NASA

IEEE

FOURTH INTERNATIONAL SYMPOSIUM ON SPACE TERAHERTZ TECHNOLOGY

The University of Michigan

UCLA

SYMPOSIUM PROCEEDINGS

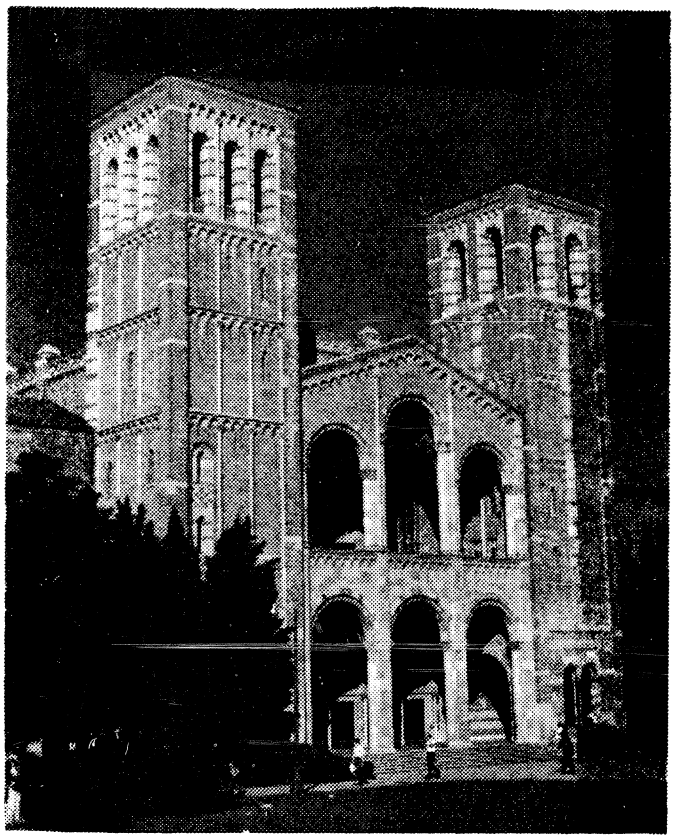

Royce Hall, UCLA

March 30-April 1, 1993
UCLA
Los Angeles, California

Sponsored by:
NASA Office of Advanced Concepts and Technology (OACT), University Space Engineering Research Centers Program, with cooperative sponsorship by the Microwave Theory and Techniques Society of IEEE.

Organized Jointly by:
The University of Michigan's NASA Center for Space Terahertz Technology and UCLA's Center for High Frequency Electronics.

Proceedings of the
FOURTH INTERNATIONAL SYMPOSIUM ON SPACE TERAHERTZ TECHNOLOGY

March 30-April 1, 1993

UCLA
Los Angeles, California

Organizing Committee

Symposium Co-chairs:	Fawwaz T. Ulaby, University of Michigan Tatsuo Itoh, UCLA
Technical Co-chairs:	Gabriel M. Rebeiz, University of Michigan Harold Fetterman, UCLA
Local Arrangements:	Dorothy Treece, UCLA David Binder, UCLA
Symposium Proceedings:	Brenda Hadley, University of Michigan

Preface

The Fourth International Symposium on Space Terahertz Technology was held at UCLA in Los Angeles, California, on March 30-April 1, 1993. The Symposium, which was attended by approximately 150 scientists and engineers from the U.S., Europe, and Japan, featured papers relevant to the generation, detection, and use of the terahertz spectral region for space astronomy and remote sensing of the Earth's upper atmosphere. The program included thirteen sessions covering a wide variety of topics including solid-state oscillators, power-combining techniques, mixers, harmonic multipliers, antennas and antenna arrays, submillimeter receivers, and measurement techniques.

The Symposium was sponsored by the University Space Engineering Research Centers Program of NASA's Office of Advanced Concepts and Technology (OACT), and organized jointly by the University of Michigan's NASA Center for Space Terahertz Technology and UCLA's Center for High Frequency Electronics. The Microwave Theory and Techniques Society of IEEE served as a cooperative sponsor of the Symposium, as well as a medium for publication of some of the papers that were presented at the Symposium in the form of a mini-special issue (April 1994) of the *IEEE-MTT Transactions*.

The Fifth International Symposium on Space Terahertz Technology will be held at the University of Michigan in Ann Arbor, Michigan on May 10-12, 1994.

Fawwaz T. Ulaby
Tatsuo Itoh

CONTENTS

* Presentation only.
**Abstract only.
+ This paper arrived late and was inserted as last paper in Proceedings.

**Abstract only.

Session 4: Antennas & Networks I **Chair: Eric Kollberg**

Session 5: Antennas & Networks II **Chair: Anthony Kerr**

Session 6: Solid State Sources I **Chair: Jim Mink**

Session 9: Josephson Effect & Novel Devices I **Chair: Jonas Zmuidzinas**

Session 10: Schottky Diode Fabrication & Receivers II **Chair: David Rutledge**

**Abstract only.

Session 11: Josephson Effect & Noval Devices II **Chair: Harold Fetterman**

Session 12: Novel Devices **Chair: Margaret Frerking**

**Abstract only.

Session 13: SIS Receivers III **Chair: Anti Räisänen**

A NEW SIS MIXER FOR THE 2-MM BAND

A. R. Kerr[1], S.-K. Pan[1], A. W. Lichtenberger[2], F. L. Lloyd[2] and N. Horner[1]

ABSTRACT

This paper describes a tunable SIS mixer for the (non-standard) 124-190 GHz waveguide band. The mixer uses a series array of Nb/Al-Al_2O_3/Nb junctions in a suspended stripline on a quartz substrate. At each end of the substrate, the stripline is coupled to a full-height waveguide. The signal and local oscillator power enter from one waveguide, while the other contains a non-contacting short-circuit which directly tunes out the series inductance of the array of junctions. Separate integrated tuning circuits on the individual junctions tune out the junction capacitance.

The dimensions of the substrate and stripline are such that the SIS junctions can either be fabricated with the stripline as a single integrated circuit, or separately on a small (0.005" x 0.010") flip-chip which is subsequently soldered in place on the stripline. The design should be suitable for scaling to ~400 GHz.

A receiver using this mixer has given an overall receiver noise temperature of 21-30 K DSB over the 130-170 GHz radio astronomy band. Typical values of mixer noise temperature and conversion loss are T_M = 6.5 K (DSB) and L = -0.1 dB (DSB).

By adding a tuner in the input waveguide behind the transition to stripline, it is possible to tune the mixer for single sideband operation. Mixers of this type are now in operation on the NRAO 12-m telescope at Kitt Peak.

---

[1]National Radio Astronomy Observatory, Charlottesville, VA 22903. The National Radio Astronomy Observatory is operated by Associated Universities, Inc. under cooperative agreement with the National Science Foundation.

[2]Department of Electrical Engineering, University of Virginia, Charlottesville, VA 22903. This work was supported in part by the National Science Foundation under Grant AST-8922155.

INTRODUCTION

Integrated tuning circuits are now widely used to tune out the capacitance of the junctions in superconductor-insulator-superconductor mixers. However, the series inductance of the junction (or array of junctions) can also limit the performance of a mixer. This inductance is usually tuned out as part of the overall impedance matching by one or two adjustable waveguide tuners [1, 2], although designs without adjustable tuners have also been successful [3, 4, 5]. In the present work we have attempted to design a versatile SIS mixer in which a mechanical tuner specifically allows the series inductance of the junctions to be tuned out, while the junction capacitance is tuned out by integrated tuning elements. Additional design requirements for this mixer were as follows:

(i) The mixer should be able to use SIS junctions on a small chip (*e.g.*, 0.005" x 0.010") or fabricated directly on a larger RF substrate. This requirement is a reflection of the fact that SIS device fabrication is still not a highly reproducible process, and when a successful wafer is made, it is desirable to have a large number of useful devices. (To this end, we normally include on each mask set a number of small SIS chips in addition to larger fully integrated designs.) A practical consequence of using small SIS chips is that the RF circuit must include bonding pads, typically 0.003" x 0.004".

(ii) Full-height waveguide should be used in the mixer block. This simplifies fabrication and allows the use of dumbbell-type tuners which have low loss and are free of resonances across the full waveguide band [6].

(iii) For compatibility with NRAO's existing SIS receivers, the tuner(s) should emerge from the face of the mixer block opposite that containing the input waveguide.

(iv) This mixer should also serve as a low-frequency prototype for future higher frequency designs. The mixer design should therefore be suitable for scaling for operation up to at least 400 GHz.

Most of these requirements are met by one or other of two existing SIS mixer designs, the GISS Type-D mixer and the NRAO 401 mixer [7, 1], and the new design incorporates the desirable aspects of each. The principal disadvantage of the Type-D design is its use of reduced (1/4) height waveguide, which is necessary to provide an acceptably low and frequency-independent embedding impedance across the waveguide band when the SIS junctions are mounted across the waveguide [8, 9, 10]. The NRAO 401 mixer's significant shortcoming is the difficulty of mounting its cantilevered stripline probes on the substrate with sufficient precision.

The new NRAO-581 mixer is shown in Fig. 1. The incoming signal and LO power are coupled into the suspended stripline from the input waveguide via a broadband probe type of transducer [3]. To accommodate future applications up to 183 GHz, a non-standard waveguide size was chosen,

0.058" x 0.029", whose nominal operating band is 124-190 GHz. (Using an extension of the EIA waveguide numbering system, we refer to this as WR-5.8 waveguide[3].)

Waveguide tuner 1 provides an adjustable reactance in series with the junctions. The two-section matching circuit just below the chip in the figure compensates for the equivalent circuit of the chip and, in conjunction with waveguide tuner 1, provides the desired embedding impedance at the SIS array. The design was originally intended to have a fixed waveguide short-circuit in place of tuner 2. However, it was found that the second tuner allowed the mixer to be tuned for true single-sideband operation, which can be of great benefit in spectral line radio astronomy.

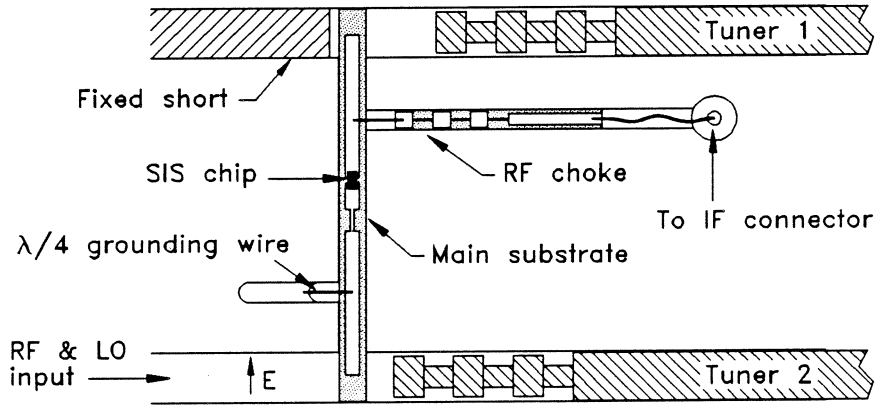

Fig. 1. NRAO-581 130-170 GHz SIS mixer. The waveguide size is WR-5.8 (0.058" x 0.029").

IF and DC connections to the SIS junctions are made via quarter-wavelength gold wires soldered to the suspended striplines either side of the chip. One wire is grounded to the block, and the other is connected to a microstrip RF choke on a second quartz substrate.

The 0.005" x 0.010" SIS chip is initially fabricated on a 0.010" thick quartz wafer, and is reduced to a thickness < 0.002" during the dicing process. It is then soldered to the stripline on the main substrate.

---

[3]In the EIA WR-# scheme, # is the inside width of the waveguide in hundredths of an inch, rounded to a whole number. For small non-standard waveguides it is logical to add a decimal point, allowing #.# to indicate the waveguide width to the nearest thousandth of an inch.

DESIGN OF THE MIXER

The choice of embedding impedances follows the procedure described in [1]. The RF source impedance, R_S, and IF load impedance were chosen, for convenience, as 50 ohms. For junctions with a given J-V curve (J is the current per unit area), it is then possible to find a value of normal resistance for which the mixer noise temperature is near its minimum, the conversion loss close to unity, and the input VSWR moderately low.

SIS junction design

For typical Nb/Al-Al_2O_3/Nb SIS mixers, this optimum normal resistance[4] $R_N = 2.4\ R_S(100/f(GHz))^{0.72}$. Accordingly, the present design assumes $R_N = 90$ ohms (for the series array of junctions). Following [1], a target value of $\omega R_N C = 2.7$ was used, corresponding to a critical current density $J_C = 2900\ A/cm^2$ (this assumes stray (overlap) capacitance to be small compared with the junction capacitance). Following [11], the specific capacitance of the junctions is taken as 45 $fF/\mu m^2$.

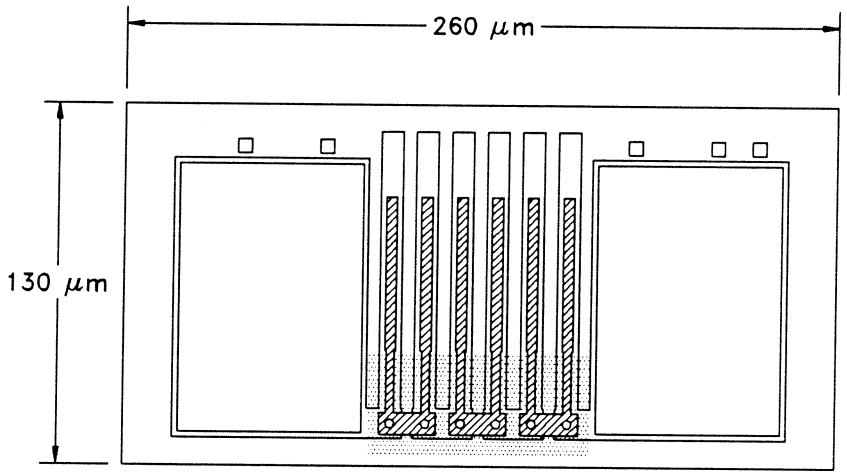

Fig. 2. Details of the SIS chip. Dotted shading indicates a 450 nm thick layer of SiO between the base electrode and the interconnection layer.

Details of the SIS chip are shown in Fig. 2. The capacitance of each junction is tuned out by a short (inductive) parallel-plate transmission line terminated in a quarter-wave open-circuit stub of very low characteristic impedance [12]. The six junctions each have a diameter

---

[4]In [1] it was found that $R_N = 2.5\ R_S(100/f(GHz))$. A more accurate mixer analysis, including five small-signal sidebands, has since shown that the formula given in the text is a better approximation [5].

of 2.3 μm and normal resistance of 15 ohms. The quarter-wave open-circuit stubs are 57 μm long and have a characteristic impedance of 2.6 ohms. The tuning inductors are each 31 μm long, with a 450 nm thick SiO dielectric over 85 nm of Nb_2O_5, and have a characteristic impedance of 19 ohms. Their electrical length is only 16°, so they can be regarded as lumped-element inductors.

Equivalent circuit of the SIS chip

The equivalent circuit of the SIS chip mounted in the suspended stripline was determined from measurements on 69 x scale models using a vector network analyzer. The measurements are well approximated up to ~200 GHz by the circuit in Fig. 3, where both reference planes TT' are at the center of the chip. The form of the equivalent circuit was chosen so its elements would represent the physical energy storage mechanisms in the actual circuit, thereby making the element values independent of frequency from DC to the highest frequency of interest. The dominant element in this circuit is the inductance, whose reactance at 150 GHz is 58 ohms.

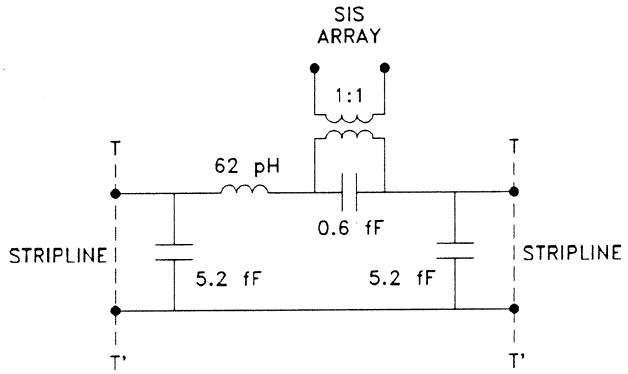

Fig. 3. Equivalent circuit of the SIS chip in suspended stripline. (Element values are for the real mixer, not the scale model.)

Main substrate

The RF circuit on the main fused quartz substrate is a Cr-Au suspended stripline, as shown in Fig. 4. Using the chip equivalent circuit in Fig. 3, the characteristic impedances Z1 and Z2, and lengths L1 and L2, were chosen to give a good match to the RF resistance of the SIS array over the desired 130-170 GHz band. Fig. 5 shows the expected input reflection coefficient as a function of frequency under the following assumptions: (i) Tuner 1 (Fig. 1) is adjusted at each frequency to tune out the series inductance of the array of junctions. (ii) Tuner 2 is set

to match the waveguide to the 50-ohm stripline[5]. (iii) When operating as a mixer, the RF small-signal impedance of each junction is 8.3 ohms (50 ohms for the whole array) in parallel with the junction capacitance.

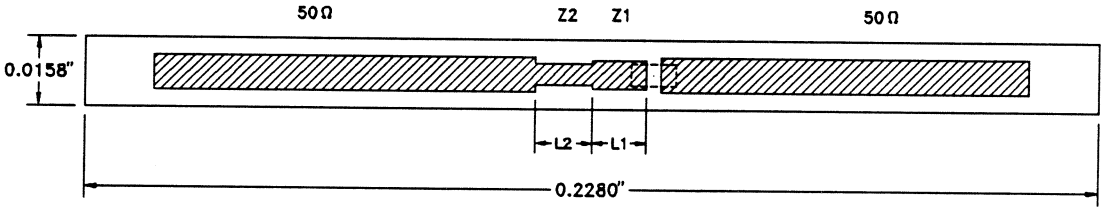

Fig. 4. The main substrate is 0.005" thick fused quartz with Cr-Au metallization. The SIS chip is soldered across the gap as indicated by the dashed outline. For this design Z1 = 60 Ω, Z2 = 70 Ω, L1 = 351 μm, and L2 = 325 μm.

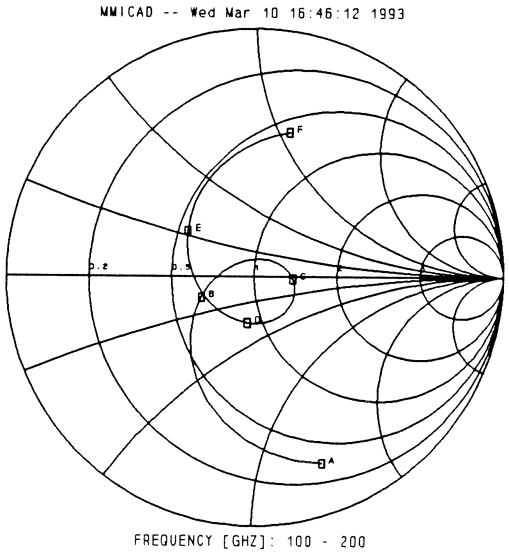

Fig. 5. Input reflection coefficient from 100 to 200 GHz when tuner 1 is adjusted to tune out the series inductance of the array of SIS junctions. Z_0 = 50 Ω. Markers are every 20 GHz.

[5]With a fixed short-circuit, the transducer has a return loss > 20 dB over the whole waveguide band.

JUNCTION FABRICATION

The Nb/Al-Al_2O_3/Nb trilayers were deposited on Infrasil 301 fused quartz wafers 0.010 inches thick using a process similar to that described in [11, 13], but with the following differences: (i) During Nb deposition, the DC magnetron power was held constant while the Ar pressure was adjusted to maintain constant current. This results in a constant deposition rate and uniform film stress from wafer to wafer over the life of the sputtering target. (ii) Nb_2O_5 was formed in the desired regions by anodization *before* patterning the trilayer. This obviates the need for the anodizing lines required to interconnect all the areas to be anodized if the trilayer is patterned before anodization.

EXPERIMENTAL RESULTS

For the mixer whose results are described here, a series array of six junctions was used, each of nominal diameter 2.8 μm. The I-V curve with and without LO power applied is shown in Fig. 6, from which a normal resistance of 58 ohms is deduced. Based on the nominal diameter, J_c = 2800 A/cm^2.

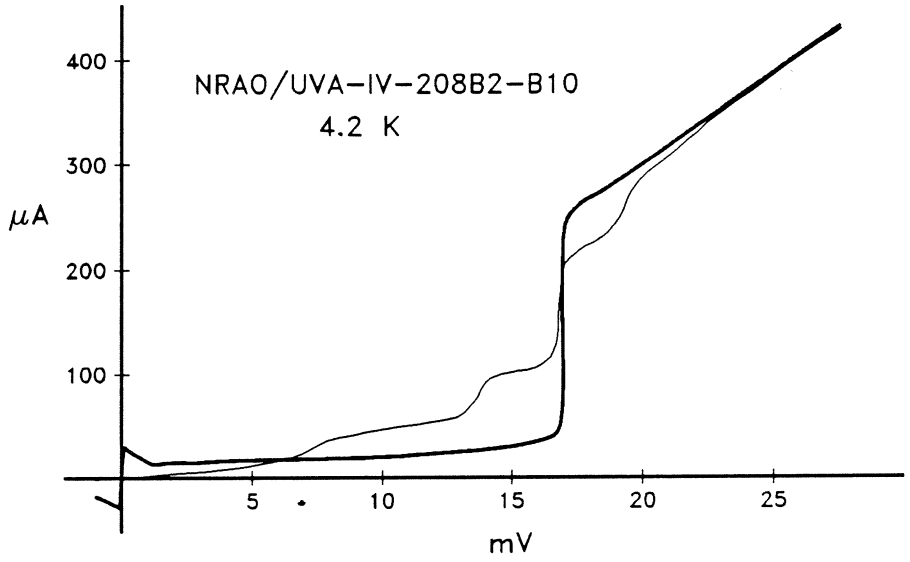

Fig. 6. I-V curve of the mixer with and without LO power. The LO frequency is 140 GHz.

The mixer was tested in a liquid helium cooled vacuum cryostat [14] containing 4.2 K IF calibration components, similar to that described in [7]. The incoming RF signal enters the cryostat through a plastic film

vacuum window supported by polystyrene foam [15]. It passes through a PTFE infrared filter at 77 K into a scalar feed horn at 4.2 K. LO power is injected through a 20 dB branch-line directional coupler, also at 4.2 K. A 1.4 GHz IF was used, and all measurements were made with a 50 MHz bandwidth. The IF noise temperature, including a coaxial switch, two isolators, and a directional coupler, was 6.5 K. No IF impedance transformer was used, and no external magnetic field was applied to the mixer.

Using a chopper wheel to switch the input beam between room temperature and 77 K loads, and a Y-factor meter synchronized to the chopper wheel, the two waveguide tuners, LO power and mixer bias voltage were adjusted for minimum receiver noise temperature at each frequency. Fig. 7 shows the DSB receiver noise temperature as a function of frequency. The dashed curve in this figure is for a receiver using the same type of mixer block with an SIS chip of comparable normal resistance but with integrated tuners designed for 90-120 GHz. The comparison demonstrates the effectiveness of the integrated tuning circuits.

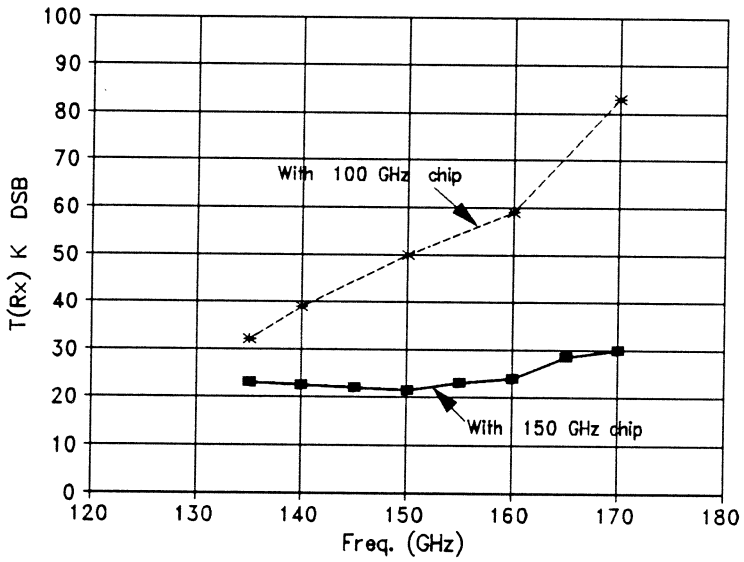

Fig. 7. DSB receiver noise temperature measured outside the cryostat. The dashed curve is for a receiver with the same type of mixer but with an SIS chip designed for 90-120 GHz.

The mixer's conversion loss, noise temperature, and output resistance were deduced from measurements with RF hot and cold loads outside the cryostat at the input of the receiver, and with IF hot and cold loads inside the cryostat connected to the input of the IF amplifier by the coaxial switch. Typical values are: L = -0.1 dB (DSB), T_M = 6.5 K (DSB), and R_{IF} = 145 ohms.

ACKNOWLEDGEMENTS

The authors thank G. Taylor and F. G. Johnson for their excellent work in fabricating and assembling the mixers, and D. M. Lea for his assistance in characterizing the SIS junctions.

REFERENCES

[1] A. R. Kerr and S.-K. Pan, "Some recent developments in the design of SIS mixers," *Int. J. Infrared Millimeter Waves*, vol. 11, no. 10, Oct. 1990.

[2] A. Karpov, M. Carter, B. Lazareff, D. Billon-Peron and K. H. Gundlach, "Modelling and performance of Nb SIS mixers in the 1.3 mm and 0.8 mm bands," *Proceedings of the Third International Symposium on Space Terahertz Technology*, pp. 244-250, March 1992.

[3] A. R. Kerr, S.-K. Pan, S. Whiteley, M. Radparvar and S. Faris, "A fully integrated SIS mixer for 75-110 GHz," *IEEE Int. Microwave Symp. Digest*, pp. 851-854, May 1990.

[4] D. Winkler, N. G. Ugras, A. H. Worsham, D. E. Prober, N. R. Erickson and P. F. Goldsmith, "A full-band waveguide SIS receiver with integrated tuning for 75-110 GHz," *IEEE Trans. Magnetics*, vol. MAG-27, no. 2, pp. 2634-2637, March 1991.

[5] A. R. Kerr, S.-K. Pan, A. W. Lichtenberger and D. M. Lea, "Progress on tunerless SIS mixers for the 200-300 GHz band," *IEEE Microwave and Guided Wave Letters*, vol. 2, no. 11, pp. 454-456, Nov. 1992.

[6] A. R. Kerr, "An adjustable short-circuit for millimeter waveguides," Electronics Division Internal Report No. 280, National Radio Astronomy Observatory, Charlottesville, VA 22903, July 1988.

[7] S.-K. Pan, A. R. Kerr, M. J. Feldman, A. Kleinsasser, J. Stasiak, R. L. Sandstrom and W. J. Gallagher, "A 85-116 GHz SIS receiver using inductively shunted edge-junctions," *IEEE Trans. Microwave Theory Tech.*, vol. MTT-37, no. 3, pp. 580-592, March 1989.

[8] R. L. Eisenhart and P. J. Khan, "Theoretical and experimental analysis of a waveguide mounting structure," *IEEE Trans. Microwave Theory Tech.*, vol. MTT-19, pp. 706-719, Aug. 1971.

[9] R. L. Eisenhart, "Understanding the waveguide diode mount," *IEEE Int. Microwave Symp. Digest*, pp. 154-156, May 1972.

[10] A. R. Kerr, "Low-noise room-temperature and cryogenic mixers for 80-120 GHz," *IEEE Trans. Microwave Theory Tech.*, vol. MTT-23, no. 10, pp. 781-787, Oct. 1975.

[11] A. W. Lichtenberger, C. P. McClay, R. J. Mattauch, M. J. Feldman, S.-K. Pan and A. R. Kerr, "Fabrication of Nb/Al-Al_2O_3/Nb junctions with extremely low leakage currents," *IEEE Trans. on Magnetics*, vol. MAG-25, no. 2, pp. 1247-1250, March 1989.

[12] A. R. Kerr, S.-K. Pan and M. J. Feldman, "Integrated tuning elements for SIS mixers," *Int. J. Infrared Millimeter Waves*, vol. 9, no. 2, pp. 203-212, Feb. 1988. This paper was presented at the International Superconductivity Electronics Conference, Tokyo, Japan, Aug. 1987.

[13] A. W. Lichtenberger, D. M. Lea, R. J. Mattauch and F. L. Lloyd, "Nb/Al-Al_2O_3/Nb junctions with inductive tuning elements for a very low noise 205-250 GHz heterodyne receiver," *IEEE Trans. Microwave Theory Tech.*, vol. MTT-40, no. 5, pp. 816-819, May 1992.

[14] Infrared Laboratories, Inc., Tucson, AZ, model HD-3(8) (modified).

[15] A. R. Kerr, N. J. Bailey, D. E. Boyd and N. Horner, "A study of materials for a broadband millimeter wave quasi-optical vacuum window," Electronics Division Internal Report No. 292, National Radio Astronomy Observatory, Charlottesville, VA 22903, Aug. 1992.

Wide Band Fixed Tuned and Tuneable SIS Mixers For 230 GHz and 345 GHz Receivers

A. Karpov, M. Carter, B. Lazareff, M. Voss, D. Billion-Pierron, and K. H. Gundlach

Single backshort waveguide mixers using SIS junctions have been developed for radioastronomy in the 180-270 GHz (1.3mm) and 300-370 GHz (0.8mm) bands. They use a series array of two Nb/Alox/Nb junctions. Parallel inductive tuning with quasi-lumped elements is optimized and allows to use the same junction area and current density for the submillimetre wavelength as for the millimetre band. Experimental measurements agree with model predictions. In particular, the same mixer can be used either in fixed-tuned, DSB mode, having an instantaneous bandwidth covering most of the band, or tuned to image-rejection (SSB) mode at each frequency.

The DSB receiver noise temperature of the 0.8 mm mixer (measured with room-temperature optics) is about 95K in the 330-340 GHz band, and remains below 120K in the 320-350 GHz band (Fig. 1). For the 1.3 mm mixer, the receiver noise temperature is about 65K in the 190-245 GHz band (Fig. 2). Using cold optics and LO injection through a cold waveguide coupler, the receiver temperature drops to 50K (Fig. 3). Fix-tuned operation is demonstrated in the 1.3 mm band: the DSB noise temperature is nearly the same as with tuning over most of the band (Fig. 4). According to the model moving the backshort away from the junction at the 6th backshort peak allows one to reject the USB by more than 15 dB (using a 4 GHz IF). The resulting SSB noise temperature is only 1.5 times the DSB value, showing a clear advantage over external filtering of the image band.

The present mixers operating in the 1.3 mm and 0.8 mm bands, are developed for operation on the 30-M IRAM radiotelescope at Pico Veleta in Spain. The first 1.3 mm mixer (Fig. 4) was installed in December 1992; the first telescope tests of the 0.8 mm mixer are planned in March 1993. New versions of both mixers are under development, with the aim of improving further frequency coverage in agreement with the atmospheric transmission windows.

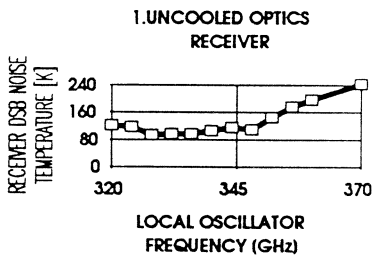

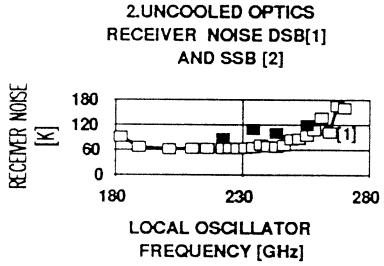

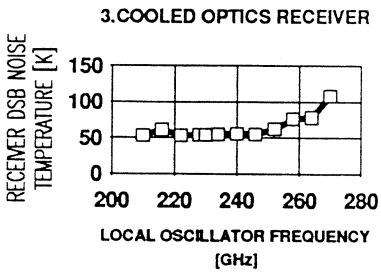

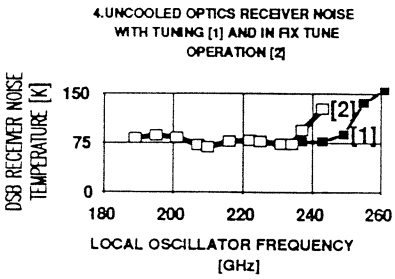

Institut de Radioastronomie Millimetrique, 300 Rue de la Piscine, Domaine Universitaire de Grenoble, F-38406 Saint Martin d'Heres, France

DEVELOPMENT OF A SIDEBAND SEPARATION RECEIVER AT 100 GHZ

R. L. Akeson[1], J. E. Carlstrom[1], D. P. Woody[1], J. Kawamura[1],
A. R. Kerr[2], S. -K. Pan[2], and K. Wan [3]

[1] California Institute of Technology

[2] NRAO

[3] University of Illinois

I. Abstract

We have built and tested a prototype SIS receiver operating at 100 GHz to test the feasibility of sideband separation through quadrature mixing at millimeter and submillimeter wavelengths. We achieved over 40 dB of separation with no degradation of the mixer noise temperature due to the sideband separation. Both the sky signal and atmospheric noise are separated, greatly reducing the system temperature for millimeter and submillimeter observations in which spectral lines are present in only one sideband.

II. Introduction

For millimeter and submillimeter–wave astronomy low–noise flexible heterodyne receivers are required. Current receivers use broadband double-sideband mixers, which output overlapped signals and noise from both sidebands. Advances in SIS mixer technology allow these receivers to operate within a factor of a few of the photon noise limit. The atmospheric noise is now the limiting factor for many observations, so for observations in which the desired signal is only in one sideband, the noise added by the image sideband can be very significant. For many astronomical spectral line observations the image sideband may have a much higher atmospheric opacity, seriously degrading the sensitivity. As shown in Figure 1, this will greatly degrade the system temperature. Calibration of spectral line observations with a double sideband receiver is difficult. To correctly calibrate lines observed with a double sideband receiver using hot/cold loads, the sideband gain ratio, which cannot be easily measured, must be known. Astronomers commonly calibrate spectral lines against a 'standard' source, such as Orion. This does not provide an absolute scale and is not possible for less common or highly doppler shifted lines. Filters can be added in front of the mixer to select one sideband, but these must be tuned for every frequency of interest and will add considerable noise unless the image sideband is carefully terminated on a cold load. Interferometers can use quadrature phase switching to separate the two sidebands, but since the signals are from two telescopes, the atmospheric noise is uncorrelated and cannot be separated. By using two mixers in a single receiver both the signal and sky noise can be separated. A sideband separation receiver can be built so that the noise of each output port is equivalent to that of a double sideband receiver in which the image sideband is terminated in a 4° K load. For systems in which the atmosphere is the main source

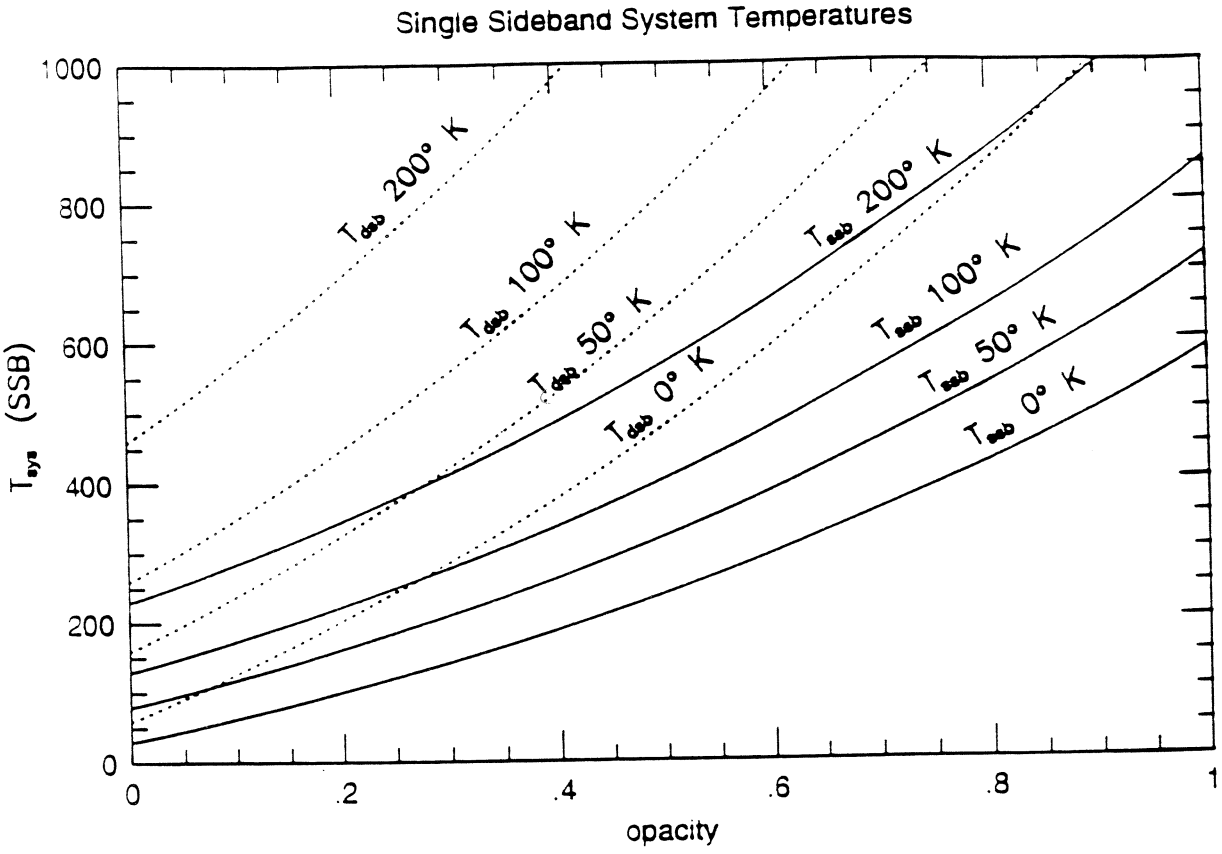

Figure 1: The single sideband system temperature referred to outside the atmosphere is shown as a function of atmospheric optical depth and the double and single sideband receiver temperatures. The beam transfer and spillover losses are assumed to be 10%. Note that the sensitivity of a single sideband system is considerably better than the double sideband system with comparable mixers for large opacities. (e.g. comparing a 50° K DSB system with a 100° K SSB system at an opacity of 0.4, the system temperature for the SSB system is 36% lower.)

of noise the single sideband receiver sensitivity is increased by up to a factor of two over a double sideband receiver with balanced sideband gains. The increase in sensitivity is even higher if the atmospheric opacity is larger in the image sideband.

III. Design

In order to test the feasibility of quadrature mixing at millimeter wavelengths with low noise SIS mixers, we built a sideband separation receiver which operates at 3 mm. This prototype uses waveguide components for convenience, though they are more lossy than other design methods. As illustrated in Figure 2, the incoming sky signal is received by a feedhorn and split by a Magic-'T'. This device equally

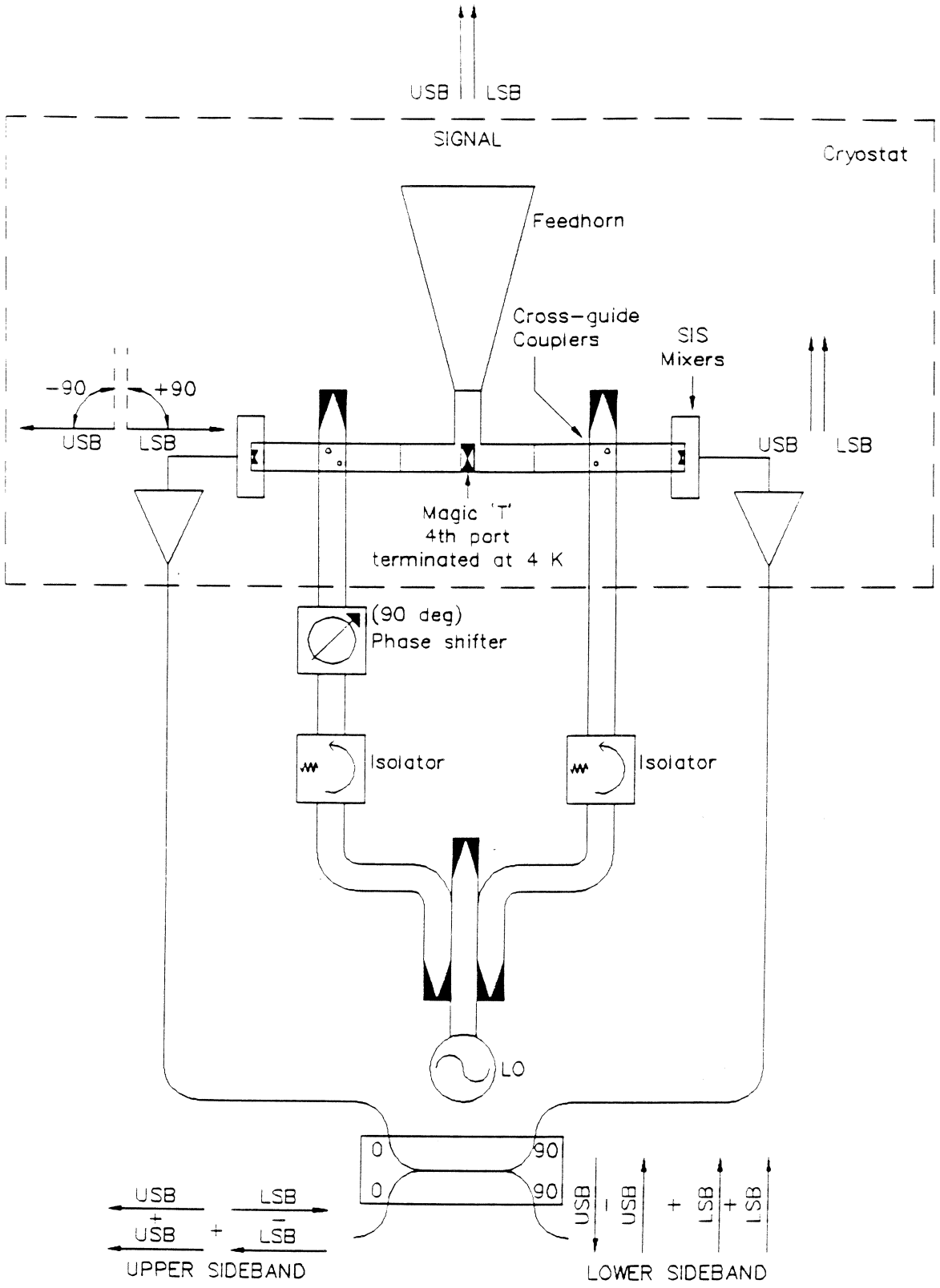

Figure 2: Prototype Sideband Separation Receiver

splits the signal from the first port into the two output ports in phase. The output ports also receive half of the power from the 4th port, which is terminated at 4° K. Any signal reflected from the output ports will be split between the feedhorn and the 4° K termination, minimizing cross talk between the mixer ports which would contaminate the separation. A Gunn oscillator provides the LO signal which is injected through isolators into two 20 dB cross guide couplers. A variable phase shifter in one of the LO paths introduces a 90° phase shift between the sky signal and LO at one mixer relative to the other. This causes a 90° phase shift in the signal received at one mixer relative to the other mixer; the relative phase shift is in the opposite sense for the two downconverted sidebands.

In this prototype, as in the next generation of receiver, we use SIS mixers. Our two mixers are integrated, tunerless devices with four Nb-AlOx-Nb junctions, developed by A.R. Kerr at NRAO with junctions made by Kelin Wan at the University of Illinois (Kerr and Pan 1990). Having two well-matched, tunerless mixers greatly simplifies operation. After the mixers, each signal is amplified by a 3 stage, FET amplifier with a 500 MHz bandpass. The two IF amplifiers were carefully tuned to be well-matched, with less than 0.5 dB difference in gain across the 1.25 to 1.75 GHz passband. They are relatively noisy with noise temperatures ~10° K. All components up to this stage were liquid helium cooled. Coaxial extenders were added to the IF paths so that small phase corrections could be made to compensate for the different IF pathlengths. The two IF signals pass through a quadrature hybrid coupler. Unshifted signal from one port is combined with 90° shifted signal from the other port. Each output consists of signals from only one of the sidebands, up to the level of separation.

IV. Results

The maximum Y factor, the ratio of the output power of the receiver seeing an ambient temperature load to that when seeing an liquid nitrogen cooled load, achieved at the output of a single mixer was 1.5, (DSB temperature = 360° K) although a more typical value was 1.45. Recall that in our receiver the effective temperature that a single mixer sees is half or less of the actual temperature. A second Gunn oscillator, matched to the input, served as an artificial source. The coaxial extenders were adjusted to compensate for the difference in IF pathlengths such that signals in the upper and lower sideband had maximum separation at the same position of the LO phase shifter. With the individual amplitudes from the mixers equalized by adjusting the IF amplifiers, the separation exceeded 40 dB. However, when the signal was switched to the lower sideband without any other adjustments, the separation was only 23 dB. This was due to unequal signal IF amplitudes, resulting from the slightly different sideband gain ratios of the two mixers. The separation in this sideband could be improved to 40 dB by equalizing the amplitudes with the IF amplifiers. Adjusting for equal signal amplitudes at a mid-IF frequency, where the IF amplifiers had matched gains, the separation across the entire IF passband was greater than 25 dB. There was no degradation of the mixer noise temperature measured at one port of the hybrid coupler compared to the

noise temperature from a single IF port, demonstrating that the noise is completely separated.

The mixer and IF contributions to the receiver noise temperature were found by analyzing the IV curve and the receiver output power when the mixers were biased above the band gap (Woody *et al.* 1985). We also measured, at room temperature, the additional loss of the Magic-'T' and cross guide couplers to be 1 dB per mixer port. The cross guide couplers were surprisingly lossy, accounting for 0.4 dB of the RF loss. After correcting for these losses we found that the mixer temperatures were 87° K and 78° K. When initially tested, these mixers had noise temperatures near 60° K, but our operating temperature was about half a degree higher. The RF losses add ~40° K to the receiver temperature. With better IF amplifiers and colder operating temperatures, the SSB receiver temperature for our prototype should be around 200° K. However, with the best available mixers and IF amplifiers and lower RF losses, we should be able to achieve single sideband temperatures around 100° K while still separating sidebands.

V. Future Developments

Despite the losses of the waveguide components, this prototype demonstrated the feasibility of a sideband separation receiver. The current separation is limited by the unequal response of the mixers across the IF band. Our easily constructed design is suitable for applications that require high separation but not extremely low noise, such as atmospheric line observations. The separation achieved was more than enough to separate the sky noise and so is already sufficient for interferometric observations. For single-dish spectral line surveys a factor of 25 dB separation is very helpful and it is possible to do much better with a more optimized system. The IF noise can be reduced by state of the art IF amplifiers, which have noise temperatures of 2-4° K and 1 GHz passbands. For applications that demand low noise as well as separation, the lossy waveguide components should be improved or replaced. The Magic-'T' and cross guide coupler could be designed and built to have much lower loss, even at higher frequencies. The design we will pursue in the next generation of receiver is a quasi-optical system (Figure 3). In the sideband separation mode the LO signal passes through a quarter-wave plate and is injected with a beam splitter. A wire grid polarizer splits the signal to the mixers. This design has the additional advantage of being easily converted to a dual polarization double sideband receiver by removing the first polarizing grid.

References

Kerr, A.R. and Pan, S. -K. 1990, *Int. J. Infrared and Millimeter Waves*, **11**, 1169.

Woody D.P., Miller, R.E. and Wengler, M.J. 1985, *IEEE Trans. Microwave Theory Tech.*, **MTT-33**, 90.

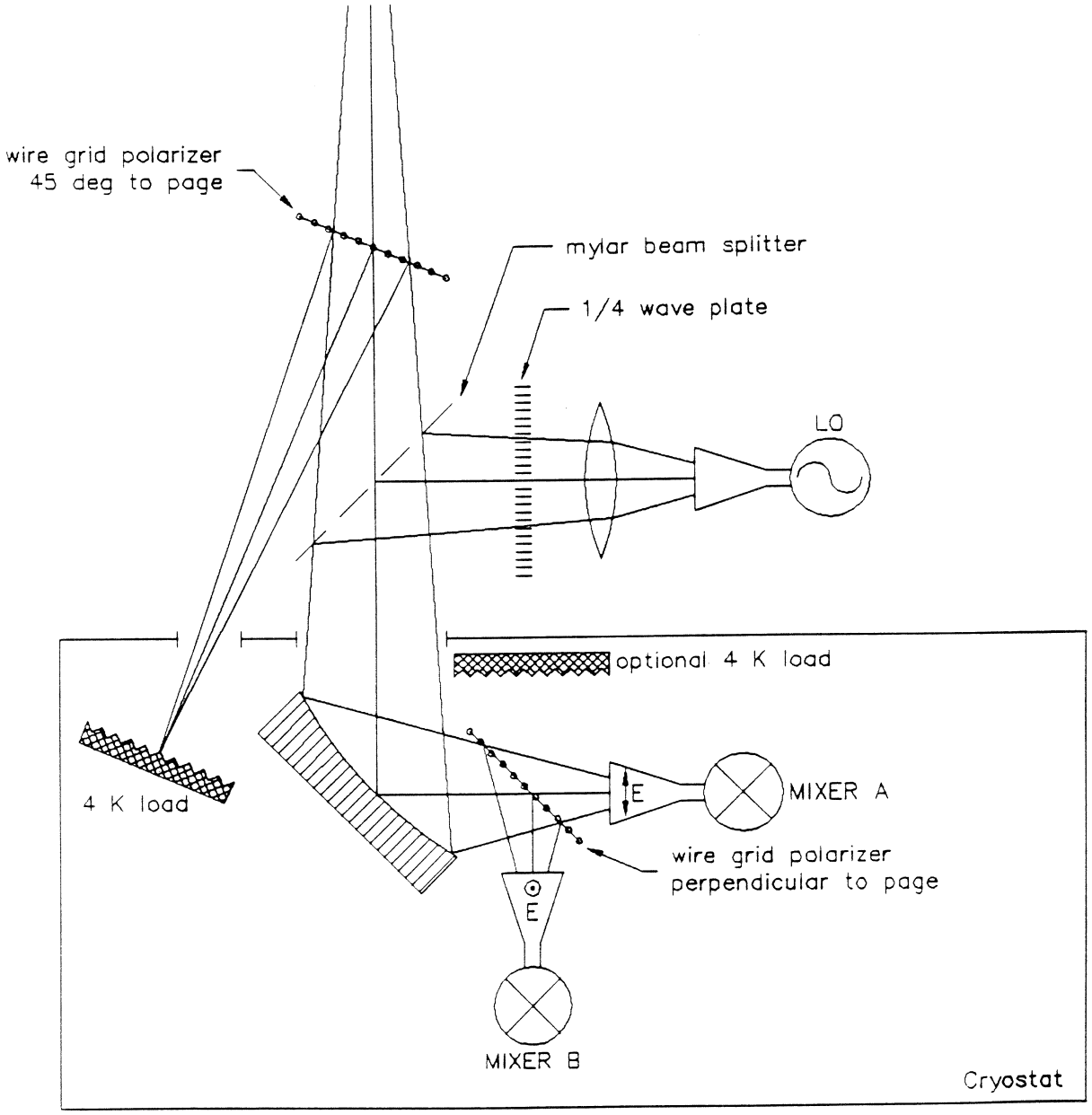

Figure 3: Quasi-optical Sideband Separation Receiver

Measuring the Quantum Efficiency of SIS Receivers

David Woody

The efficiency with which RF photons are absorbed and converted to DC current is a fundamental parameter for determining the noise performance of millimeter and sub-millimeter heterodyne receivers. According to the photodiode theory of mixing, this quantum efficiency determines the noise contribution associated with the down conversion process. This noise must necessarily dominate in receivers whose noise is close to the quantum limit and is found to be a major component in all of the SIS receivers we have evaluated. Other noise contributions arise from the "dark current" and the IF amplifier chain.

This paper describes a method for measuring the quantum efficiency of heterodyne receivers. The method does not require a calibrated RF source, but uses the same ambient and LN_2 cooled loads used for receiver noise measurements to calibrate a CW oscillator. This calibration technique automatically includes the optical losses in the signal path in the quantum efficiency measurement. The measured quantum efficiencies of several SIS receivers operating at frequencies from 85 to 270 GHz are presented. Photodiode theory is used to interpret the measurements and quantitatively evaluate the different contributions to the receiver noise.

The measurement procedures described in this paper can be applied to most heterodyne receivers and the photodiode interpretation does not depend upon a detailed theory for the mixing process. These techniques should thus prove useful for evaluating the performance of a wide variety of heterodyne receivers operating at terahertz frequencies and beyond.

Owens Valley Radio Observatory, California Institute of Technology, Big Pine, CA 93513

PHOTON NOISE IN THE SIS DETECTOR

Noshir B. Dubash, Gordana Pance, Michael J. Wengler
Electrical Engineering
University of Rochester, Rochester, NY 14627

Abstract

The dominant source of noise in an SIS mixer is the noise in the photon-induced dc current. We have made accurate measurements of noise induced in SIS junctions by 95 GHz photons. The noise in the dc current was measured at 1.5 GHz using a low-noise cryogenic measurement system. Noise measurements have been made on single $Nb/AlO_x/Nb$ junctions which are poorly coupled to the radiation due to their large parasitic capacitance. Noise in these SIS's is nearly perfectly predicted by Tucker's theory augmented by a vacuum/thermal noise term. Measurements of series arrays of these junctions also agree with this theory showing that the noise of each SIS in the array is independent. We have also measured SIS's which are well coupled to the radiation because of integrated tuning structures. The photon induced noise in these SIS's deviated significantly from theoretical predictions. We do not yet have an explanation or an alternate theory for this case.

I. Introduction

For small rf power, on the first photon step, the superconductor-insulator-superconductor (SIS) diode should behave as a photodiode and the noise in the photon-induced current should be equal to shot noise [1]. At higher rf power, and at dc bias other than on the first photon step, Tucker's theory [2] augmented by the vacuum noise term proposed by Wengler and Woody [3] must be used to predict the noise in the photon induced current. The predictions of Tucker's theory are based on a detailed microscopic theory of electronic states, and electron tunneling in the presence of radiation. Thus the measurement of this noise provides a detailed insight into the mechanism of current transport across the SIS.

Accurate measurement of SIS mixer noise have been made by several groups [4-6]. These measurements have provided valuable information about receiver sensitivity. The noise reported is often larger than that predicted by Tucker's theory. It is also difficult to determine if the excess mixer noise temperature is due to a lower mixer gain or a higher than expected noise at the mixer output.

We have chosen to make direct measurements of photon noise by injecting the photons through a cold 4.2 K attenuator to eliminate the thermal background. Our measurements of noise
can now be directly related to the statistics of the photon absorption process in the SIS. For instance, we can confirm that some SIS's have photon induced shot noise on their first photon step, and we can see how that shot noise saturates at higher photon fluxes. These measurements will lead to a better understanding of the fundamental processes that limit the sensitivity of the SIS mixer.

II. Experimental Set-up and Measurement Technique

To make calibrated measurements of available noise power at the SIS we need: 1) a low-noise and high-gain amplification system, 2) a way to accurately measure the gain and noise of this system, and 3) a way to measure the reflection coefficient at the SIS. Such a system has been designed and built. Our system uses noise measurement techniques developed by McGrath *et al.* [7] and is similar to one described by Pan *et al.* [8]. A schematic diagram of the measurement system is shown in figure 1. The high gain is provided by an ultra-low-noise HEMT amplifier. The temperature loads are used to calibrate the gain and noise of the system. The reflection coefficient is determined by injecting an external noise signal through the circulator, which can be reflected off the SIS or the short. The coaxial switch is used to switch to the temperature loads for the gain and noise calibration, and between the short and the SIS in the reflection coefficient measurement. All the microwave components in the system are optimized to operate in a 400 MHz bandwidth centered at 1.5 GHz. All noise measurements reported in this paper were made in this bandwidth. The SIS block consists of the SIS mounted in a 4.2 K cavity, and the bias tee which enables the dc biasing and capacitively couples the 1.5 GHz output. The SIS block has the capability of being temperature controlled up to 20 K for measurements above the superconducting transition temperature, and Johnson noise calibration.

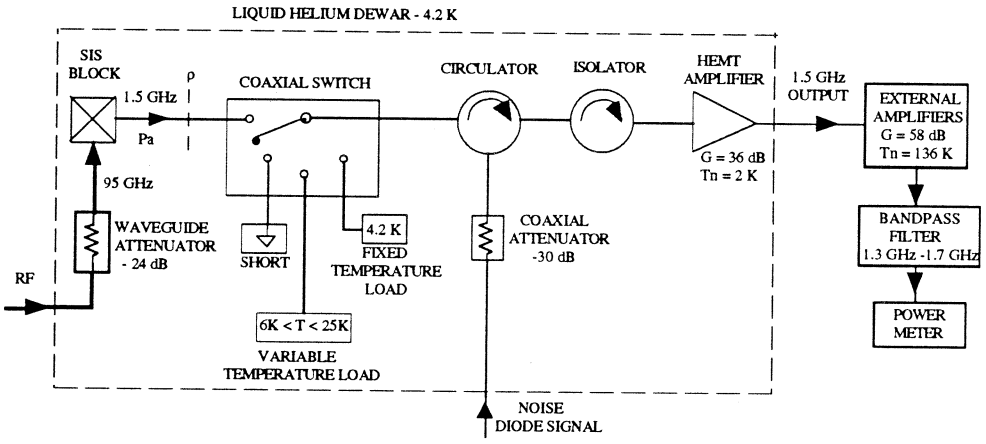

Figure 1 Schematic diagram of low-noise 1.5 GHz cryogenic measurement system

The circulator and isolator together provide 40 dB of isolation between the SIS and the HEMT amplifier. This level of isolation was found to be necessary to provide accurate measurements when the SIS was poorly matched to the amplifier. Noise waves from the input of the amplifier get reflected off the SIS and add coherently to the amplifier noise, thus increasing the effective system noise. This increase would not be detected in the calibration with the matched temperature loads.

We also measure the loss between the coaxial switch and the SIS, which is primarily the loss in the bias tee. This loss is measured by reflecting the noise signal off the SIS biased on the supercurrent. The reflected power is then compared to the power reflected off the short. If there is no series resistance in the supercurrent the SIS should look like a perfect short when current biased on the supercurrent. The noise signal must not be large enough to switch the SIS into the voltage state. The loss measured using this method is typically about 0.2 dB.

The system noise and gain is calibrated by measuring the output power for several load temperatures between 6 and 15 K. These data points are then fitted to a straight line to obtain the gain and noise of the system. The fitting error is typically less than 0.1%. The gain and noise temperature of the system measured at 4.2 K is typically 94.80 dB and 4.38 K respectively. We estimate the accuracy of the noise temperature measurement to be 0.1 to 0.4 K. The added noise power due to the loss in the stainless steel coaxial cable connecting the load to the coaxial switch is included in the calibration.

We need to determine the *available* noise power in the SIS at 1.5 GHz. Due to reflection and transmission loss we cannot successfully couple all the available power out of the SIS. The calibration of the system gain and noise allows us to measure the power successfully coupled out of the SIS. Using the measured loss and reflection coefficient we can then determine what the available power at the SIS was. The available output power P_a at the SIS is then given by

$$P_a = \frac{(P_{out} - \rho P_0)/G - P_n(1-\rho) - P_{eff}(\rho + t)}{(t - \rho/t)} \qquad (1)$$

where P_{out} is the SIS output measured on the power meter. P_0 corresponds to the power from the cold attenuator connected to the circulator, G and P_n are the measured gain and noise power of the system respectively, ρ is the measured power reflection coefficient at the SIS, t is power transmission coefficient of the measured loss, and P_{eff} is the effective noise power of the loss.

The measured loss is treated as a matched attenuation at the temperature of the SIS block. The noise added by the insertion loss of the isolator and circulator at 4.2 K is included in the system noise obtained from the calibration. The percentage error in the measurement of P_a will in general depend on the impedance of the SIS since the error in the reflection coefficient is magnified at larger values of reflection coefficient because of the very small powers that can be coupled out of the SIS. Since the directivity of the circulator is 20 dB the accuracy in the measurement of the reflection coefficient is at best 1%. Including all other random and systematic losses we estimate the accuracy in P_a to be between 1% and 5% for impedances between 3 Ω and 1000 Ω. This level of accuracy has been verified using an unbiased SIS above its superconducting transition temperature as a Johnson noise source.

The 95.5 GHz rf enters the dewar through a WR-10 waveguide port. It is then injected through a 24 dB waveguide attenuator which is cooled to 4.2 K. The attenuator consists of a nichrome-coated vane which is inserted into the broad side of the WR-10 waveguide. The vane is well heat sunk to 4.2 K. Treating this as a matched attenuator with 295 K at the input, the thermal radiation at the output of the attenuator is estimated to be 5.1 K.

The SIS output power P_a can also be expressed as an equivalent temperature using the Rayleigh-Jeans law: $P_a = kT_aB$. B is the bandwidth in which P_a is measured and k is Boltzmann's constant. We use this presentation when measuring P_a from an SIS above its superconducting transition temperature. With no dc bias on it, this SIS is a Johnson noise source with T_a equal to the actual physical temperature of the SIS. These measurements are used to verify the accuracy of our measurement system, and are described below.

We will most often express the noise in units of current. A noise source can be represented by an ideal noise current generator shunted by R_d, the dynamic impedance of the noise source. The noise current generator that would produce power P_a has mean square value $\langle i^2 \rangle = 4 P_a / R_d$, where R_d is the dynamic impedance of the SIS. The dynamic resistance R_d is determined by modulating the dc bias with a small ac voltage signal at 200 Hz, and detecting the current response with a lock-in amplifier.

The measured noise expressed as a current that we use is

$$\frac{\langle i^2 \rangle}{2eB} = \frac{2P_a}{eBR_d} \qquad (2)$$

The point of expressing noise in this way is to allow easy comparison with shot noise. If a dc current I_0 generates shot noise, then its equivalent noise current generator has $\langle i^2 \rangle = 2eI_0B$. If the SIS whose output noise we are measuring is behaving as an ideal shot noise source, then a comparison of $\langle i^2 \rangle/2eB$ with the SIS's dc current I_0 will find them identical. As theory predicts, and our measurements show, the SIS is operating as a perfect shot noise source under many circumstances.

III. Junction Description

The junctions tested were fabricated at Hypres and at IBM. The Hypres junctions come from their all-refractory niobium tri-layer process. These $Nb/AlO_x/Nb$ junctions have an area of 11 μm^2, specific capacitance of 38 $fF/\mu m^2$, and current density of about 950 A/cm^2. The normal resistance is about 22 Ω and the ωR_nC product at 95.5 GHz is about 5.5. The junctions in the series arrays are identical to the single junction. All junctions and arrays were fabricated at the center of a self complimentary log-periodic antenna which has an impedance of 75 Ω on the silicon substrate. These junctions were poorly coupled to the 95.5 GHz rf radiation due to their large area and hence large parasitic capacitance. This capacitance can be tuned out using integrated tuning circuits. We tested a single junction with a tuning circuit. The tuning circuit consists of an inductive section that tunes out the junction capacitance, and a quarter-wavelength microstripline transformer that matches the rf resistance of the junction to the antenna [9].

We also tested a $Nb/AlO_x/Nb$ junction that was fabricated at IBM. This junction had an area of ~ 4 μm^2, specific capacitance of ~ 50 $fF/\mu m^2$, and current density of ~ 2400 A/cm^2. The normal resistance was 21.2 Ω, giving an ωR_nC product of about 2.7 at 95.5 GHz. The junction was fabricated at the center of the same 75 Ω log-periodic antenna, and had a similar integrated tuning circuit as the one described above.

IV. Experimental Results and Analysis

A. Noise measurements with no rf power and a 4.2 K background

(i) NIN measurement and Johnson noise calibration

For this measurement the SIS block was heated above the superconducting transition of the niobium SIS junction, and maintained at a temperature of 10.79 K using a temperature controller. At this temperature, the SIS becomes a Normal-metal-Insulator-Normal-metal (NIN) junction. While an SIS is highly non-linear, the NIN provides an ohmic IV curve. At zero voltage bias, the NIN is a perfect Johnson noise source while at high voltage bias the NIN approaches a perfect shot noise source.

In the NIN measurement, there are losses in the niobium circuit that are negligible below the superconducting transition temperature. These losses can not be measured by the method described in section II, which involves reflecting a noise signal off the SIS biased on the supercurrent. There is a series resistance of about 2.2 Ω due to the resistance of the niobium thin film antenna leads in the normal state. This resistance acts as an additional loss between the SIS and the coaxial switch. There is also loss due to the heating of the stainless steel coaxial cable connecting the SIS to the coaxial switch. The total loss was calculated by comparing the

measured reflection coefficient off the NIN to that expected from its normal resistance matching to the load resistance. This loss was then calibrated out of the measurement. There was also a thermal gradient of 0.71 K between the temperature sensor and the SIS. This was calculated by recording the temperature at which the antenna leads went superconducting, and comparing that to the transition temperature for Niobium.

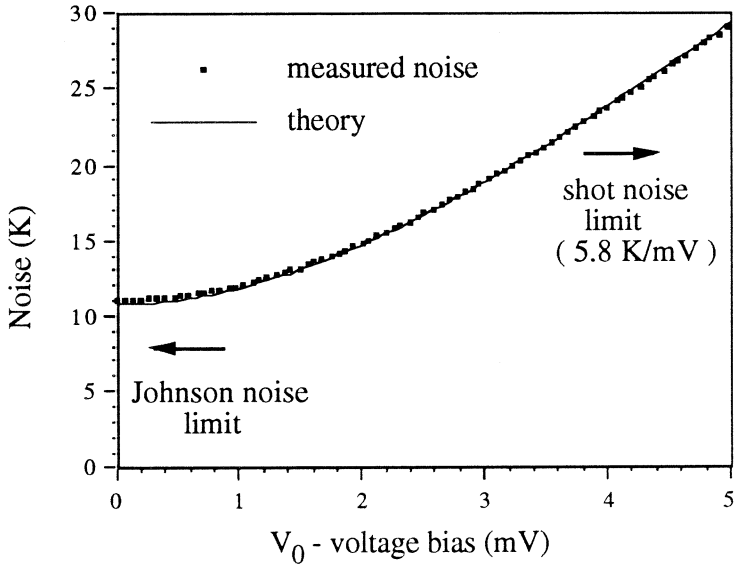

Figure 2 Measured and theoretical noise for a single niobium tunnel junction in its NIN state at a temperature of 10.79 K. The theory is calculated from the fluctuation dissipation relation of equation 4.

Figure 2 shows the measured noise compared to the theoretical noise in an NIN tunnel junction. The theoretical noise is calculated from the fluctuation dissipation relation derived by Rogovin and Scalapino [10]. The mean-square current noise or fluctuation for an NIN tunnel junction is given by:

$$\left\langle i_n^2 \right\rangle = 2e \frac{V_0}{R_n} B \coth\left[\frac{eV_0}{2kT}\right] \tag{3}$$

where V_0 is the dc voltage bias, R_n is the normal resistance, B is the bandwidth of the measurement, and T is the ambient temperature. This noise can be expressed as a temperature T_n using the Rayleigh-Jeans law.

$$T_n = \frac{eV_0}{2k} \coth\left[\frac{eV_0}{2kT}\right] \tag{4}$$

The measured noise agrees very well with this theoretical hyperbolic cotangent function. For very small V_0, $\coth(eV_0/2kT) \approx 2kT/eV_0$, and T_n is equal to the ambient temperature T, which corresponds to Johnson noise. At large V_0 the hyperbolic cotangent approaches unity and T_n approaches shot noise given by $T_{shot} = eV_0/2k = 5.8$ K/mV.

The bias was then turned off and the NIN junction was further heated and the power measured for several temperatures between 10 K and 15 K. The unbiased NIN behaves as a resistor which allows us to calibrate our system with Johnson noise. The measured noise was within 3 % of the theoretical Johnson noise.

(ii) SIS single junctions

We measured the noise in three SIS junctions with no rf power: the Hypres single junction, the Hypres single junction with the tuning circuit, and the IBM junction with the tuning circuit. Figure 3 shows the noise measured for two of these junctions. Since the measured noise is plotted as $\langle i^2 \rangle / 2eB$, the equivalent shot noise is then simply given by the dc IV curve. Tucker's theory predicts that SIS junctions with no radiation present are perfect shot noise sources.

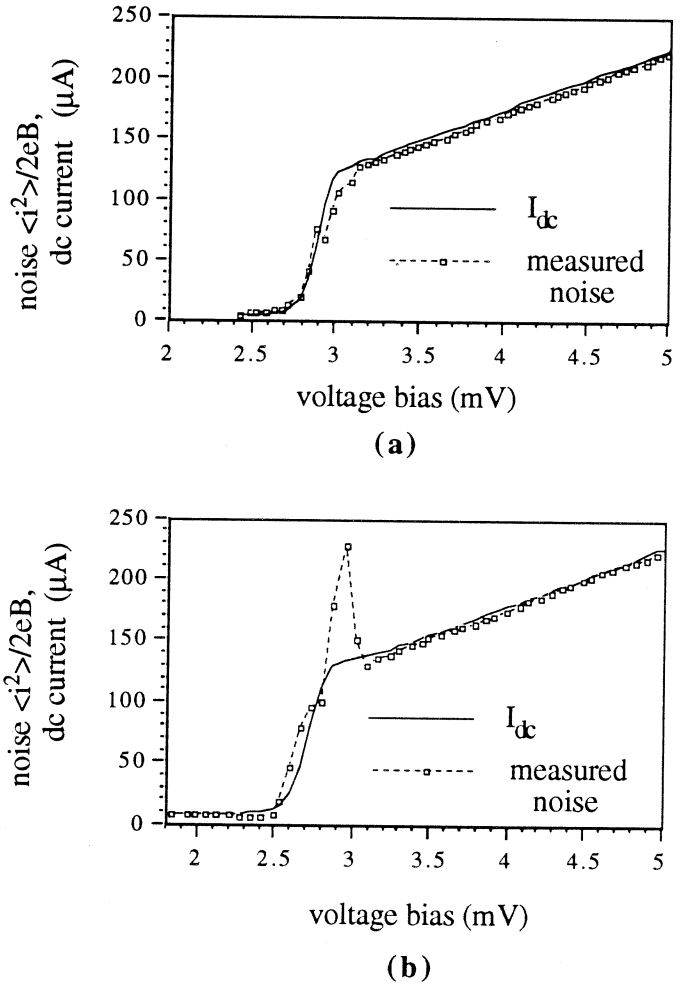

Figure 3 Measured noise in an SIS with no incident rf power for, (a) a single IBM junction, and (b) a single Hypres junction. The noise is expressed in units of current and may directly be compared to the measured dc current I_{dc} for comparison to shot noise.

In all three junctions the measured noise agreed very well with shot noise; in the leakage current region below the gap, and in the resistive region above the gap. We expected the noise in the resistive region to be equal to shot noise, but it was not clear that the noise in the leakage current should be shot noise, since the mechanism that leads to the leakage current is not well understood. We have verified that the leakage current is due to the independent tunneling of quasiparticles.

The peak that appears to be excess noise above the gap was consistently seen in all the Hypres junctions but was not seen in the IBM junction. Applied magnetic field partially suppressed this peak without affecting the noise elsewhere. This leads us to suggest the possibility that the excess noise might be due to some interaction of quasiparticles with Josephson currents.

(iii) Series arrays of SIS junctions

If the junctions in the array are identical and if the shot noise sources of the individual junctions are not correlated with each other, then the shot noise of the array is given by $\langle i^2 \rangle = 2eI_0B/N$ where N is the number of junctions in the array [11]. We measured two series arrays of two and four SIS junctions. In figure 4 we compare the measured noise $\langle i^2 \rangle/2eB$ to I_0/N. The measured noise fits the incoherent addition of noise exactly.

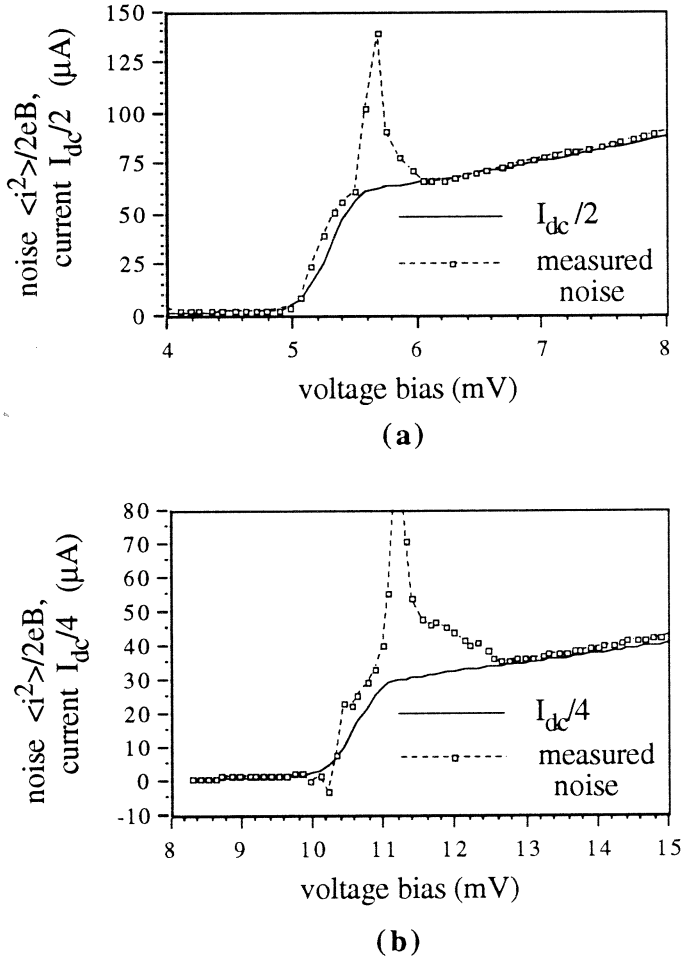

Figure 4 Measured noise in series arrays of SIS junctions with no incident rf power. (a) is a two junction array and (b) is a four junction array. Also plotted is the dc IV curve with the current scaled down by the number of junctions in the array.

On the linear part of the array IV curve at higher dc bias voltages, the available power has a slope of 5.8/N K/mV, expressed in terms of equivalent Rayleigh-Jeans temperature. This slope can be used for calibrating IF amplifier noise in SIS array mixers in a simple method described by Woody *et al* .[12].

Excess noise is detected above the gap as with the single junction. Applied magnetic field partially suppresses this noise as with the single junction.

B. Photon noise measurements: rf injection at 95.5 GHz and a 5.1 K background

Photon noise measurements were made for three single junctions and the four junction series array. Since the single junctions have different source impedances determined by the junction capacitance and the tuning structure, their measurements will be presented separately. Photon noise measurements were made as a function of dc bias voltage at a fixed rf power with $\alpha \approx 1$, and as a function of rf power biased on the middle of the first photon step. $\alpha = eV_{rf} / h\nu$ and will be referred to as the normalized rf voltage, where V_{rf} is the amplitude of the rf voltage at the SIS and ν is the rf frequency. For fixed external rf power, α will change as a function of dc bias on the SIS because the rf impedance of the SIS varies with dc bias.

The theoretical noise is calculated the using the three-port model of Tucker's theory [13], with the addition of the vacuum noise that arises from the quantization of the radiation field [3]. The total mean-sqaure current noise in the SIS can then be written as,

$$\langle i^2 \rangle = B \sum_{m,m'=-1}^{+1} \lambda_{0m} \lambda^*_{0m'} H_{mm'} + 4G_s \left|\lambda_{01}\right|^2 h\nu B \coth\left[\frac{h\nu}{2kT}\right] . \tag{5}$$

The first term is the noise predicted by Tucker's theory, where $H_{mm'}$ is the current correlation matrix. Expressions for $H_{mm'}$ and $|\lambda_{01}|^2$ for a three-port mixer model with the small IF approximation are given by Tucker and Feldman [2]. The second term represents the vacuum noise in the thermal background at temperature T. For our measurements T = 5.1 K, as explained in section II. $|\lambda_{01}|^2$ is related to the mixer gain. We assume the double sideband case, in which the upper sideband gain is equal to the lower sideband gain, which implies that $\lambda_{01} = \lambda_{0-1}$. G_s is the real part of the source admittance Y_s. The source admittance Y_s was determined from the antenna impedance, junction capacitance, and impedance of the tuning circuit, if any. The admittance obtained was fairly close to that obtained by curve fitting the theoretical pumped IV curve to the measured curve.

(i) Hypres single junction with no tuning circuit

The measured and theoretical noise for this junction as a function of dc bias are shown in figure 5. The rf power corresponds to $\alpha = 0.85$ at a dc bias of 2.45 mV. The measured noise shows good agreement with the theory below the gap voltage. Both the measured and theoretical noise do not deviate much from shot noise at biases below the gap voltage. However, the theory's deviation from shot noise on the first step at about 2.65 mV is maintained in the measurement. The comparisons to shot noise are made by comparison to the dc current I_0. There is some structure in the noise above the gap that is not predicted by the theory. This structure is partially suppressed by applied magnetic field.

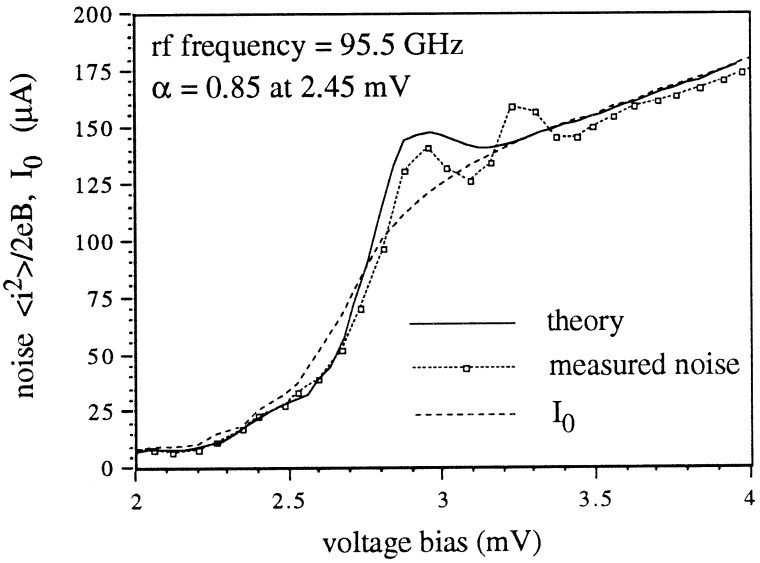

Figure 5 Photon-induced noise in a single Hypres junction as a function of dc bias voltage. The theory is calculated from Tucker's theory, including the contribution from vacuum noise. Also plotted is the measured dc current I_0 which includes the photon induced current. The dc IV curve, with no incident radiation, for this junction is shown in figure 3(b).

The noise as a function of the square of the normalized rf voltage is shown in figure 6. The SIS is biased on the first photon step at 2.45 mV. The measured noise is in good agreement with the theory, maintaining the same deviation from shot noise that the theory does. At low rf power the noise is exactly equal to shot noise as predicted by photodiode mixer theory [1].

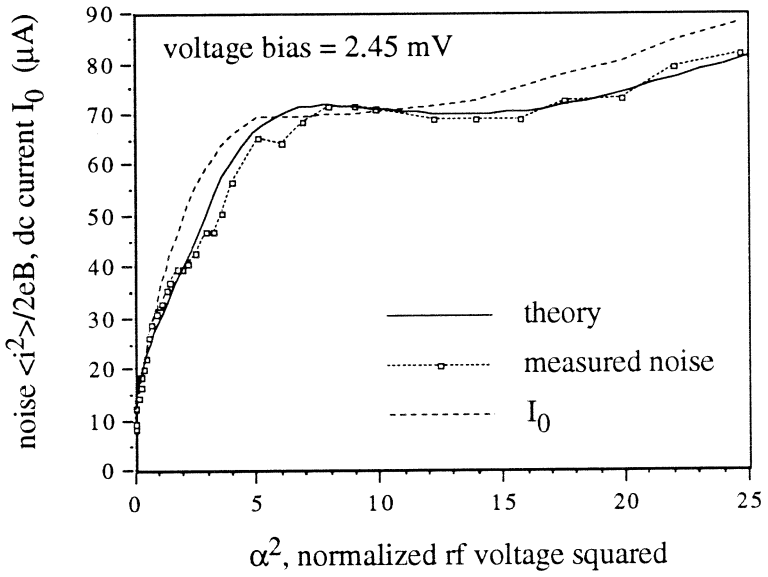

Figure 6 Photon-induced noise in the single Hypres SIS junction as a function of the normalized rf voltage squared. The junction was biased on the first photon step at 2.45 mV. Also shown is the measured dc current for comparison to shot noise.

(ii) Hypres four junction series array (no tuning circuit)

The noise measurements for the four junction array and the comparison to theory are illustrated in figures 7 and 8. The measurements agree very well with the theory except for region above the gap, and are very similar to the single junction measurements with the currents and voltages scaled appropriately. The theory was calculated using the "equivalent single

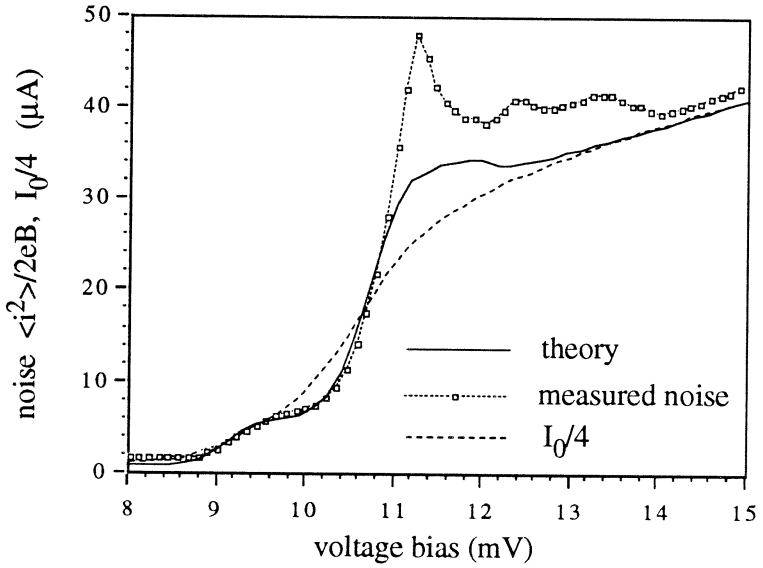

Figure 7 Photon induced noise in a four junction series array as a function of the bias voltage. Also plotted is the measured dc current divided by the number of junctions in the array, for comparison to shot noise. The rf power power corresponds to $\alpha = 1.0$ at 9.87 mV and rf frequency is 95.5 GHz.

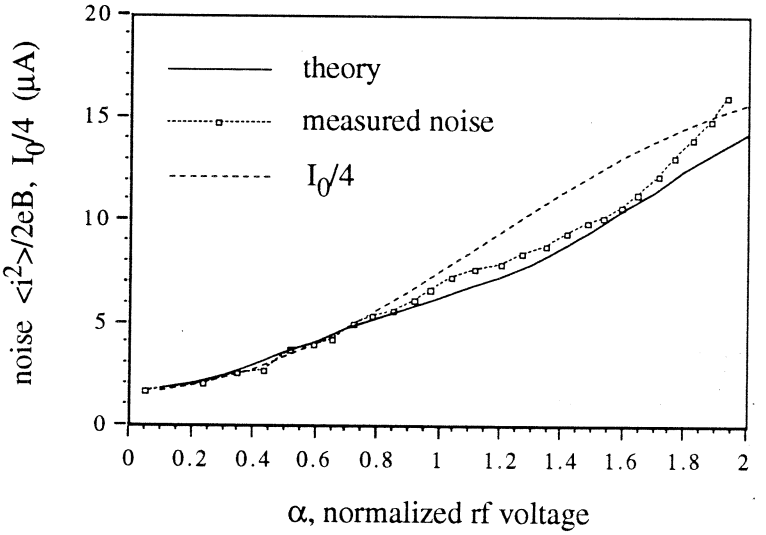

Figure 8 Photon induced noise in a four junction series array as a function of normalized rf voltage. The array was biased on its first photon step at 9.87 mV. Also plotted is the measured dc current divided by the number of junctions in the array, for comparison to shot noise.

junction" approach developed by Feldman and Rudner [11], assuming that the noise from each junction adds incoherently. Thus agreement of measurement with the theory verifies that the noise in the photon induced currents in each junction of an SIS array add independently. Incoherent addition of noise implies that the SIS mixer noise is independent of the number of junctions. Thus our measurements are in agreement with measurements done by Crété *et al.* [14] which showed that mixer noise in SIS arrays showed no significant dependence on the number of junctions for large $\omega R_n C$.

(iii) IBM single junction with tuning circuit

The photon induced noise measured for this junction is shown in figures 9 and 10. The measured noise shows very poor agreement with theory. As seen from figure 9 the theory underestimates the noise on the first photon step and overestimates the noise on the second photon step. The measured noise is about 1.6 times that predicted by theory in the middle of the first photon step at about 2.7 mV. In figure 10 we see that the deviation of measured noise from the theory, on the first photon step, gets more significant as the rf power increases.

This junction had an excellent IV curve that was very similar to the single Hypres junction as was shown in figure 3(a) and (b). However it's $\omega R_n C$ product was about half that of the Hypres junction and the integrated tuning circuit further improved the rf coupling. Thus it had a different source impedance which produced different theoretical noise. But the theory did not agree with our measurement. This seems to indicate that Tucker's noise theory works well for junctions with large $\omega R_n C$ and low rf coupling, but does not work well for small $\omega R_n C$ junctions or strong rf coupling.

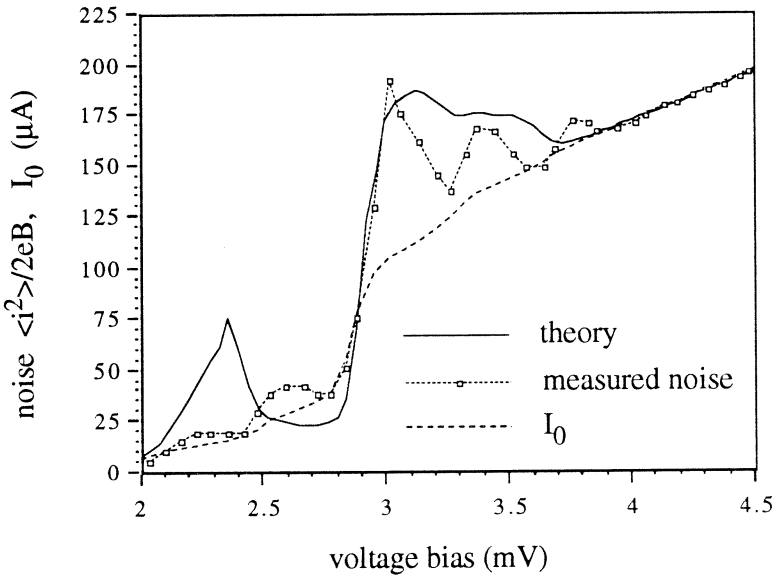

Figure 9 Photon noise in single IBM junction as a function of the voltage bias. The rf power corresponded to $\alpha = 1.10$ at 2.68 mV. The rf frequency is 95.5 GHz. Also plotted is the measured dc current, for comparison to shot noise.

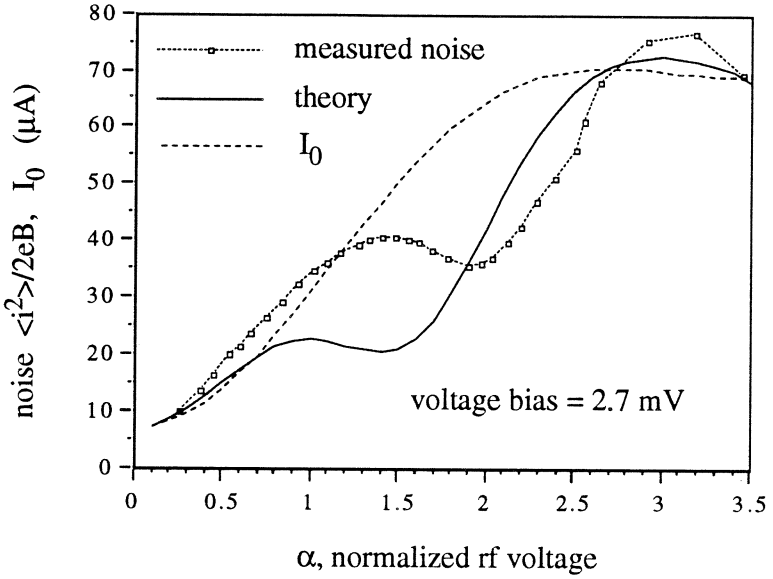

Figure 10 Photon induced noise in the single IBM junction as a function of normalized rf voltage. The junction was biased on the first step at 2.7 mV. Also shown is the measured dc current, for comparison to shot noise.

(iv) Hypres junction with tuning circuit

In order to verify that this deviation from theory was not dependent on the fabrication process, we also measured the photon induced noise in a Hypres junction with an integrated tuning circuit that was similar to the IBM junction. We could not bias stably on the first photon step of this junction, due to the very large or negative dynamic impedance in that region. However the noise measured on the second step was significantly less than that predicted by theory just as in the IBM junction.

Conclusions

We have built a very accurate system for measuring the amplitude of noise current sources in SIS junctions built in niobium mixer circuits. We have verified the accuracy of this system by measuring Johnson noise from the SIS at various temperatures above its superconducting transition.

We have experimentally verified that Tucker's theory of noise in SIS mixers [2] accurately predicts the output noise of SIS junctions with no radiation present, and that this noise is simply shot noise in the dc current of the SIS. Further, we have experimentally verified that Tucker's theory, combined with a vacuum noise term due to Wengler and Woody [3], is accurate for SIS junctions which are poorly coupled to a 95 GHz radiation field.

We have experimentally determined that the noise in arrays of two and four SIS junctions are not mutually coherent. This verifies the "equivalent single junction" model of Feldman *et al.* [11]. It is consistent with an SIS mixer temperature which is independent of N, the number of SIS's in the array, as was found by Crété *et al.*[14]. Since we did the array measurement with high capacitance junctions, we cannot make a statement about low capacitance junctions which had higher mixer noise temperatures as N increased [14].

We have found that SIS mixers with tuning circuits which produce strong coupling to the 95 GHz radiation do not fit Tucker's noise theory for the three-port model. We have ruled out some simple reasons like a misestimate of the amount of thermal noise coupled to the SIS, and a misestimate of radiation coupling to the SIS. We find that the measured noise is higher than theory predicts by about 60% on the first photon step below the gap. This may account for the higher than theoretical mixer temperatures which are often measured in well coupled SIS mixers.

We intend to extend this work in two main directions. First, we are constructing a system to do photon injection measurements at 490 GHz to see if the interaction with these more energetic photons yields any different results. Second, we will measure the noise currents of SIS's at low frequencies to determine if there are 1/f components in SIS noise.

Acknowledgement

This work was supported by NASA grant NAGW-2510. We are grateful for superconducting niobium integrated circuits fabricated for us at Hypres in Elmsford, NY and at IBM in Yorktown Heights, NY.

References

1. Wengler, M.J., "Submillimeter wave detection with superconducting tunnel diodes," *Proc. IEEE,* vol. 80, pp. 1810-1826, November, 1992.

2. Tucker, J.R. and M.J. Feldman, "Quantum detection at millimeter wavelengths," *Rev. Mod. Phys.,* vol. 57, pp. 1055-1113, 1985.

3. Wengler, M.J. and D.P. Woody, "Quantum noise in heterodyne detection," *IEEE J. Quantum Electron.,* vol. QE-23, pp. 613-622, May, 1987.

4. McGrath, W.R., P.L. Richards, D.W. Face, D.E. Prober, and F.L. Lloyd, "Accurate experimental and theoretical comparisons between superconductor-insulator-superconductor mixers showing weak and strong quantum effects," *J. Appl. Phys.,* vol. 63, pp. 2479-2491, 1988.

5. Mears, C.A., Q. Hu, P.L. Richards, A.H. Worsham, D.E. Prober, and A.V. Räisänen, "Quantum limited quasiparticle mixers at 100 GHz," *IEEE Trans. Magn.,* vol. 27, pp. 3363-3369, March, 1991.

6. Winkler, D., N.G. Ugras, A.H. Worsham, D.E. Prober, N.R. Erickson, and P.F. Goldsmith, "A full-band waveguide SIS receiver with integrated tuning for 75-110 GHz," *IEEE Trans. Magn.,* vol. 27, pp. 2634-2637, March, 1991.

7. McGrath, W.R., A.V. Räisänen, and P.L. Richards, "Variable-temperature loads for use in accurate noise measurements of cryogenically-cooled microwave amplifiers and mixers," *Int. J. of IR and MM Waves,* vol. 7, pp. 543-553, April, 1986.

8. Pan, S.-K., A.R. Kerr, M.J. Feldman, A.W. Kleinsasser, J.W. Stasiak, R.L. Sandstrom, and W.J. Gallagher, "An 85-116 GHz SIS receiver using inductively shunted edge-junctions," *IEEE Trans. Microwave Theory Tech.,* vol. 37, pp. 580-592, March, 1989.

9. Pance, G. and M.J. Wengler. "Integrated tuning elements for millimeter and submillimeter SIS mixers," in *IEEE MTT-S.* Albuquerque: June 1-5, 1992.

10. Rogovin, D. and D.J. Scalapino, "Fluctuation phenomena in tunnel junctions," *Annals of Physics,* vol. 86, pp. 1-90, July, 1974.

11. Feldman, M.J. and S. Rudner, "Mixing with SIS arrays," in *Reviews of Infrared and Millimeter Waves,* K.J. Button, Editor. 1983, Plenum: New York. p. 47-75.

12. Woody, D.P., R.E. Miller, and M.J. Wengler, "85-115 GHz receivers for radio astronomy," *IEEE Trans. Microwave Theory Tech.,* vol. MTT-33, pp. 90-95, February, 1985.

13. Tucker, J.R., "Quantum limited detection in tunnel junction mixers," *IEEE J. Quantum Electron.,* vol. QE-15, pp. 1234-1258, November, 1979.

14. Crété, D.-G., W.R. McGrath, P.L. Richards, and F.L. Lloyd, "Performance of arrays of SIS junctions in heterodyne mixers," *IEEE Trans. Microwave Theory Tech.,* vol. MTT-35, pp. 435-440, April, 1987.

A TECHNIQUE FOR ACCURATE NOISE TEMPERATURE MEASUREMENTS FOR THE SUPERCONDUCTING QUASIPARTICLE RECEIVER

Qing Ke and M. J. Feldman

Department of Electrical Engineering
University of Rochester, Rochester, NY 14627

ABSTRACT

We propose an extremely simple new technique to determine the noise temperature of the rf input section of a superconducting quasiparticle heterodyne receiver. Our method uses standard hot/cold-load measurements of the receiver driven by local oscillator power levels below optimum. We present both analytic and computed results based on Tucker's quantum theory of mixing (no experimental data are at present available) to assess the accuracy and the precision of this new technique.

INTRODUCTION

Lossy components in the rf input section of a heterodyne receiver contribute to the receiver noise temperature. For cryogenic receivers this rf input section noise has proven extremely difficult to measure. This is because the noise is the aggregate of thermal radiation arising from quite small losses at various temperatures ranging from room temperature down to the cryogenic operating temperature. The magnitude of each loss, and the temperature at which it is incurred, cannot be accurately estimated. This is an important problem for practical superconductor-insulator-superconductor (SIS) quasiparticle receivers, because this rf input section noise can dominate the entire receiver noise temperature.

For example, in Ref [1] the detailed sources of noise in a 114 GHz SIS receiver were quantitatively analyzed. The input section noise temperature was determined by two separate methods. In spite of careful and elaborate measurements, both methods yielded an uncertainty in the input section noise of about 16 K, which was by far the greatest

source of uncertainty in inferring the mixer noise temperature. This problem can be much more severe for submillimeter wavelength receivers: quasi-optical components are generally used, measurement equipment and technique are more rudimentary, and material properties are less favorable and often less well determined at the higher frequencies.

We propose a new technique to determine the input section noise temperature of an SIS receiver. Our method uses standard hot/cold-load measurements of a receiver driven by local oscillator power levels less than the receiver optimum. (The possibility of using such measurements as a diagnostic was suggested in Ref. [2].) The measurement is so simple that it may be performed during each experiment, to make sure that the input section noise temperature (i.e. beam-pattern matching, junction placement, etc.) has not changed. We present both analytic and computed results based on Tucker's quantum theory of mixing (no experimental data are at present available) to assess the accuracy and the precision of this new technique.

THE INTERSECTING LINES TECHNIQUE

The noise temperature of a microwave receiver is generally determined, quite accurately, by the so-called Y-factor method: Hot and cold matched loads, at temperatures T_h and T_c, are alternately placed at the receiver input and the total receiver IF output powers, P_h and P_c respectively, are measured. The receiver noise temperature T_R is then given by the equation

$$T_R = (T_h - YT_c)/(Y - 1)\,, \qquad (1)$$

where $Y = P_h / P_c$. This procedure can be performed graphically: The receiver output power is plotted against the load temperature, and the straight line connecting the points (P_h, T_h) and (P_c, T_c) is extrapolated back to intersect the load temperature axis. The temperature given by that intersection point is the negative of T_R.

Blundell, Miller, and Gundlach [2] recently described a remarkable and curious property of such hot/cold-load measurements of SIS receivers. They showed that if this graphical procedure is performed for a variety of local oscillator (LO) power levels less than the receiver optimum, the hot/cold-load straight lines for each LO level all intersect at a single point. Figure 1, copied from Ref. [2], is an example of this. The measured receiver output power is plotted for $T_h = 295$ K and $T_c = 77$ K and a straight line is drawn connecting these two points, for each of five different LO levels. These five lines all quite precisely intersect.

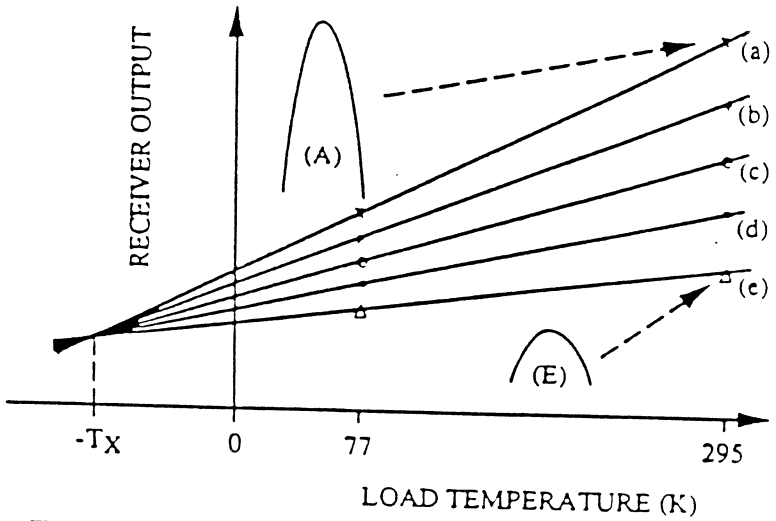

Fig. 1. The output power from an SIS receiver is plotted for hot and cold loads and a straight line is drawn connecting these two points, for each of five different LO levels. This figure is copied from Ref. [2].

In the remainder of this paper we will examine the equations describing the SIS receiver to understand the reason for this intersection. We will show that the load temperature corresponding to this intersection point, which we call $-T_X$, is the (negative of the) equivalent input noise temperature of the rf input section of the receiver: $T_{RF} = T_X$. Thus T_{RF} is for the first time amenable to easy measurement.

EXPLANATION OF THE TECHNIQUE

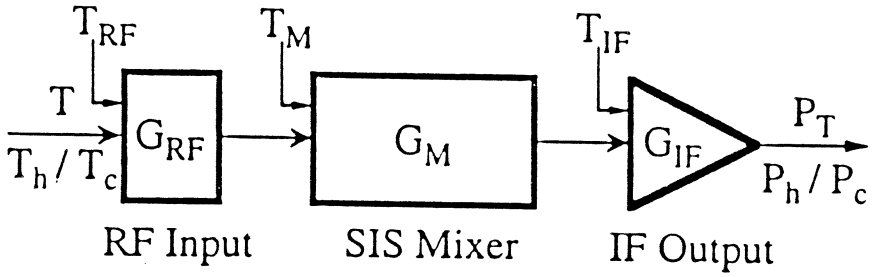

Fig. 2. A standard block diagram of a heterodyne receiver.

Our proposed technique relies on the fact that the SIS mixer output noise temperature [3] is largely independent of mixer gain for low local oscillator power. Figure 2 shows a standard diagram of a heterodyne receiver. The receiver consists of three blocks: the rf input section, the mixer, and the IF amplifier; with respective gains G_{RF}, G_M, and G_{IF}; and with respective equivalent input noise temperatures T_{RF}, T_M, and

T_{IF}. Cascading these blocks, the total output power P_T from the receiver when a matched load at temperature T is placed at the receiver input is given by

$$P_T = [(T+T_{RF})G_{RF}G_M + T^{out} + T_{IF}]\,kBG_{IF}\,, \qquad (2)$$

where we define the equivalent output noise temperature of the mixer

$$T^{out} \equiv T_M G_M\,. \qquad (3)$$

In functional form, Eq. 2 simply states that $P_T(T)$ is a straight line. Equation 2 could also be written $P_T = (T+T_R)\,kBG_{RF}G_MG_{IF}$, so that $P_T = 0$ for $T = -T_R$, which is a restatement of the graphical Y-factor method of determining T_R.

Let us now hypothesize that T^{out} is independent of the LO power, P_{LO}, for low LO power levels. (We will discuss the accuracy and the range of validity of this hypothesis for SIS mixers, below.) Then in Eq. 2 only G_M will depend upon P_{LO}, and so P_T is independent of P_{LO} for some (negative) input load temperature $T = -T_X = -T_{RF}$. Therefore our hypothesis implies that we can read $T_{RF} = T_X$ directly from the intersection point on a graph like Fig. 1. Contributions to P_T are sketched in Fig. 3.

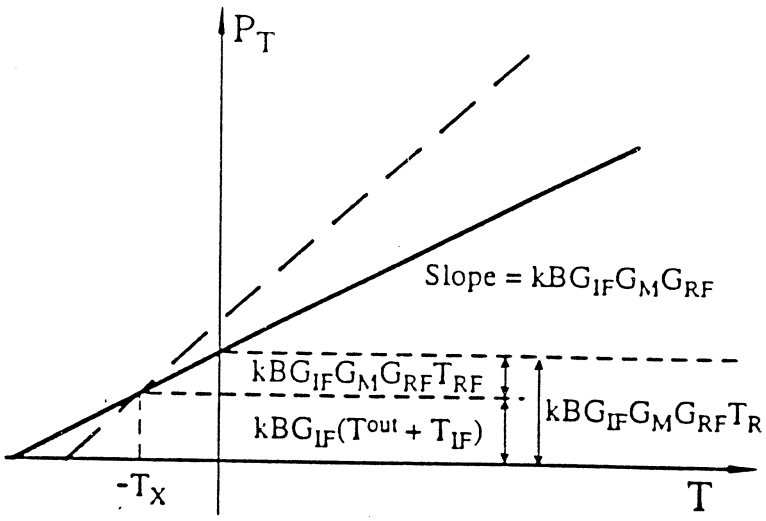

Fig. 3. Contributions to the receiver output power for interpreting the intersecting lines technique are sketched.

What if our hypothesis is not completely true? Consider the possibility that T^{out} also has a component which is proportional to G_M. Call this component τG_M. Then Eq. 2 shows that the $P_T(T)$ lines for various P_{LO} still intersect at a point, but in this case T_X is no longer equal to T_{RF} but to $T_{RF} + \tau$, which can be as large as $T_{RF}+T_M$. (We take $G_{RF} \approx 1$ for convenience.) Consider further the possibility that T^{out} has a component with some more complicated dependence upon G_M as P_{LO} is changed. Then Eq. 2 shows that the

$P_T(T)$ lines for various P_{LO} will not intersect at a point, and T_X is not defined. This happens in fact for SIS mixers at higher P_{LO} levels.

It is instructive to apply the intersecting lines technique to the ideal exponential Schottky diode mixer receiver [4]. In this case $T^{out} = (1 - 2G_M)T_D$, where the diode noise temperature T_D is constant [5]. Equation 2 then remarkably predicts that *all* $P_T(T)$ lines will intersect at a point, for *every* value of P_{LO}. The intersection point, however, gives $T_X = T_{RF} - 2T_D$, which can be considerably smaller than T_{RF}. Nevertheless, Schottky receiver engineers are likely to find the intersecting lines technique helpful in characterizing their receivers.

ANALYSIS

The LO power of an SIS mixer is characterized by the parameter $\alpha \equiv eV_{LO}/\hbar\omega$, where V_{LO} is the LO voltage across the SIS junction and ω is the LO frequency. We are interested in P_{LO} levels less than the receiver optimum so it is appropriate to expand the equations from Tucker's quantum mixer theory [6] which describe the SIS mixer in a power series in α. The analysis presented in this section is based on such a small-α limit expansion [7]. All of the conclusions are confirmed and delineated by numerical computations from the quantum mixer theory. The techniques used and the approximations made for the numerical computations are presented in Ref. [3].

G_M is proportional to α^2 to lowest order. T^{out} has a more complicated dependence. T^{out} consists of three types of noise [3]. First, there is the "uncorrelated" noise arising from the leakage current shot noise of the SIS junction; this is independent of α. Second, there is the "correlated" LO-induced shot noise, which is conventionally represented by correlated noise sources placed at the mixer's signal, image, and IF terminations; this is proportional to α^4 to lowest order. Third, T^{out} can include quantum noise, but for now we consider a double-sideband mixer which is perfectly matched to the LO source, so quantum noise is entirely included in the factor $(T+T_{RF})$ in Eq. 2 and does not appear as a component of T^{out}.

This discussion shows that T^{out} is independent of α and hence independent of P_{LO} for low LO power levels for a matched SIS mixer. There is no α^2 term. We conclude that the intersecting lines technique works perfectly.

This is not precisely true. The separation between "uncorrelated" and "correlated" noise is not perfect because they are coupled by the SIS mixer's nonlinearity. This produces a small α^2 term in T^{out}, which causes a small error in the equation $T_{RF} = T_X$. But this is negligible; numerical computations show that the error in the estimation of T_{RF} is always less than 0.1 K for reasonable mixer parameters.

If the SIS mixer is not perfectly matched to the LO source there are two other processes producing small α^2 terms in T^{out} and hence small errors in the intersecting lines technique. We will discuss this for a resistive mismatch, and assume that a reactive mismatch gives the same result. We define the photon point currents $I_n \equiv I_{dc}(V_n)$ and slopes $G_n \equiv dI_{dc}(V_n)/dV$, where $I_{dc}(V)$ is the unmodulated dc I-V curve of the SIS junction, $V_n \equiv V_0 + n\hbar\omega/e$, and V_0 is the dc bias voltage. The mismatch is characterized by the parameter $g \equiv 2\hbar\omega G_s/eI_1$, where G_s is the mixer's LO source conductance. The mixer is perfectly matched to the LO source when $g = 1$.

First, the leakage current shot noise which is coupled into the IF amplifier depends upon the output admittance of the mixer, and this is affected by the LO level. This produces an α^2 term in T^{out} with an effective input temperature

$$\tau_1 = \frac{I_0}{I_1} \frac{2G_1}{G_L+G_0} \frac{1-g^2}{4g} T_Q , \qquad (4)$$

where $T_Q \equiv \hbar\omega/k$ and G_L is the IF load conductance seen by the mixer. Second, the quantum noise which appears as a component of T^{out} is to lowest order α^2 and gives an effective input temperature

$$\tau_2 = \frac{(g-1)^2}{4g} T_Q . \qquad (5)$$

The error (in degrees K) in the equation $T_{RF} = T_X$ is the sum of Eqs. 4 and 5. It is clear that these two terms can become large if g is very large or very small, but in general these terms are not a serious problem. Our conclusion remains that the intersecting lines technique works satisfactorily.

AN EXAMPLE

Figure 4 shows a blow-up of the intersection region for a 235 GHz receiver using a six-junction array SIS mixer. The data, the output power from the receiver using hot and cold matched loads, for optimum LO power (line 1) and subsequently decreasing LO power (lines 2 to 6), was supplied by S.-K. Pan of the National Radio Astronomy Observatory. Line 1 gives $T_R = 73.0$ K. We see that lines 2 to 6 intersect in a rather narrow region, and that line 1 gives somewhat larger output power, as expected. Because the uncertainty in each power measurement was $\pm$ 0.5 μW, Fig. 4 gives $T_{RF} = 48.3 \pm 1.7$ K. More extensive data should narrow this uncertainty to $\pm$ 0.6 K, the same as the uncertainty of the Y-factor measurement of T_R. Systematic errors should also be the same as for the Y-factor measurement of T_R. Unfortunately, the rf input section noise of this receiver is not otherwise known, so the accuracy of the intersecting lines technique cannot be experimentally verified at present.

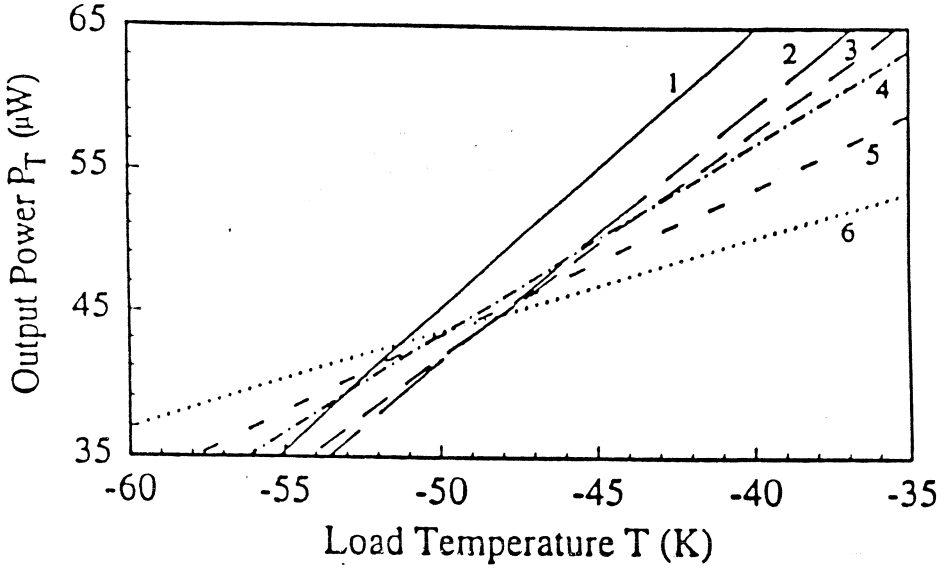

Fig. 4. A blow-up of the intersection region for a 235 GHz receiver, showing the experimental precision of the intersection. The data implies that the rf input section of this SIS receiver has noise temperature = 48.3 ± 1.7 K.

CONCLUSION

We have presented an extremely simple new technique to determine the noise temperature of the rf input section of a superconducting quasiparticle heterodyne receiver. The accuracy and the precision of this new technique are supported by analytic and computed results based on Tucker's quantum theory of mixing.

Acknowledgment: We are indebted to A.R. Kerr and S.-K. Pan for sharing unpublished experimental data with us, and for considerable contributions to the subject matter of this paper. This work was supported by NSF Grant #AST-8922301.

REFERENCES

[1] S.-K. Pan, A.R. Kerr, M.J. Feldman, A. Kleinsasser, J. Stasiak, R.L. Sandstrom, and W.J. Gallagher, "An 85-116 GHz SIS receiver using inductively shunted edge junctions," IEEE Trans. Microwave Theory Tech. **MTT-37**, 580 (1989).

[2] R. Blundell, R.E. Miller, and K.H. Gundlach, "Understanding noise in SIS receivers," Int. J. Infrared Millimeter Waves **13**, 3 (1992).

[3] Qing Ke and M.J. Feldman, "Constant output noise temperature of the superconducting quasiparticle mixer," IEEE Trans. Applied Superconductivity, to be published.

[4] A.R. Kerr and S.-K. Pan, private communication.

[5] A.R. Kerr, "Shot-noise in resistive-diode mixers and the attenuator noise model," IEEE Trans. Microwave Theory Tech. **MTT-27**, 135 (1979).

[6] J.R. Tucker, "Quantum limited detection in tunnel junction mixers," IEEE J. Quantum Electronics **QE-15**, 1234 (1979).

[7] M.J. Feldman, "An analytic investigation of the superconducting quasiparticle mixer in the low power limit," IEEE Trans. Magnetics **MAG-27**, 2646 (1991).

Quantum limited responsivity of a $Nb/Al_2O_3/Nb$ SIS waveguide mixer at 460 GHz and first results at 750 and 840 GHz.

G. de Lange[#], C.E. Honingh[*], M.M.T.M. Dierichs[#], H.H.A. Schaeffer[*], H. Kuipers[#], R.A. Panhuyzen[#], T.M. Klapwijk[#], H. van de Stadt[*], M.W.M de Graauw[*], E. Armandillo[+].
[#]Dept. of Applied Physics and Materials Science Centre, University of Groningen, Nijenborgh 4, 9747 AG Groningen;
[*]Space Research Organisation of the Netherlands, Landleven 12, 9747 AD Groningen.
[+] ESTEC, Postbus 299, 2200 AG Noordwijk.

The noise and gain behaviour of a $Nb/Al_2O_3/Nb$ SIS waveguide mixer, with a on chip integrated tuning element, is analyzed at 460 GHz. The receiver sensitivity of the whole system, including the beamsplitter, window and lenses is 116 K DSB. The mixer noise temperature is 35 ± 20 K. Within the experimental error this is as low as the quantum limit at 460 GHz. This is the first measurement of quantum limited sensitivity above 400 GHz. We compare data of the pumped I-V curves with the Werthamer-Tucker theory and demonstrate an excellent agreement at 460 GHz. A comparison of the measured IF-output noise versus bias voltage with the quantum theory of mixing shows a good agreement, indicating for the first time the applicability of this theory, to Nb tunnel junctions up to 500 GHz.

During the last decade the application of heterodyne receivers based on superconducting tunnel junctions shifted from the millimetre into the sub-millimetre range. The high sensitivity and low LO-power requirements make this type of receiver very attractive for ground-based astronomical observations. Several telescopes now use SIS-mixers for observations in the sub-millimetre range. The highest frequency at which SIS-mixers are used is around 500 GHz. Despite the large efforts spent to increase the working frequency of SIS-mixers, relatively little attention is paid to the comparison of measured results with the quantum theory of mixing as developed by Tucker [1,2,3]. In a previous article [4] we showed the performance of a low noise two tuner waveguide mixer in the frequency range 400-500 GHz, using various kinds of mixing elements. An excellent agreement between measured and calculated pumped I-V curves was obtained, and a good qualitative agreement on the noise behaviour of the mixer was shown. In this work the performance of a single junction mixer with an integrated matching circuit is analyzed at 460 GHz. This frequency is close to the resonance frequency of the stripline, and therefore we find a nearly perfect broadband matching of the LO, USB and LSB signals, resulting in a mixer noise temperature on quantum limit level.

The mixer block used in the 400-500 GHz work is a scaled version of the 345 GHz receiver described by Honingh et al.[3] This waveguide system has two moving shorts (backshort and E-plane tuner) as tuning elements, each with a quarter wave choke section to improve the quality of the short. The signal and LO-power are combined by a 15 μm Mylar beamsplitter and enter the cryostat via a 1 mm thick HDP (High Density Polyethylene) window of 3 cm diameter. On the 77 K radiation shield a 200 μm thick quartz plate serves as a heat filter. A diagonal horn with an aperture size of 3.18 mm, a length of 12 mm and a flare angle of 11 degrees is used. Laboratory tests of this horn showed a good Gaussian beam-coupling (side lobes <-15db), equal beamwidths in E-,D- and H- planes and a low

cross-polarisation (<-15 dB). A diagonal horn and a F=31.4 mm HDP lens is used. The lens is mounted in a holder which can be directly mounted on the mixerblock. The mixer block is cut in OFHC. The full height waveguide has dimensions 0.44×0.22 mm. The substrate, containing the junctions and RF-filter, is glued parallel to the sidewalls of the waveguide in a substrate channel of dimensions 0.1×0.165 mm. The E-plane tuner is placed half a guide wavelength (at 492 Ghz) in front of the junction position. A magnet coil with 10,000 turns of 0.1 mm Nb wire is placed around the horn, in front of the mixer block.
The cooled IF-chain consists of a Radiall R443533 T-bias, a Pamtech LTE 1290 isolator and a Berkshire Technologies L-1.4-30H IF-amplifier (40 dB). Outside the dewar a further 47 dB amplification of the IF-signals is provided. The IF power is measured with a HP 8481A powersensor at a center frequency of 1.4 GHz and a bandwidth of 80 MHz. The LO-power in the 400-500 GHz range is supplied by a Thomson carcinotron or a Radiometer Physics Gunn and multipliers system. The noise temperature of the system is measured by using a piece of "ECCOSORB" foam at two different temperatures as a calibrated broadband black-body signal source ("Y-factor" method).

The Nb tunnel junctions are fabricated with the use of a novel process (SNOEP Selective Niobium Over-Etch Process). Junctions with area's as small as .8 um^2 can routinely be made with a high processing yield. The details of this process are described elsewhere [5]. The junctions are fabricated (together with the RF-filters) on a 200 micron thick fused quartz wafer. After the fabrication process the wafer is diced in widths of 150 μm and polished down to 65 μm thickness. The results in this work are obtained on a single junction with an area of 1 μm^2 and a resistance of 31 Ω. The width of the open ended stripline integrated

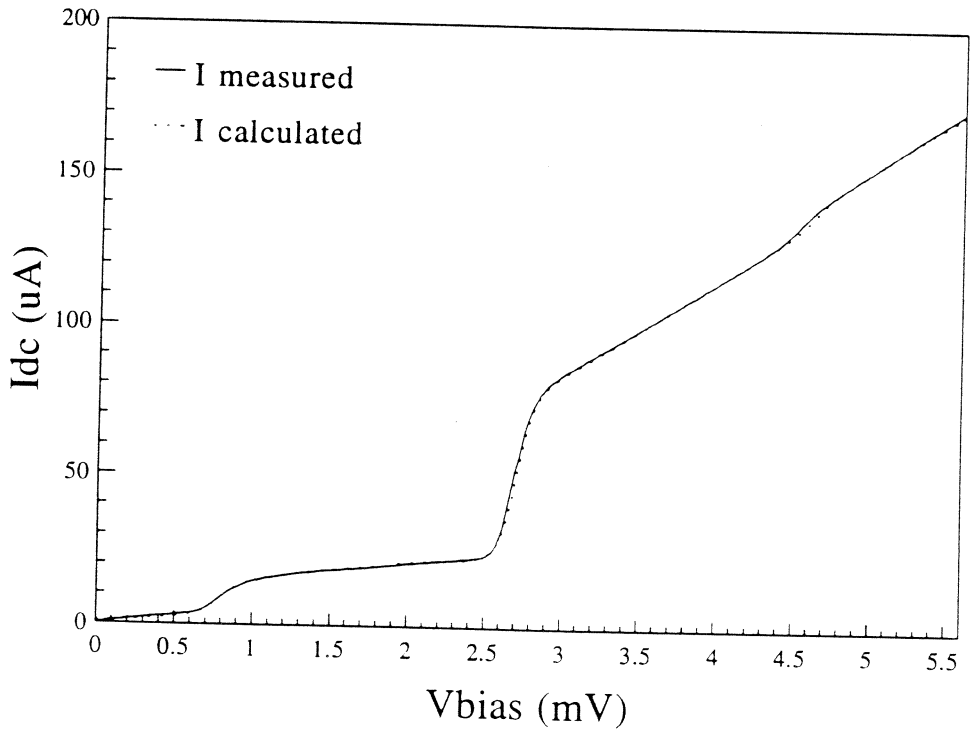

Figure 1. Measured and Calculated IV-curve at 460 GHz and LO-power giving minimum noise temperature.

matching is 5 μm, the length is 86 μm and the thickness of the SiO_2 dielectric layer is 290 nm.

The tuned bandwidth of this mixer is below 140 K in the frequency range 430-495 GHz. At 460 GHz the receiver noise temperature, including the losses of the beamsplitter, window and lens, has a minimum of 116 K. The instantaneous bandwidth of the mixer, measured with fixed tuner settings, is approximately 40 GHz. This is 10 times larger than the bandwidth of a comparable junction without integrated tuning, indicating the large influence of the integrated tuning element.

The pumped IV-curve measured at the 460 GHz LO-frequency and at optimum LO-power is shown in Fig.1, together with a calculated pumped IV-curve, using the Tucker theory. The values of the embedding parameters used in this calculation are G=0.87 and

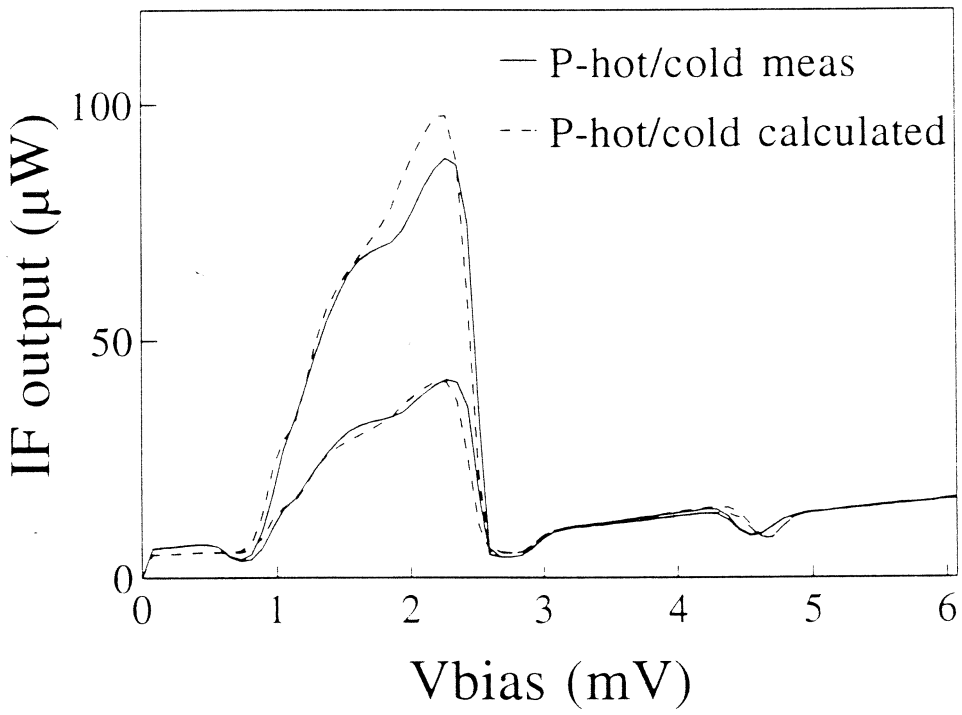

Figure 2. Measured and calculated IF output power at hot and cold input load, as a function of bias voltage

B=0.25 (normalized to the normal state conductance of the junction $G_N = 31^{-1}$ Mho). The embedding parameters for the USB and LSB frequencies are found by tuning the RF-source 1.4 GHz above or below the LO-frequency and performing the same analysis. The fits are of the same quality as shown in Fig. 1 and the values for the USB and LSB admittance are $Y_{USB}=0.87 + 0.70j$, $Y_{LSB}=0.83 + 0.31j$ respectively. The bias voltage dependence of the IF-output is shown in Fig. 2. The figure displays the IF-output with both a hot (293 K) and a cold (77 K) input signal. The gain and noise parameters of the system are found by respectively subtracting and dividing these two curves. The results are shown in Fig. 3. The gain curve in Fig. 3 shows a large conversion on the first photonstep below the gap and almost no conversion above or below this step. Fig. 3 also shows the division of the hot and the cold IF output (the Y-factor) on a linear scale. The nearly constant value of the Y-factor

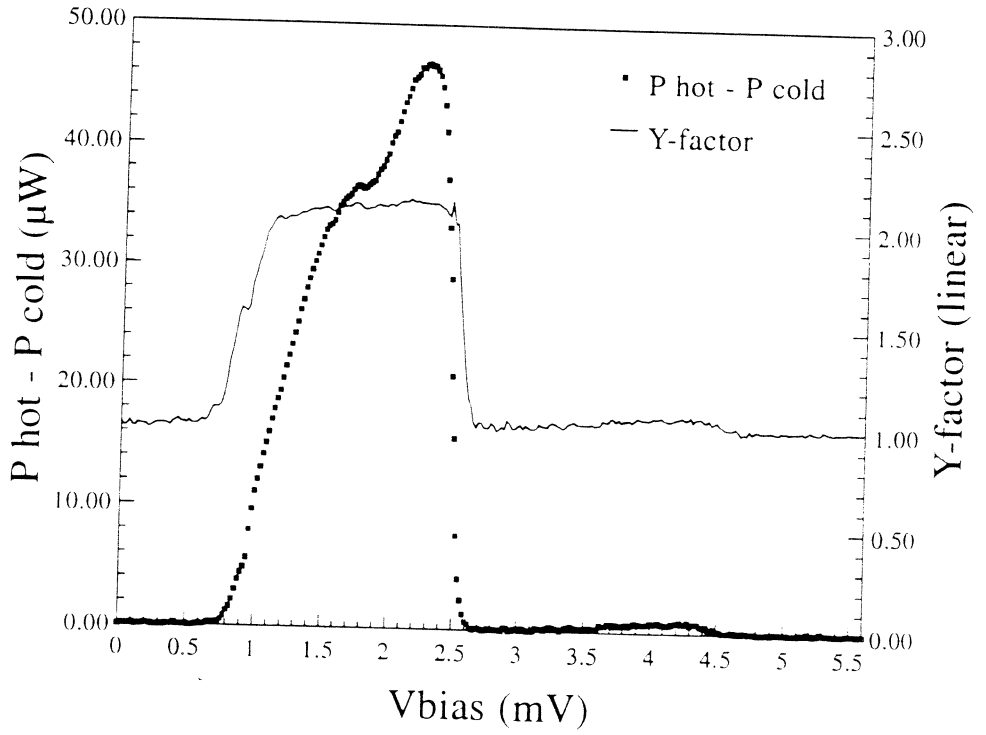

Figure 3. Measured gain and Y-factor as a function of bias voltage

on the fist photon step below the gap indicates that the influence of Josephson effects is sufficiently suppressed.

In the analysis of the mixer noise, the noise contributions of the RF-input and the IF-output have to be taken into account. The gain and noise parameters of the IF-chain (T-bias, isolator, IF-amplifier) are measured by using the unpumped junction as a calibrated noise source at the input of the IF-chain. The values thus found are: G_{IF}=85.7 ± 0.1 dB, T_{IF}=4.8 ± 0.2 K. The total gain and noise contributions of the RF-input are G_{RF}=0.77 ± 0.1, T_{RF}=56 ± 20 K (based on transmission measurements of the beamsplitter, HDP window and quartz filter).

The mixer noise and gain are calculated using the measured output powers shown in Fig. 2. The values for the mixer gain and noise are: G_{mix}=-4.6 ± 0.6 dB, T_{mix}=35 ± 20 K. The value of the measured mixer noise is within the errors equal to the quantum noise limit of 23 K at this frequency.

The measured data on the bias voltage dependence of the mixer gain (as shown in Fig. 2) are compared with the quantum theory of mixing in the three port, low IF approximation. The result of the calculated IF-gain is also shown in Fig. 2. The maximum gain thus found is G_{calc}=-3.6 dB, 1 dB higher than the measured gain.

First results of the 750 GHz mixer (last minute addition)

The measurements at 750 and 840 GHz are performed in the same dewar as the 460 GHz measurements. The 750 GHz mixerblock has a full height waveguide with dimensions 150 x 300 μm (cut-off frequency 500 GHz) and only one tuner element (backshort). This block

uses also a diagonal horn and the dimensions of the substrate channel are 50 x 100 μm. The LO-power at 750 GHz is supplied by a Thomson 340-390 GHz carcinotron in combination with a doubler of Radiometer Physics. The measurements at 840 GHz are performed with a 840-930 GHz Thomson Carcinotron.
The junctions are implemented with different kinds of integrated tuning elements, including open ended, quarter lambda shorted and end loaded striplines. The results shown in this paper are obtained with a structure where the junctions are placed at the outer edge of the stripline (end loaded).

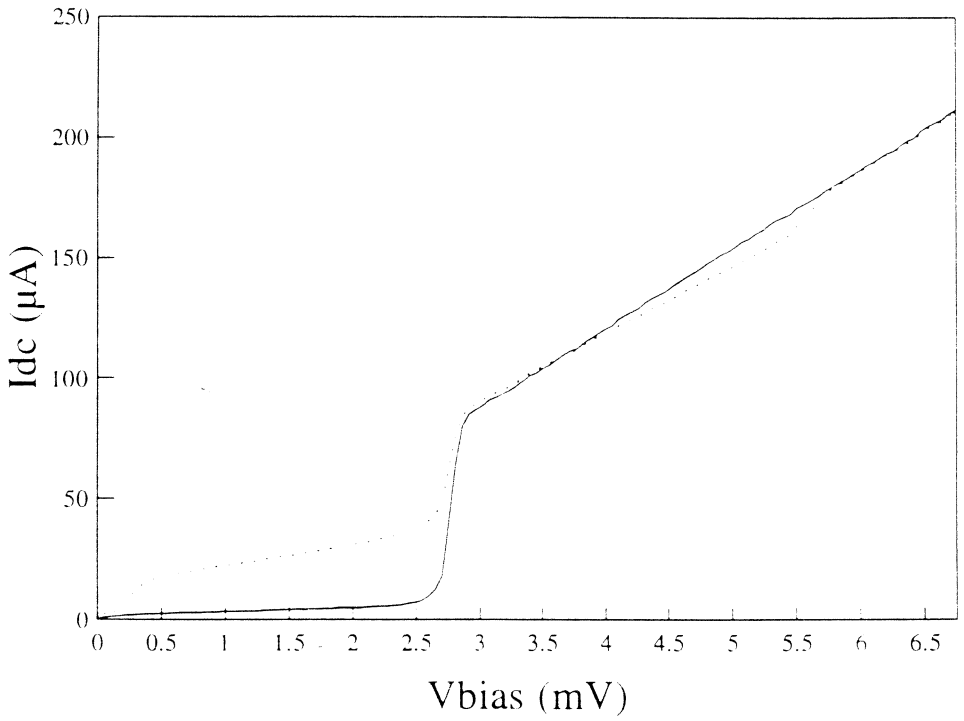

Figure 4. Pumped and unpumped curve with 750 GHz LO frequency. This measurement was performed with the 400-500 GHz mixerblock.

As a test of the 750 GHz doubler, it was placed in front of the 490 GHz receiver. The results of this measurement are shown in Fig. 4. Due to the bad coupling of the 750 GHz radiation in the 490 GHz mixer, a mirror (instead of a beamsplitter) is used to couple in the radiation. Therefore a hot/cold measurement could not be performed. Fig. 4 shows a clear developed 750 GHz photonstep, both above and below the gap. The photon energy at this frequency is above the gap-energy and the first photonsteps below the positive and negative gap voltage start overlapping each other near the zero voltage bias region. In this bias region part of the (positive) DC-current induced by photon assisted tunnelling from the left to the right superconducting electrode is cancelled by a (negative) DC-current from the induced current from the right to the left electrode. Therefore the photonsteps below the gap seems to be less wide than the value hf/e = 3.1 mV. The gap voltage of the junctions shows only a slight decrease, probably due to heating. This indicates that, although the total amount of power reflected at the junction is of the order of several microwatts, exceeding the gap-frequency does not dramatically influence the photon assisted tunnelling.

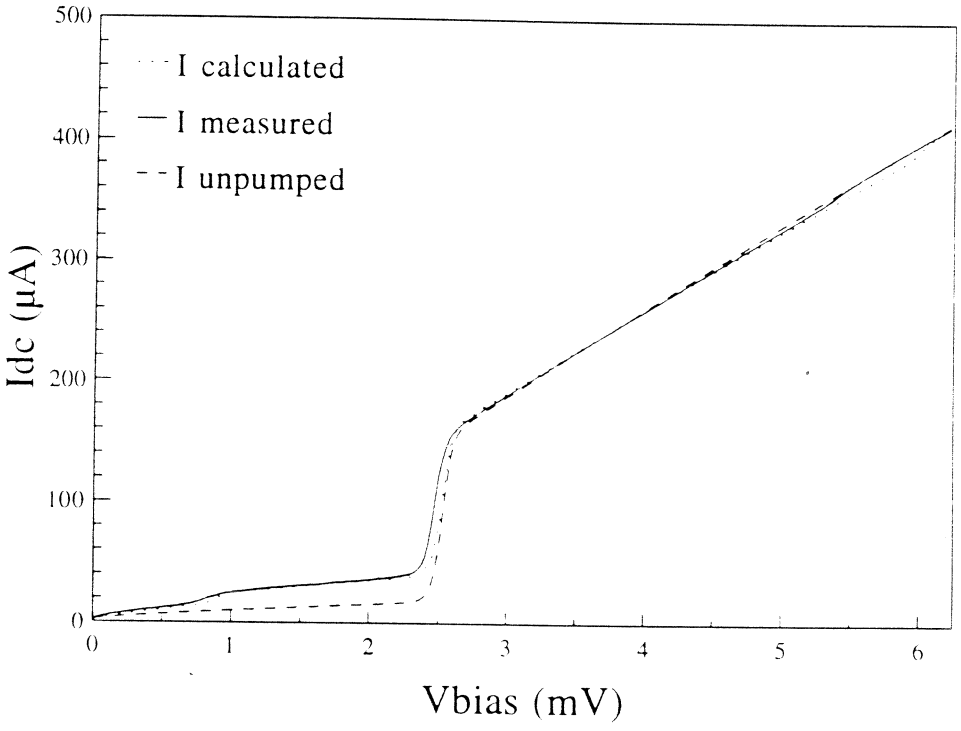

Figure 5. Measured pumped and unpumped I-V curve at 840 GHz and calculated I-V curve.

After this initial test the doubler broke down and was not available at the time the junctions for 750 GHz became available. The 750 GHz mixer was therefore tested with the 840-930 carcinotron. Two single junctions are tested with end loaded striplines with dimensions 10x40 μm and 10x43 μm. The first measurement with the longest stripline resulted in a noise temperature of 3000 K DSB, corrected for the loss of the 90 μm beamsplitter used in this measurement (55 % transmission). The second junction with the 40 μm long stripline showed a hot/cold response of 0.3 dB. Corrected for the beamsplitter loss this gives a 1500 K DSB noise temperature. The gain of the mixer is -17 dB. These values are better than the state of the art Schottky receivers at this frequency. The difference between the two measurements shows that the striplines still improve the RF-coupling at frequencies far above the gap frequency.

The measured I-V curve and the hot/cold response are shown in Figs. 5 and 6. The junctions have a relatively large subgap current and low gapvoltage (2.55 mV). In the DC I-V curve measured without a magnetic field, a self resonant peak was observed at a voltage corresponding to a resonant frequency of 720 GHz. The 840 GHz LO is thus far above the frequency where optimum performance is expected. The 2.55 mV gap corresponds with a 640 GHz gap frequency. The LO frequency is in this case 1.3 times the gap frequency.

In Fig. 5 the measured pumped and unpumped curves are shown, together with a calculated pumped curve. The measured and calculated curves show a good agreement below the gap. The effect of the overlap of photonsteps is more pronounced than at the 750 GHz measurement and this effect is well described by theory. Near and above the gap voltage the theoretical curve deviates from the measured one. In the measured curve the photonstep above the gap is nearly visible and a decrease in gap voltage is observed. These effects are probably

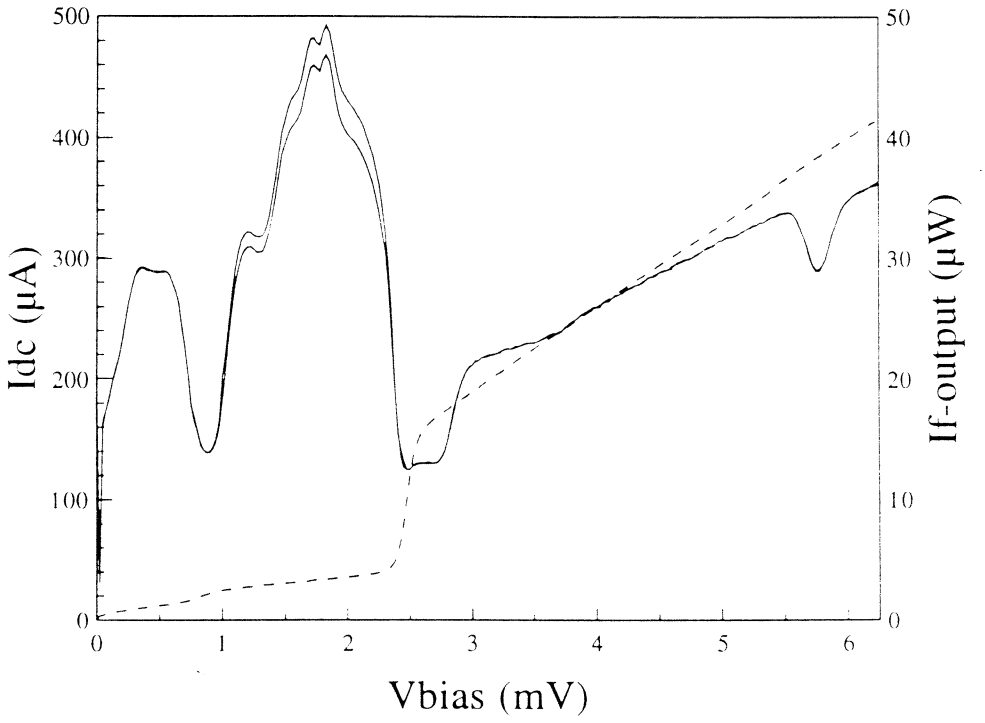

Figure 6. Measured IF-output power at 840 GHz with hot and cold input load. Also shown is the pumped I-V curve.

due to heating. The fact that the incident power on the junction is much larger than the actually coupled power and the relative poor quality of the Nb layer will enhance heating effects.

Fig. 6 shows the measured IF-output power with a hot and cold input load. Subtracting these curves results in a qualitative figure of the gain, as shown in Fig. 7. As can be seen in Figs. 6 and 7 the bias voltage region with hot/cold response (gain) is reduced to the region between the gap voltage and the bias voltage were the 840 GHz photonsteps start to overlap. This behaviour is well described by theory. Preliminary calculations show a good qualitative agreement between the measured and calculated gain curve. The power dependence of the mixergain also shows a qualitative agreement with theoretical predictions. From theory it is known that maximum gain is achieved at a pump power resulting in a pump parameter α of approximately 1. At higher pump levels the gain starts to decrease. This behaviour is observed in the experiments. The measured IF-output power shows some reminiscent Josephson effect at 1.8 mV (giving a dip in the measured gain), but qualitative agreement between calculated and measured gain and the power dependence of the gain (and noise temperature) indicate true heterodyne quasi-particle mixing.

Summary

In summary we have measured the performance of a Nb SIS mixer with an integrated tuning element in the 400-500 GHz range and at 840 GHz. The minimum receiver noise temperature of the 400-500 GHz mixer is 116 K DSB at 460 GHz. The mixer noise temperature is 35 ± 20 K which is at the quantum limit level at this frequency. We show a nearly perfect

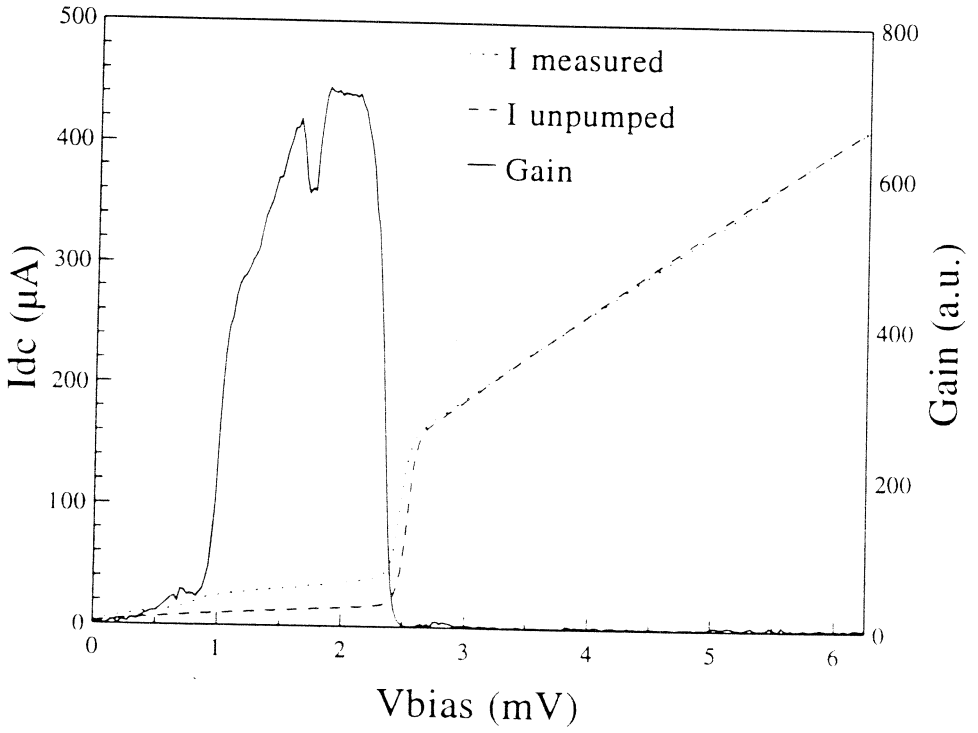

Figure 7. Measured (qualitative) gain of 840 GHz measurement, obtained by subtracting the curves shown in Fig. 6. The region of gain agrees with the theoretical calculated region (not shown).

agreement between the measured pumped I-V curves and the Werthamer-Tucker theory. The measured and calculated bias voltage dependence of the IF-output noise also show a good agreement, indicating for the first time the applicability of the quantum theory of mixing for Nb tunnel junctions up to 500 GHz.
The receiver noise temperature at 840 GHz (corrected for the 55 % loss) is 1500 K DSB. The gain of the mixer is -17 dB. This is the first succesfull measurements of Nb SIS mixers at a frequency above the gap frequency. First comparisons with theory show a good quantitative agreement between the measured and calculated pumped IV-curve.

Acknowledgements:
This work was also supported by the European Space Agency under contract No. 7898/88/NL/PB(SC), the Stichting Technische Wetenschappen and the Stichting voor Fundamenteel Onderzoek der Materie. We wish to acknowledge assistance of Van Duc Nguyen and H. Golstein in preparing the junctions and the measurement system.

References

[1] J.R. Tucker, M.J. Feldman, "Quantum detection at millimeter wavelengts",Rev. Mod. Phys., 57, 1985, 1055.
[2] C.A. Mears, Quing Hu, P.L. Richards, A.H. Worsham, D.E. Prober, A.V.

Räisänen,"Quantum-limited heterodyne detection of millimeter waves using superconducting tantalum junctions", Appl.Phys. Lett, 57, 1990, 2487.
[3] C.E. Honingh, G. de Lange, M.M.T.M. Dierichs, H.H.A. Schaeffer, Th. de Graauw, T.M. Klapwijk,"Performance of a two junction array SIS-mixer operating at 345 GHz", Submitted to IEEE Trans. MTT, Mini Special Issue on Space Terahartz Technology (March 1993).
[4] G de Lange, C.E. Honingh, M.M.T.M. Dierichs et al,"A low noise 410-490 GHz $Nb/Al_2O_3/Nb$ Waveguide mixer, IEEE Transactions on Applied Superconductivity, March 1993.
[9] M.M.T.M. Dierichs et al, Appl.Phys.Lett, 62, 774, 1993.

A SUBMILLIMETER WAVE SIS RECEIVER FOR 547 GHz

W.R. McGrath, P. Febvre[1], P. Batelaan, H.G. LeDuc,
B. Bumble, M.A. Frerking, J. Hernichel[2]

Jet Propulsion Laboratory, California Institute of Technology, Pasadena, CA 91109

1. Permanent address: DEMIRM-Observatoire de Meudon, 92195 Meudon Cedex, France
2. Permanent address: Universität Köln, 5000 Köln 41, Germany

ABSTRACT

A heterodyne receiver using an SIS waveguide mixer with two mechanical tuners has been built and characterized over a frequency range of 460 GHz to 630 GHz. The mixer uses high current density, 0.25 μm^2, $Nb/AlO_x/Nb$ SIS tunnel junctions with integrated superconductive RF circuits to tune the junction capacitance. A DSB receiver noise temperature as low as 200 ± 17 K has been obtained at 540 GHz. In addition, negative differential resistance has been observed in the DC I-V curve at 487-491 GHz.

I. INTRODUCTION

The most sensitive heterodyne receivers used for millimeter wave and submillimeter wave radioastronomy employ Superconductor-Insulator-Superconductor (SIS) tunnel junctions as the nonlinear mixing element. Good performance has been reported for SIS junctions used in planar mixer circuits [1, 2] and waveguide mixers [3-8] from about 300 GHz to 500 GHz. In general, however very few SIS mixers have been demonstrated at these high frequencies. We have developed a submillimeter wave SIS heterodyne receiver for observing important rotational transitions of molecules in the interstellar medium, and in particular the ground state transitions of $H_2{}^{18}O$ at 547 GHz and HCl at 626 GHz. This receiver is based on a waveguide mixer with an adjustable backshort and E-plane tuner [9]. The mixer uses a high current density, submicron area $Nb/AlO_x/Nb$ tunnel junction. The large capacitive susceptance of the junction at high frequencies will shunt the signal away from the nonlinear conductance and hence must be properly tuned for optimum performance. This is accomplished here through the use of carefully designed superconductive microstrip circuits to match the complex impedance of the junction to the available tuning range of the waveguide mount. The receiver performance has been measured over the frequency range 460 GHz to 630 GHz. A DSB receiver noise temperature as low as 200 ± 17 K has been achieved at 540 GHz, and represents one of the best values reported to date at this frequency. The noise temperature rises to only 1100 K at 627 GHz which is an excellent result at this frequency. In addition, negative differential resistance has been observed in the DC I-V curve at frequencies around 491 GHz. These results indicate that the superconductive Nb microstrip transmission lines used in the tuning circuits are low-loss and perform well up to at least 80% of the energy gap frequency.

II. SIS JUNCTIONS WITH INTEGRATED TUNING CIRCUITS

High quality $Nb/AlO_x/Nb$ tunnel junctions have been fabricated using a trilayer deposition and self-aligned insulator lift-off process [10]. The junction area of 0.25 μm^2 is defined by

electron beam lithography, while the junction leads and RF filter structure are produced by conventional photolithography. The Nb films are DC sputter deposited. The base electrode is 1600 Å thick and the top electrode is 2300 Å. The junctions have an estimated specific capacitance of 85-100 fF/μm^2, current densities in the range 7,000-13,000 A/cm^2, and normal state resistances R_N in the range 60 Ω - 120 Ω. The integrated RF tuning circuits are defined by the Nb wiring electrode on a 2000 Å thick SiO insulating layer. Figure 5 shows a typical I-V curve.

Two different integrated RF tuning circuits that resonate the junction capacitance have been designed and tested in order to optimize the mixer. Each circuit configuration has been designed for center frequencies near both 550 GHz and 630 GHz. One is a 3-section series microstrip transformer [11] as shown in Figure 1. The other is a parallel microstrip line terminated in a radial stub as shown in Figure 2. For the series transformer, the first section of superconducting microstrip line (starting at the SIS junction) transforms the SIS junction complex impedance to a low real impedance of ~ 2 Ω. The characteristic impedance Z_0 of this line was chosen close to $(2\pi f_S C_J)^{-1}$ to optimize the bandwidth (f_S is the signal frequency and C_J is the junction capacitance). The low real impedance is then transformed to 50 Ω with a 2-step Chebyscheff transformer. Each step is one quarter of a guide wavelength, λg, long. The adjustable waveguide circuit (discussed below), can readily provide 50 Ω to couple to the microstrip circuit.

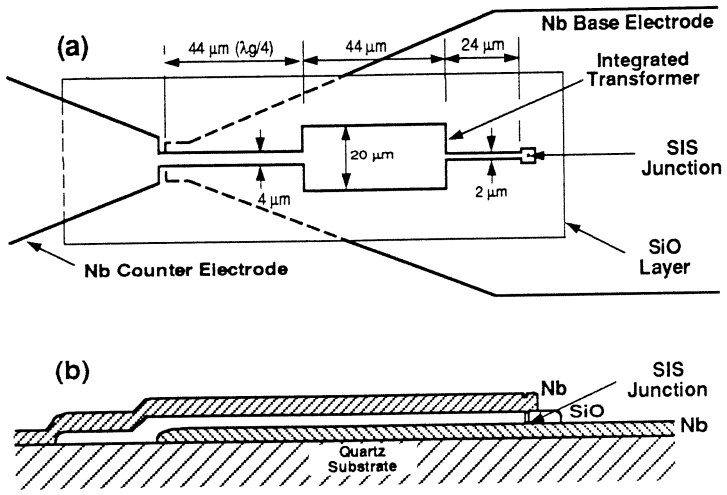

Figure 1: SIS tunnel junction with an integrated series microstrip transformer circuit.
(a) Top view showing transmission line dimensions.
(b) Cross section view showing film topology.

For the parallel circuit, shown in Figure 2, a radial stub is used to provide an RF short over a broad bandwidth. The stub dimensions were designed using an effective dielectric constant, which accounts for the penetration of the magnetic field into the superconductor. The short is then transformed to an inductance by an appropriate section of microstrip line to compensate the capacitance of the junction.

The superconducting microstrip line is a slow-wave line due to the penetration of the magnetic field into the Nb films over a distance comparable to the SiO dielectric thickness. In order to properly design these microstrip circuits, the characteristic impedance Z_0 and phase velocity v of the line must be known.

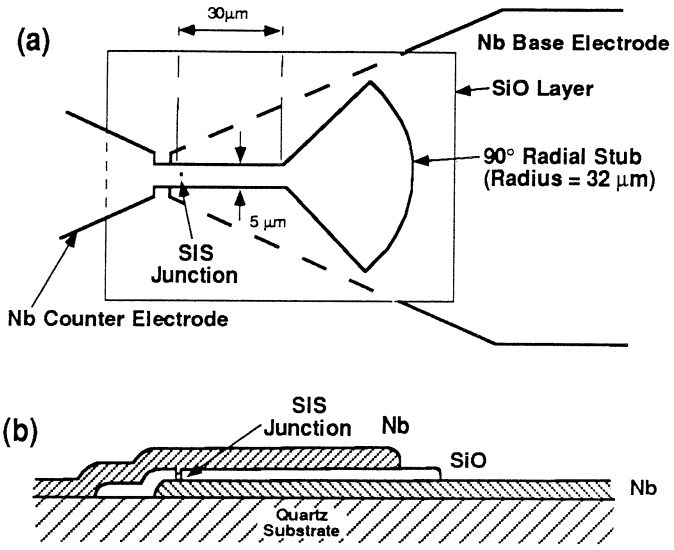

Figure 2: SIS tunnel junction with an integrated parallel microstrip tuning circuit.
(a) Top view showing transmission line dimensions.
(b) Cross section view showing film topology.

These are given by $Z_o = \sqrt{L/C}$ and $v = 1/\sqrt{LC}$ where L is the inductance per unit length of line and C is the capacitance per unit length. Convenient expressions [12, 13] for L and C valid below the gap frequency, are given by:

$$C = k\varepsilon_r\varepsilon_o \, w/t_d \qquad (1)$$

and

$$L = \frac{\mu_o}{kw}\left[t_d + \lambda\left[\coth\left(t_1/\lambda\right) + \coth\left(t_2/\lambda\right)\right]\right] \qquad (2)$$

where w is the width of the microstrip, t_1 and t_2 are the thicknesses of the top and bottom Nb films respectively, t_d is the thickness of the SiO insulting layer, $\varepsilon_r = 5.5$ is the dielectric constant of SiO, and k is a fringing field factor. k varies between 1.05 and 1.37 as a function of the width of the line [14]. Equations (1) and (2) are valid for $w/t_d >> 1$. A penetration depth λ = 750 Å [15] was used as the nominal value.

As indicated by both theory and experiment [15], the dispersion and loss in these Nb transmission lines can be neglected in this application up to about 550 GHz (reference [15] contains an improved theoretical model of the dispersion in superconductive microstrip line which agrees well with measurements). Thus we have not included these effects in our design. In addition, the step and end discontinuities on the microstrip line have also been neglected since the large width-to-height ratio makes these corrections very small. These circuits have been designed to resonate the junction capacitance based on a specific capacitance ranging from 60 to 100 fF/μm^2; a value which is dependent on the current density of the junction. Several RF tuning circuits have been designed based on this range of capacitance, and a systematic study of mixer performance for these different circuits will be published at a later date [16].

III. RECEIVER DESIGN AND MEASUREMENT TECHNIQUES

The SIS tunnel junction, integrated tuning circuit, and low-pass RF filter are fabricated on 50 μm thick quartz which is cut to a width of 150 μm. This substrate is installed into the waveguide mixer mount and wire bonded to the 50 Ω IF output connector. The waveguide mixer was designed using a low-frequency model to maximize the accessible region of impedances on the Smith chart over an equivalent frequency range of 500 GHz to 600 GHz [9]. This mixer has an adjustable backshort and E-plane tuner which provide a wide range of impedances to the SIS junction. RF signals are coupled into the waveguide mount by a dual mode conical horn [17].

Figure 3 shows a block diagram of the receiver. The local oscillator (LO) source consists of two whisker-contacted Schottky varactor frequency multipliers (x2x3) [18] driven by a Gunn oscillator at 91.5 GHz, the center frequency to detect $H_2{}^{18}O$. We varied this Gunn oscillator frequency and used two other Gunn sources to make measurements in the 460 GHz to 630 GHz frequency range. The signal and LO are combined in a folded Fabry-Perot diplexer and injected into the cryostat through a differentially-pumped window using two 125 μm thick mylar vacuum

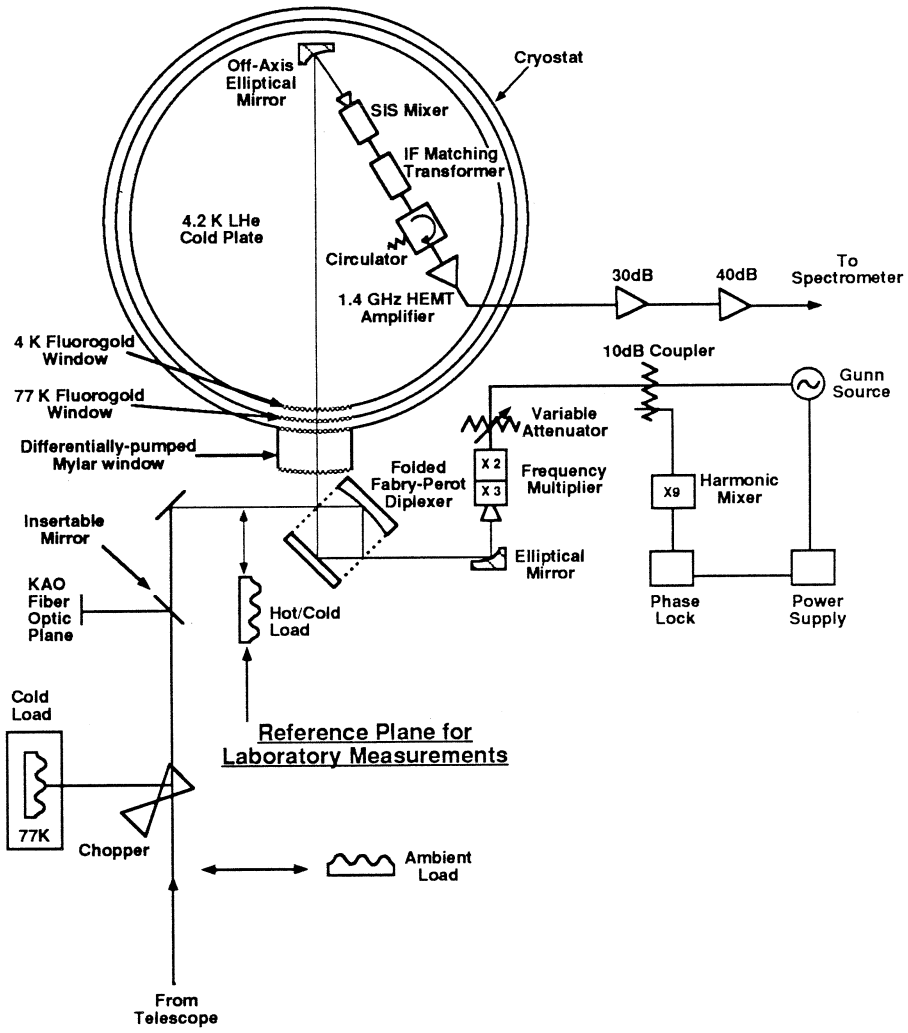

Figure 3: Block diagram of SIS heterodyne receiver. Noise measurements are referred to the reference plane at the signal input port of the Fabry-Perot diplexer.

windows. Fluorogold far IR filters, one wavelength thick at 547 GHz, on the 77 K and 4 K stages, block room temperature radiation from saturating the mixer. An off-axis elliptical mirror reflects the combined LO and signal radiation into the mixer, which is installed on the 4 K stage of the cryostat. The 1.4 GHz IF output of the mixer is transformed to the required 50 Ω input impedance of the low noise HEMT amplifier by a 2 step Chebyscheff microstrip transformer made on a 1.27 mm thick Duroid substrate with $\varepsilon_r = 10.5$. The IF is further amplified by two high gain room temperature amplifiers. The bandwidth for noise measurements is 300 MHz. A superconducting magnet is used to suppress unwanted Josephson interference and thus improve receiver performance. It has been designed to provide a magnetic field of about 800 gauss near the junction for a current through the coil of 1 ampere. This is sufficient since 1 flux quantum in our junction corresponds to about 340 gauss.

The total receiver noise temperature is determined by the Y-factor method using hot (295 K) and cold (82 K) loads. The reference plane for these measurements is the input of the diplexer (see Figure 3). Due to the very high frequency of this receiver, we have calculated the radiation power from the loads using the full Planck expression. The classical formula $P = kTB$ is replaced by $P = h\nu B/(\exp(h\nu/kT)-1)$ where k is Boltzmann's constant and ν is the LO frequency. However, the noise power per unit bandwidth of the receiver is expressed as a temperature using the classical expression.

IV. RESULTS AND DISCUSSION

IV.A. Receiver performance

The receiver performance has been measured over an LO frequency range from 460 GHz to 630 GHz. Three different SIS junctions with integrated tuning circuits have been measured. Figure 4 shows the DSB receiver noise temperature as a function of the LO frequency. Junction A used the 3-section series transformer (see Figure 1). While junction B and C used the parallel tuning circuit with the radial stub (see Figure 2). For each data point in Figure 4, the waveguide backshort and E-plane tuner, LO level, and DC bias voltage were optimized. The best performance was for junction C which gave T_R = 200 K (Y-factor = 1.78) at 540 GHz. The receiver performance was very good with this junction, yielding $T_R \leq 300$ K over the frequency range from 463 GHz to 549 GHz. The only exception was a few points near 490 GHz, where the noise increased due to the appearance of negative differential resistance (this is discussed in more detail below). The receiver also performed well up to 627 GHz with a noise temperature of 1100 K, which is the best result to date at this frequency. This junction, which had the lowest normal state resistance, R_N = 63 Ω, gave better results than the two other junctions with R_N = 110 Ω. One reason is that the junction IF impedance, which is about three times R_N, is better coupled by the IF transformer to the 50 Ω IF system, than the high impedance junctions. This difference in coupling efficiency, however, does not fully explain the observed difference in noise performance. Further theoretical analysis of the mixer performance is required.

Figure 5 shows the unpumped and LO pumped I-V curves, at 540 GHz of junction C, which gave the best performance. The unpumped curve shows very low subgap current and a sharp gap structure at 2.85 mV. The photon step is clearly seen on the pumped I-V curve. Also shown in this figure is the IF output power from the receiver for both hot and cold loads as broadband signal sources at the RF input. It can be seen that the IF power is low near zero voltage which indicates that the Josephson current has been almost completely suppressed with the magnetic field of the superconducting coil corresponding to about 2 flux quanta. However, there is some structure in the IF power curves near 1.1 mV corresponding to the first RF induced Shapiro step, but it does not create any noticeable additive noise or instabilities at the operating bias voltage

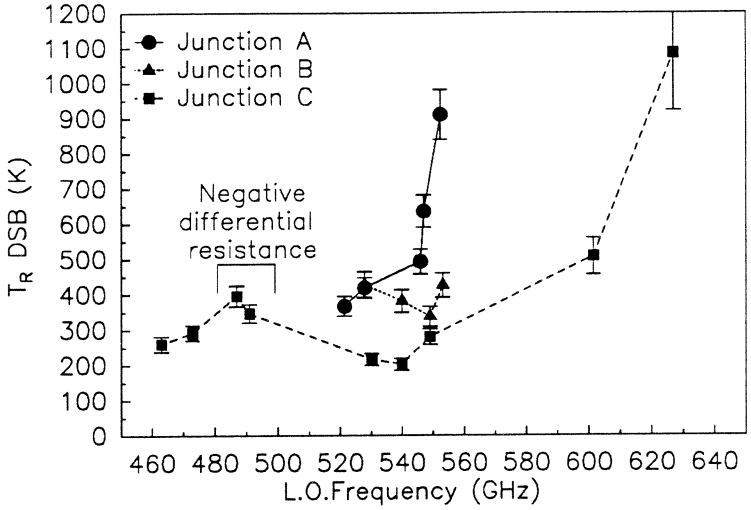

Figure 4: Receiver noise temperature as a function of the LO frequency for 3 different SIS junctions. Junction A uses a series transformer tuning circuit and junctions B and C use a parallel circuit with a radial stub (see text). Very good performance is obtained from 463 GHz to 627 GHz, with the best result T_R = 200 K at 540 GHz for junction C. Negative resistance is also observed near 490 GHz.

at about 2 mV. It may, however, suggest that the SIS junction barrier is not uniform over its surface. This effect has not been observed with the two other junctions of lower current densities. These junctions may have a more uniform barrier and a Josephson current which is easier to suppress with an external magnetic field.

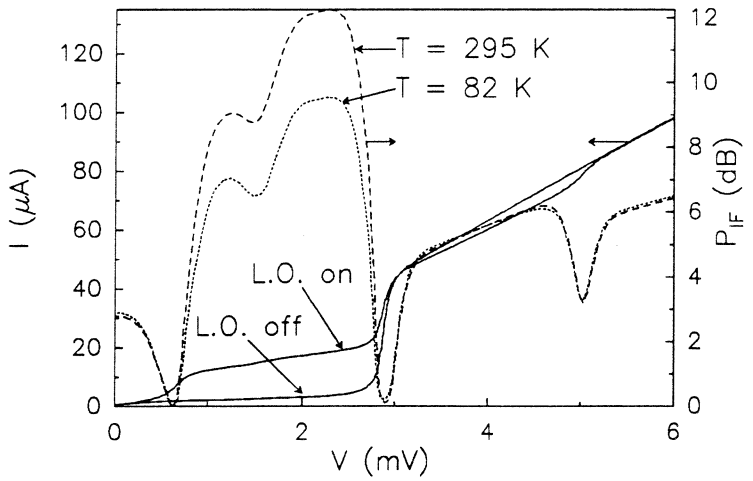

Figure 5: Current vs. voltage characteristic (solid lines) for junction C with and without LO power applied at 540 GHz. Receiver IF output power, P_{IF} (dashed lines) for broadband hot and cold load signals at the RF input.

IV.B. Negative differential resistance

A DC negative differential resistance has been observed on the 1st photon step at LO frequencies of 487 GHz and 491 GHz. This is a quantum mechanical effect which is not predicted by classical theory. Also, negative resistance implies that the available mixer gain can be infinite in theory. When the mixer was biased in the negative resistance region, the IF output power was very high and unstable, probably due to low frequency oscillations. As a result, the receiver is unstable and noisier at these frequencies. However, since the negative resistance did not extend completely across the photon step, it was possible to bias the junction at these frequencies though not at an optimum point. As seen in Figure 4, the receiver noise is higher by 100 K - 200 K in this region.

The negative resistance at 491 GHz could not be eliminated by adjusting the backshort and E-plane tuner. This indicated that the microstrip tuning circuit had at least fully compensated the junction capacitance and was very strongly coupled to the junction. Also, the microstrip losses must be very low. A similar result has been previously reported at 230 GHz [19]. The LO source does not cover the range 500-520 GHz, so the full bandwidth over which this tuning circuit resonates well is not known. This circuit was nominally designed for 547 GHz. This result shows that it actually resonates at a lower frequency than expected (in agreement with Josephson resonances, as discussed below).

IV.C. Mixer noise temperature and conversion efficiency

The shot-noise produced by the linear resistance of the SIS junction I-V curve for voltages higher than the gap voltage was used to calibrate the IF system. This is a simple technique to calibrate the IF system noise and gain, thus allowing the mixer noise and conversion efficiency to be estimated from the measured receiver performance. The SIS junction acts as a variable temperature load when biased on the linear part of its I-V curve. The IF system output power as a function of this temperature is a straight line: its slope is the gain of the IF system and the temperature at zero IF power is the IF system noise. From this calibration, the junction which exhibited 200 K noise temperature at 540 GHz, has a mixer DSB noise temperature of about 170 K with a coupled conversion efficiency (including the IF mismatch) of about -7 dB. The largest contribution to the receiver noise comes from the mixer noise. The mixer noise includes the RF mismatch and all the losses in the optics, the windows and the Fabry-Perot diplexer.

IV.D. High frequency limits

As seen in Figure 4, the receiver noise begins to increase near 550 GHz for each junction tested. We conjecture this is due, in part, to the bandwidth of the tuning circuits. These circuits were designed to resonate the junction capacitance near 547 GHz, however, resonant peaks in the DC I-V curve suggest the circuits resonate at lower frequencies. That is, an SIS junction biased at a voltage V_0 produces a high frequency oscillation given by f = 484 GHz x V_0 (mV) due to the AC Josephson effect. Generally, at high frequencies, the capacitance of the junction shunts these oscillations. But at the frequencies where the tuning circuit resonates the capacitance i.e. at the DC voltages corresponding to these frequencies, these Josephson oscillations interact with the non-linear resistance of the SIS junction and give a DC current peak on the I-V curve [20]. Peaks we observed at about 0.95 mV, corresponding to 460 GHz, for junctions with the series transformer and at about 1.08 mV, corresponding to 520 GHz for the junctions B and C with the parallel tuning circuits. Thus for frequencies well above the resonance, the waveguide backshort and E-plane tuner are not able to completely compensate the junction capacitance and the receiver noise begins to increase due to a degraded RF match.

Another source of noise increase near 545-550 GHz is due to the presence of a strong water line at 557 GHz. The line absorbs part of the signal coming from the cold load and emits at room-temperature. By putting the cold load at different positions: close to the Fabry-Perot diplexer and up to 9 cm away, a difference in the receiver temperature is clearly observed. From this increase of temperature, it is possible to determine the absorption due to the water line. An absorption of about 0.037 dB/cm at 549 GHz was deduced. This measured value is in reasonable agreement with the theoretically calculated absorption given the error in the measurement technique. Such an absorption can add at least 30 K at 549 GHz to the receiver temperature due to the signal path length up to the cryostat window. All junctions show some increase in the receiver temperature above about 545 GHz.

V. CONCLUSION

A receiver for radioastronomy applications in the range 460-630 GHz has been demonstrated. The best result is a DSB receiver temperature as low as 200 K at 540 GHz. The mixer noise is about 170 K and the conversion efficiency is around -7 dB. The optics have been designed to work in the 500-600 GHz RF frequency range. Nevertheless, this receiver was tested at lower and higher frequencies to determine the behavior of the integrated tuning circuits which resonate with the SIS junction capacitance. A differential negative resistance has been observed at 487 GHz and 491 GHz which indicates that the circuits work better at frequencies lower than designed. This is also confirmed by the resonances resulting from the AC Josephson current and observed on the unpumped I-V curves. At frequencies higher than 600 GHz, the receiver noise increases which is partly due to the roll off of the tuning circuit.

In addition, we have begun measuring the performance of this receiver using a series array of two junctions made by optical lithography techniques [21]. A noise temperature T_R (DSB) = 330 K has so far been achieved at 491 GHz. This work is in progress and will be reported later.

VI. ACKNOWLEDGEMENTS

We wish to acknowledge the fabrication of the array junctions by P. Feautrier and the contribution of T. Kuiper for calculating the theoretical atmosphere water line absorption near 550 GHz. This work was supported in part by the Jet Propulsion Laboratory, California Institute of Technology, under contract to the National Aeronautics and Space Administration and the Innovative Science and Technology Office of the Strategic Defense Initiative Organization. Pascal Febvre has been partly sponsored by Matra Marconi Space, Toulouse, France and the DEMIRM (Département de Radioastronomie Millimétrique), Observatoire de Meudon, France.

VII. REFERENCES

[1] J. Zmuidzinas and H.G. LeDuc, "Quasioptical slot antenna SIS mixers," IEEE Trans. Microwave Theory Tech., in press, 1992.

[2] T.H. Büttgenbach, H.G. LeDuc, P.D. Maker and T.G. Phillips, "A fixed tuned broadband matching structure for submillimeter astronomy," IEEE Trans. Appl. Superconductivity, September 1992.

[3] G. de Lange, C.E. Honingh, M.M.T.M. Dierichs, R.A. Panhuyzen, H.H.A. Schaeffer, T.M. Klapwijk, H. van de Stadt, M.W.M. de Graauw, "A low noise 410-495 Heterodyne two tuner mixer using submicron Nb/Al_2O_3/Nb tunnel junctions," Proceedings of the 3rd Int'l Symp. Space Terahertz Tech., pp. 210-221, Ann Arbor, MI, March 24-26, 1992.

[4] C.K. Walker, J.W. Kooi, M. Chant, H.G. LeDuc, P.L. Schaffer, J.E. Carlstrom, and T.G. Phillips, "A low noise 492 GHz SIS waveguide receiver," Int. J. IR mm Waves, pp. 785-798, vol. 13, No. 6, 1992.

[5] P. Febvre, P. Feautrier, C. Robert, J.C. Pernot, A. Germont, M. Hanus, R. Maoli, M. Gheudin, G. Beaudin, P. Encrenaz, "A 380 GHz SIS Receiver using Nb/AlOx/Nb junctions for a radioastronomical balloon-borne experiment: PRONAOS," Proceedings 3rd Int'l Symp. Space Terahertz Tech., pp. 189-209, Ann Arbor, MI, March 24-26, 1992.

[6] B.N. Ellison, P.L. Schaffer, W. Schaal, D. Vail and R.E. Miller, "A 345 GHz SIS receiver for radioastronomy," Int. J. IR mm Waves Vol. 10, No. 8, 1989.

[7] A. Karpov, M. Carter, B. Lazareff, M. Voss, D. Billon-Pierron, K. H. Gundlach, "The 350 GHz and 230 GHz mixers with the tuned SIS junctions," Digest of the 17th Int'l Conf. on IR and mm Waves, pp. 340-341, California Institute of Technology, Pasadena, CA, December 14-17, 1992.

[8] C.E. Honingh, G. de Lange, M.M.T.M. Dierichs, H.H.A. Schaeffer, J. Wezelman, J. v.d. Kuur, Th. de Graauw and T.M. Klapwijk, "Comparison of Measured and Predicted Performance of a SIS Waveguide Mixer at 345 GHz," Proceedings of the 3rd Int'l Symp. on Space Terahertz Tech., pp. 251-265, Ann Arbor, MI, March 24-26, 1992.

[9] W.R. McGrath, K. Jacobs, J. Stern, H.G. LeDuc, R.E. Miller, M.A. Frerking, "Development of a 600- to 700-GHz SIS receiver," Proceedings of the 1st Int'l Symposium on Space Terahertz Technology, pp. 409-433, Ann Arbor, MI, March 5-6, 1990.

[10] H.G. LeDuc, B. Bumble, S.R. Cypher, A.J. Judas, J.A. Stern, "Submicron area Nb/AlOx/Nb tunnel junctions for submillimeter mixer applications," Proceedings of the 3rd Int'l Symposium on Space Terahertz Technology, pp. 408-418, Ann Arbor, MI, March 24-26, 1992.

[11] K. Jacobs, U. Kotthaus, and B. Vowinkel, "Simulated performance and model measurements of an SIS Waveguide mixer using integrated tuning structures," Int. J. IR mm Waves, vol. 13, No. 1, 1992.

[12] J.C. Swilhart, "Field solution for a thin film superconducting strip transmission line," J. Appl. Phys. 32, 461-469 (1961).

[13] T.R. Gheewala, "Design of 2.5-micrometer Josephson current injection logic," IBM J. Res. Develop. 24, 130-142 (1980).

[14] W.M. Chang, "The inductance of a superconducting strip transmission line," J. Appl. Phys. 50, 8129-8134 (1979).

[15] H.H.S. Javadi, W.R. McGrath, B. Bumble, and H.G. LeDuc, "Dispersion in Nb microstrip transmission lines at submillimeter wave frequencies," Appl. Phys. Lett. 61, 2712-2714 (1992).

[16] P. Fabvre, W.R. McGrath, P. Batelaan, H.G. LeDuc, B. Bumble, to be published.

[17] H.M. Pickett, J.C. Hardy, J. Farhoomand, "Characterization of a dual-mode horn for submillimeter wavelengths," IEEE Trans. Microwave Theory Tech. MTT-32, 936 (1984).

[18] Made by Radiometer Physics, Meckenheim, Germany

[19] K. Jacobs, U. Kotthaus, "Performance of a 230 GHz SIS receiver using Broadband Integrated Matching Structures," Digest of the 17th Int'l Conf. on IR and mm Waves, pp. 332-333, California Institute of Technology, Pasadena, CA, December 14-17, 1992.

[20] R.E. Eck, D.J. Scalapino and B.N. Taylor, "Self-detection of the ac Josephson current," Phys. Rev. Lett., **13**, no. 1, pp. 15-18, July 6, 1964.

[21] P. Feautrier, M. Hanus and P. Febvre, "Nb/Al-AlOx/Nb junctions for a 380 GHz SIS Receiver," Supercond. Sci. Technol., pp. 564-568, **5**, 1992.

Double Dipole Antenna SIS Receivers at Frequencies above 500 GHz*

J. Mees[a], A. Skalare[a], M.M.T.M. Dierichs[a,b], H. van de Stadt[a], R.A. Panhuyzen[a], Th. de Graauw[a], T.M. Klapwijk[b], and E. Armandillo[c]

a) Space Research Organisation Netherlands (SRON), Postbox 800, 9700 AV Groningen, The Netherlands
b) Dept. of Applied Physics and Materials Science Center, University of Groningen, Nijenborgh 4, 9747 AG Groningen, The Netherlands
c) ESTEC, Postbox 299, 2200 AG Noordwijk, The Netherlands

Abstract

Resonances of simple tuning circuits up to 1 THz coupled to SIS tunnel junctions were obtained by means of FTS measurements and compared with calculations based on the Mattis-Bardeen theory. We developed a new sort of devices for frequencies above 700 GHz using gold instead of Nb for the rf-parts. First measurements of the video and heterodyne response of all-Nb SIS receivers have been made at frequencies between 720 and 890 GHz. We measured a possible heterodyne response of 1.1 dB due to a hot/cold load at 830 GHz. The video response of the unpumped junction was 0.3 dB due to the hot/cold load.

Introduction

Planar double dipole antennas consisting out of two half-wave dipoles are well suited for the construction of sensitive broad band heterodyne SIS-receivers. Previously published results [1,2,4] with small area Nb-tunnel junctions including simple tuning structures have shown an excellent performance at frequencies up to 500 GHz. In order to develop mixers above the gap frequency of Nb up to 1 THz we are investigating in several items.

Resonances of open-ended tuning stubs coupled to SIS-tunnel junctions are studied and compared with calculations based on the Mattis-Bardeen theory. Since the conductivity of Nb decreases strongly above the superconducting gap frequency we are proposing improved performance using instead of Nb films made out of a normal conductor. We are developing therefore devices with antennas and integrated tuning network out of gold and Nb-tunnel junctions as detection elements. First results of these new devices are promising.

Besides this we are investigating in measurements of all-Nb elements above 500 GHz. Resonances of the integrated tuning network above the gap frequency could be obtained by means of measurements with a Fourier-Transform-Spectrometer (FTS). First measurements of the video and heterodyne response have been carried out at frequencies between 700 and 900 GHz.

---

* Proceedings of the 4. International Symposium Space TeraHertz Technology (1993), Los Angeles

Resonances of the Integrated Tuning Network

Integrated tuning network is necessary to compensate for the junction capacitance or to transform its impedance to the antenna impedance. This is especially true for SIS-mixer receivers based on planar antennas since there is no other tuning possibility available. In order to understand the frequency dependent behavior of superconducting transmissionlines we measured the video response of SIS-junctions coupled to open-ended stubs by means of an Fourier-Transform-Spectrometer. We used an array of 2 junctions in a log-periodic antenna each coupled to one stub. Multiple resonances (Fig. 1) up to the gap frequency of Nb were detected. The solid line Fig. 1 shows the result for an all-Nb microstrip and the dashed line for the same geometry but with a upper conductor out of gold instead. For better comparison the curves in Fig. 1 are fitted to at the same height in the first resonance. The splitting of the first resonance of the Nb-line is presumably due to unsymmetry in the junction sizes or widths of the microstrip lines.

These measurements show again that the conductivity of Niobium is superior than of gold for frequencies below 700 GHz. The lower conductivity of gold results in a more washed out shape of the resonances in Fig. 1. There is an offset in the minima and the maxima of the gold measurements does not reach the same height as in the Nb measurements.

We made also calculations to model the measurements of Fig. 1. They are based on the Mattis-Bardeen theory (MB-theory) for the conductivity of the Nb-films and formulas of Kautz and Matick for the performance of superconducting and normal conducting striplines. They also includes terms out of Tuckers theory for the video response for the detector. The comparison of the Nb case and the calculations shows good agreement of measurements and theory in the frequency dependence of the resonances. That means the dispersion of the line and the general shape of the sensitivity. Nevertheless there is a significant difference in the height of the resonances which is increasing to higher frequencies. This is presumably due to radiation losses of the microstrip or to losses in the dielectric (sputtered SiO_2) which separates the upper and lower conductor. A more detailed discussion can be found in [3].

These results fit very well with the common picture of the conductivity of gold and Nb at high frequencies. Fig. 2 shows the calculated attenuation of superconducting striplines (MB-theory) out of Nb and NbN based on literature values for the conductivity. We measured the DC-conductivity of sputtered gold films as those used in the FTS-measurements and calculated the high frequency performance of such a stripline shown in Fig. 2. Due to our production process the conductivity of gold is less than in literature. Nevertheless there will be a clear advantage in the use of gold or other good conductors like copper for antennas and transmissionlines at frequencies above ~ 670 GHz.

Gold Antennas

The discussion in the chapter before has led us to the development of SIS-mixers with gold antennas and microstrips for frequencies above 700 GHz. As shown in Fig. 3 two small pads of trilayer are deposited on one side of the antenna for the SIS-junction and the lumped capacitor. The actual size of those is defined by two (smaller) windows in the SiO_2. The wiring layer with the other half of the antenna is deposited on top of that. Fig. 4 shows the cross-section with upper and lower conductor out of gold and in-between the trilayer with the junction in the middle. A new recipe has had to be developed for the production of these devices. First results are very promising. Measurements of the DC-IV-curves show clearly self-resonant steps at around 700 GHz.

Resonances above the Gap

Besides the development of the gold devices we are still investigating in all-Nb elements. We have been able to obtain for the first time second harmonic resonances of several devices above the gap frequency of Nb. An example for a lumped element tuning circuit (like in Fig. 3) is shown in Fig. 5 with the second resonance at 830 GHz. The dip at 560 GHz in the first resonance is due to an absorbing waterline since the FTS was not evaporated. The dashed line shows the probable shape of the resonance without waterline.

Video and Heterodyne Response above 700 GHz

Since there was no device available with a first resonance peak above 700 GHz we investigated in measurements of the video and heterodyne response of the device shown in Fig. 5. The experimental setup is shown in Fig. 6. We used a carcinotron with a frequency range from 830-930 GHz as local oscillator. The radiation from the hot/cold load (300 K / 77 K) was coupled into the cryostat by means of a 60 μm thick mylar beamsplitter. Two lenses focused the radiation of the carcinotron on a hemispherical lens. The antenna was mounted on the back side of the hemispherical lens with a quarter-lambda thick metalized plate on the back as reflector. A more detailed description of the receiver setup is given by [1,4].

We measured the video response of to different devices at frequencies ranging from 700 GHz to 900 GHz. Fig. 7 and 8 show the video response at 720 GHz and 830 GHz, respectively. We used a 350 GHz carcinotron together with a doubler for the measurements at 720 GHz. The device measured in Fig. 7 shows a much higher leakage current than that shown in Fig. 8, which is the same as in Fig. 5 and 9. The measurements were hardly influenced by the Josephson effect, although we could not suppress it completely. At 720 GHz the width of the responsivity steps in the subgap is already smaller than the width of one photon step hf/e. This is due to the interfering effect of the photon steps from the positive and negative parts of the IV-curve at zero volt. This effect is much more severe at 830 GHz (Fig. 8).

First measurements of the heterodyne response were done at frequencies between 830 GHz and 890 GHz. The best performance was obtained at 830 GHz. Fig. 9 shows the hot/cold response of the IF-line at 830 GHz together with the pumped DC-IV curve. The best hot/cold response was measured at about 1.4 mV. The shape of the IF-curve here is reasonable good. At the lower end this region is limited by the self-resonant step at ~ 1 mV and at the upper end through the AC-Josephson effect at ~ 1.8 mV that could not be completely suppressed. The structure below 1 mV is due to the interfering effect of photon steps of the positive and negative part of the IV-curve.

The junction area was 1.75 μm^2 and the normal resistance R_N=16 Ω. The best measured Y-factor was Y=1.1 dB. Assuming heterodyne response, this would correspond to a receiver noise temperature of T_{DSB}~670 K. This is not corrected for losses due to the 60 μm thick mylar beamsplitter which has a transmission of about 60%. The hot and cold load was assumed to be 300 K and 77 K, respectively. The video response of the unpumped junction was 0.3 dB at the same bias point.

These very first results of heterodyne and video experiments at frequencies above the gap frequency of Nb are very promising, although the interpretation is not yet clear. More work has to be done to verify and analyze the quasiparticle heterodyne response, e.g. with line measurements, and distinguish the quasiparticle heterodyne detection from Josephson and video effects.

Conclusions

Resonances of all-Nb and mixed Nb-gold open-ended stubs were measured up to the gap frequency. Calculations based on the Mattis-Bardeen theory agree fairly good with the measurements. Differences in the height of the resonances at higher frequencies are probably due to losses in the sputtered SiO_2 or to radiation losses of the microstrip.

For mixers above the gap frequencies a new sort of devices with gold antennas were developed. DC-IV curves from first devices show self-resonant steps at ~ 700 GHz.

Measurements of all-Nb elements were performed at frequencies above 700 GHz. FTS measurements of several devices show 2. resonances of the tuning structures at frequencies between 800 and 1000 GHz. We measured a possible heterodyne response due to a hot/cold load of Y=1.1 dB at 830 GHz. Assuming a quasiparticle heterodyne response this would correspond to a receiver noise temperature of T_{DSB}=670 K The video response for the unpumped junction was 0.3 dB. Further analysis has to be done.

Acknowledgments

This work was supported by the European Space Agency under contract No. 7898/88/NL/PB(SC), the Stichting Technische Wetenschappen and the Stichting voor Fundamenteel Onderzoek der Materie. We acknowledge the assistance of H. Golstein, H. Schaffer and J. Wezelman for helpful discussions and in the preparation of the experiments.

References

[1] A. Skalare, H. van de Stadt, Th. de Graauw, R.A. Panhuyzen, and M.M.T.M. Dierichs, 3. International Symposium Space TeraHertz Technology (1992)

[2] A. Skalare, H. van de Stadt, Th. de Graauw, Microwave and Optical Letters, Vol. 4(1), (1991)

[3] M.M.T.M. Dierichs, C.E. Honingh, R.A. Panhuyzen, B.J. Feenstra, A. Skalare, J.J. Wijnbergen, H. van de Stadt, Th. de Graauw, IEEE Trans. Microwave Theory Tech., to be published in March 1993.

[4] A. Skalare, M.M.T.M. Dierichs, J. Mees, H. van de Stadt, R.A. Panhuyzen, Th. de Graauw, T.M. Klapwijk, 4. International Symposium Space TeraHertz Technology (1993)

Figure Captions

Fig. 1: Measured resonances of a series of 2 SIS-junctions coupled to an open-ended stub each: a) upper and lower conductor are Nb and b) upper conductor is gold.

Fig. 2: Calculated attenuation (MB-theory) of microstrips out of Nb and NbN. The dashed line represents calculations for a line completely out of gold based on measurements of the DC-conductivity of sputtered films.

Fig. 3: The geometry of the gold antennas

Fig. 4: Cross-section of the new devices. The trilayer with the SIS-junctions is shown in the middle.

Fig. 5: The Fourier-Transform-Spectrum of a lumped element circuit shows the rf-coupling of the junction to the antenna. The second resonant peak at ~ 830 GHz was used for video and heterodyne measurements.

Fig. 6: Experimental setup for video and heterodyne measurements.

Fig. 7: Video response at 720 GHz. (Different device with a higher leakage current than that in Fig. 5, 8 and 9)

Fig. 8: Video response at 830 GHz. (Same device than in Fig. 5)

Fig. 9: Hot/cold response of a pumped junction at 830 GHz. The Josephson effect at ~ 1.75 mV could not be suppressed completely. Also visible is the self-resonance at ~ 1 mV, corresponding to the first resonance at ~ 510 GHz. (Same device than in Fig. 5)

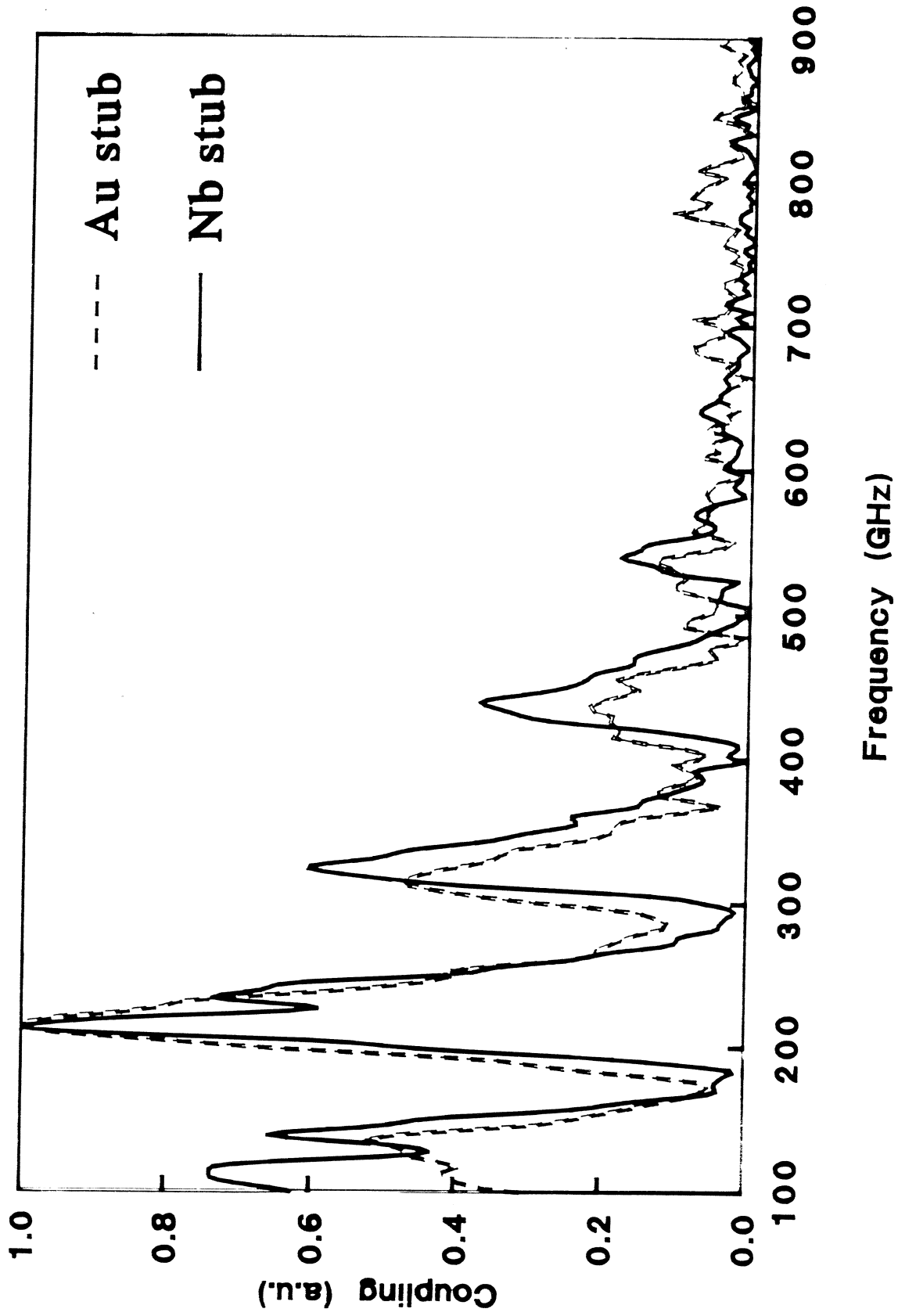
Au stub
Nb stub
Coupling (a.u.)
1.0
0.8
0.6
0.4
0.2
0.0
100
200
300
400
500
600
700
800
900
Frequency (GHz)

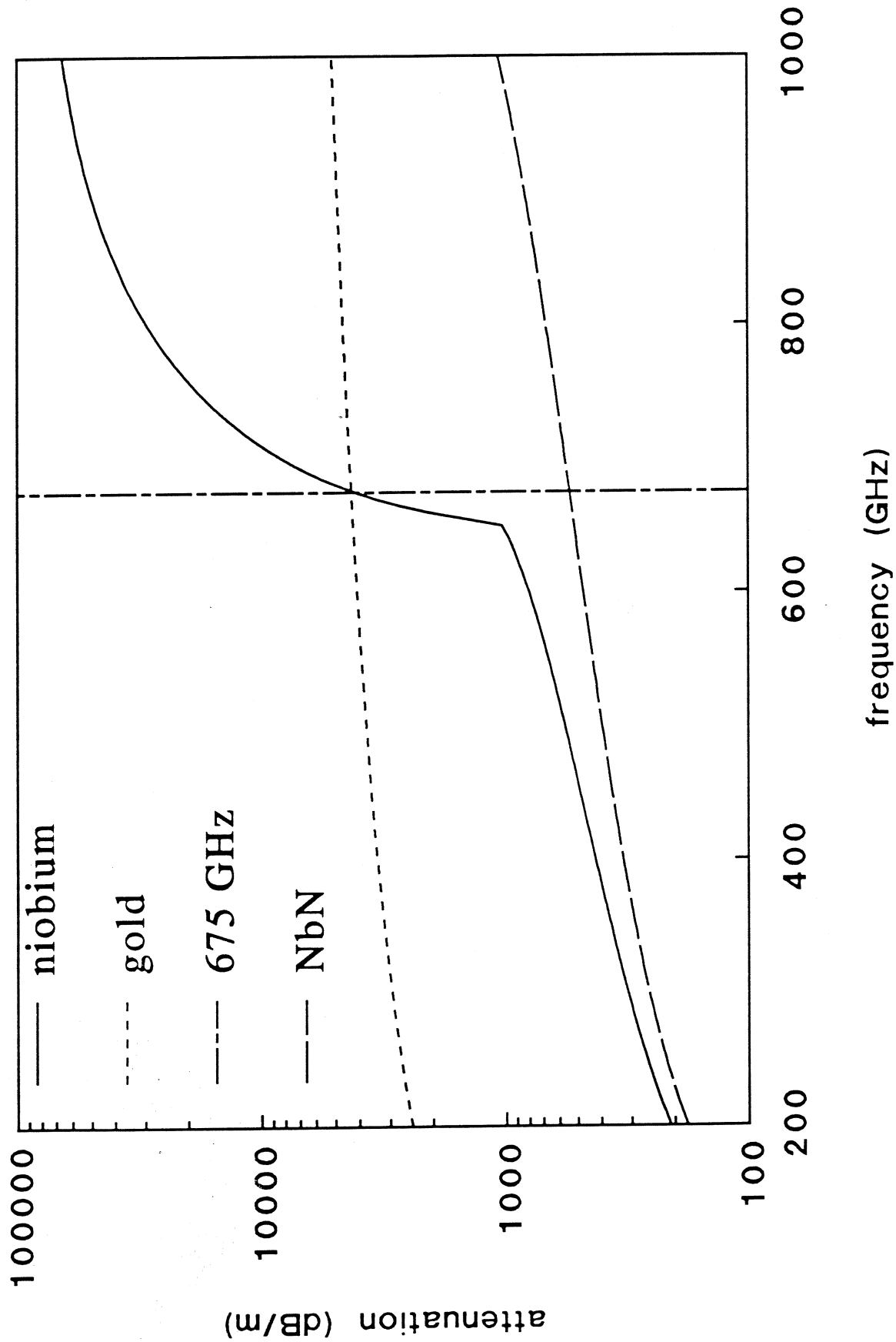
niobium
gold
675 GHz
NbN
100000
10000
1000
100
attenuation (dB/m)
200
400
600
800
1000
frequency (GHz)

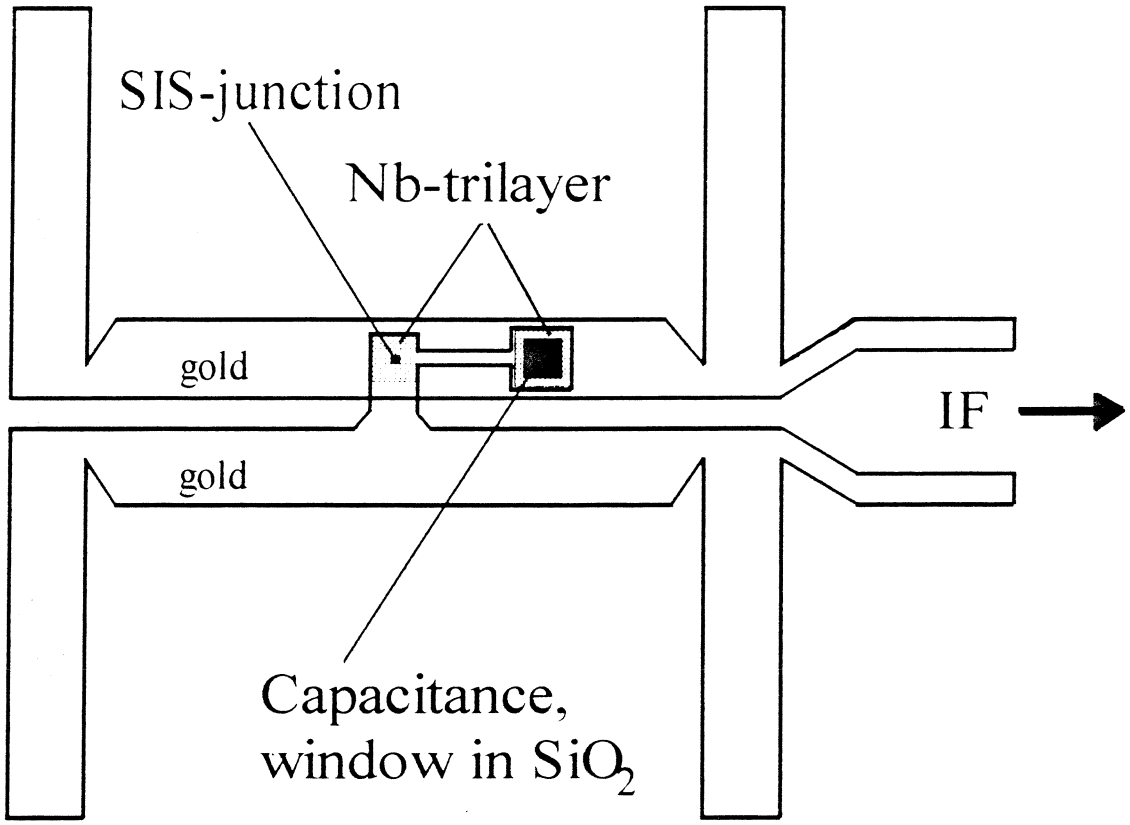
SIS-junction
Nb-trilayer
gold
gold
IF
Capacitance,
window in SiO2

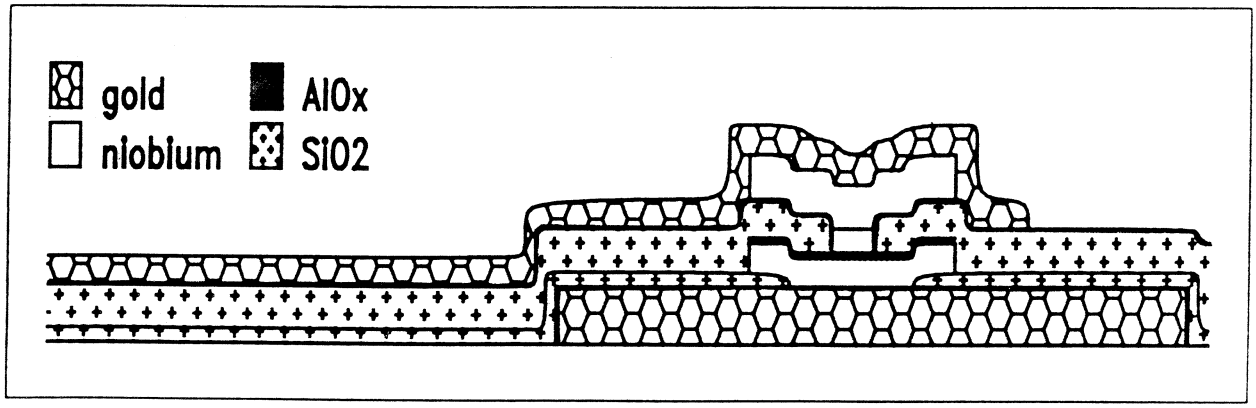
gold
niobium
AlOx
SiO2

Experimental Setup

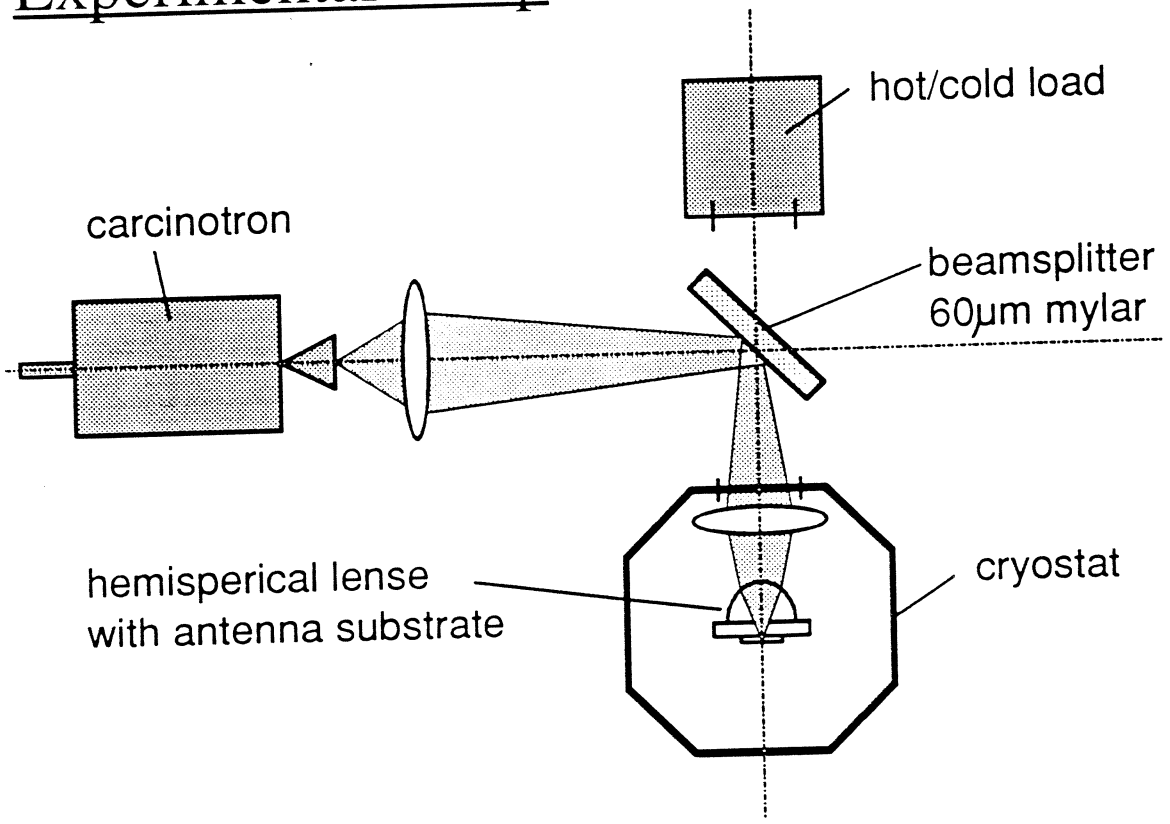

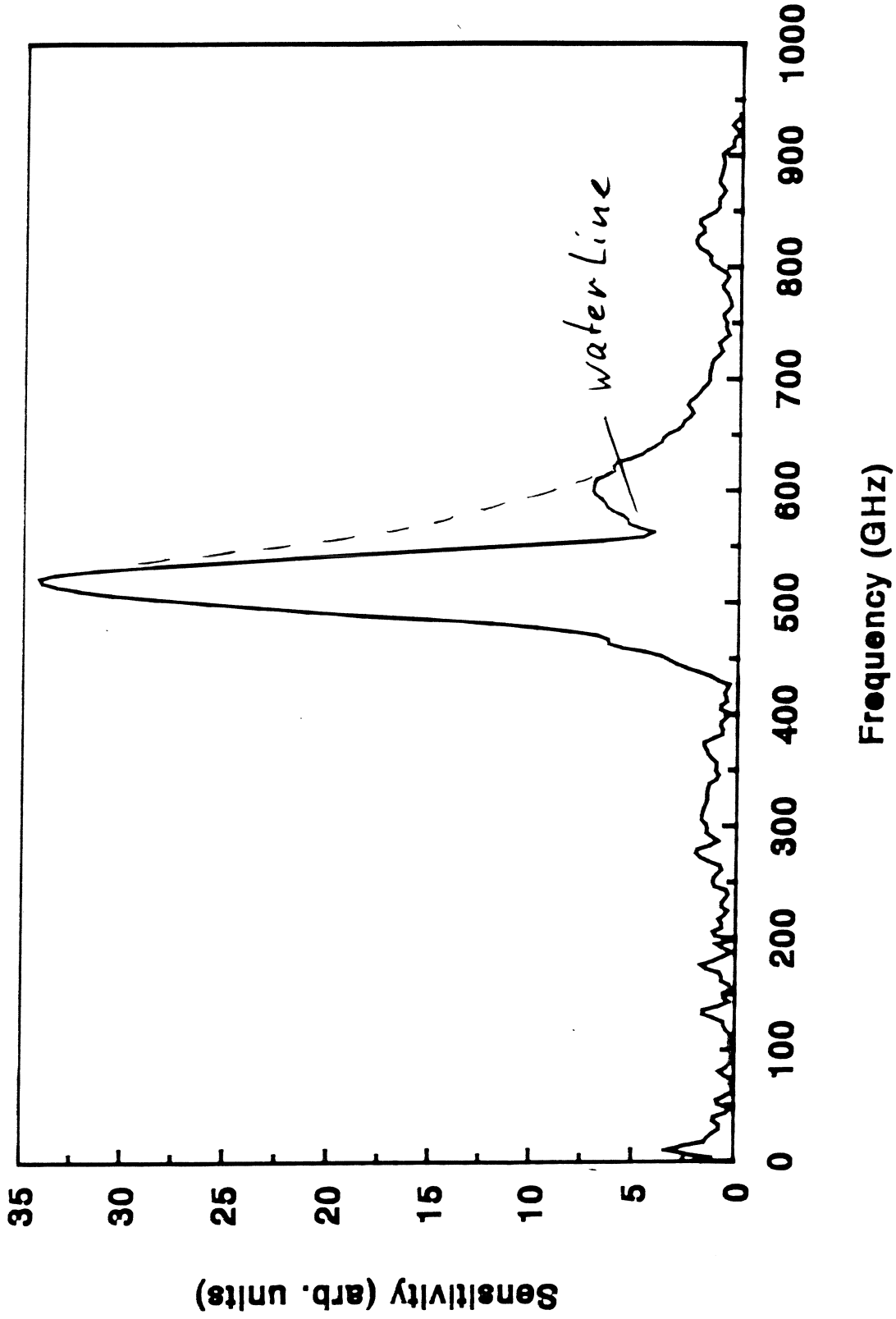
water Line
Sensitivity (arb. units)
0
5
10
15
20
25
30
35
0
100
200
300
400
500
600
700
800
900
1000
Frequency (GHz)

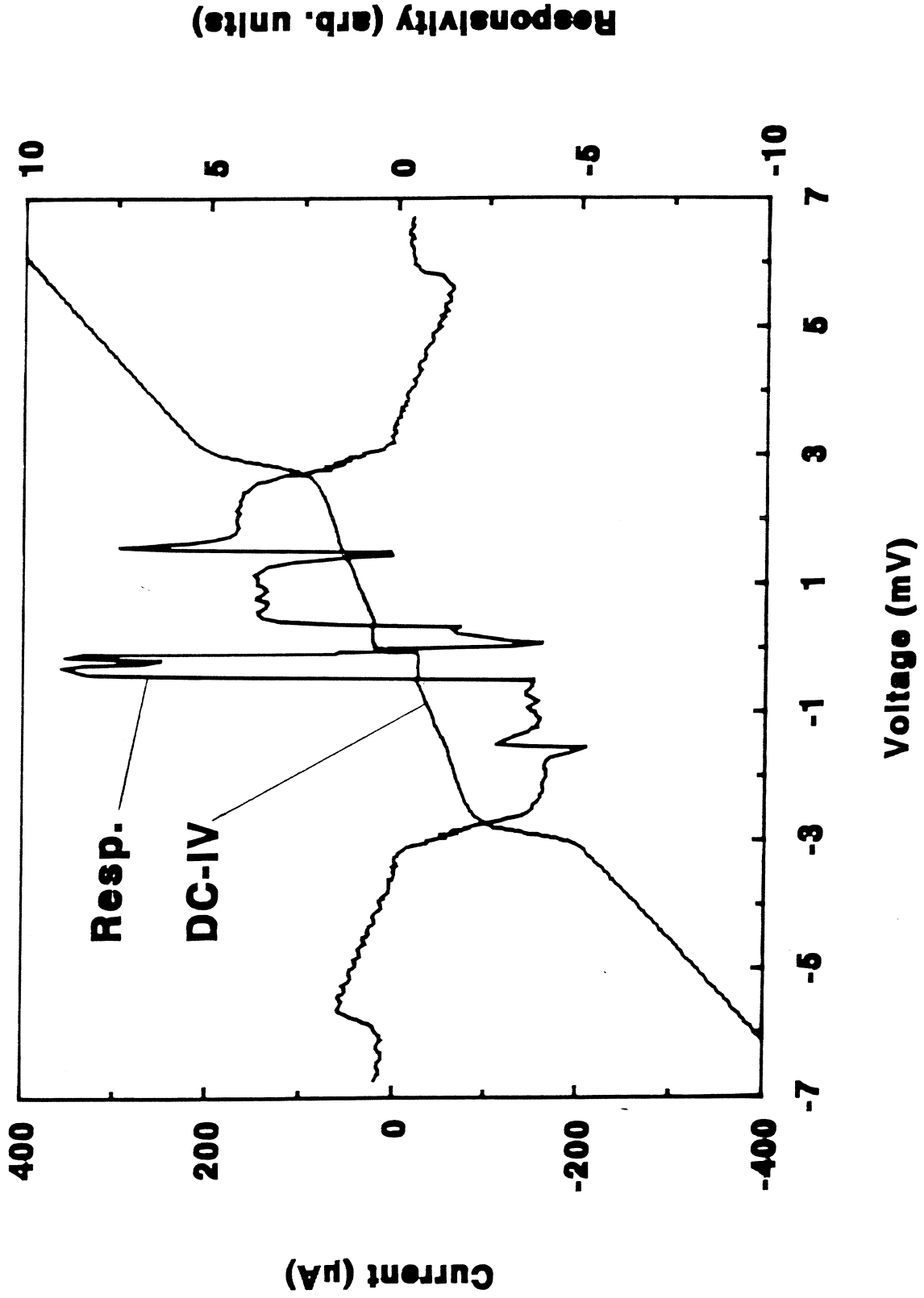
Responsivity (arb. units)
10
5
0
-5
-10
7
5
3
1
-1
-3
-5
-7
Voltage (mV)
Resp.
DC-IV
400
200
0
-200
-400
Current (μA)

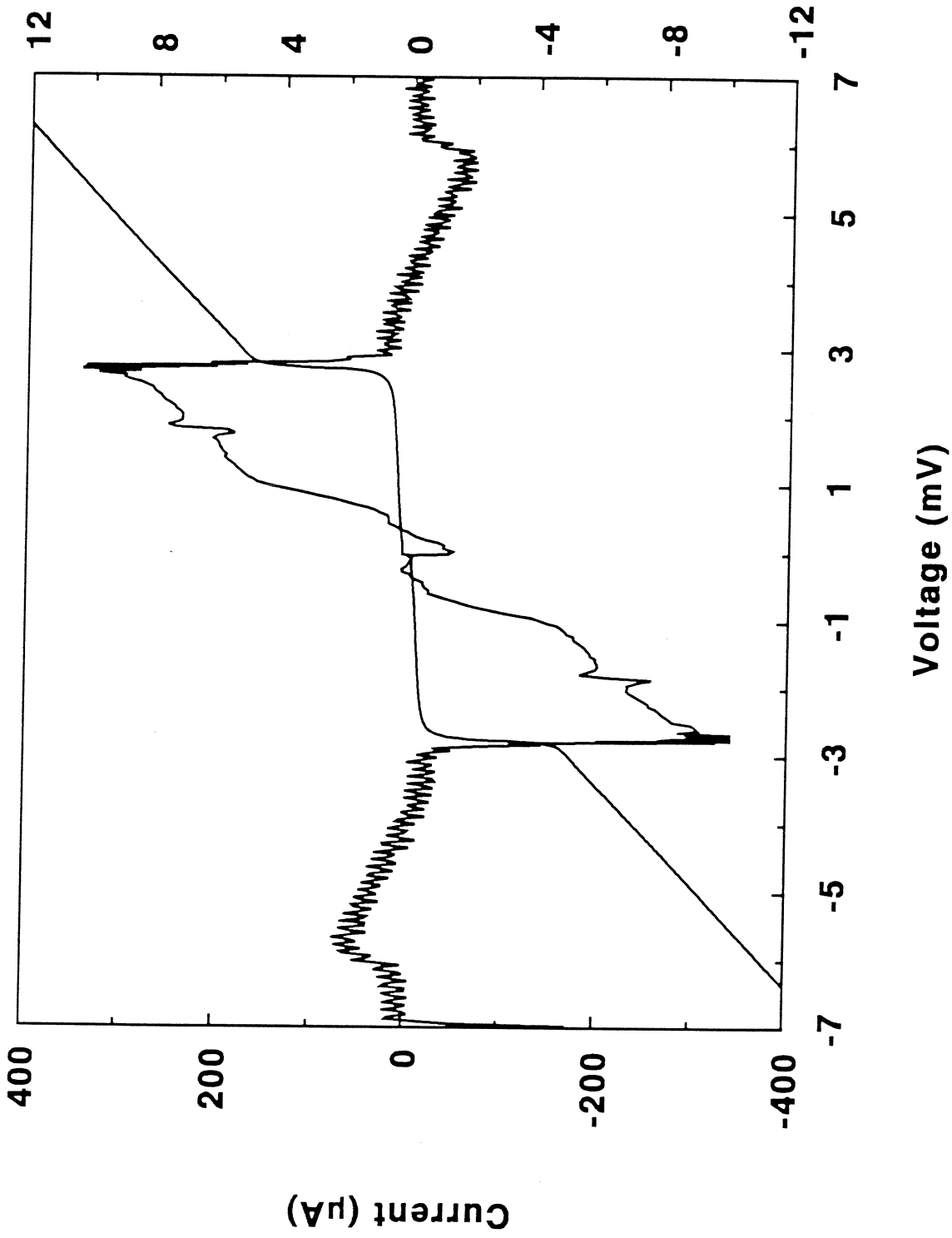
Responsivity (arb. units)
12
8
4
0
-4
-8
-12
Current (μA)
400
200
0
-200
-400
Voltage (mV)
7
5
3
1
-1
-3
-5
-7

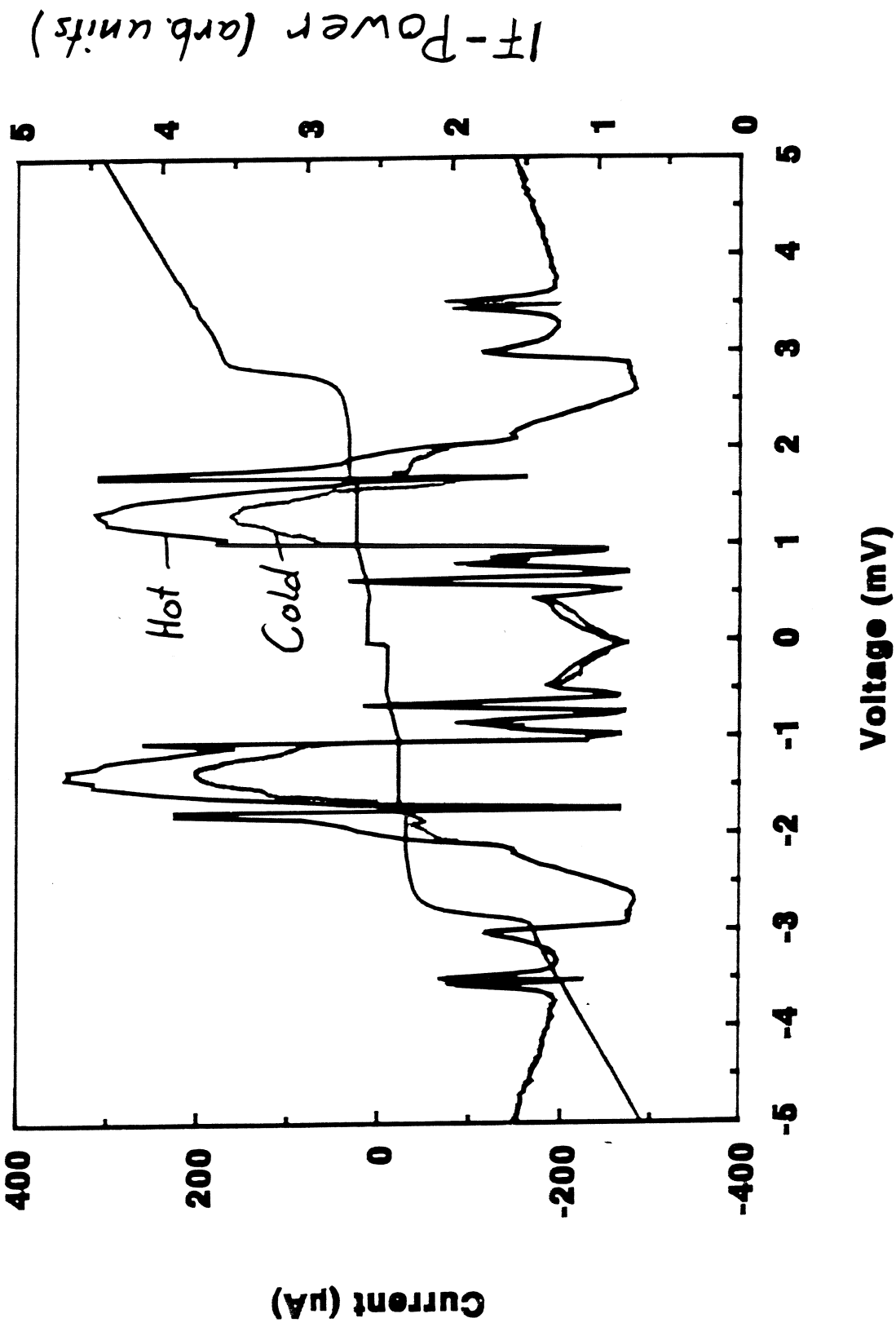
IF-Power (arb. units)
Hot
Cold
Current (μA)
400
200
0
-200
-400
5
4
3
2
1
0
-5
-4
-3
-2
-1
0
1
2
3
4
5
Voltage (mV)

Slot-Antenna SIS Mixers with Novel Tuning Circuits

Jonas Zmuidzinas*, H.G. LeDuc**, J.A. Stern** and S.R. Cypher**

SIS mixers operating at submillimeter wavelengths require tuning elements to compensate for the SIS junction capacitance in order to achieve optimum sensitivity. In particular, on-chip lithographic tuning elements are needed because they can be used either in quasi-optical or in waveguide mixers, and also because their typical broad-band response allows the construction of fixed-tuned mixers which are preferred for aperture-synthesis or focal-plane array instruments. Although such tuning circuits are now gaining acceptance in millimeter-wave SIS mixers, most of the circuits proposed to date do not scale well to the short submillimeter wavelengths. Some circuits become quite narrow-band when scaled to frequencies $\geq$ 500 GHz, while others become difficult to implement and are subject to large variations due to lithographic registration errors, etc. Our solution to this problem is to use a two-junction configuration, in which the two junctions are separated by an inductor which together with the junction capacitances forms a C-L-C "π"-circuit. This circuit can either be fed from one end only (asymmetrically) or from both ends with equal amplitude but opposite phase excitation (antisymmetrically). Because the inductance is controlled by the separation of the two junctions which are defined simultaneously in the fabrication process, the inductance can be precisely controlled and is nearly immune to lithographic registration errors. Furthermore, the predicted bandwidth of these circuits either approaches (for the asymmetric feed) or matches (for the antisymmetric feed) the bandwidth of an ideal inductively-shunted junction.

These tuning circuits could be used in a broad variety of SIS mixers, including both waveguide and quasi-optical designs. We have designed quasi-optical twin-slot antenna SIS mixers with both asymmetric and antisymmetric two-junction tuning circuits. In the asymmetric case, each slot antenna is coupled to its own two-junction circuit and the two IF outputs are combined; thus a total of four junctions are needed in this mixer. These devices were fabricated using direct-write electron-beam lithography and have been tested over the range 360-580 GHz, and receiver noise temperatures in the range 250-500 K (DSB) were measured. In addition, a receiver using this mixer design was flown aboard the NASA Kuiper Airborne Observatory in order to obtain astronomical observations over the range 490-580 GHz. We are now in the process of fabricating twin-slot mixers with antisymmetric tuning circuits. These devices need only two junctions and can be fabricated using optical lithography, even at frequencies approaching 700 GHz.

---

*Downs Laboratory of Physics, 320-47, California Institute of Technology, Pasadena, CA 91125

**Jet Propulsion Laboratory, 302-231, Pasadena, CA 91109

Progress on a Fixed Tuned Waveguide Receiver Using a Series–Parallel Array of SIS Junctions

Nils W. Halverson[1], John E. Carlstrom[1], David P. Woody[1],
Henry G. Leduc[2], and Jeffrey A. Stern[2]

I. Introduction

We are developing a 200 – 300 GHz receiver that incorporates multiple SIS junctions in a "series-parallel" configuration to achieve broadband impedance matching. At RF frequencies the junctions appear in series through capacitors, and at DC and IF frequencies they appear in parallel through inductors, so that the junctions are impedance matched to both the waveguide and the IF amplifier. Using a single fixed backshort and a full height waveguide, the receiver is designed to have a bandwidth of 100 GHz in the 230 GHz band. A similar design has been tested at frequencies around 100 GHz with excellent results by Shitov et al. (1991) and Vystavkin et al. (1993). Although our initial receiver is designed operate in the 200 – 300 GHz band, the design may be readily scaled to higher frequencies. In this paper we discuss computer and scale modeling of the device, fabrication, and preliminary test results.

II. The Design

By matching impedances at both the RF and IF ports, the sensitivity of the receiver is optimized through efficient coupling of the RF power into the junctions, and efficient coupling of the IF power into the IF amplifier. In a single SIS junction the RF input impedance is lower than the IF output impedance. At the same time the RF signal impedance in a waveguide is a few hundred ohms, while the standard IF amplifier input impedance is 50 ohms. This makes it difficult to match a single junction at both the RF and IF ports. In addition the junction has some parasitic capacitance which must be tuned out at the frequencies of interest. We have used electrically short ($<< \lambda/2$) integrated capacitors and inductors to connect an array of four SIS junctions in a series at the RF, and in parallel at the IF and DC, eliminating the mismatch problem (see Figure 1).

The series–parallel configuration also provides several other advantages. The inductors which connect the junctions in parallel are also used to tune out the junctions' parasitic capacitance. Junction uniformity is not critical since the junctions are DC biased in parallel through the inductors. Also, the match is broadband with a bandwidth of $\sim$ 100 GHz using a fixed backshort. This feature is particularly useful for the sideband separation receiver being developed at Caltech by Akeson et al. (1993), in focal plane arrays, and in multiple antenna arrays such as the forty dish Submillimeter Array proposed by NRAO. Lastly, a full height waveguide may be used, making the receiver easier to fabricate at higher frequencies.

---

[1] California Institute of Technology, Pasadena, CA
[2] Jet Propulsion Laboratory, Pasadena, CA

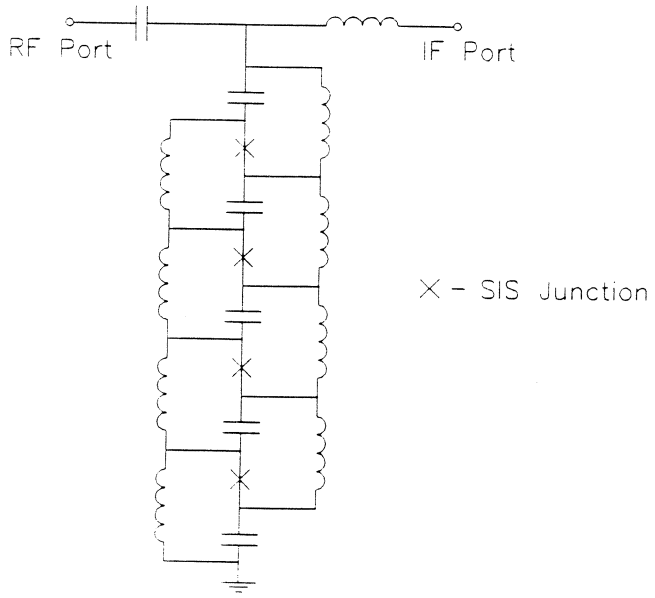

FIGURE 1. Schematic diagram for the series–parallel array of SIS junctions. The junctions, including parasitic capacitance, are represented by X's. The junctions are connected in parallel at the IF through inductors and in series at the RF through capacitors.

III. Computer and Scale Modeling

The device was computer modeled and optimized using EEsof's Touchstone[1] microwave circuit simulation program. The inductors and capacitors were modeled as lumped circuit elements, and the SIS junctions were simulated with parallel resistors and capacitors. Two basic designs were modeled, one in which the tuning elements were designed to couple RF power uniformly into each junction, and one which was stagger tuned for broader bandwidth (see Figure 2). In the stagger tuned design, the simple computer model did not take into account the variations in impedances between junctions due to unevenly coupled LO power. Testing of these devices in the near future will shed light on their feasiblity. Computer modeling predicted 40 GHz and 100 GHz bandwidth respectively for the two designs.

The tuning structures were scale modeled at 1 – 2 GHz, a scale factor of 175, in L-band full height waveguide. Terminated coplanar transmission line formulas were used to calculate inductor lengths. The circuit was etched on single sided PC board using chip capacitors and resistors to simulate the series capacitors and junctions. Delrin plastic with a dielectric constant $\epsilon_r \sim 3.8$ was used to simulate the quartz substrate. Initially, the resonance band of the scale model was significantly lower than computer model predictions, most likely due to mutual inductance between the coplanar inductors. This was

[1] EEsof Incorporated, Westlake Village, CA 91362

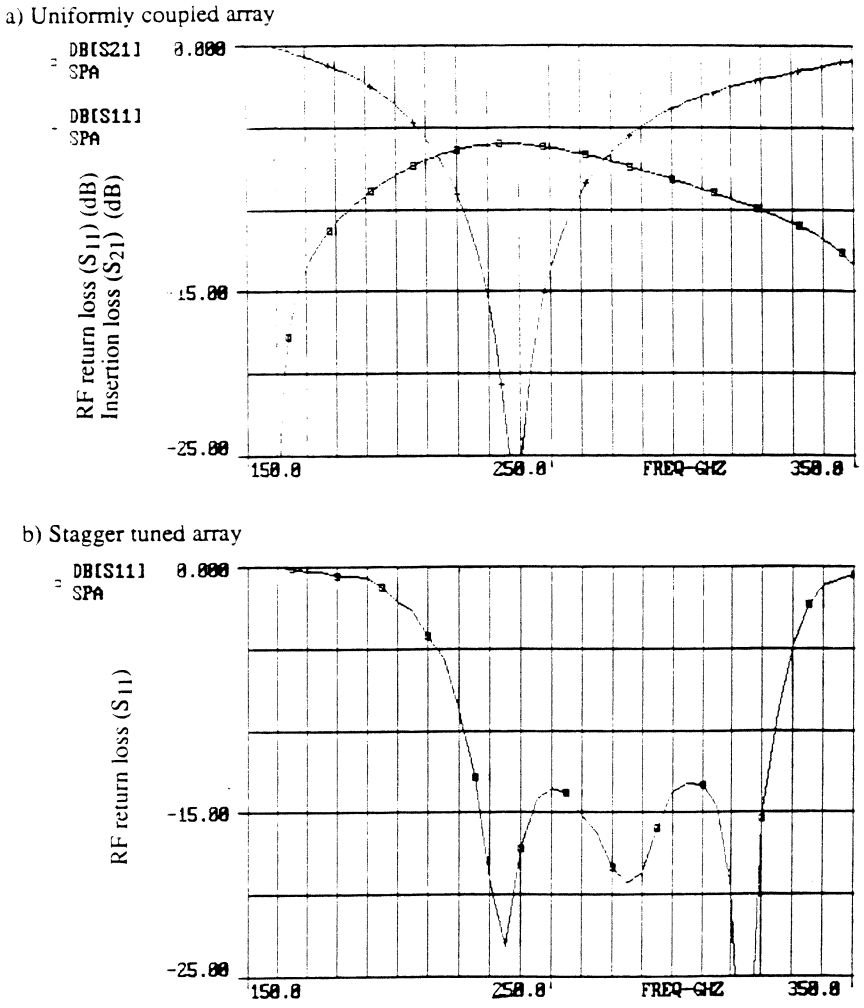

FIGURE 2. Series–Parallel array computer model predictions using lumped element circuit analysis and parallel resistors and capacitors to model the junctions. a) RF return loss and single junction insertion loss for a uniformly coupled array of 4 junctions. Each junction absorbs -6 dB of the input power at the design frequency, with 40 GHz bandwidth. The backshort is postioned 450μm from the array. b) RF return loss for a stagger tuned design, with 100 GHz bandwidth. The backshort is positioned 420μm from the array.

corrected empirically in the computer model. Figure 3 shows scale model results for uniformly coupled and stagger tuned arrays, with scaled bandwidths of 90 GHz and 50 GHz respectively, using a fixed backshort. Additional tuning flexibility is gained if the backshort is allowed to be adjusted. Structural complexities not modeled in the lumped circuit computer analysis caused the scale model resonances to differ somewhat from those predicted by Touchstone. In particular, the unexpectedly large bandwidth of the uniformly coupled array was surprising but encouraging. Despite these discrepencies the relatively simple computer models were a useful tool for predicting scale model performance. In the future we plan to simulate the device more accurately with a high frequency structure simulator.

a) Uniformly coupled array

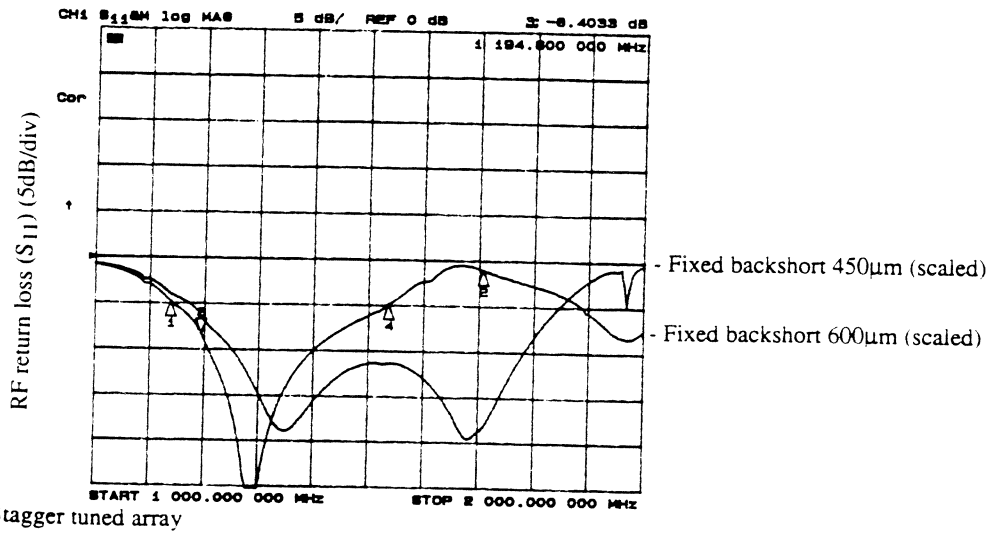

b) Stagger tuned array

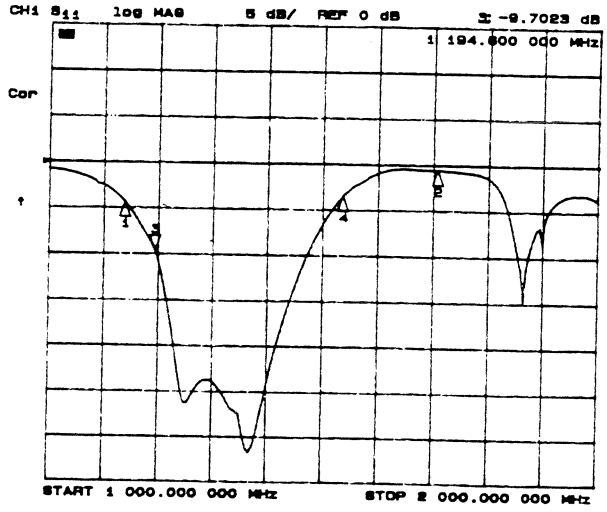

FIGURE 3. Series–Parallel array scale model measurements of RF return loss vs. frequency. Markers 1 and 2 represent scale frequencies of 200 and 300 GHz, respectively. a) Uniformly coupled array, with measurements for two backshort positions, $450\mu m$ and $600\mu m$ scaled. With backshort postion optimized the bandwidth is ~90 GHz. b) Stagger tuned array with backshort at $560\mu m$ scaled, and a bandwidth of ~50 GHz.

IV. Fabrication and Preliminary Test Results

The mixers were fabricated at the JPL Micodevices Laboratory using $Nb/AlO_x/Nb$ trilayer with critical current density $J_c \sim 10$ kA/cm^2. E-beam lithography was used to etch the $0.6\mu m \times 0.6\mu m$ junctions. The measured R_n is 16Ω for the array, near the designed value, with an ωRC product of 2.5. A photomicrograph of the uniformly coupled junction design is shown in Figure 4, with the SIS junction positions darkened for contrast.

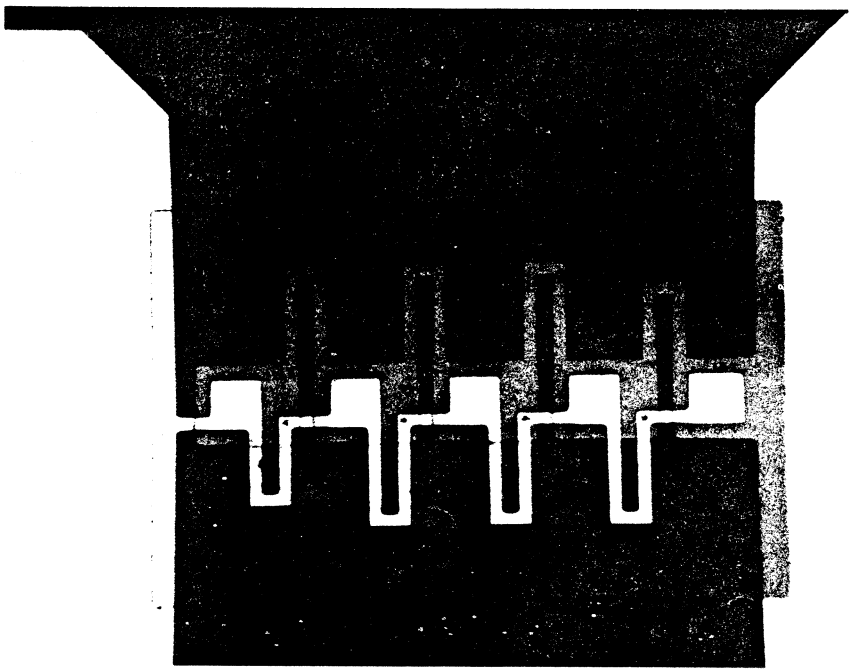

FIGURE 4. Photomicrograph of one of the uniformly coupled arrays. SIS junction locations are darkened for contrast. End inductors are shorter in order to couple RF power uniformly between junctions.

The outer inductors are shorter in order to couple RF power uniformly between the four junctions.

Before this conference there was only time to test one array from the first fabrication run. A full height waveguide for which the mixer was optimized was not available, and a reduced height waveguide was used instead. In initial tests of the uniformly coupled array a receiver noise temperature of 65 K was obtained at 210 GHz with a conversion loss of 4 dB calculated using the shot noise technique of Woody et al. (1985). As shown in the sample I-V curve in Figure 5, the junctions are well behaved thoughout the region of interest, with clearly defined LO steps and no apparent instabilities due to the Josephson effect.

In the test mixer block, a limited range of movement prevented the backshort from being placed at the optimal position 450μm from the array, as predicted by the scale model. Noise temperatures ranging from 65 to 140 K were obtained by tuning the backshort around the $3\lambda/4$ range at each frequency. With the backshort in a fixed position at $\sim 600\mu$m, we obtained receiver noise temperatures of 120 to 240 K throughout the range of the local oscillator, as seen in Figure 6.

These preliminary results are very encouraging, yielding respectable noise temperatures and demonstrating the broad bandwidth of the device. We are presently working on testing variations of the uniformly coupled and stagger tuned arrays in a full height waveguide mixer block. We expect that in proper testing conditions the noise temperatures demonstrated with the first array will be significantly reduced. We look forward to

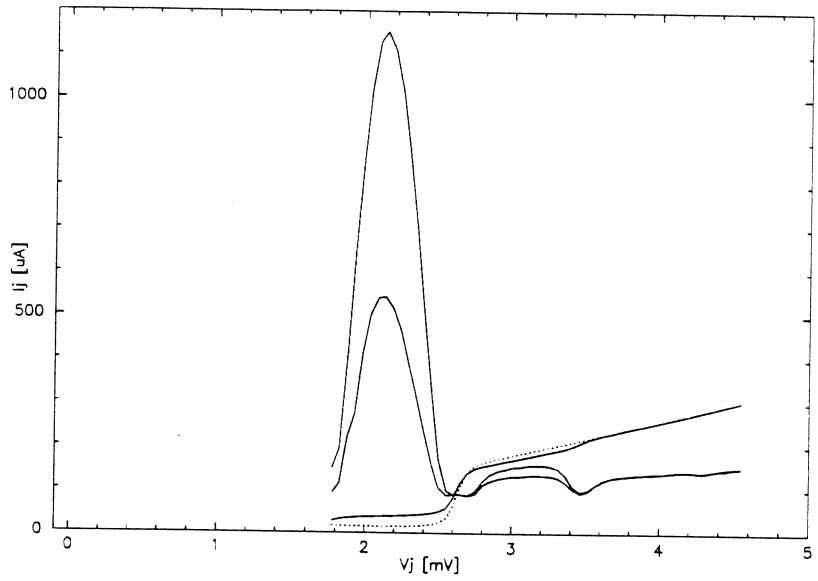

FIGURE 5. A sample I-V curve with LO off and with LO applied, and IF power with hot and cold loads. The junctions are well behaved thoughout the region of interest.

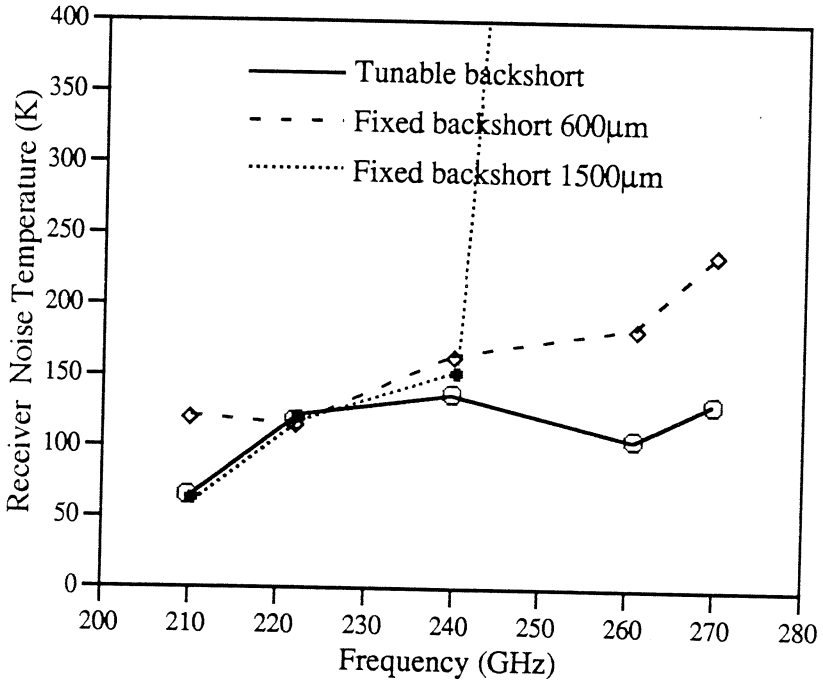

FIGURE 6. Preliminary measurements of receiver noise temperatures for the series–parallel array. The three lines represent noise temperatures using a tunable backshort, a fixed backshort at $\sim 600\mu$m and at $\sim 1500\mu$m. Tests were conducted using a reduced height waveguide mixer block. The array was optimized for a full height waveguide, but one was not available at the time the measurements were taken.

continued testing of the devices, and submillimeter devices in future iterations. We plan to implement successful devices at the Owens Valley Millimeter Array.

References

R. L. Akeson, J. E. Carlstrom, D. P. Woody, J. Kawamura, A. R. Kerr, S. -K. Pan, and K. Wan, "Development of a Sideband Separation Receiver at 100 GHz," 1993, *Fourth International Symposium on Space Terahertz Technology*, (In these proceedings).

S. V. Shitov, V.P. Koshelets, S.A. Kovtonyuk, A. B. Ermakov, N.D. Whyborn, and C.O. Lindstrom, "Ultra-Low-Noise 100 GHz Receiver Based on Parallel Biased SIS Arrays," 1991, *Supercond. Sci. Tech.*, Vol. 4, pp. 406-408.

A.N. Vystavkin, V.P. Koshelets, V. Y. Belitsky, G.V. Prokopenko, A.V. Shchukin, S.V. Shitov, and M.A. Tarasov, "Integration of SIS Mixers, Superconducting Local Oscillators and Other Elements into Receiver chips for 100 – 700 GHz," 1993, *Fourth International Symposium on Space Terahertz Technology*, (In these proceedings).

D.P. Woody, R.E. Miller, and M.J. Wengler, "85 – 115 GHz Receivers for Radio Astronomy," 1985, *IEEE Trans. Microwave Theory Tech.*, Vol. 33, pp.90-95.

PLANAR GRID OSCILLATORS FOR QUASI-OPTICAL POWER COMBINING AT 37 GHz

A. Torabi, H. M. Harris, R. W. McMillan, S. M. Halpern, J. C. Wiltse, D. Gagnon[1], D. W. Griffin[2] and C. J. Summers
Electro-Optics and Physical Sciences Laboratory
Georgia Tech Research Institute
Atlanta, Georgia 30332

Abstract

We have investigated a planar grid array of HEMTs placed in a semi-confocal open resonator to explore quasi-optical power combining at Ka-band. The grids were designed for 38 GHz, 30 GHz, and 25 GHz and they operated at 37.4 GHz, 29.3 GHz and 24.8 GHz, respectively. Under the conditions of these tests, the grid geometry is the dominant factor in setting the frequency of oscillation. We have measured 8 mW from a column of three devices placed in a grid with at least 6% DC to RF conversion efficiency.

Introduction:

Solid state semiconductor millimeter wave (MMW) sources are small, inexpensive, lightweight, operate at low power, can operate up to terahertz frequencies, and can be integrated into circuits with a large number of devices. To achieve high output power, it is necessary to combine the power from these sources. Ideally such combiners should accommodate a large number of devices in the form of a compact array that operates as a synchronized assembly free of multimoding problems.

An attractive scheme for power combining has been suggested by Mink (1) and has been studied by several investigators (2-4) at frequencies up to Ku-band. In this technique, single devices are embedded in a two dimensional array such that they operate and produce a uniformly coherent beam perpendicular to the array. The array is placed in a Fabry-Perot resonator to provide the feedback to synchronize all oscillators and stabilize the frequency. The mutual coupling between the devices in the array is governed by the

---

[1] Naval Air Warfare Center, Weapons Division, China Lake, CA. 93555.

[2] On leave from University of Adelaide, Australia.

geometry of the grid. An advantage of this method of power combining is that the combining occurs in free space where the losses are close to zero. A theoretical analysis of the grid oscillator has been given by Popović et al. (2) and by Weikle (5), where an equivalent circuit for the grid in the quasi-optical resonator is presented, along with formulae for calculating equivalent circuit values.

This analysis has been used to design grids for operation between 25-40 GHz. Modifications to an ideal grid geometry were necessary to incorporate the high electron mobility transistor (HEMTs) millimeter wave sources at the lattice sites of the array. The nature of coupling as well as grid performance have been studied by fabricating grids with single device, 1x3, 3x1, 3x3 and 4x4 arrays. The grid design and the testing of the arrays are presented here.

Grid Design:

Following Weikle, the grid was modeled as an infinite two dimensional array with transistors set in a periodic fashion in two directions. Figure 1a shows the actual grid layout, which nearly fulfills our assumption. It is further assumed that each cell of the periodic grid with the transistor at the center is square and can be modeled as an equivalent waveguide with sides "a" and electric and magnetic walls at the boundaries as shown in Figure 1b. The vertical lines are drain and source connections and the horizontal line at the middle of the square is the gate control. The horizontal lines at the upper and lower boundaries are the drain and source bias lines. The inductance L due to vertical fingers used as drain and source millimeter circuit components, the distributed inductance L_m and the distributed capacitance C_m due to horizontal bias supply lines have been calculated. When these results are combined with the transistor parameters, the loop gain for the grid transistor oscillator can be obtained.

For a square unit cell of dimensions a, we obtain the inductance of the vertical finger leads from:

$$L(f,a) = \frac{a\mu}{\pi} \times \sum_{p=1}^{\infty} \frac{Sinc^2(p \cdot K)}{(\sqrt{(p^2 - f^2 a^2 \epsilon\mu)})} \qquad (1)$$

The distributed inductance due to the horizontal leads is:

$$L_m(f,a) = \frac{4\mu a}{(2\pi)^3} \sum_{p=1}^{\infty} \sum_{n=1}^{\infty} \frac{(Sin(nM)\,Sinc(pK)\,Sinc(nQ))^2}{[p^2+(n/2)^2]} \times \frac{[(2p/n)+(n/(2p(1-w/a)))]^2}{\sqrt{[(p^2+(n/2)^2-(fa)^2\epsilon\mu]}} \qquad (2)$$

and the distributed capacitance due to horizontal lines is:

$$\frac{1}{C_m(f,a)} = \frac{1}{a\pi\epsilon}\left[\sum_{n=1}^{\infty}\left(\frac{2}{n}Sin(nM)\,Sinc(nQ)\right)^2 \times \sqrt{\left[\left(\frac{n}{2}\right)^2-(fa)^2\epsilon\mu\right)} + 2\sum_{n=1}^{\infty}\sum_{p=1}^{\infty}(Sin(nM)\,Sinc(pK)\,Sinc(nQ))^2 \times \left(\frac{\sqrt{\left[p^2+\left(\frac{n}{2}\right)^2-(fa)^2\epsilon\mu\right)} \times (1-1/(1-w/a))^2}{p^2+(n/2)^2}\right)\right] \qquad (3)$$

where p=m/2 and m and n are TE and TM mode numbers, K=πw/a, M=π/2, Q=πw$_s$/2a, a is the unit cell size, w and w$_s$ are the widths of the vertical and horizontal lines and are set to 0.1a, f is the frequency, ϵ is the substrate dielectric constant and μ is the permeability of the substrate.

Figure 2 shows L as a function of frequency and unit cell size. The vertical lead inductance, L, is a relatively slowly varying function at low frequencies, but as the frequency approaches a particular value for each unit cell size, L rapidly increases to infinity. Above this frequency L is complex and below it L is real. We have plotted only the real part of L, since it is the real part of the inductance that directly couples with the fields. The imaginary part of the inductance appears to be associated with evanescent modes. The value of L slowly increases with increasing unit cell size as can be observed from equation 1. The discontinuities in this figure indicate where L becomes infinite; however, it appears as finite because of the incremental steps of calculation. The heights of the discontinuities in this figure are not very significant, but their positions indicate the frequencies at which the impedances associated with vertical fingers pass through resonance. Figure 3 shows a similar plot for L_m. Both the frequency and unit cell size dependencies are similar to figure 2.

The distributed capacitance C_m of the grid due to the horizontal lines was similarly calculated and is shown in figure 4. Here even though C_m has a similar behavior to L and L_m, the first singularity occurs at a much lower frequency, that is, for given parameters, C_m becomes complex at a much lower frequency than L and L_m.

In evaluating grid parameters, we found that the above calculation provides an acceptable means of obtaining L, L_m and C_m at frequencies well below the singularities, but not in their vicinities. Immediately below their singularities these parameters vary rapidly and one cannot extract an accurate value for them at a given frequency.

The singularities occur because a term in the denominator of each expression becomes zero at a particular frequency. In equation 3, the lowest frequency at which C_m increases rapidly and becomes complex, occurs when p=0 and n=1 and:

$$[(n/2)^2 - (fa)^2\mu\epsilon]^{1/2}=0$$

$$f=[2a(\mu\epsilon)^{1/2}]^{-1} \qquad (4)$$

which is the resonant frequency of a half wave dipole antenna. Based on this method, we have calculated the frequency and spectral dependance of grids and have designed, fabricated and tested them.

Grid Fabrication and Cavity Design:

Quartz was used as the substrate material based on the requirement of having a substrate material with a low dielectric constant, high heat conductivity as well as chemical compatibility with photolithography techniques. For this study, we have used substrates with thicknesses from 1.0 to 2.5 mm corresponding to dimensions equivalent to $\lambda/4$ to $5\lambda/8$ of the radiating fields.

RF sputtering was used to deposit chrome-gold metallization on quartz substrates, which were then electroplated to 2 μm with gold. This thickness is over four skin depths of gold at Ka-band. Photolithographic techniques were employed to pattern the metallization. The HEMT chips which have dimensions of 0.45 mm X 0.34 mm were then die attached to the gate bias line at the center of each unit cell. The electrical connections to the HEMTs are made by wire bonding the drain, source and gate to the grid using 0.7 mil gold wire. The width of the grid lines is one tenth of the unit cell size or 0.2 mm to 0.3 mm. This is considerably less than the size of the HEMT chip, which forced us to deviate from an ideal symmetric grid in order to keep the source connections parallel with the gate and drain connections. Figure 5 shows the bonding and placement of a single HEMT in the final grid design.

The drain, source and gate pads along the edges of the grid were wired to external power supplies. We have used ferrite beads on each connecting wire to eliminate low

frequency oscillations. This assembly was attached to a polished aluminium plate which was also the back reflector of the Fabry-Perot resonator. The front reflector is a spherical partially reflecting mesh whose details are given elsewhere (6). This reflector had a reflectivity of 85% and was placed about 25 cm away from the grid. The resonator was tuned by adjusting the position of the back reflector relative to the front reflector. Figure 6 presents a schematic diagram of the power combining cavity assembly.

The sources used are Mitsubishi MGFC-4414 pseudomorphic HEMTs with gate length of 0.3 μm and gate width of 150 μm. These devices are low-noise transistors with a unity gain frequency of greater than 60 GHz. Since our goal was to demonstrate feasibility of power combining at Ka-band, these transistors fit our requirements.

Figure 7 presents a schematic of the test and measurement system. After a grid was installed within the resonator and connected to the power supplies, the signals were collected by a lens and focused into a horn. A 10dB directional coupler provides input to a spectrum analyzer via a mixer and IF amplifier. The rest of the output was fed to a thermistor to measure power. We estimate that the measuring system intercepts 20% of the power radiated by the grid oscillator.

Results and Discussion:

Grid oscillators of various dimensions were fabricated and tested. As a test of Weikle's formulation, which assumes plane TEM waves incident on the grid, we performed reflectance measurements from 30 GHz to 50 GHz on designed grids and compared these results with the calculated values. Details of the technique have been published previously (7). The magnitude and phase of the reflectance for three different grid designs are shown in Figures 8a, 8b, and 8c along with a comparison with the model. Figures 8a and 8b show measurement results of earlier grid designs and figure 8c shows the results of the final grid design. A comparison of the data shows that as the grid designs deviated from an ideal symmetric grid, the magnitude and phase of the reflectance deviated from the theoretical model and as we refined the grid design by extending the vertical fingers a better agreement with the model was achieved. Based on these measurements we designed the final grid geometries.

To test Equation (4), grids of different unit cell size were evaluated. To coarsely measure the grid oscillation frequency, we placed a wavemeter in series with the power meter and searched for a dip in the magnitude of the signal by tuning the wavemeter from 26 to 40 GHz and in a separate

assembly from 18 to 26 GHz to look for the absence of subharmonics. Further we tuned the open resonator length and found that oscillations appeared at $\lambda/2$ intervals. Table 1 lists the results of these evaluations. Figure 9 shows a plot of the frequency dependence of Equation (4) compared with the experimentally determined oscillation frequencies of the grids fabricated in this work, as well as those in the literature.

Table 1. Grid arrays tested in Ka-band.

Grid array	Unit cell size (mm)	Predicted Frequency (GHz)	Measured frequency (GHz)
3x3	2.0	38	37.4
1x3	2.5	30	29.3
1x3	3.0	25	24.8
1x3	2.15	35	
1x3	2.3	33	

From the above results it is apparent that the dominant factor in frequency determination is the grid geometry and specifically the unit cell size. Other factors such as the active device, the Fabry-Perot cavity and the grid line widths have lesser influence. It should be stated that this frequency is for an unobstructed grid coupled to the free space within or outside the open resonator. Placement of the grid within a closed cavity that alters the effective impedance at the grid will change this frequency to a lower value.

Figure 10 shows the spectra of the 1x3 grid with 2.5 mm unit cell. Figure 10a indicates a narrow spectrum, while Figure 10b shows the purity of the signal. The spectra of Figure 10 is nearly the same for a single HEMT in the grid or for 1x3 or 3x3 arrays. This is another indication that the grid geometry is the dominant factor in frequency and spectrum determination.

The oscillation frequency was tunable over 12 MHz by either the gate bias or the cavity tuning, however this tuning was at the expense of a decrease in output power. Figure 11 shows the electronic tuning range for a 3x3 grid at 37.4 GHz.

In measuring the radiated power from the grid outside the cavity, it is estimated that less than 20% of the radiation is intercepted. Considering that the grid radiates into one half of free space, with an impedance of 377Ω, any

disturbance of this arrangement by placing a collector horn near the grid alters the impedance that is presented to the transistor grid and hence a reduction in output power may occur. We have measured the emitted power from the 1x3 array by bringing a high gain horn in close contact with the ground plane and measured 8 mW of output power. The grid was operated at 2.5 V drain to source bias and 53 mA, which results in 6% DC to RF conversion efficiency. It should be noted that this is the minimum power radiated by the grid. When the grid is oscillating in the open resonator or in unobstructed free space, the output RF power and efficiencies should be higher.

To study the role of substrate thickness on the power we varied the substrate thickness from 1.5 to 2.5 mm ($3\lambda/8$ to $5\lambda/8$) and observed the variation shown in Figure 12. The peak power appears at a substrate thickness of $\lambda/2$. The line through the data points is empirical.

Conclusions:

We have designed, fabricated and tested a series of planar grid oscillator arrays at Ka-band. The experimental frequency determinations agree well with those obtained for half wave dipole antenna resonances. The fabricated grids oscillate at 37.4, 29.3 and 24.8 GHz. We have obtained 8 mW of power from a 1x3 array with 6% DC to RF conversion efficiency.

We acknowledge the US Army Research Office and SDIO/US Army Strategic Defense Command support for funding this work under contract number DAAL03-91-G-0160. Opinions, interpretations, conclusions and recommendations are those of the authors and are not necessarily endorsed by the US Army.

References:

1. James W. Mink, "Quasi-Optical Power Combining of Solid State Millimeter Wave Sources" IEEE Trans. Microwave Theory Tech., MTT-34, pp. 225-279, February, 1986.

2. Z. B. Popović, R. M. Weikle, II, M. Kim, and D. B. Rutledge, "A 100 MESFET planar grid oscillator," IEEE Trans. on Microwave Theory and Techniques, Vol. 39, Feb. 1991, pp. 193-200.

3. Z. B. Popović, R. M. Weikle, II, M. Kim, K. A. Potter, and D. B. Rutledge, "Bar Grid Oscillators," IEEE Trans. on Microwave Theory and Techniques, Vol. 38, Mar. 1990, pp. 225-230.

4. R. M. Weikle, II, M. Kim, J. B. Hacker, M. P. DeLisio, and D. B. Rutledge, "Planar MESFET Grid Oscillators Using Gate Feedback," IEEE Trans. on Microwave Theory and Techniques, Vol. 40, Nov. 1992, pp. 1997-2003.

5. R. M. Weikle, II, "Quasi-optical Planar Grids for Microwave and Millimeter-Wave Power Combining," Ph.D. thesis, California Institute of Technology, 1992.

6. H. M. Harris, A. Torabi, R. W. McMillan, C. J. Summers, J. C. Wiltse, S. M. Halpern, and D. W. Griffin, "Quasi-Optical Power Combining of Solid State Sources in Ka-Band," accepted for presentation at the IEEE MTT-S International Microwave Symposium, Atlanta, Georgia, June 15, 1993.

7. D. R. Gagnon, "Highly Sensitive Measurements with a Lens Focussed Reflectometer," IEEE MTT-S International Symposium Digest, Vol. 3, pp. 1017-108, Boston, Ma., 1991.

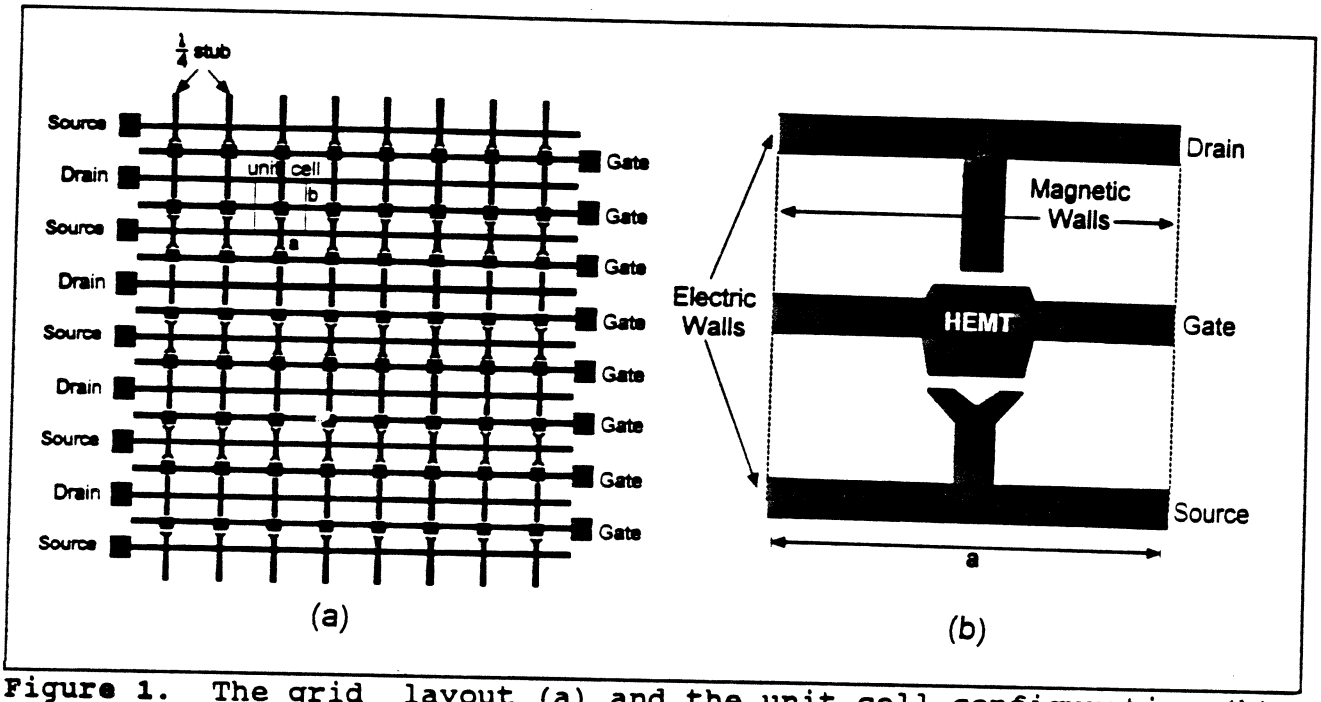

Figure 1. The grid layout (a) and the unit cell configuration (b).

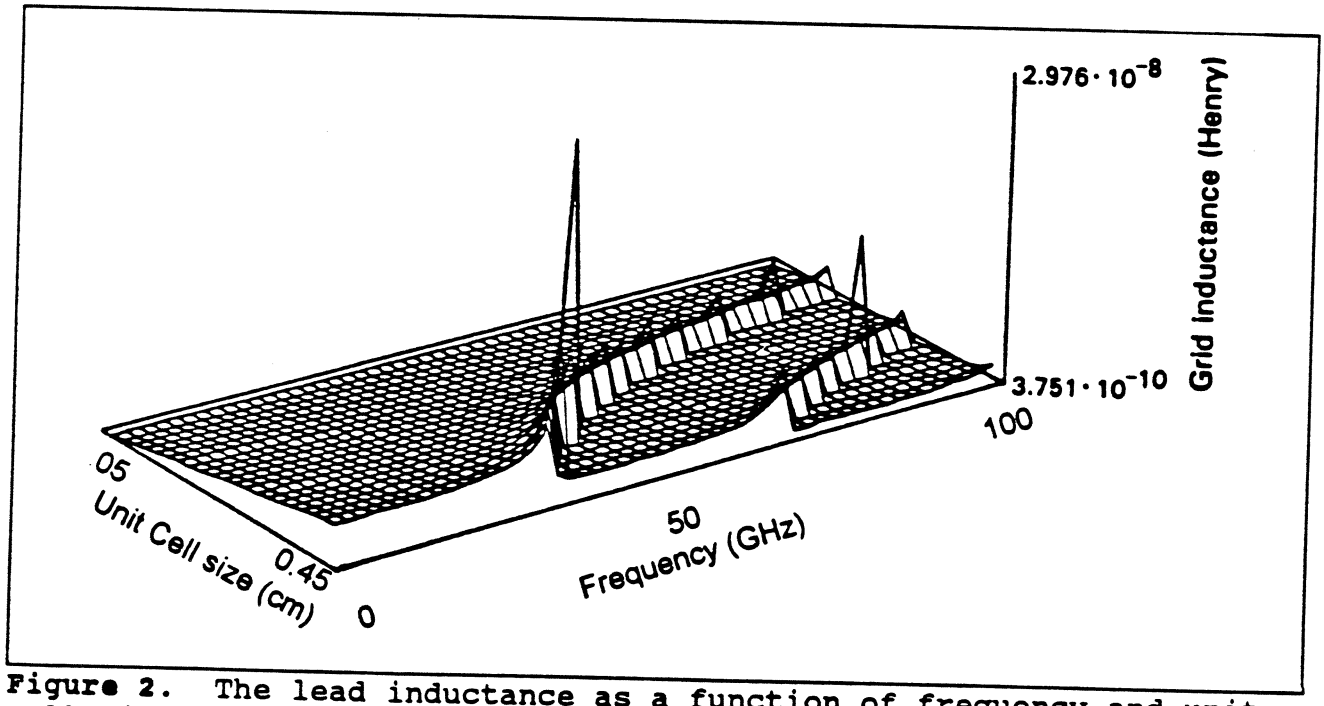

Figure 2. The lead inductance as a function of frequency and unit cell size.

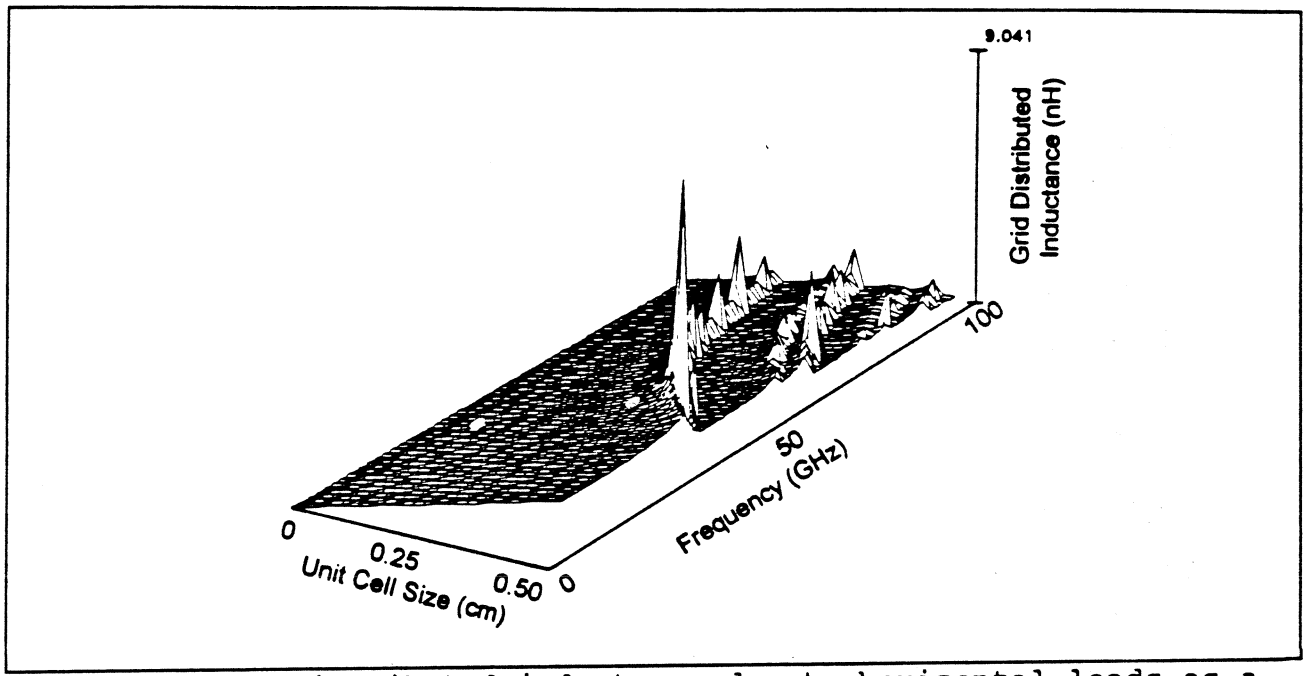

Figure 3. The distributed inductance due to horizontal leads as a function of frequency and unit cell size.

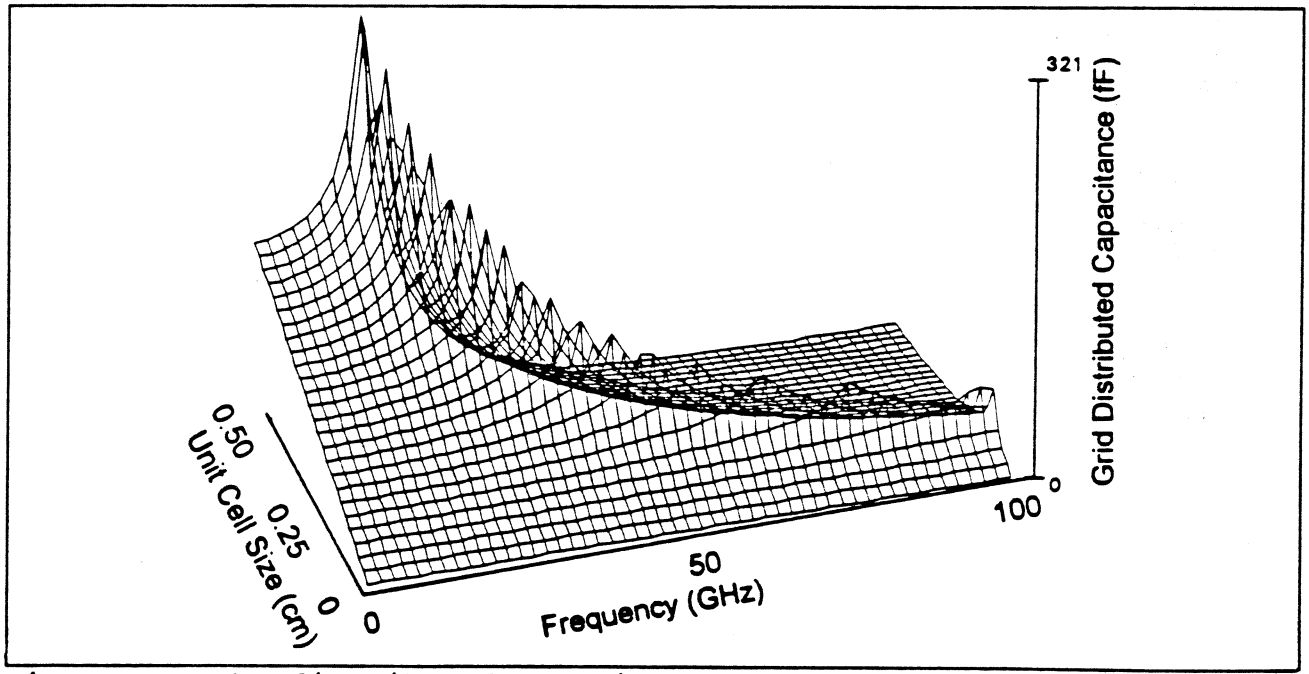

Figure 4. The distributed capacitance due to horizontal leads as a function of frequency and unit cell size.

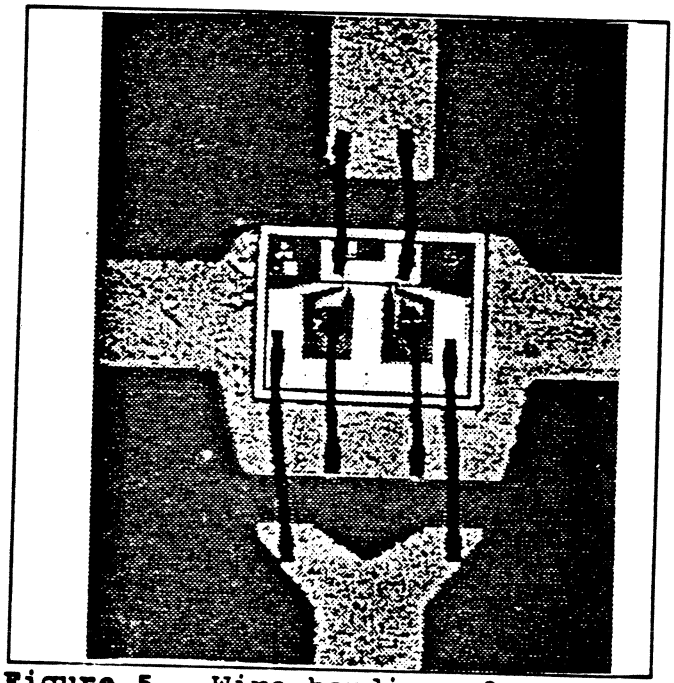

Figure 5. Wire bonding of a HEMT in the grid oscillator array.

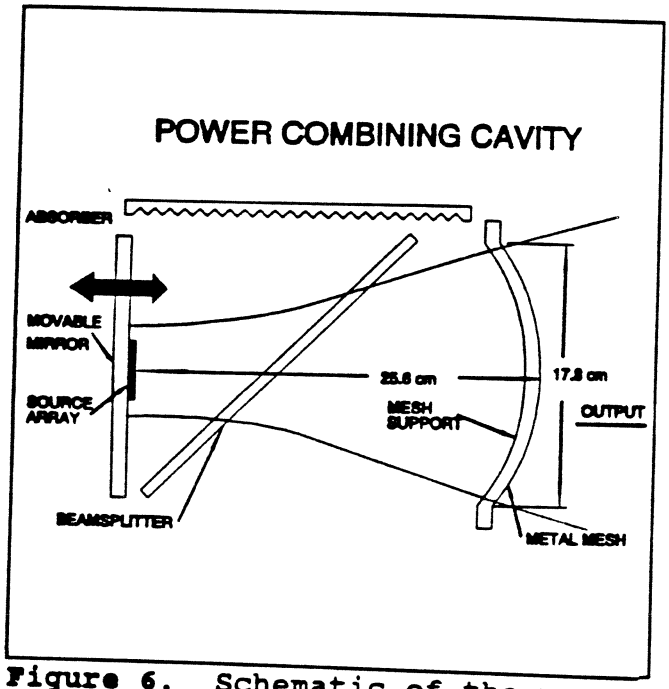

Figure 6. Schematic of the power combining cavity.

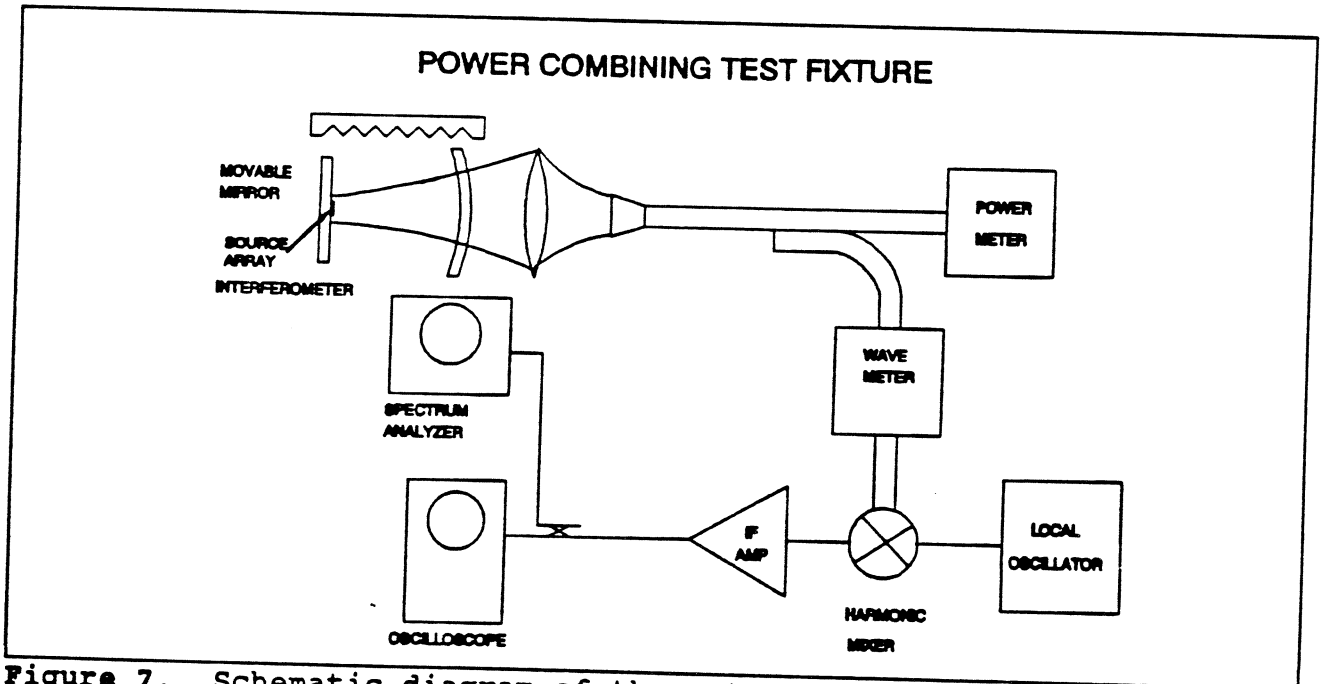

Figure 7. Schematic diagram of the output power and spectrum measurement system.

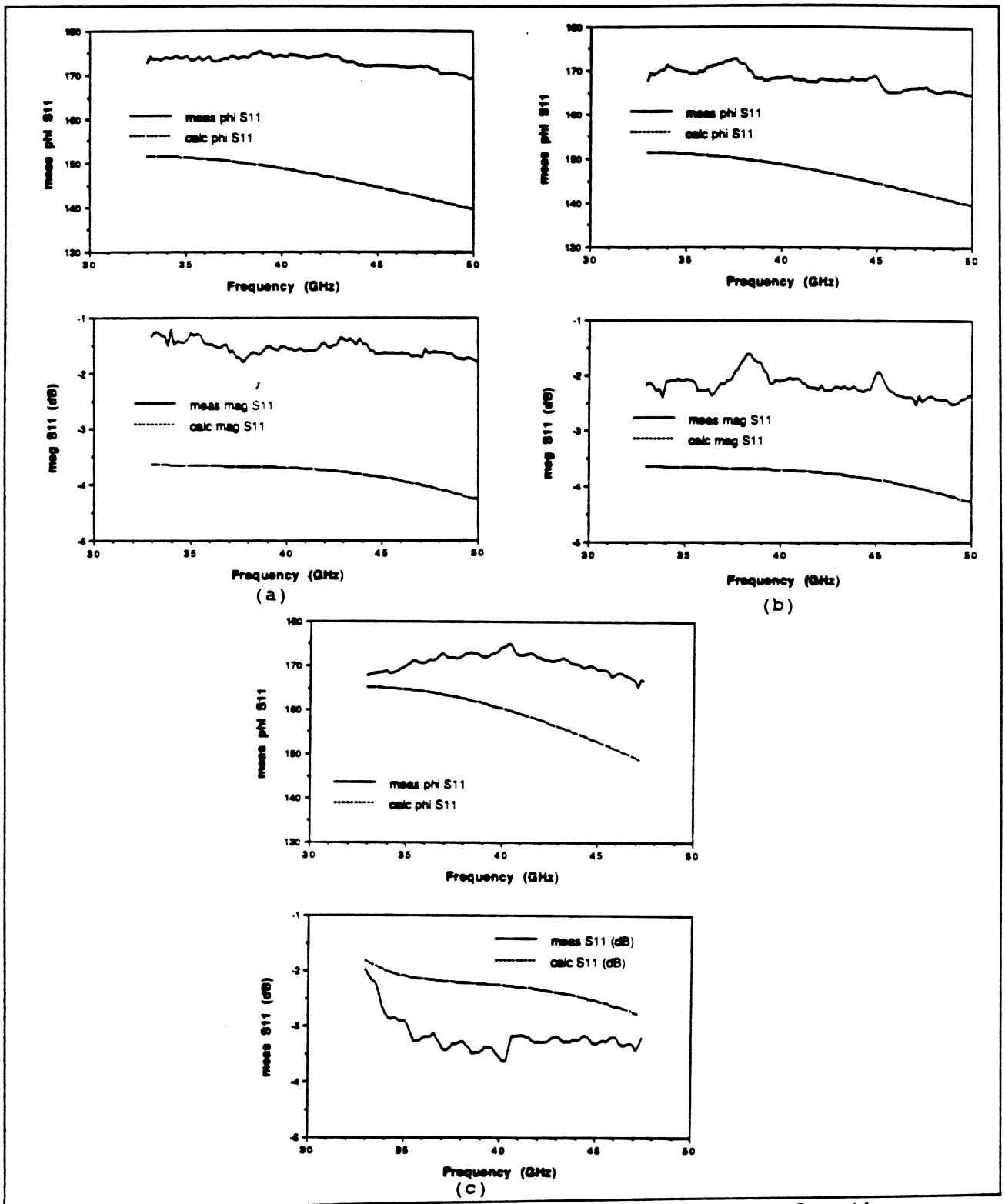

Figure 8. The magnitude and phase of the reflectance for three different grid designs. Design (c) was used in the final grid.

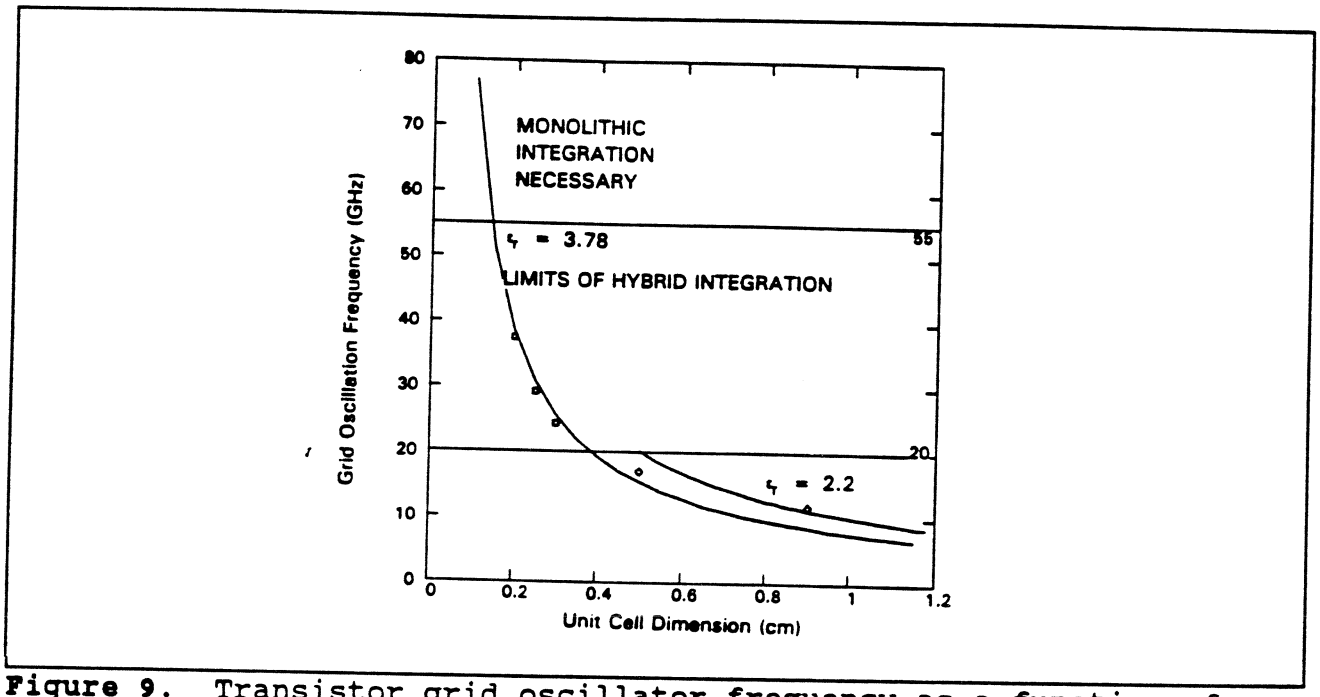

Figure 9. Transistor grid oscillator frequency as a function of unit cell size. The squares are experimentally measured frequencies and the diamonds are from reference 5.

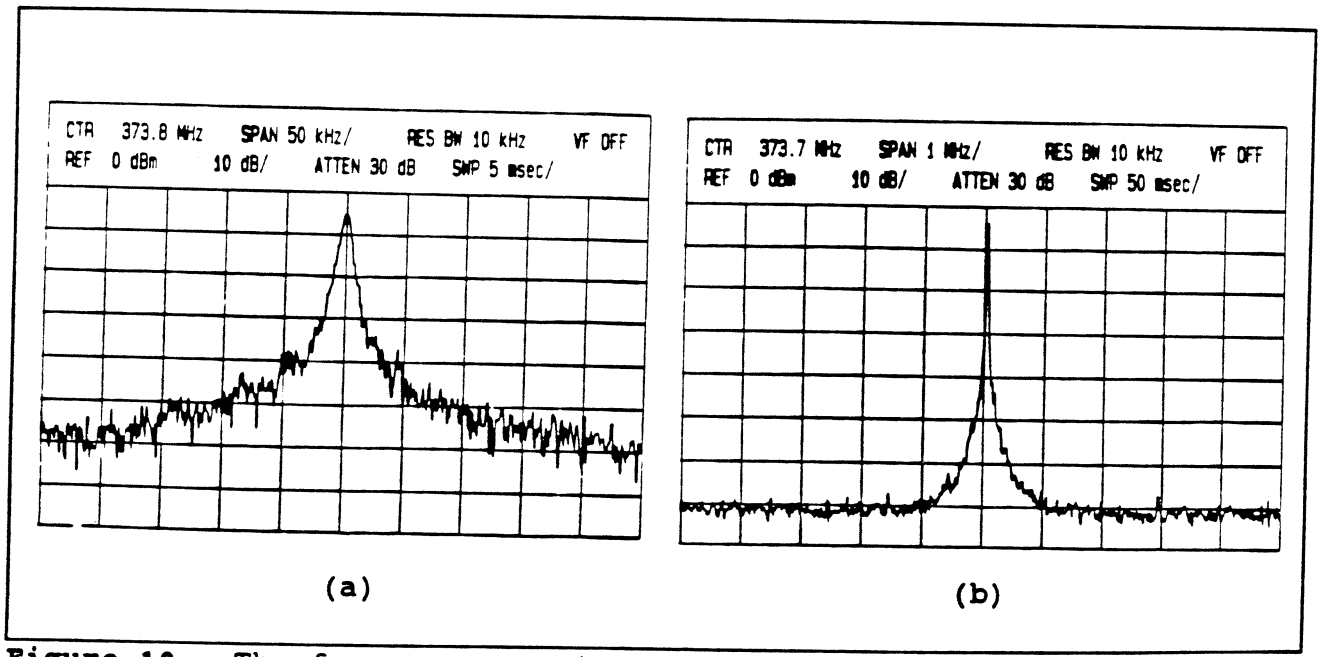

Figure 10. The frequency spectra measured for a 1x3 grid oscillator.

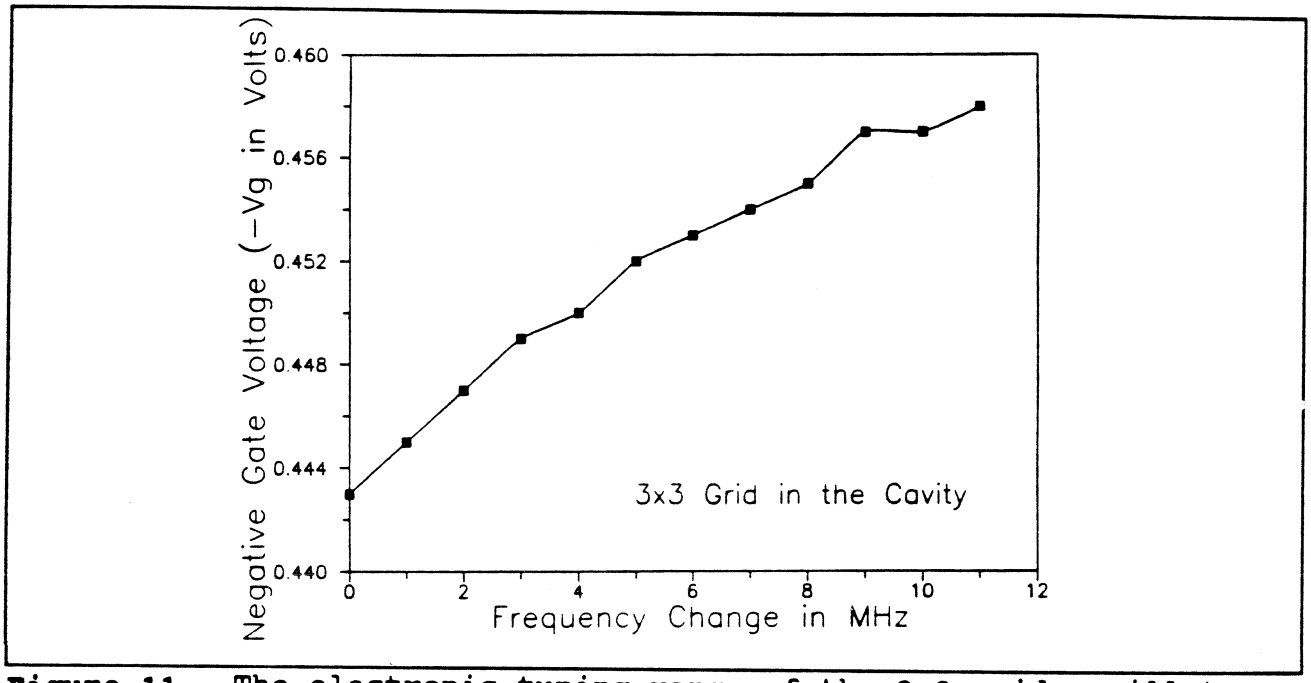

Figure 11. The electronic tuning range of the 3x3 grid oscillator.

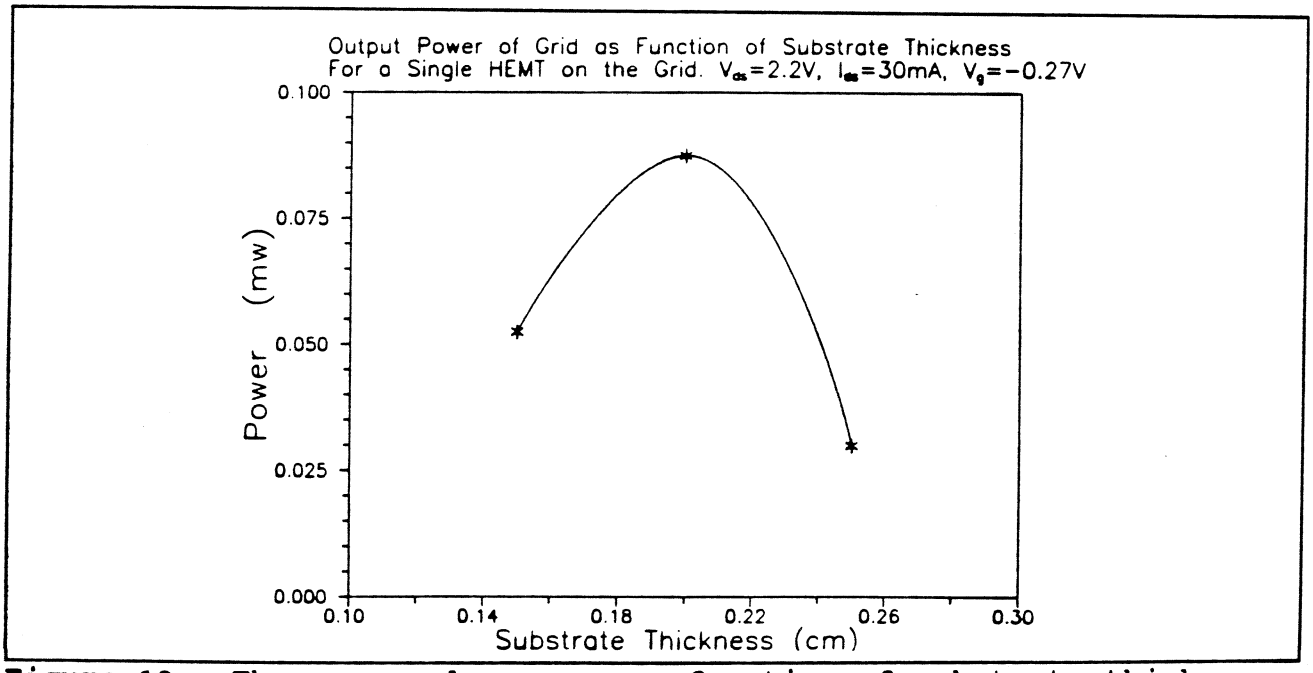

Figure 12. The measured power as a function of substrate thickness.

COMPARISON OF A 4-ELEMENT LINEAR ARRAY AND A 2x2 PLANAR ARRAY

Jenshan Lin and Tatsuo Itoh
Department of Electrical Engineering, University of California at Los Angeles
405 Hilgard Avenue, Los Angeles, CA 90024, USA

ABSTRACT

Spatial power-combining arrays integrating single oscillator units are designed in two types of configurations. The first type is a 4-element linear array which connects single oscillator units in a straight line. The other type is a 2x2 planar array which connects single oscillator units in a loop. The oscillation modes of these two types of arrays are analyzed. The measurement results are compared. In each type of array, the oscillator units can be connected by metal strips or chip resistors. In the 4-element linear array, connecting with chip resistors can achieve the stable in-phase mode oscillation while connecting with metal strips cannot. In the 2x2 planar array, both types of connection are able to achieve the in-phase mode oscillation. The result shows that, for the power combining of 4 oscillator units, connecting them in loop does not require using resistors to stabilize the in-phase mode. The measured radiation patterns of both types of arrays are compared to the theoretical patterns.

INTRODUCTION

Power combining of solid state sources is of growing interest since the available power from a single device decreases as the frequency increases[1]. The quasi-optical power-combining technique has been proven to be a very efficient method to achieve high power from solid-state oscillators in millimeter wave region[2][3]. Several types of quasi-optical power-combining techniques have been reported. To combine the power spatially, individual oscillators can be synchronized by the Fabry-Perot resonator[4], an external injected signal[5], or through the mutual coupling[6][7]. The stability of oscillation modes in a spatial power-combining array with strongly coupled oscillators has been analyzed and an effective method of stabilizing the in-phase mode was proposed[8]. The use of resistors in the coupling line suppresses the undesired modes and stabilizes the in-phase mode.

However, the analysis in [8] discussed the case of linear arrays only. In the application of two-dimensional arrays, other types of connections are of interest, e.g., connecting the oscillators in a loop. In this paper, the oscillation modes of a 2x2 array in which oscillators are connected in a loop-structure are analyzed. The result is compared to the mode analysis of a 4-element linear array. Both types of the circuits are fabricated using Gunn diodes and microstrip patch antennas. The radiation patterns are measured and compared to the theoretical patterns. The arrays containing up to eight elements are analyzed and discussed.

CIRCUIT STRUCTURE

(i) 4-element linear array

The structure of the 4-element linear array is shown in Fig. 1. The circuit integrates four identical oscillators. Each oscillator unit consists of a Gunn diode as the source and a microstrip patch antenna as the radiator. The oscillators are connected by a microstrip coupling line for strong coupling. The length of the coupling line between

oscillators is $1\lambda_g$, where λ_g is the guided wavelength of the in-phase mode frequency. The junctions at the mid-points of the coupling lines are designed for connecting oscillators with metal strips or chip resistors. The circuit is designed to have the in-phase mode oscillation at 12.45 GHz.

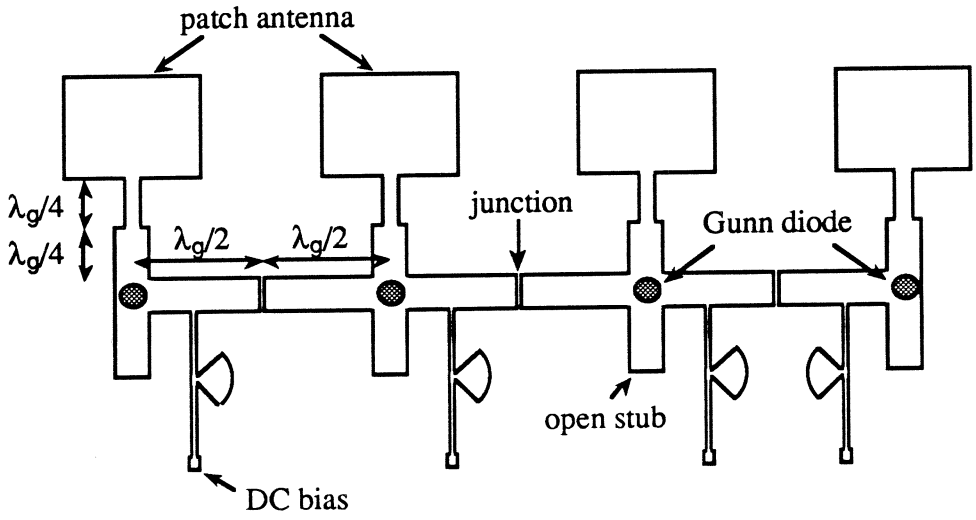

Fig. 1 Circuit structure of the 4-element linear array

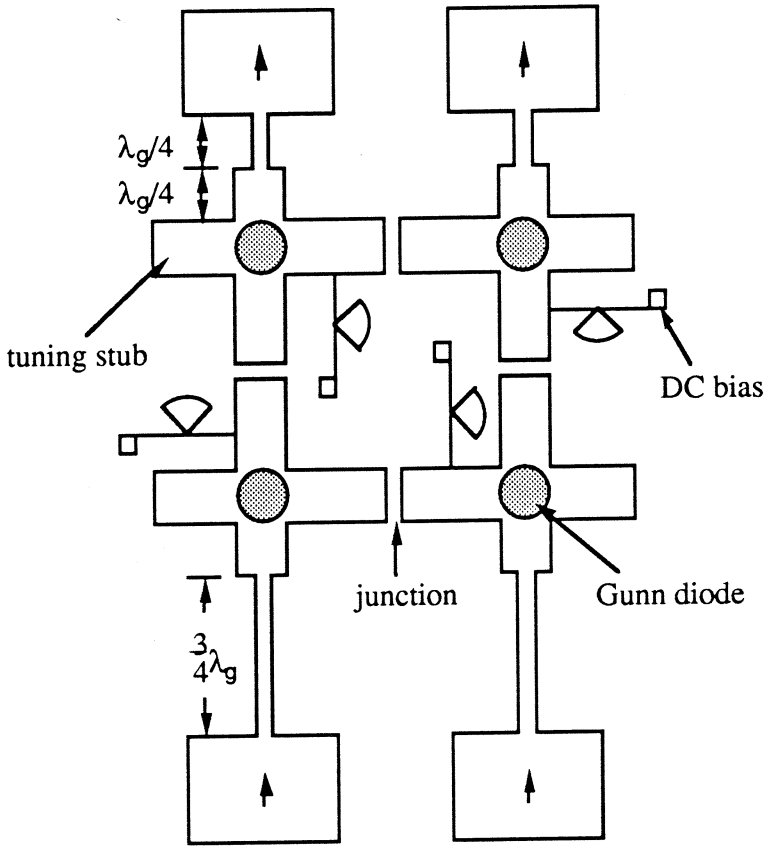

Fig. 2 Circuit structure of the 2x2 planar array

(ii) 2x2 planar array

The structure of the 2x2 planar array is shown in Fig. 2. Unlike the linear array, this 2x2 array is connected by a microstrip coupling line in the loop-structure. Each oscillator unit in this array is the same as in the 4-element linear array except that two of the feed lines are extended by $\lambda_g/2$ to compensate the phase shift of 180 degrees when two of the patch antennas are reversed. If these two feed lines are not extended, a difference pattern in E-plane will be obtained. The junctions are designed for connecting oscillators with metal strips or chip resistors. The operating frequency is also designed at 12.45 GHz.

MODE ANALYSIS

(i) 4-element linear array

The frequencies and the voltage distributions of normal modes in the linear array can be determined by the reactive system of the circuit(Fig. 3). The circuit equations are

$$j(b+b_d)V_1 + jb_tV_2 = 0 \quad (1.a)$$

$$jb_tV_{k-1} + j(b+2b_d)V_k + jb_tV_{k+1} = 0 \qquad k=2,3,...,N-1 \quad (1.b)$$

$$jb_tV_{N-1} + j(b+b_d)V_N = 0 \quad (1.c)$$

where

$$b = (\omega C - 1/\omega L)/Y_0 = Q_{ex}(\Omega - 1/\Omega) \quad (2.a)$$

$$b_d = -\cot(\phi) = -\cot(\phi_0\Omega) \quad (2.b)$$

$$b_t = \mathrm{cosec}(\phi) = \mathrm{cosec}(\phi_0\Omega) \quad (2.c)$$

$$\omega_0 = 1/\sqrt{LC} \quad (2.d)$$

$$\Omega = \omega/\omega_0 \quad (2.e)$$

$$\phi_0 = \beta(\omega_0)d \quad (2.f)$$

$$Q_{ex} = \omega_0 C/Y_0 \quad (2.g)$$

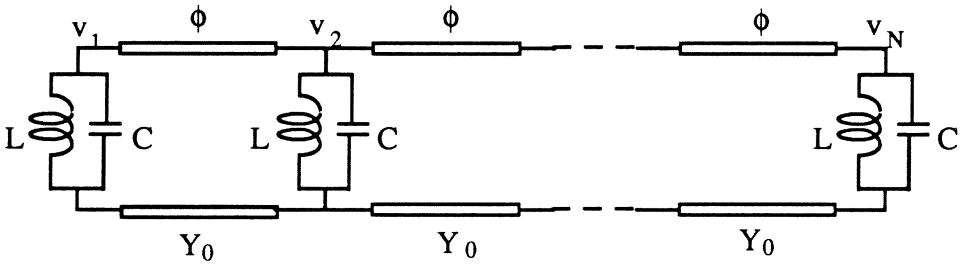

Fig. 3 Reactive system of the linear array

Eq.(1) can be written in a matrix form as

$$jb\begin{bmatrix} V_1 \\ V_2 \\ \vdots \\ V_N \end{bmatrix} + jb_t\mathbf{B}\begin{bmatrix} V_1 \\ V_2 \\ \vdots \\ V_N \end{bmatrix} = 0 \tag{3}$$

where

$$\mathbf{B} = \begin{bmatrix} \gamma & 1 & & & & \\ 1 & 2\gamma & 1 & & 0 & \\ & 1 & 2\gamma & 1 & & \\ & & \ddots & \ddots & \ddots & \\ & & & 1 & 2\gamma & 1 \\ & 0 & & & 1 & 2\gamma & 1 \\ & & & & & 1 & \gamma \end{bmatrix} \tag{4.a}$$

with

$$\gamma = b_d/b_t = -\cos(\phi_0\Omega) \tag{4.b}$$

The frequencies and the voltage distributions of the normal modes can be obtained from the eigenvalues and eigenvectors of matrix **B**, respectively. The value of Q_{ex}=5.5 is used, which is calculated from the simulation result of EEsof® EMSim. For the 4-element linear array in Fig. 1, N=4 so that four modes exist. By using the averaged potential theory and nonlinear device model, the stability of each mode is analyzed[8][9]. Here the van der Pol type of oscillator model is used. Two modes are stable single modes and the other two are stable double modes. The spectrum of the possible stable oscillation modes is shown in Fig. 4. For the purpose of power combining, the mode i=1 is required. This mode is called the desired mode or the in-phase mode, since the oscillator units oscillate in the same phase and with the same amplitude. Other modes are called undesired modes. Each undesired mode can oscillate at two frequencies of which one is higher than ω_0 and the other is lower than ω_0. They are then denoted by 2^H, 2^L, 3^H, 3^L, 4^H, and 4^L, respectively. The voltage distributions and the stabilities of all the modes are listed in Table 1.

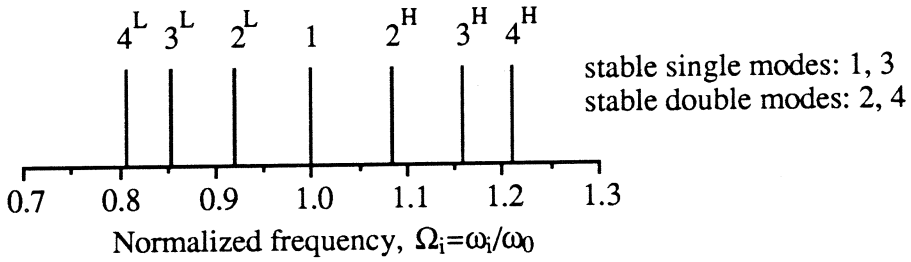

Fig. 4 Spectrum of the stable oscillation modes in the 4-element linear array

mode	voltage distribution	stability
1	1 1 1 1	stable, single
2^H	-.6487 -.2814 .2814 .6487	stable, double, with 4^H or 4^L
2^L	-.6489 -.2810 .2810 .6489	stable, double, with 4^H or 4^L
3^H	-.5519 .4421 .4421 -.5519	stable, single
3^L	-.5465 .4487 .4487 -.5465	stable, single
4^H	.3424 -.6187 .6187 -.3424	stable, double, with 2^H or 2^L
4^L	.3270 -.6269 .6269 -.3270	stable, double, with 2^H or 2^L

Table 1 Oscillation modes in the 4-element linear array

(ii) 2x2 planar array

The frequencies and the voltage distributions of normal modes in the planar array with loop-structure are determined by the reactive system of the circuit, which is similar to Fig. 3 but with a coupling line connecting the two ends to form a loop. The circuit equations then become

$$jb_tV_N + j(b+2b_d)V_1 + jb_tV_2 = 0 \quad (5.a)$$

$$jb_tV_{k-1} + j(b+2b_d)V_k + jb_tV_{k+1} = 0 \qquad k=2,3,...,N-1 \quad (5.b)$$

$$jb_tV_{N-1} + j(b+2b_d)V_N + jb_tV_1 = 0 \quad (5.c)$$

The corresponding matrix equation is similar to Eq. (3) but with

$$\mathbf{B} = \begin{bmatrix} 2\gamma & 1 & & & & & 1 \\ 1 & 2\gamma & 1 & & & & \\ & 1 & 2\gamma & 1 & & & \\ & & \ddots & \ddots & \ddots & & \\ 0 & & & 1 & 2\gamma & 1 & \\ & & & & 1 & 2\gamma & 1 \\ 1 & & & & & 1 & 2\gamma \end{bmatrix} \quad (6)$$

Usually there are N modes in a system of N elements. However, in the loop-structure degeneracy occurs and the number of modes is reduced. For N=4, three modes exist. The stability of each mode is analyzed by using the averaged potential theory. Of these three modes, two are stable single modes and one is unstable. The spectrum of the possible stable oscillation modes is shown in Fig. 5. The mode i=1 is the desired power-combining mode and has the in-phase oscillation condition. Compared to the spectrum of linear array(Fig. 4), the separation between modes is larger and the number of possible oscillation modes is reduced. The voltage distributions and the stabilities of all the modes are listed in Table 2.

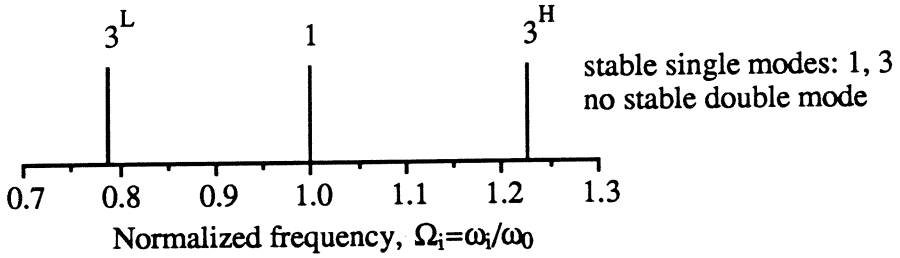

Fig. 5 Spectrum of the stable oscillation modes in the 2x2 planar array

mode	voltage distribution	stability
1	1 1 1 1	stable, single
2^H	.7071 0 -.7071 0	not stable
2^L	.7071 0 -.7071 0	not stable
3^H	.5 -.5 .5 -.5	stable, single
3^L	.5 -.5 .5 -.5	stable, single

Table 2 Oscillation modes in the 2x2 planar array

EXPERIMENT

The oscillator units in the circuits were connected by metal strips or chip resistors at the junctions. The oscillation frequencies and the far-field radiation patterns were measured. The purpose of using resistors is to suppress the undesired modes, since the current distributions at the junctions are zero for the in-phase mode but are not zero for all the undesired modes. Resistors of 4.7Ω were chosen based on the theory of [8] for the coupling line with Z_0=50Ω. The insertion of metal strips at the junctions has no effect on the suppression of undesired modes since the resistance of metal is nearly zero. The measured radiation patterns are compared to the theoretical patterns to confirm the in-phase mode oscillation.

(i) 4-element linear array

The use of chip resistors was able to achieve the stable in-phase mode oscillation while the use of metal strips was not. When the chip resistors were used, the stable in-phase mode oscillation at 12.423 GHz was observed, which was only 0.2% deviated from the designed frequency 12.45 GHz. When the metal strips were used, the array could not oscillate at the in-phase mode and a spectrum of multi-frequencies was observed. The measured radiation patterns of the array with resistors are compared to the theoretical patterns(Fig. 6). The agreement between the measured patterns and the theoretical patterns confirms the in-phase mode oscillation. The Effective Radiated Power(ERP) was 25.1 dBm.

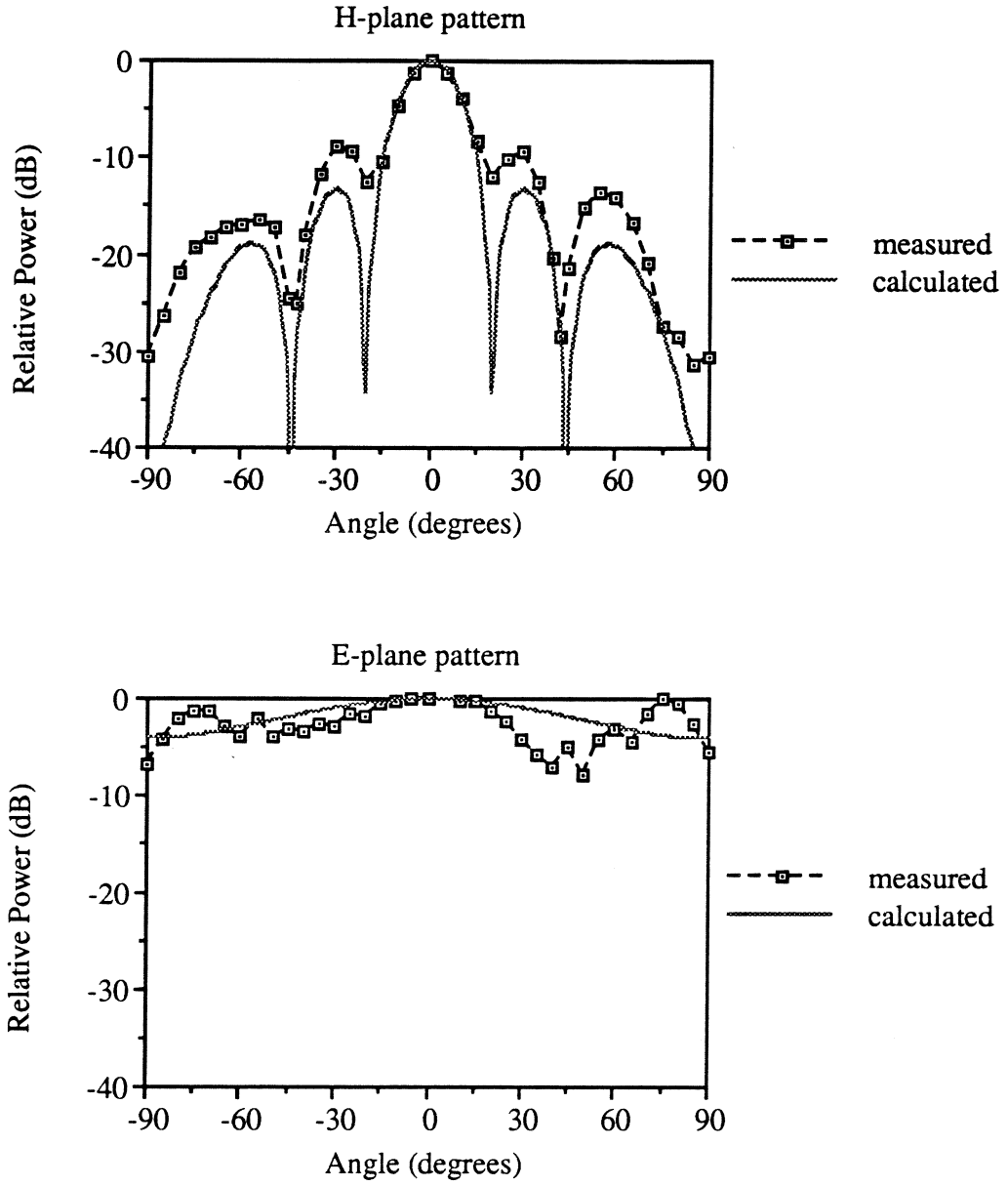

Fig. 6 Radiation patterns of the 4-element linear array

(ii) 2x2 planar array

The stable in-phase mode oscillation was obtained by using the chip resistors or the metal strips. Since the use of metal strips was not able to suppress the undesired modes, the success of stable in-phase mode means that there was only one stable mode in the circuit. This can be explained by the spectrum in Fig. 5. In Fig. 5, there are three possible oscillation frequencies. However, the difference between frequencies of the undesired mode and the in-phase mode is over 20% of the in-phase mode oscillation frequency ω_0. Due to the limited bandwidths of the Gunn diode and the patch antenna, the undesired mode 3^H and 3^L become unstable and the only stable oscillation mode is the in-phase mode. The oscillation frequency of the array was 12.395 GHz, which was 0.4% deviated from the designed frequency 12.45 GHz. The radiation patterns were

measured and compared to the theoretical patterns(Fig. 7). The agreement between the measured patterns and the theoretical patterns confirms the in-phase mode oscillation. The ERP was 25.1 dBm, which was the same as in the linear array. The grating lobes in the E-plane can be eliminated by modifying the circuit design, e.g., separating the antenna elements from the feed network in multi-layer structure[10].

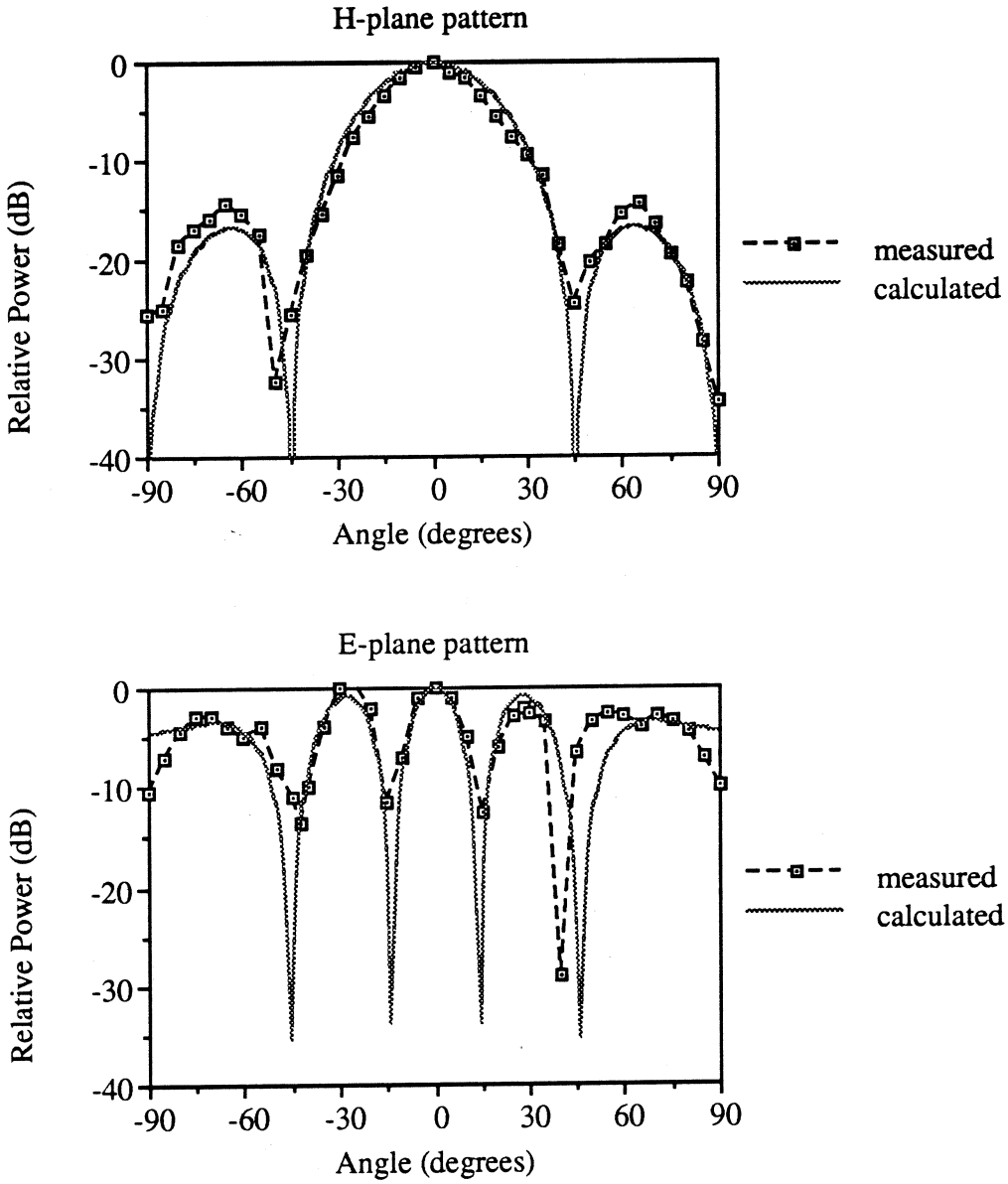

Fig. 7 Radiation patterns of the 2x2 planar array

DISCUSSION

The experimental result of achieving the in-phase mode oscillation in the 2x2 planar array without the use of chip resistors does not imply that such loop-structure power-combining arrays are free from the multi-moding problem. In fact, the number of modes increases and the frequencies of modes get closer when the number of oscillators increases. The comparison of modes in two different structures for the case of N=4, 5, 6, 8 is listed in Table 3. With the same number of devices, the loop-structure has fewer modes than the line-structure due to the degeneracy of modes. However, the total number of stable modes in loop-structure still increases and the use of chip resistors is needed for the effective suppression of undesired modes.

number of elements N	Total number of modes		stable modes of LINE-structure		stable modes of LOOP-structure	
	LINE	LOOP	single	double	single	double
4	4	3	2	2	2	0
5	5	3	1	4	3	0
6	6	4	2	4	4	0
8	8	5	2	6	4	0

Table 3 Comparison of modes in line-structure and loop-structure

CONCLUSION

Two types of configurations of the power-combining arrays with strongly coupled oscillator units are discussed. The theoretical analysis and the experimental investigation have been done. Oscillation modes in both types of arrays are analyzed and compared. The experimental results of the 4-element linear array and the 2x2 planar array are compared. Both types of structures can be applied to the circuit layout of the 2-dimensional arrays with strongly coupled elements.

ACKNOWLEDGMENT

This work was supported by the US Army Research Office under contract DAAH04-93-6-0068 and in part by the Joint Services Electronics Program F49620-92-C-0055.

REFERENCES

[1] K. Chang and C. Sun, "Millimeter-wave power combining techniques," *IEEE Trans. Microwave Theory Tech.*, vol. MTT-31, pp. 91-107, Feb. 1983.

[2] D. B. Rutledge, Z. B. Popovič, R. M. Weikle,II, M. Kim, K. A. Potter, R. C. Compton, R. A. York, "Quasi-optical power-combining arrays," *IEEE MTT-S Int'l Microwave Symp. Digest*, pp. 1201-1204, June 1990.

[3] J. W. Mink, "Quasi-optical power combining of solid-state millimeter-wave sources," *IEEE Trans. Microwave Theory Tech.*, vol. MTT-34, pp. 273-279, Feb. 1986.

[4] Z. B. Popović, R. M. Weikle,II, M. Kim, and D. B. Rutledge, "A 100-MESFET planar grid oscillator," *IEEE Tran. Microwave Theory Tech.*, vol. MTT-39, pp. 193-200, Feb. 1991.

[5] J. Birkeland and T. Itoh, "A 16-element quasi-optical FET oscillator power-combining array with external injection locking," *IEEE Trans. Microwave Theory Tech.*, vol. MTT-40, pp. 475-481, March 1992.

[6] R. A. York and R. C. Compton, "Quasi-optical power combining using mutually synchronized oscillator arrays," *IEEE Trans. Microwave Theory Tech.*, vol. MTT-39, pp. 1000-1009, Feb. 1991.

[7] A. Mortazawi, H. D. Foltz, and T. Itoh, "A periodic second harmonic spatial power-combining oscillator," *IEEE Trans. Microwave Theory Tech.*, vol. MTT-40, pp. 851-856, May 1992.

[8] S. Nogi, J. Lin and T. Itoh, "Mode analysis and stabilization of a spatial power-combining array with strongly coupled oscillators," to be published in the special issue on Quasi-Optical Techniques of *IEEE Trans. Microwave Theory Tech.*, Oct. 1993.

[9] M. Kuramitsu and F. Takase, "Analytical method for multimode oscillators using the averaged potential," *Elec. Commun. Japan*, vol. 66-A, pp. 10-19, 1983.

[10] J. Lin and T. Itoh, "A 4x4 spatial power-combining array with strongly coupled oscillators in multi-layer structure," to be published in the *IEEE MTT-S Int'l Microwave Symp. Digest*, June 1993.

The material presented below is for review only and has been submitted for publication in IEEE Trans. on Microwave Theory and Techniques.

A 75 GHz to 115 GHz Quasi-Optical Amplifier

Thomas P. Budka†, Michael W. Trippe ‡, Sander Weinreb‡ and Gabriel M. Rebeiz†

†NASA/Center for Space Terahertz Technology
University of Michigan, Ann Arbor, MI 48109-2122

‡Martin Marietta Laboratories, Baltimore, MD 21227

ABSTRACT

A wideband quasi-optical amplifier employing two pyramidal back-to-back horns has been developed. Using a four-stage W-band low noise amplifier (LNA) designed and fabricated by Martin Marietta Laboratories [1], the quasi-optical amplifier gives a system gain greater than 11 dB from 86 GHz to 113 GHz without any low frequency oscillations. A peak system gain of 15.5 dB is measured at 102 GHz, and the measured noise figure of the system is 7.4 dB at 94 GHz. The quasi-optical amplifier design maintains the same polarization of the received and transmitted signal while providing good isolation and can be fabricated monolithically at millimeter-wave frequencies.

INTRODUCTION

Recent advances in transistor technology at Martin Marietta Laboratories have led to the development of a four-stage W-band low noise amplifier (LNA) using pseudomorphic InGaAs Modulation-Doped Field Effect Transistors (MODFET's). These amplifiers have demonstrated gains up to 23 dB in a waveguide environment [1]. The amplifiers typically employ a waveguide-to-microstrip or waveguide-to-coplanar waveguide transition [1], and the waveguide test fixture is expensive to build at frequencies higher than 100 GHz. It is therefore advantageous to incorporate these amplifiers directly within a radiating structure that can be fabricated monolithically and can be easily scaled to frequencies higher than 100 GHz.

This approach has been done at lower frequencies by Kim et al. [2] and Chi et al. [3]. In both techniques, the quasi-optical amplifier employ polarization diplexing and a differential amplifier stage. In this paper, a new quasi-optical amplifier design based on the integrated horn structure [4] is presented. There is no need for tuning polarizers and therefore this design allows a wide operating bandwidth. The design maintains the same polarization and is compatible with very high gain monolithic millimeter wave amplifiers.

QUASI-OPTICAL AMPLIFIER DESIGN

The quasi-optical amplifier consists of two back-to-back pyramidal horns each with openings of $1.35\lambda_o$ x $1.35\lambda_o$ at the design frequency of 94 GHz. A 4.25 mm x 1.25 mm Martin Marietta Laboratories LNA chip is placed approximately $\lambda_o/2$ above the apex of each pyramidal horn (Fig. 1a). Two back-to-back pyramidal horns are fabricated by anisotropically etching <110> silicon wafers from opposite sides and stacking eight 385 μm-thick horn sections and one 200 μm cavity spacing section. The LNA is hybrid mounted in the etched cavity connecting the two integrated horns (Fig. 1b). The cavity is 3.0 mm wide by 200 μm high. The thickness of the LNA GaAs substrate is 100 μm. The sidewalls of the horns and the sides of the cavity are metallized with 0.7 μm of gold through angle evaporation.

The position of the chip within the horn cavity is chosen using a 3 GHz (equivalent to 94 GHz) microwave scale model for a probe of length 600 μm and width of 190 μm on a 100 μm thick GaAs substrate (at 94 GHz). An input match (S_{11}) better than -20 dB from 2.75 GHz to 3.25 GHz (equivalent to 86.5 GHz to 102 GHz) is measured with the probe facing the interior of the horn - the input horn (Fig. 2a). An input match better than -10 dB is measured with the probe facing out of the horn - the output horn - over the same frequency range (Fig. 2b). The probe radiates preferentially into the dielectric side, thereby resulting in a better match for the input horn.

The LNA is mounted on a silicon wafer containing the bias lines, bias resistors and bypass capacitors (Fig. 3). The four gates are biased at 0.25 V. The drains are biased separately

and optimized for maximum gain. The bias voltages for the drains, from input to output, are 4.5 V, 3.8 V, 3.5 V, and 3.5 V, respectively. The total source-to-drain current for all four MODFET's is 24 mA. The source is grounded on the back side of the LNA chip along the receiving horn sidewall using silver epoxy and 0.7 mil gold ribbon.

MEASUREMENTS

Patterns taken from a 3 GHz microwave model show a very high cross- polarization level of both the input and output integrated horns (Fig. 4). This is attributed to the short length and large width of the waveguide-to-CPW probe. Since the probe dimensions of the LNA are fixed, we are not able to decrease the cross-polarization level. We recommend that a longer narrower probe be used for future quasi-optical amplifier applications which will result in reduced cross-polarization levels [6]. The short monopole probe also results in an asymmetry in the E-plane copolarization pattern. No pattern measurements are done at other frequencies, but the same behavior is expected over the 2.75-3.25 GHz band (equivalent to 86.5 GHz to 102 GHz). Notice that the input pattern is better than the output pattern because the monopole probe radiates preferentially into the dielectric side of the substrate.

The gain of the quasi-optical amplifier structure is measured in a plane-wave experiment similar to [2]. First, the system is calibrated without the quasi-optical amplifier present. The power received during calibration, P_c, is determined from Frii's transmission formula:

$$\mathrm{P}_c = P_t \left(\frac{G_t G_r}{4\pi (2r)^2} \right) \tag{1}$$

where $2r$ is the distance between the transmitting and receiving horns, P_t is the transmitted power, G_t is the gain of the transmitting antenna (a WR-10 pyramidal horn), and G_r is the gain of the receiving antenna (a WR-10 pyramidal horn). Next, the power received, P_r, with the quasi-optical amplifier in place is given by:

$$\mathrm{P}_r = P_t \left(\frac{G_t A_{input}^{eff}}{4\pi r^2} \right) G \left(\frac{G_r A_{output}^{eff}}{4\pi r^2} \right) \tag{2}$$

where G is the gain of the LNA, A_{input}^{eff} is the effective aperture area of the input horn, A_{output}^{eff} is the effective aperture area of the output horn and r is the distance between the transmitting or receiving horn and the quasi-optical amplifier. Since the effective apertures of the input and output integrated horns are not known accurately, the aperture efficiencies are separated from the physical area of the input and output integrated horns:

$$\mathrm{P}_r = P_t \left(\frac{G_t \varepsilon_{input}^{eff} A_{phys.}}{4\pi r^2} \right) G \left(\frac{G_r \varepsilon_{output}^{eff} A_{phys.}}{4\pi r^2} \right) \tag{3}$$

where A_{phys} is the physical area of the input and output horns, $\varepsilon_{input}^{eff}$ is the effective aperture efficiency of the input horn, and $\varepsilon_{output}^{eff}$ is the effective aperture efficiency of the output horn. The gain of the quasi-optical system, G_{SYS}, is then found by dividing (1) by (3) and solving for $G\varepsilon_{input}^{eff}\varepsilon_{output}^{eff}$.

$$\mathrm{G}_{SYS} = G\varepsilon_{input}^{eff}\varepsilon_{output}^{eff} = \left(\frac{P_r}{P_c} \right) \left(\frac{\lambda r}{2A_{phys.}} \right)^2 \tag{4}$$

The system gain is measured over the frequency range of 75 GHz to 115 GHz. The gain of the quasi-optical amplifier, G_{SYS}, is greater than 11 dB from 85 GHz to 113 GHz and greater than 3 dB gain from 75 GHz to 115 GHz (Fig. 5). No oscillations are found on the bias lines or in free space and isolation is perfect when the bias is removed. The dips and peaks of the gain curve occur because the antenna pattern and cross-polarization levels change with frequency. From microwave pattern modeling, we expect the co-polarized aperture efficiency of each horn to be below 60% at 94 GHz. Thus the lower limit of the gain of the amplifier chip itself would be at least 4 dB above the curve in Figure 4. Although the exact gain of the LNA is not known, histograms of the gains of 44 different LNA's fabricated at the same time suggest a mean LNA gain of 16.3 dB around 90 GHz and a standard deviation of 3.2 dB.

This value corresponds closely with the measured system gains of 12.9 dB at 94 GHz and 15.5 dB at 102 GHz. If the effective aperture efficiencies were deembedded from the gain calculation, the gain would increase by more than 4 dB to 16.9 dB at 94 GHz.

Figure 6 displays the experiment for measuring the noise figure of the quasi-optical amplifier. The IF chain gain and input noise temperature is measured to be 97.0 dB and 55.3K, respectively, at 94 GHz. The conversion loss of the balanced mixer is measured to be 4.6 dB with a mixer input noise temperature of 821K. The loss of the teflon lens (f/D=0.85) is determined to be 0.30 dB. Next, we measure the noise figure of the quasi-optical amplifier to be 7.4 dB at 94 GHz using standard hot/cold load techniques. This value matches with an expected 7-8 dB noise figure from these specific LNA's. New LNA's from Martin Marietta Laboratories that have 23 dB gain and 4.3 dB noise figure [1] would greatly improve the performance of the quasi-optical amplifier.

CONCLUSIONS

In this paper we report a single element quasi-optical amplifier that is based on an integrated horn antenna using a LNA originally designed for operation within waveguide. Using the waveguide-to-CPW probe as the radiating element for the structure, a peak system gain of 15.5 dB at 102 GHz is measured and higher than 11 dB system gain is measured over a 27% bandwidth. The quasi-optical horn antenna can be designed to result in a much lower cross-polarization level using a long monopole probe and to couple efficiently to a Gaussian beam system using an integrated horn extension [4]. The quasi-optical amplifier maintains the same polarization of the incoming and outgoing signal. The absence of tuning polarizers allow a wider operating bandwidth for this design.

ACKNOWLEDGEMENTS

Research supported by NASA/Center for Space Terahertz Technology, United States Army Research Office and by Martin Marietta Laboratories. We appreciate the help of Dr. Thomas

Burke, United States Army Research Laboratory and Dr. James Mink, United States Army Research Office for their support of this project.

REFERENCES

[1] M. W. Trippe, S. Weinreb, S. W. Duncan, A. Eskandarian, B. A. Golja, D. C. Martel, G. Mendenilla, B. Power, H. B. Sequeira, S. B. Southwick, S. P. Svensson, D-W. Tu, and N. E. Byer, "mm-Wave MIMIC Receiver Components," *IEEE 1991 Monolithic Circuits Symposium Digest*, pp. 51-54, 1991.

[2] M. Kim, J.J. Rosenberg, R.P. Smith, R.M. Weikle II, J.B. Hacker, M.P. Delisio and D.B. Rutledge, "A grid amplifier," *IEEE Microwave GuidedWave Letters* vol. 1, No. 11, 1991.

[3] C. Chi and G. M. Rebeiz, "A Quasi-Optical Amplifier," *Submitted to IEEE-Microwave and Guided Wave Letters*, January, 1993.

[4] G.V. Eleftheriades, W.A. Ali-Ahmad, L.P. Katehi and G.M. Rebeiz, "Millimeter-wave integrated horn antennas: Part I: Theory and Part II: Experiment," IEEE-Transactions Antennas Propag., vol. AP-39, pp. 1575-1586, November 1991.

[5] G.V. Eleftheriades and G.M. Rebeiz, "Design and Analysis of Quasi-Integrated Horn Antennas for Millimeter and Submillimeter-Wave Applications," to be published in the IEEE-Transactions on Microwave Theory and Techniques, May, 1993.

[6] G. V. Eleftheriades, "Design and Analysis of Quasi-Integrated Horn Antennas for Millimeter and Submillimeter-Wave Applications," Ph.D. Thesis, University of Michigan, Ann Arbor, Michigan, 1993.

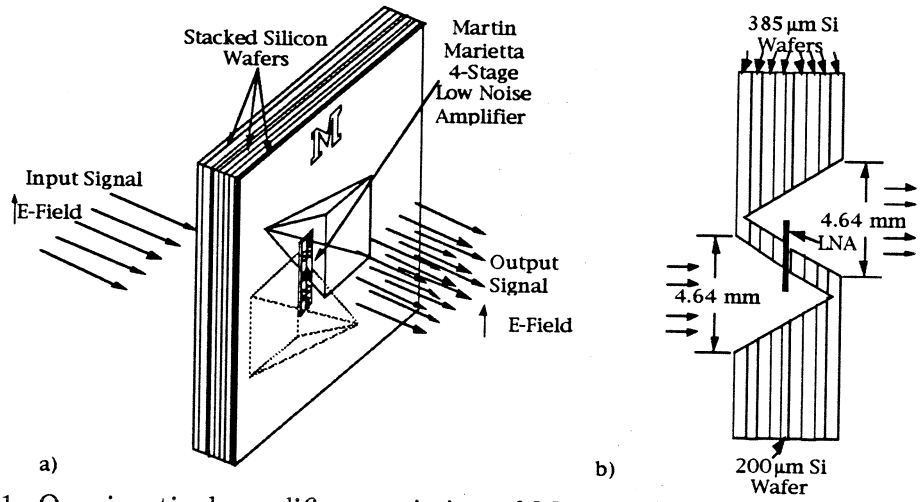

Figure 1: Quasi-optical amplifier consisting of Martin Marietta Laboratories' low noise amplifier between two back-to-back pyramidal horns. A plane wave input signal is amplified and repeated on the opposite side with the same polarization. a) Isogonal view. b) Side view.

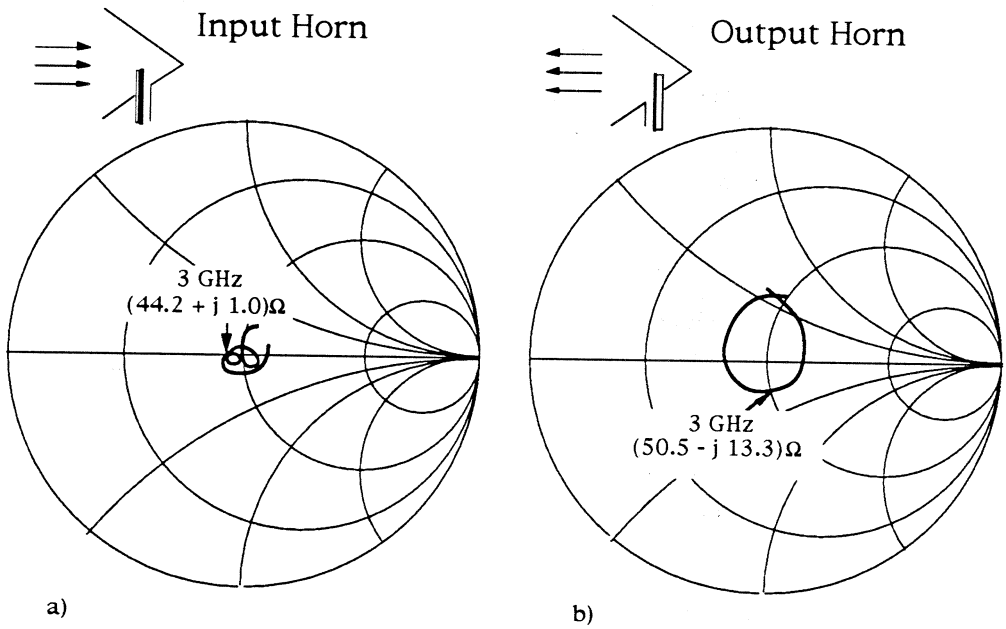

Figure 2: a) Input impedance of monopole inside the input pyramidal horn of a microwave model measured from 2.75 GHz to 3.25 GHz (equivalent to 86.5 GHz to 102 GHz). b) Input impedance of output pyramidal horn of quasi-optical amplifier microwave model measured from 2.75 GHz to 3.25 GHz.

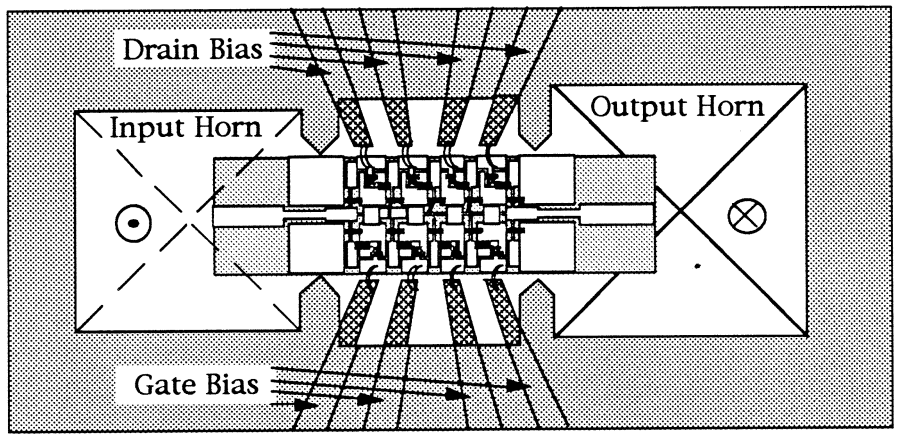

Figure 3: Martin Marietta Laboratories' low noise amplifier (LNA) chip placed in a cavity between two horn openings. Eight bias lines supply voltage to the four drains and gates while the source is grounded from the back side of the LNA chip. The LNA chip dimensions are 4.25 mm by 1.25 mm.

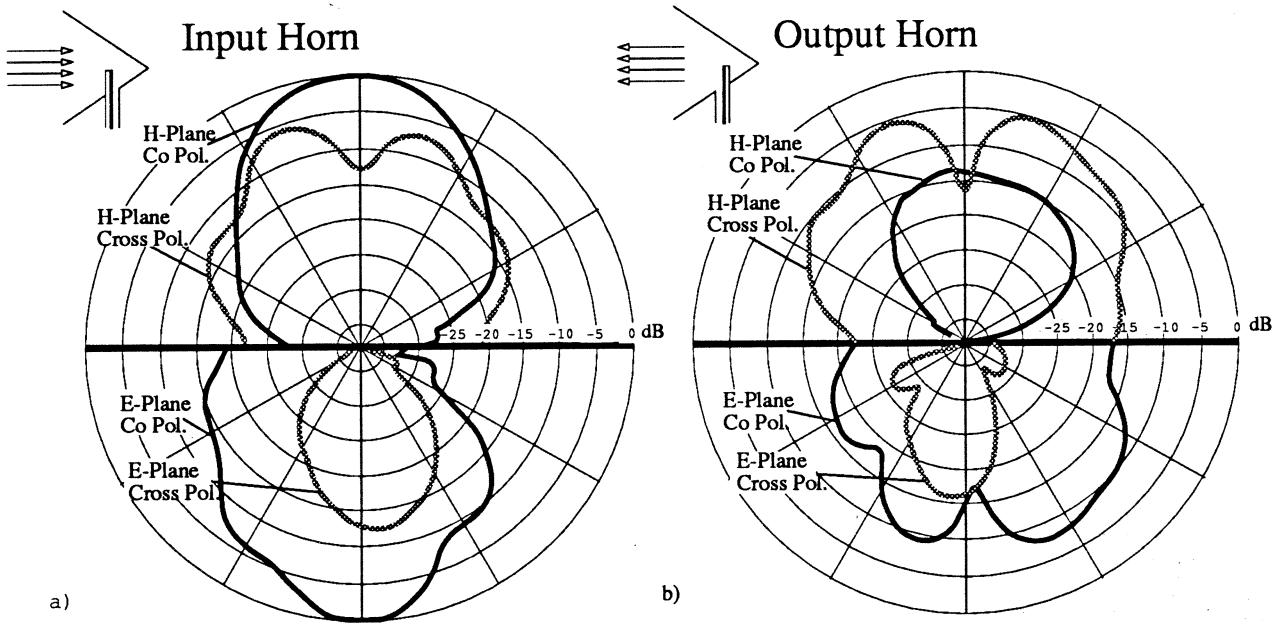

Figure 4: Quasi-optical amplifier 3 GHz microwave model (equivalent to 94 GHz) antenna patterns. a) Antenna patterns with monopole facing the interior of the horn. b) Antenna patterns with monopole facing the exterior of the horn.

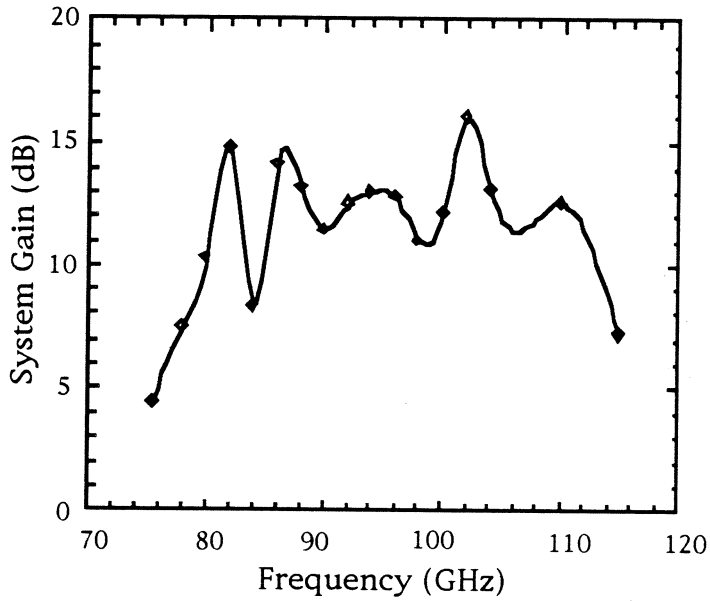

Figure 5: Quasi-optical amplifier system gain versus frequency. The system gain includes loss due to input and output horn aperture efficiency. The peaks and dips in the plot are due to the changing cross-polarization levels and antenna patterns with frequency.

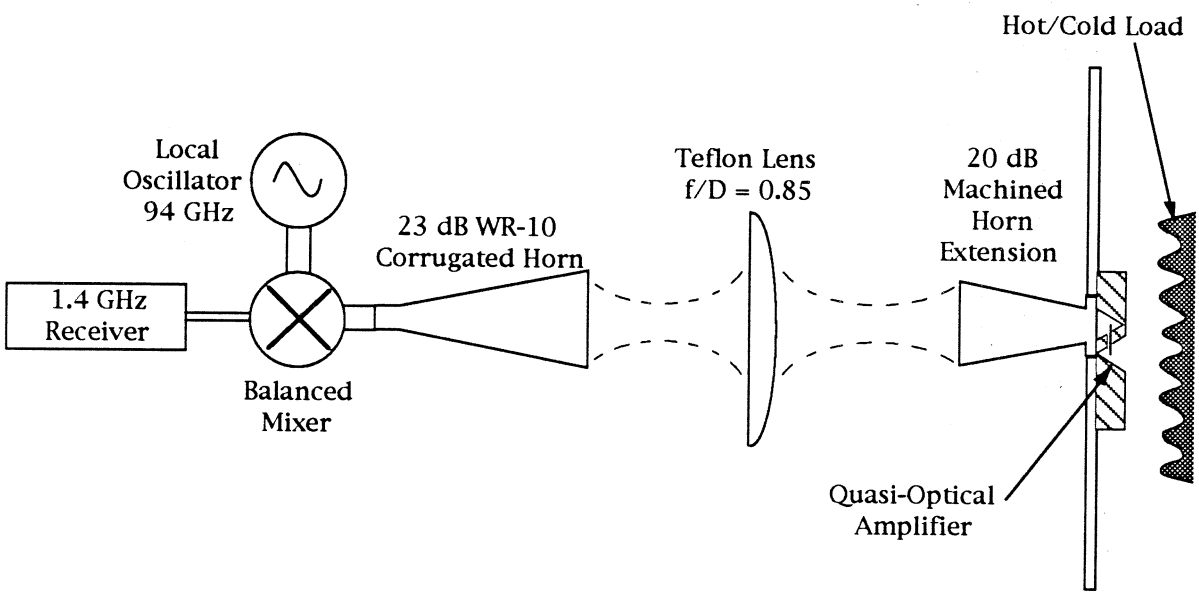

Figure 6: Noise figure experiment using an LO frequency of 94 GHz and an IF of 1.4 GHz.

A Subharmonically Pumped HFET Grid Mixer

Robert M. Weikle, II†, Niklas Rorsman, Herbert Zirath
and Erik L. Kollberg

Chalmers University of Technology
S-412 96 Göteborg SWEDEN

† University of Virginia
Charlottesville, VA 22903-2442 U.S.A.

Abstract— **In this work, we report the demonstration of a quasi-optical subharmonically pumped grid mixer. The grid consists of a 4×4 array of dual gate Heterojunction Field Effect Transistors (HFET's) which are connected in a crossed dipole configuration. Both the drains and sources of the devices are grounded, thus eliminating possible instabilities. The LO and RF signals are applied to the grid quasi-optically and with orthogonal polarizations. This enhances the isolation between the LO and RF as well as allowing for the possibility of independent impedance tuning for both signals. The IF signal is removed from the bias lines with an SMA connector. The grid was designed for and tested in the *K*-band (18-26.5 GHz), where a minimum conversion loss of 16 dB was obtained at an RF frequency of 19 GHz and an LO power of 3 dBm per device. This is comparable to conventional dual gate HFET mixers which typically have a conversion loss between 10 dB and 15 dB for the same LO power.**

I. Introduction

The development of quasi-optical arrays as a means of power generation at millimeter-wave frequencies continues to be a subject of growing interest. Planar arrays or grids of transistors have produced output powers at frequencies as high as 35 GHz [1,2] and with DC-to-RF conversion efficiencies as high as 20 % [3]. In addition to oscillators, a variety of other components have been demonstrated as quasi-optical grids, including phase shifters [4], multipliers [5], amplifiers [6], and mixers [7]. One benefit gained by using quasi-optical grids is an enhancement of power-handling capability or dynamic range. This is particularly important at millimeter-wave and submillimeter-wave frequencies where free-space power combining can be most efficient. However, even with an increased dynamic range, other important grid parameters, such as noise performance and conversion loss or gain, are expected to be comparable with those for circuits containing a single device. The increase in dynamic range is particularly important for applications

such as power combining or frequency multiplication. It could also prove useful in receiver applications, especially when the power handling of the nonlinear mixing element is fundamentally limited as it is for SIS junctions.

Unfortunately, the increased dynamic range of a grid mixer implies a corresponding increase in the LO power required for pumping. This can be a serious drawback, especially at millimeter-wave frequencies where higher power comes at a much higher cost. One possible solution is to use a power combining array for the LO signal. An alternative is to use a lower frequency, higher power source in conjunction with a multiplier. Each of these suggestions merit investigation. A different approach is to explore grid mixer configurations that allow subharmonic pumping. This permits the use of a lower frequency LO source without the need for additional multipliers. In this paper, we present the design and demonstration of a subharmonically pumped grid mixer which uses dual gate HFET's as the mixing element.

II. The Dual Gate HFET

A photograph of the dual gate HFET is shown in Fig. 1. This device was fabricated at Chalmers and consists of two HFET cells connected in parallel and fabricated on a δ-doped psuedomorphic AlGaAs-InGaAs-GaAs substrate grown by Quantum Epitaxial

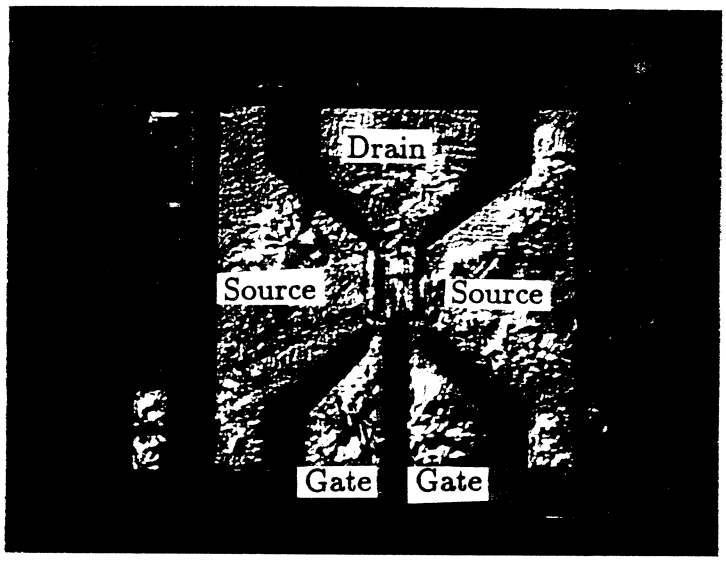

Figure 1. Photograph of the dual gate HFET. In a subharmonic mixer, the gates are driven 180° out of phase.

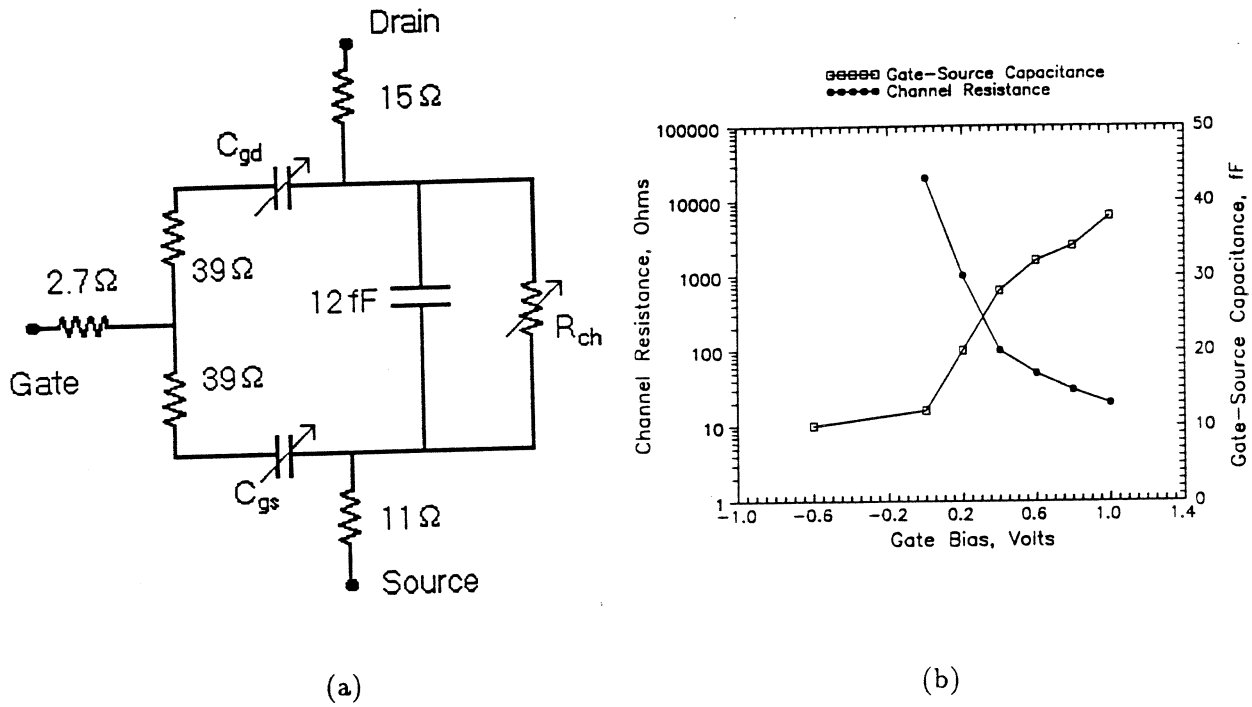

(a) (b)

Figure 2. (a) Lumped-element circuit model for one cell of the dual gate HFET. The model was determined from DC and *s*-parameter measurements up to 60 GHz . (b) HFET channel resistance and gate-source capacitance as a function of DC gate voltage.

Design, Inc. (QED). The 2-DEG sheet concentration was determined by Hall measurements to be $3.5 \times 10^{12}\,\mathrm{cm}^{-3}$, and the electron mobility to be 4800 cm^2/V-s at room temperature. Mushroom shaped gates where fabricated using electron beam lithography and a two-layer resist lift-off procedure. The gate length is approximately 0.15 μm. The drain and source ohmic contacts were formed using a Au/Ge/Au/Ni/Au metallization and annealing at 350°C for about 60 sec. An equivalent circuit model for the HFET was found from DC and *s*-parameter measurements up to 60 GHz. The f_{max} of the device is estimated to be 120 GHz and the f_T to be 100 GHz. The HFET model, with $V_{ds} = 0$ is shown in Fig. 2(a).

When used as a resistive mixer, an LO signal is applied to the gate. This signal modulates the gate voltage which in turn modulates the resistance of the drain-source channel. The dependence of the channel resistance on DC gate bias is shown in Fig. 2(b). This dependence is described relatively well by the empirical expression [8] :

$$R_{ch} = R_o e^{-kv_{gs}} + R_1$$

The sum of R_o and R_1 corresponds to the channel resistance at zero gate bias and k

determines the slope of the $\log(R_{ch})$ vs. v_{gs} characteristic. R_1 is the minimum channel resistance determined by the 2-DEG concentration and geometrical parameters.

III. Grid Design

A photograph of the grid is shown in Fig. 3(a). The grid consists of an array of identical unit cells, each of which contains a single dual-gate HFET chip. Copper strips running across the dielectric substrate in both the vertical and horizontal directions allow DC bias connections and serve to couple the devices to incident radiation. Referring to Figure 3(b), the horizontal leads (which are 100 μm wide) are wire-bonded to the HFET gates. In this configuration, an incident wave polarized parallel to the gate leads induces currents which drive the gates of each device out of phase. As a result, the combined channel resistance of the paralleled HFET's is modulated at *twice* the frequency of the incident LO signal. The 600 μm wide vertical leads are wire-bonded to the drain and sources of each device. Radiation incident on the grid with a vertical polarization sees the inductance of these leads in series with the modulated channel resistance. Mixing products are thus generated across the drain and source leads of each unit cell.

The substrate of the grid is Rogers *Duroid* 6010 with a dielectric constant of 10.5 and thickness of 635 μm. The drains and sources of the HFET's are grounded through 1 cm long gold bond wires (diameter of 1 mil). Gate bias is brought in from the sides, also on gold bond wire. An IF signal is removed from the top and bottom bias lines of the grid with an SMA connector.

The grid was designed using the equivalent circuit model shown in Fig. 4 along with the HFET lumped element model and Hewlett-Packard's *Microwave Design System* software [9]. Vertical and horizontal leads are represented by lumped inductors whose values are calculated using the EMF method [10,11]. A section of transmission line represents the dielectric substrate. Shunt admittances Y_{LO} and Y_{RF} account for reflections and losses presented to the LO and RF signals from the opposite side of the grid. In our simulations, these admittances model polarizers that are adjusted to independently tune the LO and RF. The size of the unit cell is 3 mm and was chosen so that the RF signal was well matched at 20 GHz.

IV. Measurements

To measure the performance of the grid, a K-band horn antenna was placed 45 cm in front of the array and the SMA IF output was connected to a Tektronics 2754P spectrum analyzer. The LO signal was injected from behind (through the dielectric substrate) with an X-band open-ended waveguide placed 5 cm from the grid. The experimental setup

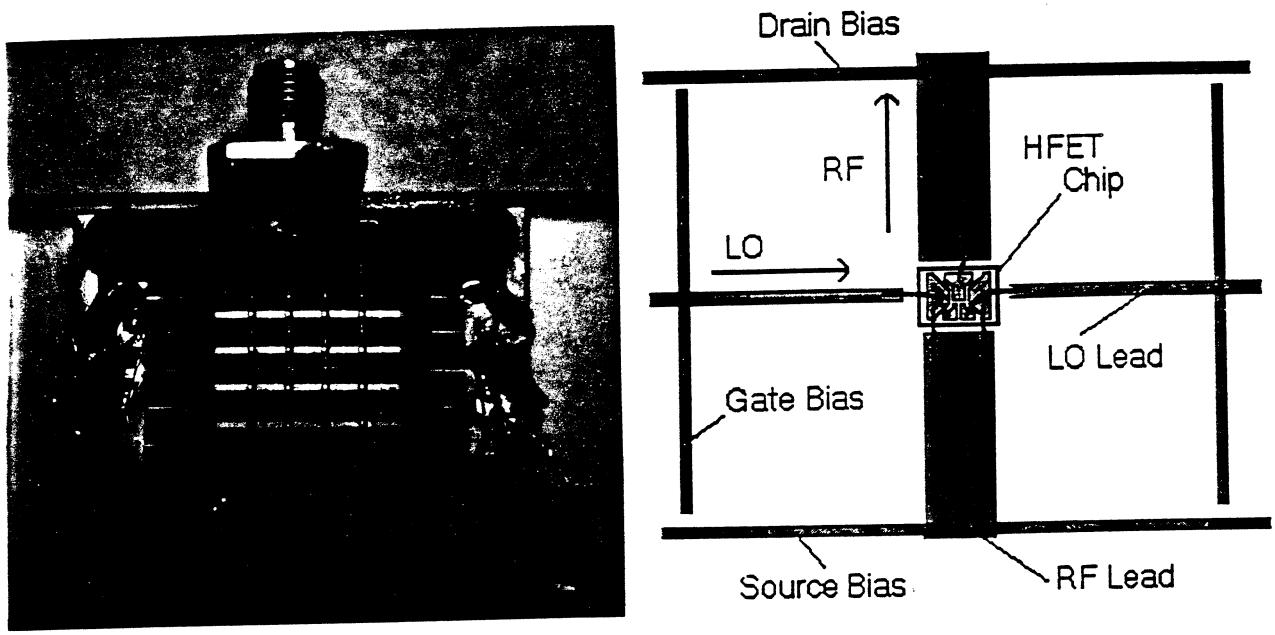

(a) (b)

Figure 3. (a) Photograph of the 16-element HFET grid mixer. The LO signal is vertically polarized and the RF horizontally polarized. (b) Schematic of the grid unit cell showing how the chip is connected with bonding wire. Note that the unit cells in Figure 3(a) are rotated by 90°

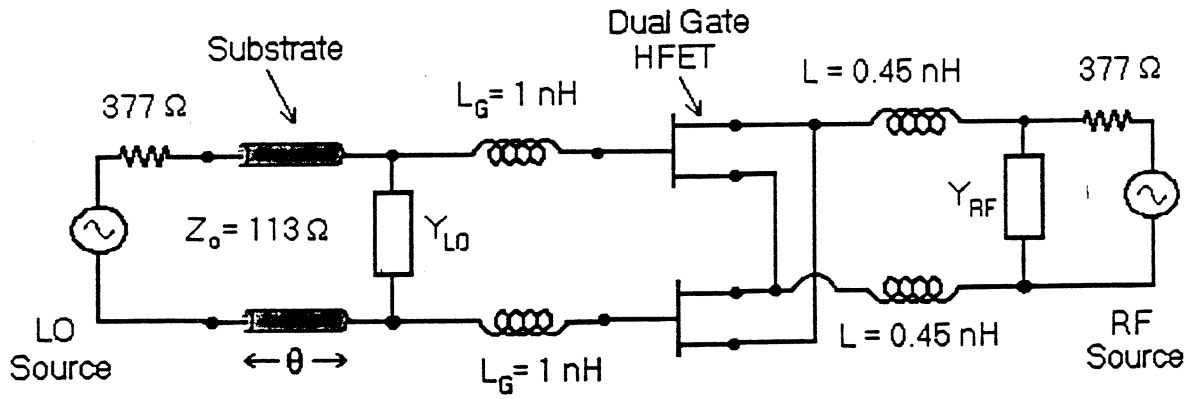

Figure 4. Equivalent circuit model for the subharmonically-pumped mixer grid..

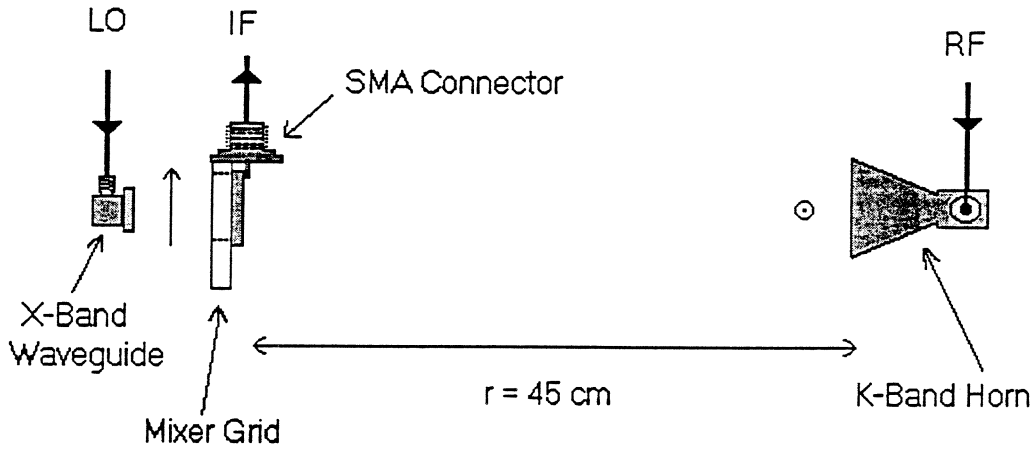

Figure 5. Experimental setup used to measure the mixer conversion loss. The LO is fed through an HP 8349B amplifier to an open-ended X-band waveguide. The IF signal is observed using a Tektronics 2754P Spectrum Analyzer.

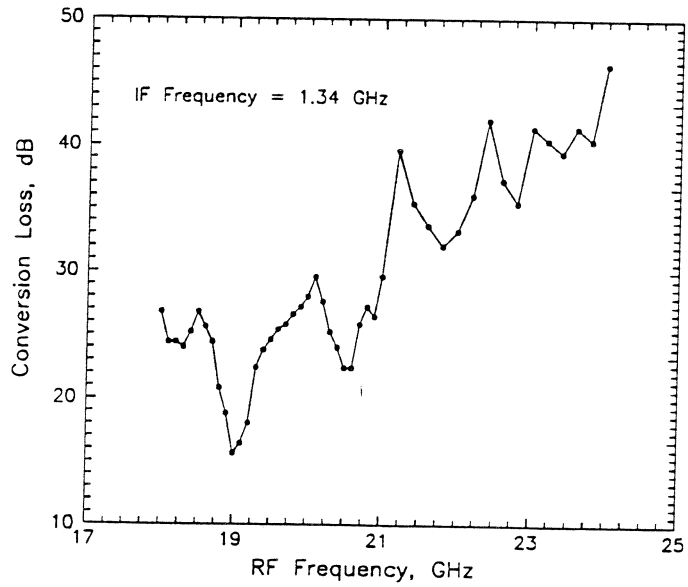

Figure 6. Conversion loss of the grid as a function of RF frequency. The IF is kept constant at 1.34 GHz.

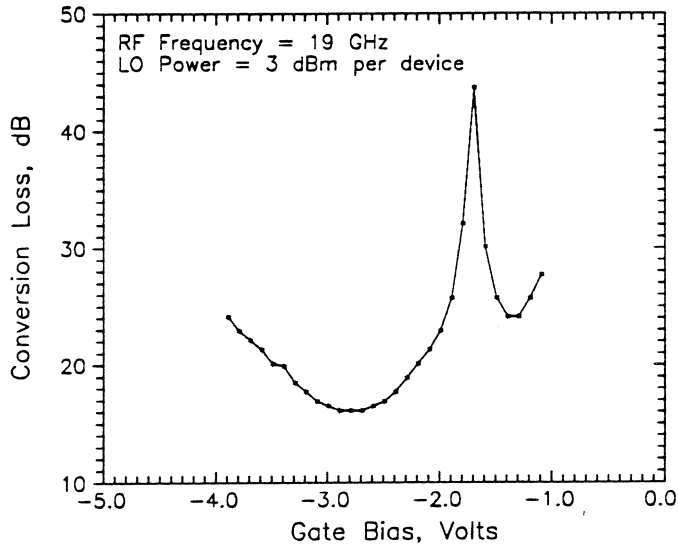

(a)

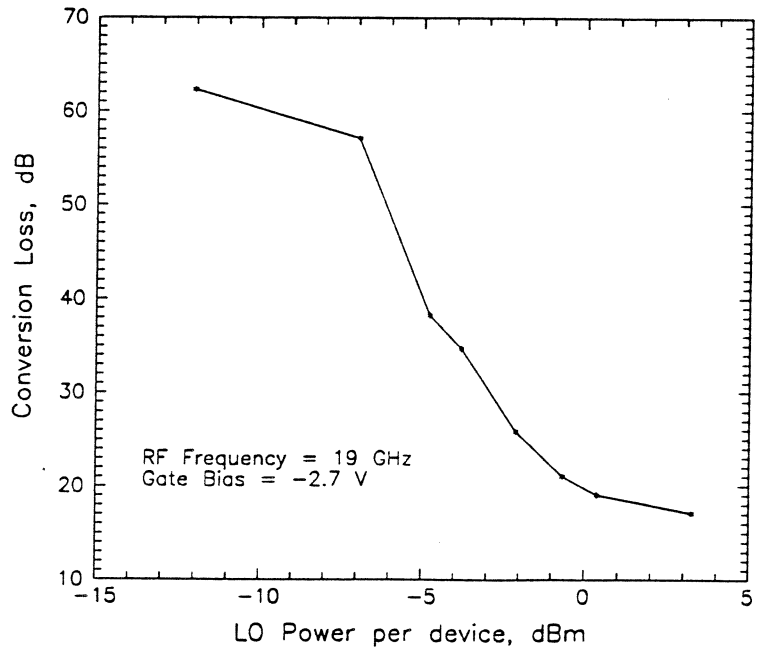

(b)

Figure 7. Conversion loss of the subharmoncially pumped grid mixer as a function of (a) gate bias and (b) LO power incident on the grid.

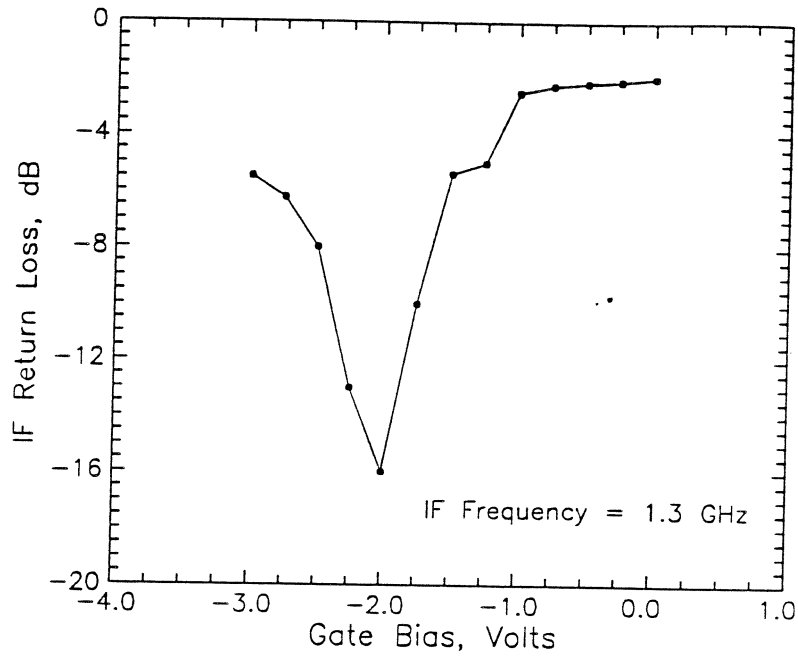

Figure 8. Measured IF return loss at 1.3 GHz as a function of DC gate bias.

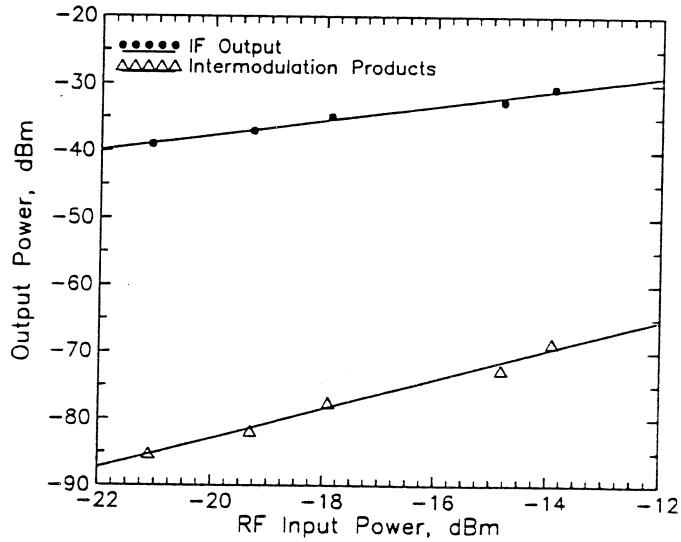

Figure 9. Measured IF output and intermodulation products of the grid mixer. Extrapolation gives a third-order intercept point of $P_{out} = 6.8$ dBm.

is shown in Fig. 5. To measure the RF power incident on the array, two identical horns were positioned facing one another and seperated by 90 cm (twice the distance to the grid). A sheet of absorber with an aperture equal to the size of the grid was placed halfway between the horns. The free-space pathloss as a function of frequency was then measured with one horn connected to a sweeper and the other connected to a power meter. A similar procedure was used to find the incident LO power.

The conversion loss of the mixer grid was measured as a function of RF frequency (with a fixed IF), DC gate bias, and incident LO power. These results are shown in Fig. 6 and Fig. 7. A minimum conversion loss of 16 dB occured at an RF frequency of 19 GHz, a gate bias of -2.7 V, and an incident LO power of 3 dBm per device. It should be noted that these measurements were done without input or output polarizers to tune the LO and RF impedances. The IF match was also measured using an HP 8510 network analyzer. Figure 8 shows the measured IF return loss at 1.3 GHz as a function of gate bias. In addition, we invesigated the linearity of the mixer and attempted to measure the third-order intercept point. The IF signal and intermodulation products as a function of incident RF power is shown in Figure 9. Because the signal levels are quite low, the validity of extrapolating to find the intercept point is questionable. However, the extrapolated intercept point $P_{out} = 6.8$ dBm agrees favorably with the expected improvement of about 11 dB over a single element subharmonically-pumped mixer.

Summary

In this paper, we have presented the design and performance of a subharmonically pumped HFET grid mixer. The grid mixer is attractive because of its quasi-optical coupling and increased dynamic range. Another attractive feature is the large degree of isolation between the LO and RF ports resulting from the physical layout of the grid. The measured conversion loss is comparable to other subharmonic mixers of similar design and could probably be improved with more careful modeling and by providing separate input and output polarizers for impedance tuning.

Acknowledgments

The authors would like to thank Dr. Ilcho Angelov, Dr. Björn Albinsson, Hans Grönqvist, and Christer Karlsson for their expertise, advice, and help with fabrication.

References

[1] E.A. Sovero, M. Kim, R.M. Weikle, II, D.S. Deakin, W.J. Ho, J.A. Higgins, and D.B. Rutledge, "A Monolithic 35 GHz HBT Quasi-Optical Grid Oscillator," *IEEE GaAs IC Symposium,* Miami, FL, October 1992.

[2] A Torabi, H.M Harris, R.W. McMillan, S.M. Halpern, J.C. Wiltse, C.J. Summers, "Planar Grid Oscillator for Quasi-Optical Power Combining at 37 GHz," *Fourth Int. Symposium on Space Terahertz Tech.,* Los Angeles, CA 1993.

[3] R.M. Weikle, II, M. Kim, J.B. Hacker, M.P. De Lisio, D.B. Rutledge, "Planar MESFET Grid Oscillators Using Gate Feedback," *IEEE Trans. Microwave Theory Tech.,* MTT-40, pp. 1997-2003, November 1992.

[4] W.W. Lam, C.F. Jou, H.Z. Chen, K.S. Stolt, N.C. Luhmann, Jr., D.B. Rutledge, "Millimeter-Wave Diode-Grid Phase Shifters," *IEEE Trans. Microwave Theory Tech.,* MTT-36, pp. 902-907, May 1988.

[5] C.F. Jou, W.W. Lam, H.Z. Chen, K.S. Stolt, N.C. Luhmann, Jr., D.B. Rutledge, "Millimeter-Wave Diode-Grid Frequency Doubler," *IEEE Trans. Microwave Theory Tech.,* MTT-36, pp. 1507-1514, November 1988.

[6] M. Kim, *et al.*, "A Grid Amplifier," *IEEE Microwave and Guided Wave Lett.,* vol. 1, no. 11, pp. 322-324, November 1991.

[7] J.B. Hacker, R.M. Weikle, II, M. Kim, M.P. De Lisio, D.B. Rutledge, "A 100-Element Planar Schottky Diode Grid Mixer," *IEEE Trans. Microwave Theory Tech.,* MTT-40, pp. 557-562, March 1992.

[8] H. Zirath, I. Angelov, N. Rorsman, "A Millimeter-Wave Subharmonically Pumped Resistive Mixer based on Heterostructure Field Effect Transistor Technology," *1992 MTT-S International Symposium Digest,* pp. 599–601, Albequerque, NM.

[9] "HP 85150B Microwave Design System," Hewlett-Packard Company, Networks Measurements Division, 1400 Fountaingrove Parkway, Santa Rosa, CA 95403, U.S.A.

[10] P.S. Carter, "Circuit Relations in Radiating Systems and Applications to Antenna Problems," *Proc. IRE,* vol. 20, pp. 1004-1041, June 1932.

[11] R.L. Eisenhart, P.J. Khan, "Theoretical and Experimental Analysis of a Waveguide Mounting Structure," *IEEE Trans. Microwave Theory Tech.,* MTT-19 pp. 706-719, August 1971.

HFET Resistive Mixers for Frequencies above 100 GHz

Herbert Zirath*, Ilcho Angelov*, Niklas Rorsman*, Christer Karlsson*,
Robert M. Weikle,II** and Erik L. Kollberg*

The development of HFETs based on InGaAs alloys has, during the last few years, pushed the frequency limit of semiconductor based amplifiers up to several hundred GHz. So far, however, mixers are usually based on either Schottky barrier diodes or SIS-diodes. In future receiver applications it would be suitable to integrate the amplifier, mixer, and even the oscillator on the same chip. For this purpose, we have investigated two different types of resistive mixers, a fundamentally pumped mixer where the LO is applied to the gate, modulating the source-drain resistance, and a subharmonically pumped resistive mixer, based on two similar HFETs in parallel, pumped at each gate with the same LO-amplitude but 180° out of phase. The pumping frequency is halved compared to the fundamentally pumped case since the combined source-drain conductance waveform varies with twice the LO-frequency. This feature is very attractive a high frequencies where it is difficult to obtain high powers. The resistive FET mixer is also attractive from the intermodulation distortion point of view.

Suitable double-delta-doped HFETs with a pseudomorphic InGaAs channel, were developed for the purpose. A harmonic balance simulation for the two mixer circuits were performed. A special fixture with a waveguide-to-microstrip transition was designed for the experimental evaluation of mixer performance above 100 GHz. For the fundamentally pumped mixer, a total conversion loss of 12 dB was obtained between 108 and 114 GHz at an LO-power of 8 dBm. The conversion loss was limited by the available LO-power. Similar performance was obtained for the subharmonically pumped mixer but with a higher conversion loss, 22 dB. These results represent the first obtained experimental results at such high frequencies and, according to our simulation, conversion loss can be improved to 8 dB for the fundamentally pumped mixer, and to 12 dB for the subharmonically pumped mixer with the same HFET structure if the parasitic bonding inductances are reduced.

---

*Chalmers University of Technology, S-412 96 Göteborg, Sweden
**University of Virginia, Charlottesville, VA 22903

Tailoring Artificial Dielectric Materials at Terahertz Frequencies

R.H. Giles, A.J. Gatesman, J. Fitzgerald, S. Fisk and J. Waldman
University of Massachusetts Lowell
Submillimeter Technology Laboratory
Lowell, Massachusetts 01854

Abstract

The Submillimeter Technology Laboratory(STL) at the University of Massachusetts Lowell has developed a methodology of tailoring the complex refractive index for artificial dielectrics at terahertz frequencies. A wide range of precisely controlled optical properties have been achieved for materials such as vinyl acetate, silicone, polyethylene and epoxy resin when combined with powdered loading agents such as boron nitride, silicon, graphite, iron oxide and stainless steel flake. Using this technology, STL has successfully fabricated both narrow-band and wide-band anechoic structures. The method of characterizing materials for the purpose of tailoring their dielectric properties at terahertz frequencies is presented along with several demonstrated applications.

2. Introduction

Because of the increase in the number of optical and quasi-optical measurement systems operating at terahertz frequencies, new materials providing alternative solutions to the design of system components are required. In response to this, STL's recent activities include an aggressive program to evaluate a wide range of materials for terahertz frequency applications[1-3]. Using in-house expertise in the technique of tailoring artificial dielectrics and the polarimetric characterization of materials, a variety of composite structures have been created as far-infrared radiation absorbing material (FIRAM)[4,5].

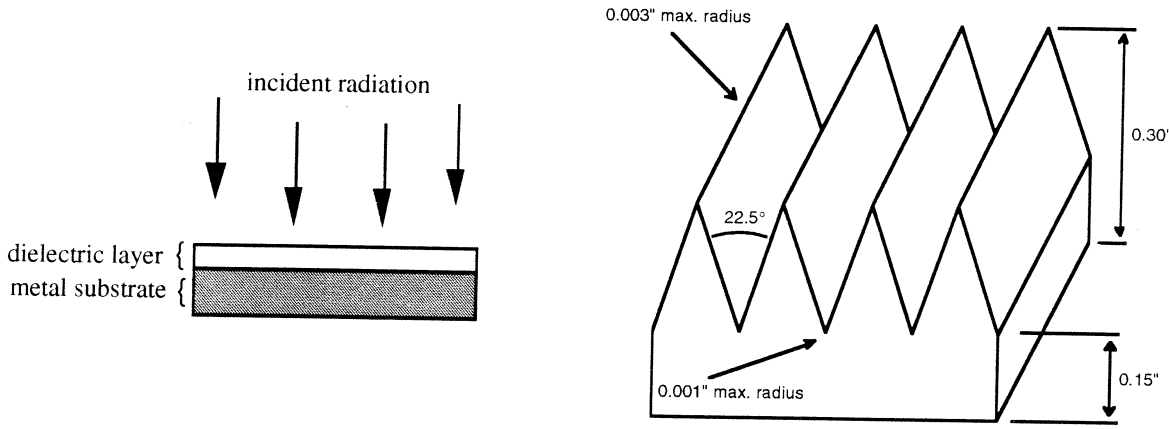

Figure 1. The FIRAM depicted on the left is a resonant absorption structure which consists of a quarter-wave thick artificial dielectric surface on a metal plate. Shown on the right are design parameters for the wedged-type anechoic implemented by STL[6].

One type of FIRAM, known at microwave frequencies as the Dällenbach layer, consists of a metal substrate coated with an evenly thick homogeneous artificial dielectric material[7]. The second type relies on a wedge-type surface geometry fabricated from a lossy silicone-based material to achieve performance as a submillimeter-wave anechoic. Examples of both FIRAM structures are shown in Figure 1. In each case a –25dB reflectivity reduction was measured at normal incidence, however when appropriately oriented within quasi-optical measurement systems these materials reduce reflections due to unwanted stray radiation by more than –50dB. Considerations such as manufacturablility and cost were addressed in choosing the methodology to implement the anechoic structures.

3. Design and Fabrication of the Dällenbach FIRAM

Realization of the Dällenbach layer as a FIRAM starts with development of a particular class of submillimeter wavelength artificial dielectric, generically referred to as metallic paints. The paint, manufactured by Stainless Steel Coatings, Inc. of Littleton, Mass, consists of resins such as vinyl acetate, silicone or polyurethane uniformly loaded with stainless steel flakes. Since the metal flakes are dimensionally small compared to the wavelength, the paint exhibits the optical properties of a homogeneous media.

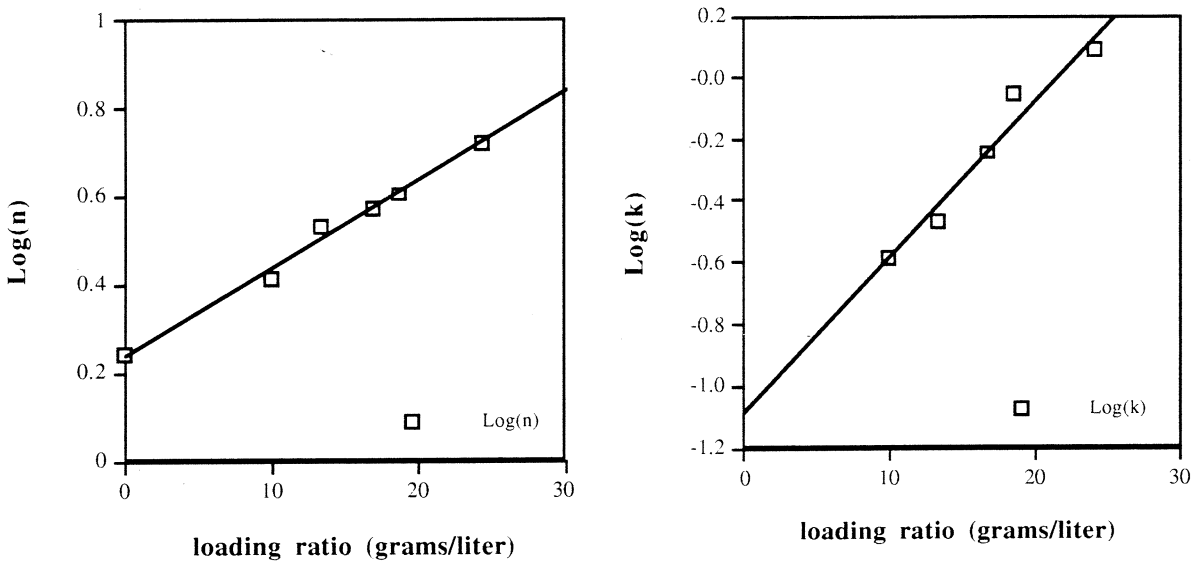

Figure 2. The complex refractive index, n – i k, for the tailored artificial dielectric as a function of the metal flake loading ratio, ρ.

Fourier transform spectroscopy (FTS) transmission and reflection measurements were performed on a series of vinyl acetate based paint samples, each with a different concentration of stainless steel flake. Using a CO_2 optically pumped submillimeter-wave laser operating at 0.584 THz, Brewster's angle was also measured. The complex refractive index, n – i k, of each sample was ascertained by fitting the FTS and laser data to the Fresnel equations. As shown in Figure 2, the material's refractive index as a function of the metal flake loading ratio, ρ, exhibits a power law

relationship. An algorithm was developed to describe the behavior analytically and is expressed as:

$$n \approx 1.73 \times 10^{(0.0201\ \rho)} \quad \text{and} \quad k \approx 0.082 \times 10^{(0.0504\ \rho)} \tag{1}$$

for a loading ratio in the regime of $0 \leq \rho \leq 30$ grams of stainless steel flake per liter of vinyl acetate binder.

This technique of characterizing and tailoring the dielectric constant of metal loaded paints at terahertz frequencies had been previously demonstrated at STL[8]. When tied to theoretical modeling of the paint's reflectivity as a function of thickness, dielectric constant and frequency using the Fresnel equations, the dielectric properties of metallic paints are ideal for providing an anechoic layer on metal surfaces. As shown in Figure 1 and Figure 2, these paints provide the vehicle for which phase and amplitude matching of the incident electric field can occur. The paint's complex refractive index model, defined by equations 1, allows calculation of the FIRAM's optical behavior using the Fresnel equations[9]. With a reflectivity of ≈ 1 for aluminum[10], the resonant structure's theoretical reflectivity was approximated by:

$$R \approx \left| \frac{r + e^{-2i\beta}}{1 + r\,e^{-2i\beta}} \right|^2 \tag{2}$$

$$\text{where} \quad r = \frac{N - 1}{N + 1} \quad \text{and} \quad \beta = (2\pi N t)/\lambda$$

are the paint's front surface reflectivity and phase thickness, respectively.

Upon evaluating equation 2 one concludes that a dielectric layer with phase thickness equal to a quarter wavelength should cause destructive interference at the material's front surface. Furthermore, if the amplitude of the electric field reflected from the paint's front surface equals that of the back surface which suffers absorption, all of the incident electric field is reflected back into the material and complete resonant absorption, i.e. the FIRAM, is established.

Using the theory described, calculations were performed to predict fabrication parameters for a range of FIRAM samples using the paint's experimentally determined dielectric properties. The far-infrared reflectivity of these samples were measured over a frequency regime of 300 GHz to 3 THz using FTS reflectivity measurements. Due to uncertainties in the refractive index model (Equation 1), the predicted fabrication parameters were only adequate for evaluating the FIRAM's general reflectivity behavior. Therefore several samples of metallic paint were prepared and tested with loading ratios ranging from 15 to 25 grams of stainless steel flake per liter of vinyl acetate binder. Also each paint sample was applied to several aluminum substrates in thicknesses which varied from 0.0005" to 0.005".

The frequency at which the reflectivity null occurred for each sample was identified and the FTS measurement results were compared to theoretical predictions. Careful analysis of the structure's multiple reflection theory at the frequency of interest (0.584 THz), allowed modification of the paint's refractive index model to achieve tighter characterization tolerances. Utilizing the modified model, the artificial dielectric layer was specifically matched in metal loading and thickness to create a Dällenbach layer which produced an RCS reduction of –27dB at

0.584 THz. See Figure 3

Reflectivity data on additional samples, shown in Figure 4, indicate the flexibility of fabricating FIRAMs for use at other frequencies. With a reflectivity null occurring at 0.584 THz for a 2.5 mil thick layer as compared to the one well above 3 THz for a 0.4 mil thick layer, one determines that the loading ratio of an artificial dielectric material could be designed and the Dällenbach FIRAM optimized at any terahertz frequency.

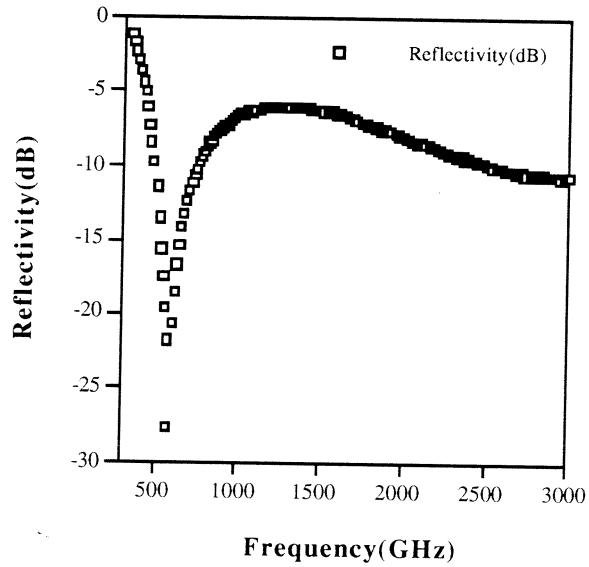

Figure 3. The reflectivity as a function of frequency for the vinyl acetate specifically matched in metal loading and thickness to provide an RCS reduction of –27dB at 0.584 THz.

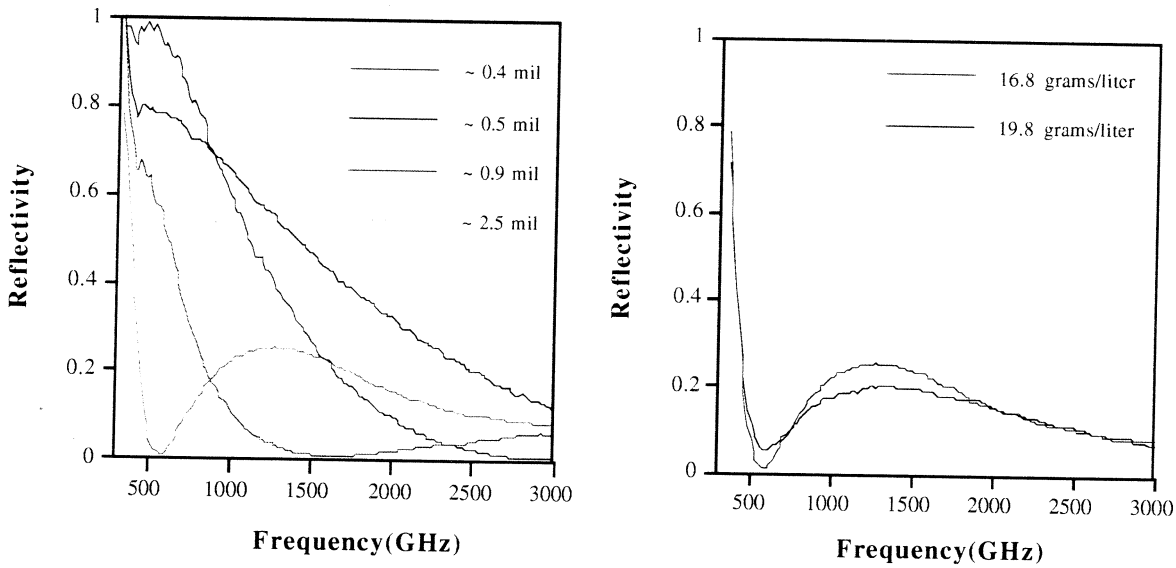

Figure 4. With a loading ratio of ρ = 19.8 grams/liter, the reflectivity of four Dällenbach layers of thickness varying from 0.4 mils to 2.5 mils is shown on the left. Optimization of the material's loading ratio is depicted on the right for two 2.5 mil thick structures.

Application of the metal loaded vinyl acetate as a Dällenbach was performed using a hand-held spray gun. While this method was suitable for prototype studies, the thickness tolerance and uniformity over large-area samples could not be achieved reliably. Techniques currently under consideration to achieve production thin-film materials are: robotic spraying, extrusion blow molding, compression molding, casting and spin coating. For this purpose, research on alternative materials such as low density polyethylene (LDPE) and epoxy resins is being conducted.

Performing FTS measurements on a series of both epoxy resin based samples and LDPE based samples, each with a different concentration of stainless steel flake, produced behavior similar to the properties described for metal loaded vinyl acetate. However, increased flexibility in tailoring the refractive index was achieved for these materials by introducing powdered silicon (a low loss, high n material) as a second loading agent. By adjusting the powdered silicon and stainless steel flake concentration levels, the real and imaginary component of a material's complex refractive index can be controlled independently. As shown in Figure 5, STL has already fabricated Dällenbach layers using the spin coating technology. Since large area, uniformly thick dielectric layers are achievable by this method, efforts to exploit this technology for applications such as AR coatings and optical band-pass filters are under consideration.

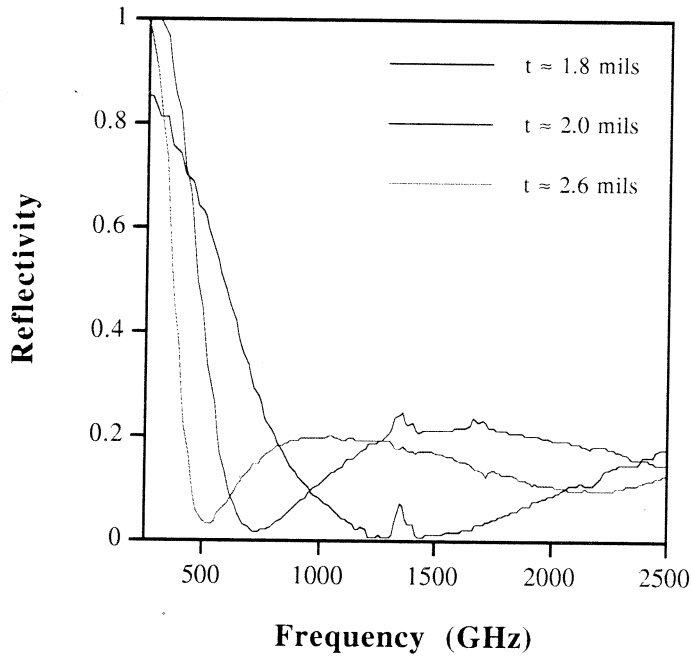

Figure 5. With an 8% loading ratio for stainless steel loaded epoxy resin, the reflectivity of three Dällenbach layers of thicknesses varying from 1.8 mils to 2.6 mils is shown.*

*The reflectivity peak observed at ≈ 1.4 THz is an artifact of the FTS measurement system.

4. Design and Manufacture of the Silicone-based Anechoic Structure

Silicone-based anechoics using wedge-type surface geometries have also been designed by STL researchers for use at terahertz frequencies. These materials provide more than –60dB of reduction in reflectivity for large-scale quasi-optical measurement systems. The geometry of the grooved surface shown in Figure 1 is manufactured in 2′ x 2′ sheets to precise tolerances through a pressure injection molding process.

As demonstrated by Janz and co-workers[11] in the millimeter wavelength regime, wedge and pyramidal–structured surface geometries improve a material's absorption properties by increasing the number of surfaces incident radiation must encounter before backscattering to the receiver occurs. Measurements performed by these and other researchers[12] have shown that the reduction in reflectivity achieved may be expressed by:

$$R_S \approx R_f^{(180°/\theta_g)} \tag{3}$$

where R_f is the material's front surface reflectivity and θ_g the structure's groove angle. Since this type of FIRAM is generally fabricated from homogeneous lossy dielectric materials which exhibit front surface reflectivities (R_f) of less than 10%, anechoic structures can be designed to provide more than –80dB of reflectivity reduction for a groove angle of 22.5° .

Using a silicone elastomer and electrically insulating siliceous filler, Prewer and Milner of Thorn EMI Technology Inc. fabricated the first samples of terahertz frequency anechoic in the form of pyramidal surface structured tiles[13]. Measurements performed during July of 1989 at STL further documented their success when specular and diffuse reflectivity levels of better than –40dB were observed at 0.584 THz for almost all incident directions. However wedge and pyramidal structured anechoic materials suitable for large-scale use at terahertz frequencies were not commercially available at that time.

Therefore STL researchers initiated a project to design and fabricate silicone-based wedge-structure anechoic material for use with its submillimeter-wave measurement systems. A method of estimating refractive indices was used to characterize a variety of materials in search for a lossy dielectric exhibiting low front surface reflectivity. Using cost-efficient molding techniques, prospective dielectric materials such as the widely available plastics and elastomers promised to provide good anechoic properties if constructed with modified surface geometries.

Chosen as most suitable due to its mechanical and optical properties was iron-oxide-loaded silicone. The front surface reflectivity for a flat 0.25" thick sample of the material was measured at 1.56 THz and found to be $R_f \approx 5.57\%$. The transmissivity was also measured and found to be $T \approx 1.8\%$ for a t = 1.9mm thick sample of the same material. The Fresnel equations for the multiple reflection theory transmissivity:

$$T = \left| \frac{(1 - r_f^2)\, e^{-2\pi N t/\lambda}}{1 - r_f^2\, e^{-4\pi N t/\lambda}} \right|^2 \tag{4}$$

and front surface reflectivity:

$$R_f = |r_f|^2 \qquad \text{where } r_f = (N-1)/(N+1)$$

were used to estimate a complex refractive index of $N \approx 1.62 - 0.03\ i$, for the iron oxide loaded silicone. With more than a –100dB reflectivity reduction expected from a structure such as the design depicted in Figure 1, STL created a 3.5" x 24" prototype aluminum mold structure for conceptual evaluation. A reduction in reflectivity of better than –80dB was realized for all incident angles except normal incidence and those angles satisfying the grating equation. At those orientations values of better than –40dB were observed.

Therefore a contract was established to manufacture 24" x 24" iron-oxide-loaded solid silicone sheets with the wedge-type surface geometry. The final anechoic structure was evaluated at 0.584 THz using a CO_2 optically pumped submillimeter laser. The reflectivity was measured by illuminating 6" x 24" samples, mounted on a rotary stage, with a 2" FWHM diameter beam. Measured values were ratioed to the measured return for a flat front surface mirror at normal incidence. Figure 6 depicts the measurement configurations used for evaluating a sample's reflectivity.

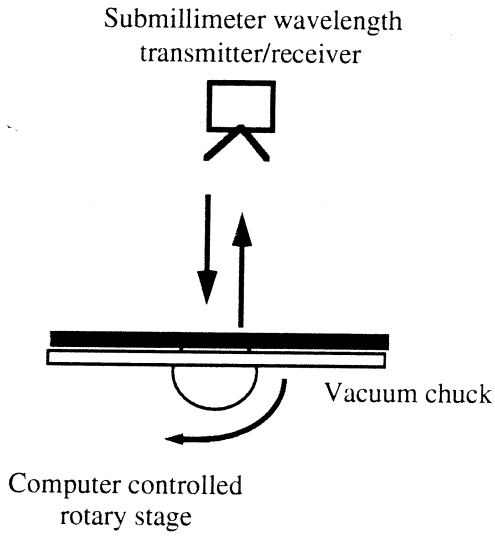

Figure 6. Shown is the configuration of the submillimeter-wave measurement system used to evaluate a material's reflectivity monostatically.

As observed in Figure 7, results for STL's silicone-based FIRAM indicate that performance is angular dependent. While the reflectivity peaks at normal incidence and those angles satisfying the grating equation have a higher value than was observed for the prototype structure, an overall performance of better than –60 dB for production grade material was considered a major success. Differences between the prototype and production grade FIRAM are strictly related to the machining limitations for each mold structure. While a peak radius of better than 0.003" was achieved during the prototype study for the milled aluminum mold, only a radius of ≈ 0.006" could be achieved for the steel precision ground production mold.

As a comparison to the evaluation of STL's FIRAM, reflectivity measurements were performed on other anechoic materials often used at terahertz frequencies. Figure 8 represents the reflectivity measurements for Thorn EMI's silicone-based RAM 100 and RAM 403. Shown in Figure 9 is reflectivity for Masland Étoile pure wool pile carpet and Emerson & Cuming's Eccosorb™ AN-73.

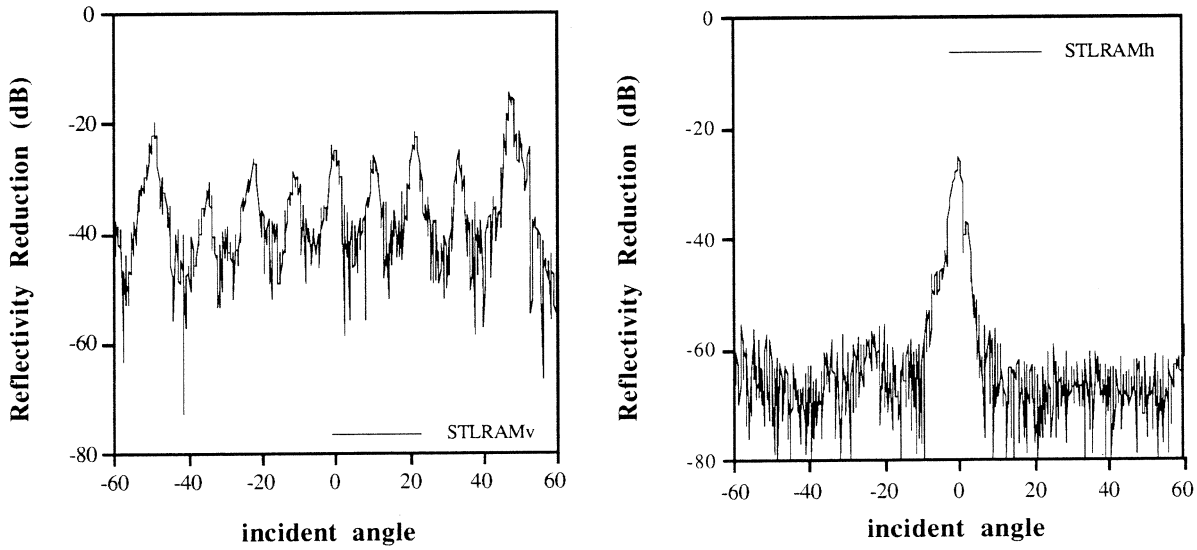

Figure 7 The reflectivity reduction for STL's FIRAM. Shown on the left, and right, are measurements performed with the structure's grooves perpendicular, and parallel, to the plane of incidence.

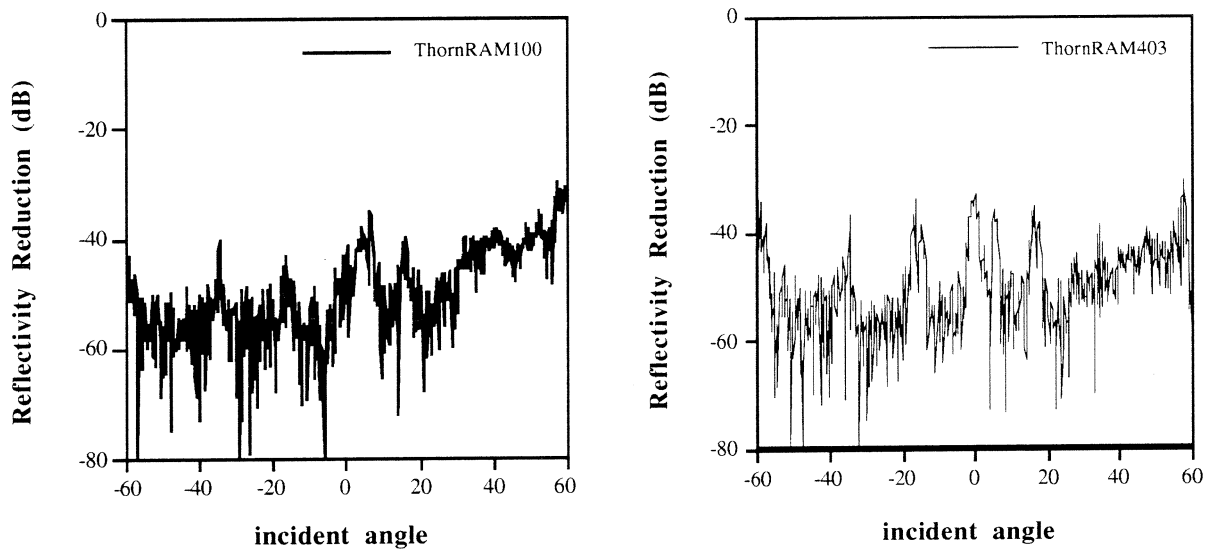

Figure 8 The diffuse reflectivity relative to a flat plate at normal incidence for Thorn EMI's RAM 100 and RAM 403.

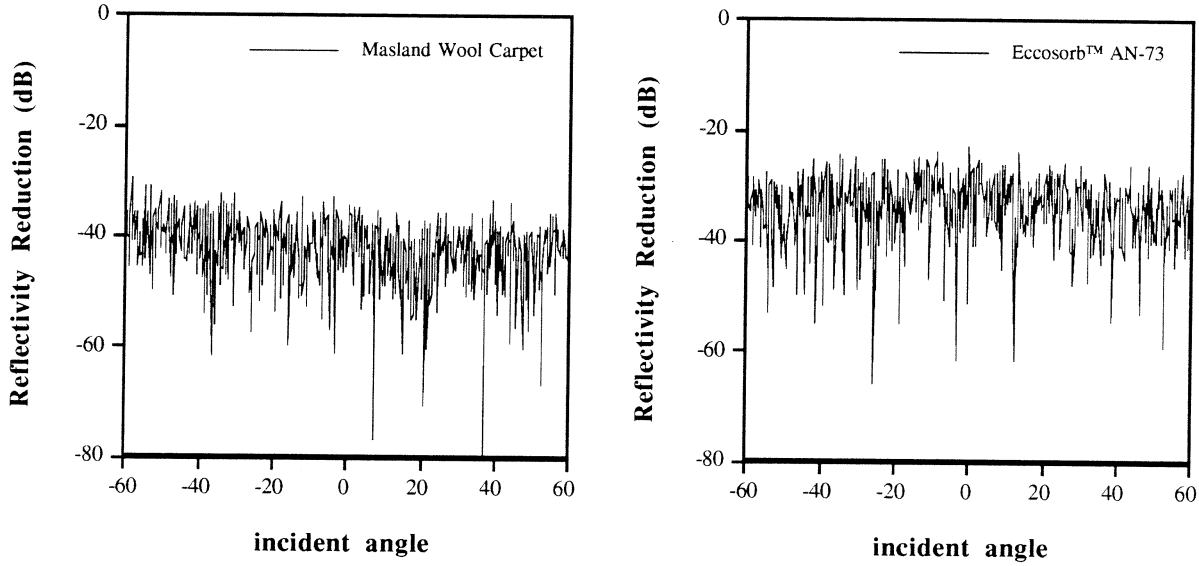

Figure 9. The diffuse reflectivity relative to a flat plate at normal incidence for Masland Étoile pure wool pile carpet and Eccosorb™ AN-73.

5. Conclusions

We have demonstrated that artificial dielectric layers can be optimized to operate as resonant absorbers for any frequency over the regime of 0.3 THz to 3 THz. We also have determined that these anechoic coatings can be designed to provide more than –25dB of reduction in reflectivity. Since the materials are relatively inexpensive and suited to commercial manufacturing methods, the technology is practical for a variety of applications at terahertz radar frequencies.

Also critical to implementation of terahertz radar systems are low cost, large area FIRAM which may be used to suppress unwanted stray radiation. Measurements performed on the silicone-based FIRAMs demonstrated that, if these materials are properly oriented, a reduction in reflectivity of better than –60dB is feasible even for large-scale operations.

6. Acknowledgements

This work was supported by a grant from the U.S. Army in conjunction with partial funding from the University of Massachusetts Lowell.

7. References

1. R.H. Giles, A.J. Gatesman, and J. Waldman, "A Study of the Far-Infrared Optical Properties of Rexolite™", International Journal of Infrared and Millimeter Waves, 11, 1299 (1990).

2. A.J. Gatesman, R.H. Giles, and J. Waldman: "Submillimeter Optical Properties of Hexagonal Boron Nitride", Proc. of MRS Society, 242, 623 (1992).

3. A.J. Gatesman, R.H. Giles, and J. Waldman, "A High Precision Reflectometer for the Study of Optical Properties of Materials in the Submillimeter", Proc. of the 17th Int. Conf. on Infrared and Millimeter Waves, Los Angeles, CA, Dec. 1992.

4. R.H. Giles, A.J. Gatesman, A.P. Ferdinand, and J. Waldman, University of Lowell: "Design and Fabrication of Narrow Band Radar Absorbing Materials at Terahertz Frequencies", IEEE Proceedings from the 15th International Conference on Infrared and Millimeter Waves, Orlando, FL, Dec. 1990

5. R.H. Giles, T.M. Horgan, and J. Waldman, "Silicon-Based Anechoics at Terahertz Frequencies", Proc. of the 17th Int. Conf. on Infrared and Millimeter Wave, Los Angeles, CA, Dec. 1992.

6. R.H. Giles and T.M. Horgan: "Silicone-Based Wedged-Surface Radiation Absorbing Material", U.S. Patent Pending

7. G.T. Ruck, D.E. Barrick, W.D. Stuart and C.K. Kirchbaum, Radar Cross Section Handbook, Volumne 2, Plenum Press 1970, Section 8.3.2.1.1.3

8. R.H. Giles, A.P. Ferdinand, M.J. Coulombe, J. Waldman, ULRF and W. Nixon, W. Reinhold, AFSTC: "Submillimeter Wavelength Modeling of Dielectric Materials in Polarimetric Radar Approaches", Proceedings of the NATO Advanced Research Workshop on Direct and Inverse Methods in Radar Polarimetry, Bad Windsheim, Federal Republic of Germany, September 1988.

9. R.M.A. Azzam and N.M. Bashara, Ellipsometry and Polarized Light, North-Holland 1979, Section 4.3

10. M.A. Ordal, R.J. Bell, R.W. Alexander, L.L.Long and M.R. Querry; "Optical Properties of Fourteen Metals in the infrared and far-infrared: Al, Co, Cu, Au, Fe, Pb, Mo, Ni, Pd, Pt, Ag, Ti, V, and W." Applied Optics, Vol. 24, No. 24, pp 4493-4499, Dec. 1985 Note on reference: *Theoretical evaluation of the frequency dependent complex refractive index for aluminum was possible using the Drude model with parameters suggested by Ordal et al. The reflectivity of Al was determined to have a value of 0.99735 at 0.584 THz.*

11. S. Janz, D.A. Boyd, and R.F. Ellis: "Reflectance Characteristics in the Submillimeter and Millimeter Wavelength Region of a Vacuum Compatible Absorber", International Journal of Infrared and Millimeter Waves, Vol. 8, No. 6, 1987, pp. 627-635

12. B.T. Dewitt: "Analysis and Measurement of Electromagnetic Scattering by Pyramidal and Wedge Absorbers", Ph.D. Dissertation, Ohio State University, 1986

13. B.E. Prewer, B. Milner: "Radiation Absorber and Method of Making It", U.S. Patent # 4,942,402 , July 17, 1990

A GAUSS-LAGUERRE ANALYSIS OF THE DUAL-MODE ('POTTER') HORN

Joakim F. Johansson

The Millimeter Wave Laboratory

Department of Radio & Space Science
with Onsala Space Observatory
Chalmers University of Technology
S–412 96 Gothenburg
Sweden

ABSTRACT

The dual-mode conical horn (a.k.a. the Potter horn) has the advantage of the relative simplicity with which it can be machined, even at small dimensions. Dual-mode horns are thus often used as substitutes for corrugated horns which are lossy and difficult (or impossible) to fabricate for submillimeter wavelengths.
A dual-mode horn with the proper combination of the circular TE_{11} and TM_{11} modes has a highly symmetrical aperture field and a relatively low cross-polarization level (≈ 1,4 % of the total radiated power). The fundamental Gaussian mode power fraction of the dual-mode horn (≈ 96,3 %) compares well with that of the corrugated horn (≈ 98,1 %).
The aperture field of the dual-mode horn has been expanded into Gauss-Laguerre modes. The symmetries of the aperture field result in a Gauss-Laguerre expansion of orders zero and two for the co-polarized part, and order two for the cross-polarized part. The expansion is rapidly convergent and truncating beyond mode number 10 would only leave out 0,026 % of the total power.
The equivalent Gaussian beam waist size and position, the radiation patterns, as well as the aperture stop requirements have been calculated and are presented as functions of the Gaussian phase slip parameter.

1. INTRODUCTION

At sub-millimeter wavelengths there is a never-ending quest for the Philosopher's Stone; The Optimum Antenna. An antenna should be easy to fabricate, have no loss, a very nice radiation pattern, and, of course, infinite bandwidth. But, as always, engineering is full of trade-offs. Each antenna type has its advantages and disadvantages. The corrugated conical horn [1, 2, 3] is a popular antenna for millimeter wavelengths, but they are lossy and difficult (or impossible) to fabricate for submillimeter wavelengths.

Easier to fabricate, but not that good in terms of symmetrical beams and cross-polarization properties is the smooth-walled conical horn [4].
Recently, the diagonal horn has been suggested as a candidate for shorter wavelengths. This horn yields a highly symmetrical beam, but has some cross-polarization [5, 6]. The diagonal horn is probably optimum for focal-plane imaging applications.
This paper will treat the dual-mode conical horn, which combines most of the advantages of the other horns [7, 8, 9, 10]. The horn is fairly easy to fabricate, the radiation pattern is highly symmetric, the cross-polarization is low, and the smooth wall yields low losses. The main disadvantage is the rather limited bandwidth [≈ 5 %].
In the following the dual-mode horn is described, and some definitions are made. The aperture field is then expressed in terms of Gauss-Laguerre modes, which makes it very simple to calculate the field at any point in front of the horn.

2. THE DUAL-MODE ('POTTER') HORN

The normal conical horn with its TE_{11} circular waveguide mode aperture field has the disadvantage of a rather non-Gaussian shape, together with abrupt field changes at the edges (E-plane). The field lines are also rather crooked, see Fig. 1. The coupling to a Gaussian beam is about 86,7 % [4], to be compared with the 98,1 % of the corrugated horn [3]. The discontinuities in the field also gives rise to marked diffractive effects, and the side-lobe level is thus fairly high in the E-plane.
The TE_{11} mode has a twin in the TM_{11} mode. The aperture field of this mode is also shown in Fig. 1. The electric field expressions for the two modes are (*cf.* [11]):

$$\bar{E}_{TE_{11}}(r,\varphi) = E_o\left(\left[J_o\left(\chi\tfrac{r}{a}\right)+J_2\left(\chi\tfrac{r}{a}\right)\right]\sin\varphi\,\hat{r}+\left[J_o\left(\chi\tfrac{r}{a}\right)-J_2\left(\chi\tfrac{r}{a}\right)\right]\cos\varphi\,\hat{\varphi}\right)=$$

$$E_o\left(J_2\left(\chi\tfrac{r}{a}\right)\sin 2\varphi\,\hat{x}+\left[J_o\left(\chi\tfrac{r}{a}\right)-J_2\left(\chi\tfrac{r}{a}\right)\cos 2\varphi\right]\hat{y}\right) \qquad (1a)$$

$$J_1'(\chi)\equiv 0 \quad\rightarrow\quad \chi\approx 1{,}841183781$$

$$\bar{E}_{TM_{11}}(r,\varphi) = E_o\left(\left[J_o\left(\xi\tfrac{r}{a}\right)-J_2\left(\xi\tfrac{r}{a}\right)\right]\sin\varphi\,\hat{r}+\left[J_o\left(\xi\tfrac{r}{a}\right)+J_2\left(\xi\tfrac{r}{a}\right)\right]\cos\varphi\,\hat{\varphi}\right)=$$

$$E_o\left(-J_2\left(\xi\tfrac{r}{a}\right)\sin 2\varphi\,\hat{x}+\left[J_o\left(\xi\tfrac{r}{a}\right)+J_2\left(\xi\tfrac{r}{a}\right)\cos 2\varphi\right]\hat{y}\right) \qquad (1b)$$

$$J_1(\xi)\equiv 0 \quad\rightarrow\quad \xi\approx 3{,}83170597$$

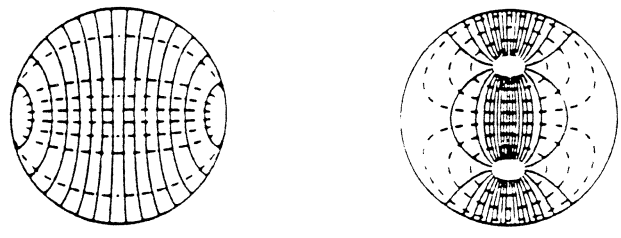

Figure 1. *The electric field patterns for the circular waveguide TE_{11} (left) and TM_{11} (right) modes (cf. [11, 12]).*

The two expression are seen to have marked similarities. It is also evident that the field lines, if combined, would be straightened out. Thus the combination of these two modes can yield a much 'nicer' aperture field, given by

$$\bar{E}(r,\varphi) = \frac{\bar{E}_{TE_{11}}(r,\varphi) + \beta\,\bar{E}_{TM_{11}}(r,\varphi)}{1+\beta} \qquad r \le a \tag{2}$$

where β is a complex mode balance constant. The total aperture field then takes the form

$$\bar{E}(r,\varphi) = E_o\left(-G\left(\frac{r}{a}\right)\sin 2\varphi\;\hat{x} + \left[F\left(\frac{r}{a}\right) + G\left(\frac{r}{a}\right)\cos 2\varphi\right]\hat{y}\right)$$

$$F(\rho) = \frac{J_o(\chi\rho) + \beta\,J_o(\xi\rho)}{1+\beta} \qquad G(\rho) = \frac{-J_2(\chi\rho) + \beta\,J_2(\xi\rho)}{1+\beta} \tag{3}$$

The idea for the dual-mode horn is thus to excite some amount of the TM_{11} mode in a mode converter and then make sure that the two modes have the correct relationship at the aperture of the conical part of the horn, see Fig. 2. Since the two modes have different cut-off frequencies, their dispersion characteristics are different. If some freedom of choice is needed in terms of horn dimensions, a phasing section is needed to ensure that the proper aperture field is achieved. All this combined makes the horn rather frequency sensitive, but this is not so important for some applications.

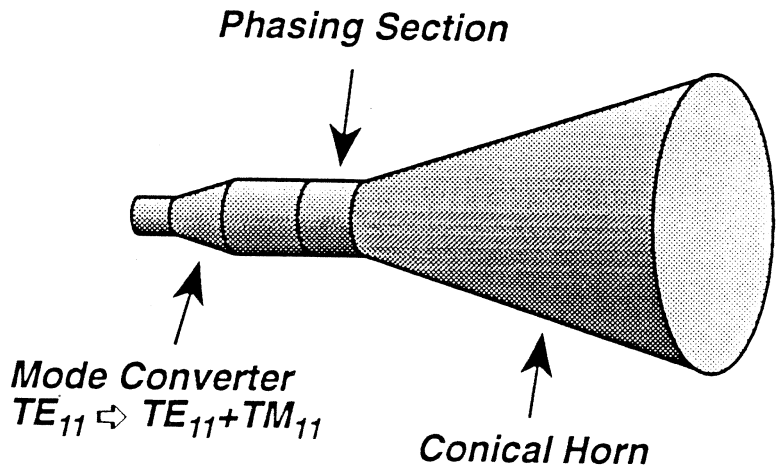

Figure 2. A schematic drawing of a dual-mode conical horn.

There are several ways to choose the relative magnitudes and phases of the two modes at the aperture plane, depending on if one wants to optimize cross-polarization, minimize sidelobes, *etc.* (*cf.* [7, 8, 13]). One way to arrange the mode excitation is to have the two modes in phase at the aperture with the mode balance constant β

chosen so that the radial field component is zero at the rim of the horn [8], *viz.*

$$\beta = \frac{J_o(\chi)}{J_2(\xi)} \approx 0{,}7846565074 \tag{4}$$

The resulting aperture field functions are then (see Fig. 3)

$$F(\rho) = \frac{J_o(\chi)\,J_o(\xi\rho) - J_o(\xi)\,J_o(\chi\rho)}{J_o(\chi) - J_o(\xi)}$$
$$G(\rho) = \frac{J_2(\chi)\,J_2(\xi\rho) - J_2(\xi)\,J_2(\chi\rho)}{J_o(\chi) - J_o(\xi)} \tag{5}$$

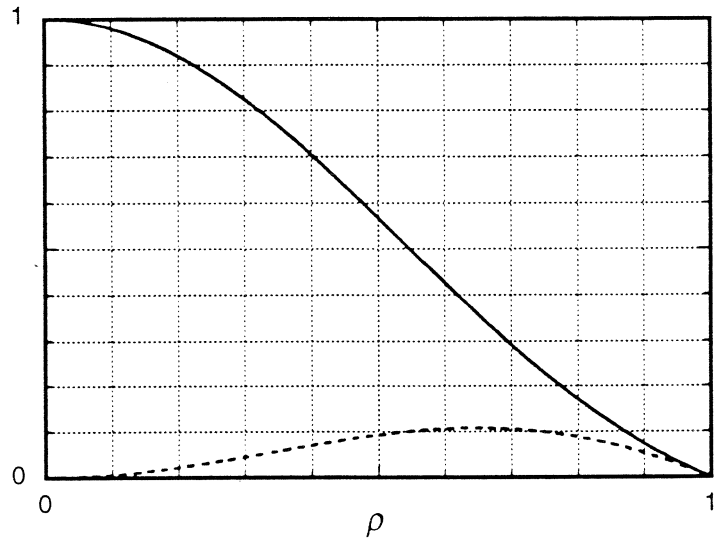

Figure 3. The functions F(ρ) (solid) and G(ρ) (dotted).

The total co-polarized field is plotted in Fig. 4. It is seen that the field *is* zero all along the rim of the aperture (which is seen from inspecting (5)). The aperture field is not fully circularly symmetrical, but the difference is seen to be rather small.
If one calculates the fraction of the power contained in the circularly symmetric part, as well as the co- and cross-polarized azimuthally varying parts, then the result is

$$\frac{P_{sym}^{co}}{P_{tot}} = \frac{1}{2} + \frac{\xi^2 + \chi^2}{\chi^2\left(\xi^2 - \chi^2\right)} \approx 0{,}9721053$$
$$\frac{P_{azi}^{co}}{P_{tot}} = \frac{P_{azi}^{cr}}{P_{tot}} = \frac{1}{4} - \frac{\xi^2 + \chi^2}{2\chi^2\left(\xi^2 - \chi^2\right)} \approx 0{,}0139474 \tag{6}$$

Thus, there is just a small amount 'lost' into unwanted radiation.

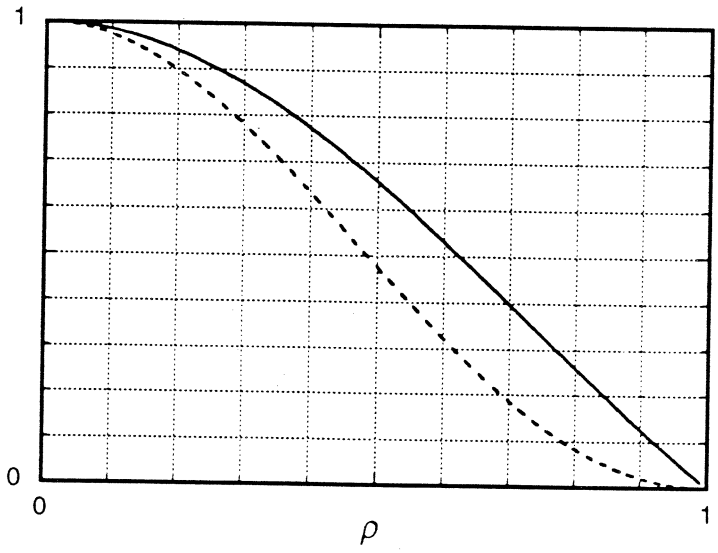

Figure 4. *The co-polarized aperture field distribution plotted for two azimuthal cuts:*
H-plane, $\varphi = 0$ (solid)
E-plane, $\varphi = \pi/2$ (dashed)

3. GAUSS-LAGUERRE MODES

The appearance of the aperture field in (3) gives a hint that the Gauss-Laguerre mode set would be appropriate to use in this case.
The general form for a Gauss-Laguerre expansion of a two-dimensional vector-valued function g is given by (*cf.* [2, 14])

$$\vec{g}(r,\varphi) = \sum_{\alpha=0}^{\infty}\sum_{n=0}^{\infty}\left(\vec{C}_n^{(\alpha)}\cos\alpha\varphi + \vec{S}_n^{(\alpha)}\sin\alpha\varphi\right) h_n^{(\alpha)}(r/w) \tag{7}$$

where the basis functions are the Gauss-Laguerre functions, *viz.*

$$h_n^{(\alpha)}(\rho) = \sqrt{\frac{2}{\pi}}\sqrt{\frac{2}{1+\delta_{0\alpha}}}\sqrt{\frac{n!}{(n+\alpha)!}}\left(\sqrt{2}\rho\right)^{\alpha} L_n^{(\alpha)}\left(2\rho^2\right) e^{-\rho^2} \tag{8}$$

and the mode coefficients are given by

$$\begin{Bmatrix}\vec{C}_n^{(\alpha)}\\ \vec{S}_n^{(\alpha)}\end{Bmatrix} = \frac{1}{w^2}\int_0^{\infty}\int_0^{2\pi}\vec{g}(r,\varphi)\, h_n^{(\alpha)}(r/w)\begin{Bmatrix}\cos\alpha\varphi\\ \sin\alpha\varphi\end{Bmatrix} r\,dr\,d\varphi \tag{9}$$

We see that except for the zeroth-order circularly symmetric Laguerre mode set, we just have to take into account the second order sets as well. If we were to use the Gauss-Hermite expansion, a lot of these symmetry properties would be lost in a jungle of modes...
The non-zero mode coefficients of the dual-mode horn can be shown to be

$$C_{n\,co}^{(0)} = E_o\sqrt{2\pi}\int_0^{a^2/w^2} F\left(\frac{w}{a}\sqrt{u}\right) L_n^{(0)}(2u)\, e^{-u}\, du$$

$$C_{n\,co}^{(2)} = -S_{n\,cr}^{(2)} = \frac{E_o\, 2\sqrt{\pi}}{\sqrt{(n+1)(n+2)}}\int_0^{a^2/w^2} G\left(\frac{w}{a}\sqrt{u}\right) L_n^{(2)}(2u)\, e^{-u}\, u\, du \qquad (10)$$

The choice of the parameter w/a is in principle arbitrary, but we choose to maximize the power in the fundamental mode. This criterion can be shown to be identical to finding the null for the mode coefficient $\vec{C}_1^{(0)}$, *viz.*

$$\int_0^{a^2/w^2}\left[J_o(\xi)J_o\left(\chi\frac{w}{a}\sqrt{u}\right) - J_o(\chi)J_o\left(\xi\frac{w}{a}\sqrt{u}\right)\right](1-2u)\, e^{-u}\, du = 0 \qquad (11)$$

The result for the dual-mode aperture field is then

$$\kappa \equiv w/a \approx 0{,}5903326584$$

where a dimensionless Gaussian beam size parameter κ has been defined. The mode coefficients for the first few modes for this choice of parameter κ are given in the table below

n	$C_{n\,co}^{(0)}/E_o$	$C_{n\,co}^{(0)}/E_o = -S_{n\,cr}^{(0)}/E_o$
0	1,35876782	0,15472432
1	≡ 0	0,03505191
2	-0,11945949	-0,02315560
3	-0,02464205	-0,02488684
4	0,02736328	-0,00709024
5	0,02522706	0,00698544
6	0,00468442	0,01078499
7	-0,01008692	0,00702175
8	-0,01278554	0,00083943
9	-0,00721838	-0,00388176
10	0,00041933	-0,00556457

Table I. *The Gauss-Laguerre mode coefficients for a dual-mode horn when $w/a \approx 0{,}590333$ (balanced for a null rim field).*

The table shows that there are just a few dominant terms, and that the rest decay quickly with increasing mode number.
The power content in the modes is given by

$$\frac{P_n^{(\alpha)}}{P_{tot}} = w^2 \frac{\vec{C}_n^{(\alpha)} \cdot \vec{C}_n^{(\alpha)*} + \vec{S}_n^{(\alpha)} \cdot \vec{S}_n^{(\alpha)*}}{\int_0^\infty \int_0^{2\pi} \vec{g}(r,\varphi) \cdot \vec{g}(r,\varphi)^* \, r \, dr \, d\varphi} \tag{12}$$

Specifically, the power fraction in the fundamental mode for the dual-mode horn is

$$\frac{P_{0\,co}^{(0)}}{P_{tot}} = \left| \frac{w/a}{\chi} \int_0^{a^2/w^2} \left(\frac{J_o\left(\chi \frac{w}{a} \sqrt{u}\right)}{J_o(\chi)} - \frac{J_o\left(\xi \frac{w}{a} \sqrt{u}\right)}{J_o(\xi)} \right) e^{-u} \, du \right|^2 \tag{13}$$

and in our case this is

$$\kappa \equiv w/a \approx 0{,}5903326584 \quad \Rightarrow \quad \frac{P_0^{(0)}}{P_{tot}} \approx 0{,}9633159142$$

The number of modes that need to be included depends on the application, but a rule of thumb is that more terms are needed for near-field calculations, and for a detailed side-lobe structure. An assessment of the effects of mode set truncation can be made if on considers the fraction of the total power that is left out. If modes above $n = 10$ are excluded, then only 0,00026 of the total power is lost, and this is probably sufficient for most purposes.
The "power budget" for the dual-mode horn can be summarized as follows

Mode(s)	Power fraction
$C_{0\,co}^{(0)}$	0,963316
$C_{n\,co}^{(0)} \quad n \geq 1$	0,008789
$C_{n\,co}^{(2)} \quad n \geq 0$	0,013947
$S_{n\,cr}^{(2)} \quad n \geq 0$	0,013947

Table II. The mode "power budget" for the dual-mode horn.

To get a comparison with other common submillimeter wave feed horns, the table below summarizes the properties of their respective 'Gaussicity'. It is seen that the dual-mode horn is only slightly worse than the corrugated horn in terms of coupling to the fundamental Gaussian mode. However, the corrugated horn couples to a larger waist, due to its less tapered aperture field distribution.

Horn	$\kappa = w/a$	$P_{0\,co}^{(0)}/P_{tot}$
Dual-Mode	0,590333	0,963316
Corrugated [3]	0,643562	0,980751
Conical [4]	0,768100	0,866621
Diagonal [5, 6]	0,863191	0,843025

Table III. A comparison between different horn antennas.

4. GAUSSIAN BEAM PROPAGATION

A multi-mode Gauss-Laguerre beam will propagate as [2, 3]

$$\bar{E}(r,\varphi,z) = \bar{\bar{g}}\left(r,\varphi,\left[\Phi(z)-\Phi_A\right]\right)\frac{w_A}{w(z)}\,e^{-jk(z-z_A)+j(\Phi(z)-\Phi_A)-j\frac{kr^2}{2R(z)}} \tag{14}$$

where

$$\bar{\bar{g}}(r,\varphi,\Delta\Phi) = \sum_{\alpha}\sum_{n}\left(\bar{C}_n^{(\alpha)}\cos\alpha\varphi + \bar{S}_n^{(\alpha)}\sin\alpha\varphi\right)h_n^{(\alpha)}(r/w)\,e^{-j(2n+\alpha)\Delta\Phi} \tag{15}$$

and

$$\begin{aligned} w(z) &= w_o\sqrt{1+\left[z/z_c\right]^2} \\ R(z) &= z\left(1+\left[z_c/z\right]^2\right) \\ \Phi(z) &= \arctan z/z_c \\ z_c &= \frac{\pi w_o^2}{\lambda} \end{aligned} \tag{16}$$

The beam parameters in the aperture plane of the horn are (see Fig. 5 for reference)

$$\begin{aligned} w_A &= w(z_A) = w_o\sqrt{1+\left[z_A/z_c\right]^2} \equiv \kappa a \\ R_A &= R(z_A) = z_A\left(1+\left[z_c/z_A\right]^2\right) \equiv L \\ \Phi_A &= \Phi(z_A) = \arctan z_A/z_c \end{aligned} \tag{17}$$

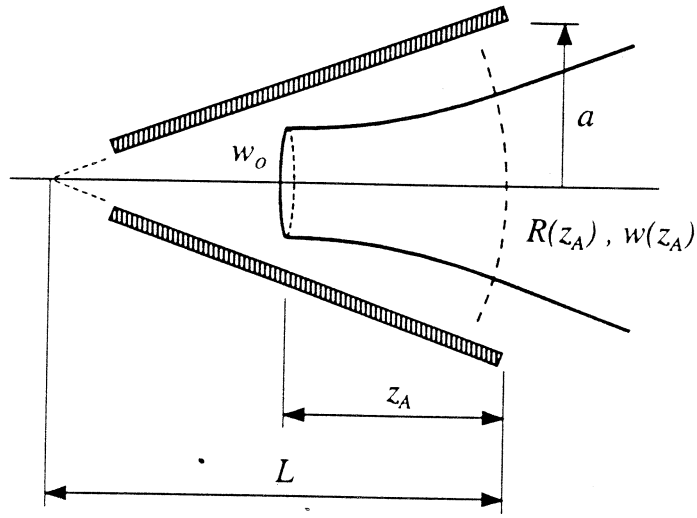

Figure 5. The geometry of a horn launching a Gaussian beam.

The equivalent waist size and position is

$$\begin{aligned} \Phi_A &= \arctan\frac{\pi\kappa^2 a^2}{\lambda L} \\ w_o &= \kappa a \cos\Phi_A \\ z_c &= \frac{L}{2}\sin 2\Phi_A \\ z_A &= L\sin^2\Phi_A \end{aligned} \tag{18}$$

It must be made clear that the equivalent waist position z_A is *not* the position of the phase center, since the different modes will combine in a complex (*sic!*) way. However, for a horn with a high fundamental Gaussian mode content, the difference between the waist position and the phase center will only be slight.

5. FIELD DISTRIBUTIONS AND RADIATION PATTERNS

The field distribution in a certain cut (such as the E-plane) can be found by combining (10), (14) and (15), resulting in the convenient form

$$\begin{aligned} E_{co}(r,\varphi,\Delta\Phi) &= E_{co}\left(r,\frac{\pi}{4},\Delta\Phi\right) - \cos 2\varphi\; E_{cr}\left(r,\frac{\pi}{4},\Delta\Phi\right) \\ E_{cr}(r,\varphi,\Delta\Phi) &= \sin 2\varphi\; E_{cr}\left(r,\frac{\pi}{4},\Delta\Phi\right) \end{aligned} \tag{19}$$

where the D-plane ($\varphi = \pi/4$) patterns are given by

$$E_{co}\left(r,\frac{\pi}{4},\Delta\Phi\right)=\sum_{n=0}^{\infty}C_{n\,co}^{(0)}\,h_n^{(0)}\left(\frac{r}{w}\right)e^{-j2n\Delta\Phi}$$
$$E_{cr}\left(r,\frac{\pi}{4},\Delta\Phi\right)=\sum_{n=0}^{\infty}S_{n\,cr}^{(2)}\,h_n^{(2)}\left(\frac{r}{w}\right)e^{-j2[n+1]\Delta\Phi} \qquad (20)$$

The different cuts are hence given by the co- and cross-polarized D-plane patterns. The field distributions when including modes $n \leq 10$ are given in the panels in Fig. 6 as functions of the parameter r/w .
If the angular far-field pattern is desired, then the following substitution should be made:

$$\left.\frac{r}{w}\right|_{Far-field}=\frac{\pi\kappa a}{\lambda}\cos\Phi_A\,\tan\theta$$
$$\left.\Delta\Phi\right|_{Far-field}=\frac{\pi}{2}-\Phi_A \qquad (21)$$

where θ is the off-boresight angle.
The -10 dB and -20 dB beamwidths calculated for the present analysis method have been checked against published data, and the results are summarized in Table IV, with the dimensions given in Table V.

Horn	E -10 dB meas.	E -10 dB calc.	E -20 dB meas.	E -20 dB calc.	H -10 dB meas.	H -10 dB calc.	H -20 dB meas.	H -20 dB calc.
Pickett *et al.* [9]	11,4°	13,1°	18,2°	19,2°	11,7°	11,9°	20,5°	19,7°
Ediss [10]	11,0°	11,2°	16,2°	17,4°	11,0°	11,2°	17,0°	17,9°

Table IV. The measured data from two published horns, and the corresponding calculated values for the beamwidths.

Horn	f [GHz]	a	γ [°]	Φ_A [°]	w_0	z_A
Pickett *et al.*	215	3,2 λ	13,5	40,1	1,44 λ	5,53 λ
Ediss	475	4 λ	13,8	47,1	1,61 λ	8,74 λ

Table V. The data for the measured horns (from references [9 10]) and some calculated parameters.

The discrepancies are probably due to the difficulty to actually ensure that the balanced condition exists at the desired frequency, as well as differences between model and reality. In the original 'Potter' horn [7], a slightly different mode balance constant was used, and it is therefore not included in the comparison.

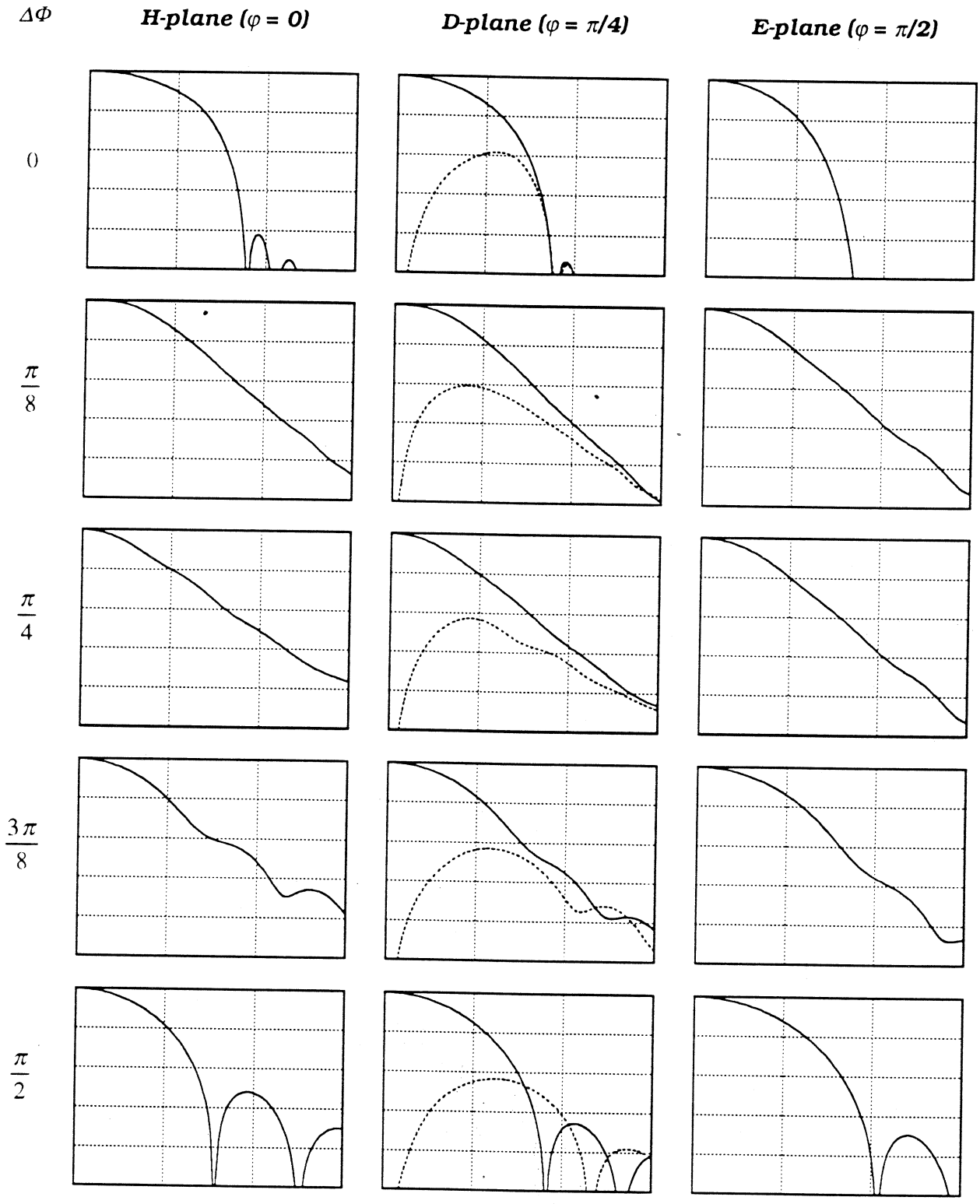

Figure 6. *The field distributions for different relative phase slips ΔΦ. Each panel shows $0 \le r/w \le 3$, with a vertical scale from −50 dB to 0 dB. Co- (solid) and cross-pol (dotted).*

6. VIGNETTING

An interesting property that should be studied when dealing with multi-mode Gaussian beams is where one is allowed to put an absorbing aperture stop in the path of the beam, see Fig. 7. The idealized case of just having the fundamental Gaussian mode yields that the power fraction vignetted by a circular aperture stop with a radius R is given by (*cf.* [1])

$$\frac{P(r \geq R)}{P_{tot}} = e^{-2R^2/w^2} \tag{22}$$

If one chooses $R = 2\ w$, then the 'lost' power fraction will be about 0,0003 . However, for a more practical, and thus finite, horn aperture distribution, the situation is more complex. The power distribution will now vary along the beam path, since the different modes combine with their respective phases.

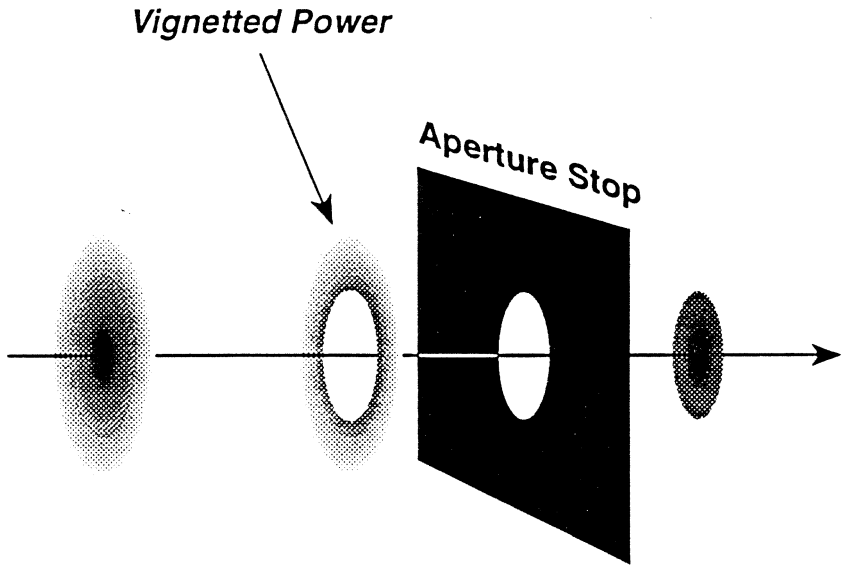

Figure 7. Vignetting of a Gaussian beam.

One can (after heavily manipulating some Laguerre polynomials) show that the power vignetted by an aperture can be written as

$$\frac{P(r \geq R)}{P_{tot}} = e^{-2R^2/w^2} \frac{\sum_{\alpha=0}^{\infty}\sum_{m=0}^{\infty}\sum_{n=0}^{\infty} Q_{mn}^{(\alpha)}\left(\frac{R}{w}\right)\left[\vec{C}_m^{(\alpha)}\cdot\vec{C}_n^{(\alpha)*} + \vec{S}_m^{(\alpha)}\cdot\vec{S}_n^{(\alpha)*}\right] e^{-j2[m-n]\Delta\Phi}}{\sum_{\alpha=0}^{\infty}\sum_{m=0}^{\infty} \vec{C}_m^{(\alpha)}\cdot\vec{C}_m^{(\alpha)*} + \vec{S}_m^{(\alpha)}\cdot\vec{S}_m^{(\alpha)*}} \tag{23}$$

where

$$Q_{mn}^{(\alpha)}(\sigma) = \sqrt{\frac{m!\,n!}{(m+\alpha)!\,(n+\alpha)!}}\; e^{2\sigma^2} \int_{2\sigma^2}^{\infty} L_m^{(\alpha)}(u)\, L_n^{(\alpha)}(u)\, e^{-u}\, u^{\alpha}\, du \qquad (24)$$

(an integral that *can* be expressed in a closed form!).
A contour plot for the vignetted power fraction can thus be plotted as is seen in Fig. 8. An example: a dual- mode horn with an aperture phase slip of $\Phi_A = 45°$ would thus need up to $R \approx 2{,}7\ w$ to vignette less than 0,001 of the total power in the far-field, whereas it would suffice with about $R \approx 1{,}6\ w$ close to the horn.

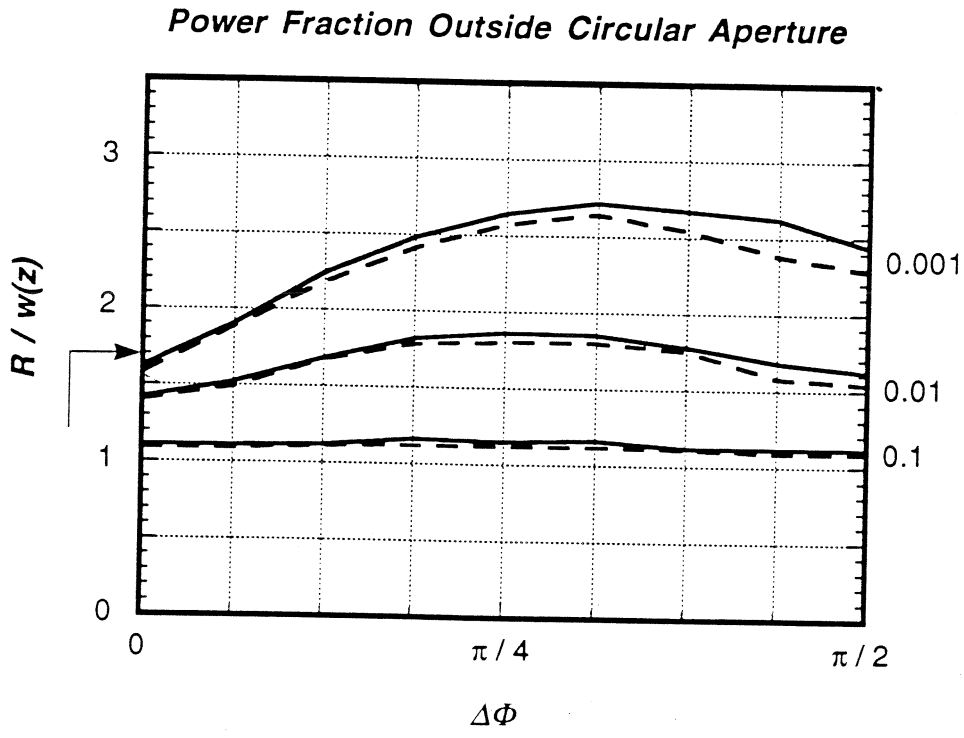

Figure 8. *A contour plot for the power fraction vignetted by a circular aperture with a radius R as a function of the differential phase slip $\Delta\Phi$ for a dual-mode horn.*
The arrow marks the horn aperture radius.
The plot shows the cases with the cross-polarized power included (solid) and excluded (dashed). $n \leq 10$.

To get a 'benchmark', the corresponding plot for the corrugated conical horn is given in Fig. 9. When comparing these plots, one finds that the dual-mode horn is superior to the corrugated horn in the vignetting sense. This is due to the more tapered aperture distribution in the dual-mode horn.

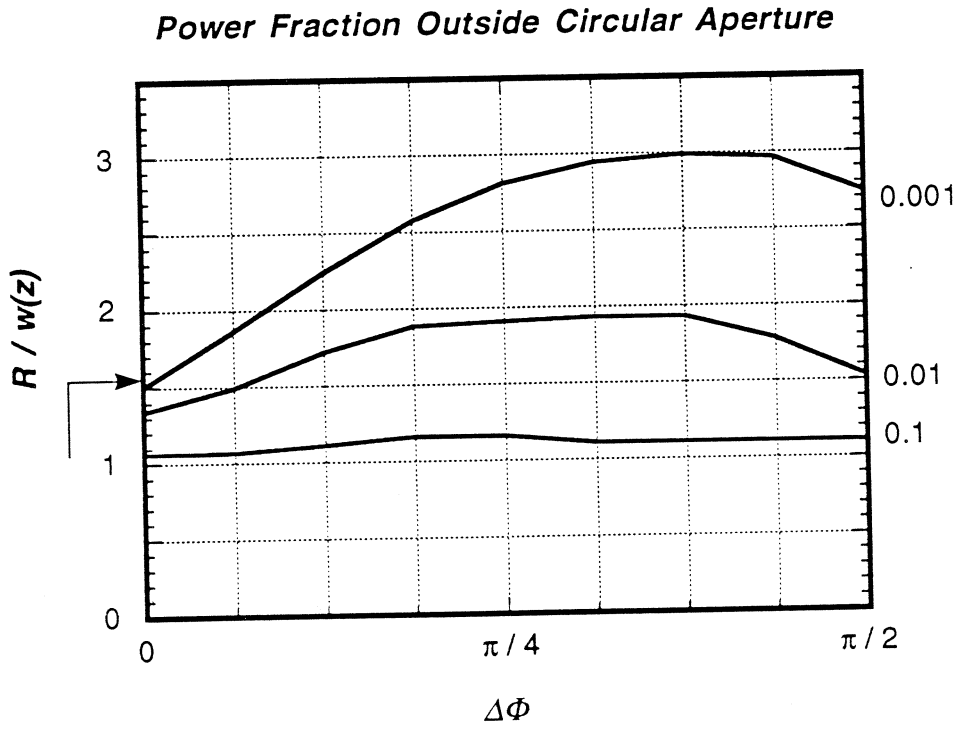

Figure 9. *A contour plot for the power fraction vignetted by a circular aperture with a radius R as a function of the differential phase slip ΔΦ for a corrugated conical horn. The arrow marks the horn aperture radius.*

7. CONCLUSIONS

The dual-mode conical horn has been shown to have a high coupling to the fundamental Gaussian mode. The cross-polarization and the circularly non-symmetric parts of the aperture field are very small. In some regards, such as vignetting sensitivity properties, the dual-mode horn is superior to the corrugated conical horn. The high coupling to the Gaussian beam also yields that a Gauss-Laguerre expansion only has to include just a few terms to accurately describe the field.

ACKNOWLEDGMENTS

Financial support from the Swedish Board for Space Activities, the Swedish Council for Planning and Coordination of Research (FRN), and the Wallenberg foundation is gratefully acknowledged.
Dr. Stafford Withington, Cavendish Laboratory, Cambridge, U.K. is thanked for introducing the author to the techniques of Gaussian beam truncation calculations.

REFERENCES

[1] P. F. Goldsmith, "Quasi-Optical Techniques at Millimeter and Submillimeter Wavelengths", Ch. 5 in ***Infrared and Millimeter Waves***, vol. 6, Ed. K.J. Button, Academic Press, 1982.

[2] D. H. Martin *et al*, ***Millimetre-Wave Optics***, (compendium), Queen Mary College, London, U.K., 1988.

[3] R. J. Wylde, "Millimetre-Wave Gaussian Beam-Mode Optics and Corrugated Feed Horns", IEE Proc., vol. 131, Pt. H, No. 4, pp. 258-262, Aug. 1984.

[4] J. A. Murphy, "Aperture Efficiencies of Large Axisymmetric Reflector Antennas Fed by Conical Horns", IEEE Trans. Antennas Propagat., vol. T-AP-36, no. 4, pp. 570-575, Apr. 1988.

[5] J. F. Johansson and N. D. Whyborn, "The Diagonal Horn as a Sub-Millimeter Wave Antenna", IEEE Trans. Microwave Theory Tech., vol. T-MTT-40, no. 5, pp. 795-800, May 1992.

[6] S. Withington and J. A. Murphy, "Analysis of Diagonal Horns Through Gaussian-Hermite Modes", IEEE Trans. Antennas Propagat., vol. T-AP-40, no. 2, pp. 198-206, Feb. 1992.

[7] P. D. Potter, "A New Horn Antenna with Suppressed Sidelobes and Equal Beamwidths", Microwave J., vol. VI, pp. 71-78, June 1963.

[8] R. H. Turrin, "Dual Mode Small-Aperture Antennas", IEEE Trans. Antennas Propagat., vol. T-AP-15, pp. 307-308, March 1967.

[9] H. M. Pickett, J. C. Hardy, and J. Farhoomand, "Characterization of a Dual-Mode Horn for Submillimeter Wavelengths", IEEE Trans. Microwave Theory Tech., vol. T-MTT-32, no. 8, pp. 936-937, Aug. 1984.

[10] G. A. Ediss, "Dual-Mode Horns at Millimetre and Submillimetre Wavelengths", IEE Proc., vol. 132, Pt. H, No. 3, pp. 215-218, June 1985.

[11] C. A. Balanis, ***Advanced Engineering Electromagnetics***, ISBN 0-471-50316-9, Wiley, New York, 1989.

[12] C. S. Lee, S. W. Lee, and S. L. Chuang, "Plot of Modal Field Distribution in Rectangular and Circular Waveguide", IEEE Trans. Microwave Theory Tech., vol. T-MTT-33, no. 3, pp. 271-274, March 1985.

[13] L. Pettersson, "Dielectric Ring Mode-Generators for Dual-Mode Radiators", Research Report No. II:35, Electron Physics II, Chalmers Univ. of Technology, Gothenburg, Sweden, Jan. 1979.

[14] A. Yariv, ***Introduction to Optical Electronics***, Holt, Rinehart and Winston, Inc., New York, 1971.

OPTICAL TUNING RANGE COMPARISON OF UNIPLANAR ACTIVE INTEGRATED ANTENNA USING MESFET, GAAS HEMT AND PSEUDOMORPHIC HEMT

Shigeo Kawasaki and Tatsuo Itoh

UCLA

Electrical Engineering Department

Los Angeles, CA 90024-1594

ABSTRACT

This paper describes experimental data from uniplanar active integrated antennas with three types of FET's; a MESFET, an AlGaAs/GaAs HEMT and AlGaAs/InGaAs pseudoumorphic HEMT. These are designed at 10 GHz and operated at 8.8 GHz, 10.4 GHz and 10.5 GHz, respectively. A maximum optical tuning range of 70 MHz was obtained from the MESFET circuit, while 7 MHz and 10 MHz were obtained from both HEMT circuits. In each case, only one DC bias was applied to the drain and the gate is floating. The optical tuning ranges of both HEMT circuits had a similar drain-voltage dependence, while the MESFET circuit had the minimum value for the optical tuning range when the drain voltage was tuned.

1. INTRODUCTION

An active integrated antenna using FET's has been of growing interest for integrated circuits operating at higher frequencies[1]. Although in the microwave region there are many FET's suitable for the active integrated antenna, it is hard to obtain an FET at submillimeter-wave frequencies. However, it is important to investigate the optical tuning range to investigate the possibility of a submillimeter-wave uniplanar optical-controlled active integrated antenna.

There are two important phenomena for optical illumination of a microwave device; a photovoltaic effect and a photoconductive effect. In the case of the photovoltaic effect, the presence of a change of the carrier distribution due to illumination results in lowering the Schottky-barrier potential. This mechanism is equivalent to the forward bias between the Schottky-barrier contact and the ground plane. Meanwhile, the photoconductive effect is a bulk type effect. The photogenerated carriers can contribute to a current flow, therefore, the conductivity of a semiconductor increases by illumination.

A MESFET and a HEMT have a Schottky-barrier contact at the gate. Therefore, the photovoltaic effect is expected for both FET's[2],[3]. However, an optically controlled quasi-optical power combining array using a HEMT can be expected to be realized at high frequencies, since a typical cut-off frequency of a MESFET is lower than that of the HEMT. Meanwhile, a wider optical absorption area of the MESFET creates a large change in the circuit parameters such as the gate-source capacitance and drain-source resistance[4]. As a result, a wide tuning range can be expected[5]. If only the photoconductive effect is desired, the photon energy of the optical source should be selected so as to be greater than the bandgap energy of the active layer but to be smaller than that of the depletion layer. This operation method is important for applications[6].

This paper reports the optical tuning ranges of active integrated antennas made of a MESFET, a GaAs HEMT or a pseudomorphic HEMT incorporated with coplanar waveguides (CPW's). Comparison of the tuning ranges of the active integrated antennas with different type of FET's is discussed.

2. DESIGN

Three types of 2-element uniplanar active integrated antennas were designed in a hybrid MIC technique. The first is the 2-element array using a GaAs MESFET, while the second is the array using an AlGaAs/GaAs HEMT. The third array uses AlGaAs/InGaAs pseudomorphic HEMT. These three FET's were used to make the difference of illumination effect clear. In order to demonstrate a topology for a uniplanar monolithic integrated circuit, a high dielectric constant substrate (ε_r=10.5 : Duroid 6010) was selected. In the case of the MESFET, the slot radiator coupled with the CPW is $0.80\lambda_s$ long and $0.062\lambda_s$ wide at 10 GHz (λ_s is a slot guided wavelength). Meanwhile, in the cases of the GaAs HEMT and the pseudomorphic HEMT, the slot is $0.51\lambda_s$ long and $0.031\lambda_s$ wide at 10 GHz. These dimensions were determined by preliminary experience.

The configuration of a 2-element active integrated antenna is shown in Fig. 1. Each oscillator was designed at 10 GHz by using small signal S-parameters. A unit active antenna has a double matching stub configuration. One matching stub consists of a CPW double stub and another constitutes a CPW-slot cross junction at the top of each unit active antenna as shown in Fig. 1. A single CPW with the length of $1\lambda_c$ and the characteristic impedance of 50 Ω was used to accomplish strong coupling between the oscillators (λ_c is a CPW guided wavelength). The moding resulting from the signal phase from each oscillator was taken into account in the design. To invoke the desired in-phase mode, the unit active antenna with a coupling line was designed by replacing one half of the coupling line with an open stub[7]. This results from the fact that a field maximum

point corresponding to an open status is located at a middle point of each oscillator. Due to use of the high dielectric constant substrate, physical separation between two slots can be reduced, keeping the length of the coupling CPW at $1\lambda_c$. In these cases, the length of $1\lambda_c$ corresponds to $0.55\lambda_o$ at 10 GHz (λ_o is a wavelength in a free space). Since the separation became less than $1\lambda_o$, problems of grating lobes are eliminated.

3. EXPERIMENTAL RESULTS

The 2-element MESFET active integrated antenna array operated at 8.8 GHz with Vds=3.58 V and Vgs=floating gate. Therefore, only one DC power supply for Vds was required to obtain the operating frequencies. The package-type FET used was NE72084. The optical control was carried out by illuminating the cap-removed package-type FET with an optical source in these three cases. As the optical source, a fiber illuminator with a halogen lamp was used. Air bridges are provided to suppress unwanted modes in the CPW circuit. The cause of the lower operating frequency may be due to parasitic unknown reactances from the CPW-slot cross and the CPW double stub. Using this circuit, an optical tuning range was measured and the maximum tuning range of 70 MHz near 8.8 GHz was obtained as shown in Fig. 2. Note that only one FET was illuminated. In addition, antenna patterns were observed. Fig. 3 shows the typical antenna patterns. No significant change occurs in the antenna pattern due to illumination. Under the active integrated antenna with strong coupling, illumination of the oscillator only creates a change of the resonant frequency.

The 2-element GaAs HEMT active integrated antenna array operated at 10.4 GHz under Vds=3.5 V and the floating gate condition. The GaAs HEMT used was NE 32184A. A relatively large receiving power results from good matching at the CPW-slot cross junction as well as the CPW cross junction. The maximum optical tuning range with single-oscillator illumination was 7 MHz at 10.4 GHz with Vds=1.5 V as shown in

Fig. 4, while a very small tuning range was measured with Vds=4.4 V at 10.4 GHz. Compared with the case of the MESFETs, the tuning range was one-tenth.

The third result is for the AlGaAs/InGaAs pseudomorphic HEMT (NE 32484) circuit operating at 10.5 GHz with Vds=2.0 V. By tuning Vds, the maximum tuning range of this circuit was 10 MHz as shown in Fig. 5. When Vds increases, the characteristic of the tuning range of the MESFET is different from that of the GaAs HEMT and the pseudomorphic HEMT as shown in Fig. 6. This may result from the difference of photo detection mechanisms. More details should be investigated by a large signal analysis with equivalent circuit parameters dependent on photon energy.

4. CONCLUSIONS

Optical illumination of FET's in the active integrated antenna circuit was demonstrated. By optically tuning the impedance of the MESFET, the circuit operating frequency was tuned near 8.8 GHz without changing the radiation pattern significantly. In addition, to investigate the illumination effect on the FET's, the GaAs HEMT operating at 10.4 GHz and pseudomorphic HEMT operating at 10.5 GHz were illuminated by the optical source. Their tuning ranges became one tenth of that of the MESFET circuit. In each case, the gate voltage was unnecessary to obtain not only the operating frequency of an active integrated antenna but the optical tuning range.

The techniques described in this paper are for a planar configuration and are suitable for a fabrication in a monolithic wafer-scale integrated circuit. Although techniques for a uniplanar active integrated antenna are still in its infancy, realization of simple, multi-functional and compact transceivers can be facilitated with potentially low cost by combining the quasi-optical technology with the optical control method. Further, this technology is very promising for application at very high frequencies where a reasonable power output is needed.

ACKNOWLEDGMENT

This work was supported by US Army Research Office under contract DAAH 04-93-G-0068.

REFERENCES

[1] T. Itoh, "Active Antennas", Journees In't De Nice Sur Les Antennes, France, Nov.1990, pp 435-438

[2] A.A.A. de Salles, "Optical Control of GaAs MESFET's", IEEE Trans. Microwave Theory Tech., vol. 31, pp 812-820, Oct. 1983.

[3] M.A. Romero, A.L.A. Cunha and A.A.A. de Salles, "Theory and experiment for the HEMTs under optical illumination", 1991 IEEE MTT-S Int'l Microwave Symposium Dig. vol. 2, Boston, MA, June 1991, pp 495-498

[4] A. Madgar, P.R. Herczfeld and A. Paolella, "Analytical Model for Optically Generated Currents in GaAs MESFET's", IEEE Trans. Microwave Theory Tech., vol. 40, pp 1681-1691, Aug. 1992

[5] S. Kawasaki and T. Itoh, "Optical Control of 2-elelment CPW Active Integrated Antenna with Strong Coupling", to be appeared in 1993 IEEE AP-S Int'l Symposium Dig., Ann Arbor MI, June 1993.

[6] R. Simons, *Optical Control of Microwave Devices*, Artech House,1990

[7] S. Kawasaki and T. Itoh, "Quasi-Optical Planar Arrays with FET's and Slots", to be appeared in IEEE Trans. Microwave Theory Tech., Oct. 1992.

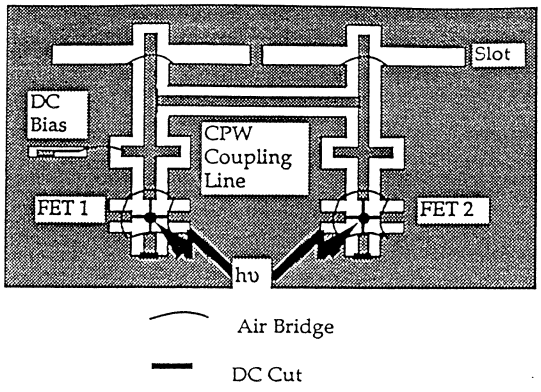

Fig.1 2-element Uniplanar Linear Array

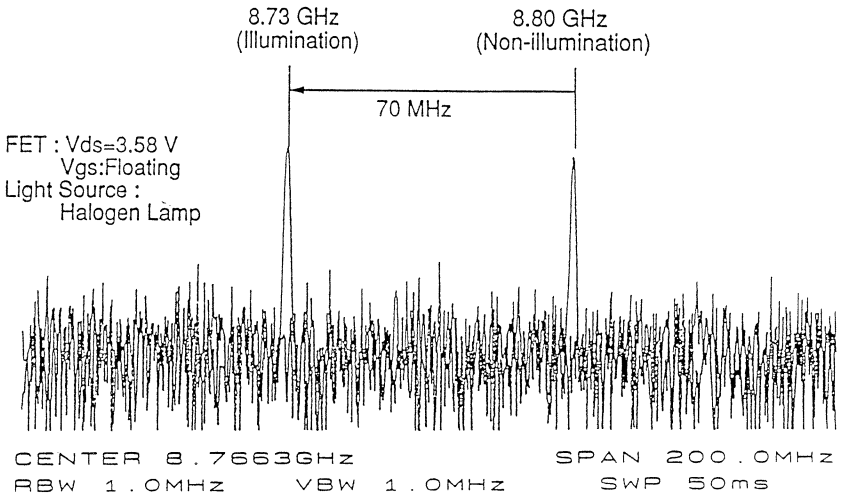

Fig.2 Operation Spectrum Shift
of Optically Controlled Active Integrated Antenna

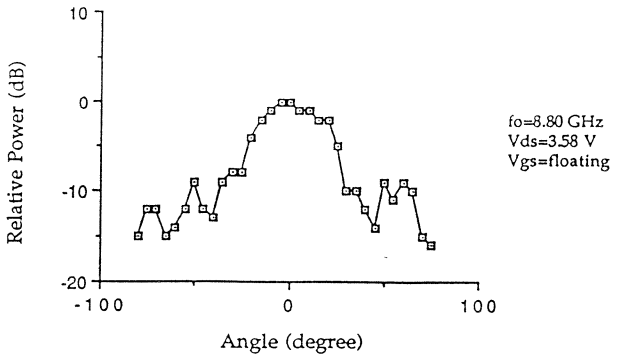

Fig.3 Antenna Pattern of 2-element
Optically Controlled Uniplanar Linear Array

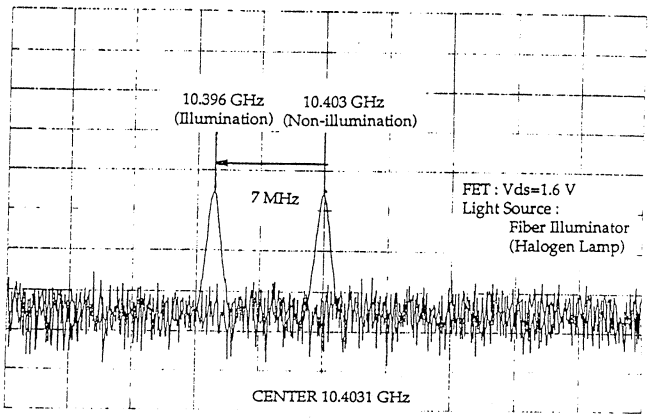

Fig.4 Operation Spectrum Shift of 2-element Optically Controlled Uniplanar Linear Array Using GaAs HEMT

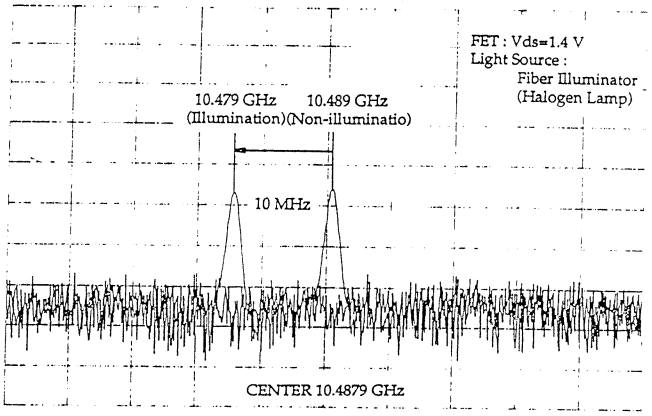

Fig.5 Operation Spectrum Shift of 2-element Optically Controlled Uniplanar Linear Array Using Pseudomorphic HEMT

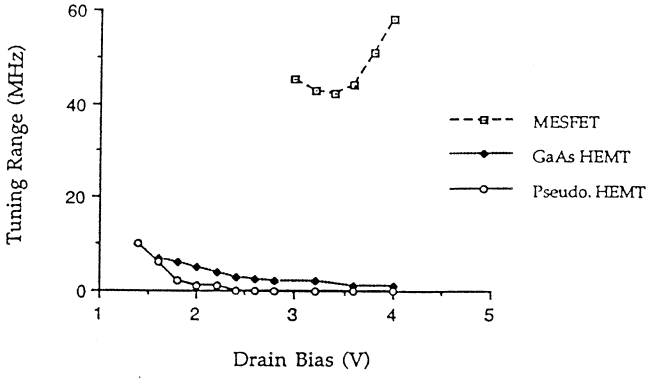

Fig.6 Comparison of Voltage Dependent Tuning Range

This paper is presented here for review only and will be published in the IEEE-MTT Oct.'93 Special Issue on Quasi-Optical Techniques.

Double-Slot Antennas on Extended Hemispherical and Elliptical Silicon Dielectric Lenses

Daniel F. Filipovic, STUDENT MEMBER, IEEE,
Steven S. Gearhart, STUDENT MEMBER, IEEE,
and Gabriel M. Rebeiz, MEMBER, IEEE.

NASA/Center for Space Terahertz Technology
Electrical Engineering and Computer Science Department
University of Michigan
Ann Arbor, MI 48109-2122

ABSTRACT

In this paper, the far-field patterns and Gaussian-beam coupling efficiencies are investigated for a double-slot antenna placed on hemispherical lenses with varying extension lengths. The radiation patterns of a double-slot antenna on a silicon dielectric lens are computed using ray-tracing inside the dielectric lens and electric and magnetic field integration on the spherical dielectric surface. The measured radiation patterns at 246GHz and Gaussian-beam coupling efficiencies show good agreement with theory. The theoretical results are presented in extension length/radius and radius/λ and therefore result in universal design curves for silicon lenses of different diameters and at different frequencies. The theoretical and experimental results indicate that for *single units*, there exists a wide range of extension lengths (ext. length/radius=0.32 to 0.35) which result in high Gaussian-coupling efficiencies (50-60%) to moderately high f#'s. These Gaussian-coupling efficiencies can be increased to 80-90% with the use of a $\lambda_m/4$ matching-cap layer. For *imaging array* applications with high packing densities, an extension length/radius=0.38 to 0.39 (depending on frequency) will result in peak directivity and a corresponding Gaussian-coupling efficiency 15-20% lower than for single units.

I. INTRODUCTION

Integrated antennas on thick dielectric substrates suffer from power loss into substrate modes [1,2]. One way to avoid this problem is to integrate the antennas on a very thin substrate, typically less than $.02\lambda_d$ for dipoles and $.04\lambda_d$ for slot antennas. However, the substrates become very thin and fragile at millimeter and submillimeter-wavelengths. One way to synthesize a thin substrate is to place the antenna on a very thin dielectric membrane [3,4,5], which is typically between 1-3μm thick. The membranes are integrated on silicon or GaAs wafers and the antennas radiate as if suspended in free-space. Therefore appropriate design methods must be used to render the patterns unidirectional. Another attractive method to eliminate substrate modes is to place the antenna on a dielectric lens. The dielectric lens has the same dielectric constant as the planar antenna wafer. The structure of the dielectric lens does not support surface-waves. Antennas placed on dielectric lenses tend to radiate most of their power into the dielectric side making the pattern unidirectional on high dielectric constant lenses. The ratio of powers between the dielectric and air is $\epsilon_r^{3/2}$ for an elementary slot antenna and ϵ_r for an elementary dipole antenna [1], where ϵ_r is the relative dielectric constant of the lens. The dielectric lens is a very attractive solution since it also provides mechanical rigidity and thermal stability.

Dielectric lenses can be hemispherical, hyperhemispherical, or ellipsoidal, and many researchers have placed various antennas on these lenses for receiver applications. The hyperhemispherical lens is a hemispherical lens with an attached extension length of R/n, where n is the index of refraction of the lens, and R is the radius of the lens. The hyperhemispherical lens was borrowed into the millimeter-wave field from optics [1,6] and it was found that radiation patterns from these lenses were broad and even multi-lobed in some cases. The hyperhemispherical lens satisfies the *sine condition*, which guarantees the absence of circular coma, and is aplanatic, implying the absence of spherical abberations [7]. The latter condition implies that if an optical system is designed such that all the rays are being focused to a point, the hyperhemispherical lens can be added to the system and all the rays will still focus to a point. In antenna terms, the hyperhemispherically shaped dielectric lens bends the rays radiated by the integrated antenna towards the broadside direction, thereby sharpening the pattern and effectively increasing the gain of the integrated antenna by n^2. The hyperhemispherical lens is capable of coupling well to a Gaussian-beam system, but couples well to a converging beam and not to a planar equiphase front. On the other hand, any antenna placed at the focus of the elliptical lens will result in a far-field pattern with a main-beam that is diffraction limited by the aperture of the elliptical lens. In a ray analysis, an elliptical lens with a source at its more distant focus refracts the emitted rays so that they emerge from the lens parallel to each other [8]. The diffraction-limited patterns have been verified for the log-periodic and spiral antennas [9], and also for a simple dipole antenna [10], a double-dipole antenna [11], and a double-slot antenna [12]. The difference between these antennas is in the sidelobe and cross-polarization levels. The elliptical lens is compatible with a large f-number imaging system due to the potential of achieving very narrow beam patterns. As will be seen later, the elliptical lens couples well to a Gaussian-beam at its minimum waist (where there is a planar equiphase front).

The log-periodic [13], spiral [14], double-slot, and double-dipole antennas have been successfully used on quartz and silicon dielectric lenses from 30GHz to 600GHz [15,16,17,18]. The antennas were placed on hyperhemispherical or elliptical dielectric lenses and were characterized by the measured far-field pattern. Recently, Büttgenbach experimentally placed a spiral antenna at a specific position behind the hyperhemispherical point (but before the elliptical focus) and achieved good patterns and a high-aperture efficiency (coupling to a plane wave)[19]. Büttgenbach based his analysis on the quality of the measured far-field power patterns and therefore did not present a full characterization of the Gaussian-coupling efficiency of an extended hemispherical lens.

The need for a full characterization of the extended hemisphere (Fig. 1) prompted us to develop a ray-optics/field-integration formulation to solve for the radiation patterns and Gaussian-coupling efficiencies of a double-slot antenna on hemispherical lenses with a varying extension length. The extended hemispherical system is very practical, since it results in an antenna/lens system which couples to a wide range of quasi-optical systems simply by varying the extension length behind the hemispherical position. It is important to note that the hyperhemispherical lens is a special case of the extended hemispherical lens. Section II shows that there also exists a specific extension length that effectively synthesizes an elliptical lens. Section III presents the theoretical analysis of extended hemispherical lenses and shows the directivity and maximum "Gaussicity" as a function of the extension length. The term "Gaussicity" is defined as the coupling efficiency of a far-field pattern of an antenna to the far-field pattern of a Gaussian-beam. The Gaussian-coupling efficiency is defined as the total coupling efficiency which is the Gaussicity multiplied by any system losses (reflection loss, backside loss, impedance mismatch loss, etc.). Section IV shows the reflection loss with and without a matching-cap layer. Section V describes the directivities and Gaussicities versus extension length as a funcion of frequency. Three particular values of extension length, 1700μm, 2200μm, and 2700μm were chosen for experimental verification. Section VI describes the measured radiation patterns at 246GHz and compares them with theory. Section VII presents the experimental setup at 246GHz used for measuring the Gaussian-coupling efficiency of an extended hemispherical lens. The theoretical and experimental results indicate that with a well designed quasi-optical system, there exists a wide range of extension lengths which yield a high Gaussian-coupling efficiency.

II. SYNTHESIS OF AN ELLIPTICAL LENS

In this section, an elliptical lens is synthesized from an extended hemispherical lens by carefully choosing a particular extension length. The analysis is done in two dimensions since the geometry is rotationally symmetric. The defining equation for an ellipse is:

$$(\frac{x}{a})^2 + (\frac{y}{b})^2 = 1 \tag{1}$$

where the foci are at $\pm c$ and $c = \sqrt{b^2 - a^2}$. It is also known from optics that for a given index of refraction n, the eccentricity of the ellipse such that the geometric focus becomes

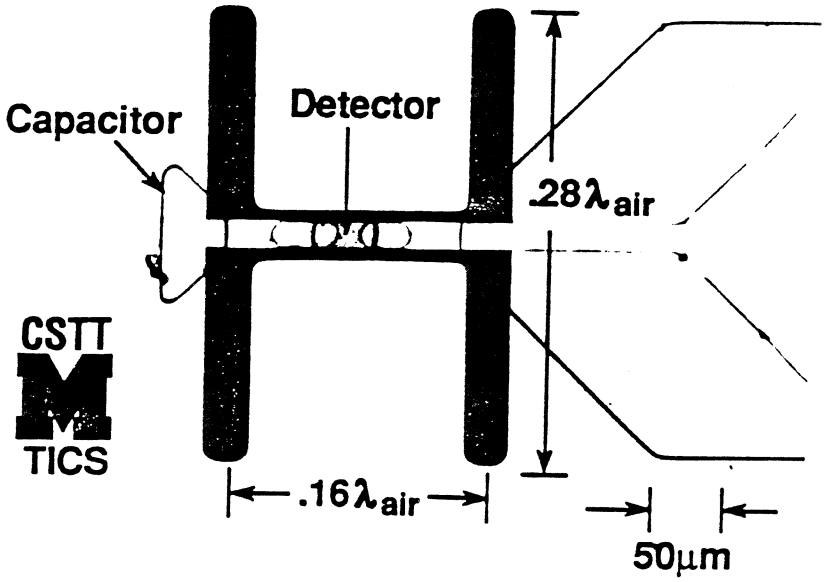

(a)

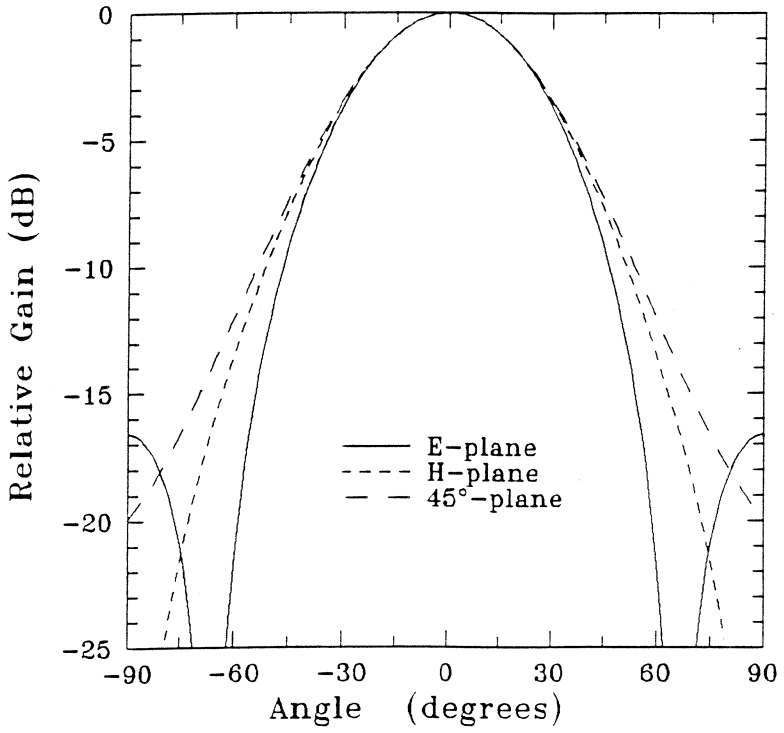

(b)

Figure 3: The double-slot antenna (a) and its radiation patterns into a silicon (ϵ_r=11.7) dielectric (b).

the optical focus is [8] :

$$\text{eccentricity} = \frac{\sqrt{b^2 - a^2}}{b} = \frac{1}{n} \tag{2}$$

From this one can derive that:

$$b = \frac{a}{\sqrt{1 - \frac{1}{n^2}}} \tag{3}$$

$$c = \frac{b}{n} \tag{4}$$

A hemisphere of unit radius is defined by $x^2 + y^2 = 1$, choosing only positive y-values. The distance from the circular tip of an extended hemisphere to the end of its extension is equal to $1 + L$, where L is the extension length. The distance from the tip of an ellipse to its more distant focus is equal to $b + c$. These distances must be equal in order to superimpose the two lenses, which yields $L = 1 - b - c$. The ellipse must be shifted down by a value $y_0 = L - c$ so that the focus of the ellipse has the same coordinates as the focus of the extended hemisphere. Thus given the index of refraction, the parameter b is varied until the extended hemisphere appears to have the closest geometrical match to an ellipse (b will lie within a narrow range no matter how this is defined). This has been done for a dielectric constant of ϵ_r =2.3 (polyethylene), 4.0 (quartz), and 11.7 (silicon), and is shown in Fig. 2. It is obvious that the higher dielectric constant yields a more exact geometrical approximation. For a silicon lens, the fitted ellipse values are a=1.03 and b=1.07691, and this yields an extension length of $L = 2670\mu m$ for a 13.7mm diameter lens. There are many ways to synthesize an ellipse [19] and it will be shown later that the synthesized silicon ellipse presented above is a very good appoximation to a true elliptical lens.

III. THEORETICAL ANALYSIS

A double-slot antenna is chosen as the feed antenna for the extended hemispherical lenses. This antenna has been used previously by Kerr et. al. in a 100GHz receiver [20] and recently Zmudzinas built a 492 GHz SIS receiver using a double-slot antenna on a quartz hyperhemispherical lens [17]. The double-slot antenna patterns are calculated assuming a sinusoidal magnetic current distribution on the slot and using an array factor in the E-plane direction [21]. The double slots lie in the x-z plane, and the slots point in the direction of the z-axis. The wavelength of the sinusoidal current distribution in the slot is the mean wavelength [22] given by $\lambda_m = \lambda_0/\sqrt{\epsilon_m}$ and $\epsilon_m = (1 + \epsilon_r)/2$. The current in the slot is given by :

$$I = I_{max}\sin[k_m(l - |z|)], \qquad l \le z \le l, \qquad l_{max} = 0.28\lambda_{air} \tag{5}$$

where $k_m = 2\pi/\lambda_m$. The corresponding normalized H-plane field pattern is:

$$\frac{\sin\theta[\cos(k_e l\cos\theta) - \cos(k_m l)]}{k_m^2 - k_e^2\cos^2\theta} \tag{6}$$

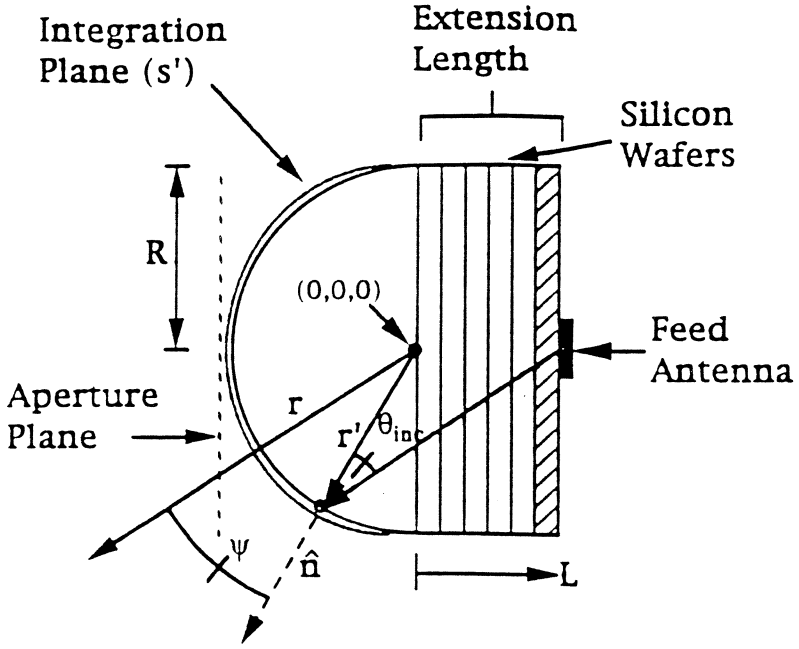

Figure 1: The extended hemispherical lens and the ray-tracing/field-integration technique.

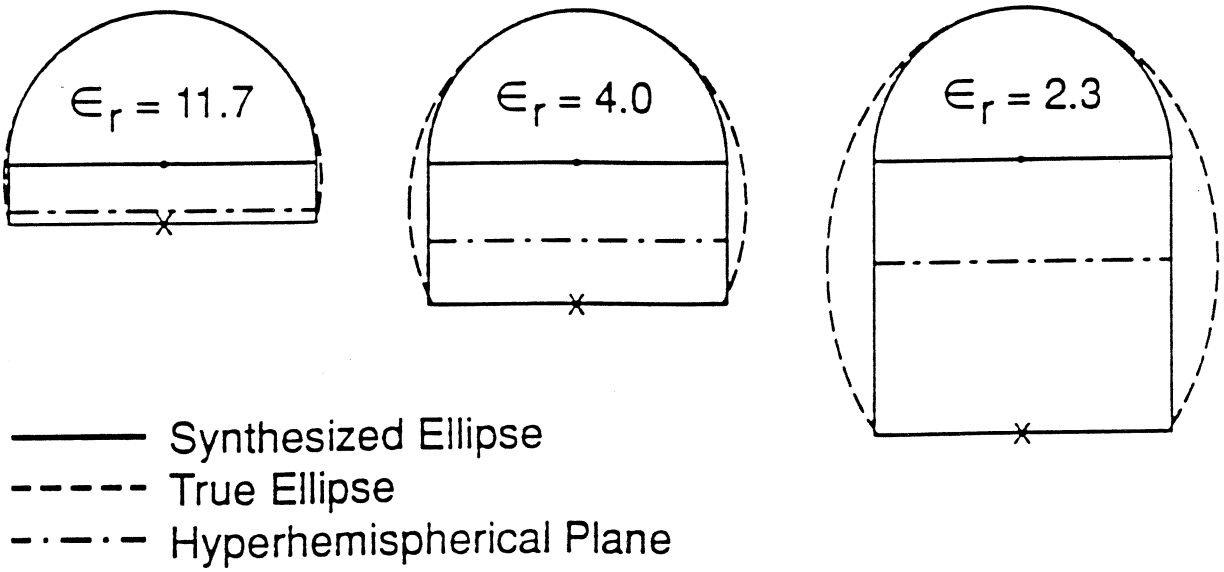

Figure 2: The synthesis of an elliptical lens from a hyperhemispherical lens and planar wafers. The extended hemisphere is a very good geometrical approximation to an elliptical lens at high dielectric constants.

where $k_e = k_{diel} = 2\pi/\lambda_{diel}$ for the dielectric side, $k_e = 2\pi/\lambda_{air}$ for the air side, and θ is the angle with respect to the z-axis. The element pattern is a constant in the E-plane. The E-plane array factor is given by:

$$\cos(k_e d \sin\theta \cos\phi) \tag{7}$$

where ϕ is the angle from the x-axis in the x-y plane, k_e is defined as above, and d is the spacing between the two slots.

Figure 3 shows the calculated radiation patterns at 246GHz of a double-slot antenna with length $l = 0.28\lambda_{air}$ and spacing $d = 0.16\lambda_{air}$ into a dielectric with a relative dielectric constant of $\epsilon_r = 11.7$. The double-slot antenna results in symmetrical patterns in the infinite dielectric half space with a -10dB beamwidth of around 48° and a cross-polarization level lower than -30dB in the 45°-plane. The phase is constant across the main-beam, and the power radiated in the main-beam illuminates the whole spherical surface of the extended hemispherical lenses considered in this paper. The patterns radiated to the air-side are broader with a -10dB beamwidth of 70° in the H-plane and a nearly uniform E-plane, and contain 9.0% of the radiated power.

The radiation patterns from the extended hemispherical lenses are computed using a ray-tracing technique [23]. The double-slot antenna patterns into the dielectric are used to calculate the distribution of the electric and magnetic fields across the spherical surface of the extended hemispherical lenses (Fig. 1). It is important to note that this analysis is not limited to double-slot antennas and is applicable to any planar antenna designed to yield similar patterns in the dielectric; for example, the double-dipole and spiral/log-periodic antennas. For a given ray, the fields are decomposed into parallel/perpendicular components at the lens/air interface, and the appropriate transmission formulas are used for each mode [24]:

$$\Gamma_{\|} = \frac{n\sqrt{1 - n^2\sin^2\theta_i} - \cos\theta_i}{n\sqrt{1 - n^2\sin^2\theta_i} + \cos\theta_i} \tag{8}$$

$$\tau_{\|} = (1 + \Gamma_{\|})\frac{\cos\theta_i}{\sqrt{1 - n^2\sin^2\theta_i}} \tag{9}$$

$$\Gamma_{\perp} = \frac{n\cos\theta_i - \sqrt{1 - n^2\sin^2\theta_i}}{n\cos\theta_i + \sqrt{1 - n^2\sin^2\theta_i}} \tag{10}$$

$$\tau_{\perp} = 1 + \Gamma_{\perp} \tag{11}$$

where n is the dielectric constant, θ_i is the angle of incidence from the normal to the spherical lens (Fig. 1), and Γ and τ are the reflection and transmission coefficients for the parallel ($\|$) and perpendicular ($\perp$) polarizations. Once the electric and magnetic fields have been found, equivalent electric and magnetic current densities [24] are calculated just outside the spherical surface using:

$$\mathbf{J_S} = \hat{n} \times \mathbf{H} \tag{12}$$

$$\mathbf{M_S} = -\hat{n} \times \mathbf{E} \tag{13}$$

where $\hat{n}$ is the normal to the interface, and $\hat{n} = \hat{a}_r$ when the origin of the coordinate system is defined to be the center of the spherical surface. In the far-field, the transverse electric field is equal to:

$$\mathbf{E}_\theta \cong -\frac{jke^{-jkr}}{4\pi r}(\mathbf{L}_\phi + \eta \mathbf{N}_\theta) \tag{14}$$

$$\mathbf{E}_\phi \cong +\frac{jke^{-jkr}}{4\pi r}(\mathbf{L}_\theta - \eta \mathbf{N}_\phi) \tag{15}$$

where $\mathbf{N}$ and $\mathbf{L}$ are defined by:

$$\mathbf{N} = \iint_S \mathbf{J_S} e^{jkr'\cos\psi} ds' \tag{16}$$

$$\mathbf{L} = \iint_S \mathbf{M_S} e^{jkr'\cos\psi} ds' \tag{17}$$

where s' is the closed surface just outside the lens, r' is the distance from the origin of the coordinate system to the equivalent electric and magnetic currents, r is the distance from the origin to the far-field point, and ψ is the angle between r and r'. A matching layer at the lens/air interface is not yet considered in this analysis.

The computed E and H-plane power patterns and the phases of the electric field in the E-plane of a 13.7mm diameter lens fed by a double-slot antenna at 246GHz are shown for extension lengths of 1600μm, 1800μm, 2000μm, 2200μm, 2400μm, 2600μm, 2800μm, and 3000μm (Fig. 4). It is seen that the patterns become progressively narrower resulting in higher directivity up to 2600μm and then the mainlobe widens and the sidelobe levels begin to increase. It is important to note that the phase of the field is not constant in the mainlobe except around the synthesized elliptical position (determined to be L = 2670μm). This is seen on the 2600μm plot where the phase is nearly constant in the mainlobe and then shifts 180° in the first sidelobe. The corresponding peak directivity and the Gaussicity (pattern coupling efficiency) as a function of the extension length are shown in Figure 5. The Gaussicity is computed using an overlap integral between the far-field patterns and the far-field Gaussian-beam expression (see Appendix). The directivity has a broad peak of 30.2dB centered at L_{pk} = 2550μm and remains within 1.0dB of the peak between 2400μm and 2800μm. The corresponding aperture efficiency (coupling to a plane wave) peaks at 84% and is above 68% between 2400μm and 2800μm. This peak position agrees well with Büttgenbach's formulation on the diffraction-limit of a lens (see [19] for more detail). In the far-field, the decrease in Gaussicity at the larger extension lengths can be interpreted as the result of the formation of out-of-phase sidelobes whose level progressively increases as the extension length is increased. It is seen that the Gaussicity is very high up to 2200μm (above 95%) and drops to 88-86% at the peak directivity and synthesized elliptical positions.

The near-field waist and radius of curvature are found from an inverse Fourier transform of the far-field Gaussian-beam [23] (Fig. 6). These are referenced to the aperture plane at the tip of the lens (Fig. 1). As expected, the radius of curvature is infinity at the synthesized elliptical position (L = 2670μm) and changes sign immediately afterwards. This means that the synthesized elliptical lens is a good approximation to a true elliptical lens

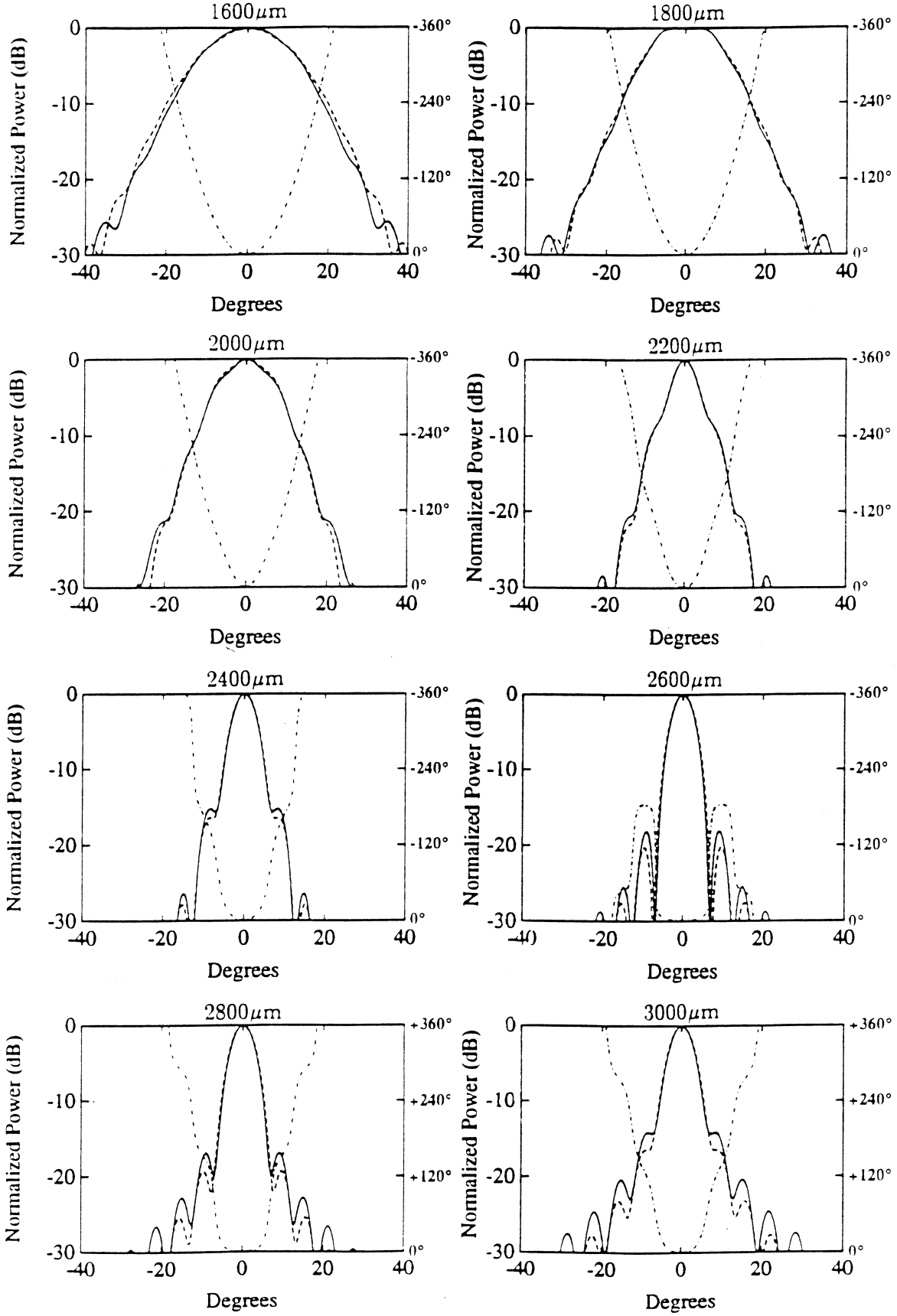

Figure 4: E and H-Plane power patterns and phase in the E-plane at 246GHz for extension lengths of 1600μm, 1800μm, 2000μm, 2200μm, 2400μm, 2600μm, 2800μm, and 3000μm The dashed/dotted line corresponds to the phase.

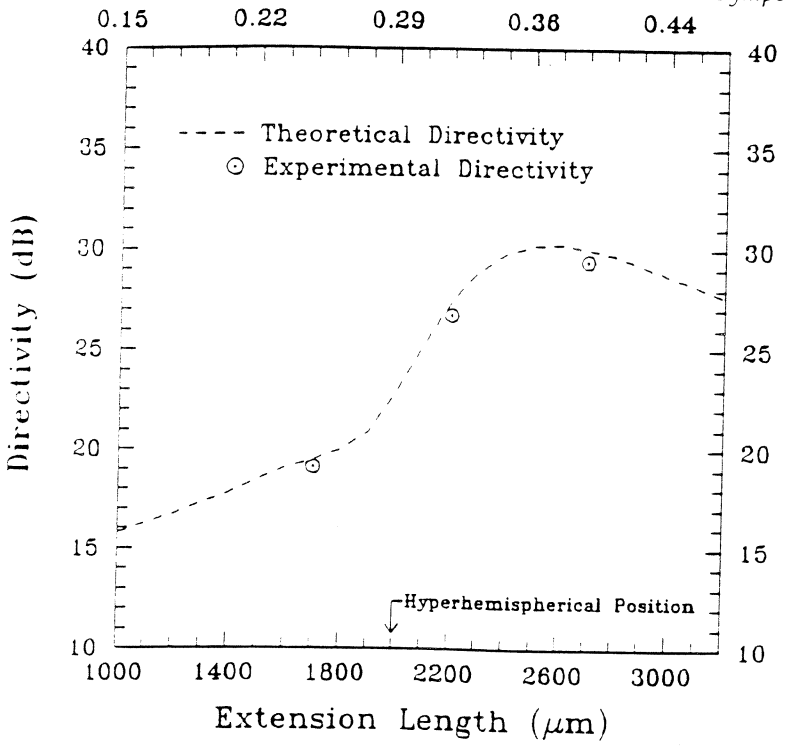

Figure 5: Directivity and maximum Gaussian-coupling efficiency as a function of extension length at 246GHz (see text).

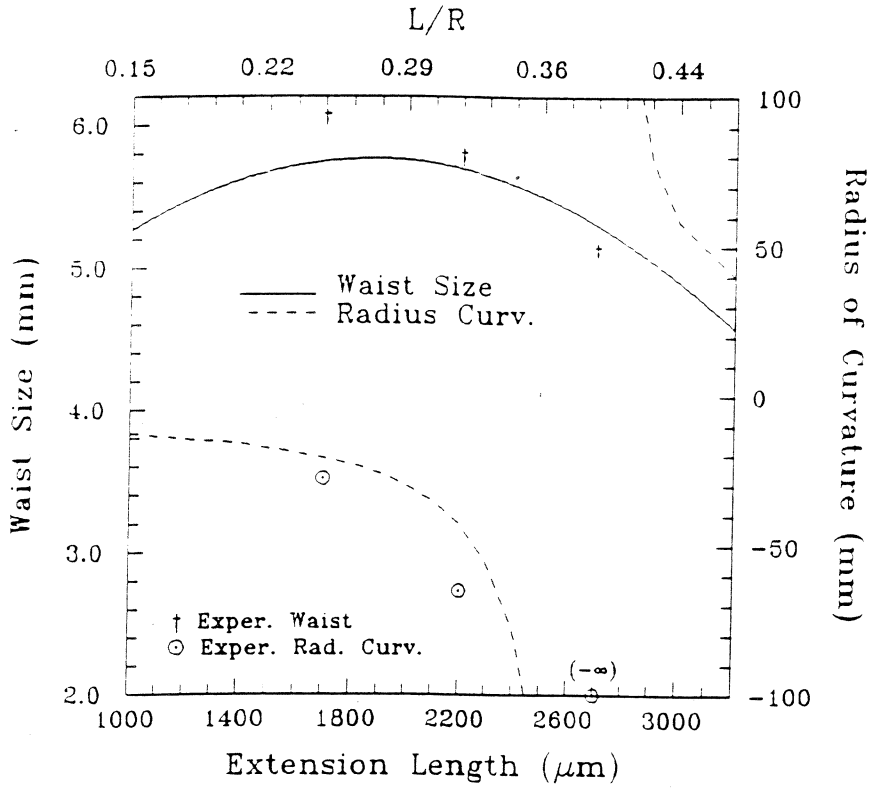

Figure 6: Waist and radius of curvature as a function of the extension length at 246GHz (see text).

and couples best to a Gaussian-beam at its minimum waist. The Gaussian-beam radius of curvature approaches the lens radius (6.858mm) when the extension length is small, as expected. The beam waist is nearly constant at 5.6±0.3mm for extension lengths between 1000μm and 2700μm and 5.8±0.1mm between 1800μm and 2300μm. It is mainly the radius of curvature that is changing from -13mm to -∞ between 1000μm and 2700μm. Therefore, the converging Gaussian-beam must be very well characterized on the lens aperture for optimal Gaussian-coupling efficiency.

In order to gain a more intuitive understanding of the optimal radius of curvature, the phase of the electric field on the aperture plane is presented in Fig. 7 for the lens system at 246GHz. The phase is calculated using a ray-optics approach all the way to the aperture-plane. This method has proven to result in a caustic with the extended lens system and is not used for far-field pattern and Gaussian-beam calculations (a caustic is a region where an infinite number of rays converge and therefore results in a singularity). However, the method does yield a physical understanding of the problem. The phase of the electric fields on the planar aperture is seen to follow a near quadratic behaviour with varying curvature depending on the extension length. For larger extension lengths (L = 2200μm and above) the phase is plotted up to the caustic region. For low extension lengths, the aperture fields extend significantly beyond the diameter of the lens due to the weak refraction of the wide angle rays, and this contributes to the high Gaussicity. This is not shown in Figure 7 since the phase is only plotted to 180°. At L = 2700μm (just near the synthesized elliptical postion) the phase is nearly constant, and then begins to increase positively for increasing extension length.

A similar analysis of a 13.7mm diameter lens was performed at 100GHz and 500GHz, assuming the same radiation patterns of the feed antenna. Figure 8 shows the patterns and phases for extension lengths of 1600μm, 1800μm, 2000μm, 2200μm, 2400μm, 2600μm, 2800μm, and 3000μm at 500GHz. The directivity and Gaussicity calculations at 100GHz, 246GHz and 500GHz are shown in Figure 9. The corresponding waists and radii of curvature are shown in Figure 10. At 100GHz, the peak in the directivity curve occurs at 2480μm and is very broad. The corresponding Gaussicity is very smooth with a drop of 10% at the synthesized elliptical position. On the other hand, at 500GHz, the directivity curve shows a distinct peak of 36.3dB centered at 2600μm (with a corresponding aperture efficiency of 72%) and drops by 0.5dB at the synthesized elliptical position. Again, this position agrees well with Büttgenbach's diffraction method (see [19] for more detail). Note that at higher frequencies, the peak directivity is closer to the synthesized elliptical position, which is the result of the geometrical optics approximation becoming more accurate. The Gaussicity peaks at 500GHz at the hyperhemispherical position of 2000μm with a value of 97% and then drops to 82% at the 2600μm-2700μm position. Again, as the frequency increases, the ray-optics approximation becomes more valid, and this explains the peak in Gaussicity at the hyperhemispherical position.

The directivity and Gaussicity are calculated for a true elliptical lens using the same approach for the extended hemispherical lens at 246GHz. The true elliptical lens is defined such that the minor axis (perpendicular to boresight) is equal to the radius of the extended

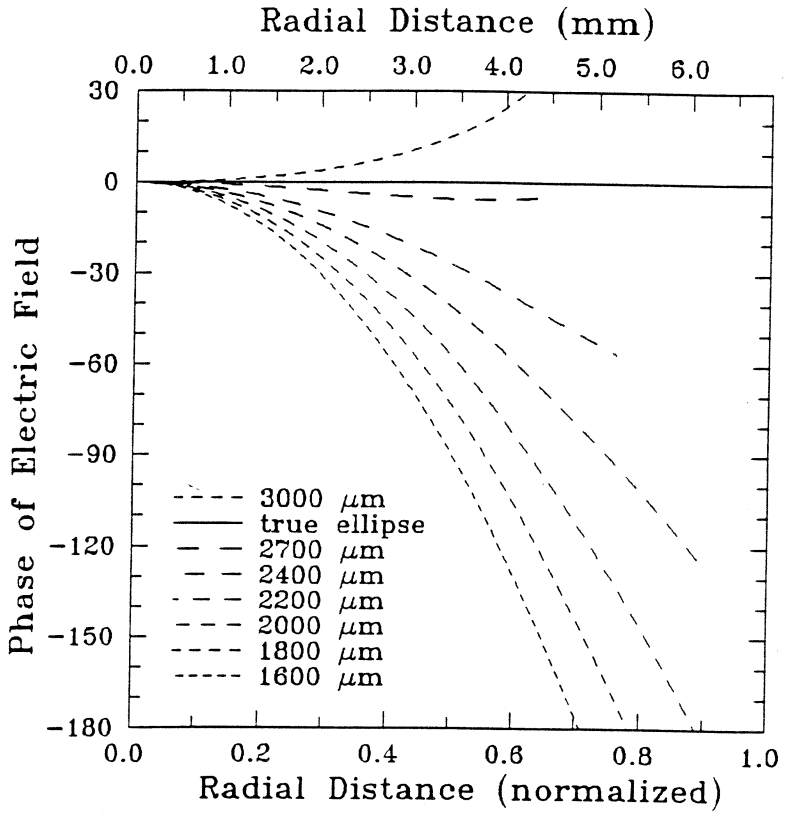

Figure 7: Phase of the aperture electric field at 246GHz for extended hemispherical lenses with different extension lengths with the double-slot antenna as the feed.

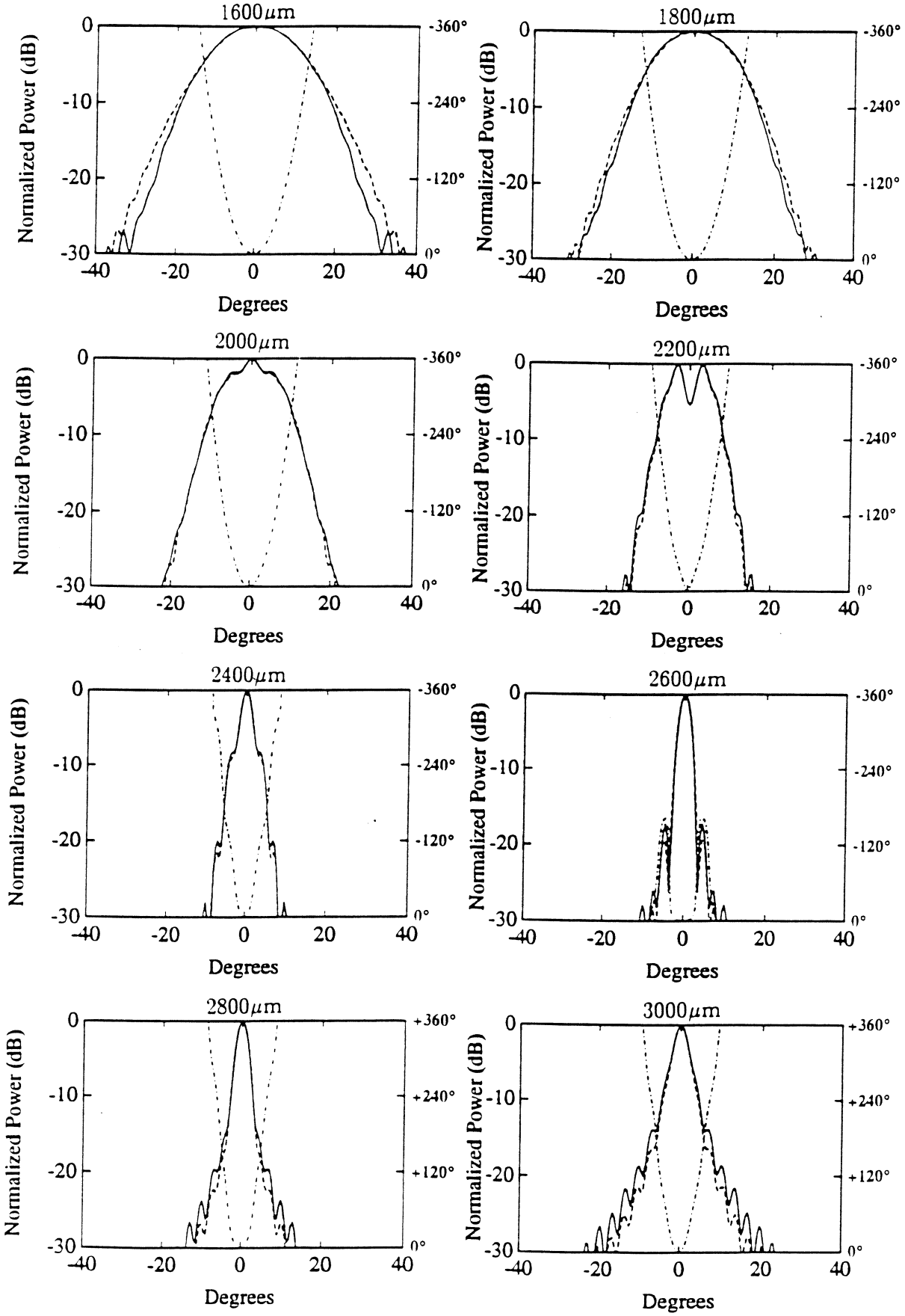

Figure 8: E and H-Plane power patterns and phase in the E-plane at 500GHz for extension lengths of 1600μm, 1800μm, 2000μm, 2200μm, 2400μm, 2600μm, 2800μm, and 3000μm. The dashed/dotted line corresponds to the phase.

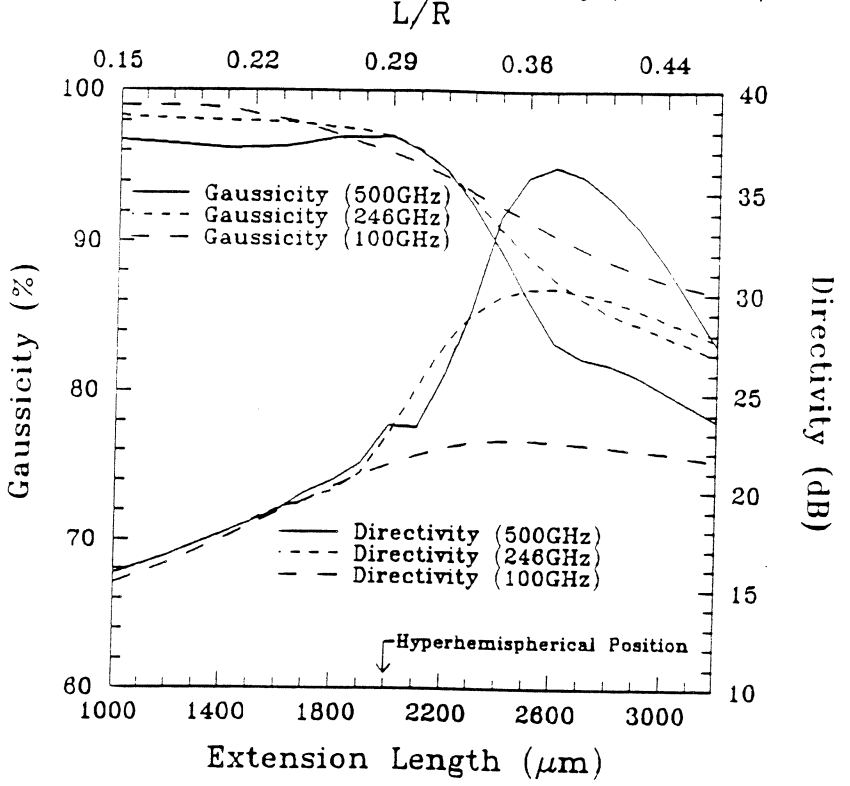

Figure 9: Directivity and maximum Gaussian-coupling efficiency as a function of extension length at 100GHz, 246GHz, and 500GHz (see text).

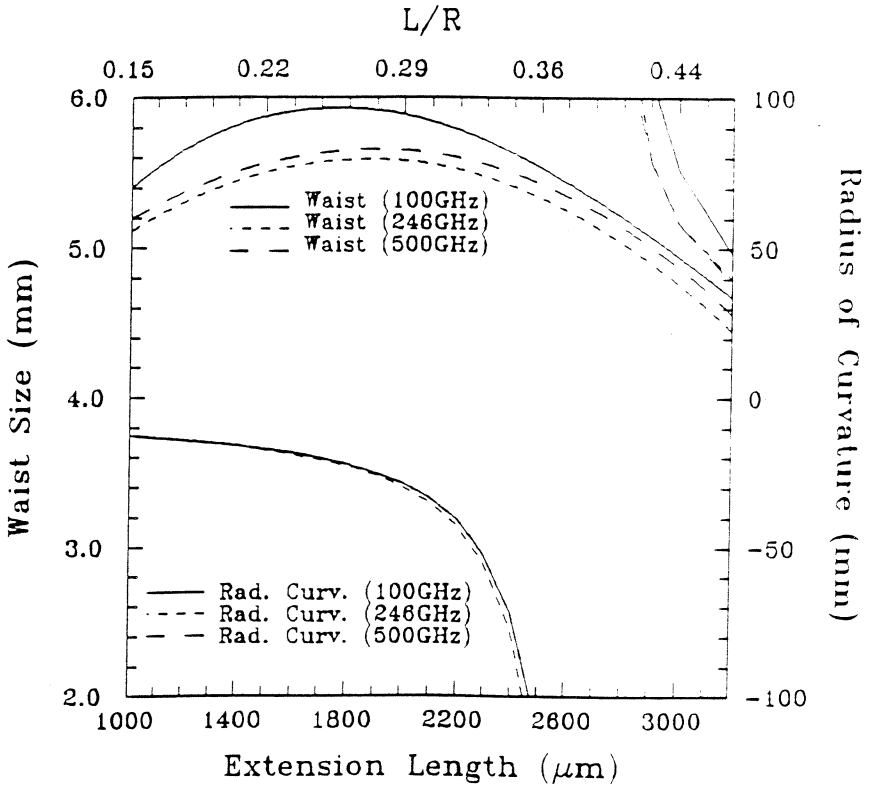

Figure 10: Waist and radius of curvature as a function of extension length at 100GHz, 246GHz, and 500GHz (see text).

hemispherical lens, so that the physical area on the aperture plane is the same for both lenses. The E and H-plane mainlobes are slightly narrower than those of the synthesized elliptical lens and have 0.5dB higher sidelobes. The directivity is 30.6dB which is 0.6dB higher than the synthesized ellipse. The elliptical lens Gaussicity is 88% and is the same to within ±1% for the synthesized elliptical lens. The corresponding minimum waist at the aperture plane is 5.6mm.

IV. REFLECTION LOSS CALCULATIONS

The ray-tracing technique presented earlier (Fig. 1) also results in a full characterization of the reflection loss at the lens-air interface as a function of the extension length (Figure 11). The reflection loss is calculated by using equations 8 and 10 and integrating the reflected power over the entire surface of the lens. At low extension lengths, the calculated loss is 1.52dB which is close to the 1.55dB predicted from simple transmission-line theory (between silicon and air). The reflection loss increases to 2.1dB at the synthesized elliptical position (L = 2670μm) due to the power loss from the total internal reflection of wide angle rays (above 65°). The Gaussian-coupling efficiency of the extended hemispherical system must include the reflection loss to result in a complete characterization of the system. This results in an *additional* decrease of 13% in the Gaussian-coupling efficiency at the synthesized elliptical positions compared to the Gaussian-coupling efficiency at the hyperhemispherical position. The calculated reflection loss at the synthesized elliptical position is 1.8dB for an antenna with a symmetrical pattern and a 10dB-beamwidth of 46° (corresponding to a directivity of 12dB) and a nearly constant 1.52dB for antennas with a 10dB-beamwidth of 40° and 31° (corresponding to a directivity of 13dB and 15dB). This means that it is advantageous to use a high gain antenna for a feed into the extended hemispherical lens. This is important at high frequencies (above 300GHz) where it may be difficult to manufacture an accurate matching layer for the silicon lens. While it is not known accurately, it is expected that the spiral antenna [19] and log-periodic antenna [13] have a pattern directivity into the lens of around 12dB. As expected, the calculated reflection loss of an elliptical lens is nearly equal to the reflection loss at the sythesized elliptical position.

Figure 11 also includes the reflection loss using a $\lambda_m/4$ matching cap layer with dielectric constant equal to $\sqrt{\epsilon_{\text{lens}}}$. The reflection loss for the double-slot antenna (directivity=11.1dB) is nearly zero up to the hyperhemispherical position, and then increases to 0.6dB at the synthesized elliptical position. The radiation patterns and the directivities remain essentially the same with the matching cap layer. As expected, the reflection loss for the higher directivity antennas are lower with a loss of 0.3dB, 0.1dB, and zero for the 12dB, 13dB, and 15dB pattern directivities at the synthesized elliptical position. No attempt is made in this paper to design an optimum matching layer (i.e. non-uniform) for the higher extension lengths.

V. GAUSSICITY VS. FREQUENCY

A comparison of the directivity and Gaussicity between the true elliptical lens, the synthesized elliptical lens, and an extended hemispherical lens at peak directivity position for

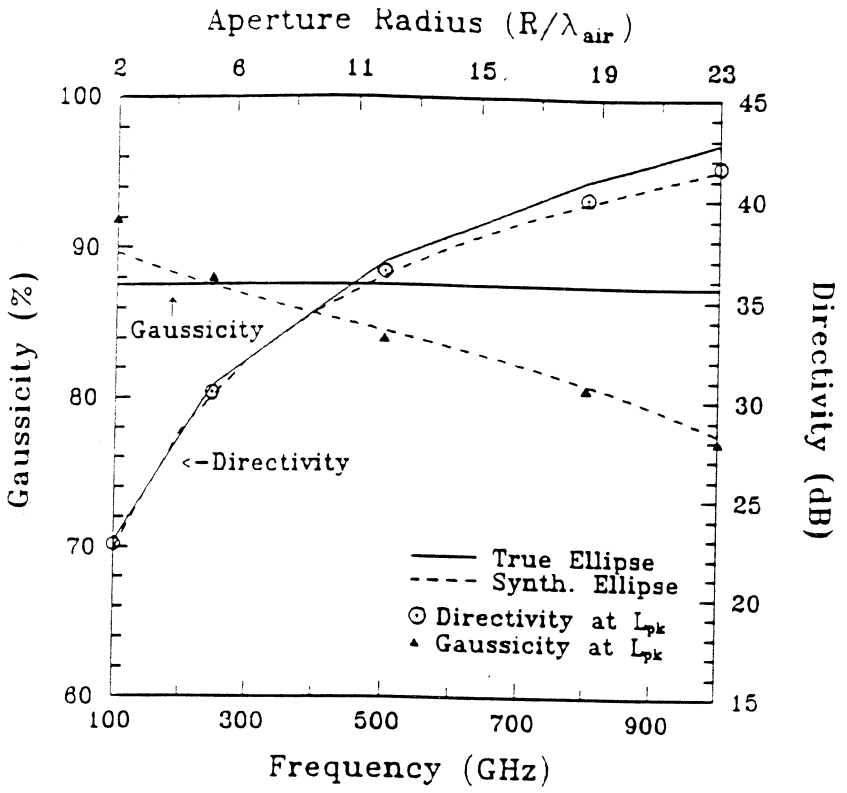

Figure 11: Reflection loss at the lens/air interface as a function of the extension length for different feed antenna directivities with and without a matching layer.

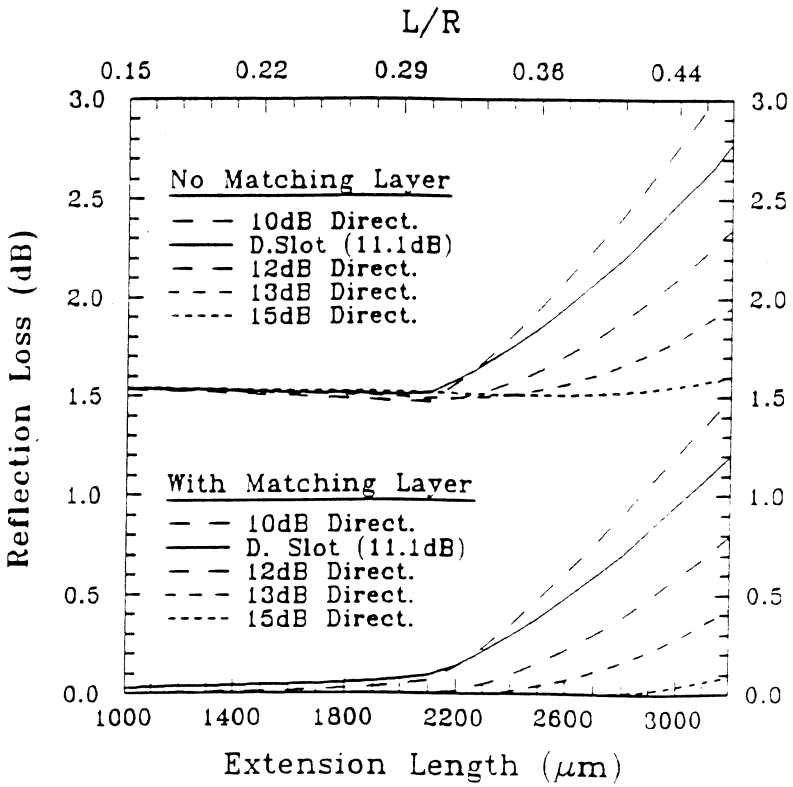

Figure 12: Directivity and maximum Gaussicity (pattern coupling efficiency) as a function of frequency (or lens radius) for a true elliptical lens, a synthesized elliptical lens, and an extended hemispherical lens at peak directivity position (L_{pk}).

100GHz-1THz is shown in Fig. 12. The true elliptical lens has a constant Gaussicity of 88% and a quadratic increase in the directivity, as expected from ray-optics calculations. The directivity of the synthesized elliptical lens shows a 1.2dB drop compared to the elliptical lens at 1THz due to the residual phase error on the planar aperture. The Gaussicity drops from about 90% at 100GHz to 78% at 1THz due to the same effect. As was seen in Fig. 9 at 246GHz and 500GHz, there exists a distinct peak in the directivity at a specific extension length (L_{pk}). Figure 13 shows that L_{pk} asymptotically approaches the synthesized elliptical position with increasing radius/wavelength (or increasing frequency for a constant radius). The peak directivity is slightly higher than the synthesized elliptical directivity and is nearly the same above 500GHz. The Gaussicities for peak directivity positions are the same as those of the synthesized elliptical position to within $\pm 1\%$ above 200GHz. At 100GHz, the peak directivity position is close to the hyperhemispherical position, and therefore results in a slightly larger Gaussicity.

The Gaussicity and directivity for extension lengths of 2000μm, 2350μm, and 2700μm are shown in Figure 14. The hyperhemispherical lens results in a constant directivity of 22dB and a constant Gaussicity of 97%. Notice that the directivity is constant with freqency due to the constant n^2 magnification of the hyperhemispherical lens. The Gaussicity at 2350μm is slightly lower than the hyperhemispherical lens and the directivity increases to around 30dB at high frequencies. The Gaussicity at 2700μm (close to the synthesized elliptical position) is the lowest of all three positions, but results in the largest directivity. The Gaussicity at the synthesized elliptical position (and at L_{pk}) drops to 78% at 1THz while the Gaussicity for the 2350μm position drops to 88% at the same frequency. Although the hyperhemispherical position shows the highest theoretical Gaussicity, it is hard to experimentally achieve this efficiency due to the difficulty in aligning to the strongly converging beams needed at the aperture of the lens (see section VII). Thus the region between 2200μm and 2400μm results in the best compromise between alignment, directivity and Gaussian-coupling efficiency.

Since all the calculations were done in terms of wavelength, Figures 12 and 14 present universal design curves to predict the performance of extended hemipsherical silicon lenses for different diameters when using the same antenna feed patterns. These graphs shows that for high gain systems, a 13.7mm diameter silicon lens can be used in an extended hemispherical configuration up to 1THz without a significant drop in the Gaussicity. For a matched load, the Gaussian-coupling efficiency is found by multiplying the Gaussicity presented above by the reflection loss at the lens-air interface (shown in Figure 11) and by 91.0% to take into account the power radiated by the double-slot antenna to the back-side (air-side). It is important to note that the reflection loss for higher extension lengths (near L_{pk} and the synthesized elliptical position) will have an *additional* loss of about 0.5dB (10%) over the hyperhemispherical position (2000μm).

VI. EXPERIMENTAL RESULTS: PATTERNS

The double-slot antenna was fabricated for 246GHz measurements using standard photolithographic techniques. All the conducting layers are 2000Å gold deposited on a high-resistivity ($4000\Omega - \text{cm}$) silicon wafer. A bismuth bolometer is placed in series at the center of the double-slot antenna using a coplanar-waveguide transmission line (Fig. 3). The series

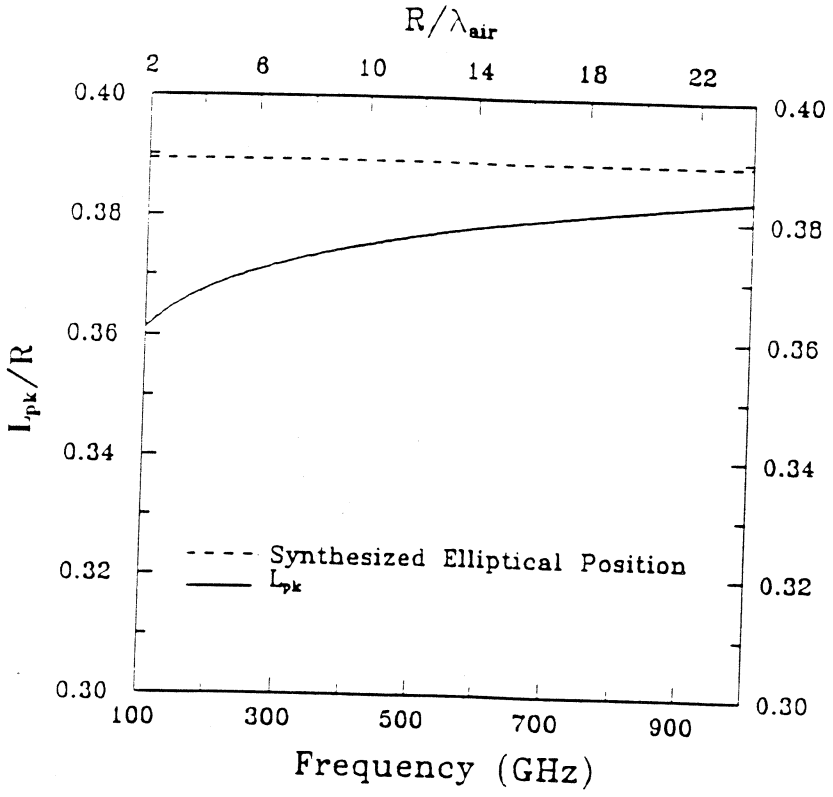

Figure 13: Extension length for peak directivity versus frequency (or R/λ).

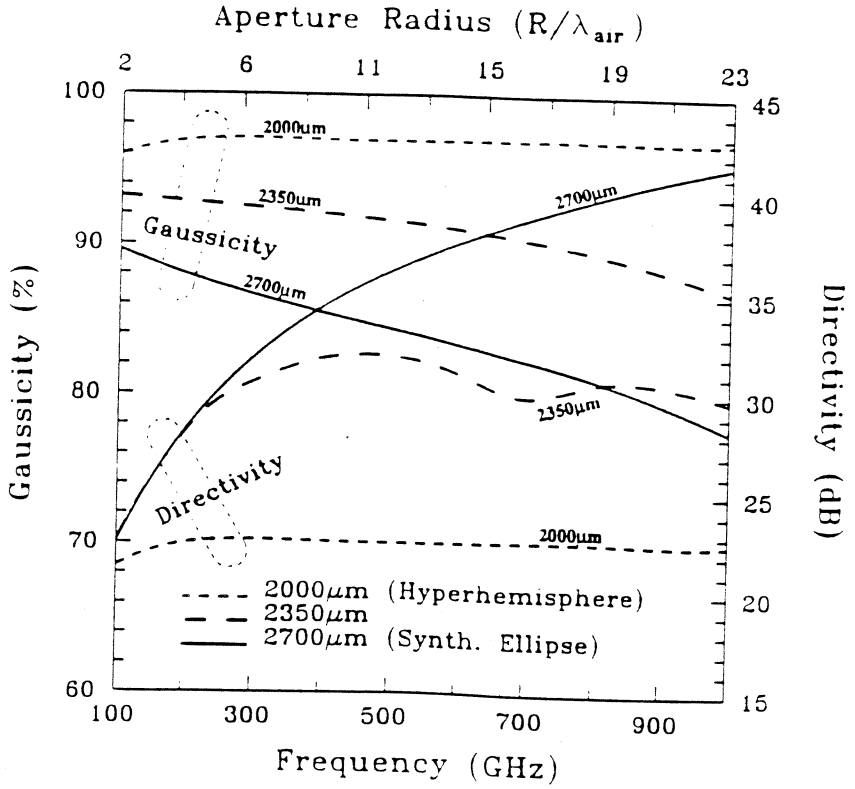

Figure 14: Directivity and Gaussicity (pattern coupling efficiency) as a function of frequency (or lens radius) for an extended hemispherical lens at L=2000μm, 2350μm, and 2700μm.

feeding is necessary in order to result in the sum mode of the double-slot antenna. The bolometer is 20μm x 15μm and is integrated on a 1.2μm thick polyimide patch for thermal insulation from the substrate. The measured DC resistance of the bolometer is 60Ω. The left and right ends of the coplanar line are terminated by a polyimide/gold capacitor which acts as an RF short. The center strip of the coplanar waveguide line runs out from the right end to a large pad for DC biasing and low frequency detection. The coplanar waveguide spacing is 15μm and the width 10μm. This yields a quasi-TEM transmission line impedance of 50Ω [25]. The measured RF impedance at the bolometer position is $60 + j50\Omega$ on a 4GHz microwave model, and results in a good match to the bolometer.

Experimental measurements at 246GHz were performed on a 13.7mm diameter silicon lens (ϵ_r=11.7) without any type of matching layer and the double-slot antenna as a feed. Three particular values of extension length were chosen for the purpose of experimental verification: 1700μm, 2200μm, and 2700μm. The extension lengths were achieved by adding high-resistivity silicon wafers. These positions were chosen based on their different properties: a phase curvature across their aperture planes of high, low, and virtually none, respectively; and a radiation pattern that is broad, narrow with nearly no sidelobes, and narrow with low sidelobes, respectively. The position of 2700μm represents the extension length where the extended hemispherical lens has effectively synthesized an elliptical lens. The hyperhemispherical position is at 2000μm and no measurements were done at this position. However, the 1700μm extension has the same features as the 2000μm position in terms of Gaussian-coupling efficiency and the small radius of curvature needed to couple well to a Gaussian-beam. No pattern measurements were done on a true elliptical lens.

The patterns were measured at 246GHz using an 82GHz Gunn source, and a wideband (220-270 GHz) tripler. The Gunn source was modulated at 1040Hz, and the output from the bolometer was fed to a lock-in amplifier. Measured patterns at the extension length of 2700μm (Fig. 15) demonstrate a directivity of 29.4dB$\pm$0.3dB with relatively low sidelobes (-16dB). The corresponding aperture efficiency (coupling to a plane wave) is 70%$\pm$5%. Notice that the theoretical analysis predicts a directivity of 29.9dB (78% aperture efficiency) at the synthesized elliptical position. Good agreement exists between the theoretical and experimental patterns (Fig. 16). Measured patterns at 2700μm for $\pm$10% of the 246GHz design frequency result in nearly the same directivity, and therefore the double-slot antenna has good pattern bandwidth. The measured power at broadside is nearly the same from 222GHz-270GHz, also indicating good impedance bandwidth for the double-slot design. The measured patterns at an extension length of 2200μm are slightly broader than the synthesized elliptical lens with a directivity of 26.7dB$\pm$0.3dB. Again, there is close agreement between theory and experiment (Fig. 17). At an extension length of 1700μm, the patterns become wide with a peak gain of 19.1dB$\pm$0.3dB, and it is considerably more difficult to laterally align the feed antenna to the focus, resulting in non-symmetric patterns with ripples (Fig. 18). As was seen earlier, this wide pattern has no detrimental effect on the coupling efficiency to a converging beam. The ratio of the 246GHz measured peak received power between the extension lengths of 2700μm and 1700μm is 10dB$\pm$0.5dB and this is the same as the difference in the measured directivities (including the effect of the different reflection losses at the lens surface).

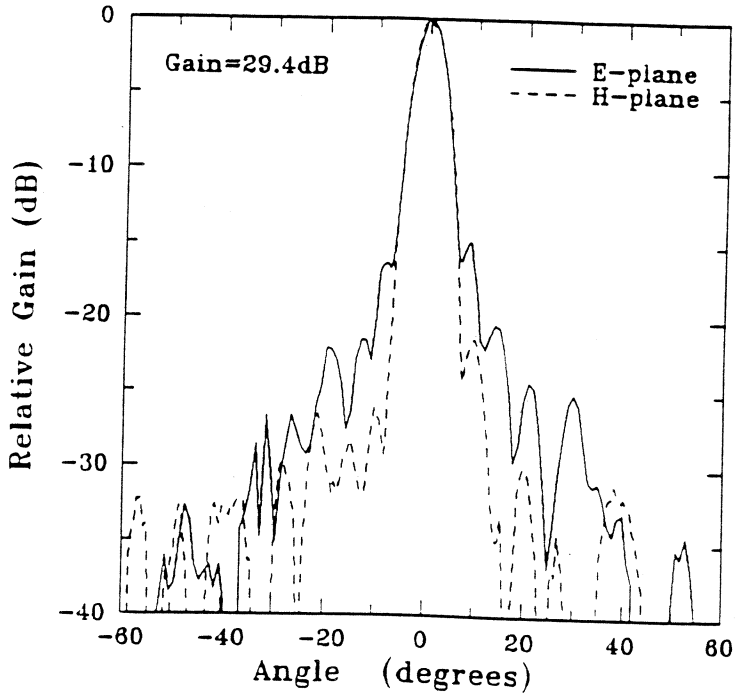

Figure 15: Measured patterns for the synthesized elliptical lens (2700μm) at 246GHz. The patterns are diffraction-limited by the size of the aperture. The S/N ratio is better than 40dB.

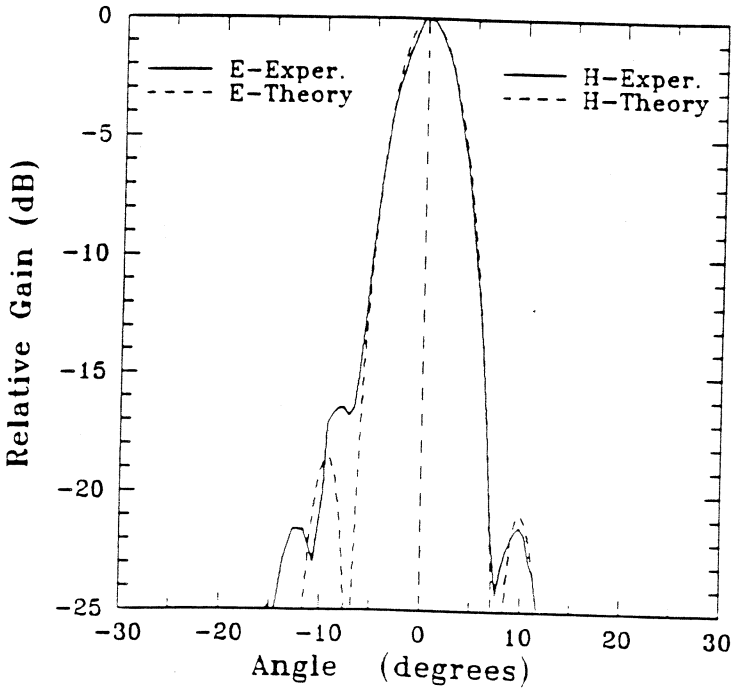

Figure 16: Comparison of the calculated patterns versus experiment at 246GHz for the double-slot antenna on a synthesized elliptical lens (extension length 2700μm).

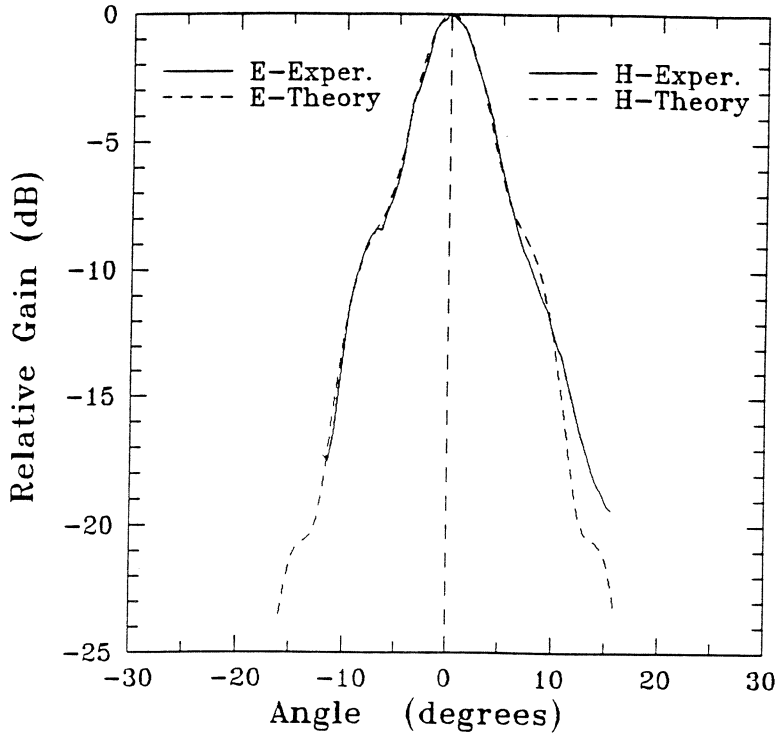

Figure 17: Comparison of the calculated patterns versus experiment at 246GHz for the double-slot antenna on an extended hemispherical lens with 2200μm extension length.

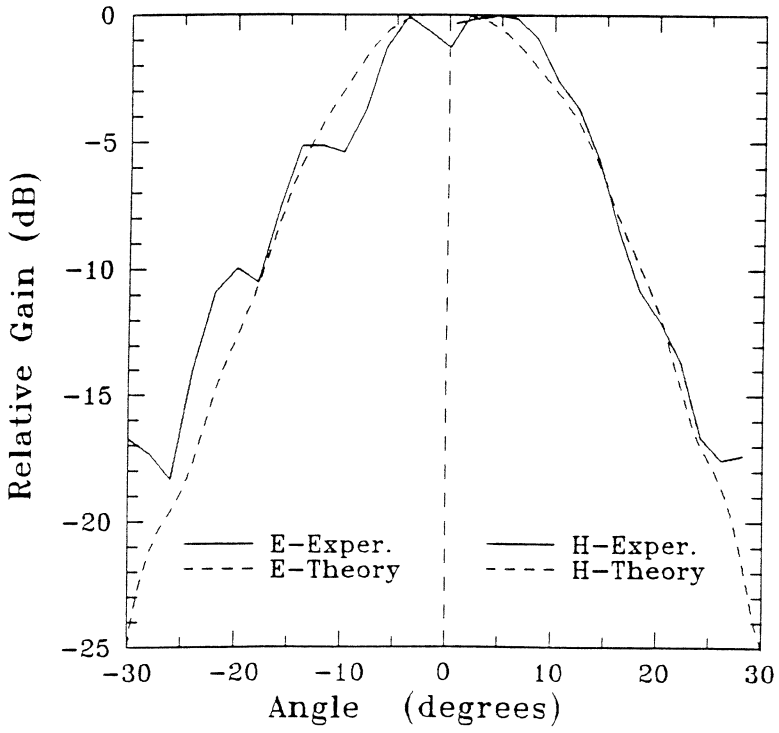

Figure 18: Comparison of the calculated patterns versus experiment at 246GHz for the double-slot antenna on an extended hemispherical lens with 1700μm extension length.

VII. EXPERIMENTAL RESULTS: GAUSSIAN-BEAM COUPLING

A Gaussian-beam experiment was performed at 246GHz with the purpose of coupling all the power radiated by a corrugated horn into the double-slot antenna/lens system. A two-lens quasi-optical system was designed which achieves a wide variety of waist sizes and radii of curvature (Fig. 19). The 10-cm Rexolite lenses used were numerically machined using parametric equations and result in no spherical aberrations [26]. The source was a WR-03 corrugated horn having symmetric E, H, and 45° patterns with a computed waist size of $w_0 = 2.1$mm. The waist can be traced through the lens system using the q-parameters [27]. In Figure 19, d1, d2, and d3 are the lens seperation distances, and f_1 and f_2 are the respective $f/\#$'s ($f/\# = $ f/D, where f is the focal length and D is the diameter of the lens). Care must be taken that the edge illumination of the lens is below the -30dB level so that the Gaussian-beam does not deform from its ideal shape. The experimental procedure went as follows: the distances d1, d2, and d3 and the $f/\#$'s f_1 and f_2 were first calculated for maximum coupling between the corrugated horn and the extended hemispherical lens system. Then, the distances d1, d2, and d3 were tuned experimentally to result in peak measured power in the bolometer.

2700μm extension length (synthesized ellipse): An equiphase wavefront is needed for the synthesized ellipse and is obtained at the minimum waist. A quasi-optical system with final values of $d_1 = 96$mm, $d_2 = 68$mm, $d_3 = 312$mm, $f_1/2.0$, and $f_2/1.4$ resulted in a peak received power with a calculated minimum beam-waist of 5.1mm at the planar lens aperture. The beam waist for optimum Gaussicity calculated from the present theory is 5.2mm. The final values of d1, d2, and d3 are within $\pm$1mm of the initially calculated values.

2200μm extension length: A quasi-optical system with final values of $d_1 = 95$mm, $d_2 = 122$mm, $d_3 = 224$mm, $f_1/2.0$, and $f_2/1.4$ resulted in peak received power. The calculated beam waist and radius of curvature were 5.78mm and -65mm, respectively. The corresponding minimum waist is 2.8λ and is located -35mm (away from the horn) from the aperture plane. The final values of d1, d2, and d3 are within $\pm$5mm of the initially calculated values.

1700μm extension length: A quasi-optical system with $d_1 = 106$mm, $d_2 = 120$mm, $d_3 = 86$mm, $f_1/0.9$, and $f_2/2.0$ resulted in peak received power. The calculated beam waist and radius of curvature were 6.07mm and -27.7mm, respectively. The corresponding minimum waist is 1.1λ (a result of the small radius of curvature necessary at the aperture of the lens). The final values of d1, d2, and d3 differ by as much as $\pm$25mm to the initially calculated values. We believe that for this extension length, the radius of curvature across the aperture is so strong that the desired aperture field distribution will distort rapidly with misalignments of the feed antenna to the lens. This is commonly seen in optics where it is difficult to align to a lens system with small f/D ratios.

The raw measured powers were 1.03, 1.18 and 1.00 for the 1700μm, 2200μm, and 2700μm positions, respectively. In the experimental setup, the 2200μm and 2700μm systems used the same set of objective lenses ($f_1/2.0$ and $f_2/1.4$) and therefore have approximately the same reflection and dielectric losses in those lenses. The 1700μm experiment required $f_1/0.9$ and $f_2/2.0$ lenses and has approximately an additional 6-10% loss due to the added

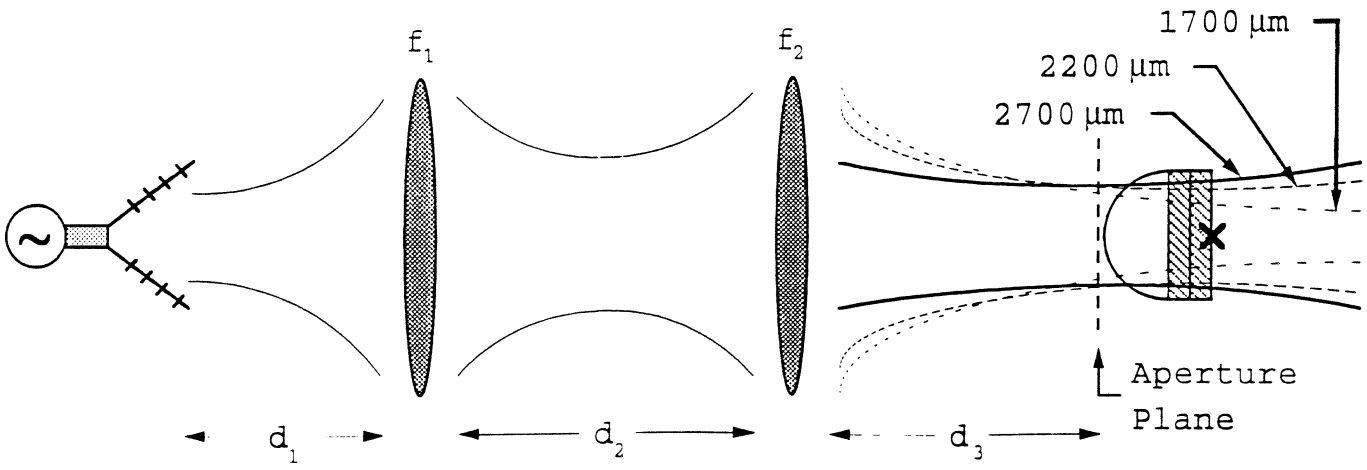

Figure 19: The setup for the Gaussian-beam coupling experiment. The waist at the aperture is 5.2-5.9mm for all three lenses, and only the radii of curvature are different.

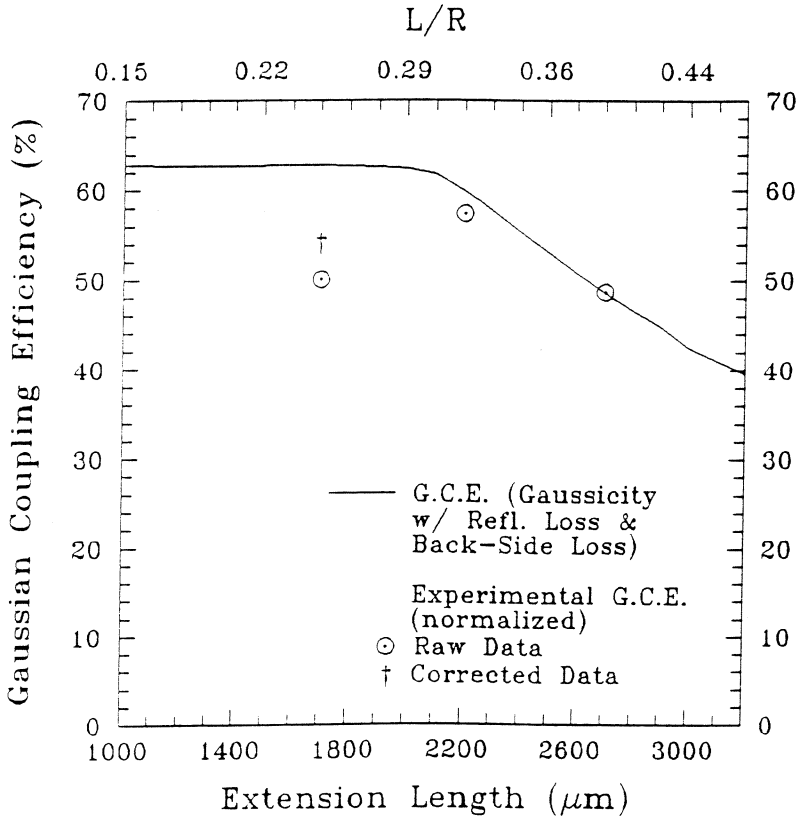

Figure 20: Measured and calculated Gaussian-coupling efficiency as a function of extension length. This takes into account reflection at the lens/air interface and power lost to the air side (91%).

thickness of the $f/0.9$ lens. The measured power at the 1700μm position is therefore multiplied by 1.08 to take into account the excess dielectric loss for the 1700μm quasi-optical system, resulting in a corrected power of 1.11 (shown as a cross in Fig. 20). The theoretical Gaussicities are multiplied by the different reflection losses at the silicon-air interface (see Fig. 11) for the three lens systems, and by the back-side power loss (91%) to yield the actual Gaussian-coupling efficiency. The theoretical Gaussian-coupling efficiencies are presented in Figure 20, together with the measured powers which have been normalized to the 2700μm position. This position was chosen for the normalization because the experimental waist and radius of curvature at 2700μm agree very well with the theoretical values. The normalization is necessary since no absolute power measurements were done at 246GHz. It is seen that within experimental error, the measured values agree well with the theoretical predictions at extension lengths of 2200μm and 2700μm. Notice that the 2700μm position results in the lowest measured Gaussian-coupling efficiency. Also, the measured Gaussian-coupling efficiency at 2200μm is 7% and 18% higher than the measured Gaussian-coupling efficiencies for the 1700μm and 2700μm positions, respectively. This agrees well with our calculations in section V which state that the 2200μm-2400μm positions (L/R= 0.32 to 0.35) result in the best compromise between directivity and Gaussian-coupling efficiency.

VIII. DISCUSSION AND CONCLUSION

In this paper, a ray-optics/field-integration approach has been used to fully characterize an extended hemispherical lens system with a double-slot antenna feed. We have also presented a formulation for synthesizing an ellipse from an extended hemispherical lens. The results show that the directivity is strongly dependent on the extension length (especially at high frequencies). The calculated Gaussicity (pattern coupling efficiency) is very high up to approximately 2200μm and then drops gradually by about 10-15% at the synthesized elliptical position (depending on frequency). The corresponding beam waist on the aperture-plane is nearly constant (5.6$\pm$0.3mm) and the radius of curvature ranges from -13mm to -∞. Thus the incident Gaussian-beam must be very well characterized on the planar aperture for optimum coupling efficiency. In fact, we have built a lens system with a 10dB difference in directivity and still succeeded in achieving nearly the same Gaussian-coupling efficiency for the low and high directivity systems. Our calculations also show that a 13.7mm diameter silicon lens can be used up to about 1THz without a significant drop in the Gaussian-coupling efficiency (maximum 20%) and has an associated directivity greater than 40dB. The Gaussian-coupling efficiency for a double-slot antenna at a position between 2200μm to 2400μm (L/R= 0.32 to 0.35) is approximately 60-50%, which includes the reflection loss and the back-side power loss. This is expected to increase to about 90-80% when a matching cap layer is used.

The question arises of where to place the antenna on a lens for the best possible performance. The answer, according to our calculations, depends on the specific application (for example, a single unit or a unit in an imaging array). For *single units*, the hyperhemispherical position is not the best place since it results in a low directivity, and requires small $f/\#$ systems that are difficult to align. This was well demonstrated by our quasi-optical set-up and we found that it was very difficult to choose the position of the lenses for best

Gaussian-coupling efficiency at the 1700μm extension length. In our opinion, one should use an extension length that results in an acceptably high directivity and therefore a large $f/\#$ for the objective lens. This also yields an easy-to-align quasi-optical system. However, the high directivity is achieved at the expense of a reduction in the Gaussian-coupling efficiency. For a 13.7mm diameter silicon lens, we believe that a good compromise between the increase in directivity and the decrease in Gaussian-coupling efficiency is achieved at 2200μm-2400μm extension length (L/R= 0.32 to 0.35). The corresponding Gaussicity is very high being always above 90% for frequencies below 1THz. This was well demonstrated in our experimental setup at 246GHz where the 2200μm positions resulted in a 7% and 18% higher coupling efficiency than either the 1700μm or 2700μm positions, respectively.

For *imaging arrays*, the extension length resulting in peak directivity should be chosen so as to result in the best possible packing density in the focal plane. For a 13.7mm diameter lens, the aperture efficiency at L_{pk} is 84% at 246GHz and 72% at 500GHz. The corresponding Gaussicity is high at 246GHz with a value of 88% and drops to 78% at 1THz. At L_{pk}, the reflection loss at the lens-air interface contributes an *additional* 0.5dB (11%) reduction in the Gaussian-coupling efficiency (with or without a $\lambda_m/4$ matching-cap layer) compared to the 2200μm position. It is possible to reduce the reflection loss with a higher directivity feed antenna. The L_{pk} position is advantageous because it results in a high-packing density with only a 15-20% drop in Gaussian-coupling efficiency when compared to the 2200μm-2400μm positions. It is also interesting to compare qualitatively the performance at this position to a corrugated horn. At peak directivity position, the extended hemispherical lens at L_{pk} will result in about 20-25% higher packing densities (i.e. aperture efficiencies) and about 25-40% lower Gaussian-coupling efficiencies (including back-side power loss and a $\lambda_m/4$ matching-cap layer) than a corrugated horn designed for the same f/# system. This is not a high penalty to pay for high-packing densities in imaging arrays.

Finally, all our calculations are presented in R/λ and L/λ and therefore present universal design curves for silicon lenses of different diameters at different frequencies. Similar calculations on quartz lenses are available from the NASA-CSTT/University of Michigan and will be published in the October 1993 International Journal of Infrared and Millimeter Waves.

ACKNOWLEDGEMENTS

This work was supported by the NASA/Center for Space Terahertz Technology at the University of Michigan. We are very grateful to Thomas Büttgenbach, Prof. Jonas Zmuidzinas and Prof. David Rutledge, all at the California Institute of Technology, for their immense contributions to this project. We are also grateful to Dr. Andy Harris, Max-Planck Institute for Extra-Terrestrial Physics, Garching bei München, and Dr. Tony Kerr, NRAO, for their detailed review of the manuscript.

APPENDIX

The electric field of a Gaussian-beam is of the form:

$$\mathbf{E}_{\text{Gauss}}(\theta) = \epsilon_{\text{co}}\, e^{-[\theta/\theta_0]^2} e^{\pm j\pi[\theta/\theta_1]^2} \tag{18}$$

where θ is the direction in the far-field from boresight (assuming circular symmetry), and ϵ_{co} is a unit vector representing the polarization of the beam. In the near-field:

$$\mathbf{E}_{\text{Gauss}}(\text{r}) = \epsilon_{\text{co}}\, e^{-[\frac{\text{r}}{\text{w}(\text{z})}]^2} e^{-\text{jk}[\frac{\text{r}^2}{2\text{R}(\text{z})}]} \tag{19}$$

where r is the radius in a planar field representation (assuming circular symmetry), $w(z)$ is the waist of the Gaussian-beam, $R(z)$ is the radius of curvature, and ϵ_{co} is a unit vector representing the polarization of the beam. The value θ_0 (or $w(z)$) controls the amplitude term and θ_1 (or $R(z)$) controls the phasing term. The coupling efficiency of an antenna to a Gaussian-beam (Gaussicity) is calculated using the formula $\eta = |< \boldsymbol{\Psi}_{Antenna} | \boldsymbol{\Psi}_{Gauss} >|^2$, which written out in the far field is [28]:

$$\eta_{Gaussicity} = \frac{|\iint[\epsilon_{\text{co}} \cdot \mathbf{F}(\theta,\phi)]\, e^{-(\theta/\theta_0)^2} e^{\pm j\pi(\theta/\theta_1)^2} \sin\theta \text{d}\theta\text{d}\phi|^2}{\iint |\mathbf{F}(\theta,\phi)|^2 \sin\theta \text{d}\theta\text{d}\phi \iint e^{-2(\theta/\theta_0)^2} \sin\theta \text{d}\theta\text{d}\phi} \tag{20}$$

and written out in the near-field is:

$$\eta_{Gaussicity} = \frac{|\iint[\epsilon_{\text{co}} \cdot \mathbf{F}(\text{r},\phi)]\, e^{-(\frac{\text{r}}{\text{w}(\text{z})})^2} e^{-\text{jk}(\frac{\text{r}^2}{2\text{R}(\text{z})})} \text{rdrd}\phi|^2}{\iint |\mathbf{F}(\text{r},\phi)|^2 \text{rdrd}\phi \iint e^{-2(\text{r}/\text{w}(\text{z}))^2} \text{rdrd}\phi} \tag{21}$$

where $\mathbf{F}(\theta,\phi)$ is the electric field in the far-field pattern of the antenna, and $\mathbf{F}(\text{r},\phi)$ is the electric field in the planar representation. The amplitude and phasing terms are varied to optimize the coupling efficiency (Gaussicity). For high coupling efficiency ($> 80\%$), the near-field Gaussian parameters can be found from a Fourier transform of the far-field Gaussian parameters [23].

REFERENCES

[1] D.B. Rutledge, D.P. Neikirk and D.P. Kasilingam, "Integrated circuit antennas," *Infrared and Millimeter-Waves*, vol. 10, K.J. Button, Ed., New York: Academic Press, pp. 1-90, 1983.

[2] G.M. Rebeiz, "Millimeter-wave and terahertz integrated circuit antenna," *Proceedings of the IEEE*, vol. 80, no. 11, pp. 1748-1770, Nov. 1992.

[3] W.Y. Ali-Ahmad, W.L. Bishop, T.W. Crowe, and G.M. Rebeiz, "An 86-106 GHz Quasi-integrated low-noise schottky receiver," to appear in the April 1993 issue of *IEEE Trans. on Microwave Theory Tech.*.

[4] S.S. Gearhart, C.G. Ling, and G.M. Rebeiz, "Integrated millimeter-wave corner-cube antennas," *IEEE Trans. Antennas Propagat.*, vol. AP-39, no. 7, pp. 1000-1006, 1987.

[5] D.F. Filipovic, W.Y. Ali-Ahmad, and G.M. Rebeiz, "Millimeter-wave double-dipole antennas for high-gain integrated reflector illumination," *IEEE Trans. on Microwave Theory Tech.*, vol. MTT-40, no. 5, pp. 962-967, 1992.

[6] D.B. Rutledge and M. Muha, "Imaging antenna arrays," *IEEE Trans. Antennas Propagat.*, vol. AP-30, pp. 535-540, 1982.
[7] M. Born and E. Wolf, *Principles of Optics* . New York: Permagon Press, pp. 252-252, 1959.
[8] E. Hecht, *Optics, 2nd Edition.* Reading, MA: Addison-Wesley, pp. 129-131, 1987.
[9] H. van de Stadt, Th. de Graauw, A. Skalare, R.A. Panhuyzen, R. Zwiggelaar, "Millimeter and submillimeter studies of planar antennas," *First Int. Symp. on Space Terahertz Technology*, Ann Arbor, MI, pp. 235-255, March 1990.
[10] C.J. Adler, C.R. Brewitt-Taylor, M. Dixon, R.D. Hodges, L.D. Irving, and H.D. Rees, "Microwave and millimeter-wave recievers with integral antennas," *IEE Proc.-H*, vol. 138, pp. 253-257, 1991.
[11] A. Skalare, Th. de Graauw, and H. van de Stadt,"A planar dipole array antenna with an elliptical lens," *Microwave and Optical Tech. Lett.*, vol. 4, no. 1, pp. 9-12, 1991.
[12] D.F. Filipovic, S.S. Gearhart, and G.M. Rebeiz, "Double-slot and log-periodic antennas on extended hemispherical dielectric lenses," in *Proc. 3rd Int. Conf. Space Terahertz Technology*, Ann Arbor, MI, pp. 382-393, March 1992.
[13] R.H. Duhamel and D.E. Isbell, "Broadband logarithmically periodic antenna structure," *IRE National Convention Record*, Part I, pp. 119-128, 1957.
[14] J.D. Dyson, "The Unidirectional Equiangular Spiral Antenna," *Trans. IRE*, AP-7, pp. 329-34, 1959.
[15] T.H. Büttgenbach, "A fixed tuned broadband matching structure for submillimeter SIS receivers," to appear in the Sept. 1992 issue of *IEEE Trans. on Applied Superconductivity.*
[16] Q. Hu, Z.A. Mears, P.L. Richards, and S.L. Loyd, "Millimeter-wave quasioptical SIS mixers," *IEEE Trans. Magn.*, vol. 25, pp. 1380-1383, 1989.
[17] J. Zmuidzinas, "Quasi-Optical Slot Antenna SIS Mixers," *IEEE Trans. on Microwave Theory Tech.*, vol. MTT-40, no. 9, pp. 1797-1804, 1991.
[18] A. Skalare, H. van de Stadt, Th. de Graauw, R.A. Panhuyzen, and M.M.T.M. Dierichs, "Double-dipole antenna SIS receivers at 100 and 400 GHz," in *Proc. 3rd Int. Conf. Space Terahertz Technology*, Ann Arbor, MI, pp. 222-233, March 1992.
[19] T.H. Büttgenbach, "An improved solution for integrated array optics in quasi-optical mm and submm receivers: the hybrid antenna," to appear in this issue of *IEEE Trans. on Microwave Theory Tech.*.
[20] A.R. Kerr, P.H. Siegel, and R.J. Mattauch,"A simple quasi-optical mixer for 100-120GHz," *IEEE-MTT Int. Microwave Symp. Digest*, pp. 96-98, 1977.
[21] R.S. Elliott, *Antenna Theory and Design.* New Jersey: Prentice-Hall, Chap. 4, 1981.
[22] M. Kominami, D.M. Pozar, and D.H. Schaubert, "Dipole and slot elements and arrays on semi-infinite substrates," *IEEE Trans. Antennas Propagat.*, vol. AP-33, pp. 600-607, June 1985.
[23] R.E. Collin, *Antennas and Radiowave Propagation.* New York: McGraw-Hill, Chap. 4, 1985.
[24] C. A. Balanis, *Antenna Theory: Analysis and Design.* New York: Wiley, Chap. 11, 1982.
[25] K.C. Gupta, R. Garg, and I.J. Bahl, *Microstrip Lines and Slotlines.* Dedham, Massachusetts: Artech House, Chap. 7, 1979.
[26] R. Johnson and H. Jasik; *Antenna Engineering Handbook, 2nd Edition.* New York: McGraw-Hill, Chap 16, 1984.
[27] A. Yariv and P. Yeh, *Optical Waves in Crystals.* New York: Wiley, Chap. 2, 1984.
[28] S.E. Schwarz, "Efficiency of quasi-optical couplers," *Int. J. Infrared Millimeter Waves*, vol. 5, pp. 1517-1525, 1984.

TRUNCATION IN BEAM WAVEGUIDES

J. Anthony Murphy,
Maynooth College, Co. Kildare, Ireland

Stafford Withington,
Cavendish Laboratory, University of Cambridge, CB3 OHE, England

Abstract

We present a technique for determining the power loss and diffraction effects that occur when the field in a beam waveguide is truncated by an axially symmetric stop. The technique is based on the principles of multimode Gaussian optics. Although the underlying theory is applicable to any long-focal-length optical system, we concentrate on beam waveguides that are fed by diagonal horns, corrugated horns, smooth-walled conical horns, and uniformly illuminated apertures. We demonstrate the technique by calculating the total loss and beam profiles in a system comprising a diagonal horn, a lens, a window, and two off-axis mirrors, with the finite size of each component taken into account.

1 INTRODUCTION

When designing the quasi-optical systems of millimetre and submillimetre-wave receivers, it is necessary to know at what radius the propagating beam can be truncated at a stop or aperture without incurring a significant loss. If the beam has been refocussed a number of times, perhaps by a series of lenses or mirrors, the loss cannot be calculated by simply integrating the far-field pattern of the feed antenna over the region defined by the stop. Also, if the beam is significantly truncated diffraction effects will occur, which will affect the subsequent behaviour of the beam.

To first order, a known field can be traced through a long-focal-length optical system by extracting the lowest-order Gaussian mode [1]. In the case of a corrugated horn, this approach is particularly attractive, since the field at the mouth of the horn is linearly polarized and can be described as a simple Gaussian to high accuracy [2]. However, for a diagonal or smooth-walled conical horn, or indeed any antenna that does not have a Gaussian aperture distribution, the situation is more complicated, because, although the simple Gaussian gives an indication of how the scale size of the beam changes as one moves through the optical system, it does not give any indication of how the sidelobe structure of the beam evolves [3] [4], [5]. This limitation is particularly troublesome when the illuminating antenna has a

highly-truncated aperture field, because then the beam changes from being spatially confined to being spatially diffuse as one moves in and out of foci. In the single-mode approximation one is therefore left with the problem of surmising how the $1/e$ Gaussian radius is related to the poorly-defined radial edge of the actual beam.

To solve this problem higher-order modes can be introduced into the theoretical description of the propagating field. (e.g. [6], [2], [7], [3]). We have devised a straightfoward technique for determining the power loss, which is based on the idea that for a multimode Gaussian beam the scale size of the beam at a plane is characterised by the Gaussian radius and the sidelobe structure of the beam is characterised by the phase slippage; hence the truncation loss is completely determined by these two quantities. It is therefore possible, for axially symmetric truncation of the beam, to summarise the results for a particular feed antenna in a single contour plot, which shows truncation loss as a function of normalised aperture size and phase slippage. We discuss how such a plot can be used together with single-mode design techniques to minimise the size of millimetre and submillimetre-wave optical systems. If diffraction effects do occur due to significant beam truncation, then these can be conveniently analysed using scattering matrix theory applied to Gaussian beam modes [8], [9]. We illustrate the approach by calculating the beam profiles in a system comprising a diagonal horn, a lens, a window and two off-axis mirrors, where the finite size of each component is taken into account.

2 APERTURE-FIELD EXPANSIONS

2.1 Associated Laguerre modes

For a circular stop that is coaxial with the direction of propagation and perfectly absorbing outside the transmitting region, the propagating fields are most conveniently described as a sum of Associated Laguerre-Gaussian modes defined by:

$$\psi_n^{\alpha,cos/sin}(r,\theta,z) = \sqrt{\frac{2(2-\delta_{0n})n!}{\pi W^2(n+\alpha)!}}\left[2\left(\frac{r}{W}\right)^2\right]^{\frac{\alpha}{2}} L_n^{\alpha}\left[2\left(\frac{r}{W}\right)^2\right]\exp\left[-\left(\frac{r}{W}\right)^2\right] \exp\left[-jk\left(z+\frac{r^2}{2R}\right)+j(2n+\alpha+1)\phi_0\right]\left\{\begin{array}{c}\cos(\alpha\theta)\\ \sin(\alpha\theta)\end{array}\right\}. \quad (1)$$

The associated Laguerre polynomials are defined as in [10]. α is an integer. W and R have their usual significance and $\phi_0(z) = \tan^{-1}(\pi W^2/\lambda R)$ is the phase slippage for the fundamental mode between the waist and the plane of interest [11]. Notice that the Associated Laguerre polynomials are defined such that the generalised power in each mode $\int\int |\psi_n^{\alpha}(r,\theta)|^2 r dr d\theta$ is unity.

We can expand the co-polar and cross-polar components of a beam in the form

$$\psi(r,\theta,z) = \sum_{n=0}^{\infty}\sum_{\alpha=0}^{\infty} A^{c}_{n\alpha}\psi^{\alpha,\cos}_{n}(r,\theta,z) + A^{s}_{n\alpha}\psi^{\alpha,\sin}_{n}(r,\theta,z)\ , \tag{2}$$

where it is understood that the $A^{s}_{0,\alpha}$ are all zero. In reality, we truncate the series once the power in the sum is close to 100 % of that in the actual beam. To determine the mode coefficients $A^{c/s}_{n\alpha}$, we evaluate the overlap integrals at the aperture of the horn. If the length of the horn is L, the field at the aperture can be written

$$\psi(r,\theta) = \begin{cases} \psi_h(r,\theta)\exp\left[-jkr^2/2L\right] & \text{for } r < a \\ 0 & \text{otherwise}\ . \end{cases} \tag{3}$$

On setting the common-mode radius of curvature equal to the length, we can determine $A^{c/s}_{n\alpha}$ through

$$\begin{aligned} A^{c/s}_{n\alpha} \;=\; & e^{j\beta_{n\alpha}}\int\int_{A} r dr d\theta \psi_h(r,\theta) \\ & \sqrt{\frac{n!2(2-\delta_{n0})}{(n+\alpha)!\pi W_h^2}}\left[2\left(\frac{r}{W_h}\right)^2\right]^{\frac{\alpha}{2}} L^{\alpha}_{n}\left(2\left(\frac{r}{W_h}\right)^2\right)\exp\left[-\left(\frac{r}{W_h}\right)^2\right]\left\{\begin{array}{c}\cos(\alpha\theta)\\ \sin(\alpha\theta)\end{array}\right\} \end{aligned} \tag{4}$$

where $\beta_{n\alpha} = kz_h - j(2n+\alpha+1)\phi_o(z_h)$. In these equations W_h is the Gaussian radius at the aperture, and z_h is the position of the aperture with respect to the virtual waist [2]. It is normal to include the phase factors $\exp(j\beta_{n\alpha})$ in the mode coefficients, since they depend only on z.

There is a complete set of orthonormal modes associated with every value of W_h, and so we are free to choose W_h in whatever way we wish. It has become common practice to use the value of W_h that maximises the power in the lowest order mode; we will call this value $W_{h,opt}$. It can be shown, however, that in general $W_{h,opt}$ does not lead to a mode set that is particularly good at sampling the aperture field. In this paper, where we are interested in accurate loss calculations, we will use the value of W_h that maximises the power in a finite number of modes [12]. Once the contour plot has been generated for this mode set, we can then transform back to the more commonly-used mode set for design purposes.

Let us now consider how the mode coefficients can be calculated for each of the horns of interest.

2.2 Corrugated conical horn

The field at the mouth of a moderately-flared corrugated horn operating under balanced-hybrid conditions can be regarded as having an HE_{11} amplitude distribution with a quadratic phase error:

$$\mathbf{E}_h(r,\theta) \propto J_0(\chi_{cc}r/a)\mathbf{j}\exp\left[-jkr^2/2L\right] \tag{5}$$

where L is the length of the horn, a is the radius of the aperture, and $\chi_{cc} = 2.405$. As described, the field is polarised in the y-direction, and all of the power is contained in the

symmetric (θ-independent) co-polarised component. Thus, only ALG modes of order 0 are required in order to describe the beam. Wylde [2] has shown that for a corrugated horn $W_{h,opt} = 0.644a$.

2.3 Smooth-walled conical horn

The modal expansion of the smooth-walled conical horn has been discussed by Murphy [4]. The field at the aperture can be regarded as having a TE_{11} amplitude distribution with a quadratic phase error:

$$\mathbf{E}_h(r,\theta) \propto [(J_0(\chi_{sc}r/a) + J_2(\chi_{sc}r/a)\cos 2\theta)\mathbf{j} + J_2(\chi_{sc}r/a)\sin(2\theta)\mathbf{i}] \exp\left[-jkr^2/2L\right] \quad (6)$$

where L is the length of the horn, a is the radius of the aperture, and $\chi_{sc} = 1.841$. It can be shown that 91.8% of the power lies in the θ-independent co-polar component, while 4.1% of the power lies in each of the θ-dependent co-polar and cross-polar components. Fortunately, we only need modes of order $\alpha = 0$ and 2 [4], since all of the field terms are either θ-independent, or else depend on $\cos(2\theta)$ or $\sin(2\theta)$. Consequently,

$$\mathbf{E}_h = \sum_{n=0}^{\infty} A^c_{n0}\psi^{0,cos}_n(r,\theta,z_h)\mathbf{j} + A^c_{n2}(\psi^{2,cos}_n(r,\theta,z_h)\mathbf{j} + \psi^{2,sin}_n(r,\theta,z_h)\mathbf{i}), \quad (7)$$

where we have used the fact that $A^c_{n2} = A^s_{n2}$. For a conical horn, it can be shown that $W_{h,opt} = 0.770a$. When $W_h = W_{h,opt}$, and the total number of modes is limited to 200 ($n_{max} = 100$), only 99.3% of the power in the actual beam is included in the expansion. By choosing $W_h = 0.140a$, however, this fraction can be increased to 99.6%, and so we have used this value in all of our calculations.

2.4 Diagonal horn

The field at the aperture of a moderately-flared diagonal horn supporting spherically-expanding TE_{10} and TE_{01} square waveguide modes can be written in the form

$$\mathbf{E}_h(r,\theta) \equiv \mathbf{E}_h(x,y) \propto [\cos(\pi y/a)\mathbf{i} + \cos(\pi x/a)\mathbf{j}] \exp(-jkr^2/2L) \quad (8)$$

where L is the length of the horn and a is the sidelength of the aperture. The co-polar direction of the hybrid field can be regarded as the $\mathbf{v} = \mathbf{i} + \mathbf{j}$ direction, and the cross-polar direction can be regarded as the $\mathbf{h} = \mathbf{i} - \mathbf{j}$ direction. The field at the aperture can then be written

$$\mathbf{E}_h = \psi_{co}\mathbf{v} + \psi_{cs}\mathbf{h} \quad (9)$$

$$\psi_{co} \propto [\cos(\pi y/a) + \cos(\pi x/a)] \quad (10)$$

$$\psi_{cs} \propto [\cos(\pi y/a) - \cos(\pi x/a)], \quad (11)$$

where co, cs denote the co-polar and cross-polar components respectively. Withington [5] has already considered the behaviour of diagonal horns in terms of Gaussian modes, but in this

paper we wish to use Laguerre polynomials rather than Hermite polynomials. This slightly more complicated expansion can be achieved by recognising that there is a 4-fold rotational symmetry associated with both the co-polar and the cross-polar fields; therefore

$$\psi_{co}(r,\theta,z) = \sum_{n=0}^{\infty}\sum_{\alpha=0}^{\infty} A^{c}_{n(4\alpha)}\psi_n^{(4\alpha),\cos}(r,\theta,z)] \tag{12}$$

$$\psi_{cs}(r,\theta,z) = \sum_{n=0}^{\infty}\sum_{\alpha=0}^{\infty} A^{s}_{n(4\alpha+2)}\psi_n^{(4\alpha+2),\sin}(r,\theta,z)\,. \tag{13}$$

The mode coefficients $A_{n\alpha}, B_{n\alpha}$ can be found by expressing r and θ, in $\psi_n^{\alpha}(r,\theta)$, in terms of x and y, and integrating over the aperture. When this Cartesian integration is carried out, it is found that $W_{h,opt} = 0.430a$. Furthermore, when $W_h = W_{h,opt}$, and the total number of modes is limited to 200 ($n_{max} = 40, l_{max} = 10$), only 98.5% of the power in the actual beam is included in the expansion. By choosing $W = 0.11a$, however, this fraction can be increased to 99.1%, and so we have used this value in all of our calculations.

2.5 Uniformly-illuminated aperture

The most difficult field to propagate through an optical system is that produced by a uniformly illuminated aperture. Although, of course, one cannot manufacture such a horn, it is precisely this field that would have to pass unimpeded through an optical system if one were trying to maximise the aperture efficiency of a reflecting antenna. It is interesting, therefore, to consider this extreme case.

The beam produced by a uniformly illuminated circular aperture has axial symmetry, and therefore the modal expansion simplifies to a sum of ψ_n^0 ALG modes. If we allow the fields at the aperture, radius a, to have phase curvature, R_h, we can write

$$\psi(r) = \begin{cases} \sqrt{\frac{1}{\pi a^2}}\exp\left[-jkr^2/2R_h\right] & \text{for } r < a \\ 0 & \text{otherwise}\,. \end{cases} \tag{14}$$

and the mode coefficients become

$$A^{c}_{n0}(a/W_h) = \frac{2\sqrt{2}}{aW_h}\int_0^a L_n^0(2(r/W_h)^2)\exp\left[-(r/W_h)^2\right] r\,dr\,. \tag{15}$$

The mode coefficients can be calculated numerically [3], but it is more efficient to use the recursion relationship

$$A^{c}_{n+1,0} = 2\frac{(L_n(2(a/W_h)^2) - L_{n+1}(2(a/W_h)^2))\exp\left[-(a/W_h)^2\right]}{\sqrt{2}a/W_h} - A^{c}_{n0} \tag{16}$$

$$A^{c}_{00} = 1 - 2\exp\left[-(a/W_h)^2\right]. \tag{17}$$

In the case of a uniformly illuminated aperture, it can be shown that $W_{h,opt} = 0.892a$. When $W_h = W_{h,opt}$, and the total number of modes is limited to 500, only 98.0% of the power in the actual beam is included in the expansion. If we choose $W_h = 0.107a$, however, this fraction can be increased to 99.9%, and so we have used this value in all of our calculations.

3 ANALYSIS OF TRUNCATION USING ALG MODES

If a beam is truncated at the plane $z = z_o$, by a coaxial circular aperture of radius r_t then the field at the aperture has the form $E_{ap}(r, \theta, z_o) = 0$ for $r > r_t$, and we can write for each component of the beam (cross-polar and co-polar):

$$E_{ap}(r,\theta,z_o) = \sum_{n,\alpha} A^c_{n\alpha} \psi^{\alpha,cos}_n(r,\theta,z_o)^T + \sum_{n,\alpha} A^s_{n\alpha} \psi^{\alpha,sin}_n(r,\theta,z_o)^T, \quad (18)$$

where T denotes a truncated mode. The $A^{c/s}_{n,\alpha}$ are the mode coefficients for the incident beam. Since a truncated mode is not a true mode of propagation, some of the power in a given incident mode will be redistributed between the other modes. Mathematically, we can write each truncated mode as a sum of true propagating modes:

$$\psi^{\alpha,cos}_n(r,\theta,z_o)^T = \sum_{m,\alpha'} S^c_{m\alpha',n\alpha} \psi^{\alpha',cos}_m(r,\theta,z_o) \text{ and } \psi^{\alpha,sin}_n(r,\theta,z_o)^T = \sum_{m,\alpha'} S^s_{m\alpha',n\alpha} \psi^{\alpha',sin}_m(r,\theta,z_o). \quad (19)$$

Because of the symmetry of the aperture, $S^c_{m\alpha',n\alpha}$ and $S^s_{m\alpha',n\alpha}$ are given by

$$S^c_{m\alpha',n\alpha} = S^s_{m\alpha',n\alpha} = \delta_{\alpha\alpha'} I^\alpha_{m,n} \exp[2(n-m)j\phi_o], \quad (20)$$

where

$$I^\alpha_{m,n}(x_t) = \int_0^{x_t} \frac{x^\alpha L^\alpha_m(x) L^\alpha_n(x) e^{-x}}{\sqrt{(m+\alpha)!(n+\alpha)!/m!n!}} dx. \quad (21)$$

and $x_t = 2(r_t/W)^2$. The field can then be re-expressed in terms of the propagating modes:

$$E_{ap}(r,\theta,z_o) = \sum_{m,\alpha'} B^c_{m\alpha'} \psi^{\alpha',cos}_m(r,\theta,z_o) + B^s_{m\alpha'} \psi^{\alpha',sin}_m(r,\theta,z_o), \quad (22)$$

where $B^{c/s}_{m\alpha'} = \sum_{n,\alpha} S^{c/s}_{m\alpha',n\alpha} A^{c/s}_{n\alpha}$. We can regard $S^{c/s}_{m\alpha',n\alpha}$ as a scattering matrix, which operates on the vector $A^{c/s}_{n\alpha}$ of incident mode coefficients to yield the vector $B^{c/s}_{m\alpha'}$ of transmitted mode coefficients. Thereafter, the beam propagates with the new set of mode coefficients until the next truncating aperture is encountered. Thus, the beam can be reconstructed anywhere along the optical path.

If we are interested in the power that is transmitted through the aperture then this is given by:

$$P_t = \int_{r=0}^{r_t} \int_{\theta=0}^{2\pi} \mathbf{E}.\mathbf{E}^* r dr d\theta = \int_{r=0}^{r_t} \int_{\theta=0}^{2\pi} |\psi_{co}(z)|^2 + |\psi_{cs}(z)|^2 r dr d\theta \quad (23)$$

where *co* and *cs* denote the co-polar and cross-polar fields respectively. In the following discussion, the co-polar and cross-polar fields ψ_{co}, ψ_{cs} have been normalised to make the total generalised power $\int_{r=0}^{\infty} \int_{\theta=0}^{2\pi} \mathbf{E}.\mathbf{E}^* r dr d\theta$ unity. The above equation can be expressed in terms of the phase slippage $\Delta\phi_0$ between the *aperture of the horn* (where the mode coefficients $A_{n\alpha}, B_{n\alpha}$ were evaluated) and the plane of interest:

$$(P_t)_{co,cs} = \sum_{m,n,\alpha}^{\infty} (A^c_{m\alpha} A^c_{n\alpha} + A^s_{m\alpha} A^s_{n\alpha})_{co,cs} I^\alpha_{m,n}(x_t) \exp[2(n-m)j\Delta\phi_0]. \quad (24)$$

The subscripts *co* and *cs* denote the co-polar and cross-polar fields respectively, and the total power transmitted P_t is the sum of the two components.

It is clear that P_t depends not only on the ratio of the truncation radius r_t to the Gaussian beam width $W(z)$, but also on the phase slippage $\Delta\phi_0(z)$. As stated earlier, the Gaussian radius characterises the scale size of the beam at a plane, and the phase slippage characterises the form (sidelobe structure) of the beam; hence one would expect the fraction of power transmitted to depend on these two quantities.

A key feature of the proposed technique for determining the truncation scattering matrix coefficients and for the truncation power loss calculations is that it is possible to derive recursion relationships for the integrals $I^{\alpha}_{m,n}(x_t)$, which enable the calculations to be evaluated easily. The relationships are:

$$I^{0}_{m+1,n+1} = I^{0}_{m,n} + (L_m(x_t) - L_{m+1}(x_t))(L_{n+1}(x_t) - L_n(x_t))e^{-x_t} \quad (25)$$

$$\sqrt{\alpha+1}\,I^{\alpha+1}_{m,0} = \sqrt{m+\alpha+1}\,I^{\alpha}_{m,0} - \sqrt{m+1}\,I^{\alpha}_{m+1,0} \text{ for } m > 0 \quad (26)$$

$$\sqrt{n+\alpha+1}\,I^{\alpha+1}_{m,n} = \sqrt{n}\,I^{\alpha+1}_{m,n-1} + \sqrt{m+\alpha+1}\,I^{\alpha}_{m,n} - \sqrt{m+1}\,I^{\alpha}_{m+1,n} \text{ for } m, n > 0 \; . \quad (27)$$

For a given plane, the Gaussian radius and the differential phase slippage are functions of the mode set chosen, and so to be precise we should write $W(z, W_h)$ and $\Delta\phi_0(z, W_h)$. For computational reasons, we have used the value of W_h that maximises the power in a finite number of modes, but from a design point of view, we would like to use the value of W_h that maximises the power in the lowest-order mode $W_{h,opt}$. For every point on the optical path, we therefore need to transform between the computationally convenient $W = W(z, W_h)$ and $\phi_0 = \phi_0(z, W_h)$, and the more commonly used $W_{opt} = W(z, W_{h,opt})$ and $\phi_{0,opt} = \phi_0(z, W_{h,opt})$. After some algebra, it can be shown that

$$\phi_{0,opt} = \arctan((W_h/W_{h,opt})^2 \tan(\phi_0)) \quad (28)$$

$$r_t/W_{opt} = (r_t/W)(W_{h,opt}\sin(\phi_{0,opt}))/(W_h \sin(\phi_0)) \; . \quad (29)$$

Hence, once the contours of constant loss have been calculated, they can be presented in terms of the more commonly used single-mode parameters.

In Figs. 1 - 4 we show, for the diagonal horn, smooth-walled conical horn, corrugated conical horn, and uniformly illuminated aperture, contours of constant loss, as a function of normalised truncation radius r_t/W_{opt} and differential phase slippage $\Delta\phi_{0,opt}$.

It can be seen that for $\Delta\phi_{0,opt}$ close to zero, the fields are spatially confined, whereas for $\Delta\phi_{0,opt}$ close to $\pi/2$, the fields are diffuse. For a diffraction limited horn, these values correspond to positions in the optical system where there are images of the aperture and Fourier transform of the aperture, respectively. It is important to realise that the central portion of this plot does not necessarily correspond to the beam waist. In fact, in the case of a physically realisable horn, the waist occurs at some negative phase slippage, and the phase slippage only becomes zero once the diverging beam has reached the aperture. As the beam propagates away from the aperture, sidelobe structure develops, and a spatial redistribution of power occurs as the image of the horn undergoes diffraction. This phenomenon shows up as P_{tr}

developing off-axis wings with increasing values of $\Delta\phi_{0,opt}$. The majority of the the power still remains within $r = W_{h,opt}$, emphasising that the simple Gaussian gives a reasonable first-order description of the diffraction process.

If one is interested in the extent of the far-field beam, then the corresponding $\Delta\phi_{0,opt}$ depends on the phase error ($s = a^2/2\lambda L$) across the mouth of the horn. If the phase error is zero then the waist occurs at the aperture, and the far-field beam pattern corresponds to $\Delta\phi_{0,opt} = \pi/2$. If there is a finite phase error, the waist is ***not*** at the aperture, and the far-field power pattern corresponds to a $\Delta\phi_{0,opt}$ of *less than* $\pi/2$ [13]. In general, if the beam propagates some distance through a waveguide before reaching the point at which it is truncated, the phase slippage corresponds to the total phase slippage accumulated *since leaving the aperture*. Notice that because $\Delta\phi_{0,opt}$ is multiplied by an even number when calculating power loss, P_t will be the same for $\Delta\phi_{0,opt}$ and $\Delta\phi_{0,opt} + n\pi$, where n is an integer. P_t is therefore only plotted for values of $\Delta\phi_{0,opt}$ lying between $-\pi/2$ and $\pi/2$. Strictly speaking only half of the plot is required because the truncation loss is symmetric; conceptually, however, it is easier, when doing calculations, if both halves are visible.

In the case of the uniformly illuminated aperture, it can be seen that there are poorly-defined sidelobes that propagate to high values of r/W as $\Delta\phi_{0,opt}$ increases. This structure is real and can be related to the number of Fresnel zones that fill the aperture. A similar structure appears in some of the other plots. It is clear from Fig. 2, that it is almost impossible to transmit the beam from a uniformly illuminated aperture through an optical system: beam spreading occurs even for small values of phase slippage, and away from the near-field region, a significant fraction of the power is diffracted to large values of (r/W).

At the other extreme, a corrugated horn only requires $r_t \geq 2.0W$ for the losses to be less than $0.035dB$, or equivalently 0.8%. Fig. 1 confirms the "rule of thumb" that, for a corrugated horn, one has to use optical components that are larger than 3 beam radii. In certain regions of the system, the components can be very much smaller, and our graph quantifies this statement.

4 USE OF CONTOUR PLOTS TO DETERMINE POWER LOSS

In the previous section, we described how to plot contours of constant loss as a function of normalized truncation and phase slippage. In this section, we explain how to use these plots to calculate the loss at any plane in a complicated optical system. We suggest the following procedure:

1. Determine the size of the beam at the aperture of the horn that maximises the power in the fundamental mode $W_{h,opt}$. For the horns considered in this paper, the options are summarised in Table 1.

Horn type	$W_{h,opt}$
top-hat	0.892a
corrugated conical	0.644a
smooth-wall conical	0.770a
diagonal pyramidal	0.430a

Table 1: The size of the beam at the mouth of the horn that maximises the power in the fundamental mode. For feeds having a circular aperture, a is the radius of the aperture, whereas for feeds having a square aperture, a is the sidelength of the aperture.

2. Once $W_{h,opt}$ is known, the mode set is completely defined, and the position and size of the waist can be calculated from:

$$z_h = \frac{L}{1+\left(\frac{\lambda L}{\pi W_{h,opt}^2}\right)^2} \text{ and } W(0,W_{h,opt}) = \frac{W_{h,opt}}{\sqrt{1+\left(\frac{\pi W_{h,opt}^2}{\lambda L}\right)^2}} . \quad (30)$$

We also need the phase slippage between the waist and the aperture:

$$\phi_0(z_h, W_{h,opt}) = \arctan\left(\frac{z_h\lambda}{\pi W(0,W_{h,opt})^2}\right) = \arctan\left(\frac{\pi W_{h,opt}^2}{\lambda L}\right) . \quad (31)$$

3. Having calculated the position and size of the waist, propagate the beam through the optical system and calculate the size of the beam at the plane of interest, W_{opt} [1]. Clearly, one can then calculate the normalised radius of the truncating stop r_t/W_{opt}. To complete the analysis, we also need the phase slippage between the aperture of the horn and the stop $\Delta\phi_{0,opt}(z) = \phi_{0,opt}(z) - \phi_{0,opt}(z_h)$, where $\phi_{0,opt}$ is the phase slippage between the waist and the stop. If there are intervening optical components, one can calculate the total phase slippage by summing the phase slippages accumulated between each of the focussing elements.

4. Once the normalised radius r_t/W_{opt} and the phase slippage $\Delta\phi_{0,opt}$ have been calculated, the appropriate contour plot can be used to determine the truncation loss. Note that if $\Delta(\phi_{0,opt}) > \pi/2$, then it should be rescaled by subtracting off an integer times π so that $\Delta(\phi_{0,opt}) - n\pi$ lies between $-\pi/2$ and $\pi/2$.

5 EXAMPLE

As an example, consider the 200 GHz to 900 GHz optical system listed in Table 2 [14], where a diagonal horn is coupled to a reflecting antenna through a lens and two off-axis mirrors. The horn is part of a superconducting mixer which is located in a cryostat, and therefore the beam has to pass through a window which must be made as small as possible. In Table 2, we list the phase slippage, normalised truncation radius, co-polar percentage power transmittion

component	separation(mm)	W(mm)	a/W	$\Delta\phi_{0,opt}$(deg.)	P_{co} (%)	Loss (%)
virtual waist		1.35		-26		
	3.8					
horn aperture		1.5		0	100.0	
	32					
lens (f=32)		6.5	3.8	52	98.3	1.8
	86					
window (50mm)		5.1	4.9	90	98.1	1.8
	280					
mirror (f=280)		14.1	2.5	-21	97.9	1.6
	280					
image		13.2		0		
	350					
mirror (f=350)		14.7	2.4	25	97.6	1.9
	350					
cass focus		6.3		90		

Table 2: Beam parameters of an optical system comprising a diagonal horn, a lens and two off-axis mirrors. The beam parameters are calculated at 400 GHz. The horn is 19.0mm long and has a 3.5mm square aperture.

from horn through relevant component and the co-polar truncation loss for each of the main optical components.

It is clear from Fig. 2 that, for diagonal horns, it is difficult to clear the beam out to a loss better than 1.5%. If we use the technique described above to calculate the amount of power lost at an individual aperture (and assuming no other truncation loss in the optical system) we arrive at the figures given in the last column. As is clear from penultimate column, it is a mistake, however, to think that if one has a cascade of truncating components, the total loss is simply given by the sum of losses associated with the individual components. Obviously, if the beam does not diffract at any of the apertures, the total loss is determined by the aperture with the greatest loss, since it is not possible to lose power twice by truncating a beam at the same normalised radius twice. If the beam does diffract then power can be lost twice. We can use the truncation contour plots using the above procedure, therefore, as a way of establishing how big an aperture should be in order to avoid truncation.

If one wants to calculate the total loss incurred in a system for which the diffraction at each component is significant, one must calculate how the beam spreads at each of the apertures. This calculation can be done by using the truncation scattering matrix technique described in section 3 to charaterise the way in which power is redistributed between modes as the beam passes through each stop [15, 8]. We have used such a scattering-parameter technique to analyse the example optical system. It turns out that the total loss (penultimate column) is, as expected, much less than the sum of the individual losses [9].

In Fig. 5, we use the mode coefficients, phase slippages, and Gaussian radii to reconstruct the beam profiles at a number of different planes. Clearly, in this particular case, the apertures are many wavelengths in diameter, and the beam diffracts only slightly after passing through each stop. Consequently, the first lens after the mixer truncates the beam, and this truncated beam passes all of the way through the optical system without much further interference. From a modal point of view, the first lens is acting as a mode filter which rejects some of the higher order modes. In low noise receivers it is, of course, desirable to reject the high-order modes at low temperatures because then less noise is coupled into the system.

6 CONCLUSIONS

We have presented a technique for determining the power loss and diffraction effects that occur when the beam in a beam waveguide is truncated by an axially-symmetric stop. The technique is based on the notion that for a multimode Gaussian beam the scale size of the beam at a plane is characterised by the Gaussian radius, and the intensity distribution of the beam is characterised by the phase slippage. Hence, the loss at a truncating aperture is completely determined by these two quantities also.

The most difficult part of an analysis lies in calculating contours of constant loss as a function of normalised truncation and phase slippage. If, however, the truncating aperture is circular, and the beam is expanded in terms of Associated Laguerre modes, the necessary integration can be reduced to evaluating a recursion relationship. The appropriate scattering matrix for an aperture can also be efficiently calculated using the same approach.

References

[1] P. F. Goldsmith, "Quasi-optical techniques at millimeter and submillimeter wavelength," in *Infrared and Millimeter Waves*, vol. 8, No. 9, pp 277-343, 1982.

[2] R. J. Wylde, "Millimeter-wave Gaussian beam-mode optics and corrugated feed horns," *Proc. Inst. Elec. Eng.*, vol. 131, pt. H, pp 258-262, 1984.

[3] R. Padman, J. A. Murphy and R. E. Hills, "Gaussian mode analysis of cassegrain antenna efficiency," *IEEE Trans. Antennas Propagat.*, vol. AP-35, pp 1093-1103, 1987.

[4] J. A. Murphy, "Aperture efficiencies of large axisymmetric reflector antennas fed by conical horns," *IEEE Trans. Antennas Propagat.*, vol. AP-36, pp 570-575, 1988.

[5] S. Withington and J. A. Murphy, "Analysis of diagonal horns through gaussian-hermite modes," *IEEE Trans. Antennas Propagat.*, vol. AP-40, pp 198-206, 1992.

[6] D. H. Martin and J. Lesurf. "Submillimetre Wave Optics", *Infrared Physics*, vol. 10, pp 105-109, 1978

[7] J. W. Lamb, "Quasi-optical coupling of Gaussian beam systems to large Cassegrain antennas," *Int. J. Infrared and Millimeter Waves*, vol. 7, pp 1511-1536, 1986.

[8] R. Padman and J. A. Murphy, "A scattering matrix formulation for Gaussian beam mode analysis," *Proceedings of the IEE/URSI 7th Int. Conference on Antennas and Propagation*, ICAP, pp 201-204, York (April, 1991).

[9] J.A.Murphy, S. Withington, and A.Egan,"Mode-conversion at diffracting apertures in millimetre and submillimetre-wave optical systems," accepted for publication in the IEEE Transactions on Microwave Theory Techniques.

[10] I. S. Gradshteyn and I. M. Ryzhik, "Table of Integrals, Series and Products," Academic Press (London), 1980.

[11] H. Kogelnik and T. Li. "Laser Beams and Resonators",*Proc. IEEE*, vol. 54, pp 1312-1329, 1966.

[12] C. Aubry and D. Bittern. "Radiation patterns of a corrugated conical horn in terms of Laguerre-Gaussian Funtions," *Electron. Lett.*, vol. 11, pp. 154-156, 1975.

[13] J. A. Murphy and R. Padman, "Phase centers of horn antennas using Gaussian beam mode analysis," *IEEE Transactions Antennas Propagat.*, vol. AP-38, pp 1306-1310, 1990.

[14] S. Withington, J. A. Murphy, A. Egan and R. E. Hills, "On the design of broadband quasioptical systems for submillimetre-wave radio-astronomy receivers," *Int. J. Infrared and Millimeter Waves*, vol.13, pp 1515-1537, 1992.

[15] P. Belland and J.P. Crenn. "Changes in the characteristics of a Gaussian beam weakly diffracted by a circular aperture," *Applied Optics*, vol. 21, pp 522-527, 1982.

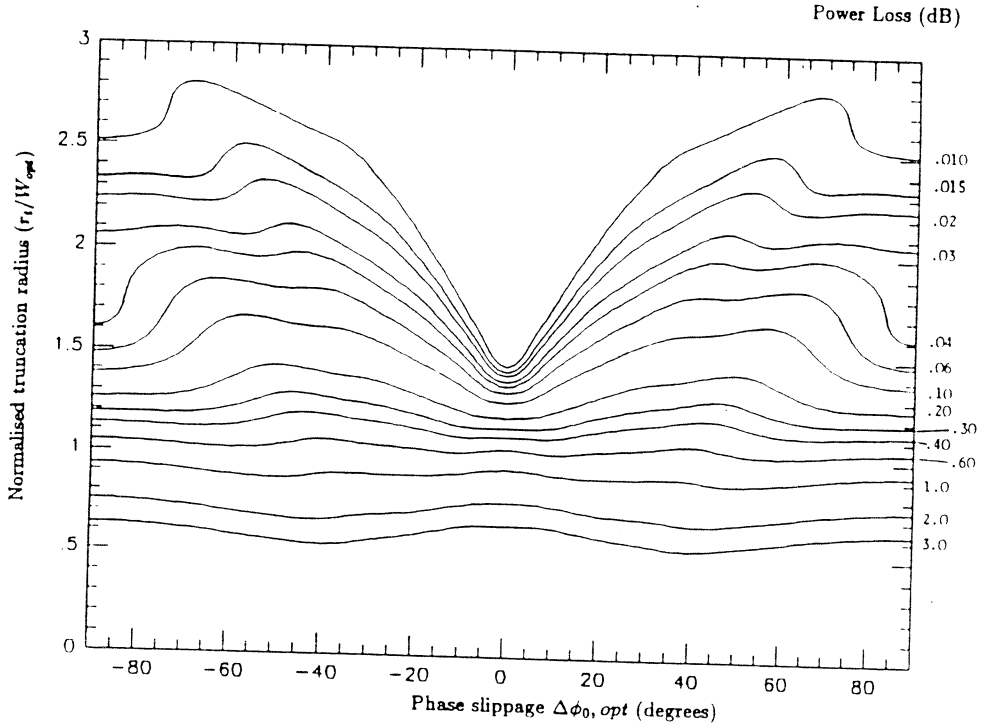

Fig. 1 Contours of constant power loss (dB) as a function of phase slippage and normalised truncation for the beam of a corrugated horn.

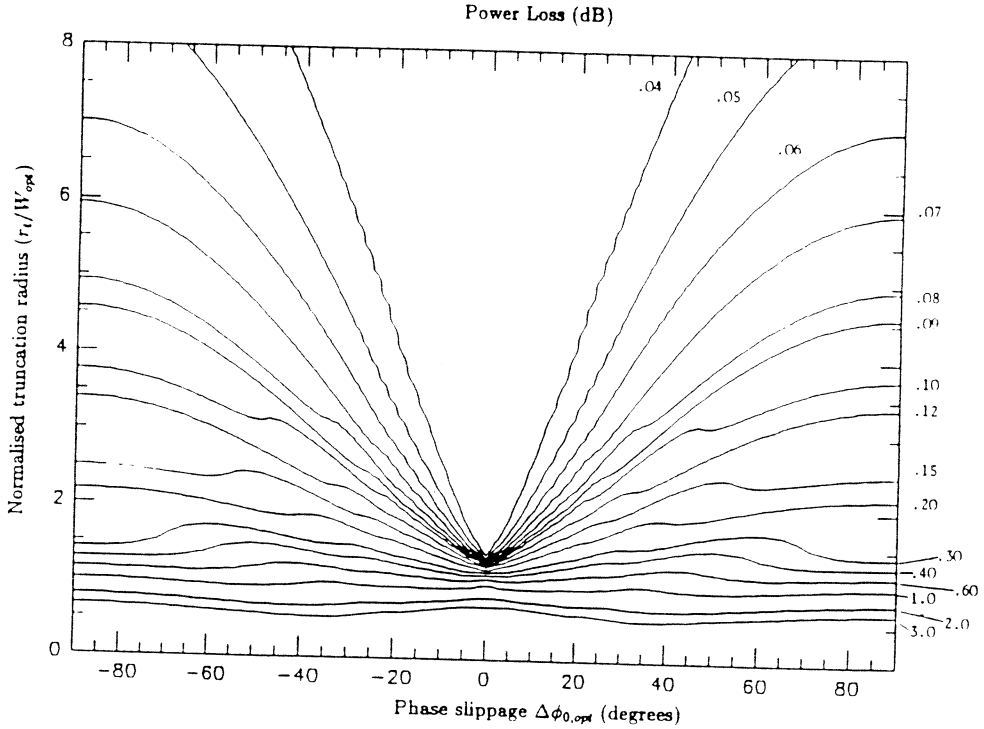

Fig. 2 Contours of constant power loss (dB) as a function of phase slippage and normalised truncation for the *co-polar* beam of a diagonal horn.

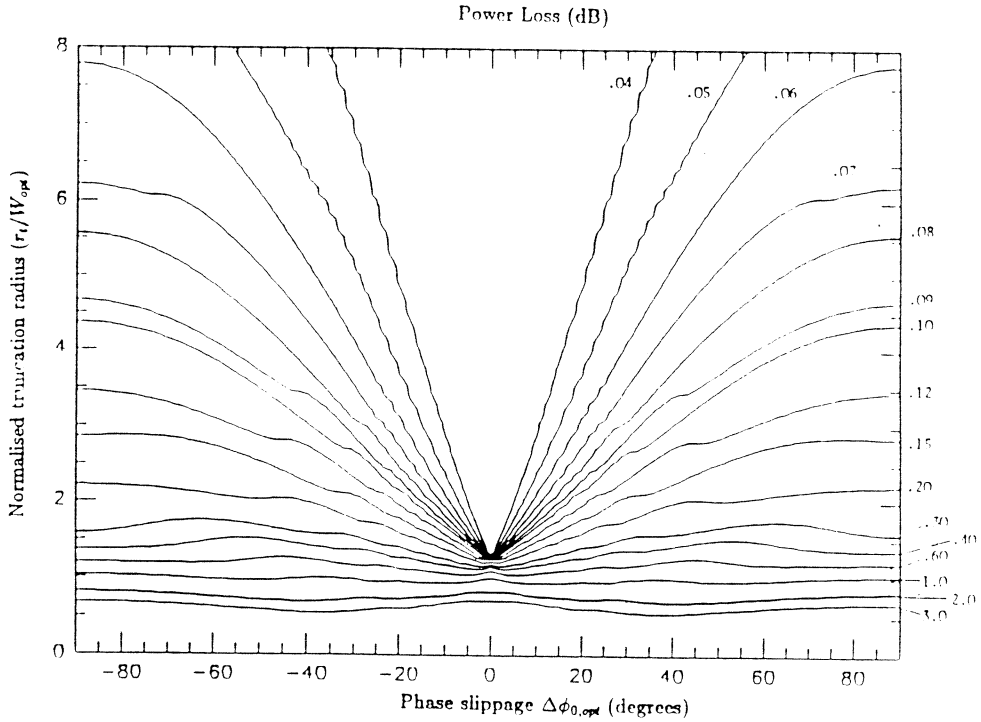

Fig. 3 Contours of constant power loss (dB) as a function of phase slippage and normalised truncation for the *co-polar* beam of a smooth-walled conical horn.

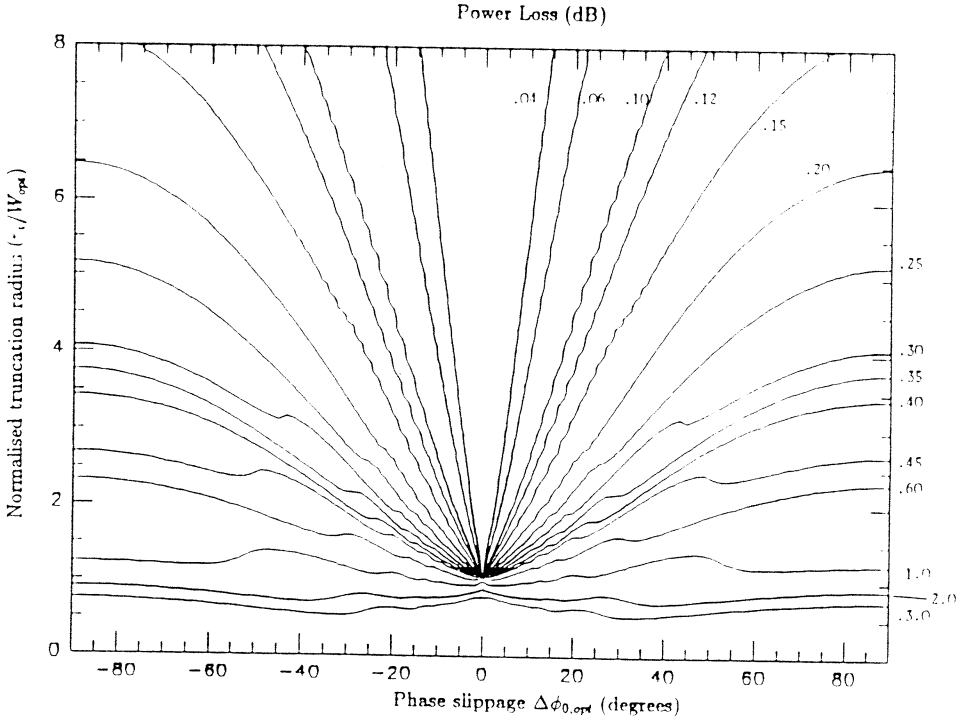

Fig. 4 Contours of constant power loss (dB) as a function of phase slippage and normalised truncation for the beam of a uniformly illuminated aperture.

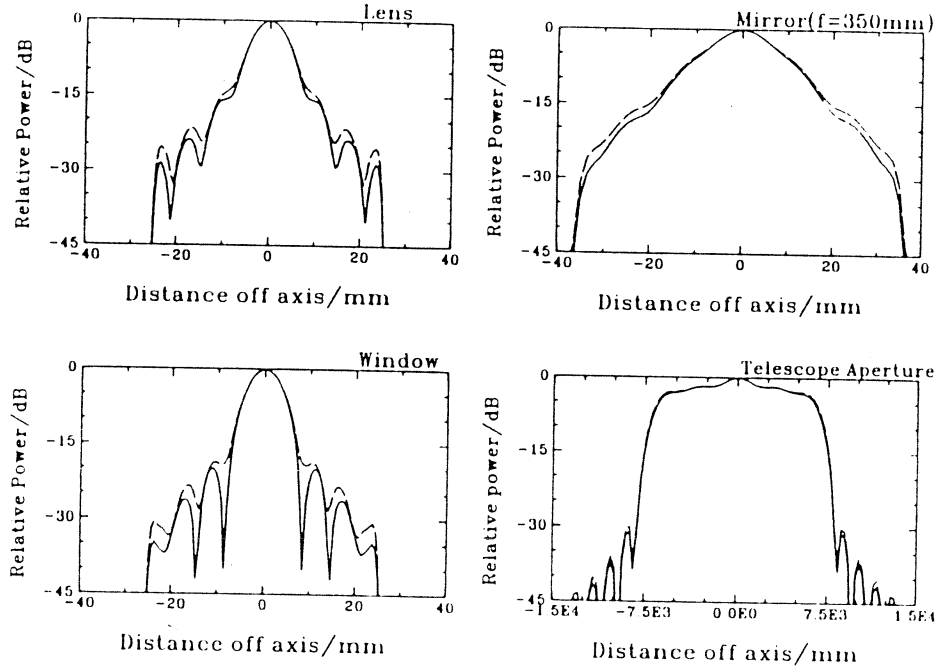

X-Y Plane Power Patterns

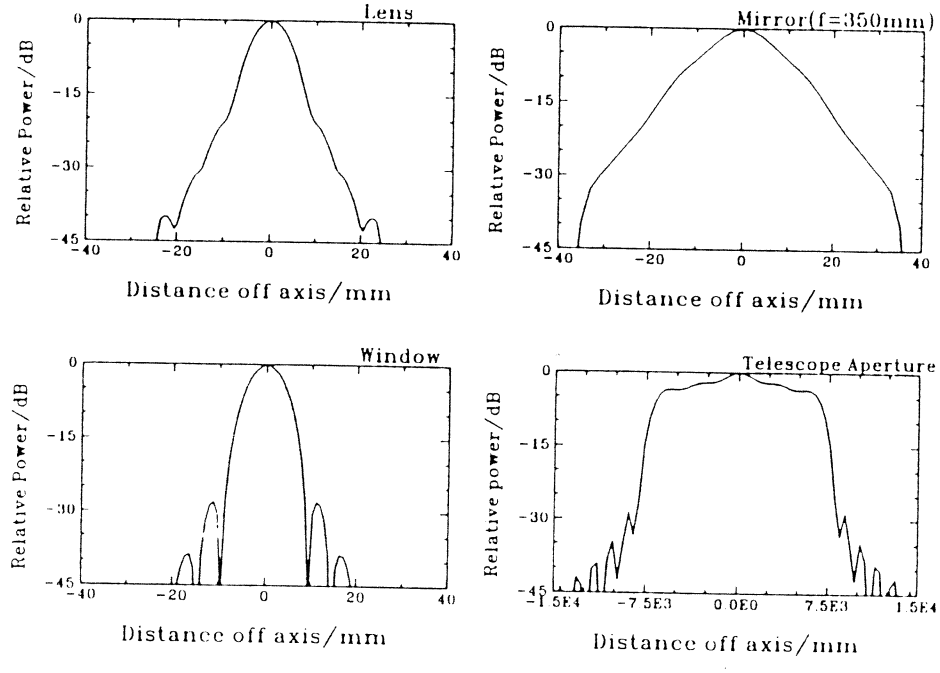

V-H Plane Power Patterns

Fig. 5 Reconstructed beam profiles at various planes in the example optical system . The two curves correspond to the copolar power (solid line) and total power (dashed line). Also

Phase Retrieval at Millimetre and Submillimetre Wavelengths using a Gaussian-Beam Formalism.

K.G. Isaak and S. Withington
Cavendish Laboratory, Madingley Rd., Cambridge, U.K.

March 26, 1993

Abstract.

In this paper, we present a technique for recovering the complex mode coefficients of a propagating beam from intensity measurements alone. Such a technique is important for experimentally characterising the behaviour of millimetre and submillimetre-wave optical systems. We describe a phase-retrieval method, based on the Gaussian-mode formalism, which is suitable for analysing the behaviour of cylindrically symmetric systems; the technique can easily be extended to cover asymmetric systems. We validate the basic procedure by recovering the complex mode coefficients of a number of different simulated amplitude distributions.

1 Introduction.

There now exists a complete range of techniques for studying and optimising the behaviour of long-focal-length millimetre and submillimetre-wave optical systems [1]. For example, a procedure exists for determining the truncation loss at any plane in a complicated quasioptical system [2], a technique has been developed for calculating the way in which power is scattered between modes at diffracting apertures [3], and a procedure has been reported for studying the aberrative effects of off-axis mirrors on collimated fields [4]. To a large extent the above techniques can only be used if the complex mode coefficients of the illuminating beam are known, and these can only be determined by evaluating the overlap integrals across some surface in the system for which the amplitude and *phase* of the field are, by some other means, already known. Indeed, the near- and far-field power patterns of corrugated [5], conical [6], and diagonal horns [7] have all been studied in this way. In many cases, however, the complex mode coefficients are difficult to determine, and a direct experimental method is required. For example, the power patterns of planar antennas and horn-lens combinations are particularly difficult to calculate, as are the power patterns of horns that have been modified for close-packed arrays. Even with nominally well-determined overlap integrals, there is often disagreement between the calculated and experimental beam patterns.

At microwave frequencies it is possible to determine the phase of a field experimentally [8] but this is much more difficult at submillimetre wavelengths, and therefore, some way of inferring phase from amplitude measurements alone is required. It should be appreciated that fitting a simple Gaussian to the far-field power pattern of a beam is of limited value, because the Gaussian only gives information about the way in which

the scale size of the beam varies as the beam propagates: it gives no information about the way in which the form of the beam varies.

In this paper, we introduce, describe, and demonstrate a phase-retrieval technique that uses the Gaussian-mode formalism. It seems that, because of its modal nature, Gaussian optics is particularly well suited to the phase retrieval process. That is to say, we should be able to measure the intensity distribution at two planes in an optical system and retrieve information abut the phase. In section 2 we give a brief outline of the history and theory of phase retrieval. In section 3 we introduce the numerical techniques and simulations that we have used to test the viability of the technique. Finally in section 4, we describe and discuss the results of a number of simulations based on the beams produced by Bessel, Gaussian and uniformly-illuminated aperture distributions.

2 Theory

The problem of recovering phase from amplitude measurements alone was first addressed by optical and electron microscopists. In the early 1970s, Gerchberg and Saxton [9] [10] suggested a technique for recovering phase from intensity measurements in the image and the diffraction planes of an electron microscope. By making use of the Fourier transform relationship between the two planes, they devised an algorithm to solve iteratively for the phase. A variation to this method was suggested by Misell [11], whereby the phase information was recovered by Fourier transforming between two slightly defocused far-field images. More recently, the technique has been applied to the microwave region for the purposes of antenna metrology [12]. According to Misell's algorithm, one makes a guess at the aperture field and then Fourier transforms this into the far field. The calculated phases are then combined with the real amplitudes to make a composite field which is transformed back to the aperture. The model antenna is then defocused, by introducing an appropriate phase term, and the far-field beam pattern recalculated. By iterating between two slightly defocused intensity distributions, the phase across the aperture can be recovered. As far as large-scale antenna metrology is concerned, the main problem is obtaining access to the far-field beam pattern. In recent times, a number of groups have concentrated on recovering phase from near-field data [13] [14] [15]. The Misell algorithm works reasonably well, although at some level problems occur due to large-scale phase errors. For example, the pointing and focusing of the actual data may differ from that of the model. Lasenby and colleagues [16] have solved this problem by using least-square fits to Zernike polynomials. In fact, they now use an algorithm where both the polynomial coefficients, and the discretised amplitudes and phases, are fitted to the intensity measurements through a least-squares procedure. This is the method preferred by an Italian group who have studied the properties of such minimisation techniques in great detail [17]. Indeed, they have devised a procedure for studying the modal content of laser beams [18], and this is essentially the technique we wish to apply to submillimetre-wave optical systems.

If the beam to be studied is circularly symmetric, the intensity distribution at some distance z from the waist can be expressed as

$$I \propto \left| \sum_n A_n L_n\left(\frac{2r^2}{w(z)^2}\right) exp\left(\frac{-r^2}{w(z)^2}\right) exp\left(j2ntan^{-1}\frac{z}{z_c}\right) \right|^2 , \qquad (1)$$

where A_n are the complex mode coefficients, r is the radial position in the measurement plane, $w(z)$ is the Gaussian beam radius at the measurement plane, and z_c the confocal

distance. The same expression can be written in the discretised form

$$I(r,z) \propto \left| \sum_n A_n \psi_n(m,i) \right|^2 \quad (2)$$

where ψ_n is a basis function appropriate to the symmetry properties of the source, and m and i characterise the data plane and data point respectively.

In the first equation, the Gaussian radius characterises the scale size of the beam at a plane, whereas the phase factor characterises the form of the beam. By noting that at large z the phase term tends to $\frac{\pi}{2}$ one can see the analogy between mode propagation and Fourier optics. It would seem that at least two intensity measurements are needed to constrain the mode coefficients. The planes used in the Gerchberg-Saxton algorithm are necessarily the diffraction and image planes, whereas in the Misell algorithm any two slightly defocused far-field planes are used. In the context of Gaussian modes, we can use any number of intensity distributions spaced in any way across phase-slippage space. Indeed, the main advantage of the Gaussian-mode approach is that one simply changes plane by changing a single parameter: the phase slippage. From a practical point of view, the Gaussian-mode approach is straightforward also, because it is possible to get access to any plane simply by inserting a long-focal-length off-axis mirror.

A key feature of the modal approach is that one does not have to calculate Fourier transforms at all, and the derivatives of the error function with respect to the real and imaginary parts of the mode coefficients are easy to calculate. The quantity we wish to minimise is

$$\chi^2 = \sum_m \sum_i \frac{(a_m |E_{mi}|^2 - D_{mi})^2}{\sigma_{mi}^2} \quad (3)$$

where we have included plane-dependent normalisation factors a_m to account for experimental variables and beam-dilution effects. In this equation, E_{mi} is the modelled field at point i on plane m, and D_{mi} is the actual data. As has already been seen, the intensity has a nonlinear dependence on the mode coefficients and hence the problem-solving process is necessarily an iterative one.

3 Numerical considerations.

The algorithm chosen to minimise the above function is based on a method suggested by Levenberg and Marquardt [19]. Close to the solution, χ^2 can be well approximated by the quadratic form. Far from the minimum, however, the second-order approximation to the Taylor expansion of χ^2 is no longer appropriate, and the best one can do is to take a step down the steepest gradient. The elegance of the Levenberg-Marquardt method lies in its ability to start with the latter process, swapping to the so-called inverse Hessian method as the minimum is approached. As minimisation proceeds, one has to determine at what point the process should be terminated. When working with noisy data it would seem meaningful to terminate the process when χ^2 = number of data points.

A problem often encountered in function minimisation is that of local minima. Rigorous studies by Isernia et al. [20] have shown that these can be largely overcome by weighting the chisquared sum by $1/D_{mi}^2$. This scaling has the effect of broadening out the quadratic surface in parameter space along which one moves as part of the minimisation process. This modification may be particularly important when analysing noisy submillimetre-wave data. The weighting means, however, that the best believable

χ^2 is no longer as above, and another convergence criterion must be used. At present, the minimisation process is allowed to continue until the fractional change between successive iterations falls below 0.005. Additional code, based on other nonlinear minimisation techniques [21], has been written to enable us to distinguish between idiosyncrasies in the minimisation procedure and undesirable features of the functional itself.

We consider hypothetical, circularly-symmetric horns as the basis for our simulations. This is merely for simplicity in the first instance. As can be seen from (2), the phase-retrieval approach is completely general and with a change of basis set, from Laguerre to associated Laguerre or Hermite polynomials, one can readily extend the phase-retrieval procedure to asymmetric beams.

Careful consideration must be given to the way in which the intensity distributions are sampled. In some sense, each Gaussian mode can be considered to represent one transverse spatial-frequency component. The intrinsic sampling can then be approximated by the Nyquist sampling rate. As one is sampling a power distribution it is necessary to sample at twice this rate. In the case of the nth Laguerre-Gaussian mode there are $\frac{(2n+1)}{4}$ periods over the extent of the mode, and therefore to sample at the Nyquist power frequency, one needs to sample $(2n+1)$ points over the power pattern. We oversample using 4n data points. It can be shown [22] that the spatial extent of a Laguerre-Gaussian polynomial is given by $w(z)\sqrt{2n+1}$ where w(z) is the Gaussian beam radius at the measurement plane. Preliminary tests indicated that sampling to $w(z)\sqrt{2n}$ produces better convergence , and it is to this limit that we sample. As the beam waist is a variable parameter, there is strictly an infinite number of mode sets that may be used to expand the propagating beam. Usually, the beam waist is set to maximise the power in the lowest-order mode: in the case of a corrugated horn this would correspond to a waist-to-aperture size ratio at the aperture of 0.6435. This value, while minimising the short comings of the propagation of a single Gaussian mode, does not necessarily sample the aperture distribution in an optimal way. Indeed, thermodynamically, this value must be wrong as it does not correctly take into account the number of degrees of freedom in the image. We have started to explore the effect of different mode sets on the efficiency of the retrieval process.

4 Results.

To demonstrate the phase-retrieval method we have produced simulated data based on the beam patterns of Gaussian, Bessel, and uniformly-illuminated aperture distributions—the Bessel-function distribution corresponds exactly to the field produced by a corrugated horn.

In each case, the data planes were oversampled out to $w(z)\sqrt{2n}$ where w(z) and n are the Gaussian beam radius at the measurement plane and the number of modes used in each data set respectively. 4n data points were used to oversample each distribution. To perform a retrieval one requires the data from two planes and an initial set of guesses to the mode coefficients: this determines the position at which one starts on the χ^2 surface. Various initial trial sets have been used: all coefficients equal, all coefficients except the fundamental set to zero, and all coefficients randomly chosen. The later was intended to simulate the random phases used as the starting condition by Misell and others. It was found that in some cases the successful recovery of the mode coefficients was dependent on the trial guess. For all of our simulations we used two far-field planes; a preliminary attempt at finding the optimum data planes failed to produce any conclusive results.

Initially, we attempted to recover phase from distributions simulated using 3 and 5 mode coefficients. The results shown in this paper are based on the recovery of 10 modes. In Figs 1,2, and 3, we show the corrugated-horn, uniformly-illuminated, and truncated-Gaussian aperture distributions that have been simulated and successfully retrieved. In each case, plot (a) shows the power distribution in each of the two far-field data planes, plot (b) shows the recovered and actual intensity distribution in the aperture, and plot (c) shows the actual and recovered phase distribution in the aperture. The plots show that excellent agreement between actual and recovered aperture distributions can be achieved. In these plots, the phase across the aperture is flat. This occurs because the Gaussian beam-mode radius of curvature is set equal to the actual field radius of curvature in the aperture. As a consequence, the mode coefficients do not contribute to the phase. A further issue is that the retrieval process does not constrain the absolute phase. We could use the retrieval process to force the imaginary part of the zeroth-order mode coefficient to zero if desired. Tables 1,2, and 3 further illustrate the success of the technique. The unconstrained phase of the fundamental mode can be clearly seen, as can the constant phase difference between the modes. This phase is simply the phase slippage associated with the dispersion of the propagating modes, and it agrees almost exactly with the expected value. Perhaps one of the most satisfying aspects of these simulations is the dynamic range that can be retrieved. For example, in the case of the corrugated horn, the fundamental and the first higher-order mode span 4 orders of magnitude.

In each case, the minimisation was allowed to continue until the weighted χ^2 between successive iterations was less than 0.005. This loop condition was found to be both under and over stringent. Reconstructions of the power patterns based on the retrieved mode coefficients taken after just a few iterations were often indistinguishable from the power patterns constructed using the final solutions. In contrast, there were a few cases where the reconstructions bore no resemblance to the simulated data set, despite the convergence criterion having, in some senses, being met. A typical retrieval of 10 mode coefficients might take around 60 iterations, although we believe that it should be possible to reduce this number significantly. Finally, the algorithm was also tested without the weighting factor $1/D_{mi}^2$. This resulted in poor convergence properties, supporting the view that weighting χ^2 reduces the problem of local minima.

5 Conclusions.

We have shown that it is possible to recover the complex mode coefficients of a propagating submillimetre-wave beam through intensity measurements alone. The mode coefficients can be recovered with high dynamic range. We are not satisfied with the performance of the Levenberg-Marquardt minimisation technique as applied to this particular phase-retrieval problem, and therefore, we are currently investigating more robust methods. The technique will be extremely useful for characterising the behaviour of millimetre- and submillimetre-wave optical systems and components.

References

[1] S. Withington, J.A. Murphy, A. Egan, and R.E. Hills,"On the design of broadband quasioptical systems for submillimetre-wave radio-astronomy receivers," Int. Journal of Infrared and Millimeter Waves, vol. 13, no. 10, pp. 1515-1537, 1992.

[2] J.A. Murphy, A. Egan, and S. Withington,"Truncation in millimetre and submillimetre-wave optical systems," To be published in IEEE Trans. Antennas and Propagat.

[3] J.A. Murphy, S. Withington, and A. Egan,"Mode conversion at diffracting apertures in millimetre and submillimetre-wave optical systems," To be published in IEEE Trans. Microwave Theory Tech.

[4] S. Withington and J.A. Murphy,"Gaussian-mode analysis of "thin" mirrors," Proceedings of the Fourth International Symposium on Space Terahertz Technology, see this issue.

[5] R.J. Wylde, "Millimeter-wave Gaussian beam-mode optics and corrugated feed horns," Proc. Inst. Elec. Eng., vol. 131, pt. H, pp. 258-262, 1984.

[6] J. A. Murphy,"Aperture efficiencies of large axisymmetric reflector antennas fed by conical horns," IEEE Trans. Antennas and Propagat., vol. AP-36, pp. 570-575, 1988.

[7] S. Withington and J. A. Murphy,"Analysis of diagonal horns through Gaussian-Hermite modes," IEEE Trans. Antennas Propagat., vol. AP-40, no. 2, pp. 198-206, 1992.

[8] G. Hygate and J.F Nye,"Measuring microwave fields directly with an optically modulated scatterer,"Meas. Sci. Technol.,vol 1., pp. 707-709, 1990.

[9] R.W. Gerchberg and W.O. Saxton,"Phase determination from image and diffraction plane pictures in the electron microscope,"Optik, vol. 34, pp. 275-284, 1971.

[10] R.W. Gerchberg and W.O. Saxton,"A practical algorithm for the determination of phase from image and diffraction plane pictures,"Optik, vol. 35, pp.237-246, 1972.

[11] D.L. Misell, "A method for the solution of the phase problem in electron microscopy," J. Phys. D:Appl.Phys.,vol. 6, L6-L9, 1973.

[12] D. Morris, "Phase retrieval in the radio holography of reflector antennas and radio telescopes," IEEE Trans. Antennas and Propagat., vol. AP-33, pp. 749-755, 1985.

[13] T. Isernia, R. Pierri, and G. Leone,"New technique for estimation of farfield from near-zone phaseless data,"Electronics Letters, vol. 27, no. 8, pp. 652-654, 1991.

[14] T. Isernia, G. Leone, and R. Pierri, "New approach to antenna testing from near field phaseless data: the cylindrical scanning," IEE Proceedings-H, vol. 139, no.4, pp.363-368, 1992.

[15] A.P Anderson and S. Sali,"New possibilities for phaseless microwave diagnostics. Part1: Error reduction techniques". IEE Proceedings-H, vol.132, no.4, pp291-298, 1986.

[16] A.N. Lasenby,"Phase retrieval using HST images,"In Proc. of Workshop on Hubble Space Telescope.

[17] T. Isernia, G. Leone, and R. Pierri,"A quadratic inverse problem: the phase retrieval,"in Inverse Methods in Action, P.C. Sabatier, ed. (Springer-Verlag, Berlin, 1990), p. 285.

[18] A. Cutolo, A. Esposito, T. Isernia, R. Pierri, and L. Zeni,"Characterization of the transverse modes in a laser beam: analysis and application to a Q-switched Nd:YAG laser,"Applied Optics, vol. 31, no. 15, pp. 2722-2733, 1992.

[19] W.H. Press, B.P. Flannery, S.A. Teukolsky, and W.T. Vetterling, "Numerical recipes in C,"Cambridge University Press, 1988.

[20] T. Isernia and R. Pierri, Private communication.

[21] The Numerical Algorithms Group Ltd, 1990.

[22] R.L. Phillips, L.C. Andrews,"Spot size and Divergence for laguerre gaussian beams of any order,"Applied Optics, vol 22, no 5, pp. 643-644, 1983.

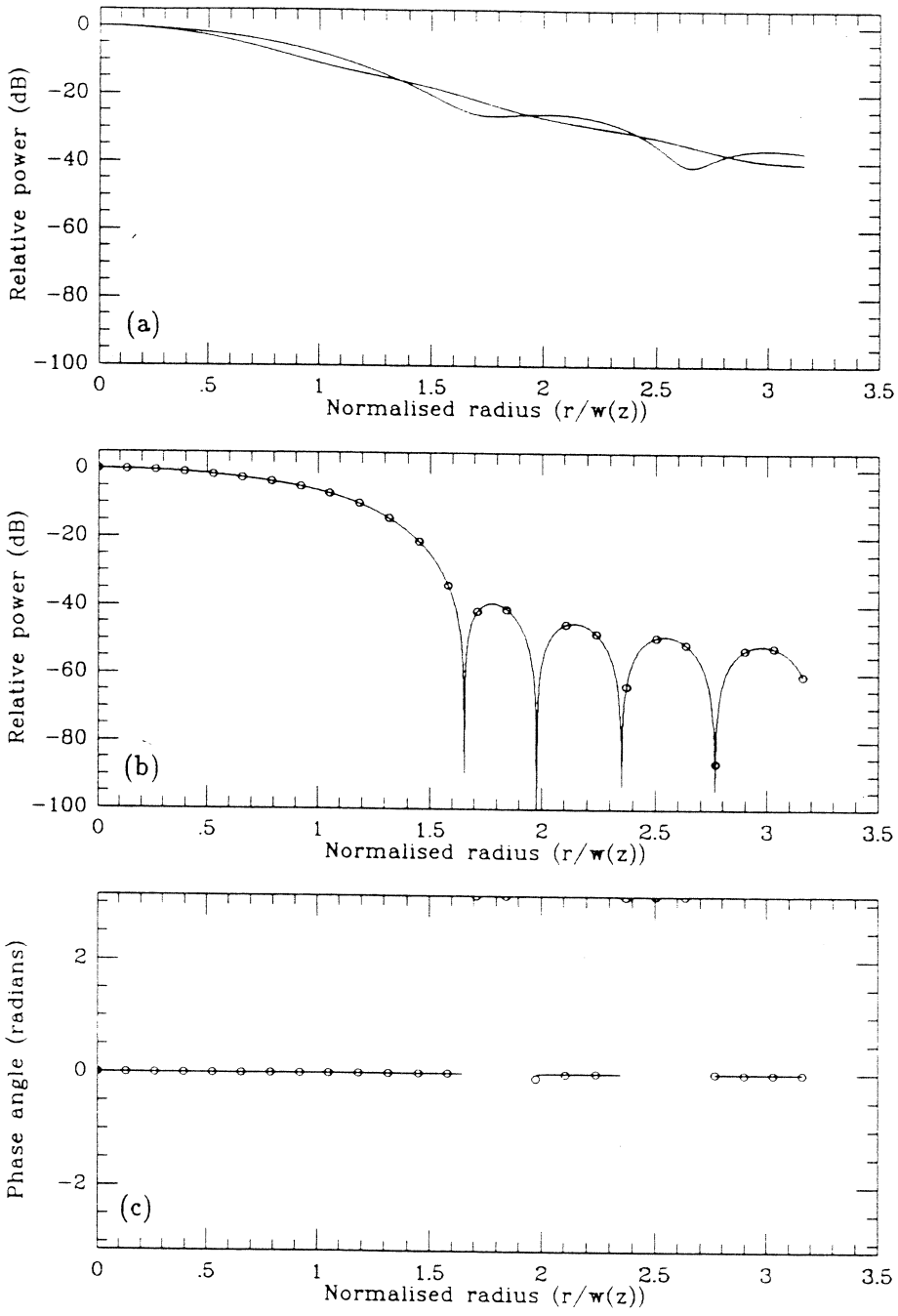

Figure 1: Retrieval of Bessel function aperture distribution. (a)Power pattern of the data planes (b) Simulated (solid line) and retrieved (open circles) power pattern as referenced to the aperture (c) Simulated (solid line) and retrieved (open circles) phase across the aperture.

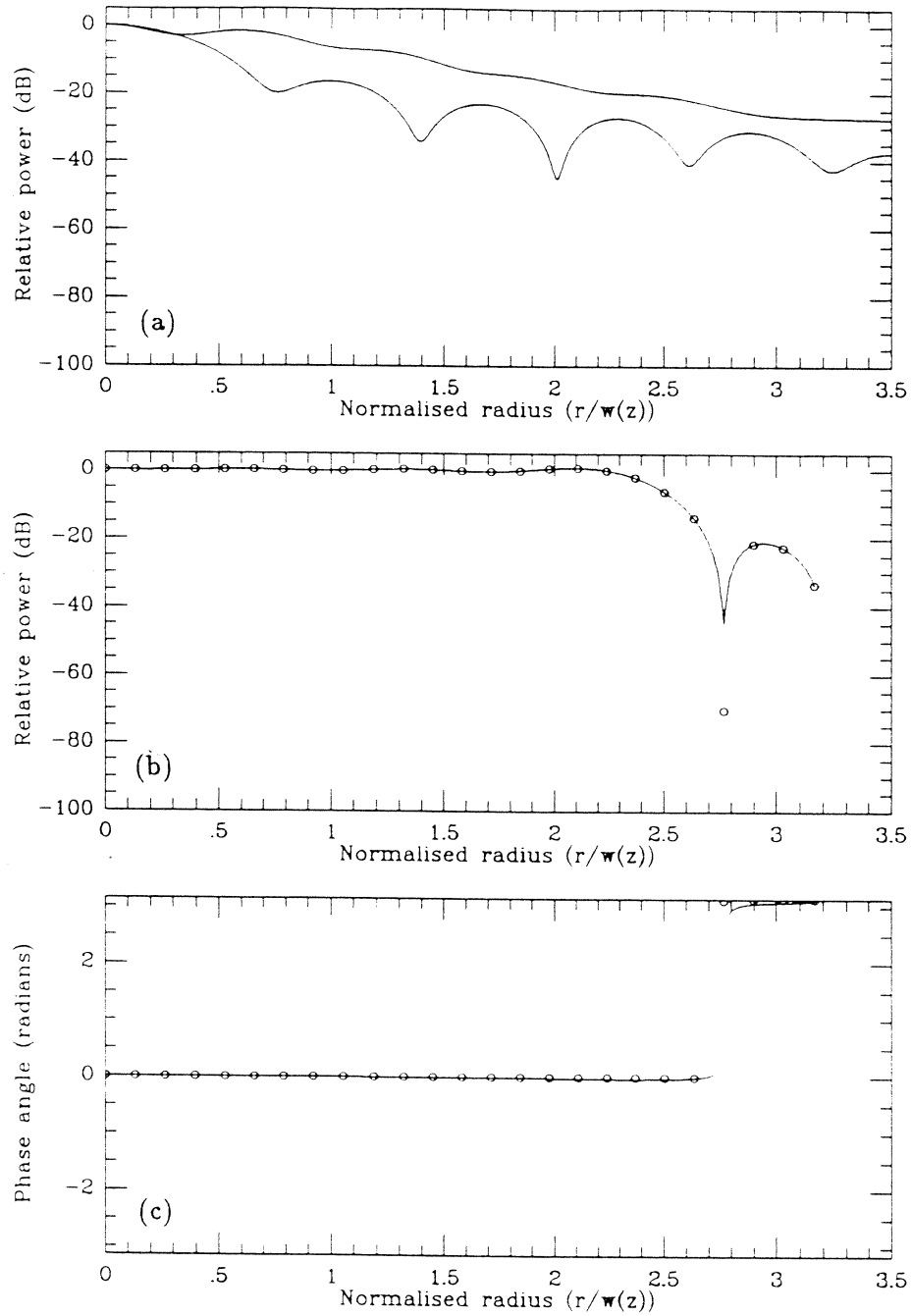

Figure 2: Retrieval of Uniformally illuminated aperture distribution. (a)Power pattern of the data planes (b) Simulated (solid line) and retrieved (open circles) power pattern as referenced to the aperture (c) Simulated (solid line) and retrieved (open circles) phase across the aperture.

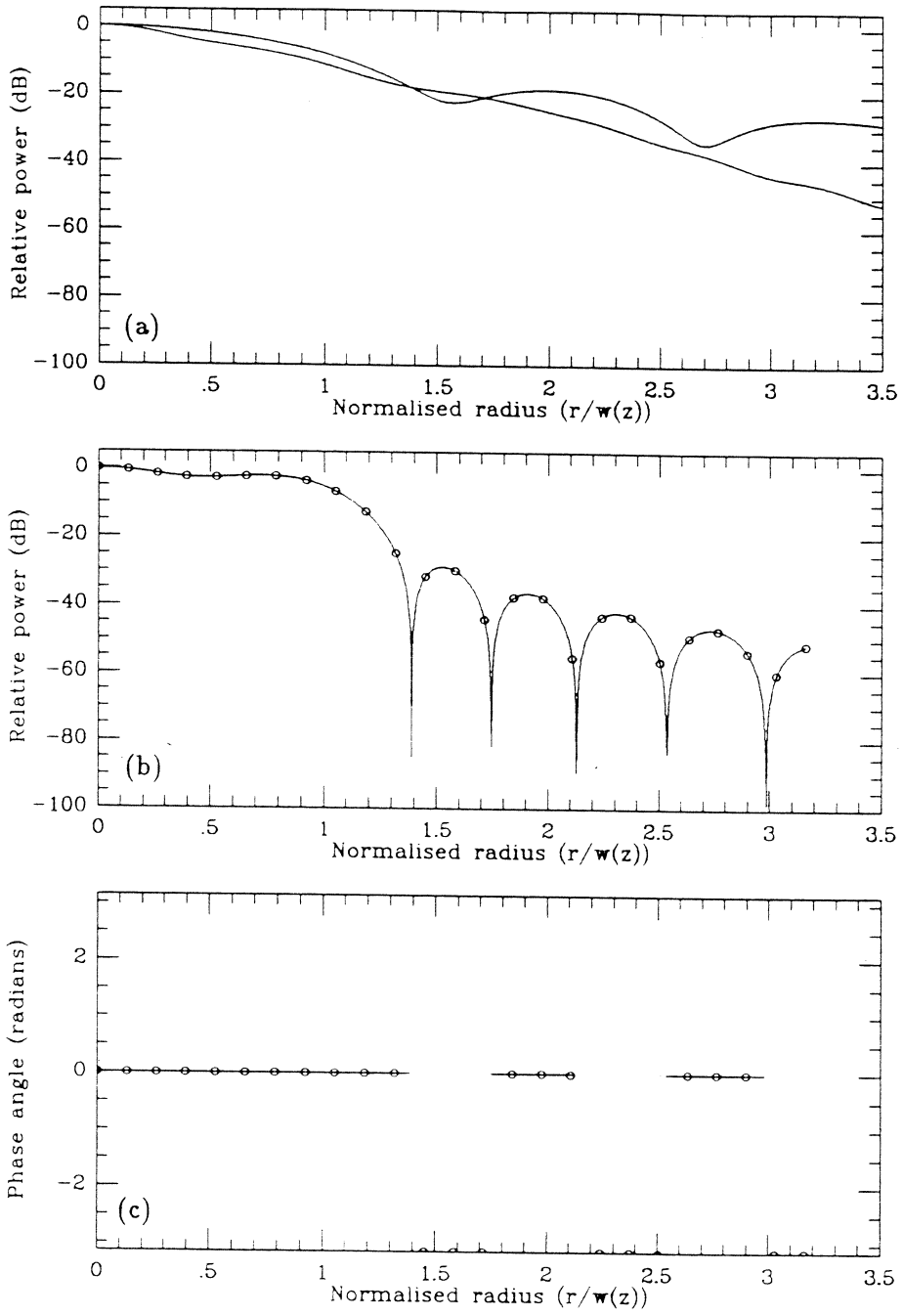

Figure 3: Retrieval of a truncated gaussian aperture distribution. (a)Power pattern of the data planes (b) Simulated (solid line) and retrieved (open circles) power pattern as referenced to the aperture (c) Simulated (solid line) and retrieved (open circles) phase across the aperture.

Table 1: Simulated and retrieved mode coefficients for a corrugated horn aperture distribution.

Simulated mode coefficients.	Corrected mode amplitudes	Retrieved mode amplitudes	Retrieved phase (radians)	Corrected Δphase between modes (radians).
0.99033	0.99059	0.99060	-1.5614	
-3.3966e-05	-3.3975e-05	1.7793e-05	0.5460	1.0342
-0.12050	-0.12054	0.12052	0.6205	-0.0744
-4.3073e-02	-4.3085e-02	4.3098e-02	0.1409	0.4795
1.9586e-02	1.9591e-02	1.9575e-02	2.8026	0.4799
3.4120e-02	3.4130e-02	3.4134e-02	2.3229	0.4797
1.9988e-02	1.9994e-02	2.0001e-02	1.8429	0.4800
1.7311e-04	1.7316e-04	1.7826e-04	1.3584	0.4844
-1.2536e-02	-1.2539e-02	1.2541e-02	-2.2579	0.4747
-1.5204e-02	-1.5298e-02	1.5211e-02	-2.7380	0.4802

note: The corrected amplitudes are renormalised to account for the fact that only 99.95% of the total power is contained within the first 10 modes.The expected phase difference between modes is $\Delta = 2arctan\frac{\pi {k_w}^2 a h^2}{4lh\lambda}$, which for the horn dimensions used is 0.4797 radians.

Table 2: Simulated and retrieved mode coefficients for a uniformly illuminated aperture distribution.

Simulated mode coefficients.	Corrected mode amplitudes	Retrieved mode amplitudes	Retrieved phase (radians)	Corrected Δphase between modes (radians).
0.56518	0.57089	0.57453	-0.4218	
-0.55150	-0.56064	0.56064	2.5314	0.1884
0.47975	0.48771	0.48771	-0.7986	0.1884
-0.28107	-0.28573	0.28573	2.1546	0.1884
-5.9638e-03	-6.0627e-03	6.0649e-03	1.9659	0.1887
0.14504	0.14745	0.14745	-1.3638	0.1881
-1.16756e-02	-1.1869e-02	1.1869e-02	1.5894	0.1883
-9.72321e-02	-9.8844e-02	9.8845e-02	1.4009	0.1885
-2.32536e-02	-2.3639e-02	2.3639e-02	1.2125	0.1884
6.10623e-02	6.2075e-02	6.2075e-02	-2.1175	0.1884

note: The corrected amplitudes are renormalised to account for the fact that only 96.76% of the total power is contained within the first 10 modes. The expected phase difference between modes is $\Delta = 2arctan\frac{\pi {k_w}^2 a h^2}{4lh\lambda}$, which for the horn dimensions used is 0.1884 radians.

Table 3: Simulated and retrieved mode coefficients for a truncated gaussian aperture distribution - truncated at $\frac{1}{e}$ point at the aperture.

Simulated mode coefficients.	Corrected mode amplitudes	Retrieved mode amplitudes	Retrieved phase (radians)	Corrected Δphase between modes (radians).
0.93843	0.95716	0.95716	0.9769	
3.0528e-02	3.1137e-02	3.1127e-02	0.1534	0.8235
-0.19301	-0.19695	0.19696	2.4715	0.8235
-0.14740	-0.15035	0.15034	1.6479	0.8236
-3.8529e-02	-3.9298e-02	3.9282e-02	0.8243	0.8236
4.6776e-02	-4.7689e-02	4.7699e-02	-3.1408	0.8236
8.4895e-02	8.6589e-02	8.6583e-02	2.3188	0.8235
8.1724e-02	8.3355e-02	8.3340e-02	1.4954	0.8231
5.3276e-02	5.4340e-02	5.4331e-02	0.6720	0.8234
1.5863e-02	1.6180e-02	1.6178e-02	-0.1515	0.8235

note: The corrected amplitudes are renormalised to account for the fact that only 96.12% of the total power is contained within the first 10 modes. The expected phase difference between modes is $\Delta = 2arctan\frac{\pi {k_w}^2\ ah^2}{4lh\lambda}$, which for the horn dimensions used is 0.8236 radians.

Gaussian-mode Analysis of "Thin" Mirrors

S. Withington
Cavendish Laboratory, University of Cambridge, UK
and
J.A. Murphy
St Patrick's College, Maynooth, Ireland

March 23, 1993

Abstract: We have developed a technique for calculating the Gaussian beam-mode scattering matrices of a shaped, off-axis mirrors. In its simplest form, the technique gives the coupling efficiency between the incoming and outgoing lowest-order Gaussian modes. In its more complete form, the technique gives the full scattering matrix between higher-order modes, which in turn characterises the aberrative behaviour of the mirror. In this paper, we model a mirror as a thin phase-transforming surface located at the tangent plane to the centre of the mirror. The scattering matrix is determined in the usual manner by evaluating the overlap integrals across some surface in the system for which the amplitude and phase of the field are known. Because, however, the modes are not orthonormal over the surface of the mirror a system of linear equations has to be solved. The shape of the mirror is simply described by the height of the surface above the tangent plane, and therefore, the technique is particularly flexible and can be used for a variety of applications. Eventually, we hope to use the technique for synthesising systems of shaped mirrors.

1 Introduction

Perhaps one of the biggest deficiencies in Gaussian beam-mode optics at the present time is the inability to describe the behaviour of shaped, off-axis mirrors. It is true that some mirrors can be described as ideal quadratic phase-transforming surfaces, but in many cases this approximation is inadequate and a more detailed analysis is required. For example, when ellipsoidal mirrors are used at frequencies away from the nominal design frequency, phase errors occur which can limit the efficiency of a system. Moreover, in array receivers most of the beams pass through the optics off-axis, and one has to worry about the distortion of individual beams in addition to the large-scale aberrations of the image. At the present time, we are particularly interested in applying phase-retrieval methods to submillimetre-wave optics, and in this case, one has to be certain that the mirror used to defocus the beam does not scatter power between modes. Another interesting application is to use the technique, together with phase-retrieval methods, for designing systems of shaped mirrors that modify beams in particular ways.

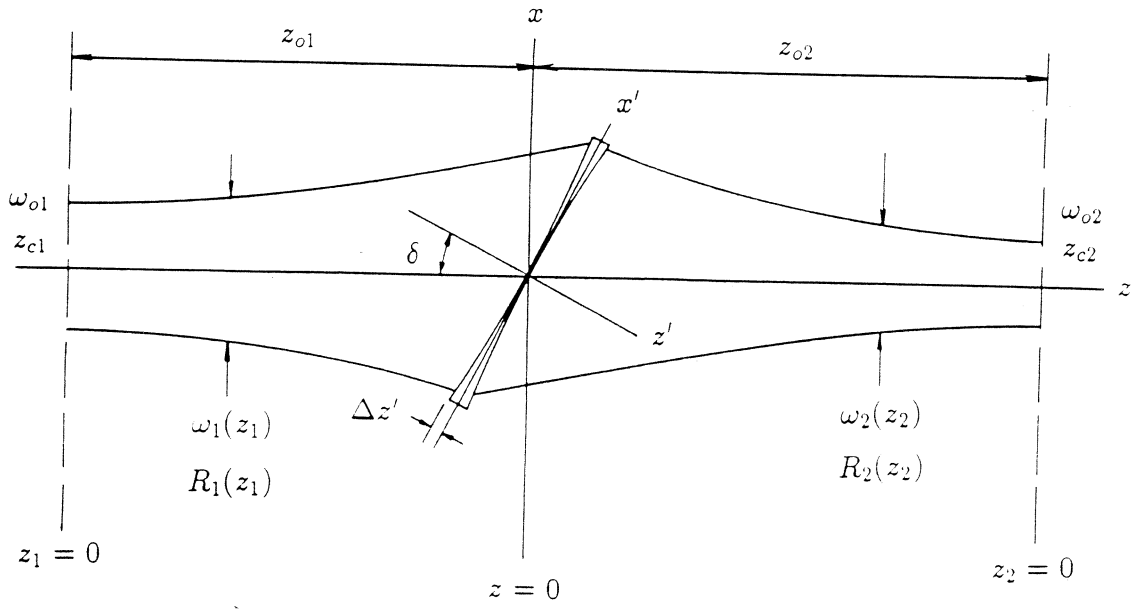

Figure 1: The coordinate system used in the analysis. The mirror is shown as though in transmission, and the tangent plane simply separates the input and output coordinate frames.

We have developed a technique for studying the behaviour of shaped, off-axis mirrors. The technique is aimed at calculating the scattering matrix relating the mode coefficients of the input beam to the mode coefficients of the output beam. To this end, we introduce the concept of a *thin* mirror. By analogy with a thin lens, we represent an off-axis mirror as a thin phase-transforming surface located at the tangent plane to the centre of the mirror. The phase transformation across the plane can be any arbitrary function, allowing ellipsoidal, paraboloidal, spherical, or other forms to be analysed. Once the reflected field is known, the scattering matrix can be determined by evaluating the overlap integrals over the surface of the mirror and inverting the system of linear equations that results from the modes not being orthogonal.

2 Scattering-matrix theory

The coordinate system to be used in the analysis is shown in Fig. 1, and a detailed view of the mirror is shown in Fig. 2. According to this scheme, the mirror is shown as though in transmission, and the tangent plane simply separates the input and output coordinate frames. If a generic point in the (x, y, z) frame is denoted by s, and a generic point in the, inclined, (x', y', z') frame is denoted by s', then the two frames are connected on the

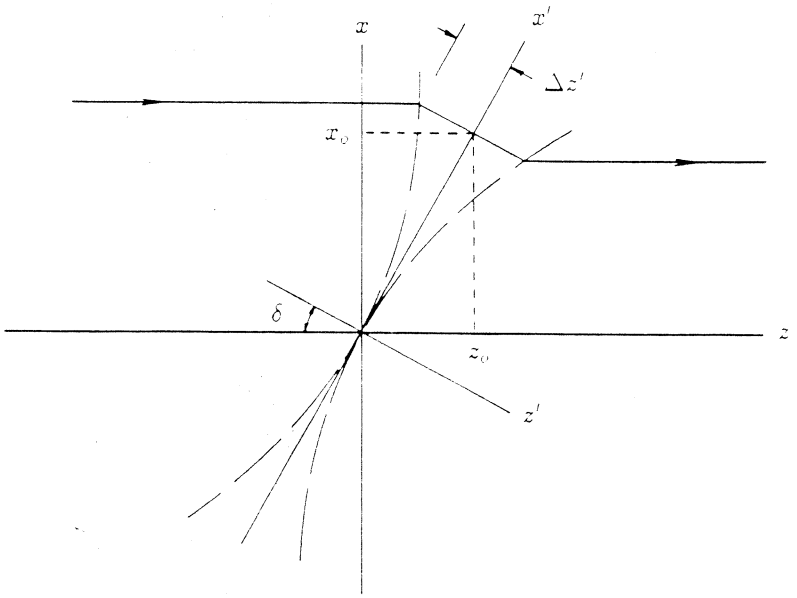

Figure 2: A detailed view of the mirror.

input surface by

$$\begin{aligned} x &= x' \cos\delta + \Delta z' \sin\delta = x_o + \Delta x \\ y &= y' = y_o \\ z &= x' \sin\delta - \Delta z' \cos\delta = z_o - \Delta z \end{aligned} \tag{1}$$

and on the output surface by

$$\begin{aligned} x &= x' \cos\delta - \Delta z' \sin\delta = x_o - \Delta x \\ y &= y' = y_o \\ z &= x' \sin\delta + \Delta z' \cos\delta = z_o + \Delta z \end{aligned} \tag{2}$$

where the form of the mirror is described by $\Delta z' = f(x', y')$. The incident and reflected fields can be written in the inclined frame to give

$$E_i(s') \exp\left[-jk(z_o - \Delta z' \cos\delta)\right] \quad \text{and} \quad E_o(s') \exp\left[-jk(z_o + \Delta z' \cos\delta)\right], \tag{3}$$

respectively, and because these points represent the same physical position, we have

$$E_o(s') = E_i(s') \exp\left[jk2\Delta z' \cos\delta\right] = E_i(s') \exp\left[j\phi(x', y')\right]. \tag{4}$$

The mirror is thus being described as an inclined phase-transforming surface, and the obliquity factor enters naturally as expected.

For long-focal-length optics, the input and output beams can be decomposed into sums of propagating free-space modes:

$$E_i(s') = \sum_{m,n} A_{mn}\psi^i_{mn}(s') \quad \text{and} \quad E_o(s') = \sum_{r,s} B_{rs}\psi^o_{rs}(s') \; . \tag{5}$$

To determine the mode coefficients, we evaluate the overlap integrals over the surface of the mirror in the output coordinate frames. Unlike usual analyses, however, the modes are not orthonormal over the plane of interest; nevertheless

$$\int_M E_o(s')\,\psi^{o*}_{ij}(s')\,dM = \int_T E_o(s')\,\psi^{o*}_{ij}(s')\left[1 + \left(\frac{\partial f}{\partial x'}\right)^2 + \left(\frac{\partial f}{\partial y'}\right)^2\right]^{\frac{1}{2}} dx\,dy' \; , \tag{6}$$

where we have projected the surface of the mirror M onto the tangent plane T. For thin mirrors

$$\left(\frac{\partial f}{\partial x'}\right)^2 \ll 1 \text{ and } \left(\frac{\partial f}{\partial y'}\right)^2 \ll 1 \; , \tag{7}$$

and the surface integral is easy to evaluate numerically. We can now project this integral onto the $z = 0$ plane by making the substitutions $x' = x_o/\cos\delta$ and $y' = y_o$ to give the s_o frame (x_o, y_o, z_o). Finally, the overlap integral becomes

$$\int_{-\infty}^{+\infty}\int_{-\infty}^{+\infty} E_o(s_o)\,\psi^{o*}_{ij}(s_o)\,J dx_o dy_o \; , \tag{8}$$

where the Jacobian is defined in the usual way through

$$dx'dy' = \begin{vmatrix} \frac{\partial x'}{\partial x_o} & \frac{\partial x'}{\partial y_o} \\ \frac{\partial y'}{\partial x_o} & \frac{\partial y'}{\partial y_o} \end{vmatrix} dx_o dy_o \; . \tag{9}$$

Because the mirror slopes in the x direction, $dx'dy' = \sec\delta\, dx_o dy_o$ where δ is the angle of incidence. Also we have $x' = x_o\sqrt{1+\tan^2\delta}$ and $y' = y_o$. At this stage, we also note that the input modes have their waists at $z_1 = 0$, and the output modes have their waists at $z_2 = 0$; consequently, the relationship between the two coordinate frames is simply $z_1 = z_2 + z_{o1} + z_{o2}$. Thus, the tangent plane is described in the frame of the input modes by $z_1 = x_o\tan\delta + z_{o1}$ and in the frame of the output modes by $z_2 = x_o\tan\delta - z_{o2}$.

Substituting the modal expansion into the overlap integrals we get

$$\int_M E_o(s')\psi^{o*}_{ij}(s')dM = \sum_{r,s} B_{rs}\beta_{ijrs}\sec\delta \tag{10}$$

where

$$\beta_{ijrs} = \int_{-\infty}^{+\infty}\int_{-\infty}^{+\infty} \psi^o_{rs}(s_o)\psi^{o*}_{ij}(s_o)dx_o dy_o \; . \tag{11}$$

Through (4), we can express the reflected field in terms of the incident field and write

$$\int_M E_o(s')\psi^{o*}_{ij}(s')dM = \int_{-\infty}^{+\infty}\int_{-\infty}^{+\infty} E_i(s_o)\exp\left[\varphi(x',y')\right]\psi^{o*}_{ij}(s_o)\,J dx_o dy_o \; . \tag{12}$$

Substituting the modal expansion then leads to

$$\int_M E_o(s')\,\psi_{ij}^{o*}(s')\,dM = \sum_{m,n} A_{m,n}\alpha_{ijmn}\sec\delta \tag{13}$$

where

$$\alpha_{ijmn} = \int_{-\infty}^{+\infty}\int_{-\infty}^{+\infty} \psi_{mn}^{i}(s_o)\exp\left[j\Delta\phi(x_o/\cos\delta, y_o)\right]\psi_{ij}^{o*}(s_o)dx_o dy_o \,. \tag{14}$$

Finally, combining these two results we find

$$\sum_{r,s} B_{rs}\beta_{ijrs} = \sum_{m,n} A_{mn}\alpha_{ijmn} \text{ for all } ij \,. \tag{15}$$

Clearly, this set of equations can be expressed in matrix form:

$$\boldsymbol{\alpha A} = \boldsymbol{\beta B} \,. \tag{16}$$

In this equation, $\boldsymbol{A}$ and $\boldsymbol{B}$ are vectors of mode coefficients, $\boldsymbol{\alpha}$ is a matrix describing the scattering of power between modes, and $\boldsymbol{\beta}$ is a matrix representing the nonorthogonality of the modes across the surface of the mirror: notice that $\boldsymbol{\beta}$ is Hermitian. We can now define a scattering matrix $\boldsymbol{S}$, relating the mode coefficients at the two waists, through

$$\boldsymbol{B} = \boldsymbol{\beta}^{-1}\boldsymbol{\alpha A} = \boldsymbol{SA} \,. \tag{17}$$

Let us choose propagating Hermite polynomials as a basis set. A suitable expansion function is

$$\begin{aligned}\psi_{ij} \;=\; & \frac{\sqrt{2}}{w(z)}h_i\left(\frac{\sqrt{2}x}{w(z)}\right)h_j\left(\frac{\sqrt{2}y}{w(z)}\right)\exp\left[-j\frac{\pi}{\lambda R(z)}\left(x^2+y^2\right)\right] \\ & \exp\left[j\,(i+j+1)\tan^{-1}\frac{z}{z_c}\right]\exp\left[-jkz\right]\end{aligned} \tag{18}$$

where

$$h_m(u) = \frac{H_m(u)\exp\left[-\frac{u^2}{2}\right]}{(\sqrt{\pi}2^m m!)^{\frac{1}{2}}} \,. \tag{19}$$

This set is normalised in the sense that the total power is unity. As shown in Fig. 1, the input beam is described in terms of coordinate z_1 and the output beam is described in terms of coordinate z_2. The waist and confocal distance of the input modes are denoted by w_{o1} and z_{c1} respectively, and the waist and confocal distance of the output modes are denoted by w_{o2} and z_{c2}. The Gaussian radii of the input and output beams are given by

$$w_2(z_2) = w_{o2}\left[1+\left(\frac{z_2}{z_{c2}}\right)^2\right]^{\frac{1}{2}} \quad \text{and} \quad w_1(z_1) = w_{o1}\left[1+\left(\frac{z_1}{z_{c1}}\right)^2\right]^{\frac{1}{2}} \,. \tag{20}$$

and the radii are curvature are given by

$$R_1(z_1) = z_1\left[1+\left(\frac{z_{c1}}{z_1}\right)^2\right] \quad \text{and} \quad R_2(z_2) = z_2\left[1+\left(\frac{z_{c2}}{z_2}\right)^2\right] \tag{21}$$

respectively.

The parameters of the modes associated with the output beam are chosen so that the waists at the centre of the mirror are equal:

$$w_1(z_{o1}) = w_2(z_{o2}) \ , \tag{22}$$

and after taking into account the focusing effect of the mirror, the radii of curvature match:

$$\frac{1}{R_1(z_{o1})} + \frac{1}{R_2(z_{o2})} = \frac{1}{f} \ , \tag{23}$$

where f is the focal length of the mirror. In some cases, it may be difficult to decide what the value of f should be. For example, an off-axis spherical mirror is astigmatic, and the sagittal and tangential focal lengths are different.

The position and size of the output waist can be found by satisfying the above two requirements [1], and this leads to

$$\frac{z_{o2}}{f} = 1 + \frac{(z_{o1}/f) - 1}{[(z_{o1}/f) - 1]^2 + (\pi w_{o1}^2/\lambda f)^2} \tag{24}$$

and

$$\left(\frac{w_{o2}}{w_{o1}}\right)^2 = \frac{1}{[(z_{o1}/f) - 1]^2 + (\pi w_{o1}^2/\lambda f)^2} \ . \tag{25}$$

Substituting the mode set into (11) gives

$$\beta_{ijrs} = \int_{-\infty}^{+\infty} \frac{2}{w_2^2(z_2 + \Delta z)} h_r\left(\frac{\sqrt{2}(x_o - \Delta x)}{w_2(z_2 + \Delta z)}\right) h_s\left(\frac{\sqrt{2}(y_o)}{w_2(z_2 + \Delta z)}\right) h_i\left(\frac{\sqrt{2}(x_o - \Delta x)}{w_2(z_2 + \Delta z)}\right)$$
$$h_j\left(\frac{\sqrt{2}(y_o)}{w_2(z_2 + \Delta z)}\right) \exp\left[j\,(r + s - i - j)\tan^{-1}\frac{(z_2 + \Delta z)}{z_{c2}}\right] dx_o dy_o \tag{26}$$

At this stage, the integral can be evaluated as it stands, or various levels of approximation can be introduced. For the purposes of this paper, we will assume that all of the offsets can be ignored when calculating the β matrix. This approximation is equivalent to following the tangent plane rather than the surface of the mirror when calculating field amplitudes. Clearly, this approximation is reasonable if the mirror is thin. After making this assumption, we can write

$$\beta_{ijrs} = \int_{-\infty}^{+\infty} \frac{\sqrt{2}}{w_2(z_2)} h_r\left(\frac{\sqrt{2}x_o}{w_2(z_2)}\right) h_i\left(\frac{\sqrt{2}x_o}{w_2(z_2)}\right) \exp\left[j\,(r - i)\tan^{-1}\frac{z_2}{z_{c2}}\right] dx\,\delta_{js} \ , \tag{27}$$

where we have taken advantage of the fact that, because the mirror is inclined in the x direction, the modes in the y direction remain orthogonal. As a consequence β becomes a block diagonal matrix; a feature which can be exploited when the matrix is inverted. Also notice that β only depends on the angle of incidence: it does not depend on the shape of the mirror. It may also be seen that, to a large extent, the modes remain orthogonal in a long-focal-length system because the waist changes very little over the region occupied by the mirror. When coupling does occur, one finds that a mode is

preferentially coupled to modes having similar orders, and this implies that some form of perturbation analysis would be appropriate.

We can also substitute the mode set into (14) to give

$$\begin{aligned}\alpha_{ijmn} = & \int_{-\infty}^{+\infty}\int_{-\infty}^{+\infty} \frac{\sqrt{2}}{w_1(z_1-\Delta z)}\frac{\sqrt{2}}{w_2(z_2+\Delta z)} h_m\left(\frac{\sqrt{2}(x_o+\Delta x)}{w_1(z_1-\Delta z)}\right) h_i\left(\frac{\sqrt{2}(x_o-\Delta x)}{w_2(z_2+\Delta z)}\right) \\ & \exp\left[j(m+n+1)\tan^{-1}\frac{(z_1-\Delta z)}{z_{c1}}\right]\exp\left[-j(i+j+1)\tan^{-1}\frac{(z_2+\Delta z)}{z_{c2}}\right] \\ & h_n\left(\frac{\sqrt{2}y_o}{w_1(z_1-\Delta z)}\right) h_j\left(\frac{\sqrt{2}y_o}{w_2(z_2+\Delta z)}\right)\exp\left[-j\frac{\pi}{\lambda R_1(z_1-\Delta z)}\left((x_o+\Delta x)^2+y_o^2\right)\right] \\ & \exp\left[+j\frac{\pi}{\lambda R_2(z_2+\Delta z)}\left((x_o-\Delta x)^2+y_o^2\right)\right]\exp\left[j\Delta\phi(x',y')\right]dy_o dx_o . \end{aligned} \tag{28}$$

This equation is rather involved, and it is not possible to simplify for the general case. Nevertheless, it is straightforward to evaluate numerically. Again we can follow the tangent plane when calculating the amplitudes. It is of course important to follow the surface of the mirror when calculating the phase. This approximation leads to

$$\begin{aligned}\alpha_{ijmn} = & \int_{-\infty}^{+\infty}\frac{2}{w_1(z_1)w_2(z_2)} h_m\left(\frac{\sqrt{2}(x_o)}{w_1(z_1)}\right) h_i\left(\frac{\sqrt{2}(x_o)}{w_2(z_2)}\right)\exp\left[j(m+n+1)\tan^{-1}\frac{z_1}{z_{c1}}\right] \\ & \exp\left[-j(i+j+1)\tan^{-1}\frac{z_2}{z_{c2}}\right]\int_{-\infty}^{+\infty} h_n\left(\frac{\sqrt{2}y_o}{w_1(z_1)}\right) h_j\left(\frac{\sqrt{2}y_o}{w_2(z_2)}\right) \\ & \exp\left[-j\frac{\pi}{\lambda R_1(z_1-\Delta z)}\left((x_o+\Delta x)^2+y_o^2\right)\right] \\ & \exp\left[+j\frac{\pi}{\lambda R_2(z_2+\Delta z)}\left((x_o-\Delta x)^2+y_o^2\right)\right]\exp\left[j\Delta\phi(x',y')\right]dy_o dx_o . \end{aligned} \tag{29}$$

To complete the analysis we need to make a modification to the last equation. The problem is that the last three terms, which constitute the phase error across the surface of the mirror, are based on the paraxial approximation. As a consequence, the equation correctly describes the long-wavelength behaviour, but does not adequately describe the short-wavelength behaviour. We can correct this deficiency, albeit in a heuristic manner, by replacing the parabolic phase front of the Gaussian mode with a spherical phase front. The appropriate phase factor is given by

$$\begin{aligned}&\exp\left[-j\left(\frac{2\pi}{\lambda}\right)\frac{(x_o+\Delta x)^2+y_o^2}{R_1(z_1-\Delta z)+\sqrt{R_1^2(z_1-\Delta z)+(x_o+\Delta x)^2+y_o^2}}\right] \\ &\exp\left[+j\left(\frac{2\pi}{\lambda}\right)\frac{(x_o-\Delta x)^2+y_o^2}{R_2(z_2+\Delta z)-\sqrt{R_2^2(z_2+\Delta z)+(x_o-\Delta x)^2+y_o^2}}\right] . \end{aligned} \tag{30}$$

Once the α and β matrices are known, the scattering matrix can be evaluated through (17).

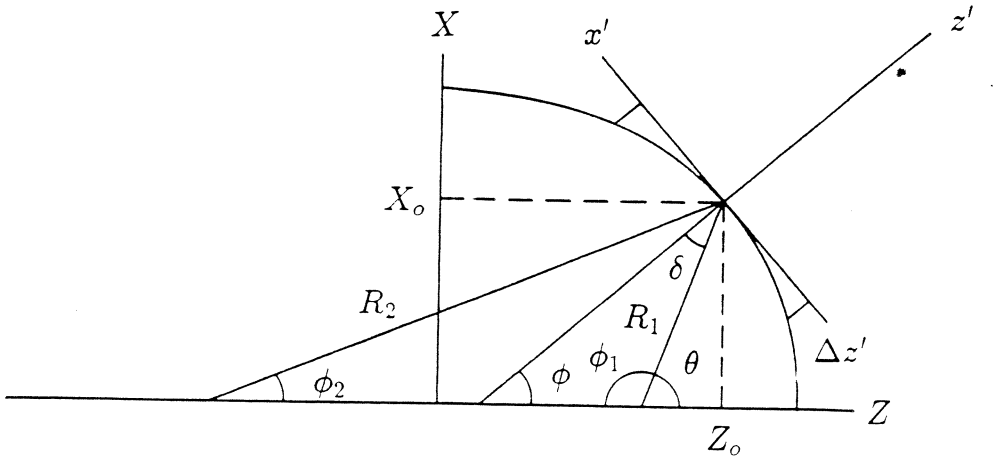

Figure 3: The geometry of an ellipsoidal mirror.

3 Ellipsoidal mirrors

To complete the analysis, we need to find the phase factors $\phi(x', y')$, for the mirrors of interest. Clearly, we need to express the height of the surface of the mirror above the tangent plane in the (x, z) coordinate frame. The geometry of an ellipsoidal surface is shown in Fig. 3.

We choose $R1$ and $R2$ to match the radii of curvature of the input and output beams respectively. Once the angle of incidence has been fixed, we can calculate the lengths of the major and minor axes through

$$a = \frac{(R1 + R2)}{2} \quad \text{and} \quad b = \sqrt{R1R2}\cos\delta \ . \tag{31}$$

We now need to determine the angle of the normal to the tangent plane with respect to the axis of rotation of the ellipsoid. Consideration of the geometry shows

$$\tan\phi 1 = \frac{\sin(2\delta)}{\left[\frac{R1}{R2} - \cos(2\delta)\right]} \tag{32}$$

and also $\phi = \pi - \phi 1 - \delta$ and $\theta = \pi - \phi 1$. The vertex of the mirror is at

$$X_o = R1\sin\theta \quad \text{and} \quad Z_o = R1\cos\theta + ae \ , \tag{33}$$

where e is the eccentricity. By shifting and rotating the (X, Z) coordinate frame through ϕ, it is straightforward to show that the thickness of the mirror can be found by solving a quadratic equation; more specifically,

$$\Delta z' = \frac{-B - \sqrt{B^2 - 4AC}}{2A} \ , \tag{34}$$

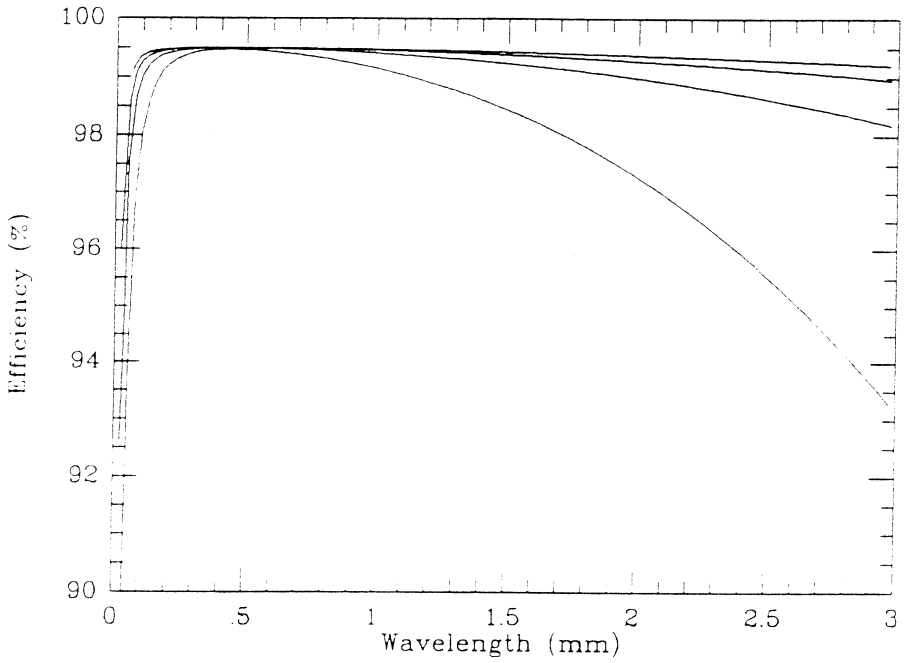

Figure 4: The fundamental-mode coupling efficiencies, as a function of wavelength, of ellipsoidal mirrors having focal lengths of 50mm, 100mm, 150mm, and 200mm. The focal ratio of the illuminating beam is 5, the design wavelength is 0.63mm, the angle of incidence is 45°, and the system is confocal.

where

$$\begin{aligned} A &= \frac{\sin^2\phi}{b^2} + \frac{\cos^2\phi}{a^2} \\ B &= \frac{2x_o\cos\phi\sin\phi}{\cos\delta}\left(\frac{1}{b^2} - \frac{1}{a^2}\right) + \frac{2X_o\sin\phi}{b^2} + \frac{2Z_o\cos\phi}{a^2} \\ C &= \frac{y_o^2}{b^2} + \left(\frac{x_o}{\cos\delta}\right)^2\left(\frac{\cos^2\phi}{b^2} + \frac{\sin^2\phi}{a^2}\right) + 2\left(\frac{x_o}{\cos\delta}\right)\left(\frac{\cos\phi X_o}{b^2} - \frac{\sin\phi Z_o}{a^2}\right) \end{aligned} \quad (35)$$

Again, this equation is easy to evaluate numerically for any design of mirror. For the purposes of finding the position of the output waist, we define the focal length of the mirror to be $f = R1R2/(R1 + R2)$.

4 Results

We have used the above technique to calculate the bandwidths of a number of ellipsoidal, off-axis mirrors. In Fig. 4 we show the fundamental-mode coupling efficiencies, as a function of wavelength, of ellipsoidal mirrors having focal lengths of 50mm, 100mm,

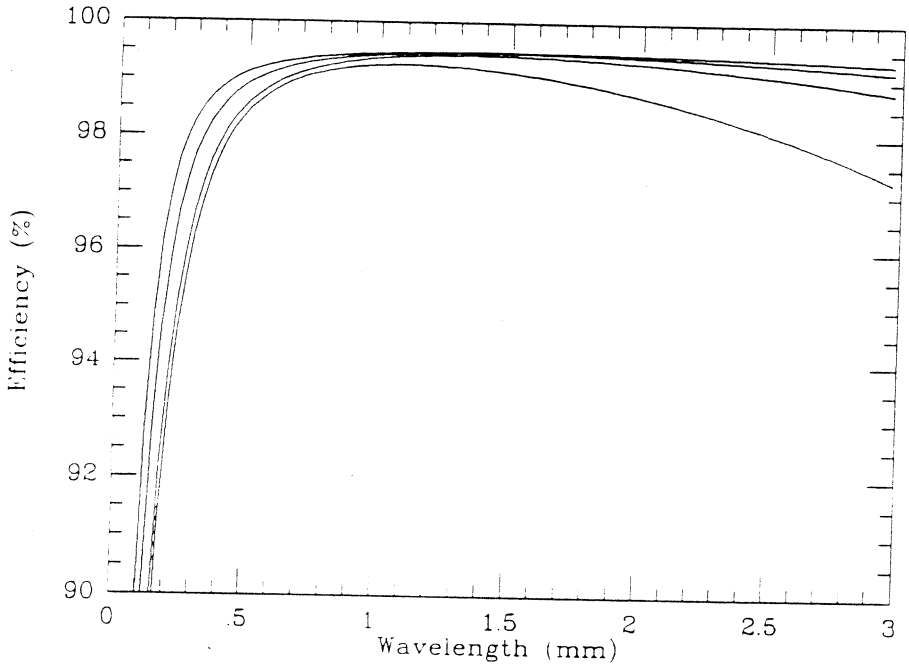

Figure 5: The fundamental-mode coupling efficiencies, as a function of wavelength, of ellipsoidal mirrors having focal lengths of 50mm, 100mm, 150mm, and 200mm. The focal ratio of the illuminating beam is 5, the design wavelength is 2.0mm, the angle of incidence is 45°, and the system is confocal.

150mm, and 200mm. At every wavelength the mirror is illuminated with a Gaussian beam having a waist focal ratio of 5. That is to say, we scale the waist with frequency so that the opening angle of the incoming beam is constant. This is the situation, for example, when a horn illuminates a reflecting antenna, in a frequency independent way, through a Gaussian-beam telescope. In each case, we have designed the mirror to match the input and output radii of curvature at a frequency of 475GHz. It can be seen that in each case the efficiency peaks at the design frequency and falls to the short and long wavelength sides due to the radii of of curvature of the incoming and outgoing beams not being matched. It is clear that high efficiencies can be achieved over a wide range of parameters as expected.

In Fig. 5 we show a similar set of plots, but in this case the mirrors are designed for a centre frequency of 150GHz. As expected, the high-frequency fall-off occurs at a lower frequency than in the previous case. Also, it can be seen that the efficiency only peaks at the design wavelength when the focal length of the mirror is reasonably large. This effect occurs because the efficiency contains two terms: one describes the degree to which the phase fronts are matched across the surface of the mirror, and the other describes the way in which the amplitudes match across the inclined plane. The amplitude projection effect is reasonably independent of wavelength, but it does depend to some extent on

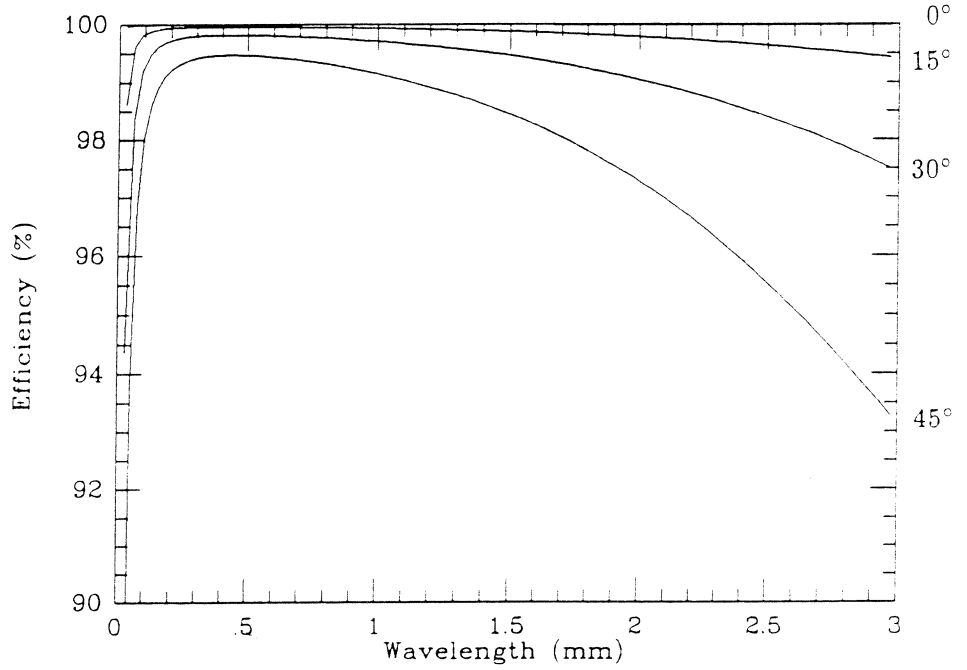

Figure 6: The fundamental-mode coupling efficiencies, as a function of wavelength, of an ellipsoidal mirror having a focal length of 50mm at various angles of incidence. The focal ratio of the illuminating beam is 5, the design wavelength is 0.63mm, and the system is confocal.

the beams involved, and in the present case peaks at the short wavelength end. The net effect is to move the maximum coupling beyond the wavelength at which the phase error is essentially zero.

Clearly, a broadband system can be made by designing the mirrors for the shortest wavelength of operation and keeping the focal lengths of the mirrors greater than about 200mm. This is essentially equivalent to designing the mirrors for far-field operation. This explains the reason for using mirrors having focal lengths of greater than 250mm in the broadband receiver we are currently building [2]. It should be noted that when a mirror is designed for a short-wavelength confocal system, the mirror becomes parabolic, and the formulation for the ellipsoidal surface given in this paper may suffer from round-off errors. There is a formulation that describes an ellipsoidal mirror in the parabolic limit in a more careful manner, but for certain designs of mirror this can introduce problems with the signs of angles, and so we have kept to the formulation described here. We have found this formulation to be perfectly adequate for most purposes.

Finally, in Fig. 6 we show the performance of a mirror, having a focal length of 50mm, which is designed to operate with a beam having a focal ratio of 5 at a wavelength of 0.63mm. The plots show how the coupling efficiency changes as the mirror is tilted. It is clear that there is a maximum efficiency for any mirror which is solely determined by the

beam and the angle of incidence. This efficiency tends to unity as the mirror is turned upright.

5 Conclusions

We have developed a technique for calculating the Gaussian beam-mode scattering matrices of shaped off-axis mirrors. The technique can be applied to any shaped mirror and can therefore be used for a variety of applications. We have demonstrated the technique by investigating the bandwidths of off-axis ellipsoidal mirrors. It is clear that very broad band submillimetre-wave optical systems can be manufactured by keeping the focal lengths of the mirrors greater than about 200mm.

Although we have not shown all of the elements of the scattering matrices, it is clear that good-quality mirrors can be used for phase-retrieval experiments. This is possible because long-focal-length mirrors do not scatter power between modes at any significant level. It may be possible to use the proposed technique, together with phase-retrieval methods, for synthesizing systems of shaped mirrors.

References

[1] P.F. Goldsmith, "Quasioptical techniques at millimeter and submillimeter wavelengths," in Infrared and Millimeter Waves, vol. 6, New York Academic, pp. 277-343, 1982.

[2] S. Withington, J.A. Murphy, A. Egan, and R.E. Hills,"On the design of broadband quasioptical systems for submillimetre-wave radio-astronomy receivers,"Int. Journal of Infrared and Millimeter Waves, vol. 3, pp.1515-1537, 1992.

FABRICATION AND CHARACTERIZATION OF MICROSHIELD CIRCUITS

T. M. Weller, L. P. Katehi, and G. M. Rebeiz
U of M NASA Center for Space Terahertz Technology

H. J. Cheng and J. F. Whitaker
Center for Ultrafast Optical Science

Abstract

Microshield is a partially shielded, planar transmission line in which the center conductor and upper ground planes are surrounded by air and supported by a 1.5 μm thick dielectric membrane. This configuration allows single-mode, TEM wave propagation over a broad bandwidth with very low dispersion and zero dielectric loss. A lower shielding cavity is used to minimize radiation loss, vary the characteristic impedance, and prevent power loss into substrate modes. These properties highlight the potential of microshield as a high performance medium for submillimeter wave transmission. Here we present an overview of the fabrication of microshield lines, and report on the recent progress in the characterization of various circuit structures. Theoretical and experimental results are shown for lowpass filters, transitions to grounded coplanar waveguide, and different resonant stub designs. A description of an ultrafast electro-optic sampling experiment using membrane-based coplanar strip transmission lines is also included, and preliminary data is presented for line losses up to 500 GHz.

I Introduction

In 1988 a submillimeter wave integrated-horn antenna was developed which contained a dipole suspended on a 1.5 μm thick dielectric membrane inside a silicon cavity [1]. The success of this technique has led to the application of the membrane technology to a variety of antenna geometries, including wideband millimeter wave power meters and corner cube arrays at 1.2 THz [2, 3]. The potential for low-loss, non-dispersive electromagnetic wave transmission eventually led to the introduction of the microshield transmission line in 1991 [4].

Microshield is a partially shielded, planar transmission line in which the center conductor and upper ground planes are surrounded by air and supported by the dielectric membrane. This configuration, which is shown in Figure 1, allows single-mode, TEM wave propagation over a broad

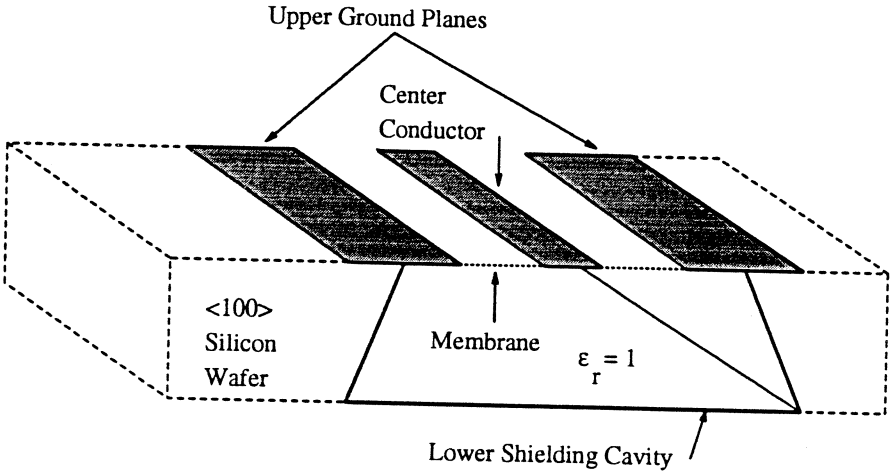

Figure 1: Illustration of the microshield transmission line geometry.

bandwidth with very low dispersion and zero dielectric loss. The lower shielding cavity is used to minimize radiation loss, vary the characteristic impedance, and prevent power loss into substrate modes. It also serves to equalize the upper ground planes, thereby eliminating the need for air-bridges or via-holes. Based on the potential high-performance from this geometry, the microshield line is currently being investigated as an alternative for submillimeter wave-guiding applications.

The characteristics of the microshield geometry were first examined in the theoretical study by Dib, et al [4, 5]. It was shown, for example, that discontinuities in microshield radiate less than comparable coplanar waveguide circuits, primarily due to the field confinement provided by the lower shielding cavity. Even on uniform transmission lines, frequency-dependent radiation into the substrate, which increases with the relative permittivity, can be significant at submillimeter wave frequencies. This loss mechanism is clearly minimized with microshield, since the conductors are completely surrounded by air. Finally, characteristic impedances ranging from around 30 Ω to over 280 Ω can easily be obtained by varying the center conductor width, upper ground plane spacing, and the height and width of the shielding cavity. Accurate, closed-form expressions for the characteristic impedance have been derived using a conformal mapping approach [5].

Here we present an overview of the fabrication of microshield lines and report on the recent progress in the characterization of various circuit structures. Theoretical and experimental results

from 20-40 GHz are shown for lowpass filters, transitions to grounded coplanar waveguide (gcpw), and two resonant stub designs. The insertion loss of a 5-section filter was measured at < .3 dB at 25 GHz, and the response compared nearly identically with ideal transmission line theory predictions. A low-loss transition to gcpw was also fabricated which had an S_{11} below -15 dB across the frequency range. The last section describes an ultra-fast optoelectronic sampling experiment using coplanar strip transmission lines printed on the dielectric membranes. Preliminary data on the loss characteristics up to 500 GHz demonstrates a definite advantage of membrane lines versus lines printed on high dielectric constant materials such as silicon or GaAs.

II Microshield Fabrication

The fabrication of microshield begins with a silicon wafer which has membrane layers on both sides. The membrane is a composite $SiO_2/Si_3N_4/SiO_2$ material which is grown using a combination thermal oxidation/chemical vapor deposition process. The wafers used here are 340 μm thick, high-resistivity silicon wafers with a $< 100 >$ orientation. The microshield structure is formed by first removing photolithographically defined regions from the membrane layer on the back side of the wafer. This pattern serves as an etch mask, allowing pyramidal [1] cavities to be opened in the wafer using anisotropic Si etchants, such as ethylene diamine pyrocatechol (EDP) or potassium hydroxide (KOH). When the wafer has been etched through to the front side, the upper membrane layer will behave as an etch stop, thereby forming the exposed membrane surface with surrounding silicon walls below.

The final step in the fabrication process is the metallization of the circuit pattern and the lower cavity sidewalls. A tri-layer photoresist/aluminum/photoresist technique with metal evaporation is used to deposit the circuit pattern on the top side of the membrane layer. Evaporation is also used for metal deposition from the backside onto the cavity sidewalls, but here some shadowing is required to protect selected areas of the membrane from metallization. A diced or micro-machined silicon mask is used to shield the region between the inner-edges of the upper ground planes and

[1]The pyramidal shape of the cavity is due to the varying rate at which the etchant attacks different surface orientations inside the silicon.

the center conductor, thus preventing metallization of the membrane below the slots. The finished circuits are then mounted on a ground plane to fully enclose the lower shielding cavity.

III Theoretical Characterization

A rigorous full-wave analysis is being developed for use in the theoretical characterization of microshield circuits. The formulation involves a space-domain integral equation (SDIE) that is generated through the application of equivalent currents. This approach has previously been applied in a variety of electromagnetic problems, such as the characterization of coplanar waveguide [6], rectangular waveguide junctions [7], and scattering from microstrip patches [8]. This method is also well-suited to the study of microshield transmission lines, as it provides a relatively simple means of studying the different types circuit geometries which are possible. These geometries include step changes in the height and width of the shielding cavity and abrupt changes in the dielectric material, in addition to discontinuities in the metallization patterns of the signal line and upper ground planes.

The first step in the analysis is to simplify the circuit geometry by applying the equivalence principle. Here fictitious metal surfaces are introduced in the slots of the metallization which transform each region of a circuit into either a closed metallic cavity (inside) or a ground plane in free space (outside). Upon each side of these surfaces magnetic currents are imposed which act as equivalent sources. To determine the strength of these unknown currents the condition of continuous tangential electric and magnetic fields is enforced over each of the fictitious planes. Since $\vec{M} = \vec{E} \times \hat{n}$, where $\hat{n}$ is the outward unit normal in each region, continuity of $\vec{E}_{tan}$ is strictly satisfied by setting $\vec{M}_{lower} = -\vec{M}_{upper} = \vec{M}$. The continuity of $\vec{H}_{tan}$ is expressed in terms of the following integral equation:

$$\hat{n} \times \int_{S'} [\bar{\bar{G}}_{ext}(\vec{r}, \vec{r'}) + \bar{\bar{G}}_{int}(\vec{r}, \vec{r'})] \cdot \vec{M}_s(\vec{r'}) ds' = \vec{J}_s \tag{1}$$

where $\bar{\bar{G}}_{ext,int}$ are the magnetic field dyadic Green's functions external and internal to the metallic cavities, respectively, and $\vec{J}_s$ is the current assumed with the ideal current source model, which

is used as the excitation. The solution to (1) is obtained by first dividing each surface into subsections, and then expanding the unknown magnetic currents using localized piecewise-sinusoidal basis functions. Equation (1) is then enforced in an average sense over each of the subsections, and is solved by using the method of moments (Galerkin's method) to generate a system of linear equations based on the mutual coupling, or admittance, between each of the currents. The solution of this system yields the complex coefficients of these basis functions, which is equivalent to finding the tangential electric field. This field is in the form of pure standing waves, such that standard transmission line theory may be then used to extract the scattering parameters of the circuit under analysis [6].

The formulation summarized above is used for the characterization of circuits which have discontinuities in just the upper metal layers. By extending this approach, it will be possible to analyze circuits such as T-junctions, shunt stubs with conformal cavities, and transitions between microshield and other planar lines such as coplanar waveguide. This extension primarily involves the use of equivalent current sheets in multiple planes, which serves to separate cavity discontinuities into homogeneous regions. The work in this area is currently in progress.

IV Theoretical and Experimental Results

In this section we present results on the performance of grounded coplanar waveguide (gcpw) to microshield transitions, stepped-impedance lowpass filters and different resonant stub designs. All measurements were made from 20-40 GHz, using an Alessi microwave probe station connected to an HP 8510B network analyzer. The system was calibrated using the TRL (thru-reflect-line) technique. For the theoretical data, ideal transmission line theory was used to characterize the lowpass filters and proved to be very accurate. The resonant stub designs were characterized using the full-wave analysis, and this section includes a study of the effect of shield-geometry variation on the stub performance. The formulation for characterization of the gcpw-microshield transitions is currently being developed, and thus only experimental data is presented.

IV.1 (Grounded) CPW to Microshield Transitions

The primary motivation for investigating the gcpw-to-microshield transition lies in optimizing the design for circuit measurements. As mentioned, these measurements are made using a microwave probe station. Since the membranes cannot reliably withstand the force of repeated probe contact, the contact pads for must be formed in gcpw, which necessitates the use of transitions from the gcpw to the microshield line under test. In order to calibrate the system, these transitions need to be designed for low reflection.

There were four microshield-gcpw-microshield transitions which were measured. The structures consist of a section of grounded cpw of length $\frac{\lambda_{g,cpw}}{2}$ at 40 GHz, which is positioned in the center of a microshield line. The design is illustrated in Figure 2. In all cases the microshield geometry has a center conductor width, s, of 350 μm and a slot width, w, of 35 μm. The characteristic impedance for this line is 75 Ω. For the four different designs, $s + 2w$ in the gcpw was also held constant at 420 μm, and center conductor widths of 35, 70, 140, and 280 μm were tested. These geometries result in characteristic impedances of 88, 71, 54, and 36 Ω, respectively.

The measured S_{11} for the transitions is given in Figure 3. The best performance, less than -15 dB from 20 to 40 GHz, is obtained with the 70 μm transition, which is the design with the closest impedance match. This transition also had a measured loss, $(1 - |S_{11}|^2 - |S_{21}|^2)$, below -15 dB across the entire band.

IV.2 Stepped-Impedance Lowpass Filters

Stepped-impedance lowpass filters were investigated since they are relatively easy to design and could demonstrate the low loss, TEM characteristics of microshield. In order to obtain the impedance ratios required to implement the chosen designs, a center conductor width ratio of 33 : 1 was necessary. The conductor widths and the impedances are shown in the schematic diagram of the 5-section filter given in Figure 4.

The measured performance for 5- and 7-section 0.5 dB ripple Chebyshev designs is shown in Figure 5. Also shown is the theoretical response obtained using ideal transmission line theory,

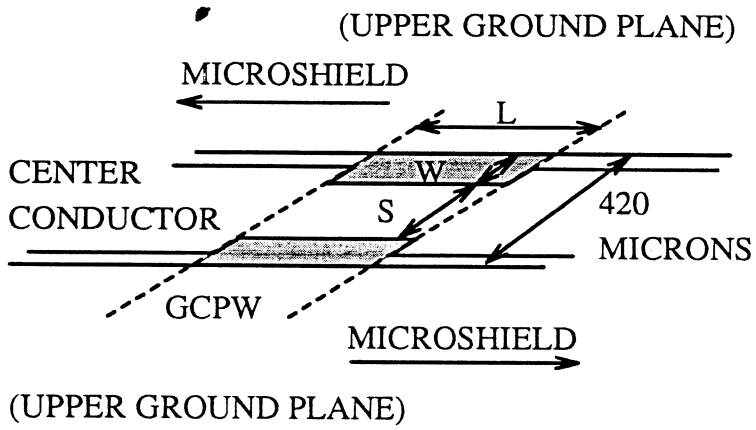

Figure 2: Illustration of the microshield to grounded cpw (coplanar waveguide) transition. The center conductor width, S, the slot width, W, and the length of the gcpw, L, are all indicated. L is $\frac{\lambda_g}{2}$ at 40 GHz. The slots in the gcpw are shaded to indicate that the substrate dielectric changes from air in the microshield to silicon in the gcpw section.

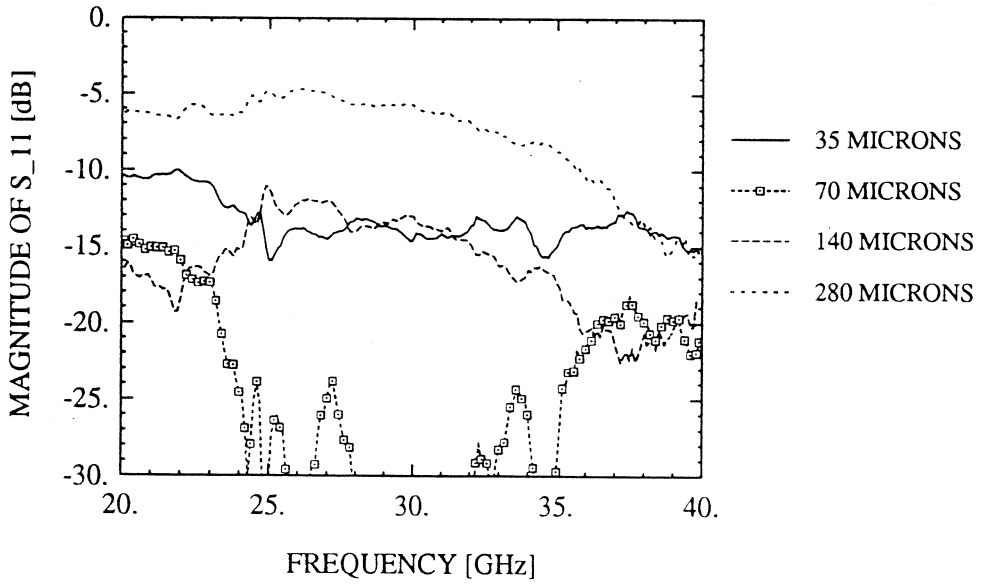

Figure 3: Measured S_{11} response of four different microshield to grounded cpw transitions. The microshield center conductor width is 350 microns. Each plot corresponds to a different center conductor width for the gcpw. In all cases, 2s+w is 420 microns for both microshield and gcpw lines.

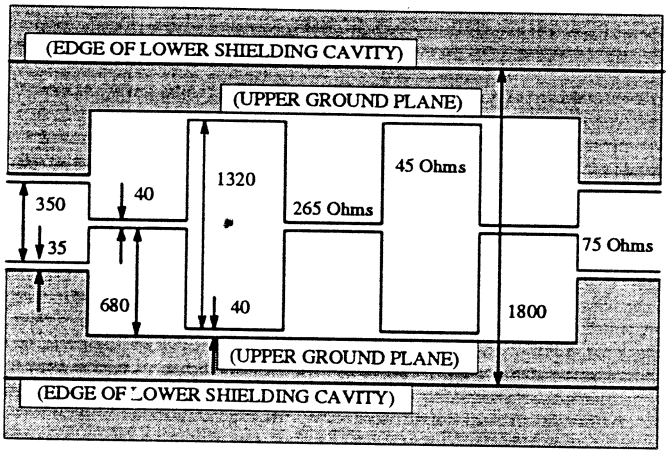

Figure 4: Diagram of the 5-section stepped-impedance lowpass filter (not to scale). Dimensions are given in μm and the different impedance sections are indicated. The shaded regions are the upper ground planes, which have been marked to indicate the positions of the lower shielding cavity sidewalls. The distance between the cavity sidewalls is 1800 μm.

with empirically-derived corrections for the effective line extension at impedance steps [9]. The agreement is quite good, and the differences near cutoff (shown in the insets) result from a peak in the measured loss which is not accounted for by the theory.

IV.3 Resonant Stubs

In this section the performance of a microshield shorted resonant stub is presented. The design which was implemented consists of a stub which is formed in the center conductor, and is of length $\frac{\lambda_g}{4}$ at the resonant frequency. This will be referred to as the in-line series shorted stub (ILS). A comparison of the measured and calculated results is first shown, followed by an illustration of the effects of varying the shielding cavity dimensions. In addition, the characteristics of the ILS stub are compared to those of a stub which is formed in the upper ground planes, which is referred to as the ground plane series stub (GPS). It is noted here that the measured ILS circuit had cavity dimensions of height, $h_c = 340$ μm, and width, $w_c = 1800$ μm, as measured at the top of the cavity.

The measured and predicted performance of the ILS stub is shown in Figure 6, where Ckt. A refers to the theoretical data. A schematic of the upper metallization pattern is also shown in the figure. The deep resonance at 28 GHz is shifted down in frequency relative to the ideal

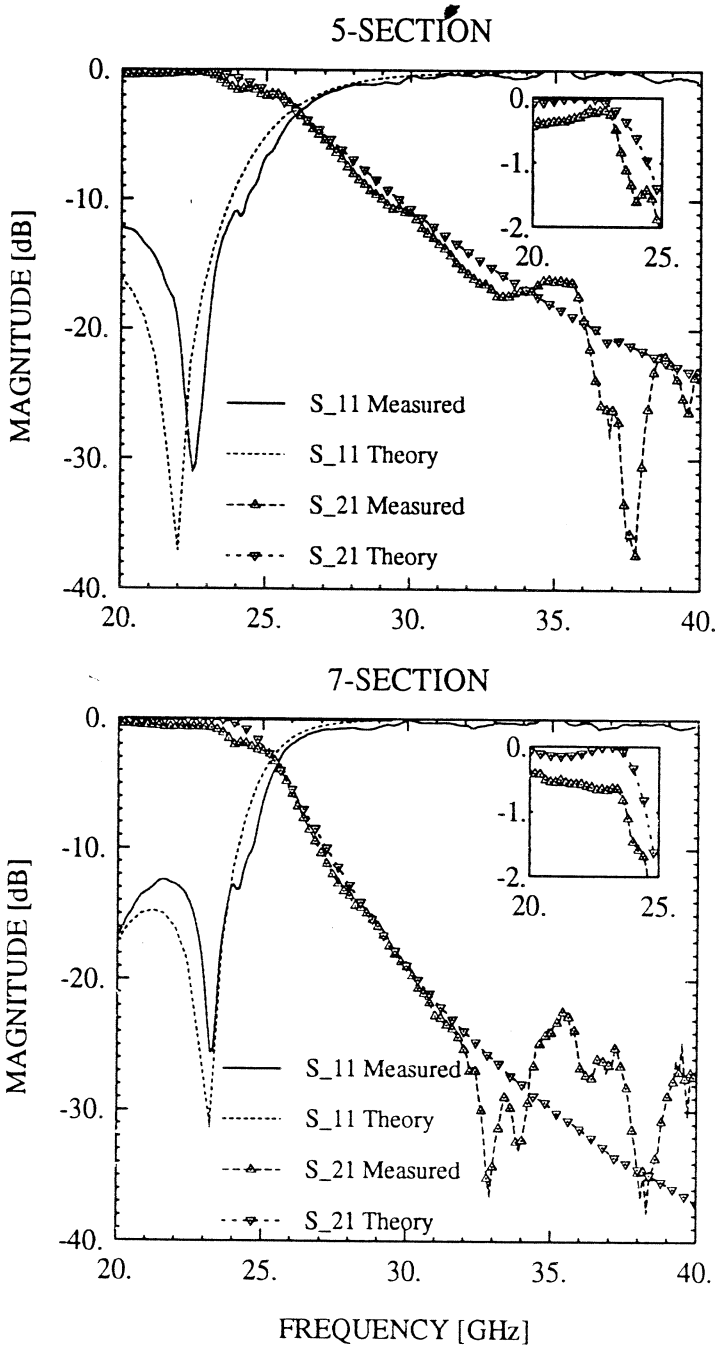

Figure 5: Measured and theoretical response of a 5- and a 7-section stepped-impedance microshield filter.

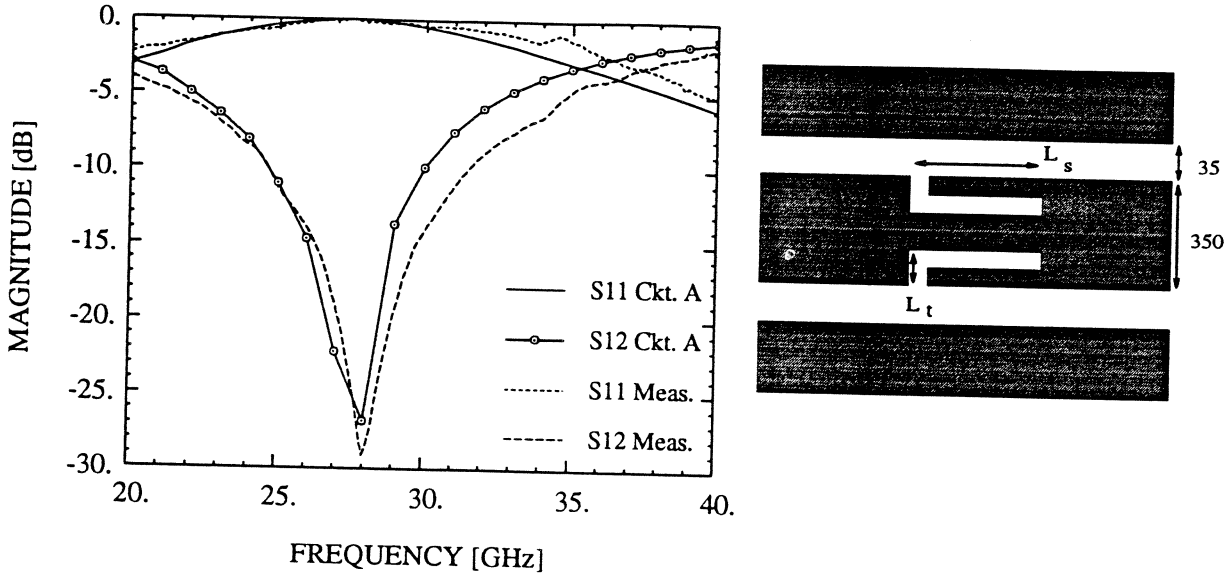

Figure 6: Measured and calculated response of the in-line series shorted stub, where Ckt. A refers to the calculated data. In the diagram on the right (not to scale), $L_s = 2500$ and $L_t = 120$. All dimensions are in μm.

response, since the physical stub length is $\frac{\lambda_g}{4}$ at $\approx$ 29.3 GHz, when account is taken of the short transverse slot lengths, L_t. In Figure 7, the effects of a reduced cavity size and upper shielding are demonstrated. The Ckt. B results represent the predicted performance with a lower cavity of dimensions $h_c = 100$ μm and $w_c = 420$ μm, which is the practical minimum cavity size for this circuit. Clearly, the cavity has only second order effects, which can be explained by the small slot width of only 35 μm. The Ckt. C results represent the predicted performance for the geometry of Ckt. A when shielded symmetrically above and below. In this case near-ideal stub performance is obtained, as the resonance has shifted to $\approx$ 29.5 GHz.

As mentioned, a comparison has been made between the in-line series shorted stub and an alternative design called the ground plane series stub. The theoretical performance of each stub, using the symmetric shielding configuration, is shown in Figure 8. The upper metallization pattern for the GPS is also given in this figure, where the total stub length is 2370 μm, corresponding to a resonant frequency of around 32 GHz. The GPS has a much narrower 3-dB bandwidth, roughly 14% versus 52% for the ILS, but will radiate much more strongly in an open environment.

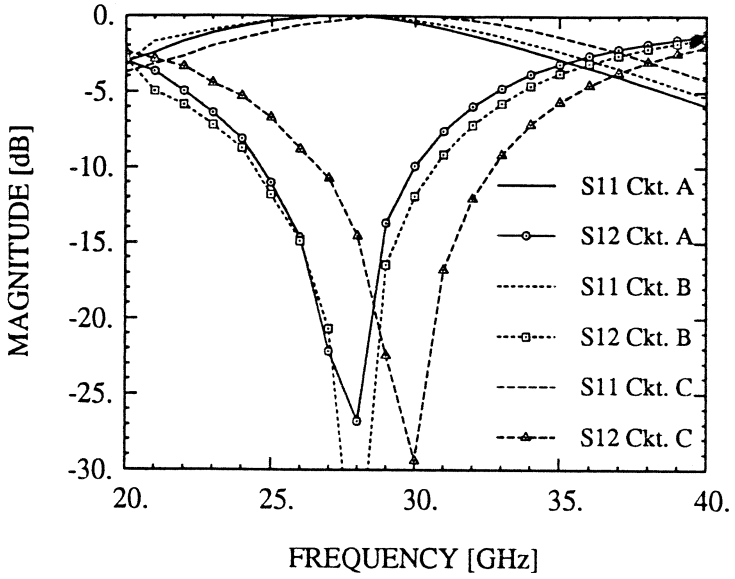

Figure 7: Theoretical response of different in-line series shorted stub geometries. Ckt. A has lower shielding cavity dimensions of 1800 × 340 μm (width by height), the Ckt. B cavity is 420 × 100 μm, and Ckt. C has the same cavity dimensions as A but is symmetrically shielded on the top and bottom.

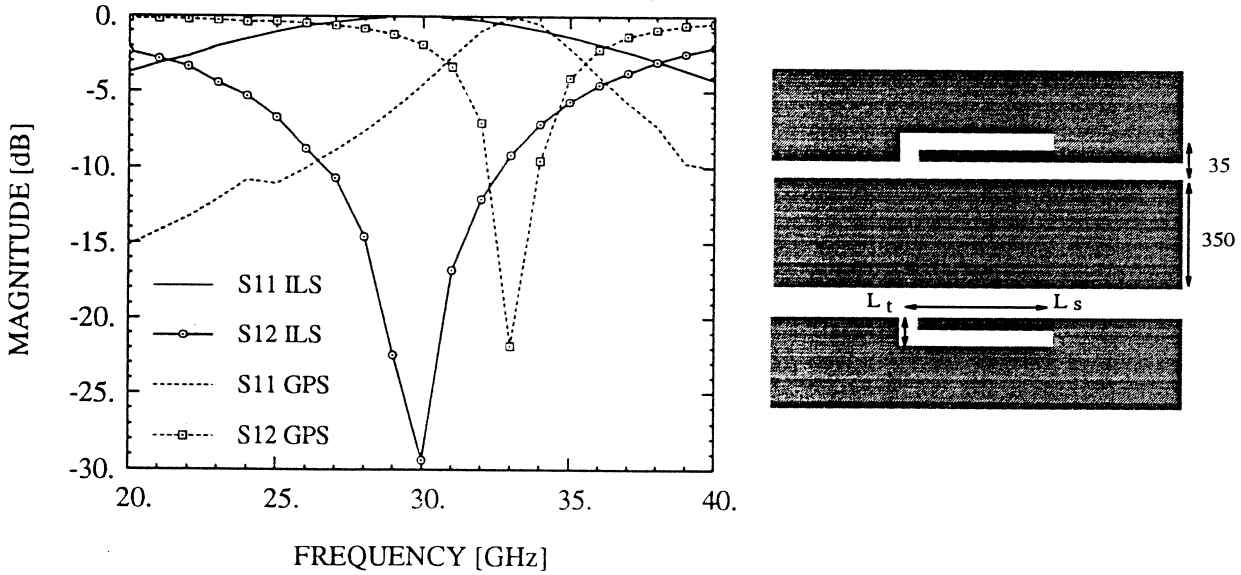

Figure 8: Theoretical response of the in-line series stub (ILS) versus the ground plane series stub configuration (GPS). The circuits are symmetrically shielded and have the same cavity dimensions as Ckt. A in Figure 7. In the diagram on the right (not to scale), L_t = 420 μm and L_s = 1950 μm.

V Electro-optic Sampling Experiment

Another interesting structure that has been fabricated on the micron-thick membranes is a simple coplanar strip transmission line (CPS). This structure, devised in order to push the limits of high-frequency, guided-wave transmission, should be capable of supporting millimeter- and submillimeter-wave electronic signals with very little induced distortion. This is due to the fact that the degree of phase velocity dispersion experienced in hybrid-mode propagation on planar transmission lines, as well as the amount of frequency-dependent radiation of energy into the substrate of such structures, increases with the permittivity of the substrate. Therefore, the electric field of a signal travelling on a uniform CPS on a membrane substrate experiences essentially a homogeneous dielectric above and below the plane of the membrane, i.e. air. This leads to propagation that has no radiation loss, no substrate dielectric loss, and no dispersion due to a frequency-dependent effective permittivity. In this preliminary investigation, we have demonstrated that pulses having subpicosecond rise times and single-picosecond durations propagate for lengths as great as 5 mm without loss of fidelity. The usable frequency content of these pulses extends from dc to nearly 1 THz, and by taking Fourier transforms, we have computed the attenuation and phase velocity of the time-domain signals on the line. Between 50 and 500 GHz, it has been observed that dispersion is negligible and attenuation is very small, arising presumably only from ohmic losses in the metal conductors. In order to generate and measure electrical pulses of such short duration and high frequency content, the optoelectronic technique of photoconductive switching, along with an ultra-high-speed electro-optic sampling characterization system, have been employed. These techniques are both based on the use of laser pulses of extremely short duration ($\leq$ 100 fs). The photoconductive source requires the ultra-short laser pulse to convert a dc bias to a subpicosecond electrical transient, while electro-optic sampling uses the optical pulse with an electro-optic crystal to produce a sampling gate having a duration of only several tenths of a picosecond. A probe tip fashioned from the electro-optic crystal is dipped into the electric field above the transmission line under test, and without any electrical contact the propagating waveform is measured. For the measurement of transients in the time domain, reflections from any source near the probing

point cause a loss of accuracy in the acquisition of clean, easily analyzed signals. Therefore, it was necessary to integrate a 200-μm-wide photoconductive-generator patch with the CPS fabricated on the membrane. This was a convenient alternative compared with transporting a short electrical transient onto the CPS via inductive wirebonds or through the use of an unwieldy flip-chip geometry. The photoconductor of choice, having subpicosecond carrier lifetime, high dark resistivity, high responsivity, and high dielectric breakdown, was a 1-μm layer of GaAs grown by molecular beam epitaxy at the low substrate temperature of $\sim$ 200 deg C (LT-GaAs). This photoconductor was lifted off its substrate to form a free-standing film through etching techniques, and then grafted to the membrane substrate using a van der Waals bonding technique. The CPS was then defined on the LT-GaAs and the membrane using standard photolithographic techniques. The pulse output after optical excitation of the photoswitch was measured at distances of 1, 3, and 5 mm from the generator, with no discernable distortion except for a small decrease in peak amplitude at the 5 mm propagation distance. The measured pulse rise time was $\leq$ 0.75 ps, and the FWHM (full width at half maximum) was $\leq$ 1.2 ps. When the Fourier transforms of the time-domain signals were compared, the phase velocity between 50 and 500 GHz was found to be flat, indicating the absence of dispersion. The attenuation, shown in Figure 9, was found to increase only slightly, to about 0.8 dB/mm at 500 GHz. This result can be directly compared to the propagation of a subpicosecond pulse along a CPS of the same dimensions on a GaAs substrate. While the attenuation at 50 GHz is only about 0.7 dB/mm for this structure, at 500 GHz it is in excess of 9.5 dB/mm. This is mainly due to the extreme radiation loss present even in uniform lines that are fabricated on high-permittivity substrates. A much larger degree of phase-velocity dispersion also results from propagation on the GaAs-substrate line, leading to pulses with rise times and durations that rapidly expand with increasing propagation distance.

VI Conclusion

This paper has presented a review of the recent progress made in the experimental and theoretical characterization of microshield transmission line circuits. Low loss transitions from microshield to grounded coplanar waveguide have been successfully designed and measured, and

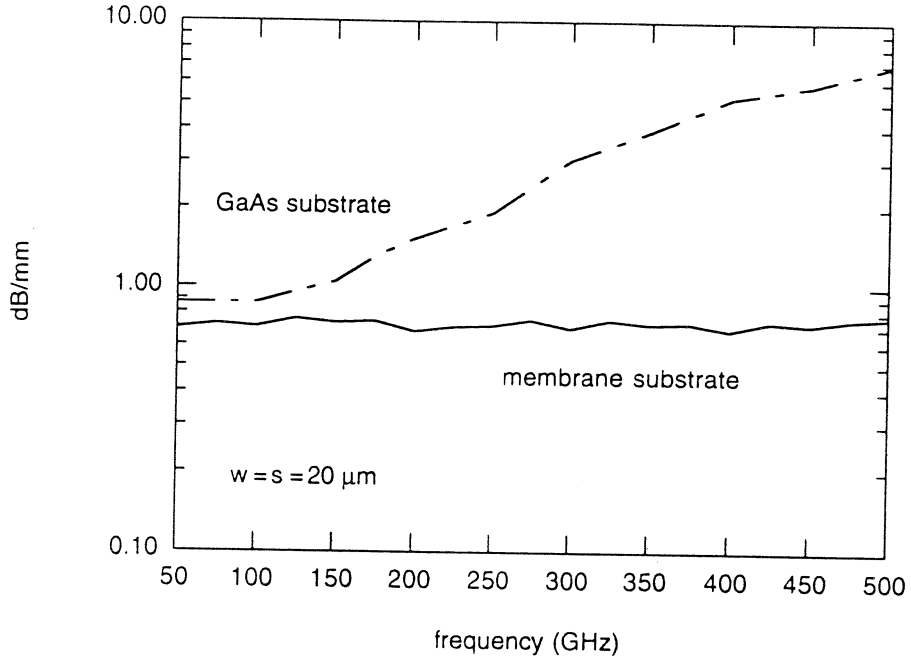

Figure 9: Measured attenuation of a coplanar stripline (CPS) printed on a GaAs substrate compared to a line printed on a dielectric membrane. The measurements were made using an electro-optic sampling technique. The conductor and slot widths of the CPS are both 20 μm.

stepped-impedance lowpass filters demonstrated very good performance and compared quite well to ideal transmission line theory. A brief study of different microshield resonant stub designs has also been presented. Finally, a preliminary study using an ultra-fast electro-optic sampling technique has shown that coplanar strip lines, printed on the dielectric membranes, show strong potential as a low loss transmission medium for THz-frequency applications.

VII Acknowledgements

This work has been supported by the Office of Naval Research under contract No. N00014-92-J-1070, the NASA Center for Space Terahertz Technology, and the NSF under the Center for Ultrafast Optical Science. The authors would like to thank Prof. G. Rebeiz's group for their assistance, and particularly Mr. Walid Ali-Ahmad.

References

[1] G. M. Rebeiz, D. P. Kasilingam, Y. Guo, P. A. Stimson and D. B. Rutledge, "Monolithic Millimeter-Wave Two-Dimensional Horn Imaging Arrays", *IEEE Trans. on Antennas and Propagation*, Vol. 38, pp. 1473-1482, Sept. 1990.

[2] Curtis C. Ling and Gabriel M. Rebeiz, "A Wide-Band Monolithic Quasi-Optical Power Meter for Millimeter- and Submillimeter-Wave Applications ", *IEEE Trans. on Antennas and Propagation*, Vol. 39, pp. 1257-1261, Aug. 1991.

[3] Steven S. Gearhart, Curtis C. Ling, Gabriel M. Rebeiz, Hemant Davee, and Gordon Chin, "Integrated 119-μm Linear Corner-Cube Array ", *IEEE Microwave and Guided Wave Letters*, Vol. 1, pp. 155-157, July 1991.

[4] N. Dib, W. Harokopus, P. Katehi, C. Ling, and G. Rebeiz, "Study of a Novel Planar Transmission Line," *1991 IEEE MTT-S International Microwave Symposium Digest*, Boston, pp. 623-626.

[5] N. I. Dib, P. B. Katehi, "Impedance Calculation for the Microshield Line," *Microwave and Guided Letters*, Vol. 2, No. 10, Oct. 1992, pp. 406-408.

[6] N. I. Dib and P. B. Katehi, "Modeling of Shielded CPW Discontinuities Using the Space Domain Integral Equation Method (SDIE)," *Journal of Electromagnetic Waves and Applications*,April 1991.

[7] Z. Shen and R. Hua, "Moment method analysis of rectangular waveguide T-junctions having arbitrary cross-sections", *Int. J. Electronics*, 1991, Vol. 71, No. 3, 463-469.

[8] K. Barkeshli and J. Volakis, "Electromagnetic Scattering from an Aperture Formed by a Rectangular Cavity Recessed in a Ground Plane," *Journal of Electromagnetic Waves and Applications*, Vol. 5, No. 7, pp. 715-734, 1991.

[9] E. O. Hammerstad and F. Bekkadal, *A Microstrip Handbook*, ELAB Report, STF 44 A74169, N7034, University of Trondheim, Norway, 1975.

EXPERIMENTAL STUDY OF MICROMACHINED CIRCUITS

Rhonda Franklin Drayton and Linda P.B. Katehi
NASA Center for Space Terahertz Technology
University of Michigan
Ann Arbor, MI 48109-2122

1.0 Abstract

Planarization of transmission lines such as microstrip, stripline, and coplanar provide enhanced flexibility in array design, compatibility to active devices and radiating elements, as well as reduced volume and weight. However, many unwanted frequency dependent mechanisms are introduced from these planar lines which cause degradation in the electrical performance of the circuit. As a result, the development of new geometries which reduce the effect of such mechanisms as ohmic loss and electromagnetic interference without affecting the monolithic character will result in extended operating frequencies and improved electrical performance of circuits and arrays. This paper presents the development of micromachined circuits which provide shielding of conventional lines using micromachining techniques. Presented is a description of the fabrication and characterization of these circuits. In addition, the study will show information about the propagation characteristics of the line and scattering parameters for a variety of micromachined circuits with comparison to theoretical and conventional circuit geometries.

2.0 Introduction

The thrust for the development of cost effective, lightweight electrical systems which exhibit improved electrical performance can be attributed to communications, commercial and military applications. One application in the area of communications is for the development of miniature satellites, microsats, which contribute to reduction in weight and improved fuel economy. Commercial applications will benefit from this development of high intelligence highway systems which require parallel processing of vast amounts of information transfer to maintain efficient operation of such systems. On the other hand, military applications will require development of PIN cards used for identifying military personel.Thus, the impetus for investigating micromachined circuits is due to the strong desire to develop inexpensive circuits that provide improved electrical performance with reduced volume and weight.

Currently, monolithic quasi-planar geometries which exhibit electrical and geometrical resemblance to waveguide shielded transmission lines and circuits are possible to implement due to recent advances in semiconductor processing techniques. Silicon based monolithic waveguides have been successfully developed for use in the sub-millimeter wave frequencies using silicon

micromachining techniques by JPL [1] and University of Michigan[2]. The waveguide is split along the broad wall and each half is formed by etching a channel through an appropriately oriented silicon wafer. Finally, a polyamide bonding technique is used to glue the etched channels to a smooth silicon wafer. In addition their performance has been measured and has been found very satisfactory[1].

Similarly, a shielded transmission line structure, Figure 1, can be developed by replacing the waveguide with a cavity which is etched into Si using KOH and then metallized using evaporation techniques. Then the planar transmission line is created by metal deposition on the Si semiconductor substrate and attached to the original wafer using electrobonding techniques. The results are lines and circuits which evolve from the conventional metallic waveguide and waveguide-shielded components with the advantages mentioned above.

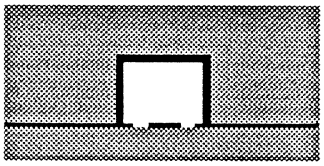

FIGURE 1. Micromachined CPW

As a result, this study will present the development of micromachined circuit, which use an etched cavity as a shield to planar geometries. After describing the fabrication and experimental procedures needed to characterize these novel circuits, scattering parameter measurements will be shown. Finally, results regarding the propagating characteristics of the line and a variety of circuit geometries will be presented and compared to theoretical models as well as conventional geometries.

3.0 Fabrication Procedure

In order to implement the development of a micromachined circuits, technology resulting from recent advances in semiconductor processes is used. These circuits are created by attaching the shielding structure to the planar line structure using electrobonding techniques. Although the shield and lines require the use of standard photolithography, the planar lines use a bilayer process technique for metal definition while the shield uses anisotropic wet etching methods for the development of the cavity structure.

Initially, a Si wafer having a membrane ($SiO_2/Si_3N_4/SiO_2$) dielectric surface is used to develop the cavity structure since depths of varying heights are required. Using photolithography to define the areas to be etched, the first oxide layer is etched using BHF while the nitride layer is etched using plasma etching. After repatterning the wafer to protect the areas to be etched later, the second oxide layer is removed while the remaining membrane layers serve as a mask for any unpatterened sections of wafer. Once the initial depth is obtained for the alignment marks, the remaining cavity areas are then exposed and etched to the required depth. The result is the development of a structure which has sections etched entirely through the wafer, the alignment marks,

and sections etched partially through, the cavities. Once the etch is complete, the shielding portion of the micromachined circuit is metallized using evaporation techniques.

Secondly, transmission lines are designed which consist of calibration standards and various circuit geometries necessary to characterize the electrical performance of the micromachined circuits. The lines, developed on a separate wafer, use photolithography to pattern circuit areas and the bilayer process to develop the appropriate line depth and width with the use of evaporation techniques.

Lastly, the micromachined circuits are developed by aligning the cavity structure to the transmission line structure. Once aligned, they are secured using electrobonding methods.

4.0 Measurement Procedure

Characterization of the circuits require the use of the following experimental arrangement: an HP 8510B Network Analyzer modified to operate up to 40 GHz, an Alessi Probe Station, and Cascade Probe Tips. To reduce the effects of possible substrate modes in the high resistivity silicon substrate, the circuits are isolated from the wafer chuck by 1/8" thick 5880 duroid, er=2.2.

To accurately measure the circuit performance of the micromachined circuits, the Thru-Reflect-Line (TRL) calibration technique is used. In order to perform this calibration, standards were fabricated using the above process. A one tier de-embedding technique was used for on-wafer calibration which calibrates the system reference plane along the transmission line. As a result, the calibration takes into account all transitions between the ANA and the reference plane.

The micromachined circuit, Figure 2, requires several transitions along the feed line to excite the micromachined circuit. The first transition is a taper between two 50 ohm sections of cpw-line. This transition is necessary to provide excitation to the desired line via the Cascade 150 μm pitch probes with minimal mismatch to the probes. The input port, having center conductor width of 100μm and slot width of 60 μm, is transitioned into a line with center conductor width of 180 μm and slot width of 130 μm. The second transition occurs between cpw and micromachined cpw circuit. The micromachined circuit is of coplanar type line which includes a micromachined shielding cavity having height of 200 μm and width of 800 μm. Subsequently, the required input line of all circuits measured will be of this type.

FIGURE 2. Micromachined circuit with various transitions

5.0 Measurements and Discussion

5.1 Philosopy of the Experimental Study

In order to facilitate a complete preliminary study of micromachined circuits, it is necessary to compare the measured results to both theoretical models as well as conventional geometries.

The *theoretical model* used for the micromachined circuits is based on the space domain integral equation (SDIE). With the appropriate Green's function for the lower half space and upper cavity region of the two dimensional circuit, unknown magnetic surface currents used to replace the slots, M_S, can be determined for a given electric source, J_S, using the method of moments. Once M_S is known, Galerkin's method is applied to reduce the above integral equation to a linear system of equations.For a given field distribution, the scattering parameters of the equivalent network is computed using standard techniques. [3,4]

The *coplanar waveguide* circuits, Figure 3b, are design to be identical in geometry to the micromachined planar circuits, Figure 3a. However, the design includes separate calibration standards for the cpw and micromachined circuits.

The resulting measurement will therefore show the response of micromachined circuits as compared to the theoretical model and conventional coplanar waveguide.

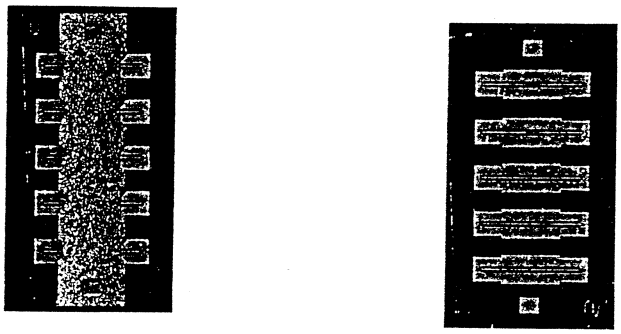

FIGURE 3. (a) Micromachined Circuits and (b) Open CPW Circuits

5.2 Measurements

A through line is used to provide information about the propagating characteristics of the micromachined transmission line. Figure 4 below shows the effective dielectric of a line having length of 2088μm and dimensions as stated above. The results show good agreement between the measured micromachined circuit and the theoretical model, which is based on Full Wave Analysis[3].

The two circuit designs presented are an open end series stub in Figure 5a, designed to have gap spacing of 30 μm, and open end gap in Figure 5b, designed to resonate at 30 GHz with resonate stub length of 1086μm

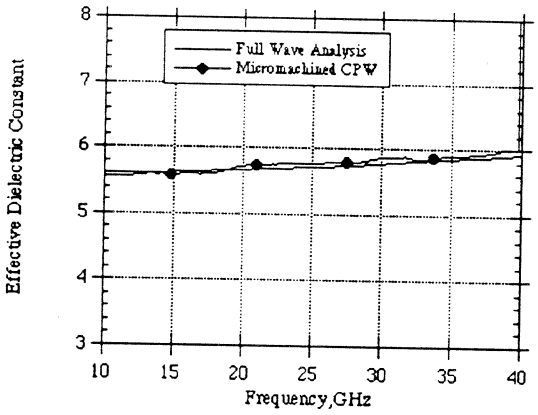

FIGURE 4. Effective Dielectric Constant

and slot width of 30 μm. The scattering parameters for the above circuits have been measured and are compared to the theoretical model for the micromachined cpw circuit. In addition they are compared to conventional cpw circuits of the same type.

(a) Open End Series Stub (b) Open End Gap

FIGURE 5. (a) Open End Series Stub and (b) Open End Gap

For the open end series stub in Figure A1.a, theory and experiment are in excellent agreement both in magnitude and phase as seen in Figures A1.b and A1.c. For the same circuit, comparison with the cpw line is shown in FiguresA2.a and A2.b. The line geometry is identical for both circuits, however, the micromachined circuit provides a shielding environment. In Figure A2.c, the total loss of this micromachined circuit varies between 6 dB and 2 dB at the high end below that of conventional cpw lines.

The open end gap in Figure B1.a, shows very close agreement in magnitude and phase with the theoretical results as seen in Figures B1.b and B1.c. As stated initially, it is very important to avoid distortion of the circuit performance when the shield is included. As a result of Figures B2.a and B2.b, comparison between the micromachined circuit and cpw show similarities in the overall circuit performance. The distinction between the lines occur when observing the total loss of the circuits. In Figure B2.c, the total loss, which is again reduced, indicates improvement in the overall performance of the circuit due to the micromachined cavity of the line.

To indicate the potential for this technology, Figure 6 shows a geometrical description of a -milled circuit as compared to the new micromachined circuits. The milled represents one circuit while the micromachined circuit represents 5 different circuits housed on the silicon wafer that is about 1/6 of a 3" wafer.

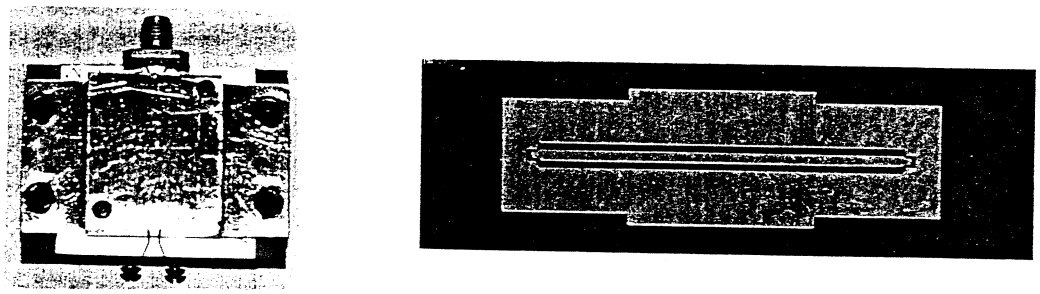

FIGURE 6. Milled Circuit and Micromachined Circuit

In addition to the physical reduction in the size and volume, circuit geometries of similar type indicate promise for applications at terahertz frequencies. However, of the two, the micromachined circuits offer the most flexibility in testing due to state of the art measurement systems available namely the probe station. These circuits and system offer more repeatable measurements along with ease in the fabrication methods used. Figure 7 shows the loss performance of similar geometries between the micromachined and milled circuit. Since the circuits are passive in nature, losses, except ohmic, can be scaled appropriately to the terahertz frequencies to give reasonable indicators of expected circuit performance.

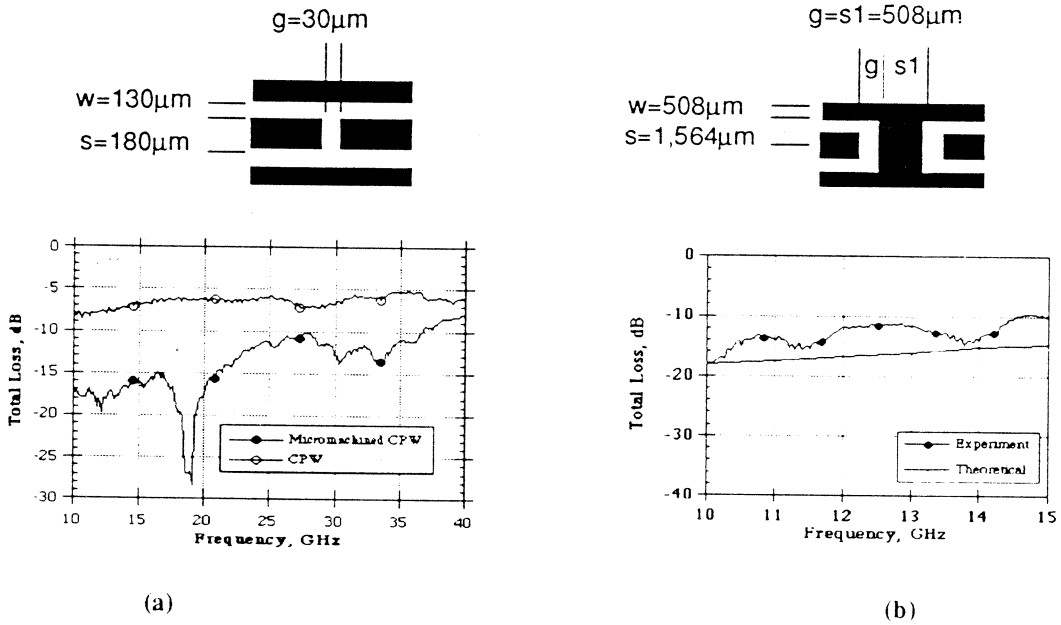

FIGURE 7. Losses of (a) Micromacnined circuit vs. (b) Milled circuit

6.0 Summary

Micromachined circuits have been built and tested. The results show that the scattering parameter measurements are in very good agreement with the theoretical model used. The study also shows comparison between the cpw and micromachined cpw. The results indicate consistently that the shielded geometry results in reduction in the total loss of the various circuits measured. When compared to machine milled circuits of similar geometry, the losses are comparable. As a result, micromachined circuits show encouraging preliminary results which warrant further development of these lines for more complicated geometries.

Acknowledgments

This work was partially supported by the Office of Naval Research and the NASA Center of Space Terahertz Technology. The authors would also like to thank Nihad Dib for theoretical model contributions.

References

1. M. Yap, Y-C Tai, W.R. McGrath and C. Walker, "Silicon Micromachined Waveguides for Millimeter and Submillimeter Wavelengths," presented in the 3rd International Symposium on Space Terahertz Technology, Ann Arbor, MI, March 1992.

2. Linda P.B. Katehi," Low-Loss Transmission Lines for Terahertz Frequency Applications," *IEEE Proceedings*, November 1992, pp.1771-1787.

3. N.I. Dib, P.B. Katehi, "Modeling of Shielded CPW Discontinuities Using the Space Domain Integral Equation Method (SDIE)," *Journal of Electromagnetic Waves and Applications (JEWA)*, Vol. 5, No 4 / 5, pp. 503-523.

4. N.I. Dib, L.P.B. Katehi, G.E. Ponchak and R.N. Simons, "Theoretical and Experimental Characterization of Coplanar Waveguide Discontinuities for Filter Applications, *IEEE Trans. on MTT*, Vol. 39, No. 5, May 1991.

Figures

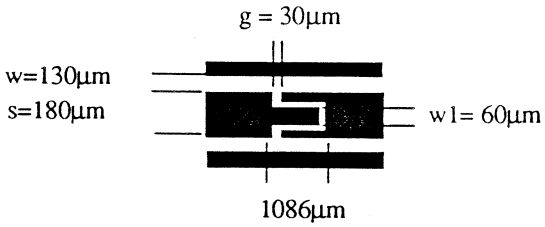

(a) Physical Geometry

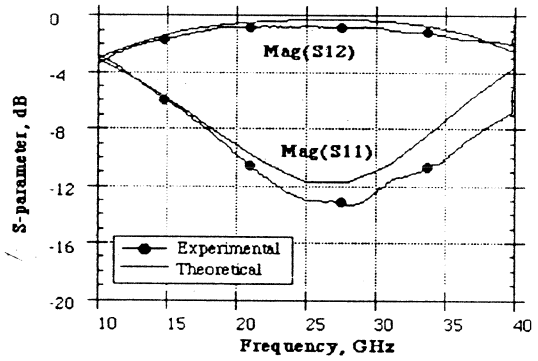

(a) Magnitude of Scattering Parameter

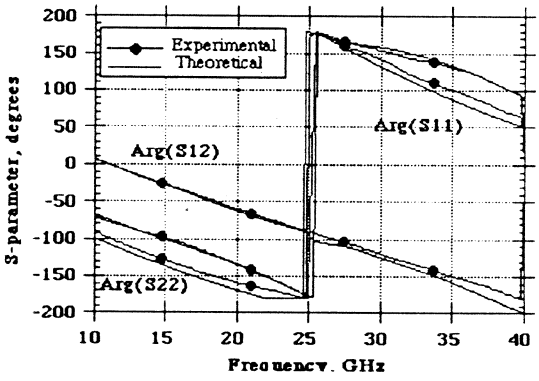

(b) Phase of Scattering Parameter

FIGURE A1. Micromachined CPW, Theoretical vs. Experimental: Open End Series Stub

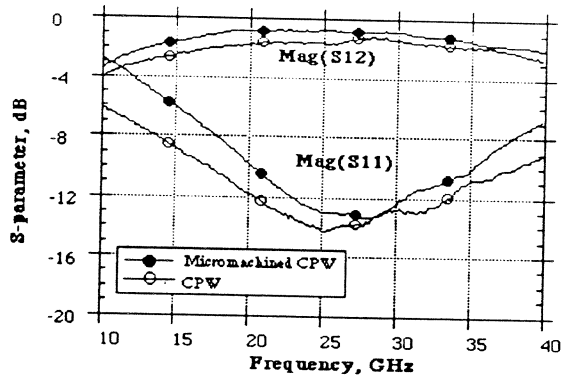

(a) Magnitude of Scattering Parameters

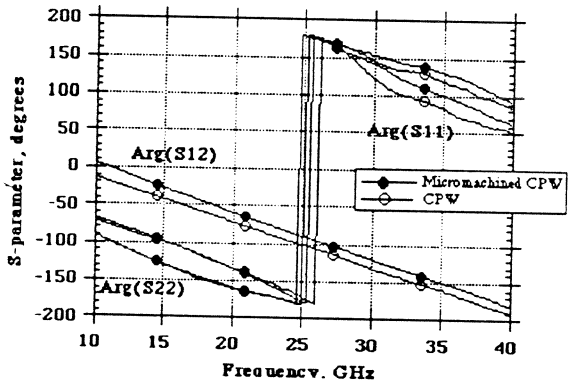

(b) Phase of Scattering Parameters

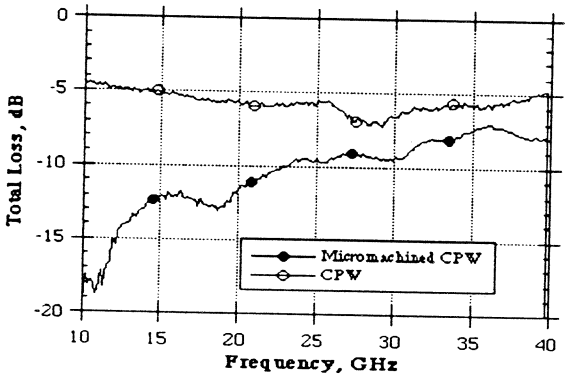

(c) Total loss

FIGURE A2. Micromachined CPW vs. CPW LIne: Open End Series Stub

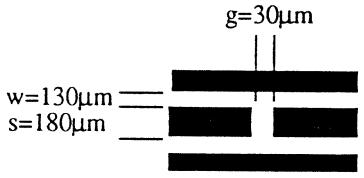

(a) Circuit geometry

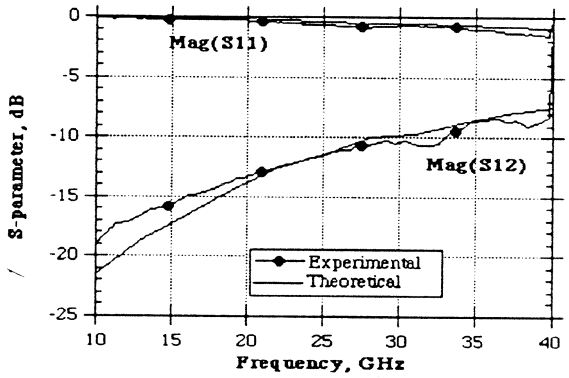

(b) Magnitude of scattering parameters

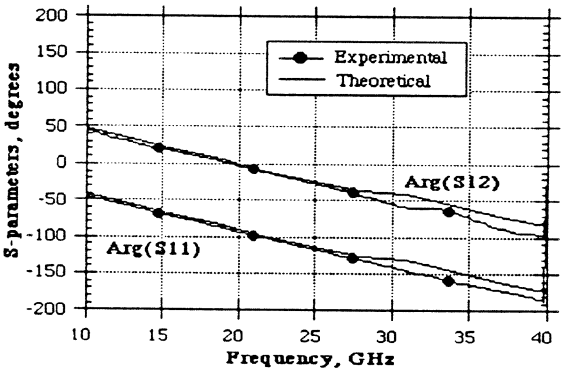

(c) Phase of scattering parameters

FIGURE B1. Micromachined CPW, Theoretical vs. Experimental: Open End Gap

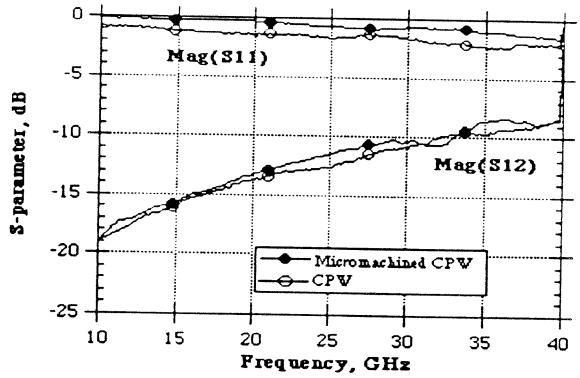

(a) Magnitude of Scattering Parameters

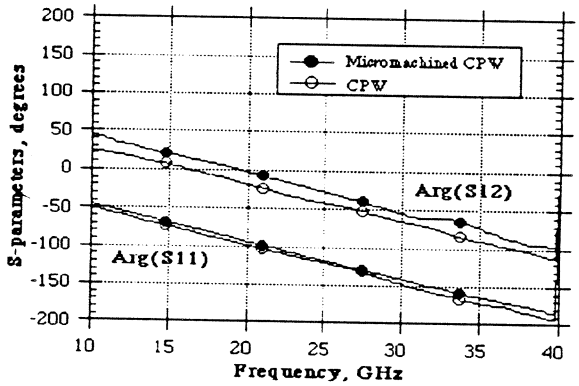

(b) Phase of Scattering Parameters

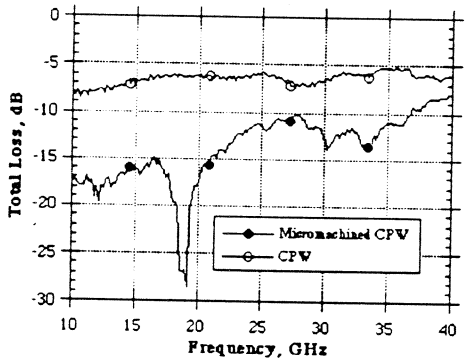

(c) Total Loss

FIGURE B2. Micromachined CPW vs. CPW Line: Open End Gap

TESTING REFLECTOR ANTENNAS IN THE THz FREQUENCY RANGE

Jussi Tuovinen

Five College Radio Astronomy Observatory
Department of Physics and Astronomy
University of Massachusetts
Amherst, MA 01003

Abstract

Possibilities of applying far-field, near-field, and compact range techniques on reflector antennas in the THz frequency range are critically discussed. In addition, other methods such as defocusing, and combining of the mechanical reflector surface measurements and the feed horn radiation patterns are discussed. The discussion of the compact range measurement method includes a description of a recently introduced hologram type of compact range. Antenna test methods in the THz range, are needed for several future scientific satellites. None of the current methods have, so far been validated for use in the THz range. One may conclude from the analysis of the different methods in this work, that the far-field method can be discarded for certain, due to the atmospheric effects. The near-field method remains a possibility, however, an expensive, high quality moving stage is needed, and phase errors caused by flexible cables have to be dealt with. In some cases, a defocusing method to bring the far-field closer may prove to be practical. Technically, the most feasible and least expensive method appears to be the hologram type of compact range. In this method, a planar amplitude hologram is used to form the required plane wave. The hologram is inexpensive to manufacture, and it is also less sensitive to surface accuracy errors than a reflector.

1 Introduction

Several scientific satellite missions with submillimeter wave radiometers operating at THz frequencies have been planned for the future. FIRST (Far Infrared and Submillimeter Space Telescope) of ESA for 500–2000 GHz and SMIM (Submillimeter Intermediate Mission) of NASA for 400–1200 GHz are two examples of this kind of mission. In both projects, the most important active elements of a radiometer, i.e., the mixers and local oscillator sources, have been selected as areas requiring significant development. Also required for a high performance radiometer, is some kind of a reflector antenna. Manufacturing a reflector antenna for space application at 1 THz is a challenging task. An additional challenging task is accurate testing of this antenna prior to launch. Presently, a convenient method for this kind of test is not readily available. In NASA's SWAS (Submillimeter Wave Astronomy Satellite) for 490–550

GHz, the antenna with an aperture size of 0.55×0.71 m, will be tested using a conventional near-field method utilizing a granite reference plate. Extending this approach for 1–2 THz testing of large antennas is difficult and promises to be extremely expensive.

One objective of this paper is to critically discuss the possibilities of applying far-field, near-field, and compact range techniques on THz antennas. In addition, other methods such as defocusing, and combining of the mechanical reflector surface measurements and the feed horn radiation patterns are discussed. The discussion of the compact range measurement method includes a description of a recently introduced hologram type of compact range. This method is considered a strong candidate for 1 THz antenna testing.

The other objective of this paper, is to stimulate discussion and raise awareness of the importance of THz antenna testing, which has often been disregarded and its difficulty underestimated in satellite technological development programs. This may lead to the situation where the mixers and solid-state sources will be ready for the satellite, but the mission will be delayed because there is not any way of adequately testing the antenna.

2 Far-field method

A natural starting point when considering an appropriate antenna test method for a particular case, is the far-field method. This method is the most direct and also, if applicable, the simplest. In the far-field method, the probe antenna is moved a distance d away from the antenna under test (AUT) so that the spherical wave from the probe antenna is virtually a plane wave in front of the AUT. The distance is usually required to be at least $d = 2D^2/\lambda$, where D is the diameter of the AUT and λ is the wavelength. This requirement for the minimum value of d, implies that a 22.5° phase change of the virtual plane wave is accepted over the aperture of the AUT. For example, for an antenna with $D = 1$ m, distance $d = 6.7$ km at 1 THz.

At microwave and low millimeter wave frequencies the large distance d is the main complication for an electrically large antenna. At higher frequencies, even though the large value of d remains a great problem, the atmospheric effects on the transmitted signal become the most significant limitation. Firstly, around 1 THz the attenuation is many tens to hundreds of dB/km [1]. Secondly, the temperature gradients and changes, and the humidity variations cause short term fluctuations in the signal path attenuation. Due to the above reasons, far-field measurements on a 1 THz reflector antenna with D > 0.2 m (d=270 m) are practically impossible.

3 Near-field method

In the near-field method, the amplitude and phase of a field over the antenna aperture is measured. The far-field is obtained then by taking a Fourier transform of the measured field. The near-field data acquisition can be carried out over a plane, a sphere or a cylinder. For a high gain antenna, like an electrically large reflector antenna, planar or cylindrical scanning are obvious choices. In planar scanning, the AUT is kept fixed and the field probe movement is realized with two linear stages. In the cylindrical case, usually the antenna is rotated and the probe is moved on a linear stage. In satellite payload antenna testing, rotating the antenna would obviously require the rotation of the whole satellite. Therefore,

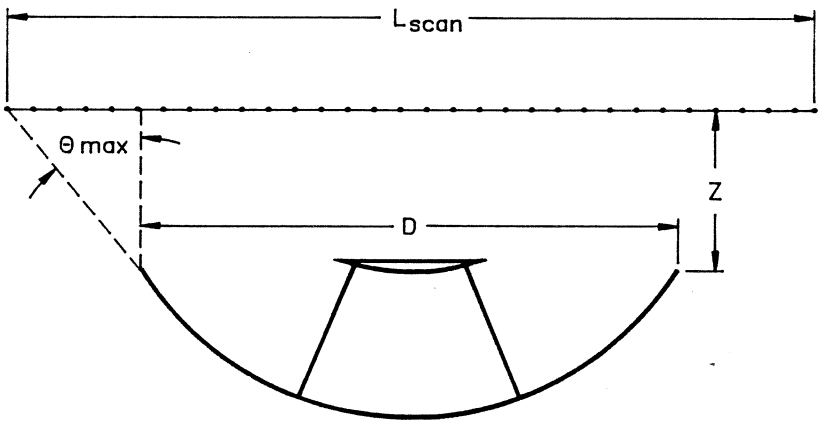

Figure 1: *Angular region of validity $\theta_{\max}$ defined by the scan length.*

for satellite antenna testing, planar scanning is the most preferable method. In this method only the probe antenna in front of the test antenna is moved. Comprehensive reviews and analysis of the near-field measurements can be found, e.g., in [2,3].

Planar near-field measurements are most frequently realized with an x-y-stage in a rectangular coordinate system. However, plane polar scanning can sometimes lead to a simpler mechanical moving stage [4,5].

Proper sampling of the near-field of an antenna requires first, to define the area required to adequately cover the aperture field and second, to choose a dense enough sampling interval. A too small sampling area and a too large sampling interval cause truncation and aliasing of the data, respectively. For a high gain reflector antenna, which even a small reflector antenna at the THz range is, truncation of the data due to a finite size scan area is not a problem. A scan area that is slightly larger than the projected area of an antenna is sufficient. The angular region for accurate far-field patterns is defined by the geometry of the antenna and the scan area, as shown in Figure 1. Angle

$$\theta_{\max} \approx \tan\left(\frac{L_{\text{scan}} - D}{2z}\right) \tag{1}$$

is the maximum angle for accurate far-field [6]. This criterion can be used to determine the minimum size of the scan plane for a given desired angular region and separation distance z. Aliasing can be fully avoided only if the Fourier transform of the measured data is band limited, and the sampling interval is $\lambda/2$ or less [6]. For an aperture field, the band limited requirement implies that the field should change smoothly and there should be no discontinuities in the field.

If band limits do not exist or if the sampling criteria is violated by using too large a data point spacing, aliasing errors occur in the use of the FFT to calculate the Fourier transform. If an antenna with a diameter of 1 m at 1 THz is sampled with a $\lambda/2$ spacing in a rectangular grid, about 11 million points are needed. Evidently, to carry out the near-field measurements, a larger data point spacing is desired. As the spacing is increased, aliasing first starts to have an effect on the far sidelobes. If only the main beam and possibly the first sidelobes are of interest, the total number of points can be reduced significantly. The

specific acceptable sampling point spacing and an estimate of the error due to aliasing can be derived from a theoretical antenna pattern along with measurements of system noise and error levels [6].

As an example, Figure 2 shows the effect of aliasing with different sample spacings. The antenna that is used in the simulations is a 1 m Cassegrain antenna with a 12 dB taper in the aperture amplitude distribution. Subreflector blockage of 70 mm in diameter is included in the analysis. In this case, the main beam and first sidelobe can be determined if the spacing of the sample points is not greater than about 100 λ.

The main concern in near-field antenna measurements at 1 THz, is the phase errors caused by the flexible cables and probe positioning errors. The error analysis for planar near-field measurements in [6], reveal that a one degree RMS phase error in the near-field measurements causes less than a 0.12 and 1.2 dB inaccuracy at -10 and -30 dB far-field amplitude pattern levels, respectively. In other words, as the pattern level decreases by 20 dB, the amplitude error caused by the near-field phase error increases by a factor of 10.

The phase errors caused by flexible cables are usually minimized by carefully selecting the flexible cable and by properly designing its mechanical attachment to the moving probe. One possible way to reduce bending of the cable, would be to use a cable with the form of a helix. The disadvantage of this would be the additional length of the cable.

Since the possibilities for directly eliminating cable phase errors are limited, schemes to first measure the phase error and then to remove the errors numerically have been developed. The method described in [7] is a simple and easy method to realize. This method is based on the measurement of the phase of the signal passing twice through the flexible cable. Therefore, it works best for low loss cables. A more complicated three cable method is described in [8]. This method enables one to measure phase errors on lossy and longer cables.

There are two techniques that can be used to overcome the phase errors caused by probe positioning inaccuracies, especially those perpendicular to the measurement plane: to design and build a very high quality moving stage, or to supply a reference plane for the measurements. The latter approach has been chosen for the tests of the 600 GHz antenna of NASA's SWAS satellite. The reference plate will be a highly flat granite plate, against which the planarity of the probe scanning area will be calibrated.

A phase retrieval method may be also used to overcome the phase problems in the near-field measurements. Much work has been done lately on this area [9]-[13]. In these methods, only amplitude data in front of the antenna is measured. The phase value of the field is then recovered from the amplitude data. The development efforts are pointed towards algorithms, which can reliably recover phase information from a single amplitude scan. Presently, most of the methods require amplitude scans over two planes, or over one plane with two focal positions of the antenna feed horn.

Phase retrieval methods entirely overcome the problem of the flexible cables (assuming obviously that the effect of the cable on the amplitude of the signal is constant) and requirements for the moving stage can be assumed to be eased somewhat. However, presently there does not exist a thorough analysis of the errors caused by factors such as probe positioning inaccuracies along the direction of the propagation and perpendicular to this direction.

Phase retrieval methods have been applied in holographic surface testing for the *far-field and Fresnel zone data* of large telescopes up to about 100 GHz (see, for example, [14]). However, so far, for the *near-field data* the methods have been used only up to high

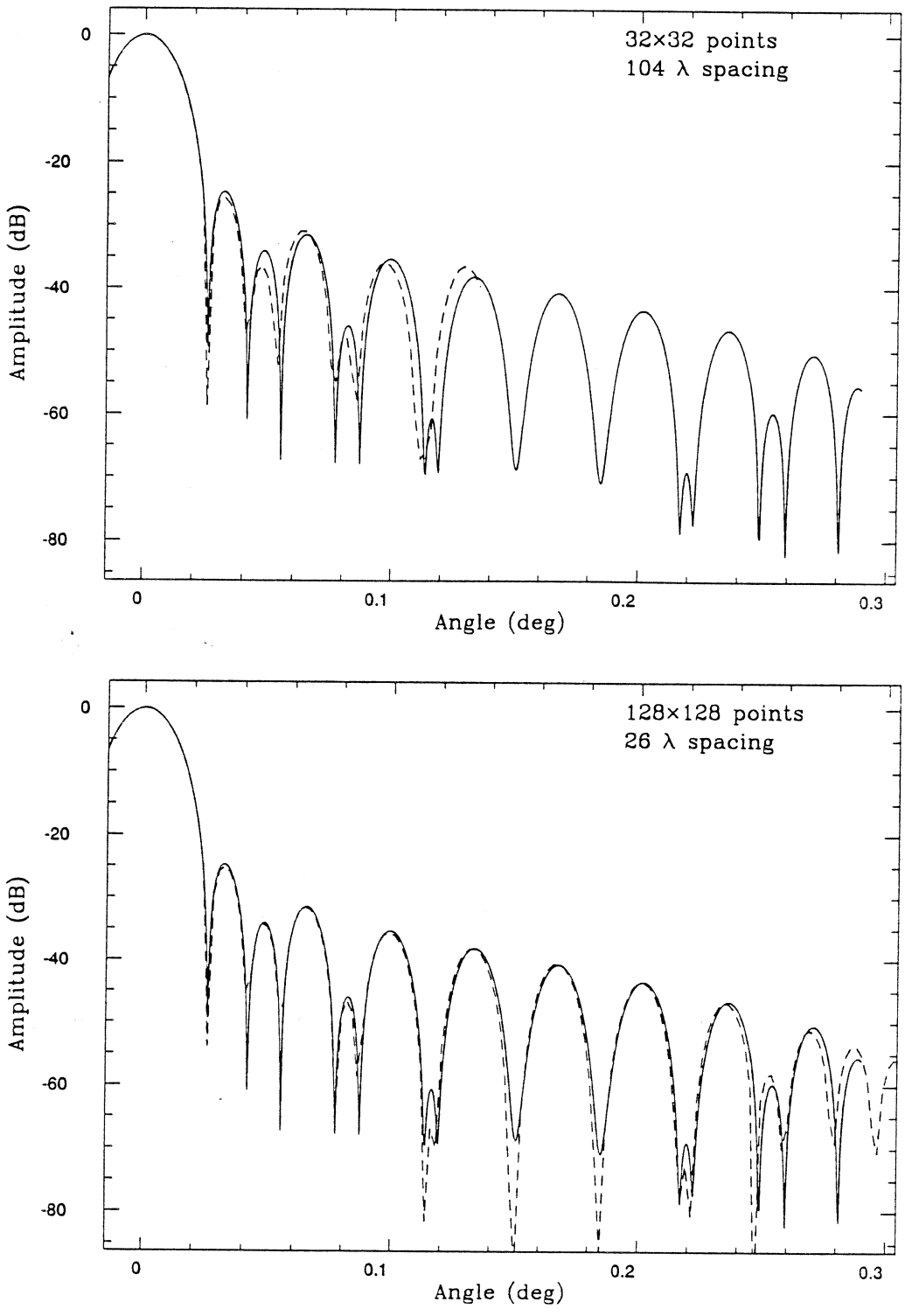

Figure 2: *Simulated effect of aliasing on a far-field pattern of a 1 m Cassegrain antenna at 1 THz. Error free far-field (——). Far-field pattern with different near-field sampling intervals (– – –).*

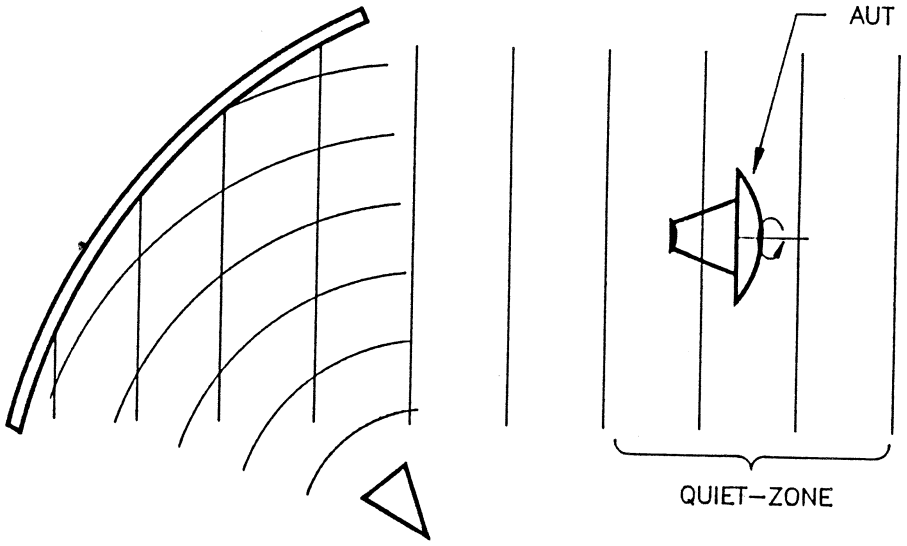

Figure 3: *A compact antenna test range (CATR) using a reflector.*

microwave frequencies (< 30 GHz) and usually for relatively small antennas. How easy it is to extend these methods to the THz frequency range is not obvious. One of the concerns is the sampling interval and whether it can be many wavelengths. A long sampling interval is essential for testing submillimeter antennas. Another concern is the required amplitude measurement accuracy. In spite of all the above unknowns, phase retrieval is an attractive alternative for testing antennas at 1 THz, especially if a near-field testing method is desired.

4 Compact antenna test range method

In a compact antenna test range (CATR) an artificial far-field plane wave is formed in front of the antenna under test (AUT). The main advantage of a CATR is that direct far-field radiation patterns can be measured the same way as in the far-field method under a controlled environment and especially in a short range.

The required plane wave is formed from a feed horn spherical wave with a focusing element, which is commonly realized with use of one or more reflectors. A typical CATR arrangement is shown in Figure 3. All of the commercial CATRs use reflectors and they are available up to about 200 GHz. The quiet-zone size, i.e., the plane wave region, defines the maximum diameter of the AUT. The diameter of the quiet-zone is usually 50–70 % of the diameter of the main reflector of the CATR. The presence of diffraction from the edges of the focusing reflector is the factor that primarily defines the useful quiet-zone area. The diffraction is reduced with a special curved or serrated edge treatment of the reflector. Edge diffraction is most pronounced at low microwave frequencies, and it gets less severe as the frequency increases. Another way of looking at this, is that the effects of diffraction are smaller, the larger the aperture (reflector) is in wavelengths.

While the diffraction effects become smaller, the high surface accuracy required for the reflectors becomes a real problem as frequency increases. Usually, a surface accuracy of $\lambda/100$ is required. Therefore, for example, the surface error should be less than 3 μm RMS

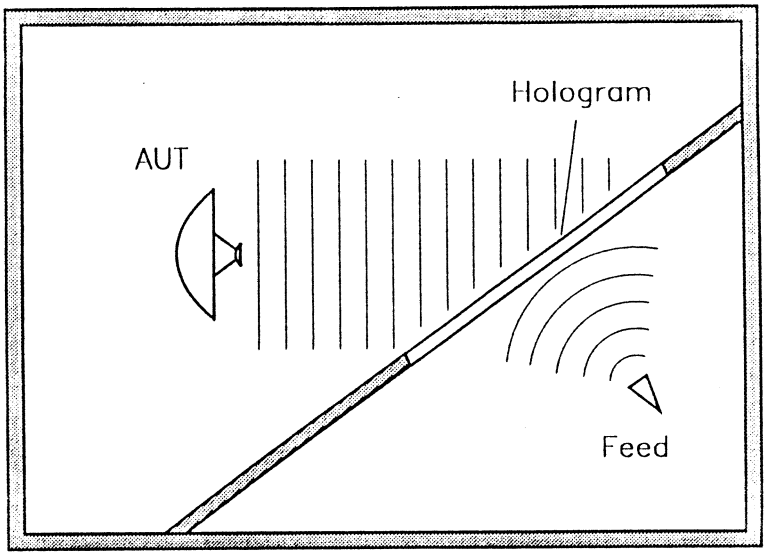

Figure 4: *A hologram type of CATR.*

at 1 THz. This implies that the cost of a reflector CATR will be very high at 1 THz.

The use of a lens instead of a reflector in a CATR has been considered as an option to overcome the high surface accuracy tolerances [15,16]. For a lens with a low dielectric constant ϵ_r, the surface accuracy requirement is much less stringent.

For a lens, the surface accuracy is weighted by the factor of $\sqrt{2}/(\sqrt{\epsilon_r}-1)$, as compared to a reflector. For example, for a foam lens with $\epsilon_r = 1.1$, the requirement for the lens surface is 90 μm RMS at 1 THz. With $\epsilon_r = 1.1$, and a focal length to lens diameter ratio $F/D = 3$, the thickness of the foam lens would be slightly less than the diameter of the lens [17]. The thickness of the lens starts to increase rapidly as ϵ_r of the lens is decreased from the value of 1.1. A lens could be a less expensive alternative than the use of a reflector. Primary concerns about the use of a foam lens at 1 THz, are the granulation of the foam and also how easily and smoothly a foam surface can be shaped.

Perhaps, the most feasible way of realizing a compact range at THz frequencies is the recently introduced hologram approach [18]. In this method, a planar, computer generated hologram structure is used as a focusing element. Figure 4 shows an arrangement for a hologram CATR. The hologram is placed at the opening in the wall, which divides the anechoic chamber into two parts.

In general, a hologram structure changes both the amplitude and phase of the field transmitted through or reflected from the structure. In practice, holograms are usually realized so that they only change the amplitude or phase of the field. In this case, the hologram is called correspondingly either an amplitude or a phase hologram. A transmitting amplitude hologram, like the one used here for the compact range, can be approximated by an appropriately shaped metallization pattern etched on a dielectric film with a thin copper layer. Figure 5 shows an example of a binary amplitude hologram pattern used at 110 GHz [18]. This pattern is generated based on a known incident field, i.e., feed horn spherical wave and the desired output plane wave. To reduce edge diffractions, the hologram is designed

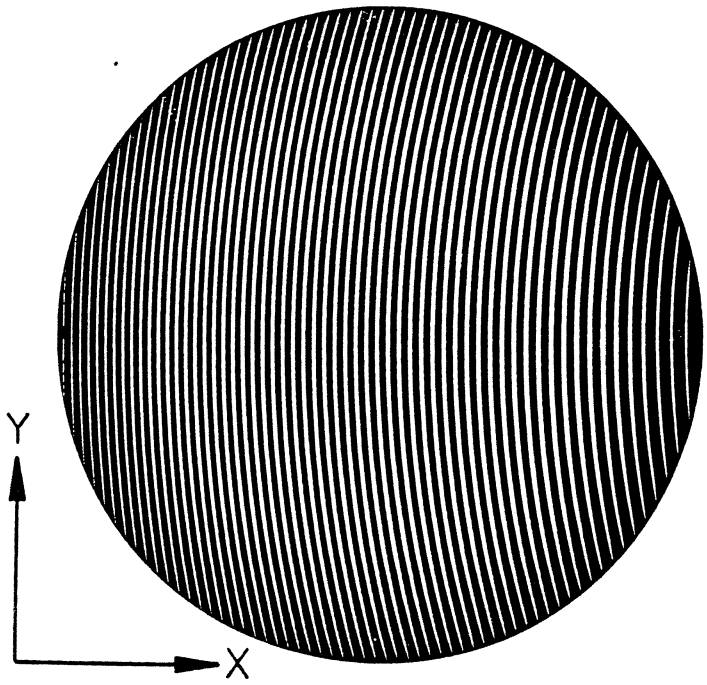

Figure 5: *An example of a binary amplitude hologram pattern. Non-transparent and transparent parts are shown with black and white, respectively.*

to give a cosine amplitude taper. Furthermore, the hologram is designed so that the plane wave leaves the hologram at an angle of about 33°. This is important to separate the desired plane wave and unwanted wavemodes, which are due to the binarization of the hologram transmittance. Using this pattern, the operation of a hologram CATR has been successfully demonstrated at 110 GHz. The diameter of the hologram was 300 mm. Figure 6 shows the measured and theoretical amplitude of the quiet-zone field. The measured ripple is about ± 1 dB and the diameter of the quiet-zone is about 2/3 of the diameter of the hologram.

Manufacturing an amplitude hologram is very inexpensive, only a few percent of the cost of a comparable curved reflector. The hologram can be manufactured with a similar etching process to the one used for making printed circuits. Since only the amplitude of the incoming spherical wave is changed, the surface accuracy requirement is much less stringent than for a reflector. Furthermore, high flatness is easy to achieve, since the hologram is simply stretched onto a frame. The only disadvantage of a hologram structure is the fairly strong frequency dependence, due to the diffractive nature of the component. This is not, however, a problem in testing antennas of scientific satellites, because they are usually designed to operate at a few specific spectral line frequencies.

As important as building the compact range well, is verifying the quality of the quiet-zone. At lower frequencies, the quiet-zone is tested by measuring amplitude and phase distribution on several cuts across the quiet-zone. Measuring amplitude cuts should not be significantly more difficult even at 1 THz. Measuring phase cuts faces basically the same problems as measuring phase in the near-field method. However, the situation in a CATR is somewhat easier, since phase is only needed on linear cuts and not on a whole plane. Making a very high quality linear moving stage is obviously much easier than to make an x-y-stage. This is

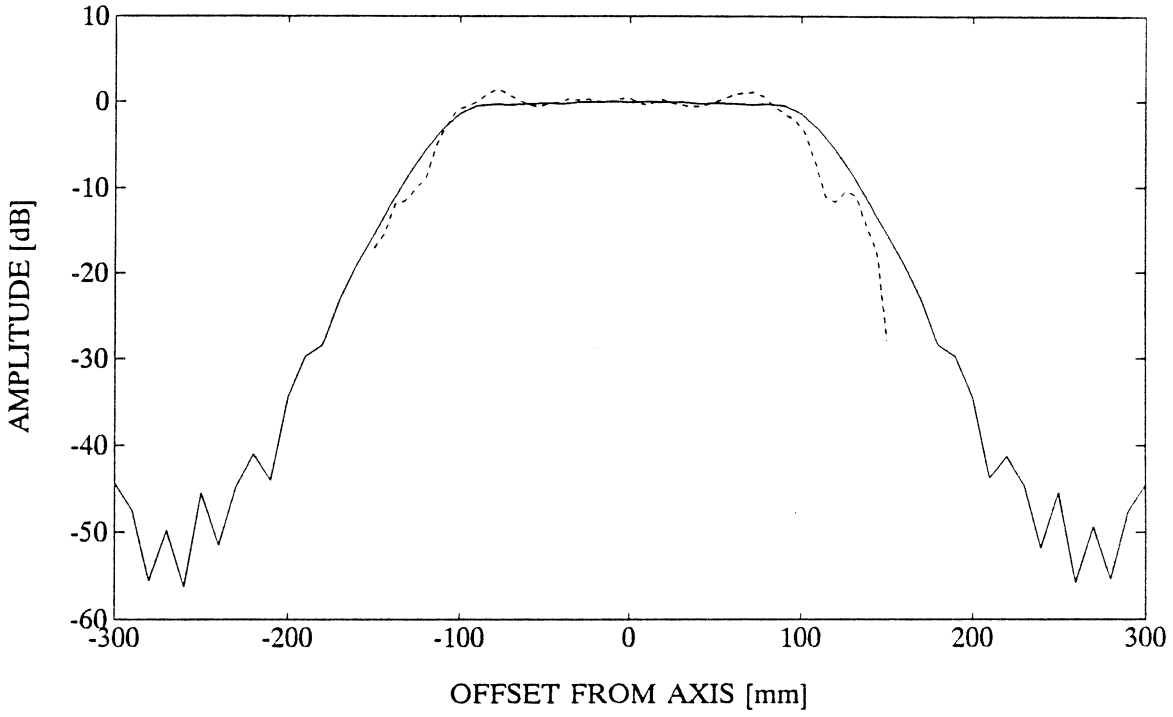

Figure 6: *Theoretical (——) and measured (- - -) amplitude of the quiet zone field at an angle of 33.06° with respect to the normal of the hologram.*

especially true, because the linear stage does not have to extend over the whole quiet-zone at one time. Therefore, phase errors due to the scanning mechanism can be neglected or at least they can be estimated quite accurately.

Phase errors caused by flexing of the cable can not be neglected. However, they are easier to handle in the case of the quiet-zone than in the near-field testing, again because of the more limited scanning requirements. Furthermore, it is possible to totally overcome the phase errors caused by the cables with the use of the differential phase method [20]. In this method, a two channel receiver is moved across the quiet-zone and the phase difference between the two channels is recorded. Then from the differential phase pattern, the normal phase information is calculated. Very short period ripple and phase front tilts are difficult to measure with this method.

Another common test is to measure the radiation pattern of a smaller reflector antenna in a CATR and then to compare it to the one measured in the far-field. This would be a valuable test to carry out in addition to the above mentioned quiet-zone tests. The size of the test reflector antenna has to be limited to about 50–100 mm in diameter. Otherwise, the far-field distance becomes too large. A comparison of the patterns of a small test antenna measured at different points of the quiet-zone indicate the uniformity of the plane wave region.

5 Other methods

In addition to the above described method, there exists some other methods, which can be considered, in general, only as marginal alternatives. However, in some specific cases, they can prove to be useful. Two such methods are described in the following section.

Defocusing

It is well known that an antenna far-field radiation pattern, which exists ideally an infinite distance away from the antenna, can be brought closer by moving the feed horn further out from the focal position [19]. This is shown in Figure 7. Interesting to note, is that for a fast optical system (F/D is small) a relatively small defocusing brings the far-field conveniently close. This can be calculated from the well known thin lens formula:

$$\frac{1}{d_2} = \frac{1}{F} - \frac{1}{d_1}. \tag{2}$$

For example, if $F = 1$ m and the defocusing distance is 20 mm ($d_1 = 1$ m $+ 20$ mm), we find that the far-field of the antenna has been brought to $d_2 = 51$ m from the antenna. Figure 8 shows theoretical far-field patterns at $2D^2/\lambda = 6.7$ km and 51 m distances in defocused and in focused cases at 1 THz. The antenna is a 1 m diameter Cassegrain antenna with $F/D = 1$. The aperture field has a 12 dB amplitude taper and a subreflector blockage 170 mm in diameter. Aperture phase distribution was calculated by ray tracing with an axial defocusing distance of 21.5 mm. This value was chosen, because it gave the best fit to an ideal spherical phase deformation, caused by a defocusing of 20 mm. The high sidelobe level of the antenna pattern is due to the large diameter of the subreflector, which is required for a $F/D = 1$ Cassegrain system. A real antenna would be rather an off-set antenna.

A drawback of the defocusing method is the need to move the feed, or alternatively, the subreflector relative to the antenna. This can be a significant problem in satellite payload antenna testing. Another disadvantage is that the accuracy of the far-field relies on the validity of the assumption that the defocusing affects only the phase distribution of the aperture field. An obvious advantage of the defocusing technique is that one may carry out measurements with the same simplicity as in conventional far-field measurements, but use a shorter range.

Combined electrical and mechanical measurements

The far-field radiation pattern of a reflector can be calculated if both the amplitude and phase pattern of the feed horn or feed system, as well as the surface of the reflector are all accurately known. Measurement of the amplitude pattern of the feed horn is fairly straight forward and includes no major problems, since a dynamic range of 30 dB should be sufficient. Measurement of the phase pattern with conventional measurement methods is difficult at 1 THz. The main problems are the complexity of the measurement set-up, and errors caused by flexing of cables needed in the system. Using the differential phase measurement method [20,21], phase pattern measurements should not be a major problem either, even at 1 THz. Mechanical antenna surface measurements can become the real bottleneck of this approach. If the antenna surface is measured with a mechanical probe, the number of surface grid

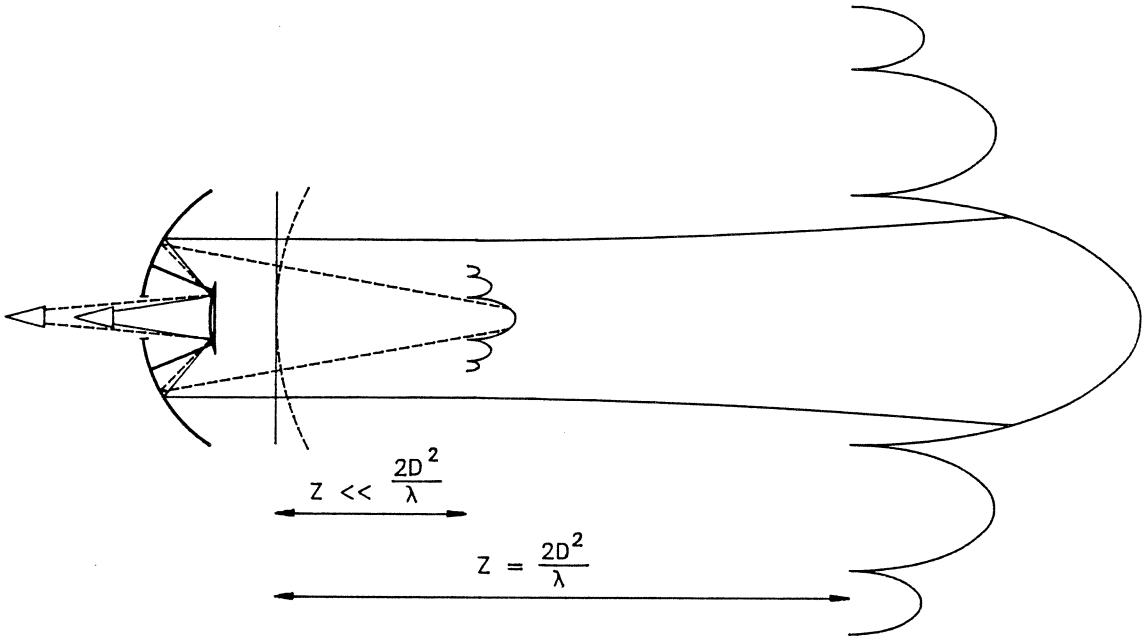

Figure 7: *Defocusing brings the far-field to a conveniently close distance.*

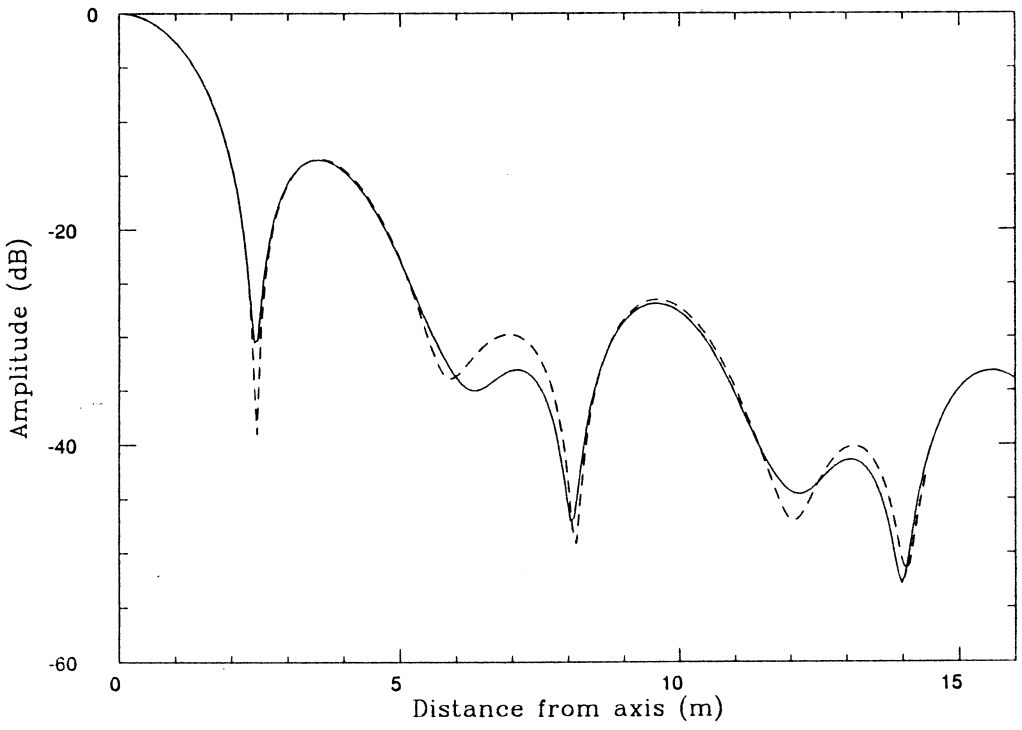

Figure 8: *Far-field pattern calculated as the antenna is in focus (——) and defocused by 21.5 mm (– – –). Calculations are based on an exact near-field integration of the aperture field of a 1 m Cassegrain antenna at 1 THz. To enable the comparison, the distance from the axis values are multiplied by 131 in the defocused case.*

points has to be limited to a fairly small number. Optical interferometric methods can be used to obtain the mechanical surface, if the antenna surface is of optical quality on a small scale.

The far-field of an off-set antenna structure can be calculated most accurately from the feed horn radiation and mechanical surface properties. In a Cassegrain system, diffraction from the subreflector and its support beams is difficult to predict, which causes inaccuracies in the far-field pattern.

6 Conclusions

Antenna test methods for measuring the far-field pattern of a reflector antenna in the THz frequency range have been reviewed. No method has so far been validated for this kind of test.

One of the conventional lower frequency methods, namely the far-field method can be discarded for certain, due to atmospheric effects.

The near-field method remains a possibility for the tests. However, a very high quality moving stage is needed, and phase errors caused by flexible cables have to be dealt with. Phase retrieval or amplitude-only methods overcome the latter problem. However, little experience exists on the use of phase retrieval methods above microwave frequencies. Therefore, these methods need more work to be validated for use in the THz range.

Technically, the most feasible and least expensive method appears to be the hologram type of compact range. In this method, a planar amplitude hologram is used to form the required plane wave. The hologram is inexpensive to manufacture, and it is also less sensitive to surface accuracy errors than a reflector.

In some cases, a defocusing method to bring the far-field closer can prove to be practical. The use of this method requires that the defocusing option has already been taken into account in the satellite's radiometer and antenna design. An alternative possibility is mechanical reflector surface measurements and accurate measurement of the feed system phase and amplitude patterns, followed by a reflector radiation pattern computation. This can be considered only as a marginal alternative, if other methods are not available.

Acknowledgments

The author would like to thank Paul F. Goldsmith, German Cortes-Medellin and Ronna Erickson for the help in preparing this paper.

References

[1] H. J. Liebe, "An updated model for millimeter wave propagation in moist air," *Radio Science*, vol. 20, pp. 1069–1089, Sep.-Oct. 1985.

[2] A. D. Yaghjian, "An overview of near-field antenna measurements," *IEEE Trans. Antennas Propagat.*, vol. AP-34, pp. 30–45, Jan. 1986.

[3] Special issue on the near-field scanning techniques, *IEEE Trans. Antennas Propagat.*, vol. AP-36, June 1988.

[4] Y. Rahmat-Samii, V. Galindo-Israel, R. Mittra, "A plane-polar approach for far-field construction from near-field measurements," *IEEE Trans. Antennas Propagat.*, vol. AP-28, pp. 216–230, Mar. 1980.

[5] L. I. Williams, Y. Rahmat-Samii, "Novel bi-polar planar near-field measurement scanner at UCLA," *IEEE Antenna Propagat. Soc. Int. Synp. Dig.*, London, Ontario, pp. 1446-1449, June 1991.

[6] A. C. Newell, "Error analysis techniques for planar near-field measurements," *IEEE Trans. Antennas Propagat.*, vol. AP-36, pp. 754–768, June 1988.

[7] J. Tuovinen, A. Lehto, A. Räisänen, "A new method for correcting phase errors caused by flexing of cables in antenna measurements," *IEEE Trans. Antennas Propagat.*, vol. AP-39, pp. 859–861, June 1991.

[8] D. W. Hess, "Principle of the three-cable method for computation of cable variations," *Proc. 14th Antenna Measurement Tech. Ass. Conf.*, Columbus, pp. 10-26–10-31, 1992.

[9] A. P. Anderson, S. Sali, "New possibilities for phaseless microwave diagnostics. Part I: Error reduction techniques," *IEE Proc.*, part H, vol. 132, no. 5, pp. 291–298, 1985.

[10] O. M. Bucci, G. D'Elia, G. Leone, R. Pierri, "Far-field pattern determination from the near-field amplitude on two surfaces", *IEEE Trans. Antennas Propagat.*, vol. AP-38, pp. 1772–1779, Nov. 1990.

[11] J. E. McCormack, G. Junkin, A. P. Anderson, "Microwave metrology of reflector antennas from a single amplitude pattern," *IEE Proc.*, part H, vol. 137, no. 5, pp. 276–284, 1990.

[12] T. Isernia, G. Leone, R. Pierri, "A new technique for far field estimation from near zone phaseless data", *Electronics Letters,* vol. 27, no. 8, pp. 652-654, 1991.

[13] R. Pierri, T. Isernia, G. Leone, "Antenna testing from near field phaseless data: the planar scanning," Final Report, ESTEC contract no. 110583, Jan. 1992.

[14] D. Morris, H. Hein, H. Steppe, J. W. M. Baars, "Phase retrieval radio holography in the Fresnel region: tests on the 30 m telescope at 86 GHz," *IEE Proc.*, part H, vol. 135, no. 2, pp. 61–64, 1988.

[15] A. D. Olver, A. A. Saleeb, "Lens-type compact antenna range," *Electronics Letters,* vol. 15, no. 14, pp. 409-410, 1979.

[16] T. Hirvonen, J. Tuovinen, A. Räisänen, "Lens-type compact antenna test range at mm-waves," *Proc. 21st European Microwave Conf.*, Stuttgart, vol. 2, pp. 1079–1083, 1991.

[17] J. Tuovinen, T. Hirvonen, A. Räisänen, "Lens-type compact antenna test range." *Proc. 14th ESA Workshop on Antenna Measurements*, Noordwijk, The Netherlands, 1991.

[18] J. Tuovinen, A. Vasara, A. Räisänen, "A new type of compact antenna test range," *Proc. 22nd European Microwave Conf.*, Espoo, vol. 1, pp. 503–508, 1992.

[19] R. C. Johnson, H. A. Ecker, J. S. Hollis, "Determination of far-field antenna patterns from near-field measurements," *Proc. IEEE*, vol. 61, pp. 1668–1694, Dec. 1973.

[20] J. Tuovinen, A. Lehto, A. Räisänen, "Phase measurements of millimeter wave antennas at 105–190 GHz with a novel differential phase method," *IEE Proc.*, part H, vol. 138, no. 2, pp. 114–120, 1991.

[21] A. Lehto, J. Tuovinen, O. Borić, A. Räisänen, "Accurate millimeter wave antenna phase pattern measurement using the differential phase method with three power meters," *IEEE Trans. Antennas Propagat.*, vol. AP-40, pp. 851–853, July 1992.

POWER GENERATION WITH IMPATT DIODES, TUNNETT DIODES AND GUNN DEVICES AT MILLIMETER AND SUBMILLIMETER WAVE FREQUENCIES

H. Eisele[1], R. Kamoua[2], G. I. Haddad[1], C. Kidner[1]

[1] Center for Space Terahertz Technology
Department of Electrical Engineering & Computer Science
The University of Michigan
Ann Arbor, Michigan 48109-2122

[2] Department of Electrical Engineering
State University of New York at Stony Brook
Stony Brook, NY 11794-2350

Abstract:

Recent experimental results have shown that GaAs IMPATT diodes can operate up to D-band frequencies. RF output power levels of up to 20 mW at 120 GHz and 15 mW at 135 GHz were obtained. Corresponding dc to RF conversion efficiencies were between 0.9 % and 1.5 %. Device simulations and preliminary experimental results indicate that the fundamental mode operation of InP Gunn devices can be extended to the upper end of the D-band. RF output power levels of 21 mW were measured at 120 GHz, 17 mW at 133 GHz and 8 mW at 155 GHz. The most promising candidate for power generation at submillimeter wave frequencies, the TUNNETT diode, has yielded RF power levels of up to 35 mW around 103 GHz with corresponding dc to RF conversion efficiencies up to 3.5 %.

IMPATT diodes, TUNNETT diodes and Gunn devices exhibit clean spectra up to the highest oscillation frequencies, which makes them useful devices for local oscillator applications.

All these devices are strongly nonlinear. Therefore power extraction at higher harmonics was also investigated. Preliminary measurements were carried out in a non-optimized circuit of a full height waveguide cavity for the fundamental frequency with a resonant cap on top of the device. 0.12 mW at 182 GHz were obtained from a GaAs W-band IMPATT diode and 13 μW at 240 GHz from a GaAs D-band IMPATT diode both at the second harmonic. W-Band TUNNETT diodes at the second harmonic gave 40 μW at 200 GHz and 0.25 mW at 224 GHz. D-band Gunn devices yielded 0.4 mW at 220 GHz and 90 μW at 228 GHz.

1. Introduction

There is a growing need for local oscillator power above 100 GHz in radioastronomy. Although impressive progress has been demonstrated for oscillators with three-terminal devices at mm-wave frequencies [1,2] two-terminal devices still hold the greatest promise in delivering significant power levels at sub-mm-wave frequencies. This paper summarizes the recent experimental results obtained from IMPATT diodes, TUNNETT diodes and Gunn devices at frequencies above 100 GHz and gives an overview of design procedures and fabrication technologies. The experimental results on D-band InP Gunn devices agree well with previously reported simulations [3] and indicate that fundamental mode operation can be extended to the upper D-band. Since IMPATT diodes, TUNNETT diodes and Gunn devices are nonlinear devices, this paper also focuses on harmonic power extraction. Preliminary results show that even in a non-optimized circuit power levels up to 0.39 mW around 220 GHz can be extracted.

2. Device Design

The design of the GaAs D-band single-drift flat-profile IMPATT diodes was based on an extended small-signal model for the avalanche region and a large-signal approximation for the drift region and followed the same procedure as previously used in the design of GaAs W-band diodes [4]. The design of the W-band TUNNETT diodes was based on a simplified large-signal model [5] and GaAs material parameters derived from measurements on heavily doped $p^{++}n^{+}$ junctions and GaAs IMPATT diodes [6]. Figures 1 and 2 show the nominal doping profiles of the D-band IMPATT diode and W-band TUNNETT diode, respectively.

An Ensemble Monte Carlo program has been developed to simulate Gunn devices. Since a Monte Carlo method requires accurate values for a large number of material parameters, first InP W-band Gunn devices with $n^{+}n^{-}n^{+}$ structures similar to published designs were fabricated and tested. The appropriate material parameters were selected by comparing dc and high-frequency measurements with results predicted by the model [3]. During this selection process two different structures for operation at D-band frequencies were designed, one with a flat doping profile and one with a graded doping profile [7]. Figures 3 and 4 give the nominal doping profiles of the two Gunn devices.

3. Fabrication Technology

A lattice matched $Al_{0.55}Ga_{0.45}As$ layer grown between the device layer of Figures 1 or 2 and the GaAs substrate or a lattice matched $In_{0.53}Ga_{0.47}As$ layer grown between the device layers of Figure 3 or 4 and the InP substrate allows the use of a selective etching technology [3,8]. This technology gives

substrateless devices on a 15 to 20 μm thick integral heat sink. Figure 5 outlines the main steps in this fabrication technology. Before the epitaxial side of the MBE-, CBE- or MOCVD-grown wafer is metallized with Ti/Pt/Au for a p^+ ohmic contact (TUNNETT diode) or Ni/Ge/Au/Ti/Au for an n^+ ohmic contact (Gunn device), grooves are selectively etched down to the etch-stop layer (AlGaAs or InGaAs) to divide the device layers into square shaped islands. This reduces the stress in the device layers during annealing. In addition, the trenches shape the evaporated metal layers and plated gold layer of the integral heat sink thus increasing the mechanical strength of the metal layers for the subsequent processing steps after the substrate and the etch-stop layer have been removed in selective etches. The top n^+ ohmic contact (Ni/Ge/Au/Ti/Au) is defined by standard lift-off technology. After an additional metallization (Ti/Au/Ti) step a second photolithography process produces a hole on top of each n^+ ohmic contact. The top Ti layer is removed and up to 3 μm of gold can be electroplated through these holes in order to ease bonding. The remaining Ti/Au/Ti layers between the contacts are removed in wet etches. Mesas are formed using a standard wet etch and the ohmic contacts are annealed on a hot plate. The heat sink is diced to give individual devices. TUNNETT diodes with nominal diameters of 25-35 μm or Gunn devices with nominal diameters of 35-45 μm are mounted on gold plated copper blocks.

The high operating current densities around 60 $kAcm^{-2}$ and corresponding high power densities in D-band IMPATT diodes require operation on diamond heat sinks. Therefore another, previously reported, selective etching technology [9] was employed in the fabrication of the IMPATT diodes. The diodes are thermocompression bonded on to metallized diamond heat sinks.

To minimize parasitic elements of the package and to find the optimum impedance transformation an open package with four stand-offs and tapered ribbons was chosen for all the IMPATT and TUNNETT diodes and for most of the Gunn devices. Some of the Gunn devices were packaged with metallized quartz rings and tapered gold ribbons.

4. Experimental results

A full-height waveguide cavity (WR-10 for W-band, WR-6 for D-band) with a resonant cap on top of the device and with a back short at one flange has been successfully used for all the two-terminal devices reported in this paper. The gold plated copper block of the heat sink forms the bottom of the waveguide. In some cases the RF output power could be slightly increased by using an E-H-tuner at the output flange of the cavity.

In Figure 6 the RF output power, the dc to RF conversion efficiency and oscillation frequency of one D-band IMPATT diode are plotted as a function of the dc bias. For the maximum applied bias current an output power of 15 mW was obtained. The corresponding efficiency was 1.5 % at the oscillation

frequency of 135.3 GHz. The highest oscillation frequency of another IMPATT diode was 137.3 GHz with an output power of 4 mW [10]. Figure 7 compares the performance of D-band IMPATTT diodes fabricated from two wafers with an active layer of a nominal width between 0.285 μm and 0.28 μm and of a nominal doping concentration between 2.7×10^{17} cm^{-3} and 2.8×10^{17} cm^{-3}. Diodes made from wafer (b) exhibit slightly higher power levels and efficiencies at frequencies above 120 GHz. Figure 8 shows the measured spectrum of a free running D-band IMPATT diode oscillator with 5 mW at 120.7 GHz and proves that the oscillations have a clean spectrum.

A plot of the RF output power and dc to RF conversion efficiency versus oscillation frequency in Figure 9 summarizes the experimental results for the eleven best devices of the W-band TUNNETT diodes that have been mounted and tested to date. The peak in output power (35 mW) and efficiency (3.5 %) at 103 GHz occurs close to the design frequency of 100 GHz and confirms that the first order design rules [5] accurately predict the operating frequency of the TUNNETT diodes. It also indicates that the average, high field, high temperature electron drift velocity in GaAs TUNNETT diodes is close to 4.6×10^6 cms^{-1} [8]. These findings have been verified by more detailed large-signal device simulation programs [11].

Figure 10 compares the experimental results obtained from the InP Gunn devices with the flat doping profile (grown by CBE) and with the graded doping profile (grown by MOCVD) between about 90 GHz and 165 GHz. The best device with the flat doping profile yielded an RF output power of 33 mW with a corresponding dc to RF conversion efficiency of 1.75 % at 108.3 GHz. To the authors' knowledge, these are the highest reported values for an $n^+n^-n^+$ structure. The decrease in performance at higher frequencies seems to be rather pronounced and may be explained by non-optimized ohmic contacts. As expected from the simulations, devices with the graded doping profile exhibit the better performance. RF output power levels of 21 mW at 120.6 GHz, 17.5 mW at 133.7 GHz and 8.4 mW at 155.4 GHz were obtained from the so far best devices. The corresponding dc to RF conversion efficiencies were 1.25 %, 1 % and 0.6 %, respectively. Oscillations up to about 165 GHz (< 1 mW) have also been detected in a reduced-height WR-4 waveguide cavity with a coaxial post.

As can be seen in Figure 11a for 14 mW at 121 GHz and in Figure 11b for 3.6 mW at 156 GHz the spectra of the free running Gunn device oscillators are clean up to the highest oscillation frequencies. Using a self-injection locking method a loaded Q value of 54 was measured at 156 GHz. This low a value indicates that the Gunn device operates in the fundamental-frequency mode. Typical loaded Q values between 30 and 105 were determined for various Gunn devices with the two doping profiles at other D-band frequencies and corroborate this conclusion.

5. Second harmonic power extraction

IMPATT diodes, TUNNETT diodes and Gunn devices are nonlinear devices and are expected to have higher harmonics in their output signal. Therefore, a 1"-long WR-3 waveguide section with a cut-off frequency of 173.28 GHz was inserted between the 1"-long WR-6 waveguide of a D-band thermistor power head (calibrated around 160 GHz) and the flange of the full height WR-10 waveguide cavity for the W-band devices or the full-height WR-6 waveguide cavity for the D-band devices. Estimated 3 dB attenuation were taken into account for the losses in the 3"-long waveguide and for the mismatch in the power head, although the correction factor for the D-band thermistor might be considerably higher at around 220 GHz.

The back short of the cavity was adjusted for maximum output power. No other additional tuning elements at the fundamental frequency, nor at the second-harmonic frequency were used in the cavity at this point.

A W-band IMPATT diode with a maximum RF output power of 140 mW and a dc to RF conversion efficiency of 4.2 % at 93.4 GHz yielded an output power of 0.12 mW at a second harmonic frequency of about 182 GHz and a bias current of about $^2/_3$ the maximum bias current. A D-band IMPATT diode with 20 mW at 120 GHz had an output power of 13 µW at the second harmonic of 240 GHz. An explanation of low up-conversion efficiency can be found in the decrease of the derivative of the ionisation rates with respect to the electric field strength at electric fields above 500 $kVcm^{-1}$ [4,12]. This decrease causes the avalanche process to become more and more linear [12] and the higher harmonics to disappear in the output signal of the diode.

Three different D-band Gunn devices yielded RF output power levels of 0.39 mW at 220 GHz with a fundamental to second-harmonic power conversion efficiency of 2.5 %, 0.09 mW at 228 GHz and 0.12 mW at 232 GHz. The power levels are similar to the values obtained with a more optimized second-harmonic oscillator circuit [13]. A W-band InP Gunn device tested in a full-height WR-10 waveguide gave 3.5 mW at 156.3 GHz with a fundamental to second-harmonic power conversion efficiency of 10 %. The second harmonic output of this W-band oscillator was measured in a WR-6 waveguide test setup.

Three different TUNNETT diodes had RF power levels of 41 µW at 200 GHz, 0.25 mW at 223.5 GHz and 0.12 mW at 225 GHz. The RF output power level of the TUNNETT diode with the 0.25 mW at the second harmonic was 14 mW at 112.5 GHz. Thus a conversion efficiency of 1.8 % between fundamental and second-harmonic output power can be calculated. This value is very similar to the unpublished result of a V-band TUNNETT diode which had a conversion efficiency of 2 % and an output power of 0.5 mW at the second-harmonic frequency of 121 GHz. The V-band diode was tested in a full-height WR-15 waveguide cavity and the second-harmonic output was measured in a WR-6 test setup. To measure the

spectrum of the W-band TUNNETT diode at the second harmonic, the D-band thermistor power head was removed and the WR-3 waveguide of a harmonic mixer (175-325 GHz) was connected to the 1"-long WR-3 waveguide piece. Figure 12 shows the spectrum of the TUNNETT diode at an RF output power of 0.2 mW and proves that the oscillations have a clean spectrum even at the second harmonic of 223.5 GHz. This is the highest reported frequency for CW operation of TUNNETT diodes.

6. Conclusion

The experimental results from the D-band IMPATT diodes are the best reported to date. The power levels and efficiencies of the W-band TUNNETT diodes above 93.5 GHz are the highest reported so far and compare favorably to the values of Gunn devices [15-17] above 100 GHz. InP Gunn devices can be operated in fundamental mode up to D-band frequencies exceeding the power levels that have been published so far. These experimental results confirm recent theoretical findings. Free running oscillators with all these two-terminal devices exhibit clean spectra which makes them excellent candidates for local oscillator applications.

Second harmonic power extraction has been successfully demonstrated with IMPATT diodes, TUNNETT diodes and Gunn devices. Useful power levels with clean spectra were extracted from TUNNETT diodes and Gunn devices. Higher power levels and harmonic power extraction at higher frequencies can be expected with more optimized circuits.

Acknowledgments

The authors wish to thank Y. Saito at TRW and Jürg M. Siegenthaler at the Swiss PTT for providing different metallized quartz rings which were used to package some of the Gunn devices. The authors would also like to thank P. Siegel at JPL for making the WR-4 waveguide cavity available. This work was supported by NASA under contract No. NAGW 1334.

References

[1] Schellenberg, J. M., Lau, C. L., Feng, M., and Brusenback, P.: "W-Band Oscillator Using Ion-Implanted InGaAs MESFET's", *IEEE Microwave and Guided Wave Letters*, **MGWL-1**(5), 1991, pp. 100-102.

[2] Kwon, Y., Pavlidis, D., Tutt, M., Ng, G. I., Lai, R., and Brock, T.: "W-Band Monolithic Oscillator Using InAlAs/InGaAs HEMT's", *Electronics Letters*, **26**(18), 1990, pp. 1425-1426.

[3] Kamoua, R., Eisele, H., East, J., Haddad, G. I., Munns, G., Sherwin, M.: "Modeling, Design, Fabrication, and Testing of InP Gunn Devices in the D-band (110 GHz - 170 GHz), *Proceedings of the Third International Symposium on Space Terahertz Technology*, Ann Arbor, Michigan, March 24-26, 1992, pp. 477-493.

[4] Eisele, H.: "GaAs W-Band IMPATT diodes: The first step to higher frequencies", *Microwave Journal*, **34**, 1991, pp. 275-282.

[5] Haddad, G. I., East, J. R., and Kidner, C.: "Tunnel Transit-Time (TUNNETT) Devices for Terahertz Sources", *Microwave and Optical Technology Letters*, **4**, 1991, pp. 23-29.

[6] Eisele, H.: "Electron properties in GaAs for the design of mm-wave IMPATTs", *International Journal of Infrared and Millimeter Waves*, **4**, 1991, pp. 345-354.

[7] Kamoua, R., Eisele, H., Haddad, G. I., Munns, G., Sherwin, M.: "High-Frequency InP Gunn Oscillators: Simulation and Experiment", these *Proceedings*.

[8] Eisele, H., Kidner, C., Haddad, G. I.: "A CW GaAs TUNNETT Diode Source for 100 GHz and Above", *Proceedings of the 22nd European Microwave Conference*, Helsinki, Finland, August 24-27, 1992, pp. 467-472.

[9] Eisele, H.: "Selective etching technology for 94 GHz GaAs IMPATT diodes on diamond heat sinks", *Solid-State Electronics*, **32**, 1989, pp. 253-257.

[10] Eisele, H., Haddad, G. I.: "GaAs single-drift flat-profile IMPATT diodes for CW operation in D band", *Electronics Letters*, **28**(23), 1992, pp. 2176-2177.

[11] Chen, C.-C., Mains, R. K., Haddad, G. I., Eisele, H.: "Numerical Simulation of TUNNETT and MITTATT Devices in the Millimeter and Submillimeter Range", these *Proceedings*.

[12] Rolland P. A., Friscourt M. R., Lippens D., Dalle C., and Nieruchalski, J. L.: "Millimeter Wave Solid-State Power Sources", *Proceedings of the International Workshop on Millimeter Waves*, Rome, Italy, April 2-4, 1986, pp. 125-177.

[13] Rydberg, A.: "High Efficency and Output Power from Second- and Third-Harmonic Millimeter-Wave InP-TED Oscillators at Frequencies Above 170 GHz", *IEEE Electron Dev. Letters*, **EDL-11**(10), 1990, pp. 439-441.

[14] Kidner, C., Eisele, H., East, J., and Haddad, G. I.: "Design, Fabrication and Evaluation of Tunnel Transit-Time Diodes for V-Band and W-Band Power Generation", *Proceedings of the 1992 IEEE MTT-S International Microwave Symposium*, Albuquerque, New Mexico, June 1 - June 5, 1992, pp 1089-1092.

[15] Wandinger, L.: "mm-Wave InP Gunn Devices: Status and Trends", *MICROWAVE JOURNAL*, **24**(3), 1981, pp. 71-78.

[16] Eddison, I. G., et al.: "Efficient fundamental frequency oscillation from mm-wave InP n^+-n-n^+ TEOs", *Electronics Letters*, **17**(20), 1981, pp. 758-760.

[17] Teng, S. J. J., Goldwasser, R. E.: "High Performance Second-Harmonic Operation W-Band GaAs Gunn Diodes", *IEEE Electron Device Letters*, **EDL-10**(9), pp. 412-414.

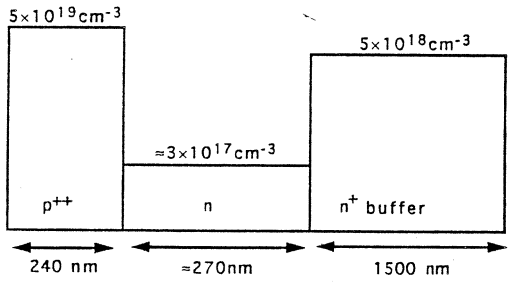

Fig. 1: Nominal device structure of a GaAs D-band single-drift flat-profile IMPATT diode.

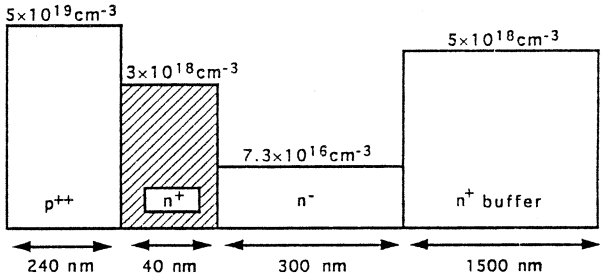

Fig. 2: Nominal device structure of a GaAs W-band single-drift TUNNETT diode.

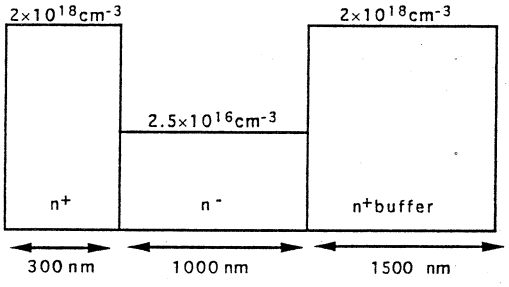

Fig. 3: Nominal device structure of an InP D-band flat-profile Gunn device.

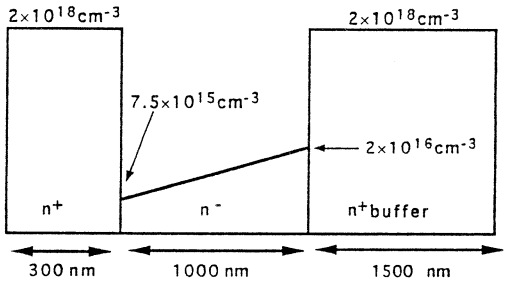

Fig. 4: Nominal device structure of an InP D-band graded-profile Gunn device.

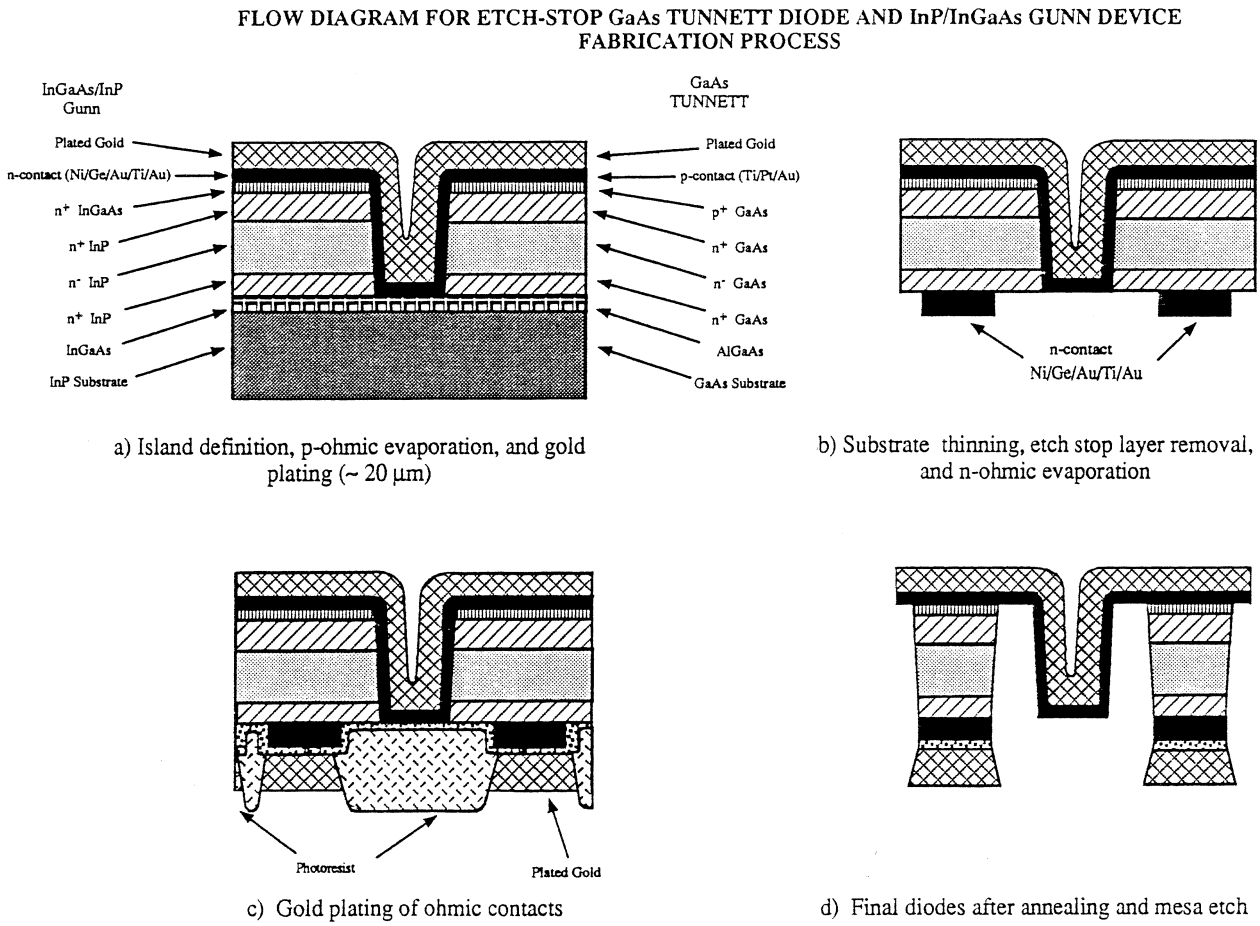

a) Island definition, p-ohmic evaporation, and gold plating (~ 20 μm)

b) Substrate thinning, etch stop layer removal, and n-ohmic evaporation

c) Gold plating of ohmic contacts

d) Final diodes after annealing and mesa etch

Fig. 5: Flow chart for mesa-type two-terminal device fabrication.

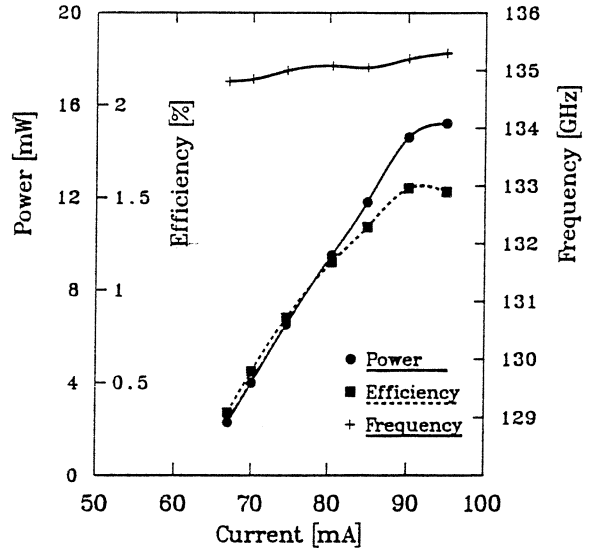

Fig. 6: Output power, efficiency and oscillation frequency as a function of bias current for a GaAs D-band single-drift flat-profile IMPATT diode.

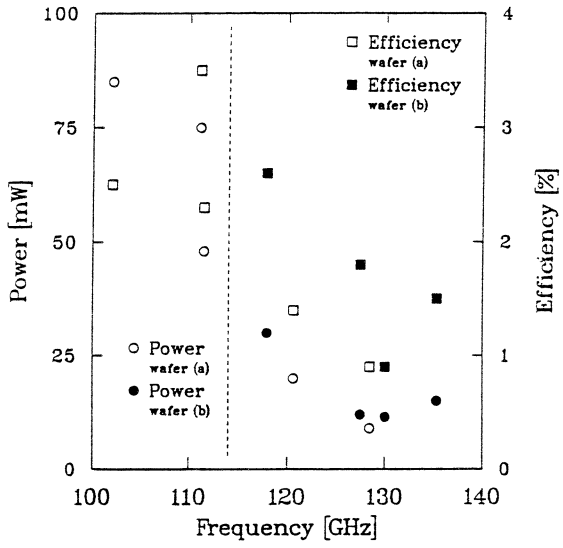

Fig. 7: Output power and efficiency versus oscillation frequency for different GaAs D-band single-drift flat-profile IMPATT diodes.

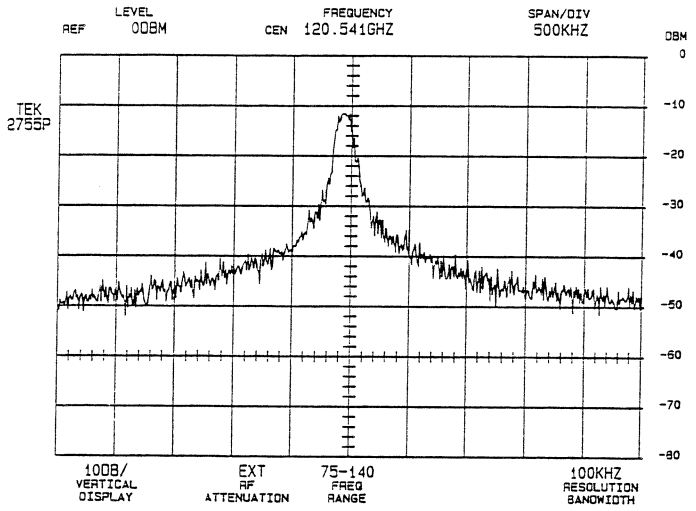

Fig. 8: Spectrum of an GaAs D-band IMPATT diode free running oscillator, power level 5.2 mW, center frequency 120.541 GHz, vertical scale 10 dB/div, horizontal scale 500 kHz/div, BW 100 kHz.

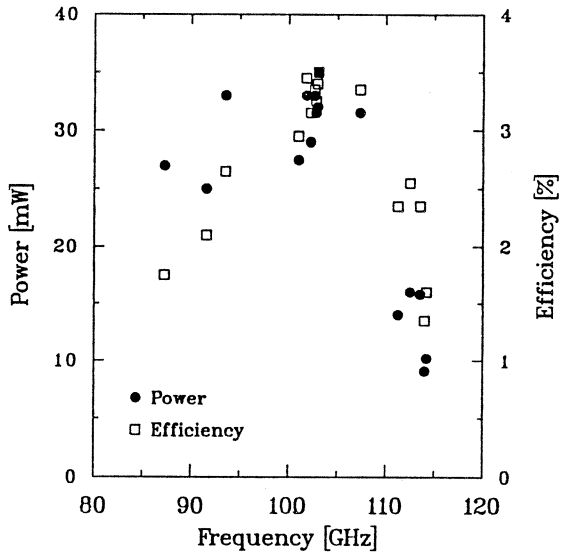

Fig. 9: Output power and efficiency versus oscillation frequency for different GaAs W-band single-drift TUNNETT diodes.

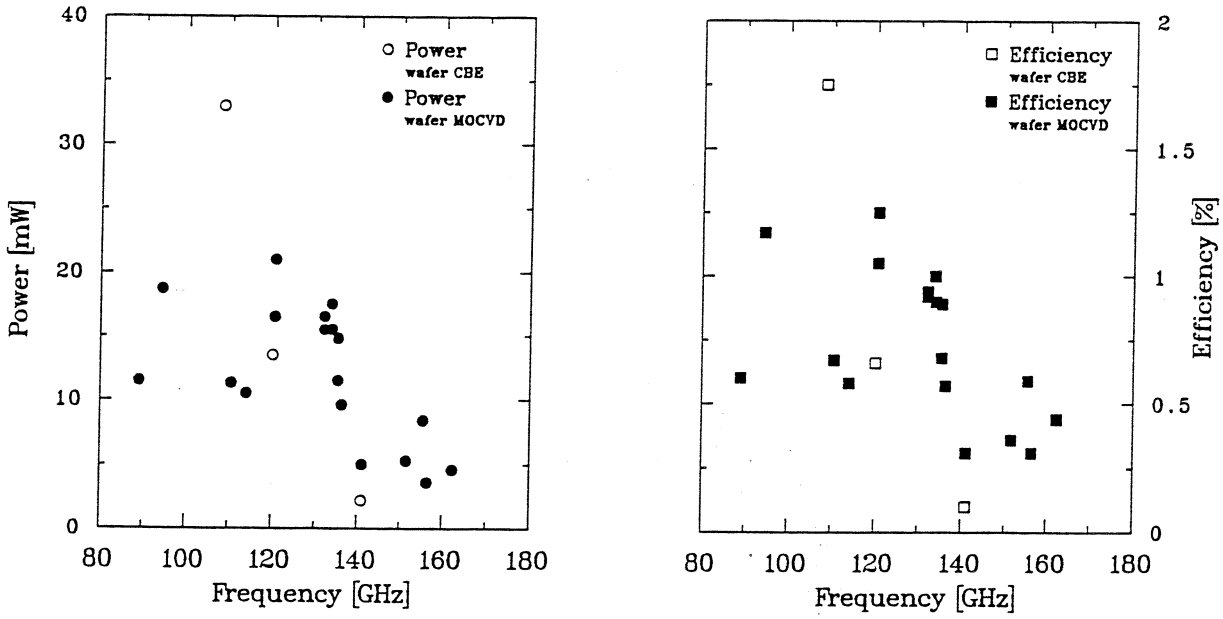

Fig. 10: Output power and efficiency versus oscillation frequency for different InP D-band Gunn devices in W-band and D-band.

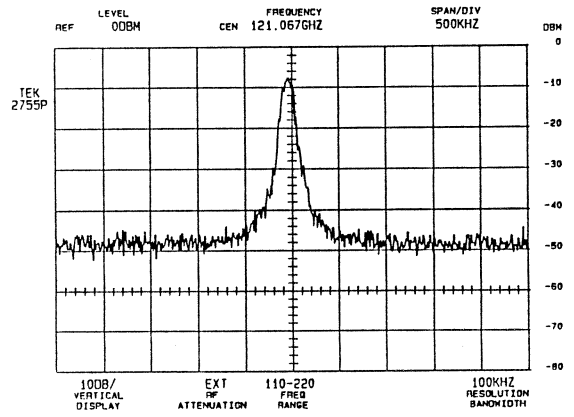

(a)

Fig. 11: Spectrum of an InP D-band Gunn device free running oscillator, power level 14 mW, center frequency 121.067 GHz, vertical scale 10 dB/div, horizontal scale 500 kHz/div, BW 100 kHz.

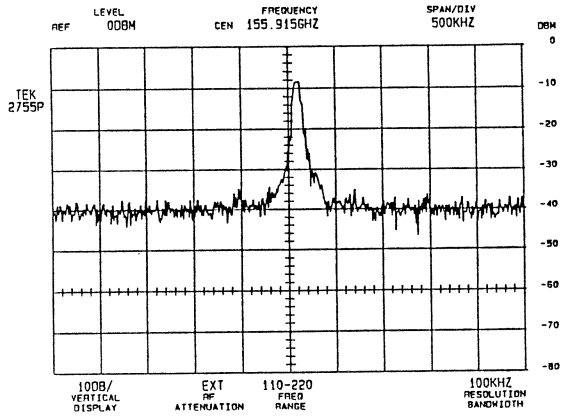

(b)

Fig. 11: Spectrum of an InP D-band Gunn device free running oscillator, power level 3.6 mW, center frequency 155.915 GHz, vertical scale 10 dB/div, horizontal scale 500 kHz/div, BW 100 kHz.

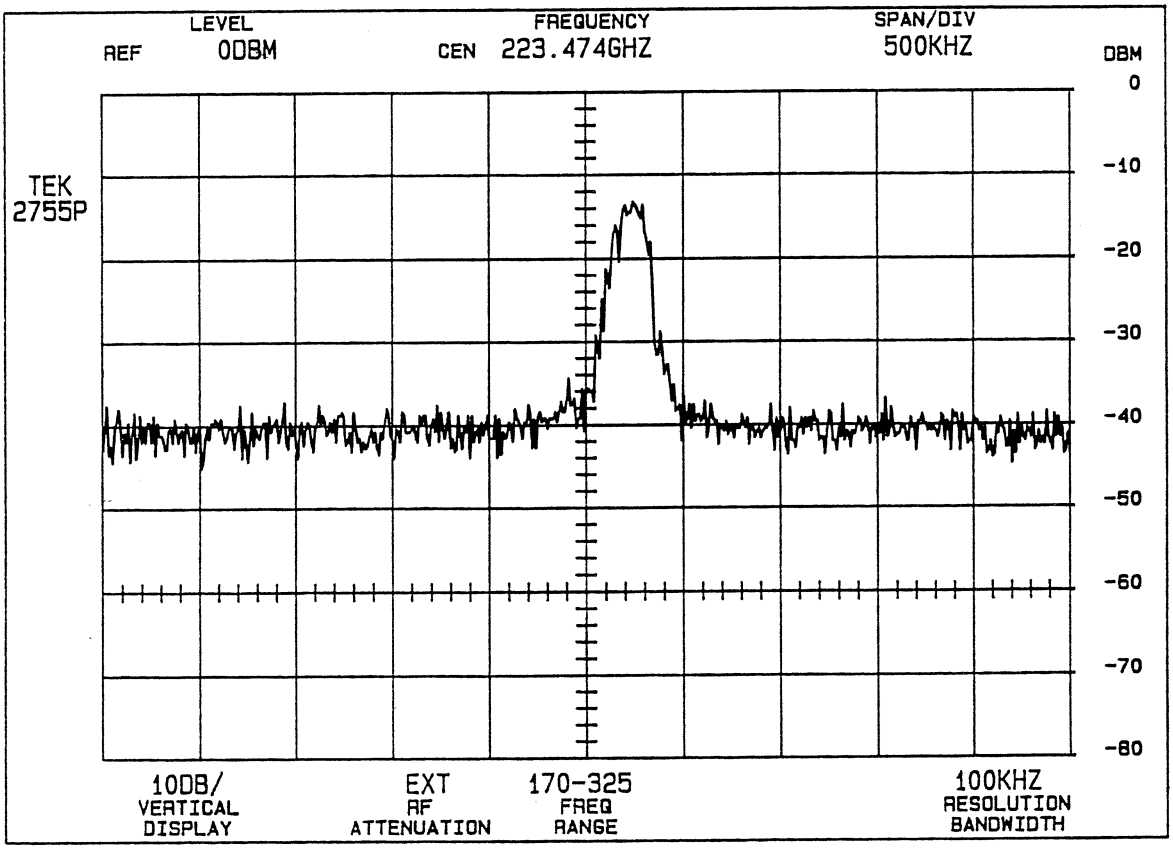

Fig. 12: Spectrum of a W-band TUNNETT diode free running oscillator in second harmonic mode, power level 0.2 mW, center frequency 223.474 GHz, vertical scale 10 dB/div, horizontal scale 500 kHz/div, BW 100 kHz.

A BACK-TO-BACK BARRIER-N-N+ (bbBNN) DIODE TRIPLER AT 200 GHz

Debabani Choudhury, Antti V. Räisänen, R. Peter Smith, and Margaret A. Frerking

Jet Propulsion Laboratory
California Institute fo Technology, Pasadena, CA 91109

ABSTRACT

This paper describes the performance of planar back-to-back Barrier-N-N+ (bbBNN) devices for mm- and submm wave multiplier applications. A technique has been developed for characterizing planar bbBNN devices with Vector Network Analyzer, which gives both the series resistance and voltage dependent capacitance of the device. Results show that bbBNN devices do not have a high series resistance like Barrier-Intrinsic-N+ (BIN) devices. Multiplication efficiency of bbBNN devices has been calculated using large signal analysis approach. A high C_{max}/C_{min} ratio is essential for high efficiency. The embedding impedance requirement has also been analyzed. So far, flange-to-flage tripling efficiency of 2.9% has been achieved using these planar devices in a 200 GHz crossed waveguide mount. The efficiency at the device is estimated to be about 6%. This is the first reported experimental result with a bbBNN waveguide frequency multiplier.

INTRODUCTION

To achieve the high sensitivity and spectrai resolution requirements of the submillimeter wave space missions, the baseline focal plane instrument consists of

heterodyne radiometers. In a heterodyne radiometer, a remote signal is downconverted to a much lower frequency by mixing with a local oscillator (LO) signal in a nonlinear device. Emphasis is placed on using technologies which are space qualifiable. The current approach is to use a solid state mm-wave Gunn oscillator driving a chain of multipliers to generate the desired frequency. One of the primary causes of failure in mm- and submm-wave mixers and multipliers is the whisker contact. Planar varactor devices are being developed to replace whisker contacted devices in order to improve the performance and ruggedness of spaceborne submillimeter wave heterodyne receivers [1]. One candidate is the planar back-to-back Barrier-N-N^+ (bbBNN) varactor device. It exhibits a very sharp change in its capacitance versus voltage resulting in very efficient harmonic generation with small input power levels. The bbBNN device has a symmetric C-V and an anti-symmetric I-V characteristics, thus generating only odd harmonics. Therefore, there is no need for an idler termination in the case of a frequency tripler. It is expected that bbBNN devices can be made to operate efficiently at frequencies over one terahertz [2-6]. Lower leakage current in these bbBNN devices provides an advantage over the conventional Schottky devices.

DEVICE DESCRIPTION

A conceptual diagram of the device is shown in Fig.1. It consists of several layers: the barrier, a sheet doping layer, a moderately doped layer and a highly doped region [6]. The layer thicknesses and compositions can be adjusted for optimum performance. When forward bias is applied, charge supplied by the sheet doping layer accumulates at the barrier, resulting in the maximum capacitance of the device, determined by the barrier thickness. When reverse bias is applied, the charge is depleted to the heavily doped n^+ region and the capacitance is minimum, determined by the barrier and the moderately doped region thickness. The architecture of the GaAs based BNN device presented in this paper is illustrated in Fig.2. The structure from the top surface down, is (i) a thin GaAs cap layer (optional), (ii) an AlGaAs layer that is sufficiently thick to preclude tunneling but sufficiently thin to allow a large capacitance per unit area (15 to 20 nm of $Al_{0.45}Ga_{0.55}As$ is typical), (iii) a highly doped (delta doped) region which introduce a built-in potential to ensure that the high capacitance mentioned above is achieved at zero voltage, (iv) a moderately doped GaAs drift/varactor region in which all of the doping can be depleted with little parasitic conduction to the metal contact

pads, and (v) a highly doped region that provides a low resistance path between the two metal contact pads. The fabrication process is described in details in [5].

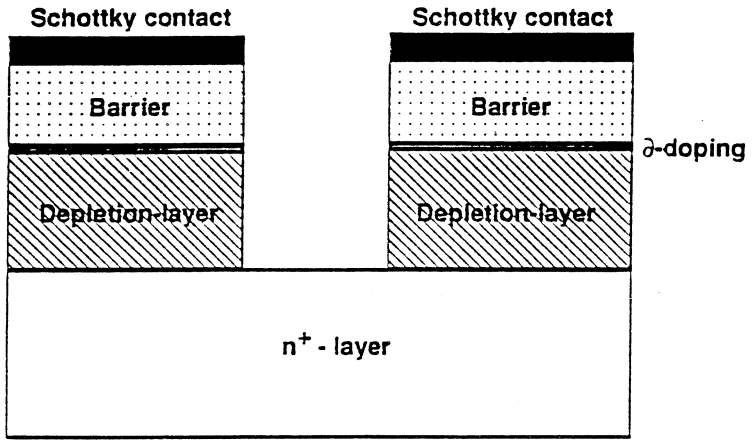

Fig.1 Back-to-back BNN varactor

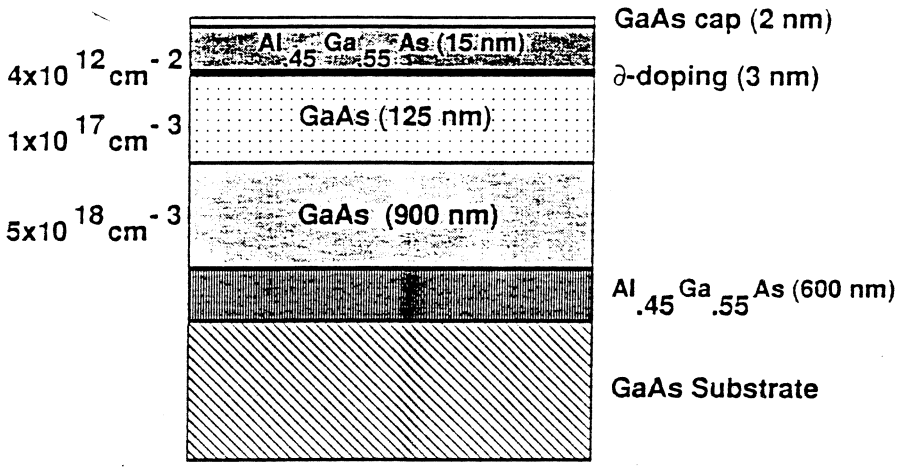

Fig.2 A typical MBE grown GaAs/AlGaAs layer structure for BNN diodes used in this study.

bbBNN VARACTOR CHARACTERIZATION

Devices were first characterized by measuring the current/voltage (I-V) and capacitance/voltage (C-V) characteristic at 1 MHz. Fig.3(a) shows the capacitance of a 2 μm X 4 μm device. Fig. 3(b) shows the DC leakage current, which is many orders of

magnitude lower than that for the conventional Schottky diodes. The series resistance of the device cannot be determined in the conventional way from the DC I-V curve. However, the remaining series resistance of some of these bbBNN devices were measured by shorting the device with an electric shock. With this technique, a DC resistance for several bbBNN devices was found to be between 7-14 Ω. This technique damages the device permanently and does not necessarily give the correct series resistance of an operating diode.

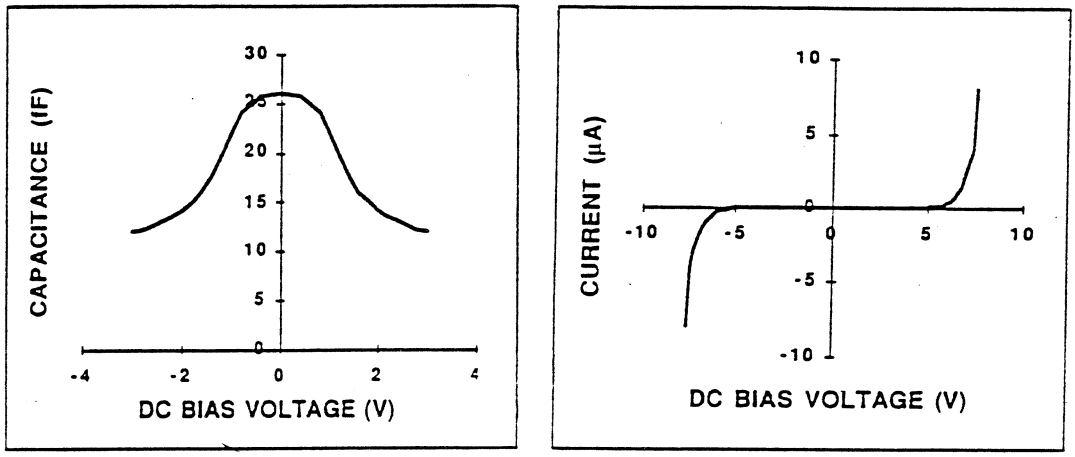

(a) (b)

Fig.3 Measured (a) C-V and (b) I-V characteristics of a 8 μm^2 bbBNN varactor diode.

In order to more accurately determine the series resistance, a special mount was designed for mounting the planar bbBNN devices to perform S-parameter measurements with a HP 8510C vector network analyzer. Measurements were done at 1-20 GHz with 10 dBm source level and 20 dB port attenuation. The bias voltage was varied from -3.0 V to +3.0 V. S11 of the device at different bias voltages was measured. The results were fitted with a linear equivalent circuit model using HP's Microwave Design System (MDS). This technique gives both the series resistance and the voltage dependent capacitance of the device. Fig. 4 shows a schematic diagram of the device mounted in a test mount (see also [7]). Fig.5 shows measured S11-response at two different bias voltages. Fig.6 illustrates the equivalent circuit of the test mount and the varactor device. Series resistance values of about 11-14 Ohm were measured using this technique for various devices having maximum capacitances of 25-60 fF.

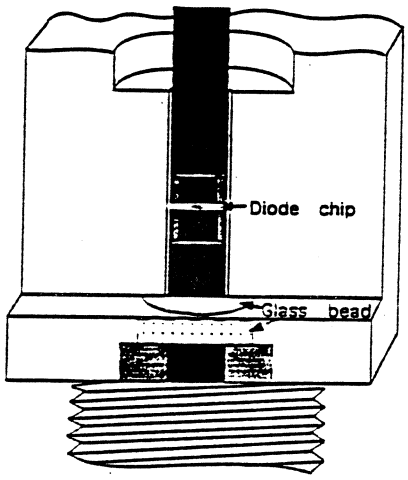

Fig.4 Schematic diagram of the planar bbBNN device in a test mount without the cover.

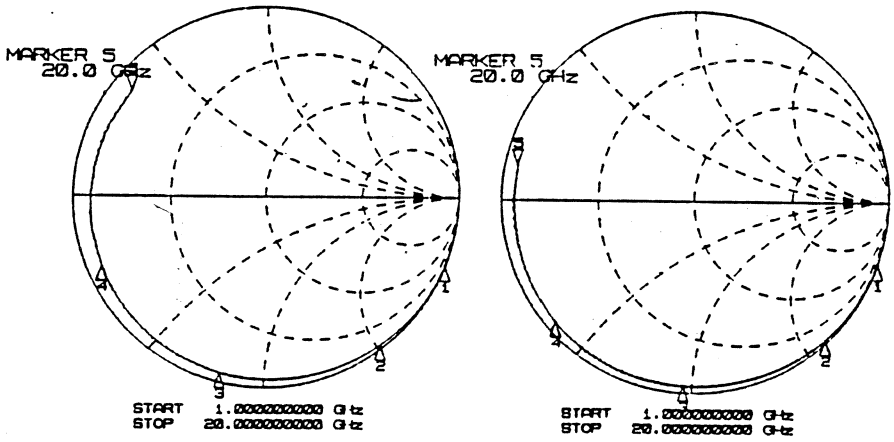

(a) (b)

Fig.5 Measured S11 - response at 1-20 GHz of the bbBNN device at (a) zero bias voltage and at (b) 2.0 volt (input reference plane inside the K-connector).

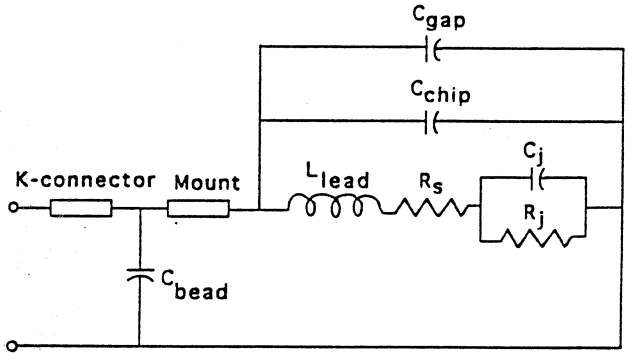

Fig.6 Equivalent circuit of the device in the test mount.

LARGE SIGNAL ANALYSIS

To achieve optimum performance of the device, it must be provided with the appropriate circuit embedding impedances. The impedances at the input and output frequencies must be set to maximize power coupling into and out of the device. The general circuit requirements are matched terminations at input and output frequencies, open circuited terminations at the higher harmonics and optimum reactive terminations at the idler frequencies.

A modified version of the nonlinear program by Siegel et. al [8], was used to calculate the tripling efficiency of the bbBNN devices. This analysis also optimized embedding impedance values. Measured C-V and I-V characteristics of a device with anode area of 8 μm^2 (as shown in Fig.3) were used to carry out large signal analysis of bbBNN devices. Since the series resistance is important in evaluating the device performance, calculations were carried out for a range of resistances. Fig.7 presents efficiency versus input power for a bbBNN tripler to 192 GHz with the series resistance of the device as a parameter. Theoretical efficiency is found to be high at low input power levels. Due to a very low leakage current, efficiency of the device does not degrade significantly when the measured I-V characteristic is included.

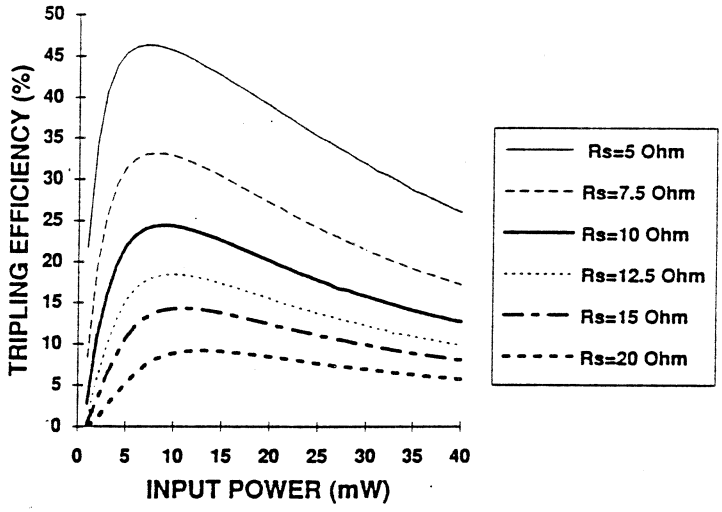

Fig.7 Calculated tripling efficiency at 200 GHz for bbBNN varactor with series resistance of the device as a parameter.

The effect of C_{max}/C_{min} ratio on the device tripling efficiency was also analysed using the large signal analysis approach. Fig.8 shows the tripling efficiency versus input power plot parameterized by the C_{max}/C_{min} ratio. Here, C_{max} is assumed to be 30 fF while C_{min} is changed. In practice this can be achieved by changing the epilayer thickness while the barrier thickness remains constant. The minimum capacitance is reached when the epilayer (in one of the back-to-back diodes) is completely depleted. The voltage required to fully deplete the epilayer depends on both the epilayer thickness and the epilayer doping. The width (FWHM) of the C-V curve was fixed by decreasing the epilayer doping to offset the effect of increasing the epilayer thickness. This has a minor effect ($\leq 1\ \Omega$) on the series resistance. In these calculations, the series resistance was assumed to be constant.

Calculated results (Fig.8) show that, the highest possible C_{max}/C_{min} value is desirable independent of the input power available.

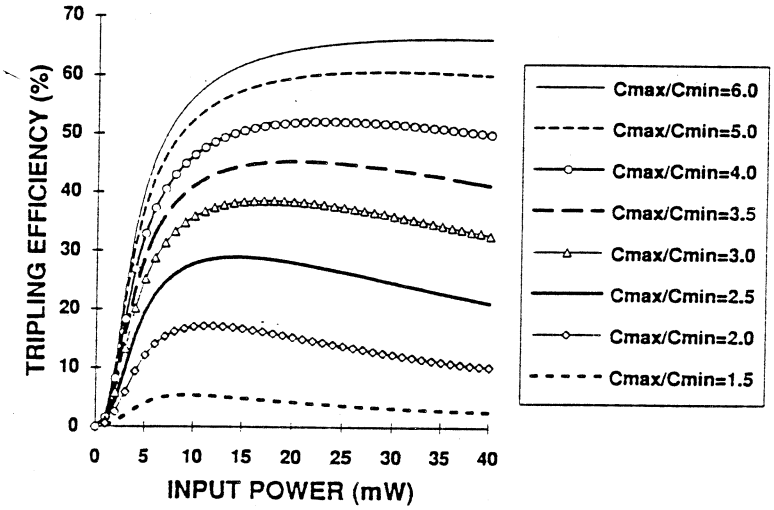

Fig.8. Tripling efficiency versus input power plot at 200 GHz parameterised by C_{max}/C_{min} (Rs=12.5 Ohm).

EXPERIMENTAL TRIPLER PERFORMANCE

The embedding impedances are provided to the planar bbBNN device by a crossed waveguide mount. A schematic of the crossed waveguide block of the 200 GHz mount is shown in Fig.9. The output waveguide in the mount is actually oriented

perpendicular to the plane of the paper.The planar bbBNN device is mounted spanning the output waveguide as shown in the diagram. The input waveguide is 0.148" x 0.074" and output waveguide is 0.039" x 0.010". The input power is coupled to the varactor in the output waveguide through a suspended substrate low-pass filter on a 76 μm thick quartz substrate. The filter prevents the second and third harmonic power from propagating back to the input waveguide and is a critical element in providing the proper embedding impedances to the varactor at the various harmonics. The output waveguide is cutoff at the fundamental and the second harmonic frequencies. Sliding backshorts in the input waveguide, in its E-plane arm and in the output waveguide as well as the proper design of the low-pass filter provide the possibility of partial optimization of the embedding impedances at the fundamental and third harmonic frequencies.

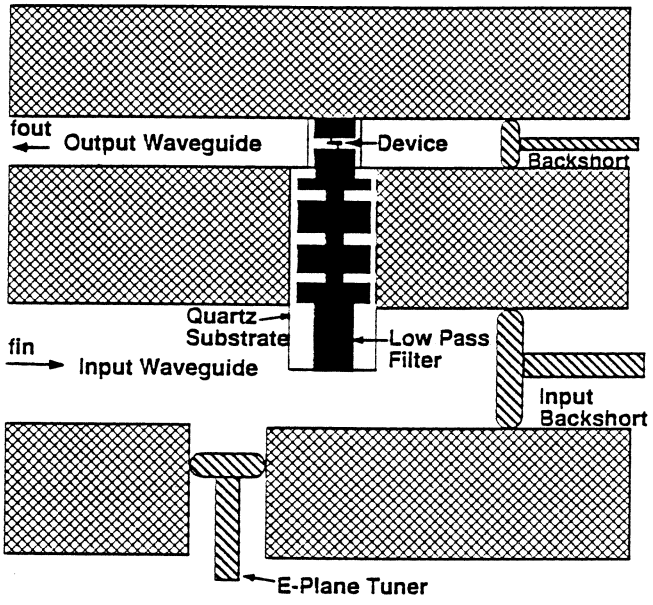

Fig.9 Schematic diagram of the 200 GHz tripler mount

The performance of the assembled tripler was measured using the set-up described in reference [9]. Backshorts and E-plane tuners were adjusted for best performance at each measurement frequency and each pump level. Fig.10 shows the measured flange-to-flange efficiency versus input power for the tripler at 188 GHz. The flange-to-flange efficiency of the tripler reaches its maximum value of 2.9% at 6 mW input power and then begins to decrease as the pump power level is increased.

In order to find out the embedding impedances available at the varactor terminals, a 20 times scaled model of the crossed waveguide mount was constructed.

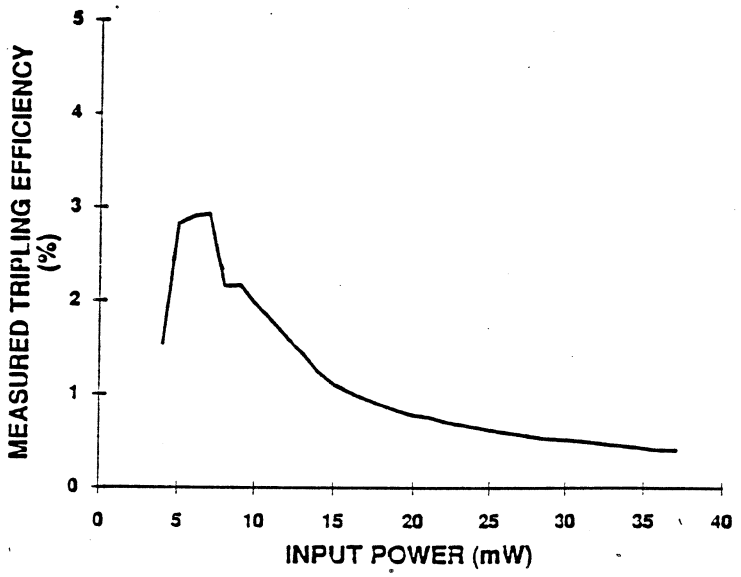

Fig.10 Measured tripling efficiency versus input power plot at 188 GHz.

The embedding impedances at the fundamental and its two higher harmonics were measured for variable mount parameters with HP 8510C vector network analyzer at 3-12 GHz. The end of a miniature coaxial cable (UT 34) was used as a probe to measure the impedances seen by the gap for the varactor diode. This technique is described in reference [10]. According to the measurements, this multiplier mount can provide a perfect impedance match at the fundamental frequency band of 60-70 GHz to any of our bbBNN devices. But, the behaviour of the third harmonic impedance at 180-210 GHz is less optimum. The output embedding impedance as a function of the output backshort position circles around the desired impedance region as shown in Fig.11. At frequencies above 200 GHz, there is a small leakage of the third harmonic signal back to the input waveguide. This is due to the suspended stripline quartz substrate of width of 635 μm which can support a parasitic waveguide mode in the filter channel.

Large signal analysis of the bbBNN device was also carried out with the available embedding impedances of the mount from the scale modeling. The effect of the third harmonic embedding impedances on the tripler efficiency was studied for five different available embedding impedance values obtained from scale model measurements (compare Fig.11). Fig.12 shows efficiency versus input power plots for the bbBNN tripler with the third harmonic embedding impedance of the mount as parameter. The embedding impedance at the fifth harmonic was found to have insignificant effect on the tripler efficiency.

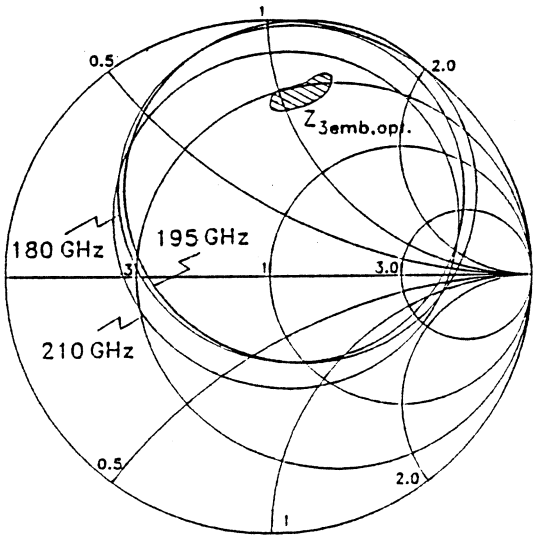

Fig.11 Smith chart showing third harmonic embedding impedances versus backshort positions obtained from the scaled model measurement of the multiplier.

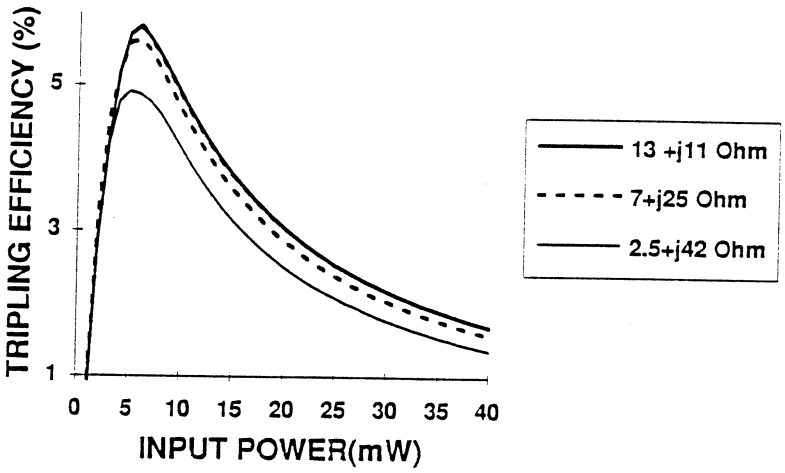

Fig.12 Calculated tripling efficiency to 188 GHz for bbBNN varactor with third harmonic embedding impedance of the crossed waveguide mount as a parameter.

Based on previous measurements of the mount (see ref. [9]), losses in the input and output waveguides and the filter are about 45%. Hence, the measured efficiency at the diode is estimated to be near 6%. This is in excellent agreement with the calculations taking into account the mismatch loss shown in Fig.12.

CONCLUSIONS

At 200 GHz, a flange-to-flange tripling efficiency of 2.9% has been obtained using planar bbBNN devices, with efficiency at the diode of about 6%. This is the first reported experimental result with a bbBNN waveguide frequency multiplier. A new technique has been developed to characterize the C-V curve and series resistance of these devices using automatic network analyzers. Measured device characteristics compare very well with those using other techniques. bbBNN varactor devices are found to have low series resistance compared to BIN devices [11]. Highest possible C_{max}/C_{min} value is also desirable for these devices. High efficiency at low input power levels makes these devices very attractive for submillimeter wave frequency multiplier applications.

ACKNOWLEDGEMENTS

The research described in this paper was carried out at the Center for Space Microelectronics, Jet Propulsion Laboratory, California Institute of Technology, under contract with the National Aeronautics and Space Administration, Office of Aeronautics, Space and Technology. Authors would like to thank Mark Natzic for mounting the device in the waveguide mount and Peter H. Siegel for various useful suggestions. Authors also would like to thank Suzanne Martin for her help in the device fabrication and John Liu for growing the bnn wafers using the MBE technique.

REFERENCES

1] W.L. Bishop, E.R. Meiburg, R.J. Mattauch and T.W. Crowe,'A micron thickness planar Schottky diode chip for terahertz applications with theoretical minimum capacitance', 1990 IEEE MTT-S Int'l Microwave Symposium Digest, vol.III,pp.1305-1308.

2] T.J.Tolmunen and M.A.Frerking,'Theoretical performance of novel multipliers at millimeter and submillimeter wavelengths', Int'l Journal of Infrared and Millimeter Waves, vol.12, no.10, pp.1111-1133, 1991.

3] M.A.Frerking and J.East,'Novel heterojunction varactors', Proceedings of IEEE, vol.80, no.11, pp.1853-1860, Nov. 1992.

4] A.V.Räisänen, 'Frequency multipliers for millimeter and submillimeter wavelengths', Proceedings of IEEE, vol.80, no.11, pp.1842-1852, Nov. 1992.

5] R.P.Smith, D.Choudhury, M.A.Frerking and S.Martin, 'A new fabrication technique for back-to-back varactor diodes', Preoceedings of Third International Symposium on Space Terahertz Technology, pp.158-163, March.24-26, 1992.

6] U.Lieneweg, T.Tolmunen, M.Frerking and J.Maserjian,'Design of planar varactor frequency multiplier devices with blocking barrier', IEEE Trans. on Microwave Theory and Tech.,Special Issue on THz Tech., vol.40, no.5, pp.839-845, May 1992.

7] O.Boric, T.J.Tolmunen, E.L.Kollberg and M.A. Frerking,'Anamolous capacitance of quantum well double-barrier diodes', Int'l Journal of Infrared and Millimeter Waves, vol.13, no.6, pp.799-814, 1992.

8] P.H.Siegel, A.R.Kerr and W.Hwang,'Topics in the Optimization of Millimeter-wave Mixers', NASA Tech. Paper 2287, 1984.

9] D.Choudhury,M.A.Frerking and P.D.Batelaan, 'A 200 GHz single barrier varactor tripler', IEEE Trans. on Microwave Theory and Technique, Mini-Special Issue on Space Terahertz Technology, 1993. (to be published).

10] A.V.Räisänen, W.R.McGrath, D.G.Crete and P.L.Richards,'Scaled model measurements of embedding impedances for SIS waveguide mixers', Int'l Journal of Infrared and Millimeter Waves, vol.6, no.12, pp.1169-1189, 1985.

11] R.J.Hwu and L.P.Sadwick,'Limitations of the back-to-back barrier-intrinsic-n^+ (BIN) diode frequency tripler', IEEE Transactions on Electron Devices, vol.39, no.8, pp.1805-1810, August 1992.

A High Power Doubler for 174 GHz Using a Planar Diode Array

N.R. Erickson
Five College Radio Astronomy Observatory
Dept. of Physics and Astronomy
University of Massachusetts

and

B.J. Rizzi and T.W. Crowe
Semiconductor Device Laboratory
Dept. of Electrical Engineering
University of Virginia

ABSTRACT

A balanced doubler for 174 GHz has been built using a planar array of four varactor diodes. The maximum output power is 55 mW, and this power is limited only by the available pump source. The peak efficiency is 25% at 150 mW input, with little saturation at higher power levels. Circuit parasitics due to the chip are not serious, and device heating is not predicted to be large at the present power levels. Higher efficiencies should be possible with minor improvements in the diode parameters.

INTRODUCTION

In the frequency range above 100 GHz, frequency multipliers can achieve high conversion efficiency at low input power, but tend to saturate in output at a rather low output power. The saturation mechanism is believed to be due to the limited carrier velocity in the GaAs epitaxial layer [1], which leads to a maximum displacement current in the varactor. This causes the efficiency to decrease rapidly above a critical power (when the peak displacement current reaches the saturated value), despite the classical prediction of increasing efficiency up to the reverse breakdown limit. Since the current increases with frequency for a given voltage swing, this becomes a major limitation for submillimeter applications. Because the saturated carrier velocity is not easily increased, except in some applications by operating at reduced temperature [2], the only alternative is to decrease the current density, through the use of several diodes or diodes with a larger area. One partial solution has been to build balanced doublers using a pair of whiskered diodes [3], but this is not extendible to larger numbers of diodes.

One of the most attractive approaches is to use series arrays of diodes, because they allow one to increase both the area and the number of diodes, while they may be treated as a single diode so far as circuit design is concerned. In an array having the same impedance level and total power handling as a single diode, the current density varies inversely with the number of diodes. Alternatively, for the same breakdown voltage per junction, the power handling increases as the number of diodes squared. While series arrays are quite impractical using whiskered diodes, they are readily fabricated using planar technology. The doubler described in this work, operating with an output frequency near 170 GHz, uses four planar diodes fabricated on a single chip. It produces two times the output power of a two diode whisker–contacted doubler at a similar frequency, clearly demonstrating the potential for such arrays.

DIODE DESIGN AND CHARACTERIZATION

The doubler circuit used is based on the balanced doubler of Erickson [3]. This circuit was chosen because it operates with very high efficiency, and is also quite simple to fabricate. Thus an initial design constraint was that the chip must fit into this multiplier mount. Diodes for this work were fabricated using the surface channel process [4], with the four diodes laid out as a linear array of discrete devices. The diode is shown in Fig. 1, with

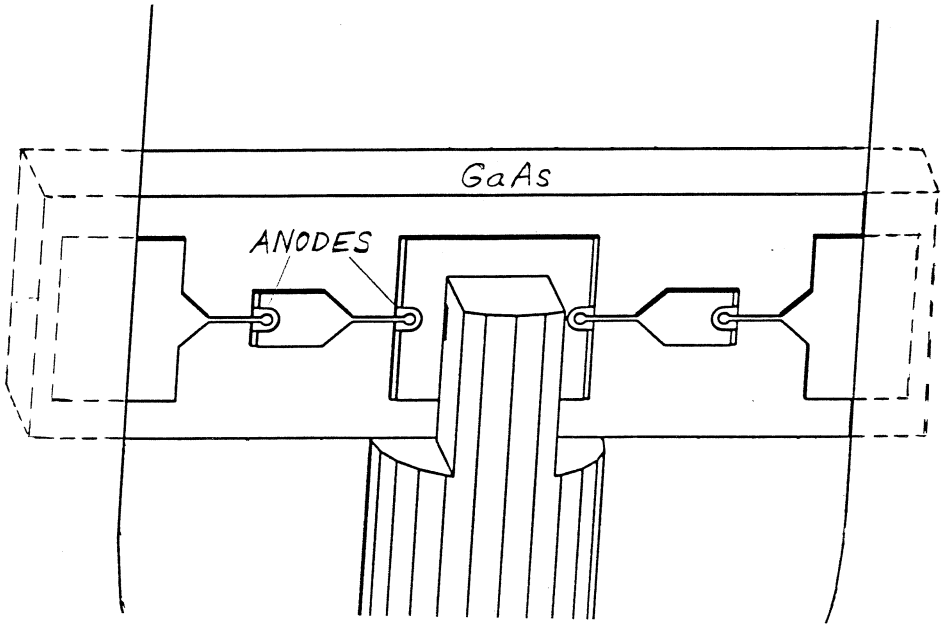

Fig. 1. Planar diode array, showing the method of installation into the circuit. The dashed ends are soldered to the input waveguide walls, while the center pad solders to a pin connecting to the output waveguide. Chip is 800x225x25μm, waveguide is 635μm high.

the connections to the doubler mount at three points. The large central pad serves as the ohmic contact for the two central diodes, as well as the output terminal. The ohmic contacts for the end diodes are the two small inner pads. The end pads are sized to permit the chip to be soldered to the top and bottom walls of the waveguide. In the absence of any detailed knowledge of the device parasitics, an effort was made to maximize the circuit inductance within the chip, since the whiskered doubler worked well with rather long whiskers (0.25 mm of 12 μm wire). After the restrictions of overall waveguide height, ohmic pad size, and central bond pad size were satisfied, the inductive "finger" length ended up being rather short. However, this geometry is easily fabricated and was adopted for initial tests of the concept. The necessity to include inductance within the chip makes planar varactors somewhat tuned to a specific frequency, while the fixed length makes them well suited only for a particular waveguide mount. Thus their advantages over whiskered diodes are partially offset by a reduced flexibility in their application.

The junction capacitance of each anode was chosen to be twice the junction capacitance of a single whiskered diode (U.Va. type 6P2) as used in the earlier balanced doubler [3]. This produces the same total capacitance as that of a single whiskered diode, about 20 fF. Breakdown voltage is less important because it is not the only limitation on useful power input in the presence of current saturation, and in this case, the available pump power required a breakdown voltage of only ~15 V. To optimize the diode parameters, the epitaxial layer doping was increased and the layer thickness decreased to achieve a lower series resistance, with a resulting reduction in V_b per junction, relative to the whiskered diodes.

Diode parameters were measured carefully to compare results with theory. DC measurements of the series resistance of diodes tend to be affected by heating of the junction, which depresses the voltage at the highest current. This lowers the measured resistance, relative to the true value. One way to avoid this difficulty is to measure the voltage immediately following the application of a fast rising pulse, but this requires special equipment. An alternative method is to make small signal resistance measurements at frequencies well above the thermal time constant of the diode using an error corrected vector network analyzer. The resistance of the diode is measured over a range of bias currents and is then fit to a behavior law:

$$R = 1/\alpha I + R_s, \text{ where } I/I_o = e^{\alpha V} - 1,$$

and $1/\alpha I$ is the small signal resistance of the ideal diode junction. The exponential slope, α, is determined from the low current portion of the IV curve measured at dc, leaving only the one free parameter R_s to be determined. In this work, the series resistance of the parallel combination of the two pairs of diodes (equivalent to a single diode) was measured in the doubler mount using an HP 8720 network analyzer at 130 MHz. Small signal (–25 dBm) impedance data were taken over a range of dc bias currents up to 50 mA. The accuracy in these measurements is ~0.1Ω for the lower impedances. The data is shown in Fig. 2, which also shows a line at the best fit value of 6.4 Ω. This contrasts to a dc value of 5.2 Ω. There is evidence for an increase in R_s by about 0.5 Ω at 50 mA (~25 mW per diode), due to heating of the junction, but this should not lead to serious problems at the highest dissipated power levels of 50 mW/jct. The resistance at the lower current values shows an increase due to the amplitude of the test port signal, which is no longer a "small signal" at the lower bias currents. Applying this signal raises the diode impedance below 5 mA, but this bias region is not essential to determine R_s.

The capacitance of each junction was measured over the range 4–10 GHz using a transmission measurement between two Cascade wafer probes, with the transmission amplitude measured with an HP 8510B network analyzer. These probes had two conductors

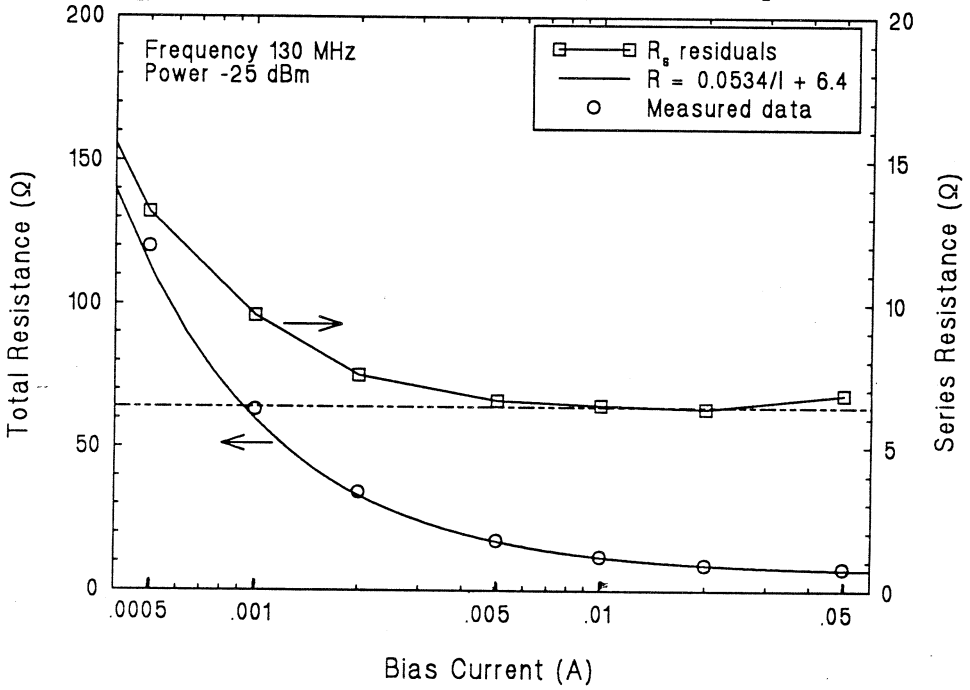

Fig. 2. Microwave resistance vs. bias current for the planar diode array. The lower curve is a fit to the data, while the upper curve shows the residuals after subtraction of the ideal diode resistance. Resistance data below 5 mA is affected by the test signal level. The dashed line is at the best fit value of 6.4 Ω.

(ground and signal) separated by 150 μm. The signal pad of each probe contacted either end of the diode under test while the grounds were connected by a parallel metal strip 30 μm from the diode chip. This transmission mode was used to enhance the accuracy of the pad–to–pad capacitance measurement, which is much less affected by probe self coupling than a single probe shunt determination. The accuracy in this measurement is ±0.2fF. Measurements of a diode with broken air bridges showed the pad to pad contribution to be 9.7 and 11 fF between the pads of the outer and inner diodes respectively. An additional capacitance of 2 fF is found between the inner and outer pads of the series pair. The remaining capacitance, assumed to be due the junction, is 38 fF, varying by ±1 fF for a range of diodes probed. The C/V characteristic of this diode is shown in Fig. 3. This data was then fit to a power law dependence of the form:

$$C(V) = C(0)/(1+V/\varphi)^{\gamma} + C_p.$$

where φ is the built in potential and C_p is a parasitic capacitance adjacent to the anode. The data can be fit by a $\gamma = 0.4$ law assuming $C_p = 0$. As an alternative, the data can also be fit by a $\gamma = 0.5$ law if one assumes that $C_p = 4$ fF. The $\gamma = 0.5$ fit is mathematically better, but there is no way to measure the parasitics very close to the anodes to verify this, and the value seems much higher than the 1–1.5 fF that is estimated from the structure.

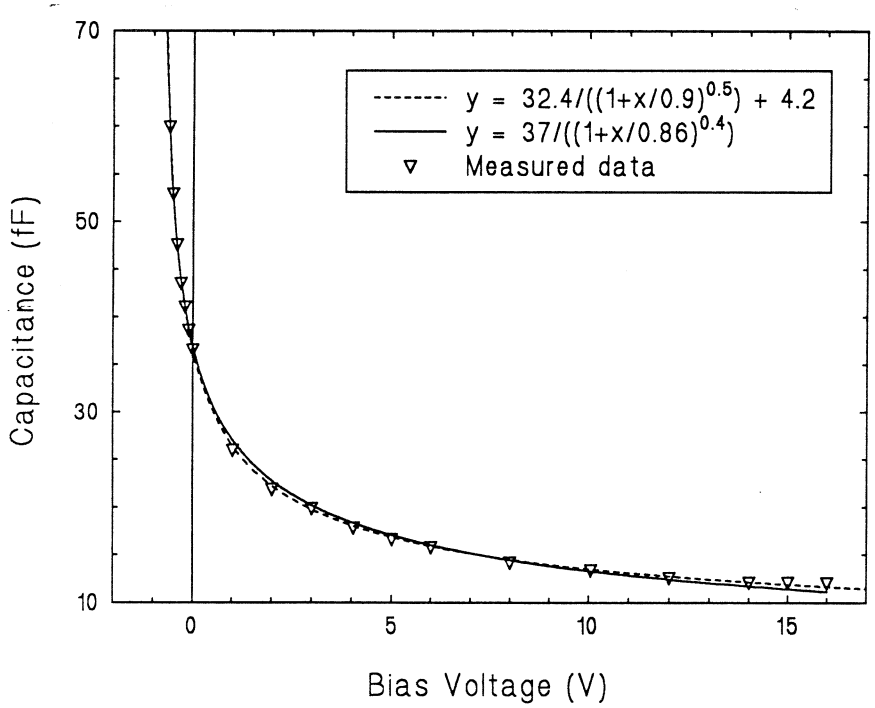

Fig. 3. Capacitance vs. voltage for one anode in the planar array.

The parasitics of the diode in an actual circuit are caused by both the pad to pad capacitance and the circuit loading by the GaAs substrate. In neither case do these cause a loss of efficiency, but they do affect the impedance matching, and the maximum useful bandwidth of a circuit. Pad–to–pad capacitance can be minimized by reducing the ohmic pad area between each series pair. The other three pads become part of the actual circuit and their areas are not critical. It is important to equalize the parasitics for each diode to achieve an equal power balance, and the present chip needs some small refinement in this respect. Circuit loading can be reduced by thinning the substrate, or by substituting a lower dielectric constant substrate such as quartz. This latter substitution would also reduce the pad–to–pad capacitance. However, the high dissipated power in varactors requires a careful study of the thermal resistance of the substrate before this can be done.

DOUBLER MOUNT AND TESTS

The doubler design is electrically equivalent to that in [3], but was redesigned for use with planar diodes. A cross section is shown in Fig. 4. All the waveguides were milled symmetrically about the center line with the coaxial sections milled with a square outer section. The pin connecting to the diode center pad is supported in one half of the block by Macor [5]. The diode is soldered to the waveguide top and bottom walls as well as to the center pin in one operation, in which the entire block is heated to 120 C. The chip is

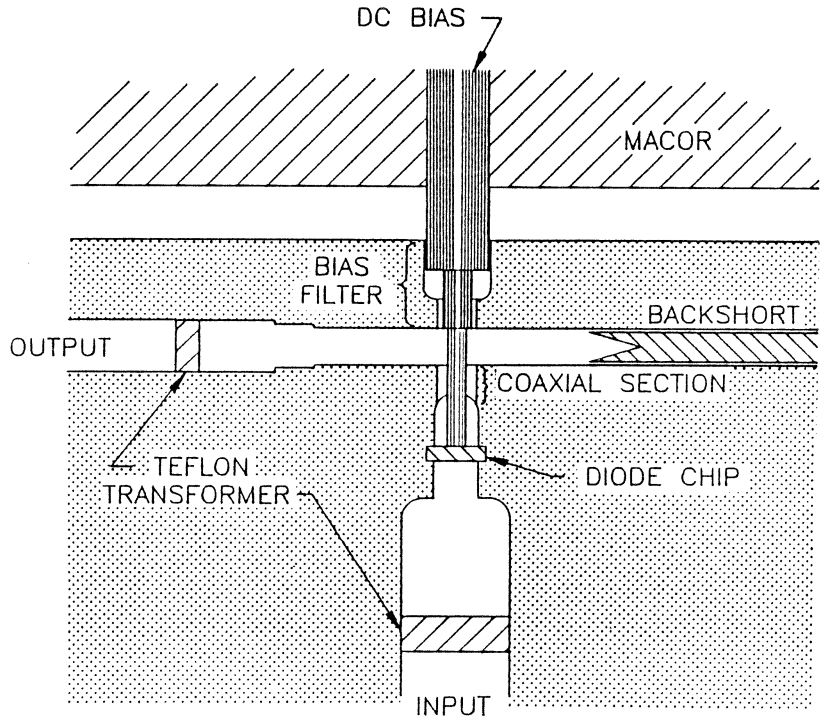

Fig. 4. Cross section through the balanced doubler mount.

unsupported except by the solder joints, but despite its apparent fragility, the structure is robust mechanically. Since the diode is face down in the soldering operation, centering of the contacts is difficult, but is aided by viewing the bottom surface in a mirror in the bottom of the waveguide.

Initial tests were made with an 80 mW Gunn oscillator source at 82 GHz, yielding an efficiency of 21% at 16.5 mW output, but these tests showed that the peak efficiency was at higher power. A klystron oscillator was then used to determine the high power behavior, but this tube produced its maximum power of 250 mW only at 87 GHz. For these tests, the input and output match were optimized using teflon quarter–wave transformers positioned in the waveguide so that the output power was maximized. These transformers can correct a maximum VSWR of:

$$\epsilon(\text{teflon})[\lambda_g/\lambda(\text{air}) \;/\; \lambda_g/\lambda(\text{teflon})]^2 \cong 2.9 \text{ (typically)}.$$

The improvement in power with the addition of the output transformer was only about 10%, meaning that the output match was very good. The input reflected power could be measured with a coupler and was 8% at 87 GHz. Bias voltage at ~250 mW input was 11–12 V, with 0.5 mA forward current. Data for the power output and efficiency vs input power, with the bias optimized at each point, are shown in Fig. 5. This shows that the

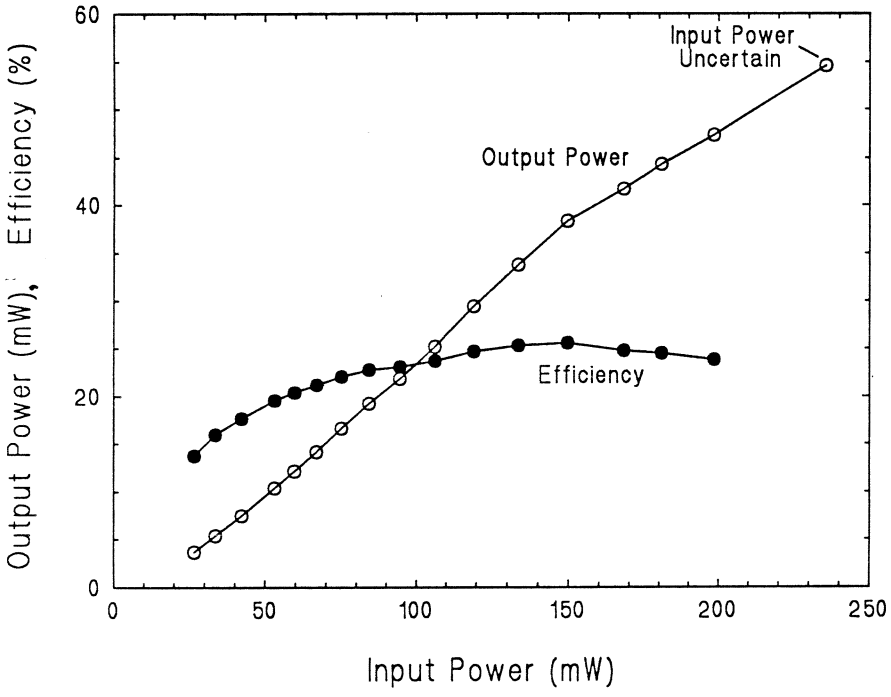

Fig. 5. Output power and efficiency for the planar array at 174 GHz output.

efficiency peaks at ~150 mW input, and has only fallen slightly by 180 mW, which is the theoretical reverse breakdown limit. Thus current saturation appears to have only a minor effect. The peak efficiency is 25% and probably would be 26–27% with a perfect input match.

The peak output power is 55 mW at an estimated input power of 240–250 mW (all other input powers were measured with a directional coupler which was removed for this final test). Input and output power calibrations were obtained with the same calorimeter built in WR–12 waveguide [6]. This maximum output power is over a factor of two higher than the previous best doubler result at a nearby frequency, and may be comparable to that available from any spectrally pure CW source. Fig. 6 shows the comparison of the array with the best previous result using a pair of whisker contacted diodes. The array shows very much less saturation, as well as operation at higher power, but its peak efficiency is lower.

The theoretical efficiency of the diode (assuming $\gamma = 0.4$, $R_s = 7\Omega$, $C_j(0) = 38$fF) is 33% at an input power of 160 mW, corresponding to the measured efficiency peak. This is somewhat less than the breakdown limit of 180 mW. The efficiency predicted for $\gamma = 0.5$ would be 40%, if the excess capacitance of 4 fF is entirely outside the series resistance.

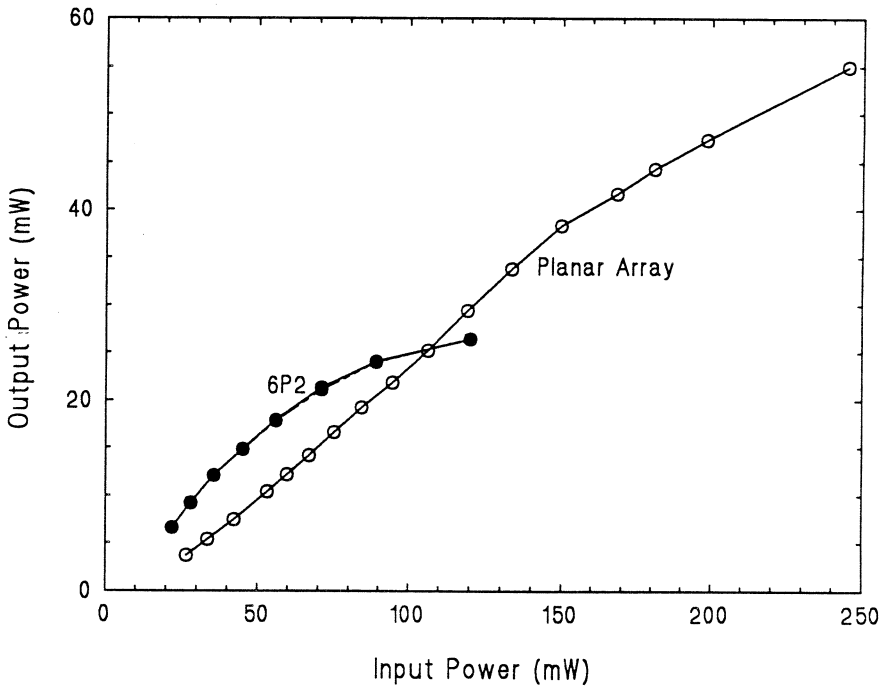

Fig. 6. Comparison of the planar doubler with a whisker contacted model. Planar array data is at 174 GHz, while the 6P2 data is at 158 GHz.

Assuming the former case, then the efficiency is consistent with 1 dB loss within the doubler block. This is consistent with the losses expected for the mount, but is rather uncertain, since there is no way to directly measure the mount losses. The data at the highest power levels is well above the classical reverse breakdown limit, but as is typical for varactors, the efficiency rolls off slowly in this region.

The quality of the impedance match that was achieved is comparable to that with whiskered diodes in the comparable mount, indicating that the parasitics of the planar diode with 25 μm substrate are small in the real circuit. Matching becomes much worse with diodes on 100 μm substrates, so thinning the GaAs appears to be important for wideband applications. This is discussed from a theoretical viewpoint in ref [7] in this same digest. In these high power applications, thermal considerations may prevent much further reduction of the substrate thickness. The thermal resistance of each junction is estimated to be 800 C/W, assuming most of the conduction is through the substrate rather than the metalization, leading to a peak temperature rise of 40 C for the junctions near the center of each span, and somewhat less for those next to the central pad.

CONCLUSIONS

We have demonstrated the first application of a planar array of diodes in the mm–wave range, and have achieved the highest output power from a frequency doubler in the 170 GHz range. The multiplier behavior is largely free of saturation effects, while the efficiency is only somewhat lower than that achieved with whiskered diodes. It appears that higher efficiency should be obtained with this type of diode if a better C/V modulation can be achieved. The series resistance is also higher than for the whiskered equivalent diode, so there is improvement possible there as well. This type of diode array seems well suited for use at even higher frequencies, where current saturation becomes a much more serious problem, and a new diode and doubler are being designed for use at ~300 GHz.

REFERENCES

[1] E.L. Kollberg, T.J. Tolmunen, M.A. Frerking and J.R. East, "Current Saturation in Submillimeter Wave Varactors," IEEE Trans. Microwave Theory Tech., Vol MTT–40, pp. 831–838, May 1992.

[2] J. Louhi, A. Raisanen, and N.R. Erickson, "Effect of Cooling on the Efficiency of Schottky Varactor Frequency Multipliers at Millimeter Waves," Proc. Third Int'l. Symp. Space THz Tech., Ann Arbor, MI., pp 134–145, Mar. 1992.

[3] N.R. Erickson, "High Efficiency Submillimeter Frequency Multipliers," 1990 IEEE MTT–S Int'l. Microwave Symp. Dig., Dallas, TX, pp. 1301–1304, May, 1992.

[4] W.L. Bishop, T.W. Crowe, R.J. Mattauch and P.H. Ostdiek, "Planar Schottky Barrier Mixer Diodes for Space Applications at Submillimeter Wavelengths," Microwave and Optical Technology Lett., Vol. 3, No. 1, pp. 44–49, Jan. 1991.

[5] Macor machinable ceramic, Corning Glass, Corning, N.Y.

[6] B. Vowinkel, "Broad–Band Calorimeter for Precision Measurement of Millimeter– and Submillimeter–Wave Power," IEEE Trans. Instrum. Meas., IM–29, pp. 183–189, 1980.

[7] J. Tuovinen and N.R. Erickson, "Finite Element Analysis of a Planar Doubler," this symposium proceedings.

Planar Varactor Diodes for Submillimeter Applications

Brian J. Rizzi, Kristan K. Rausch, Thomas W. Crowe, Philip J. Koh, William C.B. Peatman,
J. Robert Jones, Stephen H. Jones and Gregory Tait
Semiconductor Device Laboratory
Department of Electrical Engineering
Thornton Hall
University of Virginia
Charlottesville, VA 22903-2442

I. INTRODUCTION

Schottky barrier varactor diodes are used as frequency multipliers to supply local oscillator power for heterodyne receivers at millimeter and submillimeter wavelengths. Whisker contacted GaAs Schottky varactor diodes are the most common high-frequency multiplier element in use today. They have been used in heterodyne receivers to frequencies as high as 700 GHz for ground based, airborne and space applications [1,2,3,4,5]. Although the whisker contacted Schottky varactor diodes have proven very effective, there remains great interest in developing technologies which are more mechanically robust, have the potential to deliver larger amounts of power and are capable of operating well into the submillimeter wavelength range. This paper reviews the work at the University of Virginia on planar varactor technology for millimeter and submillimeter wavelength applications.

A multiplier chain to 1 THz using planar varactor diodes is being developed. The system consists of two doublers (80 to 160 GHz and 160 to 320 GHz) and a tripler (320 to 960 GHz). In Section II planar Schottky barrier varactor diode development is reviewed. An important goal is to demonstrate that planar diodes can replace whiskered devices without degrading performance. Preliminary results for a diode designed to replace the very successful U.Va.-6P4 whisker contacted diode are presented.

The doubler chips for the 1 THz multiplier chain incorporate multiple diodes for increased power handling ability, and are designed to be used in a balanced doubler circuit designed by Erickson [4]. The RF results for the 160 GHz doubler and the prototype design for the 320 GHz doubler are presented in Section III.

Developing a tripler to 1 THz is the most challenging part of the multiplier chain. The best devices today for this application are whiskered contacted Schottky diodes. To develop a planar tripler chip, we need to investigate novel varactor structures. A number of devices are being investigated as potential frequency doublers and triplers, and this work is presented in Section IV. An anti-series δ-doped varactor pair designed for tripling to 200-300 GHz is discussed first. This device technology is being evaluated as a potential tripler to 1 THz. A 2-DEG/Schottky varactor diode to be used as a frequency doubler has also been developed, and initial RF results are presented. Heterostructure barrier varactors are being investigated with emphasis on two material systems, GaAs/AlGaAs and GaAs/InGaAs/AlGaAs. Section V is a summary of the planar varactor diode work.

II. PLANAR SCHOTTKY BARRIER VARACTOR DIODE DEVELOPMENT

An initial goal in our development of planar Schottky barrier varactor diodes is to fabricate a planar device to replace the 6P4 diode, a very successful whiskered varactor diode used for doubling in the millimeter wavelength range. The parameters of this device are shown in Table I.

Prototype planar varactor diodes have been fabricated using the surface channel procedure [6,7,8]. A sketch of the surface channel structure is shown in Fig.1. The most challenging aspect of designing planar varactor diodes is reducing the shunt capacitance which is due mainly to the fringing field between the two contact pads. This added capacitance degrades the multiplier performance considerably. In addition, the anode contact finger length is fixed so device inductance cannot be tuned as it can be with a whiskered diode whose whisker length can be varied.

The first prototype planar varactor is designated SC6T1. Its parameters are also listed in Table I. Although this diode was designed as a replacement for the 6P4, its series resistance is substantially higher than the 6P4's, and the planar diode has a very large parasitic shunt capacitance of 12 fF. Preliminary RF measurements have been disappointing. A second generation device has been designed and fabricated with characteristics closer to those of the 6P4. An SEM photograph of the new device, designated SC6T2, is shown in Fig. 1, and the diode parameters are listed in Table I. The series resistance of the second batch of devices was decreased by reducing the epitaxial layer thickness and increasing the epitaxial doping density at the expense of a reduced breakdown voltage.

The shunt capacitance of the SC6T2 diodes was reduced to approximately 3-5 fF by shrinking the pad dimensions and increasing the pad separation. The pad size has been reduced to 30 μm x 60 μm, which is about the minimum size to which most users feel comfortable making a solder contact. Further reductions in pad size are also limited by the SnNi/Ni/Au ohmic contacts which have resistivities of $10^{-5}\Omega cm^2$ or slightly less. The SC6T2 diodes also have several finger lengths, ranging from 50 - 150 μm, which allows evaluation of RF performance as a function of pad-to-pad capacitance and finger inductance.

A tripler mount designed for whisker contacted diodes at the National Radio Astronomy Observatory has been obtained, and modified slightly to allow testing of planar diodes [9]. In Fig. 2 preliminary RF results for the SC6T2 planar varactors and 5M2 whiskered diodes (for which the mount was designed) are presented. It can be seen from the data that the efficiency of the SC6T2 diode increases as the 5M2 efficiency

Table I: Schottky Barrier Varactor Diodes

batch #	type	t_{epi} (μm)	N_{epi} (cm^{-3})	diam (μm)	C_{j0} (fF)	C_{shunt} (fF)	R_s (Ω)	V_{bkdn} (V)
6P4	whiskered	1.0	$3x10^{16}$	6.0	20	-	9.5	20
SC6T1	planar	1.3	$2x10^{16}$	6.2	20	12	20	30
SC6T2	planar	0.86	$4x10^{16}$	6.0	25	3-7	6	15

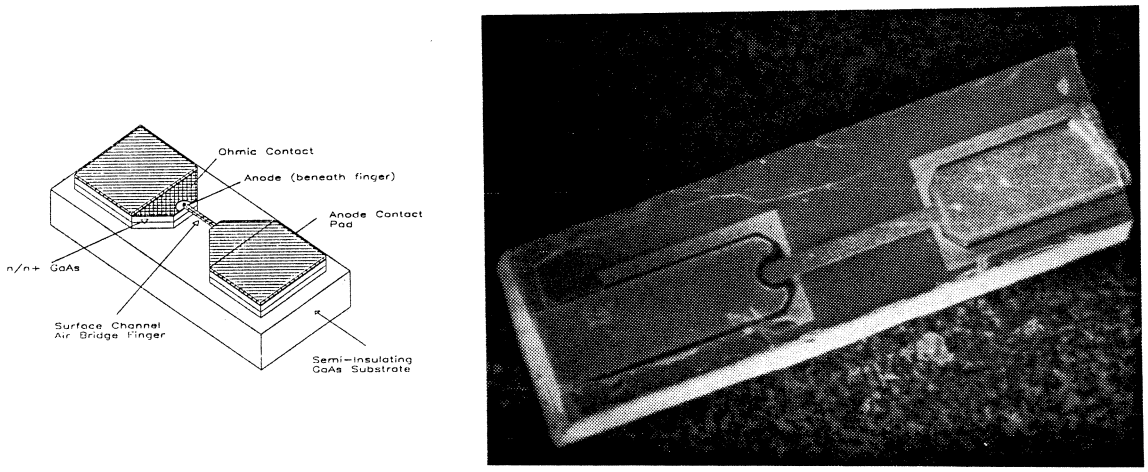

Fig. 1: SEM photo of SC6T2 varactor and sketch of the surface channel diode.

decreases at an output frequency of approximately 250 GHz. This indicates the SC6T2 diode may be most efficient at higher frequencies. New diodes will be fabricated which have higher junction capacitances, in an attempt to produce an improved match to the existing mount. Further evaluation will also be done to determine the optimum finger length at a given frequency for this multiplier. These RF results indicate that the SC6T2 is a comparable frequency multiplier to the 6P4 diode at millimeter wavelengths. However, the optimized RF performance will only be achieved when the planar diodes are used in a mount that is specifically designed for these devices.

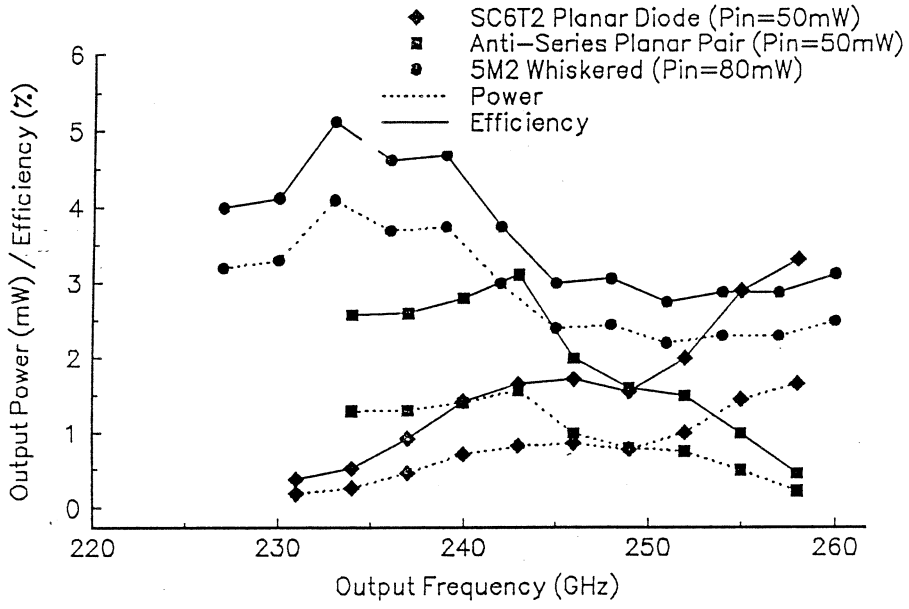

Fig. 2: SC6T2 RF performance.

III. PLANAR VARACTOR DIODES FOR BALANCED DOUBLING

In the proposed 1 THz multiplier chain, the first stage is a doubler from 80 to 160 GHz. This multiplier is designed to handle large input powers while remaining an efficient device so that it can generate as much power as possible to drive the second stage multiplier. A planar doubler chip has been developed that is based upon the balanced doubler of Erickson, which delivers up to 25 mW at 160 GHz using two whiskered varactor diodes [4].

The planar doubler chip consists of four GaAs Schottky varactor diodes, with a series diode pair for each leg of the balanced doubler. A scanning electron micrograph of the chip is shown in Fig. 3. Series diodes were used in an attempt to increase the power handling of the doubler chip, since the breakdown voltage of the diode pair is twice that of a single diode.

Four batches of doubler chips have been fabricated, and their design parameters and dc characteristics are listed in Table II. The junction capacitance of each diode was chosen so each series pair had approximately the same capacitance (20 fF) as the single whiskered diode used by Erickson. The first batch of diodes, designated SC10T1, had excessive series resistance and very large breakdown voltage. In the subsequent batches the doping density was increased and the epitaxial layer thickness decreased to reduce the device series resistance at the expense of lower breakdown voltage.

The SC10V2 diodes have been the most successful, and results of RF evaluation performed at 174 GHz by Dr. Erickson are presented in Fig. 4 [10,11]. The peak efficiency is 25% at an input power of 150 mW. The peak output power is 55 mW at an estimated input power of 250 mW. This maximum output power is more than twice the previous best doubler result at a similar frequency.

Generally, frequency multipliers tend to saturate in output at rather low power levels in the frequency range above 100 GHz. This saturation is believed to be due to the finite maximum carrier velocity in GaAs [12], which limits the displacement current in the diode. As a result, the efficiency tends to decrease rapidly above a critical power

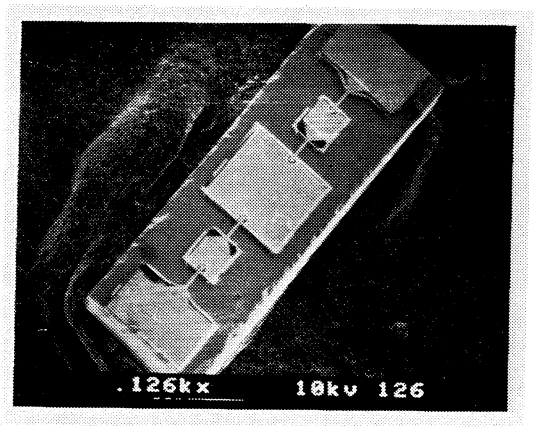

Fig.3: SEM photograph of the balanced doubler chip to 160 GHz.

Table II: Balanced Doubler Chip Characteristics							
batch #	t_{chip} (μm)	t_{epi} (μm)	N_{epi} (cm^{-3})	diam. (μm)	C_T^* (fF)	diode pair R_s (ohms)	diode pair V_{bkdn} (V)
SC10T1	100	1.3	$1.8x10^{16}$	10	43	24	45
SC10T2	100	1.2	$2.5x10^{16}$	10	50	14	35
SC10V1	100	0.64	$4.5x10^{16}$	10	60	6	30
SC10V2	25	0.64	$4.5x10^{16}$	9	47	11	29

*C_T includes the junction capacitance and 9 fF fringing capacitance.

prior to reaching device breakdown. It can be seen from the data in Fig. 4, however that the efficiency of the planar balanced multiplier levels off for input powers above approximately 100 mW. This indicates that the velocity saturation effects are reduced by the series diode structure.

In the past, varactor diodes have been designed for maximum power handling by maximizing reverse breakdown voltage. It can be seen from Fig. 4, however that the SC10V2 series diodes can operate at more than twice the input power as the single 6P2 whiskered diodes, while having a modestly increased breakdown voltage (29 V for the diode pair compared to 20 V for the 6P2 diodes). It is now believed that current saturation, not breakdown voltage, is the major limitation on the amount of input power a varactor diode can handle.

Integrating diodes in series allows the area and number of diodes to be increased, while as far as the circuit design is concerened they may be treated as a single diode. A series combination of n identical diodes of individual area nA behaves the same as an nxn array of similar diodes which have individual area A. Therefore, the series array can handle n^2 times the power as a single diode (with area A) without increasing the current density or changing the impedance level.

Since the first stage multiplier has been very successful, work has begun on developing a planar chip for the doubler to 320 GHz. This multiplier will also be a balanced doubler and will be similar in structure to the 160 GHz device. A sketch of the new doubler chip is shown in Fig. 5. Since this multiplier will not have to handle as much power as the first stage, it can be optimized for high efficiency rather than power handling.

In our first attempt, the junction capacitance and chip size of the 160 GHz doubler structure will be scaled to operate at 320 GHz. Since the 320 GHz chip is much smaller (20 mils in length) than the 160 GHz chip (30 mils in length), the pad sizes must be significantly reduced. However, this will require improved ohmic contacts. Our standard SnNi/Ni/Au alloyed ohmic contact will be replaced by an evaporated Ni/Ge/Au ohmic contact which reliably obtains resistivities of $10^{-6}\Omega cm^2$. It is hoped that the first chips will be available for RF evaluation this spring.

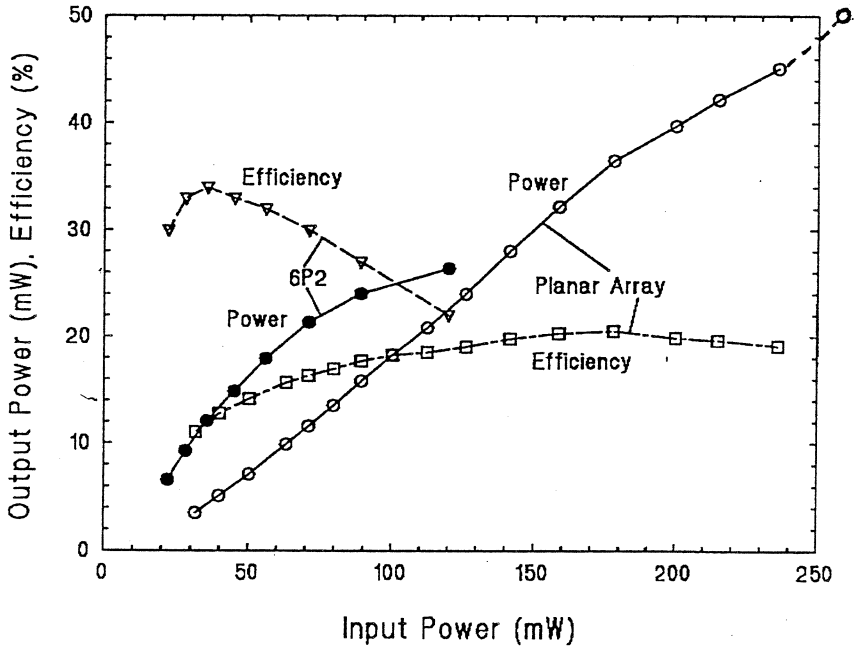

Fig. 4: RF data for the planar balanced doubler at 174 GHz.

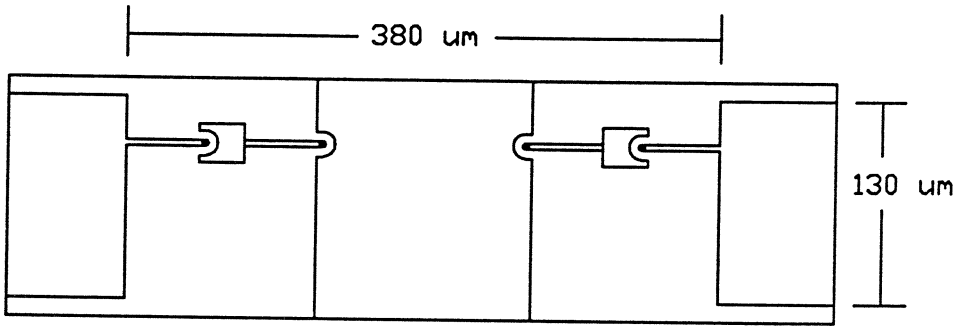

Fig. 5: Sketch of the prototype balanced doubler chip to 320 GHz.

IV. NOVEL VARACTORS

Several novel device structures are being investigated to determine their potential as frequency multipliers. In this section three of these devices are discussed. The integrated δ-doped varactor pair and the Schottky/two-dimensional-electron-gas (Schottky/2-DEG) are considered, and the numerical simulation of heterostructure barrier varactors is discussed.

Anti-Series δ-Doped Varactor Diode

A planar chip in which two δ-doped varactor diodes are integrated in an anti-series configuration has been designed to be used as a frequency tripler to 200-300 GHz. A scanning electron micrograph of the prototype chip is shown in Fig. 6. The anti-series pair produces a symmetric C-V characteristic, which offers significant benefits for tripling applications since an idler circuit at the second harmonic is not needed. The δ-doped varactor diodes have been shown to have a very sharp C-V characteristic [13,14] which is an advantage particularly at high frequencies where available input power is quite low.

C-V data for the prototype tripler chip is shown in Fig. 7. Each diode pair has a capacitance ratio (C_{max}/C_{min}) of approximately 1.8 and a breakdown voltage of 4.5 V. The zero-bias capacitance of the pair is approximately 38 fF, including 3 fF shunt capacitance. The results of an initial RF evaluation are shown in Fig. 2 along with the results for the SC6T2 diodes. The peak efficiency of the anti-series tripler is greater than 3% at about 243 GHz. The maximum power output of approximately 1.5 mW also occurs at this frequency. This preliminary data indicates that the prototype δ-doped tripler chip is a comparable frequency tripler to available whisker contacted diodes in the 200 GHz frequency range.

Design changes to improve device performance may include a lower active layer doping density than the present $2x10^{17}cm^{-3}$, and an increase in the active layer thickness to achieve a better capacitance ratio. Based upon the results of this research we hope to determine whether the anti-series δ-doped pair has the potential to be a high efficiency multiplier to 1 THz.

The Schottky/2-DEG Varactor Diode

The Schottky/2-DEG varactor diode is based on the lateral junction between the metal and the 2-dimensional electron gas [15-17], as shown in Fig. 8. In [17], we reported the C(V), the I(V) between 20-300K and the first millimeter wave multiplier measurements of the Schottky/2-DEG diode. These preliminary results were very

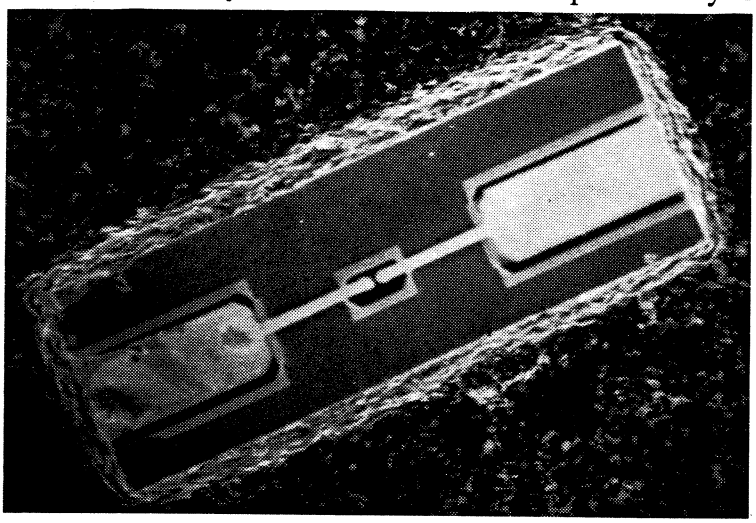

Fig. 6: SEM photograph of the prototype δ-doped tripler chip to 200 GHz

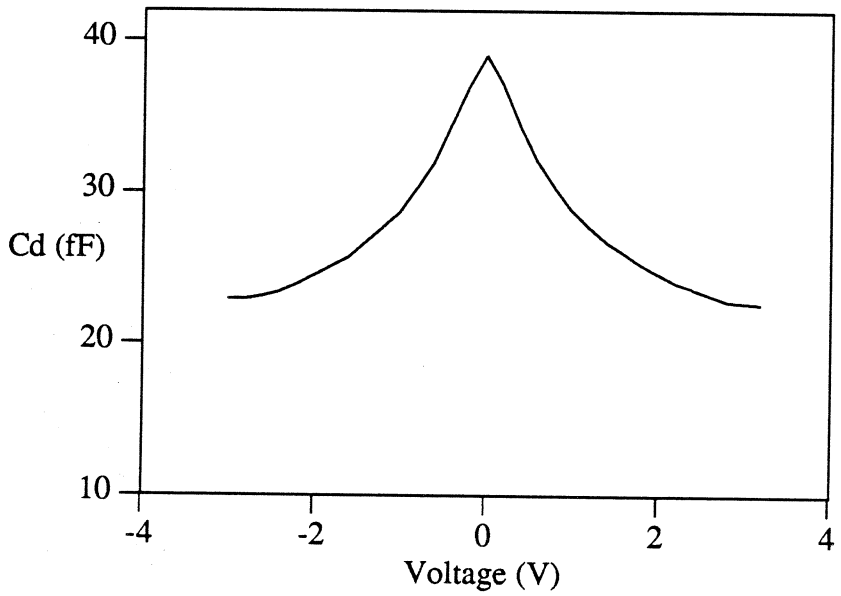

Fig. 7: C-V characteristic for δ-doped tripler chip to 200 GHz.

encouraging yet were unoptimized with regard to the series resistance and to the lack of a suitable planar diode multiplier mount for millimeter wavelengths. A new, more general theory for the C-V characteristic of the Schottky/2-DEG diode was also developed [18]. In this Section, we report recent progress in reducing the series resistance and briefly evaluate the potential performance of optimized devices. The new devices discussed here use the evaporated Ni/Au/Ge ohmic contact which should eventually yield lower resistance than the electroplated SnNi/Ni/Au contact.

The series resistance of the Schottky/2-DEG diode is due primarily to the sheet resistance of the undepleted 2-dimensional electron gas (Fig. 8) and to the ohmic contact resistance. The sheet resistance of the pseudomorphic AlGaAs/InGaAs material used to date is approximately 500 Ω / □ (100 Ω / □) at 300K (77K). Recent devices having 1 micron channel length and 90 micron channel width were evaluated at room temperature. The lowest series resistance measured was 9 Ω from which we deduce the ohmic contact resistance to be about 0.4 Ω-mm. This is the first Schottky/2-DEG diode batch fabricated using the evaporated Ni/Ge/Au ohmic contact which is still being optimized. From the literature, we expect to achieve 0.1-0.2 Ω-mm ohmic contact resistivity. Thus we expect to significantly reduce the series resistance in future devices.

The C-V characteristic of the $L = 1\ \mu m$, $W = 90\ \mu m$ device is shown in Fig. 9 (squares). Also shown is the C-V characteristic of the $L = 3\ \mu m$, $W = 80\ \mu m$ device (diamonds) reported in [17]. We measured the shunt capacitance of 19 fF for the new devices by etching away the 2-DEG in the channel. Thus, the zero-bias junction capacitance is approximately 22-25 fF/100 μm, whereas for punch-through limited devices, the minimum capacitance is nearly equal to the shunt capacitance.

A single room temperature millimeter wave tripler measurement of the 1 micron channel length device was made using the NRAO tripler (described in [9]), which was designed for whisker-contacted diodes. The multiplier measurements are shown in

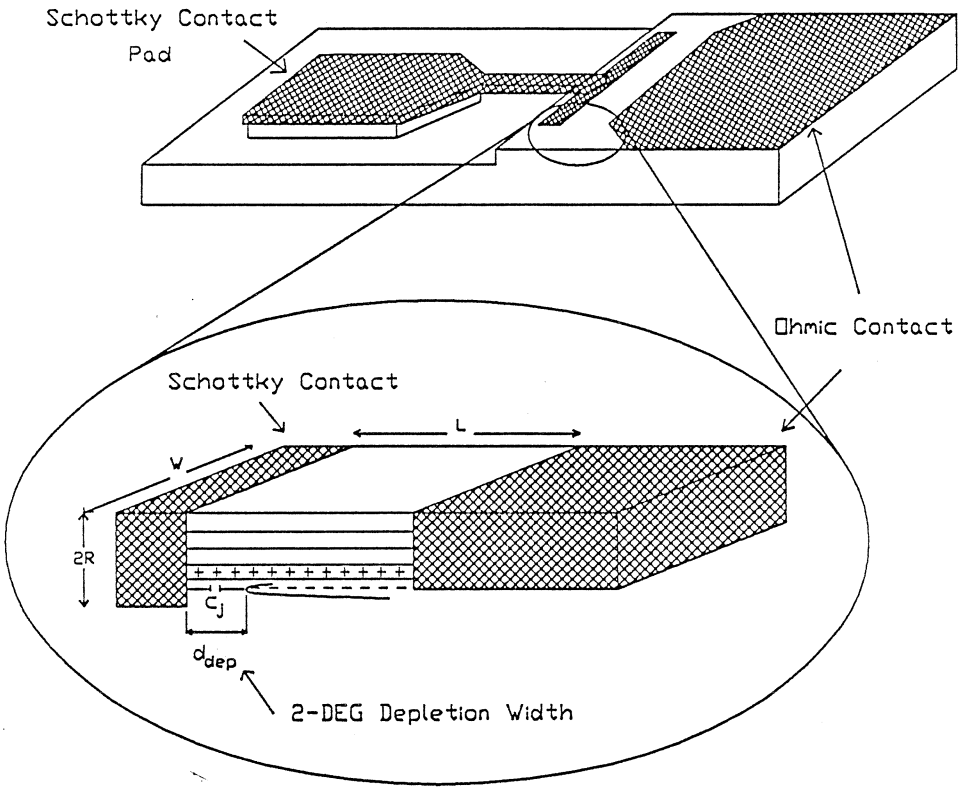

Fig. 8: Sketch of the Schottky/2-DEG multiplier diode.

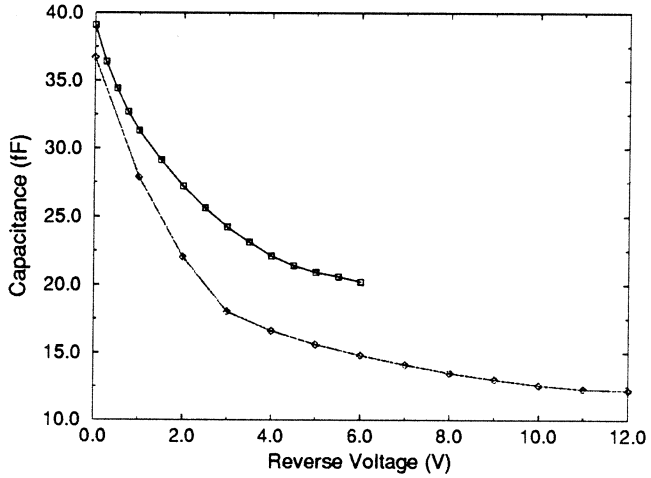

Fig. 9: C-V characteristic of the 1 μm length, 90 μm width Schottky/2-DEG diode (squares). Also shown is the C-V characteristic of the 3 micron length, 80 micron width device (diamonds) reported in [16].

Fig. 10. The output power at 225 GHz was 355 μ*W* with 50 mW input for an efficiency of 0.7 percent, compared with 186 μW measured previously [17] on longer channel devices. The higher efficiency is due either to a better impedance match between the diode and the multiplier or to the lower series resistance, or both. However, it is not clear whether significantly higher efficiency can be achieved using this multiplier mount.

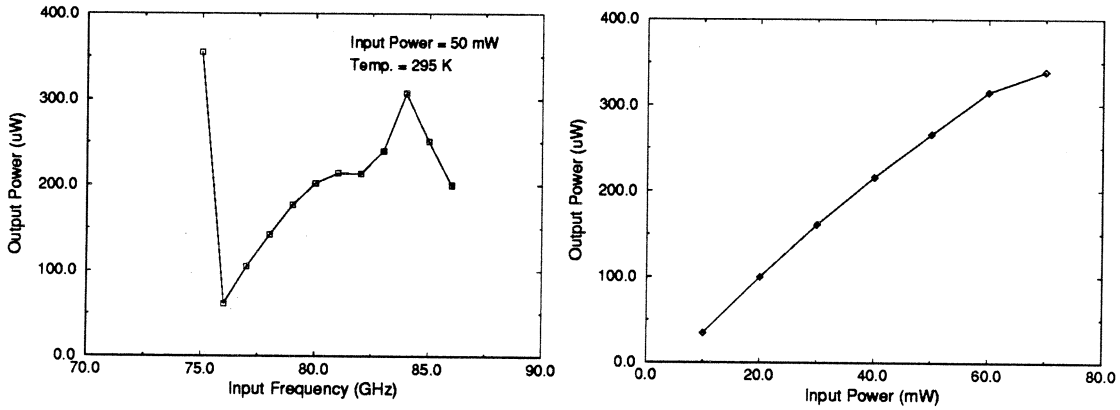

Fig. 10: Output power versus input frequency (left) and input power at 84 GHz (right) for the 1 micron length Schottky/2-DEG diode at room temperature.

The optimization of the Schottky/2-DEG diode for millimeter wave applications will focus on device designs which are suitable for insertion into the planar balanced doubler discussed in Section III. In this multiplier, the impedance match between the diodes and the multiplier circuit was excellent and the doubler performance was outstanding. A Schottky/2-DEG varactor, made using the present heterostructure material to have a similar capacitance range as each diode in the balanced doubler, would have a channel width of about 150 μm and a channel length of 1 μm. The series resistance of this device, assuming an ohmic contact resistance of 0.2 Ω-mm, would be about 2 Ω (5 Ω) at 77K (300K), compared with about 6 Ω for the standard balanced doubler. The breakdown voltage would be about 10 V compared to the 15 V breakdown of the standard balanced doubler, however, it appears this will be sufficient assuming reasonable input power levels. Thus we expect comparable performance of the Schottky/2-DEG diode at room temperature and superior performance at low temperatures.

Heterostructure Barrier Varactors

The Heterostructure Barrier Varactor (HBV) is an attractive alternative to Schottky barrier varactors for frequency multiplication in the millimeter to submillimeter wavelength ranges. A single barrier HBV consists of a high band gap semiconductor sandwiched between symmetric capacitive modulation regions of lower band gap material such that the device has an evenly symmetric nonlinear capacitance-voltage (C-V) relationship. The evenly symmetric C-V characteristic eliminates the even harmonic components of the current waveform yielding more efficient third harmonic frequency multipliers. By epitaxially stacking many single barrier HBVs, high device cut-off frequencies with moderate breakdown voltages are attainable. Also, superior device reliabilties are expected for stacked HBVs since the terminal voltage is distributed over multiple barriers. HBVs have an added advantage over Schottky barrier varactors in that the semiconductor alloy composition and doping profiles, as well as the barrier thickness, device area, and the number of barriers can be independently varied to achieve the optimum C-V characteristic. Thus, the C-V characteristic can be designed to simultaneously achieve optimum third harmonic operation and optimum device/circuit

matching. Ultimately, this should yield a very efficient single device with potentially higher power generation capabilities compared to multiple Schottky diode multiplier configurations.

With this in mind, the overall goal of our HBV research is to develop a fully self-consistent time-dependent (AC) simulator for GaAs/InGaAs/AlGaAs HBVs such that the device geometry, doping profile, and alloy composition profile can be chosen for optimal circuit performance. Our present discussion focuses on the details of the numerical device time-independent (DC) simulator that is used to predict the nonlinear I-V characteristics of GaAs/InGaAs/AlGaAs HBV structures.

The numerical DC simulator is based on the Alloy Ramp Diode DC simulator developed by Tait [19]. Any combination of abrupt heterojunctions and alloy ramps in the GaAs/InGaAs/AlGaAs material system can be simulated. Carrier transport through the device is modeled using the one-dimensional semiconductor drift-diffusion equations for electrons cast such that the state variables are the electron current $J_n(x)$, electron quasi-fermi level $\phi_n(x)$, electrostatic potential $\psi(x)$, and displacement vector $D(x)$. These equations are

$$
\begin{aligned}
dJ_n / dx &= 0 \\
d\phi_n / dx &= (-J_n / \mu_n(x)\, n_i)\ \exp\left(-\psi(x) - V_n(x) + \phi_n(x)\right) \\
d\psi / dx &= -D(x) / \varepsilon_r(x) \\
d(D(x)) / dx &= N_D(x) - n_i\ \exp\left(\psi(x) + V_n(x) - \phi_n(x)\right)
\end{aligned}
$$

where $\mu_n(x)$ is the material-dependent electron mobility, n_i is the intrinsic electron concentration in GaAs, $\varepsilon_r(x)$ is the material-dependent relative permittivity, and $V_n(x)$ is the alloy potential relative to GaAs [20]. The carrier transport equations are solved in two steps. First, the thermal equilibrium values of the state variables are obtained from the discretized nonlinear Poisson equation using a globally convergent nonlinear iterative technique [21]. The carrier transport equations are then solved using a finite-difference discretization scheme over a non-uniform mesh via the Newton-Raphson method with the thermal equilibrium solution serving as the starting point for the method. The given state variable set and the formulation of the drift-diffusion state equations as first-order differential equations has been chosen because of their superior accuracy and convergence properties when combined with the chosen numerical solution method [19].

In order to accurately predict the current across the abrupt heterointerfaces of an HBV, thermionic-emission of carriers over the barrier is included in the model via appropriate current boundary conditions at the abrupt heterointerfaces [19]. The thermionic-emission boundary condition reduces to an electron "fluid-outflow" boundary condition under appropriate biasing conditions, i.e. at the right heterointerfaces in Figures 11a and 11b. Tunneling through the barrier is modeled by reducing the barrier height. The effective barrier height reduction is calculated from the WKB approximation for tunneling through the tip of a triangular barrier [22]. For the present discussion, we restrict ourselves to a single barrier HBV such that solutions to the drift-diffusion equations are found in the three regions of the device after the domain of the original HBV is "folded". This yields a total of ten carrier transport equations with both ohmic and heterointerface boundary conditions imposed at both domain boundaries.

The GaAs and AlGaAs material parameters required for the model are taken from several sources including Adachi [23], Blakemore [24], Saxena [25], and Tait [19]. Of particular importance for the GaAs/AlGaAs material system is the Γ conduction band offset of 60% which yields a conduction band discontinuity of 235 meV for a $GaAs/Al_{0.7}Ga_{0.3}As$ heterointerface. The InGaAs material parameters required for the model are taken from several sources including Adachi [26] and Pearsall [27]. It is assumed that all InGaAs layers of interest are coherently strained such that the strain correction to the energy gap calculated by Anderson [28] is valid. For the AlGaAs/InGaAs material system the Γ conduction band offset is 55% [29] which yields a conduction band discontinuity of 376 meV for a pseudomorphic $In_{0.2}Ga_{0.8}As/Al_{0.7}Ga_{0.3}As$ heterointerface.

The simulated devices consisted of a 215 A undoped ($1x\,10^{14}cm^{-3}$) $Al_{0.7}Ga_{0.3}As$ barrier surrounded by 55 A undoped ($1x\,10^{14}cm^{-3}$) spacer layers ($GaAs$ or $In_{0.2}Ga_{0.8}As$) and 1500 A doped ($1x\,10^{17}cm^{-3}$) modulation layers ($GaAs$, or 1000 A $GaAs$ with 500 A graded $In_{0.0-0.2}Ga_{1.0-0.8}As$). For all simulations, A* was taken to be 0.15 A/K^2cm^2 for the $Al_{0.7}Ga_{0.3}As$ barrier [30], the electron mobility in the barrier was taken to be $2000cm^2/Vs$, the electron mobility elsewhere was taken to be $4000cm^2/Vs$, and barrier tunneling was assumed to occur via the AlGaAs X conduction band where the relevant electron effective mass is the transverse effective mass of $0.202m_o$. The WKB tunneling probability was assumed to be e^{-1} for all structures simulated.

Figure 11 shows typical band structure diagrams for a $GaAs/Al_{0.7}Ga_{0.3}As$ HBV and a $GaAs/In_{0.0-0.2}Ga_{1.0-0.8}As/In_{0.2}Ga_{0.8}As/Al_{0.7}Ga_{0.3}As$ HBV biased at 0.25 V. As indicated in the figure, the $GaAs/In_{0.0-0.2}Ga_{1.0-0.8}As/In_{0.2}Ga_{0.8}As/Al_{0.7}Ga_{0.3}As$ structure has an appreciably larger abrupt barrier as well as an alloy ramp. The simulated I-V relationship for the GaAs/AlGaAs structures is shown in Figure 12 along with the experimental data of Nilsen et al. [31] for diodes having an area of 625 μm^2. The simulated I-V relationship for diodes with graded InGaAs layers and A*=0.15 A/K^2cm^2 showed significantly reduced currents over the same bias range due to the increased barrier height. However, it is not clear what value of A* should be used for such a structure since strain effects significantly alter the band structure of the InGaAs and could significantly alter A*.

V. SUMMARY

Whisker contacted Schottky barrier varactor diodes have proven to be very reliable and effective multiplier elements for millimeter and submillimeter wavelength applications. However, planar varactor diodes offer improved performance and reliability. Improvements in chip design have made the prototype planar Schottky varactors competitive to whiskered diodes at millimeter wavelengths. By integrating several diodes on a single chip, increased power handling ability has been achieved with the integrated balanced doubler. This balanced doubler design is now being scaled to produce a doubler to 320 GHz.

Several novel device technologies have also been reviewed as possible multiplier elements. The anti-series δ-doped varactor diode produces a symmetric C-V characteristic which is beneficial for tripling applications. Prototype devices have shown promising initial results, and their potential as a tripler to 1 THz is being evaluated. The 2-DEG/Schottky diode benefits from increased electron mobility, and has shown promise

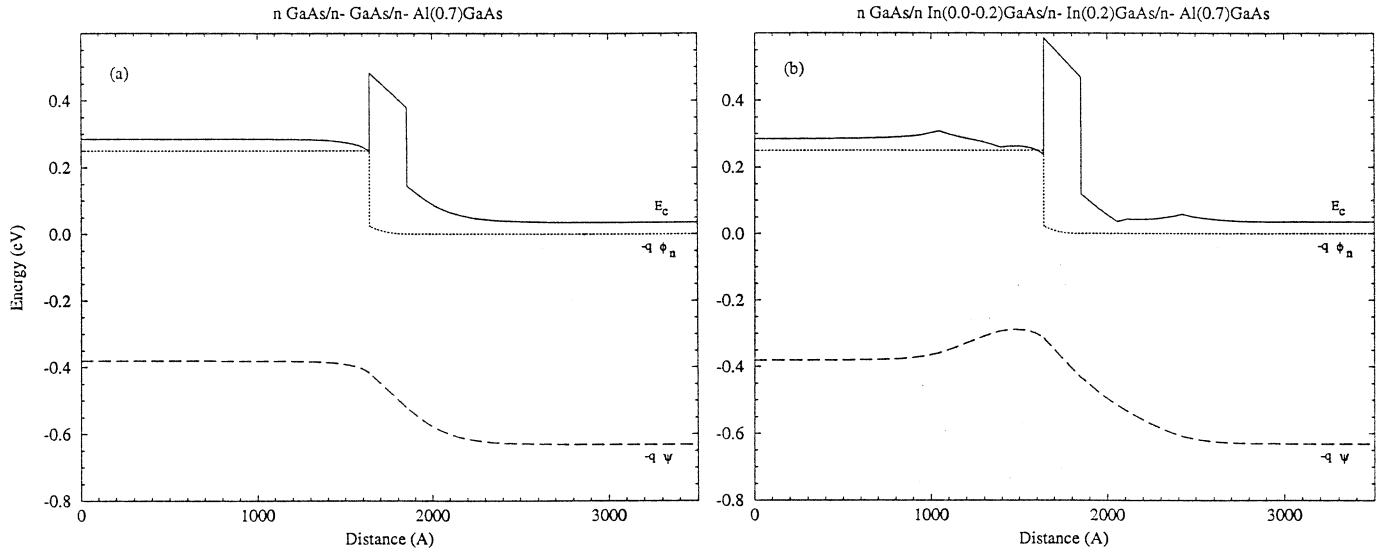

Fig. 11: Band structure of a $GaAs/Al_{0.7}Ga_{0.3}As$ HBV (a) and a $GaAs/In_{0.2}Ga_{0.8}As/Al_{0.7}Ga_{0.3}As$ HBV (b) biased at 0.25 V.

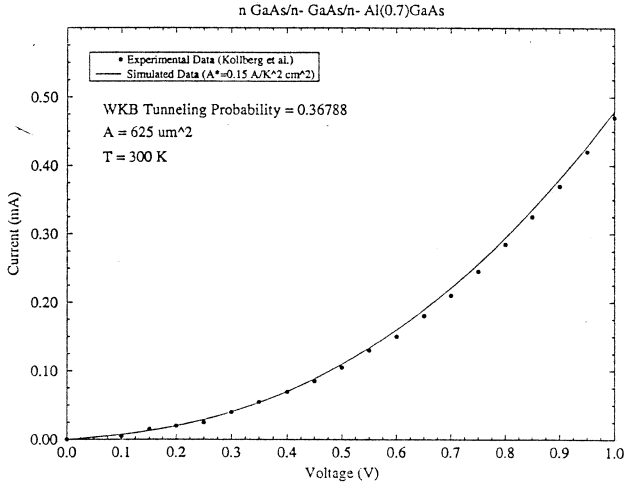

Fig. 12: Simulated I-V curve for the HBV of Figure 11a. Experimental data is taken from Nilsen et al. [31].

as a millimeter wave multiplier element. The device structure is now being optimized for reduced series resistance. Heterostructure barrier varactors show promise in high frequency multiplier applications, and a numerical model to simulate their I-V and C-V characteristics is being developed. Fabrication of initial HBV devices in the GaAs/AlGaAs and GaAs/InGaAs/AlGaAs material systems has begun. One of the main problems in producing optimum performance for the novel multipliers, is that the best RF performance will not be achieved until mounts specifically designed for these devices are made available.

It is our goal to develop a multiplier chain to 1THz suitable for space applications using planar technology. The first step is the high-power doubler which has produced record output power at 174 GHz. For the first time a planar device has displayed superior performance to a whisker contacted multiplier. This not only shows the great potential for diode arrays as frequency multipliers, but also for planar varactor diodes in general.

ACKNOWLEDGEMENT

The authors would like to thank Dr. Neal Erickson (U. Mass, Amherst) for supplying RF measurements on the balanced doubler. This work is supported by NASA (GSRP-4979-91, NAGW-2377 and NAGW-2430), JPL (#958202 and #959189), the U.S. Army (DAHC90-91-0030), and the U.S. Air Force (EE-SCEEE-5551-92).

REFERENCES

[1] R. Zimmermann, R. Zimmermann and P. Zimmermann, "All Solid-State Radiometers for Environmental Studies to 700 GHz," Third Int'l Symp. Space THz Tech., Ann Arbor, MI, March 1992.

[2] H. Nett, S. Crewell, K. Kunzi, "A 625-650 GHz Heterodyne Receiver for Airborne Operation," 16th Int'l Conf. IR and MM Waves, Lausanne, Switzerland, August 1991.

[3] S. Crewell and H. Nett, "Measurements of the Single Sideband Suppression for a 650 GHz Heterodyne Receiver," Third Int'l Symp. Space THz Tech., Ann Arbor, MI, March 1992.

[4] N.R. Erickson, "High Efficiency Submillimeter Frequency Multipliers," 1990 IEEE MTT-S Int'l Microwave Symp., Dallas, TX, May 1990.

[5] A. Rydberg, B.B. Lyons and S. Lidholm, "On the Development of a High Efficiency 750 GHz Frequency Tripler for THz Heterodyne Systems," IEEE Trans. Microwave Theory Tech., Vol. MTT-40, No. 5, pp. 827-830, May 1992.

[6] W.L. Bishop, K. McKinney, R.J. Mattauch, T.W. Crowe and G. Green "A Novel Whiskerless Schottky Diode for Millimeter and Submillimeter Wave Applications," Proc. 1987 IEEE MTT-S Intl. Symp., Las Vegas, NV, 607-610, June 1987.

[7] W.L. Bishop, T.W. Crowe, R.J. Mattauch and P.H. Ostdiek, "Planar Schottky Barrier Mixer Diodes for Space Applications at Submillimeter Wavelengths," Microwave and Optical Technology Lett., Special Issue on Space THz Tech., Vol. 3, No. 1, pp. 44-49, Jan. 1991.

[8] W.L. Bishop, E.R. Meiburg, R.J. Mattauch and T.W. Crowe, "A Micron Thickness, Planar Schottky Barrier Diode Chip for Terahertz Applications with Theoretical Minimum Parasitic Capacitance," 1990 IEEE MTT-S Int. Microwave Symp., Dallas, TX, May 1990.

[9] R. Bradley, "The Application of Planar Monolithic Technology to Schottky Varactor Millimeter-wave Frequency Multipliers," Ph.D. Thesis, University of Virginia, May, 1992.

[10] B.J. Rizzi, T.W. Crowe and N.R. Erickson, "A High Power Millimeter Wave Frequency Doubler Using a Planar Diode Array," Accepted for Publication, 1993 IEEE MTT-S Microwave and Guided Wave Letters.

[11] N.R. Erickson, B.J. Rizzi and T.W. Crowe, "A 174 GHz High Power Doubler Using a Planar Diode Array," Fourth Int'l Symp. Space THz Tech., Los Angeles, CA, March 1993.

[12] E.L. Kollberg, T.J. Tolmunen, M.A. Frerking and J.R. East, "Current Saturation in Submillimeter Wave Varactors," IEEE Trans. Microwave Theory Tech., Vol. MTT-40, No.5, pp. 831-838, May 1992.

[13] B.J. Rizzi, T.W. Crowe and W.C.B. Peatman, "A δ-Doped Varactor Diode for Submillimeter Wavelengths, "Digest of the 15th Int'l Conf. on IR and MM Waves, pp. 478-480, Orlando, Dec. 1990.

[14] T.W. Crowe, W.C.B. Peatman and W.L. Bishop, "GaAs Schottky Barrier Diodes for Space Based Applications at Submillimeter Wavelengths," The First Int'l Symp. Space THz Tech.

Proceedings, pp. 256-272, Ann Arbor, MI, March 1990.

[15] W.C.B. Peatman, T.W. Crowe and M. Shur, "Design and Fabrication of Heterostructure Varactor Diodes for Millimeter and Submillimeter Wave Multiplier Applications," Proc., IEEE/Cornell Conf. on Advanced Concepts in High Speed Semic. Dev. and Circuits, Ithaca, NY, pp. 49-57, August 1991.

[16] W.C.B. Peatman, T.W. Crowe and M. Shur, "A Novel Schottky/2-DEG Diode for Millimeter and Submillimeter Wave Multiplier Applications," *IEEE Electron Device Lett.*, Vol. 13, No. 1, pp. 11-13, January 1992.

[17] W.C.B. Peatman, T.W. Crowe, M. Shur and B. Gelmont, "A Schottky/2-DEG Varactor Diode for Millimeter and Submillimeter Wave Multiplier Applications," Proc. Third Int'l. Symp. on Space THz Tech., Ann Arbor, MI, pp. 93-109, March 24-26, 1992.

[18] B.L. Gelmont, W. Peatman, and M. Shur, "Heterodimensional Schottky Metal-Two Dimensional Electron Gas Interfaces," 20th Conf. Physics and Chem. of Semic. Interfaces, Williamsburg, VA, Jan. 25-29, 1993, also to be published in J. Vac. Sci. Tech. B, July/Aug. 1993.

[19] G. B. Tait, "Electron Transport in Rectifying Semiconductor Alloy Ramp Heterostructures," PhD Dissertation, The Johns Hopkins University, 1992.

[20] M. S. Lundstrom and R. J. Schuelke, "Numerical Analysis of Heterostructure Semiconductor Devices," IEEE Trans. Electron Devices, Vol. ED-30, No. 9, pp. 1151-1159, 1983.

[21] G. B. Tait, "Heterostructure Semiconductor Device Analysis: A Globally Convergent Solution Method for the Nonlinear Poisson Equation," Solid-State Electron., Vol. 32, No. 5, pp. 369-376, 1989.

[22] E. H. Rhoderick and R. H. Williams, "Metal-Semiconductor Contacts, 2nd Edition," Oxford, England: Claredon, 1988.

[23] S. Adachi, "GaAs, AlAs, and AlGaAs: Material Parameters for Use in Research and Device Applications," J. Appl. Phys., Vol. 58, No. 3, pp. R1-R29, 1985.

[24] J. S. Blakemore, "Semiconducting and Other Major Properties of Gallium Arsenide," J. Appl. Phys., Vol. 53, No. 10, pp. R123-R181, 1982.

[25] A. K. Saxena, Phys. Status Solidi (b), Vol. 105, p. 777, 1981.

[26] S. Adachi, "Material Parameters of InGaAsP and Related Binaries," J. Appl. Phys., Vol. 53, No. 12, pp. 8775-8792, 1982.

[27] T. P. Pearsall (ed.), "GaInAsP Alloy Semiconductors," New York, N.Y.: John Wiley & Sons, Inc., pp. 456-457, 1982.

[28] N. G. Anderson, "Strained-Layer InGaAs-GaAs Heterojunctions, Quantum Wells, and Superlattices: Electronic Structure and Optical Properties," PhD Dissertation, North Carolina State University, 1988.

[29] D. C. Bertolet, J. Hsu, S. H. Jones, and K. M. Lau, "Pseudomorphic GaAs/InGaAs Single Quantum Wells by Atmospheric Pressure Organometallic Chemical Vapor Deposition," Appl. Phys. Lett., Vol. 52, No. 4, pp. 293-295, 1988.

[30] P. M. Solomon, S. L. Wright, and C. Lanza, "Perpendicular Transport Across (Al,Ga)As and the G to X Transition," Superlatt. Microstruc., Vol. 2, No. 6, pp. 521-525, 1986.

[31] S. M. Nilsen, H. Gronqvist, H. Hjelmgren, A. Rydberg, and E. L. Kollberg, "Progress on Single Barrier Varactors for Submillimeter Wave Power Generation," Third Int. Symp. Space THz Tech., Ann Arbor, MI, March 1992.

Performance Limitations of Varactor Multipliers*

Jack East
Center for Space Terahertz Technology, The University of Michigan
Erik Kollberg
Chalmers University of Technology
Margaret Frerking
NASA/JPL

ABSTRACT

Large signal nonlinear device circuit modeling tools are used to design varactor harmonic multipliers for use as millimeter and submillimeter wave local oscillator pump sources. The results predicted by these models are in reasonable agreement with experimental results at lower frequencies, but the agreement becomes worse as the power level or frequency increases. We will discuss an improved varactor device model and compare results from the new model with both conventional models and experimental data.

I. Introduction

The Schottky barrier varactor frequency multiplier is a critical component of millimeter wave and submillimeter wave receiver systems. A variety of modeling tools are available to help in the design of the multipliers. The modeling is a combination of linear and nonlinear analysis to find the current and voltage waveforms across the varactor placed in the multiplier circuit. The conventional approach uses the harmonic balance[1,2] or multiple reflection technique[3]. These techniques start with a time domain approximation for the voltage across the device and time domain information for the nonlinear device and frequency domain information from the linear circuit to find the final waveforms across the device. These techniques are available in many commercial circuit simulators[1,2] and in more specialized mixer programs[3–5].

These techniques require an equivalent circuit to describe the varactor. Measured or calculated information on the capacitance and current vs. voltage can be used. The multiplier performance also depends on the series resistance of the device. This is more difficult to obtain from low frequency measurements, so a variety of approximations are used. These techniques have been used to design multipliers over a wide range of frequencies. The results are encouraging at lower frequencies. However, as the frequency or power level goes up the predicted powers and efficiencies are typically lower than experimental results. There are several possible explanations. High frequency multiplier circuits are small and difficult to fabricate. Skin effect and backshort loss both increase with frequency. These losses can be taken into account in the simulation, but the required

*This work was supported by the Center for Space Terahertz Technology under contract No. NAGW-1334.

loss values tend to be relatively large when compared with other information about waveguide and mount loss. The impedance presented to the device by the circuit is sometime inferred from scale model measurements at much lower frequencies. As the operating frequency increases mechanical tolerance limitations make it more difficult to predict the operating conditions from scale models. Another problem is the varactor diodes themselves. There are a limited number of varactor designs at high frequencies, so scaling over frequency is difficult. Another problem is the equivalent circuit used to describe the nonlinear varactor. At high frequencies or power levels, a simple lumped element equivalent circuit can have problems representing the actual operation of the varactor. A recent paper by Kollberg et al[6] described saturation effects in varactors using a lumped element representation for the varactor with elements that depended on the current level. That paper is the starting point for the present work.

We will discuss a varactor model in this paper that takes the device physics into account in more detail, and then use the proposed new model to study multiplier performance. The next section of the paper describes the details of the new model. Section 3 will discuss the results of including the new effects on the performance of a multiplier operating between 80 and 160 GHz. The paper will be summarized in section 4.

II. Improved Varactor Model

There are two extremes in device models; analytic or equivalent circuit models that are used in a variety of circuit simulators like SPICE and the nonlinear models discussed in the introduction, and more complete semiconductor models that solve for the internal physics in more detail. These more complete models typically solve a combination of the time dependent current continuity and Poissons' equation to find the terminal characteristics of the device. This type of solution is commonly used for IMPATT diodes[7,8] and Gunn devices[9,10]. Problems occur when a detailed numerical model is connected to a nonlinear circuit simulation to study harmonic multiplication. The time scale of the circuit simulation is some fraction of an RF period, typically picoseconds. The time scale of the semiconductor simulation is on the order of the dielectric relaxation time, which is femtoseconds. The computer time required to time step through an RF cycle is much larger than in the conventional equivalent circuit case. We propose an alternative model that includes most of the varactor physics to better understand the operation, but can be used in a nonlinear algorithm with reasonable amounts of computer time.

An improved varactor model can be found by first studying the operation of a typical varactor diode using a drift-diffusion semiconductor simulation. This simulation solves the electron current continuity equation and Poissons' equation as a function of time and position to describe the terminal characteristics of a varactor diode. The diode is 0.6 microns long and is doped at $3\times10^{16}/\mathrm{cm}^3$, similar to the experimental device in section III. The results of a two volt switching transient are shown in Fig. 1. The width of the depletion layer increases by removing electrons from the depletion layer edge and out of

the device. This is shown in Fig. 1a. The resulting electric field as a function of time is shown in Fig. 1b. The voltage step at the start of the transient produces a modified electric field inside the device. For very short times the electrons in the device can not rearrange themselves. The effect of the voltage increase is to increase the field in the entire device by an amount

$$\Delta E = \Delta V/\text{width}. \tag{1}$$

The two volt step produces a 33 KV/cm field increase across the entire device. The field increases in the depletion region where the electron density is small, and also in the undepleted region where the electron density is large. Since the electron density in the undepleted region is approximately constant the field produces an electron conduction current of

$$J_n = q \times n \times v_n(E), \tag{2}$$

where

J_n = electron current,
n = electron density,
v_n(E) = electron velocity,
E = electric field.

The particle current in the undepleted region and the displacement current in the depletion region as a function of time are shown as solid lines in Fig. 2. The first difference between the semiconductor model and an equivalent circuit model occurs as a result of equation 2. Most varactor models include a voltage dependent capacitance and a constant or voltage variable series resistance. The result of a switching transient would be an exponential decay of current with time, with a small variation due to the changing depletion layer capacitance. However, for the results in Fig. 2, the current depends on the electric field, and both the velocity and the current are limited to peak values by the semiconductor physics. The electric field in the entire device is above the saturation field at the start of the transient. Since the electron momentum relaxation time or the time required to reach the equilibrium vilocity is much shorter than the time scale under consideration, all the electrons are moving at the saturated velocity. The electron current changes slowly during the first 1.5 picoseconds of the transient because of this saturation. The electron current in Fig. 2 is caused by electrons exiting the device and increasing the depletion layer width. This electron motion changes the electric field distribution within the device and supports displacement current in the depletion layer. The field profiles vs. time in Fig. 1 show the effect of the electron redistribution. The field at the Schottky contact becomes larger (more negative) and the field at the ohmic contact becomes smaller (less negative) during the transient. The resulting time change in the field produces the current vs. time information shown in Fig. 2. Fig. 2 points out a second difference with the lumped circuit models. The total current at any point in the device is the sum of the particle and displacement currents, and is constant with position and varies with time. The difference between the displacement current in the depletion region and the electron current in the undepleted region is accounted for by displacement current in the otherwise resistive portion of the device, shown as curve c. The changing electric field in the undepleted region supports this displacement current. The time scale

and voltage change in Figs. 1 and 2 are similar to the picosecond time scale and several volts RF level associated with multipliers operating above 100 GHz. The results show the importance of the displacement current and velocity saturation. However a typical reflection algorithm goes through many RF periods in the course of a solution and the computer time required to combine this exact description with the nonlinear solution quickly becomes excessive. We will discuss a simple model that includes many of these saturation effects next.

The information from the complete semiconductor model discussed in the last paragraph can be used as a starting point for a numerically efficient varactor model. The model uses a combination of the depletion layer approximation and equation 2 to describe the device. The voltage drop associated with the depletion region is

$$V_{dep} = q \times N_d \times W_{dep}/2\epsilon, \tag{3}$$

where V_{dep} = depletion layer voltage,
N_d = doping and,
W_{dep} = depletion layer width.
W_{dep} at the start of a transient is dependent on the initial voltage across the device and the built-in barrier potential, and changes as a result of electron current in the device. When a voltage step is applied, W_{dep}, V_{dep} and J_n can be found by using equations 2 and 3 along with an expression for the field in the neutral region,

$$E = -(V_{terminal} + V_{bi} - V_{dep})/x_{total}, \tag{4}$$

where $V_{terminal}$ = external voltage from the circuit,
V_{bi} = built-n potential, and
x_{total} = overall device epitaxial length.
These three equations can be solved as a function of time and terminal voltage to produce the varactor current waveform. These equations have most of the characteristics of the more complete semiconductor model, but run in a small fraction of the computer time. The transient results predicted by these three equations are shown as dashed lines in Fig. 2.

The model described in the last paragraph is an ideal varactor. However, with a large enough voltage swing, the device can conduct in the forward direction if the junction is forward biased and conduct in the reverse direction if the voltage is above the breakdown voltage. These two currents should be included in the model. The forward current can be approximated by a thermionic emission current that depends on the voltage across the depletion layer inside the device

$$I_{th} = A \times A^* T^2 \exp(-V_{dep}/kT), \tag{5}$$

where A = area,
A* = Richardson's constant, and

T = temperature.

Under moderate voltage low frequency conditions, the depletion layer voltage is close to the terminal voltage. As the forward voltage increases, the thermionic current increases and a portion of the terminal voltage drops in the undepleted region. This voltage drop limits the forward current and device capacitance, even for terminal voltages beyond flatband. Under high frequency operation, the undepleted region must support both the forward junction current and the junction displacement current. This will further limit the current. The current and voltage waveforms predicted using a lumped element varactor model in a nonlinear simulator can swing the device beyond the measured DC breakdown voltage. Breakdown effects need to be included in the varactor model. A detailed description of breakdown effects is given by Sze[11]. The ionization current is small for reverse bias voltages below the breakdown voltage and increases rapidly above the breakdown voltage. The breakdown current can be modeled as a current generator that depends on the voltage above the breakdown voltage. The ionization current will flow through the depletion layer and be limited by the space charge resistance, (equation 12 page 214 in Sze[11])

$$R_{space\ charge} = W_{dep}^2/(2 \times A\epsilon \times v_{sat}), \tag{6}$$

where

v_{sat} = saturated velocity in the depletion layer.

The avalanche current becomes

$$\begin{aligned} I_{avalanche} &= 0 \text{ if } V_{dep} < V_{breakdown}, \text{ and} \\ &= A^*(V_{dep} - V_{breakdown})/R_{space\ charge} \text{ otherwise.} \end{aligned} \tag{7}$$

This avalanche current will also flow through the undepleted region of the device and will have the same saturation effects as the other currents under consideration. This expression for the avalanche current neglects time delays associated with the avalanche response time and transit time effects in the depletion layer.

A varactor model that includes the current effects in equations 2, 5 and 7 along with the depletion layer effects in equations 3 and 4 has been written and interfaced to a modified version of the program DIODEMX described by Maas[5]. The combined varactor and nonlinear multiplier program has been used to study doubler performance.

Section III. Multiplier Performance

The varactor effects discussed in the last section have been included in a multiple reflection multiplier program to study the performance of a doubler operating between 90 and 180 GHz. The varactor parameters and operating conditions have been chosen to match an experimental doubler discussed by Erickson[12] to allow comparison with experimental data. The varactors have a doping of $3\times10^{16}/cm^3$, two devices with an area of $38\times10^{-8}cm^2$ each, a series resistance of 10 ohms and a breakdown voltage of 20 volts. The solutions were found at the experimental bias points that were obtained from Erickson[13] and Raissanen[14].

Fig. 3 shows the experimental efficiency and the predicted efficiency for a conventional diode model. Curve (a) is the measured efficiency. The estimated output circuit loss was 1.3 dB. Curve (b) is the estimated power generated at the device with the output loss removed. Curve (c) is the output efficiency predicted by the conventional varactor model. The simple varactor model does a reasonable job of predicting the multiplier performance at low power levels, but has problems for pump powers above 30 milliwatts. The various effects discussed above can be included to better understand this difference.

The effects of current saturation can be included in the varactor program by using equations 2, 3, 4, 5 and 7 to describe the device performance. The model requires an expression for the velocity vs. electric field in equation 2. A simple expression for velocity vs. field has a constant low field mobility at low electric fields and a constant saturated velocity at higher fields. The choice of mobility and saturated velocity values will effect the performance predictions. The simplest velocity vs. field expression is a constant mobility with no velocity saturation effects included. Except for a modulation of the series resistance because of a modulation of the undepleted layer width, this varactor approximation is the same as the conventional model. The resulting efficiency vs. local oscillator power is shown in Fig. 4 for mobilities between 3000 and 6000 cm^2/Volt-sec. Since breakdown and current saturation effects are not included, the efficiencies have the same monotonic increase as the data in Fig. 3. Based on the device dimensions, doping and experimental low frequency series resistance, the estimated experimental mobility is 4000 to 4500 cm^2/Volt-sec. The best approximation to the experimental data below about 35 milliwatts pump power is the 3000 cm^2/Volt-sec data, a lower than expected result. One possible explanation is a frequency dependent series resistance due to the change in skin depth with frequency. This difference can also be explained by including displacement current in the varactor model.

There is displacement current flowing through the entire length of the varactor during its operation. This bulk displacement current is a small fraction of the electron current, but it is usually of the opposite sign. The effect of the displacement current on the efficiency vs. pump power level is shown in Fig. 5. The efficiencies in Fig. 5 are lower than the corresponding efficiencies in Fig. 4. A low field mobility of 4500 cm^2/Volt-sec gives a match to the experimental data, and is also reasonable when compared with the low frequency series resistance.

The model parameters in Fig. 5 do a good job of predicting the low power performance of the multiplier, and the choice of a low field mobility of 4500 cm^2/Volt-sec is a good match to both the RF data and the measured low frequency series resistance. However, the model efficiency still has a monotonic increase with power level while the experimental data efficiency decreases above about 40 milliwatts pump power. The next step is to include velocity saturation effects in the model. Figure 6 shows the efficiency vs. pump power for saturated velocities between 2.5×10^7 and 4×10^7cm/sec. All the curves show the saturation effects of the experimental data. The effect of the finite saturated velocity is to limit the maximum conduction current through the device. This in turn limits the

rate of change of the depletion layer with and thus the nonlinear capacitance. circuit. Reducing the saturated velocity reduces the electric field and pump power required to saturate the device. The saturation point for the curves in Fig. 6 varies between about 30 milliwatts for the lowest velocity(curve d) to about 60 milliwatts for the highest velocity(curve a). A saturated velocity of 3.5×10^7cm/sec gives a reasonable fit to the experimental data.

The best fit velocity in Fig. 6 is higher than the typical measured saturation velocity in GaAs. However, the measured velocity characteristic are based on DC measurements of long samples. Velocity saturation occurs in GaAs because of electron heating and valley transfer. Valley transfer only occurs when the electrons obtain a minimum threshold energy. In the varactor structure the distances are small and the field is changing rapidly. As a check on the solution, the voltage drop in the undepleted portion of the varactor was displayed. Although the electric field was high, the maximum voltage drop in the undepleted region was below the valley transfer threshold in GaAs for all the cases in Fig. 6. Thus a velocity vs. electric field based on central valley transport with a high saturated velocity is reasonable.

The effects of undepleted region displacement current and velocity saturation account for most of the reduction in efficiency for low and medium pump power levels. However, the device is biased past the breakdown voltage for higher pump levels. The effect of adding the breakdown current to the model of Fig. 6 is shown in Fig. 7. The three dashed curves correspond to source resistances of 800, 1000 and 1200 ohms. The model also includes the displacement current and velocity saturation effects. The device is pumped past the breakdown voltage for pump power levels above 40 to 50 milliwatts. The peak voltage across the device when breakdown effects are not included is about 34 volts. Including breakdown effects lowers the peak voltage to about 26 volts. The reduced voltage swing reduces the capacitance swing and the nonlinearity of the junction capacitance. The breakdown also adds an in- phase current to the total device current. The combined effect is a lower efficiency at higher pump power levels.

IV. Conclusions

This paper has discussed the large signal nonlinear modeling of varactor multipliers. Earlier multiplier models have used a lumped element voltage dependence model to describe the varactor. This approach does not match the experimental results at higher frequencies and power levels. This paper has described a new varactor model more closely based on the semiconductor device operation. Three effects in the new model modify the varactor and multiplier performance. At low pump power levels the changing electric field in the undepleted portion of the device produces a displacement current. This current reduces the low power efficiency. At medium pump power levels the electron velocity begins to saturate and an additional reduction in efficiency occurs. The total voltage drops in the undepleted region are small, so the velocity characteristics depend on the properties of central valley electrons in the GaAs. For higher pump powers the varactor

voltage is above the breakdown voltage and avalanche current flows. This further reduces the efficiency. The model was tested for a range of material and device parameters and compared with experimental data. The parameters needed to match the experimental results are all physically reasonable.

Acknowledgments: The authors would like to thank Dr. Neal Erickson and Dr. Antti Raissanen for useful discussions and for unpublished experimental information on experimental multiplier performance.

List of Figures

References

1. *LIBRA Users Guide*, EESOF, 5601 Lindero Canyon Road, Westlake Village, California, 91362.

2. Compact Software, 483 McLean Blvd., Patterson, New Jersey, 07504.

3. A. R. Kerr, "A Technique for Determining the Local Oscillator Waveform in a Microwave Mixer," *IEEE Trans. on Microwave Theory and Techniques*, volume MTT-23, 1975, p. 828.

4. P. Siegel, A. Kerr and W. Hwang, "Topics in the Optimization of Millimeter Wave Mixers," NASA Technical Paper 2287, March, 1984.

5. S. Maas, *Microwave Mixers,* Artech House, Norwood, Mass. 1986, chapter 4 and appendix A.

6. E. L. Kollberg, T. J. Tolmunen. M. A. Frerking and J. R. East, "Current Saturation in Submillimeter Wave Varactors," *IEEE Trans. on MTT,* volume MTT-40, 1992, p. 831-838.

7. D. L. Scharfetter and H. K. Gummel, "Large Signal Analysis of a Silicon Read Diode Oscillator," *IEEE Trans. on Electron Devices*, volume ED-16, pp. 64, 1969.

8. W. E. Schroeder and G. I. Haddad, "Nonlinear Properties of IMPATT Devices," Proc. IEEE, vol. 61, pp 153, 1973.

9. J. A. Copeland, "A new mode od oscillation for bulk negative resistance oscillators," Proc. IEEE(letters), vol. 54, no. 10, pp. 1479- 1480, Oct. 1966.

10. D. D. Khandelwal and W. R. Curtice, "A study of the single-frequency quenched-domain mode Gunn-effect oscillator," *IEEE Trans. on Microwave Theory and Technique*, vol. MTT-18, no. 4, pp. 178-187, April, 1970.

11. S.M. Sze, *Physics of Semiconductor Devices,* Wiley, 2nd edition,1981.

12. N. Erickson, "High efficiency submillimeter frequency multipliers," 1990 IEEE S Int. Microwave Symposium Digest, vol. III, pp. 1301-1304.

13. Neal Erickson personal communication.

14. Antti Raissanen personal communication.

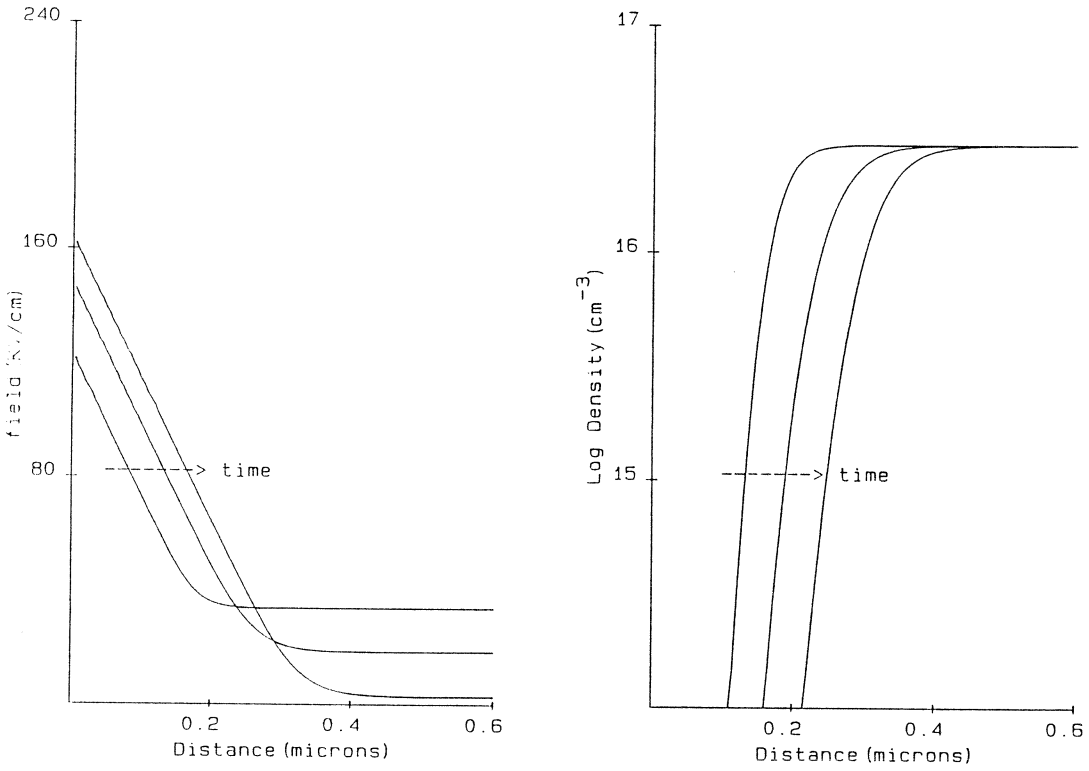

Figure 1

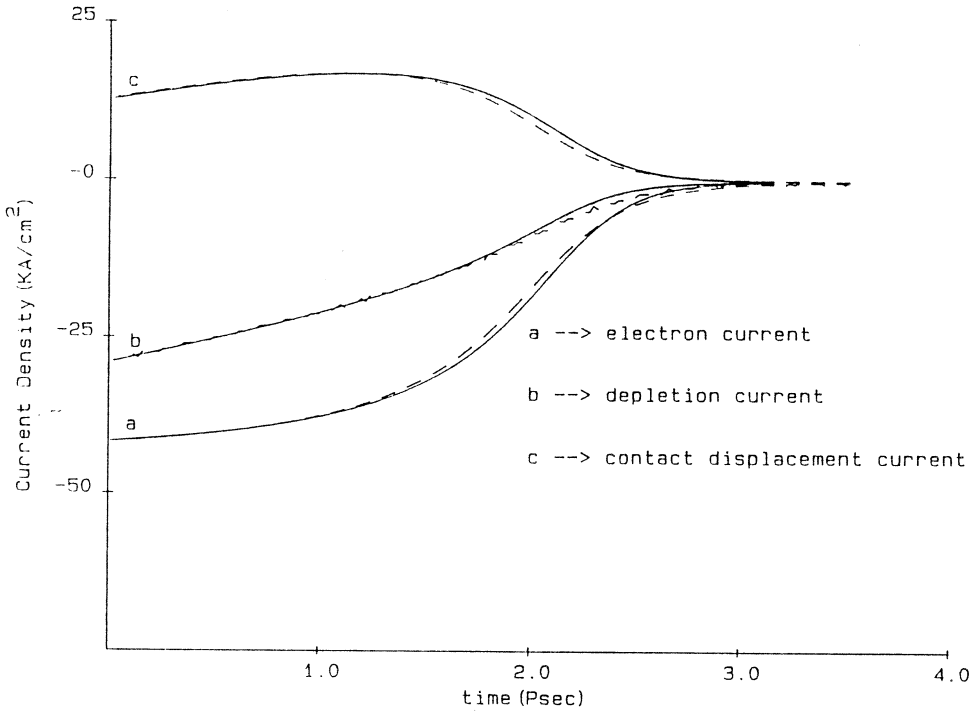

Figure 2

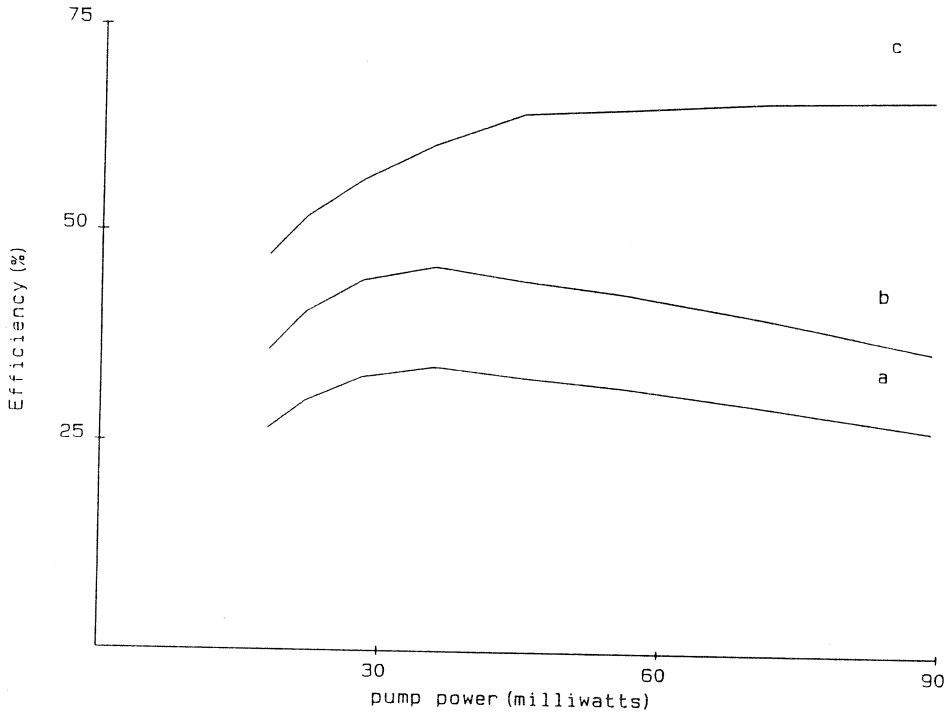

Figure 3

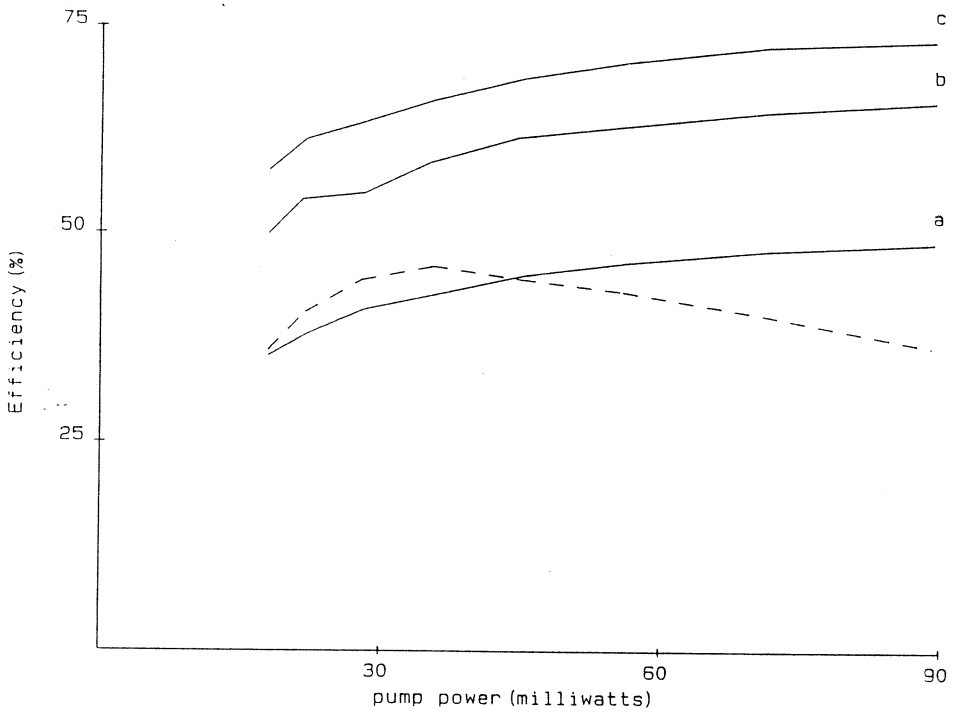

Figure 4

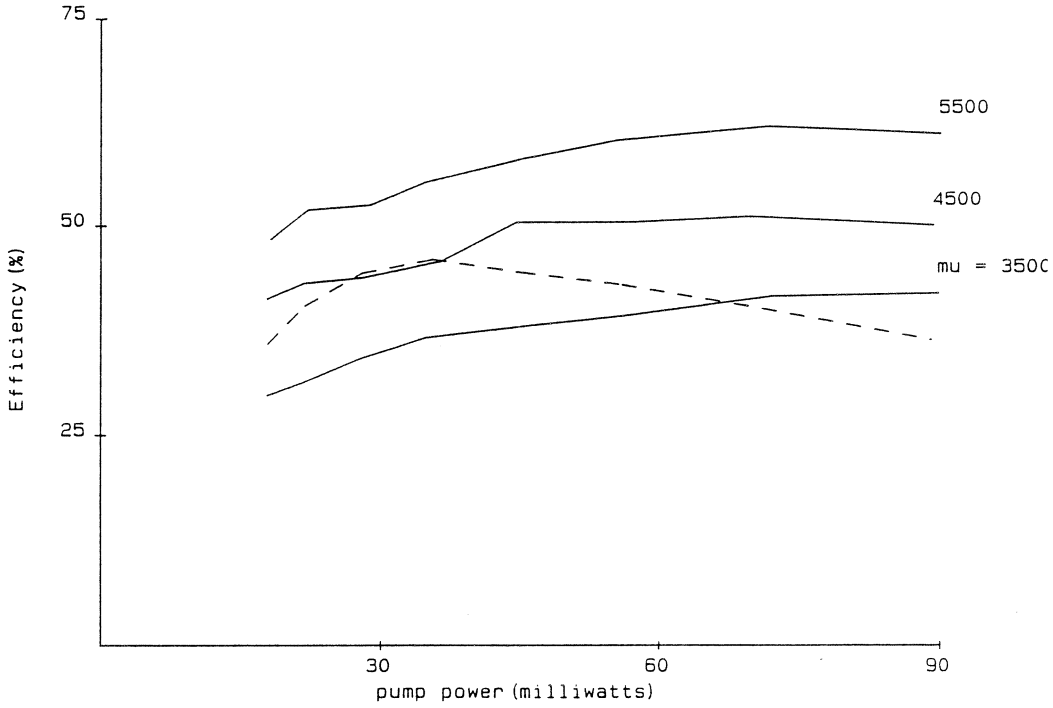

Figure 5

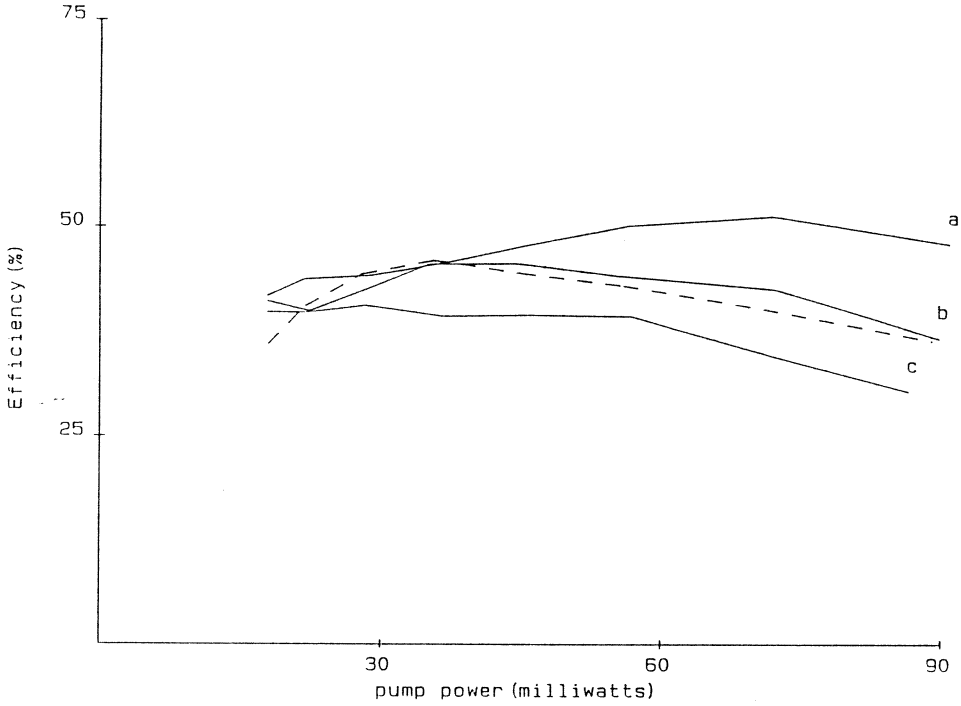

Figure 6

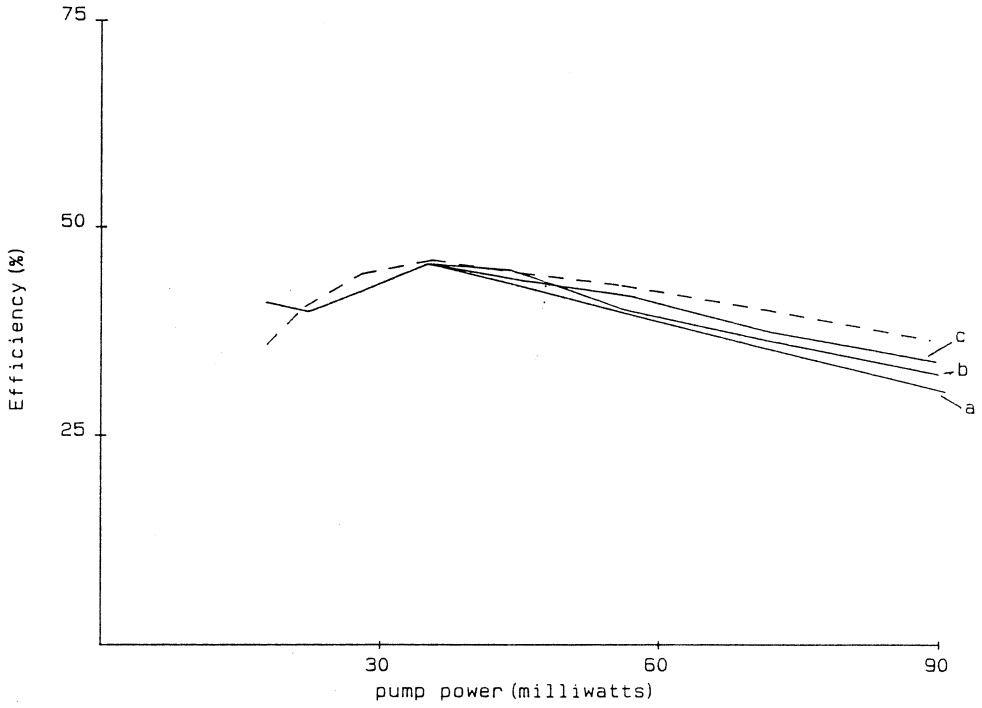

Figure 7

FINITE ELEMENT ANALYSIS OF A PLANAR DIODE DOUBLER

Jussi Tuovinen and Neal R. Erickson

Five College Radio Astronomy Observatory
Department of Physics and Astronomy
University of Massachusetts
Amherst, MA 01003

Abstract

Finite element analysis of the input circuit of a planar diode multiplier from 85 to 170 GHz is described. In the analysis, the High Frequency Structure Simulator program (HFSS) by Hewlett-Packard was used. To optimize the diode design the de-embedded diode terminal impedance was studied. The analysis revealed that the matching of the diode impedance to the waveguide impedance can be improved by thinning the GaAs substrate, and that 100 μm of quartz gives better matching than 25 μm of GaAs. The effect of air bridges in the diode is only marginally beneficial for large capacitance diode junctions, and a slight power imbalance between the diode junction was found.

1 Introduction

Solid-state local oscillator sources in the THz range are needed for a wide range of applications including laboratory spectroscopy, spaceborn radio astronomy and observations of the earth's atmosphere. This source can be made using a low frequency fundamental oscillator followed by a chain of frequency multipliers. One possibility to realize a source for 1 THz would be to have a Gunn-oscillator at 83 GHz, followed by a frequency doubler, another doubler and finally a tripler. To obtain 0.1 mW output power at 1 THz it is important that the first doubler have an output power of about 50 mW. This much output power can not be obtained with a single diode, because of the limited power handling, both due to breakdown voltage and saturation effects. Therefore, an array of diodes is needed. Recent tests at the University of Massachusetts have proved the usefulness of an array of planar diodes in series over a single diode in high power multiplication at 174 GHz [2]. The planar structure with four diodes on a single GaAs substrate has been developed at the University of Virginia. Figure 1 shows the multiplier and diode that was used in the tests. The diode was designed without any benefits of modeling. To improve the planar diode design, good modeling of the device is now highly desirable, which must include the interaction of the diode circuit with a waveguide mounting structure. This is particularly important because the manufacturing of a planar diode is a time consuming and expensive process. In this paper we describe the finite element analysis we have carried out on a planar diode doubler from 85 to 170 GHz.

Conventional scaled model measurements, because of the wide range of sizes ($> 1000/1$), are difficult when one considers the smallest important features on the diode relative to the size of a waveguide mount. Another major problem is how to provide the small coaxial probes to the diode locations. Also, manufacturing of the model includes mechanical inaccuracies, for example, with attaching metal tapes as are often used [1]. We have chosen instead to do numerical electromagnetic simulations on the multiplier. The advantages of the numerical analysis are that they make it easy to study dielectric thickness effects, optimum inductances in the diode package, power balance between the diodes, and the origin of the parasitic effects. Other advantages are the provision for multiple probe ports, and the ease with which the structure can be split into pieces and with which parts of the structure can be added or deleted to see their effects.

2 Approach to the analysis

In the analysis, the HP85180A High Frequency Structure Simulator program (HFSS) by Hewlett-Packard was used. This program performs finite element analysis on closed arbitrary geometries with lossy and lossless metals and dielectric materials. The HFSS includes only linear analysis, while a varactor diode is a very nonlinear load. The non-linear analysis to determine optimum source and load impedances was done separately with a harmonic-balance analysis program of the HP85150B Microwave Design System circuit simulator (MDS) by Hewlett-Packard.

Figure 1 shows the doubler from 85 to 170 GHz that was analyzed. In our finite element analysis, the non-linear parts of the doubler were treated in two ways. 1) Small probes were connected to the diode locations in a similar way to that which would be done in scaled model measurements. 2) The non-linear Schottky contact was substituted with a linear lossy capacitor, which had a series resistance and reactance equivalent to the diode impedance at the frequency of the analysis. Figure 2 shows schematically these two cases.

In both cases, the diode impedance was calculated with the harmonic-balance analysis, by finding the optimum input and output embedding impedances under optimum bias conditions. In the electromagnetic analysis the equivalent input and output circuits of the multiplier were used. Figure 3 shows the equivalent input circuit of the multiplier shown in Figure 1. Due to the symmetry, only half of the circuit is needed. To reduce computational requirements in the finite element analysis, it is important to take full advantage of electric and magnetic field symmetries. However, this should be done with care since physical symmetry of the structure does not necessarily imply electrical symmetry. The input waveguide TE_{10}-mode does not couple to the TEM-mode in the coaxial line between input and output waveguides. Therefore, the input circuit ends at the fixed curved backshort of the input waveguide. Comparison of the results showed that the backshort can be included either in the finite element analysis or later in the circuit analysis. Because the latter alternative was chosen, the equivalent input waveguide circuit is just a simple piece of waveguide with a port in each end. This approach is more flexible from the de-embedding point of view. The equivalent input circuit, as well as Figure 1, does not include a waveguide step, which is part of the $\lambda/4$ impedance transformer in the actual doubler.

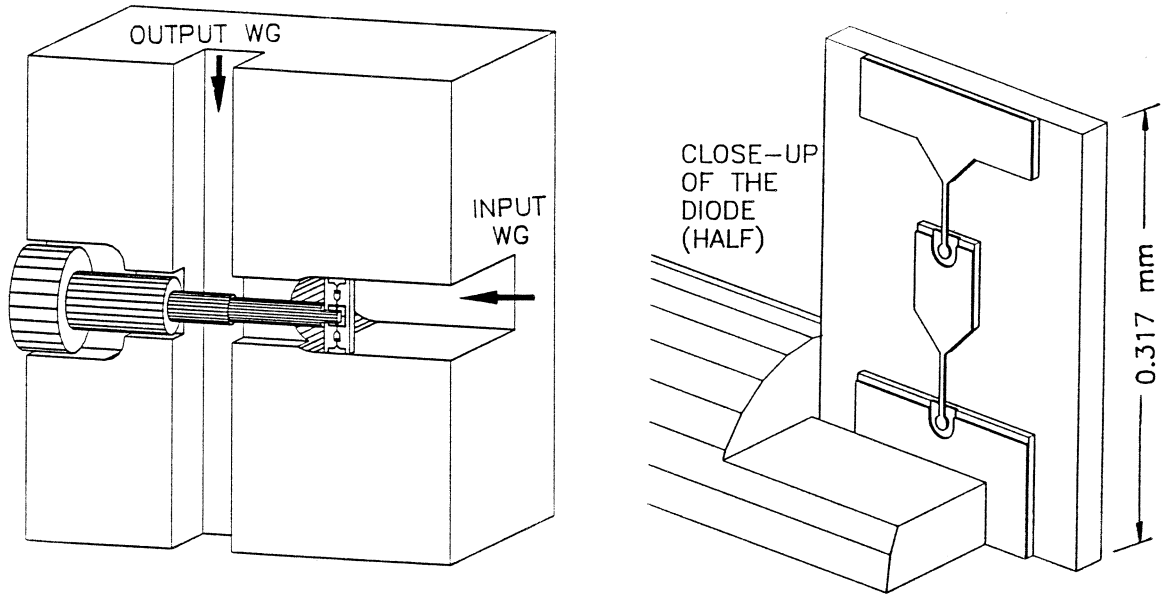

Figure 1: *The planar diode frequency doubler from 85 to 170 GHz used in the tests and in the finite element analysis.*

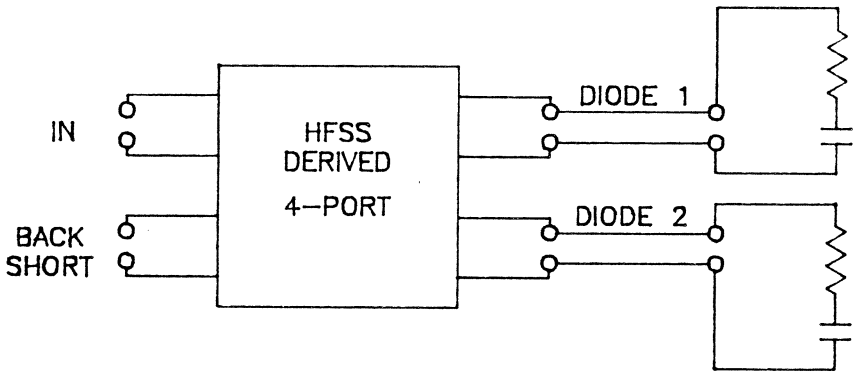

(a)

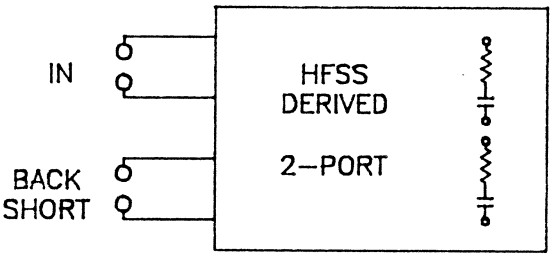

(b)

Figure 2: *Theoretical analysis circuit with (a) small probes to the diode locations and (b) lossy capacitor approach.*

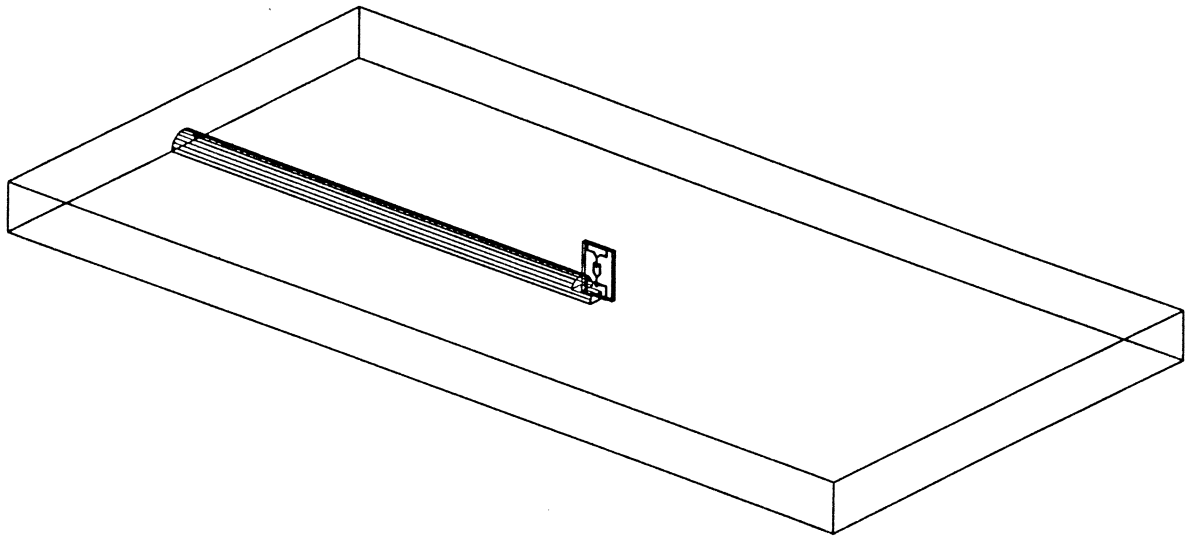

Figure 3: *Equivalent input circuit.*

Probe ports to the diode locations

Figure 4 shows schematically the theoretical analyzing process in the case when small probe ports are used to the diode locations and Figure 5 shows the cross-section of a diode location with a small probe. The output of the finite element analysis is a generalized 4-port S-matrix. There is one port to each diode location and one port in each end of the input waveguide with the S-parameters of each port normalized to the impedance of the cross section at the port. The 4-port S-matrix is combined into an embedding circuit in a circuit simulator, where diode impedances from the harmonic-balanced analysis are connected to the diode ports. To enable de-embedding and variation of the backshort position in the circuit simulator, circuits corresponding to the waveguide are connected to the waveguide ports. The waveguide circuit with the center bias pin is terminated with a backshort. The input impedance of the structure can now be calculated at the end of the other waveguide circuit.

De-embedding process, to obtain the diode terminal impedance, includes addition of waveguides with negative length and correct dispersion and impedance characteristics to the ports. Furthermore, the backshort is substituted with an open circuit. Balance between the absorbed power of the diodes can also be easily calculated from the currents and voltages in the diode ports of the S-matrix.

Diodes modeled as lossy capacitor

Instead of leading small probes to the diode locations in the finite element analysis, the correct load impedance may be placed at the diode location with a series RC circuit. In the finite element analysis, the RC circuit is easiest to realize by using a capacitor with lossy dielectric. Figure 6 shows the overall analyzing process in this case. The cross-section of the diode location, where a lossy capacitor has been placed is shown in Figure 7. The

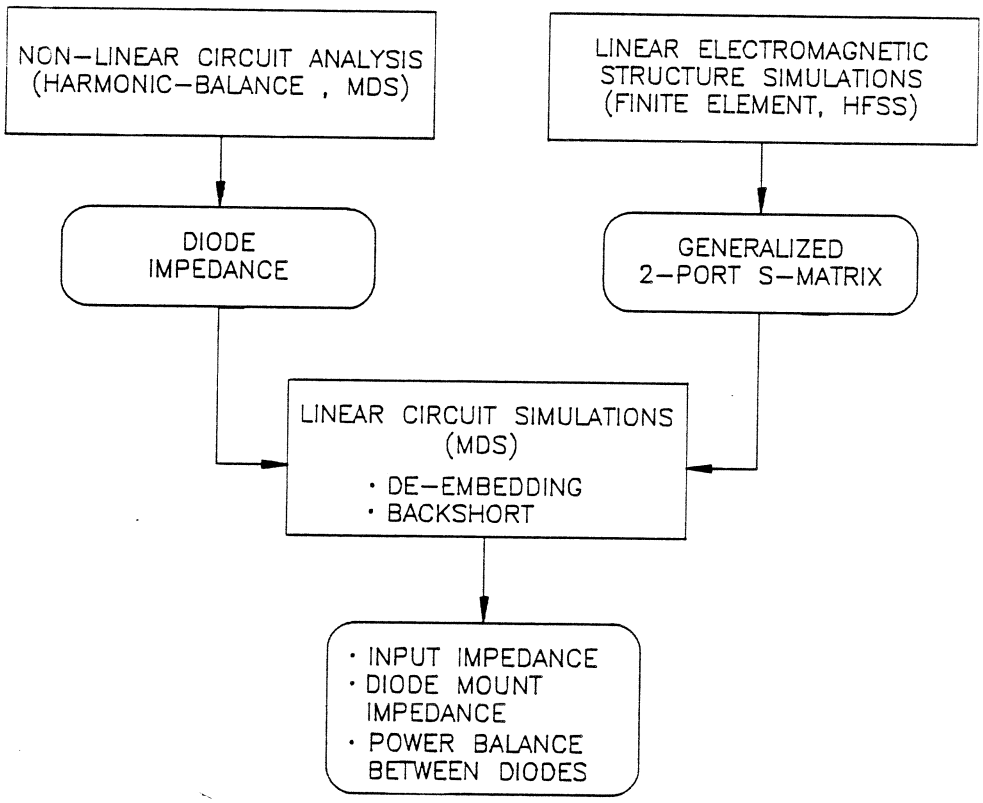

Figure 4: *Theoretical analyzing process with small probes to the diode locations.*

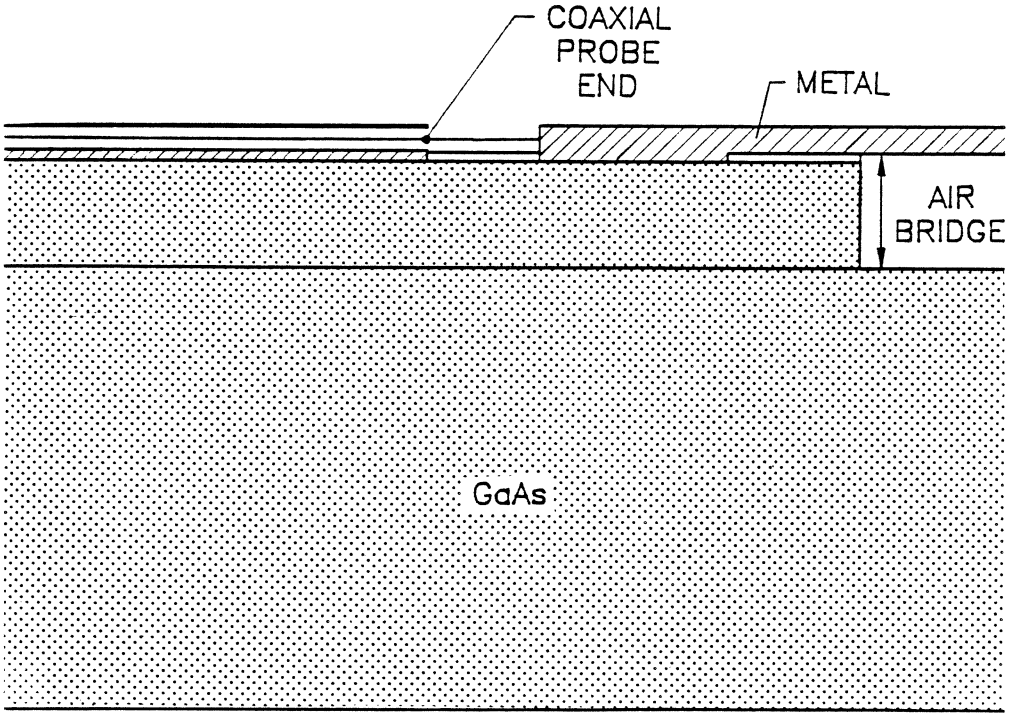

Figure 5: *Cross-sectional view of the diode junction area with a small coaxial probe.*

capacitor thickness is 2 μm, which is about two times the thickness of the n-type epilayer of a real Schottky contact. The heavily doped n^+-substrate, under the epilayer, is modeled as a perfectly conducting metal. The equivalent circuit for a lossy capacitor is shown in Figure 8. Losses in the dielectric can be expressed through a complex dielectric constant

$$\hat{\epsilon}\epsilon_0 = (\epsilon' - j\epsilon'')\epsilon_0 \tag{1}$$

where $\epsilon' = \epsilon_r$ is the real part of relative dielectric constant, ϵ'' is the imaginary part and corresponds to the losses in the material, and ϵ_0 is the dielectric constant of a vacuum. The equivalent series capacitance C_s is

$$C_s = C_0 \frac{\epsilon'^2 + \epsilon''^2}{\epsilon'}, \tag{2}$$

and the equivalent series resistance r_s is

$$r_s = \frac{\epsilon''}{\omega C_0(\epsilon'^2 + \epsilon''^2)}, \tag{3}$$

where $C_0 = \epsilon_0 A/d$ for a plate capacitor, A is area of the plates and d is the separation between the plates, ω is the angular frequency.

The advantage of using lossy capacitors over the small probes is that physically the model corresponds better to a real diode. Due to this, for example, fringing fields around the diode pad can be calculated more accurately. Also, the number of finite elements in the analysis is smaller with a lossy capacitor. This can be a significant advantage, because the complexity of the analysis is limited by the computer memory resources.

The disadvantage of the lossy capacitor approach is that the analysis relies on the assumption that the frequency dependence of the lossy capacitor impedance is the same as that of the diode, which is true only over a limited bandwidth. Another disadvantage is that the calculation of the division of the absorbed power by each diode junction is not as easy as with the diode probe ports. With lossy capacitors the power division can be obtained by calculating the pointing vector over a closed surface covering the lossy dielectric.

3 Numerical considerations

Even with the relatively large capabilities of present workstation computers, finite element analysis are often limited by the memory and processing speed of the computers. The discussion given here on the numerical limitations and requirements, and on how the analysis is done is based only on the experience with the HFSS finite element program. However, it may be assumed that the discussion serves as a general guide line to this type of analysis.

In the finite element analysis, the 2-D and 3-D structures are divided into triangular and tetrahedral sections, respectively. Figure 9 shows an example of the mesh associated with the volume in front of the diode. The structure must be closed with a metal surface. Inputs and outputs to the structure are obtained through ports on the outside surface. In each port the desired number of propagating modes are calculated, based on the cross-section of the port. Usually, the port is designed so that only the lowest order mode is supported at the frequency of the analysis. The waveguide attached to each port should extend far enough from the structure with the same cross-section so that all the evanescent modes have

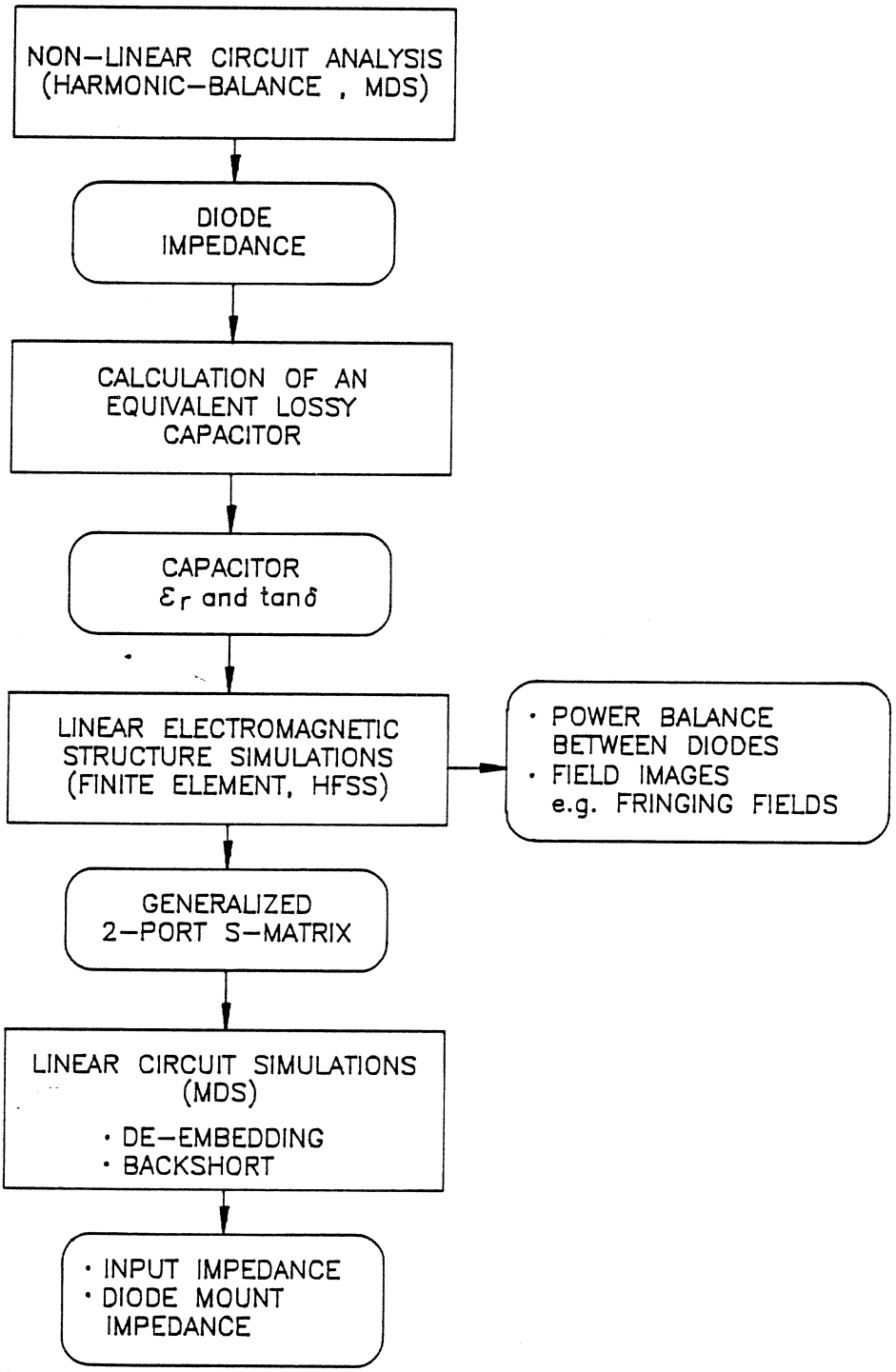

Figure 6: *Theoretical analyzing process with lossy capacitors.*

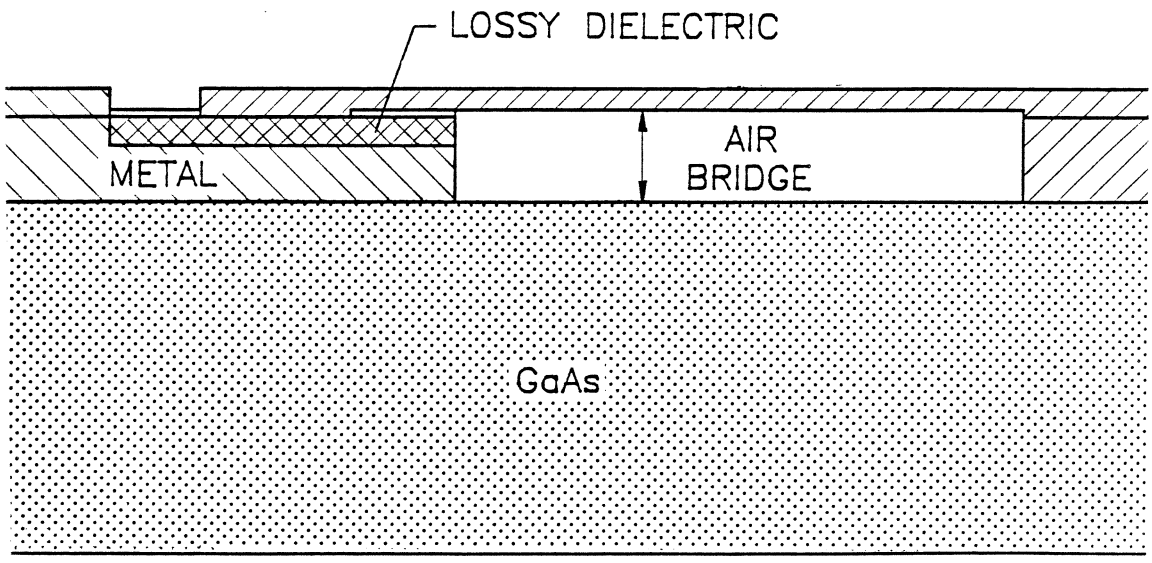

Figure 7: *Cross-sectional view of the diode junction area modeled as a lossy capacitor.*

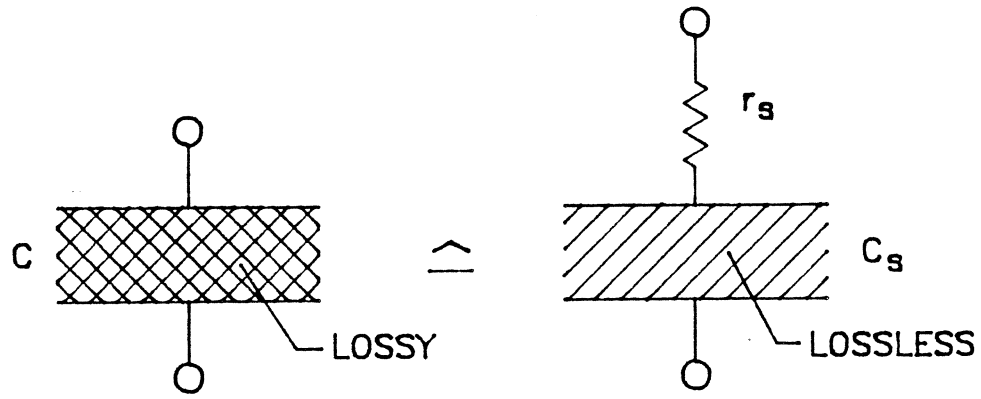

Figure 8: *Equivalent circuit of a lossy capacitor.*

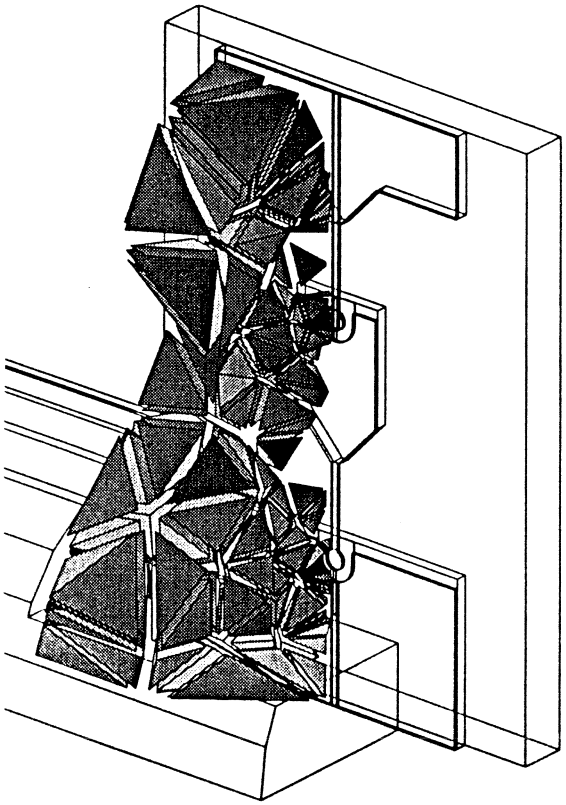

Figure 9: *Shaded view of a part of the finite element mesh in front of the diode.*

been attenuated at least 30–40 dB. This typically means that the length of the waveguide should be at least 1–3 times its width. After the mode(s) in the ports are calculated and the mesh generated, the full electromagnetic field pattern inside the structure, resulting from an excitation wave from one port is computed. This field solution is based on solving the wave equation inside the structure. The S-parameters are obtained by calculating coupling of the field inside the structure to the propagating mode(s) of each port.

From the point of view of numerical computations, the size of the mesh, i.e., the number of tetrahedra, is the most significant limiting factor. To save computer resources, the mesh is adaptively refined until the desired accuracy (convergence) for the S-parameters is obtained. In the process the mesh points are added iteratively so that the size of the tetrahedron is small compared to the length along which the field changes. Usually, 5-7 adaptive passes were used to obtain $\Delta S = 0.01$ (change of S-parameters compared to the previous adaptive pass).

The computer used in the analysis, was Sun Sparc II, with 64 MB of RAM, 219 MB of SWAP space, and a 1.5 GB harddisk. With this configuration the maximum mesh size was 34000 tetrahedra and 9 adaptive passes could be carried out for the input circuit shown in Figure 3. The memory requirement during the analysis when the matrix was solved was over 200 MB (of the RAM/SWAP memory area). In addition to these, over 350 MB of temporary file space was needed on the harddisk.

Analysis of the input circuit, was carried out from 75–95 GHz, and the mesh was generated in the middle of the band at 85 GHz. Practically no difference was observed in the results as mesh was generated at 75 or 95 GHz. In a circuit with strong resonances the mesh generated at one frequency might not be useful at another frequency. Convergence

and repeatability of the analysis were good: starting from different initial mesh gave the same results.

4 Results of the analysis

Effect of the thickness of the GaAs substrate

Experimental tests showed [2] a mismatch between the diode and waveguide mount impedances. This was due to the real part of the diode impedance being lower than that of the mount. Furthermore, the tests showed that better matching was obtained by using a thinner GaAs substrate. The original and thinner substrate were about 100 and 25 μm thick, respectively. For the comparison, finite element analyses were carried out for these two cases as well as for the imaginary extreme case of no substrate at all.

The results for the de-embedded diode terminal impedances are shown in Figure 10. This figure shows that a higher real part of the impedance is obtained as the substrate is made thinner. Therefore, better matching can be obtained with a thinner substrate. The slope of the curve of the imaginary part of the impedance indicates the resonance between the diode capacitance and the inductance of the embedding circuit of the diode junction. We see that the extra capacitance due to the thicker substrate lowers the resonance frequency of the chip, but also increases the Q of this resonance. For best bandwidth, the imaginary part of the impedance should go to zero near the midband of operation while the Q should be as low as possible. Therefore, the thinner substrate would ideally require more inductance in the package. This argument does not consider the matching at the second harmonic, which may require a lower inductance for the best results.

Quartz vs. GaAs substrate

Another possibility to improve diode matching to the waveguide impedance is to use substrate with a lower dielectric constant than that of GaAs (ϵ_r=13.0). Quartz (ϵ_r=3.8) is one such a material. Quartz is, however, more difficult than GaAs to make thin. The thinnest GaAs substrate that is reasonable to fabricate and to handle is about 25 μm. The question is what thickness quartz substrate would be better than this thinnest GaAs substrate. To find this out, the analysis was carried out for a quartz thickness of 100 μm (which would be also a very reasonable thickness to realize in practice). Figure 11 shows the de-embedded diode terminal impedance for 25 μm GaAs and 100 μm quartz substrates.

Comparison of the impedances shows that a 100 μm quartz substrate gives a slightly higher real part of the impedance. Therefore, if the quartz is used it should be made thinner than about 100 μm. The smaller thermal conductivity of the quartz over GaAs is one limitation for the use of a quartz substrate.

No air bridge

Planar diodes are generally designed with an air bridge as a lead to the Schottky contact pads. The air bridge provides a break in the n^+ substrate to avoid a dc short circuit across the diode, a need which would otherwise require a proton isolation of the region. An additional

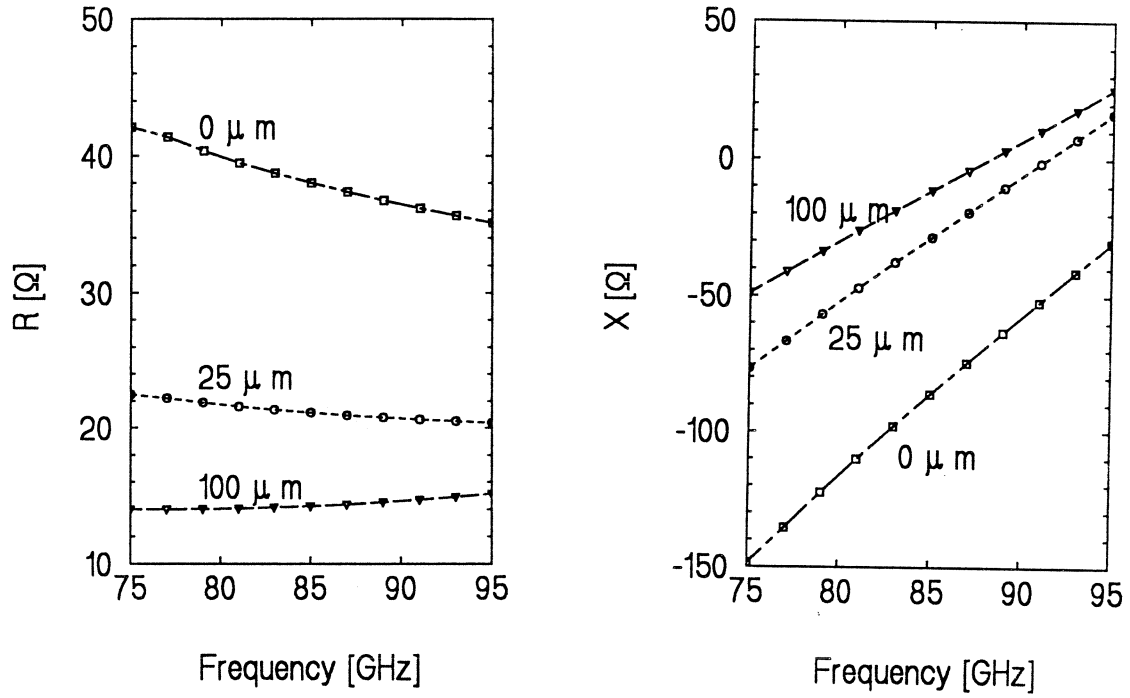

Figure 10: *Real and imaginary part of the de-embedded diode terminal impedances with 0, 25 and 100 μm GaAs substrate thicknesses.*

advantage is that air bridges reduce the shunt capacitance over the planar diode junction. However, most of the shunt capacitance is due to the fringing field between the relatively large contact pads through the high dielectric constant GaAs [3]. To study the electrical advantage of the air bridge geometry, analysis was carried out with the space under the air bridge filled with GaAs.

Figure 12 compares the de-embedded diode terminal impedances with and without the air bridge. The substrate is a 25 μm thick GaAs in both cases. The comparison shows that electrically the air bridge is only marginally effective with high capacitance varactors ($C_{j0} \approx 40$ fF). For lower capacitance planar diodes, used for example in mixers, the effect of the air bridge can be more significant. Avoiding the use of an air bridge would improve the handling and mechanical strength of the diode. Also the length of the inductive finger would not be limited, for example, when contact pads are brought further apart to reduce fringing capacitances.

Power balance between the diodes

To enable efficient use and biasing of all four diodes on the same chip, the absorbed power should be equal for each of them. For all the structures that were analyzed, the power balance between the diodes (inner diode, which is closer to the bias pin, and outer diode, which is closer to the waveguide wall) was practically frequency independent. However, depending on the structure, the power imbalance varied from 2.7 to 12.2 %. Table 1 summerises the

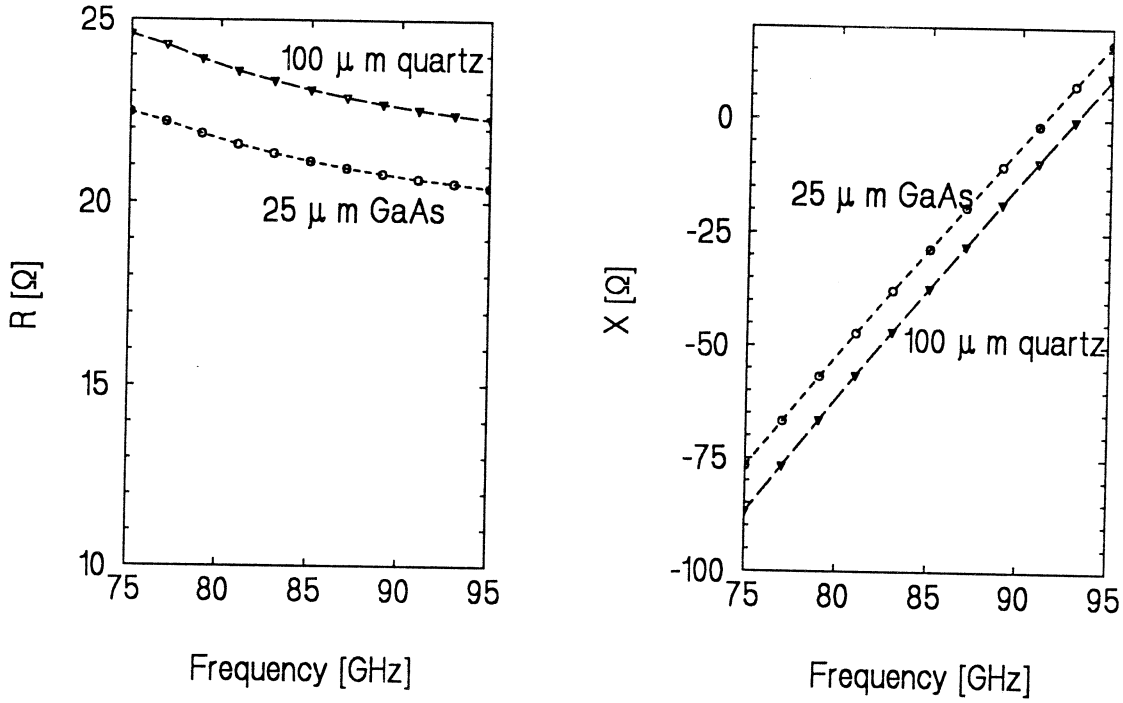

Figure 11: *Real and imaginary part of the de-embedded diode terminal impedances with 25 μm GaAs and 100 μm quartz substrates.*

power imbalance observed in different cases. The power imbalance is defined here as

$$\Delta P = \frac{P_{\text{outer}} - P_{\text{inner}}}{P_{\text{inner}}}. \tag{4}$$

A positive percentage value means, therefore, that the outer diodes are absorbing more power than the inner diodes.

The values in Table 1 imply that the environment of the diodes are not symmetric and to optimize the diode operation the symmetry should be improved. The primary contribution to the imbalance is the different sizes of the metallization areas around the diodes. A larger metallization area around the diode junction increases the shunt capacitance and therefore decreases the absorbed power. The addition to the shunt capacitance of the inner diodes due to the bias pin is less than afew percent, even though size of the pin is large compared to the center contact pad. This can be understood by realizing that the fringing fields are concentrated in the high dielectric substrate material.

5 Conclusions

Finite element analysis was shown to be useful in analyzing a planar diode multiplier structure from 85 to 170 GHz.

The diode that was fabricated and analyzed here is a good first step. To optimize the diode design, the de-embedded diode terminal impedance in the input circuit was studied.

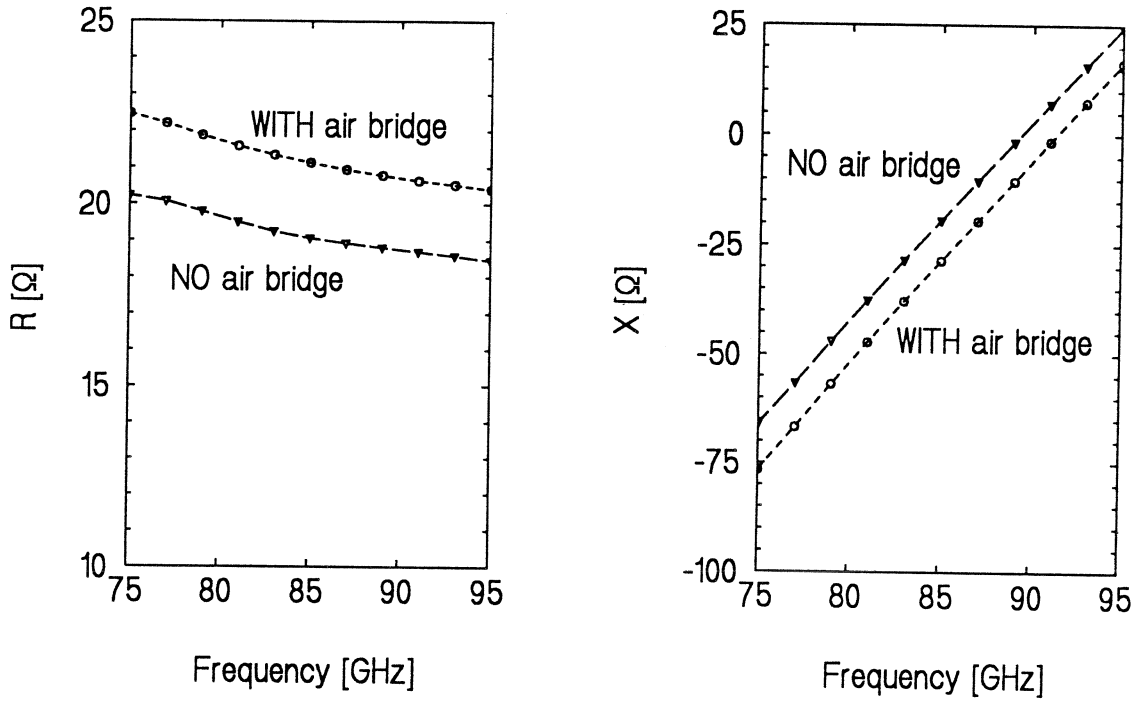

Figure 12: *Real and imaginary part of the input and diode mount impedances with and with out air bridge (25μm GaAs substrate).*

Table 1: *Absorbed power imbalance between the inner and outer diode junctions. A positive percentage means that the outer diode junctions are absorbing more power than the inner diode junctions.*

Substrate	Power imbalance ΔP
GaAs 0 μm	2.7 %
GaAs 25 μm	8.9 %
GaAs 100 μm	9.2 %
GaAs 25 μm (no air bridge)	12.2 %
GaAs 25 μm (no bias pin)	7.4 %
Quartz 100 μm	3.1 %

The analysis showed that thinner substrate thickness gives a better matching for the diode impedance to the waveguide impedance. If quartz substrate is used instead of GaAs, to improve the matching, it has to be thinner than 100 μm. This is based on the assumption that GaAs substrate can not be made thinner than 25 μm.

The analysis revealed that from the electrical point of view air bridges in the diode were only marginally effective for high capacitance varactors.

A slight absorbed power imbalance was also found between the diodes. To improve the power balance, the symmetry of the environment of the diodes has to be improved by changing the diode metal pad sizes.

Acknowledgment

We acknowledge the financial support of the European Space Agency through a ESA Fellowship for one of the authors and the National Aeronautics and Space Administration under grant NAGW2430.

References

[1] R. F. Bradley, "The application of planar monolithic technology to Schottky varactor millimeter wave frequency multipliers ," Ph.D. dissertation, University of Virginia, May 1992.

[2] N. R. Erickson, B. J. Rizzi, T. W. Crowe, "A 174 GHz high power doubler using a planar diode array," This proceedings.

[3] B. J. Rizzi, J. L. Hesler, H. Dossal, T. W. Crowe, "Varactor diode for millimeter and submillimeter wavelengths," *Proc. Third Int. Symp. Space Teraherz Tech.*, Ann Arbor, pp. 73–92, March 1992.

HIGH-FREQUENCY INP GUNN OSCILLATORS: SIMULATION AND EXPERIMENT

R. Kamoua[†], H. Eisele[‡], G. I. Haddad[‡], G. Munns[‡], and M. Sherwin[‡]

[†] Department of Electrical Engineering,
State University of New York at Stony Brook,
Stony Brook, NY 11794-2350

[‡] Center for Space Terahertz Technology
Department of Electrical Engineering and Computer Science
The University of Michigan, Ann Arbor, MI 48109-2122

Abstract

A self consistent ensemble Monte Carlo model for the simulation of InP Gunn devices has been developed and was presented in an earlier report [1]. The choice of the InP material parameters has been found to be critical to the validity of the model. Appropriate parameters were estimated by comparing the model predictions and experimental results. However, only experimental data around 83 GHz were available at that time.

Recently, very promising experimental results were obtained from 1 μm InP Gunn structures. Two doping profiles were chosen: a uniform doping of 2.5×10^{16} cm^{-3} and a graded doping increasing linearly from 7.5×10^{15} cm^{-3} at the cathode to 2.0×10^{16} cm^{-3} at the anode. Diodes having the flat doped structure gave 33 mW of RF power at 108.3 GHz while diodes with the graded structure yielded 20 mW at 120 GHz, 10 mW at 136 GHz and 8 mW at 155 GHz. Low measured Q values indicated that these results correspond to a fundamental mode of operation. Details of the experimental results will be presented in a separate paper. With this additional experimental data, a better estimation of InP material parameters is possible. A comparison of the resulting Monte Carlo model predictions and the experimental results is carried out. The potential of InP Gunn devices for power generation in the D-band (110 GHz - 170 GHz) is then discussed.

[1] R. Kamoua, H. Eisele, J.R. East, G. I. Haddad, G. Munns, and M. Sherwin, "Modeling, Design, Fabrication, and Testing of InP Gunn Devices in the D-band ", *Third International Symposium on Space Terahertz Technology* March 24-26, 1992, Ann Arbor, MI.

1 Introduction

InP is recognized to have superior characteristics compared to GaAs for power generation in the millimeter wave region [1, 2]. Fundamental mode operation up to 110 GHz has been achieved with InP Gunn devices whereas GaAs Gunn devices are believed to operate in second harmonic mode at around 94 GHz [3]. This paper reports on the development of InP Gunn devices in the D-band (110 GHz - 170 GHz).

A physical model based on the Monte Carlo technique is developed to simulate, design, and predict the performance of Gunn structures for high frequency operation. A characteristic of the Monte Carlo method, as applied to the simulation of semiconductor devices, is the requirement of accurate values for a large number of material parameters. This is not an easy task, especially for the less technologically developed compounds such as InP. The typical material parameters given in the literature have been found to be inadequate in predicting our experimental data. Based on comparisons between the model and experimental results from a well characterized InP Gunn diode, more accurate material parameters were estimated.

2 Simulation Model

The self-consistent Ensemble Monte Carlo model is used to estimate the performance of InP Gunn devices at millimeter wave frequencies. This model is an extension of the one-particle Monte Carlo technique [4]. The simulation algorithm monitors the evolution in real space and momentum space of an ensemble of electrons. The simulation time is partitioned into time steps ($\Delta t = 5 \times 10^{-15}$ sec), and each time step is terminated by a call to a Poisson equation solver in order to update the electric field. In each time step, every electron is submitted to successive free flights terminated by a scattering process which is selected using a random number generator. When all electrons are simulated for one time step, the carrier density is calculated and the electric field is updated.

To predict the performance of a particular Gunn structure a sinusoidal RF voltage is applied across the device and the current response is simulated over many RF periods (about 10). A Fourier analysis of the resulting particle current density gives the current's fundamental component which is subsequently used to determine the device admittance per unit area. To estimate the RF output power, the Gunn device is assumed to be connected to a resonant circuit represented by a load resistance and a resonating inductance. A series resistance is included in the equivalent circuit to take into account effects of contact resistances, any substrate resistances, and skin effect losses.

3 Estimation of InP Material Parameters

In this section, the material parameters needed for the Monte Carlo model are estimated. The accuracy of the model is strongly dependent on the accuracy of the material parameters used. Unfortunately, a wide range of values is given in the literature. In particular, some of the material parameters that are important to the Gunn effect have the following range of values ([5, 6, 7, 8, 9]):

$\Gamma - L$ valley separation (eV)	0.4	$\longleftrightarrow$	0.832,
L valley effective mass ratio ($\frac{m}{m_0}$)	0.26	$\longleftrightarrow$	0.4,
$\Gamma - L$ coupling constant ($\times 10^9$ eV/cm)	0.1	$\longleftrightarrow$	2.5,
$\Gamma - X$ coupling constant ($\times 10^9$ eV/cm)	0.43	$\longleftrightarrow$	1.0.

There is more than an order of magnitude uncertainty in the Γ to L intervally coupling constant. The appropriate material parameters are determined by comparing measurements at high frequencies with results predicted by the model. The structure considered for comparison is shown in figure 1. It has a 1.7 μm long active 1×10^{16} cm^{-3}, a 0.1 μm cathode region doped at 3×10^{17} cm^{-3}, and a 0.2 μm anode region doped at 3×10^{17} cm^{-3}.

An InP wafer with this structure has been processed. Diodes with various sizes have been mounted on copper heat sinks. Tapered leads were thermocompression bonded to

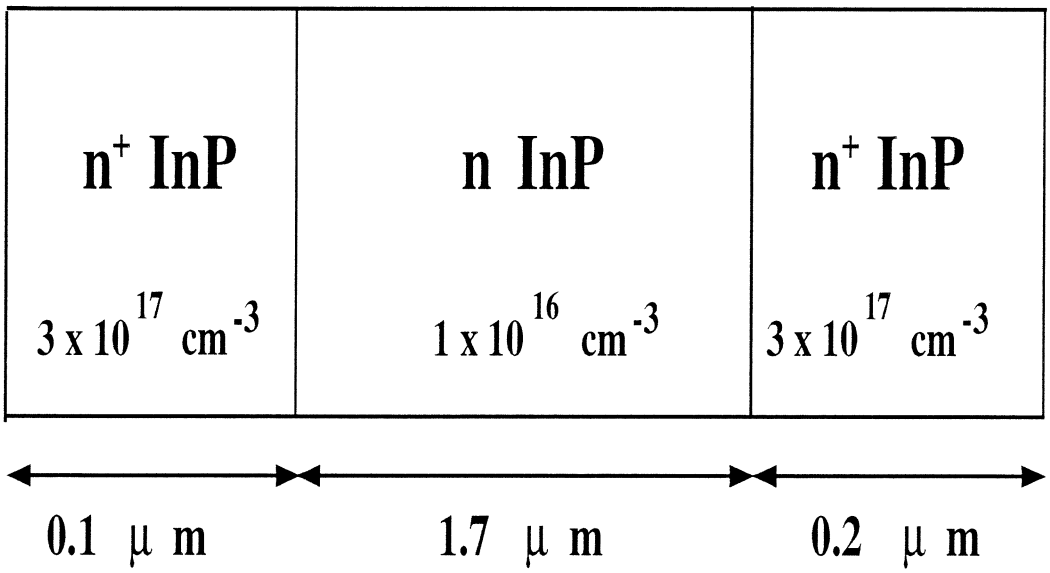

Figure 1: Gunn structure used in the model to determine more accurate InP material parameters.

the diode and to four metallized quartz standoffs. For some diodes, a metallized quartz ring was used instead of the standoffs.

A 50 μm diode was tested in a W-band resonant cavity with the following results: 40.0 mW output power at an oscillation frequency of 80.0 GHz and an efficiency of 1.6 %. The bias voltage was 5.0 V and the dc current was 500 mA. The structure shown in figure 1 is simulated using the Monte Carlo model. The dc bias voltage is set to 5.0 V and the temperature to 450 K. A starting set of material parameters is assumed and is taken from various sources in the literature. These parameters are listed in the second column of table 1 and constitute the the initial parameter set. No oscillations were obtained with these values for frequencies ranging from 75 GHz to 120 GHz. It appears that the $\Gamma - L$ intervalley energy separation of 0.8 eV is too large.

A systematic procedure for changing the values of the different parameters is adopted. In particular the values used for the intervalley energy separation and the effective mass in each valley are targeted. It is expected that the occurrence of oscillations will be enhanced if the electron effective mass in the satellite valleys is increased, the intervalley

parameter		typical value	this paper
Energy Separation (eV)	Γ-L	0.832	0.45
	Γ-X	1.5	0.775
Effective Mass ($\frac{m}{m_0}$)	Γ	0.082	0.082
	L	0.26	0.5
	X	0.325	0.5
Nonparabolicity factor (1/eV)	Γ	0.83	0.83
	L	0.23	0.23
	X	0.38	0.38
Intervalley Coupling Constant (10^9 eV/cm)	Γ-L	0.506	1.0
	Γ-X	0.498	1.0
	L-X	0.468	0.468
	L-L	0.575	0.575
	X-X	0.28	0.28
Acoustic Deformation Potential (eV)	Γ	7	5
	L	7	5
	X	7	5
LO Phonon Energy (eV)	Γ	0.043	0.043
	L	0.0423	0.0423
	X	0.0416	0.0416
Static Dielectric Constant		12.61	12.61
Optical Dielectric Constant		9.61	9.61

Table 1: InP material parameters: typical values and values used in this paper.

energy separation is reduced, and the scattering rates to the satellite valleys are increased. The combined effect of these changes is to increase the transfer to the satellite valleys for the same bias voltage and reduce the average electron velocity at high electric fields. As a consequence a larger negative differential mobility is obtained which is more favorable for nucleating space charge layers. Upon making the above changes a set of parameters, listed in the last column of table 1, was obtained which will be shown to yield good agreement with the experimental results.

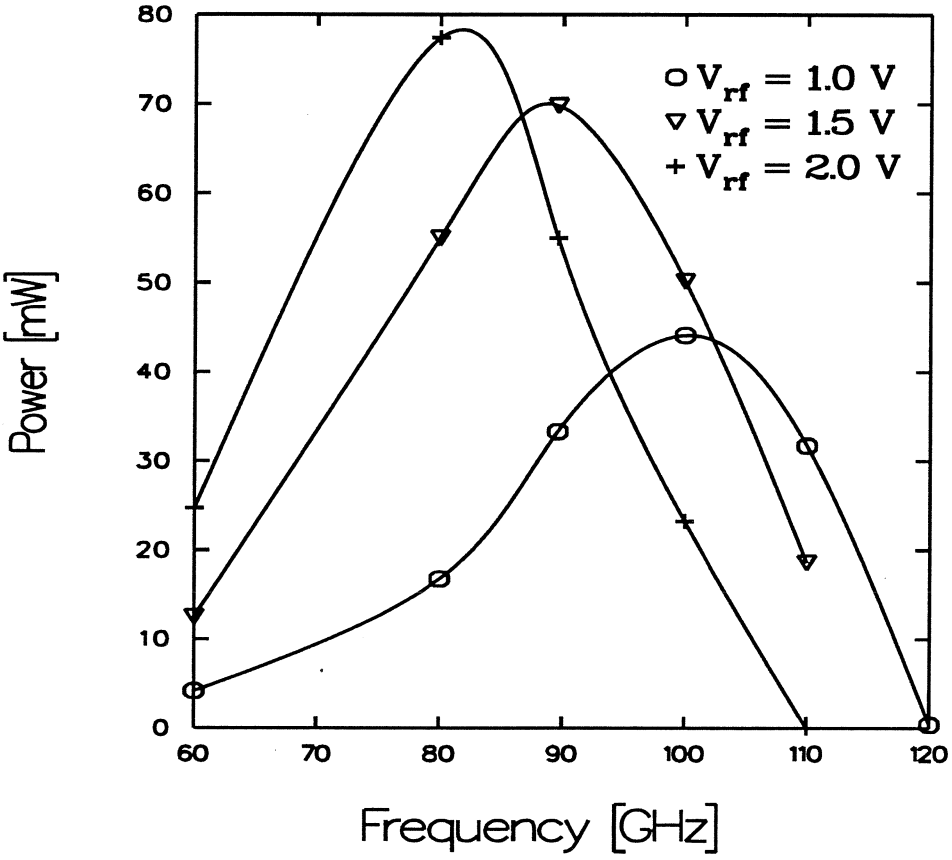

Figure 2: Predicted output power as a function of frequency from the W-band structure for three RF voltages (1.0 V, 1.5 V, and 2.0 V). The dc voltage is 4.0 V and the operating temperature is 450 K.

In order to compare the theoretical predictions with the experimental results, the diameter of the device is set to 50 μm which corresponds to the size of the tested diode. As a result, the load resistance of the resonant circuit is adjusted until the oscillation condition is satisfied. This procedure is repeated at various frequencies and RF voltages. Figure 2 shows the predicted output power as a function of frequency for three RF voltages (1.0 V, 1.5 V, and 2.0 V). At a given RF voltage, the power curve exhibits a peak as a function of frequency. This peak occurs at 100 GHz for an RF voltage of 1 V and has a value of 43 mW. As the RF voltage amplitude is increased, the peak value increases and shifts to lower frequencies: 90 GHz for an RF voltage of 1.5 V and 80 GHz for an

RF voltage of 2.0 V. A peak is obtained because the power is directly proportional to the RF voltage amplitude and the device equivalent negative conductance. The conductance decreases as the RF voltage is increased, therefore the product of the conductance and the RF voltage amplitude exhibits a maximum. The simulation predicts oscillations in a wide-band of frequencies from 60 GHz to 110 GHz. This is in agreement with the known behavior of Gunn devices as well as our experimental results. The model predicts up to 80 mW at 80 GHz with an RF voltage of 2.0 V.

It is now possible to compare the experimental with the theoretical results. Referring to figure 2 reveals that the predicted output power at 80 GHz varies from 15 mW to near 80 mW as the RF voltage is increased from 1.0 V to 2.0 V. Therefore there exists an intermediate RF voltage that yields an output power of 40 mW which is the experimentally obtained value. It is important to realize that higher power levels could be predicted by increasing the dc voltage and changing the RF voltage. However such operation point might correspond to an excessive temperature rise or require unrealistic load impedance level. In the actual operation of the Gunn device, the resonant cavity determines the oscillation frequency according to the impedance it provides to the diode terminals.

4 1.0 μm InP Gunn Structures

In order to achieve higher fundamental frequencies, it is necessary to decrease the device length and increase the doping level in the active region. In this section, two 1 μm structures with different doping profiles are considered.

4.1 Flat Doping Profile

A 1.0 μm InP structure has been designed with a flat doping profile. The wafer was grown by CBE (Chemical Beam Epitaxy). The doping in the active region was estimated to be 2.5×10^{16} cm^{-3} from C-V measurements. This doping is slightly higher than what

is typically used for 1 μm structures. The wafer was processed and 35 μm diodes were packaged and tested in a resonant cap waveguide cavity. Oscillations were obtained at 108.3 GHz with 33 mW CW output power and 1.87 % efficiency. The diode was biased at 4.1 V and has a dc current of 430 mA.

A structure similar to the experimental device has been simulated. The bias voltage was set to 4.1 V and the operating temperature to 480 K. The actual device operating temperature is estimated to be close to 500 K since most of the devices failed as the bias voltage is increased beyond 5 to 5.5 V. The performance was evaluated as a function of frequency and for different RF voltages (1.0 V, 1.5 V, 2.0 V, and 2.5 V). Figure 3 shows the RF output power versus frequency. More than 60 mW output power is predicted near 120 GHz. For an RF voltage of 2.5 V, the power peaks near 108 GHz and the oscillation bandwidth becomes smaller compared with lower RF voltages. The predicted power at 108.3 GHz in this case is approximately 50 mW. This value is in good agreement with the experimental results when taking into account cavity losses.

4.2 Graded Doping Profile

This section examines ways of enhancing the performance of InP Gunn devices in the D-band. One method consists of specifying a nonuniform doping profile in the active region and in particular, a linearly graded profile. In this case, the doping should increase from the cathode region toward the anode region, otherwise the performance is likely to be worsened [10]. The advantages of a linearly doping profile include reducing the peak electric field, lowering the current density, and improving the efficiency and output power. The peak electric field in a Gunn structure occurs near the anode region. With a linear doping profile, the peak is reduced because electrons diffuse from the high doped region near the anode to the low doped region at the cathode. The reduction in the field has two desired effects: first, a higher cathode field results in a larger fraction of the electrons transferring to the upper valleys over shorter distance, second a lower anode

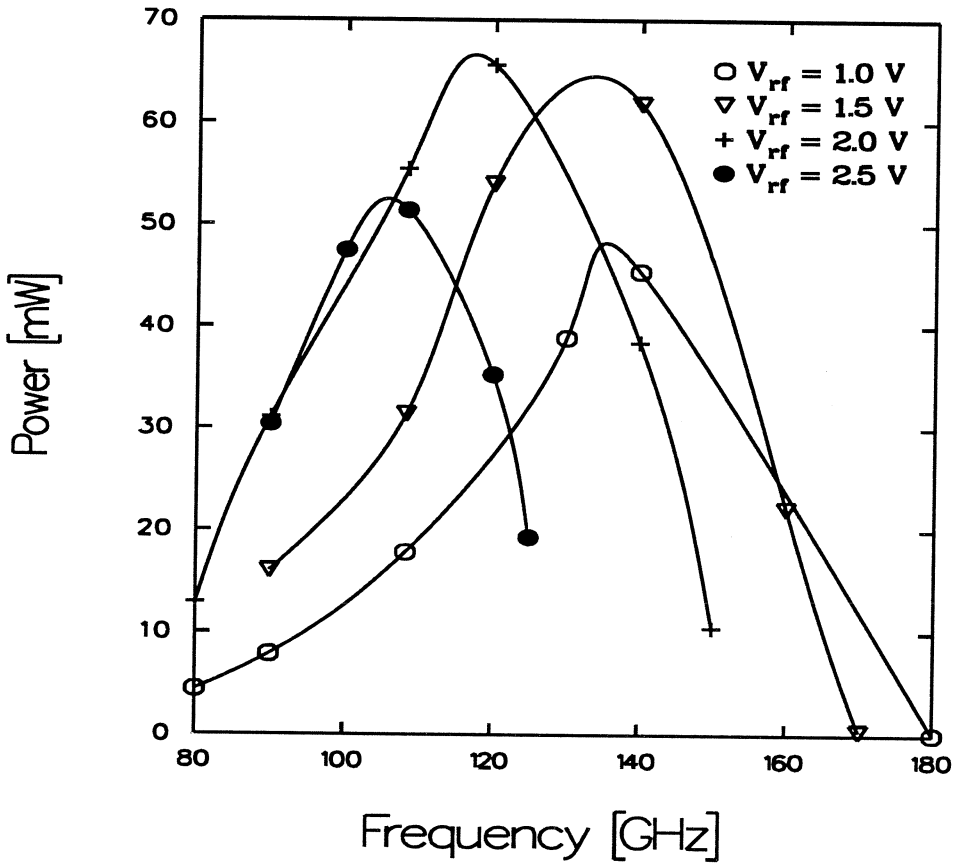

Figure 3: Predicted output power as a function of frequency for a 1 μm Gunn structure with flat doping profile. The dc voltage is 4.1 V and the operating temperature is 480 K.

field allows the application of a larger dc bias without reaching breakdown. These effects improve the the efficiency and the output power. A graded doping profile also results in a lower current density than would be obtained from a uniformly doped structure with similar doping level. This behavior is a consequence of the higher fraction of electrons in the upper valleys which reduces the average velocity.

A wafer with a graded doping profile was designed and grown by MOCVD. The structure has a 1 μm active region with a doping linearly increasing from 7.5×10^{15} cm^{-3} at the cathode side of the active region to 2.0×10^{16} cm^{-3} at the anode side. Samples were processed with integrated heat sinks consisting of plated gold and silver layers. 45

μm diodes were mounted on copper heat sinks and tested in a D-band waveguide cavity. Oscillations were obtained with 20 mW at 120 GHz, 10 mW at 136 GHz and 8 mW at 155 GHz. These devices are believed to operate in the fundamental mode since the measured Q values were between 30 and 100 around 120 GHz using a self-injection locking method. Low Q values are not a characteristic of a harmonic mode operation [11, 12]. These results represent the best performance from Gunn Devices reported at these frequencies.

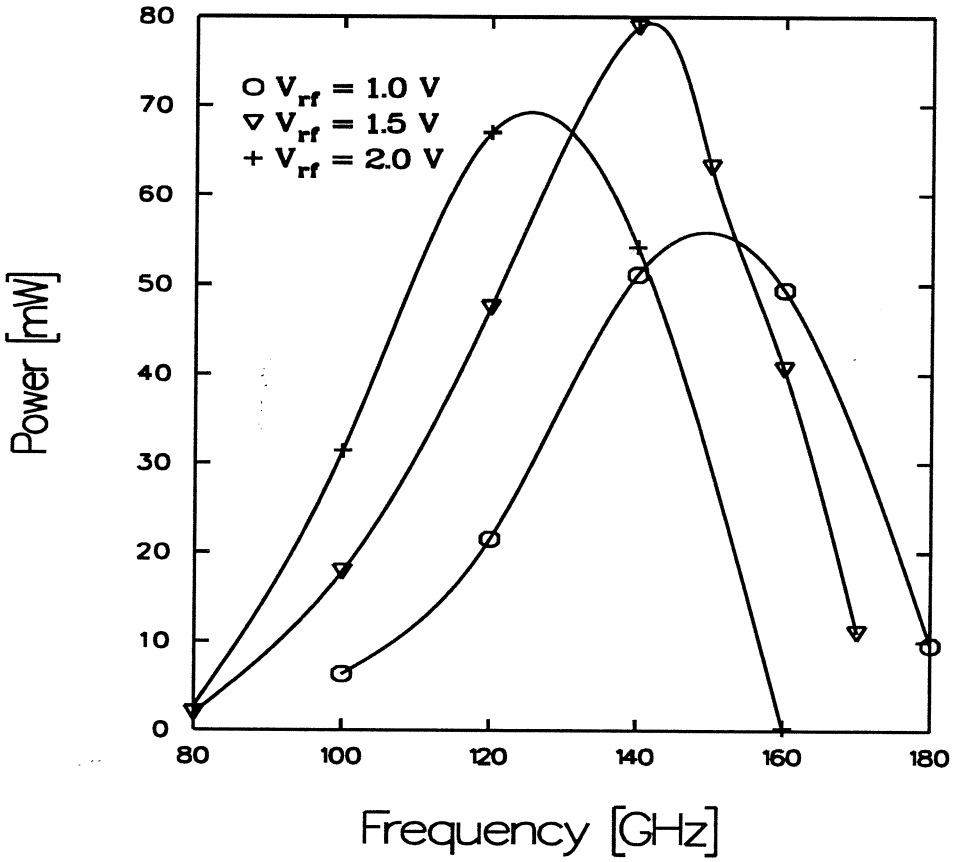

Figure 4: Predicted output power as a function of frequency for a 1 μm Gunn structure with graded doping profile. The dc voltage is 4.1 V and the operating temperature is 400 K.

Simulations were carried out on a similar structure using the Monte Carlo model. The dc bias voltage was set to 4.1 V, the operating temperature at 400 K, and the device diameter was fixed at 45 μm. Figure 4 shows the predicted output power as a function

of frequency at various RF voltages. The oscillations occur at frequencies ranging from 80 GHz to 180 GHz, however at the two extremes the oscillation condition requires load resistances less than 1 Ω. The output power peaks near 140 GHz where 80 mW is predicted for an RF voltage of 1.5 V. The simulation predicts oscillations in a frequency range corresponding to what has been observed experimentally, but with higher output power levels. Although the experimental results are very promising, more work need to be done to further improve the performance of the graded structures in the D-band.

5 Conclusions

A method has been developed for estimating the material parameters used in the Monte Carlo model. By comparing simulation and experimental results at high frequencies, more accurate material parameters were obtained. It was found necessary to use low values for the intervalley energy separation and high values for the deformation potentials than normally used in the literature. A possible reason for these trends is the high operating temperature of the Gunn device.

Simulation results have shown that it is possible to operate fundamental mode InP Gunn devices in the D-band frequency region. The operation requires structures with near micron dimensions. Two such structures have been designed, modeled, fabricated, and tested. The first structure consisted of a 1 μm active region uniformly doped at 2.5 $\times$ 10^{16} cm^{-3}. The second structure had a linearly graded doping profile increasing from 7.5 $\times$ 10^{15} cm^{-3} at the cathode side to 2.0 $\times$ 10^{16} cm^{-3} at the anode side. Experimental results from these structures were very encouraging and represent the state of the art at these frequencies. Both structures operated over roughly the same frequency range, however the graded structure yielded better performance at the high frequency end. This observation confirms the claim that nonuniform doping profiles are superior to flat doping profiles in terms of performance and high frequency capabilities.

The theoretical simulations with the improved material parameters predict even higher power levels at these frequencies. It is the opinion of the authors that better experimental results could be achieved around 140 GHz. This requires optimizing the doping profile, reducing further the contact resistances, developing better heat sinks and packaging techniques, and employing current limiting contacts.

Acknowledgements

The authors would like to thank Yoshio Saito at TRW and Jürg M. Siegenthaler at the Swiss PTT for providing different quartz rings which were used to package some of the Gunn devices. This work was supported by the Center for Space Terahertz Technology under Contract No. NAGW-1334.

References

[1] L. Wandinger, *The Microwave Journal*, p. 71 March (1981).

[2] B. Fank, *Microwave Journal,* p. 95, (1984).

[3] W. H. Haydl, *Electronics Letters,* **17**, No. 22, p. 825 (1981).

[4] W. Fawcett, A. D. Boardman and S. Swain, *J. Phys. Chem. Solids,* **30**, p. 643 (1969).

[5] K. Brennan, K. Hess, J. Y. Tang, and G. J. Iafrate, *IEEE Trans. on Electron Dev.,* **ED-30**, No. 12, p. 1750 (1983).

[6] D. C. Herbert, W. Fawcett, and C. Hilsum, *J. Phys. C: Solid State Phys.,* **9**, p. 3969 (1976).

[7] G. H. Glover, *J. Appl. Phys.,* **44**, No. 3, p 1295 (1973).

[8] T. J. Maloney, and J. Frey, *J. Appl. Phys.,* **48**, No. 2, p. 781 (1977).

[9] M. V. Fischetti, *IEEE Trans. on Electron Dev.,* **ED-38**, No. 3, p. 634 (1991).

[10] Michihisa Suga, and Kenji Sekido, *IEEE Trans. on Electron Dev.,* **ED-17**, p. 275 (1970).

[11] H. Barth, *IEEE MTT-S Digest,* p. 179 (1986).

[12] I. G. Eddison, and D. M. Brookbanks, *Electronics Letters,* **17**, No. 3, p. 112 (1981).

Novel 100 GHz GaAs/AlGaAs MQW IMPATT Oscillators :p^+n Single-Drift Structures on p^+ Substrates

C. C. Meng#, S. W. Siao and H. R. Fetterman
Department of Electrical Engineering
University of California, Los Angeles
Los Angeles, CA 90024

D. C. Streit, T. R. Block and Y. Saito
TRW
Space & Electronics Group
Redondo Beach, CA 90278
Currently working at Avantek/Hewlett Packard

I Introduction

We have successfully fabricated and tested GaAs/$Al_{0.3}Ga_{0.7}As$ MQW (Multiquantum Well) IMPATT (IMPact ionization Avalanche Transit Time) oscillators at 100 GHz. For the first time to our knowledge, CW operation of MQW IMPATT devices at 100 GHz has been achieved. Conventional GaAs IMPATT devices show a fall-off in efficiency at the frequencies above 50 GHz because of the saturation of the ionization rates at high electric fields. Recently, MQW structures have been proposed to reduce the ionization rate saturation limitations[1]-[3]. Efficiencies of 13% at 100 GHz and 10% at 140 GHz were projected for GaAs/AlGaAs single-drift flat-profile MQW IMPATT devices[3]. Preliminary results yielded 6.4 mW CW power at 100.3 GHz and 364 mA bias current in a non-optimized circuit. Experimental efforts are underway to optimize the circuit parameters and significantly higher powers are anticipated.

II Impact Ionization in MQW Structures

Ionization rate saturation limitations occur when an IMPATT device is biased at high electric fields for high frequency operations. The saturation of ionization rates at high electric fields results in a broaden injected current pulse in a less localized avalanche region and degrades the device efficiency[4]. The ionization rate saturation limitations can be reduced by replacing the bulk avalanche region by a GaAs/AlGaAs MQW structure. Impact ionization is characterized by an ionization threshold energy. A wider bandgap material has a higher impact ionization threshold energy and the ionization rate at any given electric field has an exponential dependence on the ionization threshold energy. Consider the case of a GaAs/AlGaAs multiquantum well structure. We use E_T for bulk GaAs ionization threshold energy and E_{TA} for bulk AlGaAs ionization threshold energy. When electrons (holes) enter the barrier region of a multiquantum well structure, electrons (holes) lose

some kinetic energy to the band discontinuity and thus the effective threshold energy (E'_{TA}) becomes higher higher. Here E'_{TA} can be expressed as $E'_{TA} = E_{TA} + \Delta E$, where ΔE is the band offset energy. The probability of impact ionization in the barrier region is reduced. If the barrier length is designed to be comparable to the energy relaxation length, then electrons (holes) can obtain energy when traveling through the barrier region. When an electron (hole) exits the barrier and enters the well, it sees a less effective threshold energy (E'_T) in the well region. E'_T can be expressed as $E'_T = E_T - (\Delta E + e\xi l_{eff})$. Here $e\xi l_{eff}$ is the energy obtained from the potential barrier, where l_{eff} is the effective energy acceleration length and is equal to the smaller value of the two quantities, (1) energy relaxation length and (2) barrier length.

Because E'_{TA} is much larger than E'_T, we can assume that impact ionization is forbidden in the barrier region and E'_T can be treated as the threshold energy for the whole multiquantum well structures. The amount of reduction in E'_T becomes higher at higher electric field and thus the amount of increase in the ionization rate also becomes higher at higher electric field. Thus, a multiquantum well structure can improve the nonlinearity of the avalanche process and reduce the ionization rate saturation limitations.

III Structure Design & Device Characteristics

The band diagram for the designed single-drift flat profile MQW IMPATT is shown in figure 1. The structure is a p^+n junction with five periods of MQWs ($100\mathring{A}$ barrier length and $100\mathring{A}$ well length) in the avalanche region. The transit time drift region is $1500\mathring{A}$ thick and the corresponding transit time angle is 0.75 π at 100 GHz when the electron saturation velocity is 4×10^6cm/sec. Doping density in the multiquantum well region is not constant. In an MBE system, n-type dopant replaces both Al and Ga atoms when Al flux is introduced during growth. Thus, the doping density is lower in AlGaAs layer for the simple growth condition of a constant Si flux rate in an MBE system. This problem can be circumvented by using two Si dopant guns or by using growth interruption to raise the Si flux rate in AlGaAs layers to compensate for this extra Al. However, an IMPATT structure can definitely tolerate deviation from the mean doping density to some degree. Therefore, the active layer doping densities of $2 \times 10^{17}/cm^3$ for GaAs layers and $1.4 \times 10^{17}/cm^3$ for $Al_{0.3}Ga_{0.7}As$ layers were designed for the simple growth condition of a constant Si flux rate in an MBE system.

The room temperature I-V curve in figure 2 for the structure in figure 1 shows the desired hard breakdown at 10 V. A 7 V punch through voltage was obtained from a C-V measurement and agrees well with the designed structure. From both I-V and C-V measurements, the device has at least 30% voltage amplitude modulation if the punch through voltage is taken to be the minimum voltage when the device oscillates.

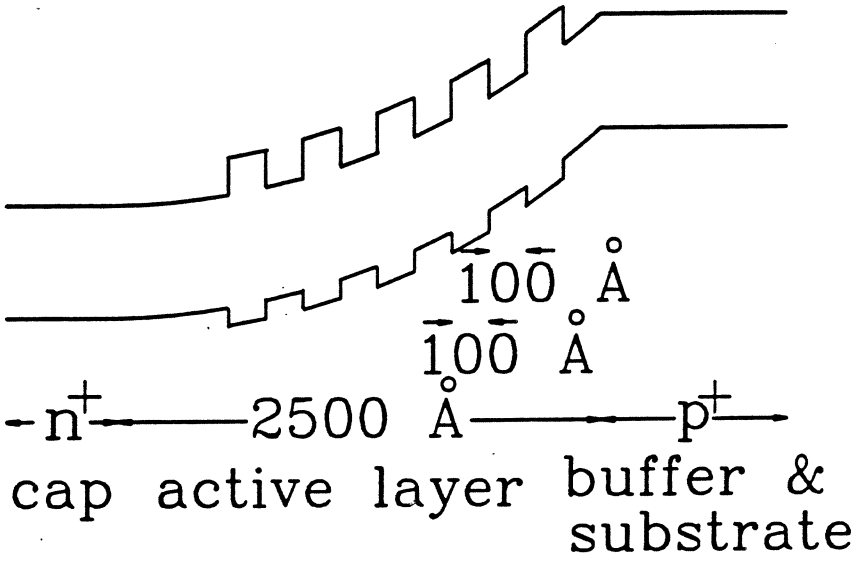

Figure 1: The band diagram of a GaAs/AlGaAs MQW IMPATT device on a p^+ GaAs substrate.

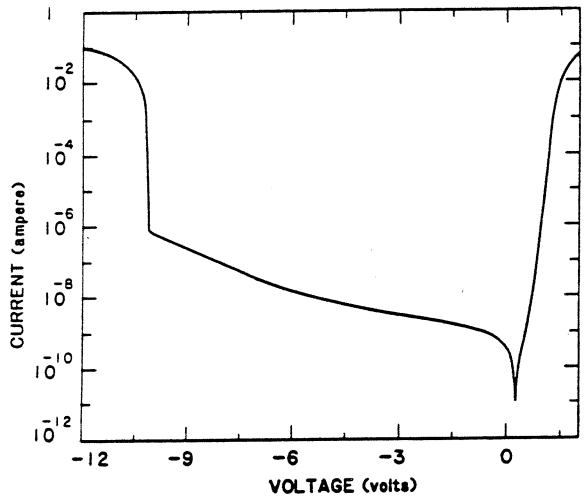

Figure 2: Room I-V curve for the GaAs/AlGaAs MQW IMPATT structure.

IV Substrate Selection and its Effect on Edge Breakdown

The structure as shown in figure 1 was grown on a p^+ GaAs substrate in an MBE system. Figure 3 illustrates a diagram of the high frequency diode on a heat sink. The p^+ substrate plays an important role in device edge breakdown. The band diagram of a GaAs/AlGaAs multiquantum well IMPATT device on a p^+ GaAs substrate was illustrated in figure 1. Because IMPATT devices are normally flip-chip mounted to dissipate heat efficiently, the edge slope of the diode mesa in figure 3 results in the equi-potential lines bending towards the p^+n junction. The band diagram near the edge (the area enclosed in a dotted square box in figure 3) is illustrated in figure 4. Because quantum wells can trap and release carriers in a dynamic way, the band bending near the edges will keep trapped holes away from the edges and push trapped electrons towards the edges. Thus, the lower effective doping near the edge makes the edge breakdown voltage to be higher and prevents early edge breakdown. On the other hand, if the p^+n multiquantum well IMPATT structure is grown on a n^+ substrate, the effective doping density at edges becomes higher when the device is biased at higher current and the lower edge breakdown voltage can cause early device failure. Because of the edge breakdown consideration, we used a p^+ substrate for the designed p^+n MQW IMPATT structure.

V Device Fabrication & Device Packaging

High frequency high power devices generate tremendous heat and are susceptible to the parasitic effects. However, semiconductors have poor thermal conductivity. Thus a flip chip mounting configuration with the junction side close to a good heat sink is used. A low parasitic quartz ring is used for device package. The tiny quartz ring requires a small device die size which is difficult to obtain by dicing. Also the resistance caused by the remaining substrate is enhanced by the skin effect at high frequencies. Thus, a novel wafer-thinning and device-separating fabrication technique has been developed to fabricate the MQW IMPATT devices.

Circular AuGe/Ni/Au metal patterns and mesas were defined on the epitaxial side of the wafer by a conventional photolithography technique. A thick layer of silver (75μm) was electroplated on the epitaxial side of the wafer before the wafer was chemically thinned down from the substrate side to facilitate the handling of this thin wafer for the rest of the fabrication process. After the wafer was chemically thinned down, circular AuGe/Ni/Au metal patterns and mesas were then also defined on the substrate side of this thin wafer. The devices were alloyed and separated by chemical etching. A diode after the separating step is 10μm thick and has AuGe($900\mathring{A}$)/Ni($150\mathring{A}$)/Au(1μm) on both sides.

The diode is T.C. bonded on a diamond heat sink and then packaged inside a 5 mil thick quartz ring (18 mil inner diameter and 30 mil outer diameter). A triple-strap ribbon connects one end of the diode to the quartz ring. The center of the triple-strap ribbon is tapered down to 2 mil to facilitate the ribbon bonding. Figure 5 illustartes the dimensions

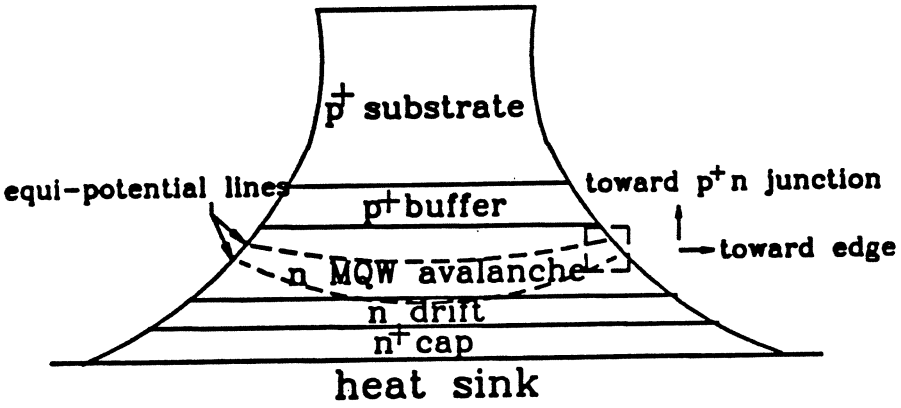

Figure 3: A flip-chip mounted GaAs/AlGaAs MQW IMPATT diode with p^+ GaAs substrate on a heat sink.

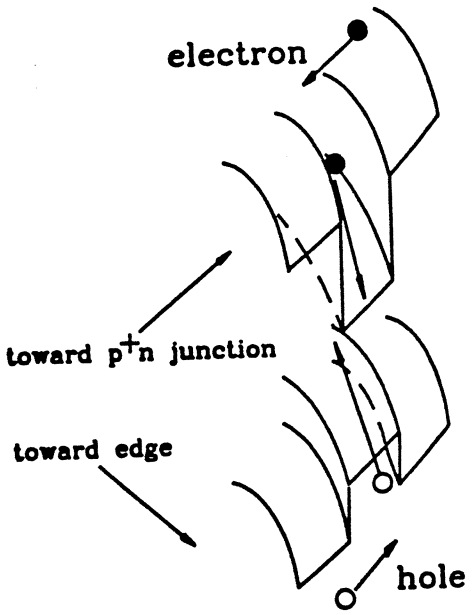

Figure 4: The band diagram near the edge (the area enclosed in a dotted rectangular box in figure 3) of a MQW IMPATT device.

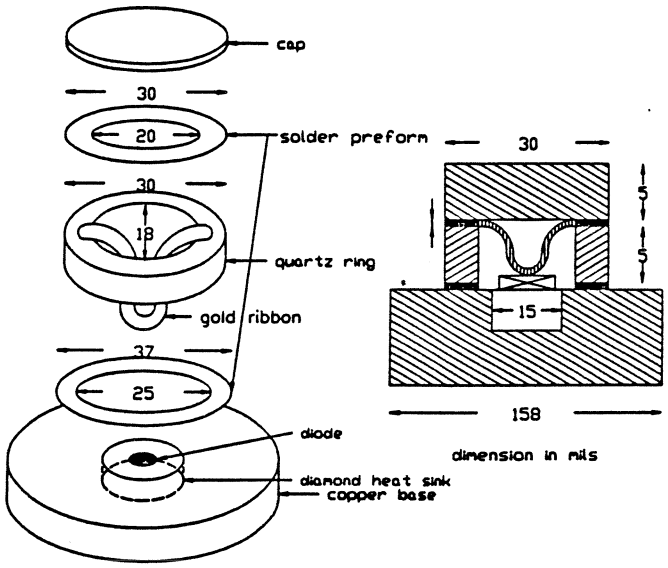

Figure 5: Dimensions for the quartz ring package.

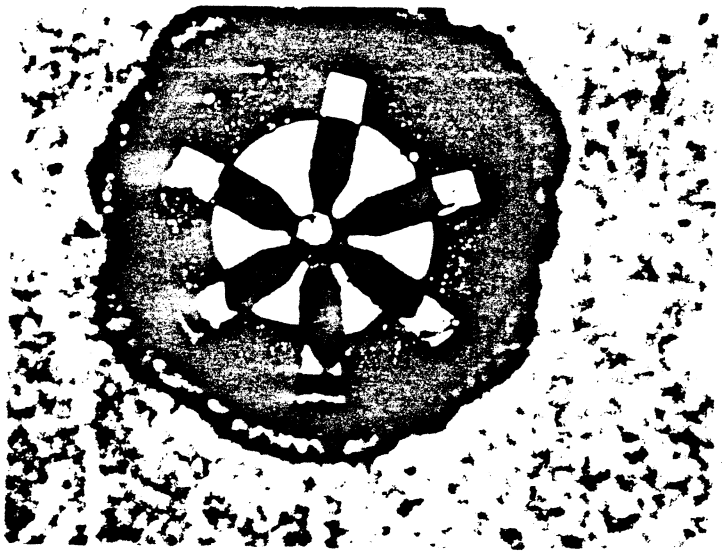

Figure 6: The picture of a triple-strap quartz ring package.

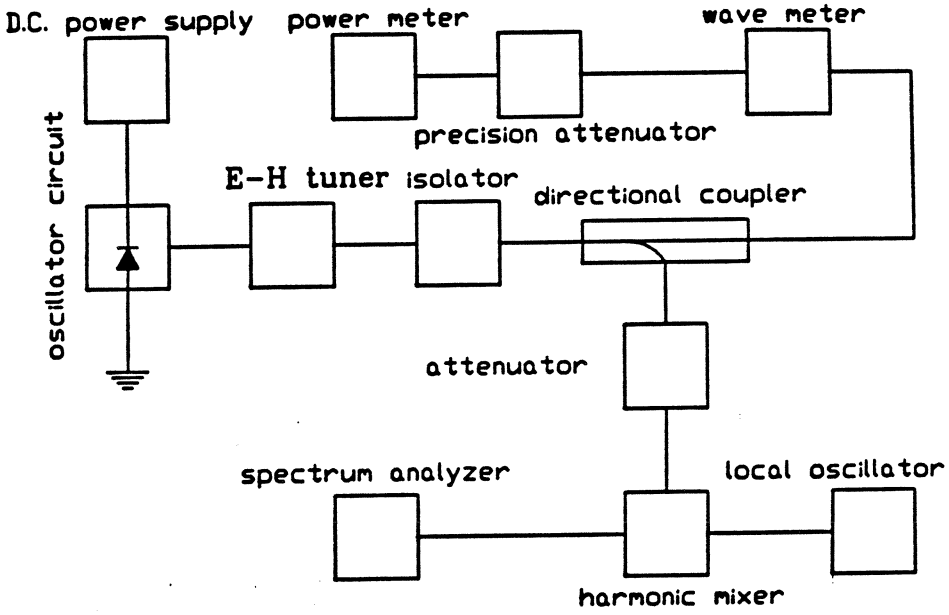

Figure 7: Measurement set-up for the W-band MQW IMPATT oscillator.

for the quartz ring package and figure 6 shows the picture of the quartz ring package. Inside the package the ribbon prevents the top contact metal from shorting to the ground, the device area is adjusted by the trim procedure to have approximate 1 pf at zero bias for r.f. testing.

VI Measurement Results and Discussions

The W-band (75-110 GHz) high frequency measurement set-up is shown in figure 7. The oscillator circuit is a Kurokawa-type oscillator circuit in a reduced waveguide. An E-H tuner was placed after the oscillator circuit to optimize the device-circuit impedance matching. The spectrum of an oscillator was measured by a heterodyne detection technique and figure 8 shows the spectrum of a CW MQW IMPATT oscillator at 101.3 GHz. Oscillation frequency and r.f. power can be directly read from a wavemeter and a calibrated thermistor power meter. CW oscillation at 100.3 GHz has been obtained with 6.4 mW at 364 mA bias current for a diode under test and the output power and oscillation frequency as a function of the bias current is illustrated in figure 9. Devices tested in a pulsed mode showed oscillation at 94 GHz with power of 127 mW and 2.2% efficiency.

No attempt has been made to optimized the device-circuit impedance and with further

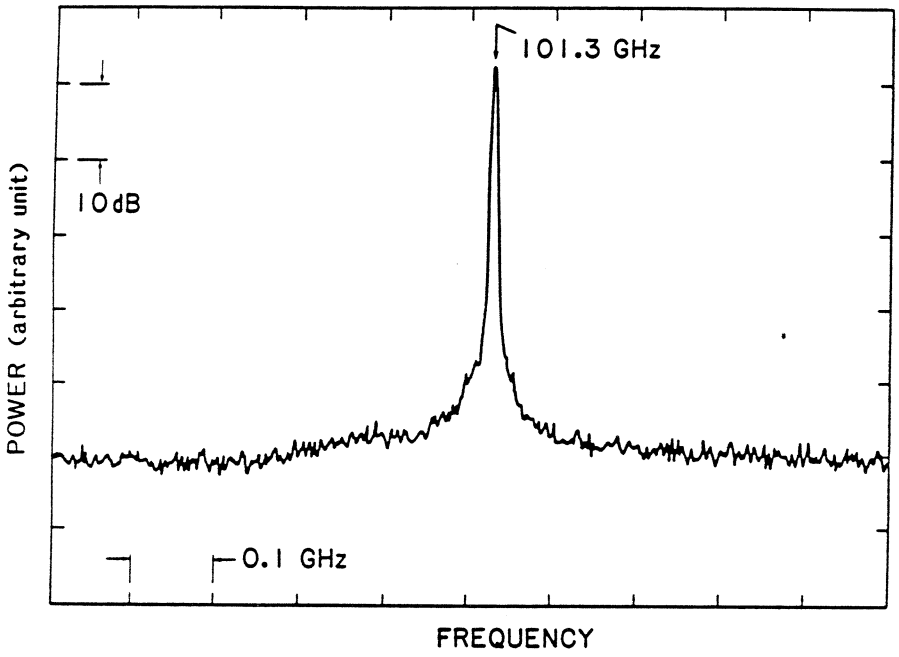

Figure 8: Spectrum of the CW MQW IMPATT diode at 101.3 GHz; the resolution bandwidth is 3 MHz.

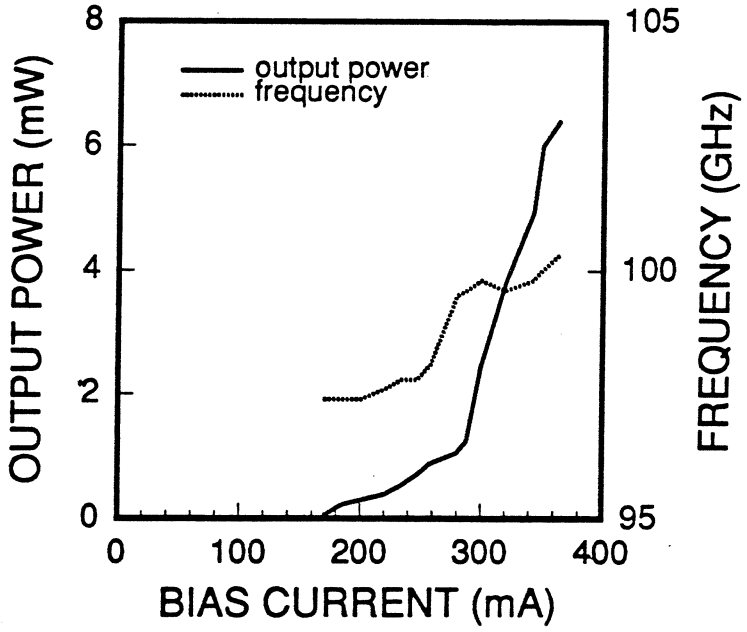

Figure 9: Output power frequency as a function of bias current for a CW MQW IMPATT oscillator.

improvement in impedance matching higher powers are expected. Also, the series resistance caused by the remaining substrate can be further minimized. The wafer-thinning technique developed can thin down the device to $1.5\mu m$ thick and a $10\mu m$ device thickness was chosen to facilitate device packaging. A device with $1.5\mu m$ thick can be packaged with further optimization in the bonding pressure, bonding temperature and bonding time. A p^+ substrate has higher ohmic loss than an n^+ substrate. A careful design on the well length, barrier length and barrier height could reduce the dynamic trapping behavior of the quantum wells at the operating current and thus an n^+ substrate can be used. Certainly, a double-drift structure with the MQW structure incorporating only into the p side can be grown on an n^+ substrate and complies with the edge breakdown consideration.

In summary, the performance of GaAs/$Al_{0.3}Ga_{0.7}$As MQW IMPATT devices at W-band frequencies was described. The operation of GaAs/AlGaAs MQW IMPATT devices at frequencies around 100 GHz opens up a new field for many millimeter-wave applications by bringing the modern epitaxy technologies to two terminal high frequency sources.

ACKNOWLEDGEMENT

This work was supported in part by the Air Force Office of Scientific Research under the direction of H. R. Schlossberg.

REFERENCES

[1] D. Lippens, O. Vanbesien and B. Lambert, " Multiquantum well GaAs/AlGaAs structures applied to avalanche transit time devices," *Journal De Physique, Vol. C5, pp. 487-290, 1987.*

[2] C. C. Meng and H. R. Fetterman, "Multiquantum well IMPATT devices in W-band frequencies," *International Semiconductor Device Research Symposium, pp. 79-82, 1991.*

[3] C. C. Meng and H. R. Fetterman, "A theoretical analysis of millimeter-wave GaAs/AlGaAs multiquantum well transit time devices by the lucky drift model," *Solid-State Electron., Vol. 36, No. 3 pp. 435-442, 1993.*

[4] T. Misawa, "High-frequency fall-off of IMPATT diode efficiency," *Solid-State Electron., Vol. 15, pp. 457-465, 1972.*

NUMERICAL SIMULATION OF TUNNETT AND MITATT DEVICES IN THE MILLIMETER AND SUBMILLIMETER RANGE†

Chien-Chung Chen, Richard K. Mains, George I. Haddad and Heribert Eisele

Solid-State Electronics Laboratory
Department of Electrical Engineering and Computer Science
The University of Michigan, Ann Arbor, Michigan 48109

Abstract — Numerical simulation programs for two-terminal transit-time devices based on drift-diffusion and energy-momentum transport models, with valence band to conduction band tunneling incorporated, have been developed. These programs can deliver accurate TUNNETT and MITATT device simulation results in the millimeter and submillimeter range. As the simulation results show, while the energy-momentum program is more accurate in the higher frequency range, the drift-diffusion program, which demands less computer resources, is suitable for W band devices.

Simulation results for GaAs TUNNETT and MITATT devices by these two methods will be presented and compared. The results obtained so far indicate that these programs provide useful tools for high frequency device structure design and optimization. In particular the energy-momentum model is required for devices operating at THz frequencies.

1 Introduction

Tunnel injection transit-time (TUNNETT) and mixed tunneling and avalanche transit-time (MITATT) diodes are two potentially useful RF power sources at extremely high frequencies[1]. The valence band to conduction band tunneling by electrons in such devices has a profound effect on the device performance. In the past, many numerical simulation programs have been developed to simulate transit-time devices, mostly for simulation of impact ionization avalanche transit-time (IMPATT) diodes[2, 3]. The free charge carrier transport models used in such simulations are the drift-diffusion model and energy-momentum model[4]. Programs based on the drift-diffusion model are more popular because of its simplicity. The energy-momentum model, due to the large number of partial differential equations to solve, is less frequently adopted in simulation.

Simulation of the interband tunneling process is still rare today. Recently Dash and Pati developed a generalized method to include the tunneling mechanism in their simulation[5]. Their simulation was based on the simple drift model (no diffusion currents), and was limited to DC or small-signal analysis. And their simulation lacks verification with measurement data for real devices.

In this work both the large-signal drift-diffusion and energy-momentum programs are developed to simulate TUNNETT and MITATT diodes. Tunneling currents are modeled and incorporated

†This work was supported by the Army Research Office under contract No. DAAL03-92-G-0109.

in the transport models. A real W-band diode is simulated using both models, and simulation results are compared with the experimental measurement. A 300 GHz diode is also designed and simulated to show the capability and limitation of such devices at this frequency.

2 Transport Theory

The two most commonly used transport models for semiconductor device simulation are the drift-diffusion (DD) model and the energy-momentum (EM) model. In the DD model, charge carriers respond immediately to the external electric field and reach steady state without any delay in time, while the energy-momentum model requires relaxation times for carriers to adjust their energy and momentum before reaching steady state. Due to this transient nature in the EM model, free carriers exhibit velocity overshoot and undershoot effects in response to the change of electric field. This kind of transient response can also be observed in the Monte Carlo simulation. By using correct relaxation times, the EM model can depict carrier behavior in remarkable agreement with Monte Carlo observations[6].

Due to the simplicity in formulation, the DD transport model is still widely used for device simulation. As long as the time and spatial variations of the electric field are small, the device simulation results by the DD model agree with those by the energy-momentum model. Even at high frequencies where the EM model is more feasible, the DD simulation is still useful in providing preliminary insight of device operation.

Two-terminal transit-time device simulation programs have been developed in our laboratory. Both include the interband tunneling and impact ionization as the major carrier generation mechanisms. In the following we briefly describe the two transport models used in the two simulation programs developed in our laboratory.

2.1 Drift-Diffusion Model

This well-known model describes the free charge carrier transport by the following equations

$$J_p = qp\mu_p(E)E - qD_p(E)\frac{\partial p}{\partial x}$$

$$J_n = qn\mu_n(E)E + qD_n(E)\frac{\partial n}{\partial x}$$

$$\frac{\partial p}{\partial t} = -\frac{1}{q}\frac{\partial J_p}{\partial x} + G$$

$$\frac{\partial n}{\partial t} = \frac{1}{q}\frac{\partial J_n}{\partial x} + G$$

where the carrier mobilities, μ_p and μ_n, and the diffusion coefficients, D_p and D_n, are functions of the electric field E, and the free carrier generation rate G is given by

$$G = G_{II} + G_T + G_{th} - R_{th}$$

with G_{II}, G_T, G_{th} and R_{th} being the impact ionization generation, interband tunneling generation, thermal generation and recombination, respectively.

2.2 Energy-Momentum Model

In the EM simulation program developed by us, holes still follow the drift-diffusion equation, while electrons are described by a variation of the two-valley drift-diffusion equation with the mobilities and diffusion coefficients being functions of electron energies instead of the electric field. Two energy equations govern the electron energies. The following equations are solved by the EM simulation program:

$$J_p = qp\mu_p(E)E - qD_p(E)\frac{\partial p}{\partial x}$$

$$J_{n1} = qn\mu_{n_1}(w_1)E + qD_{n_1}(w_1)\frac{\partial n1}{\partial x}$$

$$J_{n2} = qn\mu_{n_2}(w_2)E + qD_{n_2}(w_2)\frac{\partial n2}{\partial x}$$

$$\frac{\partial w_1}{\partial t} = -\frac{J_{n1}E}{n_1} - \frac{w_1 - w_{th}}{\tau_{w1}(w1)}$$

$$\frac{\partial w_2}{\partial t} = -\frac{J_{n2}E}{n_2} - \frac{w_2 - w_{th}}{\tau_{w2}(w2)}$$

$$\frac{\partial p}{\partial t} = -\frac{1}{q}\frac{\partial J_p}{\partial x} + G_p$$

$$\frac{\partial n1}{\partial t} = \frac{1}{q}\frac{\partial J_{n1}}{\partial x} + G_{n1}$$

$$\frac{\partial n2}{\partial t} = \frac{1}{q}\frac{\partial J_{n2}}{\partial x} + G_{n2}$$

where $w_{th} = \frac{3}{2}k_BT$ is the thermal equilibrium energy for electrons, and G_p, G_{n1} and G_{n2} are given by

$$G_p = G_{II} + G_T + G_{th} - R_{th}$$

$$G_{n1} = G_T + G_{th} - R_{th} + \frac{n2}{\tau_{n_{2\to1}}(w2)} - \frac{n1}{\tau_{n_{1\to2}}(w1)}$$

$$G_{n2} = G_{II} - \frac{n2}{\tau_{n_{2\to1}}(w2)} + \frac{n1}{\tau_{n_{1\to2}}(w1)}.$$

Close examination of the above equations reveals that the momentum relaxation times for electrons are actually neglected in the program. This is justified by the fact that the momentum relaxation times are generally much smaller than the energy relaxation times.

3 Material Parameters

The material used for devices in this work is GaAs. Since these devices are intended for RF power generation, the material lattice temperature is usually very high. 500°K is assumed throughout this work. The majority of the material parameters used by the simulation programs are generated by a traditional Monte Carlo (MC) program[7]. This MC program provides the values of electron

velocities, diffusion coefficients, relaxation times and electron energies as functions of the electric field up to 1000 kV/cm.[1] Beyond 1000 kV/cm, the material parameters are extrapolated from the MC results. The methods used to evaluate the relaxation times are similar to those proposed by Stewart *et. al.*[6], while the electron (longitudinal) diffusion coefficients are calculated in the MC program using the method discribed by Fawcett[9]. Other electron parameters such as the material intrinsic concentration and electron-hole recombination lifetime and all the hole parameters are set according to empirical expressions or assumed values.

Two important material parameters used by the simulation programs are the impact ionization and tunneling rates. They have very profound effects on the device operation, but still lack adequate determination in the electric field range where the devices are operated (up to 3000 kV/cm). For the impact ionization rate, we use values that enhance the generation rate in the high field slightly to account for the bandgap narrowing effect in the heavily doped region. The impact ionization generation rate is expressed as

$$G_{II} = (\alpha_n J_n + \alpha_p J_p)/q$$

with α_n and α_p being given by

$$\alpha_n = A_n \exp\left[-(B_n/E)^2\right]$$

$$\alpha_p = A_p \exp\left[-(B_p/E)^2\right]$$

For GaAs at 500°K, we use

$$A_n = A_p = 2.7 \times 10^5 \quad \mathrm{cm}^{-1}$$

$$B_n = B_p = 7.1 \times 10^5 \quad \mathrm{V/cm}$$

As to the interband tunneling rate, we adopt the expression which complies with the highly idealized form proposed by Kane[10] as shown below

$$G_T = A_T E^2 \exp(-B_T/E)$$

For GaAs at 500°K, we use the following values for A_T and B_T

$$A_T = 1.5 \times 10^{20} \quad \mathrm{cm}^{-1}\mathrm{s}^{-1}\mathrm{V}^{-2}$$

$$B_T = 1.5785 \times 10^7 \quad \mathrm{V/cm}$$

In the EM program, all material parameters for electrons except the tunneling rate are tabulated according to the electron energy. In other words, they are treated as functions of the electron energy instead of the electric field. The tunneling rate is considered as a function of the electric field since it is related more to the electric field that electrons in the valence band experience than to the energy of electrons in the conduction band. Figure 1 shows the impact ionization and tunneling generation rates for 500°K GaAs that are used in the simulation programs.

[1]Actually our MC program's validity should not extend to this high field. For electric fields of hundreds of kV/cm, a more comprehensive MC technique that takes into account the actual band-structure should be used instead[8]. A similar program is currently under development in our laboratory.

4 Simulation Results and Discussion

Two transit-time device structures are simulated by the two programs discussed in the preceding sections. One is a 94 GHz diode which has already been fabricated and tested in our laboratory[11]. The other is a diode designed for 300 GHz operation. Simulation on the 94 GHz diode is to verify the validity of material parameters used in the programs, and by adopting the same material parameters for the 300 GHz simulation, the TUNNETT and MITATT diode's performance at higher frequencies can be investigated. Figure 2 shows the schematic diode structures.

Design of the 300 GHz diode comes from modification of the 94 GHz diode. For diodes operating at 300 GHz, the drift region becomes short, and the efficiency drops should the generation region remain the same. In order to reduce the generation region length, the n^+ doping concentration is set to 4×10^{18} cm^{-3}, which is close to the maximum n-type doping level achievable by MBE. The n-type drift region doping concentration is increased significantly to accommodate the high current density (250 kA/cm^2). Such high current density is required to obtain enough negative resistance from the diode to overcome the contact resistance. To understand the need of high bias current for high negative resistance, we write down the negative resistance of the diode as

$$-R = \frac{-G}{G^2 + B^2}$$

where B and $-G$ are diode's susceptance and negative conductance, respectively. At frequencies as high as 300 GHz, B is usually dominated by the diode's capacitance C and is much higher than $-G$. Therefore the diode's negative resistance is approximated by

$$-R \approx \frac{-G}{\omega^2 C^2}$$

In the above expression for negative resistance, the capacitance is essentially independent of the bias current density. To increase $-R$, we may try to increase $-G$. Increasing the bias current density has the effect of increasing the negative conductance since at higher current density the same amount of V_{rf} causes greater AC current. This explains the reason why we bias the 300 GHz diode at very high current density. Simulation shows the diode's bias voltage is about 6 Volts at 250 kA/cm^2. The DC power density is as high as 1.5 MW/cm^2. Dissipation of excessive heat is critical for such high power density.

The following presents the simulation results and discussion for the two diodes.

4.1 94 GHz Diode Simulation

The 94 GHz diode is a single-drift device with strong tunneling current. When biased under the DC condition, the bias voltage at $I_{dc} = 0.14$ A ranges from 9.5 to 11 Volts among different samples with 30 μm as the nominal diameter. Due to the small uncertainty of the diode's area from the undercut phenomenon during mesa etching, the actual current density used to test the diode is also uncertain. By assuming the diode area to be 5.6×10^{-6} cm^2, $J_{dc} = 25$ kA/cm^2 is used in the simulation. The maximum RF output power measured at 94 GHz is 33 mW with the efficiency being 2.65% and bias voltage being 9 Volts.

Both the DD and EM simulations include the heavily doped contact regions for more realistic results, although doing so makes the simulation process extremely slow. Simulating such contact regions is especially desirable for single-drift devices since the p^{++} region is part of the narrow yet important carrier generation zone. Specifying a lower doping for the p^{++} region or neglecting it in simulation leads to a very different result.

DC Simulation at 25 kA/cm^2

Figure 3 shows the electron concentration and electric field obtained from both the DD and EM DC simulation. The electron concentration in the drift region by the EM program is higher than by the DD program, which gives rise to the higher electric field and higher bias voltage by the EM program due to the higher space charge effect. Also the higher electron concentration in the drift region by the EM program needs lower electron drift velocity to achieve the same DC current. This explains why the optimum frequency by the EM program is slightly lower than by the DD program as shown in the AC simulation results later. It is also interesting to note that a large amount of electrons appear near the junction of the generation region and drift region by the EM program, which phenomenon can be explained by the significantly higher electron energy than in equilibrium in this region as shown in Figure 4. The higher electron energy also expands the effective avalanche region length. When the diode operating frequency gets higher, this avalanche region expanding effect may cause lower diode efficiency. In the drift region the slightly higher electron energy than in equilibrium leads to a slower electron velocity, which is also known as the velocity undershoot effect. On the other hand, the higher electron energy in the drift region means lower electron diffusion current, which is one of the reasons why the EM program usually predicts better diode efficiency than the DD program.

The DC bias voltage at 25 kA/cm^2 obtained by the DD and EM simulation is 10.5 and 10.7 Volts, respectively. The tunneling current is 9.1 kA/cm^2 by the DD program and 9.2 kA/cm^2 by the EM program.

AC Simulation at 25 kA/cm^2

Both DD and EM AC simulations at 94 GHz are carried out on the 94 GHz diode. Figure 5 shows the voltage and current waveforms for V_{rf} = 4.5 Volts at 94 GHz by both models. Comparison of the induced current waveforms by both models shows that electrons experience the velocity undershoot effect from ωt=90° to ωt=270° where the external voltage is decreasing, and the velocity overshoot effect for the rest of the cycle. The bias voltage at V_{rf} = 4.5 Volts is 8.9 Volts by the DD program and 9.2 Volts by the EM program.

AC simulation results at 94 GHz are summarized in Figure 6, which shows the RF output power and efficiency with and without considering the 1.5×10^{-6} Ω nominal contact resistance. The diode area is assumed to be 5.6×10^{-6} cm^2 for RF output power calculation. Even with the contact resistance being considered, both models predict better output power and efficiency than the measurement results. The bias voltage at which the maximum RF output power occurs is 8.9 Volts by both models. From the figure, it can be easily seen that the EM program gives higher efficiency, RF output power and larger RF voltage swing, although the differences are not very

significant. For frequencies up to W band, the DD program provides a very good tool for diode design and preliminary performance analysis, while the EM program is indispensable for more accurate analysis and better understanding of the device physics.

As mentioned in the discussion of DC simulation, the EM model is expected to give lower optimum frequency than the DD model. This is verified in Figure 7, in which the optimum frequency at V_{rf} = 5 Volts is 103 GHz by the DD model and 97 GHz by the EM model. At V_{rf} = 5.5 Volts, the optimum frequency by the EM model is 99 GHz, a slight increase from 97 GHz at V_{rf} = 5 Volts. With increased V_{rf} the diode's optimum frequency tends to increase. This is because the average electric field in the device tends to decrease as V_{rf} increases, and thus results in increased average electron velocity and optimum frequency.

4.2 Simulation of the Diode Designed for 300 GHz

Like the 94 GHz diode, the 300 GHz diode is a single-drift diode with heavily doped p^{++} contact region. For simulation accuracy, both the DD and EM programs include the heavily doped p^{++} and n^{+} contact regions, although doing so significantly slows down the simulation speed.

DC Simulation at 250 kA/cm^2

The DC simulation results by both programs are shown in Figure 8 and 9. The electron concentration predicted by the EM program significantly departs from the DD program's. Also the EM program predicts even higher electron energy above the equilibrium energy than in the 94 GHz, which indicates the electron velocity would be significantly slower than expected by the DD program due to the velocity undershoot effect. Therefore we anticipate the EM program will give a lower optimum frequency than the DD program. Also note the avalanche region expanding effect by the EM program. At 300 GHz the total diode length is short. The expansion of the avalanche region actually disperses the injected charge pulse spatially, and thus results in low efficiency.

The DC bias voltage at 250 kA/cm^2 is 6.33 Volts by the DD program and 6.36 Volts by the EM program with the respective tunneling currents being 60.1 and 56.7 kA/cm^2. The higher avalanche current by the EM program comes from the longer effective avalanche region.

AC Simulation at 250 kA/cm^2

Frequencies around 300 GHz have been swept by the two programs to determine the optimum frequency. Since the diode structure was originally designed with the help of the DD program, the maximum efficiency occurs at 300 GHz by the DD program. Due to the slower electron velocity in the drift region by the EM program, the optimum frequency by the EM program, 260 GHz, is significantly lower than by the DD program. We believe that in this extremely high frequency range electrons no longer follow the DD transport model. Therefore, in the following discussion only the EM program's results are presented.

A series of AC simulations at 260 GHz are carried out with small steps of V_{rf} to search for the

maximum output power. Figure 10 shows the current waveforms for V_{rf} = 2 Volts at 260 GHz. From it, one can see that at this high frequency impact ionization, instead of interband tunneling, still dominates the charge generation process. Two factors contribute to the dominance of impact ionization — one is the high bias current density, which enhances only the impact ionization; the other is the significant generation region expansion phenomenon for impact ionization at this high frequency.

Figure 11 shows the predicted diode output power, efficiency and negative resistance for a 10 μm diameter diode at 260 GHz with bias current density being 250 kA/cm^2 by the EM program. These P_{rf} and efficiency values are calculated without including any contact resistance. When the contact resistance is included in the calculation, P_{rf} and efficiency drop drastically since the diode's negative resistance is low. The actual maximum P_{rf} and efficiency after taking into account the nonzero contact resistance are plotted in Figure 12 with the load resistance also being shown. This figure reveals that the diode's performance is severely degraded by the contact resistance. From another point of view, as long as the contact resistance can be reduced to 5×10^{-7} Ω·cm^2, 18 mW of RF power can be provided by this diode at 260 GHz.

In addition to reduction of the contact resistance, many measures can be taken to improve the negative resistance at high frequencies. One way to increase the negative resistance is to increase the diode length without affecting the diode's operating frequency. For example, we may design the diode in such a way that the electric field in the drift region is lower than it is now to increase the electron drift velocity; or we may build the diode with InP, which has higher electron drift velocity at high electric field; or we may reduce the diode temperature by cooling it in liquid nitrogen to achieve high electron drift velocity. Another way is to build the diode using low bandgap materials such as InGaAs to increase the diode's negative conductance.

5 Conclusion

Interband tunneling has been included in both drift-diffusion and energy-momentum transport model programs to simulate operation of TUNNETT and MITATT diodes. Simulation using both programs is presented for an experimental diode. Both programs agree with the RF performance at 94 GHz that was measured in our laboratory. Simulation shows that the energy-momentum model gives slightly better diode performance at 94 GHz. A 300 GHz diode is also designed and simulated. The simulation results show that the drift-diffusion model deviates significantly from the energy-momentum model at such high frequencies. To accurately predict the diode's performance at terahertz frequencies, the energy-momentum program should be used. However, the fast drift-diffusion program is useful for preliminary diode structure design.

At terahertz frequencies, TUNNETT and MITATT diodes' performance is severely limited by the contact resistance. To extend the use of such devices into the terahertz range, the low-resistance ohmic contact technique is highly desired.

References

[1] G. I. Haddad *et. al.*, "Tunnel transit-time (TUNNETT) devices for terahertz sources," *Microw. Opt. Technol. Lett.*, Vol. 4, No. 1, pp. 23–29, 1991.

[2] P. E. Bauhahn, "Properties of semiconductor materials and microwave transit-time devices." Ph. D. Thesis, University of Michigan.

[3] R. K. Mains *et. al.*, "Simulation of GaAs IMPATT diodes including energy and velocity transport equations," *IEEE Trans. Electron Devices*, Vol. 30, No. 6, pp. 1327–1338, 1983.

[4] K. Bløtekjær "Transport Equations for Electrons in Two-Valley Semiconductors," *IEEE Trans. Electron Devices*, Vol. 17, pp. 38–47, 1970.

[5] G. N. Dash and S. P. Pati, "A generalized simulation method for MITATT-mode operation and studies on the influence of tunnel current on IMPATT properties," *Semicond. Sci. Technol.*, Vol. 7, pp. 222–230, 1992.

[6] R. A. Stewart *et. al.*, "Improved relaxation-time formulation of collision terms for two-band hydrodynamic models," *Solid-State Electronics*, Vol. 32, No. 6, pp. 497–502, 1989.

[7] C. Jacoboni and Paolo Lugli, "The Monte Carlo method for semiconductor device simulation," Springer-Verlag, Vienna, 1989.

[8] M. V. Fischetti and S. E. Laux, "Monte Carlo analysis of electron transport in small semiconductor devices including band-structure and space-charge effects," *Phys. Rev.*, Vol. 38, No. 14, pp. 9721–9745, 1988.

[9] W. Fawcett, "Non-ohmic transport in semiconductors," *Electrons in Crystalline Solids*, International Atomic Energy Agency, Vienna, pp. 531–618, 1973.

[10] E. O. Kane, "Zener tunneling in semiconductors," *J. Phys. Chem. Solid*, vol. 12, pp. 181–188, 1959.

[11] C. Kidner *et. al.*, "Tunnel injection transit-time diodes for W-band power generation," *Electron. Lett.*, Vol. 28, No. 5, pp. 511–513, 1992.

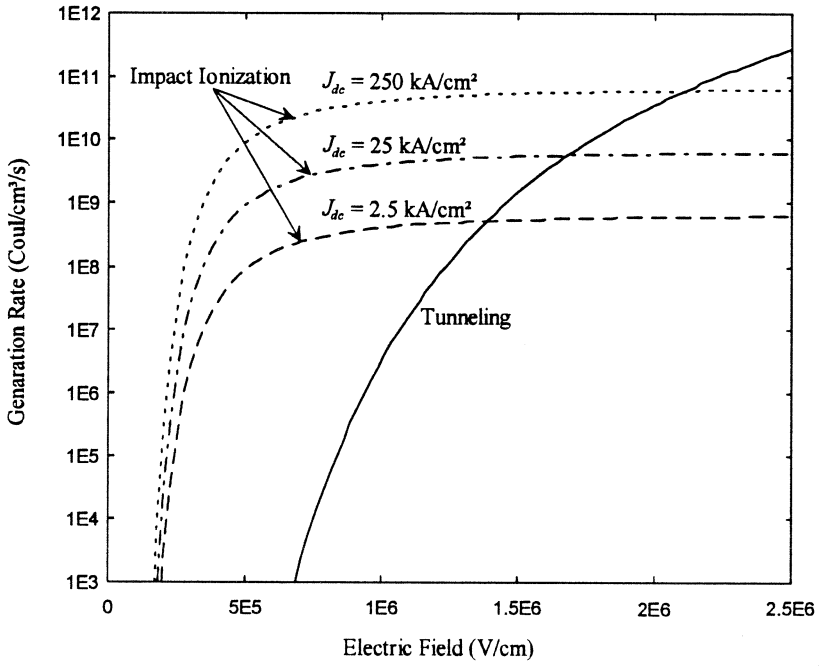

Figure 1: The impact ionization and tunneling generation rates for GaAs at 500°K.

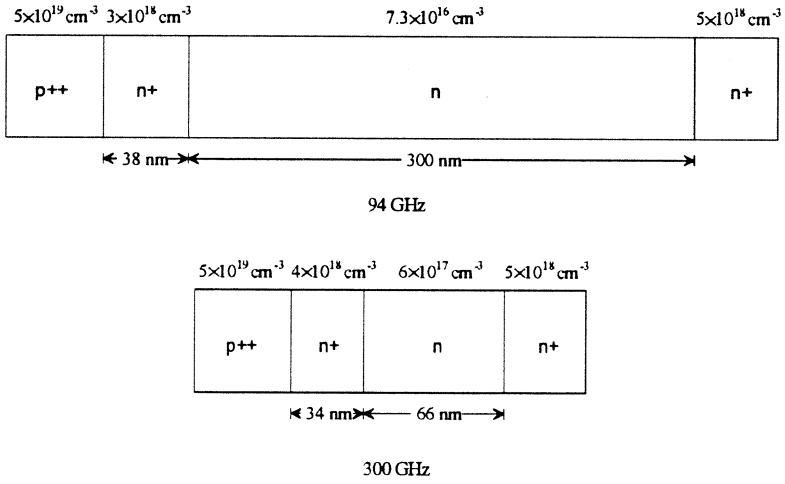

Figure 2: Doping structure of the two diodes simulated.

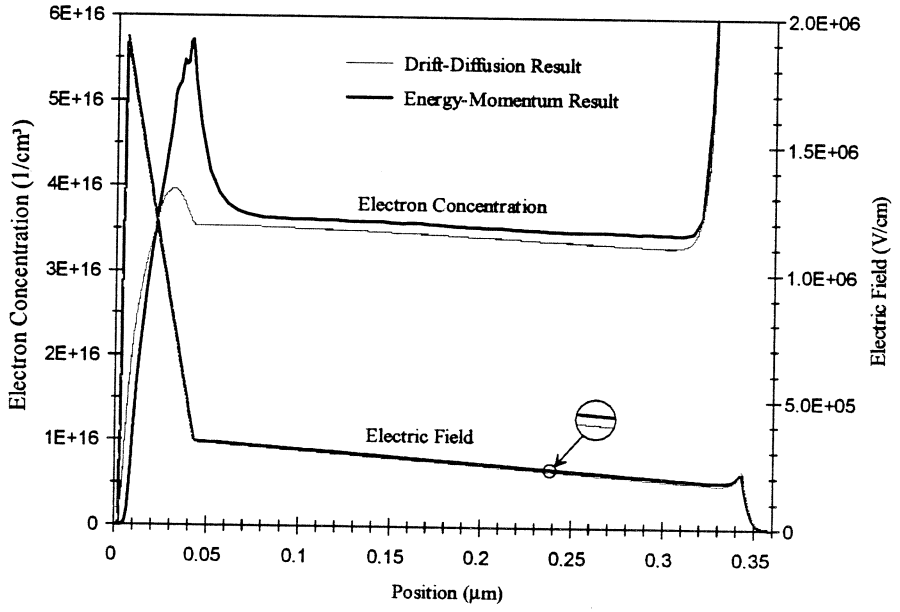

Figure 3: The DC solution for the 94 GHz diode's electron concentration and electric field.

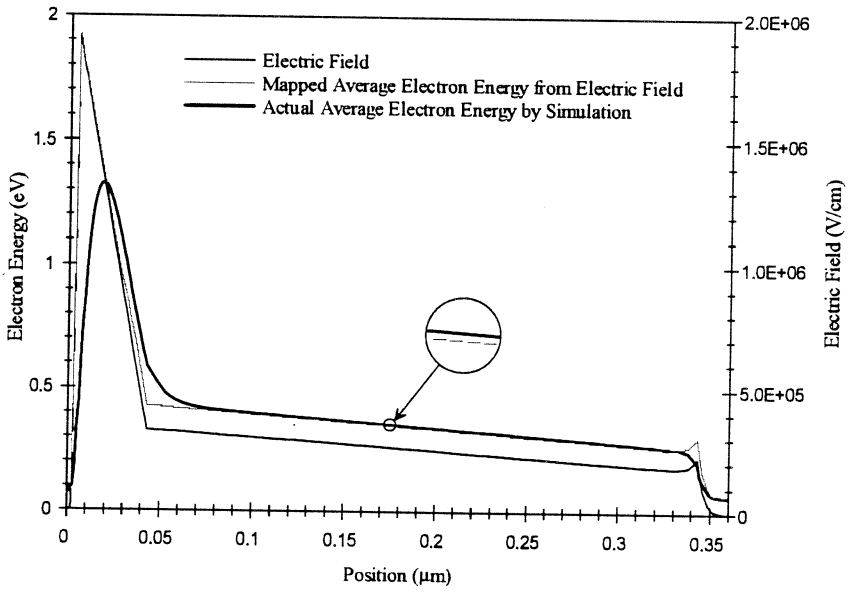

Figure 4: The electron energy in the upper valley for the 94 GHz diode by the EM program.

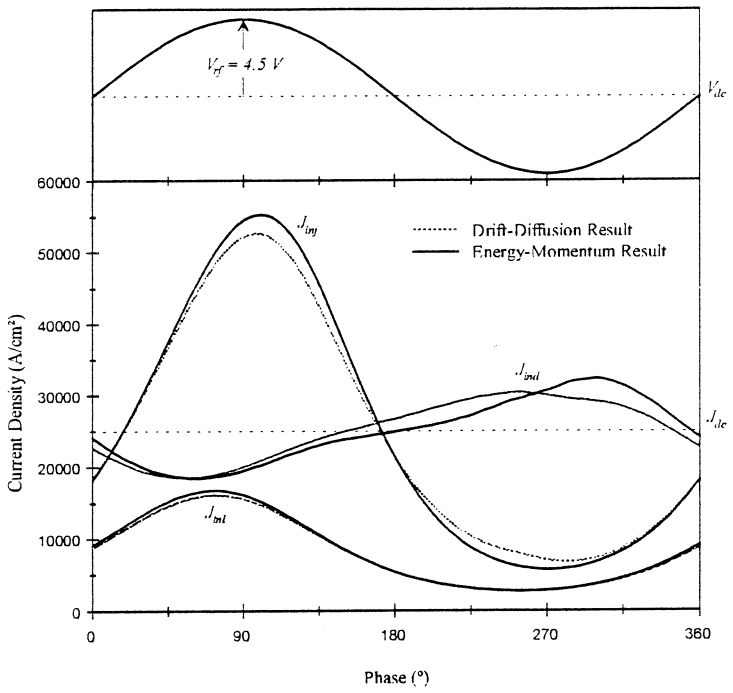

Figure 5: Voltage and current waveforms for $V_{rf} = 4.5$ Volts at 94 GHz.

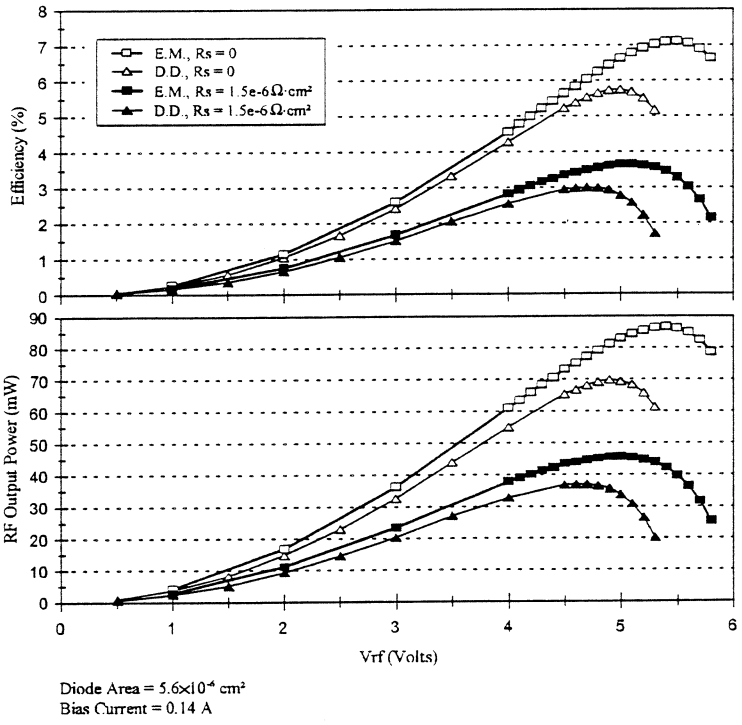

Figure 6: The 94 GHz large-signal simulation results.

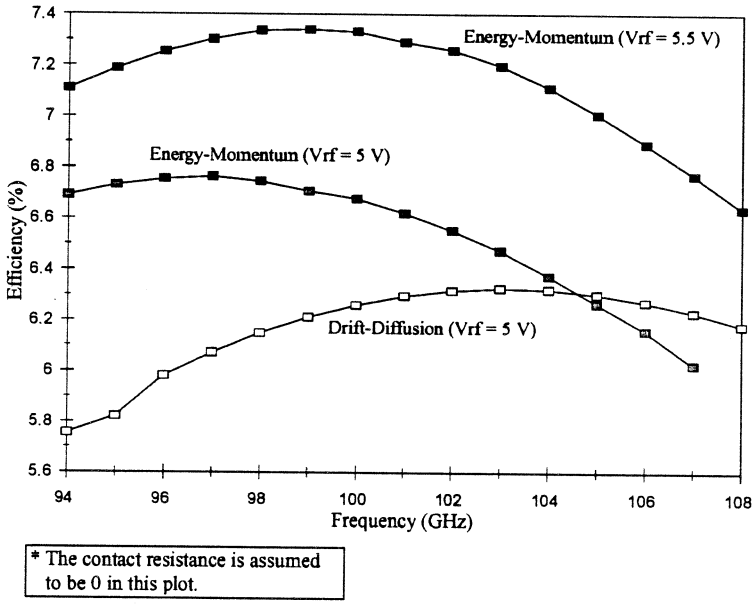

Figure 7: The 94 GHz diode efficiency versus frequency.

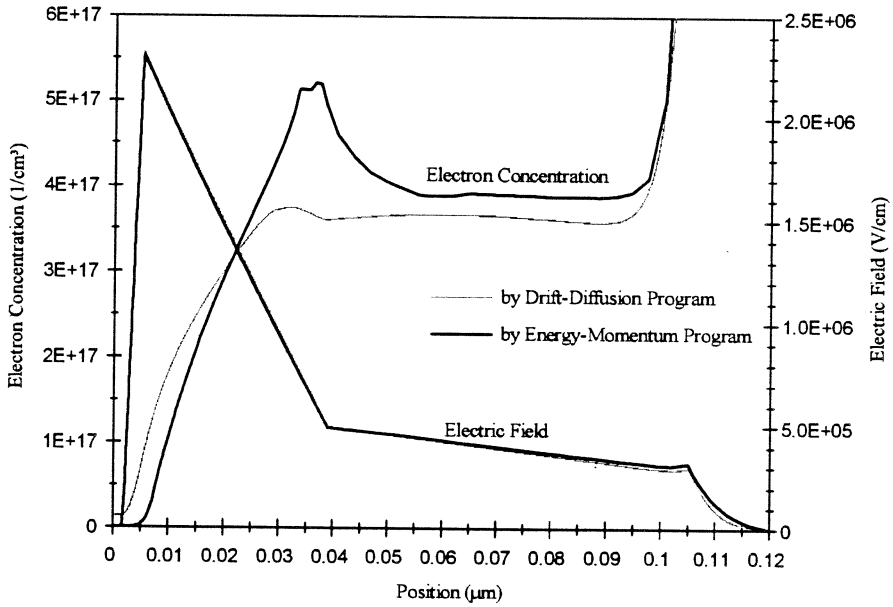

Figure 8: The DC solution for the 300 GHz diode's electron concentration and electric field.

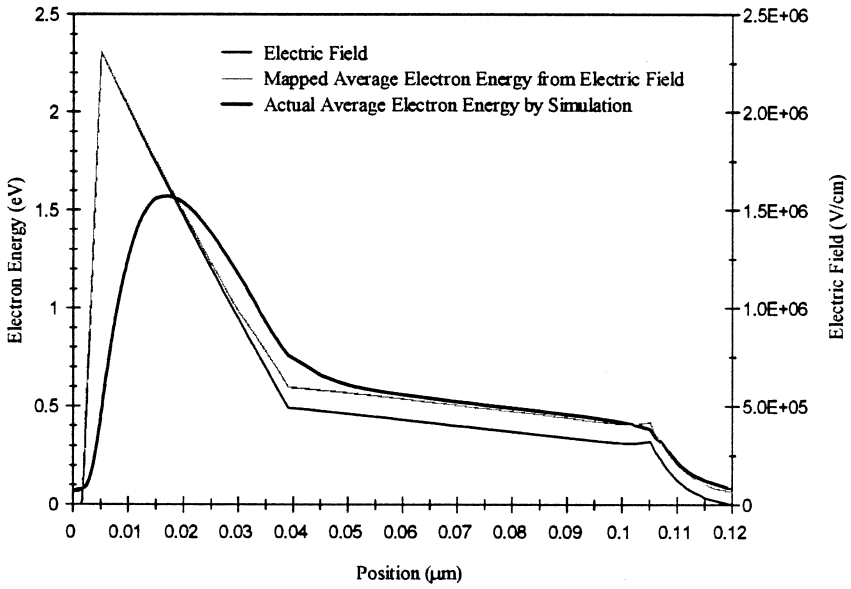

Figure 9: The electron energy in the upper valley for the 300 GHz diode by the EM program.

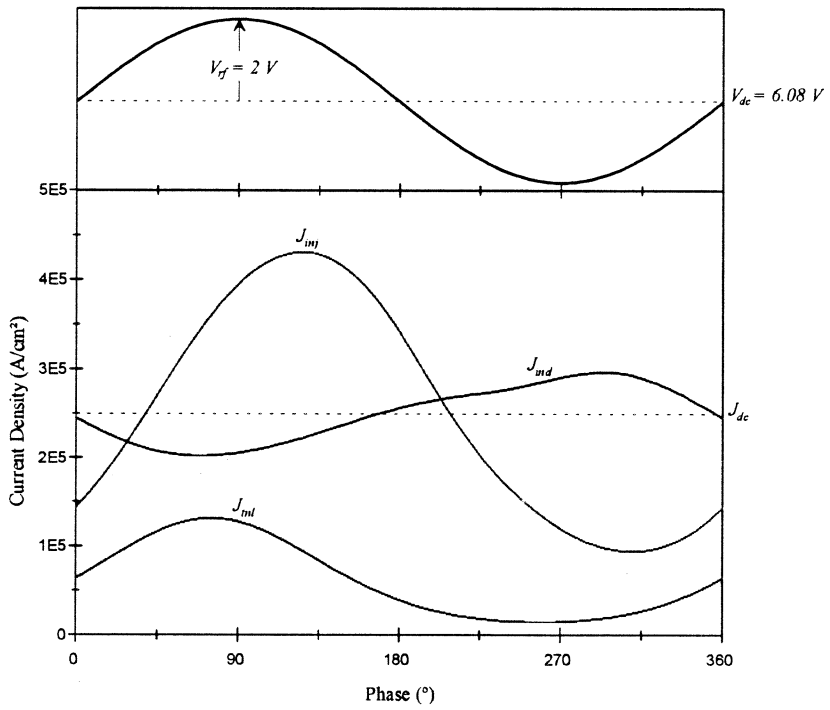

Figure 10: Voltage and current waveforms for $V_{rf} = 2$ Volts at 260 GHz.

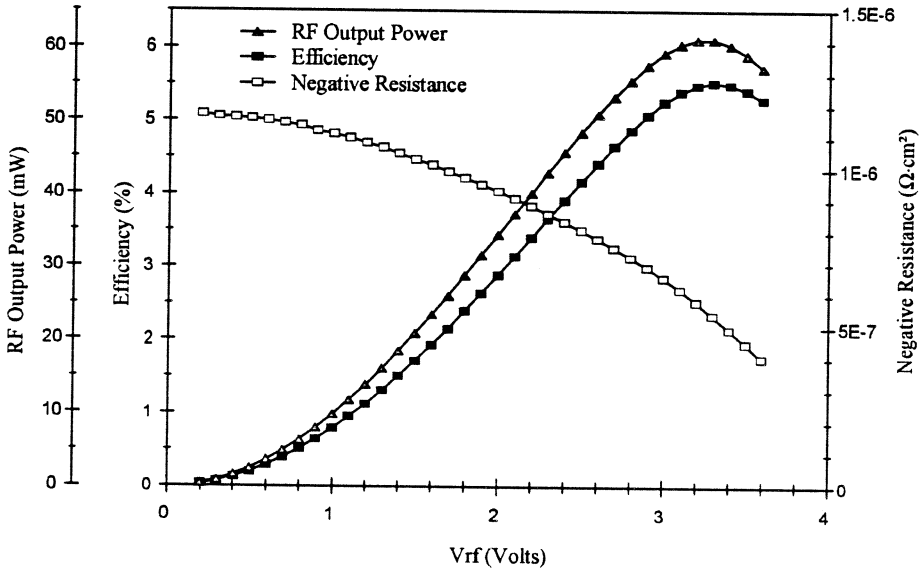

Figure 11: Predicted diode RF output power, efficiency and negative resistance at 260 GHz with current density 250 kA/cm^2 and diode diameter 10 μm.

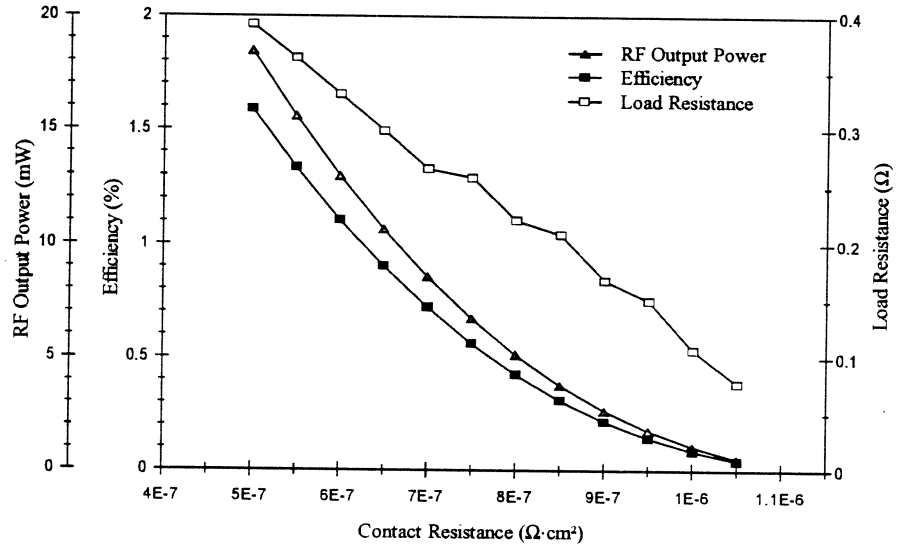

Figure 12: Predicted diode maximum RF output power and corresponding efficiency versus the contact resistance at 260 GHz with the diode diameter 10 μm.

GaAs SCHOTTKY DIODES FOR THz MIXING APPLICATIONS

P.A.D. Wood, W.C.B. Peatman, D.W. Porterfield, and T.W. Crowe

Semiconductor Device Laboratory
Department of Electrical Engineering
University of Virginia
Charlottesville, VA 22903

ABSTRACT

GaAs Schottky diodes are currently the most sensitive heterodyne receiver elements for applications above 1 THz which require high spectral resolution and broad bandwidth. Diode performance can be further improved by optimizing parameters such as anode diameter and doping concentration. Based on previous experimental and theoretical research, improved diodes have been fabricated in the Semiconductor Device Laboratory of the University of Virginia. These diodes have an epitaxial layer doping density of $1x10^{18}$ cm^{-3} and zero-bias junction capacitance as low as 0.25 fF. Diode performance was evaluated using video responsivity, mixer noise temperature and mixer conversion loss. These measurements have confirmed earlier predictions that for higher frequencies higher doping densities and smaller anode diameters must be used.

I. BACKGROUND

Several current and planned NASA programs require high sensitivity heterodyne receivers for the frequency range from 600 GHz through 2.5 THz. These include both atmospheric and radio astronomy missions. The Microwave Limb Sounder (MLS), which will be flown on the Earth Observing System, will have receivers at 215 GHz, 440 GHz, 640 GHz and 2.5 THz for atmospheric measurements related to ozone depletion [1]. A planned astronomy mission (SMIM) will require receivers covering the spectrum from 400 GHz through 1.2 THz [2]. Although superconducting technology is being pursued in these frequency ranges, and is in fact better than Schottky technology by at least a factor of two at 500 GHz [3,4,5], it is not clear when, or if, the SIS junctions will be extended to THz frequencies. Also, Schottky diodes are much more convenient for many applications due to their ability to operate at any temperature in the range

from below 20K to above 300K. In the frequency range above about 600 GHz the only receivers presently available for these missions are based on GaAs Schottky mixer diodes. Thus, any improvement in the performance of these diodes can have a great impact on these NASA programs.

GaAs Schottky diodes were first used in heterodyne receivers at microwave and millimeter wavelengths. In the 1970s it was shown that diodes with low epitaxial layer doping density can be extremely sensitive mixer elements when operated at low temperature [6]. This led to the development of greatly improved Schottky receivers at millimeter wavelengths, including a system that yielded a mixer noise temperature of only 35K DSB at about 100 GHz (<8 hv/k) [7]. It is remarkable that nearly ten years later this result is quite comparable to the best results obtained with SIS receivers at this frequency, particularly when one considers that the Schottky receiver need only be cooled to 20K.

Based on this success, there has been a large bias toward using low doped diodes at all frequencies. However, recent investigations of submillimeter wavelength receivers have shown that this may not be the optimum diode design. In 1989 Harris et. al published a detailed study of noise in an 800 GHz Schottky receiver [8]. This study was later extended to consider the diode noise [9]. It was shown that at 800 GHz the receiver noise was not dominated by the diode shot noise, as was the case at millimeter wavelengths, but rather by hot-electron noise. Thus, it was proposed that diodes with higher doping density and smaller anode diameter would reduce receiver noise by lessening the hot-electron noise.

Other studies have led to similar conclusions. For example, Bhapkar investigated the series impedance of the Schottky diodes by a finite difference technique that included all of the most important phenomena at THz frequencies [10]. This work showed clearly that higher doping density and smaller anodes were required to increase the cut-off frequency (related to the R_sC_{j0} product) to the point where THz performance was optimized. At the same time several empirical studies were indicating that such diodes always performed better at high frequency than the older, lower doped diodes. Thus, in 1991 we decided to fabricate diodes with epitaxial layer doping densities as high as $1x10^{18}$ cm^{-3} and anode diameters substantially below one micron. The fabrication and RF performance of these diodes is described in the remainder of this paper.

II. DIODE FABRICATION

The best Schottky diodes at submillimeter wavelength are of the "honey-comb" type first developed by Young and Irvin [11], as shown in Fig. 1. The GaAs substrate is highly doped to reduce its contribution to the series resistance. The epitaxial layer doping density and thickness are chosen to optimize the diode performance based on a variety of trade-offs [12]. The fabrication process has been described in various previous papers [13,14], and will only be outlined here. First, the epitaxial layer doping density is measured by a capacitance-voltage profiling technique. An anodic oxidation process is then used to remove a carefully controlled amount of the epitaxial layer, leaving behind the thickness required by the diode design. Once the soft anodic oxide is removed in an acidic etch, a thin layer of SiO_2 is deposited on the wafer by chemical vapor deposition.

Following oxide deposition, the wafer is processed by standard photolithographic techniques to define holes in the oxide. For our diodes with anodes greater than about 0.5 μm in diameter, this step is carried out with contact lithography and a UV light source. However, to achieve

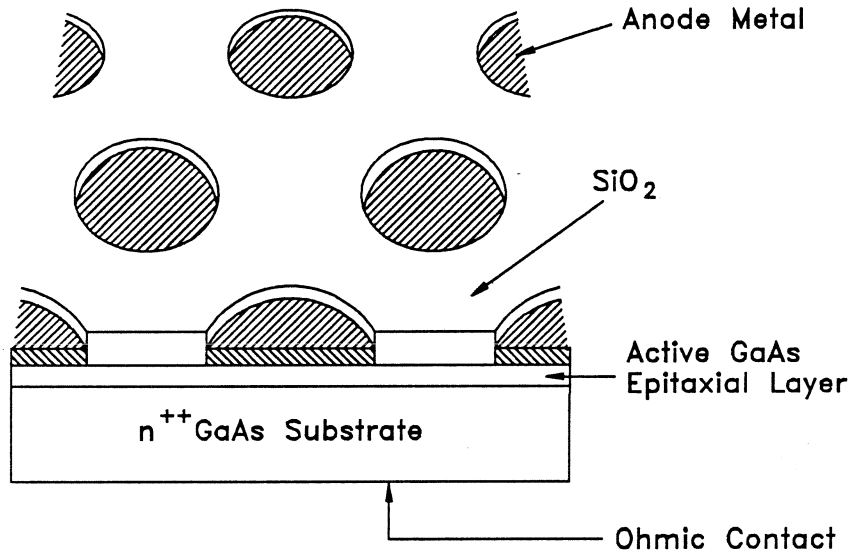

Fig. 1. A sketch of the honey-comb diode chip. The large number of closely packed anodes yields a high probability that a randomly placed whisker will contact on one of the anodes.

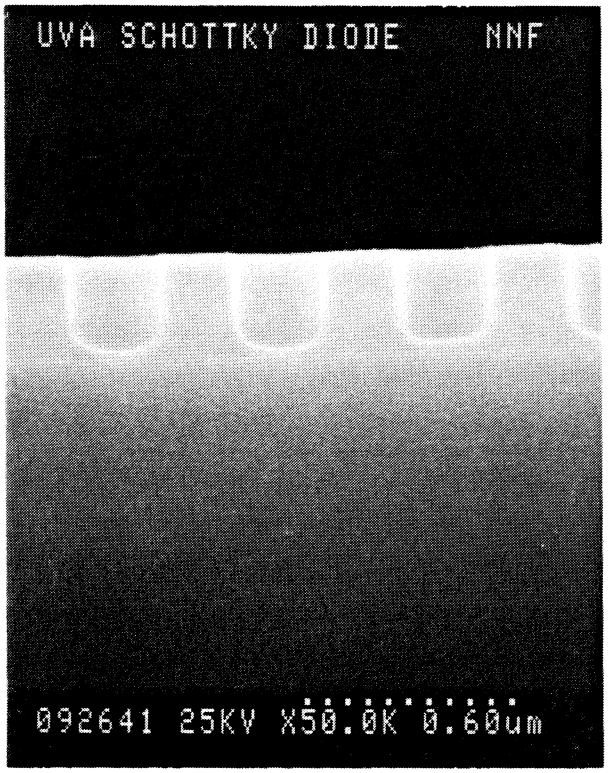

Fig. 2. A scanning electron micrograph (SEM) cross section of an oxide layer with quarter micron holes in GaAs. A small amount of oxide is left in the holes to protect the GaAs surface.

quarter-micron anodes direct-write electron beam lithography was required. This critical step was performed at the National Nanofabrication Facility at Cornell University. For all diodes, the photolithographic pattern is transferred to the oxide by reactive ion etching. This technology allows us to maintain the small size of the features and to control the depth of the etch. The control of etch depth is critical because there is evidence that the RIE etch can damage the GaAs surface, possibly creating traps and excess diode noise. Also, we would like to leave a thin layer of oxide to protect the GaAs surface during subsequent processing steps. In our process, the etch is stopped several hundred angstroms before the GaAs is exposed. Fig. 2 is an scanning electron micrograph (SEM) cross-section of a quarter micron diameter hole in SiO_2 on GaAs. The remaining oxide thickness is of order 200Å.

After RIE, the photoresist is removed and the back-side ohmic contact is formed. This involves carefully lapping the wafer to the desired thickness (of order 100 μm), electroplating the ohmic contact metals and alloying. Throughout this process, the oxide protects the top surface of the wafer. After the ohmic contact is complete, the wafer is diced into square chips, typically 250 μm wide. Individual chips are then soldered onto metal posts for anode formation.

To form the anodes, the remaining oxide in the anode holes is removed by a wet chemical etch, and the Pt/Au Schottky contact is plated onto the exposed GaAs surface. The diodes are then tested for electrical quality (forward IV and zero-bias capacitance). An SEM of a completed quarter-micron diameter chip is shown in Fig. 3. This figure shows that the anodes are well defined and that there is sufficient oxide to help hold the contact-whisker in place. In fact, this figure is virtually identical to older SEMs of our two micron diameter diodes fabricated ten years

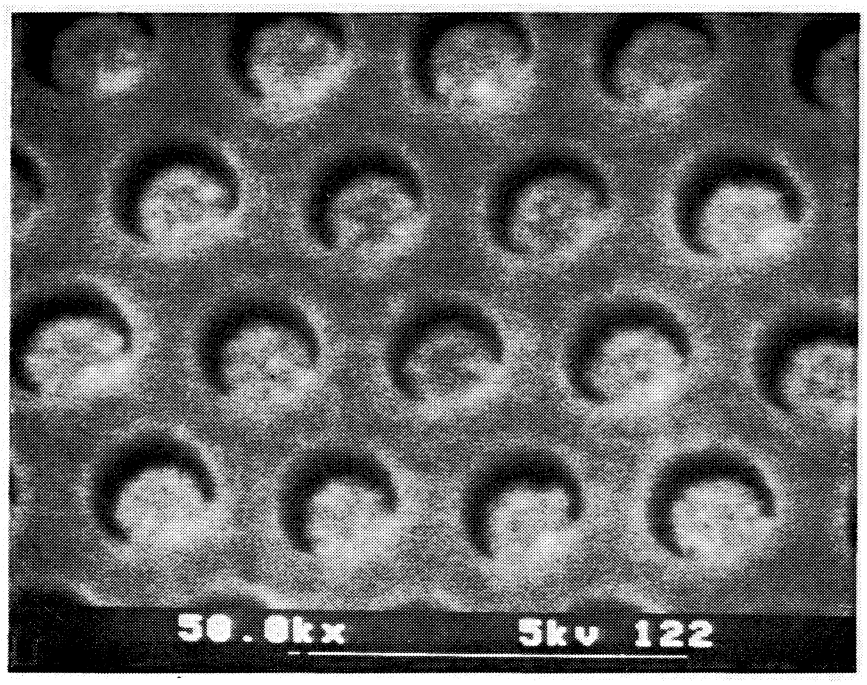

Fig. 3. A scanning electron micrograph of a completed diode chip with quarter-micron diameter anodes.

ago, except for the change in scale and the slight reduction of resolution at the higher magnification.

The characteristics of the new diodes are shown in Table I and compared to two previous batches of diodes that were fabricated on lower doped epitaxial layers. As expected, the new diodes have substantially reduced capacitance and lower R_sC_{j0} product at the expense of increased ideality factor. However, based on the theoretical analyses, it is clear that this is a beneficial trade-off.

Table I: Diode Parameters

Diode	Epilayer Doping N_d (cm^{-3})	Anode Diameter d (μm)	Epilayer Thickness t_e (Å)	Series Resistance R_s (Ω)	Zero-Bias Capacitance C_{j0} (fF)	ΔV at 10-100 μA (mV)	Ideality Factor, η 10-100 μA (mV)	Cut-off Frequency $\nu_{co} \equiv 1/2\pi R_sC_{j0}$ (THz)
1T14	$1x10^{18}$	0.45	400	8-10	0.9-1.1	85-90	1.4-1.5	18
1T15	$1x10^{18}$	0.25	300	25	0.3	90	1.5	25
1T6	$4x10^{17}$	0.45	1000	40	0.4	81-83	1.35-1.4	10
1I7	$3x10^{17}$	0.8	800	10-13	0.8-1.4	77	1.3	12.6

III. RF RESULTS

We measured the video responsivity and receiver noise temperature of several diodes with zero-bias junction capacitance, C_{j0}, ranging from 0.25 fF to 2.3 fF. These diodes were divided into two groups; those with low doping of $2\text{-}4x10^{17}$ cm^{-3} and those with high doping of 10^{18} cm^{-3}.

The video responsivity for these diodes is shown in Fig. 4. The video responsivity follows a roughly linear increase as C_{j0} is decreased. Video response is a measure of the RF induced voltage developed across the diode junction resistance, R_j, with a high impedance lock-in amplifier. The largest video response occurs when the junction resistance is much larger than the

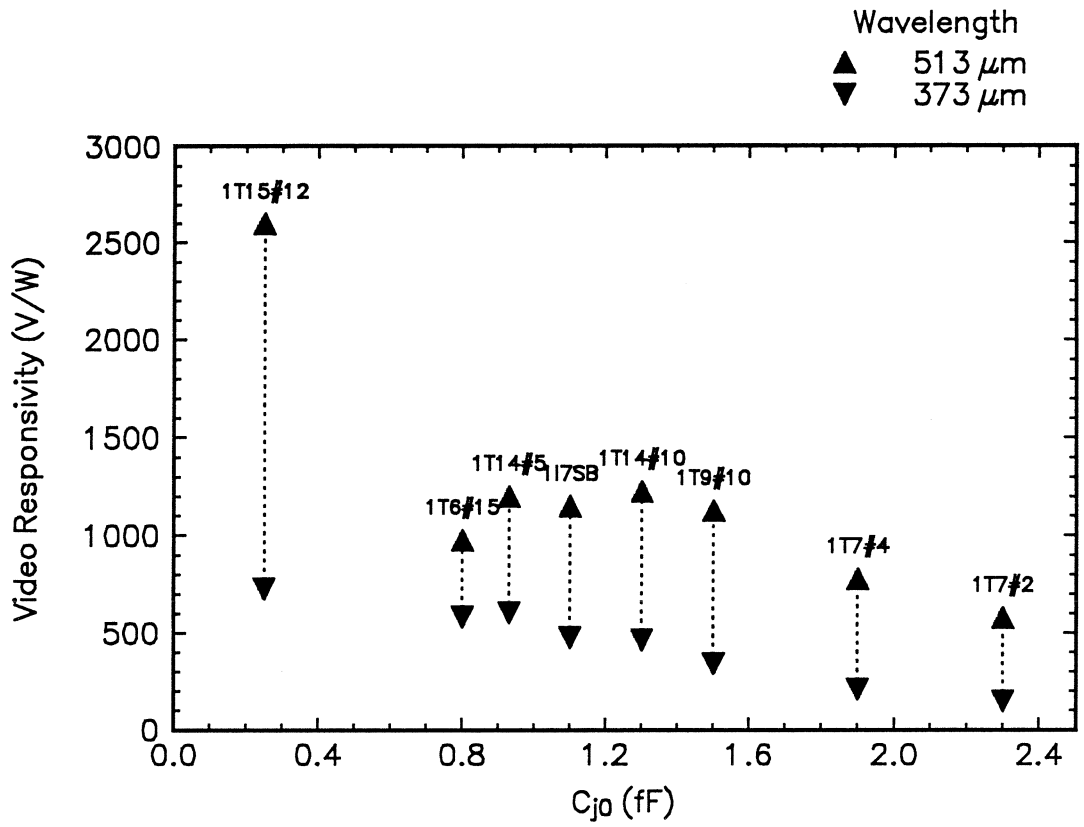

Fig. 4. Video responsivity versus zero bias junction capacitance, C_{jo}, at 585 GHz (λ = 513 μm) and 803 GHz (λ = 373 μm).

series resistance, R_s. R_j and R_s form a voltage divider and we ideally want all the voltage dropped across R_j, which requires either a small R_s or a large R_j. The junction capacitance, which shunts R_j, is the dominant parasitic element. The data shown in Fig. 4 was taken at a bias current of 1 μA. Our data does not indicate any difference in the video performance between the high doped diodes (1T14 and 1T15) and the low doped diodes, provided the capacitance is the same.

The noise measurements were performed using a hot-cold load. The hot load was room temperature Eccosorb AN-73 material. The cold load was AN-73 material submerged in liquid nitrogen. All measurements were made with the diode and the IF receiver at room temperature. The IF receiver had a noise temperature of 103K. No corrections for atmospheric absorption or diplexer loss were incorporated into the data.

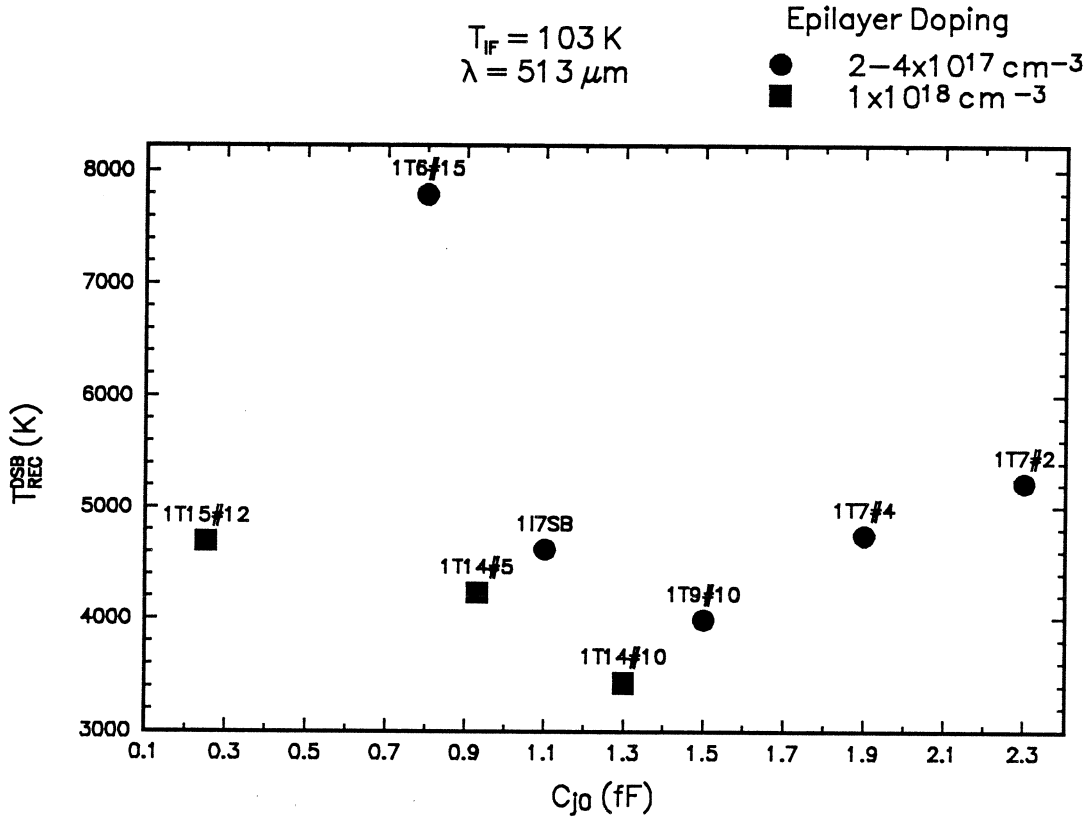

Fig. 5. Receiver noise temperature results at 585 GHz.

A summary of receiver noise temperatures is shown in Figs. 5, 6 and 7. The results for 585 GHz (λ = 513 μm) are shown in Fig 5. The lowest noise temperature was the high doped 1T14#10 with a receiver noise temperature (DSB)[1] of 3450K. For any given capacitance, the high doped diodes had a lower noise temperature than the low doped diodes. Both the high and low doped series of diodes yield a minimum noise temperature at one value of C_{j0}. At 585 GHz this minimum appears to be about 1.3 to 1.5 fF.

The results at 803 GHz (λ = 373 μm) are shown in Fig. 6. At 803 GHz the lowest receiver noise temperature was 3150K with the 1T14#5 diode. Once again, the high doped diodes have a lower noise temperature than the low doped diodes for a given capacitance. Also there is a

[1]Double sideband temperatures and conversion losses will be used throughout this paper.

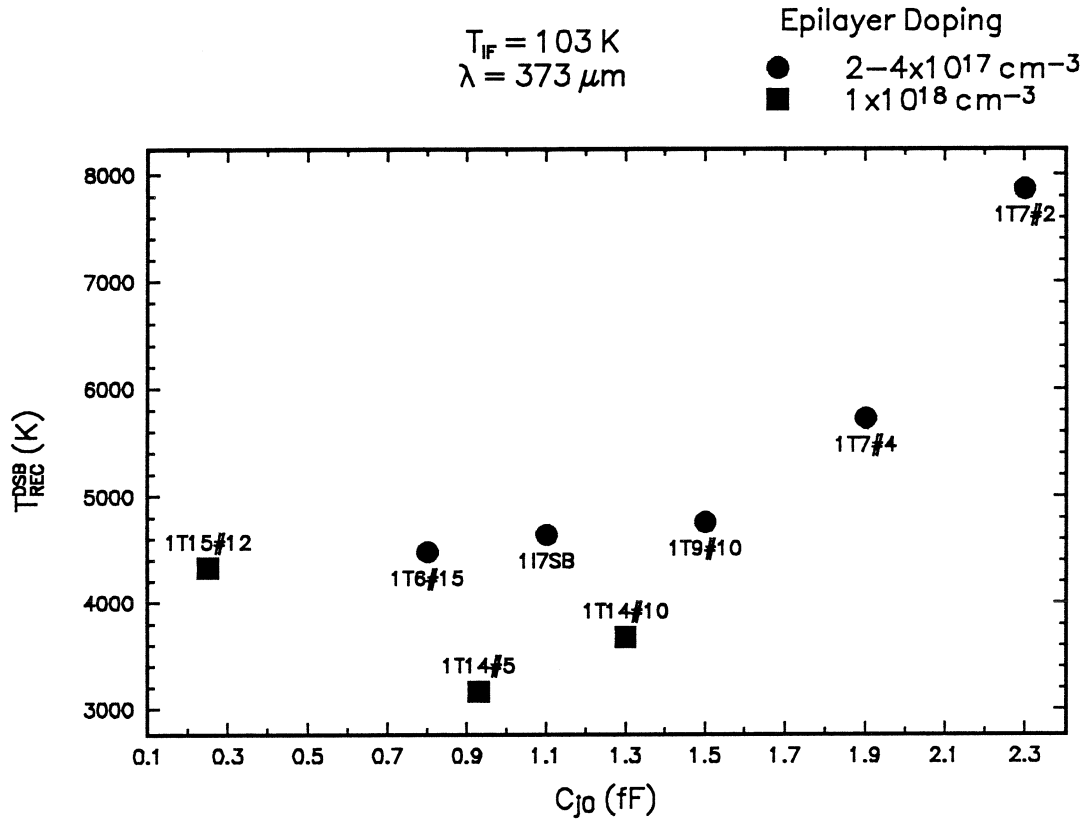

Fig. 6. Receiver noise temperature results at 803 GHz.

minimum in the receiver noise temperature versus C_{j0} at about 0.9 fF.

Receiver noise temperature versus frequency is plotted in Fig. 7 for select diodes. The best diodes at 585 and 803 GHz are the two 1T14 diodes. At 1.6 THz the 1T15#12 diode has the lowest receiver noise temperature.

IV. DISCUSSION

Crowe and Peatman [9] suggested that higher doping would lower the receiver noise temperature by decreasing the noise contribution of the diode. This noise comes from the conversion loss of the mixer and the from the diode's shot noise and hot-electron noise. To determine the contribution from all sources an analysis similar to that done by Harris [8] was

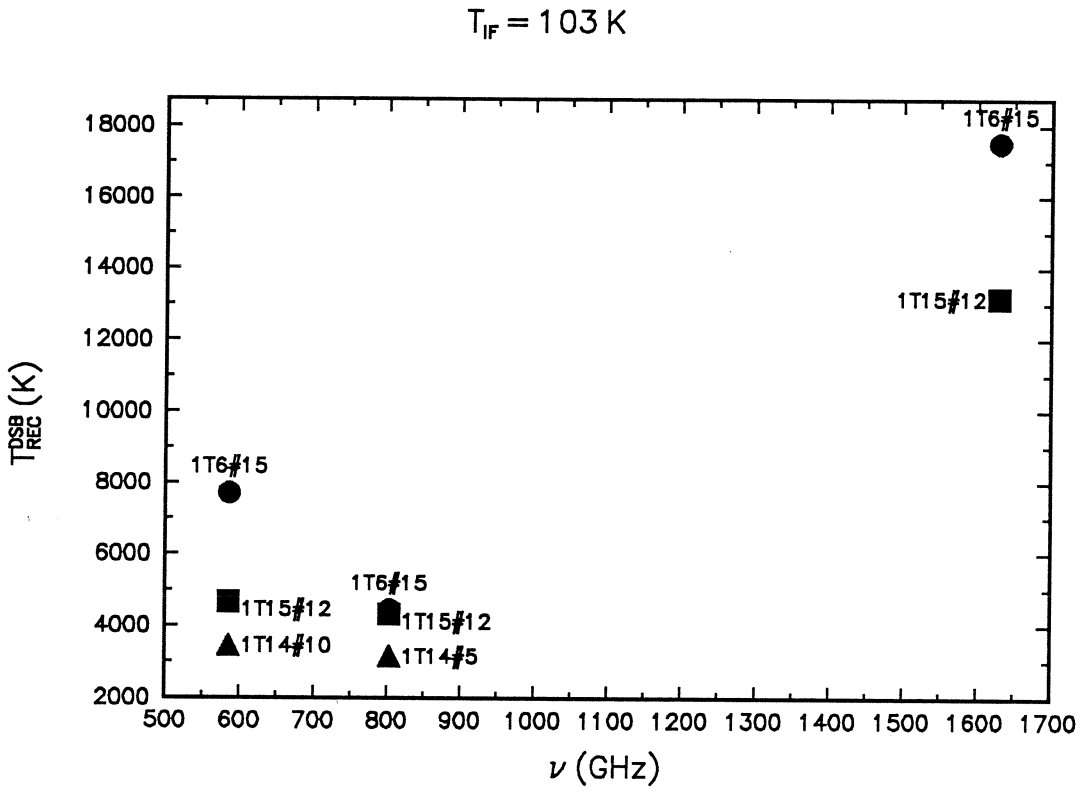

Fig. 7. Receiver noise temperature versus frequency for selected diodes.

carried out. A basic heterodyne receiver is shown in Fig. 8. The relationship between the measured mixer temperature, T'_M, measured mixer conversion loss, L'_M, and receiver temperature is given by;

$$T_{REC}=T'_M+L'_M T_{IF} \tag{1}$$

These terms include optical coupling efficiency into the corner cube, η_0, and the IF mismatch, Γ^2, as shown in Fig. 8. Eqns. 2, 3 and 4 are used to extract the diode temperature from the measured data [8, 9].

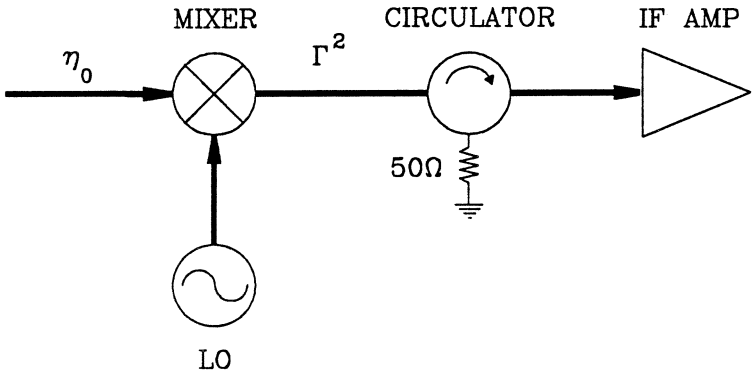

Fig. 8. A basic heterodyne receiver including the optical coupling efficiency, η_0, and IF mismatch, Γ^2. The load resistor of the circulator is at room temperature.

$$T_M' = L_M' \Gamma^2 T_{t,RJ} + \frac{T_M}{\eta_0} \tag{2}$$

$$L_M' = \frac{L_M}{\eta_0 (1-\Gamma^2)} \tag{3}$$

$$T_M = (L_M - 1) T_{D,avg} \tag{4}$$

where T_M is the true mixer temperature, L_M is the true mixer conversion loss, $T_{t,RJ}$ is the temperature of the load resistor on the circulator (300K for this analysis) and $T_{D,avg}$ is the diode noise temperature averaged over an LO cycle.

The noise breakdown for each diode at 585 GHz and 803 GHz are summarized in Tables II and III. The tables are divided into two sections for high and low doped diodes. The optical coupling coefficient, η_0, was assumed to be 0.5 for all calculations. Measurements with an HP8720C vector network analyzer of various diodes indicated that the SWR looking into the corner cube with impedance matching transformer was never more than 1.3. Therefore the reflection coefficient, Γ^2, was assumed to be 0.017.

Table II. Summary of RF Performance at 585 GHz. All temperatures and conversion losses are double sideband.

Epilayer Doping (cm^{-3})	Diode	Zero Bias C_{j0} (fF)	Receiver Noise T_{REC} (K)	Mixer Noise T_M' (K)	Mixer Loss L_M' (dB)	Minimum LO Power (mW)	Corrected Mixer Noise, T_M (K)	Corrected Mixer Loss, L_M (dB)	Diode Noise T_D (K)
$2\text{-}4x10^{17}$	1T7#2	2.3	5200	4100	10.3	1.4	2050	7.2	480
	1T7#4	1.9	4750	3800	9.7	1.2	1900	6.6	515
	1T9#10	1.5	4000	3150	9.0	0.6	1550	5.9	545
	1I7SB	1.1	4600	3600	9.8	0.7	1800	6.8	480
	1T6#15	0.8	7800	6200	11.9	0.4	3050	8.7	455
10^{18}	1T14#10	1.3	3450	2750	8.3	1.0	1350	5.2	580
	1T14#5	0.93	4250	3350	9.4	0.7	1650	6.3	500
	1T15#12	0.25	4700	3750	9.5	0.3	1850	6.4	550

The high doped diodes have a lower receiver noise temperature than the comparable capacitance low doped diodes. Comparing the diode noise, T_D, the high doped diodes perform similarly to the low doped diodes for a given capacitance. The conversion loss, however, is lower for the high doped diodes and this appears to be have resulted in the improved receiver noise temperature. Our primary goal in producing diodes with higher epitaxial layer doping density was to reduce the receiver noise by increasing the current at which hot-electron noise became important. The idea was that such diodes could be used in a shot-noise-limited mode (unaffected by hot-electron noise) and the average diode noise temperature would be the diode shot noise temperature, given by $T_{shot} = \eta T/2$. Thus, even though the higher doping increases the shot noise temperature by increasing η, the elimination of hot electron noise would drastically improve performance. In actuality, we have found that the average diode temperature has remained virtually constant, while the mixer conversion loss has been decreased.

To understand this discrepancy, it is important to realize that the mixer bias and LO power are adjusted to achieve the lowest possible receiver temperature. There is always a direct trade-off between mixer conversion loss and diode noise. As the bias current and LO power are increased, the conversion loss is decreased (the diode is pumped harder). However, at some point the diode

Table III. Summary of RF Performance at 803 GHz. All temperatures and conversion losses are double sideband.

Epilayer Doping (cm^{-3})	Diode	Zero Bias C_{j0} (fF)	Receiver Noise T_{REC} (K)	Mixer Noise T_M' (K)	Mixer Loss L_M' (dB)	Minimum LO Power (mW)	Corrected Mixer Noise, T_M (K)	Corrected Mixer Loss, L_M (dB)	Diode Noise T_D (K)
$2\text{-}4x10^{17}$	1T7#2	2.3	7850	6250	12	2.0	3100	8.9	455
	1T7#4	1.9	5750	4600	10.5	1.9	2250	7.4	505
	1T9#10	1.5	4750	3800	9.7	1.4	1900	6.6	530
	1I7SB	1.1	4650	3650	9.8	1.0	1800	6.8	480
	1T6#15	0.8	4500	3500	9.8	0.5	1700	6.7	470
10^{18}	1T14#10	1.3	3650	2900	8.6	1.3	1450	5.5	560
	1T14#5	0.93	3150	2450	8.4	1.1	1200	5.3	510
	1T15#12	0.25	4350	3350	9.8	0.2	1650	6.7	440

noise temperature begins to increase due to the hot-electron noise. Beyond the optimum point the increase in diode noise outweighs the benefit of lower conversion loss, and the total receiver sensitivity is degraded. It is our belief that the new higher doped diodes achieve greater sensitivity because they can be pumped to a lower conversion loss before the increase in the diode's hot-electron noise becomes the dominating factor.

V. SUMMARY

Schottky diodes are currently the most sensitive mixers available for frequencies in the terahertz range, but more sensitive receivers will be required for future NASA missions. For this reason we have investigated improvements that will lower the noise temperature of the diode mixer. These improvements have centered on decreasing the anode diameter and increasing the epitaxial layer doping.

Diodes with an epitaxial layer doping of 10^{18} cm^{-3} were fabricated. Contact lithography and a UV light source were used for anode diameters greater than 0.5 μm. Direct-write electron beam

lithography, performed at the National Nanofabrication Facility at Cornell University, was needed to create 0.25 μm anode diameters.

In going to a higher epitaxial layer doping we have attempted to achieve shot-noise-limited performance for the mixer. We measured the receiver noise temperature for several diodes with varying capacitance and epitaxial layer doping densities. The high doped diodes had the lowest receiver noise temperatures for a given junction capacitance. The 1T14 diode, with a 0.5 μm anode diameter, achieved a minimum double sideband receiver noise temperature of 3450K at 585 GHz and 3150K at 803 GHz. The 1T15 diode, with a 0.25 μm anode diameter, had a double sideband receiver noise temperature of 13150K at 1.63 THz. The high doped diodes had about the same diode noise temperature as low doped diodes, but the conversion loss was less. The increased doping density allowed the new diodes to be operated at a higher bias current, thereby decreasing the conversion loss without increasing the diode noise temperature.

VI. ACKNOWLEDGEMENTS

This work has been supported by the National Science Foundation (ECS-9113123) and the U.S. Army Foreign Science Technology Center (DAHC90-91-C-0030).

VII. REFERENCES

[1] J.W. Waters and P.H. Siegel, "Applications of Millimeter and Submillimeter Technology to Earth's Upper Atmosphere: Results To Date and Potential for the Future," Fourth International Symposium on Space THz Technology, Los Angeles, CA, March 1993.

[2] M.A. Frerking, "The Submillimeter Mission Heterodyne Instrument," The Second International Symposium on Space THz Technology Proc., Pasadena, CA, pp. 17-31, Feb. 1991.

[3] J. Hernichel, R. Schieder, J. Stutzki, B. Vowinkel, G. Winnewisser, and P. Zimmermann, "A 492 GHz Cooled Schottky Receiver for Radio Astronomy," Proceedings Third Intl. Symp. Space Terahertz Tech., Ann Arbor, MI, pp. 724-730, March 1992.

[4] C.K. Walker, J.W. Kooi, M. Chan, H.G. LeDuc, P.L. Schaffer, J.E. Carlstrom, T.G. Phillips, "A Low Noise 492 GHz SIS Waveguide Receiver," Third International Symposium on Space THz Technology Proceedings, Ann Arbor, MI, pp. 266-279, March 1992.

[5] G. De Lange, C.E. Honingh, M.M.T.M. Dierichs, R.A. Panhuyzen, H.H.A. Schaefer, T.M. Klapwijk, H. Van De Stadt, M.W.M. De Graauw, "A Low Noise 410-495 Heterodyne Two Tuner Mixer, Using Submicron $Nb/Al_2O_3/Nb$ Tunneljunctions," Proceedings Third Intl. Symp. Space Terahertz Tech., Ann Arbor, MI, pp. 210-233, March 1992.

[6] S. Weinreb and A.R. Kerr, "Cryogenic Cooling of Mixers for Millimeter and Submillimeter Wavelengths," IEEE J. Solid State Circuits, Vol. SC-8, pp. 58-63, Feb. 1973.

[7] C.R. Predmore, A.R. Räisänen, N.R. Erickson, P.F. Goldsmith, and J.L.R. Marrero, "A Broad-Band, Ultra-Low-Noise Schottky Diode Mixer Receiver for 80 to 115 GHz," IEEE Trans. Microwave Theory Tech., Vol. MTT-32, pp. 498-506, May 1984.

[8] A.I. Harris, J. Stutzki, U.U. Graf, and R. Genzel, "Measured Mixer Noise Temperature and Conversion Loss of a Cryogenic Schottky Diode Mixer Near 800 GHz," Intl. J. Infrared and Millimeter Waves, Vol. 10, No. 11, Nov. 1989.

[9] T.W. Crowe and W.C.B. Peatman, "GaAs Schottky Barrier Diodes for Space Based Applications at Submillimeter Wavelengths," The 2nd Int'l. Symp. Space THz Tech. Proc., Pasadena, CA, Feb. 1991.

[10] U.V. Bhapkar and T.W. Crowe, "Analysis of the High Frequency Series Impedance of GaAs Schottky Diodes by a Finite Difference Technique," IEEE Trans. Microwave Theory Tech., Vol. 40, No. 5, pp. 886-894, May 1992.

[11] D.T. Young and J.C. Irvin, "Millimeter Frequency Conversion Using Au-n-Type GaAs Schottky Barrier Epitaxial Diodes with a Novel Contacting Technique," Proc. IEEE, pp. 2130-2131, Dec. 1965.

[12] T.W. Crowe, R.J. Mattauch, H.P. Röser, W.L. Bishop, W.C.B. Peatman, "GaAs Schottky Diodes for THz Mixing Application," Invited paper, Proc. of the IEEE, Special Issue on Terahertz Technology, Vol. 80, No. 11, Nov. 1992.

[13] W.C.B. Peatman and T.W. Crowe, "Design and Fabrication of 0.5 micron GaAs Schottky Barrier Diodes for Low-Noise Terahertz Receiver Applications,"Int. Journal on Infrared and Millimeter Waves, Vol. 11, No. 3, pp. 355-365, 1990.

[14] P.A. Verlangieri and M.V. Schneider. "Microfabrication of GaAs Schottky barrier diodes for multipliers, mixers and modulators," Int. J. of IR and MM Waves, Vol. 6, pp. 1191-1202, 1985.

PLANAR THZ SCHOTTKY DIODE BASED ON A QUASI VERTICAL DIODE STRUCTURE

A. Simon, A. Grüb, V. Krozer, K. Beilenhoff, H.L. Hartnagel

Institut für Hochfrequenztechnik, Technische Hochschule Darmstadt, Merckstr. 25, D-6100 Darmstadt, Germany, Phone: +49 6151 162162, Fax: +49 6151 164367

Abstract

Whisker contacted GaAs Schottky barrier diodes are presently the standard devices for heterodyne mixing applications at THz frequencies. Due to reliability and handling problems and with regards to the recently proposed integrated antenna structures, much effort has been undertaken to develop planar whiskerless Schottky diodes. Recent approaches to planar diodes, based on FET–like structures, could not overcome the principal problems leading to a high parasitic shunt capacitance and a high series resistance. In this paper we present a novel approach for the planar diode concept. It is directly deduced from the vertical structure of the whisker contacted diode, making use of the many advantages and mature technology of the whisker contacted Schottky diode concept. On top of a mesa, the anode is connected with an airbridge to a contact pad. By means of via hole etching, the backside ohmic contact is connected with a contact pad at the surface. We have developed a technology for fabricating these diodes and describe the structure and the main technological aspects. Simulations have shown that in comparison to the recent approaches this concept shows some very promising features. In particular the minimum series resistance is comparable to the series resistance of the whisker contacted diode, due to the vertical current flow through the mesa, which is similar to the whisker Schottky diode structures operable at THz frequencies. This structure also exhibits a low parasitic shunt capacitance, due to a combined via hole and air bridge technology.

Introduction

For a variety of applications including radio astronomy, atmospheric studies and plasma diagnostics, heterodyne reception is the most promising technique in the Terahertz frequency range. There exist two different approaches to the realization of the nonlinear mixer element which is the key component of the receiver front end. The SIS device, which demonstrated record sensitivity at millimeter and long submillimeter wavelengths [1] and the GaAs Schottky barrier diode. Due to the required cryogenic cooling and a frequency limitation to about 700 GHz of SIS elements, GaAs Schottky barrier diodes are at the moment the most widely used mixer elements at submillimeter wavelengths and also in applications where cryogenic cooling is either too expensive or too heavy.

Whisker contacted Schottky barrier diodes have demonstrated excellent performance up to 2.5 THz [2]. They benefit from a minimum parasitic capacitance and a simple and highly mature fabrication. However, they are costly to assemble, show reliability problems due to the whisker contact and are impractical for systems using more than one diode. With the need for cheap and reliable mixer elements, the developement of planar Schottky diodes is an important topic of investigation. The essential drawback of these devices with respect to THz applications is the high parasitic capacitance and the increased series resistance compared to whisker contacted diodes.

In this paper we present a new approach to planar GaAs Schottky diodes which are designed for minimum parasitic capacitance and series resistance. The first section illustrates the design of the novel planar diode and gives an analysis of the parasitic resistance and the capacitance of FET–like planar diodes and the quasi–vertical diode. The second section describes the technological steps for the fabrication of the diode.

Concepts of planar diodes

In contrast to whisker contacted diodes an insulating substrate is used for planar diodes. The anode is connected to a contact pad by means of an air bridge. The common approach to the realization of planar Schottky diodes utilize FET–like structures [3]. Fig. 1 illustrates the structure. The ohmic contact pad is placed on the n^+–layer as closely as possible to the Schottky contact [3, 4]. The anode of the diode is contacted by an air bridge to the second contact pad.

The novel approach proposed in this contribution, is the quasi vertical structure il-

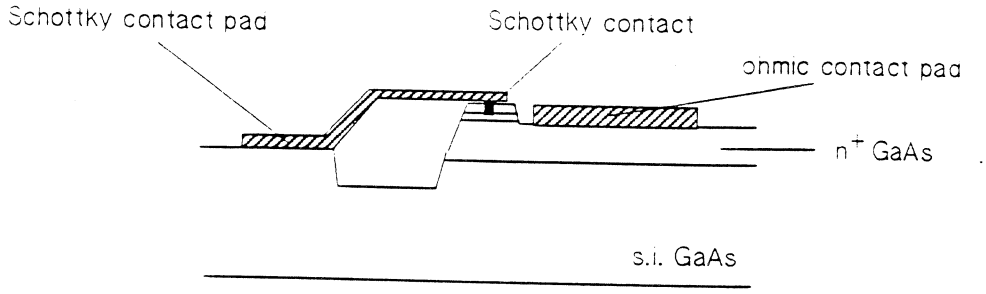

Figure 1: Structure of a FET–like planar diode

lustrated in fig. 2. This planar diode is directly derived from the whisker contacted diode. The Schottky contact is located on top of a small n/n^+ mesa. The mesa is placed on a metal island, forming the ohmic backside contact. The ohmic contact pad at the surface is connected to this backside metallization. The anode of this diode structure is also contacted by means of an air bridge to the second contact pad.

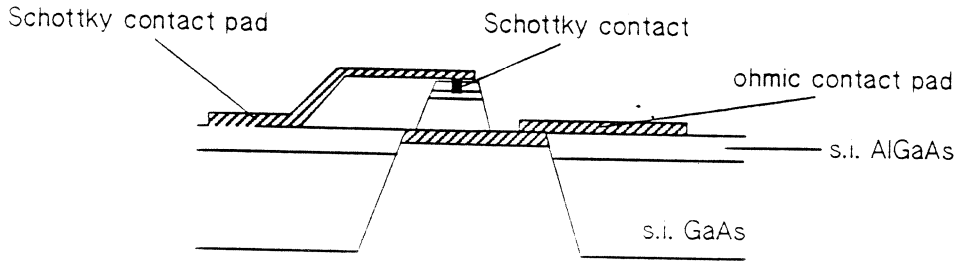

Figure 2: Structure of the quasi vertical planar diode

In the following sections, a comparison of the two concepts concerning the most important parameters for high frequency applications, the series resistance and the capacitance of the diodes, is presented.

With respect to future developements a possible resolution of 0.5 μm for the seperation between the Schottky and the ohmic metallization, an anode diameter of 0.5 μm

and a width of the air bridge of 1 μm have been assumed for the FET–like structure. For the quasi vertical diode a smallest mesa diameter of 2.5 μm, a possible via hole width of 2.5 μm, an anode diameter of 0.5 μm and a width of the air bridge of 1 μm have been chosen.

Analysis of the series resistance

The analysis presented here, gives an estimate of the parasitic resistance R_p for the two diode concepts. This resistance takes into account the ohmic contribution of the n^+ layer R_{n+} and the ohmic contact resistance R_{con} between the n^+ layer and the ohmic contact pad. For the total series resistance the contribution of the epi layer R_n has to be added to R_p. R_n depends on the anode diameter and the thickness and doping concentration of the epi layer. Typical values of THz diodes for R_n are in the range of 10–20 Ω.

Integrated antenna structures for THz applications require the smallest possible structure size [3]. Due to the required reduction of the contact areas the influence of the parasitic resistance increases dramatically. For a realistic estimation a calculation of the R_p dependance on the structure dimensions has been made. It will be demonstrated that the influence of R_p is a limiting factor for the reduction of the planar diode structures.

For the calculation of R_{con} and R_{n+} of the planar contact the following equations have been used [5]:

$$R_{con} = \frac{R_s L_T}{-2\pi R_b} \left\{ \frac{I_0\left(\frac{R_b}{L_T}\right) - \frac{I_0'(R_c/L_T)}{K_0'(R_c/L_T)} K_0\left(\frac{R_b}{L_T}\right)}{I_0'\left(\frac{R_b}{L_T}\right) - \frac{I_0'(R_c/L_T)}{K_0'(R_c/L_T)} K_0'\left(\frac{R_b}{L_T}\right)} \right\} \tag{1}$$

with

$$L_T = \sqrt{\rho_c / R_s} \tag{2}$$

I_0 and K_0 represent the modified Bessel functions of the first and second kind. R_b is the shortest distance between the center of the anode and the edge of the radial

ohmic contact pad. R_c denotes the distance between the center of the anode and the far end of the ohmic contact pad.

$$R_s = \frac{1}{q\, N_{ds}\, \mu \min(d_{n+},\, R_b)} \tag{3}$$

$$R_{n+} = \frac{1}{2\,\pi\, q\, N_{ds}\, \mu\, R_a} \tan^{-1}\left(\frac{R_b}{R_a}\right) + \frac{1}{2\,\pi\, q\, N_{ds}\, \mu\, \delta_s} \ln\left(\frac{R_b}{R_a}\right) \tag{4}$$

Due to the vertical contact, the calculation of R_p for the quasi vertical structure is straight forward.

The following material and technological parameters have been used:

specific contact resistance	ρ_c	$5 \cdot 10^{-7}\, \Omega cm^2$
electron mobility	μ	$1500\ \frac{cm^2}{V\,s}$
doping concentration of n^+ layer	N_{ds}	$5 \cdot 10^{18}\, cm^{-3}$
thickness of n^+ layer (FET–like)	d_{n+}	$1.5\ \mu m$
bridge width	L_g	$1\ \mu m$
anode diameter	R_a	$0.25\ \mu m$
skin depth at 1 THz	δ_s	$1.5\ \mu m$

Fig. 3 shows the results for a FET–like structure and a quasi vertical structure. For mesa heights smaller than the skin depth the effective contact area is not affected by the skin effect. Therefore, a mesa height of 1 μm has been chosen. It can be inferred that for all values of the structure width the parasitic resistance of the quasi vertical structure is smaller than that of the FET–like structure. The difference increases with a reduction of the structure width. For structure widths between 5 and 20 μm the difference between the two concepts is about 10 Ω. This lower series resistance would enable to reduce the typical epi–layer doping concentration of $1 \cdot 10^{18}\, cm^{-3}$ to $2 \cdot 10^{17}\, cm^{-3}$. A quasi vertical diode with the same series resistance as a FET-like diode therefore could achieve a lower ideality factor and a smaller junction capacitance. For both diodes a reduction below $\sim 2.5\, \mu m$ leads to a strong increase of R_p values which even exceed the epi–layer resistance. This is due to the rapid decrease of the contact area. Therefore, apart from the technological problems, the fabrication of diodes seems not to be reasonable with an overall structure width of less than $\sim 2.5\, \mu m$. The resulting high values of R_p ultimately limit the performance of both concepts.

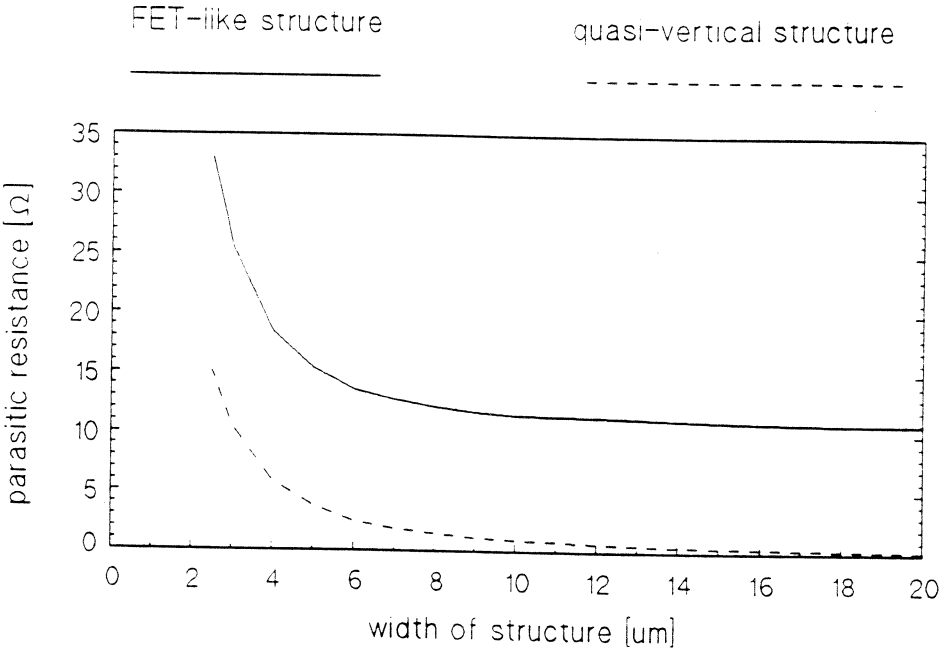

Figure 3: The parasitic resistance R_p for the two diode concepts as a function of the structure width

Analysis of the parasitic capacitance

The parasitic capacitance of the quasi–vertical structure is mainly determined by the area of the ohmic contact and the air bridge dimensions. In the FET–like structure, the main contribution to the parasitic capacitance originates from the small distance between the anode and the ohmic contact. A general–purpose 3–dimensional CAD finite–difference (F3D) program package has been developed for the calculation of passive microwave structures in the frequency domain and for static problems [6, 7]. The capabilities of the F3D CAD–package have been utilized for the calculation of the static parasitic capacitance of the quasi vertical diode structure. Based on these capabilities, simulations with varying dimensions have been carried out.

The main contribution to the capacitance of a single diode is caused by the contact pads. However, in typical applications this parasitic capacitance can be incorporated into the circuit design and is therefore generally less important. Giving an estimation of the performance of integrated diodes, the influence of these contact pads has been neglected. Assuming a via hole size of (mesa diameter)· (mesa diameter + 5 μm) the following capacitances depending on the mesa diameter, mesa height and air bridge length were calculated:

Mesa diameter [μm]	Mesa height [μm]	Bridge length [μm]	Capacitance [fF]
10	3	0	0.24
10	1	20	0.82
10	3	20	0.71
10	1	0	0.27
4	1	20	0.74
4	3	20	0.60
2	1	5	0.41
2	3	5	0.29
2	1	20	0.67
2	3	20	0.50

The decreasing mesa diameter and mesa height lead to a slight change of the parasitic capacitance. The length of the air bridge influences the capacitance to a much higher extent. However, the parasitic capacitance of this basic diode element does not exceed $1\,fF$ and is comparable to the junction capacitance of a $0.5\mu m$ anode. This indicates that the total capacitance of the quasi vertical diode can be close to that of a whisker contacted diode. Simulations of the parasitic capacitance of FET-like structures show that there is no remarkable difference between the two planar diode concepts if the structure size is reduced.

Simulating a single quasi vertical diode with $50\,\mu m \cdot 50\,\mu m$ contact pads, a $2\mu m$ anode, $50\mu m$ air bridge length and $5\mu m$ air bridge width we obtained a parasitic capacitance of $13\,fF$.

Technological Aspects

The fabrication process of the quasi-vertical diode is described in this section. The technological process is very similar to the fabrication of whisker contacted diodes, only the $GaAs$ material differs considerably. As substrate semi-insulating (s.i.) GaAs $(50 - 100\,\mu m)$ is used. The epitaxial structure consists of a s.i. AlGaAs etch stop layer $(1\,\mu m)$, a several micron thick and heavily doped epitaxially grown n^+-GaAs layer $(1 - 5\,\mu m)$ and a thin epitaxial n-GaAs layer $(50 - 100\,nm)$ at the top. A thin SiO_2 film is evaporated onto the top of the wafer, providing passivation of the surface for the following technological steps. Using AlGaAs as an etch stop layer, holes necessary for the backside ohmic contact are etched into the s.i. substrate. After a

selective etching of the remaining AlGaAs an ohmic contact consisting of Ni/AuGe/Ni is formed to the n^+–layer followed by an annealing step and a subsequent Au plating (fig. 4). The n/n^+ mesa is defined using a HCl based etching solution (fig. 5). The

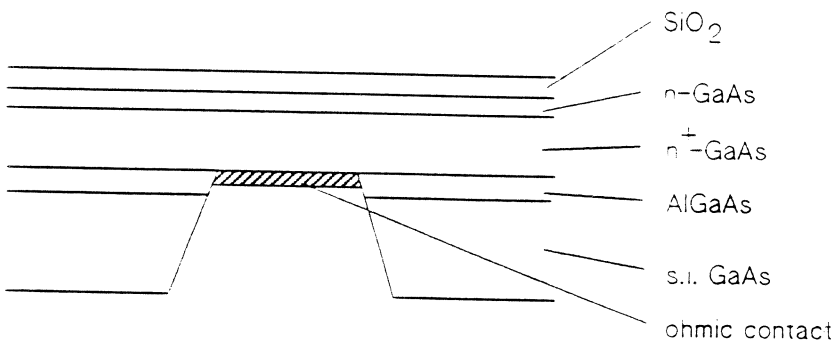

Figure 4: Structure with SiO_2 layer and ohmic contact

anode is formed by a RIE process with subsequent electrolytic Pt deposition (fig. 7). Then the air bridge and the contact pads are defined. The plating of the bridge and the contact pads completes the fabrication procedure (fig. 6). Fig. 8 and 9 show SEM photographs of the diode structure without the ohmic backside contact.

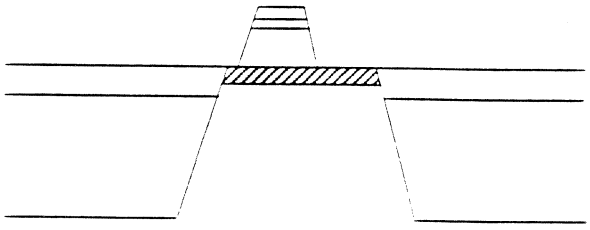

Figure 5: Definition of the mesa

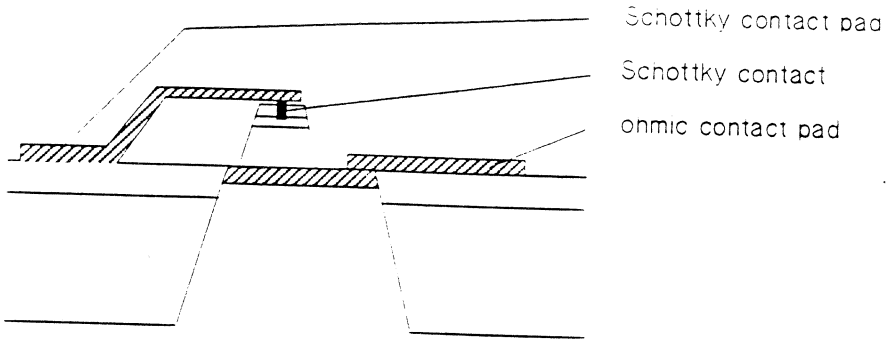

Figure 6: Quasi vertical diode

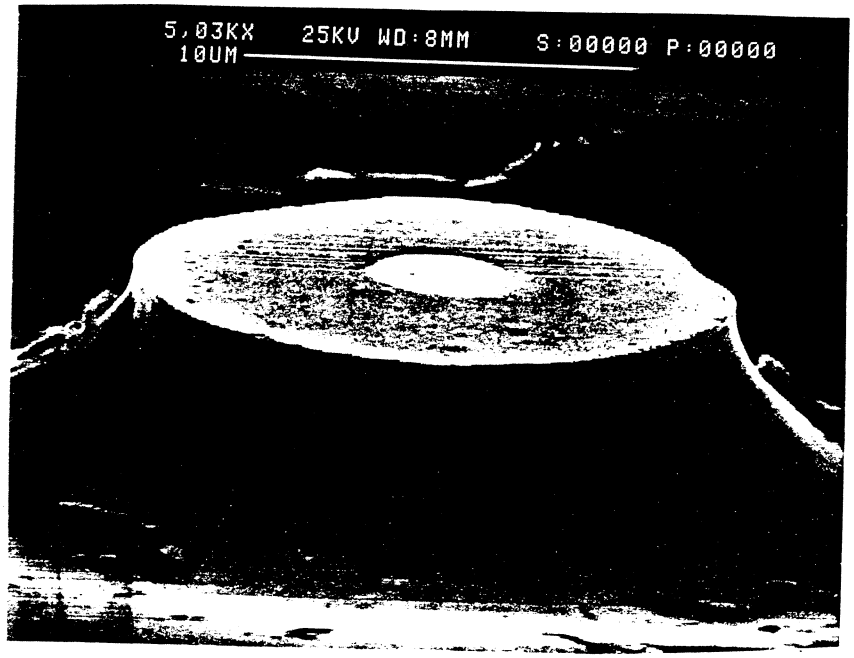

Figure 7: Mesa structure with 3 μm anode

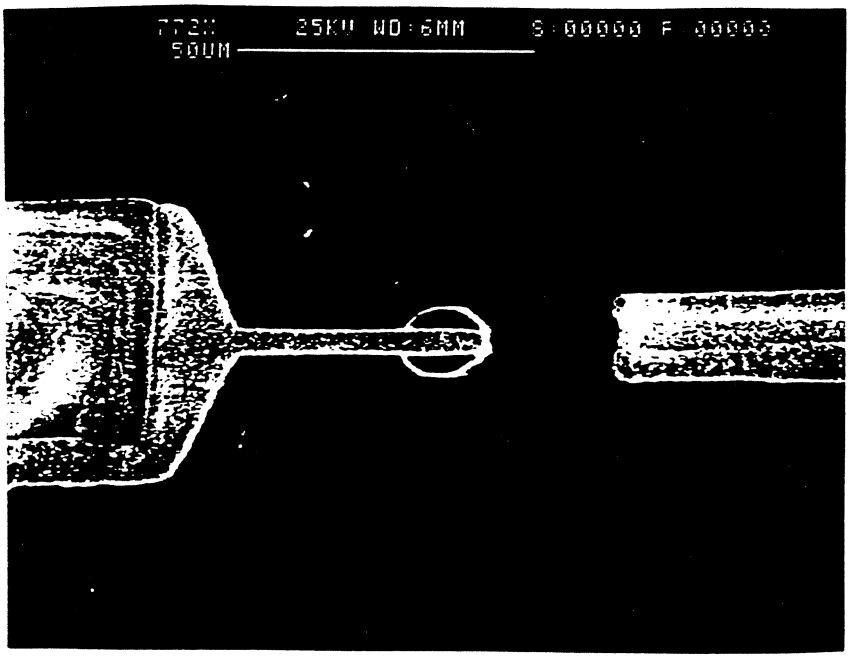

Figure 8: Top view of the diode with mesa (diameter 14 μm, height 5 μm) and air bridge (length 40 μm, width 4 μm)

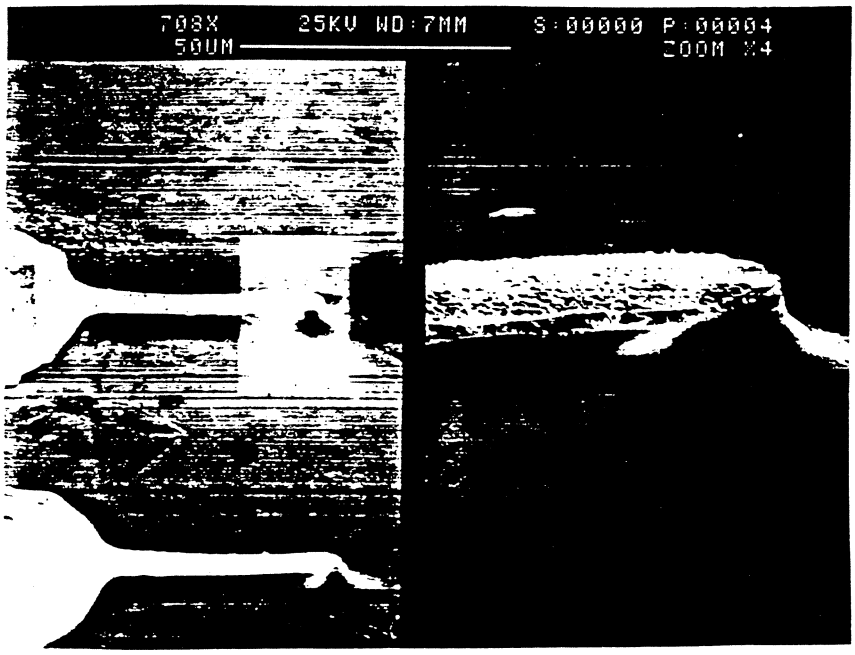

Figure 9: Side view of a diode with mesa (diameter 3.5 μm, height 5 μm and air bridge (length 40 μm, width 4 μm)

Conclusion

In this paper a novel approach has been presented for the realization of planar Schottky diodes suitable for operation at THz frequencies. The features of this structure as compared to the FET–like structure have been discussed in detail. Especially, the values for the parasitic diode capacitance and series resistance for both structures have been determined and a comparison reveals that the proposed novel structure exhibits a lower series resistance and similar shunt capacitance. The strong increase of the series resistance seems to be a limitation for the reduction of the total diode width below values of $\sim 2.5\,\mu m$. The simulations have shown that further technological improvements are necessary to reduce the shunt capacitance of planar structures to values which are comparable to whisker contacted diodes.

Acknowledgements

The authors would like to express their acknowledgements to Dr. H. Grothe and Dr. J. Freyer, both from the Technical University of Munich, Germany, for supplying the high–quality epitaxial material.

This work has been funded partly by the Deutsche Forschungsgemeinschaft (DFG) whose support is acknowledged.

References

[1] S.K. Pan, A.R. Kerr, M.J. Feldman, A.W. Kleinsasser, J. Stasiak, R.L Sandstrom, andW.J. Gallagher: An 85–116 GHz SIS receiver using inductively shunted edge–junctions, *IEEE Trans. Microwave Theory & Techniques*, vol. MTT–37, no.3, 1989, pp.580–592.

[2] W.C.B. Peatman and T.W. Crowe: Design and fabrication of $0.5\mu m$ $GaAs$ Schottky barrier diodes for low–noise Terahertz receiver applications, *Int. J. Infrared and Millimeter Waves*, vol. 11, no.3, 1990, pp.355–365.

[3] W.L. Bishop, T.W. Crowe, R.J. Mattauch, andH. Dossal: Planar GaAs diodes for THz frequency mixing applications, *Proc. of* 3^{rd} *Int. Symp. on Space Terahertz Technoloy*, vol. Ann Arbor, Michigan, USA, 1992, pp.600–615.

[4] J.W. Archer, R.A. Batchelor, andC.J. Smith: Low–parasitic, planar Schottky diodes for millimeter–wave integrated circuits, *IEEE Trans. Microwave Theory & Techniques*, vol. MTT–38, no.1, 1990, pp.15–22.

[5] K. Bhaumik, B. Gelmont, R.J. Mattauch, andM. Shur: Series impedance of GaAs planar Schottky diodes operated to 500 GHz, *IEEE Trans. Microwave Theory & Techniques*, vol. MTT–40, no.5, 1992, pp.880–885.

[6] A. Christ and H.L. Hartnagel: Three–dimensional Finite–Difference method for the analysis of microwave device embedding, *IEEE Trans. Microwave Theory & Techniques*, vol. MTT–35, 1987, pp.688–699.

[7] K. Beilenhoff, W. Heinrich, andH.L. Hartnagel: Finite Difference analysis of open and short circuits in coplanar MMICs including finite metallization thickness ansd mode conversion, *IEEE Int. Microwave Symposium Digest*, vol. 1, 1992, pp.103–106.

Low-Frequency Noise Characteristics of GaAs Schottky Diodes Fabricated by In-Situ Electrochemical Process and comparison to Evaporation Process

P. Marsh, D Pavlidis, and M. Tutt,
Dept. of EECS
The University of Michigan,
Ann Arbor MI. 48109-2122

T. Hashizume
Hokkaido Polytechnic College,
Zenibako 3-190,
Otaru 047-02, Japan

H. Hasegawa and T. Sawada
Research Center for Interface Quantum Electronics
Hokkaido University
Sapporo 060, Japan

A. Grüb and H.L. Hartnagel,
Institut fur Hochfrequentztechnik
Technische Hochschule Darmstadt
W-6100 Darmstadt, Germany

Abstract

GaAs Schottky diodes grown by MBE have been characterized by DLTS and low-frequency noise techniques. DLTS characteristics of diodes with conventional E-beam evaporated-metal anodes revealed three process-induced trap levels, S_1, S_2, and S_3; with activation energies of 0.08, 0.27, and 0.55eV respectively. Electrochemically processed diodes showed an absence of S_1, S_2 traps. The S_1-S_3 trap densities were significant to only a depth of 1000Å. A study of the signature plots showed the similarity of these defects to those produced by irradiation. Low-frequency noise spectra were studied as functions of dc current and temperature over the frequency range of 10Hz to 10MHz. In both types of diodes noise current fell with temperature and increased with dc current. Measurements at 300K and 10mA indicated that the electrochemically processed diodes had significantly lower generation-recombination current and lower noise above 6KHz than those processed by E-beam.

I. Introduction

Currently, the lack of low-noise amplifiers at submillimeter and THz frequencies means that the mixer is the first component seen by the incoming signal. Therefore, the mixer's equivalent input noise temperature sets the lower limit of a receiver's noise.

GaAs Schottky diodes are a key element in heterodyne mm and sub-mm wave receivers. Techniques for the realization of their Schottky contacts include evaporation of Pt or Ti by electron-beam and in-situ anodic pulse etching followed by electrochemical Pt deposition [1]-[3]. Noise characteristics are a key factor in successful use of Schottky diodes in sub-mm wave receivers. Since traps can play a significant role in the noise performance of Schottky diodes, it is consequently very important to evaluate process techniques that show potential for reduction of trap densities and consequently, noise. This paper addresses such issues for diodes prepared by the novel in-situ electrochemical etching/plating process and conventional E-beam evaporation techniques.

Traps have often been correlated to bulk defects and interface states at the Schottky-semiconductor boundary. Low concentrations of these traps are usually accompanied by good ideality factors, small reverse-bias leakage, low recombination currents and most importantly, lower noise temperatures in mixers. This provides a motivation for the

---

Work supported by NASA under contract NAGW-1334.

implementation of fabrication techniques which reduce these trap concentrations. Using Deep Level Transient Spectroscopy (DLTS) characterization, it was shown that a novel electrochemical anodic etch followed by in-situ Pt plating technique (hereafter referred to as electrochemical etch/plating) resulted in the virtual elimination of two of three traps normally found in anodes fabricated via E-beam metal evaporation (hereafter referred to as evaporation). The electrochemically etched/plated anodes also tended to exhibit superior ideality factors compared to those of the E-beam anodes. Since the electrochemical etch/plating technique appears to result in overall improved diode characteristics, it is of considerable interest to study whether it can improve noise performance as well. The purpose of this paper is to compare the low-frequency noise performance of diodes fabricated by E-beam evaporated metal (hereafter referred to as evaporated diodes) against those fabricated via in-situ electrochemical etch/plating (hereafter referred to as plated diodes).

In section II, the trap characteristics of evaporated and plated diodes are compared by DLTS. Section III compares the I-V and low-frequency noise properties of evaporated and plated diodes. Finally, conclusions are discussed in section IV.

II. DLTS Study of Diodes

II-A. Device Structure and Fabrication

All diodes characterized here via DLTS were fabricated on the same n+ GaAs wafer having a 0.2μm GaAs epilayer grown by molecular beam epitaxy (MBE) and doped with Si at n = $2x10^{16}/cm^3$. Both evaporated and plated Schottky's were formed from Pt covered by Au and then passivated with SiO_2. The evaporated diodes' anodes were formed via conventional E-beam evaporation of Pt while plated diodes were formed using the new electrochemical etch/plating process illustrated below in Fig 1.

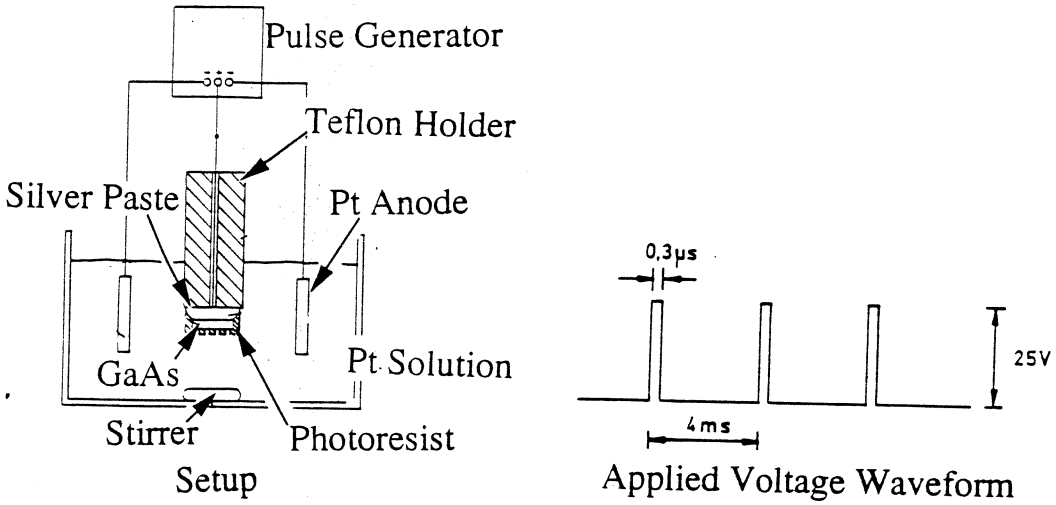

Figure 1. Pulse anodic etch followed by in-situ platinum plating process technique.

In the electrochemical etch/plating process, the Pt plating solution serves both to etch the semiconductor and form the electroplated anodes. First, the anode regions are etched to expose a high-quality semiconductor surface. Etching is accomplished by pulsing the semiconductor positive while it is in the acid Pt plating solution. While the

semiconductor is positive, holes appearing at the solution-semiconductor interface oxidize the semiconductor surface. During the relatively long intervals between pulses, oxidation stops and reaction products dissipate, allowing anisotropic etching [4]. The low pH of the etching solution acts to remove oxides. In this work, the etch rate was 40Å/pulse. Immediately after etching, the semiconductor is pulsed negative to plate Pt onto the anode regions. It is believed that this in-situ process achieves superior Schottky contacts by reducing the amount of oxides and other contaminants under the Schottky metal.

II-B. I-V Results

Fig. 2 illustrates evaporated and plated I-V curves. I-V curves of the evaporated diodes showed barrier heights (ϕ_b) in the range 0.80-0.85eV [1]. Plated diodes had higher ϕ_b's in the range of 0.95-1.00eV. Plated diodes exhibited ideality factors (η) $\leq$ 1.05, while evaporated diodes had $\eta > 1.1$.

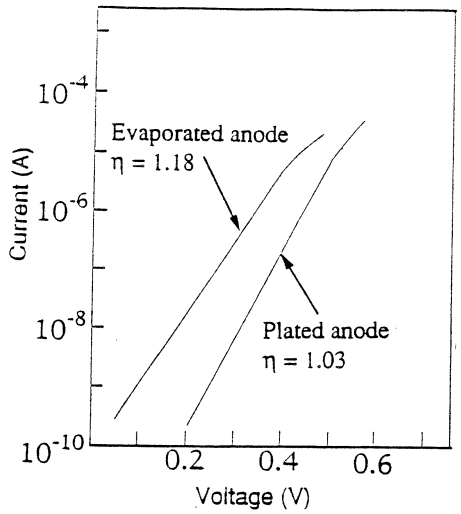

Figure 2. Evaporated and plated diode I-V curves.

II-C. DLTS Analysis

DLTS measurements showed the appearance of several traps not normally found in native bulk GaAs [1]. These traps are thought to be process-induced because they do not appear in bulk MBE GaAs and their concentrations are significant to a depth of only about 1000Å (Fig. 3). The evaporated diodes exhibited the process-induced traps S_1, S_2, and S_3 while the plated diodes exhibited only one such trap, S_3', having properties very close to those of S_3. Activation energies (E_a) of S_1, S_2, and S_3 were 0.08, 0.27, and 0.55eV, respectively. Fig. 3 indicates that in 200µm anodes, the concentration of S_3', was higher than that of S_3. However, when the anode diameter is reduced to 15µm, the situation is reversed, i.e. the DLTS signal of S_3' is now less than that of S_3. Thus, at a depth of 500Å, the 15µm plated diode has a total trap concentration of $\leq 2.7 \times 10^{14}/cm^3$ vs. $4.7 \times 10^{14}/cm^3$ for the evaporated diode. The dependence of S_3' on anode size is believed to be the result of optimizing the electrochemical etch/plating for the 15µm diodes, inadvertently resulting in suboptimal processing of the larger diodes. Recently, it has been determined that reduction of the etch rate in the electrochemical etch/plating process resulted in reduced levels of S_3' in 500µm diameter diodes [5].

The signature plots of S_1-S_3 traps are very similar to those of traps in GaAs arising from irradiation by γ rays and high-energy (1 MeV) electrons [1]. Furthermore, low-energy ($\approx$3KeV) electrons produce traps having signature plots similar to those of the MeV electrons [1]. Since irradiation by low-energy stray electrons is likely during the E-beam metal evaporation-deposition process, the traps S_1-S_3 are thought to be the result of defects formed by the stray electrons during this process.

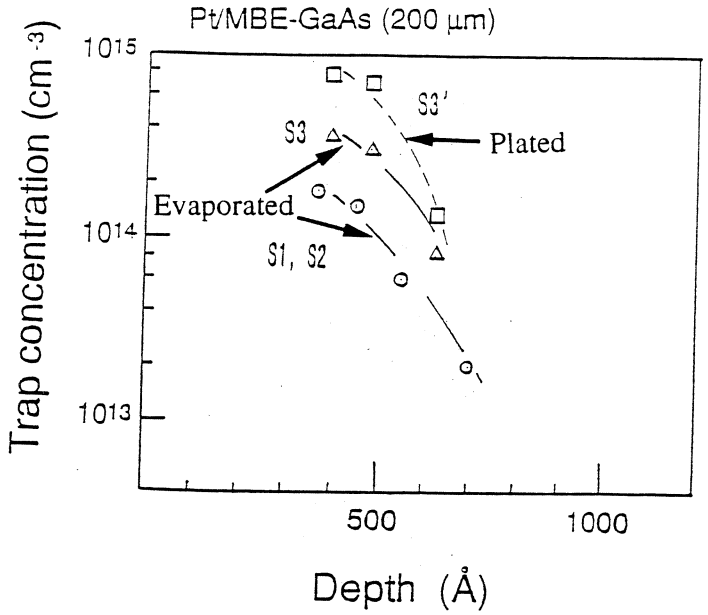

Figure 3. Trap concentrations vs. depth.

III. Low-Frequency Noise Characterization

III-A. Theory of Trap Noise

The spectral characteristic of the mean noise current squared, $S_I(f)$, from an ensemble of identical traps typically exhibits a Lorentzian behavior having the form [6]:

$$S_I(f) = \frac{C_2 \tau F_t (1-F_t)}{1 + (\omega\tau)^2} \quad (A^2/Hz) \qquad (1)$$

Where:
$V_b = q\phi_b$
C_2 = constant.
τ = characteristics trap time constant.
F_t = occupation probability of the trap.
ω = the radian frequency.

For electron traps [6], at low current densities the characteristic time, τ follows:

$$\tau \propto \exp\left(\frac{E_a}{KT}\right) \qquad (2)$$

Where: E_a = trap activation energy
K = Boltzmann's constant,
T = temperature in Kelvin.

Also, it is possible to define a characteristic trap frequency $f_{tr} = \frac{1}{2\pi\tau}$.

Since the quantity $F_t(1-F_t)$ is a maximum at $F_t = 0.5$ i.e. the only traps that will contribute significantly to the noise are those the lie near the local Fermi level, i.e. are statistically half occupied. For the case where traps are distributed uniformly in E_a and space, the resulting continuum of time constants has the proper distribution to give $S_I(f)$ a 1/f form over a region of frequencies [7]. At a sufficiently low frequency, $S_I(f)$ will plateau. In the 1/f range, $S_I(f)$ will be proportional to the anode current squared (I_d^2) [7]. At very low frequencies where $S_I(f)$ becomes constant, $S_I(f)$ is proportional to $I_d^{1.5}$ [7].

III-B. Device Structure and Fabrication

The evaporated and plated diodes characterized for low-frequency noise have the same cross-section and epilayer doping as the diodes discussed in section II, except that the epilayer is 0.9μm. All characterized devices had anode diameters of 50μm and were from the same MBE GaAs wafer.

Prior to anode deposition, the evaporated diodes' anode areas were etched using $NH_4OH/H_2O_2/H_2O$ in a (2:1:300) ratio. Next, E-beam evaporated metals in the sequence Ti/Pt/Au were deposited. Finally, Au was plated onto the anodes to facilitate wirebonding and probing.

The plated diodes' anodes were anodically etched then plated in-situ with Pt as discussed in section II-A. The plated Pt anodes were then completed with an Au deposition over the Pt.

III-C. Measurements Performed

Several diodes from both the plated anode and evaporated anode samples were subjected to the following comparative tests:

1. I-V characteristics vs. temperature.
2. $S_I(f)$ vs. I_d, $10Hz \leq f \leq 10MHz$, at room temperature (≈300K).
3. $S_I(f)$ ($10Hz \leq f \leq 10MHz$) vs. temperature (125K - 300K) with $I_d = 10mA$.

III-D. Measurement Setup and Procedure

Both the evaporated and plated samples were mounted on gold metallized alumina coplanar chip carriers designed for a coplanar waveguide microwave test fixture. Diodes were wirebonded to the chip carrier transmission lines to eliminate vibration-induced contacting noise. Room temperature testing was performed with the chip carrier mounted into the microwave test fixture, whereas variable-temperature measurements were performed in a cold stage. The measurement setup is shown below in Fig. 4 below.

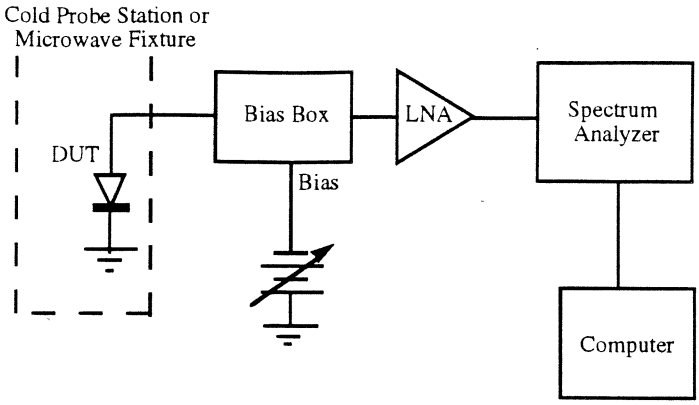

Figure 4. Measurement test setup for low-frequency noise characterization of diodes.

At measurement frequencies below 100KHz, the spectrum analyzer was an HP 3561A dynamic signal analyzer. The 100KHz to 10MHz frequency range was covered by a Tektronix 2755P spectrum analyzer.

$S_I(f)$ (A^2/Hz) is derived from $V_{mn}(f)(V/\sqrt{Hz})$, the RMS noise voltage at the diode terminals, via the use of a diode noise model. The diode model consists of R_{ohm} in series with the parallel combination of R_i, and the noise current source, $I_n(f)$ ($A/\sqrt{Hz}$). R_{ohm} is the portion of the diode resistance due to ohmic resistance from the conductive mounting paint, n+ GaAs substrate, and finally the undepleted portion of the n- epilayer. R_i is due to the dynamic resistance of the Schottky barrier itself. The total resistance presented to the diode by the bias box and LNA during the noise tests is represented by R_L. $V_{mn}(f)$, is extracted by subtracting the noise floor power from the raw spectrum analyzer reading, then referring the result to the LNA input. Next, $I_n(f)$ is extracted from $V_{mn}(f)$ using the diode noise model. Finally, $S_I(f)$ is derived from:

$$S_I(f) = \langle |I_n(f)|^2 \rangle \qquad (3)$$

This model assumes that all diode noise mechanisms originate entirely within the depletion region. This is believed to be accurate for the analysis here since electron traps should be mostly inactive within the undepleted GaAs as they will be always filled. Also, the low current densities used here should not cause significant additional noise due to hot electrons.

Extraction of the diode model's resistances, R_i, and R_{ohm}, make use of the diode relation:

$$\log(R_i) = m \bullet \log(I_d) + b \qquad \text{m and b are constants} \qquad (4)$$

Due to nonzero R_{ohm} and other effects, the relation (4) is accurate only over a limited range of I_d. Here, (4) was found to be quite accurate for $I_d = 100\mu A$. Also at $I_d = 100\mu A$ $R_i \approx \frac{\Delta V_d}{\Delta I_d}$. To find $R_i|_{I_d'}$ (R_i at the diode current I_d'):

$$R_i|_{I_d'} = \left(\frac{100\mu A}{I_d'}\right)\left(\frac{\Delta V_d}{\Delta I_d}|_{I_d = 100\mu A}\right) \qquad (5)$$

And:

$$R_{ohm}|_{I_d'} = \frac{\Delta V_d}{\Delta I_d}|_{I_d'} - R_i|_{I_d'} \qquad (6)$$

III-E. I-V Results

I-V characteristics of several evaporated and plated diodes were plotted in Fig. 5. The in-situ anode plating process yields higher barrier potentials (ϕ_b) and lower generation-recombination current than the evaporated anode process. At I_d = 10mA and 300K, R_i and R_{ohm} for the evaporated and plated diodes are nominally 2.4Ω and 1.4Ω respectively. At 300K ideality factors (η) of the evaporated and plated diodes have nominal values of 1.19 and 1.14, respectively. As temperatures fall, tunneling becomes more significant resulting in the evaporated diode's η rising to 1.54 at 125K. Similarly, the plated diode's η rose to 1.50 at 125K. Barrier height was calculated via:

$$\gamma \equiv \ln\left(\frac{I_d}{T^2}\right) - \frac{V_d}{\eta KT} = \ln\left(A_e A^*\right) - \left(\frac{V_b}{K}\right)\frac{1}{T} \qquad (7)$$

where: $V_b = q\phi_b$
A_e = effective anode area,
A^* = effective Richardson's constant and
V_d = applied diode voltage.

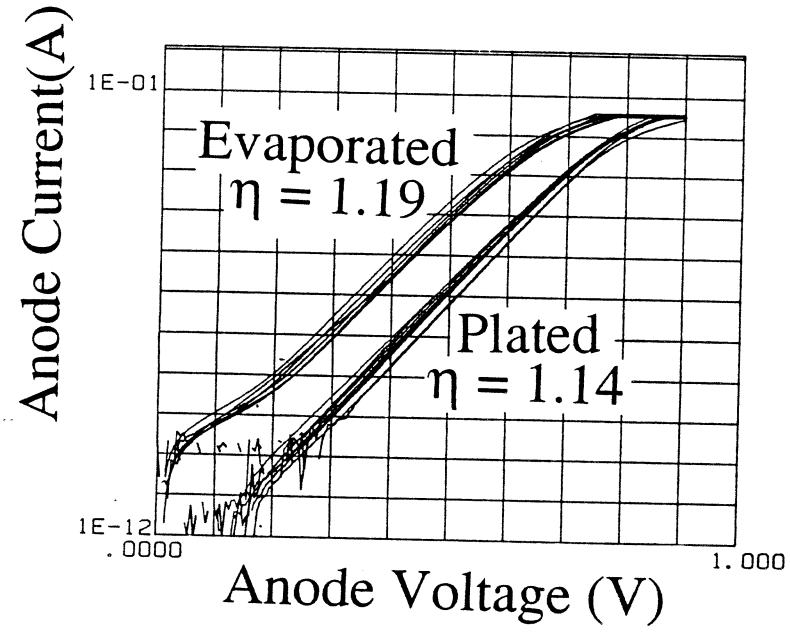

Figure 5. IV curves of several plated and evaporated diodes.

Barrier heights (ϕ_b) were obtained from the slope of a least-squares linear fit of γ vs. $\frac{1}{T}$ over 225K to 300K. At low temperatures γ deviates upward from the linear fit because of rising η. One of the evaporated diodes (Ti) had ϕ_b = 0.651eV vs. ϕ_b = 0.832eV for a

plated (Pt) diode. In comparison, Ti and Pt Schottky's on GaAs are reported to have measured ϕ_b's of 0.82eV and 0.86eV respectively [8].

III-F. Low-Frequency Noise Results

1. Noise vs. I_d @ 300K

Figs. 6 and 7. illustrate 10Hz-10MHz noise spectra vs. I_d for an evaporated diode and a plated diode. Noise was characterized at 300K and I_d = 0.316, 1.0, 3.16, 10.0, and 31.6mA.

Noise spectra for the evaporated diode follow a 1/f dependence up to about 100Hz. Above 100Hz the frequency dependence is reduced and then increases again past about 100KHz. This plateau followed by the rapid rolloff is indicative of a group of traps having f_{tr}'s ranging from ≈ 10kHz -10MHz.

In contrast, the plated diode's 1/f range extends to roughly 1kHz. Also beyond 100kHz, the plated diode's noise tends to roll off faster than that of the evaporated diode's, pointing to a more ideal 1/f behavior. Above 1MHz and at Id = 0.316mA, both diodes' noise approached the system noise floor. The flat region of $S_I(f>2MHz)$ at 1mA, for both diodes, is also due to the measurement system noise floor. However, at Id = 1mA, the shot noise level is 3.2×10^{-22} A^2/Hz, so that the actual $S_I(f)$ at 1mA would not appear much different than those in Figs. 6 and 7.

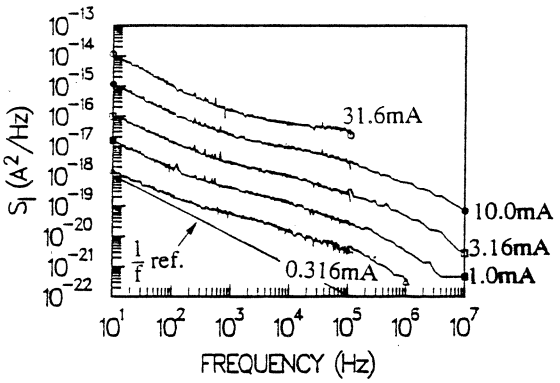

Figure 6. $S_I(f)$ vs. current for an evaporated diode (T=300k).

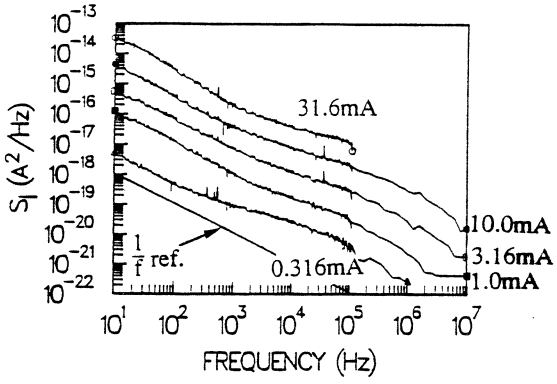

Figure 7. $S_I(f)$ vs. current for a plated diode (T=300k).

In order to draw conclusions about device parameters, several devices per type were measured. Fig. 8 represents the averages of $S_I(f)$ over ensembles of evaporated and plated diodes. At I_d=10mA and below 6KHz, the evaporated diodes show better noise performance than the plated, while above 6KHz, the reverse is true. Let f_c be defined as the frequency where S_I(evaporated)=S_I(plated). Fig. 9 shows that f_c falls as I_d increases. It is reasonable to presume that f_c largely depends on current density rather than absolute current. Since the diodes tested here are much larger than those that would be actually used in real submillimeter and THz receivers, actual current densities would greatly exceed those used here. Thus with realistic anode sizes, f_c would be considerably lower than shown in Fig. 9, giving plated diodes an even stronger noise performance advantage over evaporated diodes.

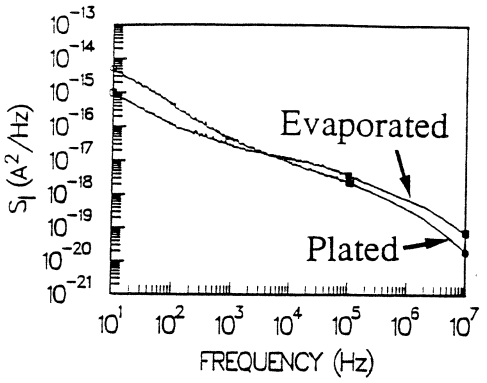

Figure 8. Average of $S_I(f)$ over several diodes of each type (T = 300K).

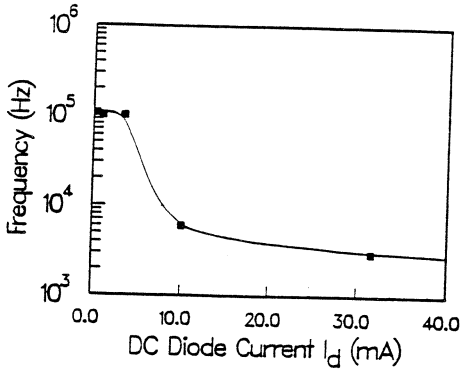

Figure 9. Crossover point (f_c) vs. I_d (T=300k).

In Fig. 10, $S_I(f)$ is plottted as a function of I_d for the plated diodes. The plated diode shows the corresponding dependency: $S_I(10Hz) \propto I_d^{1.81}$. Similarly, the evaporated diode's current dependency is: $S_I(10Hz) \propto I_d^{1.92}$. These results agree well with [7] where, for an ensemble of traps distributed uniformly in energy and space throughout the depletion region, $S_I(f) \propto I_d^{2.0}$.

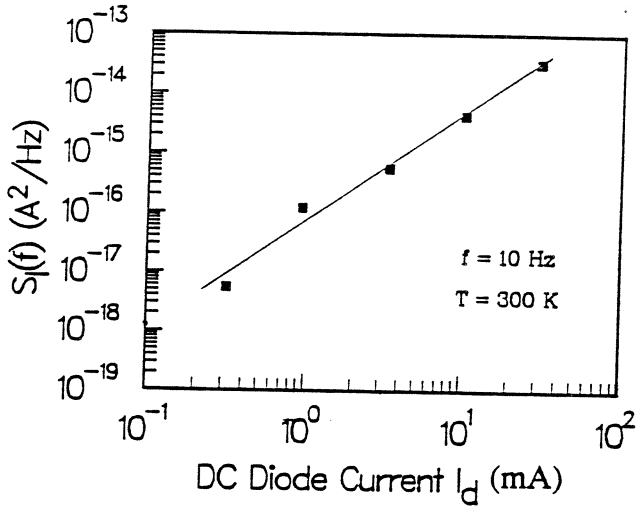

Figure 10 Plated diode noise vs. I_d (T=300K).

2. Noise vs. Temperature (I_d=10mA)

The evaporated diode's $S_I(f)$ vs. T seems interesting in that there appear to be several characteristic trap frequencies, f_{tr}, which cause a noise bulge for 10KHz < f < 100kHz. The noise bulge is most likely formed from the traps, giving rise to noise components having Lorentz dependencies. As expected from theory, this noise bulge becomes more prominent and shifts to lower frequencies as the temperature falls. The noise bulge's very slight movement in frequency is indicative of the very small values of activation energies (E_a's) of the traps causing the bulge. The noise bulge's amplitude is more strongly

affected by temperature than the 1/f portion of $S_I(f)$ as would be expected from the theory concerning Lorentz-type $S_I(f)$ functions.

In contrast, as temperature falls, the plated diode's $S_I(f)$ increases in amplitude with very little change in shape. Unlike the evaporated diode, no noise bulges appear in the range 10Hz - 100KHz, thus indicating that the plated diode apparently has no distinct traps with f_{tr}'s between 10Hz-100kHz.

The least-squares linear fit of Fig. 11 shows that $S_I(10Hz) \propto T^{-2.2}$ and $S_I(10Hz) \propto T^{-2.9}$ for the evaporated and plated diodes respectively. This is in contrast to theory which predicts $S_I(f) \propto T^{-1.5}$, for regions of $S_I(f)$ having a 1/f frequency dependence [7]. The discrepancy of theoretical temperature dependence with respect to that measured may be due to a difference in noise mechanisms for devices here and those postulated in [7]. Also, for evaporated and plated diodes, $S_I(100KHz) \propto T^{-4.2}$ and $S_I(100KHz) \propto T^{-2.9}$ respectively (fig. 11). The evaporated diode's increase of temperature dependency at 100KHz reflects the effects of the Lorentz-like noise hump discussed earlier.

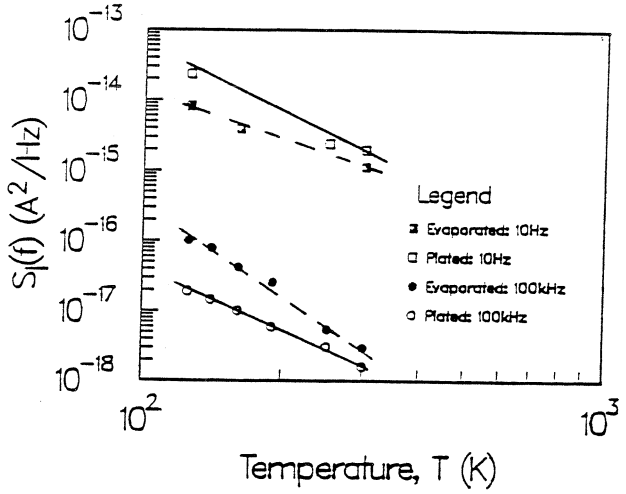

Figure 11. Noise vs. temperature at selected frequencies.

IV. Conclusions

Schottky diodes fabricated using conventional evaporated anodes were compared with those fabricated using a novel anodic and plating technique. DLTS characterization shows that plated diodes have only one process-induced trap whereas evaporated diodes show three such traps. These traps are only significant to a depth of 1000Å and are similar to those induced by irradiation. Optimized plated diodes also show lower overall trap densities. For example, at 500Å depth, an optimized plated diode yielded process-induced trap concentrations of $\leq 2.7 \times 10^{14}/cm^3$, vs. $4.7 \times 10^{14}/cm^3$ for the evaporated-anode process In contrast to the evaporated diodes, plated diodes show no detectable generation-recombination current, an η(plated) of 1.14 vs. η (evaporated) of 1.19, and a ϕ_b(plated) of 0.83eV vs. ϕ_b(evaporated) of 0.65eV. At Id = 10mA and 300K, S_I(10MHz) of the plated diode is lower than that of the evaporated diode and S_I(plated) remains

lower than S_I(evaporated) for $f > f_c = 6KHz$. Since f_c falls with current density, actual THz diodes are expected to have an f_c considerably below the 6KHz for the large diodes measured here. Temperature dependent measurements revealed the presence of shallow traps in evaporated diodes not observed in plated diodes. In conclusion, the work presented here shows that the new in-situ plating process has significantly improved junction quality and noise performance over diodes fabricated using the more-conventional E-beam evaporated metal process. The advantage of the in-situ etch-plating process is expected to increase as this process becomes better understood and optimized.

References

[1] T. Hashizume, H. Hasegawa, T. Sawada, A. Grüb and H.L Hartnagel, "Deep Level Characterization of Submillimeter-Wave GaAs Schottky Diodes Produced by a Novel In-Situ Electrochemical Process", Japanese Journal of Applied Physics Vol. 32 Part 1, No. 1B, Jan. 1993 pp. 486-490.

[2] T. Hashizume, H. Hasegawa, T. Sawada, A. Grüb and H.L Hartnagel, "Deep Level Characterization of Submillimeter-Wave GaAs Schottky Diodes Produced by a Novel In-Situ Electrochemical Process", 1992 Intl. Conf. on SSDM, pp. 257-259.

[3] A. Grüb, K. Fricke, and H.L. Hartnagel, "Highly Controllable Etching of Epitaxial GaAs Layers by the Pulse Etching Method", J Electrochem. Soc. 138, pp 856-857 (1991).

[4] A. Jelenski, A. Grüb, V. Krozer, H.L. Hartnagel "A New Approach to the Design of Schottky-Barrier Diodes for THz Mixers" Third International Symposium on Space Terahertz Technology March 24-26 1992, pp 631-642.

[5] T. Hashizume, Private Communications.

[6] H.S. Lin, P.A. Colestock, P. Fang, T.M. Chen, "Generation-Recombination Noise in GaAs p+in+ Diodes", IEEE Proceedings - 1989 Southeastcon pp 1295-1297.

[7] Sheng T. Hsu "Low-Frequency Excess Noise in Metal-Silicon Schottky Barrier Diodes", IEEE Transactions on Electron Devices Vol. ED-15, No. 7 July 1970, pp. 496-506.

[8] Ralph E. Williams, "Gallium Arsenide Processing Techniques", Artech House Inc., 1984.

PLANAR GaAs SCHOTTKY DIODE FABRICATION: PROGRESS AND CHALLENGES

William L. Bishop, Thomas W. Crowe and Robert J. Mattauch
Semiconductor Device Laboratory
Department of Electrical Engineering
Thornton Hall
University of Virginia
Charlottesville, VA 22903

I. Introduction

Schottky barrier diodes for high frequency mixer applications are usually made by forming a honey-comb array of circular metal anodes on n-type GaAs. One of these micron to sub-micron sized anodes is contacted with a sharpened wire (whisker) and a large-area backside ohmic contact completes the device. This structure is relatively simple to fabricate and it benefits from the very low shunt capacitance presented by the whisker. However, production of high quality whisker contacts is technically demanding and multiple diode arrangements are difficult to implement. Also, electrical and mechanical qualification of whisker-contacted diodes for use in space is expensive and time consuming [1,2].

Planar or whiskerless diodes were developed to overcome the problems and limitations of whisker-contacted devices. High quality planar GaAs Schottky barrier diodes from this and other laboratories have demonstrated excellent RF performance at millimeter wavelengths [3,4,5,6]. These devices are replacing whisker-contacted diodes in many applications and some have been qualified for use in space systems. This change is driven by the need to reduce the time required for mixer assembly and qualification and to simplify the fabrication of multiple diode receivers. There are a variety of more advanced mixer designs which incorporate multiple diodes and promise improved performance. Although such designs are virtually impossible to implement with whisker-contacted diodes, they are relatively easy to achieve with planar technology.

The purpose of this paper is to discuss recent diode fabrication progress at the University of Virginia and to explain the major obstacles in fabricating planar diodes for operation at submillimeter wavelengths. In Section II we discuss the structure and fabrication of the surface channel diode and in section III we summarize the latest diode fabrication results. In section IV we examine the major challenges for planar diode fabrication and possible solutions to these problems. Section V presents a new planarization technology which will greatly improve the isolation of planar structures and ultimately lead to lower shunt capacitance and greater freedom in the design of these devices.

II. Planar Diode Structure and Fabrication

Planar Schottky diodes fabricated at the University of Virginia utilize the surface channel structure as illustrated in Fig. 1 [3,7]. The cathode pad is an ohmic contact formed on the highly doped n-type GaAs (n^+ buffer layer). The anode pad may also be an ohmic contact or it may be a non-ohmic metallization on GaAs or on a silicon dioxide layer above the GaAs. A single circular Schottky barrier diode is formed near the ohmic contact pad. The forward electron current path is from the ohmic contact metallization through the n^+ buffer layer to the n-type GaAs below

This work has been supported by the Jet Propulsion Laboratory (958202), the NASA Ceneter for Space Terahertz Technology (NAGW-1334), and Aerojet Electronics Systems (10320).

the anode. From here, the electrons are emitted into the anode metal, travel along the finger and into the anode contact pad. The semi-insulating substrate and the surface channel ensure that all conduction current passes through the Schottky contact. The parasitic elements are actually more complex than illustrated and, furthermore, they are distributed. The circuit nodes for shunt capacitance are deliberately omitted to emphasize this unknown distribution. This simplified circuit is, however, most useful for discussion of chip design.

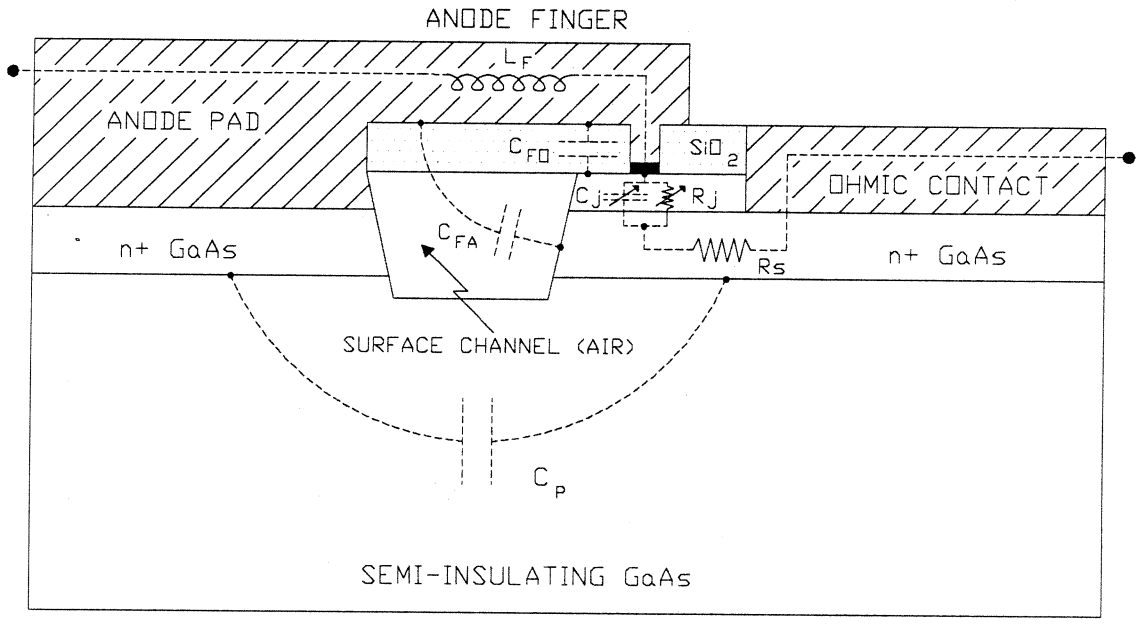

Figure 1. Surface Channel Planar Diode Structure With Major Circuit Elements

Shunt capacitance limits the cutoff frequency and bandwidth of any mixer [8]. Shunt capacitance for the surface channel structure can be divided into three major parts: (1) C_P, pad-to-pad capacitance, primarily through the high dielectric constant GaAs substrate; (2) C_{FO}, the parallel plate capacitance from the portion of the finger which overlies conductive GaAs, with SiO_2 as the dielectric; and (3) C_{FA}, the capacitance from the air-bridged portion of the finger to the cathode. The surface channel geometry produces diode chips with low shunt capacitance compared to either proton bombarded or mesa structures. Large scale models and numerical analysis indicate that pad-to-pad capacitance is reduced by increasing the depth of the trench and by producing trench sidewalls which have vertical or retrograde slope [9, 10]. Also, a contact finger which is surrounded by air for most of its length will exhibit lower parasitic capacitance than one which has high dielectric constant GaAs on one side (proton isolated). Futhermore, surface channel mask design and the fabrication process allow the surface channel (trench) wall to be positioned within one micron of the anode to minimize finger overlay capacitance.

The fabrication sequence of the surface channel planar diode offers additional benefits compared to other diode structures. The ohmic contact, anode and anode contact pad and finger are formed before the isolation trench. The highly planar surface which is available for these critical steps is conducive to high resolution lithography. By orienting the anode contact finger

in the [011] direction and using orientation dependent wet chemical etching, a trench as illustrated in Fig. 2 is formed. Undercut towards the anode is minimal. The bottom surface of the trench is flat with no remnant of the finger. The sidewall of the trench is also flat, even beneath the finger. The trench forms with essentially the same geometry as would be produced without the finger. This surprising result occurs when the channel etch depth and finger length are large compared to the width of the finger. In this case, the orientation dependent nature of the wet etch dominates the process.

Such a perfect trench could not be formed using an isotropic dry etch process of the type suggested by Hur [11]. Isotropic etchants used to undercut the finger require deeper etching and require a much greater initial mask offset from the anode location. A large mask offset limits the minimum length of the finger and causes greater variation in finger overlay capacitance due to inevitable local variation in lateral etch rate.

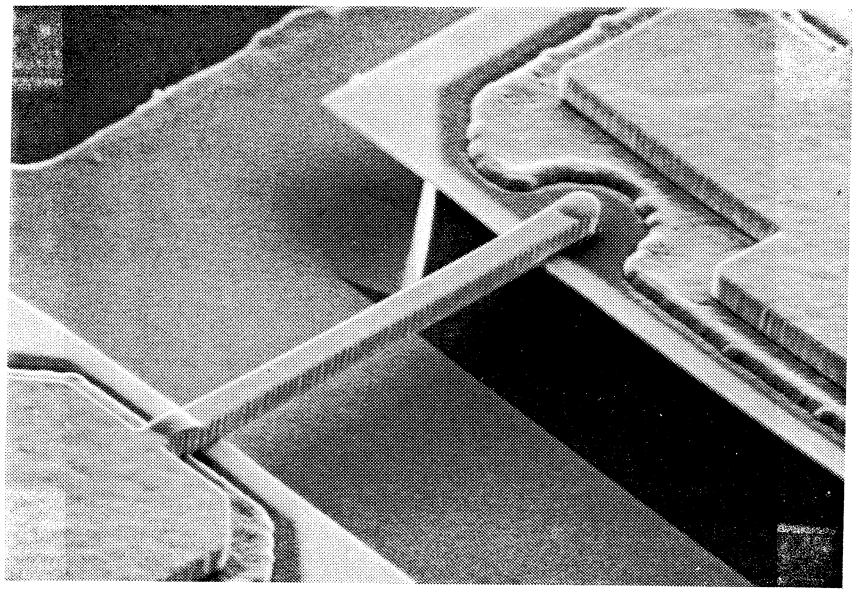

Figure 2. SD2T5 Surface Channel Planar Diode

A variety of planar mixer diodes have been produced at the University of Virginia, including: single anode chips for use as fundamentally pumped mixers, dual anode antiparallel configurations for subharmonically pumped mixers, and separately biasable dual anode chips for balanced mixers [12]. A technology has also been developed to replace the GaAs substrate with quartz for lower pad-to-pad capacitance [13]. Chip dimensions range from approximately 10 x 10 mils to 3 x 8 mils with chip thickness as small as 0.5 mil. All of the devices are intended to be inverted and soldered to the circuit (flip chip mounting).

These devices have been RF tested in both waveguide and quasi-optical mixers by several research groups. A summary of these results are given in Tables I and II.

Table I. Room Temperature Waveguide Mixer Results Using UVa Planar Diodes

Diode Type	Mixer Type	Signal Frequency (GHz)	Mixer Noise Temperature (K SSB)	Conversion Loss (dB SSB)	LO Pwr (mW)	Research Group
SC2R2 Single Anode 5x15x5 mil	Fundamental	94	520	5.3	2.6	Garfield UVa/NRAO [14]
SC1T4 Antiparallel 3x8x2 mil	Subharmonic	205	1590	8.7	5.7	Siegel JPL [15]
SC2T1 Single Anode 5x15x0.5 mil	Fundamental	345	2740	9.5	1.4	Newman UVa/NRAO [16]
2 x SC2R4 Single Anode 5x15x4 mil	Fundamental (Balanced)	74-114 (16 GHz Inst. BW)	5.2 dB Noise Figure (DSB Receiver)		10-20	Haas Aerojet [17]

Table II. Room Temperature Quasi-Optical Mixer Results Using UVa Planar Diodes

Diode Type	Mixer Type	Signal Frequency (GHz)	Mixer Noise Temperature (K DSB)	Conversion Loss (dB DSB)	LO Pwr (mW)	Research Group
SC2T3 Single Anode 5 x 15 x 2 mil	Fundamental Dipole on Membrane Integrated Horn	86 92 106	870 725 830	6.2 5.5 6.2	2.0 to 2.5	Ali-Ahmad U. Mich [18]
SC1T4-S20 Single Anode 3 x 8 x 1.5 mil	Fundamental Dipole on Membrane Integrated Horn	243 249 258 264	1850 1420 1310 1500	8.4 7.3 7.2 7.5	1.0 to 1.5	Ali-Ahmad U. Mich [19]
SR2T1 Antiparallel 5 x 10 x 2 mil (Quartz Substrate)	Subharmonic Log-Periodic Silicon Lens	90 182	1080 1820	6.7 8.5	9	Kormanyos U. Mich [20]

III. Recent Planar Diode Fabrication Progress

State-of-the-art receivers in the terahertz frequency range are currently constructed with a whisker-contacted diode. The RF signal and local oscillator energy are coupled to a long wire antenna in a corner cube assembly. This quasi-optical technique has a coupling efficiency of only about 50% [21].

The surface channel diode has recently been integrated with a monolithic antenna structure to improve energy coupling to the diode and to eliminate the fabrication and reliability problems associated with the corner-cube system. The SA1T2 antenna-diode chip, designed in collaboration with the University of Michigan, is shown in Fig. 3. This chip consists of a log-periodic antenna structure with a single 0.8 micron diameter Schottky diode located near the center. The antenna consists of ohmic contact metallization and 5 microns of highly doped n^+ GaAs. The surface channel follows this antenna pattern and is etched approximately 5 microns into the semi-insulating GaAs substrate. The anode contact finger is approximately 7 microns long and 2.5 microns wide.

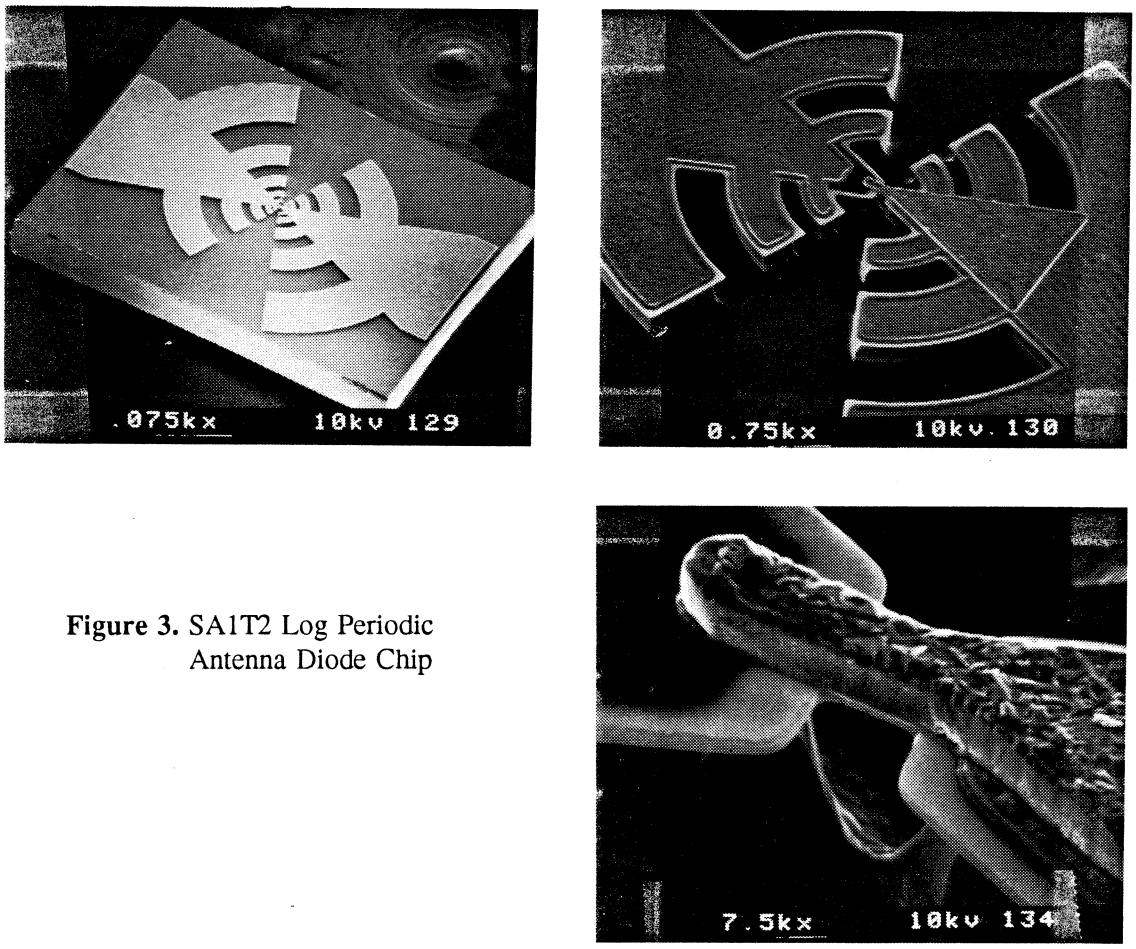

Figure 3. SA1T2 Log Periodic Antenna Diode Chip

Wet chemical etching of the surface channel was not attempted in fabricating the log-periodic antenna diode because of the short contact finger. Instead, a combination of chlorine-based reactive ion etching (RIE) and wet chemical etching was utilized. RIE was first used to vertically etch approximately 8 microns into the GaAs. This left a 2 micron thick wall of GaAs directly beneath the finger. This conductive material was removed by wet chemical etching which also moved the wall of the channel approximately 2 microns towards the anode. Because of some local variations in the wet etch rate, this remaining GaAs was not completely removed on all devices and some were short circuited. This experience illustrates the limitations of the current surface channel formation technology.

A quasi-optical mixer was constructed by placing the SA1T2 log periodic antenna-diode on a hyperhemispherical lens made of high resistivity silicon. The system exhibited excellent antenna patterns and good mixer noise temperature and loss performance at 762 GHz. The details of this RF testing are presented by Gearhardt in the Conference Proceedings [22]. This is the first planar Schottky diode to achieve reasonable mixer noise temperature at such a high frequency.

IV. Planar Diode Fabrication Challenges

Although surface channel planar diodes have done well at millimeter wavelengths, the greatest interest and challenge lies in pushing the diode performance to the terahertz frequency range. Fabrication technology will play a major role in achieving the goal of improved high frequency performance. Following is a discussion of the most important fabrication issues:

Reduce R_s x C_{j0}

Theoretical studies and practical results with whisker-contacted diode mixers show improved high frequency performance as the R_sC_{j0} product is reduced [8]. This is achieved by reducing anode diameter and choosing optimum active layer doping and thickness. For terahertz frequencies this requires anode diameters in the 0.5 micron range. While circular anodes with diameters of one micron and above are relatively easy to fabricate, submicron devices are difficult to uniformly and repeatably produce. Few, if any, commercial mask makers will guarantee submicron circular features due to a lack of measurement methods (lines are much easier). Uniform submicron masks, deep UV lithography and reactive ion etching (RIE) may facilitate the fabrication of high frequency planar diodes. Direct wafer patterning with electron beam lithography (direct write) is also a proven method [23]. Alternative anode etch mask formation in which a relatively large mask feature is reduced (electroplating, oxygen plasma etching), or where some layer thickness (photoresist, oxide, etc) is transformed into a mask opening, may be effective [24,25,26].

The problem of planar diode anode formation extends beyond that of a uniform submicron mask. The technology requires that circular wells be RIE etched into the silicon dioxide leaving a thin layer (≅300 Å) to protect the underlying GaAs from damage. This thin oxide in the bottom of the anode wells is removed with buffered hydroflouric acid (BHF) just prior to electroplating the platinum anode metallization. If this final wet chemical etch is insufficient, the resulting device may be an open circuit or may exhibit high resistance. If the etch is overdone, the resulting diode may be too large. Uniformity is important for discrete devices but even more so for multiple anode chips and arrays. The uniformity and repeatability of the process depends on accurate

determination of the thickness of the remaining silicon dioxide and its wet etch rate.

In the case of whisker-contacted diodes, the removal of this thin oxide and anode plating are performed on a chip-by-chip basis, thus providing chips for experimentation to determine the etch time for a given batch. Planar diodes, by contrast, are etched and plated on a wafer basis, with no opportunity for fine tuning. For better process control and ultimately more uniform anode diameters, a bilayer or trilayer insulation layer could be used [12]. For example, a thin (300 Å) layer of silicon dioxide could be deposited on the active GaAs and its thickness could be measured. A relatively thick layer of polyimide or other suitable polymer could next be deposited on this thin oxide. This polymer layer could be patterned with an oxygen RIE etch step which would stop at the thin SiO_2 layer. The known thickness of SiO_2 could then be wet etched prior to anode plating. This process would relax the etch rate accuracy requirement and would leave a known amount of oxide to be removed. A process of this type would probably require a substantial research effort to test polymers for chemical and thermal process compatability and reliability but would yield great potential benefits.

Optimized Chip Geometry

The geometry of the planar diode chip has a major effect on the capacitance and inductance presented to the mixer circuit. Fabrication technology limits the geometry which can be produced. Even though the surface channel diode structure is referred to as a "planar" device, we are actually concerned with all three dimensions.

Capacitance between the contact pads is normally the largest shunt conductance [10]. This capacitance can be minimized by: reducing contact pad area, separating the pads as much as possible, providing the deepest possible channel, making the channel sidewalls vertical or retrograde, or removing non-essential GaAs substrate. Technology for most of these requirements has already been developed at UVa. For example, our smallest chips have contact pads which are only 30 x 60 microns with overall chip dimensions of 75 x 200 x 25 microns. A chip with smaller pads would be very difficult to handle and bond to the circuit. A technique has been developed to completely remove the GaAs substrate and replace it with quartz. The quartz can even be removed once the chip is soldered in place [13]. As discussed previously in connection with the log-periodic antenna diode, vertical channel sidewalls are most important for short finger designs but are difficult to achieve with wet etching or a combination of RIE and wet chemical etch. A planarization method which will allow the channel to be formed before the finger could solve this problem.

Shunt capacitance from the finger must also be minimized. This can be done by reducing the width of the finger, etching the surface channel as close as possible to the anode, increasing the dielectric thickness between the n-type GaAs and the finger, or producing an upward arch in the finger. Present UVa planar mixer diodes have a 2 micron finger width. A new mask set reduces this to 1 micron for the final 5 microns of the finger length. A lower limit for width is set by considerations of alignment and mechanical strength as well as concerns about the finger resistance and inductance. A thicker dielectric would reduce the finger overlay capacitance and could be facilitated by the multilayer scheme described above. The upper limit for dielectric thickness is determined by film stress and cracking in the case of oxides. Polymers could be very

thick but may be limited by an inability to electroplate into very deep, small diameter wells. Finally, an upwardly arched finger could be a beneficial byproduct of a polymer planarization.

The optimum length and geometry of the anode contact finger in a planar diode is a topic of great interest. Some modeling has been done by Siegel to determine the effect of length on mixer noise and loss [27]. Erikson has found that finger inductance can be useful in tuning out capacitance for planar varactors [28]. Additional modeling is needed but researchers must be careful not to blindly accept model predictions. A new mask set is now available for antiparallel mixer diodes with fingers from 10 to 50 microns in length on the same wafer. RF testing of these devices will provide greater understanding of this question.

Minimize Ohmic Contact Resistance

Series resistance added by the ohmic contact is small for many planar diode chips, especially those designed to operate at millimeter wavengths. For example, a 10^{-5} Ω-cm^2 ohmic will add approximately one ohm if the contact is 30 x 30 microns. Since ohmic contacts of this quality are easily achieved and since this pad size is at the lower limit for flip-chip bonding, simple planar diode chips are probably not seriously affected by the ohmic contact. However, devices which require ohmic contacts which are very small (< 100 μm^2) will be seriously affected unless they can be made with correspondingly lower specific contact resistance.

For example, it is desirable to reduce the ohmic contact size to minimize pad-to-pad capacitance. In these cases, a small ohmic contact could be connected to a larger bonding pad on a quartz substrate or to a beam lead pad. Also, some pads in multiple diode configurations are not needed for bonding. Smaller ohmics could thus be made to reduce shunt capacitance. Via holes may reduce the area available for the ohmic contact.

An important example of the need for the lowest possible ohmic contact resistance are integrated antenna-diodes. These devices will perform best when current flows in the metallization rather than in the buffer layer. For the log-periodic structure shown above, the contact area available adjacent to the anode and ahead of the 1 THz active antenna region (the first tooth) is only about 40 um^2. Thus, a one ohm contact resistance will require a specific contact resistance of about 4×10^{-7} Ω-cm^2.

Present UVa planar diodes utilize an electroplated Sn/Ni-Ni-Au alloyed ohmic contact. This contact has been measured with TLM techniques by Slade at 10^{-5} to 10^{-6} Ω-cm^2 [29]. However, measurements on device pads indicate that the specific contact resistance must be in the low 10^{-6} range. Gold germanium contact systems are reported to have specific contact resistance in the 10^{-6} to 10^{-7} Ω-cm^2 range and this contact has recently been applied to planar diodes in our laboratory. Ohmic contacts on highly doped InGaAs are reported to be as low as 5×10^{-9} Ω-cm^2 [30].

Improve Energy Coupling

Energy coupling to the planar diode can be improved with an integrated or hybrid planar antenna. However, antenna structures must be optimized to prevent energy loss. In the log-periodic antenna diode, for example, radiation is coupled through the semi-insulating GaAs substrate and

may be partially dissipated in the buffer layer below the antenna metallization. This loss can be reduced by using a thinner buffer layer or by limiting the buffer layer to a small region near the anode with proton isolation or selective epitaxy. Coupling may also be improved by integrating tuning structures with the antenna-diode.

V. A New Planarization Process

As previously mentioned, the present surface channel diode fabrication sequence (i.e., finger formed before channel) is not without disadvantages: (1) The isolation trench is difficult to properly form if the finger is very short or wide and devices can be shorted by conductive material which is left between the pads; (2) The geometry of the contact finger is limited to relatively simple, narrow shapes while RF performance may benefit from some other finger geometry; (3) The distance from the sidewall of the trench to the anode, which determines the finger overlay capacitance, is difficult to minimize since the anode is hidden by the finger (the finger cannot be used as a reference for the anode due to alignment errors). A conservative etch time may yield higher capacitance while overetch may produce open circuits or high resistance if the anodes are undercut. Surface channel diode fabrication would benefit from a temporary planarization process which would allow the formation of the surface channel isolation prior to formation of the contact finger. The anode contact finger could then be formed on top of this planarization layer and afterwards the material could be removed to form the air-bridge.

A planarization material for surface channel diode fabrication must meet numerous criteria: (1) easy to remove, (2) unaffected by process chemicals (including resist solvents), (3) easy to pattern, (4) low skrinkage, (5) good adhesion to GaAs, SiO_2, and gold, (6) sufficient elongation to prevent the formation of voids, (7) low viscosity, (8) and low cure temperature. The material and its method of application must produce a high level of planarization for deep trenches. Available planarization materials include Novolac-based photoresist, polyimides and other polymers [31-36]. Excellent planarization has been achieved with multiple spun-on coatings and/or thermal reflow before final curing. However, photoresist is not compatible with all of our process chemistry and cure temperatures for polyimides generally exceed 160 °C, with much higher temperatures for thermal reflow.

Workers in the multichip module (MCM) fabrication area have been planarizing metal interconnect lines for several years [37]. One of the most effective planarizing systems for this application is benzocylobutene (BCB). BCB's are low molecular weight, thermoset polymers which have demonstrated greater than 90% planarization of metal lines with a single spin application and excellent chemical resistance [38]. They are being actively developed as permanent planarizing dielectrics for GaAs IC fabrication [39]. However, BCB's require 200 to 250 °C for full cure and may be difficult to completely remove from beneath the contact finger. BCB which has been partially cured at reduced temperature may be easier to remove.

Dill of IBM proposed a simple planarization technique in 1984 which he referred to as the "top cap" method [40]. This technique consists essentially of applying a droplet of thermosetting polymer or liquid thermplastic polymer to a wafer and then covering this with a flat superstrate. Once the polymer hardened, the superstrate is removed. Dill suggested that capillary action would spread the liquid polymer to form a thin, uniform film. This technology was never demonstrated by IBM and to our knowledge it has not been demonstrated or developed by any other research

group. The method is related to a very old technique used to "polish" the surface of polymer-embedded specimens. Instead of laborious lapping and mechanical polishing of a block of cured thermoset ploymer, a rough lapped surface can be "glued" to a glass plate (treated with a release compound) with the same polymer. Once the resin has set, the block is separated from the glass. The lapped surface is filled in with the polymer and the exposed surface replicates the polished glass surface.

We have developed this technique, illustrated in Fig. 4, for device applications. A wafer with trenches is first patterned with photoresist shims near the corners. The shims are used to control the thickness of the planarizing layer and must be formed in areas on a plane which is parallel to the original GaAs epitaxy (i.e., not on metallized or etched regions with different heights). Photoresist must be completely removed from all other regions. This can be assured during development of the shims by providing a high exposure level or even a second long exposure to areas where resist may be hidden from direct exposure, such as under overhanging structures. The shims are baked at relatively high temperature (120 °C) and exposed to short wavelength UV (deep UV cure) to prevent chemical attack by the liquid polymer. Next, a low viscosity thermoset polymer is applied to the wafer. A flat, smooth superstrate is then placed atop the wafer. The weight of this superstrate (plus any added force) pushes it to the level of the shims and expels excess polymer. The polymer is cured in this position and finally the superstrate is removed.

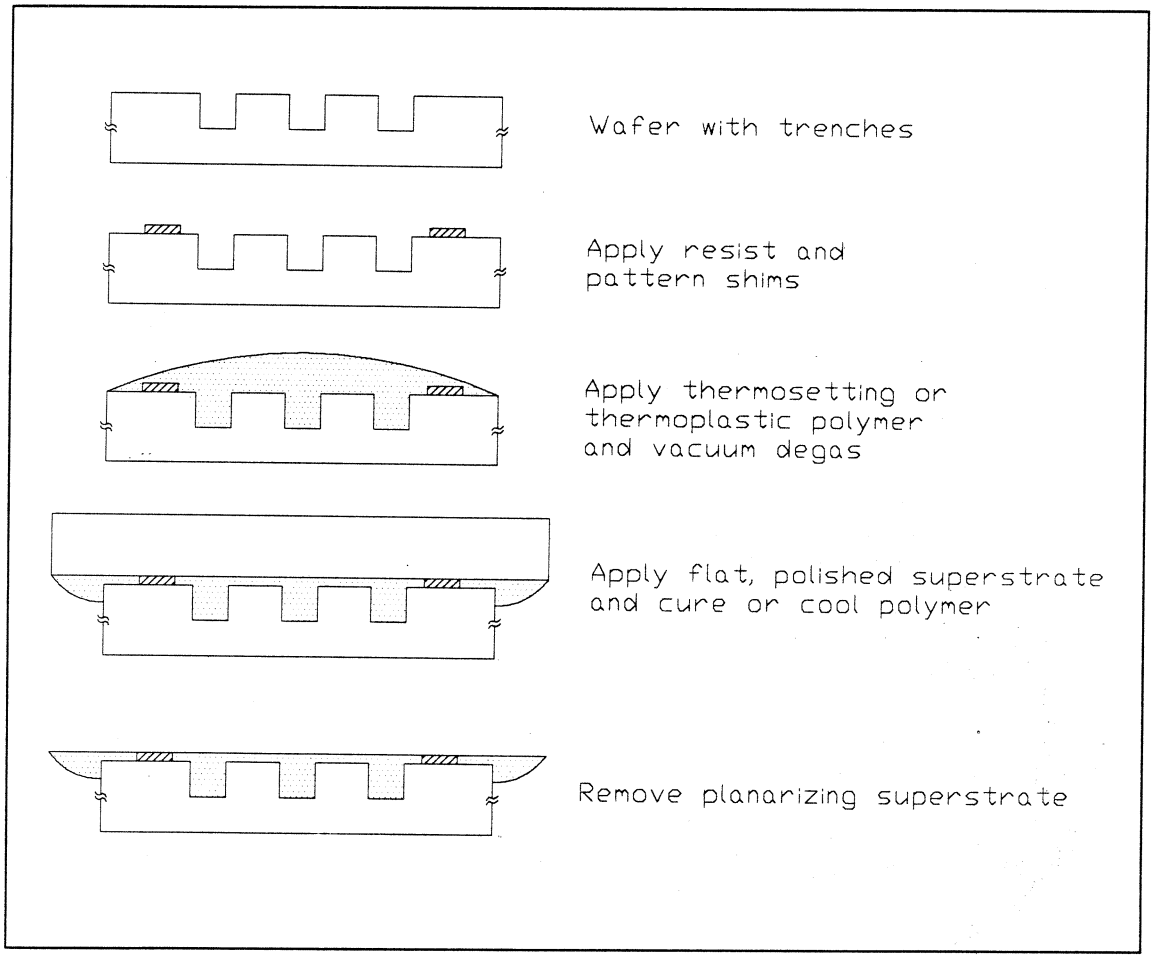

Figure 4. Superstrate Replica Planarization

In practice the wafer is inverted and placed onto the superstrate. A "curing stack" consisting of glass plates and thin Mylar sheets has been developed to align and hold the wafer and superstrate and to apply a controlled pressure to the sandwich. In addition to this fixturing, the choice of polymer and superstrate are most critical. Epoxy resins were considered to be promising candidates. Many epoxy formulations are available with generally excellent adhesion, low shrinkage, good adhesion, high elongation, and good chemical resistance. A number of epoxy resins were tested and our current material of choice is Epotek 377. It can be cured at temperatures as low as 120 °C and has excellent resistance to chemicals used in our process. It can be repeatedly patterened with photoresist and the resist can be stripped with acetone. The cured polymer can be readily etched in oxygen RIE or oxygen plasma with no apparent residue. As with most other polymer etching with oxygen, a polymer platter must be used at low pressure to avoid residue from backsputtered material.

The superstrate must be flat and smooth and must be removable. A suitable release layer may eventually be found so that a high quality optical flat or silicon wafer could function as a reusable superstrate. For this preliminary work a simpler approach was taken. A polished optical window made of sodium chloride was used. Inexpensive NaCl windows are available for infrared spectroscopy [41]. High quality, optically flat NaCl windows designed for infrared laser work are available at higher cost. These windows are rapidly removed with water which has no effect on the epoxy. The adhesion of the epoxy to the NaCl is excellent.

This procedure has been tested by planarizing GaAs wafers which have a series of deep trenches etched into the surface. The SEM photographs in Fig. 5 show a cross section which has been diced through one of the planarized wafers. The trench is approximately 14 microns deep and 80 microns wide. The wet etch used to form the trench produced a retrograde sidewall. The dark layer is cured epoxy which is approximately 2 microns thick over the unetched region. The trenches are almost perfectly planarized. Profilometer measurements indicate a 0.5 micron drop over the trench which represents a 95% planarization level.

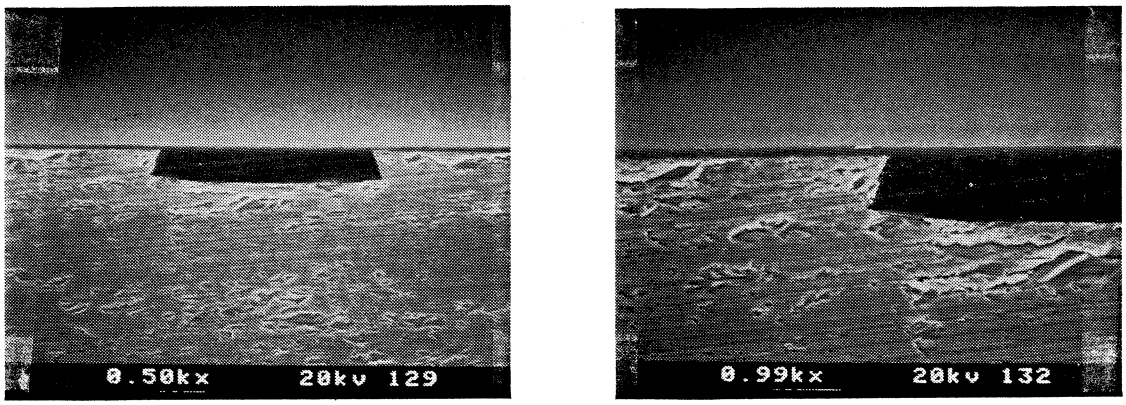

Figure 5. Trench Planarized By SRP Method

Figure 6 shows plan and cross sectional views of proposed SRP planarization and contact finger formation for the log-periodic antenna diode. After the anodes and ohmic contacts are produced, the surface channel trench is formed. The initial etching will be done with RIE to establish a vertical-walled, flat-bottomed trench. Slow wet etching of the gallium arsenide can then be used to "trim" away excess GaAs and move the channel wall as close as possible (0.5 micron) to the anode. Visual inspection and re-etch can be used to control this step.

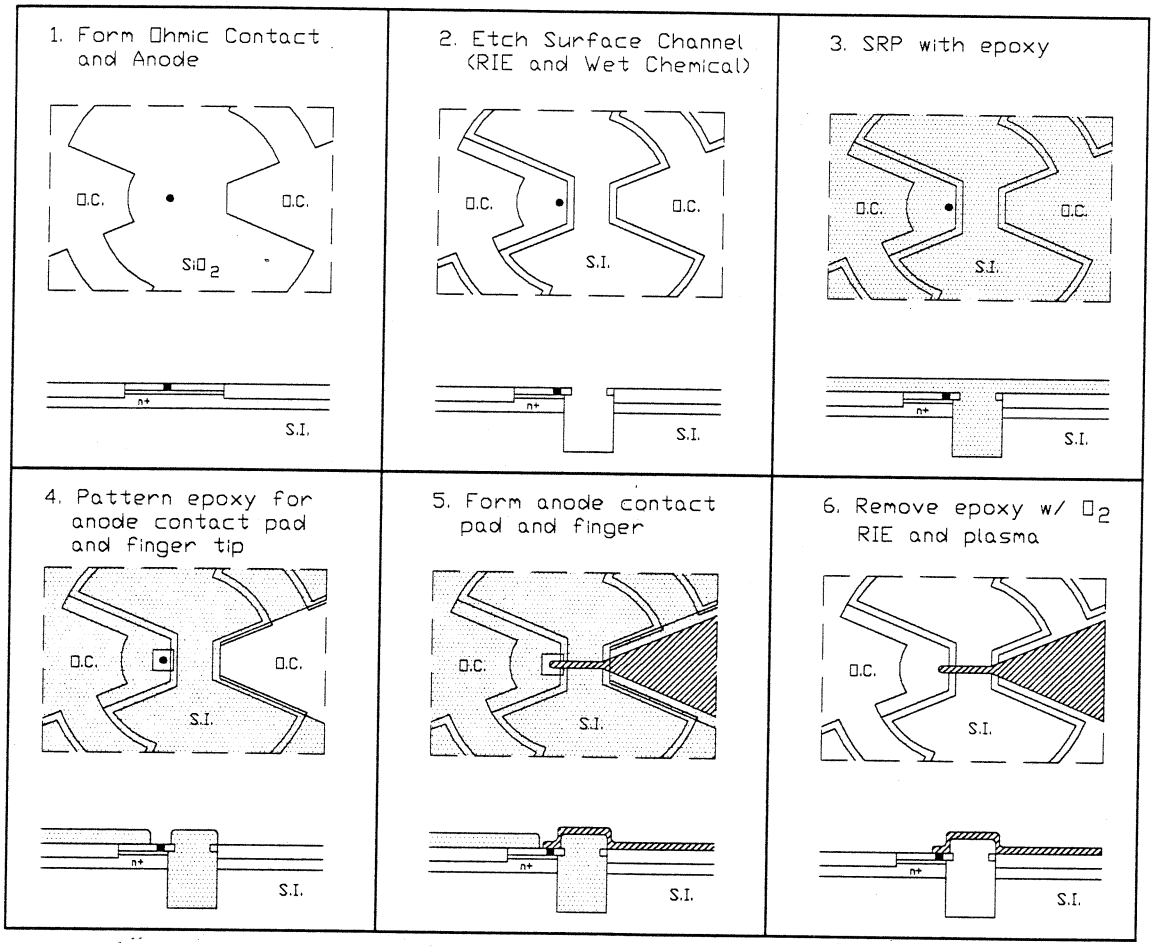

Figure 6. Surface Channel Fabrication With Planarization

Summary

Planar technology is now replacing whisker-contacted diodes at millimeter wavelengths. This technology shows great promise for submillimeter wavelengths, both as heterodyne receiver elements and as a frequency multipliers. Integration of multiple diodes and antennas will improve performance, expand the range of receiver designs and simplify their construction. The integrated log-periodic antenna diode has demonstrated great promise for rugged, broad band terahertz receivers.

The greatest challenges in fabricating planar diodes for submillimeter wavelengths are uniform, repeatable submicron anode formation and improved surface channel formation. The submicron anode problem will be solved with better mask formation techniques, possibly aided by multilayer dielectrics. Planarization technology, especially with polymers, is expected to improve the surface channel isolation process which will reduce the shunt capacitance of the diodes, improve uniformity and yield, and remove some design constraints which presently limit the geometry of the diodes.

Innovation and refinement of fabrication techniques will play a major role in the effort to improve Schottky diode performance, along with device theory, epitaxial layer engineering and RF design. New fabrication technology can drive the design of planar diode circuitry much in the same way that manufacturing technology influences mechanical design and production. These new fabrication techniques will require a significant research effort to bring them to maturity.

Acknowledgements

The authors are grateful to Israel Galin and Robert Haas of Aerojet Electronic Systems and to Peter Seigel of JPL for their continued support and advise in this effort. Sandy Armstrong of Epotek suggested the use of Epotek 377 and Epotek provided samples for testing. Jim Smith of Eastech Chemicals, Michael Rhodes of Anhydrides and Chemicals, Wells Carter of Union Carbide, Bob Pernice of Epotek and Walter Brenner of Master Bond provided invaluable information on epoxy technology and samples of epoxy components.

References

[1] J.W. Waters, "A Proposal of the Earth Observing System, Microwave Limb Sounder," Jet Propulsion Laboratory, California Institute of Tech, July 1988.

[2] M.A. Frerking, "The Submillimeter Mission (SMMM) Heterodyne Instrument," 2nd Int'l. Symp. Space Terahertz Tech., pp.17-31, Feb. 1991.

[3] W.L. Bishop, K. Mckinney, R.J. Mattauch, T.W. Crowe, and G. Green, "A Novel Whiskerless Schottky Diode for Millimeter and Submillimeter Wave Applications," Proc. 1987 IEEE MTT-S Int'l Symp, pp.607-610, June 1987.

[4] J.W. Archer, R.A. Batchelor, and C.J. Smith, "Low-Parasitic, Planar Schottky Diodes for Millimeter-Wave Integrated Circuits," IEEE Trans. Microwave Theory Tech., Vol. MTT-38, No. 1, pp. 15-25, Jan. 1990.

[5] N.J. Cronin, and V.J. Law, "Planar Millimeter-Wave Diode Mixer," IEEE Trans. on Microwave Theory Tech., Vol. MTT-33, No. 9, pp. 827-830, Sept. 1985.

[6] J.A. Calviello, S. Nussbaum, and P.R. Bie, "High Performance GaAs Beam-Lead Mixer Diodes for Millimeter and Submillimeter Applications," Proc. of Int'l. Electron Device Meeting, pp. Dec. 7-9, 1981.

[7] W.L. Bishop, K.A. McLeod, R.J. Mattauch, "Whiskerless Schottky Diode," U.S. Patent 5,041,881, Aug. 20, 1991.

[8] T.W. Crowe, R.J. Mattauch, H.P. Roser, W.L. Bishop, W.C.B. Peatman, "GaAs Schottky Diodes for THz Mixing Application," Invited paper, Proc. of the IEEE, Special Issue on Terahertz Technology, Vol. 80, No. 11, pp.1827-1841, Nov. 1992.

[9] P.H. Ostdiek, T.W. Crowe, "Integration of an Anti-parallel Pair of Schottky Barrier Diodes in Millimeter Wave Mixers," Fifteenth Int'l. Conf. on IR and MM Waves, Vol. 1514, pp.401-403, Dec. 10-14, 1990.

[10] J.A. Wells, N.J. Cronin, "Effects of Air Bridging and Additional Fabrication Techniques on the Capacitance of Planar Subharmonic Mixer Diodes," submitted to IEEE MTT.

[11] K.Y. Hur, R.C. Compton, "Fabrication of Overpass Microstructures in GaAs Using Isotropic Reactive Ion Etching," Journal of Vacuum Science and Tech. B, Vol. 10, No. 6, pp. 2486-2487, Nov./Dec. 1992.

[12] W.L. Bishop, T. W. Crowe, R.J. Mattauch and H. Dossal, "Planar GaAs Diodes for THz Frequency Mixing Applications," Proc. of the Third Intl. Symp. on Space Terahertz Technology, pp. 600-615, March 24-26, 1992.

[13] W.L. Bishop, E.R. Meiburg, R.J. Mattauch, T.W. Crowe, and L. Poli, "A Micron-Thickness, Planar Schottky Diode Chip For Terahertz Applications with Theoretical Minimum Parasitic Capacitance," Proc. 1990 IEEE MTT-S Int'l. Symp., pp. 1305-1308, May, 1990.

[14] D.G. Garfield, R.J. Mattauch, S. Weinreb, "RF Performance of a Novel Planar Millimeter-Wave Diode Incorporating an Etched Surface Channel," IEEE Trans. on Microwave Theory and Techniques, Vol. 39, No.1, January 1991.

[15] P.H. Siegel, R.J. Dengler, I. Mehdi, W.L. Bishop, T.W. Crowe, "A 200 GHz Planar Diode Subharmonically Pumped Waveguide Mixer with State-of-the-Art Performance," Presented at the 1992 IEEE-S Intl. Microwave Symp., Paper O-5, June 1992.

[16] T. Newman, W.L. Bishop, K.T. Ng, and S. Weinreb, "A Novel Planar Diode Mixer for Submillimeter-Wave Applications," IEEE MTT special issue on the 1991 Intl. Microwave Symp., Vol. 39, No. 12, pp. 1964-1971, December 1991, .

[17] R. Haas, Aerojet Electronics Systems Div., unpublished data, March 1992.

[18] Ali-Ahmad, W.Y., Rebeiz, G.M., Bishop, W.L., Crowe, T.W., "An 86-106 GHz Quasi-Integrated Low Noise Schottky Receiver," IEEE Trans. on Microwave Theory and Tech., to appear in May 1993.

[19] Ali-Ahmad, W.Y., Rebeiz, G.M., Bishop, W.L., Crowe, T.W., "A 250 GHz Planar Low Noise Schottky Receiver," Int'l. Jour. of IR and MM Waves, to appear in April 1993.

[20] Kormanyos, B.K., Ostdiek, P.H., Bishop, W.L., Crowe, T.W., and Rebeiz, G.M., "A Planar Wideband 80-200 GHz Subharmonic Receiver," submitted for publication in Oct. 1993 IEEE-MTT Special Issue on Quasi-Optical Techniques.

[21] B. Vowinkel, "The Main Beam Efficiency of Corner Cube Reflectors," Int'l. Jour. of IR and MM Waves, Vol. 7, No. 1, pp. 155-170, Jan. 1986.

[22] S.S. Gearhardt, J. Hesler, W.L. Bishop, T.W. Crowe, G.M. Rebiez, "A Wideband 760 GHz Integrated Schottky Receiver," these proceedings.

[23] W.C.B Peatman, P.A.D. Wood, D. Poterfield, T.W. Crowe and M.J. Rooks, "A Quarter-Micron GaAs Schottky Barrier Diode with High Video Responsivity at 118 Microns," submitted to the Appl. Physics Lett., Feb. 1992.

[24] W.L. Bishop, T.W. Crowe, R.J. Mattauch, P.H. Ostdiek, W.C. Peatman, H. Dossal, B.J. Rizzi, "Planar Diode Technology for Millimeter and Submillimeter Wavelengths," Proc. of the Int'l. Semiconductor Device Reasearch Symposium, pp.49-52, Dec. 4-6, 1991.

[25] K.D. Pedrotti, G.D. Robinson, F. Vachss, "A Novel Lithographic Process for Fabrication of Sub-Half-Micron Schottky Barrier Gate Structures," Suss Report, Vol. 3, No. 4, pp. 1-6, Nov. 1990.

[26] G.A. Garfunkel, M.B. Weissman, "Fabrication Techniques for Nanometer Scale Resistors: A Poor Man's Nanolithography," Jour. of Vacuum Science and Tech. B, Vol 8, No. 5, pp. 1087-1092, Sept./Oct. 1990.

[27] P.H. Siegel, I. Medhi, R.J. Dengler, J.E. Oswald, T.W. Crowe, W.L. Bishop, F. Li, R.J. Mattauch, S. Weinreb, J. East, T. Lee, "Heterodyne Radiometer Development for the Earth Observing System Microwave Limb Sounder," to appear in SPIE Conf. Proc. 1874, IR and MM Wave Engineering, May 1993.

[28] B.J. Rizzi, T.W. Crowe, N.R. Erikson, "A High Power Millimeter Wave Frequency Doubler Using A Planar Diode Array," to appear in IEEE Microwave and Guided Wave Letters, March, 1993.

[29] H. Slade, W.C. Peatman, "A Study of Electroplated and Evaporated Low-Resistance Ohmic Contacts to n-type GaAs," IEEE Southeastcon '93, Charlotte, N.C., Oct 4-7, 1993.

[30] T. Nittono, H. Ito, O. Nakajima, "Non-Alloyed Ohmic Contacts to n-GaAs Using Compositionally Graded $In_xGa_{1-x}As$ Layers," Japanese Jour. of Applied Physics, Vol. 27, pp. 1718-1722, 1988.

[31] T.R. Pampalone, J.J. DiPiazza, D.P. Kanen, "Novolac Resin Planarization Layers for Multilayer Resist Imaging Systems," Jour. of the Electrochemical Society, Vol. 133, No. 11, pp. 2394-2398, Nov. 1986.

[32] A. Schiltz, P. Abraham, E. Dechenaux, "Improvement of Photoresist Planarization Properties by Thermal Cure," Jour. of the Electrochemical Society, Vol. 134, No. 1, pp. 190-194, Jan. 1987.

[33] D.E. Bornside, "Mechanism for the Local Planarization of Microscopically Rough Surfaces by Drying Films of Spin-Coated Polymer/Solvent Solutions, " Jour. of the Electrochemical Society, Vol. 137, No. 8, pp. 2589-2594, Aug. 1990.

[34] L.B. Rothman, "Properties of Thin Polyimide Films," Jour. of the Electrochemical Society, Vol. 127, No. 10, pp. 2216-2220, Oct. 1980.

[35] H. Uzezaki, N. Koyama, R. Suzuki, "Planar Process for 16 Mb Bubble Memory Devices Using Thermal Reflow-Type Polyimide," Jour. of the Electrochemical Society, Vol. 136, No. 8, pp. 2357-2360, Oct. 1989.

[36] H. Gokan, M. Mukainaru, N. Endo, "Uniform Polymer Coating Technique for an Etch-Back Planarization Process Using Low Molecular Weight Polymers," Jour. of the Electrochemical Society, Vol. 135, No. 4, pp. 1019-1021, Oct. 1988.

[37] J.J.H. Reche, "Fabrication of High Density Multichip Modules," IEEE Trans. on Components, Hybrids, and Manufacturing Tech., Vol. 13, No. 3, Sept. 1990.

[38] P. Garrou, "Polymer Dielectrics for Multichip Module Packaging," Proc. of the IEEE, Vol.80, No. 12, pp. 1992-1954, Dec. 1992.

[39] P. Garrou, personal communication, March 29, 1993.

[40] F.H. Dill, "Planarization Layers," IBM Tech. Disclosure Bulletin, Vol 27, No. 1B, pp. 591-592, June 1984.

[41] International Crystal Laboratories, 11 Erie Street, Garfield, NJ 07026.

A STUDY OF RELIABILITY AND PHYSICAL PROPERTIES OF SCHOTTKY BARRIERS WITH RESPECT TO THZ APPLICATIONS

A. Grüb, V. Krozer, A. Simon, H.L. Hartnagel

Institut für Hochfrequenztechnik, Technische Hochschule Darmstadt, Merckstr. 25, D-6100 Darmstadt, Germany, Phone: +49 6151 162162, Fax: +49 6151 164367

Abstract

Whisker contacted GaAs Schottky barrier diodes are the standard devices for mixing and multiplier applications in the THz frequency range. With the decreasing size of Schottky diodes for operation at higher frequencies, the reliability and the physical understanding of the Schottky barrier becomes increasingly important.

In this contribution, we present new results concerning the reliability of Schottky diodes and new insight into the physical properties of Schottky junctions, especially at low current densities. For these purposes a number of different Schottky diodes have been fabricated with varying epi–layer doping concentrations and anode diameters.

It can be inferred from the measured I/V characteristics that the diode current deviates normally considerably from the ideal thermionic current behavior with decreasing diode diameter. This deviation shows an exponential dependance on the diode voltage and is a function of the doping concentration. For a given doping concentration in the epi–layer and decreasing anode diameter, this phenomenon shifts the minimum of the ideality factor towards higher current densities. It is speculated that this is caused by the crystallinity difference of the polycrystalline Pt films on the GaAs films for decreasing SiO_2 aperture size when the Pt mobility in the electrolyte of the hole is reduced.

The reliability of Schottky barrier diodes under thermal and electrical stress has been investigated on different THz Schottky diode structures. The results show that the barrier height and the ideality factor of the fabricated structures is not affected by thermal stress. Electrical stress induced by large forward currents up to a current density of 10 kA/mm^2 even leads to a slight increase of the barrier height and a reduction of the series resistance.

Introduction

The physical properties of Schottky contacts on GaAs are well–known and have been a subject of investigation since the beginning of GaAs technology [1]. But this is not the case for small–area Schottky barrier junctions which are the key element for mixing applications at far infrared frequencies. Diodes for this purpose usually have the so called honeycomb design [2]with anode areas of less than 1 μm^2 [3].

For this study a number of different diodes has been fabricated in order to investigate the influence of the diode diameter and the epi–layer doping concentration on the physical diode properties determined from the I/V characteristics. When talking about Schottky barriers, the most important parameter is the barrier height Φ_b or the current–dependent ideality factor $n_{(I)}$ which describes the lowering mechanisms of the barrier. It has been already shown earlier that the current through Schottky diodes for THz applications at medium and high forward bias can be described by thermionic emission and thermionic field emission when effects such as current spreading, heating of electrons etc. are taken into account [4, 5, 6, 7]. In the range of small currents (less than approx. 100 nA), a considerable deviation from the above theory can be observed, especially for small and highly doped diodes.

With the decreasing diode diameter of Schottky diodes for THz mixing applications, the reliability and stability of the contacts become more important. This is mainly due to the increased current densities under mixing conditions where a typical bias current between 200 and 500 μA leads to current densities of up to 1000 A/mm^2. Another problem with small anode areas is the semiconductor surface technology which becomes more critical with decreasing Schottky contact area. Therefore, it is necessary to know how Schottky diodes behave under extreme thermal and electrical conditions.

Diode fabrication and characterization

The epitaxial layers for the diodes were all grown by the same supplier [1]. Layers with doping concentrations between $2 \cdot 10^{16}$ cm^{-3} and $3 \cdot 10^{17}$ cm^{-3} have been used for the fabrication of Schottky diodes with diameters between 7 and 0.8 μm. All diodes investigated in this study have been fabricated with the same process making use of in situ anodic pulse etching and electrolytic Pt deposition. The features of this technique have been presented earlier and are described in [7, 8, 9]. The only exception is the diode D_{ox} which has been exposed to air for

[1] Drs. H. Grothe and J. Freyer, Technical University of Munich, Germany

10 *min* prior to the electrolytic Schottky metal deposition. Therefore, this diode is expected to have an interfacial native oxide layer of about 1 *nm* thickness.

The diodes were characterized by I/V and C/V measurements using a *HP4151B Semiconductor Parameter Analyzer* and a *HP4279A C/V-Meter*, respectively. Additionally, noise measurements at 1.5 GHz have been carried out using a *HP8970B Noise Figure Meter*. The noise temperature of the THz diodes A, C, E is shown in fig. 1. A comparison of the diode parameters is given in the following table:

diode	diameter $[\mu m]$	N_{de} $10^{17}\ [cm^{-3}]$	d_e $[nm]$	C_{j0} $[fF]$	$R_s^{(1)}$ $[\Omega]$	n_{min}	$-V_{br}^{(2)}$ $[V]$
A	0.8	3	70	1	20	1.23	4.9
B	0.8	2	100	0.9	25	1.18	6.3
C	1	2	100	1.2	15	1.18	6.3
D	1.3	2	100	2.1	12	1.15	4.9
D_{ox}	1.3	2	100	2.1	14	1.25	5.5
E	0.8	$gr^{(3)}$	90	0.8	28	1.15	6.5
F	1.1	$gr^{(3)}$	90	1.1	21	1.13	6.4
G	1.3	$gr^{(3)}$	90	2.2	19	1.10	7.0
H	2.2	0.8	100	5.6	12	1.11	7.1
I	1.3	0.2	100	1.2	18	1.08	9.0
J	3	0.2	100	6.3	13	1.06	9.1
K	7	0.2	100	33	6	1.04	9.1

(1): minimum of the differential measured I/V characteristic

(2): measured at a reverse current of $-1\,\mu A$

(3): graded doping, from $2 \cdot 10^{16}\,cm^{-3}$ at the surface to substrate doping within 90 *nm*

Physical properties

Diodes fabricated according to the above in-situ electrochemical etching and deposition process show near-ideal I/V characteristics. The measured I/V characteristics were used to characterize and to determine the physical properties of the diodes. One of the most suitable parameters for the characterization of the physical properties is the diode ideality factor n. Schottky diodes with large contact areas can be described in a wide current range by a more or less constant

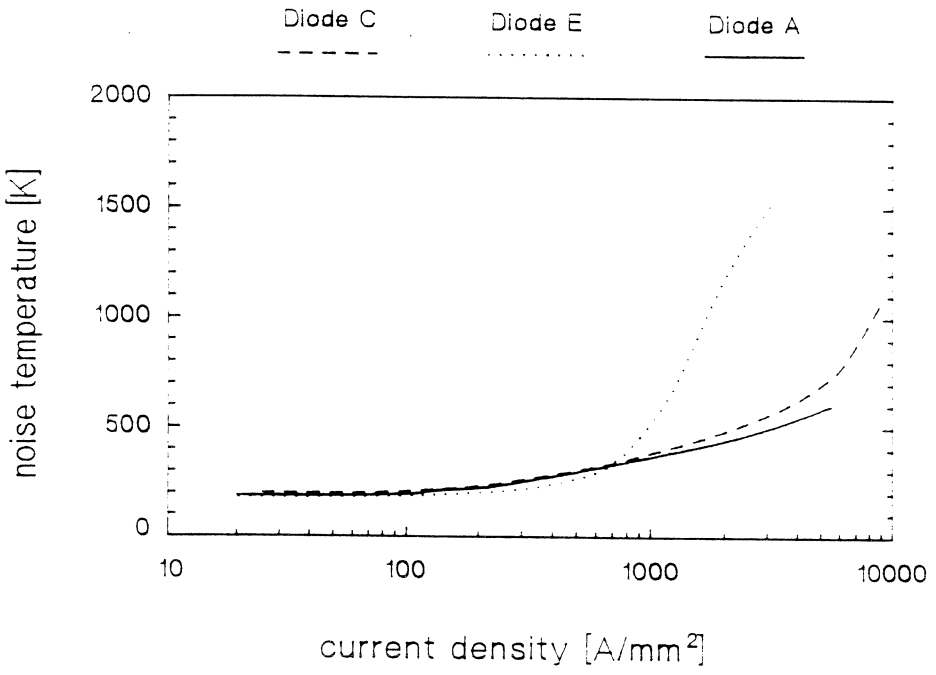

Fig. 1: The noise temperature of various THz mixer diodes measured at 1.5 GHz as a function of the diode current density

ideality factor. This approach is not applicable for diodes with small junction areas such as utilized for THz mixing applications. The current–dependance of the ideality factor cannot be neglected for these diodes. The current–dependant ideality factor $n_{(I)}$, which physically means the sum of barrier–lowering mechanisms, can easily be obtained from the measured I/V characteristics according to eq. 1.

$$n_{(I)} = \frac{1}{V_T} \frac{\delta V}{\ln \delta I} \tag{1}$$

The ideality factor of near–ideal diodes can be described by contributions due to the image force n_{if} (eq. 2, 3) and the thermionic field emission n_{tf} (eq. 4, 5, 6) [7, 10]. The ideality factor due to these two mechanisms is close to one and depends only on the doping concentration. Other barrier lowering mechanisms for example due to interfacial states can then be neglected. The ideality factor can be calculated according to the following set of equations [10].

$$n_{if} = \frac{1}{1 - \frac{\Delta\Phi_b}{4\,V_{fb}} \left(1 - \frac{V}{V_{fb}}\right)^{-3/4}} \tag{2}$$

with

$$\Delta\Phi_b = \left[\frac{q^3 N_{de} V_{fb}}{8\pi^2 \epsilon_s'^2 \epsilon_s \epsilon_0^3}\right]^{1/4} \tag{3}$$

$$n_{tf} = \left[\frac{V_T}{E_0} - \frac{V_T}{2(V_{fb} - V)}\right]^{-1} \tag{4}$$

with

$$E_0 = E_{00} \coth\left(\frac{E_{00}}{V_T}\right) \tag{5}$$

and

$$E_{00} = \frac{h}{4\pi}\left[\frac{N_{de}}{m^* \epsilon_0 \epsilon_s}\right]^{1/2} \tag{6}$$

In eq. 2- 6 the following nomenclature has been used: Flat-band voltage V_{fb}, barrier lowering $\Delta\Phi_b$, epi-layer doping concentration N_{de}, thermal voltage V_T.

The combination of eq. 2- 6 leads to

$$n = 1 + (n_{if} - 1) + (n_{tf} - 1) \tag{7}$$

It could be shown that Schottky diodes with diameters larger than 3 μm which are fabricated on low doped epitaxial layers ($N_{de} = 2 \cdot 10^{16}\, cm^{-3}$) can be completely described by the above theory. This reveals that the fabrication process for the diodes does not create any other interfacial surface states than these required for Fermi-level pinning. However, for doping concentrations larger than $N_{de} = 2 \cdot 10^{17}\, cm^{-3}$ the ideality factor determined from the I/V characteristics is slightly higher ($\Delta n \approx 0.05$) than predicted by eq. 7. The corresponding current for ideal diodes I_{id} is given by eq. 8.

$$I_{id} = I_s \exp\left(\frac{V}{n_{(I)} V_T}\right) \tag{8}$$

Although all diodes have been fabricated according to the same fabrication techniques, a comparison of the different I/V characteristics reveals that diodes with a smaller diameter than approx. 3 μm exhibit a considerable deviation from the simple theory, especially at low bias voltages. Fig. 2 shows the ideality factor as a function of the diode current density. The small diode exhibits a large increase in n at low current densities which cannot be explained in terms of image force and thermionic field emission.

Fig. 2 also shows that the small diode has a minimum in the ideality factor. The current corresponding to this value of n depends on the doping concentration and the diode diameter.

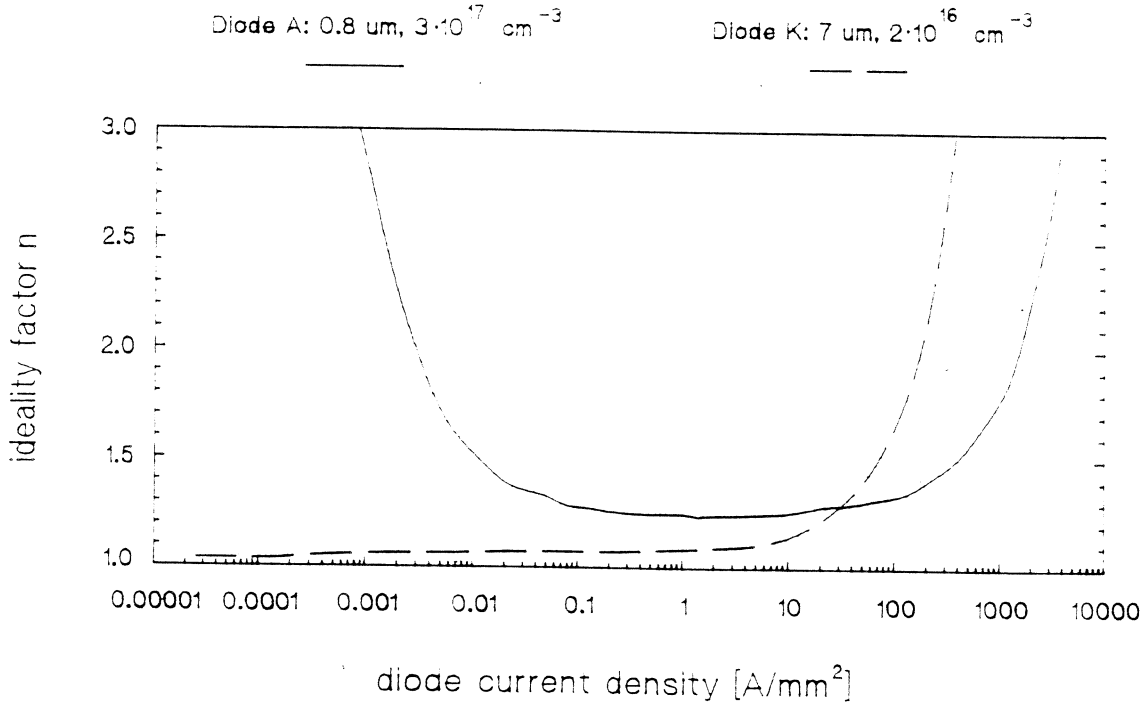

Fig. 2: The diode ideality factor as a function of the diode current density

For larger forward currents the ideality factor can be calculated according to eq. 7. The current range towards small current densities can be described by an additional current contribution ΔI to the diode current I_{id}.

$$I = I_{id} + \Delta I \tag{9}$$

In fig. 3 this additional contribution ΔI is presented for different diodes as a function of the diode voltage. Fig. 3 clearly demonstrates the exponential behavior of ΔI with the diode voltage. This implies that ΔI can be described by the following equation:

$$\Delta I = I_{sm} \exp\left(\frac{V}{m\, V_T}\right) \tag{10}$$

I_{sm} is the intercept of ΔI with the ΔI-axis and m is the slope parameter of ΔI.

The corresponding values for the slope parameter m are in the range of $m \sim 2...5$. Such large values cannot be explained by barrier lowering through image force and thermionic field emission. This means that the contribution ΔI does not originate from a simple parallel parasitic diode. However, the fact that ΔI is more pronounced in small diodes suggests that this additio-

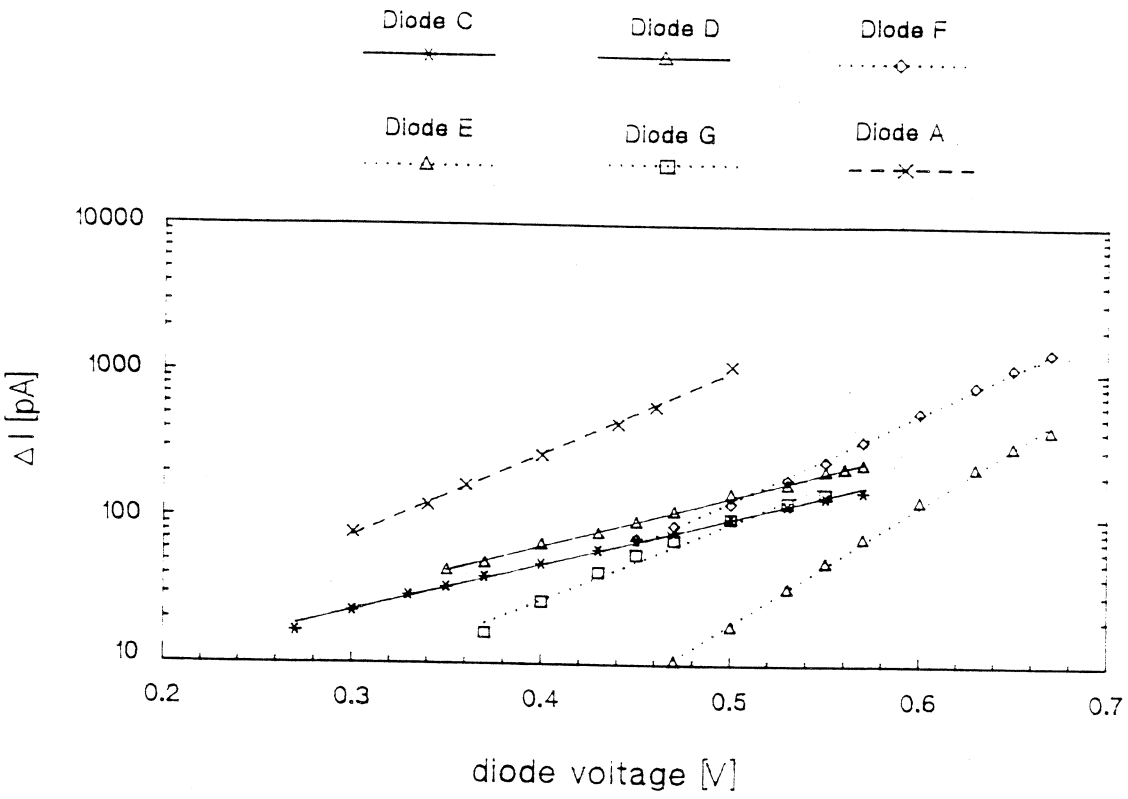

Fig. 3: The additional current contribution ΔI as a function of the diode voltage for different diodes

nal current is caused by edge effects. The area of the possible parasitic diode can be determined from I_{sm} in eq. 8. Assuming a realistic barrier height for the parasitic diode between 0.5 - 1.2 eV yields areas in the range of several square nanometers. This corresponds to a ring around the original contact with a width of less than 1 Å. Therefore, the additional contribution ΔI cannot be due to simple edge effects. We suggest that ΔI is caused by interface effects at the metal semicondutor junction. This assumption is supported by experimental results which are presented in fig. 4. This shows the ratio of the additional current contribution ΔI to the total diode current I as a function of the diode voltage for a number of diodes with different diameters and a doping concentration of $2 \cdot 10^{17}\, cm^{-3}$. At low bias voltages the diode current is entirely determined by the parasitic contribution ΔI. This behavior is more pronounced for diodes with small diameters which suggests that this effect is dependant on the junction area. Furthermore, fig. 4 indicates that the contribution ΔI to the total diode current depends on the metal semiconductor transition. This can be inferred from the comparison of the diodes D and D_{ox}. These diodes are identical but diode D_{ox} has an interfacial oxide layer. The change in the interface morphology and therefore a deviation from the ideal metal semiconductor junction leads to an increase of the influence of this parasitic effect on the diode current.

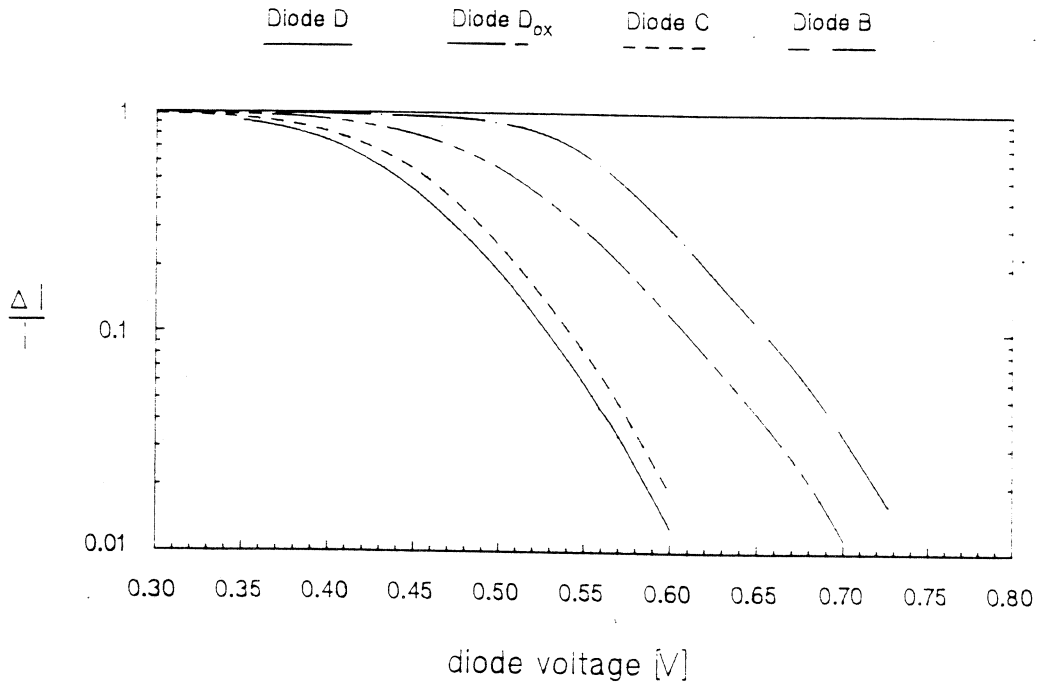

Fig. 4: $\Delta I/I$ as a function of the diode voltage

A possible explanation for the area–dependance of the parasitic current contribution ΔI could be a change of the size and number of Pt growth centers resulting in differences in crystallite sizes and intercrystalline boundary material at the interface to GaAs with decreasing Schottky contact diameter. These differences are produced by different mobilities of the Pt in the electrolyte before deposition for narrow and wide SiO_2 apertures. The adhesion of Pt during the electrolytic deposition depends on the potential distribution between the semiconductor surface and the electrolyte. The inhomogeneous field pattern at the edge of the SiO_2 window affects the Pt growth centers and therefore the Schottky metal morphology [11].

Reliability

The diodes A, D, D_{ox} have been thermally stressed under various conditions. Diode A has been tested for instrument survival with all power off in a temperature cycle ranging between -30 C and +65 C for 24 h [12]. No change in the ideality factor, the barrier height and the overall I/V characteristic could be observed. The noise temperature measured at 1.5 GHz shows that there occurs no degradation of the contacts due to the thermal stress. In order to get additional information about the influence of a thermal stress with all power off, the diodes D and D_{ox} were stressed for 1000 h in an experiment with temperatures between -50 C and

+100 C (duty cylcle 2 h). The results are illustrated in fig. 5 where the ideality factor is shown as a function of the diode current. Diode D which was fabricated according to the optimized process shows no changes in the electrical performance. For diode D_{ox} a slight increase of the ideality factor is observed in the overall forward bias range. This indicates that the in situ etching and deposition techniques utilized for the fabrication of diode D is more suitable for reliable diodes than fabrication techniques where the GaAs surface is in contact with air prior to the Schottky metal deposition.

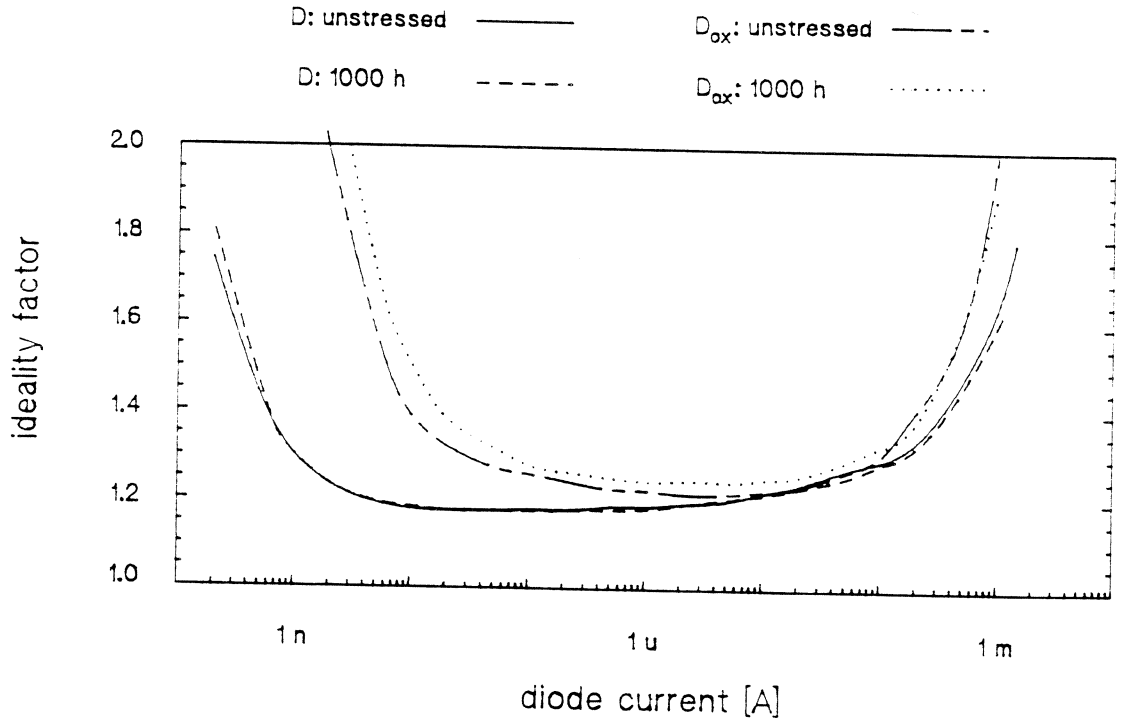

Fig. 5: Ideality factor as a function of the diode current for different diodes before and after thermal stress

The high current densities (up to 1000 A/mm^2) at which THz diodes are operated require diodes which show stable performance under electrical stress. Diode A has been stressed clearly beyond the maximum operating current densities. Operated for 48 hours at 2 mA (4000 A/mm^2) and subsequently for 48 hours at 5 mA (10000 A/mm^2), the diodes show no degradation. Even a slight reduction of the series resistance ($\sim 2\,\Omega$) in combination with a decrease of the ideality factor was observed ($\Delta n \sim 0.05$) (fig. 6). These improvements are probably due to a modification of the Pt morphology at the Schottky interface. A further increase of the current density to 14000 A/mm^2 leads to a strong degradation of the Schottky contact within 30 minutes. Fig. 6 illustrates these results. All observed changes (improvements as well as

degradations) occured within 30 min after the application of the electrical stress.

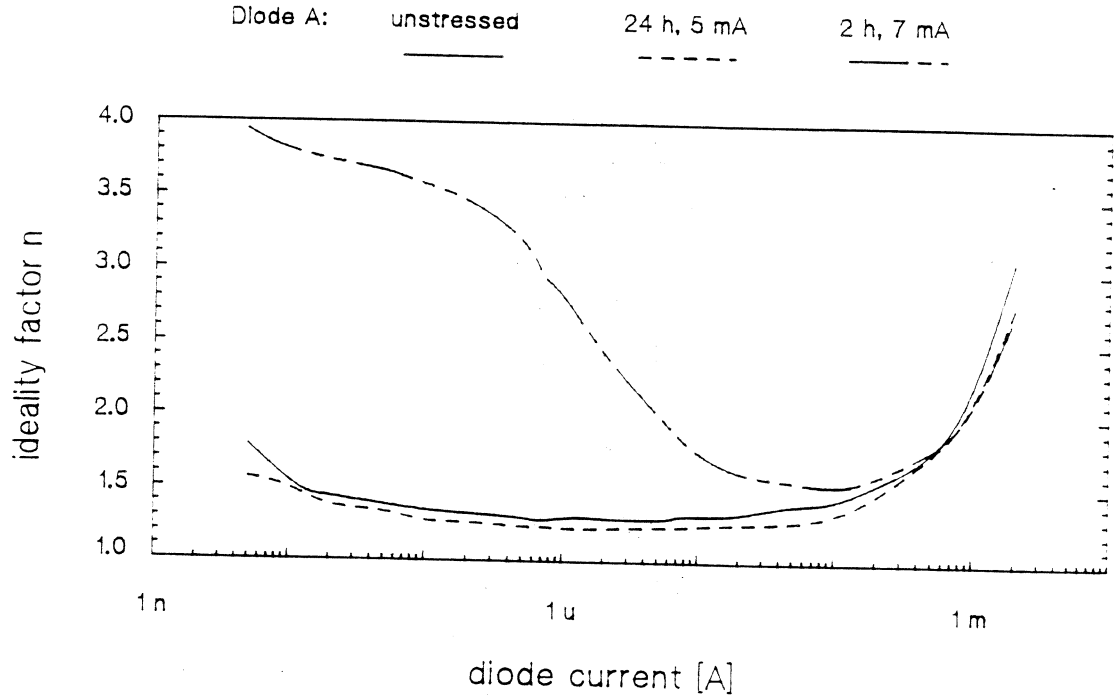

Fig. 6: The ideality factor of diode A as a function of the current before and after electrical stress

Conclusions

It has been demonstrated that small area diodes such as utilized in THz mixers can only be described in a relatively small current range by an ideality factor which is calculated according to the image force and thermionic field emission. At low bias voltages there exists a deviation from the theoretical ideality factor which is the more pronounced the smaller the diode area is. There exists experimental evidence that this deviation depends on the interface morphology of the metal/semiconductor junction.

THz mixer diodes which have been fabricated by the optimized in situ electrochemical process show no degradation after 1000 h of thermal stress. It has been also demonstrated that the diodes are reliable under long–time electrical stress up to a current density of $10000\,A/mm^2$.

Acknowledgements

The authors would like to express their acknowledgements to Dr. H. Grothe and Dr. J. Freyer, both from the Technical University of Munich, Germany, for supplying the high-quality epitaxial material and to Prof. A. Jelenski, Institute of Electronic Materials Technology, Warsaw, Poland, for stimulating discussions.

This work has been funded partly by the Deutsche Forschungsgemeinschaft (DFG) whose support is acknowledged.

References

[1] L. Brillson, "Chemical reaction and charge redistribution at metal-semiconductor interfaces," *J. of Vacuum Science & Technology*, vol. 15, (1978), no. 4, pp. 1378–1383.

[2] D. Young and J. Irvin, "Millimeter frequency conversion using $Au-n$-type $GaAs$ Schottky barrier epitaxial diodes with a novel contacting technique," *Proceedings of the IEEE*, vol. 53, (1965), pp. 2130–2131.

[3] W. Peatman and T. Crowe, "Design and fabrication of $0.5\mu m$ $GaAs$ Schottky barrier diodes for low-noise Terahertz receiver applications," *Int. J. Infrared and Millimeter Waves*, vol. 11, (1990), no. 3, pp. 355–365.

[4] A. Jelenski, A. Grüb, V. Krozer and H. Hartnagel, "A new approach to the design of Schottky barrier diodes for THz mixers," *Proc. 3rd Symp. on Space Terahertz Technology*, (1992), pp. 631–642.

[5] V. Krozer, *Verfahren der Kleinsignal- und Großsignal-Analyse und Charakterisierung von Mikrowellenschaltungen und Bauelementen mit Hilfe der Volterra Reihe.* VDI-Verlag, series 9, nr. 142, Düsseldorf, (1992).

[6] V. Krozer and A. Grüb, "A novel fabrication process and analytical model for $Pt/GaAs$ Schottky barrier mixer diodes," *Solid-State Electronics*, (submitted).

[7] A. Jelenski, A. Grüb, V. Krozer and H. Hartnagel, "New approach to the design and fabrication of THz Schottky barrier diodes," *IEEE Trans. Microwave Theory & Techniques*, vol. MTT-41, (1993), no. 3.

[8] A. Grüb, *Technologieentwicklung für THz-Schottkydioden und Nanometerstrukturen.* VDI-Verlag, series 21, nr. 110, Düsseldorf, (1992).

[9] A. Grüb, K. Fricke and H. Hartnagel, "Highly controllable etching of epitaxial $GaAs$ layers by the pulse etching method," *J. of Electrochemical Society*, vol. 138, (1991), no. 3, pp. 856–857.

[10] E. Rhoderick and R. Williams, *Metal–Semiconductor Contacts. Monographs in Electrical and Electron. Eng., No. 19*, Oxford Science Publ., 2 ed., (1988).

[11] F. Walsh and M. Herron, "Electrocrystallization and electrochemical control of crystal growth: Fundamental considerations and electrodeposition of metals," *J. Phys. D: Applied Physics*, vol. 24, (1991), pp. 217–225.

[12] P. Siegel *private communication.*

JOSEPHSON-EFFECT MIXERS USING SHUNTED Nb AND NbN TUNNEL JUNCTIONS

R.J. Schoelkopf, T.G. Phillips, J. Zmuidzinas
Downs Laboratory of Physics
California Institute of Technology
Pasadena, CA 91125

and

J.A. Stern
Center for Space Microelectronics Technology
Jet Propulsion Laboratory
California Institute of Technology
Pasadena, CA 91109

Abstract

We present test results of a 100 GHz waveguide receiver using resistively-shunted Nb and NbN tunnel junctions. These junctions were fabricated with a process similar to that used previously with Nb junctions [1], which produces non-hysteretic devices with normal-state resistances of 30-50 Ohms, and I_cR_n products of 0.5-0.75 mV. The best receiver temperature obtained to date with NbN is 270 K (DSB) with 6-7 dB of conversion loss. A receiver temperature of 390 K (DSB) was previously obtained with Nb junctions; these devices showed qualitative agreement with the predictions of the simple DC and RF current-biased RSJ model. The improvement in receiver performance is probably due to improved RF coupling of the junctions, and due to the higher I_cR_n products of NbN. However, these NbN devices display different pumped I-V curves and IF power curves than predicted by the RSJ model. We show that these effects can be caused by the strong interaction of the junction with the embedding circuit, and conclude that an accurate model of the impedance presented to the junction will have to be included in the RSJ simulations to compare with the observed performance.

Introduction

We are studying the performance of Josephson-effect mixers using resistively-shunted tunnel junctions in order to develop a better understanding of their behavior, the sources of noise and its limitation, and to determine how to optimize their performance. Also, we wish to compare the observed behavior and performance with the theoretical predictions of the so-called RSJ (resistively shunted junction) model, so that there will be a guide to the expected performance for different frequency regimes and device parameters. This work may be important as high-Tc SNS devices become available [P.A. Rosenthal and E.N. Grossman, these proceedings] with large $I_c R_n$ products, for they provide the possibility of using Josephson mixers at frequencies in the terahertz range, above the range where SIS mixers are currently available. In contrast, due to the extremely short coherence lengths of the high-Tc materials, junctions suitable for quasiparticle (SIS) mixers may not be feasible with these materials.

Device Fabrication

We have applied the technique used for creating non-hysteretic Nb Josephson devices[1] to NbN/MgO/NbN tunnel junctions. First the junction trilayer is fabricated, then the junction areas are patterned by electron-beam lithography and subsequently etched using reactive-ion etching (RIE) in the standard method [3]. After planarization of the etched area with evaporated SiO, a AuGe resistor is fabricated on top of the SiO, and the junction and resistor are then contacted with another layer of NbN. A photomicrograph of a completed Nb junction is shown in Figure 1a. Since the bottom of the etched trilayer lies under the resistor, it acts as a ground plane, and the resistor structure can be analyzed as a lossy transmission line. The impedance of this short microstrip structure is purely real, even up to frequencies comparable to the gap frequency of the superconductor, thus providing the desired broadband shunt. However, the section of

superconductor which contacts the junction and resistor creates a non-negligible parasitic capacitance when compared to the very small area tunnel junctions used, and therefore the area of this contact pad must be kept to a minimum. From a knowledge of the geometry and thickness of the insulator (SiO), we estimate this parasitic capacitance to be 7-8 fF.

Shunting of the junction is necessary to reduce the McCumber beta parameter ($\beta_c = 2eI_cR_N^2C/\hbar$) of the unshunted tunnel junctions. Junctions with β_c values greater than one have hysteretic I-V curves [4], and their dynamics can be complicated, including the possibility of chaos. Reduction of β_c is accomplished by resistive shunting, which reduces β by the square of the ratio of the initial junction resistance to the final resistance of the parallel combination of the junction and the resistive shunt. However, this shunting has the undesirable effect of reducing the I_cR_n product of the junction. For the NbN junctions used, the critical current density was about $33kA/cm^2$, and the specific capacitance is estimated to be about $150fF/\mu m^2$ [5], giving an unshunted β of about 12. Thus the optimal shunted junction for these parameters would have a shunt resistance of about one-fourth of R_n, and thus an I_cR_n reduced from the unshunted value of 3.0 mV to 0.8 mV. In order to maintain high enough resistances for the final device, very small ($0.3\mu m$ on a side) area junctions must be used, and the parasitic capacitance will be comparable to the junction capacitance. This further reduces the final I_cR_n product attainable. The I-V curve of a typical device is shown in Figure 1b. This device had a critical current of 11 microamps and a normal state resistance of 39 Ohms, giving an I_cR_n product of 430 microvolts. The I-V curve is nonhysteretic and follows the RSJ model.

Mixer Modelling

Mixer performance can be predicted using the RSJ model, in a method similar to that used by Taur[6], but extended to the case of finite junction capacitance. The

RSJ model assumes a simple linear resistance and an ideal Josephson element, whose current is given by $I_c sin\phi$. Nonzero junction capacitance can be included as well. The circuit is shown in Figure 2. Using the customary normalized units;

$$v = \frac{V}{I_c R_n} \qquad i = \frac{I}{I_c} \qquad \tau = t\,\omega_c$$

$$z = \frac{Z}{R_n} \qquad \Omega = \frac{\omega}{\omega_c}$$

$$\beta_c = \frac{2e}{\hbar} I_c R_n^2 C \qquad \omega_c = \frac{2e}{\hbar} I_c R_n$$

the equations of motion are given by:

$$v = \dot{\phi}$$

$$\beta_c \ddot{\phi} = i_{DC} + i_{LO} \sin(\Omega_{LO}\tau) - \sin(\phi) - v$$

where the differentiation is with respect to the normalized time, τ.

The bias current provided to the junction includes the DC bias, a local oscillator current, and noise currents due to the Johnson noise of the resistor. These differential equations can be integrated to determine a voltage waveform, which is then Fourier transformed. From this information, we determine the three-port mixer conversion matrix and noise correlation matrix. Mixer performance can then be optimized as a function of IF and RF impedances using standard linear circuit analysis. In this approach the embedding impedances are implicitly assumed not to affect the nonlinear dynamics of the junction; the noise and conversion matrices are determined using the infinite embedding impedance (i.e. current bias), and are assumed to be independent of the impedances connected (in very narrow frequency ranges) to the ports.

For this current-biased RSJ model, we find that the best mixer performance is expected for normalized frequencies of about a half ($\Omega_{LO} = 0.5$), with β values of about

0.8. Predicted mixer noise temperature and conversion efficiency for an optimized case are shown in Figure 3. Here, the best RF impedance (assumed to be the same at both sidebands) is about 3 to 5 times the junction normal state resistance, and real or with a small inductance. The IF impedance is about 3 times R_n. Notice that for nonhysteretic junctions, the ωRC product at the LO frequency is less than one, so compensation for the reactance of the junction capacitance (i.e. tuning circuits) should not be important for the performance. Also, since the preferred impedances are high compared to the junction impedance, the current biased approximation should be valid. Very good mixer performance is predicted under these assumptions, with double-sideband mixer temperatures of about 25 K, and a conversion gain of - 3 dB.

Nb Mixer Results

The Nb and NbN shunted junctions were both tested in a waveguide receiver similar in design to those used at the CSO [7,8]. The junctions are fabricated on thin quartz substrates, with an integrated RF choke structure on the substrate. This choke structure functions to short the superconductor to the waveguide walls at RF frequencies, while passing the IF and DC bias. This substrate is then mounted across a full-height waveguide mount with two adjustable (backshort and E-plane) tuners. The waveguide feeds a horn and polyethylene lens, with the beam coupled out through a mylar dewar window. Cooled filters of quartz/black polyethylene and fluorogold prevent IR radiation from heating the junctions. The IF signal is fed to a cooled HEMT amplifier with a noise temperature of about 10 K and gain of 30 dB. Receiver performance is estimated using the standard hot/cold load technique.

The pumped I-V curve and hot/cold IF power response as a function of bias voltage for a Nb Josephson device at 94 GHz are shown in Figure 4a. As expected the best response is found in the middle of the first photon step (i.e. between the 0-th

and 1st Shapiro steps, at about 100 microvolts), with a local oscillator power applied which is sufficient to suppress the critical current (i.e. 0-th Shapiro step) to about half its initial value. The best receiver performance observed was 390 K (DSB) receiver temperature, and -6.5 dB conversion gain. This device was not optimal in several ways, however. First, this device was too strongly shunted, and had an I_cR_n product of only about 200 microvolts. Secondly, this first batch of devices was fabricated on 0.2 mm thick substrates, while the integrated choke structure was designed assuming a 0.1 mm substrate. This probably had the effect of reducing the coupling to the waveguide, and reducing the effectiveness of the adjustable tuners, thereby limiting the range of embedding impedances possible.

Figure 4b shows the I-V curve and low frequency noise power in the absence of signal (i.e. a 0 K load at the input) from a current-biased RSJ simulation using parameters corresponding to the Nb data. The similar shapes of the I-V curve and output power curve suggest that the current-biased model adequately describes this junction. The best mixer performance was found at the maximum output power of the mixer, and with the backshort adjusted for maximum LO coupling. The slope of the photon steps was basically independent of tuner position. The optimal RF embedding impedance for this device was predicted by the current-bias RSJ model to be about 1 to 2 times R_n (or 30-60 Ohms and real), due to its lower I_cR_n product. The model further predicts mixer noise temperatures of 100-200 K (DSB), which is still substantially lower than the observed 350 K. Some of this discrepancy might be due to imperfect coupling due to the unoptimized choke structure and front end losses.

NbN Mixer Results

NbN junctions produced using the resistive-shunting process were also tested in the same receiver. These devices were superior in two respects: the I_cR_n product of

400-500 microvolts was optimal for frequencies of about 100 GHz, and they were fabricated on thinner substrates, thus improving their coupling to the waveguide. The effect of the tuners on the LO coupling and pumped I-V curves was much stronger. Indeed the photon step varied from the case where the slope was about 0.5 to 1.0 times the normal state resistance of the device, to the case where there were nearly infinite impedance steps, depending on the backshort position. The best receiver response was found on relatively low slopes, despite the fact that best IF match should occur at about 3-4 times R_n. The current-biased RSJ model predicts that the best performance would coincide with relatively large output impedances of perhaps 10 times R_n (i.e. steep slope on the photon step), but we were unable to obtain mixer results for these conditions, because the bias circuit oscillated. We intend to modify the DC bias circuit to allow operation in this regime. A hot/cold response curve and pumped I-V curve are shown in Figure 5a. The best receiver temperature of 270 K (DSB) at 105 GHz was obtained in the center of the photon step, and the conversion efficiency was about -7 dB.

Obviously, this device shows a qualitatively different behavior from the more weakly coupled Nb devices or the current-biased RSJ model. Furthermore, the difference in IF power curves for the hot and cold loads raises the possibility that nonheterodyne response or saturation could be occurring. It is unlikely that this difference is due to the different material, but is most likely due to the strong coupling of the junction to the external circuit. An extremely simple model for the embedding circuit, shown in Figure 2b, suggests that this is true. We modified the RSJ equations of motion to include a simple R-L-C series circuit, connected in parallel with the junction. The LO current was injected in parallel with the external resistor, and the L and C serve to couple this external circuit to the junction only in some frequency range near the LO

frequency. The pumped I-V curve and low frequency power simulated using this model with arbitrary parameter choices of R about 1/2 R_n and a Q of about 4. are shown in Figure 5b. The slope of the I-V curve has been greatly reduced from the typical value from the current-biased RSJ model of about 3 times R_n, and the power curve shows a shape suggestive of the observed double-humped behavior.

Clearly, an accurate representation of the impedances presented to the junction by the waveguide mount will be necessary to understand the behavior observed with the NbN junctions. The qualitatively different character of these devices may mean that the dynamics of the junction have changed significantly due to the influence of the external circuit. This in turn could have implications for the optimization of mixer performance different from those inferred from the current-biased modelling. Furthermore, it may be that certain quasioptical coupling schemes which present a real, slowly varying impedance over a wide frequency range (e.g. spiral antennas, [9]) may be advantageous, as they better approximate the current-biased case. Finally, it is possible to include the broadband signal from hot/cold loads coupled into the device once the embedding circuit is included in the simulations, which would allow the investigation of possible saturation effects.

Conclusions

We have tested Josephson-effect mixers using Nb and NbN shunted junctions at 100 GHz, and obtained receiver temperatures of 390 K (DSB) and 270 K (DSB), respectively. The NbN junctions were well coupled to the waveguide mount, and showed behavior qualitatively different from either the Nb junctions or the simulations using the current-biased RSJ model. We believe that this effect is due to the effect of the embedding circuit on the junction's dynamics. More study will be needed to compare in detail with the simulations, and to investigate the optimization of the mixer under these conditions.

The modelling performed so far predicts that receiver temperatures less than 100 K are possible. It will be important to understand the behavior of these mixers and their optimization so that this experience can be applied at higher frequencies with high-Tc devices.

Research supported by NASA Grant NAGW-107, NASA Code R funding to JPL, SDIO/IST, and a NASA Graduate Student Researcher Fellowship (R. Schoelkopf).

References

[1] R.J. Schoelkopf, T.G. Phillips, and J. Zmuidzinas, "A 100 GHz Josephson Mixer Using Resistively-Shunted Nb Tunnel Junctions," IEEE Trans. Appl. Supercond, , pp. 1993, in press.

[2] P.A. Rosenthal and E.N. Grossman, these proceedings.

[3] J.A. Stern and H.G. LeDuc, "Characterization of NbN Films and Junctions," IEEE Trans. Magn., MAG-27, pp. 3196-3199, March 1991.

[4] K. K. Likharev, *Dynamics of Josephson Junctions and Circuits*, New York: Gordon and Breach, 1986, pp. 14, 332-342, 423-424.

[5] J.A. Stern, H.G. LeDuc, and A.J. Judas, "Fabrication and Characterization of High Current-Density, Submicron NbN/MgO/NbN Tunnel Junctions," in *Proceedings of the 3rd International Symposium on Space Terahertz Technology*, Ann Arbor, MI, March 1992.

[6] Y. Taur, "Josephson-junction mixer analysis using frequency-conversion and noise-correlation matrices," IEEE Trans. Elect. Devices, ED-27, pp. 1921-1928, October 1980.

[7] B. N. Ellison et al., "A 345 GHz SIS receiver for radio astronomy," Int. J. of Infra. and MM Waves, 10, pp. 937-947, August 1989.

[8] J. Kooi et al., "A Low noise 230 GHz heterodyne receiver employing 0.25 μm^2 area Nb/AlOx/Nb Tunnel Junctions," IEEE Trans. MTT, 40, pp. 812-815, May 1992.

[9] T.H. Buettgenbach et al., "A Broad-Band Low-Noise SIS Receiver for Submillimeter Astronomy," IEEE Trans. MTT, 36, pp. 1720-1726, December 1988.

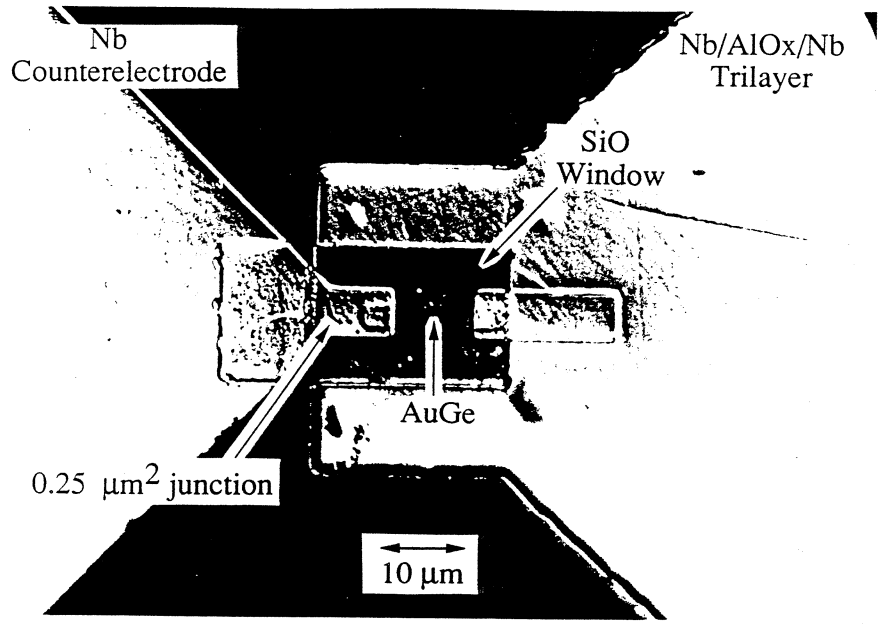

FIGURE 1a)

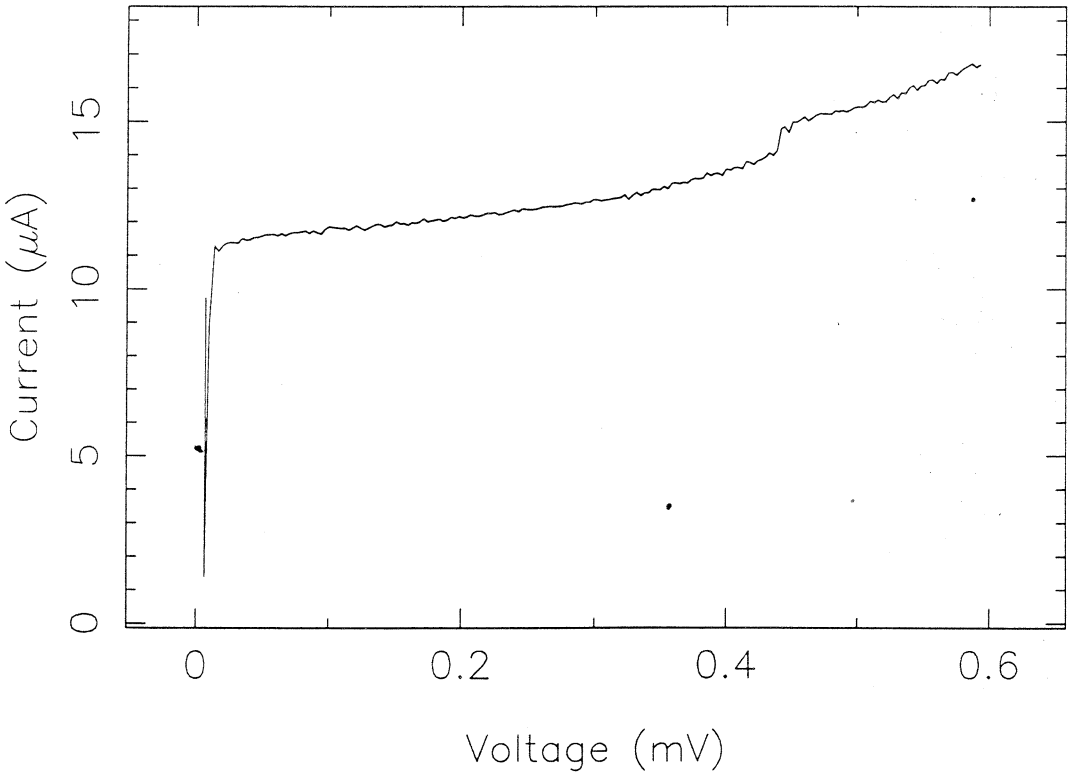

FIGURE 1 b)

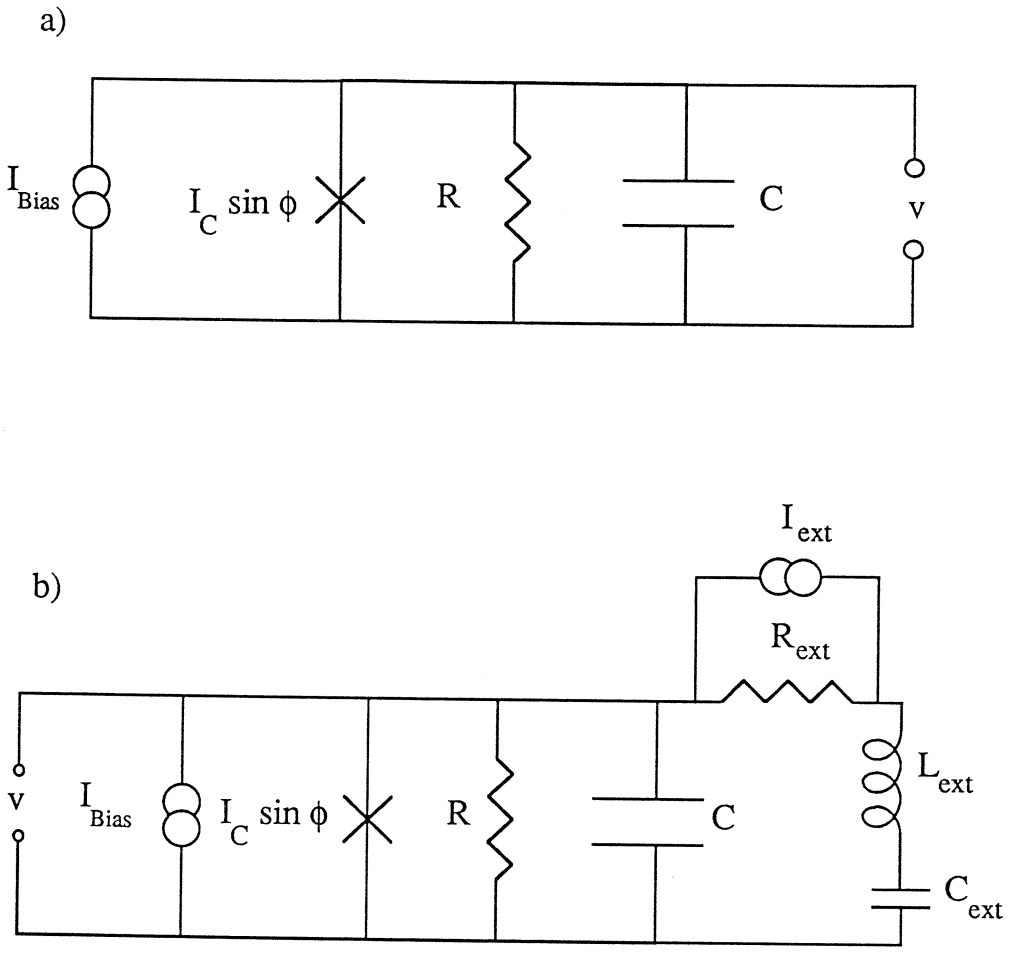

Figure 2: a) The current-biased RSJ model, consisting of a linear resistor, capacitor, and ideal Josephson element with sinusoidal current dependenence on phase.
b) A simplistic model of the RSJ junction plus external circuit. The external L and C serve to couple the external resistance and current source only over some frequency range. This circuit can at least qualitatively reproduce the behavior seen in strongly-coupled junctions.

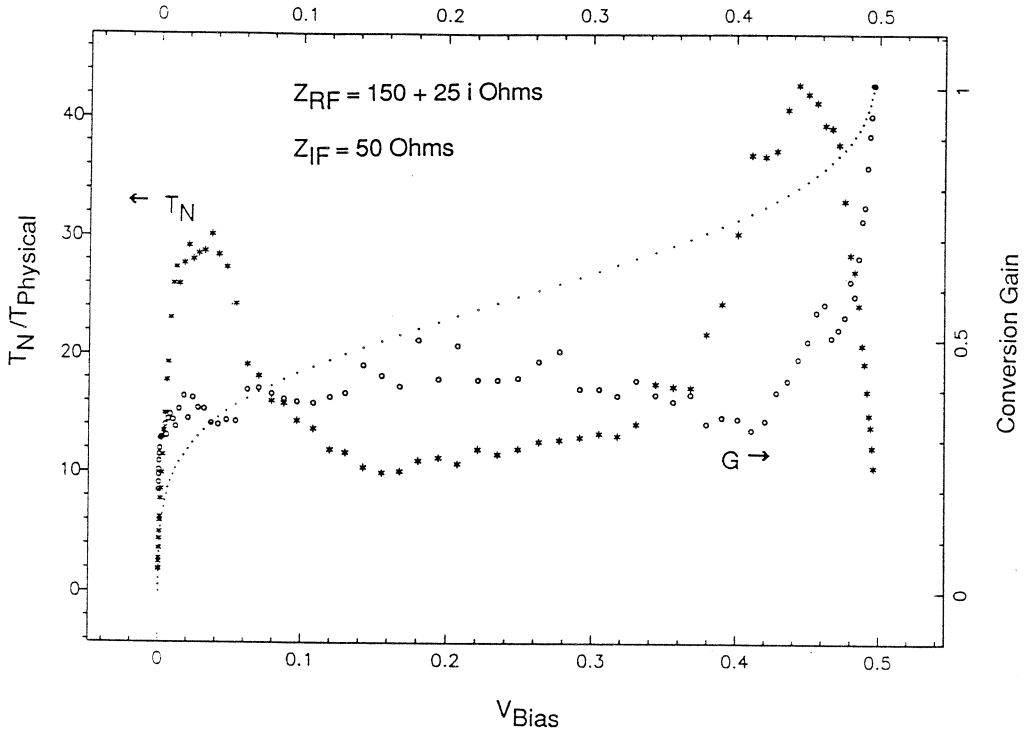

Figure 3: Mixer noise temperature and conversion efficiency as predicted by current-biased RSJ simulations for a Josephson mixer operated at 100 GHz with an IcRn product of 0.4 mV and a normal-state resistance of 50 Ohms. Filled dots are pumped I-V curve, showing first Shapiro step. Asterisks are single-sideband mixer temperature normalized to the physical temperature. Open circles are conversion efficiency, in linear units. Model predicts receiver temperatures of about 50 K (DSB), with 3 dB conversion loss.

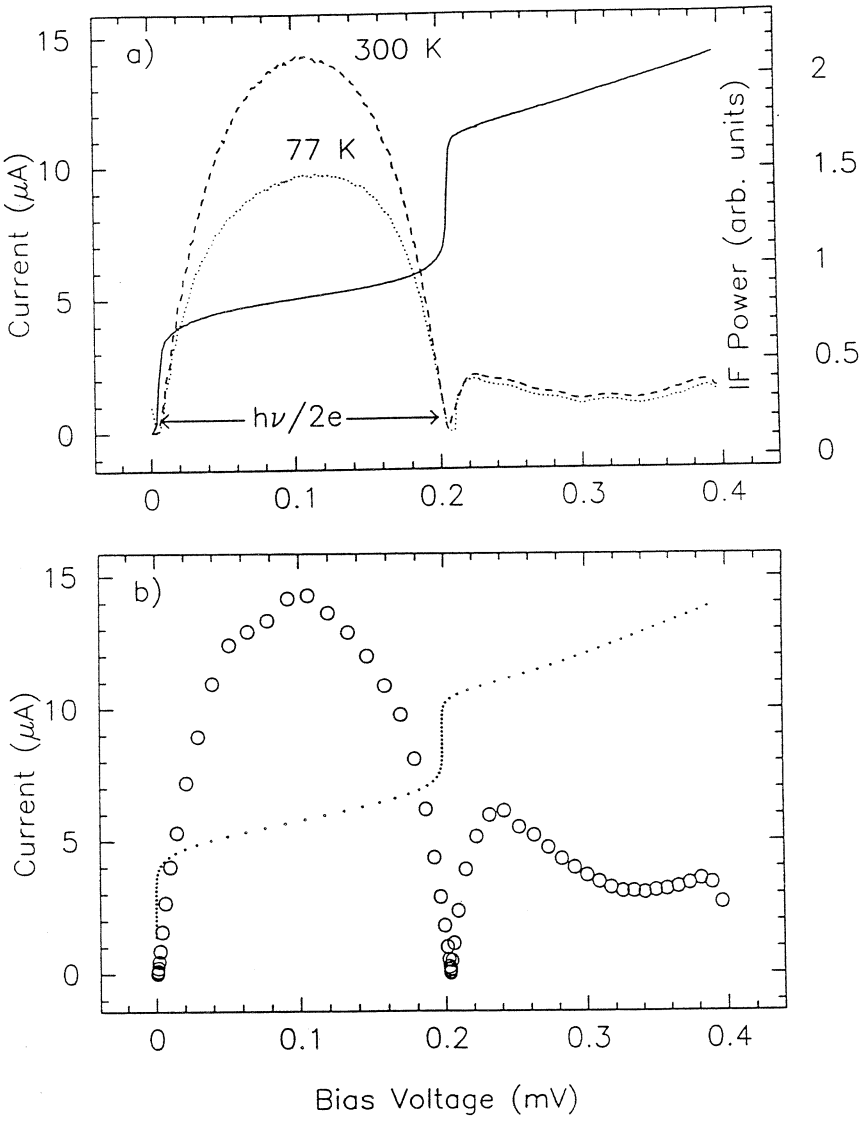

Figure 4: Heterodyne response of Nb Josephson-effect mixer.
a) Shows I-V curve with local oscillator applied (solid line). IF output power vs. bias voltage is shown for room temperature (dashed line) and 77 K loads at the receiver's input. Receiver has noise temperature of 400 K (DSB) and conversion efficiency of 0.2 (i.e. -6.5 dB).
b) Low frequency output noise expected from numerical simulations of current-biased RSJ model in the absence of signal (i.e. for a 0 K load). Mixer shows good qualitative agreement with model predictions.

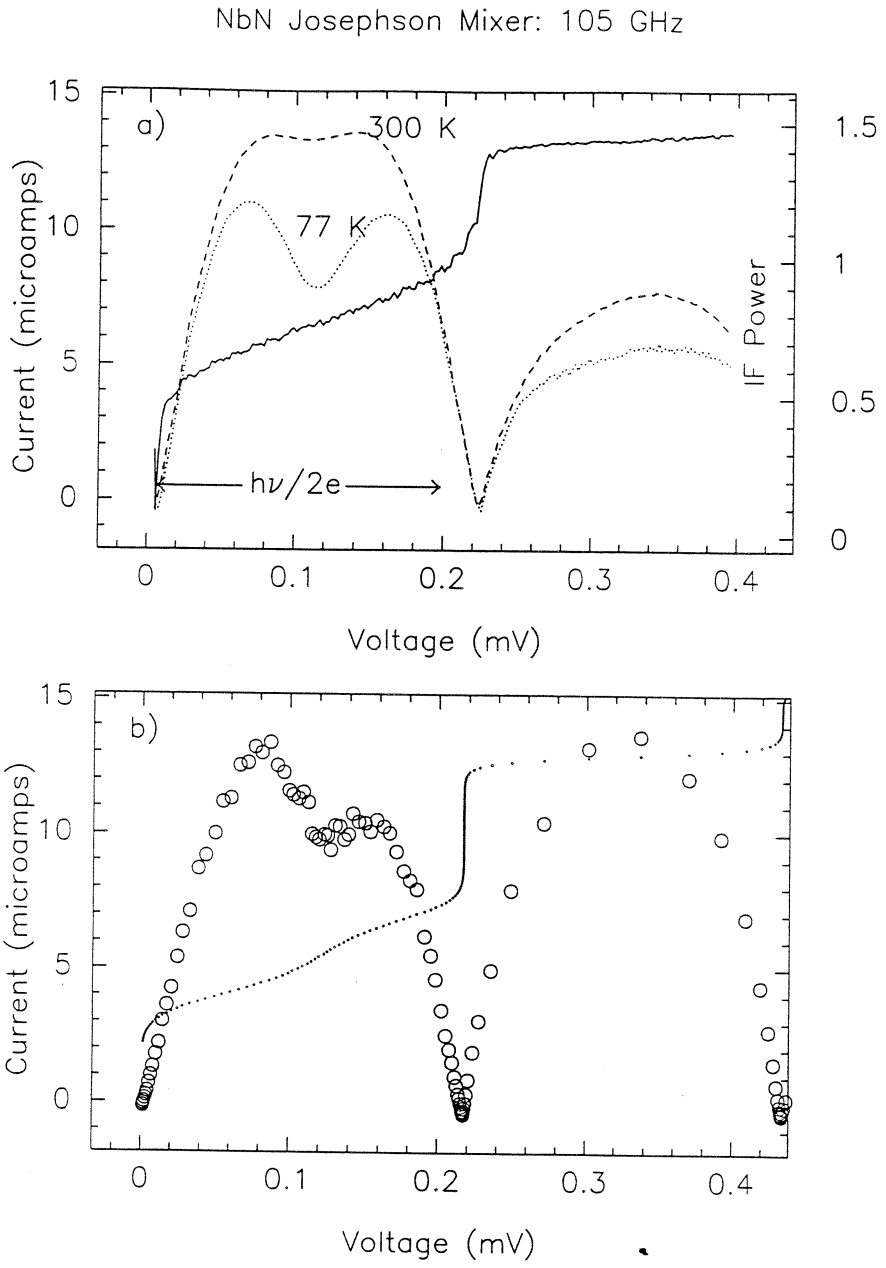

Figure 5: Heterodyne response of NbN Josephson-effect mixer.
a) Shows I-V curve with local oscillator applied (solid line). IF output power vs. bias voltage is shown for room temperature (dashed line) and 77 K loads at the receiver's input. Receiver has noise temperature of 270 K (DSB) and conversion efficiency of -7 dB.
b) Low frequency output noise expected from numerical simulations of RSJ model driven by RLC series circuit (see Fig 2 b). Model reproduces the shapes of pumped I-V curve and IF power curve.

QUASI-OPTICAL 2-D JOSEPHSON JUNCTION ARRAY OSCILLATORS WITH ON-CHIP INDUCTIVE TUNING STRUCTURES

Bin Liu and Michael J. Wengler
Department of Electrical Engineering
University of Rochester
Rochester, NY 14627

ABSTRACT

Progress in understanding the mechanism of coherent oscillation in two-dimensional (2-D) Josephson junction arrays has been made through analysis of the coupling circuit between two Josephson junctions. For a 2-D array to oscillate in phase, capacitive coupling is required for adjacent junctions in the same row and inductive coupling for adjacent junctions in the same column of the array. Computer simulation has been developed for two junctions coupled through a general circuit to find the optimum coupling between two junctions. The junctions in the array are also integrated with inductive tuning elements to tune out the junctions' parasitic capacitance. We have built 2-D Josephson junction arrays but no coherent oscillation has yet been observed.

I. INTRODUCTION

A Josephson junction is a voltage tunable oscillator with typical voltage scales of mV and an oscillation frequency f_J = 484 GHz per mV of dc bias. It is a natural choice for a millimeter and submillimeter oscillator. Such an oscillator will find many applications, e.g., as a local oscillator for SIS receiver systems. There are several problems commonly associated with a single Josephson oscillator: very low output power, broad radiation linewidth, poor coupling between a Josephson oscillator and the outside world, and a large harmonic content in the oscillation. One solution to these problems is to use an array of junctions. Josephson junction array oscillators have been demonstrated at Stony Brook [1] and NIST [2].

Recently we proposed a new scheme of Josephson array oscillators [3]. It is a two-dimensional Josephson junction array with integrated coupling structures called the Quasioptical Josephson Oscillator (QJO). Fig. 1 shows a functional schematic of the QJO. The junction array is fabricated on one side of a substrate. The other side of the substrate is metalized to form a cavity behind the array. The cavity functions in two ways. In one way it provides a mean field to the array to lock all junctions in phase. In the other way it

tunes out the junctions' capacitance. Such distributed arrays have been fabricated but no coherent oscillation has been observed [4, 5]. Two possible problems are those of phase-locking and the junction parasitic shunt capacitance. The back mirror is proposed to tune out the junctions capacitance. But this requires the array to oscillate in phase. Therefore the local coupling circuit between junctions is crucial in determining the mutual phase-locking of the junctions in the array. On the other hand, the large capacitive shunt reduces the locking range dramatically even if the local coupling circuit makes the junctions locked in phase. The small locking range will be easily broken up by the noise in the system. One solution to this problem is to integrate junctions in the array with inductive tuning elements to tune out junction capacitances at one particular operating frequency. In this paper we discuss the coupling circuit for in-phase and out-of-phase locking between junctions and their implication to 2-D arrays, and the on-chip integrated tuning structures.

II. MUTUAL PHASE-LOCKING IN 2-D DISTRIBUTED ARRAYS

To solve the mutual phase-locking problem in 2-D distributed arrays is an immense task. As a first step we can look the mutual phase-locking of two junctions and infer the results to 2-D arrays. Here only high frequency electromagnetic coupling is investigated, and low frequency coupling associated with flux quantization is not considered in this paper.

A. Circuit model of two coupled junctions

A real tunnel junction can be modeled as a bare Josephson junction shunted by a parasitic capacitor and resistor. We apply a two port network to the circuit connecting the two junctions (as shown in Fig. 2). Here J_1 and J_2 are bare Josephson junctions with parasitic capacitors and resistors included in the two port network. In general a two port network can be represented by a Y-matrix:

$$\mathbf{Y} = \begin{pmatrix} Y_{11} & Y_{12} \\ Y_{21} & Y_{22} \end{pmatrix}.$$

For a reciprocal two-port network the Y matrix is symmetric. The terminal currents are related to the voltages by the Y matrix:

$$I_1 = I_{11} + I_{12} = Y_{11} \times V_1 + Y_{12} \times V_2 \qquad (1)$$

$$I_2 = I_{21} + I_{22} = Y_{21} \times V_1 + Y_{22} \times V_2. \qquad (2)$$

An equivalent circuit described by (1) and (2) is the Π network as shown in Fig. 2 (b).

B. Phase relation of two weakly coupled junctions

Both perturbation analysis [6] and two-port network analysis [7] indicate that two resistively shunted junctions (RSJ's) will be locked in phase if they are coupled by a capacitor, and will be locked out of phase if they are coupled by an inductor (as shown in Fig. 3). To find the phase relation between two Josephson junctions through all the coupling range including strong coupling, we developed a computer simulation program. Some interesting results will be discussed below.

C. Computer simulation of two Josephson junction phase-locking

The algorithm for simulation of two junctions is an extension of the algorithm we developed for a single junction circuit [8]. We still use the harmonic balance method and update the voltage waveforms across the two terminals in the two-port network in each iteration. The following normalized variables are used in our computer simulation:

impedance:	$z = Z/R_N$
current:	$i = I/I_C$
voltage:	$v = V/V_N$, $V_N = I_C R_N$
capacitance:	$c = C/C_N$, $C_N = \Phi_0/I_C R_N^2$
inductance:	$l = L/L_N$, $L_N = \Phi_0/I_C$
time:	$t = T/T_N$, $T_N = 1/\Phi_0 I_C R_N$
frequency:	$f = F/F_N$, $F_N = \Phi_0 V_O$
power:	$p = P/P_N$, $P_N = I_C^2 R_N$.

Here I_C is the critical current of the junction, R_N is the normal state resistance of the tunnel junction, v_O is dc biasing voltage, and $\Phi_0 = 2e/h$ is the flux quantum. In normalized units, $f_J = v_O$ and the Josephson relations become:

$$i(t) = \sin(\phi(t)) \tag{3}$$

$$\frac{d\phi(t)}{dt} = 2\pi v(t). \tag{4}$$

For a typical niobium junction used in our arrays, the junction area A = 12 μm^2, I_C = 120 μA, R_N = 18 Ω, C = 456 fF. The normalization units for this junction are: V_N = 2.16 mV, C_N = 53 fF, L_N = 17 pH, F_N = 1045 GHz.

Simulation algorithm

1) Assume the junction voltage $v_{J1}(t)$ and $v_{J2}(t)$. We always set $v_{J1}(t) = v_{J1}(t) = v_O$ as the initial value, where v_O is the dc bias voltage.
2) Fourier transform $v_{J1}(t)$ and $v_{J2}(t)$ to $v_{J1}(\omega)$ and $v_{J2}(\omega)$.
3) Use the Fourier transform of the second Josephson relation (4)

$$j\omega\phi_1(\omega) = 2\pi v_{J1}(\omega)$$

$$j\omega\phi_2(\omega) = 2\pi v_{J2}(\omega)$$

to find $\phi_1(\omega)$ and $\phi_2(\omega)$.

4) Inverse Fourier transform $\phi_1(\omega)$ and $\phi_2(\omega)$ to $\phi_1(t)$ and $\phi_2(t)$.

5) Use the first Josephson relation (3) to find the junction current in the time domain $i_{J1}(t)$ and $i_{J2}(t)$.

6) Fourier transform $i_{J1}(t)$ and $i_{J2}(t)$ to $i_{J1}(\omega)$ and $i_{J2}(\omega)$.

7) Find the voltage across the two-port terminals

$$v_1(\omega) =(-i_{J1}(\omega))z_{11}(\omega) + (-i_{J2}(\omega))z_{12}(\omega)$$

$$v_2(\omega) = (-i_{J1}(\omega))z_{21}(\omega) + (-i_{J2}(\omega))z_{22}(\omega).$$

8) Compare $v_1(\omega)$ and $v_2(\omega)$ with $v_{J1}(\omega)$ and $v_{J2}(\omega)$. If the magnitude of the error is larger than the preset precision parameter, go back to step 3) and use $v_1(\omega)$ and $v_2(\omega)$ as $v_{J1}(\omega)$ and $v_{J2}(\omega)$. Otherwise the simulation is done.

In all the iterations, the dc component of the junction voltage is kept constant at v_O, the dc bias voltage. The initial phase of one junction is fixed at 0 as the phase reference and the phase of the other junction is allowed to vary. The second junction is current biased at i_{BIAS} and the phase is found by applying the following load line constraint:

$$\phi_{NEW}=\phi_{OLD} - p^*(i_{DC} - i_{BIAS})$$

where p is a positive constant, i_{DC} is the dc component of Josephson current, ϕ_{OLD} is the junction initial phase in current iteration and ϕ_{NEW} is the initial phase for next iteration.

Simulation Results

All simulations presented here were made at a fixed biasing voltage v_O=1 in normalized units.

1) Two coupled resistively shunted junctions

Our simulation results confirm our analysis above about the phase relation between two coupled resistively shunted Josephson junctions. Besides phase relations, the simulation also gives a quantitative locking range. For two mutually phase-locked junctions coupled by a capacitor, the dc currents through the junctions are depicted in Fig. 4. The horizontal axis in Fig. 4 is the phase difference between the two junctions. If we define the maximum allowable current difference between the junctions as the locking range ΔI, and the maximum allowable phase variation across the locking range as the phase span $\Delta\Psi$, we found that locking ranges are small at both weak and strong coupling. The maximum locking range is at intermediate coupling strength. Another interesting thing we found with the simulation is that the phase span $\Delta\Psi$ decreases with increasing coupling strength. Such locking behavior is depicted in Fig. 5 for two capacitively coupled resistively shunted Josephson junctions. The locking behavior for inductive coupled two

junctions is similar to that of capacitive coupled two except the phase difference is centered around π.

Another interesting thing we checked with the simulation is the pure resistively coupled two resistively shunted Josephson junctions. The locking range is zero for two identical junctions. The results we obtained are consistent with previous work [6, 9].

2) Two inductively coupled resistively-capacitively shunted junctions
Even though two inductively coupled resistively shunted junctions oscillate out of phase, the junction parasitic shunt capacitors change the two junction phase relation when they convert the inductive coupling to capacitive. A realistic circuit for two coupled tunnel junctions looks like that shown in Fig. 6. The simulation result for $L = 4$, $C_1 = C_2 = 8.6$ in the normalized units, which are typical parameters of Nb tunnel junction we used, showed that the phase difference between two Josephson junctions is around 0 at the center of locking range, opposite to the pure inductive coupling situation. The locking range is very small , $\Delta I = 1.4 \times 10^{-5}$, in this situation because of the large capacitive shunts.

Implication of the results of two junction mutual phase-locking to 2-D arrays
If the coupling circuit between two adjacent junctions in the same row of a 2-D array is right to have the two junctions locked in phase, the whole row will be locked in phase. The interesting thing here is that we need inductive coupling for the adjacent junctions in the same column of a 2-D array to lock in phase. This is the only situation a 2-D array will oscillate coherently. Any other situation, such as inductive coupling between two adjacent junctions in the same row or the capacitive coupling between two adjacent junction in the same column, will not have a 2-D array oscillate coherently.

III. On-Chip Integrated Matching Circuit

Various tuning structures have been used by people working on SIS mixers [10]. We mainly adapted these designs because we use the same tunnel junctions. The concern, however, is different. We are concerned about the effect of scattering of junction capacitances in the array. If the capacitance variation is δC, the resonant frequency will shift by $\delta\omega = (d\omega/dC)\delta C$. In design of tuning elements we want to ensure that the maximum resonant frequency shift due to the capacitance variation is within half of the 3 dB bandwidth of the resonant circuit. That is:

$$\delta\omega_{max} < \Delta\omega. \qquad (5)$$

Here we use $\delta\omega$ for resonant frequency shift due to the capacitance variation and $\Delta\omega$ for half of the 3 dB bandwidth of the resonant circuit. The interesting thing we found is that for a given δC, $\delta\omega$ scales with $\Delta\omega$. This scaling relation can proved easily as shown in the following.

A. Effect of junction capacitance scattering

In general a tuning circuit can be represented as $jB(\omega)$ in parallel with the capacitor it tunes out as shown in Fig. 6. The total admittance of the circuit including junction parasitic resistor and capacitor is:

$$Y_{total} = G + j\omega C + jB(\omega). \tag{6}$$

At resonance:

$$\omega_0 C + B(\omega_0) = 0. \tag{7}$$

To find the bandwidth of the circuit we consider the change of admittance with frequency:

$$\frac{dY_{total}}{d\omega} = jC + j\frac{dB(\omega)}{d\omega}. \tag{8}$$

With $\Delta\omega$ approximated by the change of admittance with frequency scaled by the real part of the admittance at resonant frequency:

$$\Delta\omega \approx \left| \frac{Re(Y_{total})}{\frac{dY_{total}}{d\omega}} \right|_{\omega=\omega_0} = \left| \frac{G}{C + \frac{dB(\omega)}{d\omega}} \right|. \tag{9}$$

Now assume the capacitance variation is δC, the resonant frequency shift can be found from eqn. (7):

$$(\omega_0 + \delta\omega_0)(C + \delta C) + B(\omega_0 + \delta\omega_0) = 0.$$

After expansion, we got:

$$\delta\omega_0 = \frac{1}{\omega_0} \left| \frac{\delta C}{C + \frac{dB(\omega)}{d\omega}} \right|. \tag{10}$$

The ratio of $\delta\omega_0$ and $\Delta\omega$ is:

$$\frac{\delta\omega_0}{\Delta\omega} = \frac{\omega_0 \delta C}{G} = Q\frac{\delta C}{C} \tag{11}$$

where $Q = \omega_0 C/G$. This result shows that a wider bandwidth tuning element has no advantage than a narrower bandwidth one in covering the resonant frequency shift due to the junction capacitance parameter scattering. But

wider bandwidth tuning structures do have advantage if we want larger tunability around the designed operating frequency. From equation (11), we can see that for given $\frac{\delta C}{C}$, if we want the resonant frequency shift no larger than half of the 3 dB bandwidth, there is a upper frequency limit for a given C or there is a upper capacitance limit for a given frequency.

B. Applicability of different tuning elements

Here we list in table 2 some tuning elements. All parameters are calculated for the HYPRES Nb fabrication process [11]. The parameters used to calculate transmission lines and 3 dB bandwidths are summarized in table 1.

Table 1. Parameters used in calculation of transmission lines and 3 dB bandwidths

Junction Capacitance	490 fF ± 5%
Gap Voltage	2.8 mV
Normal State Resistance	18 Ω
Physical Temperature	4.2 K
Center Frequency	100 GHz
Film Thickness of Bottom Electrode	150 nm
Film Thickness of Top Electrode	300 nm
Penetration Depth of Nb	90 nm
Thickness of Dielectric	200 nm
Dielectric Constant	4.7

Table 2. Different inductive tuning elements and their fractional bandwidths

Tuning Elements	Fractional Bandwidth
Lumped Inductor	18 %
Open-ended Stub	6.3 %
Short-ended Stub	14 %
End-loaded Stub	18 %

Essentially all the listed tuning elements can be use with 2-D arrays. The lumped inductor requires somehow a dc open circuit, which will make design more difficult. Among the listed tuning elements, the shorted-ended stub is a good choice. It has reasonably large bandwidth, and simple design when considering the coupling circuit. The end of the stub is RF shorted but

dc open. This can be achieved by using a quarter wave radial stub, which is a broad band short. Another tuning element we considered is the resistor-terminated stub as shown in Fig. 8. The advantage of this tuning circuit is that the termination resistor cuts the low frequency noise on the junction, and make the resonant steps easier to bias on. The tradeoff is the power loss to the termination resistor.

IV. Testing Results

2-D Arrays with capacitive coupling and on-chip resistor terminated tuning elements have been fabricated and tested. The optical micrograph of one of the arrays and the I-V curve are shown in Fig. 8 and Fig. 9. The adjacent junctions in the same row are coupled capacitively, and the coupling capacitor also serves to break the two junction SQUID loop. The I-V curve is close to that of a RSJ and showed a very slight bump corresponding to the resonant frequency 100 GHz of the tuning circuit. Using a liquid helium cooled bolometer, the output power from the arrays was determined to be less than 50 pW, indicating a lack of coherent oscillation. More analysis is under way.

V. Conclusion

For a 2-D array to oscillate in phase, capacitive coupling is required for adjacent junctions in the same row and inductive coupling for adjacent junctions in the same column of the array. Computer simulation of two coupled junctions showed that stronger coupling does not yield a larger locking range above a certain coupling strength. There is an optimal coupling strength which results in a maximum locking range. Integrating junctions in an array with tuning elements is a good solution to the parasitic capacitive shunt of junctions. For any inductive tuning structure, the resonant frequency shift due to capacitance variation is proportional to the 3 dB bandwidth of the tuning circuit.

Acknowledgment

This work is supported by grant AFOSR-90-0233 from the Air Force Office of Scientific Research.

References

[1] K. Wan, A.K. Jain, and J.E. Lukens, "Submillimeter wave generation using Josephson junction arrays," *Appl. Phys. Lett.*, vol.54, pp. 1805-1807, 1989.

[2] S.P. Benz and C.J. Burroughs, "Coherent emission from two-dimensional Josephson junction arrays," *Appl. Phys. Lett.*, vol.54, pp. 1805-1807, 1991.

[3] M.J. Wengler, A.Pance, B. Liu, and R.E. Miller, "Quasioptical Josephson Oscillator," *IEEE Trans. Magn.*, vol. 27, pp. 2708-2711, March, 1991.

[4] J. A. Stern, H. G. LeDuc and J. Zmuidzinas, "Quasi-optical josephson-junction oscillator arrays," *Proceedings of 1992 Applied Superconductivity Conference*

[5] B. Liu, M.J. Wengler and Arthur W. Lichtenberger, "Two Dimensional Josephson Junction Array Oscillators," to be published in *Digest of Technical Papers of the 17th International conference on Infrared and Millimeter Waves,*, December, 1992

[6] A.K. Jain, K.K. Likharev, J.E. Lukens, and J.E. Sauvageau, "Mutual phase-locking in Josephson junction arrays," *Physics Reports*, Vol. 109, pp. 309-426, 1984.

[7] B. Liu, "Mutual Phase-Locking of Two Josephson Oscillators due to High Frequency Coupling," Internal Report, Superconducting Electronics Group, University of Rochester, Feb., 1993

[8] B. Liu and M.J. Wengler, "Modeling of Quasioptical Josephson Oscillator," *IEEE Trans. on Applied Superconductivity*, Vol. 1, pp. 150-156, 1991

[9] M. A. H. Nerenberg, J. A. Blackburn and D. W. Jillie, "Voltage locking and other interactions in coupled superconducting weak links. I. Theory," *Physical Review*, B, Vol. 21, pp. 118 - 124, 1980.

[10] M. J. Wengler, "Submillimeter-wave detection with superconducting tunnel diodes," *Proc. IEEE*, Vol. 80, pp. 1810-1826, 1992.

[11] Niobium Design Rules, HYPRES Document Number 22-80601

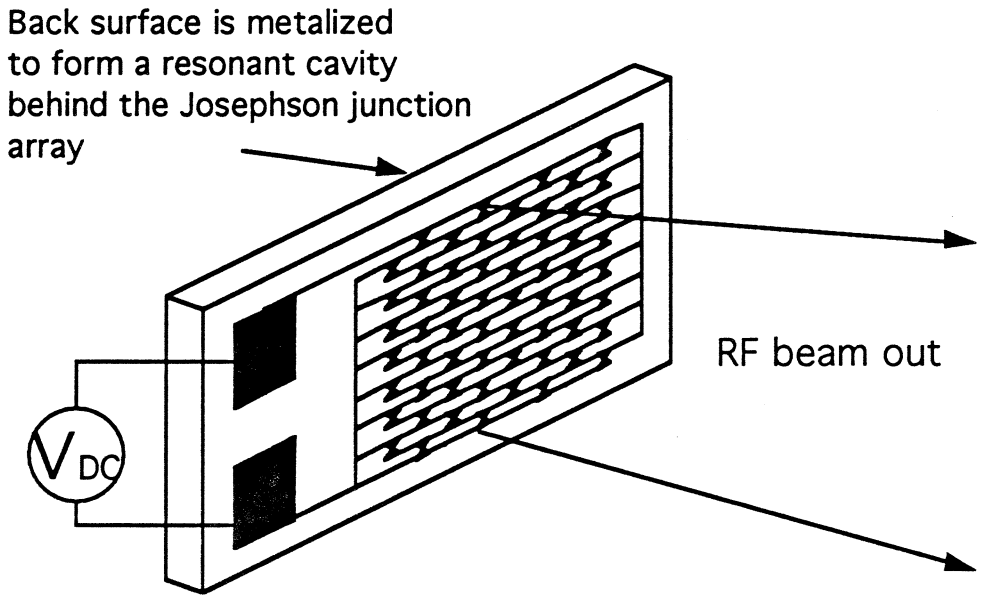

Fig. 1. A schematic design of the quasi optical Josephson oscillator with integrated bowtie antennas. There is one junction at the center of each bow-tie dipole antenna. The power is combined quasi-optically and coupled out from the broad side of the 2-D array of Josephson junctions. The dc wiring is shown so that all junctions are biased in parallel.

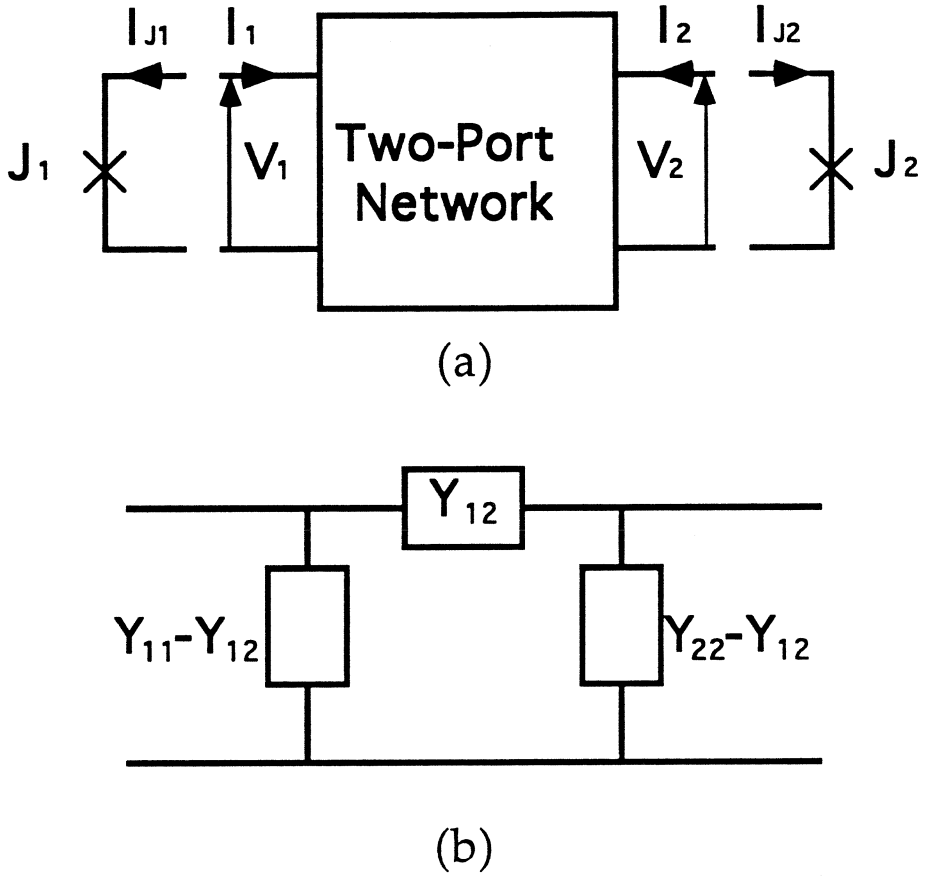

Fig. 2 Circuit model for two Josephson junctions coupled through a general complex circuit which is modeled as a two-port network (a), and the Π network equivalent circuit (b). Here J_1 and J_2 are bare Josephson junctions with parasitic capacitors and resistors included in the two port network.

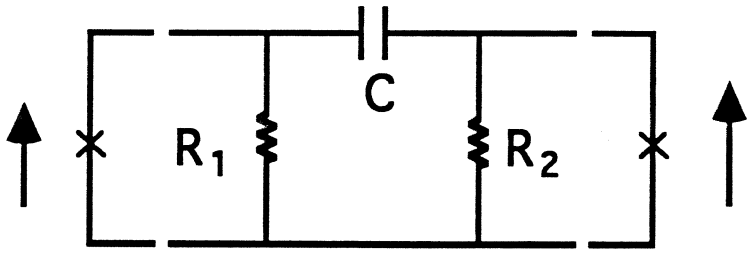

$\phi_1 - \phi_2 \approx 0$ at center of the locking range

(a)

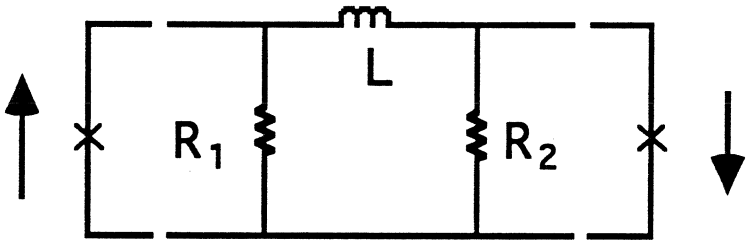

$\phi_1 - \phi_2 \approx \pi$ at center of the locking range

(b)

Fig. 3 Circuits of capacitively (a) and inductively (b) coupled two RSJs. The arrows indicate the Josephson current in the junctions. The ϕ_1 and ϕ_2 are phases of the two junctions respectively.

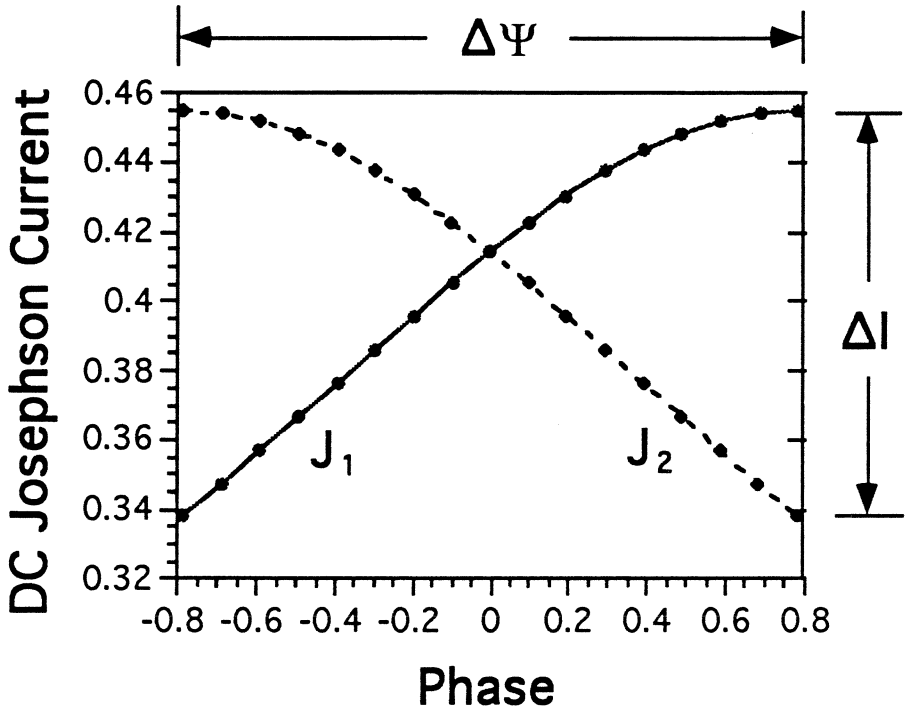

Fig. 4 The dc Josephson currents through two mutually phase-locked junctions by capacitive coupling versus the phase difference between the two junctions. The phase difference is $\Delta\phi = \phi_1 - \phi_2$. The locking range ΔI and the phase span across the locking range $\Delta\Psi$ are also shown in the graph.

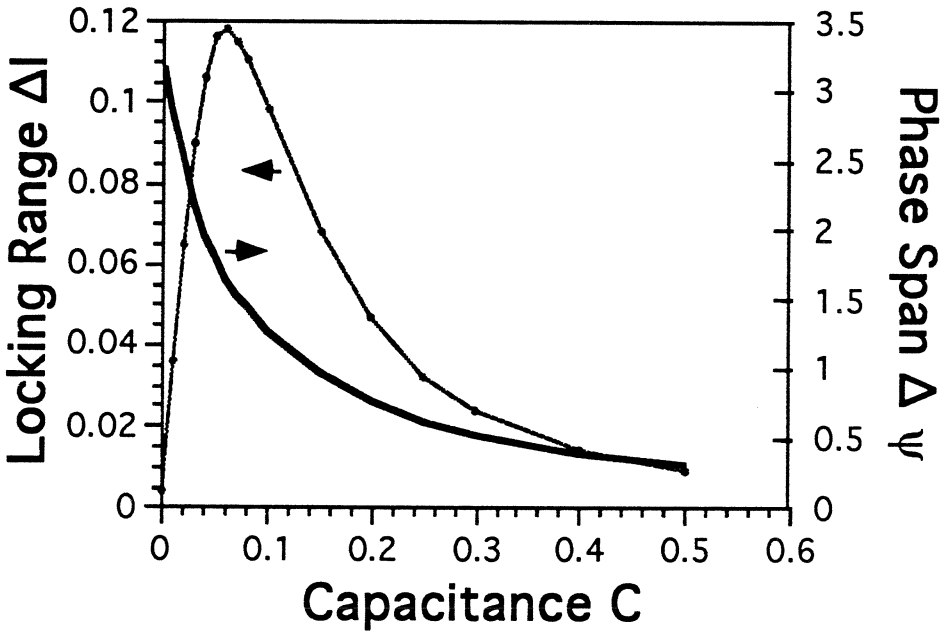

Fig. 5 The locking behavior for two capacitively coupled resistively shunted Josephson junctions as shown in Fig.4 (a). The left hand vertical axis is the locking range and the right hand vertical axis is the phase span across the locking range. Both ΔI and C are in the normalized units.

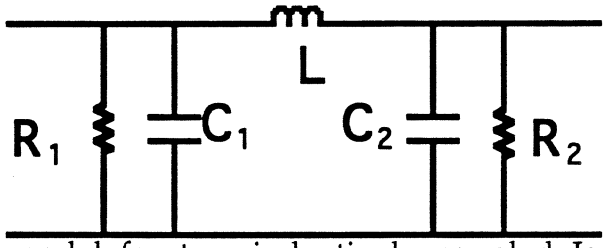

Fig. 6 Circuit model for two inductively coupled Josephson tunnel junctions. The ideal Josephson junctions are not shown.

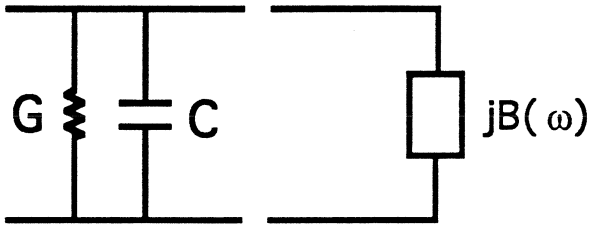

Fig. 7 The circuit model of a Josephson junction with an integrated tuning element. The G and C are the junction parasitic conductance and capacitance, and B(ω) is susceptance of the tuning element.

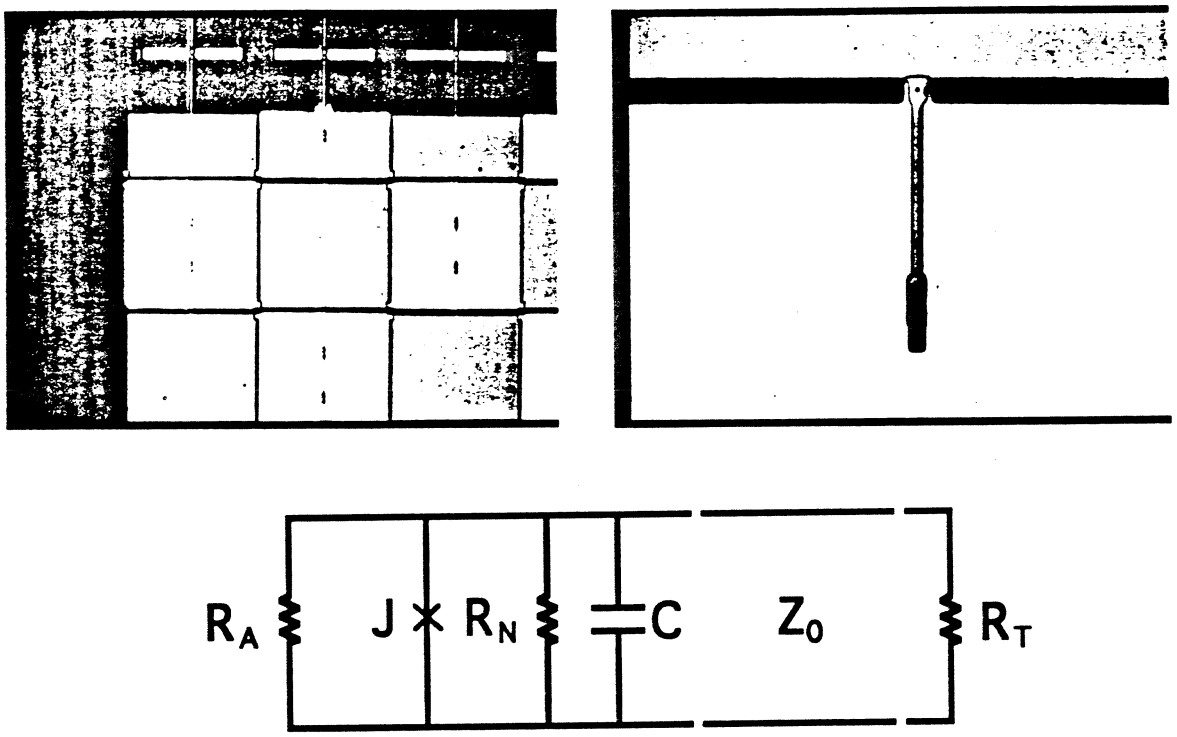

Fig. 8 Optical micrographs of a 2-D array of Josephson junctions with on-chip tuning elements fabricated at HYPRES, and the equivalent circuit of a unit cell in the array. There is a capacitor between two adjacent junctions to make the coupling between them capacitive. The tuning element is a resistor terminated microstrip transmission line. The Z_0 is the transmission line characteristic impedance, R_T the terminating resistor, R_N and C the junction parasitic resistance and capacitance, and R_A the antenna impedance.

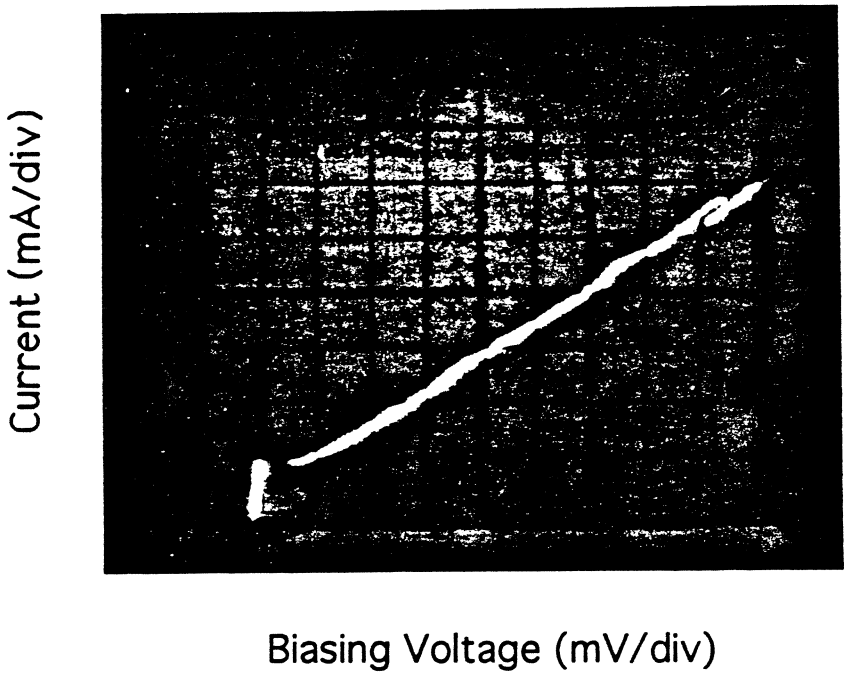

Fig. 9 I-V curve of a 2-D array of 14x14 Josephson junctions with on-chip resistor terminated tuning elements. The biasing scheme is that junctions in a same column are series biased, and all columns are parallel biased.

High Power Submillimeter Wave Source using Series Biased Linear Josephson Effect Array

Siyuan Han, Baokang Bi, Wenxing Zhang, A. H. Worsham, and J. E. Lukens
Department of Physics, SUNY at Stony Brook
Stony Brook, NY 11794, U.S.A.

As millimeter and submillimeter sources, phase-locked array of N Josephson junctions can overcome many shortcomings of the single junction source such as low source impedance, low output power, and large linewidth. In recent years it has been demonstrated that small linear arrays ($N \leq 100$) are capable of delivering several μW power to a load of 10 to 60 Ω in the frequency range of ~ 200 GHz to ~ 600 GHz with linewidth $\Delta f/f < 5$ x 10^{-6} [1-4]. For many applications one would like to have higher power and narrower linewidth which can be achieved by increasing the number of junctions deployed in the array since the output power increase as N^2 and linewidth decreases as $1/N^2$ for arrays having $NR_J = R_L$, where R_J and R_L are the junction's shunt resistance and the load resistance, respectively. There are two basic designs for the medium size ($N \sim 10^2$) and large size ($N \sim 10^3$) linear Josephson array: the quasi-lumped array and distributed array [4, 5]. In a quasi-lumped array the distance between two adjacent junctions is λ_0 (wavelength at designed operating frequency). In a distributed array a group of m junctions are closely packed together and the distance between two adjacent groups is λ_0. In both types of array the junctions are embedded in the transmission line structure which provides the long-range high-frequency electromagnetic couplings between the junctions. This coupling is essential to achieve mutual phase locking in the linear array. Compared to the quasi-lumped array, the distributed array requires less space and has smaller internal rf loss (especially as f_0 approaches the superconducting gap frequency of ~ 700 GHz for Nb).

The output rf power coupled to a load R_L from an linear array of N junctions can be written as

$$P_N = \frac{(\gamma N V_C)^2 R_L}{2(NR_J + R_L)^2} \tag{1}$$

when the source impedance matches to the load Eq. (1) becomes

$$P_N = \frac{(\gamma N V_c)^2}{8R_L} \tag{2}$$

where $V_c \equiv I_c R_J$ is the characteristic frequency of the junction, I_c is the critical current of the junction. γ depends on the dc bias voltage and is usually less than unity.

We have designed medium size ($N = 500$) distributed array ($m = 10$) oscillators for operation around 400 GHz. Each resistively shunted Nb/AlO/Nb tunnel junction is 5.2 μm^2 in size and has designed parameters of $I_c = 1.4$ mA ($J_c = 27000$ A/cm^2) and $R_J = 0..5\ \Omega$ which give $V_c = 0.7$ mV, $\beta_c \equiv 2\pi V_c R_J C_J/\Phi_0$ $\simeq 0.25$ and $\beta_L \equiv 2\pi I_c L_s/\Phi_0 \simeq 0.8$, where C_J and L_s are the shunt capacitance of the junction and the parasitic inductance associated with the shunt resistor, respectively. Φ_0 is the flux quantum. The total length of the array is about 50 λ_0 (at ~ 400 GHz). The Nb microstrip line is 250 nm thick and 8 μm wide with 670 nm thermally evaporated SiO between the microstrip line and the 340 nm thick Nb ground plane. This gives $Z_0 \simeq 12\ \Omega$. The designed output power to the 50 Ω load is about 100 μW around 400 GHz.

The Nb/AlO/Nb trilayer films were made at AT&T Bell Laboratory and the arrays were fabricated at IBM using the PARTS process developed by Ketchen et. al [6]. The measured parameters of a typical single junction from wafer #8 are $I_c = 2.5$ mA, $R_J = 0.56\ \Omega$ and $V_c = 1.4$ mV at 4.2 K. This corresponding to a Jc of about 50000 A/cm^2 which is about twice of the designed value. This results in a value of $\beta_c \simeq 0.56$ and $\beta_L \simeq 1.6$ which are quite far away from the designed value and unfavorable for phase-locking. The measured load resistance is 62 Ω.

The output rf power to the load resistor has been measured using the on-chip Josephson junction detectors. The amplitude of the rf current through the detector junction is estimated by comparing the size of the first Shapiro step and the suppression of the critical current to those obtained from the numerical simulations using measured V_c, I_c, and R_J. The estimated output rf power P_{rf} is 45 ± 15 μW using the suppression of I_c and is 50 ± 25 μW using the size of the first Shapiro step. The measured rf power is consistent with $P_{rf} = 65$ μW calculated from Eq. (1) [7]. The measurement of the output power spectrum $P_{rf}(f)$ is currently in progress.

In summary, a linear Josephson effect array oscillator with series dc bias has been designed to deliver rf power of about 100 μW to a 50 Ω load. The measured output power to the 62 Ω load at $\sim$400 GHz is 50 μW, lower than designed value., due to the difference between the target critical current and that of the sample.

This work is supported in part by SDIO-IST through the RADC, with support for the sample fabrication provided by CSE which is supported in part by DARPA, and by IBM and AT&T. We gratefully thank R.E. Miller and W.H. Mallison for making Nb/AlO/Nb trilayer films used in this work and M. Ketchen and A. Kleinsasser for fabricating the sample. We also thank A. Jain for valuable discussion.

[1] K. Wan, A.K. Jain, and J.E. Lukens, "Submillimeter wave generation using Josephson junctions arrays," Appl. Phys. Lett., Vol. 54, pp. 1805-1807, May 1989.

[2] K. Wan, B. Bi, A.K. Jain, L.A. Fetter, S. Han, W.H. Mallison, and J.E. Lukens, "Refractory submillimeter Josephson effect sources," IEEE Tran. Mag., Vol. 27, pp. 3339-3342, March 1991.

[3] Baokng Bi, Siyuan Han, and J.E. Lukens, "Radiation Linewidth of Phase Locked Distributed Array in the Submillimeter Wave Range", to be published in Appl. Phys. Lett.

[4] Siyuan Han, A.H. Worsham, and J.E. Lukens, "Complete Phase-Locking in a One-Dimensional Series Biased Josephson-Junction Array", to be published in the Proceedings of 1992 Applied Superconductivity Conference.

[5] Baokang Bi, Siyuan Han, and J.E. Lukens, "Distributed Josephson Junction Arrays as Local Oscillators", to be published in the Proceedings of 1992 Applied Superconductivity Conference.

[6] M.B. Ketchen, D. Pearson, A. Kleinsasser, C.-K. Hu, M. Smyth, J. Logan, K. Stawiasz, M. Jaso, K. Petrillo, M. Manny, S. Basavaiah, S. Brodsky, S.B. Kaplan, W.J. Gallagher, and M. Bhushan, "Sub-μm, planarized, Nb-AlO_x-Nb Josephson process for 125 mm wafers developed in partnership with Si technology," Appl. Phys. Lett., Vol. 59, pp. 2609-2611, November 1991.

[7] In deriving Eq. (1) it is assumed the junctions can be approximated well by the RSJ model. However, this condition is not met by the junctions used in this work. Thus Eq. (1) can be used only to give a rough estimate of P_{rf}.

CENTRAL FREQUENCY/WIDEBAND QUASIOPTICAL JOSEPHSON OSCILLATOR ARRAYS

Aleksandar Pance*, Gordana Pance and Michael J. Wengler
University of Rochester
Department of Electrical Engineering
Rochester, NY 14627

Abstract

In this paper we present new design of quasioptical Josephson oscillators: the Central Frequency/ Wideband design. In this design, tuning structures composed of inductances, radial stubs and quarter wave transformers are integrated with every junction of the array in order to tune out the junction capacitance and match the junction impedance to the antenna impedance for the efficient output power coupling. Each junction feeds an antenna and power from individual junctions is quasioptically combined. We present a variation of the design where a sub-array replaces every single junction of the array. Preliminary results for the array designed for 98 GHz fundamental frequency and fabricated in Hypres Nb/AlO_x/Nb technology are presented.

Introduction

In recent years there has been a growing effort within the superconducting research community to develop oscillators based on Josephson junction arrays. Submillimeter Josephson oscillator arrays with power levels of the order of 1μW have been made at Stony Brook [1] and NIST [2]. Two-dimensional array of parallel biased Josephson junctions coupled to small antennas with quasioptically combined output power has been proposed as a promising approach for achieving larger power levels and reasonable radiation linewidths [3]. It has been shown that the performance of these arrays would critically depend on the way the Josephson junctions' capacitances are tuned out [4]. We have proposed arrays with microstrip tuning structures integrated with every junction as potentially the best solution [4]. Because of inherent frequency limitations of tuning circuits, these arrays are designed for one central frequency with the requirement of as large bandwidth as possible. This design will be referred to as the Central Frequency/Wideband (CFW) Design. Here we describe the basic CFW design and one of its modifications, and present preliminary results obtained from arrays fabricated in Nb/AlO_x/Nb technology.

Generic CFW array oscillator design

The generic CFW design is presented in Figure 1. MS2 is a very short length transmission line whose inductance tunes out the junction capacitance. A radial stub at the end of MS2 serves as the broadband short. MS1 is the quarter wave transformer that matches the junction impedance to the antenna impedance. That way, all of the rf power produced by the junction is coupled to the

---

* Present address: Conductus, Inc., 969 West Maude Ave, Sunnyvale, CA 94086

antenna and radiated in the broadside direction. This design has successfully been used in SIS mixers [5] (see elsewhere in this issue). A detailed account of this and other applicable designs of tuning elements can be found in [6].

We have designed 492 GHz CFW arrays for the following parameters: critical current density j_c = 4000 A/cm^2, junction capacitance C_j = 60 fF/μm^2 and junction area A = 7 μm^2. The impedance of the log-periodic antenna is around 79 Ω on silicon substrate and is independent of frequency in the designed frequency range. Since there is a basic trade-off between the coupling and the bandwidth, careful design of the tuning elements provides a predicted bandwidth of 80 GHz with 75% power coupling at the central frequency of 492 GHz (Figure 2). The design of the tuning structure is performed in Touchstone [7] with effects of the superconducting kinetic inductance accounted for. The tuning element design values are: Z_1 = 18 Ω, l_1 = 62.5 μm (MS1) and l_2 = 3.5 μm, Z_2 = 15 Ω (MS2). The 360 junction array is predicted to deliver 20μW of RF power at 492 GHz. A dramatic increase in performance, in terms of both the bandwidth and the coupling is possible with advanced sub-micron and high current density fabrication processes.

Figure 3 shows the fabricated 492 GHz array. It employs 360 log-periodic antennas on a chip 6 mm X 6 mm in size, with integrated tuning structures on one arm of the antenna. All junctions are DC biased in parallel. The array periods are d_X = 240 μm, d_Y = 264 μm. Unfortunately, this fabrication run did not yield working devices because of the minor problem during fabrication. New fabrication runs should be performed in the near future.

Antenna-coupled lumped array

A ready extension of the generic CFW design can be made for arrays at relatively smaller frequencies. Single junction can be replaced by a lumped parallel sub-array of junctions in order to increase the output power. The overall size of the sub-array must be much smaller than the wavelength at the desired operation frequency. Usual tuning structures can be used to tune out the capacitance of the sub-array and to transform the small impedance of the sub-array to the large antenna impedance. If an oscillator is composed of several antennas and sub-arrays biased in parallel, the power from different sub-arrays would be quasioptically combined.

Figure 4a shows a single sub-array oscillator fabricated in Nb/AlO_X/Nb technology at Hypres, Inc. A compact parallel array of 64 Josephson junctions is placed on one arm of log-periodic antenna on a silicon substrate (Figure 4b). A microstrip transmission line is used as a coupling structure between the sub-array and the antenna. Its electrical length is somewhat bigger than 90° so that the excess portion tunes out the big capacitance of the sub-array and the 90° portion serves as an impedance transformer. Although the bandwidth of this design is rather narrow, it has a nice feature that it works not only at the designed frequency f_0, but at a set of frequencies approximately given by the sequence

$$f_0, 3f_0, 5f_0, ...(2k-1)\ f_0. \qquad (1)$$

Array from Fig. 4 was designed for the fundamental frequency of f_0 = 98 GHz. The fabrication process parameters were j_c=983A/cm^2, C_j=38fF/μm^2, A=12.2 μm^2, R_N=16.4 Ω. In order to increase the available power, we have placed identical microstrip-coupled sub-array on the opposite arm of the antenna. The two sub-arrays feed the antenna in parallel. The schematic of the electrical circuit is given in Figure 5. The microstrip line was designed with impedance of Z=1.42 Ω and electrical length of 93° at 98 GHz. The measured dc I-V curve of the whole array reveals a series of seven resonant peaks (Figure 6a). A small amount of DC magnetic field was applied

along the chip surface to enhance the resonances. When no magnetic field is applied (Figure 6.b) one of the steps (5^{th} counted from $V_{dc}=0$) has disappeared. The visible critical current (1.25mA , Fig. 6b) is much smaller than about 15mA expected from the size of the quasiparticle current rise at the gap voltage, which we attribute to noise. The approximate frequencies of resonant peaks are inferred from the I-V curve and are given in Table 1 below.

Resonant step #	Frequency [GHz]
1	81
2	129
3	210
4	243
5	356
6	405
7	518

Table 1. Resonant steps from the I-V curve (Figure 6) of the array in Figure 4.

The first step is at the fundamental frequency f_0 = 81 GHz and is down-shifted from the designed 98 GHz value because of the slight discrepancy between the designed and obtained fabrication parameters. Steps #4 and #6 correspond to higher "oscillator" modes given by k=2 and k=3 (1). At these three frequencies, the two sub-arrays work coherently supplying the RF power to the antenna. The remaining resonant peaks roughly correspond to the sequence of modes with resonant frequencies $(2j-1)\frac{f_0}{2}$, where j = 2, 3, 5 and 6 for the steps #2, #3, #5 and #7, respectively. In these modes, one sub-array supplies the RF power to the other sub-array, and practically no power is radiated through the antenna.

From the size of the resonant steps in the "oscillator" modes we estimate that the available RF power is less than a μW. The experiments for coupling the array radiation to the off-chip SIS detector are in progress . For radiated power in the range of μW, a two-dimensional array of parallel biased antenna/sub-arrays should be employed.

Discussion and Summary

We have presented a new Central Frequency/Wideband design of quasioptical Josephson oscillator arrays that effectively deals with the parasitic junction capacitances. Because of the independent tuning of individual junction capacitances, CFW oscillators would tolerate large scattering in process parameters. Further, because of impedance matching between the junctions and the antennas, these arrays would be very efficient sources. The major disadvantage of the CFW design is the size of the unit cell, i.e. much smaller number of junctions can be utilized per given array area, compared to compact 2-D arrays. This disadvantage is offset by the array efficiency. First fabricated arrays show evidence of likely coherent array operation at a set of frequencies. The design promises Josephson submillimeter oscillators of unprecedented performance.

Acknowledgments

We are pleased to acknowledge Hypres, Inc. for the fabrication of the antenna-coupled lumped-array oscillator. This work was supported by the Air Force Office of Scientific Research grant AFOSR-90-0233. Gordana Pance was partially supported by the IEEE Microwave Theory and Techniques Society Graduate Fellowship.

References

1. K. Wan, B. Bi, A.K. Jain, S.H. L. A. Fetter and J.E. Lukens, "Refractory submillimeter josephson effect sources," *IEEE Trans. Magn.*, vol. 27(2), 1991.

2. S.P. Benz and C.J. Burroughs, "Coherent emission from two-dimensional Josephson junction arrays," *Appl. Phys. Lett.*, vol. 58(19), pp. 2162-2164, 1991.

3. M.J. Wengler, A. Pance, B. Liu and R.E. Miller, "Quasioptical Josephson Oscillator," *IEEE Trans. Magn.*, vol. 27(2), pp. 2708-2711, 1991.

4. A. Pance, *Two-Dimensional Josephson Arrays for Submillimeter Coherent Sources*, Ph.D. Thesis, University of Rochester, 1992.

5. G. Pance and M.J. Wengler, "Broadband Quasioptical SIS Mixers with Large Area Junctions," in *Proceedings of Fourth International Symposium of Space Terahertz Technology,* University of California, Los Angeles, 1993.

6. G. Pance and M.J. Wengler, "Integrated Tuning Elements for Millimeter and Submillimeter SIS Mixers," in *Proceedings of 1992 IEEE International Microwave Symposium,* Albuquerque, NM, 1992.

7. *EESOF Inc., Westlake Village*, CA.

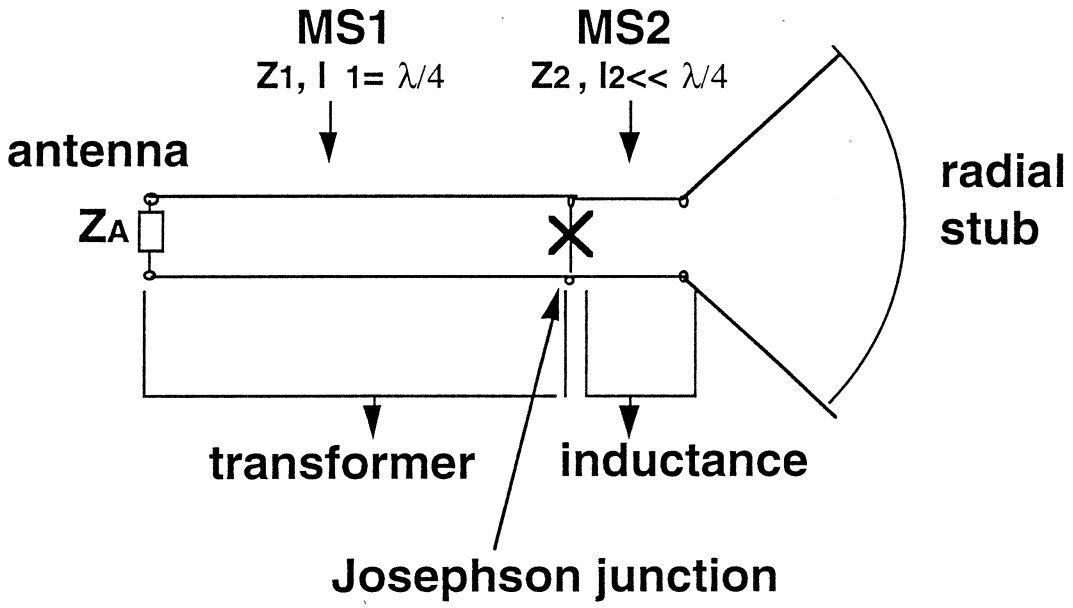

Figure 1. Electrical circuit of the tuning structure for the generic CFW design.

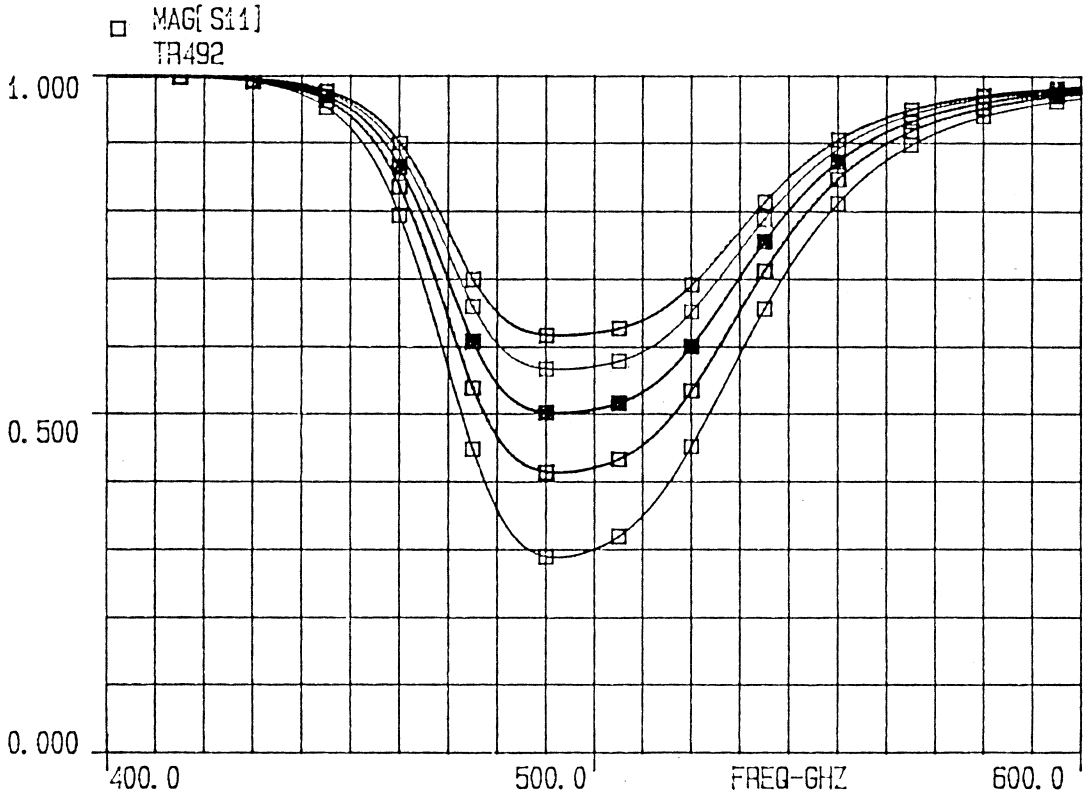

Figure 2. Predicted coupling between the junction and the log-periodic antenna for the 492 GHz CFW design of Figure 1. Different traces are for variation of junction critical current from the designed value: -20% (topmost trace), -10%, 0%, 10% and 20% (bottom trace).

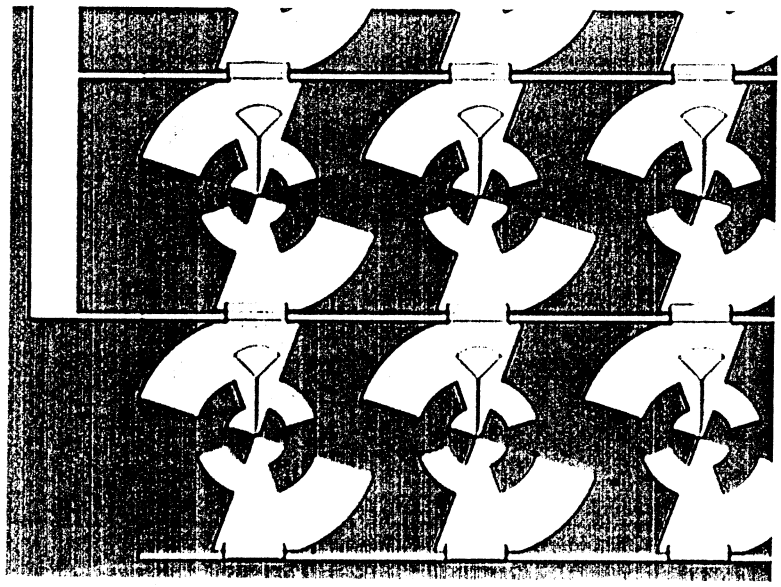

Figure 3. Photograph of a portion of the 360 junction 492 GHz CFW array fabricated in $Nb/AlO_X/Nb$ technology.

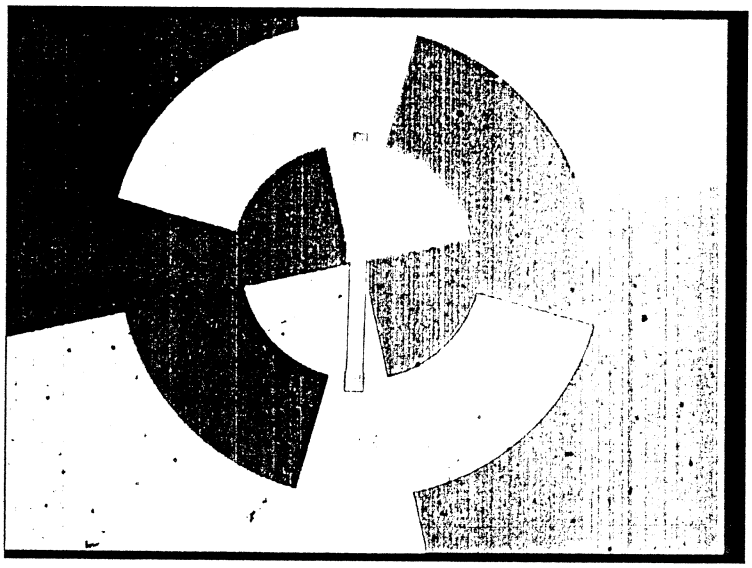

Figure 4a. Photograph of th antenna-coupled 98 GHz lumped array of 128 junctions fabricated at Hypres, Inc.

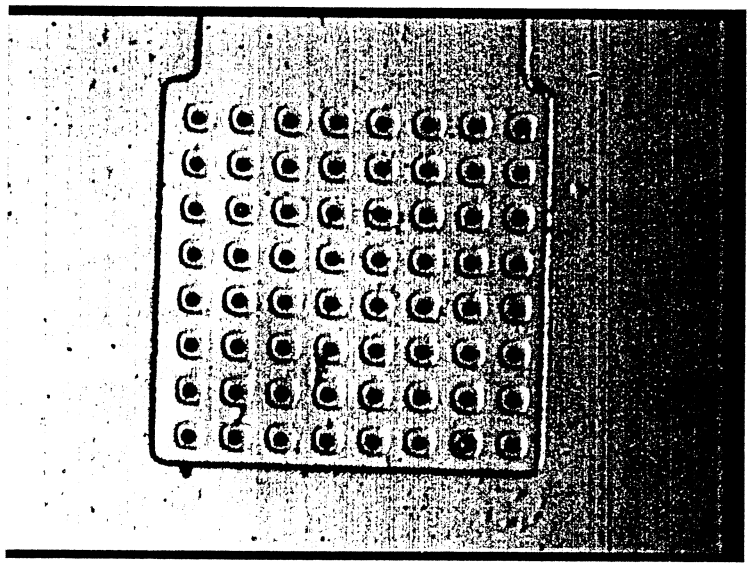

Figure 4b. Detail showing the 8 x 8 sub-array of 12 μm^2 junctions on one arm of the antenna.

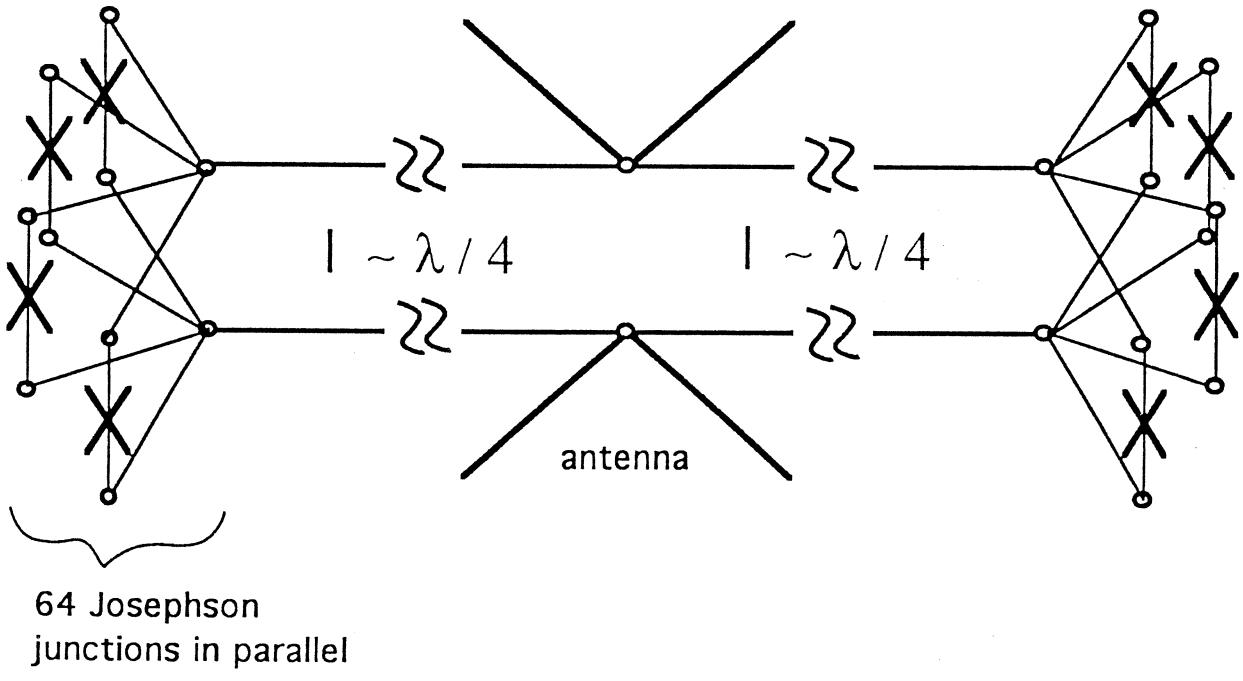

Figure 5. Electrical circuit of the array in Figure 4.

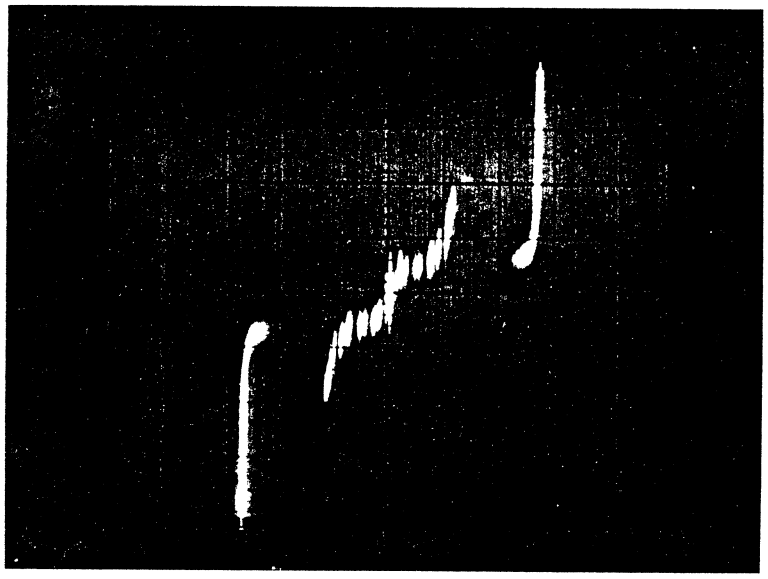

(A)

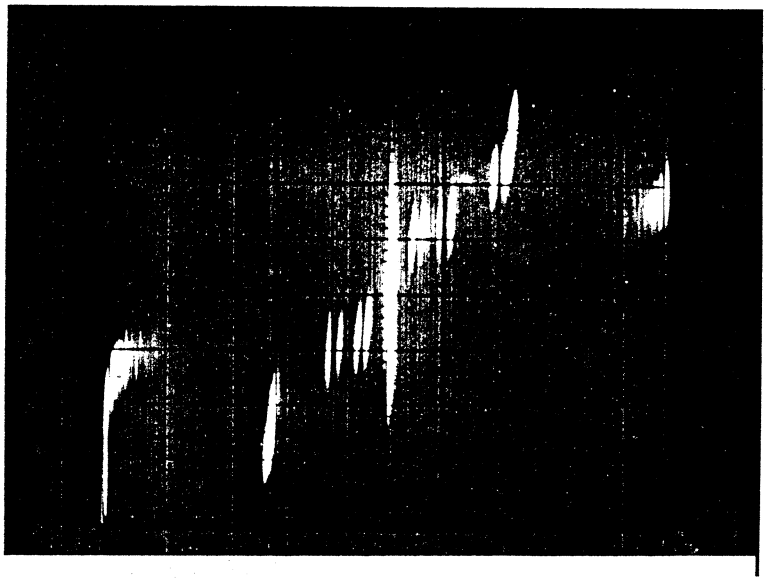

(B)

Figure 6. Measured dc I-V curve of the array from Fig. 4: (A) with small amount of applied magnetic field (scale: 1mA/div.; 1mV/div.) and (B) with no magnetic field applied (scale: 0.5mA/div.; 0.5 mV/div.).

LINEWIDTH MEASUREMENTS OF FLUX-FLOW JOSEPHSON OSCILLATORS USING A CAD DESIGNED INTEGRATED SUB-MM WAVE RECEIVER

Y.M. Zhang, D. Winkler, and T. Claeson
Department of Physics
Chalmers University of Technology
S-412 96 Göteborg, SWEDEN

ABSTRACT

By using a superconducting integrated sub-mm wave receiver, the linewidth of a flux-flow type Josephson oscillator (FFO) was measured to be less than 2.1 MHz in the band 280–330 GHz. The output power coupled to a 10 Ω microstripline was about 0.5 μW, and could be adjusted by changing the current bias of the oscillator junction.

The integrated receiver consists of two identical Josephson flux-flow oscillators and an SIS (superconductor-insulator-superconductor) mixer. We can determine the composite linewidth of the oscillators by mixing them down to an intermediate frequency in the SIS mixer. The FFOs are connected to the SIS mixer via centerfed interdigital capacitors. One FFO is well coupled to the SIS mixer by using a 3-step Chebychev microstripline transformer and a fairly large interdigital capacitor, while the second FFO has about 15 - 20 dB weaker coupling. A strip inductor, *rf*-terminated by a radial stub resonates out the SIS junction capacitance at about 340 GHz. Radial stubs were also used as RF chokes for the *if*-line (4 GHz). The FFOs and the SIS element are made of Nb/Nb-oxide/PbBi tunnel junctions.

The circuit was optimized by careful CAD modeling (HP Microwave Design System). Normal conductors were used with the resistivity set to zero. Microstripline widths and lengths were recalculated for the superconducting case with the London penetration depths of the electrodes (Nb and PbBi) taken into account. After adjusting the area of the SIS element and the length of the tuning strip inductor, a good response was observed from 280 to 330 GHz, with the LC resonance at 340 GHz. The power was high enough to pump the SIS mixer.

1. INTRODUCTION

For space born missions, low weight and small volume are required. When it comes to imaging arrays, this is even more of a concern. By using SIS (superconductor-insulator-superconductor) mixers with much less local oscillator (LO) power requirements some of the problems can be alleviated. Even better would be if the external LO could be replaced with an on-chip fully integrated source. The concept of using superconducting technology for the construction of low-noise, integrated millimeter or submillimeter-wave receivers has been considered as a promising idea for many years. However, not until recently has sufficient progress been made to

really demonstrate the possibilities. One way to achieve practical oscillators is by using coherent, mutually phase-locking arrays. Bi *et al.* [1] measured a 10 MHz linewidth by mixing two Josephson array oscillators at 250 GHz. Sufficient available power existed to pump an SIS mixer, but the number of junctions in the oscillator or the coupling strength to the SIS mixer had to be fixed at the design stage to obtain the optimum local oscillator power for the design frequency .

Another way to achieve a practical oscillator is by using the fluxon (flux quantum $\Phi_0=h/2e$) propagation in a long Josephson tunnel junction (LJJ), either in a resonant mode (back and forth propagation of solitons) or in a unidirectional flux-flow mode. A soliton (fluxon) is an electromagnetic pulse and gives rise to the emission of a pulse of electromagnetic energy when it hits the end of the junction. If the arrival of solitons at one end of the junction is periodic, *rf* radiation is emitted. The propagation mode of the fluxon in a LJJ depends on the junction quality factor Q_J, which is related to the junction losses as [2]

$$Q_J = ((\omega_0/\omega_J)^2 \beta + \alpha)^{-1} \quad , \qquad (1)$$

where $\omega_0=(2\pi/\Phi_0)V_{dc}$ is the frequency of Josephson oscillation (V_{dc} is the dc voltage of the junction, ω_J is the Josephson plasma frequency, β is the surface loss, and α is the quasiparticle loss).

The first type of fluxon oscillator is called resonant soliton oscillator (RSO), which uses a long junction with a high quality factor Q_J (low quasiparticle loss α). In order to achieve a high Q_J, the junction should have a low critical current density j_c [3]. Driven by the bias current, a fluxon travels along the junction until it reaches the junction boundary, where it is reflected as an anti-fluxon, which in turn is driven in the opposite direction. This process is repeated, resulting in a microwave emission at a frequency given by [4]

$$f = V_{dc} / 2\Phi_0 = n u / 2L \quad , \qquad (2)$$

where u is the average fluxon velocity, n is the number of fluxons moving in the junction of length L. A RSO is operated at zero or a relatively weak external magnetic field. Its oscillation frequency is determined mainly by the junction length L rather than the applied field and bias

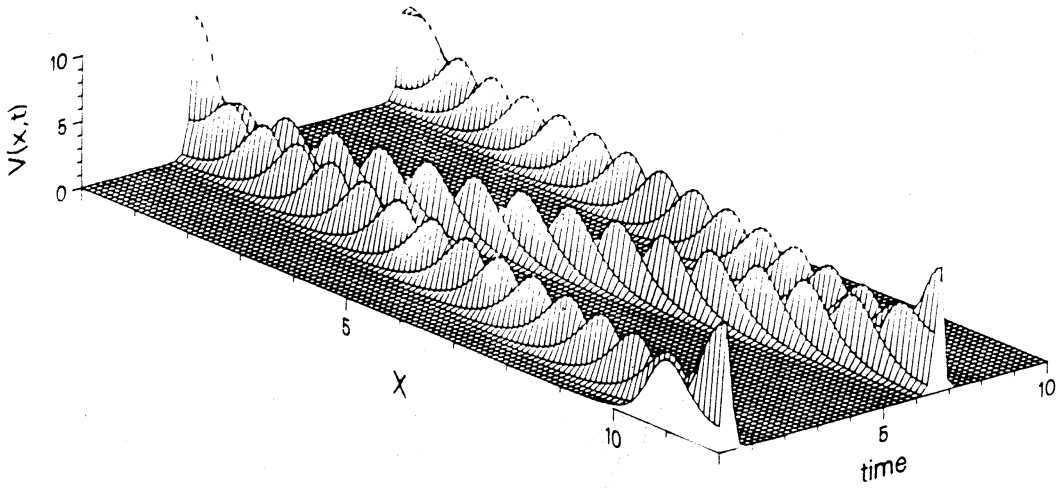

Fig.1 Computer simulation showing time-dependent junction voltage V(x,t) of a LJJ in the single resonant soliton (n=1) case for parameters: $L/\lambda_J=12$, $\alpha=0.05$, $\beta=0.02$, $\gamma=0.35$ (at zero magnetic field).

current. This suggests a rather well defined frequency. The resulting resonant step in the characteristic is commonly called a zero field step (ZFS). When the oscillator is biased on a zero field step, the emitted radiation is characterized by a very narrow output linewidth - about 1 kHz at 10 GHz [5]. A main weakness of this kind of oscillators is its low output power - reported powers coupled to SIS detectors are less than 10 nW at ~100 GHz [6]. However, Cirillo *et al.*[7] have estimated a power of ~100 nW at 75 GHz into a tightly coupled small junction. The low output power is partially due to the low j_c requirement for a RSO. Also, the output voltage waveform of a RSO consists of fairly sharp spikes, which suggests that the output power is delivered into a broad range of harmonics rather than being concentrated at the fundamental frequency. In Fig.1, we show a computer simulation for the single soliton propagation in a LJJ with overlap geometry. Note that this figure is in normalized units: distance x is normalized to the Josephson penetration depth λ_J, time is normalized to the inverse of ω_J, and γ is the bias current I_B normalized to the maximum zero-voltage Josephson current I_c. Another weakness of a RSO is its upper oscillation frequency limited by the junction length L which should be much larger than the Josephson penetration depth λ_J. This makes it difficult to operate at sub-mm wavelengths.

The second type of fluxon oscillator is called flux-flow Josephson oscillator (FFO). It is based on a long Josephson junction working in the viscous unidirectional flux-flow regime. In order to maintain fluxons moving unidirectionally under the Lorentz force, a dc magnetic field H_e is applied in the plane of the junction, and the junction should have a low quality factor Q_J (high quasiparticle loss α). This means a high j_c value is necessary for an FFO [6]. When the velocity of the flux-flow u approaches that of the electromagnetic wave $\bar{c}$ propagating along a LJJ, a resonant like current step appears in the I-V characteristic. This resulting step is commonly called velocity-matching step (VMS). A computer simulation illustrating flux-flow in a LJJ with overlap geometry is shown in Fig.2. The oscillation frequency can be tuned over a wide range by changing the applied field

$$f = V_{dc}/\Phi_0 = ud\mu_0 H_e/\Phi_0 \quad . \qquad (3)$$

Here, d is the effective magnetic thickness of the junction barrier and μ_0 is the permeability of free space. The FFO was early investigated both experimentally and by computer modeling by Nagatsuma *et al.* [2,8,9] and Zhang and Wu [10]. Relatively large output power in the sub millimeter wave band was obtained for this type of oscillator, e.g., powers of about 1 μW (into a small junction detector) up to 400 GHz was reported early [8], and power of about 0.5 μW coupled to a 10 Ω microstripline at 280 - 330 GHz was recently reported [11]. The high output power of an FFO is due to two reasons: i) high current density leads to a high bias current; ii) fluxons reach the output end in a tightly packed unidirectional train, thus the output voltage waveform is nearly sinusoidal, which suggests the output power is largely concentrated at the fundamental frequency. In principle, there is no limitation to the operation frequency of this kind of oscillator up to the energy gap of the superconducting electrode. However, there were serious doubts about its usefulness since no linewidth measurements had been done until recently. Its oscillation frequency, which relates to the vortex density inside the junction, depends strongly on the value of the external magnetic field. This means there exists another source of fluctuations that might broaden the output spectral linewidth. Ustinov *et al.* [12] have measured a linewidth of 120 kHz of an FFO working at 76 GHz. Koshelets *et al.* [13] have used an FFO integrated with an SIS mixer. They mixed the signal of a backward wave oscillator with the LO signal produced by the FFO in the SIS element, and measured an upper value of the linewidth to be about 1 MHz in the band 82 - 112 GHz.

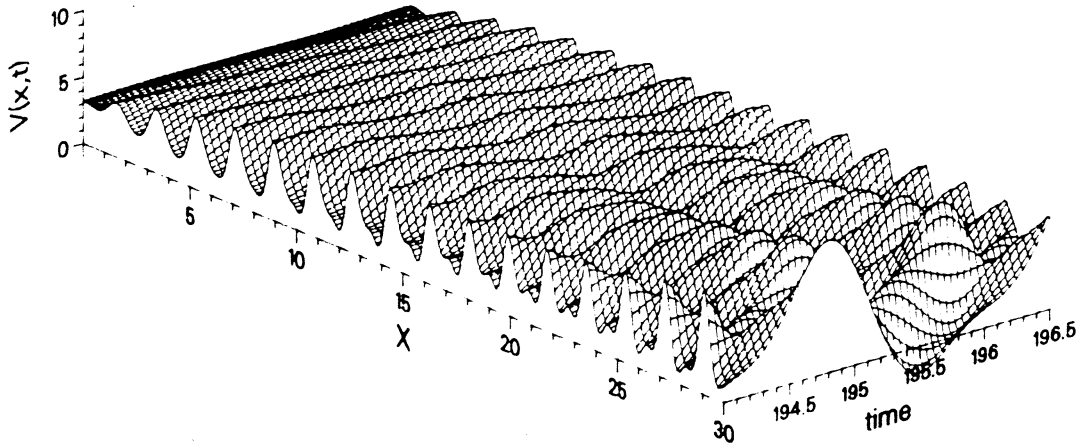

Fig.2 Computer simulation showing time-dependent junction voltage V(x,t) of a LJJ in the flux-flow regime for parameters: $L/\lambda_J=30$, $\alpha=0.25$, $\beta=0.001$, $\gamma=1.015$ (in normalized units and at normalized magnetic field βe [10]).

In this paper, we report the design of an integrated receiver in which we mix the output oscillations from two identical fluxon oscillators in a small SIS mixer and determine the linewidth of the oscillators from the intermediate frequency (*if*) with a spectrum analyzer. The circuit was optimized by using CAD modeling. We also show that a long-junction oscillator could be operated in either the resonant propagation mode or the flux-flow mode, depending on the critical current density of the oscillator junction.

2. DESIGN

To avoid problems of coupling mm- and sub-mm waves between different wave guide systems, and to be able investigate a variety of frequencies, we decided to make a fully integrated receiver where the output signals (local oscillator f_{LO} and a weaker signal f_S) of two fluxon oscillators are mixed in an SIS element to a lower intermediate frequency ($f_{if}=|f_{LO}-f_S|$). In this way, the two fluxon oscillators and the SIS mixer could be (i) fabricated all on the same chip, (ii) coupled by microstripline circuitry, and (iii) analyzed using only one coaxial line and dc-bias leads.

The circuit, which was designed to operate around 350 GHz, is outlined in Fig.3. Before describing the *rf* design of the total circuit and the CAD modeling, we will first examine the requirements on the fluxon oscillators and the SIS mixer.

2.1 Oscillators

In Fig.4, we show a SEM photograph for a receiver circuit. The long Josephson junctions (LJJ) are constructed in an overlap geometry with a length $L=400\mu m$ ($>>\lambda_J$). The bias current I_B is applied perpendicular to the long dimension of the junction. In order to reduce the self field at the end where vortices are nucleated, a projection length of $50\mu m$ is employed (e.g., see left end of FFO1 in Fig.4). The characteristic impedance of a LJJ of width w is given by

$$Z_0 = \frac{120\pi}{w\sqrt{\varepsilon_r}}\sqrt{td} \qquad (4)$$

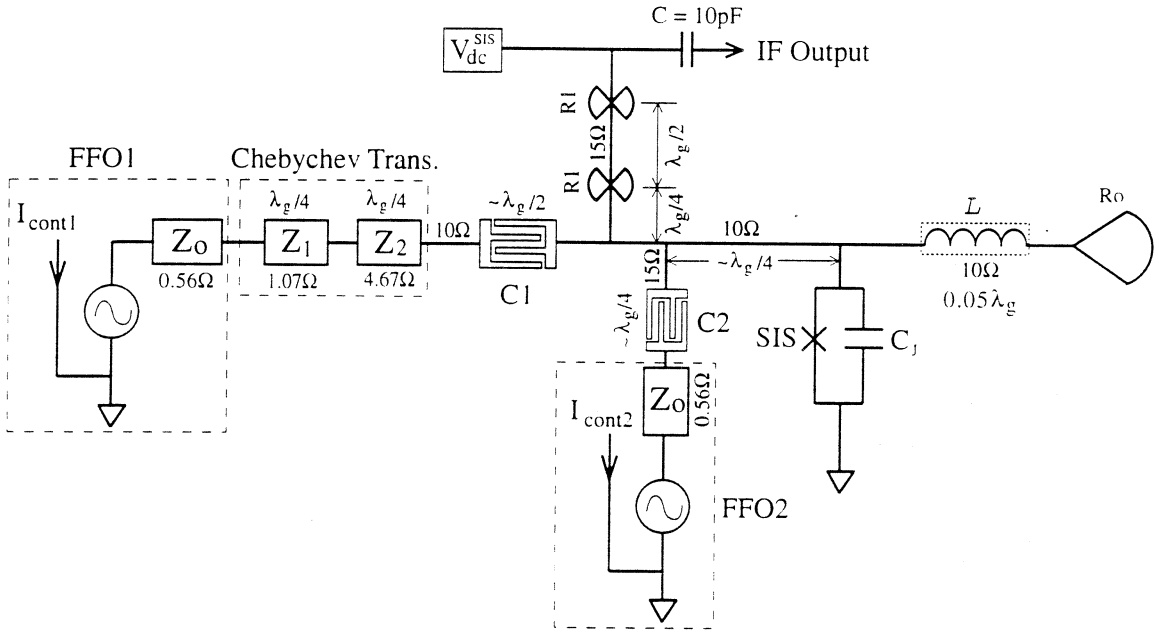

Fig.3 The modeling circuit for measuring the linewidth of FFOs. By mixing two similar FFOs in the SIS element, we can determine the combine linewidth of the FFOs from the *if* product. FFO1 is used as a local oscillator, while FFO2 serves as the signal source.

For Nb/NbOx/PbBi junctions, the dielectric constant of the junction barrier (Nb_2O_5) $\varepsilon_r = 29$, the barrier thickness t ≈2 nm, and the magnetic thickness $d = t + \lambda_{Nb} + \lambda_{PbBi} \approx 287$ nm. In order to match the output impedance Z_o of the oscillator to the load, and to avoid resonant modes along the small dimension of the junction, we choose a narrow width ($w = 3\ \mu m$) for the LJJs ($Z_o = 0.56\ \Omega$).

The junction critical current density, j_c, is an important fabrication parameter that controls the operation mode of a LJJ. We have shown that a long-junction oscillator could be operated in either the resonant propagation mode or the flux-flow mode, depending on the junction current density [6]. Here, we give a rough estimate of the lowest j_c value for the flux flow mode. For simplicity, we use the junction normal state resistance R_n instead of the dynamic resistance R_d of the quasiparticle current at $V = V_{dc}$. Thus, the quasiparticle loss α can be written as [3]

$$\alpha = \frac{1}{I_c R_n}\sqrt{\frac{j_c \Phi_o}{2\pi C}} \quad , \tag{5}$$

where C is the junction capacitance per unit area. The Josephson penetration depth λ_J is given by

$$\lambda_J = \sqrt{\frac{\Phi_o}{2\pi \mu_o j_c d}} \quad . \tag{6}$$

Combining Eq.(4) and (6) together, we get

$$\alpha L/\lambda_J = \frac{j_c L w Z_o}{I_c R_n} \quad . \tag{7}$$

The condition for supporting the unidirectional flux-flow is $\alpha L/\lambda_J \geq 2$. Taking the typical value for Nb/NbOx/PbBi junctions $I_c R_n = 1.8$ mV, we get $j_c \geq 540\ A/cm^2$ ($L = 400\ \mu m$, $w = 3\ \mu m$,

$Z_O = 0.56\Omega$). Actually j_c of an FFO should be at least 2 times higher than this value, because the dynamic resistance R_d is usually a few times higher than R_n.

The external magnetic field to sustain the flux motion in a LJJ can be provided by injecting *dc* current through the base electrodes or through a separate control line (another Nb layer) under the LJJs. Two separate local fields were applied to FFO1 and FFO2 (as indicated by I_{cont1} and I_{cont2} in Fig.3). For obtaining a uniform distribution of bias current along the LJJ, we used multi-finger bias leads for both base and top electrodes (see Fig.4).

2.2 SIS detector

The SIS element should be well matched to the LJJ. A small junction area (i.e. small capacitance) is needed to get a reasonably large value of the tuning inductance for resonating out the junction capacitance at 340GHz. The junction capacitance C_J is inductively compensated by a strip inductance L and *rf* terminated by a radial stub R_0. The outer radius r_2 of the radial stub was calculated approximately from [14]

$$r_2 - r_1 = \lambda_g / 2\pi \quad , \tag{8}$$

where the inner radius r_1 was taken as the half width of the 10 Ω microstripline (λ_g is the wavelength in the microstripline). The width of the 10 Ω microstripline is 6.9 μm for the superconducting case and 5.4 μm for the normal conductor. The outer radius was then optimized by the CAD simulation and recalculated for the superconductor case (r_2=35.2 μm).

The LC resonance frequency, given by $f_0 = 1/2\pi\sqrt{LC_J}$, is very sensitive to the length of the strip inductance and the area of the SIS junction. Fortunately, the resonance frequency could usually be determined from the I-V curve of the SIS mixer, which had an additional step structure at the corresponding Josephson frequency ($f_0 = 2eV/h$). From the LC resonance and by measuring the actual junction area in an SEM, we could get a fairly good control of the tuning of the SIS mixer for the second batch of samples that was fabricated. We varied junction sizes from 0.5 μm^2 to 4 μm^2 for different chips. The inductance length is 13.5 μm long for a junction size of 0.65 μm^2. For a 4μm^2 large junction, the inductor length would only be 2.2 μm long, which should be compared to the junction width and the microstripline width of 6.9 μm. Hence, the actual dimensions of the inductance is very critical. To avoid this difficulty, we have also made circuits, where two (about twice as long) inductors with separate radial stubs have been connected in parallel with the SIS element. The bandwidth of the SIS mixer around LC resonant frequency f_0 is given by

$$\frac{\Delta f}{f_0} = \frac{1}{\omega_0 R_n C_J} = \frac{j_c}{\omega_0 (I_c R_n) C} \quad . \tag{9}$$

Thus, the available bandwidth of the mixer is not dependent on the junction area, but depends on its j_c value [15,16]. Knowing for Nb/NbOx/PbBi junctions, $I_c R_n = 1.8$mV, $C = 140$ fF/μm^2, we acquire $\Delta f = 6.3$ GHz for j_c=1 kA/cm^2. By increasing j_c ten times to 10 kA/cm^2, we can have a quite wide bandwidth of 63 GHz. This indicates the importance of having a high j_c SIS junction for a broad band response. Since both FFOs and the SIS junction on a chip were made within the same process steps, they had almost the same j_c value. This means that for a LJJ working in the resonant mode, the response band for an SIS detector on the same chip is very narrow because of low j_c. That is why in experiments we found it was quite difficult to observe radiation from a low j_c sample.

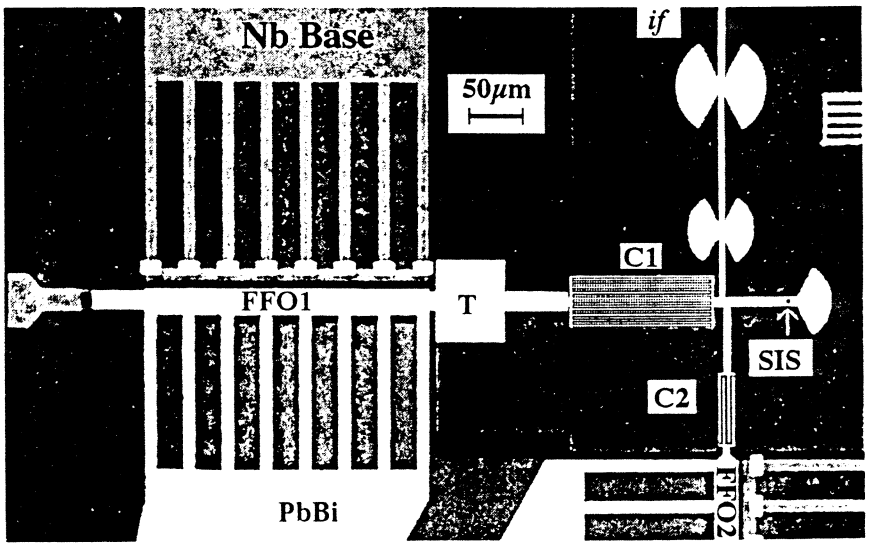

Fig.4 SEM picture of the integrated receiver. The FFOs (3 μm wide by 350 μm long) are connected to an SIS mixer via centerfed interdigital capacitors (C1 and C2). T is the first section of the impedance transformer (Z_1 in Fig.3). The FFOs and the SIS element are made of Nb/Nb-oxide/PbBi tunnel junctions.

2.3 *rf* circuit

The *rf* performances of the circuit design was optimized by careful CAD modeling (HP 85150B Microwave Design System) with the center frequency at 350GHz. Normal conductors were used with the resistivity set to zero. Microstripline widths and lengths were recalculated for the superconducting case with the London penetration depths of the electrodes taken into account [17,18]. We take λ_L(Nb)=85 nm and λ_L(PbBi)=200 nm [19] for superconducting microstriplines Nb(200nm)/SiO(400nm)/PbBi(400nm) in the circuit. Also, we take ε_r = 5.5 [20] for the SiO dielectric layer with the assumption that this holds also at 350 GHz.

Both oscillator junctions are connected to the SIS mixer via center-fed interdigital capacitors (see Fig. 3). These capacitors are necessary for separating the dc-biases of the FFOs and the SIS element. One oscillator (FFO1) is well coupled to the SIS mixer by using a 3-step Chebychev microstripline transformer and a fairly large interdigital capacitor C1 with 20 strips (see Fig.5 for detail). The center frequency of the Chebychev transformer [21] is 350 GHz, and its 3dB bandwidth is 80 GHz. It transforms the low impedance of the oscillator Z_0 (= 0.5 Ω) to the 10 Ω microstripline impedance through two λ/4 long microstriplines Z_1(= 1.07 Ω) and Z_2 (=4.67 Ω). The length of the finger coupler C1 has to be about λ/2 long rather than λ/4 to give sufficient coupling with available lithography. The problem is caused by the unfavorable small aspect ratio of the dielectric thickness (400 nm) and the strip separation (0.8 - 1 μm). CAD modeling showed that this capacitor could have 50 GHz bandwith (3 dB loss). The second FFO has about 15 - 20dB weaker coupling. It only contains four strips (63μm long, 2μm wide, and 2 μm as the gap). In this way the interaction between the two oscillators is fairly small. In Fig.5, we show the CAD modeled *rf* response of the circuit (for the normal conductor case). The transmitted power (S12) from the local oscillator (FFO1) to the SIS element has a bandwidth of 50 GHz. An additional window at around 100GHz, however with ~20 dB loss, is also seen in the calculation. Although this window is very narrow, we observe radiation from the oscillator to the SIS detector in this band.

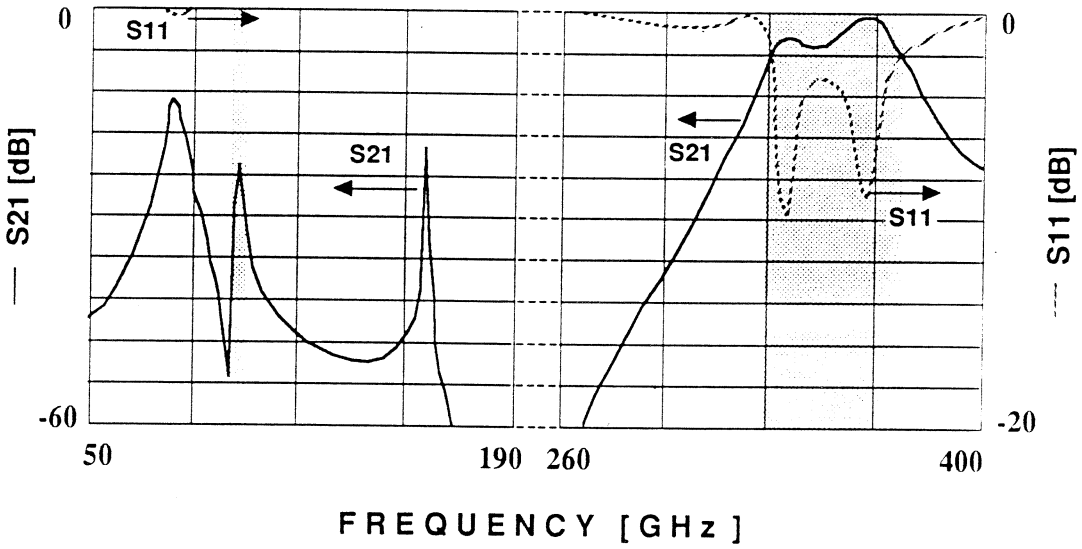

Fig.5 *rf* characteristics of the modeling circuit. Microstriplines are based on lossless metals separated by a 400nm thick insulator layer with ε_r of 5.5. S11 is the reflection from FFO1, S21 is the transmitted power from the FFO1 to the SIS element. We choose 10Ω for the resistance R_n of the SIS mixer, and 560 fF for its capacitance C_J. Note that for the 260GHz response (see below), the actual circuit differed somewhat from this one.

The intermediate frequency (*if*) signal is transmitted through a 15 Ω microstripline (4 μm wide) filtered by two pairs of radial stubs (R1 in Fig.3). The radial stubs were used as *rf* chokes for the *if*-line. The outer radius of the radial stubs was calculated from Eq.(8), r_2=46.1 μm and r_2'=34 μm. The position of the *if*-line on the 10 Ω microstrip was optimized by CAD simulation (to minimize the effect of the *if*-line to the rf characteristics of the circuit). The 15 Ω microstripline was then transferred to a finline via a balun construction. One electrode of the finline (PbBi) is connected to a thin film capacitor (10pF), while the other is electrically connected to the Nb ground plane. The *if* characteristics of this circuit was simulated by CAD, and showed a flat transmission from the SIS element to IF output at the band around 4 GHz with a loss less than 1 dB. Before the thin film capacitor, the *if*-line also serves as the dc-bias line for the SIS mixer.

3. FABRICATION PROCEDURES

Low doped silicon wafers were used as substrates. About fifty 6 x 3.8 mm^2 chips of different designs were fabricated simultaneously, before dicing the wafer. The pattern of the last layer (PbBi) was defined by a direct electron beam writing for a single chip or a couple of chips at a time. This made adjustments of the circuit parameters very easy.

Both FFOs and the SIS element are fabricated by using Nb (200 nm) as base-electrodes, windows in SiO (400 nm) defining the junction areas, and PbBi (400 nm) as top-electrodes. First, a lift-off stencil for defining the Nb base electrodes is prepared with S1813 photoresist. Nb film is dc sputted at a rate of 0.5 nm/s. This Nb layer is also the ground plane for the microstriplines. Then, on top of the Nb patterns, another lift-off stencil for defining the Au contact pads is prepared. The Au layer is formed by thermal evaporation of 20 nm NiCr (0.1 nm/s) followed by 250 nm Au (1 nm/s). For a good contact between the Au and Nb layers,

Ar-ion beam etching is used just before the evaporation without breaking the vacuum to provide a fresh Nb surface.

Lift-off stencils for defining the junction windows in SiO as well as the top-electrodes are made by using electron-beam writing on PMMA/Copolymer double layer e-beam resist: copolymer (poly[methyl methacrylate/methacrylic acid] copolymer) 11% (650 nm) at the bottom and PMMA (poly[methyl methacrylate]) 3% (150 nm) on the top with an exposure dose of 220 $\mu C/cm^2$ at 50 kV. This high exposure dose works well for the lift-off process of the finger coupler which has 20 fingers (see Fig.6). SiO was thermally evaporated at a rate of 2.5 nm/s. The Nb/NbOx/PbBi tunnel junctions were formed by Ar-ion beam etching followed by reactive ion beam oxidation and a thermally evaporated PbBi (1nm/s) top electrode. The critical current density of the junction is controlled by the oxidation time and can be varied from 200 A/cm^2 to 20 kA/cm^2.

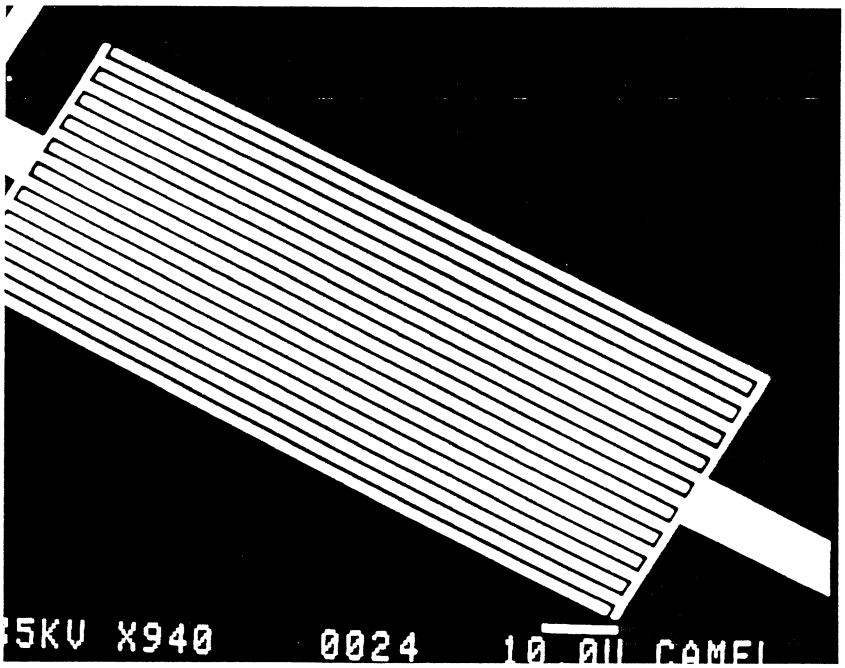

Fig.6 SEM micrograph of a finger coupler (C1) made of 400nm PbBi. The coupler has 20 fingers (1.2μm wide, 180μm long and 0.8μm separation). It provides good rf-coupling and dc-block between FFO1 and the SIS element. Its length is about $\lambda/2$ long of the center frequency for the pass band. It is the most difficult part of this circuit, from the fabrication point of view.

4. EXPERIMENTAL

The integrated oscillators and SIS circuit was mounted in a 22 pin IC package. Gold pads on the chip were connected to the package by thermosonic wire bonding. The IC package was mounted onto an IC socket at the bottom of a closed-end dipstick (0.75 inch in diameter). Two pins on the IC socket are soldered to a UT85 coaxial cable (a 1nF chip capacitor on the outer jacket of the coax gives dc-isolation also on the ground side). Bias leads were filtered by low pass filters. The oscillators, SIS, and control currents were driven by stabilized battery sources. The chip package was shielded by Pb foil. The dipstick was immersed into a μ-metal shielded helium cryostat, and the measurements were done inside a screen room. The sample temperature could be adjusted from 4.2K to about 1K by pumping the liquid helium. The *if* signal was

transmitted through the coaxial line to room temperature *if* amplifiers (f_{if} ~ 4 GHz, gain 57 dB) and either a square law detector or a spectrum analyzer.

For the initial circuits, the LC resonance of the SIS mixer fell outside the band of the rest of the circuitry, and the best response of the SIS mixer was obtained at about 100 and 260 GHz. Weak responses at about 350 GHz were also seen in this case. The response was mapped out in a couple of slightly different geometries, and the passbands were well described by the predictions obtained from CAD modeling.

4.1 Detection of resonant soliton oscillation

When j_c was less than 1 kA/cm^2, strong responses were observed in the SIS detector junction to radiation at around 100 GHz from resonant motion of fluxons in the LJJs. Shapiro steps and photon-assisted-tunneling steps in the dc I-V curves of the SIS detectors agree with the radiation frequency given by Eq.2. An independent check of the oscillation mode can be done by changing the bias of a LJJ, from a resonant step (ZFS) in the positive branch to the negative branch. For a RSO, its radiation can be detected in both bias branches, while for an FFO, the direction of the radiation is dependent on the Lorentz force given by the vector product of the current and the magnetic field. Thus, for the FFO, the velocity-matching step is more pronounced in one branch, and so is the radiation.

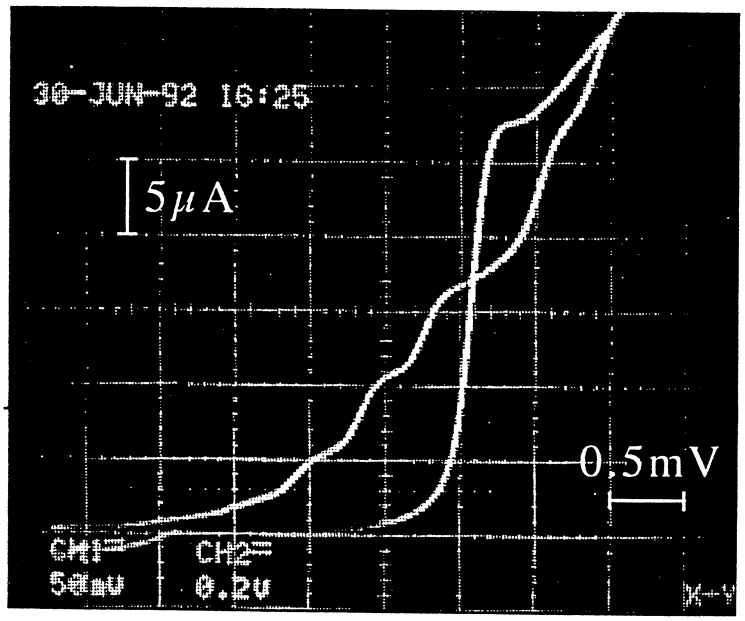

Fig.7 Detection of radiation from a low j_c RSO (j_c =250 A/cm^2) at about 106 GHz. dc I-V curves for an SIS detector junction at 4.2 K with and without radiation. The LJJ is biased on a resonant step at V_{osc} = 439.7 μV, I_{osc} = 0.963 mA.

In Fig.7, we show the response of an SIS detector to the radiation from a resonant soliton oscillator that has a low j_c value. When the LJJ was biased on a ZFS (~440 μV) enhanced by a weak magnetic field, clear photon assisted tunneling steps corresponding to the radiation frequency (~106 GHz) appeared in the I-V curve of the detector. We believe the radiation is from the resonant motion of multi-fluxons in a bunched configuration. In this figure, the Josephson pair current was suppressed. When the Josephson current was present, we also observed Shapiro steps in the I-V curve which corresponded to the 106 GHz radiation.

The embedding circuitry (admittance $Y_S=G_S+jB_S$ as well as the magnitude of an equivalent current source I_S) for the SIS element can be calculated from Tucker's quantum theory of mixing [22] by using the pumped and unpumped I-V curves [23].The *rf* voltage amplitude V_{rf} across the SIS detector can then be calculated from

$$V_{rf} = \frac{I_S}{|Y_S + Y_{f,k}|} \quad , \tag{10}$$

where $Y_{f,k}$ is the non-linear admittance at the bias point. The incident available power P_{LO} and the absorbed power P_{det} in the SIS can be calculated from

$$P_{LO} = \frac{I_S^2}{8G_S} \quad , \tag{11a}$$

$$P_{det} = V_{rf}^2 \mathrm{Re}(Y_{f,k})/2 \quad . \tag{11b}$$

For the I-V curves in Fig.7, we calculated $V_{rf}=0.77\,\mathrm{mV}$, $P_{LO}=4.1\,\mathrm{nW}$, and $P_{det}=3.2\,\mathrm{nW}$. For the LJJ, the current step height times the step voltage gives $0.33\,\mu\mathrm{W}$ for the LJJ. This dc-bias level fits well with the CAD modeling (i.e. about 20dB loss for this window). It also implies that the output power should be more than 20dB larger at the output end of the LJJ. For this sample, we also detected weak radiation around 106 GHz when the oscillator was biased on a resonant steps at around $\pm 220\,\mu\mathrm{V}$. This radiation could come from the second harmonic oscillation of a resonant soliton motion which has its fundamental frequency at 53 GHz.

4.2 Detection of flux-flow oscillation

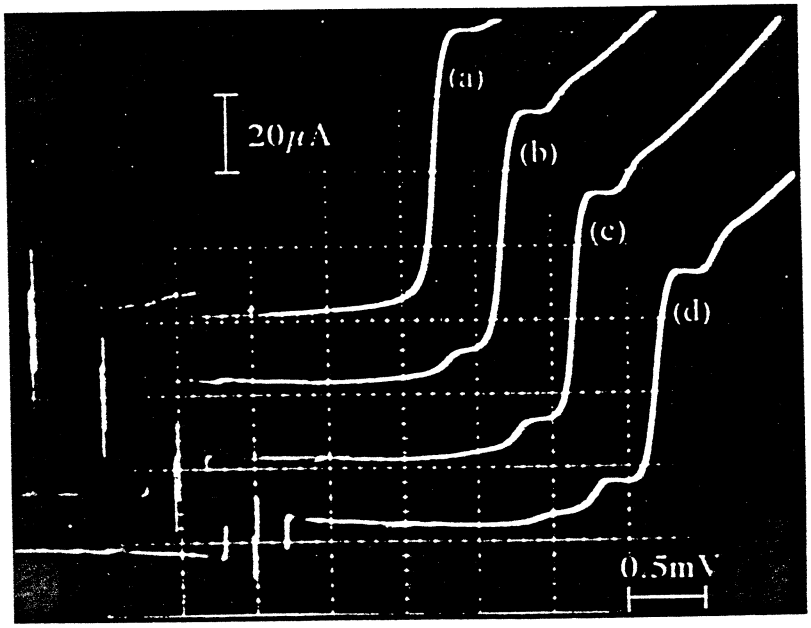

Fig.8 Detection of radiation from an FFO at about 98GHz. The dc I-V curves for an SIS detector junction at 4.2K is shown with no radiation (a) and (b-d) for increasing LO powers. The LJJ is biased on a VM step at V_{osc}=202.6 μV, I_{osc}=1.903 mA, 1.983 mA and 2.111 mA for curves (b), (c), and (d), respectively. Negative dynamic resistance appears at the first photon induced step for enough pumping powers. This indicates that the junction capacitance is tuned out at this frequency. Shapiro steps were also obtained for large pump powers.

Measurements showed that, for LJJs which had $j_c > 1\,kA/cm^2$, VM steps due to the unidirectional flux-flow motion were easily induced and their voltages could be tuned by an external field linearly over a wide range, typically from 0.2mV (100GHz) to 1.2mV (600GHz), for our Nb/NbOx/PbBi junctions. As the voltage of a VM step was gradually increased with the field, the step height decreased and the step steepness decreased. This indicates that the output power decreases and the linewidth increases with increasing oscillator frequency. Above a certain bias close to 1.4mV, the step suddenly disappeared, which may be due to the flux flow oscillation reaching the gap frequency.

We observed radiation from the flux-flow motion at around 100GHz and 260GHz [6], and in the band 280 - 330GHz [11]. At these three frequencies, both Shapiro steps and photon-assisted tunneling were clearly seen in the SIS element. The oscillation mode was confirmed by changing the bias polarity and from Eq.3. Radiations at 350GHz, 400GHz, and 600GHz were also observed from the first Shapiro step at 0.72mV, 0.83mV, and 1.24mV, respectively.

We show in Fig.8 the response of an SIS detector ($R_n = 32.3\Omega$) to the radiation from a flux-flow oscillator with $j_c = 1.4\,kA/cm^2$. Both photon assisted tunneling steps and Shapiro steps corresponding to radiation at 98 GHz was observed. The response became more and more pronounced (Fig.8 b-d) when the oscillator's bias was moved from the bottom of the step to the top. The oscillator was biased at around 203 μV. Using Eqs.(10) and (11), we obtain $V_{rf} = 0.27\,mV$, $P_{LO} = 3.7\,nW$, and $P_{det} = 2.8\,nW$. Calculations also show that the SIS mixer has a conversion gain of +2dB (for curve d in Fig.8) due to the appearance of a negative dynamic resistance at the first photon-induced step. The SIS junction area was $4\,\mu m^2$ for this sample.

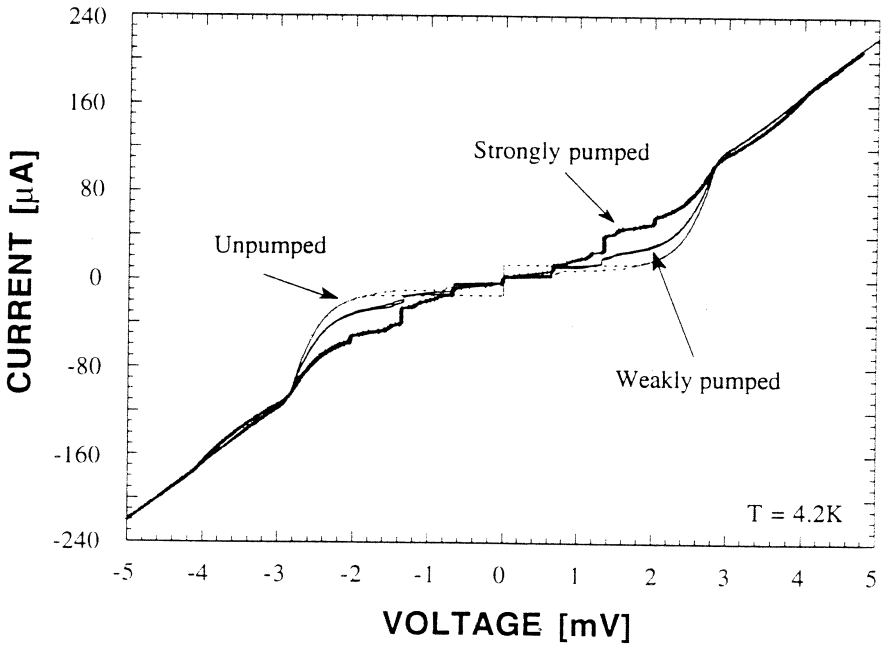

Fig.9 Response of the SIS detector to radiation from FFO1. For the weakly pumped I-V, the FFO1 was biased at V_{osc}=651 μV (315GHz), and the calculated available power P_{LO} is 110nW. For the strongly pumped case, V_{osc}=663 μV (330GHz) and P_{LO}=430nw. The same external field was supplied in both cases.

After adjusting the area of the element and the length of the tuning strip inductance carefully, the LC resonance moved to the desired center frequency, and a good response was observed from 280 to 330GHz (580μV to 690μV) with the LC resonance at 340GHz, as shown in Fig.9. This response bandwidth (Δf=50GHz) fits well with the CAD simulation. The *rf* power from the oscillator, which could be tuned by changing the current bias along the VM step, is high enough to pump the SIS element for mixing purpose. The maximum response was at 330GHz (660μV), with a calculated power $P_{LO}=430\mu W$. This sample had quite a high j_c value ~12kA/cm^2, which gave a broad detection bandwidth (around the LC resonant frequency) for the SIS element. The SIS junction had a small junction area of 0.65μm^2, compensated by a 13μm long strip inductance.

5. LINEWIDTH MEASUREMENTS OF THE FLUX-FLOW OSCILLATOR

The linewidth was determined for the flux-flow type oscillator, i.e. for the viscous unidirectional fluxon motion. Since two FFOs were mixed in an SIS element, the experimental set-up became fairly elaborate. For the dc-biasing of the FFOs and the mixer we needed 5 bias supplies - 2 for each oscillator and one for the mixer. Since the *if* amplifiers were operating at 4 GHz and had a bandwidth of about 1 GHz, the difference in voltage bias of the two oscillators had to be in the regime 7 – 10μV. First the control currents for the oscillators were adjusted to give a velocity matching (VM) step near a voltage corresponding to the band of interest. The response of the SIS mixer was monitored for each oscillator separately, and after adjusting the control currents and the oscillator biases, the amplified *if* signal was measured with a square law detector and monitored versus the voltage bias of the SIS element, as shown in Fig.10. This picture resembles the typical *if* output power versus voltage bias of the SIS mixer. However, this may not be a proof for mixing of two harmonic signals. Indeed, in some cases we found that even though the *if* output power from the SIS mixer was high and the bias dependence reasonable, the weakly coupled oscillator usually was too much off-set in bias from the strongly coupled one, and only an increased noise level with no additional structure could be seen when the spectrum analyzer was connected.

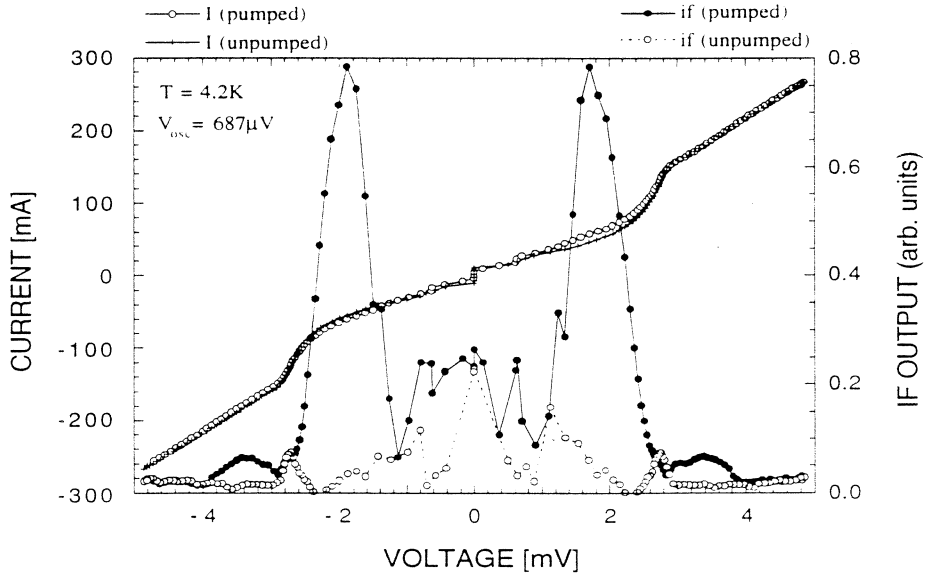

Fig.10 dc I-V curves of the SIS mixer and the *if*-output power, with and without radiation. Both FFOs oscillate at around 330GHz.

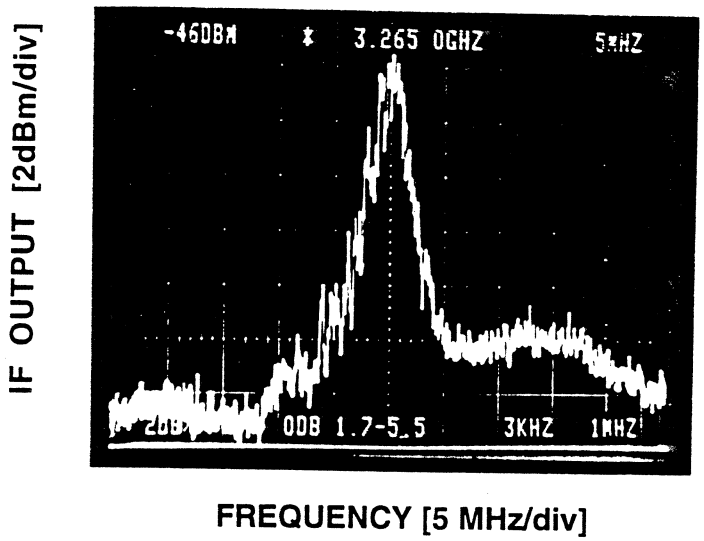

Fig.11 Spectrum of the *if*-power at 1.4 K when the signal of FFO2 is mixed with the FFO1 (as the local oscillator) in the SIS mixer at around 320GHz. The center *if* frequency is 3.265 GHz.

After the response such as the one seen in Fig. 10 was obtained, the signal was brought to a spectrum analyzer instead. Fig.11 shows a typical recording of the *if* output, when spectral response showed mixing from coherent signals. This spectral response (with somewhat different amplitudes) was seen from 280 GHz to 330 GHz. Although, the drawback of our method is that we obtain the composite linewidth of the two oscillators, we do not have to deal with an external source of a different kind, which could add uncertainties of the upper limit of the linewidth. The composite linewidth (- 3 dB) of the FFOs in our measurement was 2.1 MHz across this band.

6. CONCLUSIONS

An integrated receiver circuit was built to investigate radiation from long Josephson junctions. The radiation from two flux-flow oscillators was detected or mixed in an SIS mixer. Extensive CAD modeling of the circuit was done before the actual receiver was built. A good agreement between the experimental data and the modeling was obtained. We measured the linewidth of the flux-flow oscillators to be less than 2 MHz in the band 280-330 GHz. The frequency was tuned by changing the control current to the FFO. The output power within the same frequency interval was 0.5μW coupled to a 10Ω microstripline. The output power from the oscillator could conveniently be tuned by changing the current bias on the velocity matching step. By varying the critical current density j_c, we could operate the long Josephson junction both in the resonant soliton regime ($j_c < 1\text{kA/cm}^2$), and in the unidirectional flux-flow regime ($j_c > 1\text{kA/cm}^2$).

ACKNOWLEDGEMENTS

We thank H. Zirath, I. Angelov and H. Ekström for their help, and N.F. Pederson, A.V. Ustinov and M. Cirillo for helpful discussions. The circuits were made in the Swedish Nanometer Laboratory. This work was supported by the Swedish National Board for Industrial and Technical Development (NUTEK) and the Swedish Research Council for Engineering Sciences (TFR).

REFERENCES

[1] B. Bi, S. Han, J.E. Lukens, and K. Wan, "Distributed Josephson junction arrays as local oscillators", IEEE Trans. Appl. Supercond., MAG-27, to be published, (1993).

[2] T. Nagatsuma, K.Enpuku, K. Yoshida, and F. Irie, "Flux-flow-type Josephson oscillator for millimeter and submillimeter wave region. II. Modeling", J. Appl. Phys., 56, 3284-3293, (1984).

[3] Y.M. Zhang, "Effect of losses on the output voltage of a flux-flow type Josephson oscillator," in *Nonlinear Superconductive Electronics and Josephson Devices*, New York: Plenum Press, G. Costabile, S. Pagano, N. F. Pederson, and M. Russo, eds., (1991), pp.145-153.

[4] N.F. Pederson, "Solitons in Josephson transmission lines," in *SOLITONS*, Amsterdam: Elsevier Science Publishers B.V., S. E. Trullinger, V. E. Zakharov, and V. L. Pokrovsky, eds., (1986), pp.469-501.

[5] E. Joergensen, V.P. Koshelets, R. Monaco, J. Mygind, M.R. Samuelsen, and M. Salerno, "Thermal fluctuations in resonant motion of fluxons on a Josephson transmission line: Theory and Experiment", Phys. Rev. Lett., 49, 1093-1096, (1982).

[6] Y.M. Zhang, D. Winkler, and T. Claeson, "Detection of mm and submm wave radiation from soliton and flux-flow modes in a long Josephson junction", IEEE Trans. Appl. Supercond., MAG-27, to be published, (1993).

[7] M. Cirillo, F. Santucci, P. Carelli, M.G. Castellano, and R. Leoni, "Coupling of long Josephson junction oscillators at millimeter-wave frequencies", IEEE Trans. Appl. Supercond., MAG-27, to be published, (1993).

[8] T. Nagatsuma, K. Enpuku, F. Irie, and K. Yoshida, "Flux-flow-type Josephson oscillator for millimeter and submillimeter wave region", J. Appl. Phys., 54, 3302-3309, (1983).

[9] T. Nagatsuma, K. Enpuku, K. Sueoka, K. Yoshida, and F. Irie, "Flux-flow-type Josephson oscillator for millimeter and submillimeter wave region. III.Oscillation stability", J. Appl. Phys, 58, 441-449, (1985).

[10] Y.M. Zhang and P.H. Wu, "Numerical calculation of the height of velocity-matching step of flux-flow type Josephson oscillator", J. Appl. Phys, 68, 4703-4109, (1990).

[11] Y.M. Zhang, D. Winkler, and T. Claeson, "Linewidth measurements of Josephson flux-flow oscillators in the band 280-330 GHz", Appl. Phys. Lett., to be published, (1993).

[12] A.V. Ustinov, T. Doderer, R.P. Huebener, J. Mygind, V.A. Oboznov, and N.F. Pedersen, "Multi-fluxon effects in long Josephson junctions", IEEE Trans Appl. Supercond., MAG-27, to be published, (1993).

[13] V.P. Koshelets, A.V. Shchukin, S.V. Shitov, and L.V. Filippenko, "Superconducting millimeter wave oscillators and SIS mixer integrated on a chip", IEEE Trans. Appl. Supercond., MAG-27, to be published, (1993).

[14] H.A. Atwater, "Microstrip reactive circuit elements", IEEE Trans on Microwave Theory and Technology, MTT-31, 488-491, (1983).

[15] A.R. Kerr and S. Pan, "Some recent developments in the design of SIS Mixers," in *First Int. Symp. on Space Terahertz Technology*, Michigan, (1990), pp.363-377.

[16] R. Blundell and D. Winkler, "The superconductor-insulator-superconductor mixer receiver - a review," in *Nonlinear Superconductive Electronics and Josephson Devices*, New York: Plenum Press, G. Costabile, S. Pagano, N. F. Pedersen, and M. Russo, eds., (1991), pp.55-72.

[17] W.H. Chang, "The inductance of a superconducting strip transmission line", J. Appl. Phys., 50, 8129-8134, (1979).

[18] W.H. Chang, "Measurement and calculation of Josephson junction device inductances", J. Appl. Phys., 52, 1417-1426, (1981).

[19] W.H. Henkels and C.J. Kircher, "Penetration depth measurements of type II superconducting films", IEEE Trans. on Magn., MAG-13, 63-66, (1977).

[20] H.K. Olsson, "Dielectric constant of evaporated SiO at frequency between 13 and 103GHz", IEEE Trans. Magn., MAG-25, 1115-1118, (1989).

[21] R.E. Collin, *Foundations for microwave engineering*, Tokyo: McGraw-Hill, 1966, Chapter 5.

[22] J.R. Tucker and M.J. Feldman, "Quantum detection at millimeter wavelengths", Rev. Mod. Phys., 57, 1055-1113, (1985).

[23] A. Skalare, *SIS Embedding Circuit Program for Macintosh*, Version 2.5, 1993.

The Fabrication and Performance of Planar Doped Barrier Subharmonic Mixer Diodes*

Trong-Huang Lee†, Jack R. East†, Chen-Yu Chi†, Robert Dengler‡, Imran Mehdi‡, Peter Siegel‡, and George I. Haddad†

† NASA/Center for Space Terahertz Technology
The University of Michigan
Ann Arbor, Michigan

‡ Jet Propulsion Laboratory
California Institute of Technology
Pasadena, California

ABSTRACT

The PDB (*P*lanar *D*oped *B*arrier) diode consists of a p^+ doping spike between two intrinsic layers and n^+ ohmic contacts. Such devices can have an anti-symmetric current vs. voltage characteristic. The capacitance is approximately constant with the applied voltage, and the barrier height and device capacitance are easily adjustable. These characteristics make the PDB a candidate for millimeter- and submillimeter-wave subharmonic mixers. We have fabricated a series of 2 and 4 μm diameter diodes with different barrier designs using a GaAs epi-layer. These devices are planarized using an air-bridge and a surface channel etch. After completely removing the substrate, the devices are mounted on quartz substrate to reduce parasitic effects. Diced diodes were tested as subharmonic mixers at 200 GHz in both a quasi-optical planar wideband subharmonic receiver and a planar-diode waveguide-mixer. The results from quasi-optical measurement show that a 0.23 V (and 0.4 V) barrier height GaAs diode with 2.0 μA (and 5 nA) of saturation current gives a DSB conversion loss of 10.8 dB (and 9.5 dB) and a noise temperature of 3795°K (and 2450°K). The results available from waveguide mixers are for a similar 0.23 V barrier height PDB and have a minimum conversion loss improved by 0.6 dB (10.2 dB) and noise temperature reduced by 220°K (3575°K), but required only less than 1 milliwatt of LO power.

1. INTRODUCTION

For space-borne applications, one of the most attractive configurations of submillimeter-wave heterodyne receiver design is the subharmonically-pumped (SHP) mixer. This type of mixer usually requires a device with an anti-symmetrical current-voltage characteristic to be able to perform signal mixing at both positive and negative voltages. Using SHP mixers at over 100 GHz has several advantages. The first is that SHP mixers only require local oscillator (LO) pumping at half of the signal (RF) frequency, which is important because the LO power above 100 GHz

* This work was supported by NASA under Grant No. NAGW-1334

currently available is small. Other advantages include the simplicity of diplexing as well as the possibility of independent impedance adjustment at the RF and LO frequencies, due to the wide separation of these two frequencies, and the suppression of the local oscillator AM noise [1]. Finally, no DC return path is needed due to zero or near zero DC currents.

The most common device for SHP mixers uses two Schottky diodes connected as an anti-parallel pair to give an anti-symmetrical current-voltage characteristic [2,3]. However, such zero-biased Schottky diode pairs still require a large amount of LO power to sweep over the diodes' turn-on voltage. This limits their usefulness at submillimeter-wave frequencies because currently-used GaAs Schottky diodes have a high barrier height, and thus require large LO power. The absence of biasing reduces the degrees of freedom to adjust differences in the current-voltage characteristics and capacitances between the two diodes of a pair. Such differences cause degradation of mixer performance [4]. To circumvent these problems, recent efforts include the use of low barrier height Schottky diodes from material systems with lower band gaps, or the use of integrated circuit design with bias circuits [5,6]. Another approach is to use Planar Doped Barrier (PDB) diodes with an anti-symmetrical current-voltage characteristic [7], which are discussed in this paper.

PDB diodes were first proposed in 1980 by Malik *et al.* [8]. They employ a thin p^+ layer sandwiched in a lightly doped region to modify potential barriers in semiconductor structures, and two n^+ regions to form the contacts. Such an n^+-i-p^+-i-n^+ structure produces a triangular barrier, and thus charge injection occurs in both directions. By carefully choosing the doping profile and length of i layers, one is able to control the barrier height, capacitance per unit area, space charge resistance, and the degree of asymmetry required in the I-V characteristics. If the p^+ doping spike is placed in the middle of the structure, the current-voltage characteristic can be made anti-symmetric. This type of PDB is a candidate for SHP mixer diode. The benefits of building SHP mixers based on such devices include: (1) a low barrier PDB diode requires lower pump power; (2) the simplicity of the device structure eliminates the occurrence of loop inductance that exists in anti-parallel diode pairs; (3) the balance of the device structure implies a well-matched anti-symmetrical I-V characteristic; (4) unlike Schottky diode pairs, PDB diodes are quite insensitive to surface states and static discharge, and thus, device handling is easier.

In this paper we present a planar fabrication process developed at the University of Michigan for PDB diodes, and their RF performances at 200 GHz in a quasi-optical planar wideband subharmonic receiver at NASA/Center for Space Terahertz Technology [9], and in a planar-diode waveguide-mixer at JPL [10]. Our GaAs PDB #1 has a barrier height of 0.23 V and RF results at both laboratories are presented; GaAs #2 has a 0.4 V barrier height but only the results measured at NASA/CSTT are currently available. The performance results include a conversion loss and noise temperature of 9.5 dB and 2450°K (DSB), measured at NASA/CSTT from PDB #2, and a required LO power less than 1 milliwatt, measured at JPL from PDB #1. Both diodes have very well matched forward and reverse characteristics, with their resulting DC currents in an external loop during the RF measurements less than 10 μA. This is at least an order of magnitude better than that of a typical Schottky anti-parallel diode pair.

The outline of the remaining portion of this paper is as follows. Section 2 describes the device physics and the planar fabrication process. Section 3 gives the device DC parameters and a description of a 91 GHz video detection measurement. The setup and results of subharmonic

mixer measurement are presented in Section 4, and finally, conclusions are given in Section 5.

2. DEVICE PHYSICS AND FABRICATION PROCESS

A. Device Physics

An idealized subharmonic planar doped barrier structure is shown in Figure 1. The device designer has control over the material profile and dimensions. The device capacitance per unit area is approximated by the width of the two i layers

$$C_{pdb} = \frac{\varepsilon}{2 l_i} , \tag{1}$$

where $2l_i$ represents the total width of the i region, and ε is the semiconductor's dielectric constant. Since the total width of the i layer is controlled by the device structure rather than by the bias conditions, the PDB capacitance is approximately constant with the bias. The zero bias barrier height is determined by the combination of the i-layer width and the amount of charge in the p^+ doping spike

$$V_{pdb} = \frac{q P_{spike} l_i}{2\varepsilon} , \tag{2}$$

where the P_{spike} is the sheet density of charge in the doping spike and q is the electronic charge. A range of barrier heights is possible with proper choice of layer thickness and spike. The charge injection of the triangular barriers can happen in both directions and can be expressed approximately by

$$J_{pdb} = J_0 (e^{\frac{qV}{2kT}} - e^{-\frac{qV}{2kT}}) , \tag{3}$$

and

$$J_0 = A^* T^2 ,$$

where V is applied bias, A^* is the Richardson constant, T is temperature, and k is Boltzmann constant.

In a conventional Schottky diode the "ideality factor" is a measure of the physics of the current transport across the barrier. It is near 1 for a good device at temperatures where tunneling current is small. The equivalent "ideality factor" for PDB diodes is at least 2 for either forward or reverse direction. The biased PDB diodes act as a voltage divider, with half of the applied bias appearing across the region to the right of the p^+ doping spike and the other half appearing to the left. This high ideality factor is a potential limitation on the performance of subharmonic PDB mixers.

Space charge resistance is another limitation of PDB devices. In high level injection, the

transport carriers screen the electric field, and thus change the shape of the barrier height and affect the current-voltage characteristic. The space charge resistance is approximately proportional to the square of total depletion width and inversely proportional to carriers' saturation velocity. This became a guideline in the design of the second PDB wafer, which cut the space charge resistance by half by reducing the *i*-layer width from 500 Å to 350 Å.

B. Fabrication Process

The device fabrication process for PDB diodes here at the University of Michigan uses an air-bridge and a surface channel etch technique [11,12], modified to include a mesa structure. This process, as shown in Figure 2, is divided into the following nine steps:

(1) Wafer preparation;
(2) Mesa definition and top metallization;
(3) Mesa etch, which uses the ohmic metal as a self-aligned mask;
(4) Bottom ohmic metallization;
(5) Dielectric deposition, which is used for passivation and mechanical support for the coming bridge;
(6) Contact area opening on the dielectric layer;
(7) Thick metal deposition for air-bridge and contact pads;
(8) Channel etch; and
(9) Quartz mounting, and on-wafer test.

If the devices have desirable characteristics, further processing is needed before mounting on RF circuits. One important step is to remove all of the semiconductor substrate, which is lossy at submillimeter-wave frequencies. This is done by a process using wax for protection and support during the substrate etch. The resulting epi-layer only device is subsequently bonded on a 3-mil quartz substrate. The bonding process can be done either via van der Waals force or by UV sensitive glue. The devices on the quartz are diced, and then mounted onto mixer circuits. This quartz stayed on the mixer circuits as our measurements were proceeding; however, if necessary, it can be separated from the GaAs layer by removing the glue between the semiconductor layer and the quartz.

Using the above technique, we have been able to fabricate 2 μm and 4 μm diameter PDB diodes with different layout sizes. A variety of bridge lengths and widths were fabricated to study the optimal design of the bridge. The effect of bridge dimensions on the mixer performance was not seen in the measurements, however, possibly because the system noise had overwhelmed the subtle effects due to the variant bridge dimensions. The sizes of the metal pads for the contacts are either 100x75 μm or 60x30 μm, and are designed to fit in the circuit mount of the planar-diode waveguide-mixer or the planar antenna of the quasi-optical wideband receiver. Figure 3 shows a typical SEM picture of a finished diode, with 2 μm diameter, a 40x2 μm bridge, and two 60x30 μm pads. Figure 4 shows a 2 μm PDB diode, with a 10x2 μm bridge and 100x75 μm pads, flipped over and epoxied on a log-periodic antenna after its substrate is removed and replaced with quartz.

The above process has several advantages. First, the large metal contacts make circuit mounting easy. In comparison to whisker-contacted diodes, planar diodes can reduce assembly

cost and improve reliability for space-borne applications. Second, the air-bridge type of interconnection is feasible for submicron devices if the electron-beam writing technique is used for diode definition. Third, the etching of the surface channel and the removal of the semiconductor substrate reduce the parasitic effects and possible losses. Finally, our planar process and device thinning-down technique are ready to be extended to integrated circuit design, but unlike the limitation of MMICs, with a further freedom of choosing adequate substrate material, not necessarily semiconductors.

3. PLANAR DOPED BARRIER DEVICE CHARACTERISTICS

GaAs PDB diodes with different barrier heights were fabricated for mixer measurements. The diced quartz pieces are 250 μm long and 85 μm wide with a 2-μm PDB diode and 100x75 μm of contact pads, plus a variety of bridge dimensions. Diode DC characteristics were measured both before and after diodes were mounted onto the antennas to avoid measuring degraded diodes.

Table 1 shows two sets of diode DC parameters under forward as well as reverse bias, PDB #1 with 0.23 V and PDB #2 with 0.4 V barrier height, both measured with the diodes mounted on the antennas. PDB #1 has a 500 Å *i*-layer, while PDB #2 has a 350 Å *i*-layer, shorter by 150 Å but with a higher p^+l_i product. The design rule employed here is: (1) to increase the barrier height by raising the p^+l_i product, and (2) to decrease the space charge resistance by cutting the *i*-layer width.

The diode capacitance is calculated by the diode nominal anode diameter, 2 μm, and the total depletion width. The diode series resistance (R_s), ideality factor (η), and saturation current (I_s) are all extracted from the measured I-V characteristics by a least squares fitting program. PDB #1 has a zero-bias capacitance of 5.3 fF, an ideality factor of 2.2, a series resistance of 20 Ω, and a saturation current of about 2 μA. PDB #2 has a zero-bias capacitance of 6.6 fF, an ideality factor of 2.7, a series resistance of 14 Ω, and a saturation current about 5 nA.

Two points are important. First, as shown in Figure 5, both PDB diodes have well matched forward and reverse current-voltage characteristics. Second, PDB #2's series resistance is reduced because the space charge resistance is cut by half. The series resistance is the sum the space charge resistance and the contact resistance, which is estimated at 10 Ω from a contact resistivity of $3x10^{-7}$ Ω-cm^2. Therefore, the space charge resistance is 10 Ω for PDB #1 and 5 Ω for PDB #2.

A 91 GHz video detection measurement was performed to estimate the devices' parasitic capacitance (C_p) of the 20x4 μm bridge PDB diodes. This experiment, as described in [9], is performed by shining a plane wave with a known power density on a log-periodic/substrate lens antenna and by measuring the output voltage across a 106K load. The transmitted power is measured through a 10 dB coupler connected to an Anritsu power meter. The power density on the detector plane can be calculated from this measured power and the distance between the transmitter and detector. The detected voltage across the load is amplified by a Stanford low noise amplifier and read from a lock-in amplifier. The video responsivity defined here is the ratio of the detected voltage to the available RF power of the log-periodic antenna. As shown in Figure 6, the peak video responsivity is about ł300 V/W for a 0.4 V barrier height PDB.

The C_p was estimated by curve-fitting the measured video responsivity. The resulting C_p is about 6 fF for a 20x4 μm bridge PDB. Their RF spreading resistances should be close to their DC values, because the skin effect dominates the current flow in the n^+ region. The theoretical predictions agree reasonably with the measured data except at the higher current region where diodes suffer from the space charge effect.

4. MIXER MEASUREMENT

A. Quasi-optical Measurement Setup

Diode performance was measured at 91-182 GHz in a quasi-optical planar wideband subharmonic receiver by a hot-and-cold load method [9]. This quasi-optical system, shown in Figure 7, consists of four categories of parts: sources, a receiver system, a diplexer, and a lens system. The sources include a 90 GHz Gunn diode as an LO source, whose output power is adjusted by a grid attenuator, and two hot-and-cold sources, made from Eccosorb 72 absorbers with their hot temperature estimated to be room temperature and cold temperature to be 85°K at millimeter-wave frequencies.

The receiver system includes a planar wideband subharmonic mixer and an IF chain. The subharmonic mixer uses a planar self-complementary log-periodic antenna designed to cover the 26 to 260 GHz band, with a PDB diode epoxied at the antenna apex. A silicon lens is placed on the top of the antenna substrate to reduce power loss and improve the pattern and gain. Such an antenna on a silicon lens has a constant input impedance of 74 Ω; it is grounded on one side and on the other side connected to an IF matching network, then an IF chain, and finally a power meter. The IF chain, consisting of a circulator, one low noise amplifier, two second-stage amplifiers, and a 100 MHz band-pass filter, is centered at 1.4 GHz and has a gain of 98.7 dB and a noise temperature of 88.7°K.

Between the sources and receiver is a Martin-Pupplett diplexer, and the lens system. The Martin-Pupplett diplexer is a complex device which contains a beam splitter, made of a 45° grid, and two corner reflectors, one for the transmitted beam and the other for the reflected beam. It is easy to configure the diplexer's path-length difference to allow the maximum LO signal and the upper and lower sideband RF signal at about twice the LO frequency. The lens system includes two lenses and two wire grids. The lenses are 10 cm diameter Rexolite and have to be put at proper places in the beam path, one before and one after the diplexer, for the best coupling of LO signal from the Gunn source to the planar receiver. The RF signal, on the other hand, will be coupled to the hot-and-cold load and pass through only the second lens. A vertical wire grid is placed between the diplexer and the sources to allow only the horizontally polarized RF signal from the RF port or vertically polarized LO signal from the LO port to reach the diplexer. In front of the receiver stands a horizontal wire grid in the 45° plane to reflect the cross-polarized components into a hot-and-cold load. The positions and angles of the grids sensitively affect the signal beam polarization and the occurrence of standing waves.

B. Results of 91-182 GHz Subharmonic Mixer Measurements

Figure 8 shows the measured double-sideband conversion loss and noise temperature versus available LO power at 91-182 GHz subharmonic mixer measurements for PDB #1 and #2. The

available LO power for the diode is estimated by measuring the Gunn diode output power and reducing this value by the attenuation factor and system losses, where the system losses include the Gaussian coupling efficiency of the pyramidal LO horn (60%), reflection and dielectric loss of the lens (0.6 dB at 91 GHz and 0.8 dB at 182 GHz), diffraction loss of diplexer (0.2 dB), loss of the silicon lens due to dielectric constant mismatch (1.57 dB), and losses at the antenna system (2.1 dB). The mixer conversion loss and noise temperature take into account diode intrinsic conversion loss, assuming an IF match, and antenna system loss, due to imperfect antenna coupling, residue reflection, and absorption of the silicon lens. The DSB results at 182 GHz have a minimum conversion loss of 10.8 dB and a noise temperature of 3750°K for PDB #1, and 9.5 dB and 2450°K for PDB #2. The LO power for the minimum conversion loss is estimated at 2.2 mW for PDB #1 and 2.7 mW for PDB #2. These results are summarized in Table 2.

Also shown in Table 2 is a result measured in JPL's planar-diode waveguide-mixer at 210 GHz for PDB #1. The DSB minimum conversion loss is 10.2 dB and the noise temperature is 3575°K. These are slightly better than those measured at NASA/CSTT, but the required LO power around 1 mW is lower, which implies that the RF match at the LO frequency at the planar-diode waveguide-mixer is better than in the antenna system. The LO efficiency can be improved by adding a RF matching network at the antenna apex, but at the expense of bandwidth.

5. CONCLUSION

In this paper, we presented the design, fabrication and measurement of GaAs PDB diodes at 200 GHz. The devices' barrier height is controlled by the product of the p^+ sheet charge doping and the intrinsic width, and the space charge resistance can be reduced by shortening the depletion region width. Diodes with 0.23 V and 0.4 V barrier height are fabricated by a planar process using an air-bridge interconnection and surface channel etching to reduce the parasitic capacitance, and further thinning the substrate and mounting on quartz to reduce losses. This process can be easily modified to make integrated receivers with a choice of substrate for THz applications. The devices have a very good anti-symmetry in current-voltage characteristics; the measured diodes show an excellent balance and the external DC loop current seen in the RF measurement is less than 10 μA, an order of magnitude less than that of a typical anti-parallel Schottky diode pair. The PDB performances are evaluated on a quasi-optical planar wideband subharmonic receiver at 182 GHz, which gives a DSB conversion loss improvement of 1 dB and noise temperature reduction of 1300°K as the diode barrier height increases from 0.23 V to 0.4 V. Also presented are the results of the 0.23 V barrier PDB measured at JPL's planar-diode waveguide-mixer at 210 GHz, which show a 1 mW of required LO power at minimum conversion loss. This implies that a more efficient LO coupling in the quasi-optical receiver system is possible by adding an RF matching network at LO frequency at the antenna apex.

ACKNOWLEDGMENTS

The authors would like to thank H. C. Sun and W. L. Chen for their preparation of materials, and B. Kormanyos and S. Gearhart for their discussions of the quasi-optical measurement. Special thanks go to Professor Gabriel Rebeiz for his help on the measurement facilities and enthusiastic advice.

REFERENCES

[1] P. S. Henry, B. S. Glance, and M. V. Schneider, "Local-Oscillator Noise Cancellation in the Subharmonically Pumped Down-Converter," *IEEE Trans. Microwave Theory Tech.*, vol. MTT-24, pp. 254-257, May 1976.

[2] M. V. Schneider, and W. W. Snell, "Stripeline Down-Converter with Subharmonically Pump," *Bell Syst. Tech. J.*, vol. 53, pp. 1179-1183, Jul.-Aug. 1974.

[3] M. Cohn, J. E. Degenford, and B. A. Newman, "Harmonic Mixing with an Antiparallel Diode Pair," *IEEE MTT Int. Symp. Digest*, pp. 171-172, Jun. 1974.

[4] R. G. Hicks and P. J. Khan, "Analysis of Balanced Subharmonically Pumped Mixers with Unsymmetrical Diodes," *Proc. IEEE Int. Microwave Symp.*, pp.457-459, Jun. 1981.

[5] U. V. Bhapkar, Y. Li, and R. J. Mattauch, " InGaAs/InP Heteroepitaxial Schottky Barrier Diodes for Terahertz Applications," *Third Int. Symp. on Space THz Tech.*, pp. 661-677, Mar. 24-26, 1992.

[6] P. H. Siegel, S. Weinreb, S. Duncan, W. Berk, A. Eskandarian, and D. W. Tu, "Design and Measurements of a 210 GHz Subharmonically Pumped GaAs MMIC Mixer," *IEEE MTT-S Int. Symp.*, pp. 603-606, June 3, 1992.

[7] T. H. Lee, J. R. East, and G. I. Haddad, "Planar Doped Barrier Subharmonic Mixers," *Third Int. Symp. on Space THz Tech.*, pp. 616-630, Mar. 24-26, 1992.

[8] R. J. Malik, T. R. Aucoin, R. L. Ross, K. Board, C. E. C. Wood and L. F. Eastman, "Planar-Doped Barriers in GaAs by Molecular Beam Epitaxy," *Electron. Lett.*, vol. 16, pp. 836-838, Oct. 1980.

[9] B. K. Kormanyos, P. H. Ostdiek, W. L. Bishop, T. W. Crowe, and G. M. Rebeiz, "A Planar Wideband 80-200 GHz Subharmonic Receiver," to be published in *IEEE Trans. Microwave Theory Tech.*, Oct., 1993

[10] P. H. Siegel, R. J. Dengler, I. Medhi, W. L. Bishop, and T. W. Crowe, "A 200 GHz Planar Diode Subharmonically Pumped Waveguide Mixer with State-of-the-Art Performance," *IEEE MTT-S Int. Symp.*, pp. 595-598, June 3, 1992.

[11] P. H. Ostdiek, T. W. Crowe, and I. Galin, "Integration of an Anti-parallel Pair of Schottky Barrier Diodes in Millimeter Wave Mixers," *IEEE Trans. Microwave Theory Tech.*, vol. MTT-38, pp. 15-22, Jan. 1990.

[12] W. L. Bishop, T. W. Crowe, R. J. Mattauch, and H. Dossal, "Planar GaAs Diodes for THz Frequency Mixing Apllications," *Third Int. Symp. on Space THz Tech.*, pp. 600-615, Mar. 24-26, 1992.

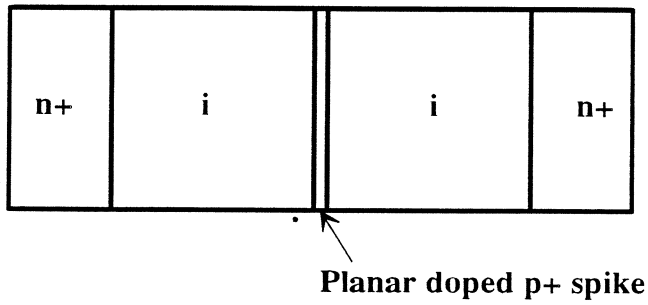

(a)

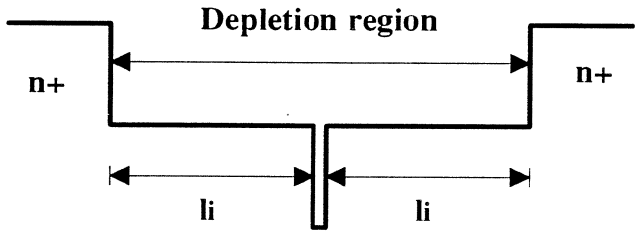

(b)

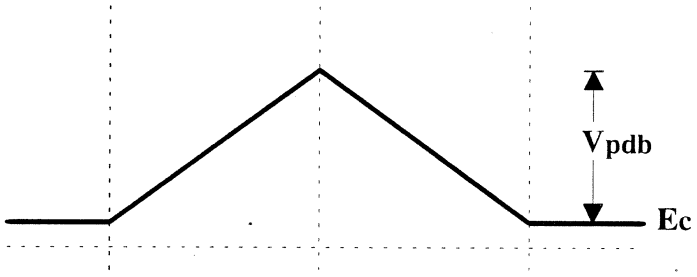

(c)

Figure 1: Planar Doped Barrier diodes include a planar doped p^+ spike sandwiched in two intrinsic regions and contact regions (a). They have a constant depletion width (b) and a triangular potential barrier (c).

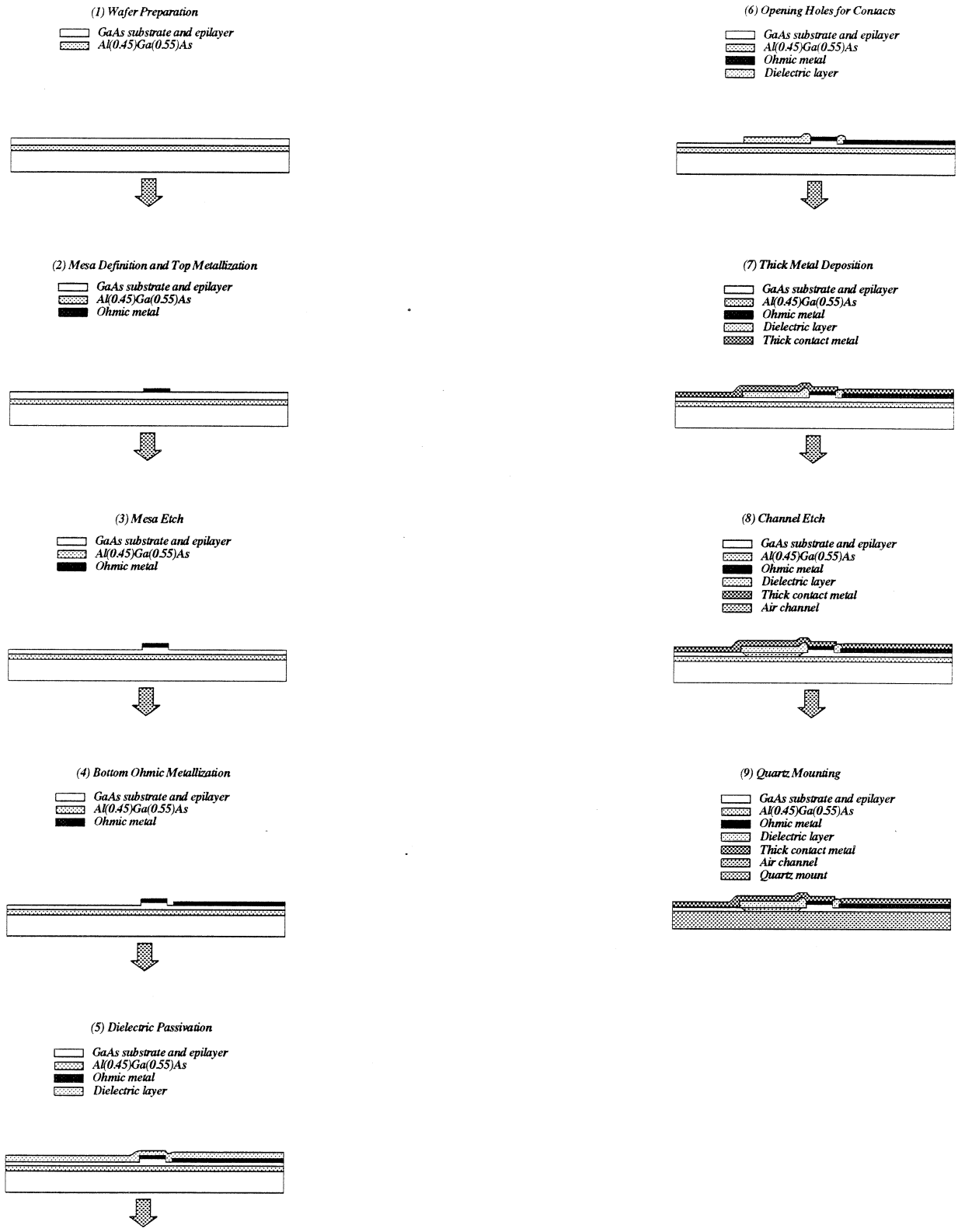

Figure 2: The planar fabrication process for GaAs PDBs using air-bridges, surface channel etching, substrate removing, and quartz mounting techniques.

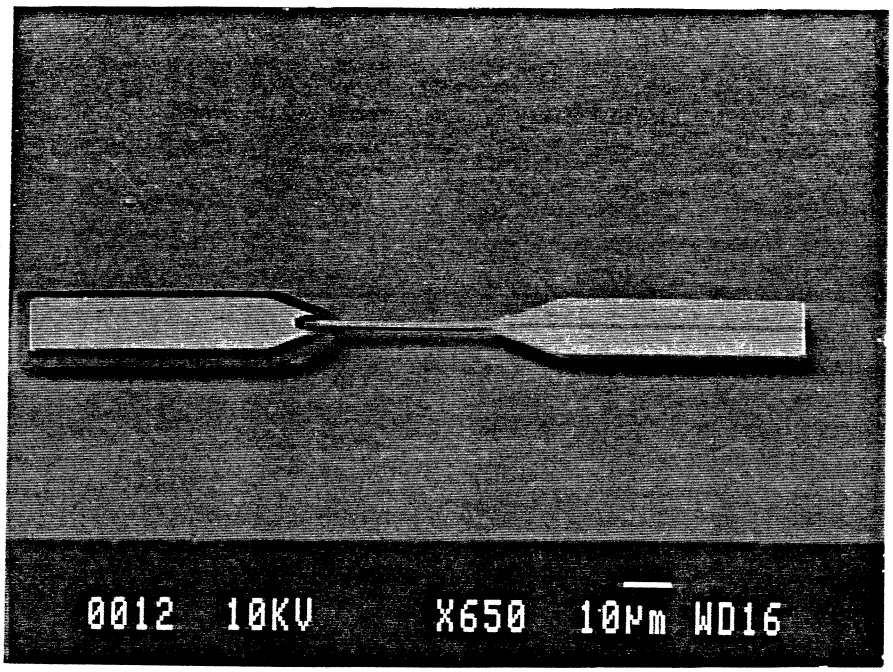

Figure 3: A PDB diode with 2 µm diameter, a 40x2 µm air-bridge, and two 30x60 µm contact pads after channel etch.

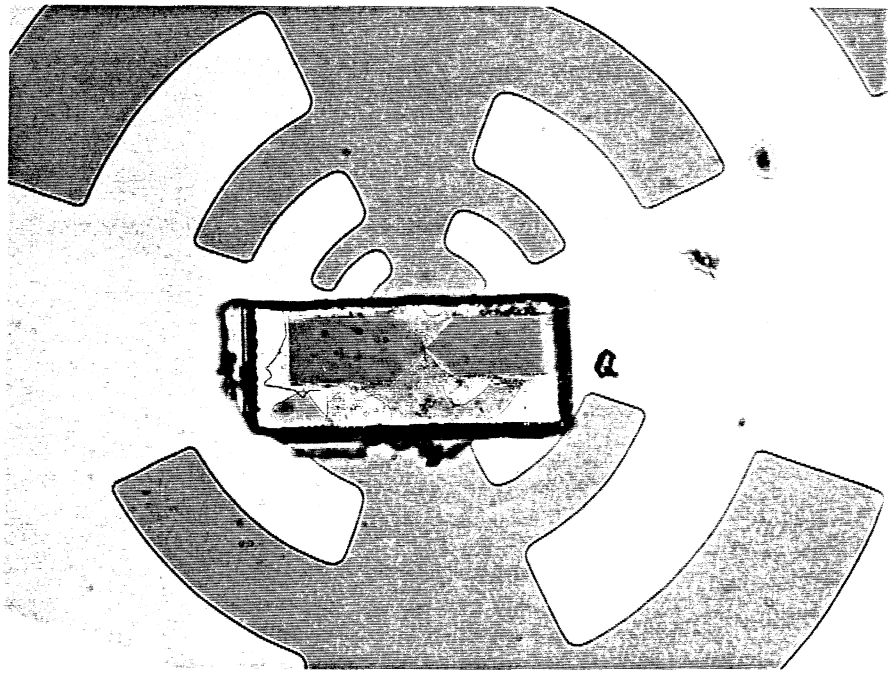

Figure 4: A PDB diode, after thinning and quartz mounting, flipped over and epoxied on a log-periodic antenna.

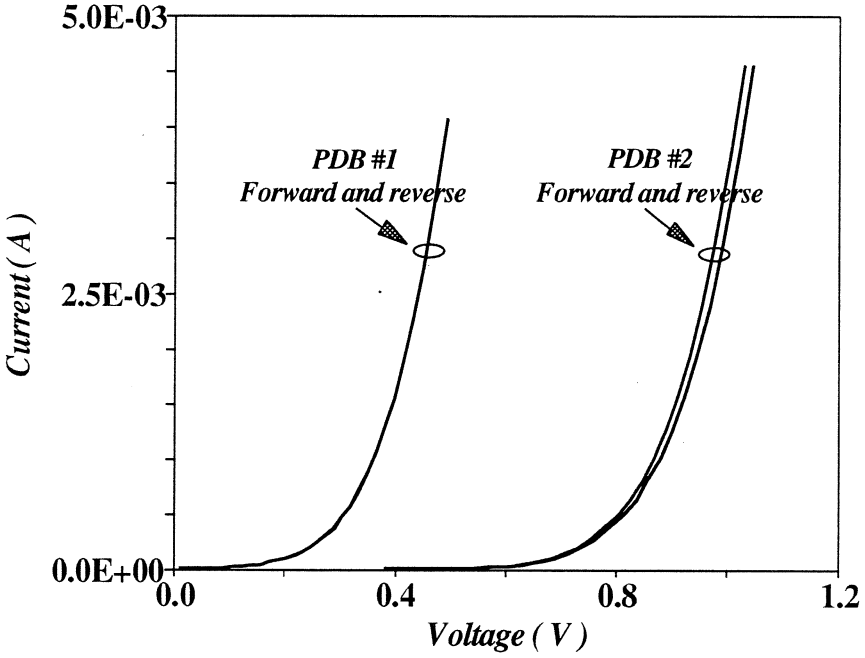

Figure 5: Current-voltage characteristics for two 2 μm GaAs PDBs.

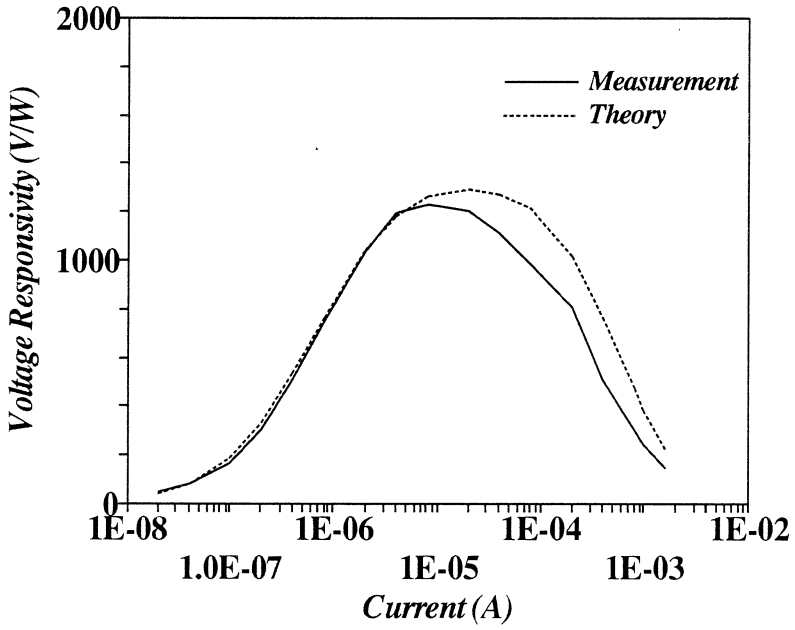

Figure 6: Video responsivity of a 0.4 V barrier height PDB at 91 GHz.

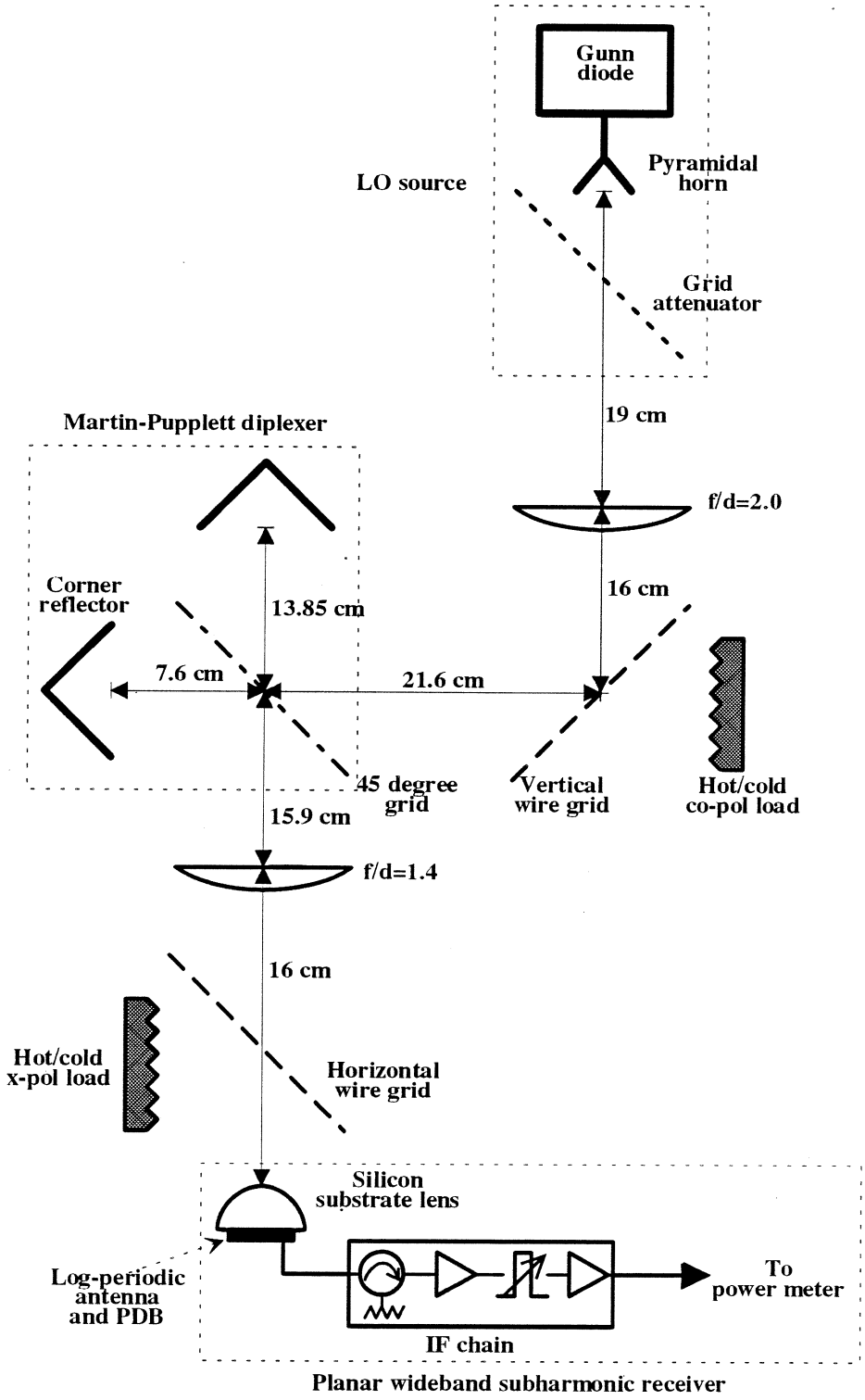

Figure 7: Mixer measurement setup of a quasi-optical planar wideband subharmonic receiver at UM NASA/CSTT.

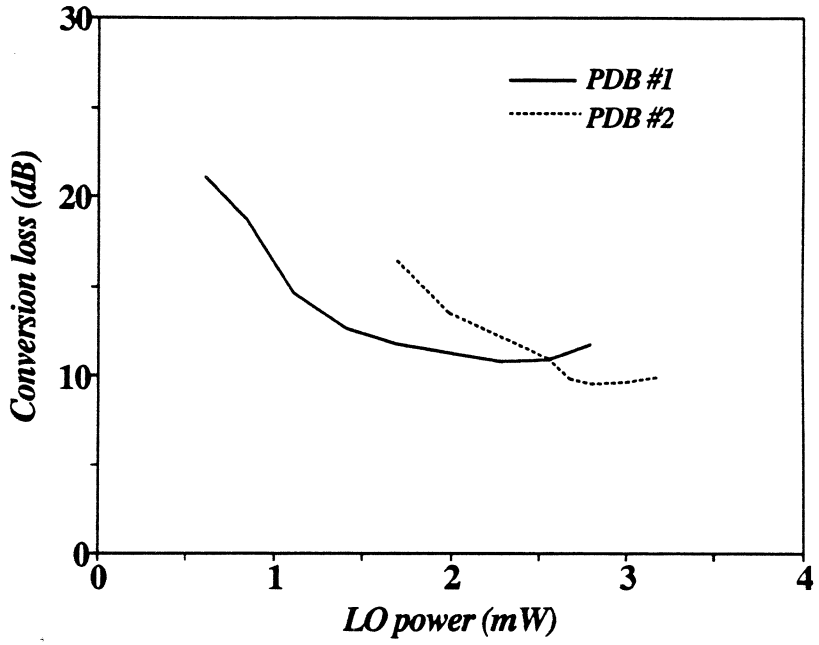

(a)

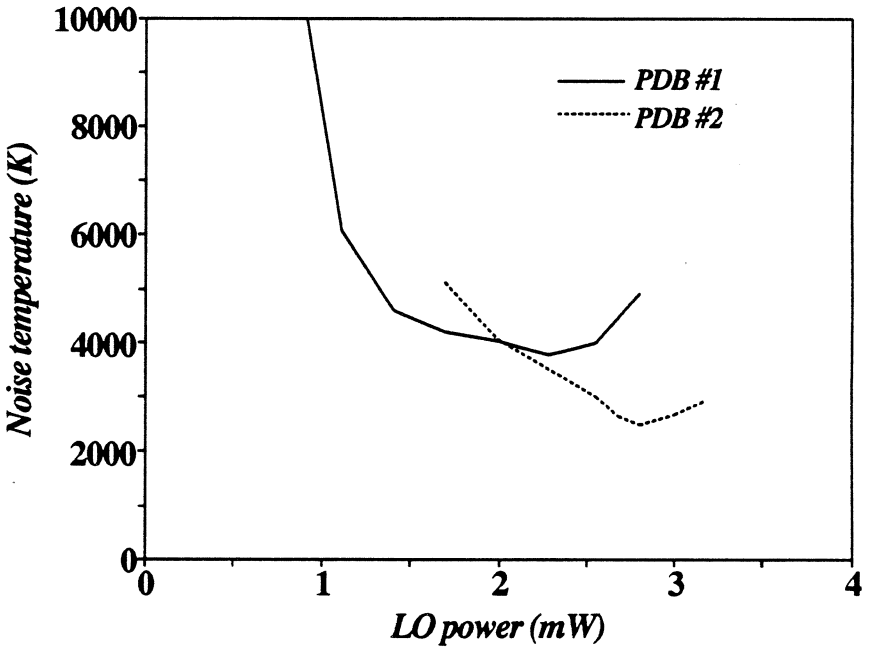

(b)

Figure 8: The diode conversion loss (a) and noise temperature (b) versus estimated LO power in the quasi-optical receiver system for PDB #1 and PDB #2.

Description	C_{j0} fF	ϕ_b V	η	R_s Ω	I_{sat} A	Anode Diam.	Finger Length	Finger Width
#1: MBE GaAs from QED - on 3 mil quartz	5.3	.245 .234	2.2 2.2	20. 20.	2.0×10^{-6} 2.0×10^{-6}	2 μm	20 μm	4 μm
#1: Same as the above	5.3	.245 .234	2.01 2.02	20.4 20.3	1.8×10^{-6} 1.9×10^{-6}	2	20	4
#2: MBE GaAs from UM - on 3 mil quartz	6.6	.398 .394	2.71 2.72	14.6 12.6	4.7×10^{-9} 5.4×10^{-9}	2	20	4

Table 1: Device parameters of PDB diodes for subharmonic mixer measurements. Note that: (1) junction capacitance is calculated from nominal anode area and total depletion width, and (2) other parameters are calculated from measured I-V data. Both forward and reverse parameters are shown.

SHP Mixer type	Diode	Frequency (GHz)	DSB T_{mixer} (°K)	DSB Loss (dB)	LO Power (mW)
JPL Planar-diode Waveguide-mixer	#1	210	3575	10.2	1.2
UM NASA/CSTT Planar Wideband Subharmonic Receiver	#1	182	3795	10.8	2.2
UM NASA/CSTT Planar Wideband Subharmonic Receiver	#2	182	2450	9.5	2.7

Table 2: Device performance at 200 GHz Subharmonic Mixer Measurements.

Cryogenic Mixers for Radioastronomical Radiometers from 660 to 810 GHz

A.I. Harris*, K.-F. Schuster*, L.J. Tacconi* and K.H. Gundlach**

The Max Planck Institute for extraterrestrial Physics has operated a radioastronomical spectrometer system in the highest-frequency atmospheric windows for the past six years. This system is now in routine use at the James Clerk Maxwell Telescope on Mauna Kea. In the course of optimizing the system sensitivity we have extensively characterized the Schottky diode mixers and have developed an experimental 691.5 GHz SIS front end. We will briefly describe the overall spectrometer and the important constraints for radio astronomical applications, discuss our measurements of Schottky diode mixer parameters, and will present results from the SIS work including nonequilibrium effects from pair breaking by LO pump photons with energy above the Nb gap.

---

*Max Planck Institute for extraterrestrial Physics, Garching bei München, Germany
**IRAM, Grenoble, France

This is a review paper. The material presented below has been submitted for publication in IEEE Microwave and Guided Wave Letters.

A Wideband 760GHz Planar Integrated Schottky Receiver

Steven S. Gearhart+, Jeffrey Hesler*, William L. Bishop*,
Thomas W. Crowe*, and Gabriel M. Rebeiz+

+NASA/Center for Space Terahertz Technology
Electrical Engineering and Computer Science Department
University of Michigan
Ann Arbor, MI 48109

*Semiconductor Device Laboratory
Department of Electrical Engineering
University of Virginia
Charlottesville, VA 22903

ABSTRACT

A wideband planar integrated heterodyne receiver has been developed for use at submillimeter-wave to far-infrared frequencies. The receiver consists of a log-periodic antenna integrated with a planar 0.8μm GaAs Schottky diode. The monolithic receiver is placed on a silicon lens and has a measured room temperature double sideband conversion loss and noise temperature of 14.9$\pm$1.0dB and 8900$\pm$500K respectively, at 761GHz. These are the best results to date for room temperature integrated receivers at this frequency.

INTRODUCTION

Open structure mixers with whisker contacted Schottky diodes are the current favorite for far-infrared receivers [1]. Problems with the open structure mixers include low coupling to gaussian beams [2], structural instability, and the lack of an RF matching network. These mixer mounts have an input impedance of approximately 150Ω which does not supply a good conjugate match for a Schottky diode. Additionally, open structure mixer mounts are expensive to array for imaging applications.

Many of these problems can be overcome with the use of a planar integrated receiver. A planar log-periodic antenna with a silicon lens can be designed to couple more than 80% of its pattern to a fundamental Gaussian mode [3,5]. Many receivers can be fabricated at once to form a two-dimensional array, and an RF matching network can be integrated at the antenna apex to conjugately match the Schottky diode impedance. Although the receiver is tested at 761GHz, with the wideband performance of the log-periodic antenna and the absence of a narrowband RF matching network, the receiver is expected to have nearly identical performance over the 500GHz to 1THz frequency range. Planar integrated receivers show great promise to replace open structure mixers for radio astronomy applications.

RECEIVER DESIGN

A planar self-complimentary log-periodic antenna with $\sigma = 0.707$ and $\tau = 0.5$ [4] is chosen for the receiver due to its wideband input impedance and radiation patterns. A self-complimentary antenna has a frequency-independent input impedance of

$$Z_{ant} = 189\Omega/\sqrt{\frac{\epsilon_r+1}{2}} = 74\Omega$$

The log-periodic antenna is linearly polarized and has a cross-polarization level of -5 to -15dB which varies periodically with frequency [5]. The antenna is designed to cover the frequency range of 100GHz to 2.4THz and allows the diode performance to be measured over a wide frequency range. The antenna and GaAs substrate are mounted on an extended hemispherical silicon lens to eliminate power loss to substrate modes. Filipovic [3] has theoretically and experimentally found the lens extension length that results in good Gaussian patterns for a double-slot antenna feed, and Kormanyos has experimentally verified that these results are also applicable for the planar log-periodic antenna [5]. At 761GHz, the log-periodic antenna is placed 1000μm behind a 6mm diameter high resistivity silicon hemispherical lens using GaAs spacer wafers.

A planar UVa GaAs Schottky diode with a 0.8μm anode diameter is integrated at the apex of the antenna. The diode consists of a 900Å n^--layer with a doping of $2x10^{17}cm^{-3}$ and a 5μm n^+-layer doped at $5x10^{18}cm^{-3}$. A finger length of 7μm separates the antenna leads. A surface channel etch is used to etch all of the n^+ material under the finger and around the log-periodic antenna (Figure 2). The diodes have a measured DC series resistance of 25Ω, a junction capacitance of 1-1.5fF, a parasitic capacitance of approximately 2fF, an ideality factor of 1.25, and a built-in potential of 0.77V.

RECEIVER MEASUREMENTS

Antenna patterns and video responsivities were measured at 184GHz and 761GHz. A Gunn diode with a multiplier is used as a source at 184GHz, and a far-infrared laser is used at 761GHz (393μm). Using measured E-, H-, and D-plane patterns, a co-pol directivity of 24±0.5dB with a 12mm diameter silicon lens and 30±1dB with a 6mm lens is calculated at 180 and 761GHz, respectively. The measured cross- polarization levels are -8dB at 184GHz and less than -16dB at 761GHz. The video responsivity measurements were performed by illuminating the receiver with a known plane wave power density and measuring the low- frequency (100Hz) diode video voltage in a 100kΩ load. With respect to the plane wave power incident upon the silicon lens, the measured video responsivity is 370V/W at 184GHz and 160V/W at 761GHz. Compensating for a reflection loss of 1.5dB at 761GHz (0.9dB at 184GHz - a matching layer is used) at the silicon-air interface, an estimated absorption loss of 0.3dB in the silicon, and the measured co-polarized effective aperture of the antenna, the peak video responsivity from a 74Ω source (the antenna terminals) is 810V/W at 184GHz and 380V/W at 761GHz. This is the highest video responsivity ever measured for a planar diode at 761GHz.

Double sideband noise temperature and conversion loss were measured at 761GHz using the hot/cold load technique. The RF and LO power were combined with a Martin-Puplett interferometer. The 1.4GHz IF chain consists of a bias-T, a circulator, a low-noise amplifier chain, a 100MHz filter centered at 1.4GHz, and a calibrated power meter. Additionally, a 10dB coupler was placed between the receiver output and IF chain for IF reflection measurements. A microstrip quarter-wave IF matching network is used to reduce the IF reflection from 2.4dB to 0.9dB. This means that the diode output IF impedance is 250Ω as expected for small diameter diodes. The double sideband conversion loss and noise temperature versus bias is shown in figure 4. At 761GHz, the minimum room temperature conversion loss of 14.9$\pm$1.0dB and noise temperature of 8900$\pm$500K occurs at a bias of 0.4V. This estimated optimum LO power level is 5mW and is large due to the high series resistance of the diode compared to the RF impedance of the junction. This noise temperature and conversion loss are 4-5dB higher than *cooled* whisker contacted 800GHz receivers and represents the best result to date for a planar room temperature integrated receiver in this frequency range.

At 761GHz, the diode series resistance is much higher than the measured DC value of 25Ω and is a primary reason for the high conversion loss and noise temperature. Increasing the n^- doping level from $2\text{x}10^{17}\text{cm}^{-3}$ to $1\text{x}10^{18}\text{cm}^{-3}$ should reduce the RF series resistance at 760GHz. For use at terahertz frequencies, the diode anode diameter should be decreased to 0.5μm for a minimum R_sC_{jo} product [6]. Additionaly, decreasing the thickness of the n^+ level should increase the overall RF coupling efficiency of the antenna.

ACKNOWLEGDMENTS

This work was supported by the NASA/Center for Space Terahertz Technology at the University of Michigan, Ann Arbor. We thank Perry Wood and Tim Scholz at the University of Virginia for their help with the far-infrared laser.

This work is supported by US Army DAHC-90-91-C-0030 and AASERT-DAAL03-92-G- 0057.

REFERENCES

[1] A.I. Harris, J. Stutzki, U.U. Graf, and R. Genzel, "Measured Mixer Noise Temperature and Conversion Loss of A Cryogenic Schottky Diode Mixer Near 800GHz," *Intern. J. Infrared Millimeter Waves,* vol.10, no.11, 1989.

[2] E.N. Grossman, "The Coupling of Submillimeter Corner-Cube Antennas to Gaussian Beams," *Infrared Physics,* vol.29, no.5, 1989.

[3] D.F. Filipovic, S.S. Gearhart, and G.M. Rebeiz, " Double-Slot Antennas on Extended Hemispherical and Elliptical Dielectric Lenses," submitted to the Oct. 1993 Quasi-Optical Techniques issue of *IEEE Trans. Microwave Theory Tech.*

[4] R.H. DuHamel, and D.E. Isbell, "Broadband Logarithmically Periodic Antenna Structures," Technical Report No. 19, Antenna Lab, Univ. of Illinois, May 1957. See also *IRE National Convention Record,* Part-1, 1957.

[5] B.K. Kormanyos, P.H. Ostdiek, W.L.Bishop, T.W. Crowe, and G.M. Rebeiz, "A Planar Wideband 80-200GHz Subharmonic Receiver," submitted to the Oct. 1993 Quasi-Optical Techniques issue of *IEEE Trans. Microwave Theory Tech.*

[6] T.W. Crowe, GaAs Schottky Barrier Mixer Diodes for the Frequency Range from 1-10THz," *Intern. J. Infrared Millimeter Waves,* vol.10, no.7, 1989.

LIST OF FIGURES

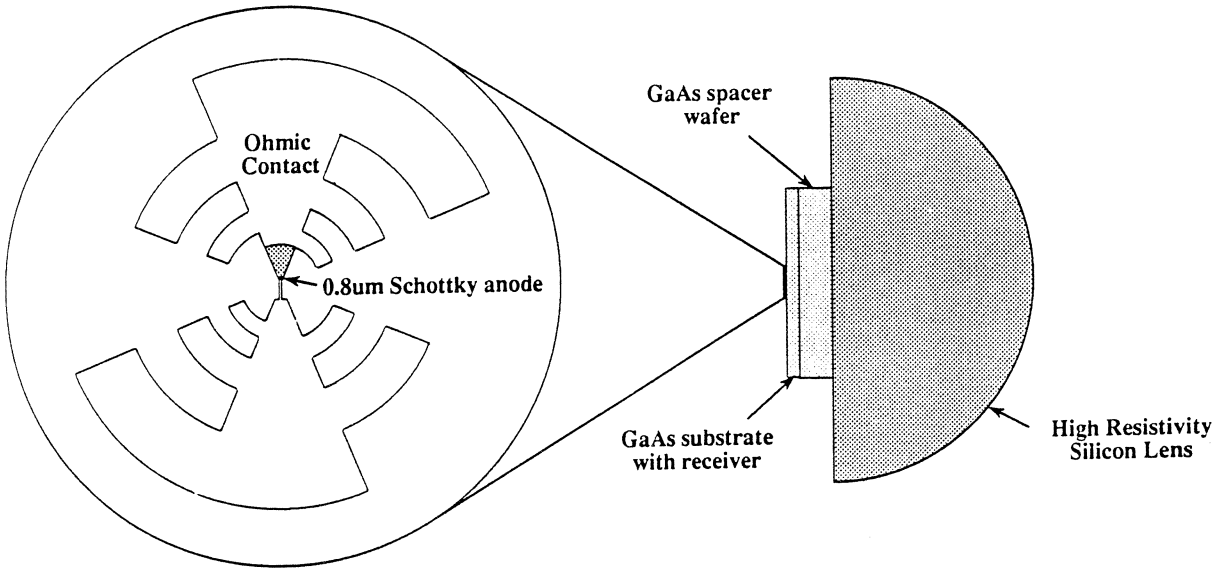

Figure 1: Planar receiver with spacer wafers and silicon lens.

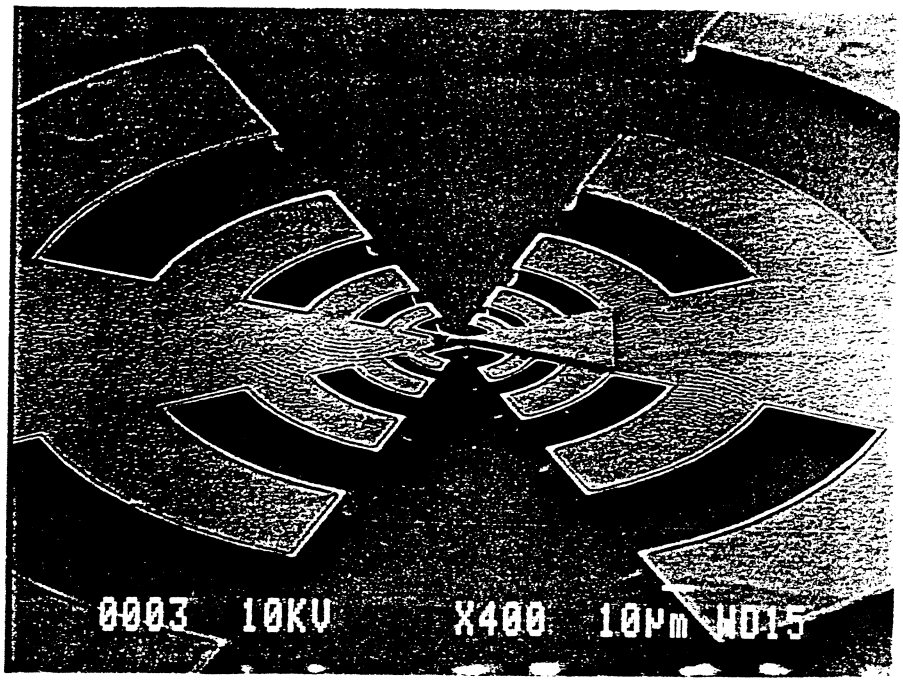

Figure 2: The integrated receiver. Due to the surface channel etch, the log-periodic antenna appears to be a 5μm-high plateau.

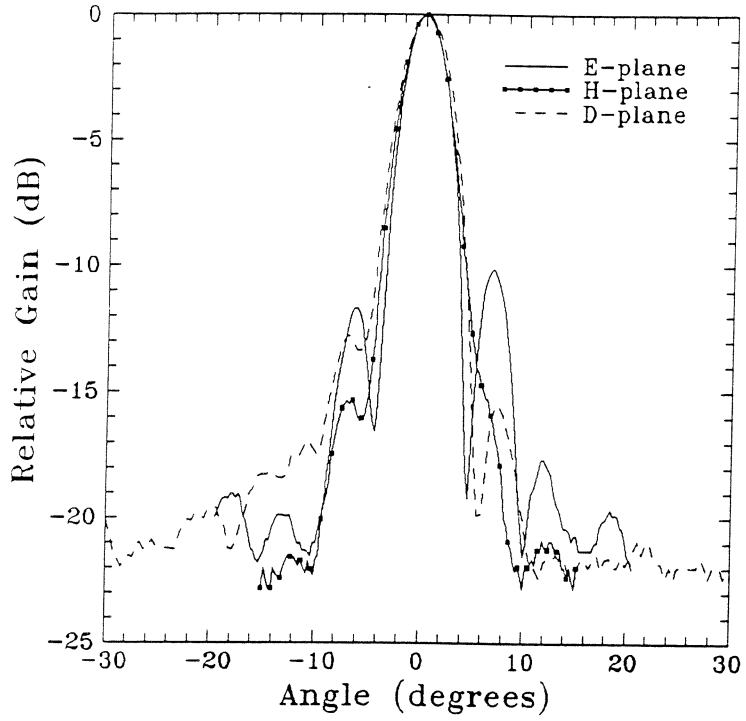

Figure 3: 761GHz antenna patterns. The cross-pol level is less than -15dB in the E-,H-, and D-planes.

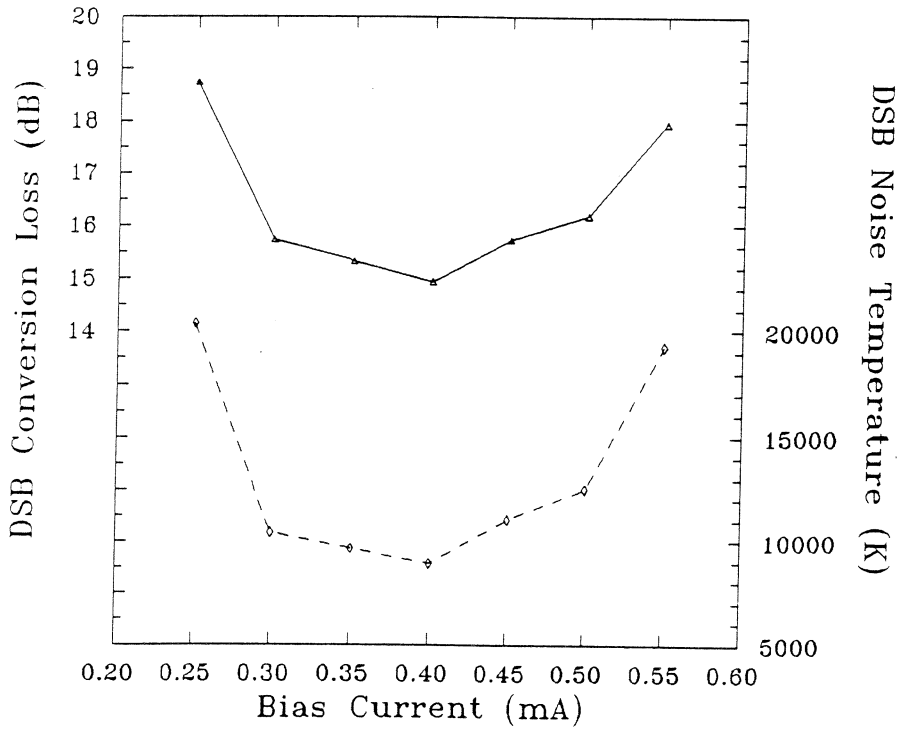

Figure 4: 761GHz DSB Conversion Loss and Noise Temperature vs. bias current.

Noise Temperatures and Conversion Losses of Submicron GaAs Schottky–Barrier Diodes

H.–W. Hübers[1], T. W. Crowe[2], G. Lundershausen[1], W. C. B. Peatman[2], H. P. Röser[1]

1) Max–Planck–Institut für Radioastronomie, Auf dem Hügel 69, D–5300 Bonn 1, Germany
2) Semiconductor Device Laboratory, University of Virginia, Charlottesville, VA 22903, USA

Abstract

We have determined system noise temperatures, mixer noise temperatures and conversion losses of two whisker–contacted submicron GaAs Schottky–barrier diodes at THz frequencies. Both diodes were fabricated with new technologies and have thin epitaxial layers with depletion thicknesses close to the optimum value of about 300 Å. The diodes have exceptional performance as THz mixer elements with noise temperatures and conversion losses 2–3 times below the best previous reported values. The effect of cooling on the diode performance is also investigated.

1 Introduction

A wealth of molecular and atomic transitions are in the THz frequency range, which consequently leads to its great importance for radio astronomy and atmospheric research. For high sensitivity and high spectral resolution measurements, THz heterodyne receivers are used [1]. The heart of this receiver is the mixer element. Above 800 GHz GaAs Schottky–barrier diodes are by far the most sensitive devices for this purpose. Therefore, the development of low noise Schottky diodes is of major importance and will have great impact on radio astronomy as well as atmospheric research.

In this work we report measurements of system noise temperatures T_{sys}, mixer noise temperatures T_{mix} and conversion losses L of two whisker–contacted GaAs Schottky–diodes, called 1T14 and 1T15. The diodes were manufactured at the University of Virginia and the National Nanofabrication Facility at Cornell University using direct–write electron beam lithography [2]. This results in a smaller diode geometry (e.g. 0.25 μm anode diameter of the 1T15), lower capacitance and higher cutoff frequency (see fig. 1). Of main importance are the thin epitaxial layers of 450 Å (1T14) and 300 Å (1T15) and depletion thicknesses close to the optimum value of about 300 Å determined by Roeser et al. [3]. At 803 GHz we have determined the system noise temperature of the diode 1T14 as a function of temperature.

2 Measurement System and Method

Measurements were performed at three different frequencies: 803 GHz, 1397 GHz and 2547 GHz by using laser lines of $^{15}NH_3$ and CH_2F_2. An optically pumped far–infrared ringlaser served

DIODE	1 I 12	1 T 14	1 T 15
ANODE DIAMETER [μm]	0.45	0.5	0.25
EPITAXIAL LAYER THICKNESS D_{epi} [Å]	600	450	~300
DEPLETION THICKNESS AT ZERO BIAS D_{depl} [Å]	500	~380	~300
EPITAXIAL LAYER DOPING $N_D \times 10^{17}$ [cm^{-3}]	4.5	10	10
CAPACITY AT ZERO BIAS C_j [fF]	0.45	0.8-0.9	0.25
SERIES RESISTANCE R_S [Ω]	33	8-12	~20
CUT-OFF FREQUENCY ν_{CO} [THz]	11	15-25	32

Figure 1: Geometrical and electrical parameters of the Schottky–diodes 1I12, 1T14 and 1T15. The capacitances are measured values.

as the local oscillator. Compared to a conventional standing wave resonator, the ringlaser has a higher amplitude and frequency stability [4]. The laser beam and the signal from a hot/cold load were spatially superimposed by a Martin–Puplett diplexer and focused onto the diode by an off axis parabola. The diodes were mounted in a 4 λ corner cube mixer block. The low noise HEMT amplifier of the first amplification stage operated at an IF frequency of 1.55 GHz (bandwidth: $\pm$ 20 MHz) and was cooled to 20 K. Its noise temperatures were 35 K (803 GHz, 1397 GHz) and 130 K (2547 GHz).

Cooling of the Schottky–diode was done with a cryocooler (CTI Cryogenics) with the diode mounted directly on the cold head. The temperature could be varied from 300 K to 20 K and was measured and stabilized with a Si–diode temperature controller (Lake Shore Cryotronics). For calibration this diode was mounted in a dummy mixer block at the position of the Schottky diode.

The system noise temperature T_{sys} has been measured by the total power method using black bodies at room temperature and at liquid nitrogen temperature. A directional coupler with an additional noise diode was used to measure the impedance mismatch (see fig. 2). According to the equations given by Stimson et al. [5] and according to

$$T_{sys} = T_{mix} + L * T_{if} \tag{1}$$

we have determined T_{mix} and L from the measured impedance mismatch and T_{sys}.

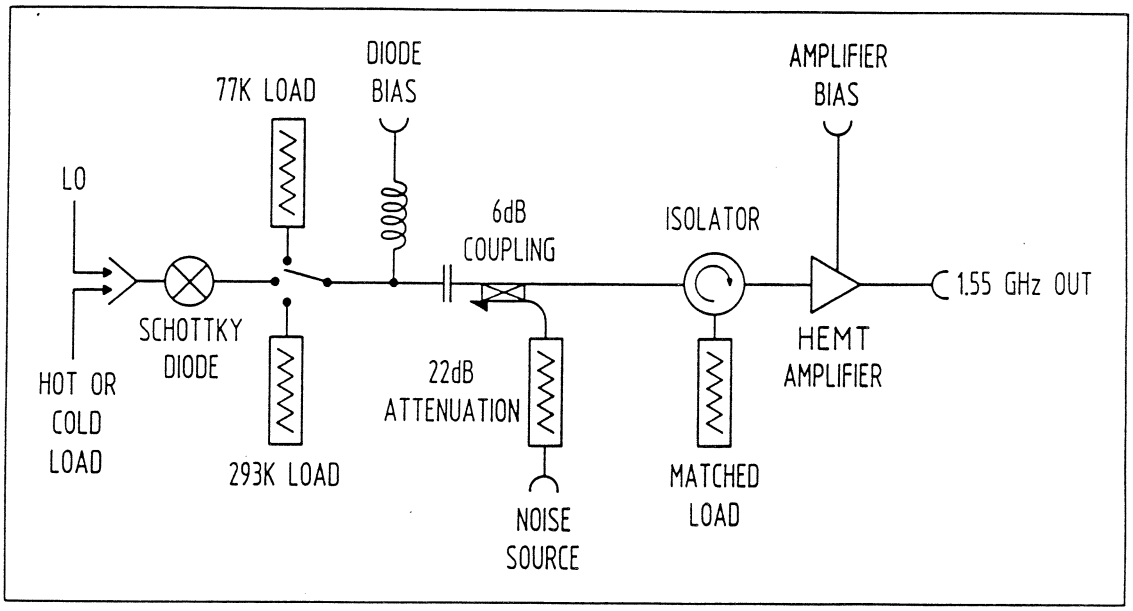

Figure 2: Block diagram for the calibrated heterodyne measurements.

3 Results

Both diodes show exceptional sensitivity (see fig. 3), which is 2–3 times better than the best previous reported results [6], [7]. Mixer noise temperatures and conversion losses are also a factor of 2–3 better than before. Figure 4 gives a summary of the main results. All values are DSB and are corrected for atmospheric losses.

At 803 GHz the diode 1T14 is the best. Its T_{mix} of 1100 K is only a factor of 29 above the quantum limit in terms of $h\nu/k$ but this ratio increases with frequency to 70 at 2547 GHz. T_{sys} (1200 K) and L (5.3 dB) at 803 GHz are also remarkably low. At higher frequencies the diode 1T15 is superior. Its quantum efficiency (defined as $\eta = kT_{mix}/h\nu$) decreases from 43 at 803 GHz to 34 at 2547 GHz. But the required local oscillator (LO) power of 1–12 mW is still high.

Figure 5 shows the improvement of T_{sys} with decreasing temperature, which is essentially due to the decreasing IF temperature. T_{mix} changes insubstantially with temperature. This is demonstrated by a comparison of the system noise temperatures of the same diode with the same contact and the same cooled HEMT amplifier at room temperature and at 20 K. But it is important to note that in the cooled diode–amplifier configuration, the diode impedance was not matched to the amplifier whereas the warm diode was matched to the amplifier.

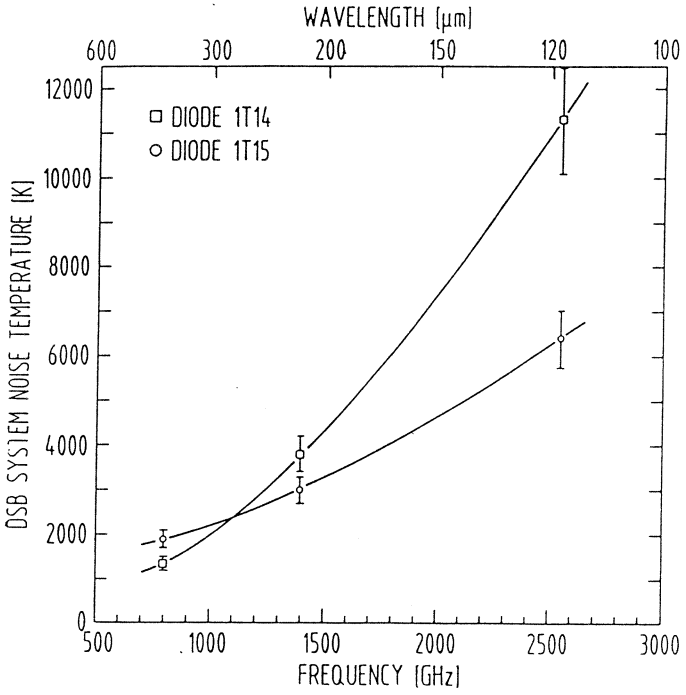

Figure 3: System noise temperature of the Schottky–diodes 1T14 and 1T15 at room temperature as a function of frequency

DIODE 1T14	803GHz	1,397GHz	2,547GHz
T_{SYS}[K]	1,200	3,700	11,300
T_{MIX}[K]	1,100	3,400	8,500
L[dB]	5.3	9	~13
P_{LO}[mW]	1	8	12

DIODE 1T15	803GHz	1,397GHz	2,547GHz
T_{SYS}[K]	1,900	3,000	6,400
T_{MIX}[K]	1,700	2,600	~4,100
L[dB]	6.5	9	~12.5
P_{LO}[mW]	1	1	10

Figure 4: System noise temperature, mixer noise temperature, conversion loss (DSB values) and required LO power for the diodes 1T14 and 1T15 at 803 GHz, 1397 GHz and 2547 GHz. At 803 GHz and 1397 GHz the IF noise temperature was 35 K whereas at 2547 GHz it was 130 K.

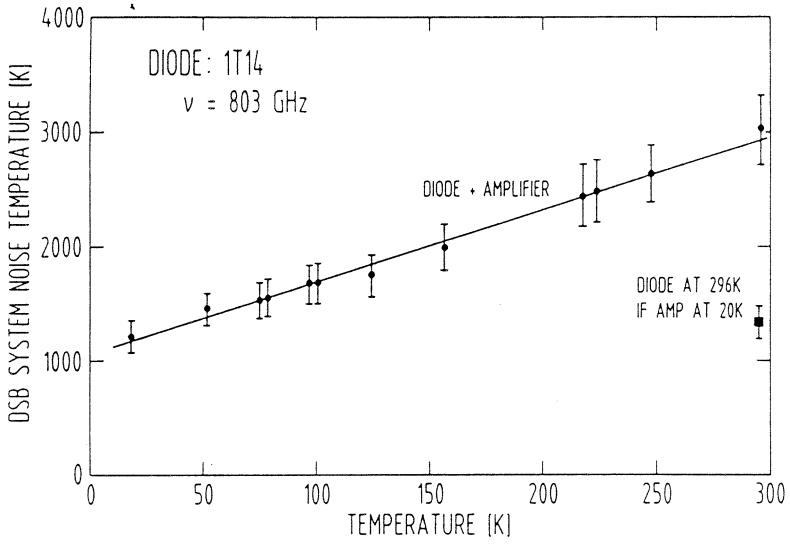

Figure 5: System noise temperature of the diode 1T14 at 803 GHz as a function of temperature. For comparison the system noise temperature of the same diode at room temperature but with a cooled (20 K) amplifier is also shown. Note, T_{if}=200 K at room temperature and T_{if}=35 K at 20 K.

4 Discussion

Experiments have shown that when the diode bias and LO power are adjusted for optimum heterodyne receiver sensitivity at a given frequency, ν, the average number of electrons that pass through the Schottky contact during each LO cycle is a constant, N_e [3]. This behaviour is expressed by the experimentally obtained equation for the optimum mixing current, I_{opt}

$$I_{opt} = N_e \, e \, \nu \,, \tag{2}$$

where N_e does not vary with frequency, but rather is a constant for each diode type. The constant charge, $N_e e$, transferred through the diode each LO cycle can be related to the diode area , A, and epitaxial doping density, N_d, according to

$$N_e = (A \, D_{depl}) \, N_d \,. \tag{3}$$

It has also been shown that the voltage drop, V_{LO}, across the diode due to the LO power at the optimum bias current for mixing is independent of the LO frequency [3],

$$V_{LO} = constant. \tag{4}$$

A voltage drop of this amount can be expressed in terms of a depletion depth in the Schottky contact as

$$V_{LO} = (D_{depl}^2 \, e \, N_d)/2\epsilon_s \,, \tag{5}$$

where ϵ_s is the dielectric permittivity of GaAs. Equations (3) and (5) both yield a depletion depth of about 300 Å for a variety of diodes tested. It appears that for a given diode a specific number of electrons, N_e, take part in the mixing process each LO cycle, regardless of the frequency. The same behaviour has been confirmed with our new diodes.

A comparison of these new results with the best previous diode, 1I12, shows that the increase in doping density and the reduction of the epitaxial layer thickness has led to significant improvements in performance. Since the new diodes have epitaxial layer thicknesses close to the value of D_{depl} obtained above, it may be that this is the primary reason for the improved performance. Also,since the epitaxial layer thickness is well below the mean free path in GaAs (typically 500–1000 Å [8]) and the Debye length $l_d < 150$ Å [8], it is possible that ballistic transport effects are becoming more important.

It is worth noting that at 803 GHz the antenna coupling loss of about 3 dB [9] is the main contribution to the mixer conversion loss of 5.3 dB. This loss can be decreased by the addition of a conical horn in the corner cube configuration, which lowers the system noise temperature about 30% [10]. Therefore, a DSB system noise temperature at 803 GHz below 1000 K seems to be achievable.

5 Summary

Record noise temperatures and conversion losses were measured, corresponding to quantum efficiencies as low as $T_{mix}=29h\nu/k$ (803 GHz), $38h\nu/k$ (1397 GHz) and $34h\nu/k$ (2547 GHz).

These results fit in the previous work [3] which indicated that a specific number of electrons per LO cycle participate in the mixing process for a given diode type regardless of the frequency. It is also clear that increased epitaxial doping and reduction of the diode epitaxial layer thickness to approximately 300 Å has led to substantially improved performance. Reduction of the diode temperature to 20 K led to no substantial improvement in the mixer noise temperature. At 803 GHz a DSB system noise temperature below 1000 K (26 $h\nu/k$) seems to be achievable with an improved antenna configuration.

Acknowledgements: We thank Ken Zelin for assisting with the diode fabrication and Walter Esch for technical support during the experiments.

References

[1] H. P Röser, IR Physics, vol. 32, pp. 385–407, 1991

[2] W. C. B. Peatman, P. A. D. Wood, D. Porterfield, T. W. Crowe, M. J. Rooks, Appl. Phys. Lett., vol. 61, no. 3, pp. 294–296, 1992

[3] H. P. Roeser, R. U. Titz, G. W. Schwaab, M. F. Kimmitt, J. Appl. Phys., vol. 72, no. 7, pp. 3194–3197, 1992

[4] H. K. E. Stadermann, P. B. van der Wal, Proc. 16th Int. Conf. IR and MM Waves, Lausanne, 1991

[5] P. A. Stimson, R. J. Dengler, P. H. Siegel, H. G. LeDuc, Proc. 3rd Symp. Spave THz Tech., Ann Arbor, USA, 1992

[6] R. U. Titz, H. P. Röser, G. W. Schwaab, H. J. Neilson, P. A. Wood, T. W. Crowe, W. C. B. Peatman, J. Prince, B. S. Deaver, H. Alius, G. Dodel, Int. J. IR and MM Waves, vol. 11, no. 7, pp. 809–820, 1990

[7] A. I. Harris, J. Stutzki, U. U. Graf, R. Genzel, Int. J. IR and MM Waves, vol. 10, no. 11, pp. 1371–1376, 1989

[8] M. Shur, GaAs Devices and Circuits, Plenum Press, New York, 1987

[9] B. Vowinkel, Int. J. IR and MM Waves, vol. 7, no. 1, pp. 155–170, 1986

[10] H. Nett, Ph. D. thesis, University of Bonn, 1988

MEASUREMENT AND STUDY OF THE EMBEDDING IMPEDANCE PRESENTED BY THE WHISKER ANTENNA OF A SCHOTTKY DIODE CORNER CUBE MIXER

C M Mann,** T Suzuki,* J J Chang,** T Nozokido,** Y Kuwano* and K Mizuno.*

ABSTRACT

A 250X scale model of a Schottky diode corner cube mixer designed for operation in the terahertz region has been built and tested. It has been successfully used to measure the embedding impedance presented to the diode at the whisker tip and also determine the impedance of the whisker antenna itself. The results are presented and their relevance to the performance of an operational mixer is considered.

* Research Institute of Electrical Communication
Tohoku University, Sendai, 980, Japan

** Photodynamics Research Centre,
The Institute of Physical and Chemical Research (Riken)
19-1399 Aza-Koeji, Naga-Machi, AobaKu, 980 Sendai, Japan.

INTRODUCTION

The technique of microwave limb sounding from space as implemented by the Upper Atmosphere Research Satellite (UARS) has been shown to be an extraordinarily powerful tool for the study of the Earth's atmosphere. The technique can be further enhanced if the observational frequency is raised, largely because of the increased strength of the signal. With the advent of NASA's and ESA's future Earth Observing Systems (EOS), impetus has now been given to the area of submillimetre wave devices to take full advantage of this fact.

This research area has been of interest to radio astronomers, plasma physicists, molecular spectroscopists and atmospheric researchers. Due to the fabrication difficulties associated with waveguide based devices at these frequencies, the emphasis has mainly been placed on mixers making use of an open or quasi-optical structure. Of these the most studied by far has been the "corner cube" mixer. The basic layout of a typical corner cube mixer is shown in figure 1.

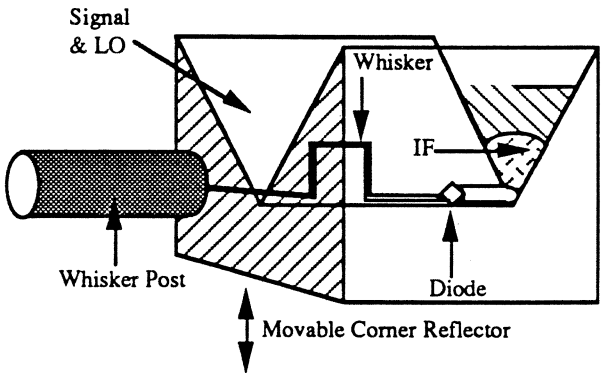

fig 1

Such mixers are comparatively easy to physically realise compared to their waveguide equivalent but such a simple format has it's associated disadvantages. From a performance perspective the most obvious is their relatively poor coupling efficiency but this is usually acceptable for most uses and is somewhat compensated for by the lower losses in the signal path. Indeed excellent performance has been obtained by various researchers using designs incorporating subtle variations of the basic concept. For space applications, however, most of the designs in current use have one serious flaw which is the need for the contact to the diode to be made via a long whisker. This is necessary because the whisker not only forms the electrical contact to the diode but also forms the main antenna element. It is usually four wavelengths (4λ) at the signal frequency in order for the coupling efficiency between the mixer and the input beam to be optimised, although recent examinations report that shorter whiskers may be appropriate [1,2]. This in itself would not be a problem if the diodes that are to be contacted were much larger than those required at terahertz frequencies ($\approx 0.5\mu m$ in diameter). Only the smallest of whisker tips can be used to contact the diode anode. As the whisker can be anything from 6-50μm in diameter it represents a large mass with respect to the whisker tips dimensions. In order to visualise the scale of this physical mismatch it useful to consider the dimensions of the scaled whisker in our model. For the thickest whisker investigated (50μm in diameter), whilst the 250X scaled whisker tip is represented by a piece of wire 0.1mm in diameter, the whisker itself is made from copper pipe that is 13mm in diameter and is over one metre in length. It is not surprising therefore that in real life once a contact to a diode has been made, the mixer has to be treated extremely carefully for the contact to stay intact. The chances of such a structure reliably surviving the vibration and

thermal environmental tests required for space flight are probably minimal. The rigours of space qualification should not be confused with those experienced in an astronomical receiver or during an airborne experiment. A device intended for space flight not only has to survive the qualification procedure, the rigours of launch but once in space has to survive for the entire duration of the mission in a stable condition and of course must **never** fail. For NASA's EOS programme the expected mission life time is 5 years. The format of the device will almost certainly have to be altered in some way in order for the corner cube to be considered a viable option.

The first part of this report therefore examines the part played by the whisker in the operation of the corner cube mixer to determine as to what extent the structure can be modified to make it more rugged. Secondly, the embedding impedances measured are used in conjunction with a computer analysis to assess the overall effect of the modifications on the mixers performance.

SCALE MODELLING OF THE CORNER CUBE MIXER

Whisker Antenna Impedance

The corner cube mixer was to be examined using a technique similar to that described by Eisenhart and Khan [3]. A HP8510C network analyser having a maximum operating frequency in coaxial line of 20GHz was available to make the measurement. For full frequency coverage a 250X model was required. Because a complete model would have been too large a 50X model of just the whisker post arrangement was first considered. This model could be examined only to a scaled frequency of 800GHz but it was hoped that this would be sufficient in also approximating the whisker posts effect at higher frequencies. This proved to be the case and it was then possible to ignore most of the whisker posts structure. The complete 250X mixer model then took the form shown in figure 2. The whisker antenna impedance is the characteristic impedance of whisker antenna minus the effect of it's tip.

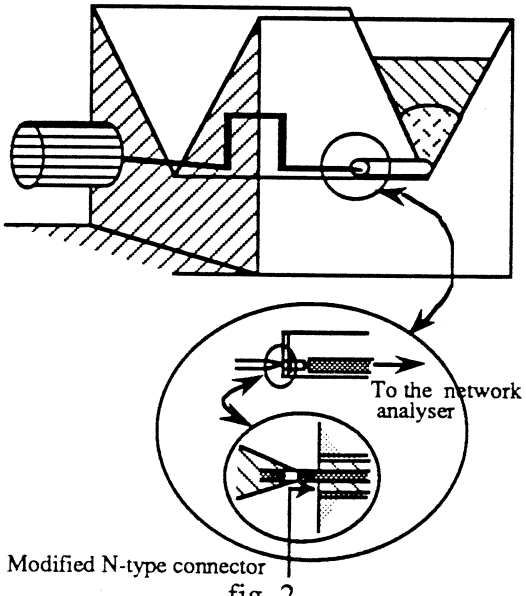

fig. 2

To measure the thickest whisker antenna's impedance it was necessary to make a simple 50Ω transformer to dimensionally match the N-type connector to the 13mm diameter scaled whisker. The signal could then be launched directly into the whisker antenna. The whisker

antenna impedance was found to be much lower than that measured at the whisker tip (30 - 50Ω versus 90 - 120Ω). The same procedure was carried out for other whisker diameters and the results are plotted in fig 3.

For tuning purposes it would be useful if the diode embedding impedance could be altered by varying the whisker dimensions. The easiest of these to change in real life would be the length of the whiskers first section. This was tried in the model. It was found that this could be altered with no effect on the impedance measured at the end of the 50Ω transformer. In order to understand this the model was again examined in the time domain and it was found that the reflections from the bend were down at the -20dB level. This was not true if the first bend was very abrupt. Provided the first bend was of the order of $\approx\lambda/4$ in radius the active part of the antenna was limited to the length of whisker between the tip and the first bend. This has also been found by Matrese and Evenson [4]. The impedance could however be changed if the whisker was terminated too soon after the bend. If this distance was several wavelengths or more the final termination had no resultant effect on the embedding impedance at the diode. It was therefore apparent that the full whisker was not required for normal mixer operation and could be replaced by a simple right angle bend with no resultant loss of performance.

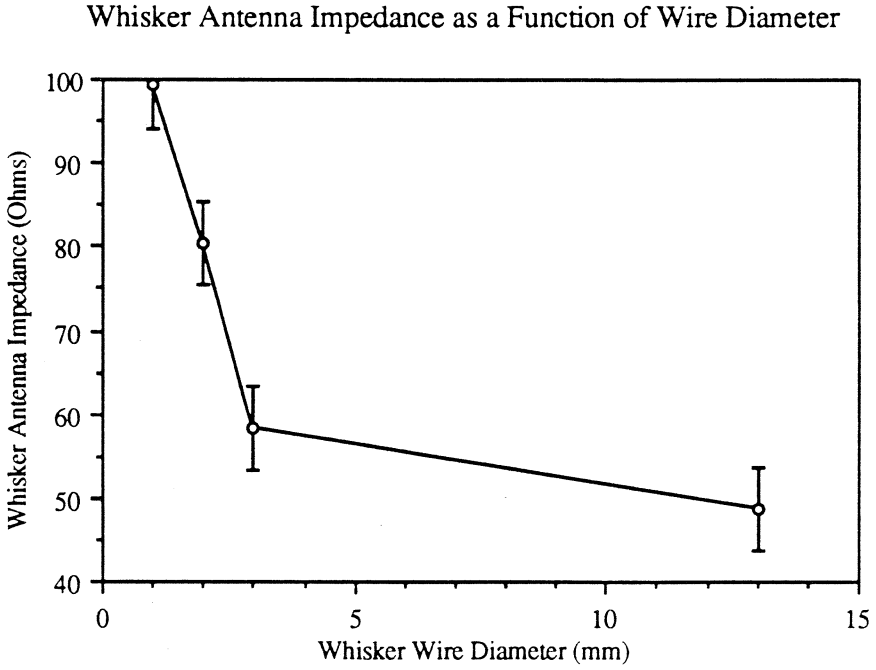

fig 3

The antenna appeared to be working as expected. The presence of the main lobe and side lobes could be established in a crude manner by placing a small metallic disc in the field and observing the magnitude of the reflection in the time domain.

Whisker Tip Impedance

This impedance was rather more difficult to measure than that of the whisker antenna itself. The main reason for this was that even for a scaling factor of 250 times, the diameter of the whisker tip was still only 0.1mm. Because of this an airline structure was used for the transition between the N-type connector and the scaled whisker tip. It was not possible to

machine a scaled version of the tip directly, instead a short length of wire (2mm) of the appropriate diameter was soldered between the whisker tip and the N-type connector pin. It was then possible to vary the effective whisker tips diameter very accurately. By using this arrangement it was possible to represent the true physical form of the whisker. The whisker could be reconnected easily in a reproducible manner, the details of the arrangement are shown in figure 4. It should be noted that for all results the distance between the whisker and antenna apex was set at 1.2λ for the scaled frequency corresponding to 1.4THz. Changing this parameter for each frequency would have made the measurement time consuming and laborious. In addition, the small change resulting in the diode embedding impedance could not have been easily resolved using this technique.

Different wire thicknesses corresponding to different tip diameters were tried for a range of whisker diameters.

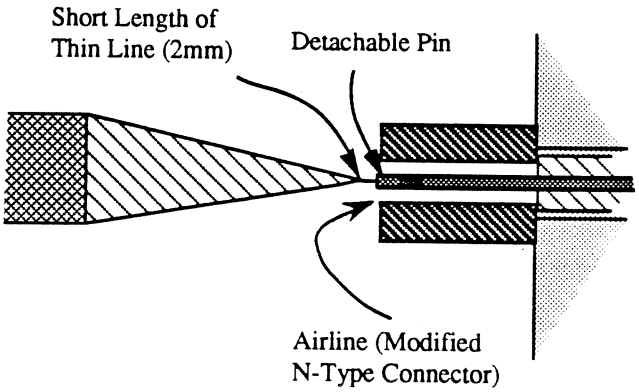

fig 4

The combined results are shown in figure 5. The parameters plotted are the real component of the normalised tip impedance versus the normalised tip diameter and are defined as the following:-

$$Z_{norm} = \frac{Z_{tip}}{Z_{ant}} \qquad \ldots 1$$

Where:-

Z_{norm} = Real component of the normalised tip impedance.
Z_{tip} = Real component of whisker tip impedance.
Z_{ant} = Real component of whisker antenna impedance.

$$D_{norm} = \frac{D_{tip}}{D_{whsr}} \qquad \ldots 2$$

Where:-

D_{norm} = Normalised tip diameter.
D_{tip} = Diameter of the whisker tip.
D_{whsr} = Diameter of the whisker.

The reactive component of the embedding impedance was not considered as it's magnitude was always less than 50 Ω and the technique was not deemed accurate enough to state the measured value reliably down at this level. The plot shows the effect of the tip diameter on the diode embedding impedance for all frequencies. For the thickest whisker wire, the cone section at the whisker tip represents a considerable fraction of a wavelength at the signal

frequency. This represents a section of non uniform transmission line, the input to which is the high impedance (≈200Ω) of the whisker tip itself.

Normalized Whisker Tip Impedance versus Normalized Tip Diameter

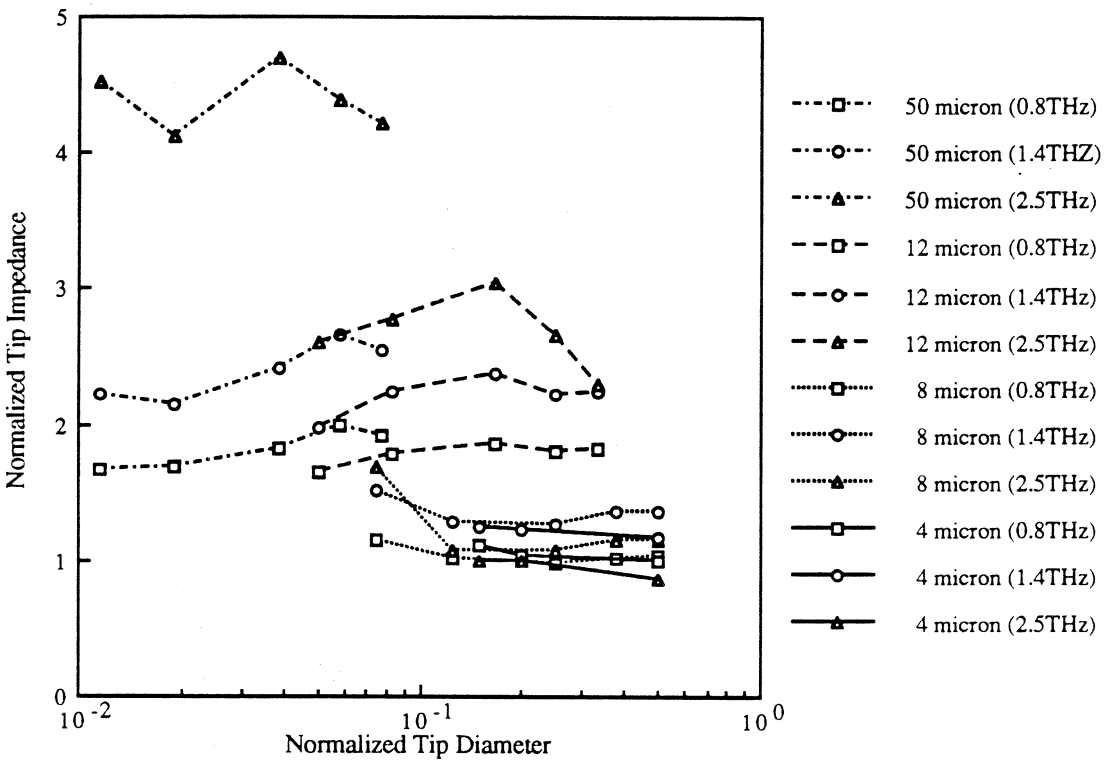

fig 5

Whisker Tip Impedance vs Frequency

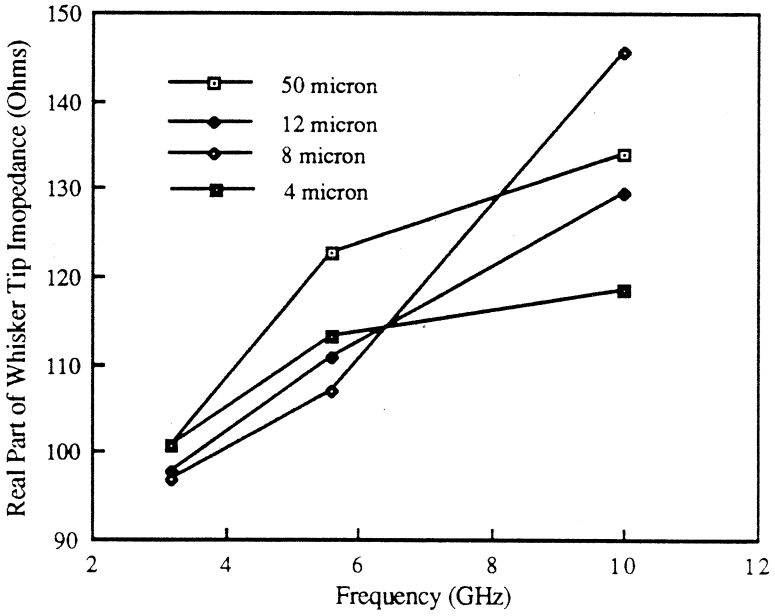

fig 6

The effect of this is to transform the lower impedance of the whisker antenna to some intermediate value. For thinner whiskers this is not the case. The geometry associated with the whisker etching process results in a much shorter cone section. Consequently the signal does not see the short length of high impedance line at the whisker tip, instead only that of the whisker antenna. The normalised impedance of the whisker tip therefore approaches the value 1.0 for successively thinner whiskers. For the typical whisker diameters currently in common use the embedding impedance is found to be approximately 120+/-20 Ω. The embedding impedance presented to the diode for different diameters of whisker wire is shown in figure 6. The diameter of the whisker tip is the same for all measurements (0.6μm). It can be seen that even though the characteristic impedances for different thickness whisker antennae vary substantially (from ≈ 30 - 100 Ω, fig 3), the impedance measured at the whisker tip is relatively similar. For the 50μm whisker antenna the embedding impedance at the diode is over four times that of the whisker antenna characteristic impedance. This effect can presumably be neglected for lower frequencies in the millimetre region where the wavelength is considerably larger than the whisker tips length.

COMPUTER MODELLING

In order to further understand mixer operation a computer model has been used. The program is a modified version of the original by P. H. Siegel et al[5] and allows for the optimisation of conversion loss and noise performance as a function of LO power and DC bias. The IF port is always assumed conjugate matched.

Whilst the computer model does not take account of additional effects that may be present at terahertz frequencies (i.e. plasma resonance, surface loss etc..) it has been used with some success at lower frequencies[7] and does provide an approximate guideline with regard to expected performance. Also, like the scale modelling it does give insight to the effects of circuit adjustment, for instance, embedding impedance and diode parameters. In this way it is possible to assess the overall action of each parameter on the mixers performance so as to establish tuning trends which can then be used to optimise the device in an understandable manner.

The diode embedding impedances obtained from the scale model were input into the computer program along with values for the diode parameters (table I). These were obtained from well known formulas but measured parameters from actual diodes were used as a reference (0.4μm diameter with an epi-layer thickness of 800Å).

Local oscillator frequency	1.4 THZ
Intermediate frequency	1.0 GHz
Mixer operating temperature	300 K
Diode reverse saturation current	7.3^{-19} A
Diode capacitance at zero bias	0.3 fF
Diode built in potential	0.96 V
Diode capacitance law exponent	0.5
Diode ideality factor	1.08
Diode series resistance at DC	83.3 Ω
Diode chip thickness -width-length	100 μm - 200 μm - 200 μm
Antenna coupling efficiency	0.5

Table I

The measured embedding impedances for the conventional 4λ whisker were as follows:-

$Z_{emb}(f_{LO}) = 133.6 - j\ 5.0$; $Z_{emb}(2f_{LO}) = 82.7 - j\ 11.0$; $Z_{emb}(3f_{LO}) = 62.5 + j\ 18.9$;

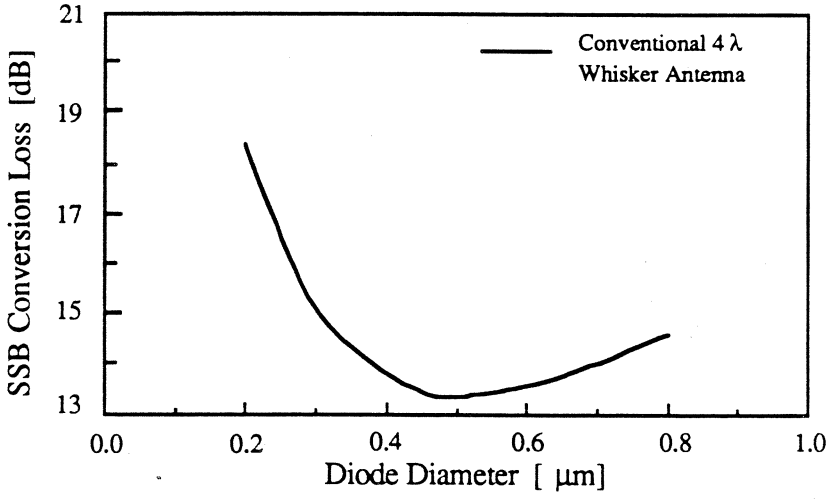

fig 7

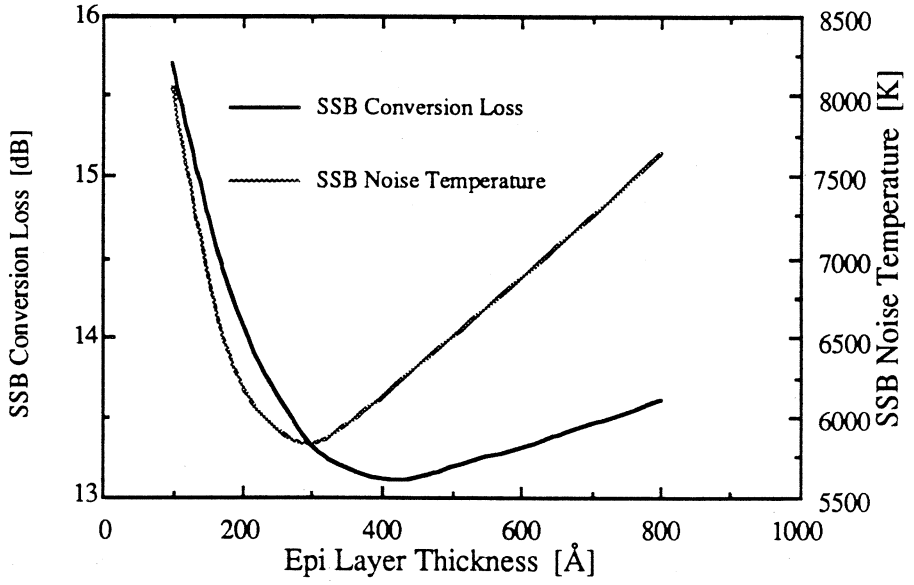

fig 8

The impedances for the signal side bands are assumed to be the same as those used for the corresponding LO harmonics. This is considered reasonable bearing in mind the low IF frequency used. The predicted performance for this mixer configuration gives reasonable agreement to that measured in the real device[6]. The program was used to determine the effect of various diode parameters. Figure 7 shows how the conversion loss of the mixer varies as function of diode diameter. Decreasing the diameter should initially give an improvement in performance which eventually reverses to a degradation for very small diodes. The effect of varying the epi-layer thickness is shown in figure 8. These trends are currently under investigation and diodes having the theoretically optimised parameters are now being fabricated for assessment. The only truly valid way of verifying the model is to vary the mixer format in a controlled way and check that the change in the device's performance agree

with the predictions. This will require a comprehensive iterative investigation during which full control over both diode and antenna parameters will be essential

DISCUSSION

The main finding of this work is that the embedding impedance presented to the diode will essentially be independent of the whiskers diameter and length of the first section. This is true provided that the first bend in the whisker is not too sharp and that the final termination is not made too close to the bend. If the first bend in the whisker is made too sharp a standing wave will be present on the whiskers first section. The reactive component of the embedding impedance can then be substantial allowing the real component to be varied as a function the first section length. A similar argument applies if the final termination of the whisker is positioned too close to the bend.

Obviously the technique used has it's limitations, for instance the scaling of the real mixers surface finish was not possible and discrepancies due to the skin effect have not been considered. However, these measurements do show the tendencies of embedding impedance variation with whisker tip parameters which will also be present in the real device. For example, when the whisker diameter is reduced, the tendency for the characteristic impedance of the whisker antenna to increase is apparent.

These results suggest that only a limited improvement in performance could be found by varying the whisker diameter (D). Experience gained during the optimisation of lower frequency (≈350Ghz) Schottky diode mixers in waveguide would suggest caution however. Mixers assembled using only 12μm diameter whisker wire displayed a wide variation in performance even though near identical whiskers were used. This was finally traced to undesirable effects related to the excess pressure exerted on the diode anode by the whisker tip. This resulted in an increase in the diode noise and a degradation of the diode characteristic. Only when these effects were removed by improving the contacting process was it possible to optimise the devices in an understandable manner. The force exerted by a whisker is proportional to D^4 so it is likely that similar effects may be present for current corner cube mixers. It is possible that the use of thinner whisker wire will result in improved performance whereas these results suggest that it should not. The reduction in the force exerted on the diode may lead to an overall improvement even though the RF match to the diode has not changed.

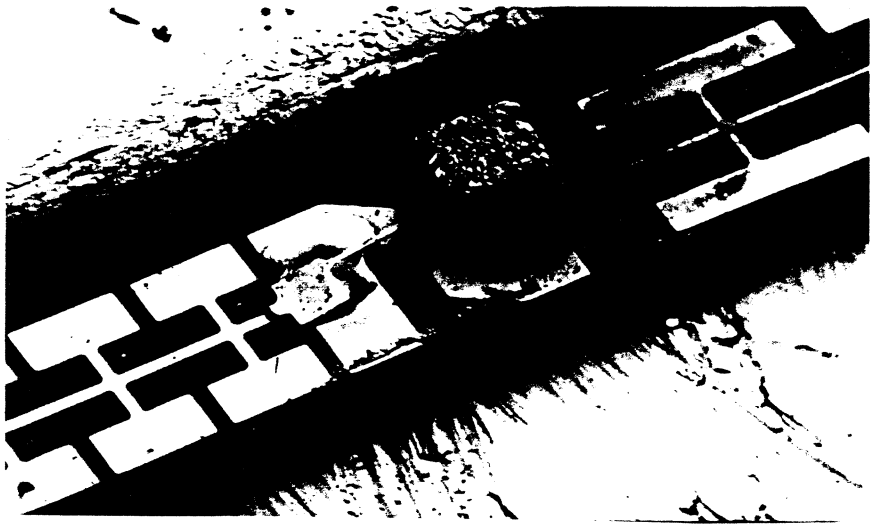

fig 9

The physical resilience of the structure could be improved dramatically if the diode were contacted using a much shorter whisker. This can achieved by fixing both the diode and the contacting whisker to a dielectric substrate[6, 7]. The antenna element of the mixer can then be fabricated using photolithographic techniques. Techniques which make the assembly of such small circuits possible are now becoming available. Figure 9 shows a circuit designed for operation in waveguide at 600GHz {fabricated by the Millimetre Wave Technology group at the Rutherford Appleton Laboratory, Oxon, UK}. The circuit has been realised using a novel 5μm wide quasi-planar whisker which is contacted to the 1μm diode and then fixed in place using Indium solder. The rough cylinder lying alongside the substrate is a human hair approximately 70μm in diameter. The contacting process is controlled with great precision using stepper motor drives and piezo-electric pressure transducers to determine safe limits for the force acting on the diode. Further work is currently underway but already the concept shows great promise and ideally lends itself to terahertz devices.

ACKNOWLEDGEMENTS

We would like to thank the Millimetre Wave Technology group at the Rutherford Appleton Laboratory for making available details of the Quasi-Planar technology.

REFERENCES

[1] "The Coupling of Submillimeter Corner-Cube Antennas to Gaussian Beams", E. N. Grossman, Infrared Phys. Vol. 29, pp.875-885, 1989

[2] "A Corner-Reflector Mixer Mount for Far Infrared Wave Lengths", J.Zmuidzinas, A. L. Betz, R. T. Boreiko, {Accepted for Publication in Infrared Physics}.

[3] "Theoretical and Experimental Analysis of a Waveguide Mounting Structure", R. L.Eisenhart and P. J. Khan, IEEE Trans. on MTT, Vol MTT 19. Pg 706-719, Aug 1971.

[4] "Improved Coupling to Infrared Whisker Diodes by use of Antenna Theory", Matrese, L.M. and Evenson, K.M., Appl. Phys. Lett., 17, no.1, pp.8-10, July 1970.

[5] P. H. Siegel, A. R. Kerr, W. Hwang, NASA Technical Paper 2287, March 1984.

[6] "Low Noise GaAs Schottky diode for Submillimeter Wave Detectors/Mixers", T. Suzuki, H. Shinohara, K. Mizuno, H. P. Roser, R. Titz, The 3rd Asia-Pacific Microwave Conference Proceedings, Tokyo, 1990

[7] "183GHz Double Diode Subharmonically Pumped Mixer", C M Mann, D N Matheson, M R B Jones. Int. J. of Infrared and Millimeter Waves. Vol.10. No 9. 1989.

[8] "A Novel 183GHz Subharmonic Schottky Diode Mixer", C M Mann, PhD Thesis, Queen Mary and Westfield College, University of London. May 1992.

0.5 THz SIS Receiver with Twin junction Tuning Circuit

V.Yu. Belitsky*, S.W. Jacobsson**, L.V. Filippenko*,
S.A. Kovtonjuk*, V.P. Koshelets*,
and
E.L. Kollberg**.

* Institute of Radio Engineering and Electronics, Russia Academy of Sciences, Mokhovaja 11, 103907, Moscow, Russia.

** Department of Microwave Technology, Chalmers University of Technology, S-412 96 Göteborg, Sweden.

Abstract

An open structure SIS mixer has been designed for operation in the frequency band 400–550 GHz and successfully tested in a laboratory receiver setup. A novel type of SIS mixer structure was implemented and integrated with an equiangular spiral antenna. In this structure two identical (twin) SIS junctions are connected so that conjugate impedance of the first exactly compensates the reactance of the second. This tuning circuit was connected to the spiral antenna via an impedance transformer. Using this combination we obtained broadband SIS mixer operation with measured instantaneous frequency range more than 80 GHz without any mechanical tuners. The Nb–AlO_X–Nb SIS junctions have each an area of 4 μm^2 and an $\omega R_n C$-product of 7.4 at 500 GHz. The relatively large area SIS junctions together with the particular topology of the twin tuning circuit make it easy to suppress the Josephson effect. The cooling to 3.5 K dramatically improved the receiver performance. Measured SIS mixer receiver noise temperatures, which include **all** losses, were below 300 K DSB across the 450–515 GHz range with the best noise temperatures <250 K DSB at 453 GHz and <270 K DSB at 512 GHz.

Response of Ramp-Type High-T_c Josephson Junctions to Near Millimeter-Wave Radiation

R. Gupta*, Qing Hu*, D. Terpstra**, G.J. Gerritsma** and H. Rogalla**

To explore the potential of using high T_c Josephson junctions as sensitive millimeter- and submillimeter-wave detectors, we have studied the response of a YBCO/PBCO/YBCO ramp-type junction to coherent radiation at 176 GHz and 270 GHz. The I-V characteristic of the junction closely resembles the prediction of the RSJ model. The I_cR_n product of the junction is 0.25 mV at 5K. The millimeter-wave radiation is coupled to the junction via a quasioptical structure which focuses the radiation onto the junction through a yttrium-stabilized ZrO_2 substrate. At 176 GHz, we have observed as many as 6 Shapiro steps at the maximum power level of our Gunn oscillator-pumped frequency doubler. These Shapiro steps are still clearly seen up to 65 K. The widths of the zeroth, first, and the second Shapiro steps as functions of the square root of the radiation power agree remarkably well with a Bessel function fit, indicating the junction is voltage biased at the radiation frequency. At 270 GHz, due to a combination of the heavy RF loss of the ZrO_2 substrate and the lack of radiation power, we have observed only the first Shapiro step.

This work was conducted under the auspices of the Consortium for Superconducting Electronics with full support by the DARPA (contract MDA972-90-C-0021).

---

*Department of Electrical Engineering and Computer Science and Research Laboratory of Electronics, Massachusetts Institute of Technology, Cambridge, MA 02139

**Department of Applied Physics/LT, University of Twente, AE Enschede, the Netherlands

TERAHERTZ SHAPIRO STEPS IN HIGH TEMPERATURE SNS JOSEPHSON JUNCTIONS*

P. A. Rosenthal and E. N. Grossman

Electromagnetic Technology Division
National Institute of Standards and Technology
325 Broadway
Boulder, CO 80303

Abstract

We have studied the far infrared behavior of high-T_C superconductor-normal metal-superconductor (SNS) microbridges with properties well suited for sub-THz and THz applications. We have fabricated YBCO junctions with $T_C > 85$ K and critical current-resistance products (I_CR_N) as high as 10 mV at 4.2 K. These are the highest I_CR_N products reported to date for micrfabricated Josephson junctions of any material. The junctions were integrated at the feeds of planar log-periodic antennas made from noble metal thin films. The junctions had D.C. normal state resistances R_N between 10 and 40 Ω, well matched to the antenna's estimated R.F. impedance of 53 Ω. A far infrared laser was focused onto the antenna-coupled junctions through the backside of the substrate via a plano-convex polyethylene lens and a hemispherical silicon lens. Radiation at 404, 760, and 992 GHz induced pronounced Shapiro steps (i.e. constant voltage steps at voltages n(hν/2e), n= 0,1,2,...) in the current voltage characteristics as well as modulation of the critical current. The amplitude of the Shapiro steps rapidly decays at voltages above 1-1.5 I_CR_N corresponding to a maximum frequency cutoff of ~ 8 THz. These are the first far infrared measurements performed on high T_C junctions. Measurements of the power, frequency, and temperature dependence of the Shapiro steps are presented and discussed in the context of a resistively and capacitively shunted junction (RCSJ) model. A value of 4.5 fF for the capacitance is inferred from the hysteresis of the slightly underdamped current-voltage characteristics.

I. Introduction

The potential of Josephson junctions for various submillimeter and THz applications has been of interest for some time.[1] Furthermore, the discovery of high temperature superconductivity and subsequent advances in the art of fabrication of Josephson junctions and thin film structures has renewed interest in various high frequency applications of Josephson junctions which are not addressed by practical low T_c devices.[2] The frequency scale for all Josephson effects is set by the I_cR_N product through the definition of the dimensionless or reduced frequency $\Omega = h\nu/(2eI_cR_N)$, where ν is the real frequency, h/2e is the flux quantum and I_c and R_N, the critical current and normal state resistance, enter in product form. The I_cR_N product or characteristic voltage is fundamentally limited by the superconducting energy gap.[3] When the junctions are strongly damped by additional shunt conductance, the characteristic voltage is substantially reduced. The most successful high T_c junction approaches to date, such as grain-boundary junctions (GBJs)[4,5], and step-edge superconductor/normal metal/superconductor (SNS) junctions[6,7] have achieved I_cR_N products of 1-2 mV, comparable to that achieved with Nb (for which the tunneling gap $2\Delta = 2.9$ mV at 4 K). However, an important distinction should be made : Nb tunnel junctions with the full gap-limited characteristic voltage are extremely underdamped whereas the high T_c junctions have generally been strongly overdamped, as most clearly evidenced by their non-hysteretic current voltage characteristics. It has been shown[8] that the strongly damped resistively shunted junction (RSJ) model describes well the power and frequency dependence of the Shapiro steps and critical currents in high Tc SNS junctions at reduced frequencies $\Omega = h\nu/(2eI_cR_N) < 1$ when the I_cR_N product is ≤ 0.5 mV. These facts suggest that high temperature superconducting Josephson junctions have the potential for much higher I_cR_N products, extending the range of useful Josephson effects to much higher frequencies.

We have recently developed a technique for fabricating low capacitance SNS junctions from $Y_1B_2Cu_3O_7$ (YBCO) with I_cR_N products as high as 10 mV, as measured from D.C. current voltage characteristics. The characteristic frequency associated with a 10 mV characteristic voltage is 4.8 THz. Our goal in this work was to determine to what extent the RSJ like behavior at low characteristic voltages and reduced frequencies persists to high characteristic voltages and high reduced and real frequencies. We believe that the high characteristic voltages and operating frequencies of these devices represent a breakthrough in THz device technology.

In this work, we investigate the high frequency behavior of selected junctions of this type using quasioptical coupling techniques and a far infrared laser. In section II of this paper we present an overview of our fabrication process for superconductor/normal metal/superconductor Josephson junctions with integrated THz bandwidth antennas. In section III we describe the optics and electronics used to perform far infrared measurements. In section IV we present the results of measurements of the power, frequency and temperature dependence of the current-voltage characteristics of selected Josephson junctions under irradiation by signals up to 1 THz. The measurements demonstrate quasioptical coupling of a far infrared laser into a high temperature superconductor (HTS) Josephson junction as evidenced by Shapiro steps induced in the junction current-voltage characteristics. We discuss the results of these measurements in the context of a resistively shunted junction model.

II. Fabrication

Junctions were fabricated by a variant of the process presented by Ono et al.[7] The processing sequence is shown in Fig. 1. First, roughly perpendicular steps approximately 100 nm deep were etched by ion milling into (100) $LaAlO_3$ substrates. It was found that, for $LaAlO_3$ substrates, 300 nm thick niobium etch masks patterned by photolithography and reactive ion etching yielded better step-edge profiles than did a simple photoresist etch mask. Because Nb etches more quickly than NbO_x we found that spraying a small amount of oxygen onto the substrates during the milling process helped to sharpen the steps and reduce the required Nb mask thickness. The substrates were rotated during the ion milling process, and a 1000 eV Ar ion beam at 1 mA/cm^2 cut the steps in approximately 10 minutes. After the steps were etched, the Nb masks were stripped off in a CF_4/O_2 plasma etch, and the samples were cleaned carefully. Next, a film of $Y_1Ba_2Cu_3O_7$ was grown on the substrate by laser deposition. The samples were held at approximately a 40° angle relative to the laser plume to cause the superconducting film to break across the step edge. The YBCO was deposited in 27 Pa (200 mT) of O_2 at a substrate temperature of 775 °C at a rate of 1.3 nm/sec, using a KrF excimer laser at 10 Hz with a measured beam energy of 120 mJ/pulse focused onto a 10 mm^2 area, for a fluence of 1.2 J/cm^2. Using our deposition parameters we routinely grow films with smooth morphologies, critical temperatures over 90 K, and critical current densities above 10^6 A/cm^2 at 77 K.[9] After the superconducting film is deposited the substrate heater is rotated to normal incidence, the deposition chamber is pumped down and a

normal metal (Au, Ag, or AuAg alloy) is deposited to a thickness of ~50 nm. The samples are then further rotated 30° and another 100 nm or so of normal metal are deposited. The normal metal films are grown by sputtering without exposing the sample to atmospheric pressure to minimize surface degradation and contact resistance at the SN interfaces, while the deposition angles help the normal metal make a robust bridge across the break in the superconductor at the step. After deposition, the samples are removed, and the SN bilayers are patterned into bridges typically 6 μm wide.

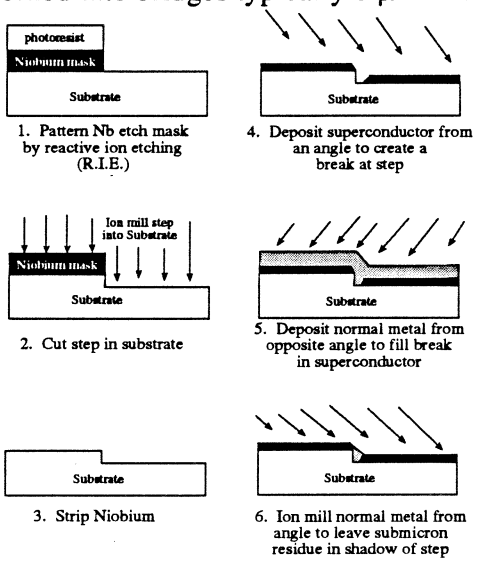

Fig. 1. Schematic of fabrication sequence to produce step-edge SNS Josephson junctions.

Antennas are fabricated by liftoff, with another deposition step consisting of a 5 nm layer of Ti for adhesion followed by a ~140 nm thick film of Ag. The antennas used in all of the far infrared measurements were of the log-periodic type[10] depicted in Fig. 2 (a) with a minimum tooth radius of ~12 μm at the feed and a maximum tooth radius of 2 mm. The bow angle was 45°, and the tooth and slot angles were each 45°. This design is self-complementary and self-similar, so to a good approximation the impedance should be purely real and almost frequency independent over a bandwidth of approximately .14 - 2.3 THz.[11] Using the quasistatic expression for the antenna impedance $Z_{ant} = Z_0 / \sqrt{[2(1+\varepsilon_r)]}$ we estimate an impedance of 53 Ω assuming a dielectric constant of 24 for the $LaAlO_3$ substrate. After the antenna liftoff, the samples were diced and tested at D.C. The best samples were selected, and the normal metal bridge was further patterned by ion milling to increase the junction resistance. We found that extreme care

was required to avoid electrostatic damage to the chips when the junction resistances exceeded 1 Ω. Fig. 2 (b) shows an optical micrograph of the feed area of a completed device.

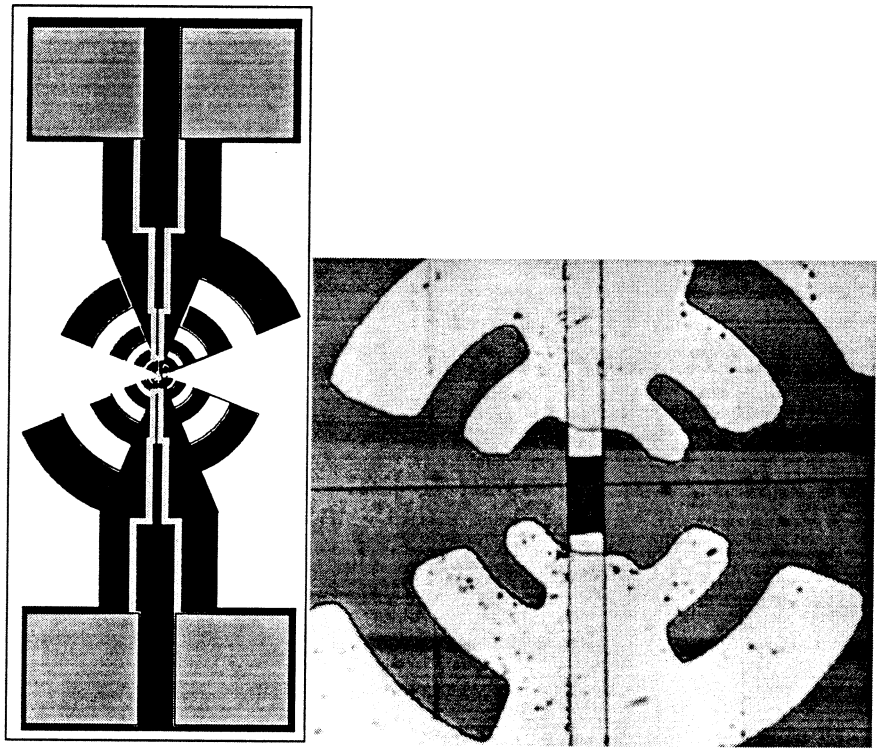

Fig. 2 (a) Schematic of normal metal planar log periodic antenna (black) and YBCO contact pad and lead (grey) configuration for the chips used in the far infrared measurements. (b) An optical micrograph of the feed area and part of an antenna from an actual chip. The junction width is 6 μm. The dark area at the feed is the YBCO exposed by the angled ion mill.

III. Measurement Apparatus

The experimental configuration is shown in Fig. 3. The samples were mounted in vacuum, on a variable temperature stage, with a 1 cm radius high resistivity Si hemisphere pressed against the backside of the substrates. A 6.5 THz cutoff lowpass filter, cooled to 4 K, was used to reduce the thermal infrared (IR) background to a manageable level. Nonetheless, residual IR power absorbed on the sample stage was sufficient to raise its temperature approximately 5 K above the liquid He bath, limiting our measurements to $T > 9$ K. The broadband IR power coupled directly into the junction

via the antenna may be estimated as P_{bg} = kTB = 30 nW, with T = 300 K and the bandwidth B limited by the filter cutoff. Plano convex lenses machined from high and low density polyethelyne were used to focus the far infrared laser into the dewar. The focussing was relatively slow, with a maximum opening angle of ~10^{o} (FWHM), which resulted in a large loss (roughly 16 dB) due to beam mismatch with the antenna. The far-IR laser, pumped by a 15 W CO_2 laser, yielded approximately 5 mW on the formic acid lines at 404, 760, and 992 GHz, and approximately 8 mW on the 2.52 THz methanol line. A substantial fraction of the laser power was directed by a (Si or mylar) beamsplitter into a pyroelectric detector to serve as a real time power monitor. Based on these rough estimates of coupling efficiencies, the maximum laser power actually delivered to the junction was in the range of 50 μW. The laser power was adjusted by varying the gas pressure. The junctions were biased through a 1 kΩ resistor. Voltages and currents were amplified by low noise instrumentation amplifiers and current voltage characteristics (IVCs) were plotted on either an xy recorder or an oscilloscope.

IV. Results

We measured two junctions with the far infrared laser. The first initially had a resistance of 16 Ω and a critical current of 0.43 mA at 4.2 K. Shortly after the far-IR measurements were begun, during a brief hiatus in the experiments, the resistance increased to 38 Ω and the critical current dropped to 0.28 mA. This change was possibly due to degradation of some portions of the junction due to prolonged contact with a vaccuum environment at room temperature. We also measured a second junction with a resistance of 12 Ω and a critical current of 0.22 mA. We have fabricated other junctions of this type, but without antennas, for studies of the temperature dependence of the critical currents. Fig. 4 shows a plot of the temperature dependence of I_cR_N and R_N for a typical high I_cR_N junction. Fig. 5 shows the current-voltage curves for the 10 mV I_cR_N junction with no applied radiation, and with radiation at 404 GHz, 760 GHz, and 992 GHz. The Shapiro steps are clearly visible with minimal rounding, and extend to high voltages, approximately 15 mV (corresponding to 7 THz) at a temperature of 9 K, and approximately 6 mV (3 THz) at a temperature of 53 K. It is also obvious that the current voltage characteristic is mildly hysteretic with no rf bias applied. Fig. 6 shows measured current-voltage characteristics at 53 K with and without 992 GHz laser radiation applied.

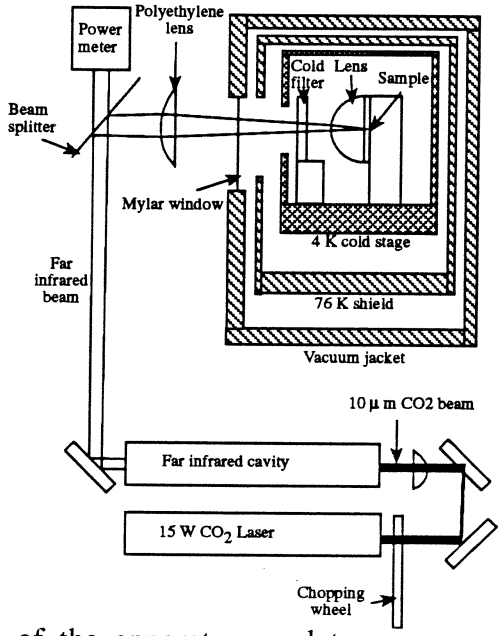

Fig. 3 Schematic of the apparatus used to measure shapiro Steps at THz Frequencies.

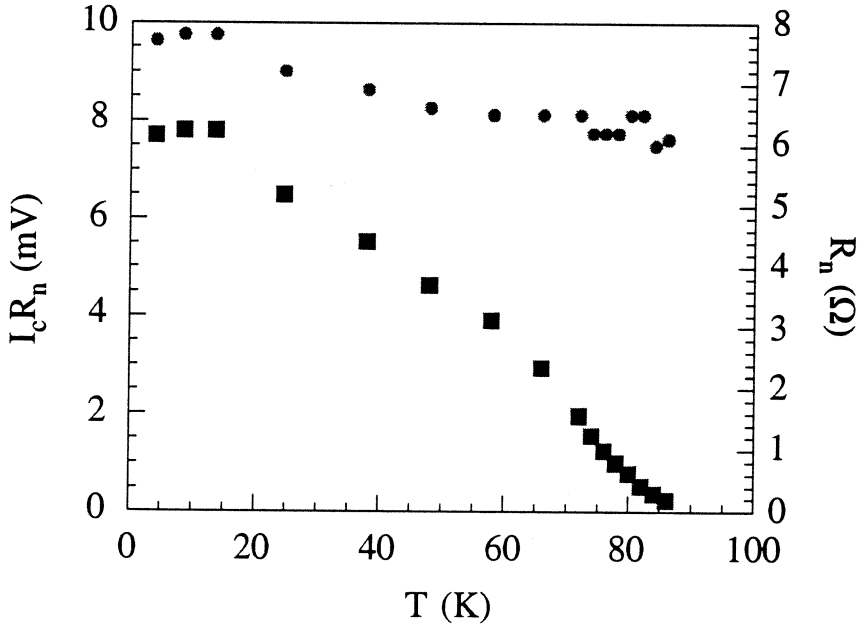

Fig. 4 Temperature dependence of the normal state resistance R_N and the I_cR_N product of a typical high resistance junction. The squares represent values of the I_cR_N product and the circles represent the normal state resistance.

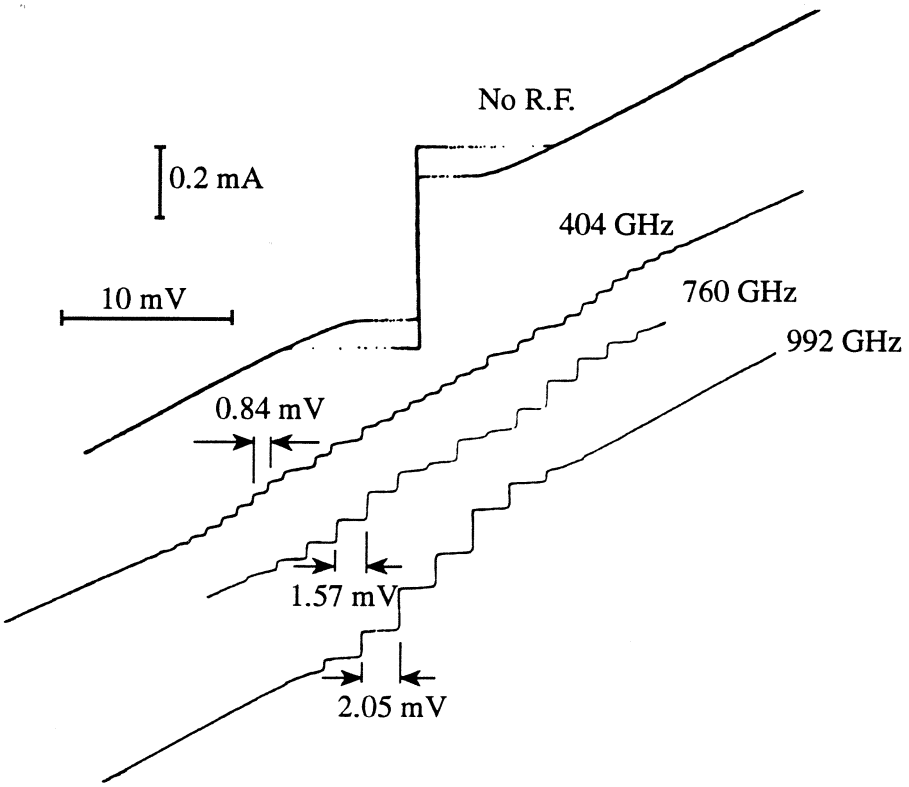

Fig. 5 dc Current Voltage characteristic taken at 9 K of a junction with a resistance of 38 Ω and a critical current of 0.28 mA. IV Curves are also shown for applied R.F. frequencies of 404 GHz (Ω = .08), 760 GHz (Ω = 0.15), and 992 GHz (Ω = 0.19) showing pronounced Shapiro steps at voltages comparable to the 10 mV I_CR_N product.

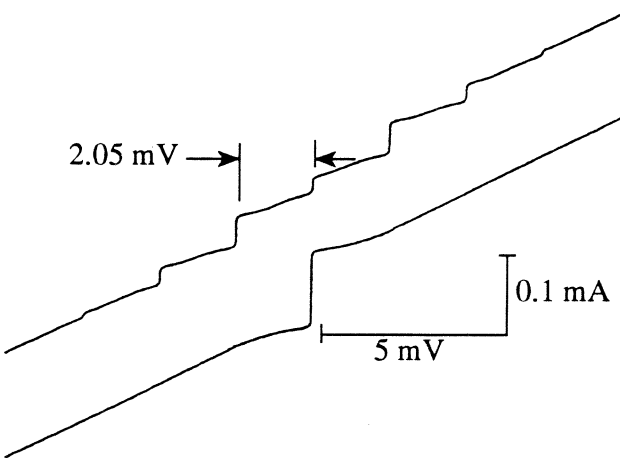

Fig. 6 Current voltage characteristics at 53 K. The upper curve shows the current voltage characteristic with 992 GHz (Ω = 1.1) radiation.

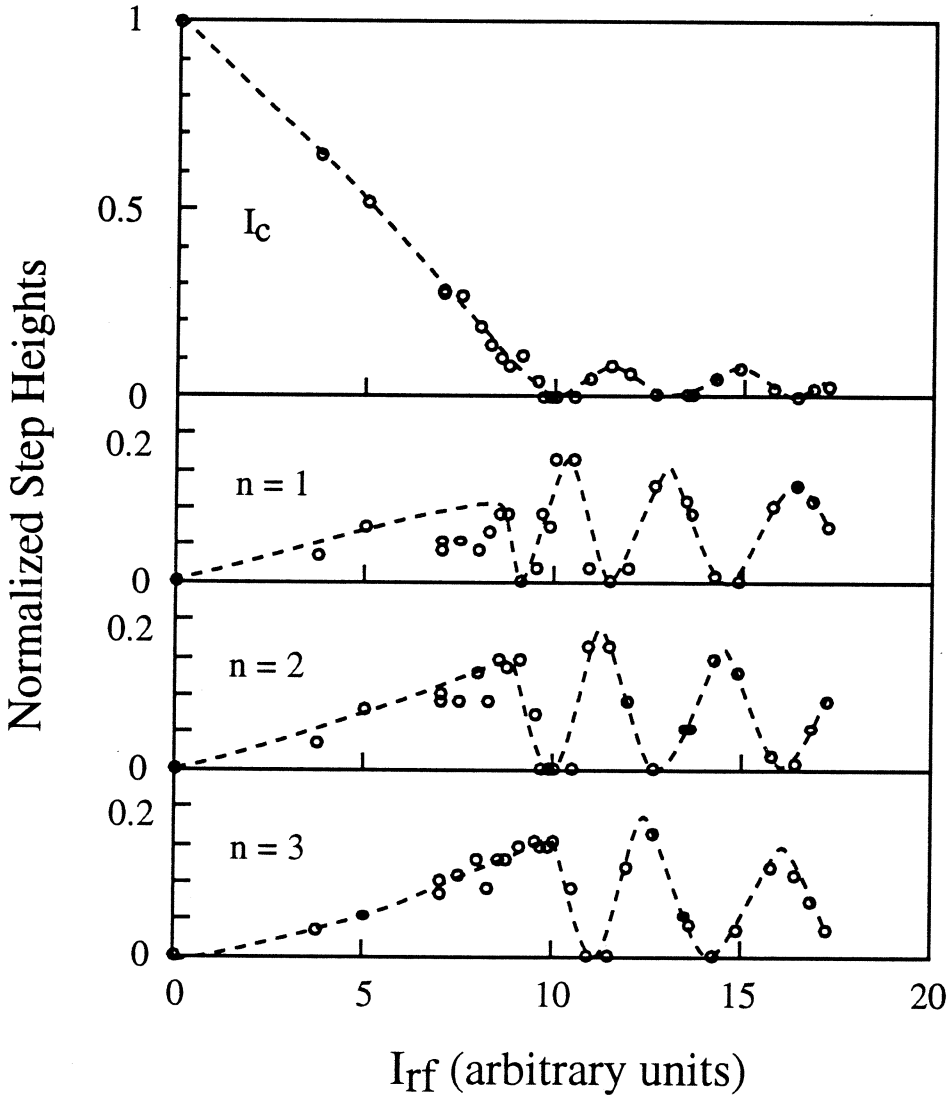

Fig. 7 Power dependence of the critical current and Shapiro step heights for a 10 mV I_CR_N junction at 9 K irradiated at 404 GHz. For the measured values of I_C and R_N of 0.28 mA and 38 Ω this corresponds to a reduced frequency $\Omega = 0.08$. The critical current and step heights are normalized to the value of the critical current with no rf applied. The R.F. current quoted in arbitrary units was assumed proportional to the square root of the measured power. The dashed lines through the points are guides to the eye.

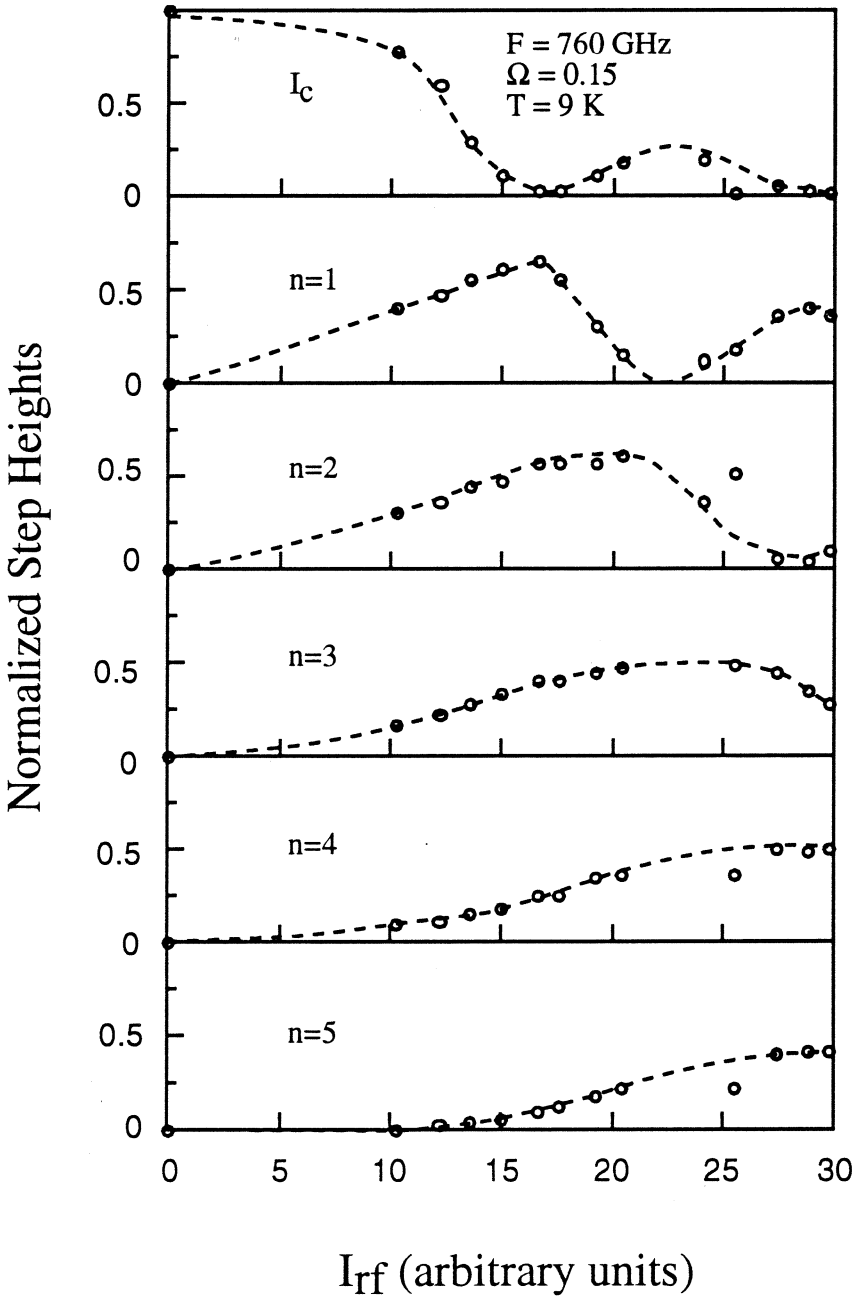

Fig. 8 Power dependence of the critical current and Shapiro step heights for a 10 mV I_CR_N junction at 9 K irradiated at 760 GHz. For the measured values of I_C and R_N of 0.28 mA and 38 Ω this corresponds to a reduced frequency $\Omega = 0.15$. The critical current and step heights are normalized to the unirradiated critical current. The rf current quoted in arbitrary units was assumed proportional to the square root of the measured power. The lines through the points are meant as guides to the eye.

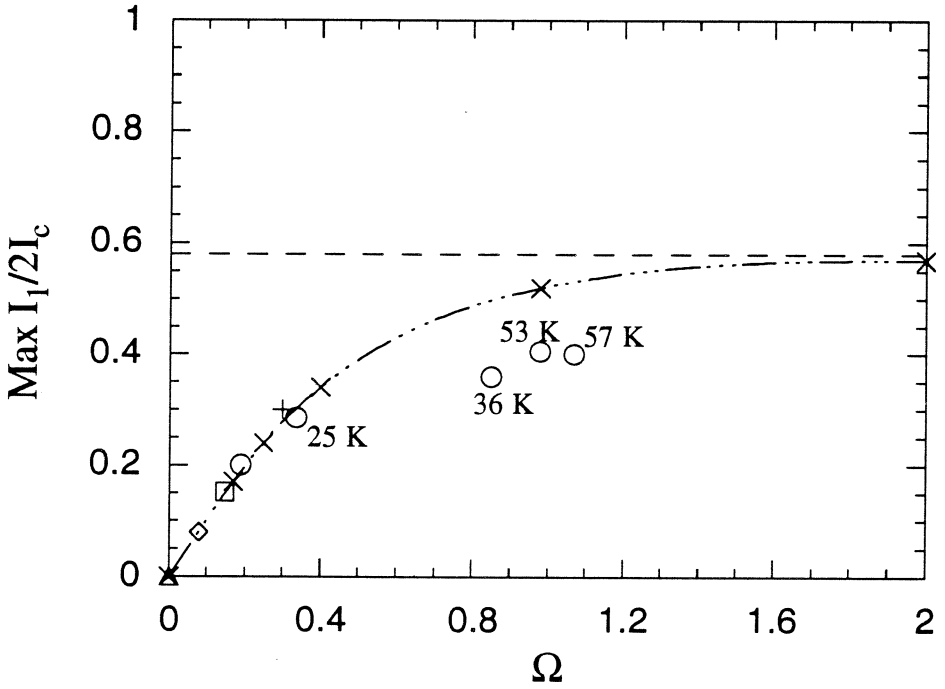

Fig. 9 Dependence of maximum normalized amplitude of first Shapiro step vs reduced frequency Ω. The circles, the square, diamond and triangle refer to data taken at 992 GHz, 760 GHz, 404 GHz and 3 GHz, respectively. The cross refers to data taken from a second device with a 3 mV I_cR_n product at 992 GHz. Points without explicitly labeled temperatures were taken at 9 K. The dashed line is the Bessel function value obtained for large β_c. The dot dashed curve and the X's are the results of simulations of the zero temperature (overdamped)RSJ model from Kautz et al[8] and from Benz.[12] Here β_c, the Stewart-McCumber parameter, is given by $\beta_c = 2\pi\ (2e/h)\ I_cR_N^2C$ where e is the electron charge, h is Planck's constant and C is the shunt capacitance.

In Figs. 7 and 8 we show the measured power dependence of the Shapiro step heights as a function of the applied power. The characteristic pattern of lobes is qualitatively similar to what would be expected from the resistively shunted junction model. The frequency dependence of the step amplitudes is a feature that can be checked against various models. This allows a direct comparison with the predictions of the R.S.J. model (or other dynamical models) without explicitly knowing the R.F. power levels. In Fig. 9 we show the maximum amplitude of the first Shapiro step normalized to twice the critical

current, from two devices, as a function of reduced frequency $\Omega = hF/2eI_cR_N$. The data shown in Fig. 9 were taken using 3 GHz, 404 GHz, 760 GHz and 990 GHz radiation over a range of temperatures so as to access a wide range of reduced frequencies. One can see that there is a systematic variation, approximately linear at low frequencies, with a slope close to 1.0, rolling off as Ω approaches unity. For comparison, some points calculated at low reduced frequency using the overdamped ($\beta_C = 0$) RSJ model are also shown in Fig. 9. From this we can see that the agreement with the RSJ model is excellent at low frequencies. At frequencies near unity the maximum step height is still somewhat lower than the high frequency Bessel function prediction ($I_1/I_C = 0.58$) of the RSJ model. Considering the uncertainties due to the frequency dependence of the embedding impedance, it is unclear to what extent the data should agree quantitatively with the RSJ model at high reduced frequencies. A further uncertainty arises because the frequency dependence of the supercurrent is unknown for frequencies comparable to the gap frequency, whereas the RSJ model assumes a frequency-independent supercurrent. These effects are all progressively more important at higher frequencies, which is exactly the region where the observed deviations from the RSJ model are most pronounced.

An correlation was observed between the junctions' characteristic voltages and the maximum observable Shapiro step frequency. For the two junctions measured we found strong Shapiro steps only up to frequencies comparable to the junction's characteristic frequency. The junction with the 10 mV characteristic voltage showed Shapiro steps up to approximately 15 mV, while the junction with the 3.0 mV characteristic voltage showed Shapiro steps only up to 4 mV with a 404 GHz source. The 3 mV junction showed only one step when biased with a 990 GHz beam. The observed proportionality of scale between the highest voltage Shapiro steps and the I_CR_N product suggests that the difference in the I_CR_N product for the two junctions measured is related to a difference in the intrinsic Josephson coupling strength. We speculate that the observed behavior is due to a combination of differing normal metal bridge length, S-N interface boundary resistance, or reduced energy gaps in the superconducting banks.[13] Junctions with identical Josephson coupling strength but differing parasitic shunt conductance would be expected to exhibit Shapiro steps out to similar maximum voltages (but with power dependence characteristic of different reduced frequencies) which we have not observed. To the extent that this observed behavior will prove to hold generally for this class of junctions we suggest that optimal high frequency locking will be achieved with junctions with the highest possible characteristic voltages. The junctions reported here have

already exhibited Shapiro steps at voltages as high as the best point contact junction results, and higher than any other high T_c technology.

The 10 mV junction exhibited no Shapiro steps when illuminated with 2.52 THz radiation. This result for the 10 mV junction is most likely not intrinsic to the junction dynamics, but rather, it is due to a combination of two extrinsic effects: the opacity of the LaO_3 substrate, which rises substantially above 1 THz, and the high frequency cutoff of the antenna. The 2.52 THz tranmissivity of an LaO substrate was separately measured to be 0.12, while reflection loss (with $\varepsilon_r = 24$) would only account for a loss of approximately 50 %.

Hysteresis in junction current voltage characteristics is most commonly due to either underdamped dynamics[14,15] or to self-heating.[16] A thermal explanation for the observed hysteresis requires invoking thermal conductances that are implausibly small. The bias heating in the junction is of the scale $I_c^2R_N$, which is 3 μW for a junction with a resistance of 38 Ω and a critical current of 0.28 mA. The observed 30% hysteresis at 9 K would require bias heating of at least 15 K. This would imply a thermal conductance between the junction and the substrate of $2*10^{-7}$ W/K, which is about two orders of magnitude smaller than is typically obtained in structures of this size. In our junctions, there is significant evidence that the hysteresis is primarily due to underdamped dynamics, i.e. the Stewart-McCumber parameter $\beta_c = 2\pi\ (2e/h)\ I_cR_N^2C \geq 1$, where e is the electron charge, h is Plancks constant, C is the shunt capacitance and I_c and R_N are the critica current and normal resistance. Using dynamical simulations within the context of the resistively shunted junction model one can calculate the β_c of a junction from its critical current, and its return or retrapping critical current.[17] We performed this procedure for the 10 mV junction. We measured the retrapping critical current over a range of temperatures (and therefore critical currents), and extracted a value for β_c, giving us the capacitance at each temperature. For these calculations we replaced the normal state resistance of the junction with the parallel combination of the estimated antenna impedance and the measured junction resistance R_N. This assumption is justified because the voltages at which the junction retrapped were all within the nominal bandwidth of the antenna, and in this way we better include the additional damping of the junction due to the antenna radiation resistance. From the simulations, we calculated a value of ~4.5 fF for the capacitance . Fig. 10 shows the capacitance extracted from the retrapping currents over a range of critical currents taken at various temperatures.

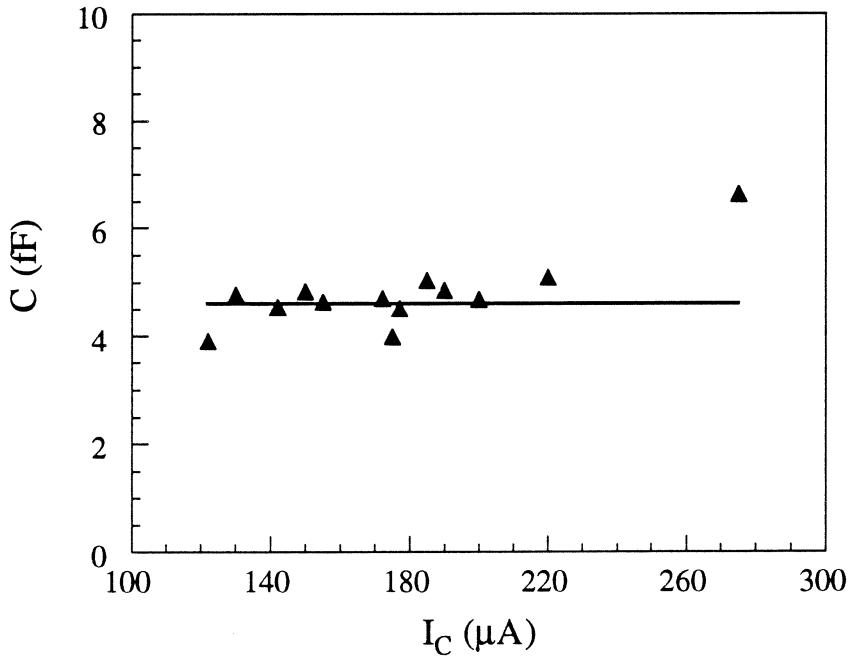

Fig. 10 Values of capacitance extracted from the retrapping and critical currents of a 10 mV IcRn Junction. Each point was taken at a different temperature, which ranged from 9 K to 45 K.

The value of the capacitance calculated in this way is within a factor of 2 of our estimate of the geometric capacitance of the electrodes within the feed of the antenna. The remarkable consistency of the capacitance over a wide temperature range (9 K to 50 K) is strong evidence that the hysteresis is due primarily to dynamical effects and that self heating is at most a second order effect. We have observed similar behavior in the other junctions that displayed hysteresis. In addition, over the regime where the current voltage characteristics were hysteretic, we observed that at sufficiently high applied far-IR power the adjacent Shapiro steps were overlapping in current. i.e.. the steps themselves were mildly hysteretic. This behavior was not observed when the D.C. I-V curves were nonhysteretic. Within the contexct of the RSJ model, such behaviour only occurs for underdamped dynamics where $\beta_c \geq 0.7024$. It is unlikely that self heating would lead to a consistent value of RSJ derived capacitance over such a wide temperature range.

To summarize, we have fabricated high temperature superconducting Josephson junctions with I_cR_N products up to 10 mV. Measurements of the Shapiro steps induced by a far infrared laser showed RSJ-like behavior with visible steps at Josephson frequencies up to 8 THz. The high resistances of this type of junction make them attractive candidates for use in antenna based quasioptical coupling schemes. The wide operating temperature range and fast non-thermal (i.e. Josephson) response mechanism gives these devices an intrinsic flexibility well suited to many applications in THz detection and mixing.

---

[1]P. L. Richards, "Semiconductors and Semimetals," V c1.12, (Academic Press, New York 1977) Chapter 6

[2] R.J. Schoelkopf, T.G. Phillips, and J. Zmuidzinas, IEEE Trans. Appl. Superconductivity, in press (1993)

[3]K.K. Likharev, Rev. Mod. Phys.,**51 (1)** 1979

[4]D. Dimos, P. Chaudhari, J. Manhart, and F. K. LeGoues, Phys. Rev. Lett, **61,** 219, (1988)

[5]K. Char, M. S. Colclough, S. M. Garrison, N. Newman, and G. Zaharchuck, Appl. Phys. Lett., **59**,733, (1991)

[6]M.S.DiIorio, S. Yoshizumi, K. Y. Yang, J. Zhang, and M. Maung, Appl. Phys. Lett., **58**, 2552, (1991)

[7]R. H. Ono, J. A. Beall,, M. W. Cromar, T. E. Harvey, M. E. Johansson, C. D. Reintsema, and D. A. Rudman, Appl. Phys. Lett., **59**, 1126, (1991)

[8]R. L. Kautz, R. H. Ono, and C. D. Reintsema, Appl. Phys. Lett. **61** (3), p. 342 (1992)

[9]N. Missert, C. D. Reintsema, J. A. Beall, T. E. Harvey, R. H. Ono, and E. A. Rudman, to be published in I.E.E.E. Trans. Applied Supercond. in the proceedings of the Applied Superconductivity Conference 1992

[10]R. H. DuHamel and D. E. Isbell, Broadband Logarithmically periodic antenna structures," *IRE Nat. Conven. Rec.*, pt. 1, 1957, pp. 119-128

[11]D. B. Rutledge, D. P. Keikirk, and D. P. Kasilingam, "Integrated Circuit Antennas," *Infrared and Millimeter Waves, Vol. 10*, (Academic Press, N.Y. 1983), p. 1.

[12]S. P. Benz private communication

[13]M. Y. Kupriyanov and K. K. Likharev, Sov. Phys. Usp. **33**,(5) May 1990

[14]W. C. Stewart, Appl. Phys. Lett., **12,** 277 (1968)

[15]D. E. McCumber, J. Appl. Phys., **39**, 3113 (1968)

[16]W.J.Skocpol, M.R.Beasley, and M.Tinkham, J. Appl. Phys., **45**, 4054 (1974)

[17] A. Barone and G. Paterno "Physics and Applications of the Josephson Effect,"John Wiley and Sons, Inc (1982)

Fourth International Symposium on Space Terahertz Technology

ELECTRON BOLOMETRIC MIXERS FOR THE THZ REGION

K.S. Yngvesson, J.-X. Yang, F. Agahi, R. Brasco, D. Dai, J. Li,
W. Grammer, C. Musante, M.A. Tischler, and K.M. Lau

ABSTRACT

This paper reports new results related to 2DEG electron bolometric mixers for THz frequencies. We have measured the charge carrier inductance of a 2DEG device at 30 GHz, as well as the intrinsic device noise temperature at 1.5 GHz. 2DEG material with an increase in 4.2 K mobility by a factor of 3-4 has been grown by OMVPE. Detection by cyclotron resonance has been studied at 94 GHz and 238 GHz, with a maximum responsitivity (uncorrected for circuit loss) of 200V/W. Mixing has not been observed, so far, in this mode. The design principles for a 1 THz mixer are developed, and the DSB receiver noise temperature is predicted to be about 1000K.

This work has been supported by the National Aeronautics and Space Administration, under grant NAGW-1659. Work on the cyclotron resonance mode 2DEG device is now supported by NSF grant ECS-9298752. Most of the authors are with the Department of Electrical and Computer Engineering, University of Massachusetts at Amherst, Amherst, MA 01003. W. Grammer is now with the Hittite Corporation, 21 Cabot Road, Woburn, MA 01801; M.A. Tischler is with Advanced Technology Materials, Inc., Danbury, CT 06810.

I. INTRODUCTION

In contributions to previous Space Terahertz Technology Symposia, we have discussed the potential advantages of bulk, or "quasi-bulk" (i.e. surface-oriented or quasi-two-dimensional) electron bolometric mixer devices for the THz range [1,2,3]. An updated graph of receiver noise temperatures for these frequencies is given in Figure 1. Above 500 GHz, the lowest noise temperatures are still the ones achieved with InSb bulk effect mixers in the mid 1980s [4]. The advantage of using the bulk configuration should become even greater as the frequency is increased further into the THz region, due to the very low parasitic reactance of a bulk device compared with junction devices such as the Schottky diode and the SIS device. Surface-oriented devices have further advantages compared with the InSb-type bulk configuration. These include ease of achieving a desired device impedance and size, as well as the feasibility of integration into monolithic circuits. We have also earlier demonstrated a roughly three orders-of-magnitude increase in the IF bandwidth (to 1.7 GHz) compared with the typical performance of InSb mixers, by using a surface-oriented medium: two-dimensional electron gas (2DEG), located at the hetero-junction between GaAs and AlGaAs [1,2,3]. It now appears that there are many different media and modes of operation which allow electron bolometric mixing [5], all with large IF bandwidth, as demonstrated in several other papers at this conference [6,7,8]. In the present paper, we will emphasize new results related to 2DEG electron bolometric mixers, and also discuss in some detail how a 2DEG mixer could be implemented in the THz range.

We need to introduce some nomenclature, in order to distinguish the different modes of operation of the 2DEG device:

(1) **Mode I.** This is a mode for which mixing has been demonstrated, with a preliminary minimum conversion loss of 18 dB, and bandwidth of 1.7 GHz, at an RF frequency of 94 GHz. The operating temperature is quite flexible, typically 20-77K, and the LO power required is about 1 mW.

(2) **Mode II.** The Mode II mixer was proposed by Smith et al.[9]. It operates at 4.2 K, and requires a moderately large magnetic field. There are two different versions of the Mode II 2DEG device: Mode IIa is tuned to cyclotron resonance with the help of a fairly low magnetic field ($< 2T$). Due to the lower operating temperature, one

predicts much lower LO power (nW-μW), and lower noise temperature. The cyclotron resonance tuning has been successfully used in InSb, and is a convenient method for reaching THz frequencies without experiencing problems with charge carrier inertia (discussed in some detail below). We describe some recent work on this mode in this paper. Mode IIb: This mode occurs in somewhat higher magnetic fields (1-5T), and appears to be connected with the Shubnikov-deHaas effect, which can be detected as oscillations of the DC resistance, when the magnetic field is varied. Detection of 94 GHz and 238 GHz radiation has been obtained in this mode, but no mixing so far.

II. MATERIALS GROWTH

2-DEG samples were grown in a horizontal low-pressure OMVPE system. The sources used were trimethylgallium (TMG), trimethylaluminum (TMA), 100% arsine and 50ppm silane diluted in hydrogen. The growth temperature was 700°C and the reactor pressure was 50 Torr. The V/III ratio was kept high (> 200) for better AlGaAs quality. The total gas flow was 4000 sccm. The estimated growth rate for GaAs and AlGaAs using these parameters were 5.5Å/s and 9 Å/s respectively. Typical 2-DEG structures include a 1.2μm GaAs buffer, a 360Å undoped AlGaAs spacer, a 500Å uniformly doped (mid-$10^{17}/cm^3$) AlGaAs, and a 130Å doped GaAs ($1 \times 10^{18}/cm^3$) contact layer. The Al composition in the AlGaAs layers is about 38%. The GaAs buffer was actually grown in two steps, 15 minutes at 650° C and then 20 minutes at 700° C. Initiation of the buffer at a lower temperature helps to preclude incorporation of impurities at the substrate and epilayer interface, which may create an undesirable parallel conduction path in the 2DEG device.

Although the maximum mobility we achieved (766,000 cm^2/V-s with 4.9×10^{11} electrons/ cm^2 at 2.2K after exposure to light) is still much lower than that obtained by MBE, to our knowledge, it is the highest by the OMVPE growth technique. Since the 2-DEGs are grown for device applications, light sensitiveness and overall thickness of the epi-layers are important considerations for device fabrication and testing. In addition to the requirement of high mobility, 2-DEG structures without the AlGaAs- related buffer are needed to minimize light sensitivity. To attain this goal, we found that deposition of AlGaAs in the reaction chamber prior to the growth of the 2-DEG structure provides a sufficient condition for producing a high mobility device. Samples grown with this type

of reactor pre-conditioning have maximum light mobilities similar to those with AlGaAs-related buffers. More significantly, these devices are much less light sensitive, specifically, the dark mobilities are typically near 80% of the light values.

To compare the effectiveness of the pre-run and the conventional AlGaAs buffer technique, 2-DEG devices with either an undoped thick AlGaAs buffer or an AlGaAs/GaAs multiple quantum well buffer were grown. The parameters used for the 2-DEG structure were identical to those described earlier.

Characterization of the resulting 2-DEG structures was performed by computerized Hall effect measurement using the van der Pauw method. A plot of the Hall mobility versus temperature for the best sample is shown in Figure 2. Similar to other high-mobility 2-DEGs, the maximum mobility was measured at the lowest temperature, 2.2K. Without the pre-run or AlGaAs-related buffer, the maximum light μ_{77} obtained with optimized parameters ranges from 100,000 to 120,000 $cm^2/V\text{-}s$. Samples grown with pre-runs or with an AlGaAs-related buffer have increased light μ_{77} in the 140,000 - 170,000 $cm^2/V\text{-}s$ range. We believe that the pre-runs leave a deposit of Al-rich compound in the reactor walls and the susceptor which effectively passivates the chamber and in subsequent experiments, helps to getter the impurities from the gas stream, allowing the growth of high purity GaAs and AlGaAs.

The most significant advantage of the samples grown with a pre-run is their reduced sensitivity to light, as evidenced by the dark to light mobility ratios shown in the table. The dark μ_{77} of these samples are typically about 80% of the light values, while the dark mobilities of samples with an AlGaAs or MQW buffer are only 50-60% of their light counterparts.

III. THE MODE I 2DEG MIXER

Measurement of the Charge Carrier Inertia Inductance

Charge carrier inertia was studied in bulk semiconductors at low temperatures in the 1960s [10]. It is not relevant under normal device conditions at room temperature, or when the electrons are accelerated substantially, unless one considers frequencies of the order of 500 GHz. In the 2DEG devices we have investigated, the electrons can have extremely high mobilities, and show charge carrier inertia phenomena at much lower frequencies. To

make this quantitative, on can show [11] that to first order the effect is equivalent to an inductance, L_B, in series with the device resistance, R_B, see Figure 3. The total device impedance is:

$$Z_B = R_B + j\omega L_B = R_0(1 + j\omega\tau_m) \tag{1}$$

where R_0 is the low-frequency resistance. We have measured this inductance in a device for which the maximum electron mobility, μ, was about 90,000 cm^2/Vs at 77 K [12]. This mobility corresponds to a τ_m of

$$\tau_m = \frac{(\mu \times m^*)}{q} = 3.4 \times 10^{-12} s \tag{2}$$

Here, m^* is the effective mass $= 0.067m_0$, and q is the electron charge. The measured DC resistance was 27.1 ohms, and the microwave value $R_B = 20\Omega$. The measured resistance includes the contact resistance (R_p). As explained below, we believe that the contact resistance is largely eliminated at 30 GHz. This conclusion is consistent with a value for R_B at 30 GHz, which is less than the DC resistance. The corresponding inductance predicted from (1) and (2), and with R_B bracketed from 20Ω to 27.1Ω, thus is in the interval 0.068 to 0.092 nH. The measured value of L_B for the frequency range of 29 to 35 GHz was 0.08 ± 0.015 nH, which shows agreement with theory within the measurement error. We believe that this is the first measurement of charge carrier inertia in the 2DEG medium. We now describe how the measurement was performed.

A 2DEG device was flip-chip mounted with indium solder across a 50 ohm slot line of width 25 μm, etched in a thin copper layer deposited on a low-loss silicon substrate with thickness 0.33 mm. Cascade microprobe measurements were then performed after designing biasable coplanar waveguide (CPW) to slotline transitions [13] on the substrate, as shown in Figure 4. A network analyzer with an upper frequency limit of 40 GHz was utilized. Calibration standards etched on the same substrate allowed us to de-embed the device parameters, using the TRL ("thru-reflect-line") method. A room temperature measurement first determined the parasitic capacitance, C_p, of the device to 70 fF. Note that at room temperature the device inductance is negligibly small, since τ_m is about an

order of magnitude shorter in this case. The parasitic inductance (L_p in Figure 3) was very small.

The substrate was next placed on top of a copper cylinder, which was surrounded by a liquid nitrogen bath, and the entire assembly substituted for the steel cylinder normally used to support substrates in the microprober. The measured and modeled response are compared in Figure 5, for three bias currents. As the bias current is increased, the inductance/resistance ratio decreases rapidly (see (1)), when the electrons begin to heat up. The inductance can then not be measured accurately at these frequencies, and future refinements in the measurement setup will have to be made to allow modeling of the device under conditions of substantial electron heating. It is clear that L_B/R_B decreases with increasing bias, however, which is the expected behavior.

Measurement of Intrinsic Device Noise

To assess the expected noise temperature of a THz mixer receiver, one can measure the device noise temperature at the IF frequency, as a DC bias current is applied. This method has previously been used for Schottky barrier diodes [14]. We have measured the available output noise temperature (T_d) from a 2DEG device connected to a CPW circuit on a silicon substrate, as a function of bias current. The device was cooled to 77K by immersion in liquid nitrogen. We corrected for the mismatch between the device and the 50Ω circuit by measuring S_{11} at the device terminals. The result is shown in Figure 6, which also gives the DC I-V-curve of the device. The noise was measured at 1.5 GHz. For a typical mixer bias point, T_d is about 100K. Note that this is close to the estimated electron temperature of 85-100 K. In future experiments, we will investigate the dependence of T_d on the physical temperature of the device, as well as on other device parameters, and the frequency at which T_d is measured.

Design of a Mode I THz 2DEG Mixer

Several design features will have to be revised in an actual THz 2DEG mixer design. The flip-chip mounting yields a much too high parallel capacitance, even if the chip is thinned considerably, as shown by the microprobe measurements. This capacitance basically disappears if the device is fabricated as an integral part of a monolithic circuit, made from semi-insulating GaAs. Coupling of the RF and LO is also best accomplished

quasi-optically. Figure 7 shows two possible integrated antennas which may be used: (a) A tapered slot antenna, etched on a silicon-oxynitride membrane [15], and (b) an extended hyper-hemispherical dielectric lens [16]. If a silicon lens is used for alternative (b), then a good dielectric match is obtained to a GaAs substrate, clamped to the back of the lens.

The low power output of THz LO sources makes it important to minimize the LO power required. The 2DEG device can be scaled down in size while maintaining a constant impedance, if both width and length are scaled by the same factor. The main factor to watch is the contact resistance, which is inversely proportional to the device width, and thus will increase. In a typical device, the vertical distance from the contact pad to the 2DEG is 0.1 μm or less, and with the pad size of about $100 \times 100\mu$m used presently, there is then a capacitance shunting the contact resistance of about 11 pF. At 100 GHz, the capacitive reactance is 0.1 ohms, much smaller than the typical contact resistance, R_c, of 10-20 ohms. This circumstance allows us to design a 1 THz device with considerably smaller area, without problems with the contact resistance. R_c does have an effect at the IF frequency, but since the optimum IF impedance is several hundred ohms, a higher R_c can be tolerated in the IF circuit. Based on a smaller device size, with a width of 10 micrometers, we estimate that LO powers in the range 10-100 μW are feasible.

Another important factor to consider is the effect of the charge carrier inertia at 1 THz. In order to estimate this, we must know the effective value for $< \tau_m >$, under conditions of electron heating. It is convenient to introduce the frequency, f_m, at which $R_B = L_B$ (see (1)). Unfortunately, the detailed physics of the heated 2DEG medium is anything but simple. From a Monte Carlo simulation of 2DEG under similar conditions to those in our mixer, we can estimate $f_m = 500$ GHz. We have used values of f_m of 300 and 500 GHz, respectively, to predict the degradation in conversion loss, assuming a simplified equivalent circuit based on (1), i.e. an inductance in series with the resistance, see Figure 8. The conclusion is that a conversion loss from about 11.5 dB to 13 dB is predicted at 1 THz, when the conversion loss at 100 GHz is 10 dB. The predicted conversion loss at 1 THz is about in the same range as for Schottky barrier mixers: therefore the comparison of the two types of mixers depends critically upon the effective noise temperature of the respective devices. We may also note that at higher frequencies than about 1 THz, one

may obtain a conversion loss which is close to that at the lowest frequencies by adding a monolithic capacitor in series with the device, and thus resonate out the effect of the charge carrier inertia inductance.

We can now proceed to an estimate of the receiver noise temperature of a Mode I hot electron mixer at 1 THz. We assume that the effective device temperature is roughly equal to the measured device noise temperature (T_d) at the IF, i.e. 100 K. With an IF amplifier noise temperature, T_{IF}, of 10 K, and $L_c = 13$ dB, we find

$$T_{R,DSB} = \left(\frac{T_d}{2}\right) \times (L_c - 2) + \frac{(T_{IF} \times L_c)}{2} = 1000K \tag{3}$$

This receiver noise temperature is about $15 \times (hf/k\ell n2))$ and would represent a significant advance in the state-of-the-art at THz frequencies. Major advantages of the 2DEG hot electron mixer, are the moderate cooling requirement (20–77K), and the completely monolithic fabrication technology.

IV. THE MODE IIa 2DEG MIXER (CYCLOTRON RESONANCE MODE)

Basic Requirements for Mode IIa

Cyclotron resonance is observable at frequencies high enough that the following conditions are fulfilled:

$$\hbar\omega_c >> kT \tag{4a}$$

and

$$\omega_c \times \tau_c > 1 \tag{4b}$$

where

$$\omega_c = eB/m^* \tag{4c}$$

is the cyclotron resonance frequency (B is the magnetic flux density). The relaxation time, τ_c, is often taken to be the same as the momentum relaxation time, τ_m, which can be derived from the mobility, and was discussed above in connection with charge carrier inertia. The scattering processes of the electrons in a magnetic field are often quite different from the case of drift in a uniform electric field, so τ_m should only be regarded as a first approximation for the value of τ_c in (4b). It is clear from the above conditions that in order

Table 1.1

Data for wafers used to study cyclotron resonance detection.

Wafer	77K		4.2K	
	$N_S(\times 10^{11})$	$\mu(cm^2/Vs)$ (light)	$N_S(\times 10^{11})$	$\mu(cm^2/Vs)$ (light)
TDEG 33 (OMVPE)	4.7	171,000	4.95	728,400
T7591 (MBE,IBM)	4.5	173,240	4.23	790,610
G587(MBE, ref.[9])	5.2	202,000	5.6	1,410,000
G585(MBE,ref.[9])	2.4	205,000	3.35	2,410,000

to observe cyclotron resonance (CR) one requires a combination of (1) a low temperature (2) a high frequency, and (3) a high mobility. The 2 DEG medium is ideal for detecting CR at reasonably low frequencies, since μ is quite high at low temperatures. One can detect CR either in absorption, or by a photoconductive effect. Smith, Cronin et al [9] showed that the 2DEG medium has a strong CR photoconductive effect at frequencies from 94 GHz to 3 THz. They employed samples with mobilities as high as 2.4×10^6 cm^2/Vs, and estimated that the maximum detector responsivity was at least 300 V/W. In order to further investigate this effect, we are performing a comparative study of 2DEG samples from different sources, including some of the samples used in [9]. The mobility at 4.2 K ranges from about 200,000 cm^2/Vs to 2.4×10^6 cm^2/Vs. The main characteristics of representative wafers are summarized in Table 1.

Experimental Results

Although the study is still ongoing, some preliminary results are very interesting, and are mentioned here. We are using a system as shown in Figure 9. A typical device configuration is as shown in Figure 10.

(1) The responsivity at 94 GHz ranges from 1 V/W for the lowest μ sample, as previously reported in [2], to over 100 V/W for the IBM sample with $\mu = 790,000$ cm^2/Vs. If mismatch losses are accounted for, we find a maximum responsivity close to 135 V/W. The responsivity at 238 GHz is higher than at 94 GHz by at least a factor of two. The responsivity saturates as the microwave power is increased, as shown in Figure 11.

(2) The linewidth measured at 238 GHz is much narrower than at 94 GHz (typically by a factor of two). Two typical recordings are given in Figure 12 (for the IBM wafer) . The linewidth also appears substantially narrower than that predicted from accepted theories (0.02T for the highest mobility device).

One can use the responsivity of the straight detector to predict mixer performance, if it is assumed that the hot electron bolometer theory of Arams et al. [17] applies. The approximate minimum conversion loss is:

$$(L_C)_{\min} \simeq 4\left(\frac{1}{\mathcal{R}I_o}\right)^2$$

where $\mathcal{R}$ is the responsivity of the device as a detector, and I_o the bias current. With currently demonstrated responsivities, we predict a conversion loss of $\sim$ 50 dB. Experiments are under way to investigate this second mode of mixing. We can potentially increase $\mathcal{R}$, which would decrease L_C to values of practical use. The expected noise temperature in this mode, if successful, should be considerably less than for the Mode I mixer. LO power should be 1 μW or less, and the bandwidth a few hundred MHz.

V. CONCLUSION

We have explored the requirements on a THz 2DEG mixer by measuring charge carrier inertia and intrinsic device noise, and by developing improved 2DEG material. The new data enable us to predict the performance of a THz 2DEG mixer with greater confidence, and a receiver noise temperature of about $15\times$ $(hf/k\ell n2)$ or less appears feasible. We have also obtained preliminary results in the cyclotron resonance mode, with strong detected signals. Further experiments are needed to determine whether mixing is possible in this mode.

VI. ACKNOWLEDGEMENTS

We gratefully acknowledge the receipt of two wafers from the IBM T.J. Watson Research Center, Yorktown Heights, NY. We would also like to thank Dr. Nigel Cronin for providing us with several high-mobility wafers, and for informative discussions regarding the CR photoconductive effect. One of the authors (KSY) would like to thank Chalmers University of Technology, Gothenburg, Sweden, for support and for providing a stimulating environment for a sabbatical leave, during which part of this work was done.

VII. REFERENCES

[1] K.S. Yngvesson, J.-X. Yang, F. Agahi, D. Dai, C. Musante, Grammer, W., and K.M. Lau, "AlGaAs/GaAs Quasi-Bulk Effect Mixers: Analysis and Experiments," Proceedings of the Third International Symposium on Space Terahertz Technology, University of Michigan, Ann Arbor, MI, p.688 (1992).

[2] J.-X. Yang, F. Agahi, D. Dai, C. Musante, W. Grammer, K.M. Lau, and K.S. Yngvesson, "Wide-Bandwidth Electron Bolometric Mixers: A 2DEG Prototype and Potential for Low-Noise THz Receivers", Accepted for publication in IEEE Trans.Microw.Theory and Techniques, Mini-Special Issue on Space THz Technology, May 1993.

[3] J.-X. Yang, "AlGaAs/GaAs Two Dimensional Electron Gas Devices: Applications in Millimeter Waves and Submillimeter Waves," Ph.D. Thesis, University of Massachusetts @ Amherst, Department of Electrical and Computer Engineering, Sept. 1992.

[4] E.R. Brown, J. Keene, and T.G. Phillips, "A Heterodyne Receiver Based on Cyclotron Resonance in InSb at Low Temperature," Intern.J.Infrared and Millimeter Waves, 6,1121 (1985).

[5] E.L. Kollberg, E.M. Gershenzon, G.N. Gol'tsman, and K.S. Yngvesson, "Hot Electron Mixers, the Potential Competition," ESA Symposium on "Photon Detectors for Space Instrumentation," November 1992.

[6] D.E. Prober, "Low Noise, Superconducting Hot-Electron Microbolometer Mixer for Heterodyne Detection at 0.5 to 2 THz with Gigahertz IF Bandwidth, this conference.

[7] E.N. Grossman, J.E. Sauvageau, and D.G. McDonald, "Optocal Performance of Photoinductive Mixers at THz Frequencies," this conference.

[8] E.M. Gershenzon, and G.N. Gol'tsman, "Hot Electron Superconductive Mixers," this conference.

[9] S.M. Smith, N.J. Cronin, R.J. Nicholas, M.A. Brummel, J.J. Harris, and C. T. Foxon, "Millimeter and Submillimeter Detection Using $Ga_{1-x}Al_xAs/GaAs$ Heterostructures", Intern. J. Infrared Millimeter Waves, 8, 793-802 (1987).

[10] K.S. Champlin, D.B. Armstrong, and P.D. Gunderson, "Charge Carrier Inertia in Semiconductors," Proc. IEEE, 52, 677 (1964).

[11] R.O Grondin, P.A. Blakey, and J.R. East, "Effects of Transient Carrier Transport in Millimeter Wave Diodes," IEEE Trans. Electron Devices, ED-31, 21 (1984).

[12] W. Grammer, "Characterization of the Two-Dimensional Electron Gas (2DEG) Device at 77K," M.Sc. Thesis in Electrical and Computer Engineering, University of Massachusetts, Sept. 1992.

[13] W. Grammer and K.S. Yngvesson, "Coplanar Waveguide Transitions to Slotline: Design and Microprobe Characterization," Accepted for publication, IEEE Trans. Microw. Theory Techn. (1993).

[14] A. Jelenski, E. Kollberg, and H. Zirath, "Broad-band Noise Mechanisms and Noise Measurements of Metal-Semiconductor Junctions," IEEE Trans. Microw. Theory Tech., MTT-34, 1193 (1986).

[15] H. Ekström et al., "348-GHz Endfire Slotline Antennas on Thin Dielectric Membranes," IEEE Microwave Guided Wave Lett., 2, 357 (1992).

[16] D.F. Filipovic, S.S. Gearhart, and G.M. Rebeiz, "Double-Slot Antennas on Extended Hemispherical and Elliptical Dielectric Lenses," this conference.

[17] F.R. Arams, C. Allen, B. Peyton, and E. Sard. "Millimeter Mixing and Detection in Bulk InSb". Proc. IEEE, 54, 612 (1966).

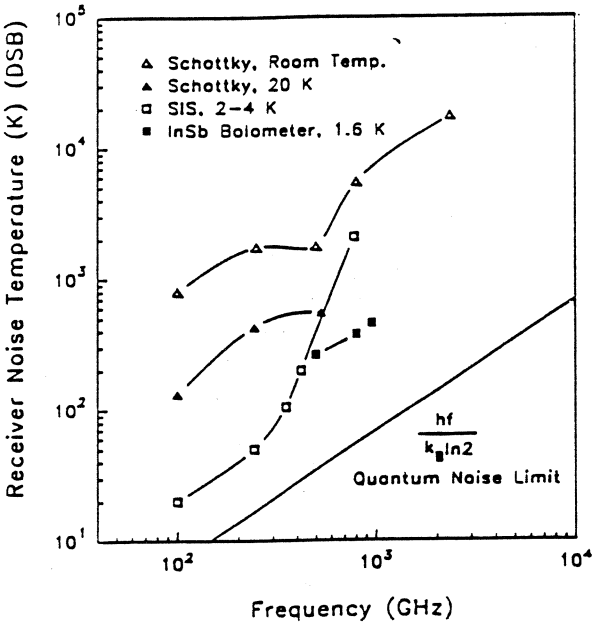

Figure 1. Receiver noise temperatures in the millimeter and submillimeter wave frequency ranges.

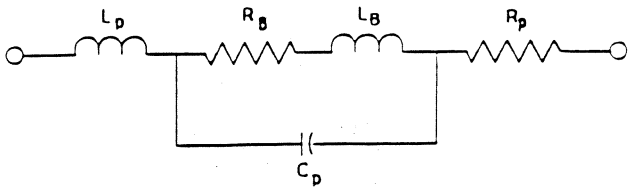

Figure 3. Equivalent circuit of the 2DEG device, including the effect of charge carrier inertia.

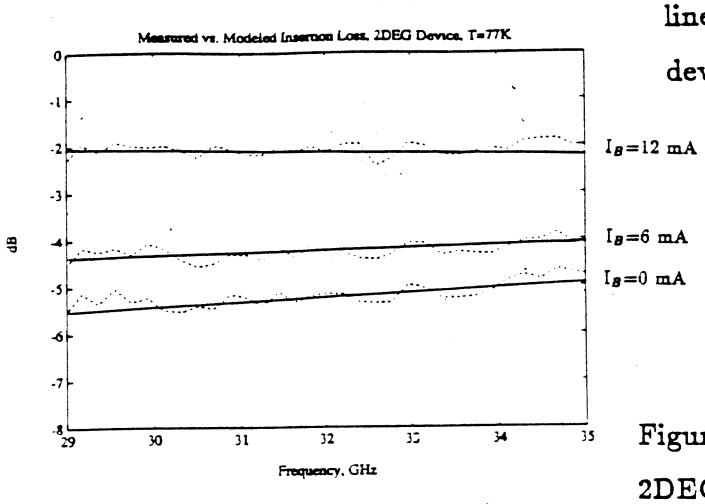

Figure 5. Measured and modeled response of a 2DEG device at 77 K, for three different bias currents.

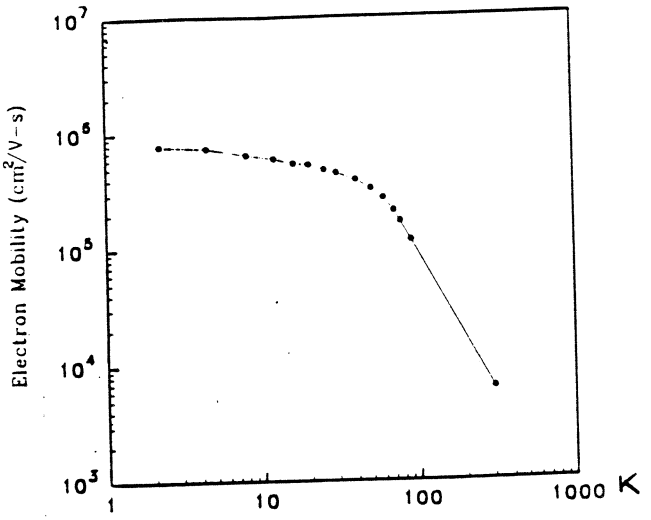

Figure 2. Mobility versus temperature for the best wafer grown by OMCVD.

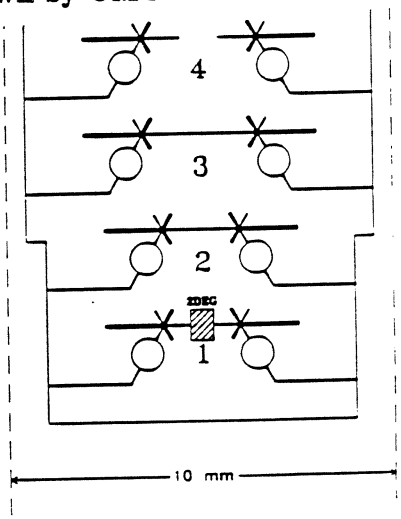

Figure 4. Back-to-back coplanar waveguide to slotline transitions, used to Cascade probe a 2DEG device.

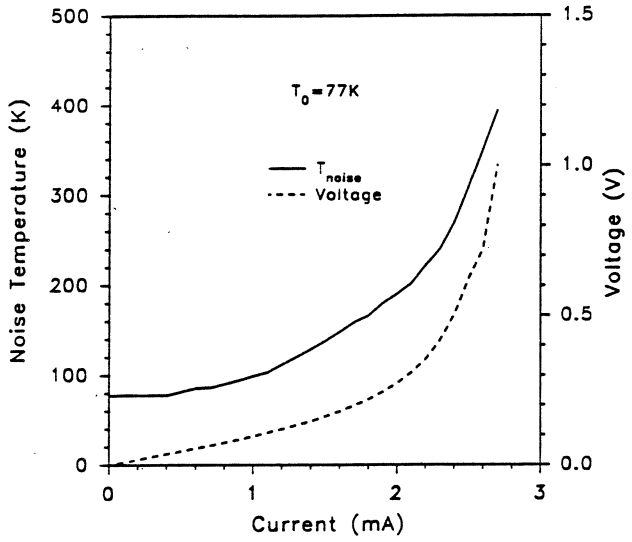

Figure 6. Measured device noise temperature at 1.5 GHz versus bias current. The DC I-V-curve is also shown.

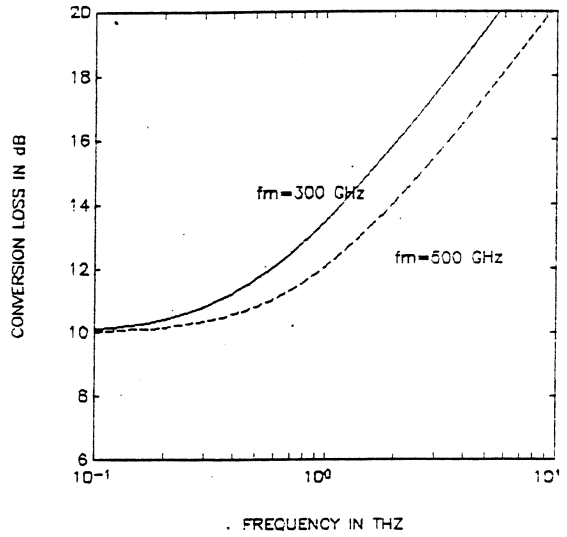

Figure 8. Predicted increase of the conversion loss of a 2DEG mixer in the THz range.

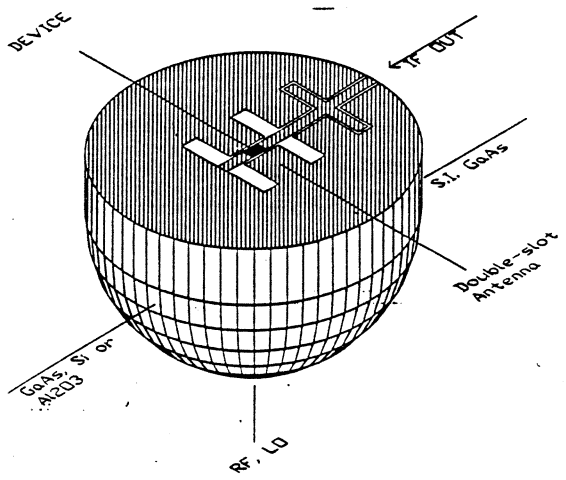

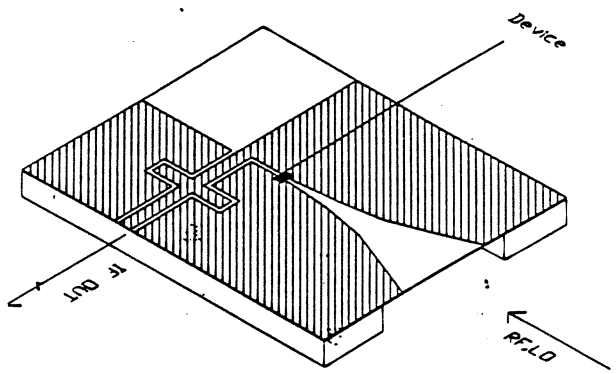

Figure 7. Integrated circuit antennas which could be used with a THz 2DEG device.

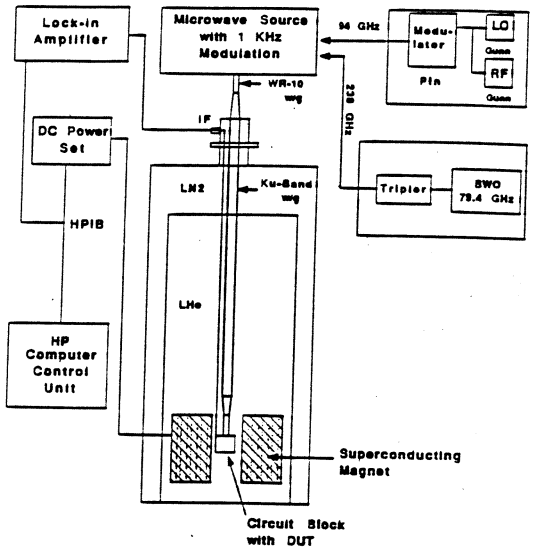

Figure 9. The system used to measure the cyclotron resonance photoconductive effect.

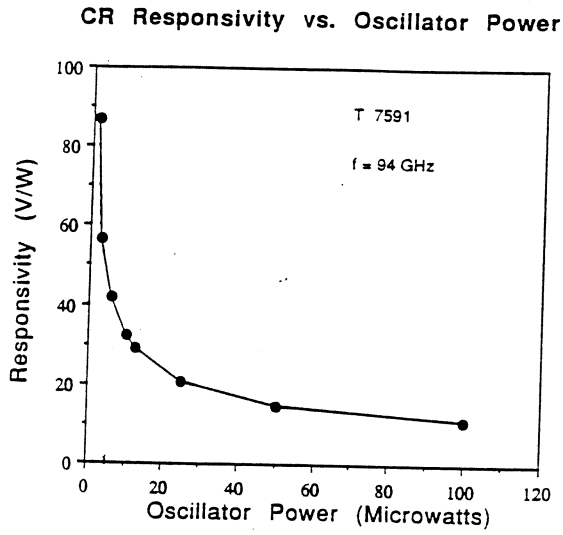

Figure 11. Responsivity versus microwave power for a device made from the IBM wafer (T7591).

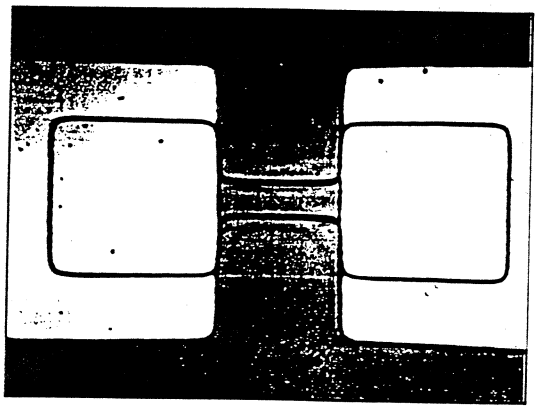

Figure 10. Typical device configuration used in the CR experiments.

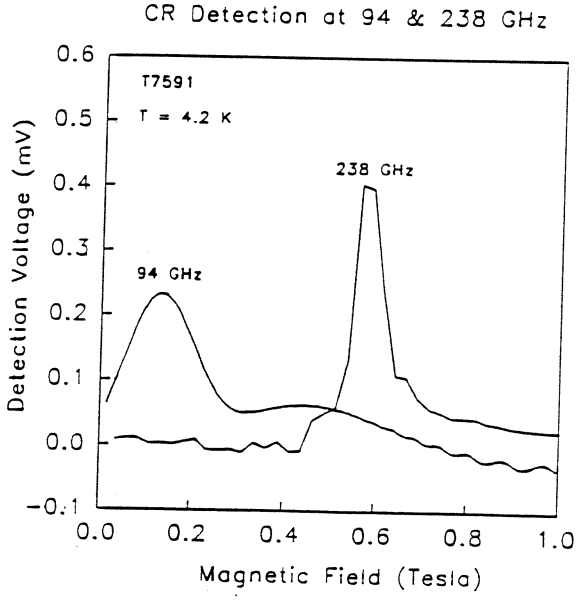

Figure 12. Recordings of CR at 94 and 238 GHz, respectively, for the same device as in Figure 11. The input power was about 5μW at both frequencies, and bias current 30μA.

Low Noise, Superconducting Hot-Electron Microbolometer Mixer for Heterodyne Detection at 0.5 to 2 THz with Gigahertz IF Bandwidth

Daniel E. Prober Dept. of Applied Physics, Yale University*
PO Box 2157, New Haven, CT 06520-2157

Abstract[1]

We present a new device concept for a mixer element for THz frequencies. This uses a superconducting transition-edge microbridge biased at the center of its superconducting transition near 4.2 K. It is fed from an antenna or waveguide structure. Power from a local oscillator and an rf signal produce a temperature and resulting resistance variation at the difference frequency. The new aspect is the use of a very short bridge in which very rapid (<0.1 ns) outdiffusion of hot electrons occurs. This gives large intermediate frequency (if) response. The mixer offers ≈4 GHz if bandwidth, ≈80 ohm rf resistive impedance, good match to the if amplifier, and requires only 1 - 20 nW of local oscillator power. The upper rf frequency is determined by antenna or waveguide properties. Predicted mixer conversion efficiency is 1/8, and predicted receiver noise temperatures are 260K and 90K for transition widths of $0.1T_c$ and $0.5\ T_c$ respectively.

* Research supported by NSF DMR 9112752 and NASA NAG 5-1244

[1] Related paper to appear in Applied Physics Letters, April 26, 1993

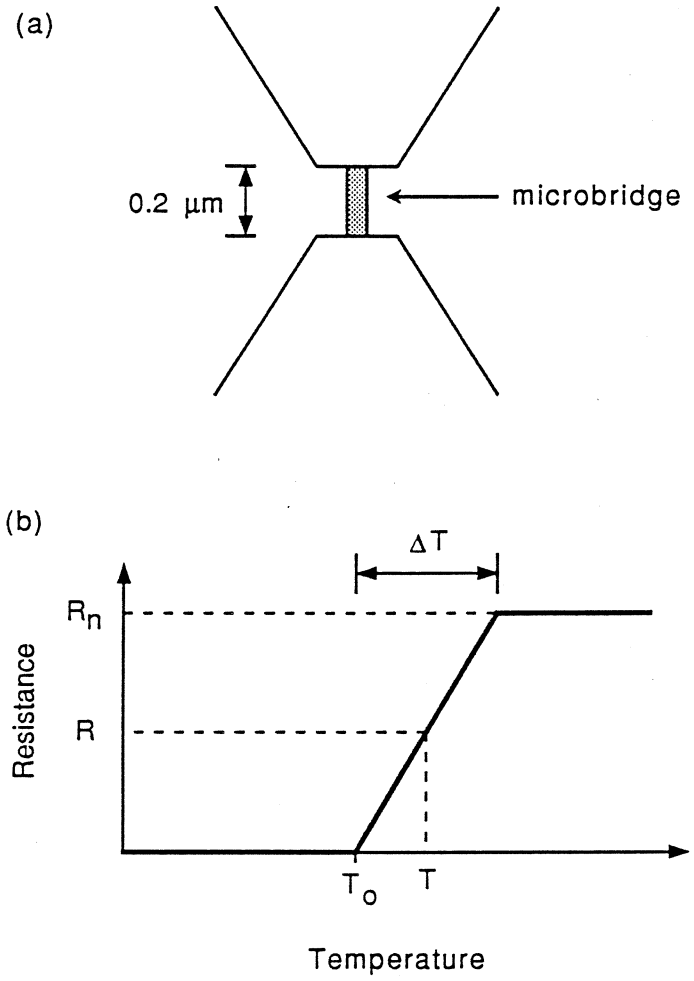

Fig. a. Layout of microbridge mixer; bridge is shaded, thick pads are unshaded; b. Resistive transition with bridge biased at R and T.

Table - Device properties for Nb microbolometer mixer, this work.

T = 4.4 K; receiver conversion efficiency η =1/10 for computation of T_R. For a planar antenna or corner-reflector mount, a smaller value of η is realistic, and the values of T_R (DSB) would be larger than given below.

R_n	80 ohms
Dimensions (μm^3)	0.2 x 0.05 x 0.01
G	0.8×10^{-8} W/K
S ($\omega = 0$) for $\Delta T = 0.1T$	1.1×10^5 V/W
P_{lo} for $\Delta T = 0.1T$	1 nW
$\Delta T = 0.5$ T	5 nW
τ	0.04 ns
IF response (-3db)	4 GHz
T_R (DSB) for $\Delta T = 0.1$ T	260 K
$\Delta T = 0.5$ T	90 K

THz SOURCES BASED ON INTERSUBBAND TRANSITIONS IN QUANTUM WELLS AND STRAINED LAYERS *

A. Afzali-Kushaa, G. I. Haddad, and T. B. Norris

Solid-State Electronic Laboratory
Department of Electrical Engineering and Computer Science
The University of Michigan, Ann Arbor, Michigan 48109

ABSTRACT

The feasibility and potential of laser sources based on intersubband transitions in quantum wells and strained layers will be presented. The basic schemes and proposed structures for both electrically and optically pumped devices are discussed. Both conduction band and valence band quantum wells as well as strained layers may be used as the active layer of these lasers. These sources can be either optically or electrically pumped with each having its own advantages. Various material systems which are appropriate for these applications will be described.

I. INTRODUCTION

Recent advances in crystal growth techniques such as MBE, CBE, and MOCVD have enabled us to grow thin layers of semiconductor materials on top of bulk materials. Depending on the thickness and the material properties of the grown layers, one can realize either a bulk like or a quantum well layer. If the thickness of the grown layer is less than the de Broglie wavelength and the energy gap of the layer is different from the surrounding layers, a quantum well can be realized in which quantum size effects become easily observable. When the carriers are confined in the valence band of the layer, the well is referred to as "valence band quantum well" while when the carriers are confined in the conduction band of the layer the well is referred to as "conduction band quantum well." The confinement of carriers in one direction and the lack of confinement in the other two directions in the structure lead to the formation of subbands of bound states. The energy separation of subbands is inversely proportional to the square of the well width. In the strained system, the lattice constant of the grown layer does not match the lattice constant of the substrate which leads to lifting the degeneracy of the of light- (LH) and heavy-hole (HH) subbands at the Brillouin zone center. If the strain is compressive, i.e., the lattice constant of the epilayer is larger than that of the substrate, the induced non-degeneracy gives rise to a smaller energy difference between the HH subband and the conduction band compared to the LH subband to conduction band energy separation. If, however, the strain is tensile, i.e., the lattice constant of the

* This work is supported by the NASA Center for Space Terahertz Technology under contract No. NAGW-1334 and the Army Research Office the URI program under contract No. DAAL03-92-G-0109.

epilayer is smaller than that of the substrate, the non-degeneracy leads to a closer LH subband to the conduction band. The energy difference between the top of the LH and HH subbands is proportional to the strain in the system. Energy separation between subbands in both quantum well and strained layers therefore can be designed properly to be in the THz range (10-20 meV) making these layers a suitable material system for detectors, modulators, and lasers in this range of frequency.

II. PROPOSED STRUCTURES

1) Intersubband Conduction Band Quantum Well Lasers

Recently, several research groups [see e.g. 1-14] have reported studies on intersubband transitions in quantum wells with applications such as infrared lasers, light modulators (switches), and detectors. Strong optical absorption [8] and spontaneous emission [9] due to intersubband transitions have been observed experimentally. Although these observations are encouraging, in order to realize intersubband lasers, enough photon gain should be achieved to compensate all the photon losses in the quantum well. The gain in a laser system is directly proportional to the population inversion in the active layer. To achieve population inversion in the quantum well, both optical and electrical pumping schemes have been suggested [1-7]. Figure 1a shows the band diagram of the simplest electrically pumped intersubband laser suggested by Mehdi *et al.* [1] and Loehr *et al* [2]. Carriers are injected from the left contact and by tunneling through the left barrier, reach to subband 2 and radiatively relax to subband 1 and finally, after tunneling through the right barrier, they are collected by the right contact. Another proposed electrically pumped intersubband laser is shown in Figure 1b. To improve population inversion in the quantum well (the active layer of the laser), resonant tunneling filters have been utilized in the structure to selectively inject carriers into subband 2 and remove carriers from subband 1 [4,5].

The major problems associated with the electrically pumped laser schemes is that the confinement factor in the system, which accounts for the reduction in gain that occurs because of the spreading of the optical energy beyond the active layer, is very low. The net gain therefore is too small which makes the laser action very difficult. This factor can be improved by utilizing the optically pumped laser scheme where one period of its active layer is shown in Figure 2. The structure may utilize 10-20 periods of the well shown in the figure to enhance the confinement factor about a factor of 100-400. The proposed scheme uses a heavily n-doped layer to provide carriers in subband 1 where a pumping laser excites carriers from the subband into subband 4. After relaxing to subband 3, these hot electrons radiatively relax to subband 2, and finally return to subband 1 and the carrier cycle completes.

In conduction band quantum wells, the symmetry of the subbands is the same. Therefore, the tunneling and relaxation rates in the well only depend on the relative energy difference of the subbands. Population

inversion, which is a crucial requirement for laser action, may be created when the injection and removal rate of the carriers from the subbands are not identical. Therefore, inverting the population of two different subbands in these wells is rather difficult.

2) Intersubband Valence Band Quantum Well Lasers

Instead of using conduction band quantum wells, one can use valence band quantum wells in similar structures. In these structures, the tunneling and relaxation rates of the hole from one subband to the other is not only dependent on the energy difference of the two subbands, but it also depends on the symmetry of the subbands. This additional feature of the subbands in valence band quantum wells, makes them an excellent choice for inter-subband quantum well lasers. The origins of different transition rates of the hole from different subbands are briefly expressed in the following:

a. The tunneling rate is a function of the carrier mass in the growth direction. The different masses of the holes in the growth direction, therefore give rise to different tunneling rates for light and heavy holes.
b. Under the application of a strong magnetic field parallel to the interface, the motion of holes passing through the barrier is altered [14]. This can be considered as a decrease of the kinetic energy in the tunneling direction or an effective increase of the tunneling barrier. The additional voltage needed, to obtain the same tunneling rate as in the case of zero magnetic field, is inversely proportional to the effective mass of the hole in the growth direction.
c. In strained systems, the barrier seen by the light hole is different from the barrier seen by the heavy hole due to the induced non-degeneracy in the system. Since the tunneling rate decreases exponentially as the barrier increases, the tunneling rate would have different values for the heavy-hole and light-hole.
d. Depending on the symmetry, namely, LH or HH, of the subband, the tunneling rate of the carriers may be different. This provides another feature which can be utilized in designing systems to obtain a better population inversion. The non-radiative relaxation rate between two subbands in the same well also might be reduced if the subbands have different symmetry.

Any of a-d or some combinations thereof may be exploited in designing structures for intersubband lasers where achieving the population inversion between the two subbands involved in the radiation is a vital requirement. The conclusion reached from the above argument suggests that the threshold of the input power (or carrier density) for lasing should be lower in properly designed valence band quantum wells compared to a similar structure but based on conduction band quantum wells. Despite the aforementioned potential of the valence band quantum well, it has not been studied as extensively as conduction band quantum wells. White *et. al.* [15] have observed population inversion with a ratio of 300/1 between LH1 and HH1 in

a p-i-n structure. The energy separation between the two subbands is 21 meV which is less than the LO phonon energy. Since the population inversion has been achieved in this simple quantum well, one can consider a simple quantum well, similar to the one shown in Figure 1a, as a potential structure for THz sources.

Figure 3 shows an electrically pumped laser scheme proposed by our group. The structure is the valence band quantum well version of the scheme shown in Figure 1b. In this structure, the transition between subband 3 and subband 1, as well as the transition between subband 2 and subband 0 are undesired and detrimental to the population inversion between subband 2 and subband 1. In the electron version, we do not have much control over reducing these rates except for adjusting the energies of the subbands. In the hole version of the proposed scheme, however, one can make use of the properties mentioned before to reduce these rates more. Figure 3 is an example of a design where due to the different symmetry between subband 3 (HH band symmetry) and subband 1 (LH band symmetry), the transition rate between these two subbands is reduced. The same argument holds for the transition from subband 2 (HH band symmetry) to subband 0 (LH band symmetry). In addition, the lighter effective mass of the carrier in subband 1 provides a higher tunneling rate for holes in this subband. This further improves the population inversion between subband 2 and subband 1.

Optically pumped laser schemes can take advantage of the relaxation properties of the holes in quantum wells. Figure 4 shows a valence band quantum well version of the optically pumped laser structure discussed earlier (see Figure 2). To invert the populations of subband 3 and subband 2, the non-radiative relaxation of holes from subband 4 to 2 as well as from subbands 3 to 1 should be as slow as possible while the non-radiative relaxation of holes from subband 4 to subband 3, as well as from subband 2 to subband 1 should be as fast as possible. A desired symmetry for the subbands of the laser is shown in the figure where unwanted relaxation corresponds to different symmetry transitions while desired relaxation occurs between the subbands with the same symmetry.

In all these proposed structures, in order to have coherent light, we would like to retain carriers in the higher energy subband as long as possible and let photons stimulate their radiation coherently. In addition, to maintain population inversion in the structure, the carriers in the lower energy subband should be emptied out as soon as possible. Consequently, relaxation times between different subbands in a quantum well, as well as tunneling rates between different subbands in adjacent quantum wells are the key factors in determining the achievable population inversion due to a certain current density or pumping rate in an intersubband quantum well laser. Several studies have previously been devoted to intersubband or interwell scattering [see e.g. 16, 17]. These studies mostly have addressed the case of simple quantum wells and transition from subband 2 to subband 1.

In order to enhance the confinement factor of the laser, the use of optically pumped structures was suggested earlier. Although, a considerable

improvement may be obtained, however, the factor is still far below unity in the frequency range of interest.

3) Bulk Strained Lasers

As has been mentioned earlier, the energy separation between LH and HH subbands in a strained layer is proportional to the amount of strain in the layer. By adjusting the strain, one can design the desired energy separation of the subbands. Depending on the strain, hoewever, the thickness of the strained layer may not exceed a certain thickness called critical thickness for the pseudomorphic or coherent layer, i.e., a layer without any dislocations. The critical thickness is *inversely* proportional to the strain on the system. For the energy separations that lead to THz radiation (around 10 to 20 meV), this thickness is more than 100 nm which can be a great advantage for THz lasers based on these systems as will be discussed later. Figure 5 shows the critical thickness for InGaAs alloys as a function of the frequency which can be radiated due to the transition of the hole from one subband to the other.

The far-infrared (FIR) amplification of the electromagnetic waves due to direct transition of the hot holes in *strong* electric and magnetic field (larger than 1 kV/cm and 1 T, respectively, induced by a voltage greater than a few kilovolts and a few Amperes) has been under investigation [see e.g. 18, 19]. The observed stimulated emission covers a broad wavelength range 80-210 μm with a line width of about 20 1/cm and with pulse emitted power up to 10W. The FIR radiation from uniaxially stressed p-type Ge in the absence of a magnetic field and at lower electric fields also has been observed [see e.g. 20, 21]. The uniaxial strain in the Ge layer split the degenerate valence band edge at the Brillouin zone center into two subbands separated by the energy Δ. In the measured structure which is a bar of the semiconductor, at zero electric field essentially all of the holes occupy the lower energy band with small effective mass in the stress direction. When an electric field is applied to the sample, the light holes heated by the field are transferred to the upper band with larger effective mass and higher density of states. The direct optical transitions may take place only due to the holes with energies above the band-split energy Δ.

Instead of using external uniaxial strain, one can use biaxial strained layers which are grown on a lattice mismatched substrate. An electrically pumped p-i-p laser structure based on strained bulk systems proposed by our group is shown in Figure 6. The active layer, which is intrinsic, is under tensile strain. When an electric field is applied to the system, the top of the emitter valence band is aligned to the top of the active layer HH band while the top of the collector valence band is aligned to the top of the active layer LH band. The applied field moves holes from the emitter valence band to the active layer HH band where holes radiatively relax to the active layer LH band. Holes are then collected by the collector layers. If the structure is designed for the light radiation with the photon frequency of 4 THz (~16 meV energy separation), the thickness of the active layer may be as high as 200

nm as can be extracted from Figure 5. Therefore, in these structures the confinement factor of the laser gain can be improved by a factor about 40 compared to that of the quantum well system.

An optically pumped laser which is based on strained bulk layers is shown in Figure 7. The active layer is under tensile strain and is p-doped. A laser pump is used to excite electrons from split-off band to LH band. Hot electrons in this band radiatively relax to HH band which create photons at a THz frequency. The relaxed holes to HH band then relax back to split-off band and complete the circle. The relaxation time between LH band and HH band will be long, if the energy separation between the HH band and the LH band at k = 0 (where k is the wave number) is less than LO phonon energy. However, the energy separation between the split-off band with the LH and HH bands are more than LO phonon energy leading to shorter transition rates between these bands.

III. Material System

Figure 8 shows different layers used to realize the strained electrically pumped laser structure shown in Figure 5. The substrate is InP and the alloy used in the injector and collector layers is $In_{0.53}Ga_{0.47}As$ which is lattice matched with the substrate. The alloy used in the strained layer is $In_{0.49}Ga_{0.51}As$ which is not lattice matched with the substrate and other layers. Since the lattice constant of the active layer is less than that of the substrate, therefore the layer is under tensile strain. The advantage of using InGaAs/InP systems is that by changing the composition of Ga (or In) in the alloy, one can have a lattice matched, compressive or tensile strained layer.

The choice of materials in none of the proposed structures is restricted to direct band gap semiconductors and indirect band gap materials, like Ge and Si, also can be utilized in the laser structure. Therefore, these system have the potential to be integrated eventually with other semiconductor devices in silicon based integrated circuits.

IV. Summary

The potential application of the transition between subbands in both conduction band and valence band quantum wells as well as the transition between HH and LH subbands in strained layers for THz sources was discussed. Both electrically and optically pumped lasers based on quantum well and strained systems were proposed. The optically pumped schemes offer a larger confinement factor compared to electrically pumped structures in the same system. At present time, the strained system seems to be the most promising system in both electrically and optically pumped lasers among the proposed structures. The confinement factor in the optically pumped laser based on strained layers can be as high as 1. In addition, the factor is higher in the proposed electrically pumped scheme compared to similar structures based on quantum wells. The choice of materials in these structures is not

limited only to the direct band gap semiconductors and indirect band gap semiconductors such as Si and Ge may be used in the active layer of these systems. To asses the performance and characteristics of the proposed structures further study is being carried out both theoretically and experimentally.

REFERENCES

1. I. Mehdi, G. I. Haddad, and R. K. Mains, Superlatt. Microstruc. 5, 443 (1989).
2. J. P. Loehr, J. Singh, R. K. Mains, and G. I. Haddad, Appl. Phys. Lett. 59(17), 2070 (1991).
3. H. C. Liu, J. Appl. Phys., 63(8), 2856, (1988).
4. Borenstain S. I. and Katz J., Applied Physics Letters, 1989, Vol 55, 654-656.
5. Hu Q. and Feng S., Applied Physics Letters, 1991, Vol 59, 2923-2925.
6. P. Yuh and K. L. Wang, Appl. Phys. Lett. 51(18),1404 (1987).
7. K. M. Lau and W. Xu, IEEE J. Quantum Electron. QE-28, 400 (1992).
8. L. C. West and S. J. Eglash, Appl. Phys. Lett. 46, 1156 (1985).
9. H. Helm, E. Colas, P. England, F. DeRosa, and S. J. Allen, Jr., Appl. Phys. Lett. 53, 1774 (1988).
10. D. D. Yang, P. Boucaud, F. H. Julien, L. Chusseau, J. M. Lourtioz, and R. Planel, Electronics Letter, Vol. 26, pp. 1531-1532, 1990.
11. S. Noda, T. Uemura, T. Yamashita, and A. Sasaki, J. Appl. Phys., vol. 68, pp. 6529-6531, 1990.
12. Oberli D. Y., Wake D. R., and Klein M. V., Physical Review Letters, 1987, Vol. 59, 696-699.
13. I. V. Altukhov, M. S. Kagan, K. A. Korol'ov, V. P. Sinis, F. A. Smirnov, Proceedings 1991 International Semiconductor Device Research symposium, 371-374.
14. R. P. G. Karunasiri and K. L. Wang, J. Vac. Sci. Technol. B 9 (4), Jul/Aug 1991, 2064-271.
15. C. R. H. White, H. B. Evans, L. Eaves, P. M. Martin, and Henini, Phys. Rev. B, 1992, pp. 9513-9516.
16. Ferreira R. and Bastard G., Physical Review B, 1989, Vol. 40, PP 1074-1086.
17. B. Deveaud, A. Chomette, F. Clerot, P. Auvray, and A. Regreny, R. Ferreira, and G. Bastard, Physical Review B, 1990, Vol. 42, 7021-7032.
18. Keilmann, V. N. Shastin, and K. Till, Appl. Phys. Lett. 1991, 58, pp. 2205-2207.
19. L. E. Vorobjev, S. N. Danilor, D. V. Dontzky, Yu. V. Kochegarov, V. I. Stadfeev, and D. A. Firsov, Proceedings: 1991 International Semiconductor Device research Symposium, pp. 387-389.
20 I. V. Altukhov, M. S. Kagha, and V.p. Sinis, Optical and Quantum Electronics, 23, No. 2, 1991, pp. S211-S216.
21 I. V. Altukhov, M. S. Kagha, K. A. Korol'ov, V.p. Sinis, and F. A. Smirnov, Proceedings: 1991 International Semiconductor Device research Symposium, pp. 371-374.

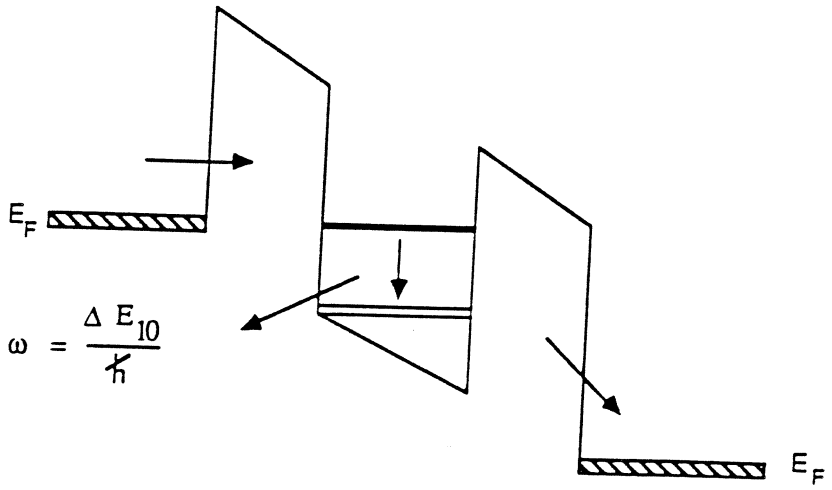

(a)

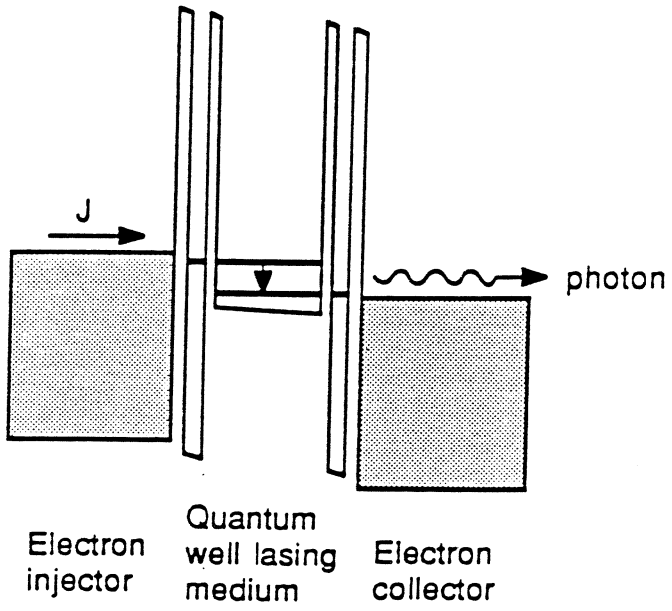

(b)

Figure 1. Electrically pumped laser based on conduction band quantum wells a) single quantum well [1,2] b) coupled quantum well [4,5].

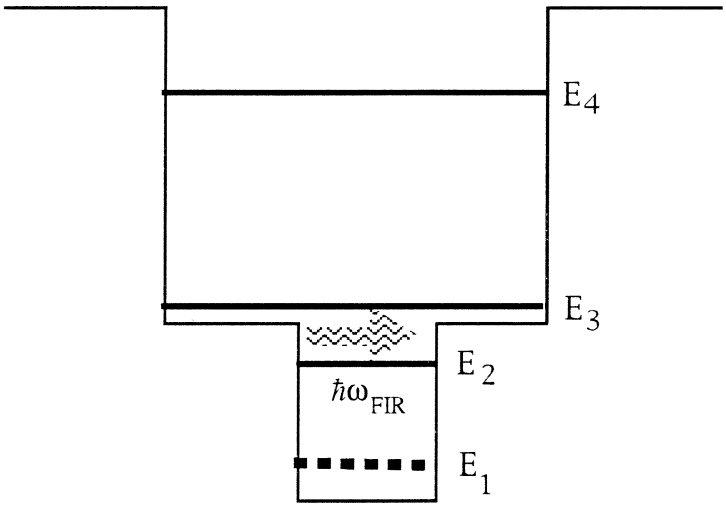

Figure 2. Optically pumped laser structure based on conduction band quantum wells.

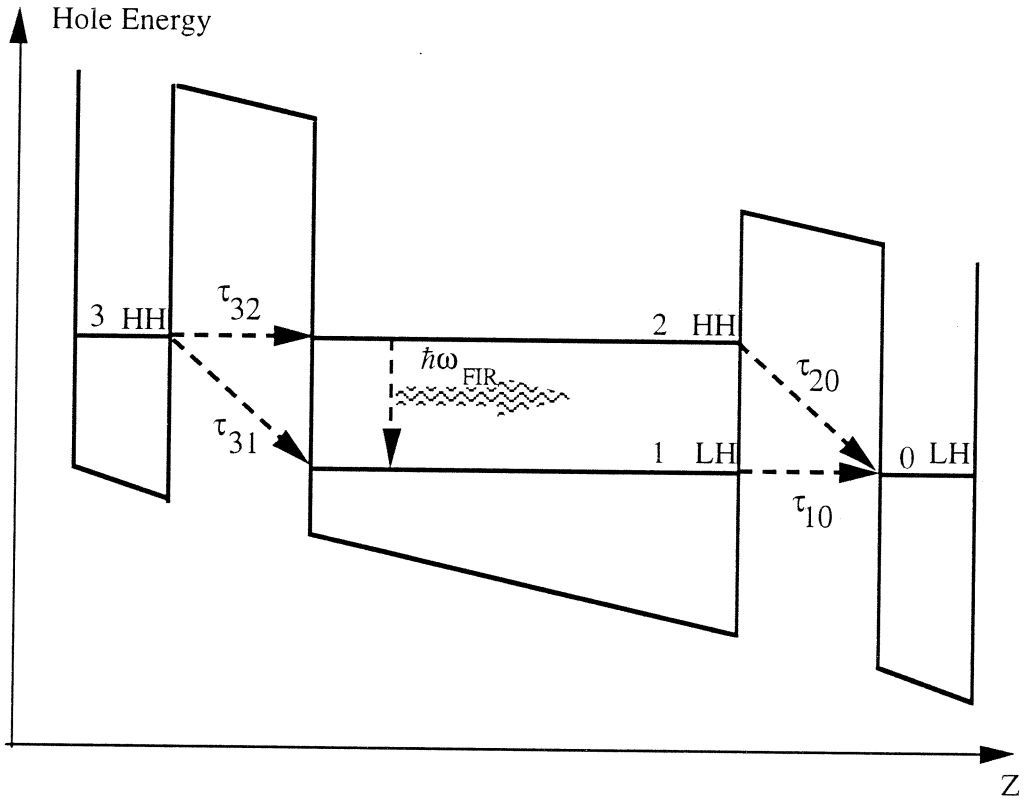

Figure 3. Electrically pumped laser based on valence band quantum wells

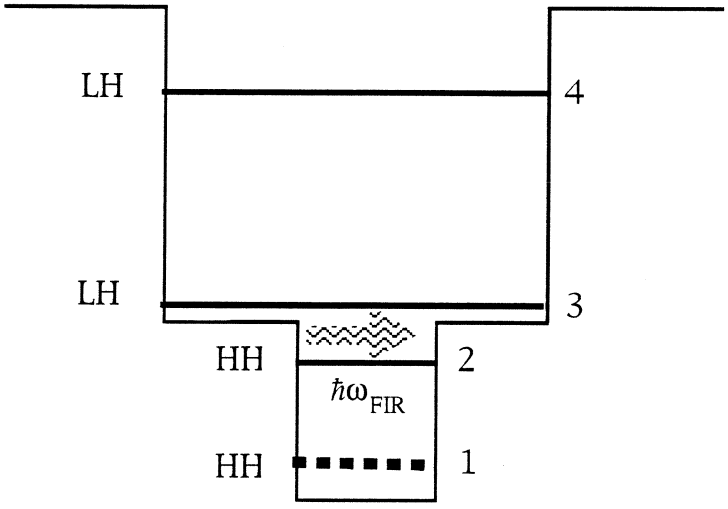

Figure 4. Optically pumped laser structure based on valence band quantum well lasers

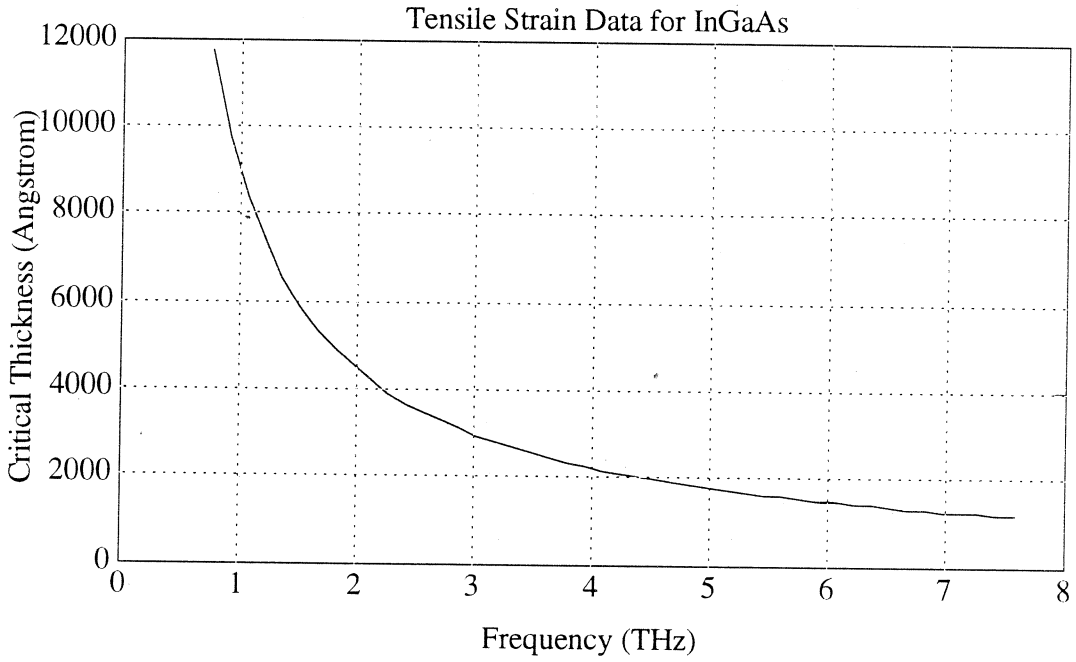

Figure 5. Critical thickness of InGaAs/GaAs systems as a function of frequency which can be radiated due to transition of holes from one subband to the other.

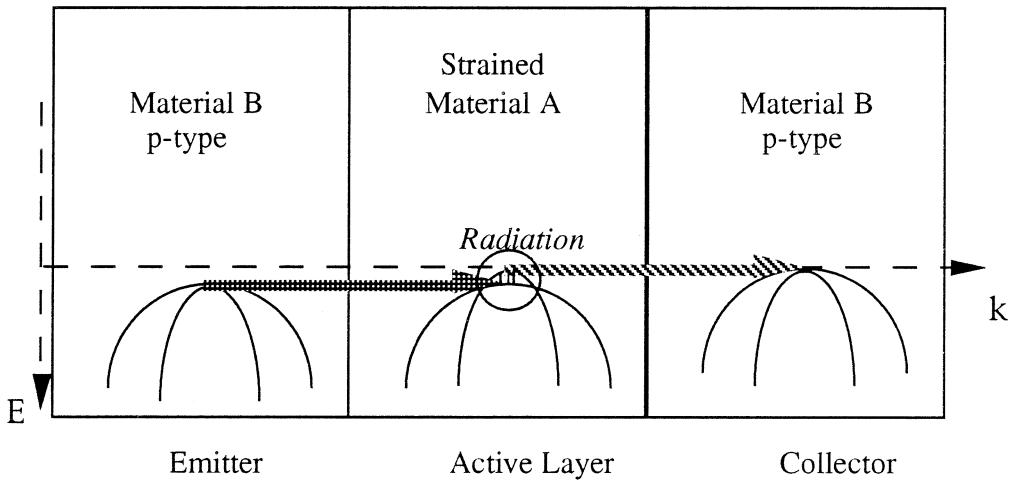

$a_{substrate} = a_B$

$a_{substrate} > a_A$ Tensile Strain

Figure 6. Electrically pumped laser structure based on strained layers

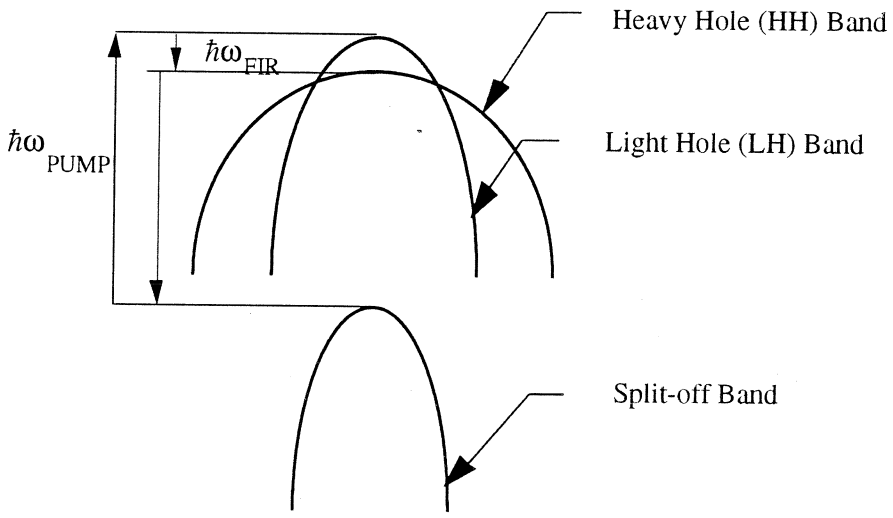

Figure 7. Optically pumped laser structure based on strained layers

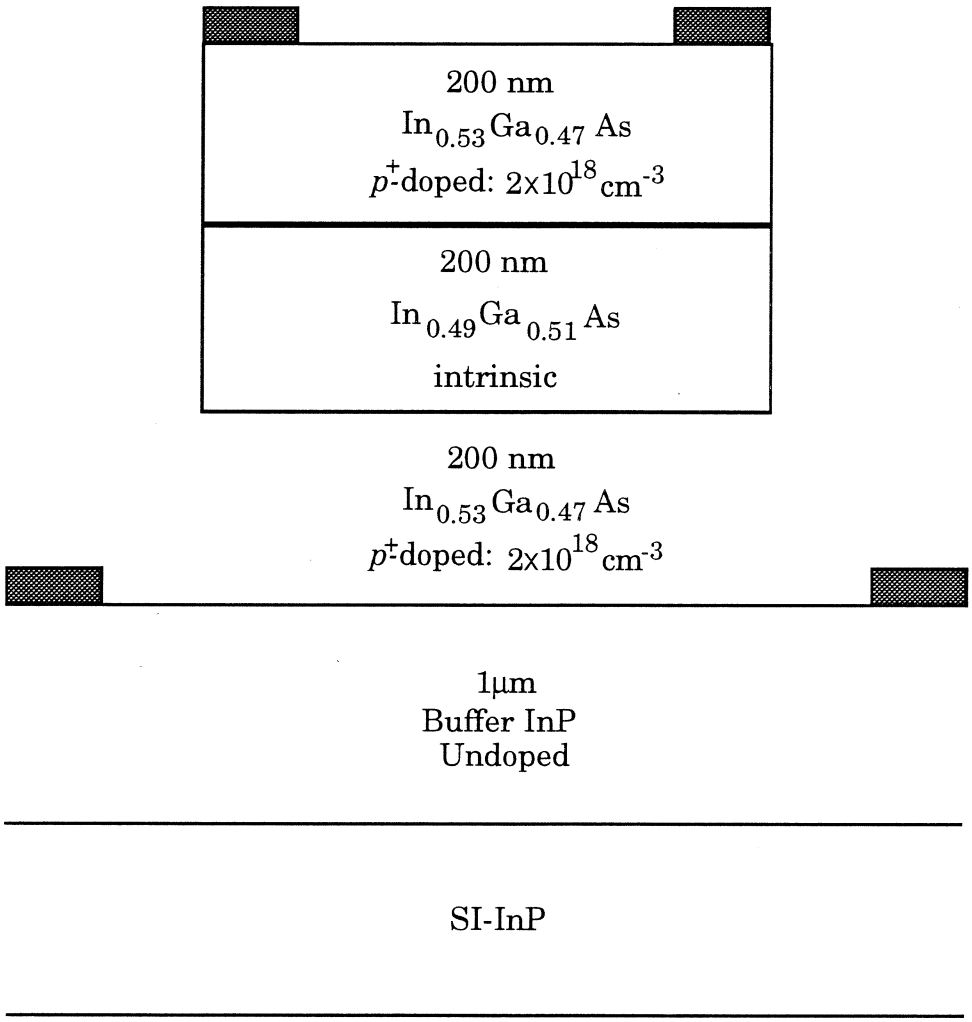

Figure 8. A realization of electrically pumped laser proposed in Figure 5.

Optical Performance of Photoinductive Mixers at Terahertz Frequencies*

E.N. Grossman, J.E. Sauvageau, and D.G. McDonald

Electromagnetic Technology Division
National Institute of Standards and Technology
325 Broadway
Boulder, CO 80303

Abstract

We have investigated the electrical and optical properties of detectors based on the change in kinetic inductance of a superconducting film with incident terahertz-frequency radiation. Two different geometric configurations, stripline and slotline, of these photoinductive detectors have been explored. Both include a loop of thin niobium coupled to the incident radiation through a lithographic antenna; the loop inductance is read out via an integrated D.C. SQUID. The slotline geometry is substantially simpler to fabricate, but electrically, the two geometries have very similar properties. The loop inductance varies with temperature in good agreement with the 2-fluid model, while thee critical current varies with temperature in agreement with Ginzburg-Landau theory. The maximum voltage-flux transfer characteristic of the SQUID varies with temperature according to the empirical relation $dV/d\Phi(max) = R/L$, where R is the resistance of the junction shunt resistors and L the loop inductance. The thermal conductance is less accurately determined experimentally, but the approximate value of $5e10^{-7}$ W/K implies a peak electrical responsivity of 2200 V/W. No excess audio frequency noise has been observed down to our amplifier's noise floor of 190 $pV/Hz^{1/2}$. This yields an electrical noise-equivalent-power (NEP) of 8×10^{-14} $W/HZ^{1/2}$, a factor of 2.5 from the expected phonon-noise limit. The response to 992 GHz laser radiation varies with reduced temperature as expected for a purely bolometric response in the limited range over which it was examined, $.78 < t < .95$. The optical power level at which the response saturates indicates that in a heterodyne mixing application, the optimum local oscillator power level would be approximately 2 nW.

I. Introduction

Terahertz-frequency detectors based on the kinetic inductance of a superconductor were originally proposed for two applications at frequencies above the superconducting gap frequency: low-noise heterodyne mixers, and low-noise bolometers compatible with large array formats and with superconducting processing electronics[1]. At frequencies above the superconducting gap frequency, the performance of mixers based on quasiparticle tunneling in tunnel junctions[2] is strongly degraded. Photoinductive mixers, which, like the resistive electron-heating mixer[3] are based on excitation of a non-thermal quasiparticle population in a superconductor, consist of a lithographic antenna, a superconducting loop thin enough to be in the kinetic inductance limit, and an integrated D.C. SQUID. In addition to a D.C. bias current through the SQUID (which passes through the two arms of the loop in parallel), a much larger D.C. bias current is passed through the loop arms in series, which creates a large D.C. magnetic flux bias. As the self-inductance of the loop varies due to power deposited in it by the antenna, the flux bias current induces a varying flux in the loop, which in turns induces a varying SQUID voltage. The photoinductor's sensitivity derives from the good impedance matching that is obtainable both at the terahertz-frequency RF, where the loop is resistive and well matched to the antenna, with impedance ~ 100 Ω, and at the IF and video frequencies, where the loop is inductive and well matched to the SQUID. Two mechanisms for far-IR response exist, direct pair-breaking, on a sub-nanosecond timescale suitable for a heterodyne mixer, and a thermal or bolometric response, on a microsecond timescale, suitable for direct detectors. The fabrication of the integrated antenna/photoinductor/SQUID devices has been significantly more difficult than originally envisioned. However, we believe we have now fabricated and tested a sufficient number of working devices that some preliminary conclusions may be drawn regarding their performance as direct detectors. The data are highly relevant to the device performance as a heterodyne mixer as well, but actual heterodyne measurements have not yet been made.

II. Device Architecture and Experimental Setup

We have fabricated and tested devices with two distinctly different geometric structures: a stripline geometry, in which the two thin photoinductive elements forming the SQUID loop lie atop one another, separated by dielectric, and a slotline or "hairpin" geometry, in which the two photoinductive elements lie side by side. These are both illustrated in fig.

1. The slotline geometry has number of advantages. Most obviously, there are fewer layers to be deposited and patterned (6 as opposed to 10 for the stripline geometry), allowing the devices to be fabricated faster, more reliably, and with fewer parameters requiring optimization In addition, since both photoinductive strips are deposited and patterned simultaneously, they can be better matched in critical current and critical temperature. Furthermore, both photoinductive elements can be left exposed during the remainder of the processing, allowing thinning or other modification after the wafer is finished and diced into individual chips. Finally, the slotline geometry does not require any part of the thin photoinductive film to cross the edge of another film. We believe that much of our difficulty in reproducibly fabricating the stripline photoinductors was related to breaks in the upper thin photoinductive film occuring where it crossed the edge of a much thicker direlectric layer underneath. On the other hand, the stripline geometry has the advantage of being more compact. It is also easier to analyze theoretically, with a simple analytic formula for its inductance. In addition, the stripline devices appear to be less susceptible to effects due to stray or trapped flux that are manifested as hysteresis and non-periodic features in the SQUID's voltage-flux characteristic, as would be expected on the basis of the stripline loop's smaller geometric area. In terms of the SQUID's voltage-flux transfer characteristic, the loop inductance, the photoinductors' critical current and temperature, and the device's total thermal conductance, the two device geometries yield very similar results.. Neither geometry therefore appears to have an advantage over the other in terms of responsivity or NEP.

All our devices were fabricated on single crystal Si substrates with 250 nm of SiO_2 thermally grown on the surface. The photoinductive films were 15 nm thick pure Nb, deposited by D.C. magnetron sputtering. The SQUID junctions were of the standard $Nb/Al/AlO_x/Nb$ type, and were shunted by resistors of either Au or Pd/Au alloy, of a thickness that yielded a D.C. sheet resistance of 1 Ω/square. In the stripline devices, the photoinductive strips were nominally 1.8 μm wide x 2.5 μm long. In the slotline devices, they were nominally 1.5 μm wide, separated by 1.5 μm, and 3.0 μm long. It is important to note that all junctions were at least 3 μm x 3 μm in area, with critical current densities no higher than 500 A/cm^2, substantially larger, and of lower Jc, (and thus easier to fabricate), than high performance SIS mixer junctions. In all cases, the photoinductor/SQUID combination was located at the feed of a self-complementary, log-periodic antenna with bow angle= 52.5^o, tooth/slot angle = 37.5^o, and scale ratios of σ = 0.5, τ = 0.25, (using the notation of reference 4). The nominal radii of the smallest and largest teeth were 2.4 μm and 147 μm respectively, providing a nominal bandwidth of

0.46 - 14 THz. 1 cm square chips were mounted circuit-side up against single-crystal Si hemispheres on a temperature-controlled stage. In the tests described here, no magnetic shielding at all was used in or around the cryostat. All optical tests were performed using a 6 THz lowpass filter cooled to 4 K to reduce the thermal IR background incident on the sample stage to a manageable level, typically 1-2 mW. Optical measurements were made using both a far-IR laser and a chopped blackbody (liquid nitrogen-cooled eccosorb) as source. The data taken with the far-IR laser are more accurate, since high enough power levels were available in that case to saturate the detector response. Far-IR laser power was monitored by directing most of the power into a pyroelectric detector, while a small fraction was directed by a (Si or mylar) beamsplitter into the cryostat.

III. Results

Considerable information can be obtained on device performance from variable temperature measurements with no far-IR radiation applied. For each device, the voltage-flux transfer characteristic was measured first, as a function of the stage temperature. That is, a bias current I_{SQUID}, typically 20 - 60 μA, was passed through the SQUID and the SQUID voltage recorded as the flux bias current I_ϕ was swept. The periodicity of the lobe pattern yields the loop inductance, via $L(T) = \Phi_0 / \Delta I_\phi$(1 period), while the maximum slope of the V-Φ characteristic is a direct measurement of the SQUID's flux responsivity, $dV/d\Phi$. The critical current of the loop, I_c, is simply the maximum I_ϕ to which the lobe pattern extends. In fig. 2, these three quantities, L(T), I_c(loop), and $dV/d\Phi$ are plotted versus temperature for our most recent slotline device. As we have found for nearly all devices tested, the fit of L(T) to the prediction of the 2-fluid model, namely $L(T) = L_0 / (1 - t^4)$, where $t = T/T_c$, the reduced temperature, is extremely good. The critical current of an isolated superconducting wire is predicted by Ginzburg-Landau theory to vary with temperature according to $I_c(T) = I_c(0) (1 - t)^{3/2}$. The critical current density implied by the $I_c(T=0)$ derived from the fit, a 15 nm thickness and 1.5 μm width, is 6×10^7 A/cm^2, which compares favorably with the depairing limit for Nb of 1.0×10^8 A/cm^2. The data on this particular device only fits the Ginzburg-Landau temperature dependence at a fairly qualitative level; other devices we have tested, however, including one from the same wafer as that shown, generally display temperature dependences of $I_c(T)$ much closer to the theoretical one. Variations in I_c from device to device are typically much larger than variations in inductance. This is not surprising, since I_c is a quantity determined by the weakest point in the loop, and therefore more susceptible to process-dependent non-uniformities in the photoinductors, while the inductance

represents an average over the entire loop perimeter. Such non-uniformities in the photoinductors are probably also the explanation for the discrepency we commonly find between the values of T_c derived from fits to L(T) as opposed to $I_c(T)$. The $I_c(T)$ fit is probably yielding the T_c of the weakest part of the photoinductor, not an average value.. The insensitivity of L(T) to device-to-device variations is remarkable. We even find very similar absolute values of inductance, namely 20 pH < L(T=0) < 30 pH, for both stripline and slotline devices, even though the loop areas vary by approximately an order of magnitude. This is at least partially a manifestation of the dominance of kinetic inductance over magnetic inductance in such thin films, with thickness t=15 nm << λ, where λ is the superconducting penetration depth.

The steepness of the V-Φ curve on the edges of the lobes, i.e. $dV/d\Phi(max)$ is of great importance to device performance, since the device responsivity is directly proportional to it. However, there is no simple analytic theory that can rigorously predict it's value; detailed simulations of the device dynamics are required. Furthermore, it is not unusual to observe irregularities of various kinds in SQUID V-Φ curves[5] which can drastically affect $dV/d\Phi(max)$, but which leave the overall periodicity of the lobe pattern and its maximum extent unchanged, and therefore would not affect our estimates of $I_c(T)$ and L(T). Irregularities which we commonly observe in the slotline devices include hysteresis, i.e. a shift in the position of a part of the lobe pattern depending on whether I_ϕ is swept upward or downward, truncated lobes, and a maintanence of exact periodicity in lobe position over only limited ranges of I_ϕ. Fig. 3a shows an example of a V-Φ curve with some of these irregularities visible. In many cases, these effects seem to be associated with trapped or stray flux present in the device. They seem to be much more common in the slotline devices than in the stripline devices, as would be expected on the basis of the slotline devices' larger loop area.

It is of great interest to measure optical responsivity as a function of temperature. By comparing such measurements with the predictions of a purely thermal response, with the free parameters determined from the variable-temperature, dark measurements described above, it is possible to separate the thermal and direct pair-breaking response mechanisms. In order to perform optical measurements over any reasonable temperature range however, some attention must be paid to the two D.C. bias currents I(SQUID) and I_ϕ. The responsivity is extremely sensitive to I_ϕ but only weakly sensitive to I(SQUID) The responsivity depends on I(SQUID) only through the latter's effect on $dV/d\Phi(max)$. At T = 4.1 K we measured $dV/d\Phi(max)$ as a function of I_{SQUID} and found only 5 %

variation over a 30 % range in current. The relative insensitivity of responsivity to I(SQUID) is not surprising, since the scale if I_{SQUID} is set by the the junction critical currents, which vary slowly with temperature because the junctions have (by design) a considerably higher T_c than the photoinductors.

On the other hand, the responsivity depends very sensitively on I_ϕ. As shown in fig. 3, over each lobe of the V_ϕ pattern, the responsivity goes through through 2 maxima (of opposite polarity). The envelope of these maxima increases (ideally) linearly with I_ϕ. Typically these maxima are quite narrow. At 5.5 K, for example, the responsivity falls to 50 % of its peak value when I_ϕ is varied from its optimum value of 650 μA (the position of the last lobe in the V-Φ pattern) by only +-2 μA. Thus, to perform measurements with reasonable accuracy, the flux bias needs to be controlled to approximately 1 part in 1000. Of course, the apparent position of the maximum varies slowly with thermal drifts, amplifier offsets, drifts in incident power, etc.

We have used two methods to circumvent the flux-bias sensitivity problem, and obtain data on optical responsivity versus temperature. (In commercial magnetometers, this problem is solved with a "flux-locked loop") In one case, we simply swept the flux bias slowly, while the SQUID voltage was synchronously demodulated on a lock-in amplifier and recorded. This yielded, in the best cases, clean plots, like that shown in fig. 3c, of far-IR response versus I_ϕ. In such cases, a straight line could be drawn through the envelope of the the responsivity peaks, and the slope of that line - basically $(dV/d\Phi)\,(dL/dT) / G$, in the context of a purely thermal response - could be measured as a function of temperature. The problem with this technique is that when the V-Φ characteristic is highly irregular, as in fig. 3a, the responsivity may be high, but the envelope of the responsivity peaks is not a straight line whose slope can be meaningfully measured. Our other method was to adjust I_ϕ so as to remain on the same lobe of the V-Φ pattern at all temperatures, continuously tweaking I_ϕ so as to hold the D.C. SQUID voltage fixed. Again, the optical radiation was chopped and synchronously demodulated. The 404 GHz points shown in fig.4 were taken by this method. Using this method, one is of course not at the optimum bias point except at the highest temperature measured. (At lower temperatures, lobes at higher values of I_ϕ are accessible, which would yield greater responsivity.). Thus one is really measuring $(dV/d\Phi)\,(dL/dT) / G$. This response is expected, for a purely thermal response mechanism, to rise monotonically at higher temperatures (in theory diverging at Tc), rather than turning over due to the falloff in $I_c(T)$.

IV. Discussion

Within the context of a purely thermal response, the "thermometric" responsivity, i.e. the change in SQUID voltage resulting from an infinitesmal change in temperature, is

$$S_T = I_C \, (dV/d\Phi) \, (dL/dT) \qquad (1)$$

As was mentioned above, our measurements of $I_C(T)$ and $L(T)$ seem to agree with theoretical expectation, both in terms of temperature dependence and absolute value, fairly well. What we have only learned fairly recently is that, at least for the two slotline devices we have examined in detail, the simple empirical relation $dV/d\Phi(max) = R/L$, where R is the shunt resistance of a single junction, seems to describe our devices remarkably well. This relation[6] is not a rigorous theoretical prediction based on the true dynamics of the junctions (which even in the simplest, resistively-shunted Josephson model are quite complicated), but as fig 5 shows, it is sufficiently accurate to draw some conclusions regarding device optimization. Substitution into (1) yields

$$S_T = I_C \, R \, (1/L \, dL/dT) \, . \qquad (2)$$

This equation has some interesting implications for photoinductive device design. Firstly, it makes clear the fact that the absolute value of L does not affect (to first order at least) the responsivity. Furthermore, the temperature dependence of S_T is a simple analytic function of reduced temperature, namely $S_T = S_T(0) \, t^3 \, (1-t)^{1/2} / (1-t^4)$, which has a reasonably broad maximum at t = .78. At higher temperatures, the responsivity falls off because the maximum attainable flux bias I_ϕ ($< I_C(T)$) is reduced, while at temperatures t < .78, the response is reduced by the falloff in dL/dT. Direct pair-breaking response would be manifested by a low temperature response above that predicted from the dL/dT rolloff. The theoretical temperature dependence of (2), along with the data (taken without incident radiation) from a slotline device are shown in fig. 6. The discrepency between theory and experiment is a manifestation of the different T_C's derived from fits to $I_C(T)$ and $L(T)$ mentioned earlier, 7.05 K and 7.66 K respectively.. This (probable) effect of process non-uniformity does not appear to suppress the responsivity very much, however, probably because the discrepency in critical temperatures is not large compared to the width of the maximum in S_T. Thus, there is little room for improvement in responsivity through higher (1/L dL/dT) or, for that matter, through higher $I_C(T)$, since the latter is already near the depairing limit. Given the assumptions underlying (2), the main avenue for increasing responsivity is making SQUIDs from higher resistance junctions. The resistance can only be increased to the extent that the junctions remain non-hysteretic; however. The McCumber parameter, $\beta_C = (2e/h) \, I_C R^2 C$ (where I_C is here the critical current of the junctions, not the

photoinductor, and C the junction capacitance) must remain < 1. Since I_c must remain fixed to hold the modulation depth, determined by $\beta_L = \pi L I_c / \Phi_0$, constant, the higher resistance SQUID must be accomplished by fabricating it from smaller (lower capacitance) Josephson junctions with higher J_c's. With our current 4 x 4 μm junctions and J_c's of 300 - 500 A/cm^2, the measured thermometric responsivities of 1.0 - 1.5 mV/K, seem to be a reproducible limiting value.

Our optical response measurements are shown in fig. 4. Unfortunately, the range of reduced temperature accessed in this set of data was only $0.78 < t < 0.95$. (This was partly because background loading raised the sample stage temperature from 4.1 K to 5.5 K, and partly because this photoinductor had a critical temperature of only 7.05 K.) Over this temperature range, no deviation of the optical response from that expected from a purely bolometric response was observed. Referring to our original calculations[1], however, the deviation from thermal response due to direct pair-breaking is only expected at $t < .7$. Obviously, our next step is to extend these measurements to lower temperature.

The total responsivity is given by S_T / G, where G is the thermal conductance from the loop to the thermal bath. The order of magnitude of G may be estimated by measuring the voltage and current, V_d and I_d, of the point on the descending branch of the (hysteretic) I-V curve of the photoinductor where it drops back into the superconducting state and calculating $G_0 = V_d I_d / (T_c - T)$. However, as has been discussed in terms of transition-edge bolometers[7], the G_0 calculated in this way is only a lumped-conductance approximation to what is actually a distributed thermal conductance. Temperature gradients within the photoinductive loop are clearly significant, as shown by curvature in the descending branch of the I-V curve before (I_d, V_d) is reached. Based on the values of G_0 computed from a variety of both stripline and slotline devices, as well as independent theoretical estimates, a value of $G = 5 \times 10^{-7}$ W/K is a reasonable estimate to use for translating our measured thermometric responsivities into total responsivities. The maximum value 1.1 +- .2 mV/K for both slotline and stripline geometries corresponds to 2200 V/W.

The key to obtaining low noise performance from photoinductive detectors is obtaining a good impedance transformation to the following amplifier. With our current 4 nV/Hz1/2 room-temperature amplifier and cooled transformer (effective turns ratio = 21) we have a noise level, referred to the SQUID output, of 190 pV/Hz$^{1/2}$. With 2 exceptions, we have not observed any excess noise from the detector above this level of amplifier noise. The

exceptions are: a) large (up to 20 dB) increases over the entire audio bandwidth within isolated ranges of I_ϕ , which seem to be correlated with irregularities in the V-Φ curve, and b) excess noise at low frequencies (< 100 Hz) when I_ϕ is set to one of the high-order lobes (for maximum responsivity), and which is most likely associated with flux-current bias drifts, that would be removed with an active bias stabilization circuit.

Combining the noise and responsivity measurements implies a noise-equivalent power, (NEP) in bolometric mode, of approximately 8×10^{-14} W / $Hz^{1/2}$, at a temperature of 6.5 K. This NEP is approximately a factor of 2.5 greater than the phonon-noise limit, $NEP_{phonon} = (4kT^2G)^{1/2}$, at this temperature. However, quantitative comparison with the phonon-noise limit has the built-in uncertainty of not being able to accurately measure (better than, say, at the 50 % level) the thermal conductance, and the conceptual difficulty of trying to describe a distributed thermal conductance with an equivalent lumped conductance.

At the higher temperatures in fig. 4, saturation of the detector with the laser is apparent. Detector saturation is interesting because, for any total-power type of mixer, it sets the scale of optimum local oscillator (L.O.) power in a heterodyne application. When saturation of the photoinductive detector is extreme (at the highest temperature displayed in the figure, for example) it is obvious in the waveform of the chopped laser signal as extra humps at corners of square wave. This arises from the lobe in the V-Φ curve at which the bias is set being shifted over far enough that the bias point rises along the lobe all the way to the maximum, goes over the top, and settles (with full laser illumination) part way down the other side. Well before that point, however, the response falls below that expected from the theoretical small-signal response using the parameters obtained from the dark measurements. Defining saturation as the point where the measured response is 3 dB below that expected on the basis of the small-signal responsivity, we find that the measured r.m.s. voltage at the SQUID output at saturation is approximately 2.7μV, in the data plotted in fig. 5. Multiplying by 2 to convert from r.m.s. to peak-to-peak signal (for a square wave), and dividing by the small-signal responsivity of 2200 V/W, we obtan a saturation power of 2.4 nW. This agrees with our original estimates[1] of optimum L.O. power in heterodyne mixing applications as a function of reduced temperature. The fact that optimum performance (i.e. maximum conversion gain) occurs for such low L.O. powers is a major advantage of the photoinductor over other types of mixer in the terahertz-frequency spectral region, where convenient high-power oscillators are not available. Whether the optimum performance of a photoinductive mixer is in fact

competitive with the optimum performance of other mixers will be determined by direct heterodyne measurements, to be performed in the near future.

V. Conclusion

We have fabricated photoinductive far-IR mixers of two different geometries, stripline and slotline, and measured some of their electrical and optical properties as a function of temperature, at audio frequencies. The inductance varies with temperature in good agreement with the 2-fluid model, and the photoinductor critical current varies with temperature in agreement with Ginzburg-Landau theory. The empirical relation for the maximum flux responsivity of the SQUID, $dV/d\Phi(max) = R/L$, appears to be surprisingly accurate over the range of temperatures and devices examined. Using this relation , we find the optimum operating temperature for use as a bolometer to be .78 T_c, and that further optimization of the device is primarily a matter of producing SQUID's from higher resistance junctions, by reducing junction area and increasing junction critical current density. The current devices, both stripline and slotline, with 4 x 4 μm, 300-500 A/cm^2 junctions, yield peak responsivities of 2200 V/W. No excess noise is seen in the devices (except low-frequency noise due to bias drift) down to our amplifier's noise level, yielding an NEP of 8 x 10^{-14} $W/Hz^{1/2}$. Measurements of detector saturation at 992 GHz using a far-IR laser indicate an optimum local oscillator power of approximately 2 nW in heterodyne applications.

VI. References

1. E.N. Grossman, D.G. McDonald, and J.E. Sauvageau, "Far-Infrared Kinetic Inductance Detectors", IEEE Trans. Mag. MAG-27, p. 2677 (1991)
2. J.R. Tucker and M.J. Feldman, "Quantum Detection at Millimeter Wavelengths", Rev. Mod. Phys., 57, p. 1055 (1985)
3. E.M. Gershonzon et al., "Millimeter and Submillimeter Range Mixer based on Electronic Heating of Superconducting Fims in the Resistive State",,Superconductivity, 3, p. 1582 (1990)
4. R.H. DuHamel and D.E. Isbell, "Broadband Logarithmically Periodic Antenna Structures", 1957 IRE National Convention Record, p. 119 (1957)
5. M. Cromar, private communication

6. M.B. Ketchen, "DC SQUIDs 1980: The State of the Art", IEEE Trans. Mag. MAG-17, p. 387, (1981)

7. E.N. Grossman, J.E. Sauvageau, and D.G. McDonald, "Electrical and Infrared Properties of Thin Niobium Microbolometers near T_c", Proc. of the 3rd Intl. Symposium on Space Terahertz Technology, Ann Arbor

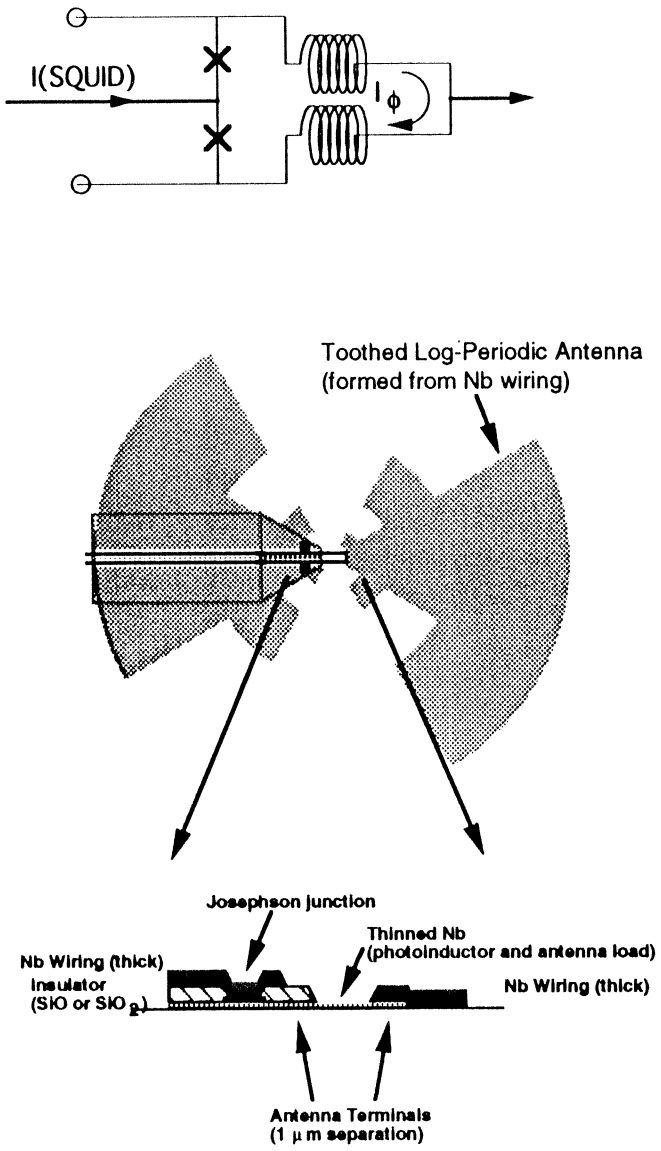

Figure 1a. Slotline geometry photoinductor

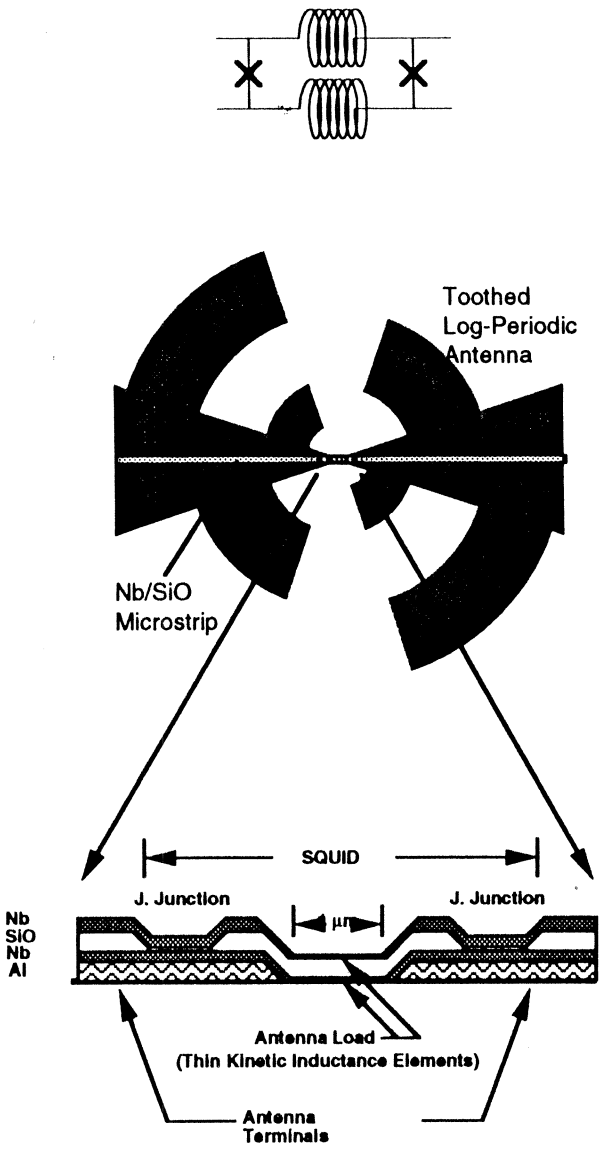

Figure 1b. Stripline geometry photoinductor. Note that SQUID bias is necessarily asymmetric in this case

Figure 2. Loop inductance, critical current, and SQUID flux responsivity, as a function of sample stage temperature, with 4K radiation shield blocking all incident far-IR.

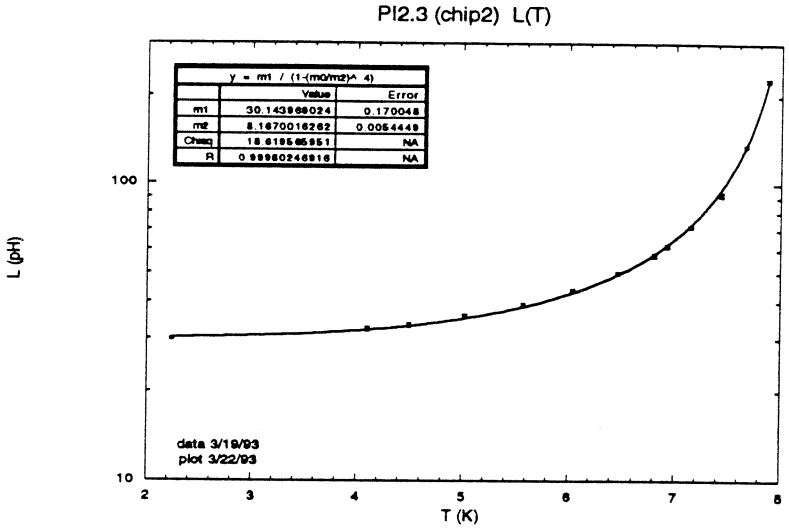

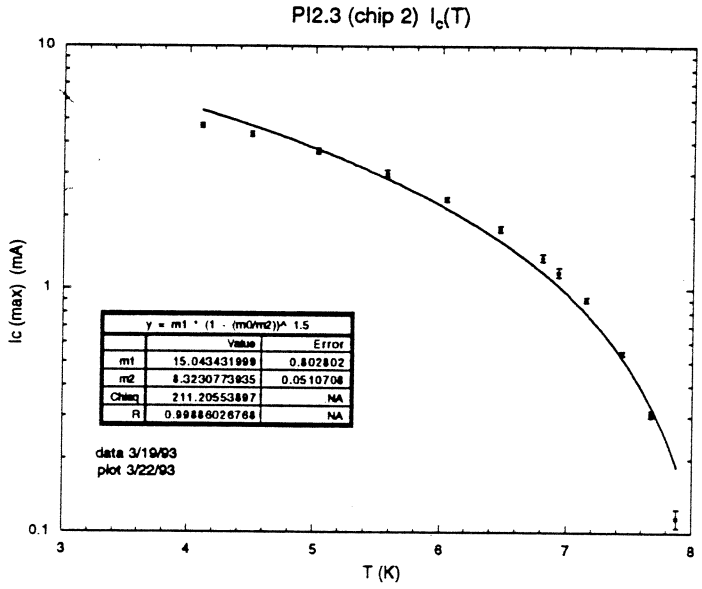

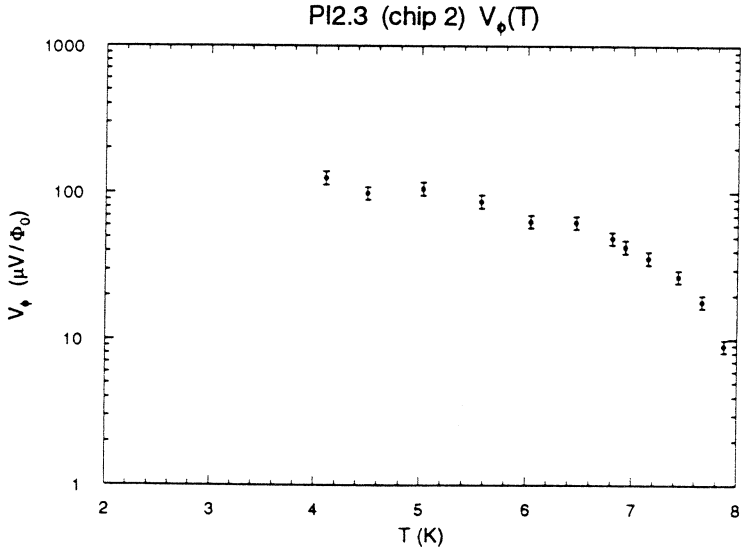

Figure 3a,b V-Φ characteristic (above) of slotline photoinductor (chip 1) at 5.48 K, and demodulated response (below) to 403 GHz laser radiation, measured simultaneously. Horizontal scale is 50 μA/division; vertical scale 5 μV/division (for. V-Φ characteristic), 1 μV r.m.s./divison (for 403 GHz response).

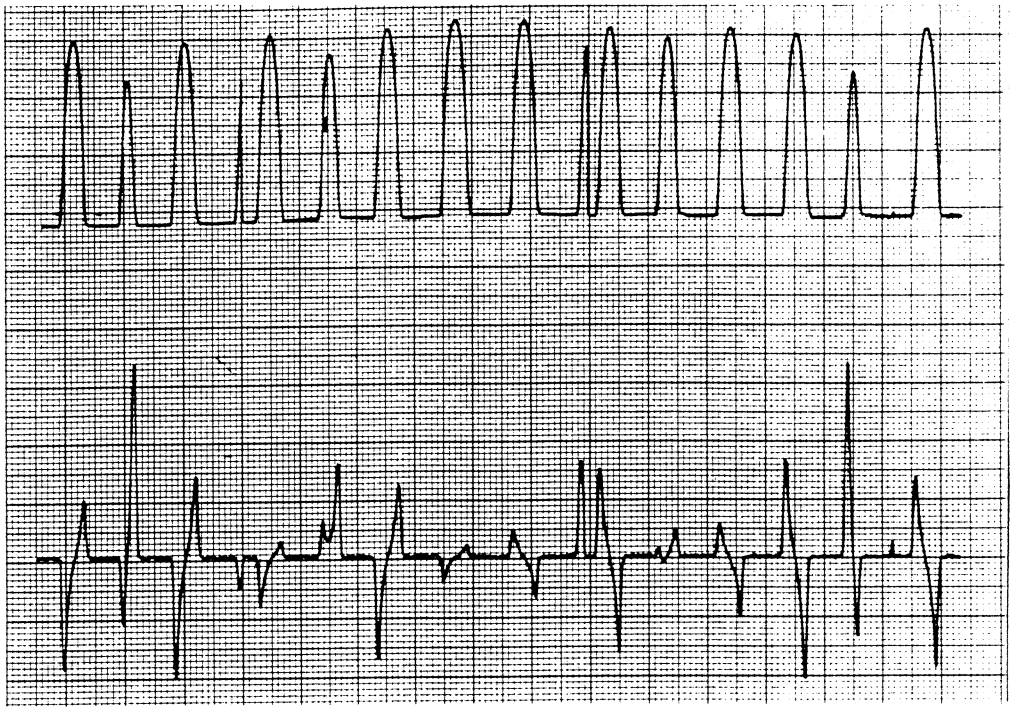

Figure 3c. Demodulated response of slotline photoinductor (chip 1) at 5.32 K, measured on a different run as data in Fig. 3a. Horizontal scale is 50 μA/divsion, vertical scale 0.2 μV r.m.s./divison.

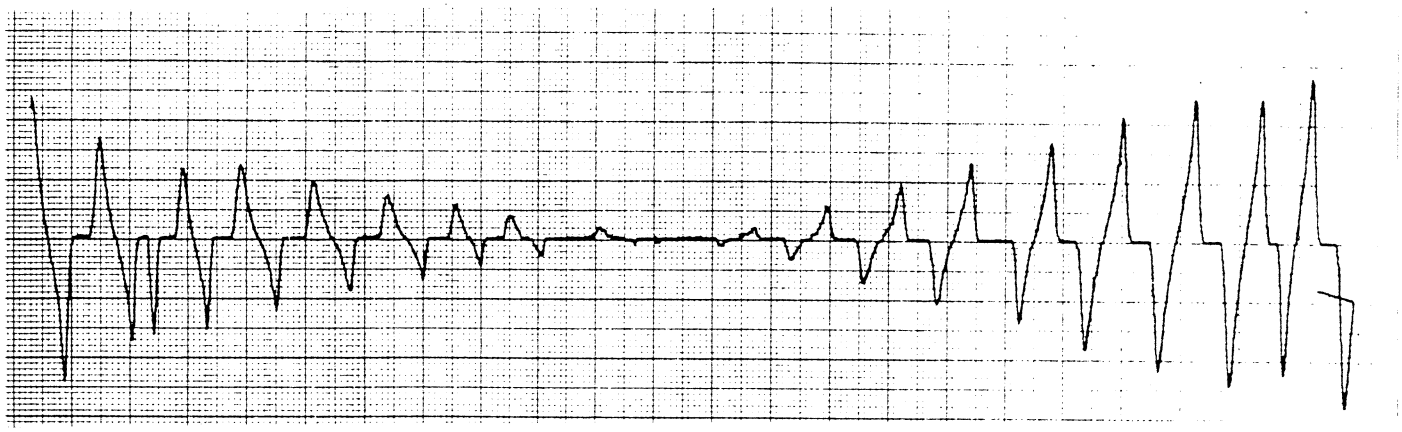

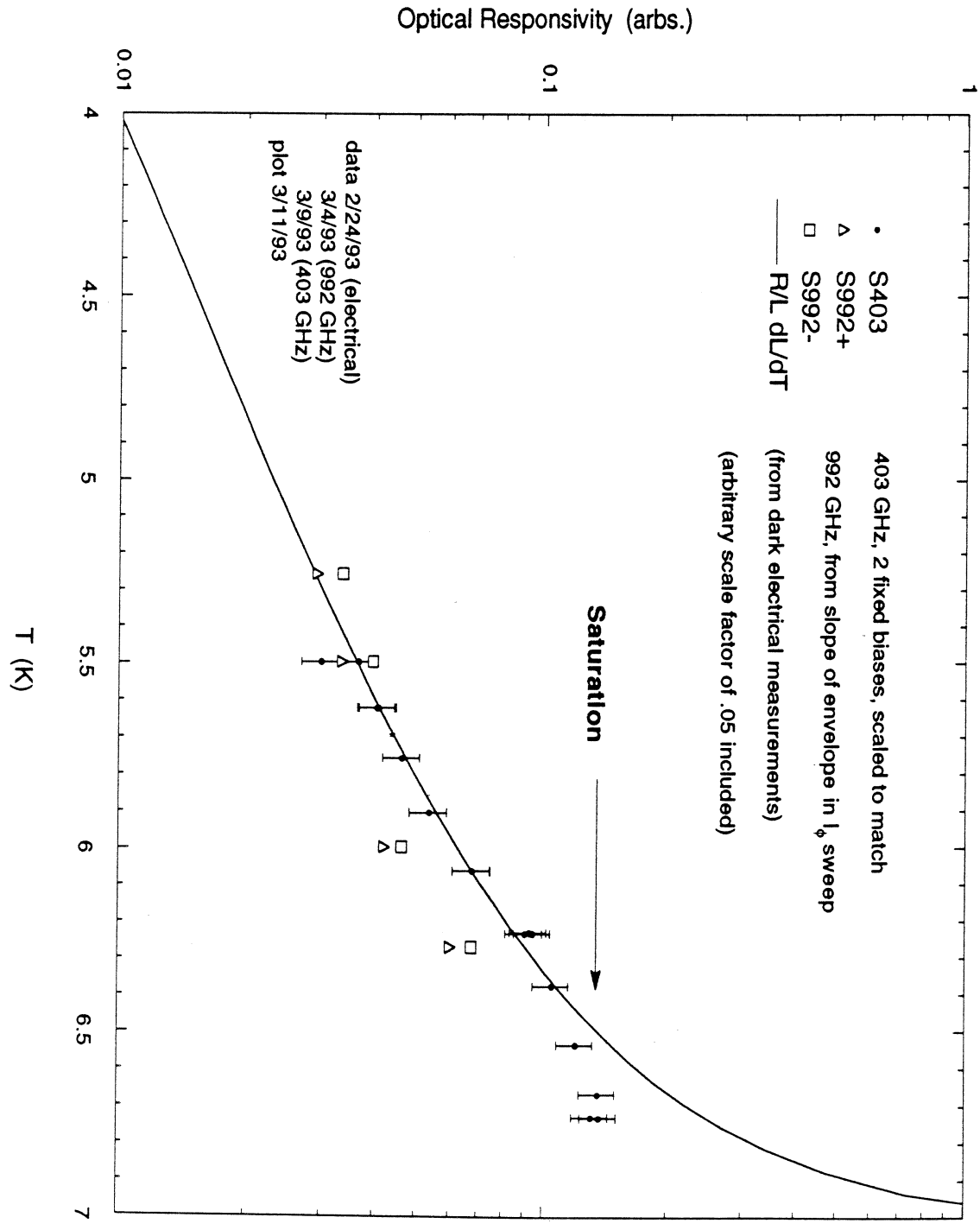

Figure 4. Response to chopped far-IR laser radiation for slotline photoinductor (chip 1). The 404 GHz data was taken at a fixed bias point on the V-Φ curve, tweaking I_ϕ so as to hold V_{SQ} fixed.

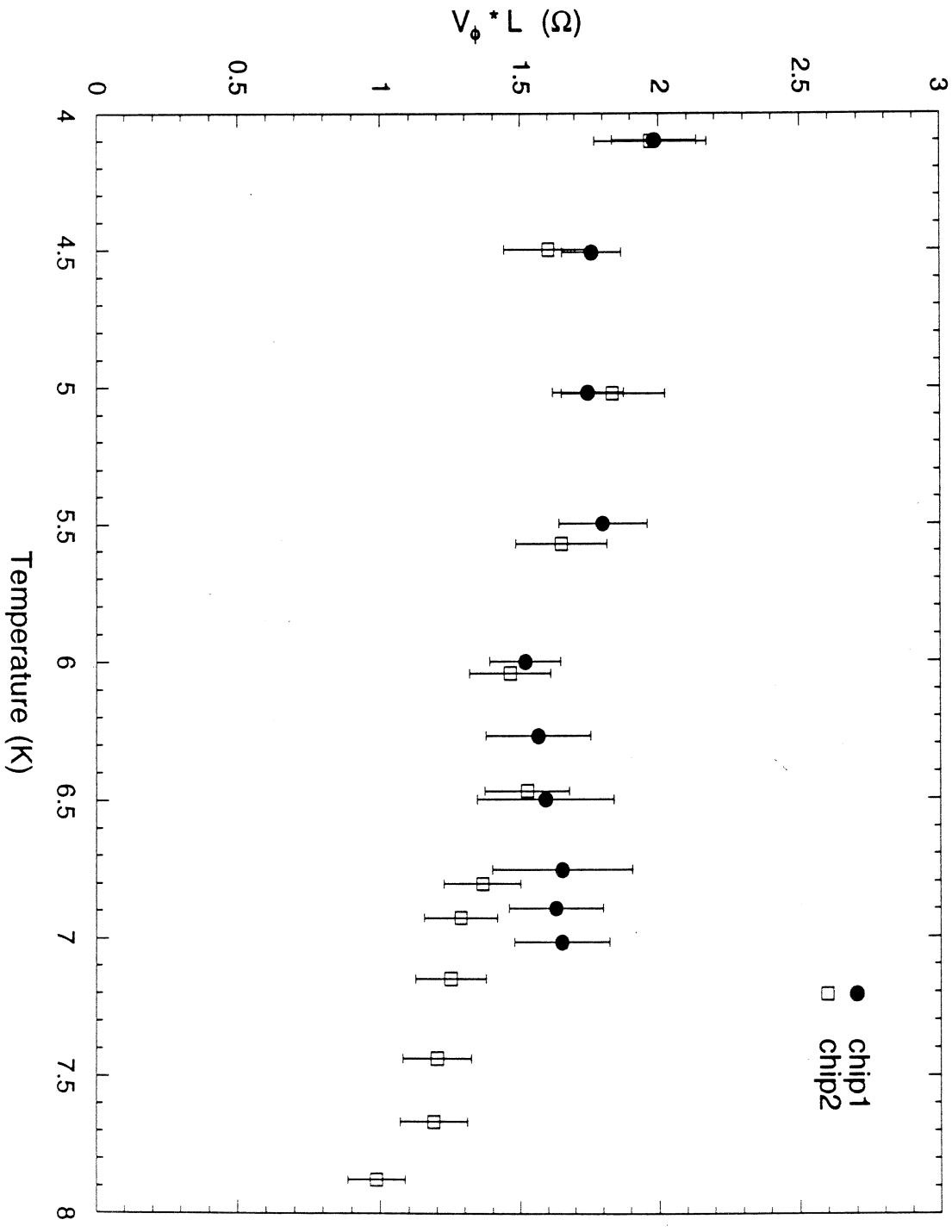

Figure 5. Test of the empirical relation $V_\phi = R/L$ for the maximum flux responsivity of a SQUID, applied to two slotline devices.

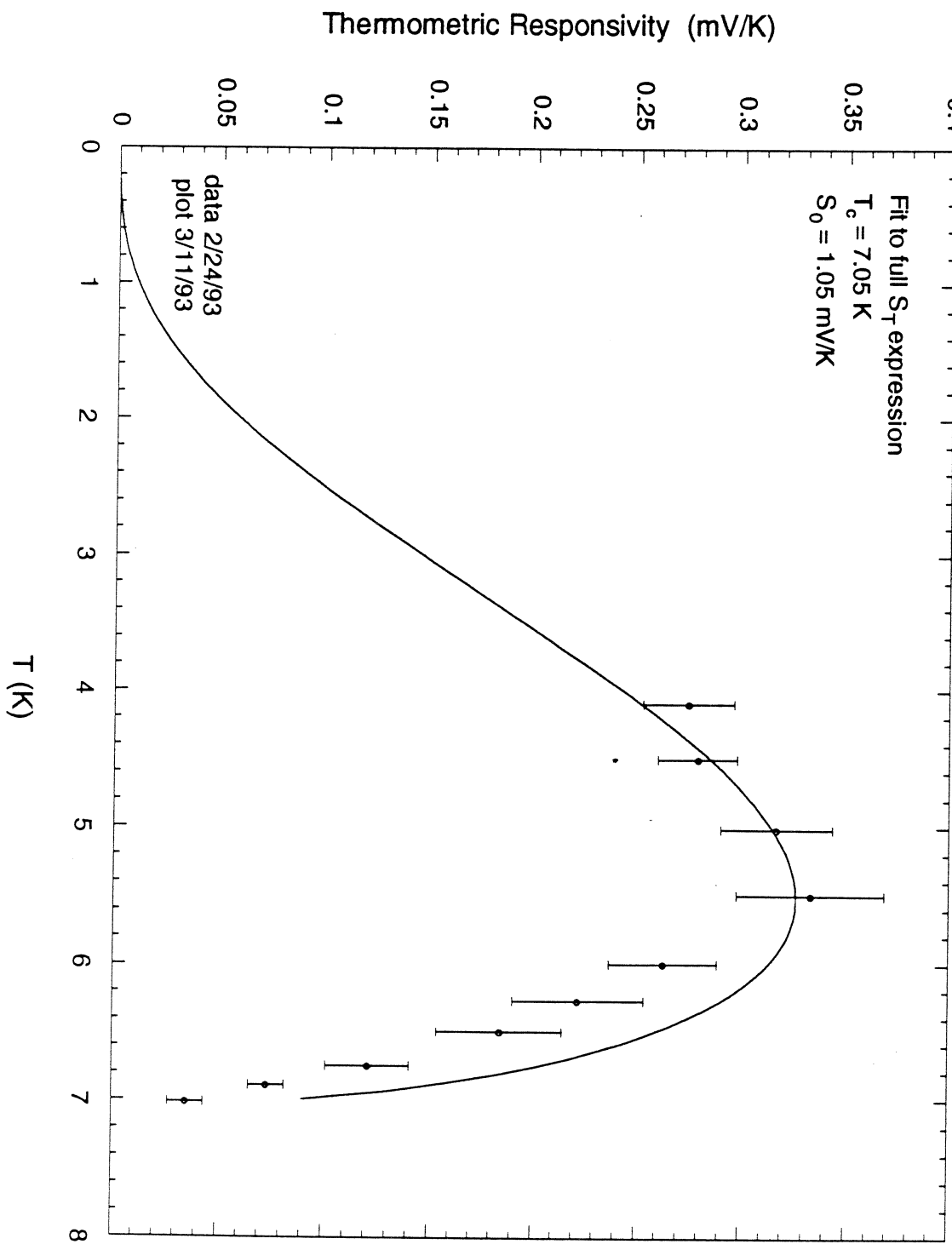

Figure 6. Comparison of the theoretical temperature dependence of S_T, (eqn. 2), assuming a single T_c and 0-temperature value, with experimental datapoints of $(2 \cdot I_c(T)$ (1/L dL/dT).

A Novel Submillimeter-Wave Detector Using Quantum Point Contacts

Qing Hu, R.A. Wyss, C.C. Eugster, J.A. del Alamo, S. Feng†, M.J. Rooks,††
and M.R. Melloch†††

Department of Electrical Engineering and Computer Science and Research Laboratory of Electronics, MIT, Cambridge, MA 02139
†Department of Physics, University of California at Los Angeles
††National Nanofabrication Facility, Cornell University
†††Department of Electrical Engineering, Purdue University

Abstract

We are developing a novel submillimeter-wave and THz detector using semiconductor quantum point contacts. The operation principle of this unique device is based on a new physical phenomenon, called *photon-assisted quantum transport*,[1] in which photons enhance the energy of ballistic transport electrons and produce a photon-induced drain/source current.

A quantum point contact is formed by depleting the 2DEG (two-dimensional electron gas) underneath a split-gate electrode on a MODFET (modulation-doped field-effect transistor) structure. For our device, the split-gate also serves as the two terminals of a planar antenna which concentrates the radiation field in the point contact region. The electrical field of the radiation near the split-gate is orthogonal to the drain/source conduction path. Intersubband transitions can therefore be excited that contribute to the drain/source conduction. It is estimated in our theory that the current responsivity of the quantum point contact detectors can be comparable to the quantum efficiency $e/\hbar\omega$ at and above 1 THz. The capacitance of this device should be small due to the planar geometry. Thus, the RC roll-off, which is inevitable in all tunnel devices such as SIS junctions and Schottky diodes, is negligible. Consequently, a very high-frequency quantum photon detector ($\geq$1 THz) could be developed.

We have fabricated several quantum point contacts with antenna/split-gate structures using a combination of optical and electron-beam lithography on a GaAs/AlGaAs MODFET structure with a 2D electron density 2.8×10^{11} cm^{-2}, and an electron mobility 200,000 cm^2/V•sec at 45 K. Under a 300 GHz coherent radiation at about 0.5 mW level, a profound photon-induced drain/source current is produced throughout the entire gate voltage region in which the quantum point contact exhibits the behavior of an 1D electron system. The amplitude of the photon-induced current is comparable to that corresponding to a quantized conductance step, i.e. $(2e^2/h)V_{DS}$, and it oscillates with the gate voltage. Our analysis suggests that the photon-induced drain/source current is mainly due to heating (or a bolometric effect). Future improvement of device parameters are discussed.

I. Introduction

Ballistic quantum transport through semiconductor quantum point contacts has been an active research area in recent years. In essence, such devices are made of very clean two-dimensional electron gas samples with a finely structured split gate on the wafer surface. Thus at low temperatures, electrons can travel from the source to drain without suffering elastic and inelastic scattering. This results in the well-known quantized drain/source conductance behavior, with a conductance quantum of $2e^2/h$.[2,3] Extensive work has been done after the discovery of this effect to study various features and extensions of this novel quantum transport device.[4] However, most of the experiments that have been performed on such devices are limited to DC transport measurements.

It is well known in the field of superconducting tunneling that photons can assist the tunneling process, provided that tunneling is elastic so that electrons do not suffer inelastic scattering.[5] The theoretical framework for photon-assisted tunneling has been well established and verified in experiments. The effect of photon-assisted tunneling has also been utilized in heterodyne receivers and radiation detectors using superconducting tunnel junctions. These devices have been demonstrated superior to other devices in terms of sensitivity and speed.[5] In a broad sense, elastic tunneling is a phase-coherent quantum transport in a classically forbidden region. Therefore, the results of photon-assisted tunneling can be applied to the study of photon-assisted quantum transport in semiconductor devices. If demonstrated successfully, novel devices based on the photon-assisted quantum transport can be developed for applications in the THz frequency range where very few devices are available.

II. Theory of Photon-assisted Quantum Transport

We consider a standard split-gate quantum point contact device, as shown in Fig. 1. The electrons are confined to two-dimensional movements at the interface of a GaAs/AlGaAs modulation-doped heterojunction. We assume that the 2D electron gas has a high mobility so that no impurity potential near the constriction region needs to be included in our calculation. Two capacitive split gates are patterned on top of the device, which form the constriction for the point contact device. The shape of the split gates can be described by the distance between them, D(x), where the x-direction is that of electron transport. Application of a negative gate voltage $-V_G$ creates subband structures in the direction perpendicular to transport (the y-direction in Fig. 1). We model the effect of this negative gate voltage on the electron gas underneath by an effective channel width of the electron gas, $d(x) \leq D(x)$, which decreases with an increasing negative gate voltage. We also assume that the variation of d(x) is slow enough so that WKB-type adiabatic semiclassical approximations for the electron wave function can be applied. Within this approximation, assume infinite potential sidewalls at $y = \pm d(x)/2$, the electron eigenstates $\psi_n(x,y)$ can be expressed as products of the longitudinal (in the x

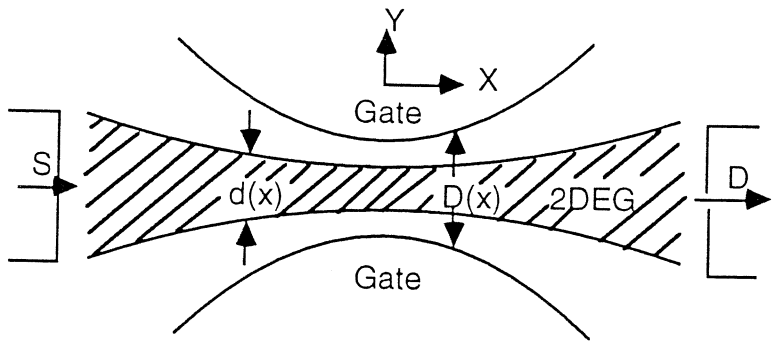

Figure 1 Geometry of the quantum point contact device under consideration. Under a negative gate voltage, electrons travel from the source (S) to the drain (D) through a channel with an x-dependent width d(x).

direction) eigenfunctions $\phi_n(x)$ and the transverse (in the y direction) standing-wave functions $\chi_n(y)$, where

$$\chi_n(y) = \sin[\frac{n\pi y}{d(x)}] , \qquad n \text{ even},$$

$$\chi_n(y) = \cos[\frac{n\pi y}{d(x)}] , \qquad n \text{ odd}, \tag{1}$$

with transverse eigenenergies given by

$$E_n(x) = \frac{n^2\pi^2\hbar^2}{2md(x)^2} . \tag{2}$$

This gives rise to the familiar subband structures so that the subband potential energies increase to their maximum values at the narrowest point of the constriction, i.e. x = 0 in Fig. 1. By substituting $\psi_n(x,y)$ in the time-independent Schrödinger equation, we reduce the original two-dimension equation into one-dimensional equations,

$$[-\frac{\hbar^2}{2m}\frac{d^2}{dx^2} + E_n(x)]\phi_n(x) = E\phi_n(x) . \tag{3}$$

Eq. (3) implies that the electrons in the nth subband are subject to a potential $E_n(x)$. The first few $E_n(x)$'s are sketched in Fig. 2(a). Using WKB approximation, electrons with energies greater than the potential barrier $E_n(0)$ will have a unity transmission coefficient from the source to the drain, while electrons with energies less than $E_n(0)$ will have a zero transmission coefficient. As the electron Fermi energy increases, more subbands will be turned on. Since each subband contributes exactly $2e^2/h$ to the drain/source conductance,[6] the total conductance of the device will increase discontinuously as the Fermi energy (or equivalently, the gate voltage) increases. This results in the well-known step structures of the drain/source conductance G_{DS} vs. the gate voltage V_{GS} curves.

The novel idea of photon-assisted quantum transport is to use far-infrared photons to enhance the energies of the 2-D electron gas in the source, so that they will be energetic enough to pass through the subbands and contribute to conduction. A schematic illustrating the idea is shown in Fig. 2(a). In this picture, the electron waveguide is pinched off so that the Fermi level lies below the energy barrier $E_n(0)$ of the n = 1 subband. Radiation photons increase the energy of electrons, so they can travel over the barrier $E_1(0)$. This photon-assisted transport will result in a photon-induced drain/source current. This idea is similar to photon-assisted tunneling in superconducting tunnel junctions. In photon-assisted tunneling, quasiparticle electrons in the valence band on one side of a junction absorb photons to enhance their energy, and subsequently tunnel to the conduction band on the other side of the junction. Because of this similarity, we call the possible photoelectric effect of the conduction through a quantum point contact "photon-assisted quantum transport."

In the presence of radiation, the total Hamiltonian will have a time-dependent component. For simplicity, here we will only consider the case in which the radiation field is in the y direction (the transverse case). The results for the longitudinal case (**E** field in the x direction) is similar to the transverse case, but the mathematics is more complicated.[7] For the transverse case, the time-dependent Hamiltonian is

$$H' = -eE_{ac}y\cos(\omega t) . \tag{4}$$

From selection rules, H' will couple subbands with opposite parities. Thus, intersubband transitions will occur. In general, the solutions of the time-dependent Schrödinger equation should include all the subband wave functions, that is,

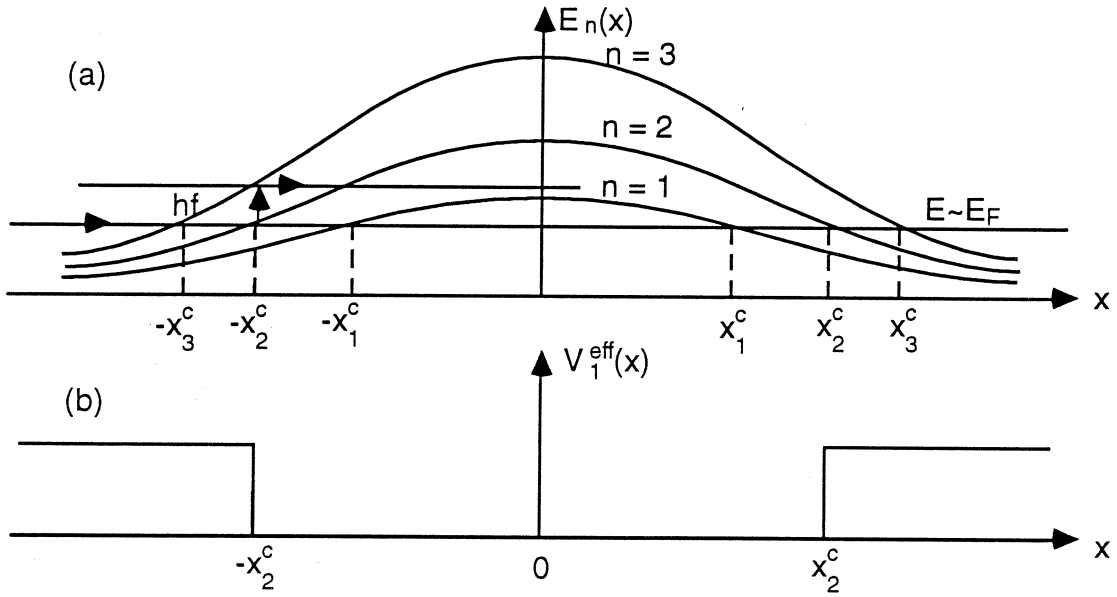

Figure 2 (a) Effective one-dimensional potential profile for the transport electrons moving from the source to drain in a quantum point contact. The barrier potential arises from the subband energies $E_n(x)$, which is x dependent (cf. Eq. (2)). Electrons from a particular subband n can propagate adiabatically through the point contact if the electron energy $E \sim E_F$ is greater than the maximum barrier height $E_n(0)$. Under radiation, electrons with energies even less than $E_n(0)$ can propagate over the barriers by absorbing an integer number of photons, as illustrated in the figure. (b) Effective AC potential V_1^{eff} for the electrons in the first subband.

$$\psi(x,y,t) = \sum_n C_n(x,t)\phi_n(x)\chi_n(y) , \tag{5}$$

and

$$[-\frac{\hbar^2}{2m}(\frac{\partial^2}{\partial x^2}+\frac{\partial^2}{\partial y^2}) - eE_{ac}(x)y\cos\omega t]\,\psi(x,y,t) = i\hbar\frac{\partial\psi(x,y,t)}{\partial t} . \tag{6}$$

We are most interested in electrons in the first subband where the dc potential barrier is the lowest. Multiplying Eq. (6) by $2\chi_1(y)/d$ and then integrating over y from -d/2 to d/2 leads to:

$$[-\frac{\hbar^2}{2m}\frac{\partial^2}{\partial x^2} + E_1(x)]\phi_1(x,t)C_1(x,t) - eE_{ac}(x)\cos\omega t \sum_{n \geq 2} D_{1n}C_n(x,t)\phi_n(x) = i\hbar\phi_1(x)\frac{\partial C_1(x,t)}{\partial t} , \tag{7}$$

where

$$D_{1n} = \frac{2}{d(x)}\int_{-d/2}^{d/2} y\chi_1(y)\chi_n(y)dy .$$

Eq. (7) is the equation of motion for the component of the electron wavefunction in the first subband, which is coupled via "dipole" moment D_{1n} to those of higher subbands with an odd parity.

The subband that mixes with the first subband most is the second subband, with a "dipole" moment given by

$$D_{12}(x) = \frac{2}{d(x)}\int_{-d/2}^{d/2} y\cos(\pi y/d(x))\,\sin(2\pi y/d(x))dy = \frac{16d(x)}{9\pi^2} \approx 0.2d(x).$$

The next subband that mixes with the first subband is the fourth subband. As the dipole moment D_{1n} decays rapidly with n (for example, $|D_{14}| = \frac{2}{25}D_{12}$), we can then make a further simplification by concentrating on the D_{12} term only, and. Eq. (7) then reduces to the form

$$[-\frac{\hbar^2}{2m}\frac{\partial^2}{\partial x^2} + E_1(x) + V_1^{eff}(x,t)]\psi_1(x,t) = i\hbar\frac{\partial\psi_1(x,t)}{\partial t}, \qquad (8)$$

where we have rewritten $\psi_1(x,t) = \phi_1(x)C_1(x,t)$, and have introduced an effective time-dependent perturbation potential

$$V_1^{eff} = -eD_{12}(x)E_{ac}(x)\cos(\omega t)\frac{\phi_2(x)C_2(x,t)}{\phi_1(x)C_1(x,t)} \approx -0.2eV_{ac}\frac{d(x)\,\phi_2(x)}{D(x)\,\phi_1(x)}\cos\omega t, \qquad (9)$$

where $V_{ac} = E_{ac}(x)D(x)$. In Eq. (9), we have approximated the two C-functions to be the same, which is certainly valid in regions far away from the classical turning points x^c. Therefore, V_1^{eff} is mainly determined by the ratio of the wave functions of the two subbands $\phi_2(x)$ and $\phi_1(x)$.

Thus, with suitable approximations, we can map the photon-assisted transport problem in the transverse case into an effective one-dimensional Schrödinger equation with an AC and a DC potential. Since $\phi_1(x) \approx \phi_2(x)$ in regions far away from the classical turning point of the second subband x_2^c (x_2^c is shown in Fig. 2(a)), the amplitude of the AC potential V_1^{eff} is approximately constant in the region $|x| > x_2^c$, and V_1^{eff} decreases exponentially for $|x| < x_2^c$. Thus to a good approximation, we can treat V_1^{eff} as a piece-wise potential with $V_1^{eff} = 0.2eV_{ac}d(x_2^c)/D(x_2^c)$ for $|x| \geq x_2^c$, and $V_1^{eff} = 0$ for $|x| < x_2^c$, as shown in Fig. 2(b).

Using this piece-wise ac potential V_1^{eff}, in the region where $|x| < x_2^c$ the solution of the Schrödinger equation is the same as the one without radiation. While in the region $|x| \geq x_2^c$, since V_1^{eff} is spatially independent, the spatial part of the wave functions remains the same while the temporal part of the wave functions has an additional phase factor[8]

$$\exp[i(eV_1^{eff}/\hbar\omega)\sin\omega t] = \sum_{n=-\infty}^{\infty} J_n(\alpha)e^{-in\omega t}, \qquad (10)$$

where J_n is the nth order Bessel function, and $\alpha = eV_1^{eff}/\hbar\omega$ is a dimensionless parameter which is proportional to the strength of the radiation field.

Eq. (10) implies that the new wave function has components with energies $E+n\hbar\omega$. Physically this means that the photon field creates new eigenstates with energies $E+n\hbar\omega$. Positive n's correspond to states where electrons have absorbed n photons, while negative n's correspond to states where electrons have emitted n photons. The amplitude of these new eigenstates is $J_n(\alpha)$, and the corresponding electron density is $J_n^2(\alpha)$.

For a simple situation, consider a bias condition where the Fermi energy E_F is suppressed at $\leq\hbar\omega$ below the first subband $E_1(0)$ of the quantum point contact, as shown in Fig. 2(a). Then the occupancy of states at $E_1(0)$ is zero at T = 0, and so is the drain/source current in the absence of radiation. In the presence of the radiation, however, there will be occupied states at $E \geq E_1(0)$, with an occupancy of $J_1^2(\alpha)$ due to one-photon absorption, and $J_n^2(\alpha)$ due to n-photon absorption. Since a fully occupied subband contributes a drain/source conductance $(2e^2/h)$, these partially occupied states will contribute to a photon-induced current of $(2e^2/h)V_{DS}\sum_{n=1}^{\infty} J_n^2(\alpha) = [1 - J_0^2(\alpha)](e^2/h)V_{DS}$, which has a maximum value of $(e^2/h)V_{DS}$. Thus, the photon-induced current

from the first subband is maximally half of the current at the first conductance step. The total photon-induced current will be the sum of the contributions from all the subbands. In the small signal limit, $\alpha << 1$, only J_1 is significant and $J_1^2(\alpha) \approx \alpha^2$, then the photon-induced current will be proportional to the square of the **E** field, or the power of the radiation. This results in a square-law or video detection. When $\alpha >> 1$, higher order Bessel functions in Eq. (10) become more important, which implies that multiphoton (or nonlinear) processes become dominant.

The situation for E_F being at $> \hbar\omega$ below $E_1(0)$ is similar to the case discussed above, except a multiphoton absorption is now required for the photon-assisted transport. Therefore, it is less efficient. The photon-induced current for a gate voltage just above the pinch off should be negative, due to a depletion of the occupied subband. In general, at frequencies much higher than the thermal broadening 3.5 k_BT, a coherent far-infrared radiation will produce ministep structures in G_{DS} vs. V_{GS} curves, as shown in Fig. 3. The width of the ministep is proportional to the frequency, and the height of the ministeps is a function of the radiation power in the form of

$$(2e^2/h)V_{DS}\sum_{n}^{\infty} J_n^2(\alpha). \qquad (11)$$

The lower limit of the summation is determined by the difference between $E_n(0)$ and E_F relative to the photon energy $\hbar\omega$.

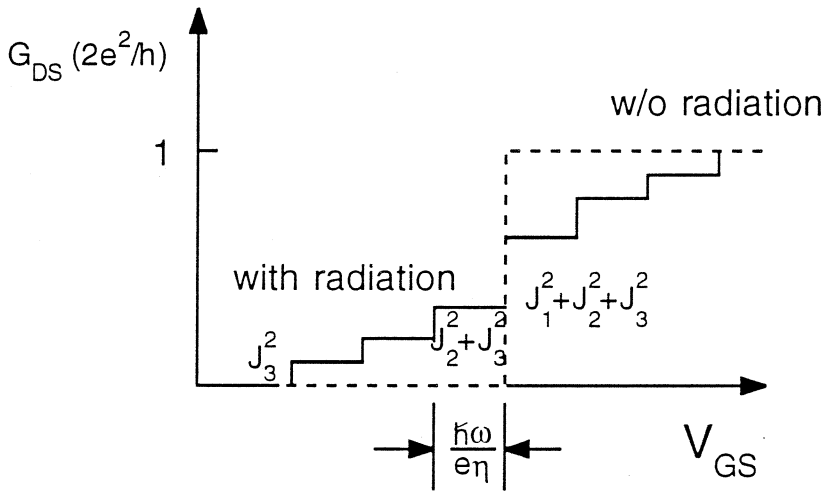

Fig. 3 Predicted G_{DS} vs. V_{GS} curves of a quantum point contact under a coherent far-infrared radiation. The range of the gate voltage is around the onset of the first conductance step. η is a dimensionless factor which is determined by the geometry of the quantum point contact which relates the gate voltage to the energy level of the subbands.

III. Preliminary experimental results

Two important technical issues need to be addressed in order to observe the effect of photon-assisted quantum transport. The first one is the required frequency range of the far-infrared radiation, and the second is how to couple this long-wavelength radiation to a quantum point contact with submicron dimensions.

At a finite temperature T, the thermally excited electrons can also contribute to a drain/source current below the pinch-off threshold. In order to observe a profound photon-induced drain/source current, the photon energy must be much greater than the thermal broadening of the Fermi surface 3.5 k_BT,[9] where k_B is the Boltzmann constant. At 1.5 K, which is the temperature of a typical helium cryostat with far-infrared access ports, 3.5 $k_BT/h \approx 100$ GHz. Thus, a submillimeter-wave radiation source at ≥ 300 GHz should provide sufficiently energetic photons to

assist the drain/source transport. A CO_2 laser-pumped far-infrared laser should provide the required radiation. Solid-state sources, such as Gunn oscillator-pumped Schottky-diode multipliers, are also adequate sources at frequencies below 500 GHz.

In order to couple far-infrared radiation (whose wavelength is typically on the order of 1 millimeter) to the quantum point contact of submicron size, a planar antenna[10] is required to concentrate the radiation field into the area where the drain/source conduction takes place. Otherwise, most of the radiation will bypass the quantum point contact. In addition, to excite the intersubband transitions, the **E** field of the radiation should be polarized in the direction transverse to the drain/source conduction path. This can be achieved by placing the antenna in such a way that its terminals also serve as the split-gate electrodes, as shown in Fig. 4(a). The radiation electric field at the antenna terminals is perpendicular to the antenna terminals, as shown in Fig. 4(b), which is roughly perpendicular to the drain/source conduction path.

It is advantageous to use broadband antennas so that radiation in a broad frequency range can be coupled to the quantum point contact in order to perform spectroscopy. One family of broadband antennas is the self-complementary antenna, in which the pattern of the metal part is the same as the dielectric part.[10] According to Booker's theorem,[10] the impedance of a self-complementary antenna is independent of frequency. The simplest self-complementary antenna is a 90^o bow-tie antenna, as shown in Fig. 4. Its wedge-shaped electrodes can also help to make the electron transport through the quantum point contact adiabatic.

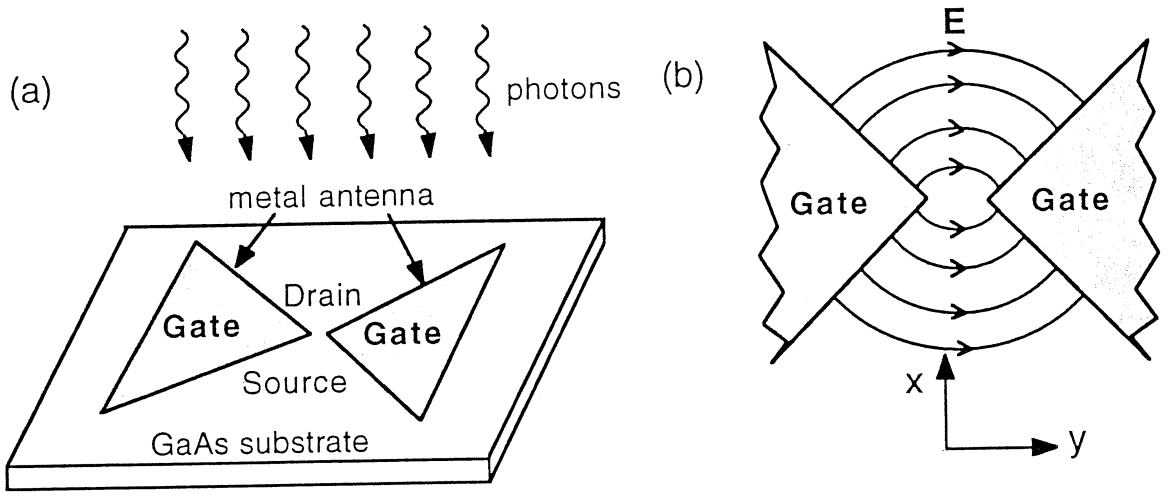

Fig.4 (a) An antenna-coupled quantum point contact. The planar antenna concentrates the radiation field into the small gap region between the two antenna terminals. (b) Central region in (a), the curved lines are the electric field of the radiation near the antenna/gate terminals.

We have successfully fabricated several quantum point contacts which are coupled with planar antennas. The fabrication was made using a combination of optical and electron-beam lithography on a GaAs/AlGaAs MODFET structure with a two-dimensional electron density $N = 2.8\times10^{11}$ cm^{-2}, and an electron mobility μ = 200,000 $cm^2/V\cdot sec$ at 45 K. The electron-beam lithography was performed at the National Nanofabrication Facility at Cornell University.[11] SEM pictures of one of the devices with a log-periodic antenna (it is also self-complementary but it has a better antenna pattern than that of bow-tie antennas) is shown in Fig. 5. The gate electrodes are shaped like 45^o wedges, and the opening of the split-gate is 0.15 μm.

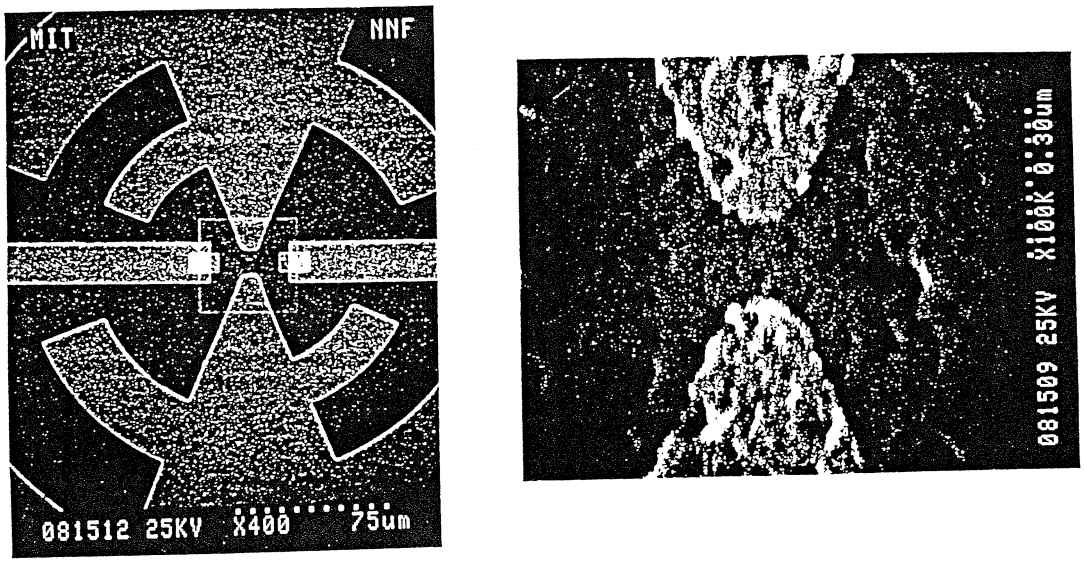

Fig. 5 SEM of a quantum point contact with a log-periodic antenna. The opening of the split-gate is 0.15 μm.

The measurement was performed in a cryostat in which the device is submerged in liquid helium. By pumping the helium bath, the device can be cooled down to 1.5 K. The cryostat has a quartz window with a low-pass black polyethylene filter which allows the pass of far-infrared radiation, and cuts off at frequencies above several THz. Extreme care was taken to minimize the ground-loop pick-up noise and to filter out undesired RF signals. Using a special home-made electronic bias circuit and amplifier, we were able to measure the voltage signals at levels below one microvolt and the current signals at levels below one nanoampere. For a quick measurement of the drain/source current as a function of voltage, we can apply a dc drain/source voltage of 150 μV and sweep the gate voltage at several ten Hz. The measured I_{DS}-V_{GS} curves is displayed on an oscilloscope, as shown in Fig. 6(a).

The I-V curve measurement can also be made using a digitally controlled voltage supply to sweep the gate voltage. The drain/source current is measured using a lock-in technique. In this way, the data can be collected by a computer and easily analyzed. Fig. 6(b) shows the drain/source conductance as a function of the gate voltage. Fifteen conductance steps are clearly seen which indicates the high quality of the device. The deviation from $n(e^2/h)$ at higher steps is due to the series resistance, which becomes more important at higher steps where the device is more conducting.

The radiation source is a tunable (75-110 GHz) Gunn oscillator-pumped Schottky frequency tripler with output frequencies at about 300 GHz. The maximum output power is 0.5 mW. The radiation beam of the frequency tripler is launched into free space through a conical horn, and then focused through the window of the cryostat by two TPX lenses. The radiation signal reaches the device from the air side of the planar antenna. At the maximum radiation power level, a profound photon-induced drain/source current is produced throughout the entire gate voltage region where the quantum point contact exhibits the behavior of a 1-D electron system. The amplitude of the photon-induced current is comparable to that corresponding to a quantized conductance step, i.e. $(2e^2/h)V_{DS}$, and it oscillates with the gate voltage, as shown in Fig. 7.

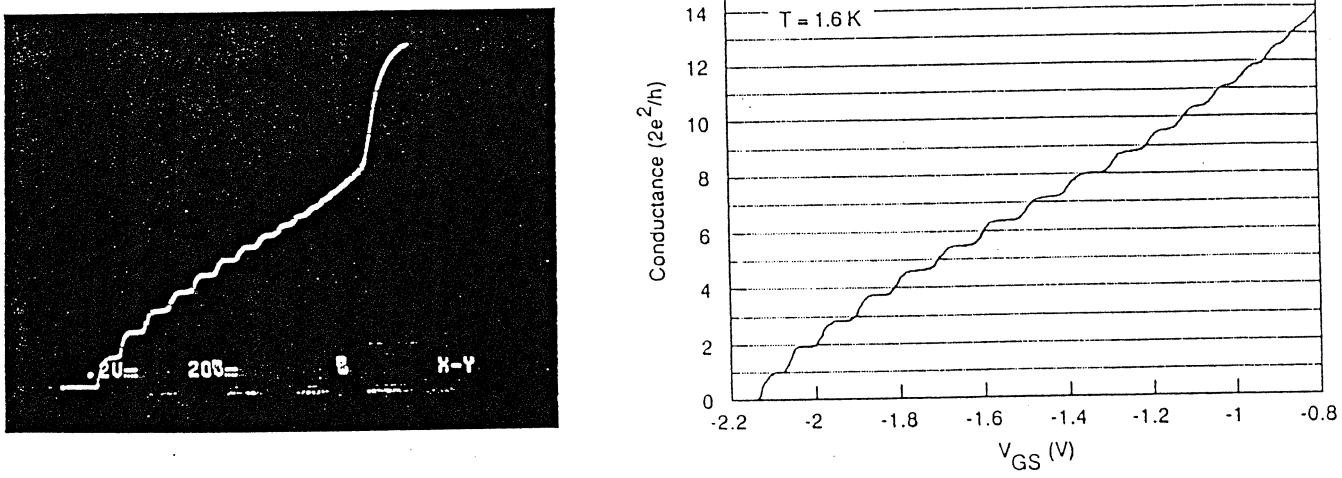

(a) (b)

Fig. 6 (a) Drain/source current as a function of the gate voltage. (b) Drain/source conductance as a function of the gate voltage.

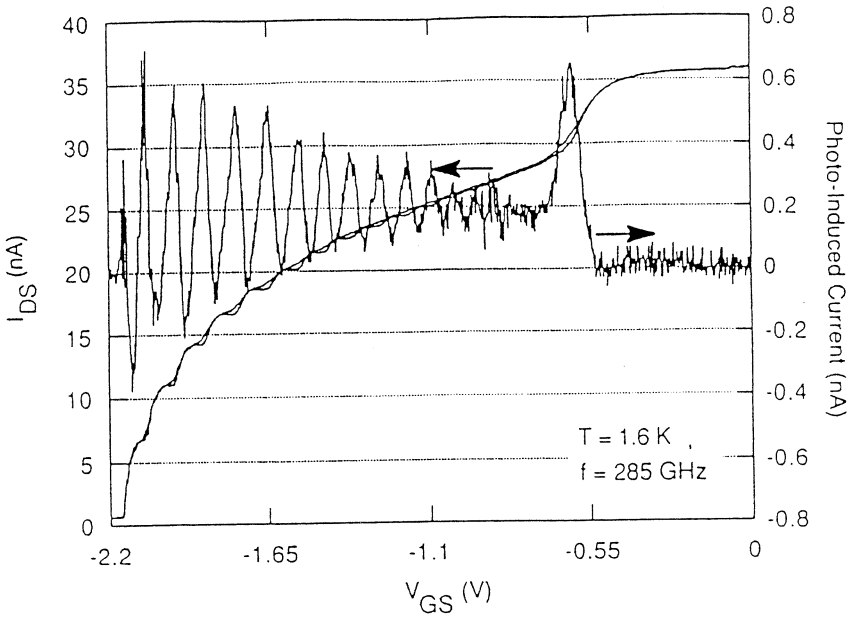

Fig. 7 Drain/source current vs. the gate voltage with and without the far-infrared radiation. The difference between the two currents is the photon-induced current, which is the oscillatory curve.

In order to compare our measurement with the theoretical predictions shown in Fig. 3, we plot the photon-induced drain/source current and the drain/source conductance measured without radiation as functions of gate voltage in a range where the conductance step structures are sharp, as shown in Fig. 8. The photon-induced current is mainly positive below the threshold of the next conductance step, and negative above the threshold of the step. This behavior qualitatively

resembles the prediction from our theory of photon-assisted quantum transport. However, no ministep structures such as those shown in Fig. 3 were seen in our measurement.

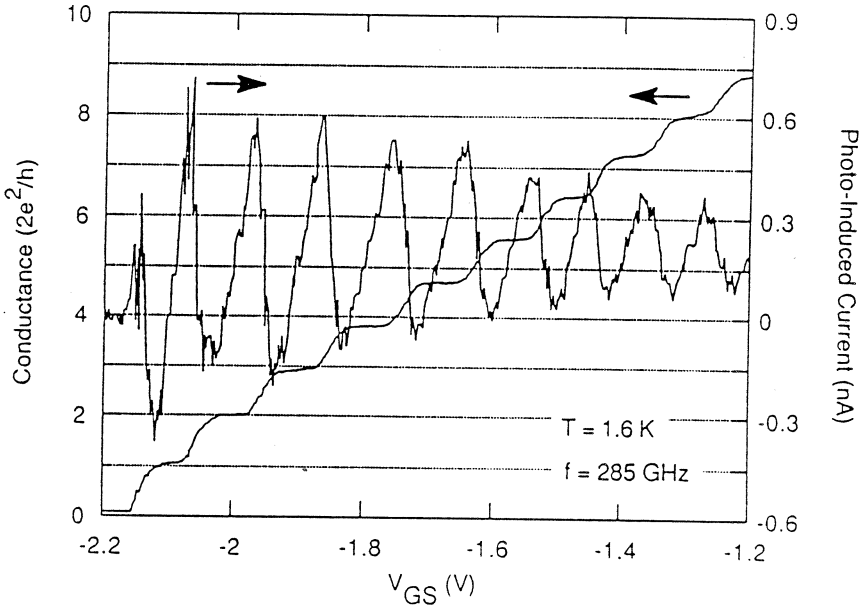

Fig. 8 Drain/source conductance and the photon-induced current as functions of the gate voltage. The photon-induced current is mainly positive below the threshold of the next conductance step and mainly negative above the threshold.

The mostly likely cause of the observed far-infrared photon-induced drain/source current is the heating of the 2DEG by the far-infrared radiation. The absorbed far-infrared radiation energy increases the temperature of the electron gas and the surrounding area, so the local temperature is higher than the temperature of the liquid helium bath. This higher local temperature broadens the Fermi surface and produces an additional drain/source current . To verify this hypothesis, we plot the difference between the drain/source current taken at 3.7 K and 1.6 K (without radiation) as a function of the gate voltage in Fig. 9. It appears quite similar to that shown in Fig. 7. Thus, this measurement supports our preliminary conclusion that the observed photon-induced drain/source current is mainly due to heating.

Our preliminary measurement and analysis then raise a difficult issue for experimentally observing the effect of photon-assisted quantum transport. Unlike photon-assisted tunneling in superconducting tunnel junctions, where the superconducting energy gap prevents energy absorption in the leads below the gap frequency, the excitation in the 2-D electron gas in a quantum point contact is, however, gapless. Thus, absorption can occur anywhere in the 2DEG, and the effect of the photon-assisted quantum transport will always be accompanied by a heating effect. In our devices, the effect of photon-assisted quantum transport is suppressed due to a device defect which was realized only recently: the central part (~10 μm) of the split-gate/antenna terminals is made of a 200 Å-thick gold film using e-beam lithography and lift-off techniques. This thickness is much thinner than the skin depth at 300 GHz (which is about 1000 Å), thus the 200 Å-thick antenna terminals are rather resistive. Therefore, as illustrated in Fig. 10, most of the radiation electric field drops within the antenna terminals instead of between them, where a strong radiation electric field is required to excite the intersubband transitions. Thus, most of the absorbed far-infrared radiation energy is consumed in increasing the temperature of the 2DEG, instead of in assisting the quantum transport processes.

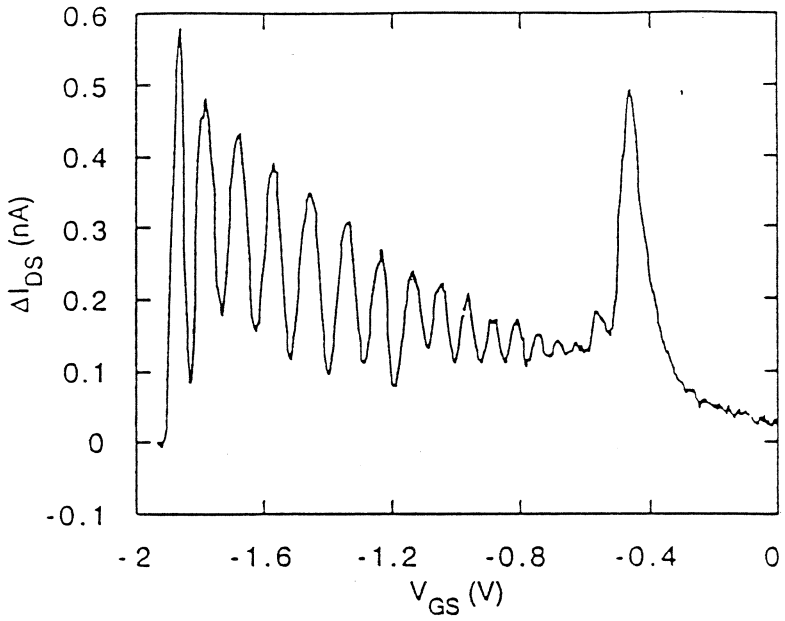

Figure 9 Thermally induced drain/source current (which is defined as the difference between the drain/source current measured at 3.7 K and 1.6 K) as a function of the gate voltage. It exhibits similar behavior as the photon-induced drain/source current, as shown in Fig. 7.

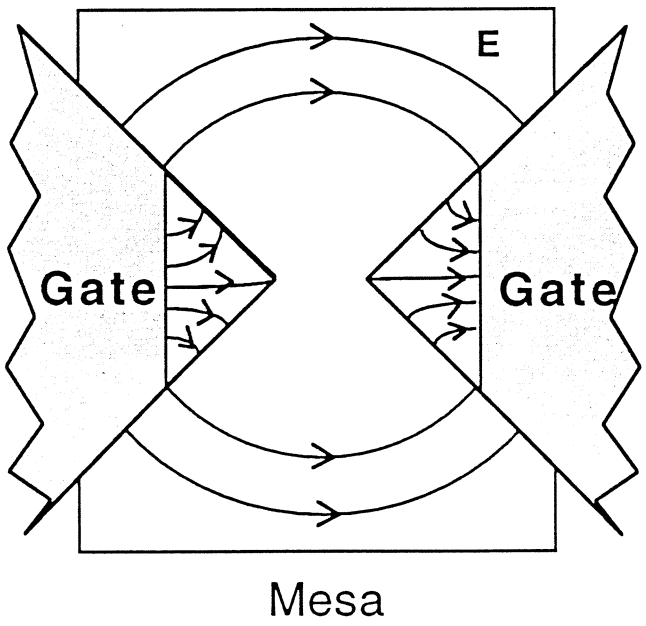

Fig. 10 Radiation electric field lines. Because of the high resistance of the antenna terminals due to a small thickness of the gold film, most of the electric field is within the antenna terminals instead of between the antenna terminals.

IV. Future improvements

In order to observe the predicted effect of photon-assisted quantum transport, we need to enhance the quantum process and minimize the thermal effect. Several steps should be taken to achieve this goal:

1. Study the response of the quantum point contact devices at frequencies much higher than 300 GHz. Since the width of the photon-induced ministeps is proportional to the radiation frequency, these ministep structures will be more profound at higher frequencies. For example, at 1 THz, the photon energy $\hbar\omega = 4$ meV, which is comparable to the intersubband spacing between the first few subbands. Thus, the width of the photon-induced ministeps will be about the same as that of the original quantized conductance steps, and they should be quite distinctive, compared to thermal broadening. In addition, the dissipation in the 2DEG is proportional to ω^{-2}, thus heating will be substantially reduced at higher frequencies.
2. Using samples with higher electron mobilities ($\mu \approx 10^6$ cm^2/V•sec). The dissipation in the 2DEG is inversely proportional to the square of the scattering time τ (which is proportional to the electron mobility μ). The heating effect will be reduced in samples with higher electron mobilities.
3. Using thicker (~2000 Å) antenna terminals. This is perhaps the most important step to take in order to observe the effect of photon-assisted quantum transport. According to the theoretical discussions in Section II, it is crucial to concentrate the radiation field near the classical turning points, which are only several hundred angstroms from the center of the point contacts. Antennas made of high-conductivity films with thicknesses greater than the skin depths are required to achieve this goal. Thus, thick (~2000 Å) PMMA photoresist layers will be required to lift off thick metal films. This will require some experimentation since the electron scattering in thick resist layers will alter fine features of the devices. An alternative approach is to use x-ray lithography to fabricate the devices. The scattering of x-ray photons in resist is negligible, thus a thick layer of resist can be used to lift off thick metal layers. Given the relatively relaxed tolerance for our devices (the distance between the split-gate electrodes can range from 0.15 to 0.3 μm), we believe that high-quality devices with desired properties can be fabricated using the existing technologies.

In summary, we have fabricated several antenna-coupled quantum point contact devices which showed good dc transport characteristics. We have observed photon-induced drain/source current when the device is irradiated with coherent radiation at 285 GHz. Our analysis suggests that the observed photon-induced current is mainly due to heating or a bolometric effect. Our analysis has also identified a device defect (the antenna/gate electrodes are too thin) which suppressed the photon-assisted quantum transport process and pointed out several improvements need to be made. Our theoretical calculation has shown that the current responsivity of an antenna-coupled quantum point contact can approach the quantum efficiency $e/\hbar\omega$ at and above one THz.

This work was supported by NSF grants 9109330-ECS and DMR-9022933 at MIT, and was performed in part at the National Nanofabrication Facility which is supported by the National Science Foundation under Grant ECS-8619049, Cornell University, and industrial affiliates.

References

1. Qing Hu, Appl. Phys. Lett. **62**, 837 (1993).
2. B.J. van Wees, H. van Houten, C.W.J. Beenakker, J.G. Williamson, L.P. Kouwenhoven, D. van der Marel, and C.T. Foxon, Phys. Rev. Lett. **60**, 848 (1988).

3. D.A. Wharam, T.J. Thornton, R. Newbury, M. Pepper, H. Ajmed, J.E.F. Frost, D.G. Hasko, D.C. Peacock, D.A. Ritchie, and G.A. C. Jones, J. Phys. C **21**, L209 (1988).
4. C. W. J. Beenakker and H. van Houten, in *Solid State Physics*, vol. 44, Edited by H. Ehrenreich and D. Turnbull, (Academic, New York, 1991), pp. 1-228, and references therein.
5. P.L. Richards and Qing Hu, IEEE Proceedings, **77**, 1233 (1989).
6. Y. Imry, in *Directions in Condensed Matter Physics*, edited by G. Grinstein and G. Mazenko (World Scientific, 1986), pp. 101-164.
7. Shechao Feng and Qing Hu, submitted to Phys. Rev. **B**, February 1993.
8. P.K. Tien and J.P. Gordon, Phys. Rev. **129**, 647 (1963).
9. P.F. Bagwell and T.P. Orlando, Phys. Rev. **B40**, 1456 (1989); P.F. Bagwell and T. P. Orlando, Phys. Rev. **B40**, 3735 (1989).
10. D. B. Rutledge, D. P. Neikirk, and D. P. Kasilingam, in *Infrared and Millimeter Waves*, Edited by K. J. Button (Academic, New York, 1983), pp. 1-90.
11. M. J. Rooks, C. C. Eugster, J. A. del Alamo, G. Snider, and E. Hu, J. Vac. Sci. Technol. **B9**, 2856 (1991).

Hot Electron Superconductive Mixers

E.M.Gershenzon, G.N.Gol'tsman

Moscow State Pedagogical University
1 Pirogovskaja Str., Moscow 119435 Russia

The creation of low noise heterodyne receivers for frequencies above 500 GHz is a prime necessity in radio astronomy. The lack of success in the development of sensitive submillimeter wave mixers is a serious problem, as several projects involving radioastronomical satellites are contemplated. For frequencies between 100 GHz to 500 GHz superconducting quasiparticle mixers (SIS-mixers) offer noise temperatures T_n below the 20-fold quantum limit T_{QL} [1]. However, for submillimeter waves at frequencies above 500 GHz SIS mixers have not yet been able to be compete with ordinary Schottky mixers. Heterodyne receivers for frequencies more than one THz have so far been realized only by using the Schottky diode mixers (see e.g. [2]) and InSb mixers. In this paper we discuss the nonlinear effect related to hot-electrons in superconductors, and their potential use in low noise submillimeter wave mixer. We also discuss the results achieved so far, as well as possible future developments.

Recently we have shown that in thin ($\sim 100\mathring{A}$) and narrow ($\sim 1\ \mu$m) superconducting strips nonlinearities are present due to hot-electron effect. Both ordinary superconductors and high-T_c superconductors have been suggested [3,4].

As radiation is absorbed, the superconductivity is being suppressed, and the quasiparticle concentration increases causing a change in V-I–characteristics as shown in Fig.1. When the current flowing through the superconducting strip exceeds its critical value, the strip's state becomes resistive. The nature of this resistive state is attributed to various physical mechanisms such as (i) phase slip centers which appear at $T \approx T_c$, (ii) flow of magnetic flux vortices at $T < T_c$ and (iii) heated normal conduction domains.

In Fig.2 energy relaxation flow within the device is illustrated. A necessary condition is that there is a strong electron-electron (Coulomb) interaction to rapidly transfer the absorbed energy to all electrons (typically the time-constant τ_{el-el} is of the order of $10^{-11} - 10^{-12}$s for $T_0 \approx T_c$). It is also required that the energy transfer from the electrons to the phonons is comparatively slow i.e. τ_{el-ph} is comparatively long (the bottleneck of the process). Hence it is required that $\tau_{el-el} \ll \tau_{el-ph}$. On the other hand, since we want the time of the detection process to be short enough to allow IF-frequencies of the order of GHz, it is also necessary that $\tau_{el-ph} < 10^{-10}$s.

The time constants can be affected by a proper choice of the dimensions of the superconducting strip. The excess electron energy must first escape to the phonons in the superconducting film (time constant τ_{el-ph} which for $T_0 \approx$

T_c is of the order of 3×10^{-10} s for Nb, 10^{-11} s for NbN, and 10^{-12} s for HTS), then τ_{ph-sub} from the phonons in the film to the substrate. It is then required that the nonequilibrium phonons escape from the film into the substrate before they could be scattered by the electrons ($\tau_{ph-sub} \ll \tau_{ph-el}$). The τ_{ph-sub} time constant is affected by the dimensions of the superconducting strip i.e. $\tau_{ph-sub} \propto d$, where d is the thickness of the superconducting film. In order to avoid reverse flux of nonequilibrium phonons from the substrate to the film, the width of the film should be smaller than 1 μm.

The results for IF frequency band measurements at 150 GHz are shown in Fig.3. Summarizing the data we can expect IF band widths for superconducting mixers made of Nb to approach 500 MHz, while NbN should yield 10 GHz and YBaCuO 100 GHz.

Experimental results of conversion losses for a 100 GHz Nb mixers have been presented in [5]. The measurements show total conversion losses of 7.5 to 11 dB. Considering the mismatch loss, the convrsion loss for the mixer process itself amounts to about 1 dB only. The calculations show that positive conversion efficiency is also possible. This is due to non-equilibrium phenomena in the film causing an effective negative resistance phenomenon (see Fig.1). The ambient temperature should of course be below the critical temperature of the film. The bias conditions will be affected by the operating temperature, but can also be affected by an external magnetic field. In Fig.4 an example is shown of calculated conversion loss vs bias current (Fig.3). So far, noise has not been experimentally established. The measurements only indicate that the noise temperature is quite low. In Fig.4 we also show the calculated noise temperature for Nb mixer, assuming that the noise is only attributed to Johnson noise and thermodynamic fluctuation type noise [5].

Since the number of static defects in ultrathin films is large, the momentum relaxation time is of the order of $\tau_m - 10^{-14} \div 10^{-15}$ s, and the film should be capable of absorbing power at any frequency, e.g. from microwave to infrared frequencies, where $\omega\tau_m = 1$. Furthermore, there should be no parasitic elements such as the junction capacitance for SIS junctions or an inductance related to electron inertia, which should greatly facilitate the design of submillimeter wave mixers.

By choosing the length of the strip (of the order a of several μm), its resistance can be adjusted to 20-300 Ω, which would make it suitable for coupling to waveguides or planar antennas. For such a strip the optimum local oscillator power is of the order 10^{-6}W for Nb, 10^{-4}W for NbN and 10^{-3}W for YBaCuO. If a large dynamic range is required, several long strips can be connected in shunt.

The hot electron mixer seems to be a promising alternative in achieving low noise temperatures in the submillimeter wave frequency range, in particular for frequencies above 500 GHz. However, a lot of work still remains to be done for the final proof of their efficiency in low noise receivers.

References

[1] Kerr A. & Pan S.K., 1990, Some recent developments in the design of SIS mixers. Int. J. of Infrared and Millimeter Waves, 11, pp.1169-1188.

[2] Zimmermann R & R & P, 1992, All solid state radiometers for environmental studies to 700 GHZ. Proceedings of the Third International Symposium on Space Terahertz Technology, pp.706-723.

[3] M.E.Gershenzon, M.E.Gershenzon, G.N.Gol'tsman, A.M.Lyul'kin, A.D.Semenov, A.V.Sergeev, Electron-phonon interaction in ultrathin Nb films. Sov.Phys.JETP **70**, 505 (1990).

[4] M.E.Gershenzon, G.N.Gol'tsman, A.D.Semenov, A.V.Sergeev, Mechanism of picosecond response of granular YBaCuO films to electromagnetic radiation. Sol.St.Commun. **76**, 493 (1990).

[5] M. E. Gershenzon, G.N.Gol'tsman, Yu. P. Gusev, A. I. Elant'ev, A. D. Semenov, Electromagnetic radiation mixer based on electron heating in resistive state of superconductive Nb and YBaCuO. IEEE Trans.Mag. **27**, 1317 (1991).

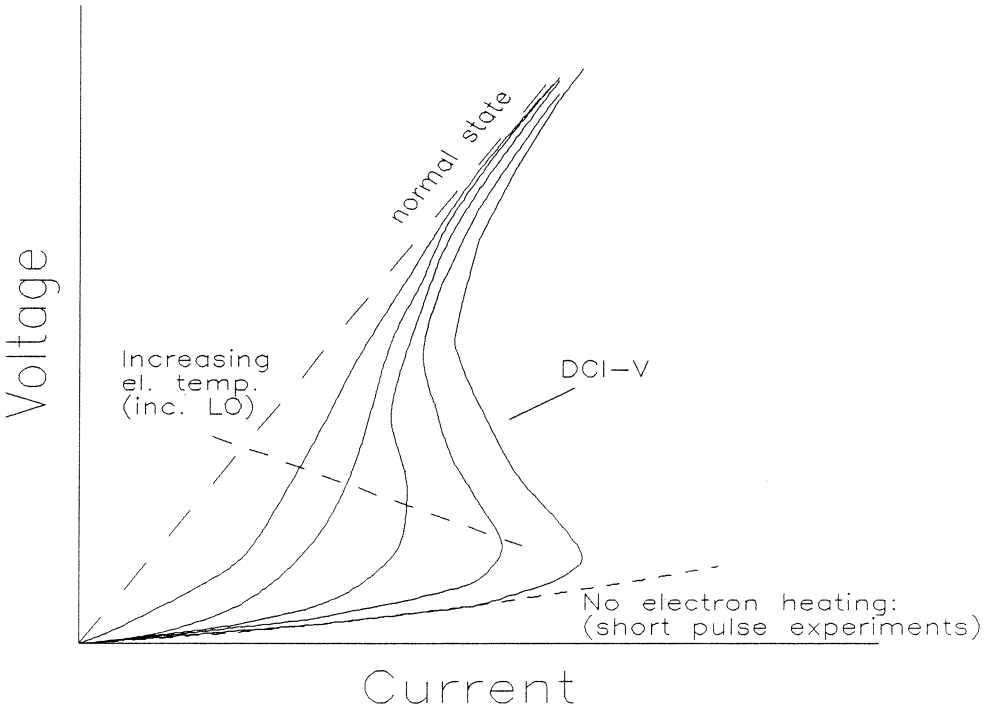

Fig.1 Schematic IV-characteristics of a thin film superconductor for different LO bias conditions.

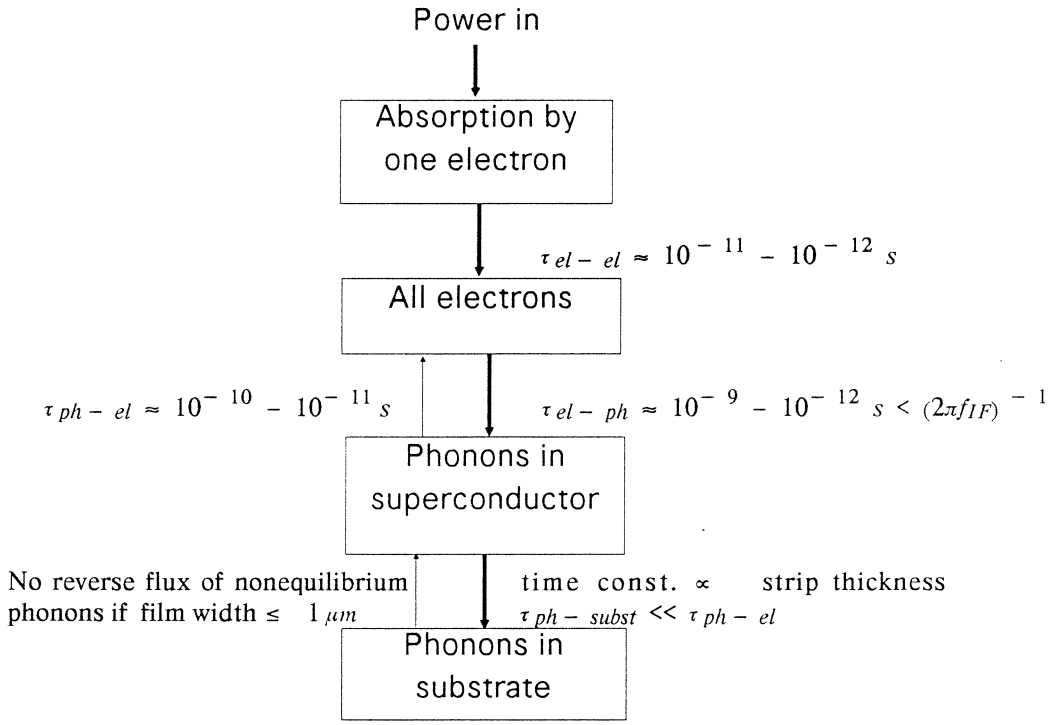

Fig 2. Shematic diagram shoing the various energy relaxation mechanisms in superconducting hot-electron devices.

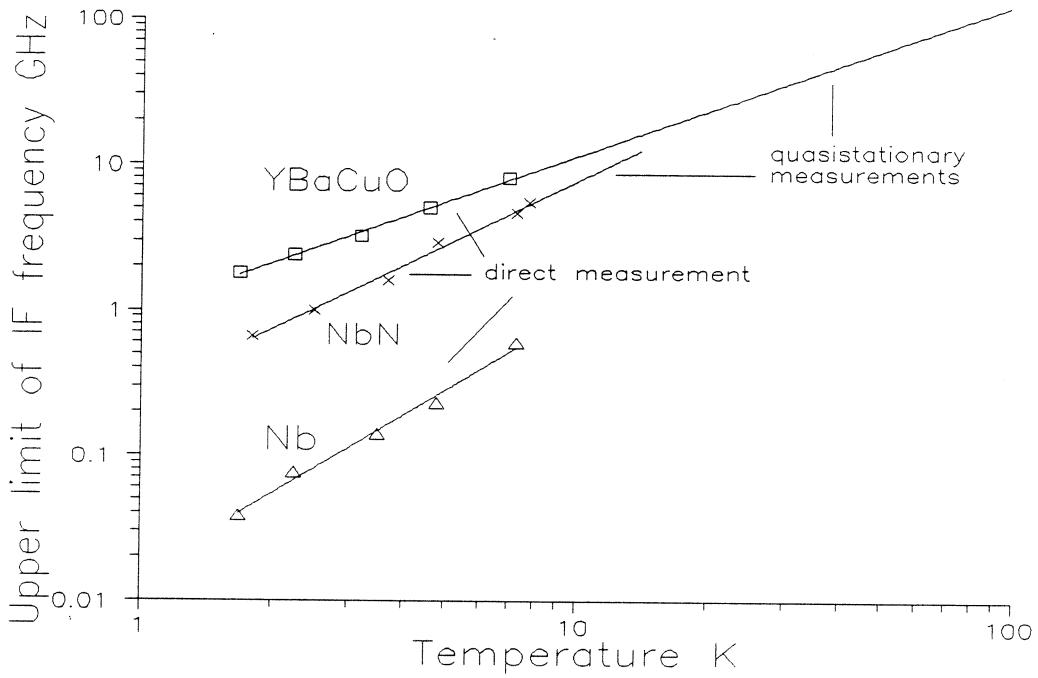

Fig.3. Upper limit of IF frequency vs temperature for Nb, NbN and YBaCuO mixers elements.

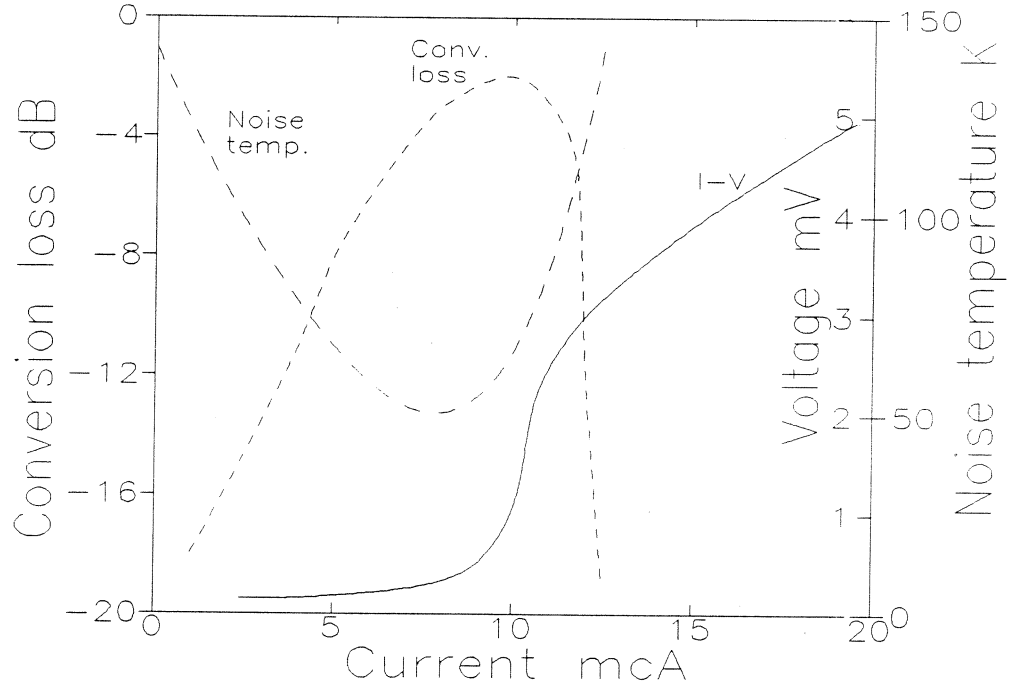

Fig.4. Culculated current dependence of conversion loss and noise temperature for a Nb mixer.

ANTENNA – COUPLED SUPERCONDUCTING ELECTRON-HEATING BOLOMETER

G.N. Gol'tsman, A.I. Elant'iev, B.S. Karasik, and E.M. Gershenzon

Moscow State Pedagogical University
1 M. Pirogovskaja str., Moscow 119435, Russia

Abstract.

We propose a novel antenna-coupled superconducting bolometer based on electron-heating in the resistive state. A short narrow ultrathin superconducting film strip (sized approximately 4x1x0.01 μm^3), which is in good thermal contact with the thermostat, serves as a resistive load for infrared or submillimeter current. In contrast to conventional isothermal superconducting bolometers, electron-heating ones can have a higher sensitivity which grows when film thickness is reduced. Response time of electron-heating bolometer does not depend on heat transfer from the film to the enviroment. To calculate the sensitivity (NEP), we have used experimental data on wideband Al, Nb and NbN bolometers which have the same underlying physical mechanism. The bolometers have been made in the form of a structure composed of a number of long narrow strips. The values of NEP have been found to be $1.5 \cdot 10^{-16}$, $1 \cdot 10^{-15}$, and $2 \cdot 10^{-14} W \cdot Hz^{-1/2}$ for Al, Nb and NbN respectively. In the paper, the prospects are also discussed of improving the picosecond YBaCuO detector, developed recently. NEP value of the detector, if combined with a microantenna, can reach the order of 10^{-10}–10^{-11} $W \cdot Hz^{-1/2}$.

Introduction.

Over the last decade, a substantial progress has been made in the creation of high-sensitive superconducting devices intended to receive electromagnetic radiation in the spectral range of 20 - 1000 μm. Due to frequency-independent response, bolometers have certain advantages over other superconducting detector types, such as Josephson junction or superconductor-insulator-superconductor structure. Further improvement in bolometer parameters can be primarily achieved by reducing the size of the bolometer, which in its turn entails the use of small antenna coupled with the sensitive unit of the bolometer [1]. This approach seems very promising for the development of radiation detectors with very low NEP values. Very recently we have proposed to utilize the electron-heating effect in thin and narrow superconducting films for radiation detection. A fundamental property of the effect is a small value of time constant as compared to the traditional bolometric effect.

The present paper views the characteristics of an antenna-coupled microbolometer whose operation is based on the electron-heating effect. It is shown that the sensitivity of the electron bolometer is enhanced both by

reducing film area and by getting the film thinner. Moreover, NEP value can be diminished in comparision to conventional bolometers, to achieve an extremely rapid action, as well as to ensure a much better matching between the bolometer and the antenna.

Results and Discussion.

Our previous papers [2-4] have demonstrated that the electron-heating effect is manifested at liquid helium temperatures in thin (thickness d $\simeq$ 100$\AA$) and narrow (width w $\simeq$ 1 μm) films of Al, Nb and NbN, deposited onto the substrates having good heat conductivity. Under these conditions one can obtain a unique combination of rapid action and high sensitivity inherent in the material. The electron heating has been most thoroughly studied in Nb films. As demonstrated in [2], a small mean free path of electrons (5-10 $\AA$) in thin disordered films leads to the enhancement of electron-electron interaction and to the weakening of electron-phonon one. As a result, unlike in pure metals, the inequality $\tau_{ee} \ll \tau_{eph}$ (τ_{ee} is the electron-electron interaction time, τ_{eph} is the electron-phonon interaction time) holds at temperatures $T \leq 10K$. Under such circumstances the Fermi-type distribution function of excited electrons with the temperature $\Theta > T$ is established during electron-electron relaxation time after radiation absorption. The next phase of relaxation is controlled by the electron temperature decay that is characterized by the time constant τ. Another peculiarity of ultrathin films is fast ballistic escape of nonequilibrium phonons from the film during the time τ_{es} smaller than the time of the back energy transfer from phonons to electrons τ_{phe}. In this case τ is defined by τ_{eph} only. For rather thick films, when the conventional bolometric effect is observed, τ coincides with the bolometric time constant $\tau_b = \tau_{es}C_e/C_p$ (C_e and C_p are specific heat capacities of electrons and phonons, respectively, and $C_e \gg C_p$ at low temperatures). Taking into account the result of [5] concerning the theoretical study of the superconducting film response to radiation as a function of the modulation frequency, one can show that if $\tau_{eph} \gg \tau_{phe}, \tau_{es}$, the bolometric response may be described by a single time constant $\tau = \tau_{eph} + \tau_b$.

It is useful to trace the transition from the electron-heating mode to the bolometric mode when film thickness is varied. As is known, the escape time of phonons is presentable by the formula $\tau_{es} = 4d/(v\eta)$, where v is the velocity of sound and η is the coefficient of transmission of a phonon through the film-substrate interface. In this way the following expression for τ can be obtained:

$$\tau = \tau_{eph} + \frac{4dC_e}{v\eta C_{ph}}. \qquad (1)$$

Such a dependence is confirmed by the experiment. The experimental data for Nb films shown in Fig.1, have been taken from [2]. The experimental curves follow the dependence given by Eq.1. Since for Nb $\tau_{eph} \sim T^{-2}$, the transition to the electron-heating regime is shifted towards the smaller

values of thickness when the temperature rises. It can be seen that the minimum response time corresponds to the electron-heating mode. In this case the time constant at the transition temperature for Al, Nb and NbN is of the order of 10^{-8} s, 10^{-9} s, and 10^{-11} s respectively.

We shall further analyze the superconducting bolometer sensitivity and determine its change while the transition to the electron heating occurs. It is well known that a minimum detectable power may be represented in the following form:

$$NEP^2 = \frac{4kT^2G}{\alpha^2} + \frac{4kTR}{S_u^2} + \frac{8\sigma kT_\phi^5 S\Omega}{\alpha} + \frac{(U_{exc})^2}{S_u^2}. \tag{2}$$

The first term in the right-hand side of the formula describes temperature fluctuations (G is the effective thermal conductance). The second describes the Johnson noise , the third describes fluctuations of the background radiation with the effective temperature T_ϕ (S is the area and Ω is the viewing angle of the device), and the fourth describes excess noise of various sources. In the formula R is the film resistance, α is the absorptivity, S_u is the responsivity. A good bolometer is characterized by a narrow superconducting transition. The typical transition widths are less than 0.01 K for Al and approximately 0.1 K for Nb and NbN. The responsivity S_u of such films is extremely high, therefore the second and the forth terms in equation (2) become negligible. So, the first term will be dominating in the absence of background radiation.

The value of effective thermal conductance at low temperatures ($C_e \gg C_p$) can be written as

$$G = \frac{C_e L w d}{\tau}, \tag{3}$$

where L is the film length. Substitutions of Eq.1 and Eq.3 into Eq.2 yield

$$NEP = \alpha^{-1}\sqrt{\frac{4kT^2C_e w L d}{\tau}}. \tag{4}$$

This is a well khown expression for NEP. For an isothermal bolometer the value of τ is defined by the thermal boundary resistance between the film and the substrate, i.e. $\tau \sim d$, and NEP does not depend on the film thickness. However, for ultrathin films this is not correct. For films having thicknesses $\leq 100\mathring{A}$ the electron heating mode is prevalent and τ reaches its minimum value τ_{eph}. In this case Eq. 4 should be re-written in the following form (Eq. 1 for τ is used):

$$NEP = \alpha^{-1}\sqrt{\frac{4kT^2C_e w L d}{\tau_{eph} + 4C_e d/(v\eta C_{ph})}}. \tag{5}$$

This formula shows that the reduction of the film thickness causes smooth transition from the conventional bolometric effect to the electron-heating effect. In the latter case τ does not depend on heat conductivity and is only controlled by τ_{eph}. In its turn the sensitivity rises with the decrease of the thickness.

Fig.2 demonstrates the dependence of NEP on thickness which follows that of Eq. (5). The dependence was calculated using experimentally measured values of τ (Fig.1) and the dimensions $w = 1$ μm and $L = 4$ μm (α is supposed to be $\sim$1). The triangle corresponds to the NEP value measured in [6] and reduced to 4 μm^2 area. The solid line corresponding to the isothermal antenna coupled bolometer with the same area from Ref. 7 is also given for the sake of comparision. One can conclude that the experimental data are consistent with those expected. The re-calculsation of the experimental data for Al at 1.6 K [6] and NbN at 10 K [8] to 4 μm^2 area gives respectively $1.5 \cdot 10^{-16}$ and $2 \cdot 10^{-14}$ W$\cdot$Hz$^{-1/2}$. Due to its small heat capacity and low critical temperature, Al can be used as a high-sensitive electron-heating bolometer with the time constant of 10 ns, whereas NbN can be used as a high-speed receiver with a response time of 20 ps.

An important problem which should be solved in developing a microbolometer is its matching with an antenna. For conventional superconducting bolometers the film impedance is complex. It has a small real part and a large imaginary part mostly defined by kinetic inductance [7]. For ultrathin films the real part of surface resistance becomes rather large. Moreover, the suppression of the energy gap in a current carrying resistive state near T_c leads to an almost frequency independent absorptivity at submillimeter and far-infrared wavelengths [3]. It means that the afore-mentioned superconducting strips in the resistive state may be treated as a pure resistive load to an antenna. The surface resistance inherent in the films (40-80 Ohms) is well suitable to be matched to antennas with an impedance of 100 - 200 Ohms.

Currently the high-T_c superconductors are very promising for the development of radiation detectors. For YBaCuO thin films, recent works [9–11] have demonstrated the presence of a fast mechanism of photoresponse in submillimeter and far-infrared as well as in optical spectral regions. The most probable nature of this phenomenon is relaxation of nonequilibrium carriers excited by radiation. The order of magnitude of the time constant of the process ($\sim$ 1–2 ps) coincides with that of the electron-phonon interaction time. Due to the reverse (compared to conventional superconductors) relationship between electron and phonon specific heats ($C_e \ll C_{ph}$), phonons serve as a heat sink for electrons during the first phase of relaxation. It is manifested as a biexponential response in pulse experiments. In [12] we have studied the sensitivity of the fast component of YBaCuO detector photoresponse and found it to be about 10^{-7} W$\cdot$Hz$^{-1/2}$. Considering the fact that the readout system used was far from perfect, and a possibility exists to significantly reduce the dimensions of detector when the antenna is

applied, we would claim the availability of an YBaCuO picosecond detector with $NEP \simeq 10^{-10} - 10^{-11}$W·Hz$^{-1/2}$.

Conclusion.

In summary, basing on experimental results we calculate the characteristics of the electron-heating microbolometer and show its availability as a high-speed antenna-coupled detector. Such a bolometer is more sensitive, rapid and easier to matching with an antenna than the isothermal bolometer. For conventional superconductors it is possible to attain the value of NEP less than 10^{-16} W·Hz$^{-1/2}$. Radiometers based on the electron-heating microbolometer are likely to have a sensitivity comparable to that of heterodyne receivers in the terahertz frequency range. Furthermore, such a bolometer will make it easier to produce matrix devices. Hot electron microbolometers based on superconductors with $T_c > 10$ K can be useful as mixers in space research applications [13].

The authors would like to thank A.V. Sergeev for helpful discussion and Yu.P.Gousev for technical assistance when preparing the manuscript.

References.

1. D.B. Rutledge, S.E. Schwarz, and A.T. Adams, Infrared Physics **18**, 713 (1978).

2. E.M.Gershenzon, M.E.Gershenzon, G.N.Gol'tsman, A.M.Lyul'kin, A. D.Semenov, A.V.Sergeev. Sov. Phys. JETP **70**, 505 (1990).

3. E.M.Gershenzon, M.E.Gershenzon, G.N.Gol'tsman, A.M.Lyul'kin, A.D.Semenov, and A.V.Sergeev, Sov.Phys.Tech.Phys. **34**, 195 (1989).

4. E.M. Gershenzon, M.E. Gershenzon, G.N. Gol'tsman, A.D. Semenov, and A.V. Sergeev, IEEE Trans. on Magn. **27**, 2836 (1991).

5. N. Perrin and C. Vanneste, Phys. Rev. B **28**, 5150 (1983).

6. E.M. Gershenzon, G.N. Gol'tsman, B.S. Karasik, G.Ya. Lugovaja, N.A. Serebrjakova, and E.V. Chinkova, Superconductivity: Physics, Chemistry, Engeneering **5**, 1129 (1992) (in Russian).

7. J.Mees, M.Nahum, and P.L.Richards, Appl.Phys.Lett. **59**, 2329 (1991).

8. G.N. Gol'tsman, A.D. Semenov, Y.P. Gousev, M.A. Zorin, I.G. Gogidze, E.M. Gershenzon, P.T. Lang, W.J. Knott and K.F. Renk, Supercond. Sci. Technol. **4**, 453 (1991).

9. E.M. Gershenzon, G.N. Gol'tsman, I.G. Gogidze, A.D. Semenov, and A.V. Sergeev, Physica C **185-189**, 1371 (1991).

10. M. Johnson, Appl.Phys.Lett. **59**, 1371 (1991).

11. A.D. Semenov, G.N. Gol'tsman, I.G. Gogidze, A.V. Sergeev, P.T. Lang, and K.F. Renk, Appl.Phys.Lett. **60**, 903 (1992).

12. R.S.Nebosis, R.Steinke, P.T.Lang, W.Schatz, M.A.Heusinger, K.F.Renk, G.N.Gol'tsman, B.S.Karasik, A.D.Semenov, and E.M. Gershenzon, J.Appl.Phys. **72**(11), 5496 (1992).

13. E.M.Gershenzon, G.N.Gol'tsman, this issue.

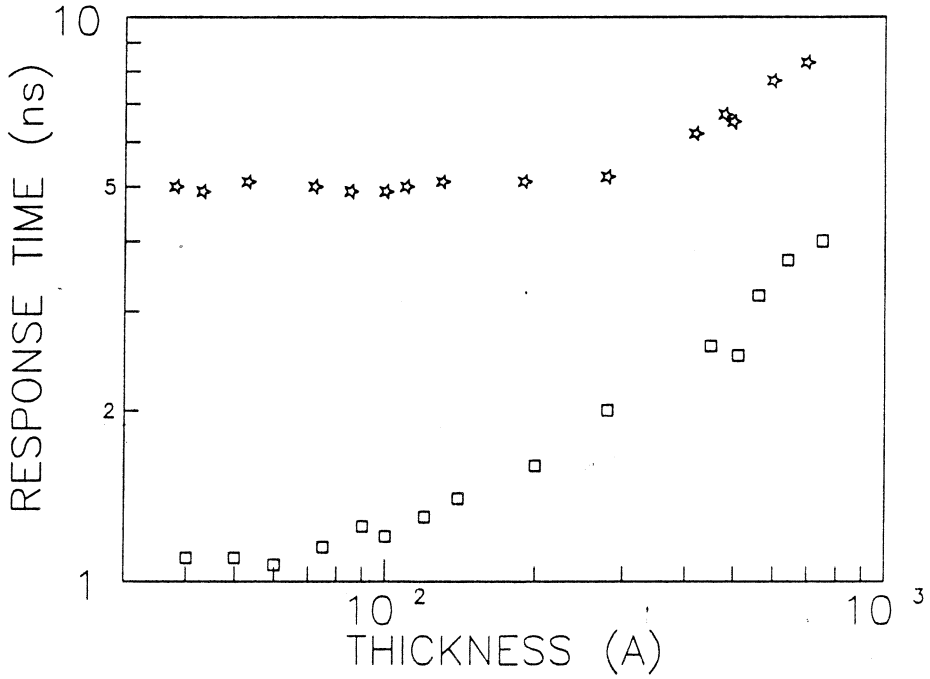

Fig. 1. The dependence of τ on d for Nb films at different temperatures. $\star$ – 1.6 K, $\sqcap$ – 4.2 K.

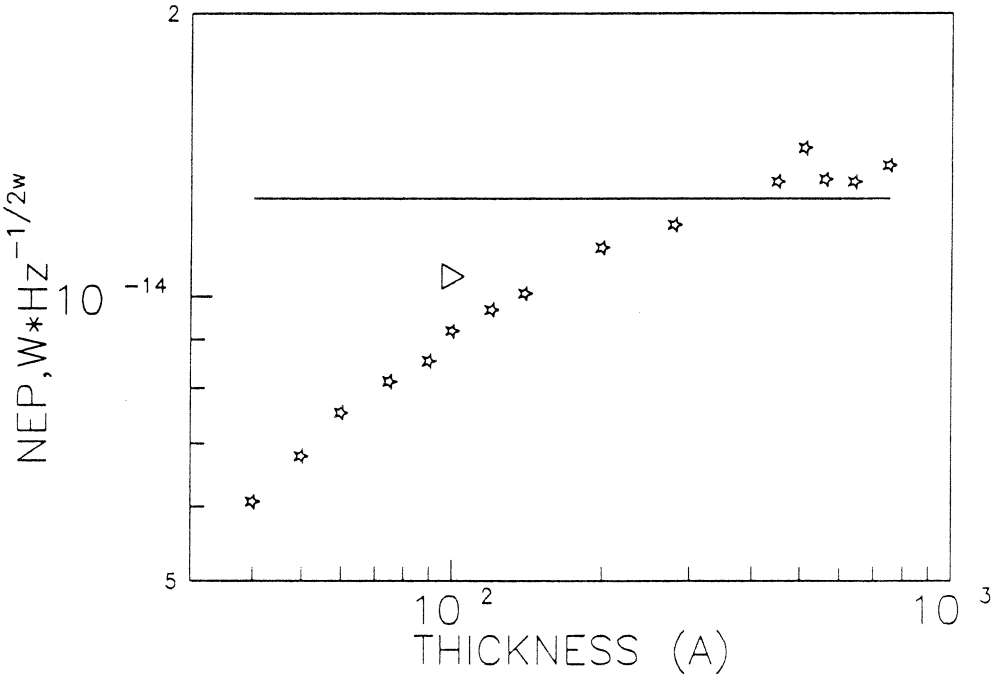

Fig. 2. The dependence of NEP on d ($\star$) at 4.2 K. $\triangle$ – recalculation of the experimental data from Ref.6, solid line – calculated value for isothermal bolometer from Ref.7.

A Superconducting Mixer Tuned By The Quantum Susceptance

N.G. Ugras, A.H. Worsham [a], D. Winkler [b], D.E. Prober,
Department of Applied Physics, Yale University
New Haven, CT 06520-2157

Abstract

The high frequency quasiparticle tunneling current in a superconducting tunnel junction has been recently measured. The ratio of the reactive component of this current to the rf voltage is the quantum susceptance. We have successfully employed this susceptance as the tuning element for a SIS mixer.

Introduction

SIS (superconductor-insulator-superconductor) mixers are now the dominant technology for receivers in radioastronomy for observations in the millimeter-wave band. There is substantial effort to extend their operation into the sub-mm range [1]. It seems most likely that future millimeter-wave observational instruments will use focal plane arrays of SIS mixers [2]. At these high frequencies, the admittance due to the geometric capacitance of the tunnel junction is significant. A finite capacitance is necessary in order to shunt noise sidebands generated by the Josephson pair currents. At 100 GHz a good compromise is achieved with a $\omega R_n C$ product of about 4, where R_n is the normal state resistance [4]. For $\omega R_n C \geq 1$ one must resonate the junction capacitance C at the frequency of operation. Waveguide backshorts have been used successfully to tune out the capacitance at high frequencies, but are impractical for array applications [2]. On-chip thin film inductors have also been successful in resonating the junction capacitance. However these inductors are not variable, so one cannot adjust the resonant frequency [3,5]. Thus there is a need for a variable integrated tuning element at millimeter-wavelengths for array applications. We demonstrate in the present work a novel electronic on-chip tuning element.

Quantum Susceptance

In this paper we will concern ourselves only with the quasiparticle currents and assume the Josephson current is suppressed by a magnetic field. The *quantum admittance* can be calculated from the quasiparticle density of states which determines the dc I-V curve [6]. For an applied voltage:

$$V(t) = V_0 + V_\omega \cos(\omega t), \qquad (1)$$

where V_0 is the dc bias voltage and V_ω is the rf signal voltage at a fixed frequency ω, the admittance is:

$$Y_Q(V_o, V_\omega) = G_Q(V_o, V_\omega) + iB_Q(V_o, V_\omega). \qquad (2)$$

The real part of this admittance is the quantum conductance, G_Q, and the imaginary part of the admittance is the quantum susceptance, B_Q.

The quasiparticle dc I-V curve of a SIS tunnel junction and its Kramers-Kronig transform are shown in Figure 1, along with the calculated quantum conductance and susceptance. These are calculated for a 90 GHz rf signal with an available power of ~ 3 pW.

The quasiparticle susceptance and conductance have recently been experimentally measured [7,8]. It has also been demonstrated that a lumped circuit model is accurate in describing the voltage dependence of these two quantities, even for a relatively large input power (α>1) [8]. For a small rf power, and within one photon energy of the gap voltage, the quasiparticle admittance can be modeled as a voltage-variable susceptance, $B_Q(V_0) = -j/\omega L(V_0)$, in parallel with a constant conductance which is about three times larger than the normal state conductance at 90 GHz.

Mixer Design

For proper tuning, the SIS junction capacitance needs to be resonated by a tuning element which is placed in rf-parallel with the mixer without shorting the dc bias current. In our design we use a series array of four tunnel junctions as the mixing element. The inductive tuning element consists of a separate series array of seven tunnel junctions which is referred to as the tuning array. This tuning array is independently dc-biased and is in rf-parallel with the mixing array. The junctions of the tuning array have the same current density and area as the junctions of the mixing array. In order to decrease the absorption of photons from the input signal by the tuning array, we have used about twice as many tuning junctions as mixing junctions. This ensures that the dominant mixing effect is from the mixing array. The use of a series array for tuning adds

less capacitance than a single junction.

Figure 2 shows the waveguide mixer mount and the microstripline circuitry [6]. The local oscillator (lo) is directed through a WR-10 cross-coupler into the input waveguide. A four-step Chebychev single ridge transformer at the end of this waveguide provides a broad-band waveguide-to-microstrip transition. The waveguide impedance is transformed to 50Ω at the last ridge section which makes rf and dc contact to the 50Ω input microstripline on the chip (position A in Fig. 2). This input section is $\lambda/4$ long at 100 GHz. The rf impedance transformation by the ridge enables the use of low impedance SIS junctions. This eases matching on the intermediate frequency (if) side since we do not employ an if impedance transformer. The SIS mixing array is placed between the end of this microstrip-line (pos. B) and a 90° radial stub (pos. C). The 90° radial stub, like an unterminated quarter wave microstripline, provides an rf ground at a well defined point with a broad bandwidth and transmits the dc-bias and if-signal. The rf signal is thus shorted to the ground plane. A second 90° radial stub, next to the one terminating the mixing array, provides a separate rf termination for the tuning array in parallel with the SIS element. The radial stubs are in close proximity relative to the wavelength and are also capacitively coupled via a 2μm wide gap between them. Thus we have two dc- and if-isolated broadband rf-ground terminations at nearly the same geometrical location, and the tuning array can be independently dc biased. The 1.4 GHz if signal is then filtered with a bias-tee. A similar filter is used for the tuning array, except with a larger contact pad. The dc and if grounds are provided by the waveguide walls.

The local oscillator signal is provided by a YIG tuned oscillator which is tripled, and fed into the mixer chip along with a test signal from a cryogenic hot/cold load [9]. By measuring the if output for different hot/cold load temperatures, the receiver noise and gain are determined. The receiver includes an electromechanical switch and various ports to test the noise, match, and gain of the if system. With these we can determine the mixer noise and mixer gain. The Nb/Al-O_X/Nb trilayer tunnel junctions used in this work each have an area of $4(\mu m)^2$ and a resistance of 11.5Ω [10].

Receiver Results and Discussion

The performance of this mixer is evaluated using our test receiver. The results are compared quantitatively with the quantum theory of mixing [6]. Initially the success of the tuning approach is evaluated from the pumped I-V

curves. In the presence of rf radiation , a SIS junction I-V curve exhibits photon assisted tunneling steps. Usually a SIS mixer is biased in the middle of the first step below the gap voltage. The if output resistance of the mixer is the differential resistance of the dc I-V curve in the middle of the first photon step. The input impedance of the if amplifier should match this differential resistance for best if coupling efficiency. Thus the shape of the tunneling steps is important in determining receiver performance.

The shape of the tunneling steps depends on the amplitude of the rf signal and the admittance presented to the device by the embedding circuitry. In our design, for optimum receiver performance the rf conductance of the mixer needs to be close to 20 mmhos while the capacitance is resonated [5,11].

Fig. 3 shows the measured dc I-V curve, and two pumped I-V curves with photon assisted tunneling steps. The step-like proximity effect feature above the gap rise is caused by the slight non-uniformity of the junction areas. These curves are taken with a 90 GHz local oscillator signal. Tunneling steps are shown for two different biasing conditions for the tuning array. These bias voltages on the tuning array are chosen to separately analyze the effects of the susceptance and the conductance. There is a distinct difference between the shapes of the pumped I-V curves. The dynamic resistance of the mixing array in the middle of the first photon step is a factor of two larger for curve b than curve a. Thus, we have altered the embedding admittance seen by the *mixing* array by changing the bias voltage of the *tuning* array.

The embedding admittance seen by the mixing array can be calculated from the shape of the tunneling steps in Figure 3. This is done using the voltage-match method in the three frequency approximation [12]. This approximation introduces an error in mixer calculations done for devices with $\omega R_n C < 4$ [2]. The mixing array modeled here is estimated to have a $\omega R_n C$ product of about 1.5.

The embedding admittance for the mixer, Y_{emb}, is obtained by fitting the pumped I-V curves for various bias voltages on the tuning array. Values of B_t and G_t are inferred from Y_{emb} by subtracting other components of the embedding admittance. These values are given in Table 1. Using this method the change in the embedding susceptance between curves a and b is inferred to be $\Delta B_t = 42$ mmhos. The theoretical value is $\Delta B_t = 49$ mmhos. This is in good agreement with the experimentally derived value.

The double-sideband receiver noise temperature, T_R of this mixer at 90

GHz is measured as a function of the dc-bias voltage of the *tuning* array. The mixer gain g_m is obtained by testing the if system independently. The receiver noise temperature depends on the mixer gain as

$$T_R = T_m + T_{if}/g_m , \qquad (3)$$

where T_m is the mixer noise temperature and T_{if} is the if amplifier noise temperature which is around 8K.

The negative susceptance of the tuning array increases as the tuning voltage, V_t approaches the gap voltage. At this voltage it resonates the array capacitance. Resonating this capacitance (at $V_t \sim V_g$) gives the largest mixer gain and the lowest receiver noise temperature. The experimental results for g_m and T_R for three specific values of V_t are given in Table I.

The theoretical mixer gain is calculated using the embedding admittances inferred from the pumped I-V curves. The experimental value of ΔB_t agrees well with the theoretical value. This verifies the validity of the lumped element circuit model we have employed, in which the quasiparticle admittance is modeled as a voltage variable susceptance in parallel with a conductance. The tuning array acts as a separate passive tuning element, and the mixer gain is significantly improved by the tuning array.

Acknowledgments

We thank N.R. Erickson and P.F. Goldsmith for discussions and loans of equipment, J.H. Kang, J.X. Przybysz, and M.J. Rooks for their help with the microfabrication, A.R. Kerr, M.J. Feldman, and M.J. Wengler for useful discussions, and A. Skalare for the simulation programs. This work was supported by NSF grant ECS-8604350, and AFOSR-88-0270. Fabrication at the National Nanofabrication Facility was supported by NSF grant ECS-8619049.

[a]Current address: Westinghouse Science & Technology Center, Pittsburgh PA 15235.
[b]Current address: Physics Department, Chalmers University of Technology, S-41296 Göteborg, Sweden.

References

[1] R. Blundell and C.-Y. E. Tong, Proc. IEEE **80**, 1702 (1992), and M.J. Wengler, Proc. IEEE **80**, 1810 (1992).

[2] A.R. Kerr, S.-K. Pan, S. Withington, to appear in IEEE Trans. Microwave Theory & Tech., March (1993).

[3] A.R.Kerr, S.-K. Pan, A.W. Lichtenberger, and D.M. Lea, IEEE Microwave and Guided Wave Lett. **2**, 454 (1992).

[4] A.R. Kerr, and S.-K. Pan, Int. J. Infrared Mm. Waves **11**, 203 (1990).

[5] D. Winkler, N.G. Ugras, A.H. Worsham, D.E. Prober, N.R. Erickson, and P.F. Goldsmith, IEEE Trans. Magn. **27**, 2634 (1991).

[6] J.R. Tucker, and M.J. Feldman, Rev. Mod. Phys. **57**, 1055 (1985).

[7]Q. Hu, C.A. Mears, P.L. Richards, and F.L. Lloyd, Phys. Rev. B **42**, 10250 (1990).

[8] A.H. Worsham, N.G. Ugras, D. Winkler, D.E. Prober, N.R. Erickson, and P.F. Goldsmith, Phys. Rev. Lett. **67**, 3034 (1991).

[9] D. Winkler, N.G. Ugras, A.H. Worsham, D.E. Prober, N.R. Erickson, and P.F. Goldsmith, in progress.

[10] A.H. Worsham, D.E. Prober, J.H. Kang, J.X. Przybysz, and M.J. Rooks, IEEE Trans. Mag., **27**, 3165 (1991).

[11] W.R. McGrath, P.L. Richards, D.W. Face, D.E. Prober, and F.L. Lloyd, J. Appl. Phys., **63** 2479 (1988).

[12] A. Skalare, Int. J. Infrared and Millimeter Waves **10**, 1339 (1989).

Table I. Values of B_t and G_t calculated by fitting the pumped I-V curves in Fig. 3, experimental and theoretical double-sideband (DSB) mixer gain and experimental receiver noise temperature for three different bias voltages of the tuning array. The bias voltages are shown in the inset of Fig. 3. The last column is for no tuning array. The conductance G_t of the tuning array does not appear to play a major role in determining the mixer gain, as seen by comparing columns b and c.

Bias Point	a	b	c	
V_t	V_g	$\approx(V_g-(\hbar\omega)/e)$	$<(V_g-(\hbar\omega)/e)$	-
B_t (mmho)	-42	0	0	0
G_t (mmho)	35	35	3	0
g_m(dB)-Calc.	-0.6	-5.3	-5	-3.3
g_m(dB)-Expt.	-1.1	-5.1	-4.3	-
T_R (K)-Expt.	47	76	65	-

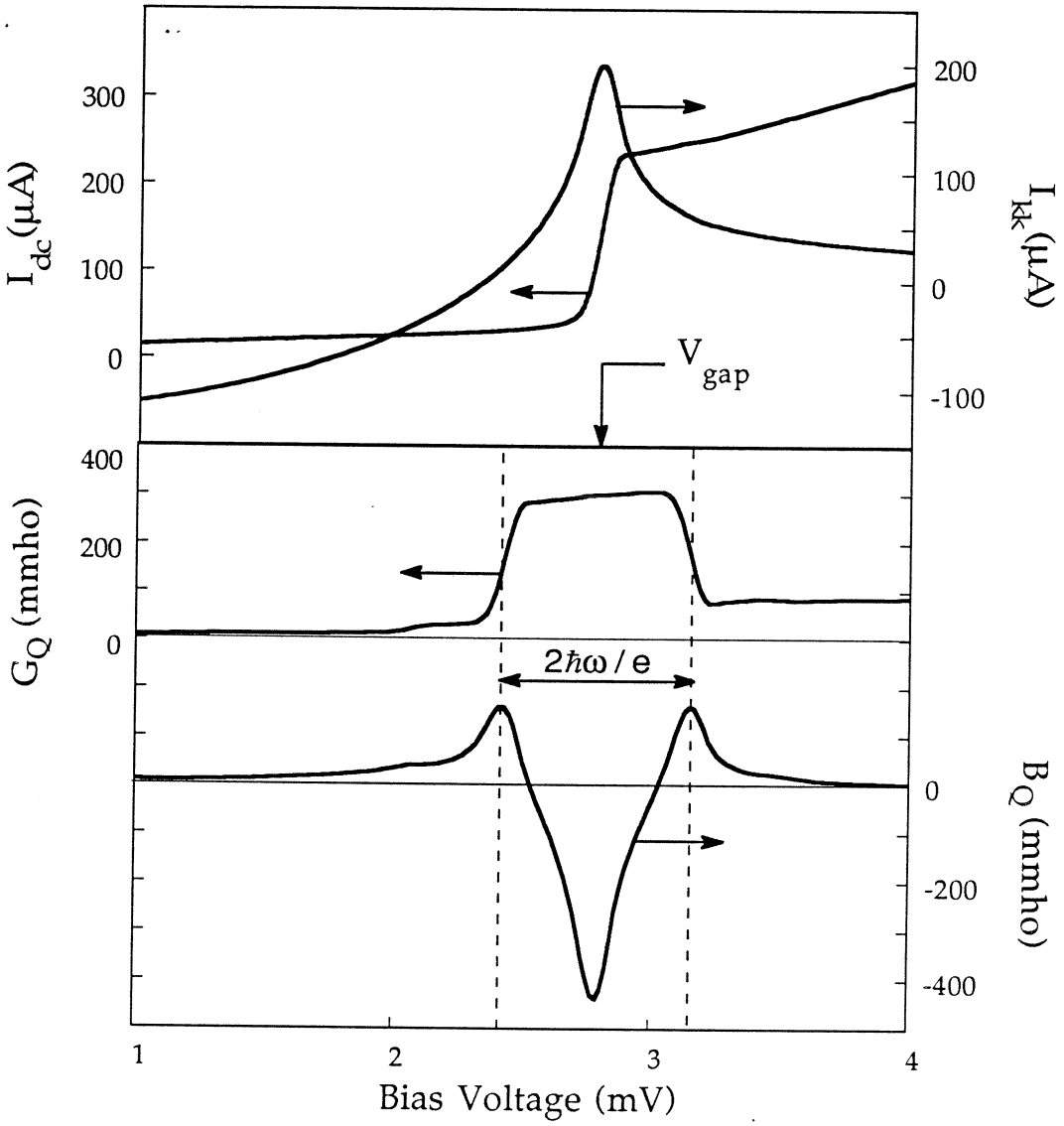

Fig. 1: DC I-V curve of a single tunnel junction and its Kramers-Kronig transform (top). The calculated quasiparticle conductance and susceptance (bottom) for a small input power at 90 GHz.

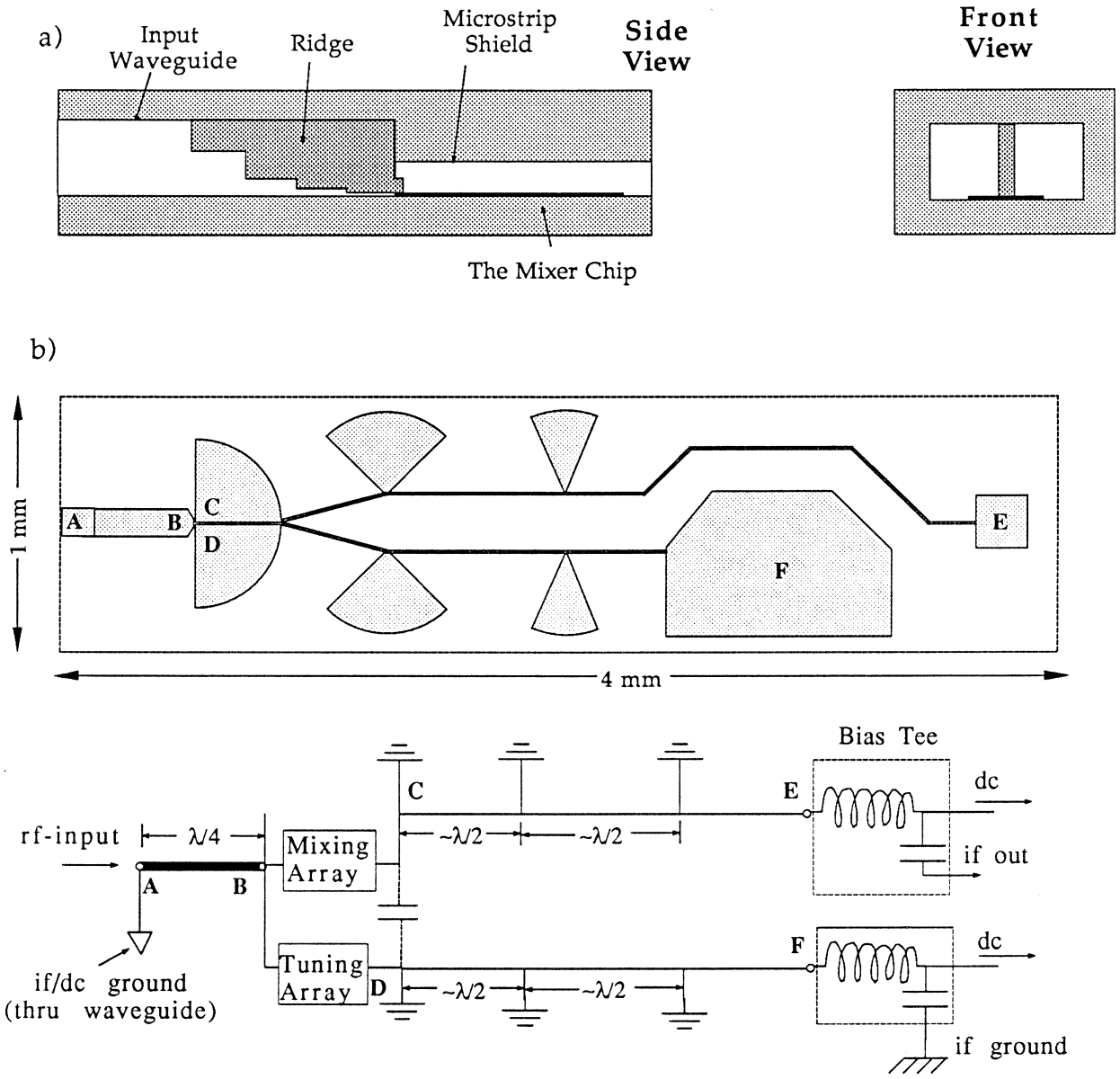

Fig. 2: The waveguide mount and the mixer chip. a) Side views of the mixer mount showing the waveguide ridge. b) The mixer chip layout (top) and the rf equivalent circuit (bottom). The test signal along with the local oscillator signal is fed into the input microstrip (A). Both arrays are terminated in 90° radial stubs providing two dc-isolated rf grounds near locations B and C, where the junctions connect. The if and dc signals are extracted at D for the mixer while the tuning array is biased through E.

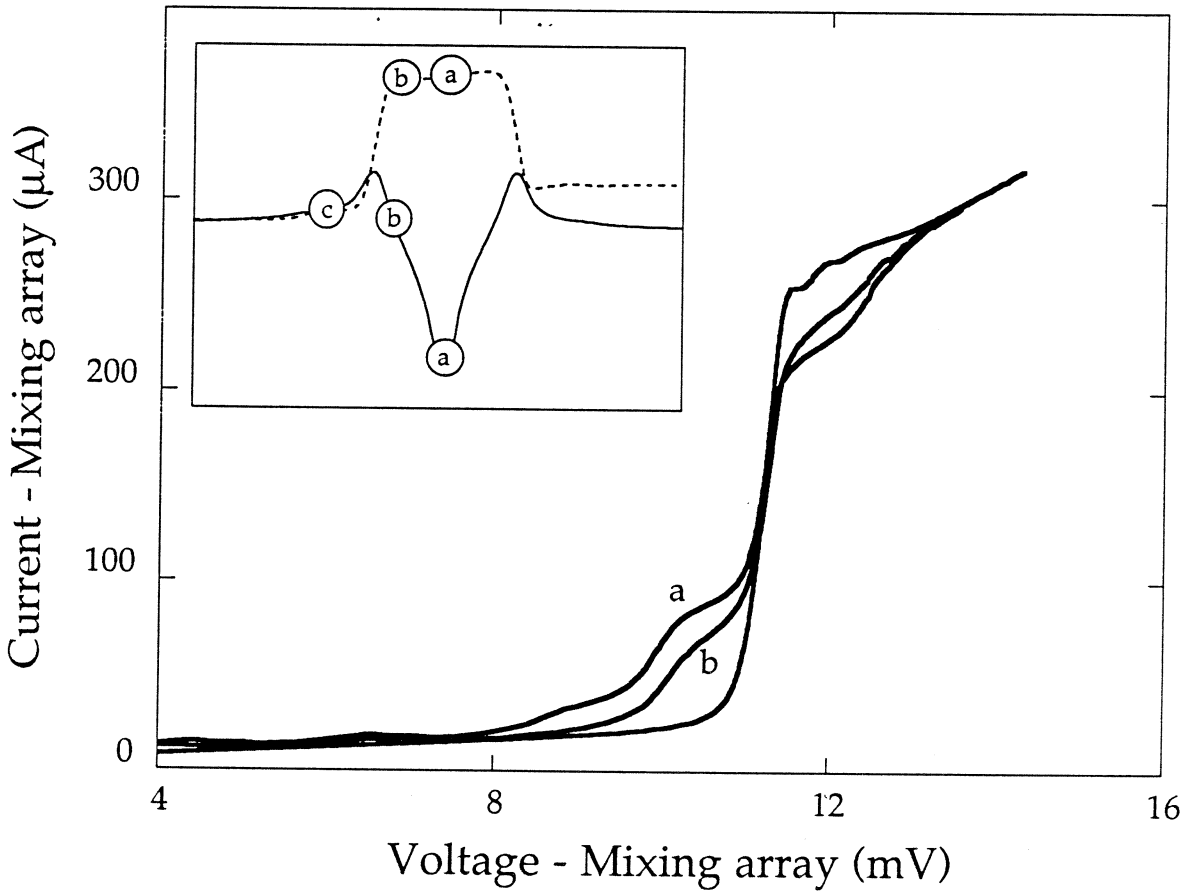

Fig.3 : Measured pumped I-V curves of the mixing array for two different bias voltages on the tuning array; also shown is the unpumped dc I-V curve. The inset shows the conductance and the susceptance of the tuning array at bias voltages a, b, and c on the tuning array.

SIS Mixers using Endfire and Broadside Double Dipole Antennas at 435 and 480 GHz

A. Skalare*,***, M.M.T.M. Dierichs*,**, J. Mees*, H. van de Stadt*, R.A. Panhuyzen*, Th. de Graauw*, T.M. Klapwijk**

* Space Research Organization Netherlands (SRON), Landleven 12, Postbus 800, 9700 AV Groningen, the Netherlands

** Dept. of Applied Physics and Materials Science Centre, University of Groningen, Nijenborgh 4, 9747 AG Groningen, the Netherlands

*** Dept. of Microwave Tech., Chalmers Univ. of Tech., S-412 96 Göteborg, Sweden

Abstract

In the article is presented a double dipole antenna endfire design, which has been fabricated with a two-junction SIS series array. An initial Y-factor measurement gave best performance at 435 GHz, where a receiver noise temperature below 500 K double sideband was achieved. Also presented are measurements with a broadside double dipole array antenna and SIS mixer. An on-chip tuning structure consisting of a short inductive stub, terminated by a lumped niobium oxide capacitor, was used. The best receiver noise temperature achieved was below 200 K DSB at 480 GHz.

1. Introduction

In the latest years, SIS mixers have been generally recognized as the most sensitive devices for heterodyne detection from the mm-wave regime up to frequencies around 500-600 GHz[1]. The most commonly used category is based on waveguide technology, where the detected signal is coupled onto a mixer chip via a horn antenna and a rectangular waveguide. One or two movable short circuits provide microwave matching between the waveguide and the rather capacitive SIS junction. Another category is that of open structure antennas such as bow-ties[2], log-periodic[3], log-spiral[4,5,6,7], ,resonant slot[7], and dipole[8,9,10,11,12,13] antennas. These are all planar structures that are usually fabricated together with the SIS junction itself. The absence of adjustable tuners means that the parasitic capacitance of the junction must be compensated by an on-chip circuit, which in most cases is realized in microstrip technology. Open structure antennas are often mounted directly to a dielectric lens for two different reasons. This is partly to focus down the wide antenna beams, but also to avoid problems associated with substrate modes in the dielectric substrate that supports the antenna and mixer junction.

We will here describe two particular SIS open structure antenna mixers, both using twin dipole arrays in conjunction with dielectric quartz lenses. In the first one the dipole elements are spaced at $\lambda/4$, and are asymmetrically fed by the SIS to create an endfire antenna beam. In the second one the two dipoles are arranged for a broadside beam.

2. An endfire dipole array antenna

2.1 Endfire antenna geometry and design

As is shown in fig. 1, the antenna consisted of two half-wave dipoles that were connected to each other by a co-planar stripline. The overall idea was to choose an appropriate value of the characteristic impedance of the stripline, so that the coupling from each of the two dipole elements to the SIS would be equal in magnitude. With the dipole spacing and the feed point as in Fig. 1, the contributions from the dipole elements add up in phase for one of the endfire directions and out of phase by $\pi/2$ for the other, Fig. 2. The far-field pattern of one of the dipole elements can be approximated by:

$$E_\theta \approx j \cdot \frac{120\pi}{\sqrt{\varepsilon_r}} \cdot \frac{I \cdot e^{-jkr}}{2\pi r} \cdot \frac{\cos\left(\frac{\pi}{2}\cos\theta\right)}{\sin\theta} \qquad \text{Eq. 1}$$

where r is the radius from the dipole to the observation point, θ is the angle between that radius and the axis of the dipole, ε_r is the dielectric constant of the surrounding medium and $k=2\pi/\lambda$. The theoretical diffraction pattern from the two dipoles would then appear as in Fig. 3. The imbalance between the two planes is due to the two extra nulls in the E-plane that are generated by Eq.1 when $\theta \rightarrow 0$ and $\theta \rightarrow \pi/2$.

The design frequency of the antenna for the SIS mixer chip was 480 GHz, so the length of the dipoles in Fig. 1 was chosen to $\lambda/2$=160 μm, where the dielectric constant of the surrounding fused silica medium was taken into account (ε_r=3.8). The width of the dipole elements was 24 μm, and the width and spacing of the coplanar stripline between them were 8 and 4 μm, respectively. The DC/IF connection to the SIS was made via the wires to the right in Fig. 1. A band stop filter consisting of 7 $\lambda/4$ sections was used to prevent RF leakage to the line. The width and spacing of the high impedance sections were 4 and 20 μm, respectively, and of the low impedance sections 20 and 4 μm. Each SIS junction was connected to a 75 μm long open ended tuning stub of width 4 μm. 250 nm of SiO_2 was used as dielectric for the stubs. The two Nb-Al/AlOx-Nb SIS junctions had an area of ≈1.5 μm^2 and a total normal resistance of 29 Ω.

The mixer chip was glued to the back plane of a fused silica lens with cyanoacrylat glue, Fig. 4. The chip was supported by two other glued-in fused silica pieces, which also ensured that the dipole antenna would be completely surrounded by the same dielectric material. The lens had a diameter of 11 mm, and had the unique ellipsoidal shape that would focus a plane wave into a point, according to geometrical optics. The edge of the mixer chip had previously been sawed so that this focal point would fall halfway between the dipoles.

2.2 Endfire antenna measurements

The fused silica lens with the endfire dipole SIS chip was placed in a fixture inside an SIS receiver cryostat. The first measurements were made with a *Fourier Transform Spectrometer* (FTS), and after that a Y-factor measurement was carried out. The

fixture holding the lens and the Y-factor measurements will be described in the later section about the broadside antenna chip measurements.

The spectrogram from the FTS measurement showed two response peaks, Fig. 5. The first was a sharp peak at 320 GHz, and the second one a slightly broader shape from 450 to 470 GHz. This latter response was the result of the tuning stubs connected to the SIS junctions, and fell within the 402-496 GHz range of the carcinotron source in our Y-factor measurement set-up. It is not known what caused the 320 GHz peak. The SIS DC bias voltage was 4.92 mV (2.46 mV per junction).

The noise measurements showed a best Y-factor response of 1.4 dB at 435 GHz, with the local oscillator power coupled in via a 60 μm Mylar™ beamsplitter at 45° angle in front of the dewar window. With the hot and cold loads at 290 and 77 K, respectively, this corresponds to a double sideband noise temperature of 483 K. As the transmission of the beamsplitter was rather low, only ≈ 62%, we feel the results could be improved significantly by using a thinner one. The same measurement set-up was used as in the broadside dipole measurements that are described below. Fig. 6 shows the noise temperature as a function of frequency, measured at an intermediate frequency of 4.3 GHz. Fig. 7 shows an unpumped and a pumped IV curve, together with the mixer output.

3. Broadside dipole array antenna

3.1 Broadside antenna geometry and design

The design and some properties of the broadside double dipole antenna have been described in the references[12,14]. As is shown in Fig. 8, the antenna consists of two planar half-wave dipoles, that are separated by slightly less than half a wavelength. The dipoles are connected by a co-planar stripline, with the feed point at the center. The DC and intermediate frequency connections are via the co-planar stripline to the right in Fig. 8. A 7-section lambda quarter bandstop filter prevents leakage of signal and local oscillator power along the line. On the mixer chip a single 1.5 μm^2 Nb-Al/AlOx-Nb SIS junction was fabricated at the feed point of the antenna. The junction capacitance was tuned by a short microstrip section, which was shunted to ground at the end by a 25 μm^2 large lumped capacitor. The microstrip had a width of 1.6 μm, and used a 250 nm thick SiO_2 layer as dielectric. Several lengths were patterned on different chips, but the measurements we report here were all made with a device where the stub length was ≈ 6.2 μm. The shunt capacitor was formed by defining a large extra SIS junction, the top electrode and oxide barrier of which was later etched away, thereby exposing the niobium of the base electrode. An extra anodization step was carried out to create approximately 50 nm of Nb_2O_5, which was used as dielectric. The purpose of the capacitor was to create an approximate short circuit at the signal and local oscillator (LO) frequencies, without shorting out the DC bias and the IF output from the mixer. At the signal and LO frequencies, this places the microstrip "inductance" in shunt with the junction capacitance. This arrangement provides a larger bandwidth than a simple open ended stub, and requires less surface space on the antenna.

The antenna chip was glued with cyanoacrylat to the back plane of a fused silica hyperhemispheric lens of 11 mm diameter, Fig. 9. An 80 μm thick fused silica chip with a deposited chromium/gold reflector on one side was glued on to the antenna chip. The thickness of the lens had been chosen so that the focus would fall on the reflector, where the phase center of this antenna should be.

The lens was held by the fixture in Fig. 10. It was cooled via the copper front and back plates and via the copper braid. An extra cooling strap of copper foil was glued directly to the reflector chip with silver paint. The flexible copper/Kapton™/copper strip line that was used for the DC and IF connections to the mixer chip is described in one of the references[14]. A superconducting magnet was placed to the side of the fixture for suppression of the Josephson effect. The same mixer fixture and magnet were also used in the measurements with the endfire antenna, but with the magnet placed directly behind the fixture instead of to the side. The objective with that was to orient the magnetic field into the plane of the SIS junctions.

3.2 Broadside antenna Y-factor measurements at 480 GHz

Y-factor measurements were carried out between 420 and 496 GHz with the set-up shown in Fig. 11. The mixer fixture and magnet were attached to the cold plate of an Infrared Labs. HD(3)-8 cryostat. The signal and local oscillator were coupled in through a TPX window, and focused onto the fixture with a polyethylene lens. A 200 μm thick fused silica sheet was used to reduce the heat flow into the cryostat. The intermediate frequency output from the mixer was connected to a Berkshire Tech. HEMT amplifier, with a best performance according to the manufacturer of 3.7 K at 4.4 GHz. This frequency was also our choice for the broadside antenna measurements.

In the first measurement, a rather thick Mylar beamsplitter was used (60 μm). This resulted in the noise temperatures shown in Fig. 12, with a best point just below 400 K DSB at 480 GHz. A second measurement was made with a 15 μm Mylar beamsplitter, which gave a best hot/cold response of 2.5 dB at 470 and 480 GHz. With the hot and cold loads at 290 and 77 K, respectively, this gives a best receiver noise temperature of just below 200 K DSB. Fig. 13 shows the unpumped IV curve together with a pumped curve and the hot and cold load responses at 480 GHz.

4. Summary

An SIS mixer using an endfire double dipole antenna was presented. A simplified theoretical analysis shows a that the main lobe is rather wide, and not of the same width in the E- and H-planes. The SIS mixer chip was mounted on the back side of an ellipsoidal fused silica lens. A measurement of the broadband coupling to the SIS was made with a Fourier transform spectrometer, which showed that the on-chip superconducting microstrip stubs tuned out the junction capacitance at around 460 GHz. Y-factor measurements showed a response slightly lower in frequency. The best noise temperature point was just below 500 K DSB at 435 GHz, measured with a 60 μm beamsplitter. This value should be improved if a thinner beamsplitter is used.

The 480 GHz receiver used a broadside double dipole antenna with a single SIS junction. The junction capacitance was tuned out with a short inductive stub that was terminated in a lumped capacitor. The mixer chip was mounted on the back side of a hyperhemispherical fused silica lens, and a Y-factor measurement was made. The best performance was at 470 and 4809 GHz, where the Y-factor was 2.5 dB. This gives a noise temperature of less than 200 K DSB. The bandwidth, measured at the 300 K DSB level, was more than 30 GHz.

Acknowledgements

We would like to acknowledge Harry Schaeffer for much mechanical design work (including the superconducting magnets) and Johan Wezelman for help with many measurements. Both are with the Space Research Organization, the Netherlands. We would also like to thank Niklas Rorsman of Chalmers University, Sweden, for manufacturing our E-beam masks. We also thank Dr. Errico Armandillo of the European Space Agency at ESA/ESTEC in Noordwijk, the Netherlands, for his financial support of this project through contract 7898/88/Pb/(Sc).

References

1 R. Blundell, Cheuk-Yu E. Tong, "Submillimeter Receivers for Radio Astronomy", Proceedings of the IEEE, Vol.80, No.11, Nov.1992.

2 X.Li, P.L. Richards, F.L. Lloyd, "SIS Quasiparticle Mixers with Bow-Tie Antennas", Int. J. of Infrared and Millimeter Waves, Vol.9, pp.101-103, 1988.

3 R.H. DuHamel, D.E. Isbell, "Broadband Logarithmically Periodic Antenna Structures", 1957 IRE National Convention Record, pt.1, pp.119-128.

4 J.D. Dyson, "The Equiangular Spiral Antenna", IRE Trans. Antennas Propag., Vol. AP-7, pp. 181-187, April 1959.

5 T.H. Büttgenbach, R.E. Miller, M.G. Wengler, D.M. Watson, T.G. Phillips, "A Broad-Band Low-Noise SIS Receiver for Submillimeter Astronomy", IEEE Trans. Microwave Theory Tech., Vol. MTT-36, pp. 1720-1726, Dec. 1985.

6 B. Yu. Belitsky, I. L. Serpuchenko, M. A. Tarasov, A. N. Vystavkin, "MM Waves Detection using Integrated Structure with SIS Junction, Stripline Transformer and Spiral Antenna", Extended Abstracts of ISEC-89, Tokyo, 1989, pp.179-182.

7 J. Zmuidzinas, H.G. LeDuc, "Quasi-Optical Slot Antenna SIS Mixers", IEEE Trans. Microwave Theory Tech., Vol.40, No.9, September 1992.

8 P. T. Parrish, T. C. L. G. Sollner, R. H. Mathews, H. R. Fetterman, C. D. Parker, P. E. Tannenwald, A. G. Cardiasmenos, "Printed Dipole-Schottky Diode Millimeter Wave Antenna Array", SPIE Millimeter Wave Technology, Vol. 337, 1982, pp.49-52

9 W. Chew, H. R. Fetterman, "Printed Circuit Antennas with Integrated FET Detectors for mm-Wave Quasi-Optics", IEEE Trans. Microwave Theory Tech., Vol. MTT-37, No. 3, 1989.

10 J. A. Taylor, T. C. L. G. Sollner, D. D. Parker, J. A. Calviello, "Planar Dipole-fed Mixer Arrays for Imaging at Millimeter and Sub-Millimeter Wavelenghts", Proc. of the 1985 Int. Conf. on IR and mm-Waves, 1985, pp.197-188.

11 H. Rothermel, D. Billon-Pierron, K. H. Gundlach, "An Open Structure SIS Mixer for 350 GHz", Presented at the 16th Int. Symp. of Infrared & Millimeter Waves, Lausanne, Switzerland, Aug. 1991.

12 A. Skalare, Th. de Graauw, H. van de Stadt, "A Planar Dipole Antenna with an Elliptical Lens", Microwave & Optical Tech. Letters, Vol.4, No.1, January 1991.

13 K. Uehara, K. Miyashita, K.-I. Natsume, K. Hatakeyama, K. Mizuno, "Lens-Coupled Imaging Arrays for the Millimeter- and Submillimeter-Wave Regions", IEEE Trans. Microwave Theory Tech., Vol. MTT-40, No. 5, 1992.

14 A. Skalare, H. van de Stadt, Th. de Graauw, R. A. Panhuyzen, M. M. T. M. Dierichs, "Double Dipole Antennas at 100 and 400 GHz", Proc. Third Int. Symp. on Space Terahertz Tech., Ann Arbor, Michigan, U.S.A., March 24-26, 1992.

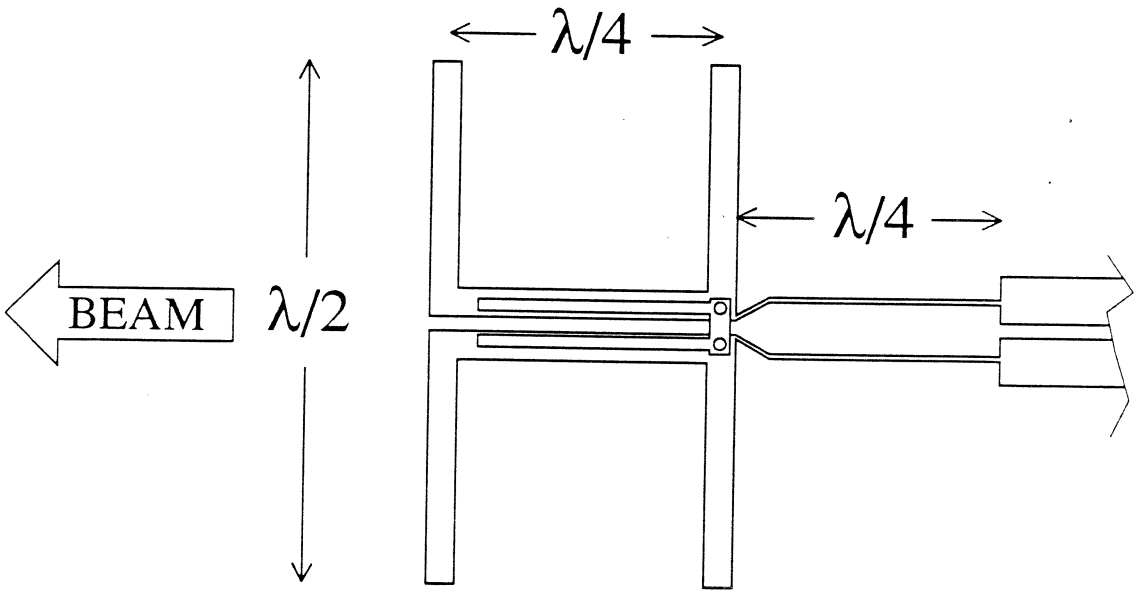

Fig. 1: The endfire double dipole antenna.

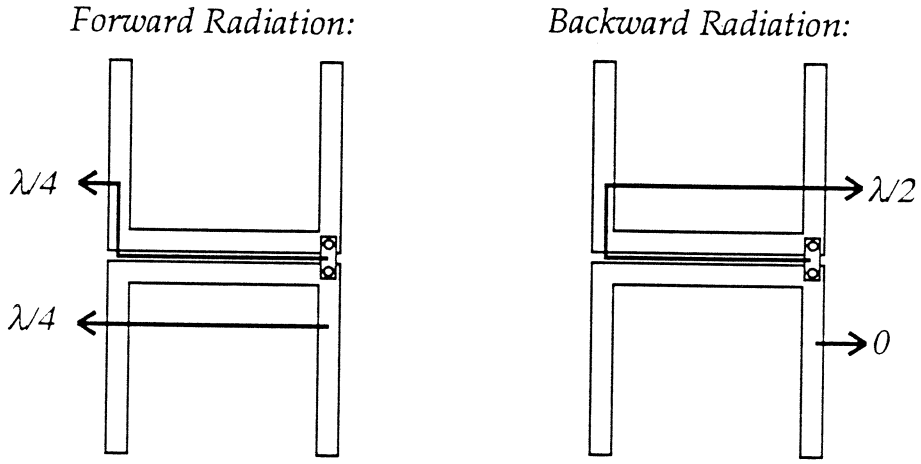

Fig. 2: The contributions from the two dipole elements add up in phase in one endfire direction, and cancel each other out in the other.

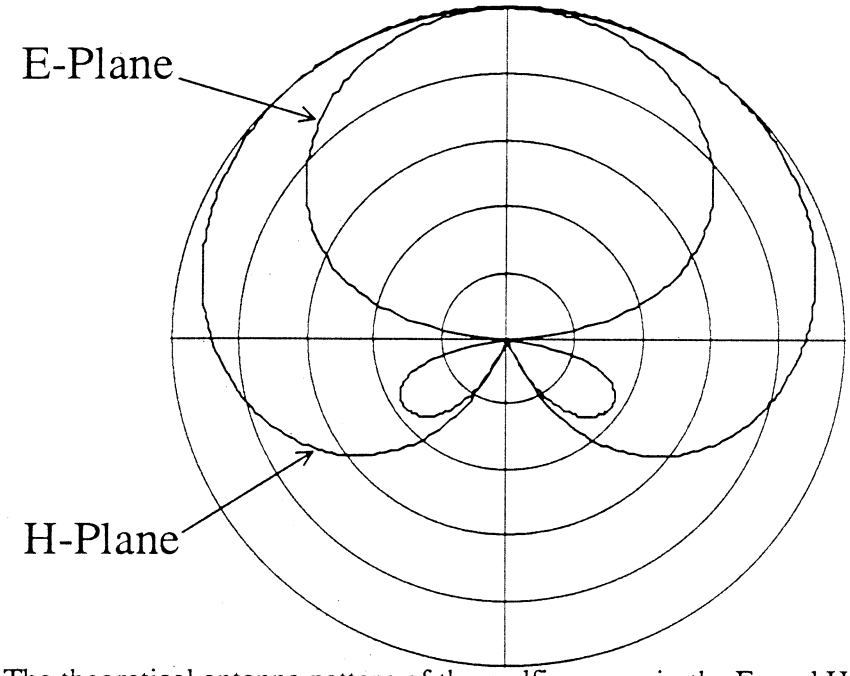

Fig. 3: The theoretical antenna pattern of the endfire array in the E- and H-planes. The radial scale is 5 dB per division.

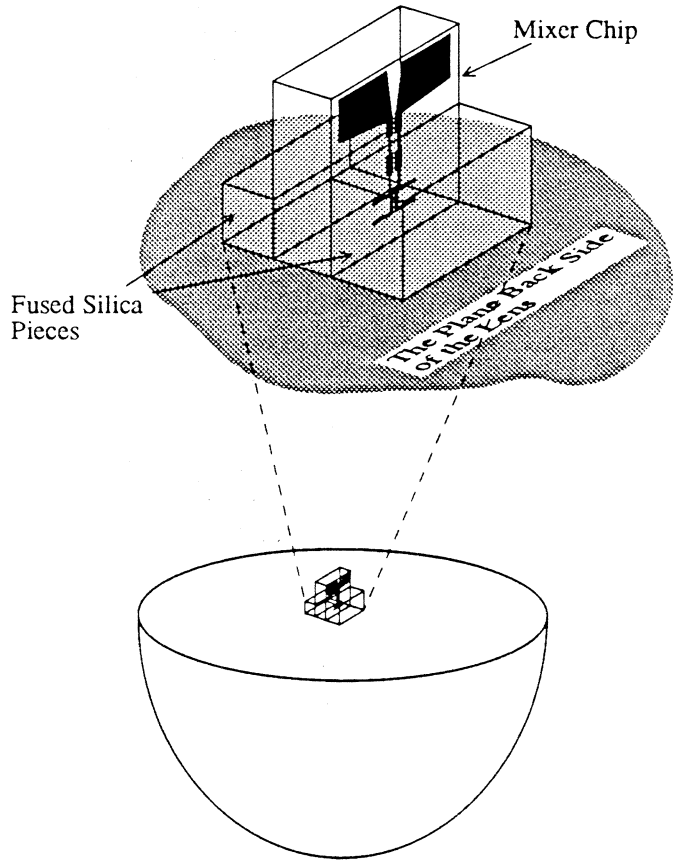

Fig. 4: How the endfire dipole chip is glued to the back plane of the lens. The figure is not true to scale.

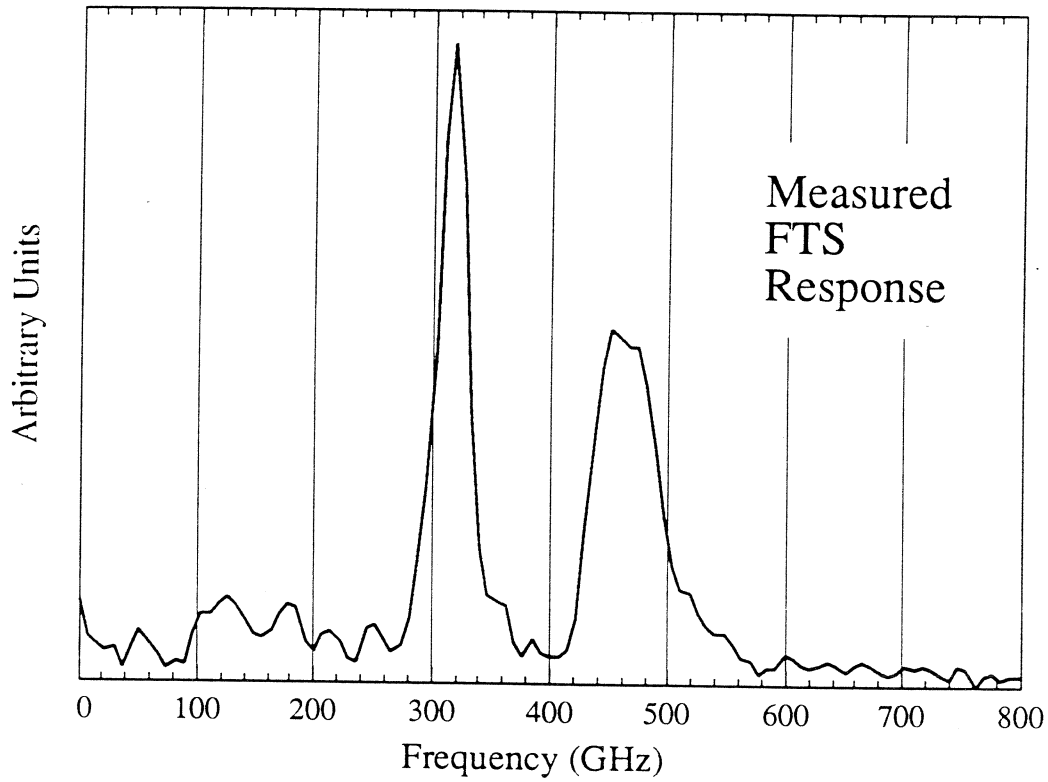

Fig. 5: Response of the SIS endfire dipole antenna chip, as measured with a Fourier transform spectrometer.

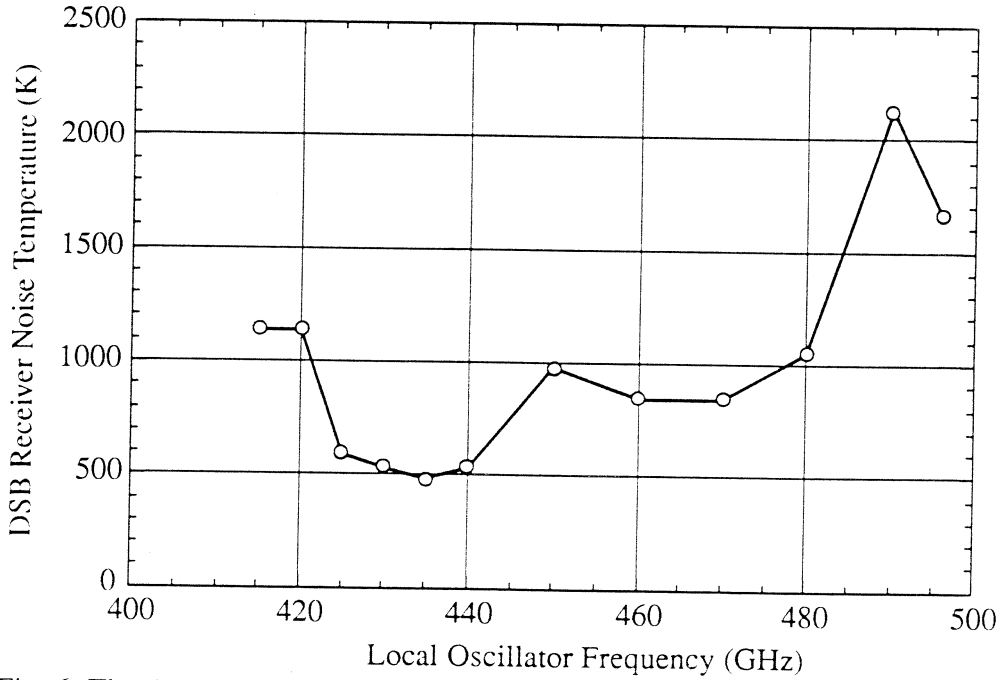

Fig. 6: The double sideband noise temperatures of the SIS endfire dipole antenna receiver.

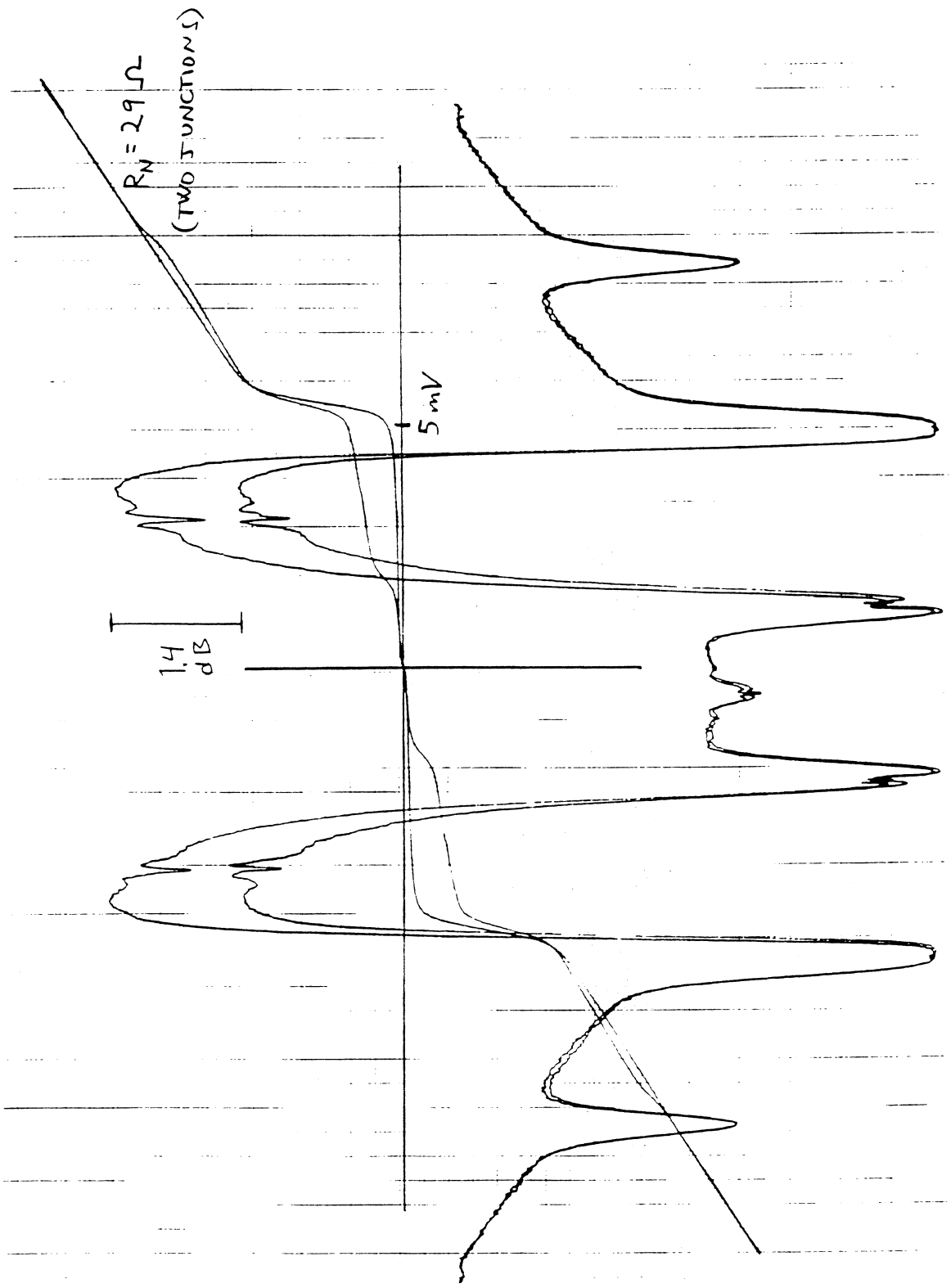

Fig. 7: Unpumped and pumped DC IV curves of the endfire antenna SIS junctions. The pump frequency was 435 GHz. Also shown is the intermediate frequency output at 4.3 GHz.

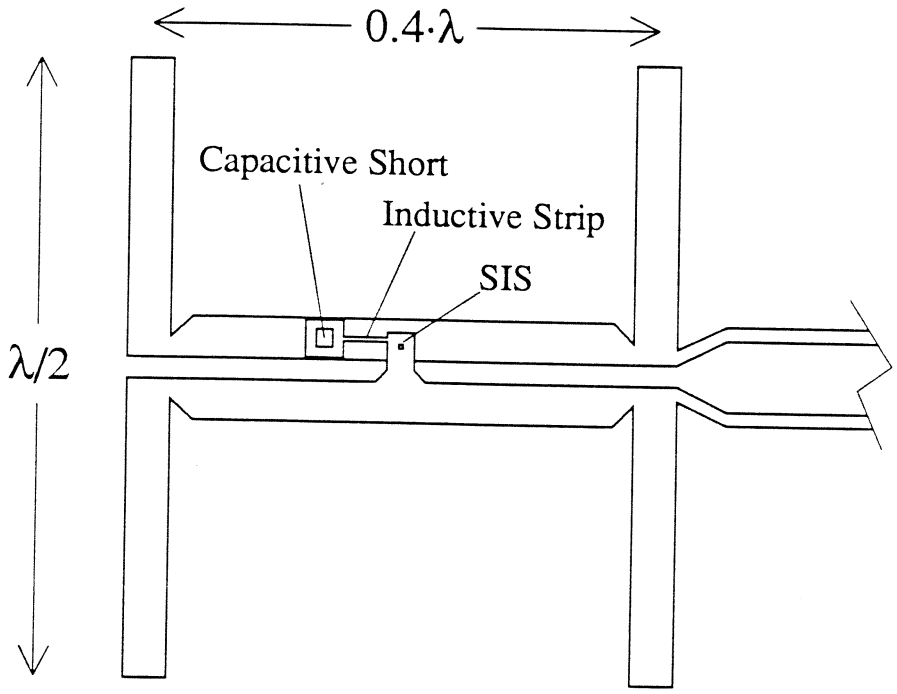

Fig. 8: The broadside dipole array antenna. "λ" is the wavelength in fused silica at 430 GHz (358 μm). All dimensions except the length of the inductive strip are shown true to scale.

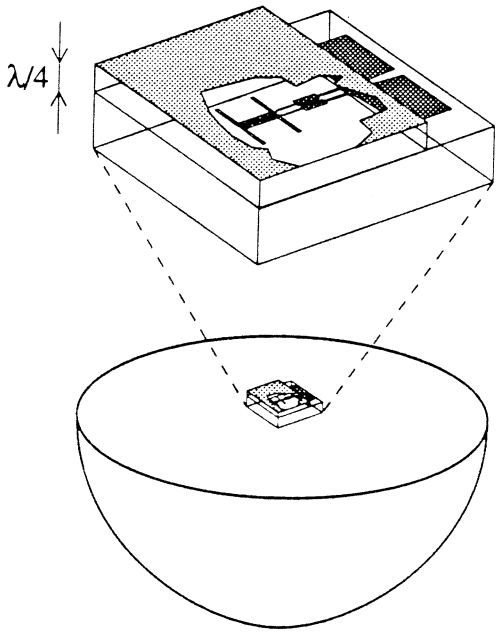

Fig. 9: A schematic view of how the broadside antenna chip is mounted to the lens. Part of the Cr/Au reflector has been removed to expose the antenna.

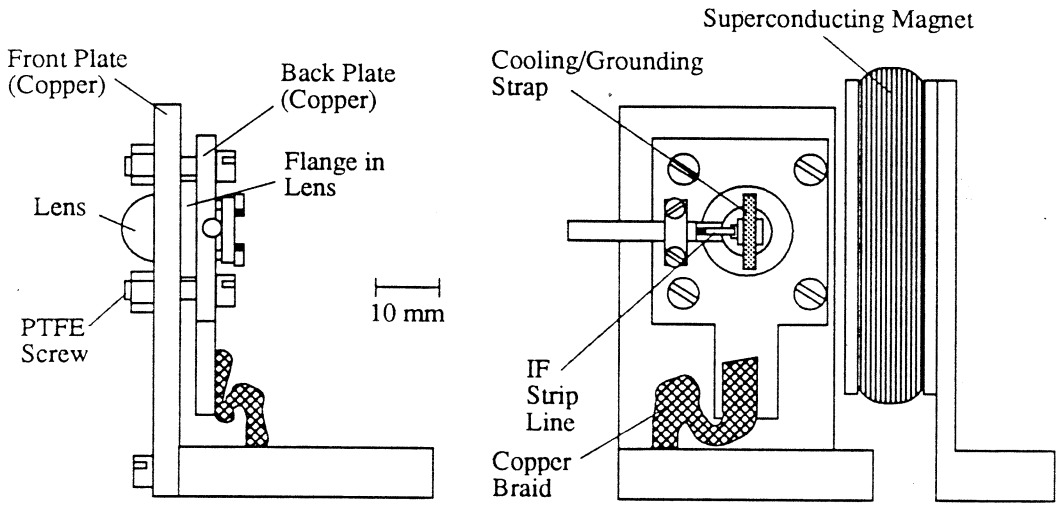

Fig. 10: The mixer fixture used in the measurements with the broadside antenna SIS chip.

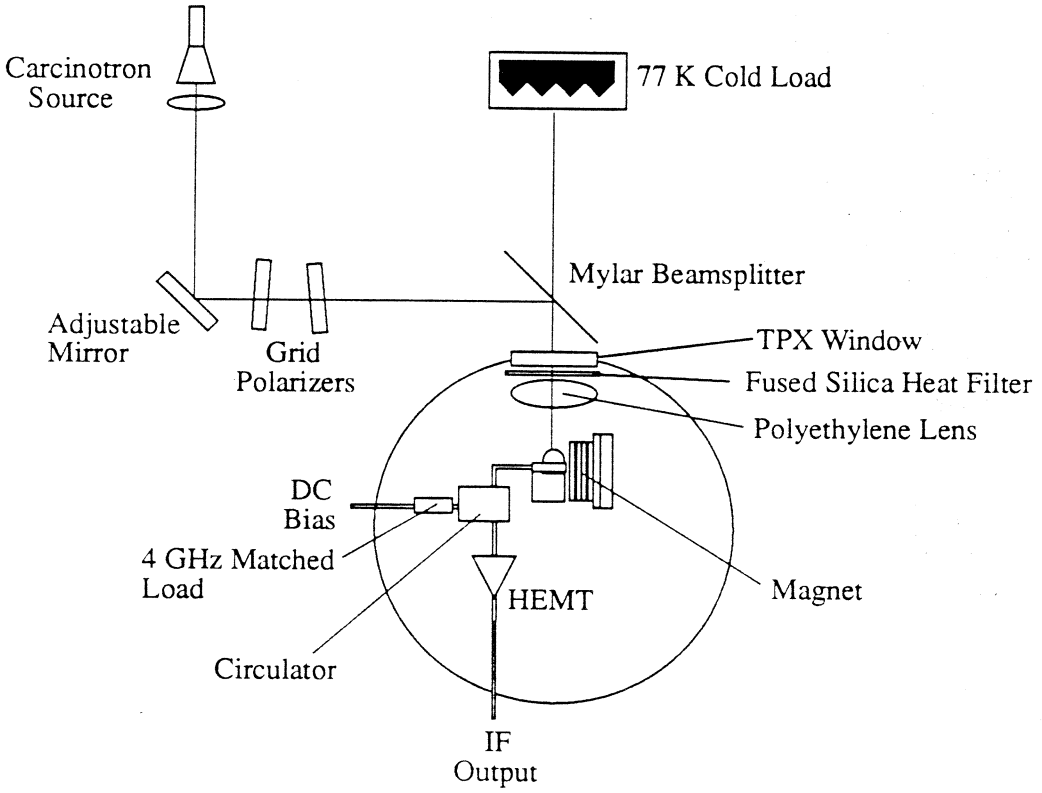

Fig. 11: The 420-496 GHz Y-factor set-up for the measurement with the broadside antenna chip.

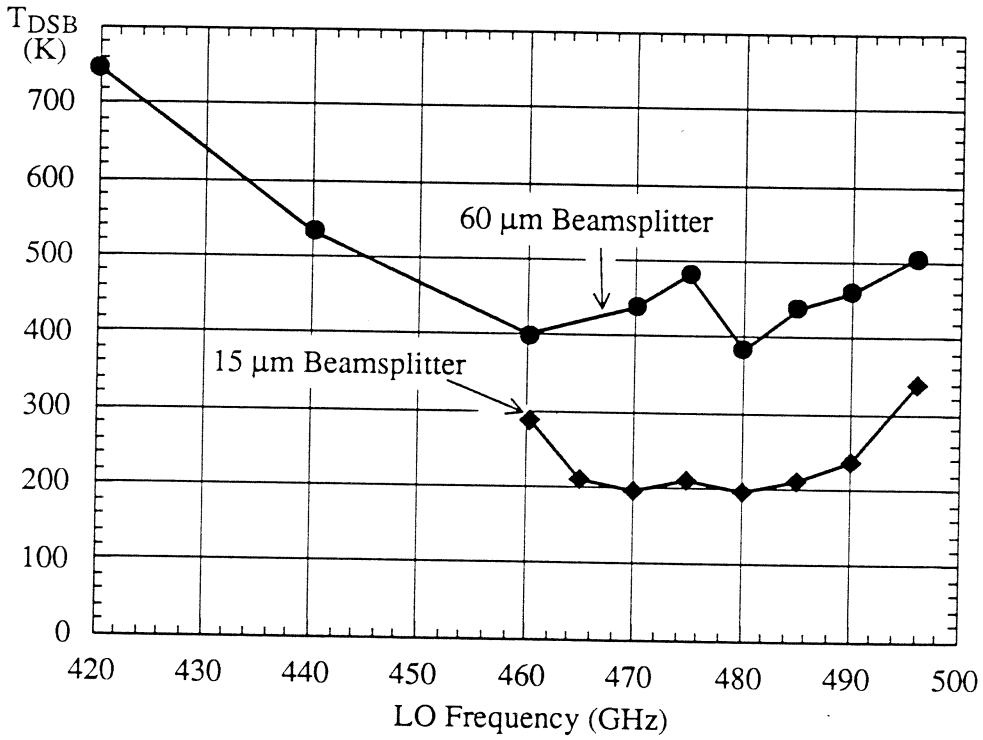

Fig. 12: Noise temperature results from the Y-factor measurements with the broadside antenna chip.

Fig. 13: Unpumped and pumped (480 GHz) DC IV curves of the broadside SIS junctions. Also shown is the intermediate frequency output at 4.3 GHz.

BROADBAND QUASIOPTICAL SIS MIXERS WITH LARGE AREA JUNCTIONS

G. Pance and M. J. Wengler
Department of Electrical Engineering
University of Rochester
Rochester, NY 14627

Abstract

We have designed and tested a broadband quasi-optical superconducting tunnel junction (SIS) mixer with integrated tuning elements. We achieve state of the art results using low critical current density, large area niobium SIS's which are commercially available from Hypres, Inc. We have performed noise measurements in the frequency range from 70 GHz to 105 GHz. The best uncorrected double sideband receiver noise is 38 K at 77 GHz, with receiver noise temperatures less than 100 K from 75 to 102 GHz.

I. Introduction

Superconducting tunnel junctions (SIS's) are used in the most sensitive detectors at frequencies from 100 GHz to 750 GHz [1]. Much of the recent progress in improving sensitivity has relied on using very small area (submicron) junctions with very high critical current densities exceeding 10 kA/cm^2 [2-5]. The large current density allows higher frequency operation of junctions, while the small junction area is necessary to match large current density junctions to moderately high impedance radiation structures. Unfortunately, submicron lithography is very expensive and not widely available, so it is time consuming and expensive to develop submicron circuits. Similarly, 1 kA/cm^2 SIS technology is well developed for digital circuit research, but higher current densities require device development separate from the larger digitally oriented efforts.

We show in this paper that large area, low current density SIS's can be used to make state of the art SIS mixers. We do this by designing our mixers for Hypres, Inc.'s standard niobium integrated circuit process. We use inductive tuning to cancel out the large capacitance of large area SIS's, and a transformer to match to high impedance antennas. We are thus able to take advantage of all of the technology development effort that has gone into digital circuits.

II. Circuit Design and Simulations

In our quasi-optical SIS receiver, the SIS junction is built integrally with a planar self-complementary log-periodic antenna on the silicon substrate [6-8]. The antenna is placed on the back of a quartz hyperhemisphere [9]. The hyperhemisphere and a teflon lens in front of it focus the radiation onto the antenna. The antenna impedance is frequency independent over several octaves and is around 76 Ω.

Tuning structures are built on one arm of the antenna which is used as their ground plane (Fig. 1). The major goal in the design of integrated tuners is a large bandwidth of good coupling. A large bandwidth design has two advantages. First, it provides a sensitive

receiver over a large frequency range. Second, it makes it likely that a particular frequency of interest will fall in the sensitive range of the receiver, even if some fabrication process parameters are different from those used in the design.

For SIS mixers without integrated tuning, it is necessary to use small area (submicron) SIS's with high current density in order to achieve good coupling over a reasonable bandwidth. Our work shows that with tuning structures, we do not require either submicron lithography or high current density to succeed. The SIS mixers we use were fabricated at Hypres, Inc. in their all-refractory niobium process. The Hypres $Nb/AlO_X/Nb$ SIS's have current density around 980 A/cm^2 and junction area of 12 μm^2. As our measurements show, we can achieve excellent results over broad bandwidths with these junctions.

The tuning circuit for the mixer we report here consists of two parts: an inductive part which tunes out junction capacitance, and a transformer which matches the junction resistance to the antenna impedance (Fig. 2). The inductive section is a combination of an open-ended radial stub and a short length high impedance microstrip line [10]. The large angle radial stub is used in order to get a broadband short on its other end. The high impedance microstrip line presents the inductance necessary to tune out the junction capacitance. As a transformer we use a quarter wavelength microstrip line which transforms the junction impedance into antenna impedance. The design presented here is applicable for different fabrication processes, and for both large and small area junctions. Table 1 shows the expected performance of the mixer with tuning circuit designed for different fabrication process parameters and different central frequencies. The 3 dB bandwidth shown is the frequency range over which the particular circuit has coupling to the antenna exceeding 0.5.

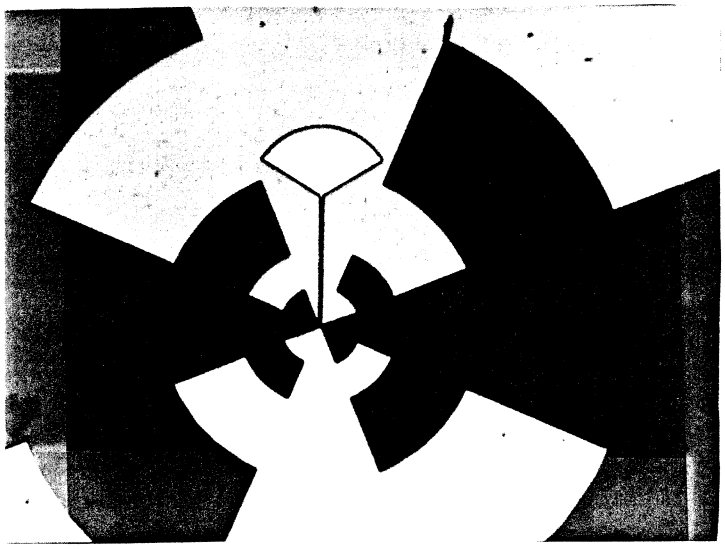

Fig. 1. Self-complementary log-periodic antenna with integrated superconducting tuning structure.

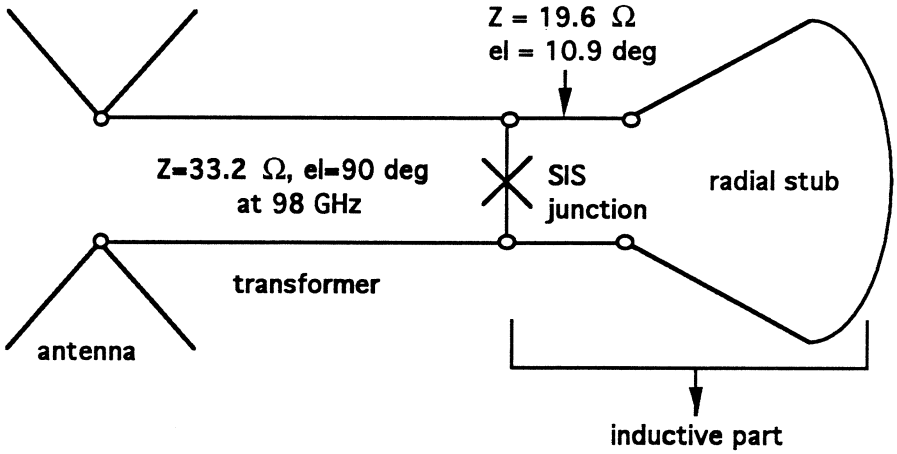

Fig. 2. The electrical circuit of the design, where Z is the characteristic impedance of the microstrip line and el is the electrical length at 98 GHz.

Central Frequency [GHz]	3 dB bandwidth [GHz]		
Jc A	1000 A/cm^2 12 μm^2	4000 A/cm^2 12 μm^2	4000 A/cm^2 1 μm^2
98	38	48	82
230	29	55	144
492	18	39	167

Table 1. Expected 3 dB bandwidth of the circuit shown in Fig. 2, designed for different fabrication process parameters and at different frequencies. Coupling at the central frequency is kept the same and it is equal to 0.9.

We used the RF simulation program *Libra* [11] to optimize circuit elements for the best coupling and the largest bandwidth. The junction is modeled as an impedance $1 / (1/R_{rf} + j\,\omega\,C_{rf})$. For typical biasing conditions R_{rf} has a value close to the normal state resistance (R_N), and the major part of the parasitic reactance is due to the geometrical junction capacitance (C_j), so that we used those values in the simulation. Junction parameters used in the design are $R_{rf} = R_N = 26.7\ \Omega$ and $C_{rf} = C_j = 432$ fF. The circuit was designed to have the best coupling of 91 % at 98 GHz and a 3 dB bandwidth of 34 GHz (Fig.3). A small mismatch at the central frequency is included to provide a larger bandwidth of the tuning circuit. After the dc IV curve of this circuit is measured, the actual junction parameters are used to run simulation program. The junction RF impedance calculated from the dc IV curve is $R_{rf} = 6\ \Omega$ and $C_{rf} = C_S + C_j = 544$ fF, where C_S is the capacitance calculated from the quantum susceptance, with the bias point in the middle of the first photon step and optimum local oscillator (LO) power [12]. Since the values for R_{rf} and C_S did not vary much at different frequencies, we assumed for simplicity R_{rf} and C_S to be constant. For the junction geometrical capacitance we have used 38 fF/μm^2, which is the typical value for the

capacitance in Hypres fabrication process. The fabricated junction size is 12.2 μm^2 and the junction normal state resistance is 18.2 Ω. The coupling curve with the actual junction parameters is shown in Fig. 3.

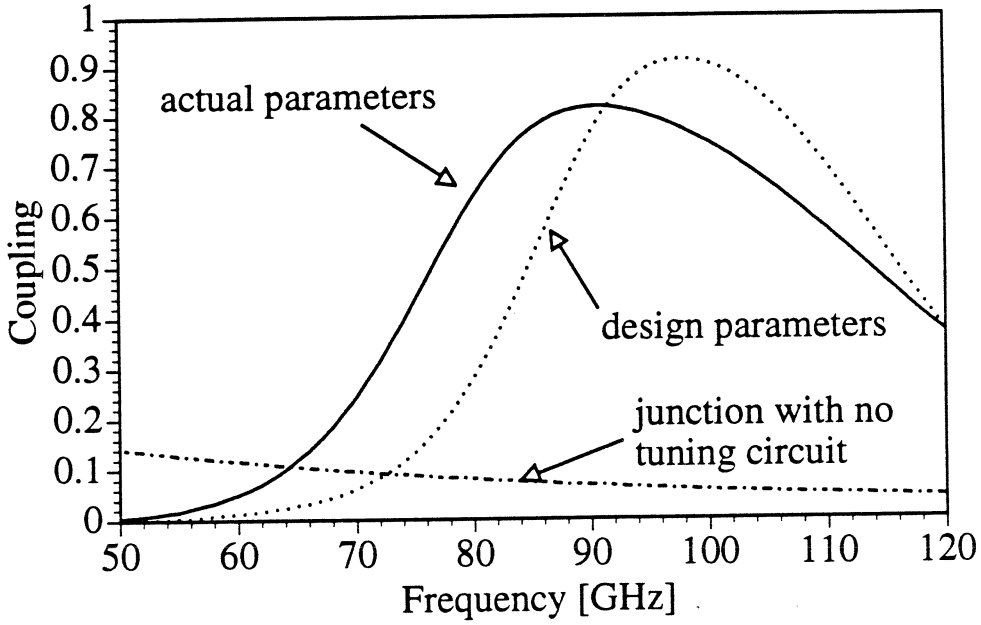

Fig. 3. Coupling coefficient between the SIS junction and the self-complementary log-periodic antenna

III. Results

The dc IV Curve Measurements

The simplest way to check the central resonance frequency of the tuning circuit is to measure its dc IV curve. We show the IV curve for dc voltage up to 0.97 mV in Fig. 4. The resonant step occurs because the tuning structure is impedance matching Josephson junction oscillations to the antenna. We translate the voltage range of this resonance step to a frequency range using the Josephson frequency relation $f_J = 2eV_0/h$. The dc IV curve in Fig. 4 shows a resonant step in the frequency range from 56 GHz - 98 GHz. The *Libra* simulation of the actual circuit shows 3 dB bandwidth from 76 GHz to 114 GHz (Fig. 3). There are a number of fabrication parameters in our real circuit that could account for the difference between theory and measurement. For example, a larger value of SIS junction capacitance than the one assumed (38 $fF/\mu m^2$) would account for the lower frequency resonance which we see.

Heterodyne Receiver Measurements

In the heterodyne receiver measurements we used a tunable Gunn oscillator as a LO, which has operation range from 70 GHz to 105 GHz. In our receiver we couple the input radiation through a set of lenses (Fig. 5). The beam from the LO is first focused by the teflon lens and then it reflected from the mylar beamsplitter toward the mylar window in the bottom of the receiver. Further on, the beam passes through the quartz window built on the 77 K shield, and through the teflon lens, 1 mil thick black polyethylene, and 40 mil thick quartz. Finally, the beam is focused by the quartz hyperhemisphere lens onto the center of

the log-periodic antenna. For the hot / cold load measurements we used absorber at 295 K and 77 K. The receiver noise temperatures we report are those measured at the place of hot / cold signal source. We make no corrections for any beam losses between the hot and cold loads, and the mixer itself.

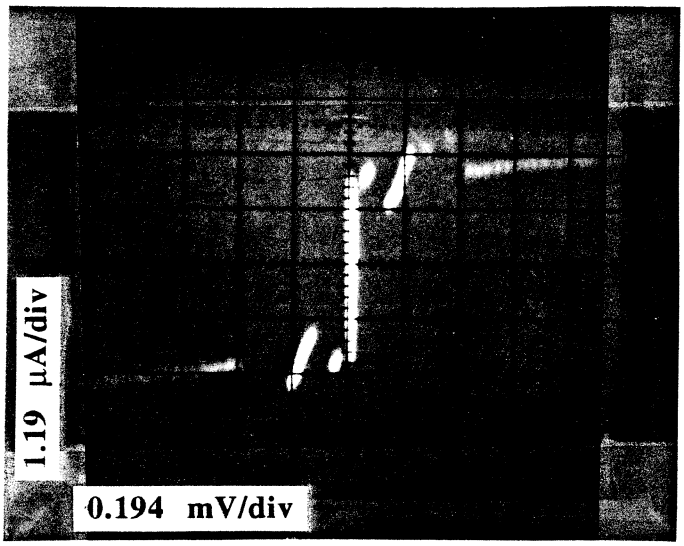

Fig. 4. The dc IV curve of the mixer with tuning structures. The self induced resonant step is in the frequency range from 56 GHz to 98 GHz.

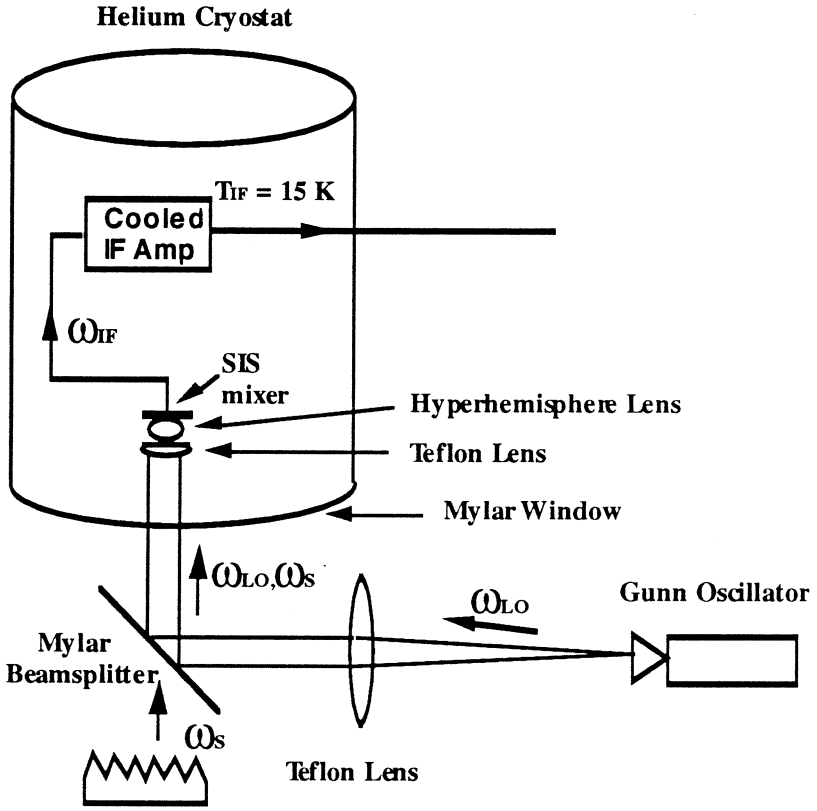

Fig. 5. The experimental setup for the hot / cold load measurements.

The dc IV curve of the mixer with the tuning structures shows flat photon steps at frequencies larger than ~ 95 GHz and steps with negative slope at some frequencies lower then 95 GHz (Fig. 6). On the first photon step we were not able to find the optimum noise temperature at all frequencies, due to the unstable bias at some regions of the LO power. Fig. 7 shows measured receiver noise temperature on the first photon step. All values that are shown in Fig. 7 are achieved with stable bias, but those marked with crosses are the frequencies where we had regions of unstable bias, so we could not obtain the noise temperature for all LO power values. The IF amplifier we use in the setup has noise temperature of T_{IF} = 15 K. The best double sideband receiver noise temperature we obtained is 38 K at the LO frequency of 77 GHz. The calibrated mixer noise at that point is 14 K with the mixer gain of -1.3 dB.

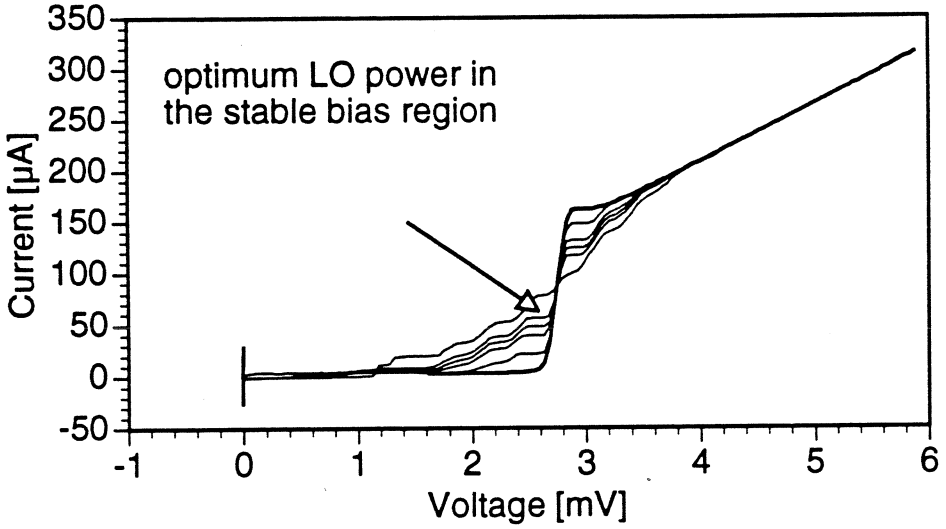

Fig. 6. The dc IV curve of the SIS mixer with integrated tuning structures. Bold line represents the dc IV curve when no LO is applied. The curve with the optimum LO power is marked on the chart. The LO frequency is 77 GHz. All measurements were made at 4.2 K.

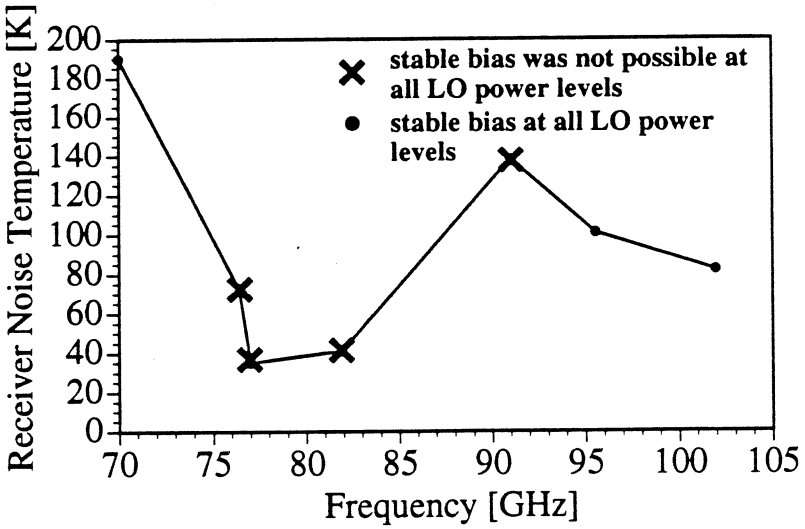

Fig. 7. Double sideband receiver noise temperature on the first photon step.

We measured the noise temperature on the second photon step where the bias was stable in the whole LO frequency range, except for one point which we skipped in the measurement. The best receiver noise temperature we obtained on the second photon step is $(T_R)_{DSB}$ = 180 K at the frequency of 89.7 GHz. The calibrated mixer noise is 141 K and the mixer gain is - 4.1 dB. As a reference, we measured a mixer with no tuning structures. In this case, the 12.2 μm^2 junction is fabricated directly at the center of the log-periodic antenna. Due to the large parasitic capacitance, photon induced steps are almost invisible in the dc IV curve. The minimum mixer noise temperature obtained with this circuit is 1478 K with the mixer gain of - 8.2 dB, when biased on the second photon step and at a frequency of 89 GHz.

The simple photodiode theory [1] predicts that the mixer noise temperature on the first photon step is inversely proportional to coupling between the SIS junction and the source. In Fig. 8 we compared the coupling obtained from the *Libra* simulation to C/T_{MIX} where T_{MIX} is the calibrated mixer noise temperature on the second photon step and C is the normalization constant. An increase in the mixer noise at the frequencies close to 70 GHz is probably caused by the performance of the antenna, which is designed to operate at a minimum frequency of ~ 72 GHz. The central frequency of the real coupling curve is, we believe, shifted toward smaller frequencies, as evidenced from the dc IV curve. These two curves do not fit very well, but they definitely show strong dependence between the noise temperature and the coupling. Using this measurement we estimated the 3 dB bandwidth of our tuning circuit to be ~ 18 GHz.

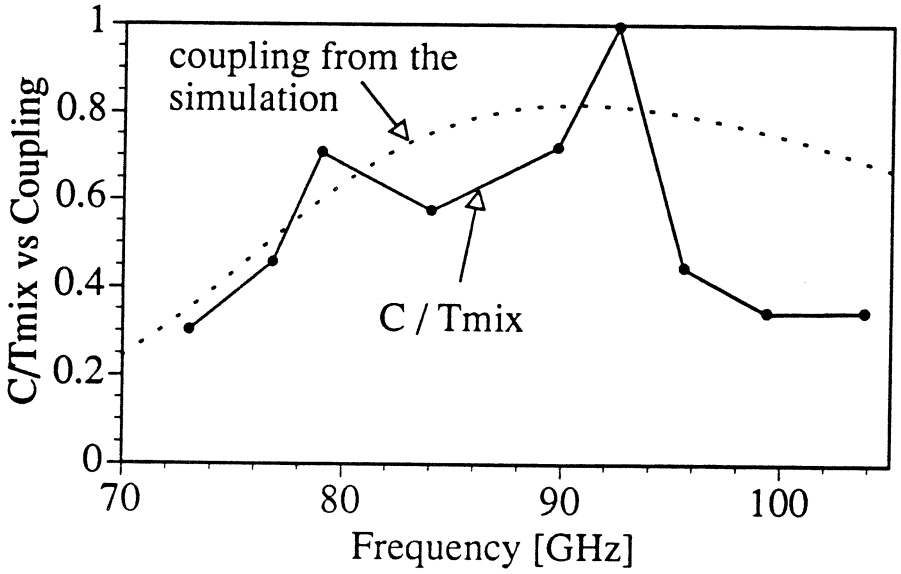

Fig. 7. Comparison between the coupling curve calculated from the *Libra* simulation program and C/T_{MIX} where T_{MIX} is the calibrated mixer noise temperature on the second photon step and C is the normalization constant.

Conclusion

We have presented results for an SIS receiver which achieves less than 100 K receiver noise over a 27 GHz bandwidth with the minimum values around 77 GHz. This is achieved using a quasioptical coupling scheme, and a fairly noisy 15 K IF amplifier. It is

achieved using low critical current density (980 A/cm^2), large area (12 μm^2) SIS junctions.

We have demonstrated that extremely low noise, fairly broad band millimeter receivers can be achieved using large area, low current density SIS junctions. This should greatly reduce the cost of producing and maintaining SIS mixers. It should make them more attractive for space-based astronomical platforms.

We have achieved these results by careful design of appropriate superconducting tuning elements. In particular, we tune out the very large parasitic capacitance of the SIS, and we use a stripline transformer to match the low junction impedance to the higher antenna impedance. We have demonstrated that we can accurately design superconducting tuning structures for millimeter wave mixers using Hypres's commercial technology.

We believe that similarly excellent results will be possible using large area junctions up to frequencies of at least 500 GHz. As we get to higher frequencies, going to higher current density junctions will allow higher bandwidth designs, but we are still capable of 18 GHz bandwidth even with 1000 A/cm^2 junctions.

Acknowledgements

We are pleased to acknowledge Hypres, Inc. for the SIS mixers fabrication. We also thank N. Dubash for many helpful discussions and for some calculations using his SIS mixer theory programs. This work was supported by a Presidential Young Investigator Award, National Science Foundation grant ECS-8857868. Gordana Pance has been partially supported by the IEEE Microwave Theory and Techniques Society Graduate Fellowship.

References

1. M. J. Wengler, "Submillimeter -wave detection with superconducting tunnel diodes", *Proceedings of the IEEE*, vol. 80, no. 11, pp 1810-1826, Nov. 1992.

2. J. W. Kooi, M. Chan, T. G. Phillips, B. Bumble and H. G. Leduc, "A low noise 230 GHz heterodyne receiver employing .25 μm^2 area Nb/AlO$_x$/Nb tunnel junctions", *IEEE Trans. Microwave Theory Tech.*, vol. 40, pp. 812-815, May 1992.

3. T. H. Büttgenbach, H. G. LeDuc, P. D.Maker and T. G. Phillips, "A fixed tuned broadband matching structure for submillimeter SIS receivers", *IEEE Trans. of Applied Supercond.*, vol. 2, pp. 165-175, Sept. 1992.

4. C. K. Walker *et al.*, "A low-noise 492 GHz SIS waveguide receiver", *International Journal of Infrared and Millimeter Waves*, vol. 13, pp. 785-798, June 1992.

5. G. de Lange *et al.* , "Low noise Nb/AlOx/Nb SIS waveguide mixers at 492 GHz and 345 GHz", *IEEE Trans. on Applied Superconductivity,* 1993, in press.

6. G. Pance, N. Dubash and M. J. Wengler, "Quasioptical SIS mixer with broadband integrated tuning elements", *IEEE Trans. on Applied Superconductivity,* 1993, in press.

7. T. H. Büttgenbach, R. E. Miller, M. J. Wengler, D. M. Watson and T. G. Phillips, "A broad-band low-noise SIS receiver for submillimeter astronomy", *IEEE Trans. Microwave Theory and Technique*, vol. 36, pp. 1720-1726, 1988.

8. M. J. Wengler, N. B. Dubash and G. Pance, "Josephson Effect Gain and Noise in SIS Mixers", *IEEE Trans. Microwave Theory and Technique*, vol. 40, no. 5, pp. 820-826, 1988.

9. M.J. Wengler, D.P. Woody, R.E. Miller and T.G. Phillips, "A low noise receiver for millimeter and submillimeter wavelengths", *International Journal of Infrared and Millimeter Waves*, vol. 6, pp. 697-706, Aug. 1985.

10. G. Pance and M.J. Wengler, "Integrated Tuning Elements for Millimeter and Sub-Millimeter SIS Mixers", *Proc. of 1992 MTT-S Symp.*, 1992.

11. EESof, Inc., Westlake Village, CA.

12. N.B. Dubash, G. Pance and M.J. Wengler, "Photon Noise in the SIS Detector", *Proc. of Fourth International Symposium on Space Terahertz Technology*, March 1993.

A Planar SIS Receiver with Logperiodic Antenna for Submillimeter Wavelengths

F. Schäfer*, E. Kreysa*
T. Lehnert**, and K.H. Gundlach**

* Max-Planck-Institut für Radioastronomie, Bonn, Germany

** Institut de Radioastronomie Millimetrique,
St. Martin d'Heres, France

We describe a quasi-optical SIS receiver, which is intended to be part of a combined Schottky/SIS system in the submm wavelength range, for the Kuiper Airborne Observatory. The SIS receiver employs a logperiodic antenna and a diffraction limited substrate-lens to couple to the incoming radiation. The antenna's amplitude and phase characteristics were measured at microwave frequencies with a scaled modell (x47) of the antenna-lens combination in the E, H and two diagonal planes. Fig. 1 shows as a representative result the E- and H-plane data taken at 12.4 GHz. From these measurements we calculate a main beam efficiency better than 85 %.

Currently we use single 1.3 μm^2 Nb-Al/AlO_x-Nb junctions fabricated with standard optical lithography techniques [1] giving an ωRC-product of roughly 10 at 345 GHz and 17 at 584 GHz. A lumped inductor is integrated parallel to the junction to compensate the junction capacitance. It is realized by terminating a short piece of superconducting transmission line with a radial stub. The frequency response of the SIS junction with integrated tuner for 345 GHz was measured using the SIS receiver as video detector in a commercial fourier transform spectrometer. The result of this measurement corresponds to resonances that can be found in the DC IV-curves of tuned junctions [2]. We have observed resonances corresponding to frequencies up to 660 GHz in the DC-IV-curve of tuned junctions with lower current density which indicates that the tuning circuit should still work properly up to that frequency.

As a first verification of the system at a lower frequency a heterodyne measurement at 345 GHz was made. An uncorrected DSB receiver noise temperature of 330 K was achieved. We used a Martin-Puplett Diplexer for injection of the LO power supplied by a solid-state source. No further efforts were taken to improve this noise temperature.

At 584 GHz a DSB receiver noise temperature of 900 +/- 70 K has been obtained recently. The conversion loss was measured to be 15.5 +/- 0.5 dB. The IF amplifier had a noise temperature of 6 +/- 0.5 K at 1.4 Ghz, reflection loss at the output of the mixer was around 1.5 dB. All measurements were taken with 60 MHz IF bandwidth. In Fig. 2 the IV characteristic of the junction with applied magnetic field is shown together with the receiver IF output power for hot/cold loads and laser LO power applied at 584 GHz by means of a 25 μm Mylar beamsplitter. The noise temperature is corrected for the measured loss of 20 % of a fluorogold-sheet provisionally placed in front of the cryostat vacuum window at 300 K to avoid supression of the junctions energy-gap by Near-IR-radiation.

An optically pumped far infrared ringlaser developed for the KAO-Schottky system supplied the local oscillator power at 584 GHz using HCOOH as FIR laser gas [3]. An active stabilization loop controls the CO_2 laser frequency [4]. A stability measurement of the overall system was made in the laboratory and is shown in Fig. 3. The upper trace shows

the DC current flowing through the junction versus time for constant voltage bias at 2 mV. It is a direct measure for the LO-power applied to the junction. The lower trace is the corresponding receiver IF-output power for a 295 K load at the receiver input. The vertical jumps on both traces indicate the points where the LO-power was restored by varying the attenuation in the LO-path. The main effect seen is a slow drift in LO power which is mainly due to a leak in the laboratory version of the ringlaser and could be easily removed with an active stabilization loop maintaining constant DC current through the junction [5]. An additional effect adding to the drift is the slow condensation of water on the cryostat window with the current IR blocking of the cryostat.
The measurement indicates the feasability of using a FIR laser as local oscillator source for SIS receivers which will be an important issue at higher frequencies or for arrays.

Acknowledgements

This work was supported by Deutsche Agentur für Raumfahrt-Angelegenheiten (DARA) under contract FKZ 50 00 9102

References

[1] K.-H. Gundlach, T. Lehnert, D. Billon-Pierron, M. Voss, P. Pasturel, "Preparation and properties of Nb/Al SIS and SIN junctions for mm and submm radioastronomical receivers", Proc. of an ESA Symposium on Photon Detectors for Space Instrumentation, pp. 313-316, ESA/ESTEC, Noordwijk, The Netherlands, Nov. 10-12, 1992

[2] T. Lehnert, F. Schäfer, K.-H. Gundlach, "Resonance effects in Josephson tunnel junctions with integrated tuning structures", submitted to the Journal of Applied Physics

[3] H.K.E. Stadermann, P.B. van der Wal, "Research on an optically pumped FIR Ringlaser", Conf. Dig. 16th Intl. Conf. on Infrared and Millimeter Waves, Lausanne, Switzerland, pp. 112-113, August 26-30, 1991

[4] H. Stuer, diploma-thesis, MPIfR Bonn, 1992

[5] S.K. Pan, M.J. Feldman, A.R. Kerr, E.S. Palmer, J.A. Grange, P. Timbie, "Superconducting tunnel junction receiver for 2.6 mm", Conf. Dig. 8th Intl. Conf. on Infrared and Millimeter Waves, M 6.2, 1983

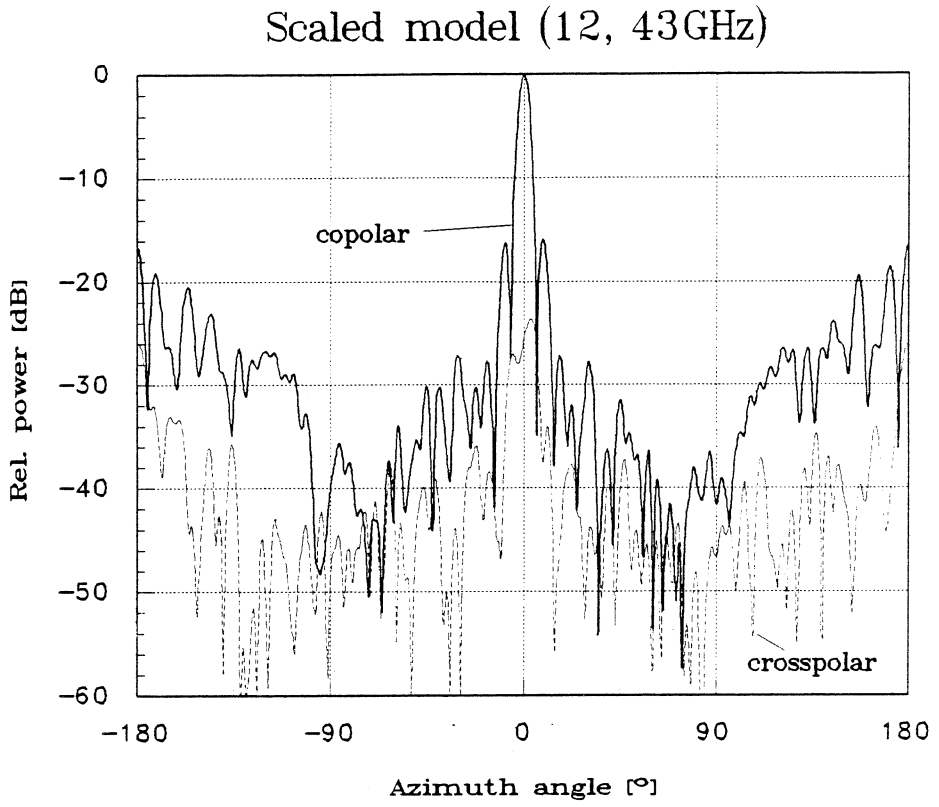

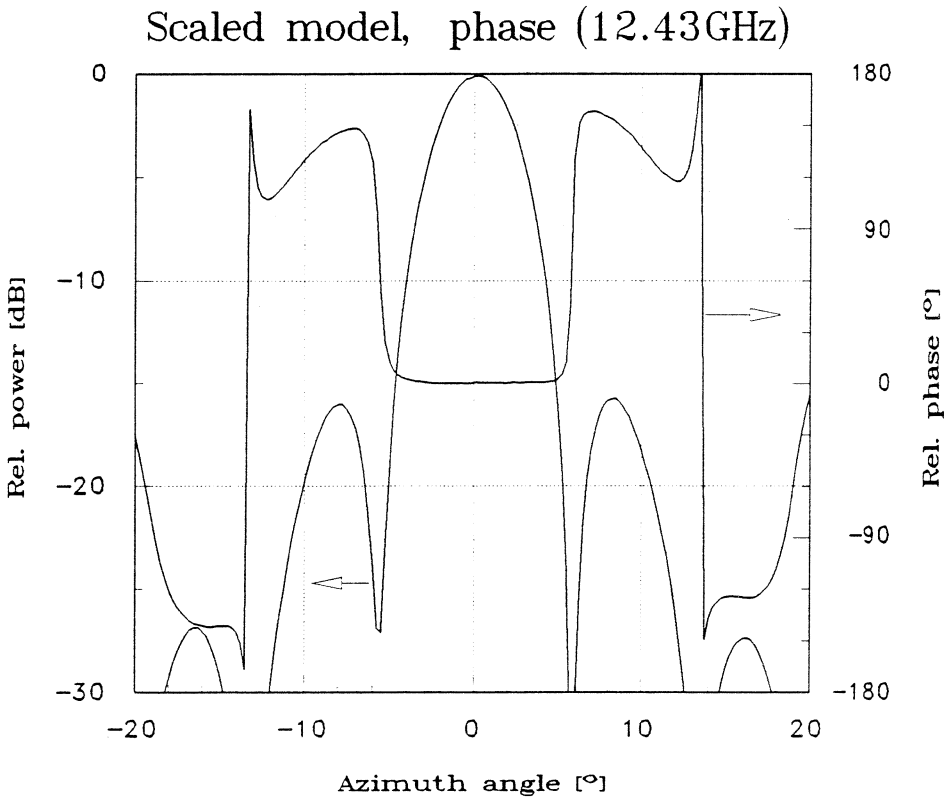

Figure 1a Scaled measurement of the antenna's E-plane characteristic at 584 GHz

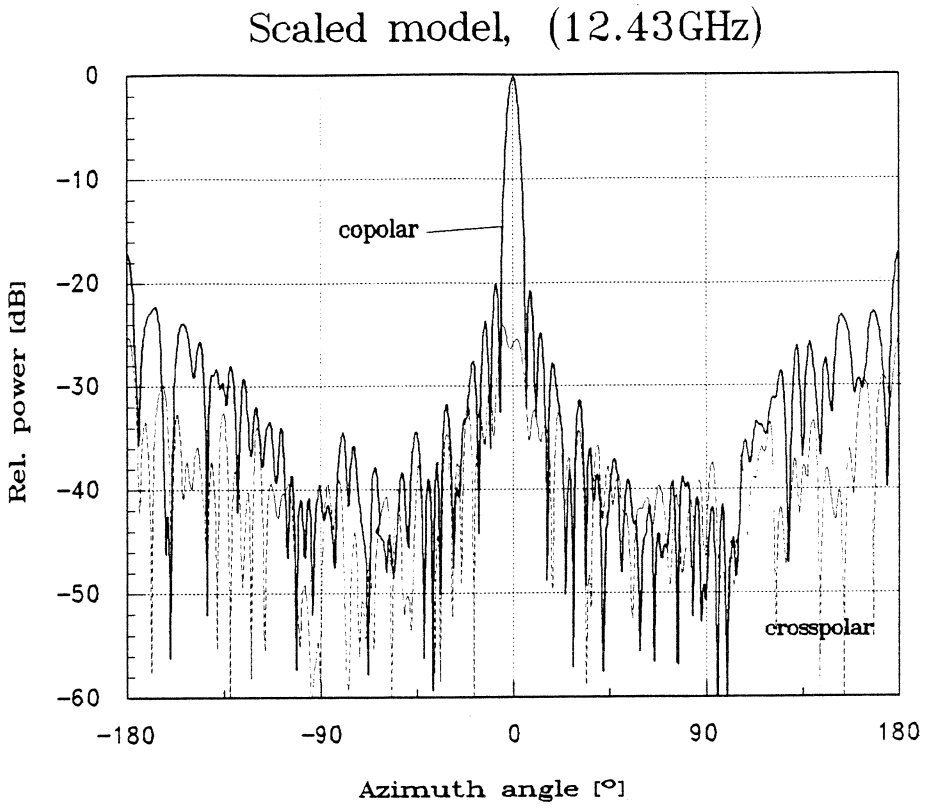

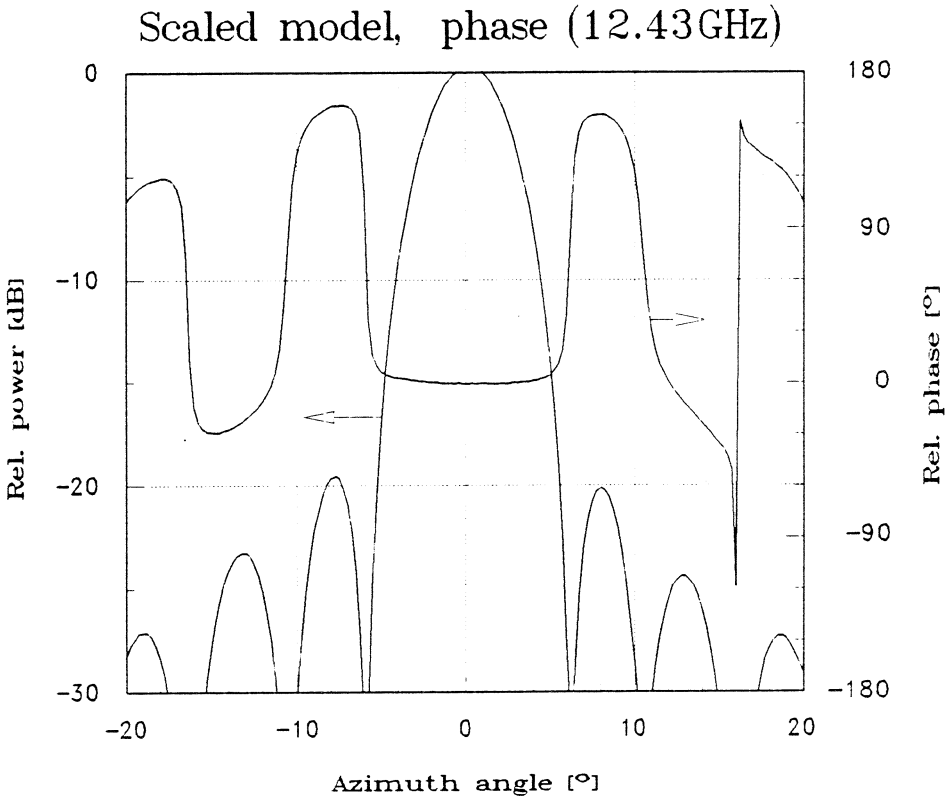

Figure 1b Scaled measurement of the antenna's H-plane characteristic at 584 GHz

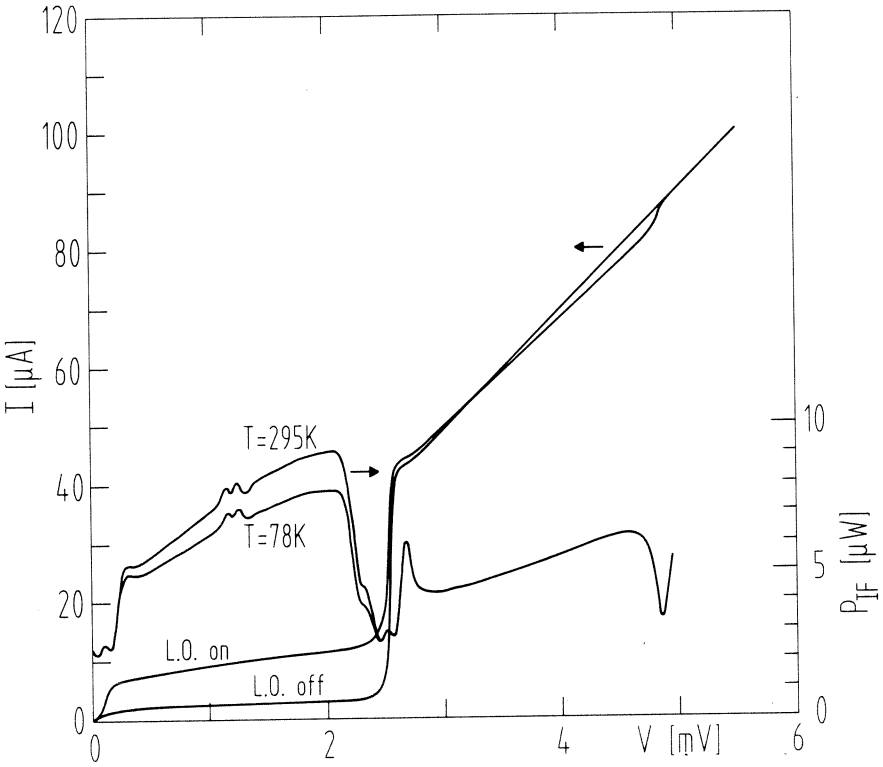

Figure 2 IV characteristic of the junction without and with applied Laser-LO at 584 GHz and receiver IF output for hot and cold loads at the input. A magnetic field is applied.

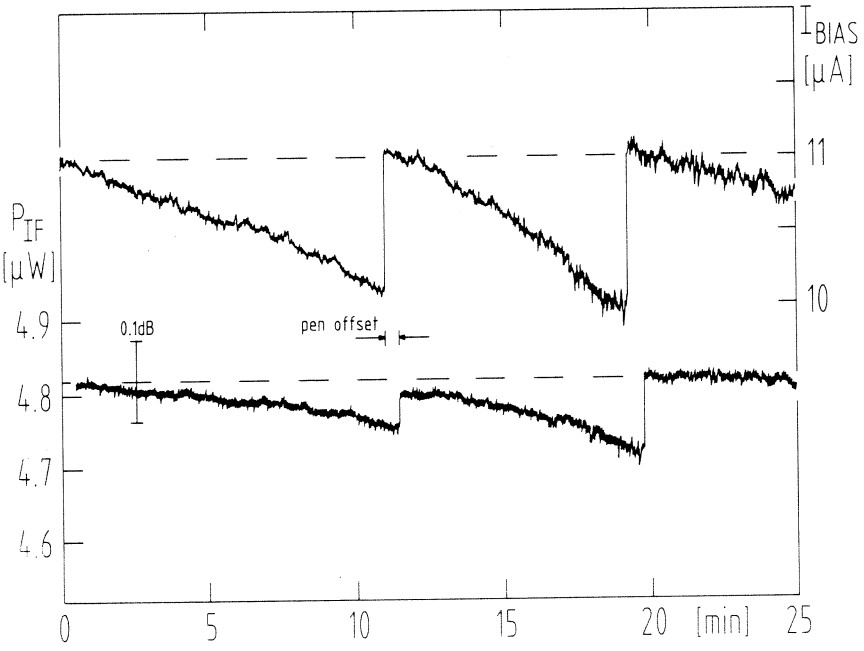

Figure 3 Stability measurement of the overall system with Laser-LO at 584 GHz

NUMERICAL AND SCALE MODELLING OF A BROADBAND WAVEGUIDE-TO-MICROSTRIP COUPLING STRUCTURE FOR A 100 GHZ SIS MIXER

Guillermo F. Delgado, Joakim F. Johansson, and Nicholas D. Whyborn

Department of Radio and Space Science
with Onsala Space Observatory
Chalmers University of Technology
S-412 96 Gothenburg, Sweden

ABSTRACT

Recently, interest has arisen in the development of fixed-tuned SIS mixers with a full waveguide-band bandwidth. There are many reasons for developing a broadband structure with a performance comparable to that of mechanically tuned ones, the main ones being the need to eliminate the risk of a mechanical failure (*e.g.* space-borne applications) and reducing the numbers of parameters to set when changing operating frequency (*e.g.* array receivers).

Nowadays, with the availability of powerful software tools such as the Hewlett-Packard HP85180A High-Frequency Structure Simulator (HFSS) package [1], it is possible to quite accurately model the coupling structure on a computer. But, in order to do this, we have to know to what extent we can rely on the simulations.

In this paper we report a comparison between scale model measurements of a broad band waveguide-to-microstrip coupler and the predictions given by a numerical model using the HFSS package.

We find that the computer modelling, though slow, gives results that are in good agreement with the measured performance of the scale model structure. Moreover, the simulations allow us to modify some parameters that otherwise would be difficult to change, such as the properties of the dielectrics and metals. This enables us to model the behaviour of more realistic mixer coupling structures, *e.g.* losses, cooled dielectrics, *etc.*

The relative advantages of each modelling method are reviewed and a broadband waveguide-to-microstrip coupler design is presented in this paper.

INTRODUCTION

There is no doubt that present coherent broadband millimeter and submillimeter wave detection is lead by the SIS mixer in terms of receiver noise temperature. There are also many groups around the world working on the improvement of this technology to guarantee that this dominance will continue, at least for the coming years [2, 3].

So far, most of the mixer designs have relied on experience gained with Schottky diode mixers that were the workhorse for sensitive receivers during the last decades. However, the matching of an SIS structure imposes different conditions on the coupling structure to those

imposed by Schottky diodes. Two approaches have been taken to couple the radiation to the SIS detector: quasioptical techniques and waveguide coupling structures.

Quasioptical techniques couple the radiation directly to the SIS detector via lenses or planar antennas, and have advantages in terms of reduced size, easy planar integration and series fabrication, but they still lack the efficiency that waveguide coupling structures have and this is a crucial factor in the design of sensitive detectors for radio astronomy.

For the mixers being built as part of the development of an imaging receiver we decided on a waveguide coupling to the SIS structure, thus we concentrate our work on the design of a transition between waveguide and microstrip and, as such, this transition should fulfil the following requirements [4]:

- Low return loss
- Low insertion loss
- Full waveguide-band bandwidth
- Easy integration to the microstrip
- Straightforward mechanical reproduction

The first step in solving the coupling problem is the necessity of matching the highly reactive component inherent to SIS junctions, so earlier designs were all based on the use of at least one (often two) backshorts. It became clear later that there were cleverer approaches to solve this problem, and the idea of embedding the tuning elements on the same substrate as the junction proved to be useful [5]. Now it remained to find the appropriate geometry of the mixer cavity and the coupling structure to have a mixer with no tuning elements.

Several different techniques have been presented elsewhere [6, 7], but they do not necessarily match what we consider to be important for our design needs. On the other hand there has been no report about a systematic design procedure based on tools available to everyone in the community.

GEOMETRY OF THE STRUCTURE

The geometry of the waveguide cavity we have investigated is shown in Figure 1. The probe can be seen with its main plane sitting parallel to the polarization direction of the incoming radiation.

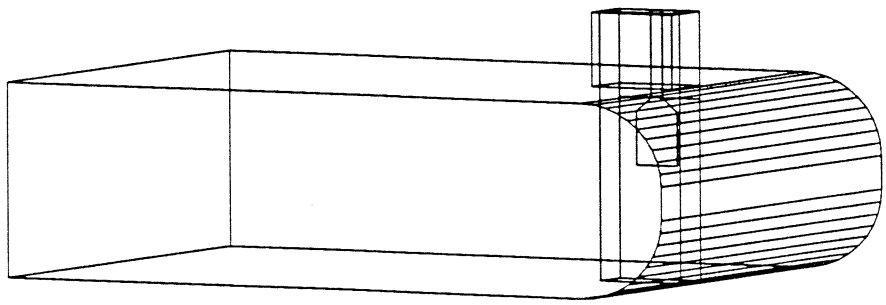

Figure 1. Geometry of the problem studied.

SCALE MODEL MEASUREMENTS

The scale model measurement was done with a standard WR-229 (IEC-R40) waveguide with 3.5 GHz and 4.8 GHz band limits that translate to 84.6 GHz and 116 GHz, respectively, with a scaling factor of 24.167.

The probe was etched on a 0.72 mm Duroid ® substrate, $\varepsilon_r = 2.34$, with a 7.2 mm superstrate of Stycast ®, $\varepsilon_r \approx 4.0$. This in order to simulate a fused quartz substrate for the final probe-mixer structure. With these dielectric constants and dimensions it was possible to calculate the 50 Ω strip line geometry [8]. This strip line terminated at an SMA connector to have access to the probe with the network analyser.

On one side of the probe cavity the non-contacting backshort structure was connected, and at the other side a commercial waveguide-to-SMA adapter was placed (Sivers Lab, type 7606/3).

We used an HP 8720B network analyser and the results of such measurements can be seen in Figures 2 and 3 for the backshort at the $3\lambda/4$ position and in Figures 4 and 5 for the backshort at the $\lambda/4$ position. This position is measured from the symmetry axis of the probe to the surface of the backshort.

NUMERICAL SIMULATIONS

The results of the simulation of the two cases measured on the scale model can be seen in Figures 2 to 5 together with the measured values.

For the backshort at $3\lambda/4$ (Figures 2 and 3) we see that HFSS predicted within 0.5 dB over the band the value of the response for $|S_{12}|^2$ and predicted quite accurately the shape of it. For $|S_{11}|^2$ the predicted values are not in such a good agreement, but the general shape is predicted. On this particular case it is quite clear that the prediction works very well, since the bandpass characteristics of the $3\lambda/4$ backshort position matching is clearly defined on the simulation.

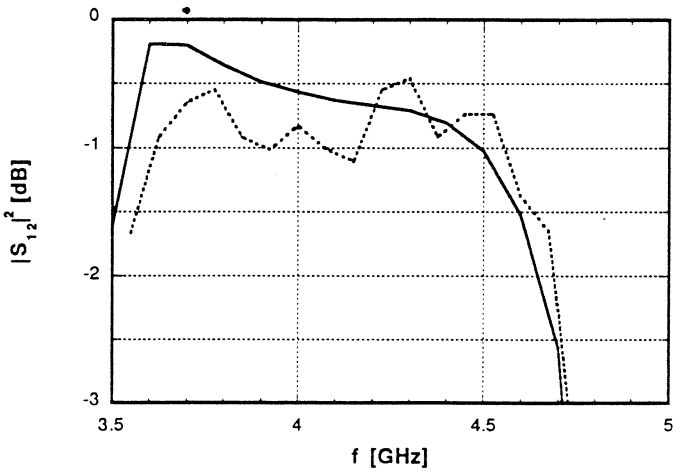

Figure 2. Measured (dashed) and simulated (continuous) results for $|S_{12}|^2$ at $3\lambda/4$ backshort position.

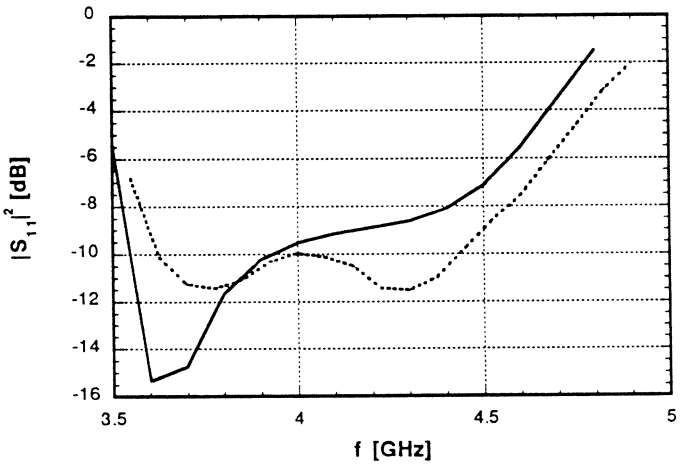

Figure 3. Measured (dashed) and simulated (continuous) results for $|S_{11}|^2$ at $3\lambda/4$ backshort position.

On the *λ/4* case, seen in Figure 4 and 5, the value predicted for $|S_{12}|^2$ is again within 0.5 dB of the measured value, predicting the general shape. For $|S_{11}|^2$ again we see that the predicted values vary more against the measured ones, but the shape of the response agrees very well with the measurements.

It is important to remark here that the HFSS program has a built in CAD user interface that is far from being a final version: it is not very user friendly and suffers from lack of flexibility. The simulation itself takes about half an hour for each point of the frequency scan, thus, for a complete simulation between 3.5 and 4.8 GHz with a resolution of 100 MHz it needs 7 hours.

It was found also that HFSS cannot predict the behaviour of superconducting metals since it cannot handle complex conductivity. This did not allow us to model the structure at its operating frequency.

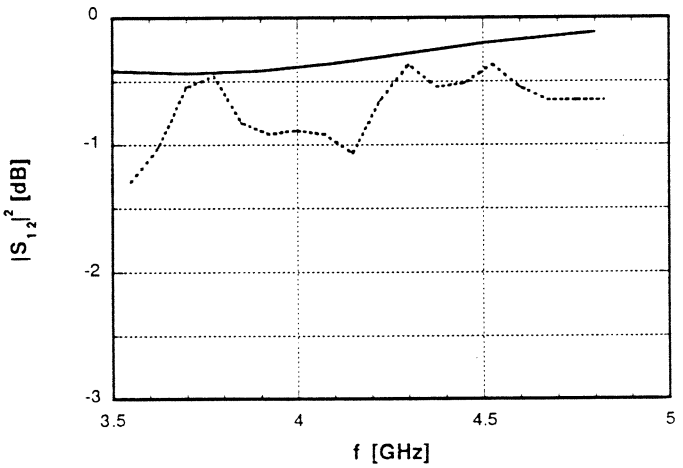

Figure 4. Measured (dashed) and simulated (continuous) results for $|S_{12}|^2$ at $\lambda/4$ backshort position.

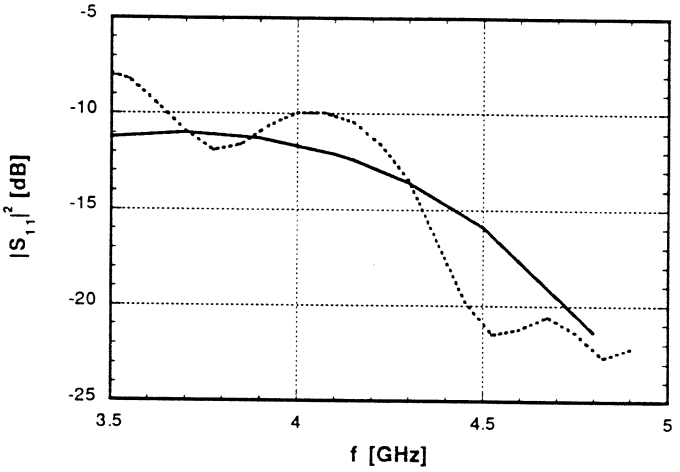

Figure 5. Measured (dashed) and simulated (continuous) results for $|S_{11}|^2$ at $\lambda/4$ backshort position.

DISCUSSION AND CONCLUSIONS

As to the results we get a working coupling structure that allows us a full waveguide-bandwidth coupling with losses less than 1 dB over a 32 GHz band. This structure is planar, thus allowing immediate integration of it to the SIS junction substrate, allowing the creation of a mixer with coupling probe, tuning structures, mixer junction, and IF matching structures, all on one piece of substrate.

The HFSS was successfully contrasted against real measurements. We can see, from a direct comparison of the results shown in Figures 2 and 3, that the simulation results are in quite good agreement with the measured ones.

The fact that the CAD phase on HFSS is cumbersome does not weigh as much when compared with the time consuming process of etching a probe (that includes the drawing and photolithography of it) or mechanically modify the mixer cavity geometry. Still it is much faster to modify anything in the geometry of the structure on the computer than on the real scale model.

It is clear that the availability of this powerful computational tool is a major step towards an easy and fast microwave design in the millimeter wave region.

ACKNOWLEDGEMENTS

The authors want to thank Mr. Carl-Olof Lindström for his patience and fundamental help during the measuring stage. Also the people at the workshop of Radio and Space Science at Chalmers University of Technology are acknowledged for their skilful work constructing the scale model.

REFERENCES

[1] A. Anger, "Software Computes Maxwell's Equations," *Microwave Journal*, pp. 170-178, February 1990.

[2] M. J. Wengler, "Submillimeter-Wave Detection with Superconducting Tunnel Diodes," *Proceedings of the IEEE*, Vol. 80, No. 11, pp. 1810-1826, Nov. 1992.

[3] S. V. Shitov, V. P. Koshelets, S. A. Kovtonyuk, A. B. Ermakov, N. D. Whyborn, and C-O . Lindström, "Ultra-Low-Noise 100 GHz Receiver Based on Parallel Biased SIS Arrays," *Supercond. Sci. Tech.*, No. 4, pp. 406-408, 1991.

[4] T. Edwards, ***Foundations for Microstrip Circuit Design***, 2nd ed., Chichester, England: John Wiley & Sons, 1992.

[5] A. V. Räisänen, W. R. McGrath, P. L. Richards, and F. L. Lloyd, "Broad-Band RF Match to a Millimeter-Wave SIS Quasi-Particle Mixer," *IEEE Transactions on Microwave Theory and Techniques*, Vol. MTT-33, No. 12, pp. 1495-1500, December 1985.

[6] A. R. Kerr, S. K. Pan, S. Whiteley, M. Radparvar, and S. Faris, "A Fully Integrated SIS Mixer for 75-110 GHz," *IEEE Int. Microwave Symp. Digest*, MTT-S, pp. 851-854, May 1990.

[7] D. Winkler, N. G. Ugras, A. H. Worsham, D. E. Prober, N. R. Erickson, and P. F. Goldsmith, "A Full-Band Waveguide SIS Receiver with Integrated Tuning for 75-110 GHz," *IEEE Transactions on Magnetics*, Vol. 27, No. 2, pp. 2634-2637, March 1991.

[8] E. Yamashita and K. Atsuki, "Strip Line with Rectangular Outer Conductor and three Dielectric Layers," *IEEE Transactions on Microwave Theory and Techniques*, Vol. MTT-18, pp. 238-244, May 1970.

INTEGRATION OF SIS MIXERS, SUPERCONDUCTING LOCAL OSCILLATORS AND OTHER ELEMENTS INTO RECEIVER CHIPS FOR 100–700 GHz

A.N.Vystavkin, V.Yu.Belitsky, V.K.Kaplunenko, V.P.Koshelets, S.A.Kovtonyuk, G.V.Prokopenko, A.V.Shchukin, S.V.Shitov, M.A.Tarasov
Institute for Radio Engineering and Electronics of the Russian Academy of Sciences
Mochovaya str. 11, Moscow 103907, RUSSIA
Fax (7 095) 203 84 14

1. INTRODUCTION

The recent progress in development of high–sensitive SIS mixers of 100–500 GHz frequency region with corresponding noise temperature 30–300 K (Fig.1) [1,2], superconducting local oscillators in this portion of spectrum [3,4] with linewidth of the order of 0.7 MHz, SQUID amplifiers of IF signals in 0.1–0.4 GHz region with noise temperature less than 1 K [5], different types of planar antennas, matching elements, filters and so on in integrated implementation and combining them into integrated structures of different complexity [6] clears the way to integrated receiving chips of mentioned frequency region. Receivers based on integrated chips comprising mentioned superconducting elements will be comparatively inexpensive, having small dimensions and weight and necessary reliability. Fabrication of such compact receiving chips opens the way to the creation of superconducting matrix for image receiver.

Results of corresponding investigations, developments and estimations of creation of entirely superconducting integrated receivers for frequencies up to 700 GHz are given. Results not published earlier are given in more details.

2. JUNCTIONS FABRICATION TECHNOLOGY AND LAYOUT DESIGN

Our technology group has the possibilities to fabricate all types of superconductive circuits that are designed and investigated in our laboratory. These possibilities based on high quality Nb–AlOx–Nb tunnel junction fabrication process which has been described previously [7,8]. In this process we use stress–free Nb films for three–layer sputtering and well–known "self aligned" process for junction geometry determination.

The junctions properties (specific capacitance, magnetic penetration depth in the Nb films) have been investigated in wide range of critical current densities [8]. The results obtained make possible to design and fabricate complex microwave receiving and Single Flux Quantum (SFQ) circuits perfectly matched in the desired frequency range.

For fabrication of SIS arrays consisting of numerous identical high critical current density Nb–AlOx–Nb junctions we utilize usual optical lithography and double step "self align" process (cross method). Here we provide usual "self align" operational procedure: lithography, RIE, anodization,

insulator deposition (SiO) and lift–off twice, defining two comparatively long (1.5x10 μm) junctions perpendicularly each other. The square junction with approximately 1 μm dimensions (decreasing dimensions is due to RIE underetching) are realized on the crossing. In our RIE setup it is possible to keep underetching at 0.4 –0.7 μm and fabricate submicrometer Nb–AlOx–Nb tunnel junctions in controllable manner.

In our laboratory a CAD system for photomask constructing was developed. It consists of different kind calculation and superconductive circuits modeling software which is specified for digital RSFQ logic and SIS mixer circuits. Based on this modeling photomasks are plotted using PC based drawing systems. Special program provides analyzing of the particular topology and converts drawing data to data convenient for an E–beam photomask processing machine. The program comprises drawing data converting module, topology analyzer (arbitry topology), and data proceeding module which is accommodated for the concrete photomask processing machine. Thus all lines from the primary drawing of the future chip ready for producing photomasks is CAD supported. Now we are using this technology for all our investigations.

3. SERIES RF / PARALLEL IF ARRAYS OF SIS JUNCTIONS FOR WAVEGUIDE MM WAVES MIXERS.

Since 1982 we have developed mixing SIS arrays which have unique design because of parallel connection between the junctions for both dc bias and IF output signal but for rf signal the connection is still in series [9] (SRF/PIF design). The original idea of this connection was appeared as a result of analysis for earlier experiments with SIS mixers which had shown number of problems [10].

This problems have been overcome by using the SRF/PIF design because it provides simultaneously:

i) low capacitance and high impedance referred to input port which are equivalent to those of series array;

ii) the same optimum voltage for all junctions in the array which is feature of an ideal array;

iii) tuning out intrinsic capacitance by means of special design of bias circuits;

iiii) low output impedance close to 50Ω without using any transformers.

Simple relationships can be established to calculate optimum number N and parameters of single junctions in the array as well. The SRF/PIF connection provides for the mixing array *increased input* impedance $NG_{\omega\omega}^{-1}$ seen by *rf* source and *decreased output* impedance G_{oo}^{-1}/N seen by IF amplifier. Here $G_{\omega\omega}^{-1}$ and G_{oo}^{-1} are input and output impedances of pumped single junction respectively [11]. The optimum number N of junctions in such array could be calculated to get *desired* both input and output impedances in followed manner [12]:

$$N^2=(G_l/G_s)(G_{\omega\omega}/G_{oo})$$

Here G_s and G_l are real parts of *rf* source and IF load admit–

tances need to be matched respectively. The ratio $G_{\omega\omega}/G_{oo}$ could be obtained from experimental junction IVC using numerical calculations based on three-port model [11].

The integrated bias circuits can be used not only as an *rf* isolation, but also as tuning elements to tune out junction's intrinsic capacitance. Fig.2 illustrates the design principle have been developed for the new arrays. It shows the transition from purely resistive nonlinear elements connected in series by mean of assembling with lumped resonant circuits toward tuned arrays with series *rf*/parallel IF connection of SIS junctions (crosses). The figures a)-c) presents the way to combine together even number of junctions. The base unit is the original two-junctions cell with three electrodes and *rf* rejection filter L_iC_i (see Fig. 2).

Two different ways could be used to tune odd number array. The examples d)-f) and g)-i) illustrate this difference which is mainly in parameters of tuning inductances and capacitances. In the case f) tuning capacitances should be equal to junction capacitance C, but for case i) only half of that. The ratio for inductances should be inverse. The tuning bandwidth is wider for the case i) if junctions parameters are kept the same.

The treatment above allows to state that one could obtain perfect matching condition for SIS mixing element without any input/output transformers if mentioned requirements are satisfied.

In Figure 3 the layout of experimental five-junction array is shown. It is an example of practical realization of variant i) from Figure 2. The tuning inductances are patterned as short circuited two wire lines. It should be noted that capacitance coupled to the tuning inductance is approximately *four* times less than for individually tuned junction. It makes easier to design inductive elements for higher frequencies, because the loop need become not too small.

Laboratory tests of the experimental receivers were carried out in liquid helium cryostat at mixer ambient temperature in range 4.2-5 K. The input signals were obtained from matched loads at 80K and 300K placed in front of the horn antenna on the top of the cryostat. The mixers have only one tuning element (backshort plunger) which can operates as an image rejecter. The output IF signal centered at 1.5 GHz was amplified by cold low-noise (≤10K) IF amplifiers and registered by spectrum analyzer.

The magnetic field up to 6000 A/m could be applied to the mixing array by superconducting coil, but it was not really used because the new arrays have suppressed critical current. The suppression is caused by weak random magnetic fields coupled to the tuning loops which are galvanically connected to the pair of junctions (see Fig.2). This configuration is very similar to *dc*-SQUID which has critical current very sensitive to magnetic field. This property is very helpful to suppress Josephson steps in sub-mm region.

The receiver noise temperature measurements have been carried out by using data acquisition system. This system is based on the AT-286 IBM compatible computer and HP8566 spect-

rum analyzer connected together by GP–IB interface. The program was written in C language and performs digital processing and graphics based on the data obtained from spectrum analyzer. It makes experiments more convenient and accurate. All variants presented in Figure 2 have been tested as mixing elements. The low–noise wide band receiver performance has been obtained even if very simple input and output circuitry was used (i.e. full height input waveguide and single tuner; absence of any output transformer).

In spite of similar results were obtained with 2, 4 and 5–junctions arrays in 2 mm band (5, 10 and 11–junctions array in 3 mm band [13]) it was found that arrays which parameters better fit the *optimum matching conception* demonstrated wider tuning range and lower noise temperatures.

In Figure 4 the summary for the best receivers tested in 40–150GHz frequency range is presented in comparison with quantum limit hf/k. This data have been obtained with parallel biased arrays as a receiver front end mixing elements.

The *optimum matching conception* have been developed for SIS array mixers and was successfully confirmed in frequency range 40–180 GHz. This conception could be applied for full height waveguide mixers and for mixers integrated with stripline structures as well. Very low noise parameters ($T_r \leq 50K$) were demonstrated in 40–150 GHz frequency region.

4. QUASIOPTICAL SIS MIXERS WITH MICROSTRIP TRANSFORMERS AND SPIRAL ANTENNAS

Another approach is associated with open structure SIS mixers based on equiangular spiral antenna with integrated on chip coupling circuitry and a single or pair stacked SIS junctions. Open structure SIS mixers are under developing in our laboratory since 1984. From the very beginning the equiangular spiral antenna was used. The first design was specified to use Si substrate placed in oversized circular waveguide at 75 GHz. Inductive loop with DC block capacitor was integrated in the antenna apex area for SIS junction capacitance compensation at 75 GHz.

Next step in the integration circuit was made in 1989: it was suggested to connect SIS junction and antenna via a microstrip impedance transformer with length little bit longer than quarter of wavelength. This additional piece of microstrip line acts as inductance for resonating out the SIS junction capacitance. Quarter wavelength microstrip transformer is used for transformation of already real impedance to spiral antenna driving impedance ~44 Ohm [14] and later was successfully applied to 115 GHz spiral antenna SIS mixer, Fig.5 shows the topology of the 115 GHz receiver chip [15].

Further developing of this technique is associated with twin SIS junctions compensation circuit which was suggested [16] to use for resonating out SIS junctions capacitance by mean conjugating of the impedance of one to compensate reactance of another. The twin junctions compensation circuit in combination with microstrip impedance transformer was

implemented for 500 GHz SIS mixer receiver.

The result which is presented at the present conference [2] was obtained in a very close collaboration with Chalmers University of Technology with a group of Prof. E.Kollberg. The receiver demonstrated noise temperature below 300 K DSB at the frequency band 450–515 GHz. Relatively large optically lithographed SIS junctions and the particular topology of the twin circuit make very easy suppression of the Josephson steps on pumped IV curve. Low normal state resistance of the junctions using both in impedance transformer and twin circuits improve saturation power of the SIS mixer. Our calculations show very good prospects of the integrated structure based on open structure SIS mixer and twin junctions tuning circuit for submm band applications up to 800–900 GHz.

5. SIS ARRAYS INTEGRATED WITH MATCHING ELEMENTS AND PLANAR ANTENNAS

Integration of SIS junction arrays with planar wide band antenna allows to increase instantaneous bandwidth of receiver up to octave in comparison with rather narrow–band traditional waveguide mixers with SIS junction arrays or planar antennas with integrated single microstrip transformer and single SIS junction. Integrated receiving structure comprising self–Babinet–complementary spiral antenna, array of SIS junctions connected in series as seen by the RF but are parallel DC–biased through the same inductances that provide the tuning for the SIS junctions capacitance has been designed and experimentally studied. Array was designed for 80–160 GHz wave band and consists of 5 SIS junctions 1.5 μm^2 area each, six inductive short–ended slot–lines and two decoupling capacitances. Effective direct detector bandwidth of such structure with quantum efficiency equals unity has been estimated as wide as 70 GHz. Noise temperature of heterodyne mixer has been measured in three–lens Gaussian beamguide by means of hot/cold loads method, yielding receiver DSB noise temperature 80 K. IF mixer port load bandwidth and thermal background radiation influence on IV curve and saturation of SIS mixer have been studied.

The waveguide type SIS mixers signal frequency increasing over achieved values ~500 GHz [17] is connected with increasing problems of mechanical elements fabrication tolerances and increasing with frequency losses in waveguides and plungers. From radioastronomy point of view it is much easier to use quasioptical methods of focusing and transmission of initial signal which is presented at the output of radio telescope as a gaussian beam.

The combining quasioptical beamguide and wide bandwidth planar antenna allows to design more broadband device than waveguide type receiver system having conversion gain and noise temperature close to the best achieved in waveguide type mixers [18]. Among disadvantages of quasioptical systems may be mentioned the absence of tuning elements and possibility of antenna–substrate interaction, which can lead to beam pattern distortion at some frequencies.

Advantages and drawbacks of both mentioned methods leads to conclusion about combining series–parallel arrays and integrated planar antennas in order to obtain effective mixer matching in wide bandwidth and increasing of central frequency up to 700 GHz and higher. Problems of external broadband thermal radiation on mixer parameters and its saturation in such system should be carefully studied.

In these experiments we used equiangular self–Babinet two–arm spiral antenna similar to [18] with shape according to relation $r=R_0 exp(a\phi)$ where r and ϕ – polar coordinates, a and R_0 – constants (see Fig. 6a). Value of a=0.36 was chosen as compromise between two cases of wider beam pattern with lower and more elliptical beam pattern with higher values. Impedance of such antenna placed on quartz hyperhemisphere corresponds to relation $Z_{ant}=Z_0/(0.5+0.5n^2)^{1/2}\simeq 114$ Ω in more than decade frequency band.

SIS junction array (Fig. 6b) consists of five junctions. Six sections of end–shorted slot lines were used for parallel connection of junctions and capacitances tuning out. The central sections are 140 μm long and outer sections are 70 μm long. Area of each junction is 1.5 μm^2 and the whole structure designed for central frequency 115 GHz is equivalent to single junction of 0.3 μm^2 area.

Such integrated circuit operates without additional choke filters in IF channel preventing signal leakage because spiral antenna itself has a useful property of automatic currents cutoff which means that only central part of antenna takes part in signal receiving. The length of such active part of antenna not exceeds the signal wavelength, i.e. 2–3 mm in our case.

In order to make direct measurements of antenna beam pattern and to adjust precisely 3–lens beamguide at room temperature we have fabricated similar structures with golden antenna of the same shape and bismuth microbolometer instead of SIS array. Bolometers were made of Bi film 200 nm thick, 30 Ω/□ resistance, 3 μm width and 9–16 μm length. Beam patterns of bare antenna on quartz substrate, the same on quartz hyperhemisphere lens and also with counterreflector behind antenna are shown in Fig. 7. Data presented in Fig.7 are normalized to maximal signal corresponding to the last case.

In IF channel the cold amplifier and circulator were used to prevent standing waves at the output of the mixer. Such amplifier was matched with SIS array in bandwidth over 0.5 GHz. It may lead to the mixer output saturation. For mixer dynamic range increase it is desirable to make IF band narrower and short–circuit its output out of this band. For this purpose we have tested two types of filters. First consists of microstrip line section and decoupling capacitor, and the second – of antenna+leads inductance and capacitor comprising together series resonant circuit.

Matching efficiency at IF was estimated from IF port noise temperature, measured with SIS junction shot noise as noise source. In general current noise in SIS junction cor–

responds to the relation $I_N^2=2eI\cdot\Delta f\cdot coth(eV/4kT)$ which is reduced to simple shot noise relation $I_N^2=2eI\cdot\Delta f$ for voltages above the energy gap. Noise temperature of the receiver was measured in DSB mode with hot (300 K) / cold (80 K) loads. In this experiments a sufficient influence of hot/cold switching on IV curve and IF noise was observed even in the absence of LO power for array with dc resistance 20 Ω. This fact is clear illustration of mixer input saturation by broadband thermal radiation of the order of 100 GHz with effective temperature 300 K. Observed in the same experiment rather high noise temperature equals to 180 K at 108 GHz is due to this saturation effect.

Another SIS array with 10 Ω normal resistance was tested with switching on and off additional cold attenuator with losses 3.8 dB. The receiver noise temperature with open attenuator was 350 K, and with closed attenuator 200 K. For another cold attenuator with 8.8 dB losses the receiver noise temperature was 250 K and 80 K for open and close cases correspondingly, see Fig.7b. These experiments show that the main problem for such very broadband SIS mixers is the output saturation and it may be solved by restricting input and output bandwidths.

6. SUPERCONDUCTING MILLIMETER WAVE RECEIVER INTEGRATED ON A CHIP

At frequencies above approximately 300GHz a problem of local oscillator for spectral receivers arises; it is especially important for satellite receivers and/or image receivers combined many mixers. This is why the idea of using superconducting local oscillators integrated with SIS mixers looks very attractive.

Josephson oscillations in long tunnel junctions due to solitons' motion along the tunnel region can be used as a microwave source. The frequency of oscillation f is dependent on the dc voltage V across the junction according to the Josephson relation:

$$f = 2eV/h$$

The soliton mode generation has very narrow linewidths [19] and the frequency is strictly determined by the junction length due to resonant properties of the junction cavity [20]. Moreover it is very difficult to obtain microwave oscillations at frequencies higher than approximately 150 GHz in the "soliton" mode. The flux-flow mode of oscillation (FFO) in the similar long junction uses viscous motion of the solitons (see, for ex. [21]) and can be tuned almost permanently up to 500 GHz with large output power. The experimental integrated receiving structure comprises SIS array mixer integrated with Flux-Flow type Josephson oscillator used as a LO source on the same substrate. The mixer was designed based on the new SRF/PIF conception (see section 3). The FFO local oscillators and SIS array mixing elements have been sputtered in the same run onto a 15x24x0.1 mm quartz substrate which then was cut down to chips of 0.5x5.3x0.1 mm size (the same size as ordinary mixing chips).

The Nb–AlOx–Nb trilayer process has been used [22] to form both generating and receiving junctions, so they have the same current density.

An equivalent circuit for the experimental structure is presented in Fig.8. It is simplified version to clarify the actual layout shown in Fig.9. Bottom electrode (1) of the structure serves as a ground plane for impedance transformer (7) and was shaped as low–pass filter to prevent leakage of microwave power along the substrate. The 5–step octave bandwidth microstrip impedance transformer with ratio 1:30 is loaded by a Ti film resistor (8) to avoid reflections and resonances in the LO part. The transition from transformer to coupling probes (9) provides isolation for the input rf signal and about –10 dB attenuation for the LO power delivered by the FFO. The 10 μm gap between probes serves as a dc–block. The substrate could be split along this gap to obtain two independent elements: FFO and mixing SIS array.

The experimental mixing section was based on two junctions array [19]. The array have an inductive tuner designed to tune out the reactance of both junctions around 150 GHz (see Fig.2a in section 3). The top electrode (3) forms a low–pass filter for the output IF signal. This filter design is based on quarter–wave coplanar and microstrip lines. The new receiving structure has to be used with three independently dc control current sources. One more source is needed to produce a magnetic field to control the FFO junction. The magnetic field was applied to the chip by a superconducting coil in the plane of the junction. The field up to only 4–8 A/m was used to provide the tuning of FFO.

The integrated receiver has been tested in the same mixer block which was used for ordinary mixing experiments. The mixing block has full height rectangular waveguide (0.8x1.6 mm) and single tuning backshort of circular shape. The input noise signal has been supplied to the mixer through a oversized waveguide. The LO power from BWO and Gunn oscillator have been introduced by means of a cold diplexer (–26 dB) mounted on the mixer block input flange.

The IF output signal (1.3–1.8 GHz) passed through cooled isolator was amplified by cooled FET amplifier. Typical noise temperature of the IF channel estimated from the SIS junction shot noise was less than 10 K.

The maximum power 80 nW coupled to the array have been estimated at a FFO frequency range 100–140GHz. It corresponds to a normalized rf voltage equal to $\alpha \cong 1$ that is sufficient to pump the SIS array mixer. However the minimum receiver noise temperatures (67K at 133 GHz and 85 K at 140 GHz) were obtained with lower powers (≅20nW).

The LO power coupled to the array changes when the backshort is moving. It is very similar to the case when external LO used. The experimental data for two different chips (#1 and #2) tested in two different laboratories in comparison with two different external LO (BWO and Gunn oscillator) are presented in Fig.10. It is surprising that the receiver noise temperatures obtained with the FFO could be somewhat lower at certain frequencies than for the case of mixer pumped by external oscillators.

It was demonstrated experimentally that a Flux–Flow LO can provide good stable and repeatable low–noise operation of a SIS receiver at short millimeter wavelengths.

7. FLUX FLOW OSCILLATORS STUDIES

Superconducting Flux–Flow Oscillators (FFO) integrated on the same chip with microwave detector have been experimentally investigated in the wide frequency range 100 – 450 GHz. A possibility to adjust the oscillator rf power by changing the bias current and /or magnetic field has been demonstrated. The detected microwave power as high as 0.3 μW has been achieved at FFO frequency 375 GHz. The linewidth of the FFO about 1 MHz has been estimated from different mixing experiments. An integrated circuit which consists of a FFO, coupling transformer sections, superconducting high frequency attenuator and microwave detector with tuned out capacitance have been designed and successfully tested.

The possibility to create a SIS receiver with integrated Flux–Flow Oscillator (FFO) has been recently demonstrated [3,4]. The frequency tuning in the range 280 – 330 GHz with linewidth 2.1 MHz have been reported in [4]; the front–end noise temperature of real integrated receiver as low as 85 K at 140 GHz has been achieved [3]. In this report we present the results of farther investigation of FFO and more complicated integrated circuits. High quality Nb–AlOx–Nb junctions ($j_c \simeq 10^3$ A/cm^2) were used as elements of the integrated circuits; technological procedure for their fabrication was published in [3,23].

A first type of the integrated circuit consists of a long Josephson junction, a coupling impedance transformer section and a microwave detector with tuned out capacitance; it is similar to described in [3]. To provide the additional dumping the long Josephson junction was shunted by low inductance Mo resistor ($R_n < R_s < R_j$). Nevertheless even for large external magnetic field together with a flux–flow step (FFS) the weak Fiske steps (FS) at $V_{FS} = n\Phi_o \upsilon/2L$ occurred (υ – is Swihart velocity, L – junction length). At changing of the magnetic field H the flux–flow step moves on IVC: $V_{FF}=\upsilon\Lambda\mu_o H$, where Λ – magnetic thickness of the junction. Flux–flow step "emphasizes" the corresponding FSs and increases their amplitude. Therefore it was possible to realize flux–flow regime at appropriate FS providing the small dynamic resistance and permanency of the generated frequency.

Fig. 11 shows the IVC of the detector for different FFO bias currents at constant magnetic field. One can see that the frequency (f≅375 GHz) is fixed and only changing of the power takes place. It should be noted that for the same H but at different bias currents the generation of 175, 375 and 450 GHz was observed. The same was also possible at constant bias current by changing the magnetic field only to provide the variation of the FFO power (similar to shown in Fig. 11) without distinguished changing of the FFO frequency.

For measuring the FFO linewidth the integrated receiver

circuits [3] have been used. The signal from external synchronized generator, f = 70 or 140 GHz (4-th or 8-th harmonic of the 15 – 22 GHz pure linewidth source) was mixed with 140 GHz FFO signals in SIS junctions array. The output signal was connected to room temperature 1.5 GHz IF amplifier. One of the measured spectrum is shown in Fig. 12, it's possible to estimate the 3 dB linewidth which is about 0.7 MHz. Theoretical estimation of the linewidth [24]

$$\delta f = (\pi kT/\Phi_o)\cdot(R_d^2/R_{dc})$$

gives a smaller value about 100 kHz. It should be mentioned that as a rule some additional modulation of the FFO signal took place. This effect was observed in quit different set-ups and probably is connected with the small instabilities of fluxon motion in long Josephson junction.

To achieve the ultimate parameters of a SIS mixer the local oscillator (LO) power should be carefully controlled without any changing of the FFO frequency. We have designed and investigated integrated circuits which comprise FFO, microwave detector, matching elements and adjustable superconducting high frequency attenuator. The action of this attenuator is based on the change of the microwave impedance at variation of the SIS junction bias. Fig. 13 shows the action of the integrated attenuator at frequency 325 GHz. Because of non optimal design there was a large enough attenuation even in open state; numerical calculations predict that the performance of the integrated attenuator circuit could be considerably improved.

8. SIS ATTENUATOR FOR FFO OSCILLATOR

To achieve the optimal performance of the SIS mixer the LO pumping level should be adjusted with the accuracy about 1 dB. It's especially important for synchronous arrays of the Josephson junctions, whereas for Flux Flow Oscillators (FFO) microwave power could be tuned within large enough range by changing the current bias and/or magnetic field. But even for FFO the adjustment of the power might results in changing frequency and/or linewidth. To provide the possibility of fine tuning of the microwave power we have introduced a new integrated element – superconducting attenuator for high frequency signals.

An action of the attenuator is based on the change of the microwave impedance Z of a superconducting tunnel junction at variation of its dc voltage bias V. The microwave impedance Z(V) is dependent also on the frequency f, but for $f < eV_g/h$ one can distinguish three basic regions on IVC of a SIS junction. At $V \gg V_g$ the real part of the impedance ReZ is equal to normal state resistance R_n, $ReZ \gg R_n$ at $|V| < (V_g - hf/e)$ and $ReZ < R_n$ at $V \cong V_g$. To realize this simplified picture the junction critical current should be suppressed and capacitance of the SIS junction has been tuned out. The attenuator junctions could be placed in microstrip line between signal source and detector in series or/and parallel; in both cases

the R_n should be about characteristic impedance of the line. The attenuator is closed at $|V|<(V_g-hf/e)$ for series connection and $V \cong V_g$ for parallel one; the "open" state takes place at opposite combination of the biasing. Numerical calculations, based on Tucker's theory, have confirmed this consideration.

The different types of the integrated microcircuits have been designed and realized to check the idea of impedance attenuator. An equivalent diagram for one of the integrated circuit is shown in Fig. 14. The 70 GHz microwave signal was introduced in the circuit through fin-line antenna and microstrip quarter wave transformer. An attenuator itself consist of three identical sections $-S_1, S_2, P$. Each sections combines two SIS junctions ($A=25\ \mu m^2$, $R_n=4-8\ \Omega$), which are connected in series for RF signals but in parallel for DC; the capacitance of the junctions are tuned out at signal frequency by small inductance. Two series attenuator sections S_1 and S_2 are connected together by large inductance L. After attenuator the microwave power through transformer T_2 was connected to the detector SIS junction ($A=5\ \mu m^2$, $R_n= 20\ \Omega$); its capacitance is tuned out by inductance of the microstrip stub.

All microcircuits which include three superconducting Nb layers and two double SiO_2 layers have been fabricated using technological procedure developed for SIS and RSFQ devices (Section 2). High quality $Nb-AlO_x-Nb$ junctions with critical current density $j_c \cong 2 \cdot 10^3$ A/cm^2 and subgap to normal state resistance ratio $R_j/R_n>20$ were used as attenuators and detectors.

Fig.15 demonstrates the action of the series attenuator (S-att) at f = 74.6 GHz; the IVC of the S-att, measured between terminals "1" and "3", is presented in the insertion. The IVCs of the detector junction were obtained at four different bias voltages on the S-att, these voltages are marked in the insertion also. One can see the significant changing of the detected microwave power at variations of S-att bias. At point "1" ($V \cong V_g$) the S-att is open ($\alpha \equiv eV_{rf}/hf \cong 2$) while at point "4" ($V \cong 0$, $\alpha\tau \approx 0.02$) IVC of the detector is close enough to the autonomous one which is shown by dashed line in Fig.15. So, it's possible to introduce the attenuation of the microwave power at least 17 dB by changing the bias of the S-att.

To investigate the dependence of the attenuation on bias voltage more carefully we have applied to the circuit modulated microwave power and measured by lock-in amplifier the response of the detector. The qualitative agreement with the numerical calculations has been found. The detailed experimental results and their comparison with the theory will be published elsewhere.

The presented results have confirmed the possibility to

create an adjustable superconducting attenuator for microwave signals. The wide dynamic range (more than 15 dB) together with small losses in the "open" state have been demonstrated in both numerical calculations and experiments. New elements could be successfully used in integrated mm wave and tera-hertz receivers as precisely controlled attenuator and micro-wave modulators.

9. IF SQUID AMPLIFIER AND ITS TESTING BY SIS JUNCTION NOISE

The noise and signal parameters of several types of the IF amplifiers based on the different SQUIDs with integrated and hybrid input coils were studied. A new type of the multiloop dc SQUID with integrated input coil and extremely low stray capacitances was designed. The inductance of a four-loop SQUID was 100 pH, the input coil inductance 1.3 nH and mutual inductance 300 pH. The noise temperature of untuned SQUID amplifier with hybrid input coil at 100 MHz was 1.2 ±1 K and the power gain has exceeded 20 dB. The tuned integrated four-loop amplifier at 450 MHz has nearly 20 dB gain in 60 MHz band. For the noise calibration of such amplifiers we used SIS junctions as a shot noise source or cooled attenuator and a room-temperature semiconductor noise source.

The main disadvantages of the previous studied SQA are relatively low operating frequency and a high influence of external magnetic fields on SQA parameters. For the signal frequency increase with preservation of the low noise tempe-rature and high gain the Josephson frequency in the SQUID loop should be increased and it means that the loop induc-tance and capacitance should be decreased. In the well-known integrated SQUID structure [25] the stray capacitance in the loop exceeds 10 pF. The capacitance between the evaporated above the loop input coil and the loop is even more and this capacitance leads to the significant stray input-output feedback.

To eliminate these disadvantages and increase the input signal frequency and band we designed a four-loop dc SQUID with an integrated input coil in the form of rectangular turns inside the loops (see Fig.16).

The SQUID loop inductance consists of the four parallel connected square loops of 200x200 μm^2 size. The input coil consists of four series connected square turns with Nb film widths 10 μm. Parallel connection of the loops allows to reduce inductance of the loop and increase the resonant fre-quency. Series connection of the input turns allows to inc-rease the input coil inductance and make easier the impedance matching with the input 50 Ohm line. The position of input turns inside the loops was chosen to reduce stray input-output capacitance.

The SQUID loop inductance in this construction is 100 pH, input coil – 1.3 nH, mutual inductance 300 pH. The stray capacitance in SQUID loop 1.8 pF, the sum junctions capaci-tance 0.8 pF, input coil capacitance 0.3 pF, loop-coil capa-citance 2.2 pF. The Nb-AlO_x-Nb shunted tunnel junctions of 2.5x2.5 μm^2 area were used as Josephson junctions. The input

coil resonant frequency is estimated to be 8 GHz and the loop resonant frequency 10 GHz.

Since the input coil inductance is rather small and its reactive impedance at 300 MHz is ~2.5 Ohm, then to match the input 50 Ohm line and the input coil we used the resonant circuit matching [26]. In the design of the matching circuit the sufficient element is series additional inductance L_s, which was in the range 5–15 nH and depends on the size of connecting leads. Scaling the input circuit elements to the input resonant circuit one may obtain the equivalent capacitance $C_r \simeq C_1 + C_0$ and resistance $R_r \simeq R(C_1/C_0)^2$. According to [27] the optimal Q–factor is $Q \simeq (1+L_s/L_i)/\alpha^2$ which in our case gives $Q_{opt} \simeq 10$ and taking into account $Q \simeq \omega L_s / R_r$ one could obtain $C_1 \simeq 0.2 C_0$.

For such matching circuit parameters the dependence of the amplified noise signal on frequency is shown in Fig.17. The measured noise temperature of such SQUID amplifier was $T_N < 0.5$ K at signal frequency $f \cong 430$ MHz in 60 MHz frequency band.

The nearest competitor of SQA is cooled HEMT amplifiers which have $T_N \sim (1–3)$ K at $f \sim (1–3)$ Ghz, but have rather high power dissipa–tion equal to tens milliwatts and nearly achieved their asymptotic parameters. On the other hand SQA has more than one order reserve in the margins of gain, noise temperature and signal frequency even on the basis of the present technology. The sufficient advantages of SQA are extremely low power dissipation of several picowatt, small size ~1 mm^2 and full electrical, material and temperature compatibility with the superconducting sensitive devices such as Josephson and SIS mixers.

For these measurements we use SIS junction as calibrated shot noise source. In such configuration the measurements layout is similar to SIS mixer with SQUID IF amplifier and may be useful to combine both of these devices in single chip. The problem is to design and fabricate integrated matching circuit with proper series and parallel capacitors. Direct connection of integrated capacitor to the input coil was unsuccessful because of too low Q–factor of input circuit. Such integrated circuit needs additional series inductance in order to increase Q–factor and to achieve high enough gain and low noise temperature.

ACKNOWLEDGEMENTS

Authors would like to acknowledge hospitality, help and many useful discussions to Prof. E.Kollberg, Prof. R.Booth, D–r S.Jacobsson, N.Whyborn, C.–O.Lindstrom from Applied Electron Physics Department of Chalmers University of Techno–logy (Gothenburg, Sweden).

Fruitful discussions with J.Mygind and A. Ustinov are gratefully acknowledged.

This research supported in part by Russian State Scien–

tific Program "HTc Superconductivity" under contracts No 90463, 91009 and by Ministry of Science, Higher education and Technical policy of Russia under order N 580.

REFERENCES

1. SIS Workshop 11–12 May 1992, Zernice Science Park, Groningen, The Netherlands.
2. V.Yu.Belitsky, et al, 0.5 THz SIS receiver with twin junction tuning circuit, this conference.
3. V.P.Koshelets et al, IEEE Trans on Appl. Supercond. (1993), to be published.
4. Y.M.Zhang, et al, Appl.Phys.Lett., 1993, to be published.
5. M.A.Tarasov, et al, IEEE ASC, v.2, N 2, 1992, 79–83.
6. A.N.Vystavkin, et al, Proc. 22 European Microwave conf., 24–27 Aug. 1992, Helsinki, Finland, v.2, 981–986.
7. An.B. Ermakov, et al, Ext. Abstr.1989 Int. Supercond. Electron. Conf. (ISEC'89), Japan, pp.294–297.
8. V.P.Koshelets, et al, IEEE MAG, v.27, pp 3141–3144.
9. A.N.Vystavkin, et al, Physica 109&110 pp 2064–2066, 1982.
V.Yu.Belitsky, V.P.Koshelets, G.A.Ovsyannikov, S.V.Shitov, "RF Detector", a.c. (USSR patent) No. 12708679, 1984.
10. A.R.Kerr and S.–K.Pan, Int. J. IR&MM Waves, v 11, N 10, pp 1169–1187, 1990.
11. J.R.Tucker, M.J.Feldman, Rev. of Mod. Phys., vol. 4, pp 1055–1113, 1985.
12. An.B.Ermakov, et al, IEEE MAG, v. 27, N 2, pp 2642–2645, 1991.
13. S.V.Shitov, et al, Supercond. Sci. Technol., v 4, pp 406–408, 1991.
14. Belitsky V.Yu., et al, Extended Abstracts of ISEC–89, TOKYO, 1989, pp 179–182.
15. Belitsky V.Yu., et al., Int. J. of IR & MM Waves, v.13, no 4, pp. 389–396, 1992.
16. V.Yu. Belitsky and M.A. Tarasov, IEEE Trans. on Magn., vol. MAG–25, 1991.
17. G.De Lange, et. al., Proc. 3 Int. Symp. on Space Terahertz Technol., Ann–Arbor, Michigan, p.16, March 1992.
18. T.H.Buttgenbach, et.al., IEEE MTT, vol.36, p.1720–1725, 1988.
19. An.B.Ermakov, et al, IEEE Trans. on Magn., MAG–27, No.2, pp 2642–2645, 1990.
20. E.Joergensen, et al, Theory and Experiment Phys. Rev. Let., vol.49, No.15, pp 1093–1096, 1982.
21. T.Nagatsuma, et al, The Trans.IECE of Japan, vol.E–66, No.11, pp 680–681, 1983.
22. V.P.Koshelets, et al, IEEE Trans. on Magn., MAG– 27, No.2, pp 3141–3144, 1990.
23. V.P.Koshelets et al, IEEE Trans on Magn, MAG–27, (1991), 2642.
24. E.Joegersen et al, Phys Rev Lett, 49, (1982), 1093.
25. M.B.Ketchen, J.M. Jaycox, Appl.Phys.Lett. –1982.–40,n8.–P.736–738.
26. T.Takami, et al, IEEE Trans. Magn. –1989.– 25,N 2.–p.1030–1033.
27. C.Hilbert, J.Clarke, J.Low Temp. Phys. –1985. –61,n3/4. –P.263–280.

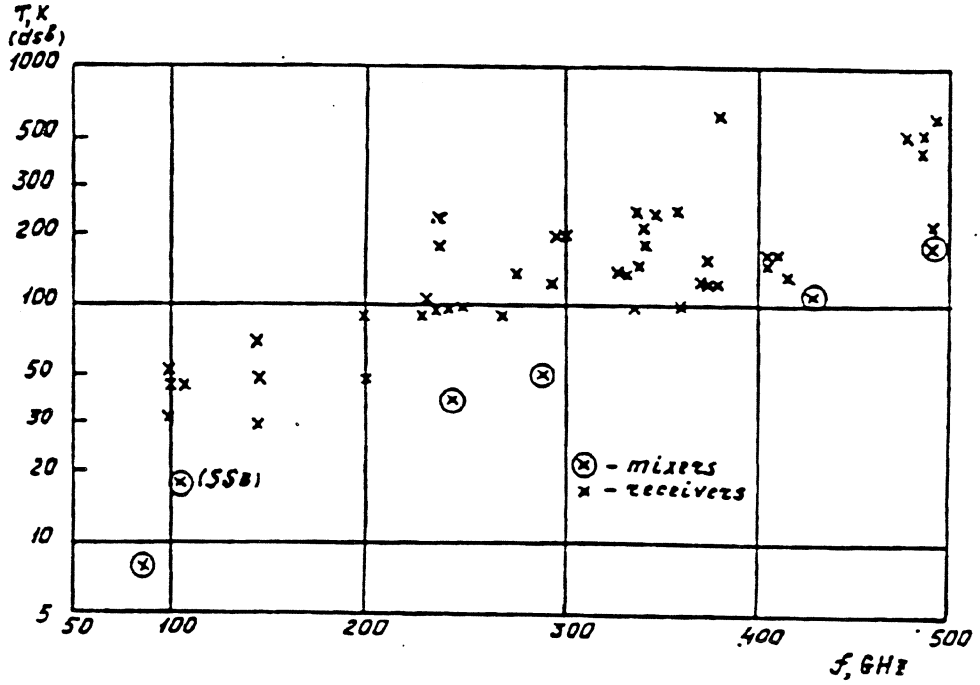

Figure 1. SIS receivers and mixers DSB noise temperatures in 50–500 GHz frequency band.

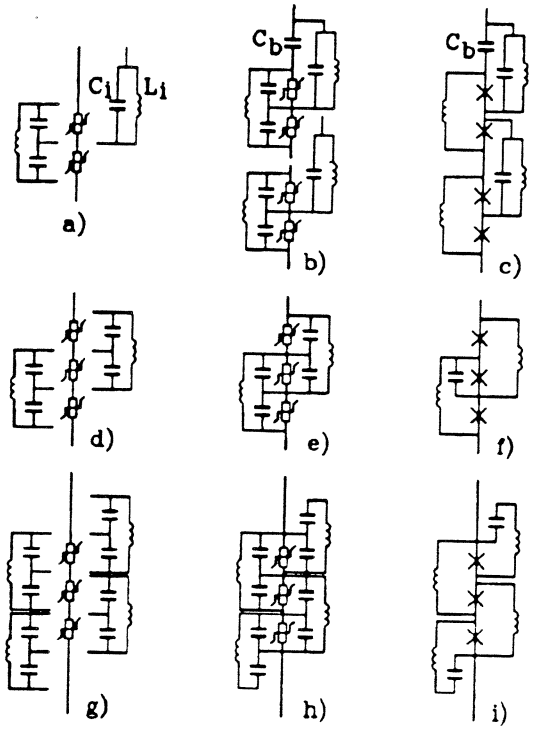

Figure 2. The illustration for the design principle developed for the parallel biased arrays: a)–c) for even number of junctions; d)–f) and g)–i) for odd number of junctions in the array.

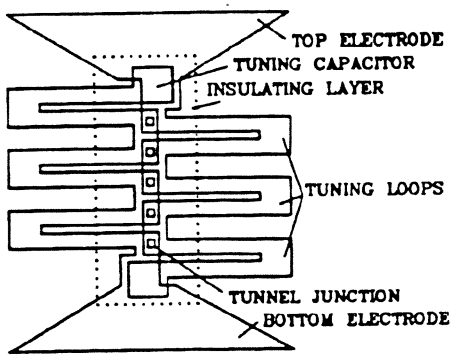

Figure 3. The layout of experimental 5–junctions array as an example of practical realization of variant i) from Figure 1.

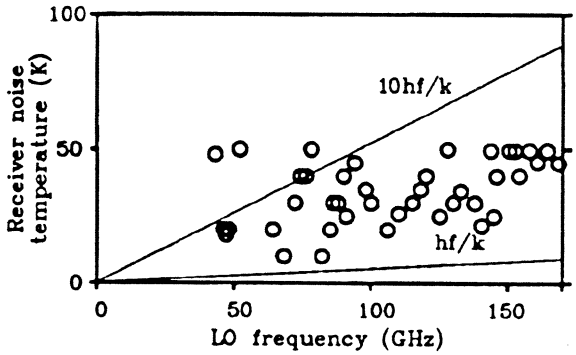

Figure 4 The summary for our best receivers tested in 40–150 GHz frequency range in comparison with quantum limit hf/k.

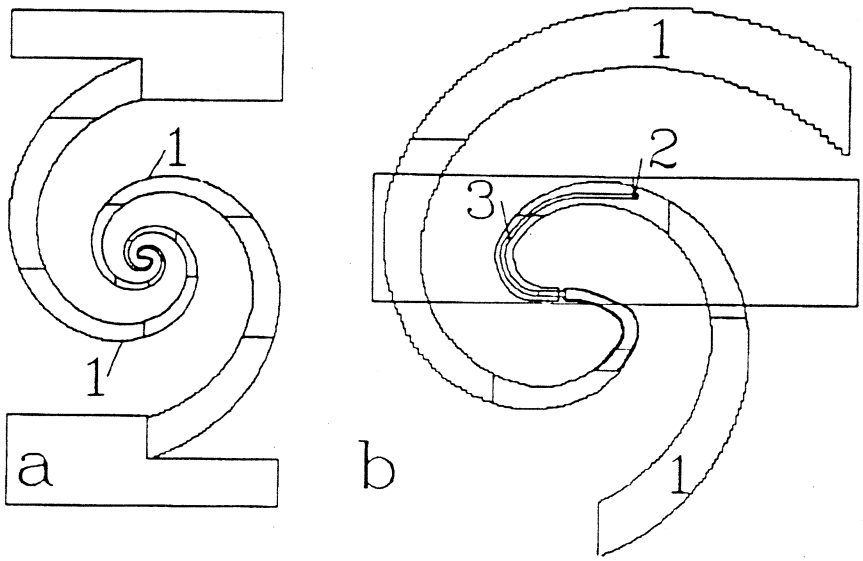

Figure 5. Quasioptical receiver structure for 115 GHz (left) and magnified central part (right) 1 – spiral antenna, 2 – VIA SIS, 3 – microstrip transformer.

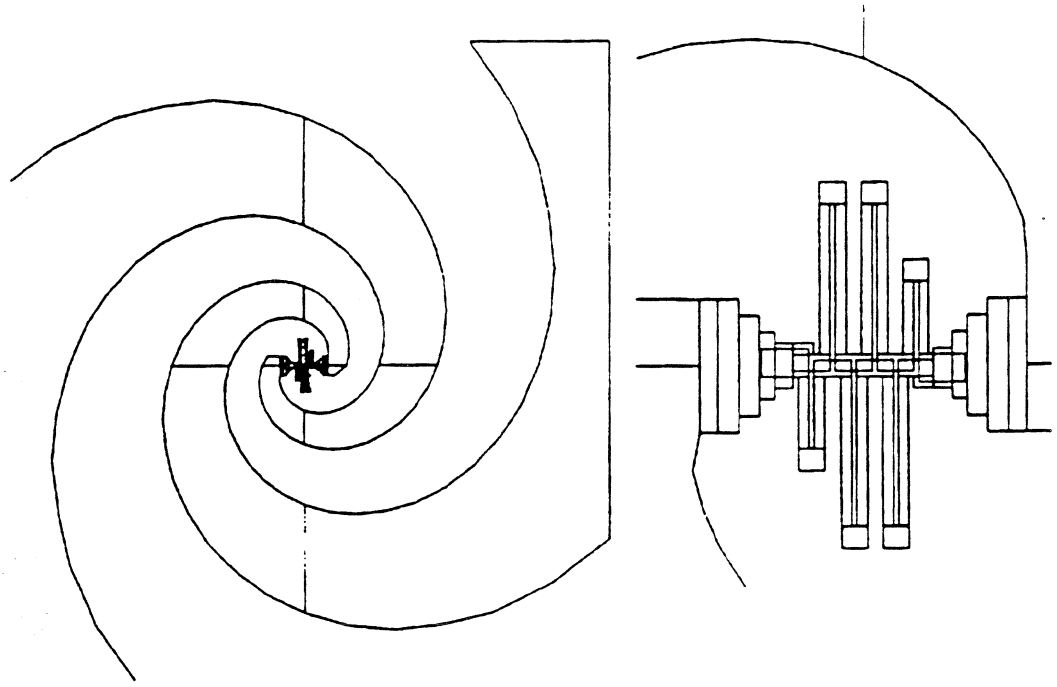

Figure 6. a) Self–babinet spiral antenna
b) Series–parallel array consisting of five SIS junctions 1.5 μm^2 area each, six inductive short–ended slot lines and two decoupling capacitances.

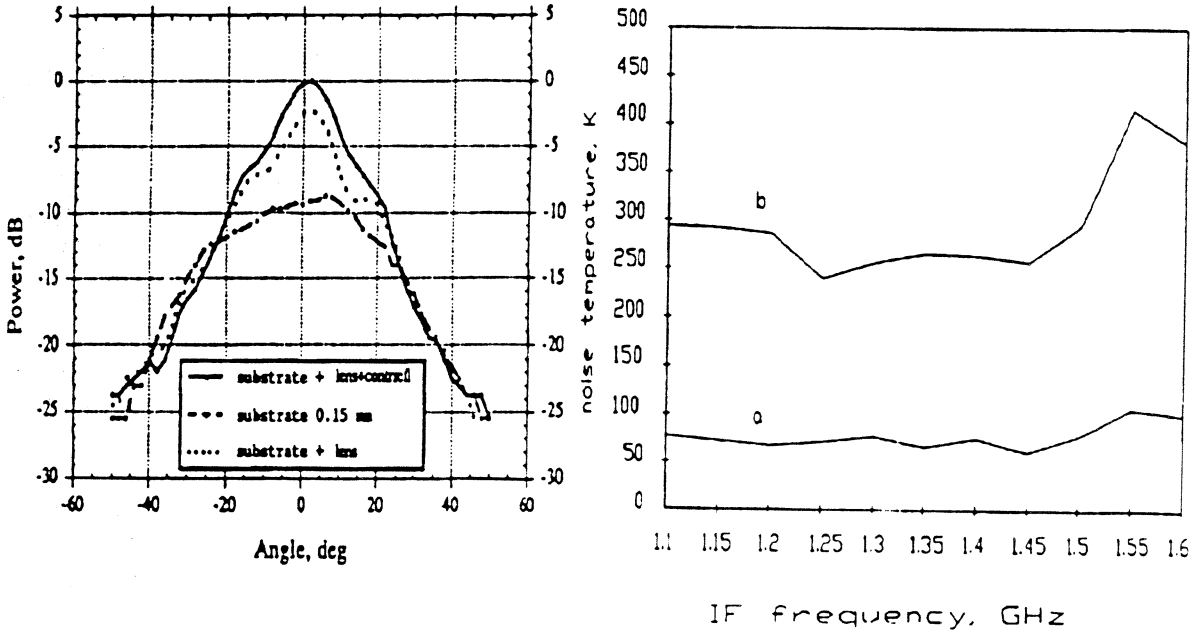

Figure 7. a) Beam patterns of spiral antenna on quartz substrate, the same on quartz hyperhemisphere lens and with counterreflector.
b) Noise temperature for closed (a) and opened (b) 8.8 db cold attenuator

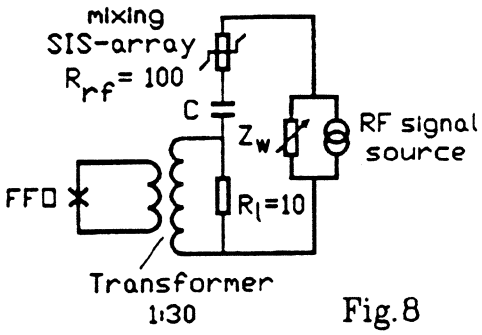

Fig.8

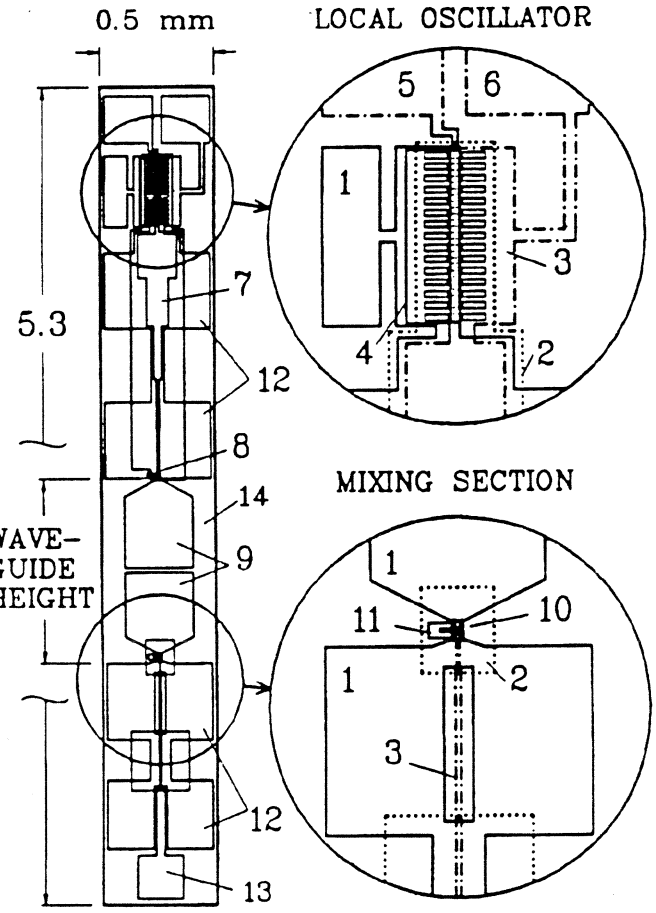

1. BOTTOM ELECTRODE (Nb)
2. INSULATION (SiO)
3. TOP ELECTRODE (Nb)
4. DAMPING RESISTOR (Ti)
5. NONUNIFORM FEED PAD
6. UNIFORM FEED PAD
7. MICROSTRIP TRANSFORMER
8. OSCILLATOR LOAD
9. COUPLING PROBES
10. SIS ARRAY
11. INDUCTIVE TUNER
12. RF LOW-PASS FILTERS
13. IF OUTPUT AND BIAS PAD
14. QUARTZ SUBSTRATE

Fig.9

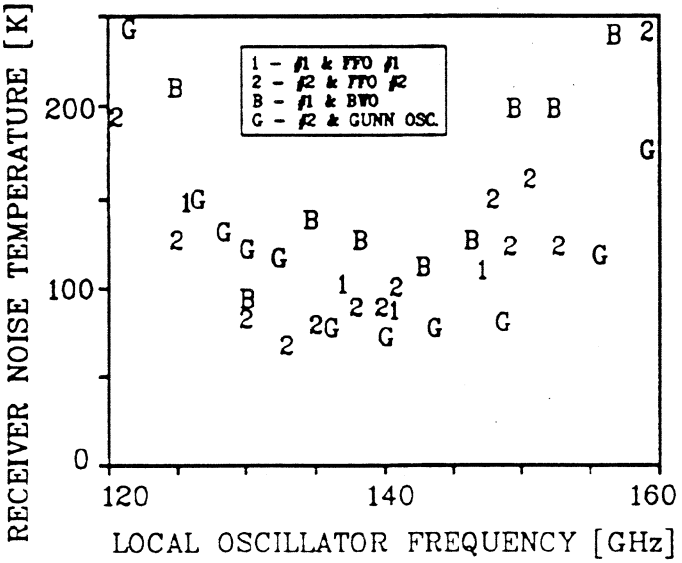

Fig.10

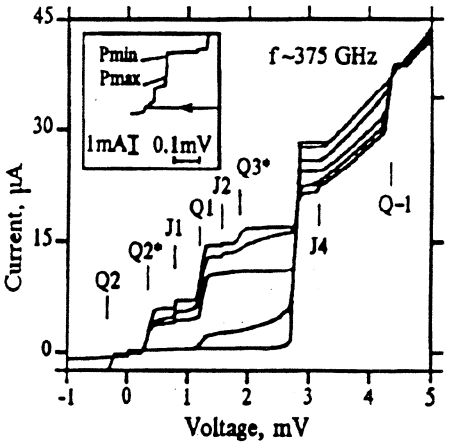

Figure 11. IVC of the detector at different levels of the FFO power adjusted by tuning the bias current at constant magnetic field.

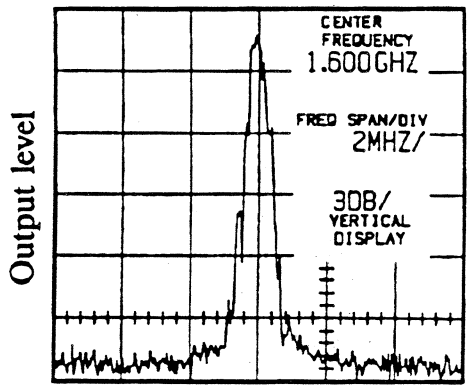

Figure 12. Spectrum of the IF output power when the signal of FFO is mixed with synchronized signal in SIS mixer at 140 GHz.

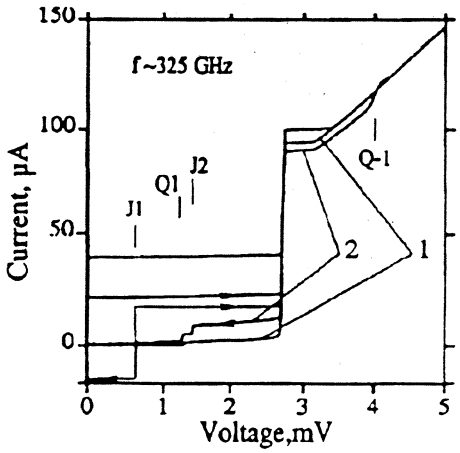

Figure 13. IVC of SIS detector at two levels of the FFO power (f=325 GHz); adjustable attenuation is introduced by integrated superconducting attenuator.

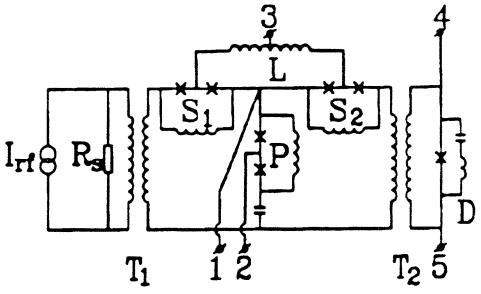

Figure 14. Equivalent diagram of the integrated attenuator circuit.

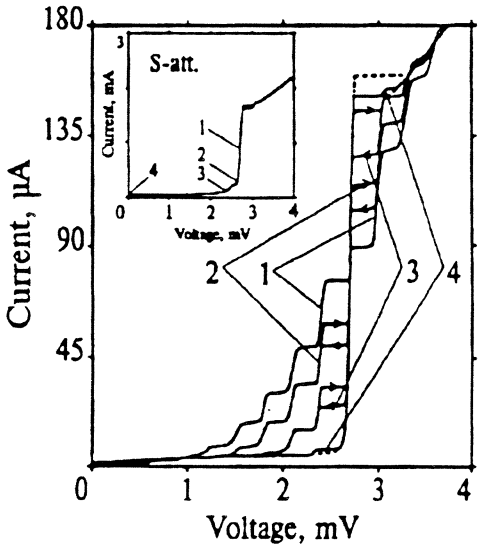

Figure 15. IVCs of the detector at four different bias voltages on the series attenuator for constant level of the input power f=74.6 GHz. IVC of S-att is shown in the insertion.

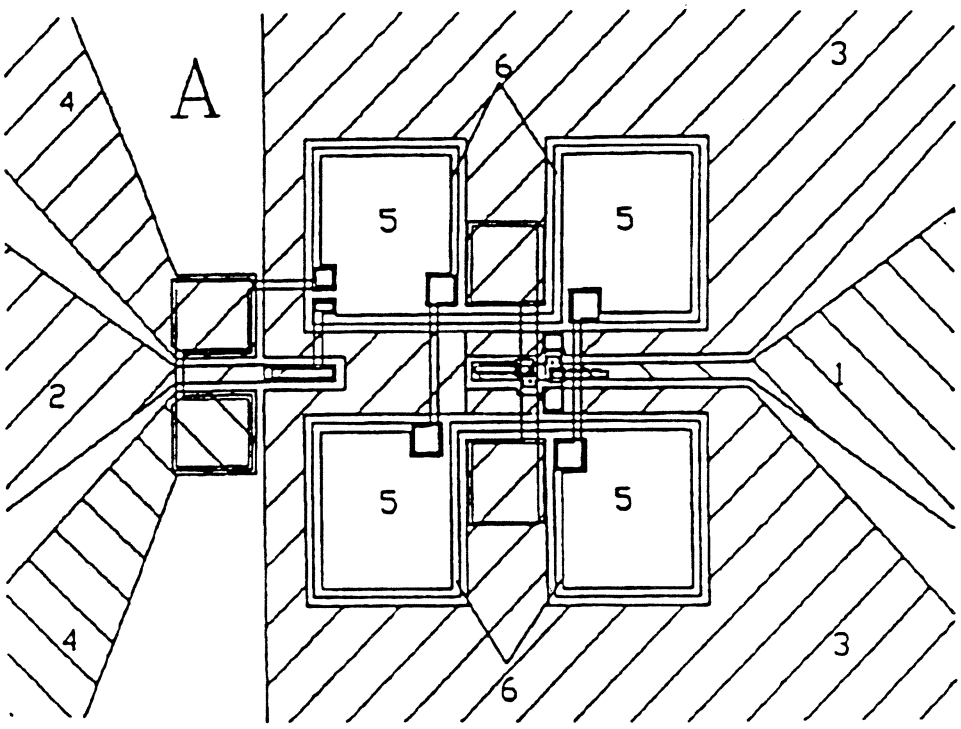

Figure 16. Four-loop planar dc SQUID with integrated input coil. (1,3) and (2,4) – output and input coplanar lines. (5) – parallel connected inductive SQUID loops each 200x200 mm^2, inside each of them single turns are arranged and connected in series to form an input coil.

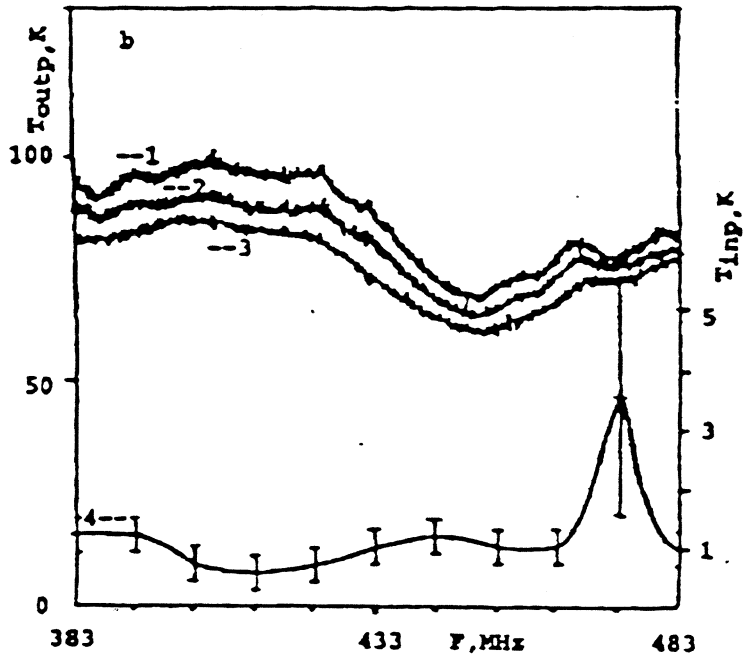

Figure 17. The dependence of the amplified noise signal on frequency. The noise temperature is lower than 0.5 K in 60 MHz band

First Results from A Small Bolometer-Array on the IRAM 30-m Telescope at 250 GHz

E. Kreysa*, E.E. Haller**, H.-P. Gemünd*, C.G.T. Haslam*, R. Lemke*, A.W. Sievers***
* Max-Planck-Institut für Radioastronomie, Bonn, Germany
** L B L, Berkeley, USA
*** I R A M, Granada, Spain

Abstract

Bolometers, cooled to temperatures below 1 K, are the most sensitive detectors of continuum radiation for mm- and submm-waves. The reason for their sensitivity is the virtually unlimited bandwidth that can be used. Processes involving continuum radiation give clues to a variety of important astronomical topics, such as star formation and active galactic nuclei. All large submm-telescopes are therefore equipped with bolometers for these studies. In a groundbased environment bolometers can be made to work close to the fundamental limit of the photon fluctuations of the thermal radiation of the atmosphere and the telescope. The same limit, at a lower level, will apply for space experiments involving passively cooled telescopes (SMIM, FIRST). In this situation further improvement of performance is possible, for the study of extended sources, by using bolometer arrays.
We report the first operation of a small bolometer array, cooled to 0.3 K, on the IRAM 30 m-telescope at a wavelength of 1.2 mm. Several observing strategies have been tried and evaluated. It is obvious from the raw data, that the noise in adjacent channels is partially correlated. This is to be expected if the noise is due to fluctuations of the sky emissivity (skynoise). One can take advantage of these correlations in order to reduce the noise of the raw data. In the near future we hope to apply these techniques to a large bolometer array for the 350 μm atmospheric window on the MPIfR/SO Submm-telescope which is under construction on Mt. Graham, Arizona.

Introduction

For the purpose of mapping extended sources, a bolometer array consisting of n elements should have an advantage of a factor of n in observing time over a single bolometer, if each array element is equivalent in performance to the single bolometer. If on the other hand, the average noise equivalent power (NEP) of the array bolometers were higher by a factor of n the array advantage would vanish. It is difficult to manufacture large numbers of bolometers of unformly high quality and to couple them efficiently to the telescope. Therefore, if some loss of performance of the individual array element is unavoidable one should favour a large number of elements. Mm/submm-bolometer systems on large groundbased telescopes are often limited by skynoise even at the best observing sites. Skynoise is that fraction of the fluctuations of atmospheric emission that remains even after sky-chopping and phase-sensitive detection. At submm-wavelengths atmospheric fluctuations are caused mainly by spatial and temporal variations of the concentration of water vapour. Work by other groups (Ref. 1) seems to indicate that skynoise is highly correlated across an array. Therefore in a skynoise limited situation even the smallest array (e.g. of two elements) could be advantageous.

The Instrument

We decided to investigate the properties of bolometer arrays experimentally with a small array of seven bolometers, arranged in a hexagonal grid with one central element. The array was designed to operate on the IRAM 30 m Millimeter Radio Telescope (MRT) in the 1 mm atmospheric window. This small array will serve as a prototype for future large arrays. The array of composite bolometers was fabricated at MPIfR, with thermometers made from NTD-germanium[1] (Ref. 2), and installed on He-3 "minifridge" (Ref. 3) on the cold surface of a standard HD-3(8) cryostat (Ref. 4). With a pumped He-4 bath the hold time of both the He-3 and He-4 stage are conveniently above 48 hours. A seven channel preamplifier with room temperature junction-FETs in the first stages is mounted on top of the cryostat. It provides a gain of 1000. As in our single channel bolometer systems (Ref. 5) each bolometer is designed to operate in the diffraction limited mode. In this way, the full spatial resolution of telescope is preserved and the array can thoroughly optimised for one wavelength. Each element of the array consists of three parts: the feed, a short length of waveguide and the bolometer cavity. In the diffraction limit the antenna theorem is valid for the feed

$$A\Omega = \lambda^2$$

and one can think of the system as a very simple waveguide receiver. The main difference to a coherent receiver is that the bolometer will accept both planes of polarisation. Unless one is interested in polarisation measurements, the feed and the waveguide should not be polarisation selective. We chose a circular waveguide with a diameter such that the cutoff frequency of the fundamental mode (TE 11) coincides with the desired long wavelength cutoff

$$\lambda_c = 1.706\ d$$

A circular waveguide allows about 30 % bandwidth of single mode propagation up to the cutoff wavelength of the next higher mode (TM 01).

$$\lambda_c = 1.307\ d$$

The waveguide can be very short (~ 2 d), because the very steep drop in transmission beyond cutoff provides an almost ideal high pass filter (Ref. 6). The definition of the system passband is completed by the addition of a low pass filter, mounted in front of the feeds. The low pass property of the filter is determined by a stack of capacitive meshes that are embedded in polyethylene (Ref. 7). These filters have to be combined with bulk absorbing materials in order to achieve the wideband blocking properties required by the bolometers. Of all possible waveguide feeds, corrugated horns have the highest efficiency, as they launch an almost ideal fundamental Gaussian mode. They would be the ideal choice for single channel diffracation limited systems, if it were not for the difficulty of manufacturing them for very high frequencies. For arrays one also has to consider the sampling efficiency. Feeds of different types have different minimum spacings in the focal plane which means that on the sky the spacing between the beams, relative to their widths is different. If for example the area to be mapped is of the same size as the array and if it is the aim to sample that area completely, then that type of feed that can be packed most densely is the best choice (Ref.

---

[1]Neutron-Transmutation-Doped germanium

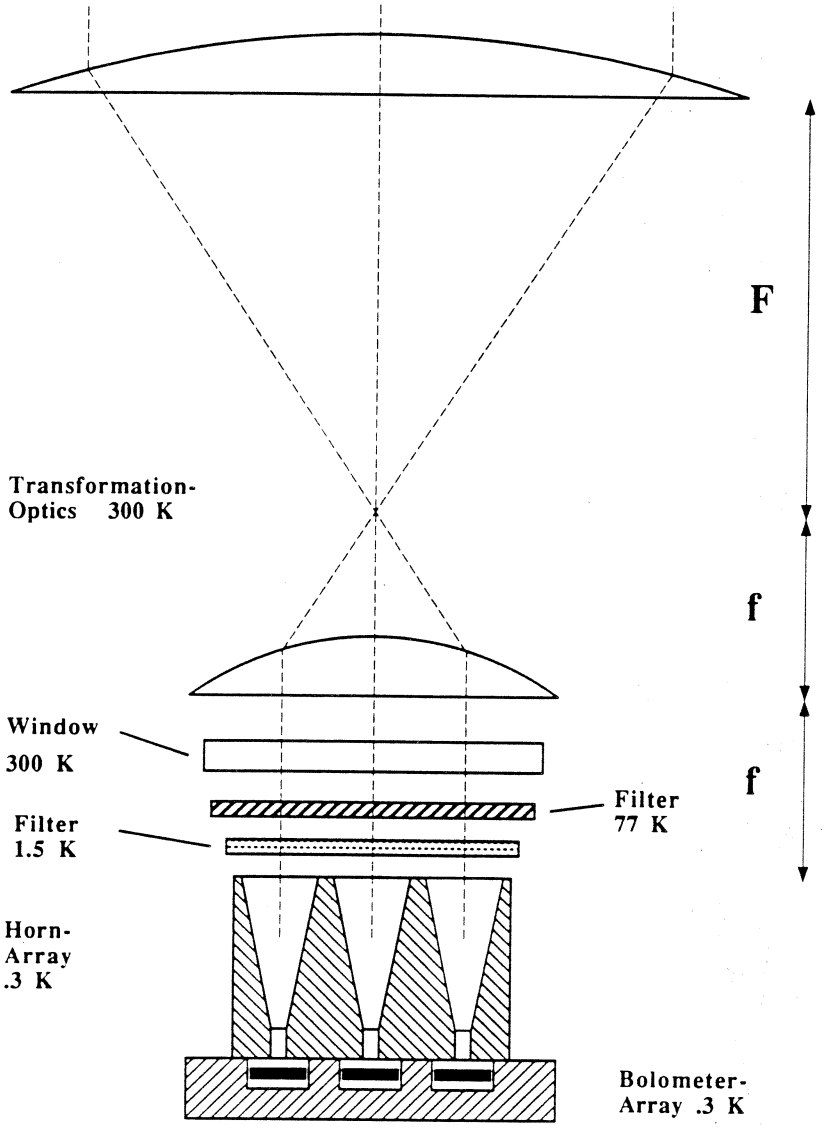

Figure 1 Schematic view of the seven element bolometer array

9). Corrugated horns, especially those of the wideband variety (Ref. 10) that would be required for bolometers, use a lot of space. For that reason a compromise between single beam efficiency and sampling efficiency is necessary. Without having done a detailed optimisation, the ease of manufacture led us to choose conical horns. The horns were made elong enough so that the maximum gain for the given aperture diameter is reached (Ref. 11). The 30m-MRT has a secondary focal ratio of

$$F/D = 9.73$$

Horns for this focal ratio would be too large and heavy to mount on the He-3 refrigerator that is used to cool the bolometers. Feeds with a small focal ratio are compact and light. They have the additional advantage of requiring only a small window in the cryostat, thereby reducing the radiative heat load. It is most convenient to fabricate both the bolometer- and the horn-arrays in a planar configuration, which means that the axes of the horns are parallel to each other. An optical system is then needed that can transform the beams to the telescope focal ratio, while maintaining the parallelism of the beams. This cannot be done with a single optical element. The solution is to use two optical elements (lenses in our case) with positive focal lengths in a telecentric configuration, i.e. with a common focal point between them (Fig. 1). In the Gaussian approximation a beamwaist in one focal plane of a single lens is transformed into a waist in the other focal plane independently of the wavelength. The ratio of the waist diameters still depends on wavelength (Ref. 12) and is given by

$$w_2 = \lambda f_1/\pi w_1$$

For the telecentric lens system if follows that

$$w_3 = f_2\, w_1/f_1$$

This means that in this configuration not only the positions of the waists are frequency independent, but also the ratio of the waist diameters. This is the principle of a Gaussian beam telescope (Ref. 8).
We use aspherical lenses, corrected for spherical aberration and machined from PTFE. The lenses have to be fairly large in order to satisfy both the Gaussian beam approximation and the field of view requirements (f_1 = 250 mm, f_2 = 50 mm). At shorter wavelengths, where there are no low loss, machinable dielectric materials one might have to use offaxis mirrors. Their design will require careful raytracing over the whole field of view and the alignment will be critical.

Results

During a test run February 1992 the array cryostat and the transformation optics were installed in Nasmyth focus of the IRAM 30 m MRT. Sky chopping in azimuth direction was done with the subreflector at 2 HZ and a throw of 30". Because of the Nasmyth configuration the beams of the array rotate around the central beam with any change in elevation. The center beam is used for pointing. This rotation occurs in addition to the usual rotation caused by the altazimuth mounting. Keeping track of each individual beam during any type of observation is therefore somewhat involved. Beam patterns obtained with the array on the planet Uranus (Fig. 2) show satisfactory beamshapes and good coupling to the

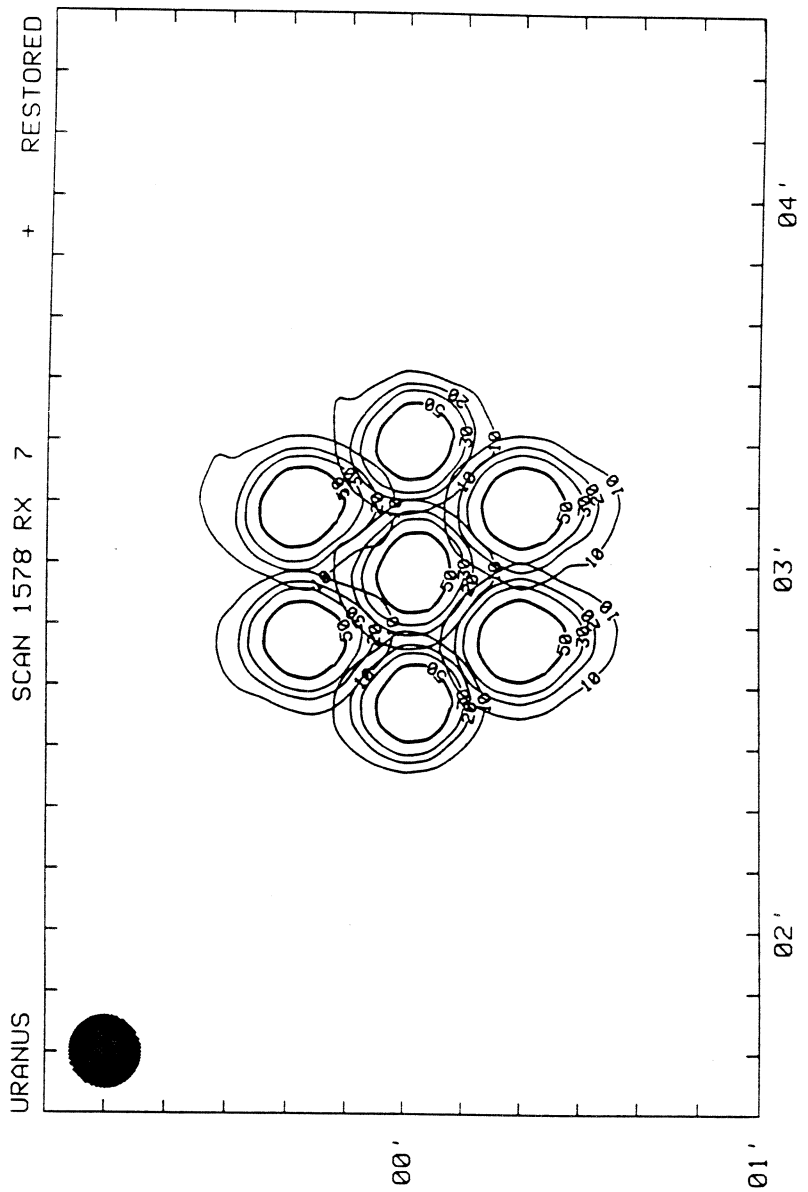

Figure 2 Beam pattern of bolometer array obtained on Uranus with the 30 m-MRT. Contour levels are in percent of peak intensity

telescope. The variation of the sensitivity among the beams is within 10 %. The average beamwidth (FWHP) is 12" at a spacing of 22" corresponding to an undersampling factor of about 5. The limiting flux density is about 50 mJy/ Hz (in perfect weather conditions), which is similar to the performance of single beam systems on this telescope.
The seven-element array has been used again extensively in Feb/March 1993 on the 30 m-MRT for different kinds of astronomical programs. The following advantages were obvious:

a) Skynoise filter algorithms are effective both for continuous mapping modes and for ON-ON observations of point sources.
b) The seven maps produced in the mapping mode have precisely known position offsets from each other. This is not necessarily true when seven coverages with a single beam system are done sequentially.
c) In deep ON-ON integrations on point sources with the central beam, the six surrounding beams can serve as control fields to check for spurious signals.

The last two advantages might also apply for space applications.
A 19-beam bolometer array for 250 GHz is nearing completion. We plan to build 37-element arrays at 250 GHz and 860 GHz for the 30 m-MRT and the 10 m-SMT (MPIfR/Steward Observatory) respectively.

References

1. Hildebrand, R., private communication
2. Haller, E.E. et al. (1984) Proc. 4th Neutron Transmutation Doping Conference, New York, Plenum Press, 21-36
3. Torre, J.P. & Chanin, G. (1985) Rev. Sci. Inst., 56, 318-320
4. Infrared Laboratories, Tucson
5. Kreysa, E. (1990) Proc. 29th Liège Int. Astrophysical Colloquium, ESA SP-314
6. Marcuvitz, N., Waveguide Handbook, MIT Radiation Laboratory Series 10, McGraw-Hill, New York, 1951
7. Whitcomb, S.E. & Keene, J. (1980), Appl. Optics, 19, 197-198
8. Goldsmith, P. (1982) Infrared and Millimetre Waves Vol. 6, N.Y. Academic Press, 277-343
9. Yngvesson, K.S. (1988) IEEE Trans. on Antennas and Propagation, AP.36, 1637
10. Thomas, B.M. (1978) IEEE Trans. on Antennas and Propagation, AP-26, 367
11. Hansen, R.C. (1988) Microwave and Optical Technology Letters, 1, 386
12. Kogelnik, H. & Li, T. (1966) Appl. Optics 5, 1550

WIDE BAND FIXED TUNED AND TUNEABLE SIS MIXERS FOR 230 GHz AND 345 GHz RECEIVERS

A. Karpov, M. Carter, B. Lazareff, M. Voss, D. Billon-Pierron, K. H. Gundlach

INSTITUT DE RADIOASRONOMIE MILLIMETRIQUE
300, rue de la Piscine,Domaine Universitaire de Grenoble, St Martin d'Hère,
38406 France

ABSTRACT

Extra-low noise SIS mixers have been developed for radioastronomy receivers in the 1.3 mm and 0.8 mm bands. A single backshort waveguide mixer design is used. The best receiver DSB noise temperatures achieved are about 55 K in the 1.3 mm band and about 72 K in the 0.8 mm band. The present mixer design uses SIS junctions in which parallel inductive tuning is implemented with quasi-lumped elements. The tuning structures have been optimized in order to allow to use the same junction area and current density for the submillimeter band as for the millimeter band. Experimental measurements agree with model predictions of the new SIS mixers performance. In particular, the same mixer can be used either in fixed-tuned, DSB mode, having an instantaneous bandwidth covering most of the waveguide band, or tuned to image band rejection (SSB) mode at each frequency. It has been found that if a mixer is tuned to SSB operation the minimum SSB receiver noise temperature is only about 75% of the SSB noise temperature in DSB regime. The new mixers have been installed at the IRAM 30-m telescope in Spain and at the telescope of the University of Grenoble in France.

INTRODUCTION

SIS mixer development is one of the main activities of the IRAM receiver group. The large investment made in the 30-m IRAM telescope at Pico Veleta and in the four 15-m antennas interferometer on Plateau de Bure gives a strong incentive for improving the receiver performance.

The objectives of the development are: to reduce the receiver noise, to extend the operating bandwidth, and to allow to tune the mixer either for single sideband (SSB) or for double sideband (DSB) operation. The reduction of the receiver noise temperature increases the data gathering efficiency of scheduled observations. An improved coverage of the atmospheric windows opens new possibilities for the observations. Mixer tuning with 10-15 dB image sideband rejection in all the mixer RF band improves the calibration accuracy of

spectroscopic observations and the SSB system temperature through rejection of atmospheric noise.

Fixed tuned, wide band mixers are attractive for their simplicity of operation. This new kind of SIS mixer appeared some years ago and is currently an area of active development [1-3]. It is interesting for all the applications were DSB operation is acceptable or the tuning to SSB is impractical. The possible domains of application in radioastronomy are multibeam arrays or large interferometers. It may be also interesting for the installation on a satellite or airborne observatory.

The capability of fixed-tuned operation was one of the main design objectives of new mixer development in IRAM. The present design is universal. The same mixer may be used either fixed-tuned (DSB mode) or tuned to SSB mode. Single backshort tuning of this mixer allows one sideband rejection allover the mixer RF band

Below we present the new 1.3 and 0.8 mm SIS mixer developments. The principal mixer features are: reduced height waveguide, single backshort design, two SIS junctions array with individual tuning structures.

The use of this mixer in a receiver is simpler than the use of a mixer with two adjustable backshorts, but the stage of mixer circuit design is more complicated. If the RF band is relatively broad (25-30 %) and if the junction $R_N C\omega$ parameter is large an accurate mixer model is required to synthesize the mixer circuit allowing the correct mixer tuning (or tuneless operation) over all the band. A reduced height waveguide single backshort SIS mixer model reported before in [4] is used for the mixer circuit design.

The SIS junctions with the integrated inductive tuning let us use for the submillimeter band (0.8 mm) the same junction size and critical current density as for millimeter band (3-1.3 mm). For example it allows to get a good mixer performance in a 25% relative band with a factor $R_N C\omega$ about 14 at 350 GHz. It is about 14 times large then the value given by the well known relation for the optimal $R_N C\omega \approx \frac{400}{F[GHz]}$ [5].

In this work we first describe the receiver conversion gain measurements and the receiver and mixer noise estimation for a 345 GHz SIS receiver. Then a test of the noise temperature of the fixed tuned and the tuneable mixers over the 180-270 GHz and the 300-360 GHz band is presented. In the last section the operation of the new mixers on the telescopes is described.

SIS RECEIVER CONVERSION GAIN MEASUREMENT

The conversion gain measurement of an SIS receiver is important for the understanding of the mixer performance. Below we show how these measurements are used for the estimation of the mixer noise temperature.

The measured receiver conversion gain depends on the frequency, the mixer tuning, the junction current, the mixer block temperature etc. In our laboratory experiments the measured receiver minimum conversion gain (SSB) is normally between about 0 dB in the 3 mm band and -3 dB in the 0.8 mm band. The in situ measurement of the IF chain noise temperature is in a good agreement with the result of an independent measurement with a variable temperature load.

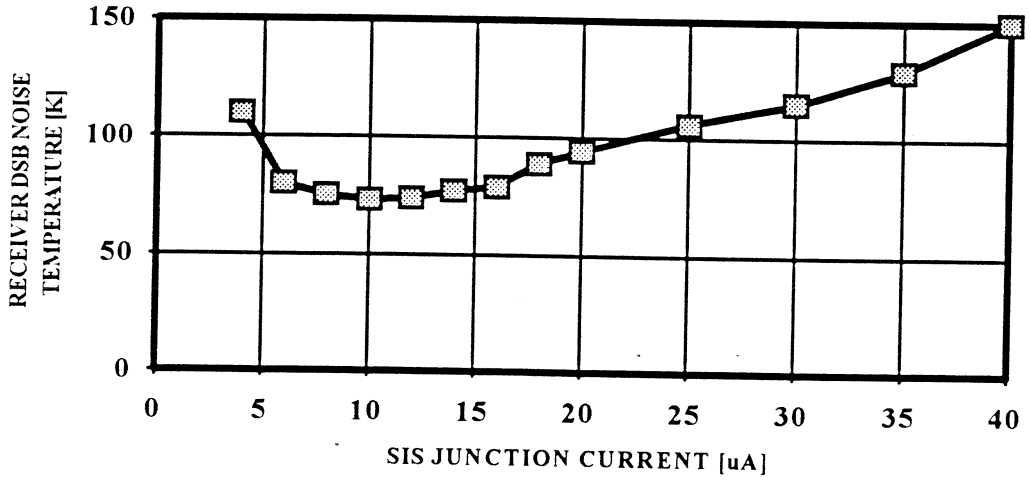

Fig. 1 SIS receiver DSB noise temperature at 318 GHz for different LO power levels as a function of the bias current. Junction bias voltage is fixed (4 mV). Junction temperature is 4.2 K.

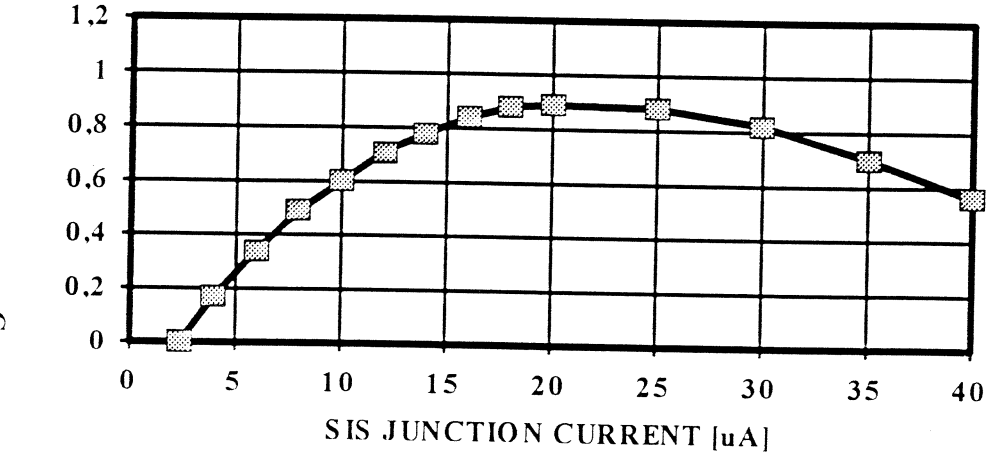

Fig. 2 SIS receiver SSB conversion gain at 318 GHz for different LO power levels as a function of the bias current. Junction bias voltage is fixed (4 mV). Junction temperature is 4.2 K.

The receiver conversion gain between the quasioptical input port and the input port of the first IF amplifier (behind an isolator) is determined in the same hot-cold loads experiment as the receiver noise temperature by a "shot noise" method [6]. In the same procedure the IF chain noise temperature is measured.

The conversion gain is calculated from the receiver IF power (P_{IF}) variation which occurs when the room temperature load (black body at T_{HOT}=295 K) is substituted at the receiver input port by the liquid nitrogen load (T_{COLD}=77 K). Then the temperature variation at the receiver input is 218 K and the equivalent noise temperature variation at the mixer output is proportional to receiver IF power variation. For the receiver in DSB operation the conversion gain (SSB) is calculated from the ratio of noise source temperature variations at the mixer output and at the receiver input.

$$Gr = \frac{1}{2}\frac{K*(P_{IFH} - P_{IFC})}{T_{HOT} - T_{COLD}} \qquad (1)$$

The IF chain should be calibrated to determine the coefficient (K) of the equivalent temperature variation at mixer output to the IF power (P_{IF}) variation.

In our experiment the IF amplifier chain between mixer output and the IF power measurement plane is calibrated in situ using as a controlled noise source the unpumped SIS junction biased beyond the gap voltage. An SIS junction biased behind the gap voltage is in a normal state and may be considered as a parallel connection of the junction normal resistance and the junction capacitance. The junction normal resistance equivalent noise temperature is calculated for the different bias current levels from the resistance shot noise density converted to an equivalent temperature T ($h\nu << kT$). The coefficient (K) relating the temperature variation at mixer output to the IF power variation is determined from two IF power measurements with different junction current levels I_{J1} , I_{J2} as :

$$K = \frac{T_2 - T_1}{P_{IF2} - P_{IF1}}, \qquad (2)$$

where T_1 and T_2 are the equivalent noise temperatures corresponding to the shot noise power available at the IF chain input for bias current levels I_{J1} and I_{J2}. The noise power available at the cooled amplifier input (behind an isolator) is calculated from the noise power available at the terminals of the SIS junction. The mixer block and IF chain equivalent circuit is used to calculate the junction coupling to the IF amplifier input port.

The IF chain noise temperature is calculated from the same data in a standard way as:

$$T_{IF} = \frac{T_2 * P_{IF1} - T_1 * P_{IF2}}{P_{IF2} - P_{IF1}}. \qquad (3)$$

Figures 1-3 show the results of a 0.8 mm receiver test. In this test the receiver noise temperature Tr and conversion gain Gr are measured for the different local oscillator power levels at a fixed frequency (318 GHz). The junctions bias voltage is fixed (4 mV) and the bias current is controlled by the local oscillator power. Measured values Tr, Gr are presented as a function of the bias current. The test has been performed at the altitude of 2850 m, where the mixer block temperature is about 4.2 K instead of 4.8 K at the sea level, resulting in performances which are better than in laboratory.

The 1.2-1.8 GHz IF chain noise temperature measured in situ is 3.5-4 K The independent test gives 3.8 K..

The minimum receiver DSB noise temperature is 73 K and maximum receiver conversion gain (SSB) is as high as 0.9 (- 0.5 dB). It is the best result observed in our 0.8 mm receiver test. Junction mismatch to the receiver input and mixer output ports accounts for a loss about -1.5 dB at this frequency. Therefore, the mixer available gain about 1 dB. It is close to the theoretical prediction in [7] of the gain in optimum regime at this frequency.

In our experiments the minimum receiver noise temperature occurs at a lower local oscillator power level than the maximum gain. It can be explained by the increase of the shot noise contribution in the receiver noise temperature when the junction current follows the increase of the local oscillator power.

In fig. 3 the receiver gain corrected for the junction coupling to the IF chain is presented. The maximum of the curve is relatively flat and corresponds to a current about 5-6 times larger than the leakage current at the operating point. It is interesting to note that the gain may be rather large (0.7) down to a current of about only 1.5 times more than the leakage current.

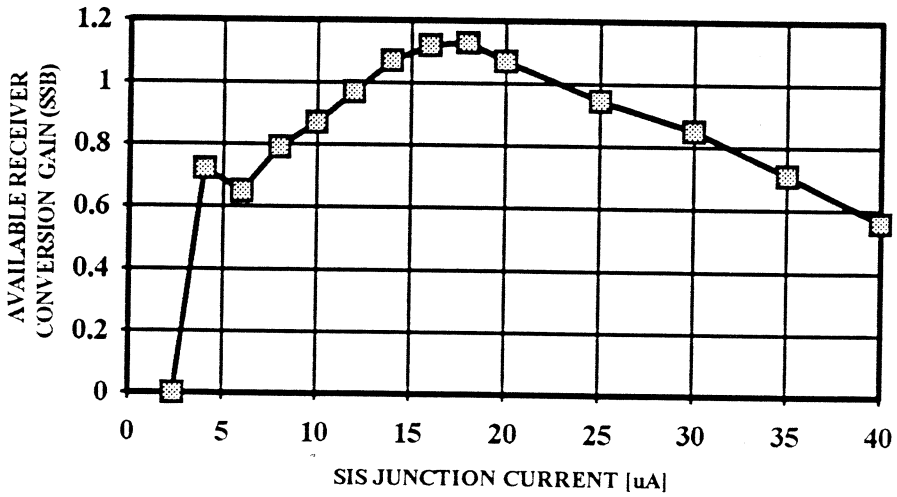

Fig. 3 SIS receiver SSB conversion gain at 318 GHz corrected for the junction to IF chain coupling.

SIS RECEIVER NOISE ESTIMATION

We use the standard relation for the receiver DSB noise

$$T_R = T_{ANT} + T_{MIX} + \frac{T_{IF}}{2G_R} \tag{4}$$

Where:

T_{ANT} is the equivalent noise temperature of the quasioptical system at the receiver entrance before the mixer. Usually a dual beam interferometer diplexer is used in IRAM receivers for the local oscillator power injection. The loss of this element is about 0.2 dB (15 K contribution in T_{ANT}). The plastic lens loss contribution (if it is not cooled) is similar. A cooled scalar corn contribution in T_{ANT} may be neglected.

T_{MIX} is the mixer DSB noise temperature.

T_{IF} is the IF chain noise temperature.

G_R is the receiver SSB conversion gain.

The receiver noise measured at 318 GHz can be broken down as follow:

T_{ANT} is about 25 K (15 K from the diplexer and 10 K from the plastic cryostat window; the mixer horn and lens are inside of the cryostat at 4.2 K stage); the measurement of T_{IF} gives 4 K; at optimal bias current (10 μA) SSB receiver conversion gain is G_R=0.6.

So, the minimum mixer DSB noise in this experiment is T_{MIX}≈45 K ($T_{MIX}=T_R-T_{ANT}-T_{IF}/2G_R$).

This value is about one order of magnitude larger than the minimum mixer noise at 345 GHz predicted in [7, 8]. Available mixer noise temperature remains still more than prediction, even corrected for the SIS junction to antenna coupling.. Corrected (available) mixer noise temperature $T_{MIX\,AV}$≈38 K is estimated according to:

$$T_R = T_{ANT} + \frac{T_{MIX\,AV}}{2G_C} + \frac{T_{IF}}{2G_C * G_M} \tag{5}$$

Where:

$T_{MIX\,AV}$ is the available mixer noise temperature.

G_C is the SIS junction coupling to the antenna. The coupling of the junction has been calculated using the mixer equivalent circuit for the different backshort positions and frequencies. At 318 GHz G_C it is estimated as 0.7 (SSB)

G_M is the mixer conversion gain; ($G_R=G_C \cdot G_M$).

The difference between the prediction of the optimal mixer noise and measured data may be related to the junction shot noise power injected in the IF chain. An estimate of the maximum shot noise can be derived by applying the standard shot nose formula, using DC bias current and the differential resistance of the pumped IV curve at the bias point. In the condition of the test at 318 GHz (fig. 1-3) it gives the equivalent noise temperature about 70

K injected in the IF chain and about 50 K contribution in the available mixer noise. The approximate agreement with the measured noise lends some support to our hypothesis.

JOSEPHSON EFFECT PROBLEM IN THE SIS MIXER

At some frequencies the Josephson effect may perturb the SIS mixer operation. If the $R_N C\omega$ product is large enough this happens when the Josephson oscillation fundamental frequency or one of its harmonics coincides with the mixer operating frequency. It results in a receiver noise increase and a perturbation of the pumped I-V curve. Usually these oscillations in the SIS junction may be suppressed if a magnetic field is applied. When a junction array is used, Josephson oscillations suppression may be more difficult due to possible asymmetries in the circuit. In this situation the oscillations in the different junctions are suppressed at slightly different field intensities and the mixer operation perturbation may be reduced but remains present.

A correct junction bias choice may improve the situation. It allows to use an SIS mixer with incomplete suppression of the Josephson effect by magnetic field and makes the choice of magnetic field density less critical. Diagram in the fig. 4 illustrates this. This drawing shows the frequency of the Josephson oscillation and its harmonics (up to 6 th) versus the bias voltage of a two junction array. Here we can choose fixed bias voltage to keep the Josephson oscillation frequency outside the RF mixer band.

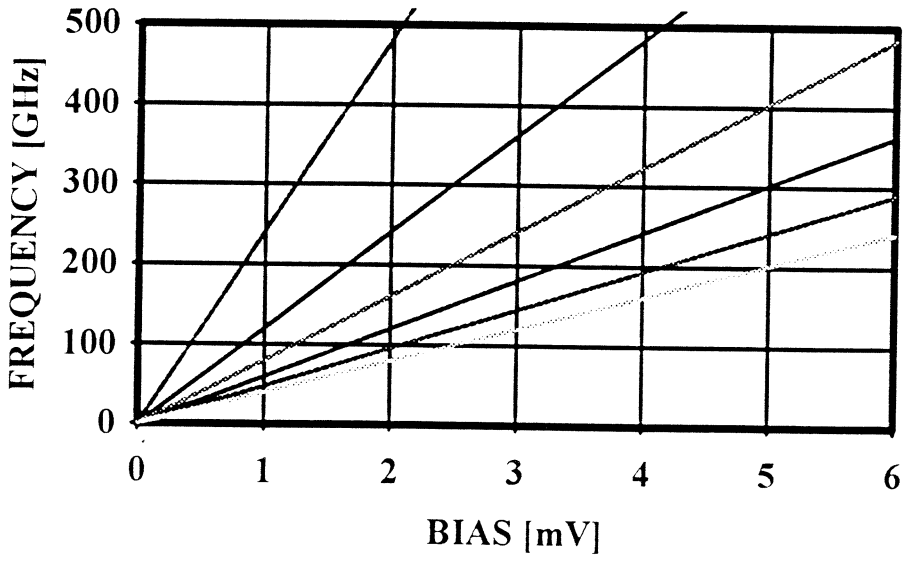

Fig. 4 Frequency of the first six harmonics of the Josephson oscillation.

For the 0.8 mm mixer fixed 4.0 mV junctions bias has been selected. The 4 mV vertical line in fig. 4 has the crossing points at 242, 323 and 484 GHz. Near these frequencies mixer

operation may be perturbed by the 4th, the 3th and the 2th Josephson oscillation harmonics excitation. The 322 GHz frequency coincides with the absorption line in the atmosphere and is not of interest for the radioastronomy. So, the 4 mV fixed bias allows to use a two junctions SIS mixer in 260-370 GHz band without important Josephson effect perturbations. On the other hand in this frequency range the 4 mV bias is sufficiently close to the middle of the first photon step, the optimal operation point.

LABORATORY RECEIVERS TEST

Fig. 5 shows a comparison of predicted performance and laboratory measurements for the 0.8 mm fixed tuned mixer. Receiver DSB noise temperature varied between 75 K and 145 K in the 300-360 GHz range. For the receiver noise estimation the junction coupling to the antenna is calculated over the band. A mixer available noise temperature estimation from the preceding section is used. In fig. 6 the measured receiver conversion gain is presented.

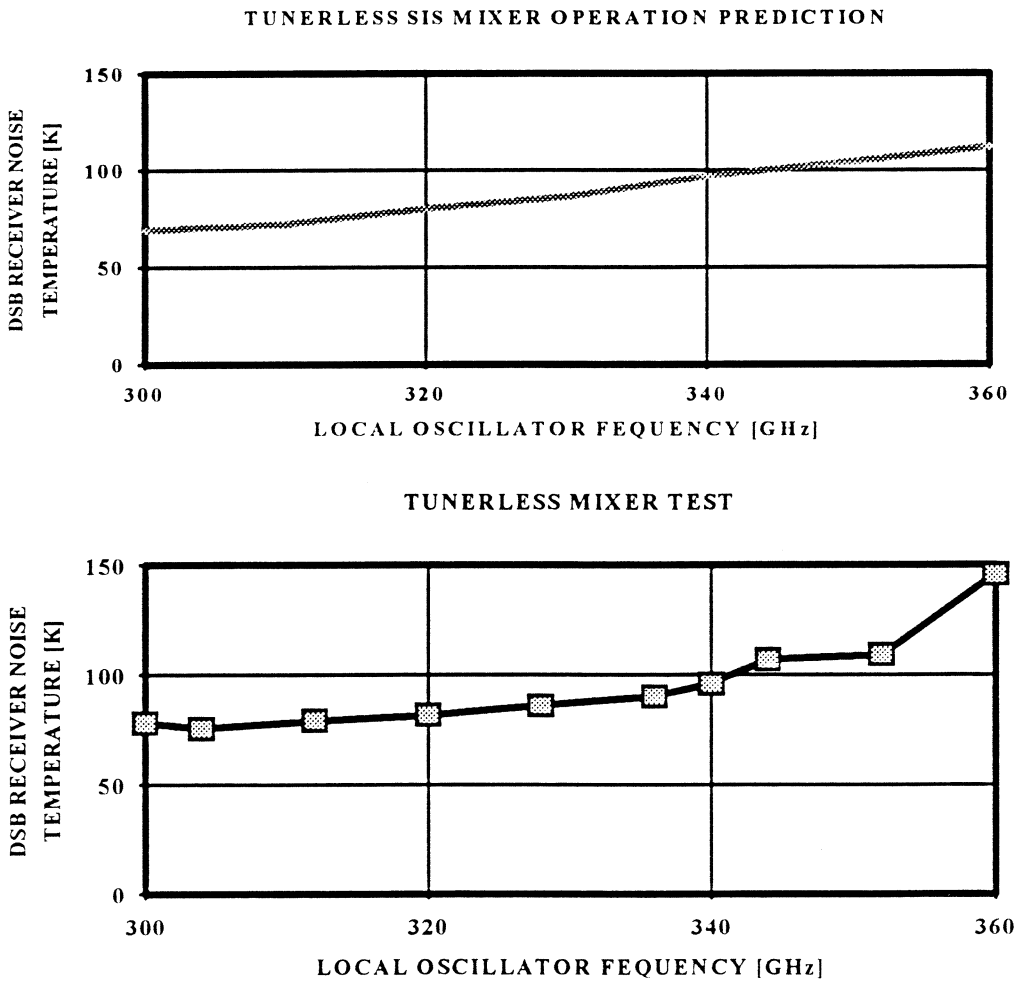

Fig. 5 Fixed tuned operation of the 0:8 mm SIS mixer.

The predicted mixer operation is in a good accord with the test result in all the 300-360 GHz band. Model prediction gives the band of the operation with the receiver DSB noise temperature below 150 K between 280 and 370 GHz but in the test the local oscillator was not available in the band 280-300 GHz. In this mixer a two Nb-Al oxide-Nb junctions array with the individual junction surface about 1 μm^2 and $RnC\omega \approx 5$ is used.

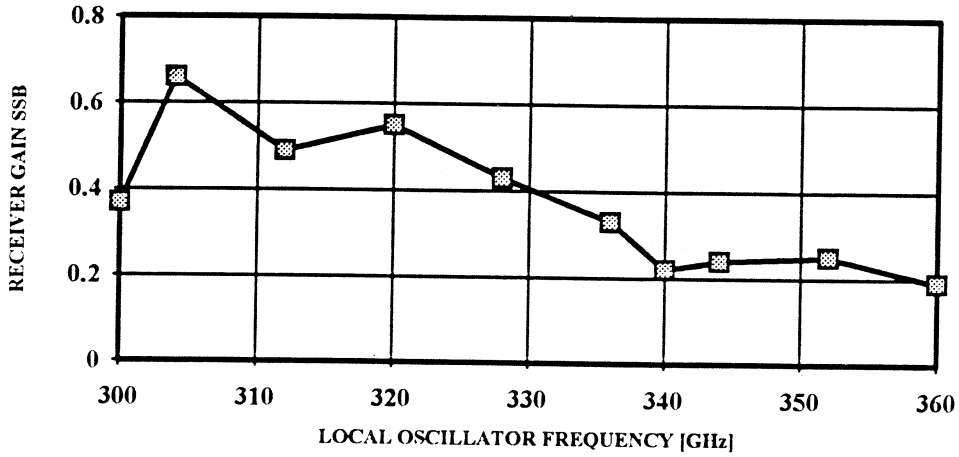

Fig. 6 Receiver conversion gain in 0.8 mm band (fixed tuned operation).

A similar design of the tuneable mixer allows to use in the same frequency range (320-360 GHz) the junctions with an individual area of about 2 μm^2 and $RnC\omega \approx 14$. The tuneable 0.8 mm mixer test is presented in fig. 7. Even though the bandwidth of this mixer is less than with smaller junctions, it is sufficient to cower the atmospheric transparency band around 345 GHz. This result is particularly interesting, because the fabrication of such junctions with traditional photolithography is relatively easy.

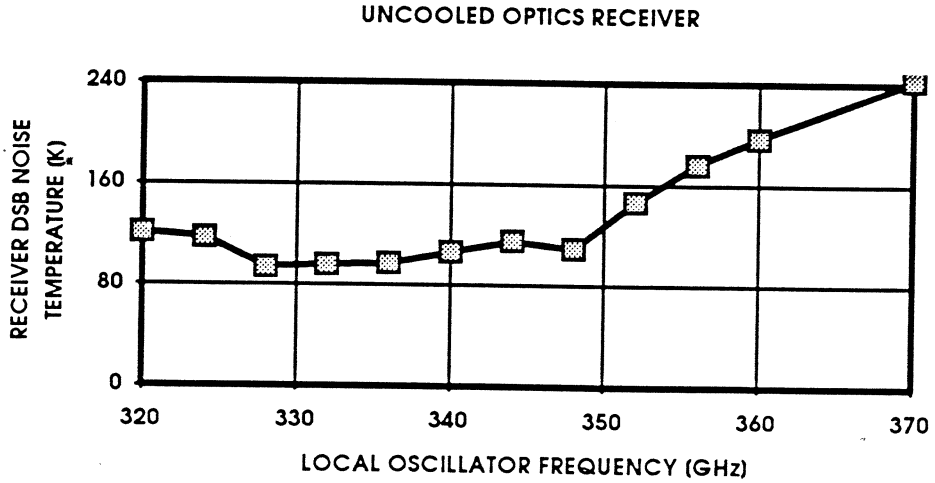

Fig. 7 A tunaeble 0;8 mm receiver operation. The junctionwith an individual area of about 2 μm^2 and $RnC\omega \approx 14$.

The test of a 1.3 mm fixed tuned mixer with uncooled optics is presented in fig. 8 (curve 1). In this receiver the diplexer and the lens are at the ambient temperature. Junctions with an area of about 2 μm^2 and $R_nC\omega \approx 5$ are used in this mixer. The minimum DSB receiver noise temperature (70-80 K) achieved in fixed tuned operation (curve 1) may be improved by the mixer tuning only in a small fraction of the band (curve 2).

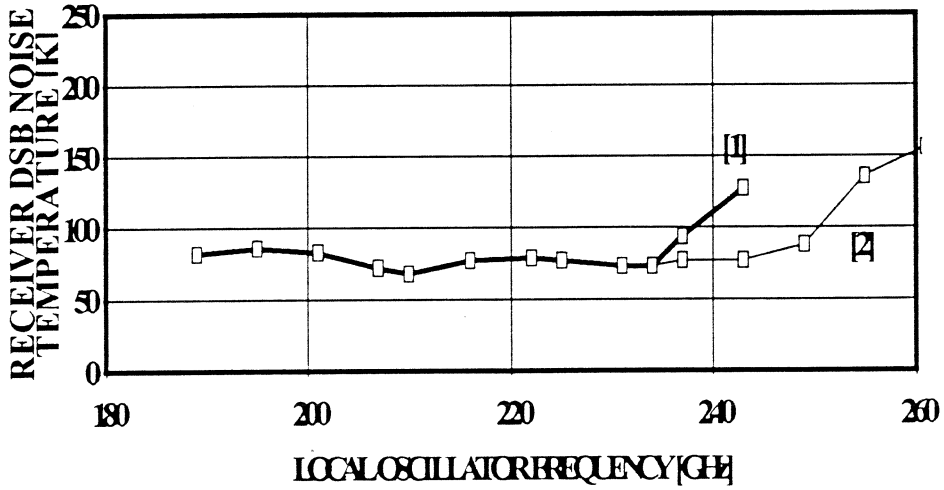

Fig. 8 Noise temperature of a 1.3 mm SIS mixer with a fixed backshort position (1) and with tuning (2)

When the cooled optics is used in the receiver noise temperature drops to the value of about 55 K in the 1.3 mm band (fig.9). In this receiver the local oscillator power is injected at the mixer input throw a cooled waveguide coupler. A plastic correcting lens of the mixer antenna is also cooled.

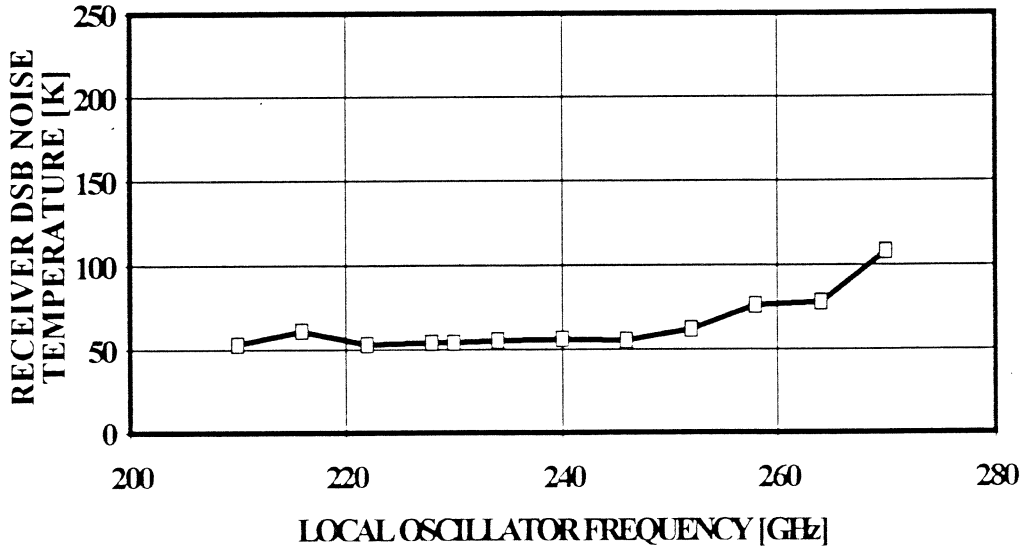

Fig. 9 The 1.3 mm receiver with a cooled optics and local oscillator power injection throw a cooled coupler.

The 1.3 mm receiver tuning to the SSB or DSB operation is presented in fig. 10 for a room temperature optics receiver. In this figure the DSB receiver noise temperature is given for the double sideband mixer operation and the SSB noise temperature for the mixer tuned for the single sideband operation. The SSB receiver noise temperature in SSB operation is about 150 % of the DSB noise temperature in DSB mode (or the SSB noise temperature of the tuned receiver is about 75% of SSB noise temperature of the receiver in wide band operation).

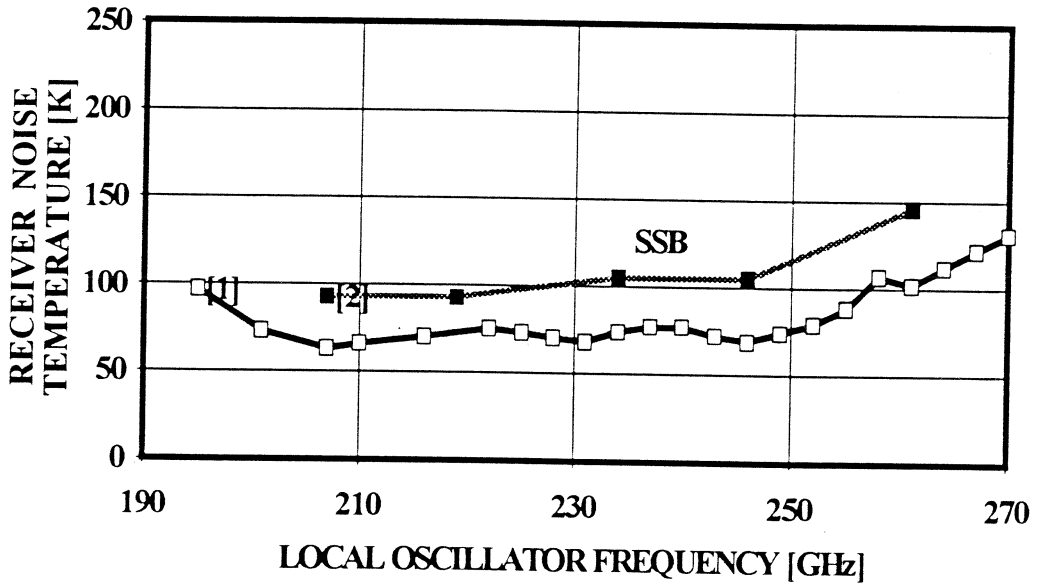

Fig 10 The tuning of a 1.3 mm receiver to the DSB and SSB operation

RECEIVERS ON THE TELESCOPES

Actually the new 230 GHz mixers are in use at two telescopes.

One SIS mixer is installed in September 1992 as a replacement of the Schottky-diode mixer at the Grenoble university telescope POM-2 [9] on Plateau de Bure in French Alps at 2500 m of altitude. It is a tuneable single-backshort mixer. Mixer is situated on the 4 K stage of the closed-cycle vacuum cryostat. Signal and local oscillator power are injected at the mixer entrance through the diplexer and uncooled lens. Measured at the telescope receiver DSB noise temperature is presented in fig. 11. In the band of receiver operation typical noise temperature is nearby 80 K.

The next 230 GHz mixer is installed at the beginning of 1993 at IRAM 30 M telescope at Pico Veleta in Spain as a replacement of the lead-junctions SIS mixer developed by R. Blundel [10]. The mixer is at 3.4 K stage in a helium gaze chamber of a traditional IRAM

liquid helium cryostat with the uncooled optics [11]. For the needs of the spectrum observations the sideband rejections is required. Using the mixer model the distance between

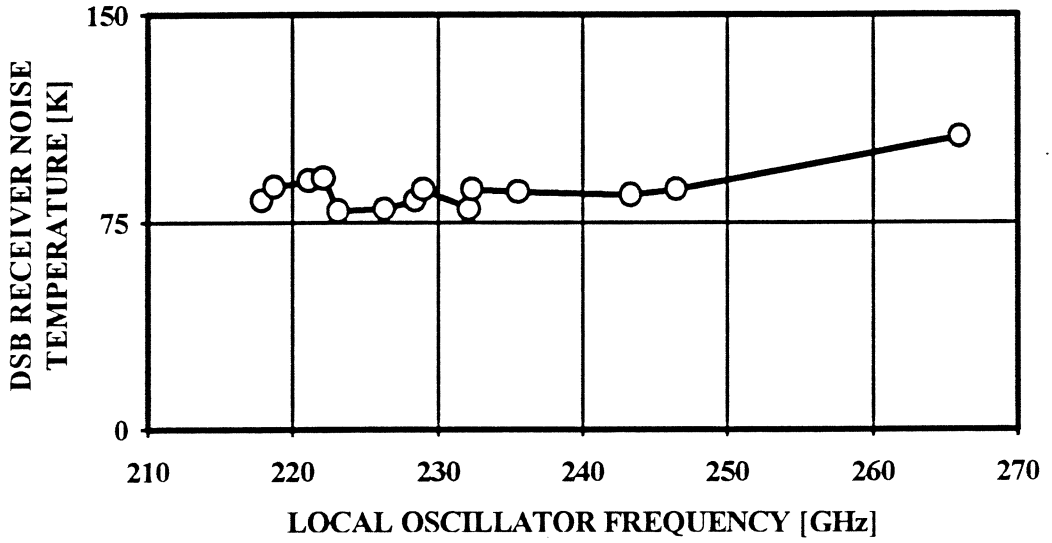

Fig. 11 Receiver with a developed SIS mixer at the telescope of Grenoble University.

the backshort and the junction is optimised. It has been found that a far backshort position (about 5-6th resonance) is convenient to provide a sufficient variation of the junction to waveguide coupling in the frequency range between the two sidebands. Receiver SSB noise temperature achieved during the performed observations is presented in fig. 12. Normally the SSB receiver noise temperature is between 80 and 100 K. In SSB operation the upper sideband is rejected by -7-10 dB.

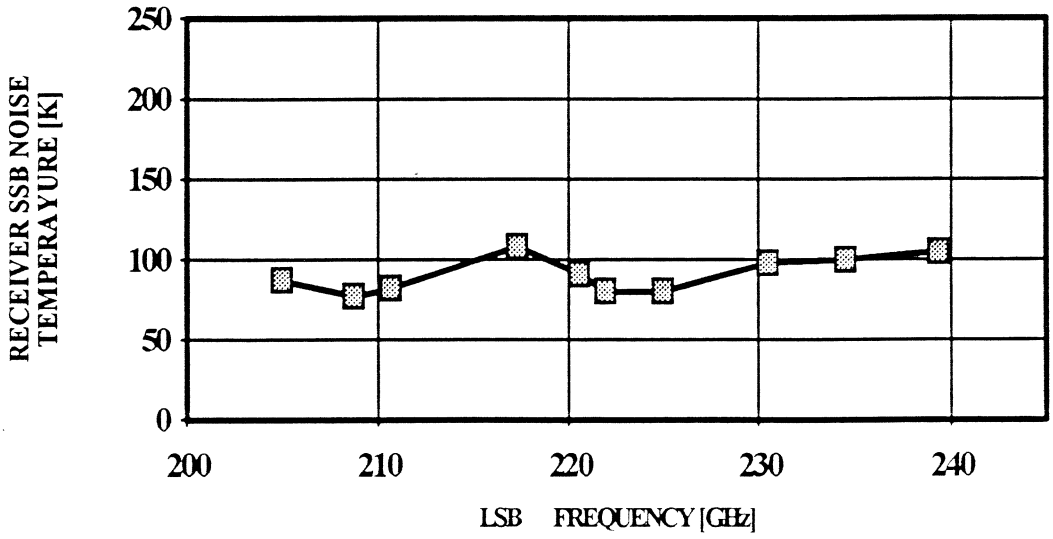

Fig. 12 Receiver with a new 1.3 mm mixer at IRAM 30-m telescope.

In the end of march 1993 a 345 GHz receiver with the new fixed tuned SIS mixer has been installed and tested at IRAM 30-m telescope. The receiver consists of the SIS mixer installed in the liquid helium Infrared Laboratory cryostat, the cooled IF amplifier situated in the same cryostat, the room temperature IF amplifier and the local oscillator. In this receiver we use the local oscillator earlier developed in MPIFR for the Schottky 345 GHz receiver. Local oscillator power is injected at the entrance of the mixer through dual beam interferometer diplexer. The mixer horn and the lens are at the 4 K stage of the cryostat. Intermediate frequency chain noise temperature is about 4K in the range 1.25-1.75 GHz.

At the telescope the fixed tuned receiver is tested in 320-360 GHz band (fig. 13). The noise temperature is found to be close to the laboratory test results (Fig. 5) and varied between 70 K and 130 K. Junction bias has been fixed at 4 mV. During the test no problem beard by the Josephson effect have been occurred. The minimum noise temperature of 70 K DSB is measured at 332 GHz. The system temperature (at the limit of the atmosphere) as low as 650 K has been achieved. Having the possibility of the low noise operation in the band between 280 and 360 GHz the new fixed tuned SIS mixer may be used as a supplement of the 1.3 mm mixer for the complete covering of the 190-310 GHz atmospheric window or for the operation in 330-360 GHz band.

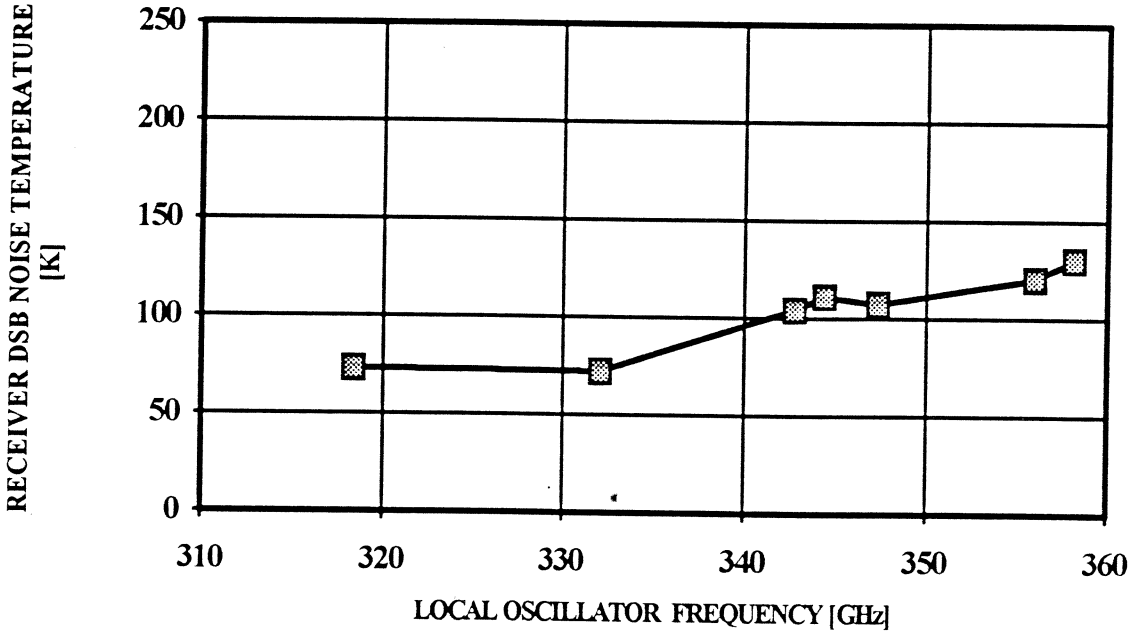

Fig. 13 Fixed tuned operation of the 0;8 mm SIS mixer on the IRAM 30-m telescope.

The junctions structures developed for a fixed-tuned 0.8 mm mixer have been provided to MPIFR (Bonn) and tested in their tunaeble two-backshort mixer being prepared for the

SMT (Arizona). Measured receiver noise temperature is close to 120 K over all the 320-370 GHz band.

CONCLUSION

The fixed tuned and tuneable SIS mixers for radioastronomy in 0.8 mm and 1.3 mm bands are developed. The receivers with this mixers are in use on the radiotelescopes. Receiver DSB noise temperature as low as 55 K and 72 K have been achieved in 1.3 mm and 0.8 mm bands.

The developed fixed tuned mixers may be used in futures multibeam arrays receivers.

REFERENCES

1. A. R. Kerr, S. -K. Pan, S. Whiteley, M. Radparvar, S.Faris, IEEE MTT-S Digest, 1990, 851-854

2. T. H. Buttgenbach, H. G. LeDuc, P. D Maker and T. G. Phillips, IEE Trans. Appl. Superconductivity, September 1992

3. D. Winkler, N. G. Ugras, A. H. Worsman, D. E. Prober, N. R. Erikson, P. F. Goldsmith, IEEE Transactions on Magnetics, 1991, v 27, N2, 2634-2637

4. A. Karpov, M. Carter, B. Lazareff, D. Billon-Pierron, K. H. Gundlach , in Proceedings of the Third International Symposium on Space Terahertz Technology, Ann Arbor, Michigan, March 24-26, 1992, p244-250

5. A. R. Kerr, S. -K. Pan Some recent development in the design of SIS mixers, International Journal of Infrared and Millimeter Waves, 1990, **11**, 10, 1169-1187

6. J. R. Tucker, M. J. Feldman, Quantum detection on millimeter wavelength, Rev. Mod. Phys. 1985, 57, 1055-1113

7. A. K. Kerr, S. -K. Pan, S. Withngton, Embedding impedance approximation in the analysis of SIS mixers, Proceedings of Third international Symposium on Space Terahertz Technology, 1992, Ann Arbor ,Michigan, p394-407.

8. Qing Ke, M. J. Feldman Source conductance for high frequency superconducting quasiparical receivers, Proceedings of Third international Symposium on Space Terahertz Technology, 1992, Ann Arbor ,Michigan, p538-547

9. A. Castets and all, Astron. Astrophys. 194, 340-343 (1988)

10. R. Blundel, M. Carter, K. H. Gundlach, Int. J. of Infrared and Millimetre Waves, 1988, N8, 361

11. E.-J. Blum A cryostat for radioastronomy receivers using superconducting mixers at millimeter wavelengths , Advances in Cryogenic Engineering, 1985, **31**